

به نام خدا



# مرکز دانلود رایگان مهندسی متالورژی و مواد

[www.Iran-mavad.com](http://www.Iran-mavad.com)



C. N. R. Rao, A. Müller,  
A. K. Cheetham (Eds.)  
**The Chemistry of  
Nanomaterials**

*The Chemistry of Nanomaterials: Synthesis, Properties and Applications.* Edited by C. N. R. Rao,  
A. Müller, A. K. Cheetham  
Copyright © 2004 WILEY-VCH Verlag GmbH & Co. KGaA, Weinheim  
ISBN: 3-527-30686-2

[www.Iran-mavad.com](http://www.Iran-mavad.com)

مرجع دانشجویان و مهندسين مواد

## ***Further Titles of Interest***

G. Schmid (Ed.)

### **Nanoparticles**

**From Theory to Application**

2004

ISBN 3-527-30507-6

V. Balzani, A. Credi, M. Venturi

### **Molecular Devices and Machines**

**A Journey into the Nanoworld**

2003

ISBN 3-527-30506-8

M. Driess, H. Nöth (Eds.)

### **Molecular Clusters of the Main Group Elements**

2004

ISBN 3-527-30654-4

G. Hodes (Ed.)

### **Electrochemistry of Nanomaterials**

2001

ISBN 3-527-29836-3

U. Schubert, N. Hüsing

### **Synthesis of Inorganic Materials**

2000

ISBN 3-527-29550-X

*C. N. R. Rao, A. Müller, A. K. Cheetham (Eds.)*

# **The Chemistry of Nanomaterials**

Synthesis, Properties and Applications in 2 Volumes

Volume 1



WILEY-VCH Verlag GmbH & Co. KGaA

[www.iran-mavad.com](http://www.iran-mavad.com)

مرجع دانشجویان و مهندسين مواد



**Prof. Dr. C. N. R. Rao**

CSIR Centre of Excellence in Chemistry  
and Chemistry and Physics of Materials  
Unit  
Jawaharlal Nehru Centre for Advanced  
Scientific Research  
Jakkur P.O.  
Bangalore – 560 064  
India

**Prof. Dr. h.c. mult. Achim Müller**

Faculty of Chemistry  
University of Bielefeld  
Postfach 10 01 31  
D-33501 Bielefeld  
Germany

**Prof. Dr. A. K. Cheetham**

Director  
Materials Research Laboratory  
University of California, Santa Barbara  
Santa Barbara, CA 93106  
USA

This book was carefully produced.  
Nevertheless, authors, editors and publisher  
do not warrant the information contained  
therein to be free of errors. Readers are  
advised to keep in mind that statements,  
data, illustrations, procedural details or  
other items may inadvertently be  
inaccurate.

**Library of Congress Card No.: applied for**

A catalogue record for this book is available  
from the British Library.

Bibliographic information published by Die  
Deutsche Bibliothek

Die Deutsche Bibliothek lists this  
publication in the Deutsche National-  
bibliografie; detailed bibliographic data is  
available in the Internet at <http://dnb.ddb.de>

© 2004 WILEY-VCH Verlag GmbH & Co.  
KgaA, Weinheim

All rights reserved (including those of  
translation in other languages). No part of  
this book may be reproduced in any form –  
by photoprinting, microfilm, or any other  
means – nor transmitted or translated into  
machine language without written  
permission from the publishers. Registered  
names, trademarks, etc. used in this book,  
even when not specifically marked as such,  
are not to be considered unprotected by law.

Printed in the Federal Republic of  
Germany.

Printed on acid-free paper.

**Composition** Asco Typesetters, Hong Kong

**Printing** betz-druck gmbh, Darmstadt

**Bookbinding** J. Schäffer GmbH & Co. KG,  
Grünstadt

**ISBN** 3-527-30686-2

## Contents

**Preface**    *xvi*

**List of Contributors**    *xviii*

### Volume 1

<b>1</b>	<b>Nanomaterials – An Introduction</b>	<b>1</b>
	<i>C. N. R. Rao, A. Müller, and A. K. Cheetham</i>	
1.1	Size Effects	3
1.2	Synthesis and Assembly	4
1.3	Techniques	5
1.4	Applications and Technology Development	8
1.5	Nanoelectronics	8
1.6	Other Aspects	9
1.7	Concluding Remarks	11
	Bibliography	11
<b>2</b>	<b>Strategies for the Scalable Synthesis of Quantum Dots and Related Nanodimensional Materials</b>	<b>12</b>
	<i>P. O'Brien and N. Pickett</i>	
2.1	Introduction	12
2.2	Defining Nanodimensional Materials	13
2.3	Potential Uses for Nanodimensional Materials	15
2.4	The General Methods Available for the Synthesis of Nanodimensional Materials	17
2.4.1	Precipitative Methods	19
2.4.2	Reactive Methods in High Boiling Point Solvents	20
2.4.3	Hydrothermal and Solvothermal Methods	22
2.4.4	Gas-Phase Synthesis of Semiconductor Nanoparticles	23
2.4.5	Synthesis in a Structured Medium	24
2.5	The Suitability of Such Methods for Scaling	25
2.6	Conclusions and Perspectives on the Future	26
	Acknowledgements	27
	References	27

<b>3</b>	<b>Moving Nanoparticles Around: Phase-Transfer Processes in Nanomaterials Synthesis</b>	<b>31</b>
	<i>M. Sastry</i>	
3.1	Introduction	31
3.2	Water-Based Gold Nanoparticle Synthesis	33
3.2.1	Advantages	33
3.2.2	Disadvantages	33
3.3	Organic Solution-Based Synthesis of Gold Nanoparticles	33
3.3.1	Advantages	33
3.3.2	Disadvantages	34
3.4	Moving Gold Nanoparticles Around	34
3.4.1	Phase Transfer of Aqueous Gold Nanoparticles to Non-Polar Organic Solvents	34
3.4.2	Transfer of Organically Soluble Gold Nanoparticles to Water	43
	Acknowledgments	48
	References	49
<b>4</b>	<b>Mesoscopic Assembly and Other Properties of Metal and Semiconductor Nanocrystals</b>	<b>51</b>
	<i>G. U. Kulkarni, P. J. Thomas, and C. N. R. Rao</i>	
	Abstract	51
4.1	Introduction	51
4.2	Synthetic Strategies	53
4.2.1	General Methods	53
4.2.2	Size Control	55
4.2.3	Shape Control	57
4.2.4	Tailoring the Ligand Shell	58
4.3	Programmed Assemblies	61
4.3.1	One-Dimensional Arrangements	61
4.3.2	Two-Dimensional Arrays	62
4.3.2.1	Arrays of Metal Nanocrystals	63
4.3.2.2	Arrays of Semiconductor Nanocrystals	65
4.3.2.3	Arrays of Oxide Nanocrystals	66
4.3.2.4	Other Two-Dimensional Arrangements	68
4.3.2.5	Stability and Phase Behaviour of Two-Dimensional Arrays	68
4.3.3	Three-Dimensional Superlattices	71
4.3.4	Superclusters	73
4.3.5	Colloidal Crystals	75
4.3.6	Nanocrystal Patterning	75
4.4	Emerging Applications	77
4.4.1	Isolated Nanocrystals	78
4.4.2	Collective Properties	82
4.4.3	Nanocomputing	86
4.5	Conclusions	86
	References	88

<b>5</b>	<b>Oxide Nanoparticles</b>	<b>94</b>
	<i>R. Seshadri</i>	
	Abstract	94
5.1	Introduction	94
5.2	Magnetite Particles in Nature	96
5.3	Routes for the Preparation of Isolated Oxide Nanoparticles	98
5.3.1	Hydrolysis	98
5.3.2	Oxidation	101
5.3.3	Thermolysis	102
5.3.4	Metathesis	103
5.3.5	Solvothermal Methods	105
5.3.5.1	Oxidation	105
5.3.5.2	Hydrolysis	105
5.3.5.3	Thermolysis	106
5.4	Prospects	108
	Acknowledgments	110
	References	110
<b>6</b>	<b>Sonochemistry and Other Novel Methods Developed for the Synthesis of Nanoparticles</b>	<b>113</b>
	<i>Y. Mastai and A. Gedanken</i>	
	Abstract	113
6.1	Sonochemistry	113
6.1.1	Sonochemical Fabrication of Nanometals	116
6.1.1.1	Sonochemical Synthesis of Powders of Metallic Nanoparticles	116
6.1.1.2	Sonochemical Synthesis of Metallic Colloids	118
6.1.1.3	Sonochemical Synthesis of Metallic Alloys	120
6.1.1.4	Sonochemical Deposition of Nanoparticles on Spherical and Flat Surfaces	121
6.1.1.5	Sonochemical Synthesis of a Polymer-Metal Composite	124
6.1.1.6	Sonochemical Synthesis of Nanometals Encapsulated in a Carbon Matrix	127
6.1.2	Sonochemical Fabrication of Nano-Metallic Oxides	129
6.1.2.1	Sonochemical Synthesis of Transition Metal Oxides from the Corresponding Carbonyls	129
6.1.2.2	Sonochemical Synthesis of Ferrites from the Corresponding Carbonyls	131
6.1.2.3	Sonochemical Preparation of Nanosized Rare-Earth Oxides	133
6.1.2.4	The Sonochemical Synthesis of Nanosized Rare-Earth Oxides	134
6.1.2.5	The Sonochemical Synthesis of Nanostructured SnO <sub>2</sub> and SnO as their Use as Electrode Materials	136
6.1.2.6	The Sonochemical Synthesis of Mesoporous Materials and the Insertion of Nanoparticles into the Mesopores by Ultrasound Radiation	137
6.1.2.7	The Sonochemical Synthesis of Mixed Oxides	143
6.1.2.8	The Sonochemical Synthesis of Nanosized Hydroxides	143

6.1.2.9	Sonochemical Preparation of Nanosized Titania	144
6.1.2.10	The Sonochemical Preparation of Other Oxides	145
6.1.2.11	Sonochemical Synthesis of Other Nanomaterials	147
6.2	Sonoelectrochemistry	148
6.2.1	Sonoelectrochemical Synthesis of Nanocrystalline Materials	149
6.3	Microwave Heating	152
6.3.1	Microwave Synthesis of Nanomaterials	155
6.3.1.1	Microwave Synthesis of Nanometallic Particles	155
6.3.1.2	The Synthesis of Nanoparticles of Metal Oxides by MWH	157
	Acknowledgements	163
	References	164
<b>7</b>	<b>Solvothermal Synthesis of Non-Oxide Nanomaterials</b>	<b>170</b>
	<i>Y. T. Qian, Y. L. Gu, and J. Lu</i>	
7.1	Introduction	170
7.2	Solvothermal Synthesis of III–V Nanomaterials	175
7.3	Synthesis of Diamond, Carbon Nanotubes and Carbides	181
7.4	Synthesis of $\text{Si}_3\text{N}_4$ , $\text{P}_3\text{N}_5$ , Metal Nitrides and Phosphides	186
7.5	Synthesis of BN, $\text{B}_4\text{C}$ , BP and Borides	189
7.6	Synthesis of One-Dimensional Metal Chalcogenide Nanocrystallites	193
7.7	Room Temperature Synthesis of Nanomaterials	198
	References	204
<b>8</b>	<b>Nanotubes and Nanowires</b>	<b>208</b>
	<i>A. Govindaraj and C. N. R. Rao</i>	
	Abstract	208
8.1	Introduction	208
8.2	Carbon Nanotubes	210
8.2.1	Synthesis	210
8.2.1.1	Multi-Walled Nanotubes	210
8.2.1.2	Aligned Carbon Nanotube Bundles	212
8.2.1.3	Single-Walled Carbon Nanotubes	214
8.2.2	Structure and Characterization	217
8.2.3	Mechanism of Formation	222
8.2.4	Chemically Modified Carbon Nanotubes	224
8.2.4.1	Doping with Boron and Nitrogen	224
8.2.4.2	Opening, Filling and Functionalizing Nanotubes	225
8.2.5	Electronic Structure, Properties and Devices	227
8.2.5.1	Electronic Structure and Properties	227
8.2.5.2	Electronic and Electrochemical Devices	228
8.3	Inorganic Nanotubes	239
8.3.1	Preliminaries	239
8.3.2	General Synthetic Strategies	244
8.3.3	Structures	246
8.3.4	Useful Properties of Inorganic Nanotubes	253

8.4	Nanowires	255
8.4.1	Preliminaries	255
8.4.2	Synthetic Strategies	255
8.4.2.1	Vapor Phase Growth of Nanowires	256
8.4.2.2	Other Processes in the Gas Phase	262
8.4.2.3	Solution-Based Growth of Nanowires	265
8.4.2.4	Growth Control	273
8.4.3	Properties of Nanowires	274
	References	275
<b>9</b>	<b>Synthesis, Assembly and Reactivity of Metallic Nanorods</b>	<b>285</b>
	<i>C. J. Murphy, N. R. Jana, L. A. Gearheart, S. O. Obare, K. K. Caswell, S. Mann, C. J. Johnson, S. A. Davis, E. Dujardin, and K. J. Edler</i>	
9.1	Introduction	285
9.2	Seed-Mediated Growth Approach to the Synthesis of Inorganic Nanorods and Nanowires	287
9.3	Assembly of Metallic Nanorods: Self-Assembly vs. Designed Chemical Linkages	293
9.4	Reactivity of Metallic Nanoparticles Depends on Aspect Ratio	299
9.5	Conclusions and Future Prospects	304
	Acknowledgements	306
	References	306
<b>10</b>	<b>Oxide-Assisted Growth of Silicon and Related Nanowires: Growth Mechanism, Structure and Properties</b>	<b>308</b>
	<i>S. T. Lee, R. Q. Zhang, and Y. Lifshitz</i>	
	Abstract	308
10.1	Introduction	309
10.2	Oxide-Assisted Nanowire Growth	311
10.2.1	Discovery of Oxide-Assisted Growth	311
10.2.2	Oxide-Assisted Nucleation Mechanism	314
10.2.3	Oxide-Assisted Growth Mechanism	316
10.2.4	Comparison between Metal Catalyst VLS Growth and OAG	317
10.3	Control of SiNW Nanostructures in OAG	319
10.3.1	Morphology Control by Substrate Temperature	319
10.3.2	Diameter Control of Nanowires	326
10.3.3	Large-Area Aligned and Long SiNWs via Flow Control	328
10.3.4	Si Nanoribbons	330
10.4	Nanowires of Si Compounds by Multistep Oxide-Assisted Synthesis	332
10.4.1	Nanocables	332
10.4.2	Metal Silicide/SiNWs from Metal Vapor Vacuum Arc Implantation	333
10.4.3	Synthesis of Oriented SiC Nanowires	334
10.5	Implementation of OAG to Different Semiconducting Materials	335
10.6	Chemical Properties of SiNWs	340
10.6.1	Stability of H-Terminated SiNW Surfaces	340

10.6.2	Reduction of Metals in Liquid Solutions	343
10.6.3	Chemical Sensing of SiNWs	345
10.6.4	Use of SiNWs as Templates for Nanomaterial Growth	346
10.7	Optical and Electrical Properties of SiNWs	347
10.7.1	Raman and PL of SiNWs	347
10.7.2	Field Emission from Different Si-Based Nanostructures	350
10.7.3	STM and STS Measurements of SiNWs and B-Doped SiNWs	351
10.7.4	Periodic Array of SiNW Heterojunctions	356
10.8	Modeling	359
10.8.1	High Reactivity of Silicon Suboxide Vapor	359
10.8.2	Thermal and Chemical Stabilities of Pure Silicon Nanostructured Materials	360
10.8.2.1	Structural Transition in Silicon Nanostructures	360
10.8.2.2	Thinnest Stable Short Silicon Nanowires	361
10.8.2.3	Silicon Nanotubes	361
10.8.3	Thermal and Chemical Stabilities of Hydrogenated Silicon Nanostructures	363
10.8.3.1	Structural Properties of Hydrogenated Silicon Nanocrystals and Nanoclusters	363
10.8.3.2	Size-Dependent Oxidation of Hydrogenated Silicon Clusters	365
10.9	Summary	365
	Acknowledgement	368
	References	369

## Volume 2

11	<b>Electronic Structure and Spectroscopy of Semiconductor Nanocrystals</b>	371
	<i>S. Sapra and D. D. Sarma</i>	
11.1	Introduction	371
11.2	Structural Transformations	372
11.3	Ultraviolet–Visible Absorption Spectroscopy	374
11.4	Fluorescence Spectroscopy	377
11.5	Electronic Structure Calculations	383
11.5.1	Effective Mass Approximation	384
11.5.2	Empirical Pseudopotential Method	385
11.5.3	Tight-Binding Method	387
11.6	Photoemission Studies	394
11.6.1	Core Level Photoemission	395
11.6.2	Valence Band Photoemission	399
11.7	Concluding Remarks	401
	References	402
12	<b>Core–Shell Semiconductor Nanocrystals for Biological Labeling</b>	405
	<i>R. E. Bailey and S. Nie</i>	
12.1	Introduction	405

12.2	Optical Properties	405
12.3	Synthesis	408
12.4	Surface Modification and Bioconjugation	410
12.5	Applications	413
	Acknowledgement	416
	References	416
<b>13</b>	<b>Large Semiconductor Molecules</b>	<b>418</b>
	<i>J. F. Corrigan and M. W. DeGroot</i>	
13.1	Introduction	418
13.2	Nickel Chalcogenides	419
13.3	Group XI Chalcogenides	423
13.3.1	Copper Sulfide and Copper Selenide Nanoclusters	424
13.3.1.1	Layered $\text{Cu}_2\text{Se}$	424
13.3.1.2	Spherical $\text{Cu}_2\text{E}$	426
13.3.2	$\text{Cu}_{2-x}\text{Te}$ and $\text{Ag}_2\text{Te}$	430
13.3.3	$\text{Ag}_2\text{S}$	433
13.3.4	$\text{Ag}_2\text{Se}$	436
13.4	Group XII-chalcogenides and the Quantum Confinement Effect	438
13.4.1	$\text{CdS}$	438
13.5	Ternary $\text{MM}'\text{E}$	444
13.6	Metal Pnictides from $\text{E}(\text{SiMe}_3)_3$ Reagents	446
13.7	Conclusions and Outlook	447
	References	448
<b>14</b>	<b>Oxomolybdates: From Structures to Functions in a New Era of Nanochemistry</b>	<b>452</b>
	<i>A. Müller and S. Roy</i>	
	Abstract	452
14.1	Introduction: Similarities between Nanotechnology in Nature and Chemistry?	452
14.2	Sizes, Shapes, and Complexity of Nano-objects are Determined by the Nature and Variety of the Constituent Building Blocks	453
14.3	Nanoscaled Clusters with Unusual Form–Function Relationships	457
14.4	Perspectives for Materials Science and Nanotechnology: En Route to Spherical-Surface, Nanoporous-Cluster, and Super-Supramolecular Chemistry Including the Option of Modelling Cell Response	465
	Acknowledgments	473
	References	473
<b>15</b>	<b>Nanostructured Polymers</b>	<b>476</b>
	<i>S. Ramakrishnan</i>	
	Abstract	476
15.1	Introduction	476
15.2	Macromolecular Structural Control	477



15.2.1	Living Polymerization	478
15.3	Polymer Conformational Control	480
15.4	Morphology of Block Copolymers	484
15.5	Nanostructures Based on Bulk Phase Separation	486
15.6	Nanostructures Based on Lyotropic Mesophases	493
15.6.1	Core-Crosslinked Systems	495
15.6.2	Shell-Crosslinked Systems	497
15.6.3	Nanocages	500
15.7	Rod-Coil Diblock Copolymers	502
15.8	Nanostructures from Polymerized Surfactant Assemblies	507
15.9	Summary and Outlook	513
	Acknowledgements	514
	References	515
<b>16</b>	<b>Recent Developments in the Chemistry and Chemical Applications of Porous Silicon</b>	<b>518</b>
	<i>J. M. Schmeltzer and J. M. Buriak</i>	
16.1	Introduction	518
16.2	Preparation and Characterization of Porous Silicon Substrates	518
16.3	Surface Chemistry of Porous Silicon Surfaces	522
16.4	Chemical Applications Based on Porous Silicon	527
16.4.1	Bioactive Porous Silicon	527
16.4.2	Micro Enzyme Reactors ( $\mu$ IMERS) and Total Analysis Systems ( $\mu$ TAS)	531
16.4.3	Porous Silicon Sensors	532
16.4.4	Explosive Porous Silicon	539
16.4.5	Desorption/Ionization on Silicon Mass Spectrometry (DIOS-MS)	540
16.5	Conclusion	546
	Acknowledgments	547
	References	547
<b>17</b>	<b>Nanocatalysis</b>	<b>551</b>
	<i>S. Abbet and U. Heiz</i>	
17.1	Introduction	551
17.2	Chemical Reactions on Point Defects of Oxide Surfaces	552
17.3	Chemical Reactions and Catalytic Processes on Free and Supported Clusters	555
17.3.1	Catalytic Processes on Free Metal Clusters	555
17.3.2	Chemical Reactions and Catalytic Cycles on Supported Clusters	562
17.3.2.1	Single Atoms on Oxide Surfaces	562
17.3.2.2	Size-Selected Clusters on Oxide Surfaces	566
17.3.3	Turn-Over Frequencies of Catalytic Reactions on Supported Clusters	578
17.3.3.1	A Newly Designed Pulsed Valve for Molecular Beam Experiments	578
17.3.3.2	Size-Distributed Clusters on Oxide Surfaces	580
17.4	Chemical Reactions Induced by Confined Electrons	582

17.5	Conclusions	586
	Acknowledgements	586
	References	586
<b>18</b>	<b>Nanoporous Materials</b>	<b>589</b>
	<i>A. K. Cheetham and P. M. Forster</i>	
18.1	Introduction	589
18.2	Stability of Open-Framework Materials	590
18.3	Aluminosilicate Zeolites	591
18.4	Open-Framework Metal Phosphates	595
18.4.1	Aluminum Phosphates	595
18.4.2	Phosphates of Gallium and Indium	598
18.4.3	Tin(II) Phosphates and Antimony(III) Phosphates	599
18.4.4	Transition Metal Phosphates	600
18.4.4.1	Molybdenum and Vanadium Phosphates	600
18.4.4.2	Iron Phosphates	601
18.4.4.3	Cobalt(II) and Manganese Phosphates	603
18.4.4.4	Copper and Nickel Phosphates	603
18.4.4.5	Zirconium and Titanium Phosphates	605
18.5	Chalcogenides, Halides, Nitrides and Oxides	606
18.5.1	Sulfides and Selenides	606
18.5.2	Halides	607
18.5.3	Nitrides	607
18.5.4	Binary Metal Oxides	607
18.5.5	Sulfates	608
18.6	Hybrid Nanoporous Materials	608
18.6.1	Coordination Polymers	609
18.6.2	Hybrid Metal Oxides	612
18.7	Conclusions	614
	References	616
<b>19</b>	<b>Photochemistry and Electrochemistry of Nanoassemblies</b>	<b>620</b>
	<i>P. V. Kamat</i>	
19.1	Metal and Semiconductor Nanostructures	620
19.2	Photoinduced Charge Transfer Processes in Semiconductor Nanoparticle Systems	620
19.3	Photoinduced Transformations of Metal Nanoparticles	622
19.3.1	Transient Bleaching of the Surface Plasmon Band	623
19.3.2	Laser Induced Fusion and Fragmentation of Metal Nanoclusters	624
19.3.3	Photoinduced Energy and Electron Transfer Process between Excited Sensitizer and Metal Nanocore	625
19.4	Electrochemistry of Semiconductor Nanostructures	627
19.4.1	Nanostructured Metal Oxide Films	627
19.4.2	Nanostructured Oxide Films Modified with Dyes and Redox Chromophores	628

19.4.3	Photocurrent Generation	630
19.5	Electrochemistry of Metal Nanostructures	631
19.6	Semiconductor–Metal Nanocomposites	632
19.6.1	Improving the Efficiency of Photocatalytic Transformations	633
19.6.2	Fermi Level Equilibration	634
19.7	Concluding Remarks	635
	Acknowledgement	636
	References	636
<b>20</b>	<b>Electrochemistry with Nanoparticles</b>	<b>646</b>
	<i>S. Devarajan and S. Sampath</i>	
	Outline	646
20.1	Introduction	646
20.2	Preparation of Nanostructures	647
20.3	Electrochemistry with Metallic Nanoparticles	649
20.3.1	Monolayer-Protected Nanoclusters	651
20.3.2	Nanoelectrode Ensembles	653
20.4	Single Electron Events	657
20.5	Probing Nanoparticles using Electrochemistry Coupled with Spectroscopy	664
20.6	Nanosensors	670
20.6.1	Biosensors	670
20.6.2	Chemical Sensors	674
20.7	Electrocatalysis	678
20.8	Summary and Perspectives	680
	Acknowledgement	681
	References	681
<b>21</b>	<b>Nanolithography and Nanomanipulation</b>	<b>688</b>
	<i>A. K. Raychaudhuri</i>	
	Abstract	688
21.1	Introduction	688
21.2	Template Fabrication	690
21.2.1	Polycarbonate Etched Track Templates	691
21.2.2	Fabrication of Anodized Alumina Membrane	693
21.2.3	Anodized Alumina Membrane as a Mask for Physical Vapor Deposition	695
21.2.4	Templates Made in Block Copolymers	696
21.3	Fabrication of Nanostructures in the Templates	697
21.3.1	Electrodeposition	698
21.3.2	Sol–Gel Method	702
21.3.3	CVD Method	704
21.4	Scanning Probe Based Anodic Oxidation as a Tool for the Fabrication of Nanostructures	706
21.4.1	Oxidation of Metallic Substrates	709

21.4.2	Oxidation of Semiconducting Substrates	710
21.5	Use of Scanning Probe Microscopy in Dip Pen Nanolithography	712
21.6	Use of Scanning Probe Microscopy in Nanomanipulation	716
21.7	Nano-Electromechanical Systems	718
	Acknowledgements	720
	References	720
	<b>Index</b>	<b>724</b>

## Preface

Nanomaterials, characterized by at least one dimension in the nanometer range, can be considered to constitute a bridge between single molecules and infinite bulk systems. Besides individual nanostructures involving clusters, nanoparticles, quantum dots, nanowires and nanotubes, collections of these nanostructures in the form of arrays and superlattices are of vital interest to the science and technology of nanomaterials. The structure and properties of nanomaterials differ significantly from those of atoms and molecules as well as those of bulk materials. Synthesis, structure, energetics, response, dynamics and a variety of other properties and related applications form the theme of the emerging area of nanoscience, and there is a large chemical component in each of these aspects. Chemistry plays a particularly important role in the synthesis and characterization of nanobuilding units such as nanocrystals of metals, oxides and semiconductors, nanoparticles and composites involving ceramics, nanotubes of carbon and inorganics, nanowires of various materials and polymers involving dendrimers and block copolymers. Assembling these units into arrays also involves chemistry. In addition, new chemistry making use of these nanounits is making great progress. Electrochemistry and photochemistry using nanoparticles and nanowires, and nanocatalysis are examples of such new chemistry. Nanoporous solids have been attracting increasing attention in the last few years. Although the area of nanoscience is young, it seems likely that new devices and technologies will emerge in the near future. This book is intended to bring together the various experimental aspects of nanoscience of interest to chemists and to show how the subject works.

The book starts with a brief introduction to nanomaterials followed by chapters dealing with the synthesis, structure and properties of various types of nanostructures. There are chapters devoted to oxomolybdates, porous silicon, polymers, electrochemistry, photochemistry, nanoporous solids and nanocatalysis. Nanomanipulation and lithography are covered in a separate chapter. In our attempt to make each contribution complete in itself, there is some unavoidable overlap amongst the chapters. Some chapters cover entire areas, while others expound on a single material or a technique. Our gratitude goes to S. Roy for his valuable support in preparing the index manuscript.

We trust that beginners, teachers and practitioners of the subject will find the

book useful and instructive. The book could profitably be used as the basis of a university course in the subject.

C. N. R. Rao  
A. Müller  
A. K. Cheetham

## List of Contributors

**S. Abbet**

University of Ulm  
Institute of Surface Science and Catalysis  
Albert-Einstein-Alle 47  
D-89069 Ulm  
Germany

**R. E. Bailey**

Departments of Biomedical Engineering and  
Chemistry  
Georgia Institute of Technology and Emory  
University  
1639 Pierce Drive, Suite 2001  
Atlanta, GA 30322  
USA

**J. M. Buriak**

National Institute of Nanotechnology  
University of Alberta  
Edmonton, AB  
T6G 2V4  
Canada

**K. K. Caswell**

Department of Chemistry and Biochemistry  
University of South Carolina  
Columbia, SC 29208  
USA

**A. K. Cheetham**

Materials Research Laboratory  
University of California, Santa Barbara  
CA 93106-5121  
USA

**J. F. Corrigan**

Department of Chemistry  
University of Western Ontario  
London, Ontario  
Canada

**S. A. Davis**

Department of Chemistry  
University of Bristol  
Bristol, BS8 1TS  
UK

**M. W. DeGroot**

Department of Chemistry  
University of Western Ontario  
London, Ontario  
Canada

**S. Devarajan**

Department of Inorganic and Physical  
Chemistry  
Indian Institute of Science  
Bangalore 560 012  
India

**E. Dujardin**

Department of Chemistry  
University of Bristol  
Bristol, BS8 1TS  
UK

**K. J. Edler**

Department of Chemistry  
University of Bath  
Bath BA2 7 AY  
UK

**P. M. Forster**

Materials Research Laboratory  
University of California, Santa Barbara  
CA 93106-5121  
USA

**L. A. Gearheart**

Department of Chemistry and Biochemistry  
University of South Carolina  
Columbia, SC 29208  
USA

**A. Gedanken**

Department of Chemistry  
Bar-Ilan University, Ramat-Gan  
Israel, 52900

**A. Govindaraj**

Chemistry and Physics of Materials Unit and  
CSIR Centre of Excellence in Chemistry  
Jawaharlal Nehru Centre for Advanced  
Scientific Research  
Jakkur P.O.  
Bangalore 560 064  
India

**Y. L. Gu**

Department of Chemistry  
University of Science and Technology of China  
Hefei, Anhui 230026  
P.R. China

**U. Heiz**

University of Ulm  
Institute of Surface Science and Catalysis  
Albert-Einstein-Alle 47  
D-89069 Ulm  
Germany

**N. R. Jana**

Department of Chemistry and Biochemistry  
University of South Carolina  
Columbia, SC 29208  
USA

**C. J. Johnson**

Department of Chemistry  
University of Bristol  
Bristol BS8 1TS  
UK

**P. V. Kamat**

Notre Dame Radiation Laboratory, Notre  
Dame  
Indiana 46556-0579  
USA

**G. U. Kulkarni**

Chemistry and Physics of Materials Unit  
Jawaharlal Nehru Centre for Advanced  
Scientific Research  
Jakkur P.O.  
Bangalore 560 064  
India

**S. T. Lee**

Center Of Super-Diamond and Advanced  
Films (COSDAF) & Department of Physics  
and Materials Science  
City University of Hong Kong

Hong Kong SAR  
China

**Y. Lifshitz**

Center Of Super-Diamond and Advanced  
Films (COSDAF) & Department of Physics  
and Materials Science  
City University of Hong Kong  
Hong Kong SAR  
China

**J. Lu**

Department of Chemistry  
University of Science and Technology of China  
Hefei, Anhui 230026  
P.R. China

**S. Mann**

Department of Chemistry  
University of Bristol  
Bristol, BS8 1TS  
UK

**Y. Mastai**

Department of Chemistry  
Bar-Ilan University, Ramat-Gan  
Israel, 52900

**A. Müller**

Faculty of Chemistry  
University of Bielefeld  
Postfach 100131  
D-33501 Bielefeld  
Germany

**C. J. Murphy**

Department of Chemistry and Biochemistry  
University of South Carolina  
Columbia, SC 29208  
USA

**S. Nie**

Departments of Biomedical Engineering and  
Chemistry  
Georgia Institute of Technology and Emory  
University  
1639 Pierce Drive, Suite 2001,  
Atlanta, GA 30322  
USA

**S. O. Obare**

Department of Chemistry and Biochemistry  
University of South Carolina  
Columbia, SC 29208  
USA

**P. O'Brien**

The Manchester Materials Science Centre and  
the Chemistry Department



The University of Manchester  
Oxford Road  
Manchester, M139PL  
UK

**N. Pickett**  
Nano Co Ltd.  
48 Grafton Street  
Manchester, M139XX  
UK

**Y. T. Qian**  
Structure Research Laboratory and  
Department of Chemistry  
University of Science and Technology of China  
Hefei, Anhui 230026  
P.R. China

**C. N. R. Rao**  
Chemistry and Physics of Materials Unit and  
CSIR Centre of Excellence in Chemistry  
Jawaharlal Nehru Centre for Advanced  
Scientific Research  
Jakkur P.O.  
Bangalore 560 064  
India

**S. Ramakrishnan**  
Department of Inorganic and Physical  
Chemistry  
Indian Institute of Science  
Bangalore 560012  
India

**A. K. Raychaudhuri**  
Department of Physics  
Indian Institute of Science  
Bangalore-560012  
India

**S. Roy**  
Faculty of Chemistry  
University of Bielefeld  
Postfach 100131  
D-33501 Bielefeld  
Germany

**S. Sampath**  
Department of Inorganic and Physical  
Chemistry  
Indian Institute of Science  
Bangalore 560 012  
India

**S. Sapra**  
Solid State and Structural Chemistry Unit  
Indian Institute of Science  
Bangalore-560012  
India

**D. D. Sarma**  
Solid State and Structural Chemistry Unit  
and Centre for Condensed Matter Theory,  
Indian  
Institute of Science Bangalore-560012  
India  
and  
Jawaharlal Nehru Centre for Advanced  
Scientific Research  
Jakkur  
Bangalore-560064  
India

**M. Sastry**  
Materials Chemistry Division  
National Chemical Laboratory  
Pune – 411 008  
India

**J. M. Schmeltzer**  
Department of Chemistry  
Purdue University  
560 Oval Drive  
West Lafayette, IN 47907-2084  
USA

**R. Seshadri**  
Materials Department  
University of California, Santa Barbara  
CA 93106-5050  
USA

**P. J. Thomas**  
Chemistry and Physics of Materials Unit  
Jawaharlal Nehru Centre for Advanced  
Scientific Research  
Jakkur P.O.  
Bangalore 560 064  
India

**R. Q. Zhang**  
Center Of Super-Diamond and Advanced  
Films (COSDAF) & Department of Physics  
and Materials Science  
City University of Hong Kong  
Hong Kong SAR  
China

## 1

**Nanomaterials – An Introduction**

*C. N. R. Rao, A. Müller, and A. K. Cheetham*

The term nanotechnology is employed to describe the creation and exploitation of materials with structural features in between those of atoms and bulk materials, with at least one dimension in the nanometer range ( $1 \text{ nm} = 10^{-9} \text{ m}$ ). In Table 1.1, we list typical nanomaterials of different dimensions. Properties of materials of nanometric dimensions are significantly different from those of atoms as well as those of bulk materials. Suitable control of the properties of nanometer-scale structures can lead to new science as well as new devices and technologies. The underlying theme of nanotechnology is miniaturization. The importance of nanotechnology was pointed out by Feynman as early as 1959, in his often-cited lecture entitled “There is plenty of room at the bottom”. The challenge is to beat Moore’s law, according to which the size of microelectronic devices shrinks by half every four years. This implies that by 2020, the size will be in the nm scale and we should be able to accommodate 1000 CDs in a wristwatch, as predicted by Whitesides.

There has been an explosive growth of nanoscience and technology in the last few years, primarily because of the availability of new strategies for the synthesis of nanomaterials and new tools for characterization and manipulation (Table 1.2). There are many examples to demonstrate the current achievements and paradigm shifts in this area. Scanning tunneling microscope (STM) images of quantum dots (e.g. germanium pyramid on a silicon surface) and of the quantum corral of 48 Fe atoms placed in a circle of 7.3 nm radius being familiar ones (Figure 1.1). Several methods of synthesizing nanoparticles, nanowires and nanotubes, and their assemblies, have been discovered. Thus, nanotubes and nanowires of a variety of inorganic materials have been discovered, besides those of carbon. Ordered arrays or superlattices of nanocrystals of metals and semiconductors have been prepared. Nanostructured polymers formed by the ordered self-assembly of triblock copolymers and nanostructured high-strength materials are other examples.

Besides the established techniques of electron microscopy, diffraction methods and spectroscopic tools, scanning probe microscopies have provided powerful means for studying nanostructures. Novel methods of fabrication of patterned nanostructures as well as new device and fabrication concepts are constantly being

Tab. 1.1. Examples of nanomaterials.

	<i>Size (approx.)</i>	<i>Materials</i>
Nanocrystals and clusters (quantum dots)	diam. 1–10 nm	Metals, semiconductors, magnetic materials
Other nanoparticles	diam. 1–100 nm	Ceramic oxides
Nanowires	diam. 1–100 nm	Metals, semiconductors, oxides, sulfides, nitrides
Nanotubes	diam. 1–100 nm	Carbon, layered metal chalcogenides
Nanoporous solids	pore diam. 0.5–10 nm	Zeolites, phosphates etc.
2-Dimensional arrays (of nano particles)	several nm <sup>2</sup> –μm <sup>2</sup>	Metals, semiconductors, magnetic materials
Surfaces and thin films	thickness 1–1000 nm	A variety of materials
3-Dimensional structures (superlattices)	Several nm in the three dimensions	Metals, semiconductors, magnetic materials

discovered. Nanostructures are also ideal for computer simulation and modelling, their size being sufficiently small to accommodate considerable rigor in treatment. In computations related to nanomaterials, one deals with a spatial scaling from 1 Å to 1 μm and a temporal scaling from 1 fs to 1 s, the limit of accuracy going beyond 1 kcal mol<sup>-1</sup>. Prototype circuits involving nanoparticles and nanotubes for nano-electronic devices have been fabricated. Quantum computing has made a beginning and appropriate quantum algorithms are being developed.

Let us not forget that not everything in nanoscience is new. Many existing technologies employ nanoscale processes, catalysis and photography being well-known examples. Our capability to synthesize, organize and tailor-make materials at the nanoscale is, however, of recent origin. Novel chemistry has been generated by employing nanoparticles, nanowires and other nanostructures. This includes electrochemical, photochemical, catalytic and other aspects. The immediate objectives of the science and technology of nanomaterials are: (i) to fully master the synthesis of isolated nanostructures (building blocks) and their assemblies with the desired properties, (ii) to explore and establish nanodevice concepts and systems architectures, (iii) to generate new classes of high performance materials, (iv) to connect

Tab. 1.2. Methods of synthesis and investigation of nanomaterials.

<i>Scale (approx.)</i>	<i>Synthetic Method</i>	<i>Structural Tool</i>	<i>Theory and simulation</i>
0.1 to ~10 nm	Covalent synthesis	Vibrational spectroscopy NMR Diffraction methods	Electronic structure
<1 to ~100 nm	Techniques of self-assembly	Scanning probe microscopies	Molecular dynamics and mechanics
100 nm to ~1 μm	Processing, modifications	SEM, TEM	Coarse-grained models etc.

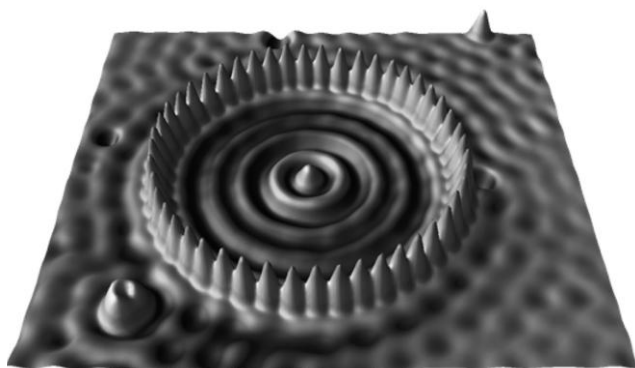


**Fig. 1.1.** STM image of a quantum corral of 48 Fe atoms placed in a circle of 7.3 nm [IBM Research].

nanoscience to molecular electronics and biology, and (v) to improve known tools while discovering better tools of investigation of nanostructures.

## 1.1

### Size Effects

Size effects constitute a fascinating aspect of nanomaterials. The effects determined by size pertain to the evolution of structural, thermodynamic, electronic, spectroscopic, electromagnetic and chemical features of these finite systems with increasing size. Size effects can be classified into two types, one dealing with specific size effects (e.g. magic numbers of atoms in metal clusters, quantum mechanical effects at small sizes) and the other involving size-scaling applicable to relatively larger nanostructures. The former includes the appearance of new features in the electronic structure. In Figure 1.2, we show how the electronic structures of metal and semiconductor nanocrystals differ from those of bulk materials and isolated atoms. In Figure 1.3, we show the size-dependence of the average energy level spacing of sodium in terms of the Kubo gap ( $E_F/N$ ) in K. In this figure, we also show the effective percentage of surface atoms as a function of particle diameter. Note that at small size, we have a high percentage of surface atoms.

Size affects the structure of nanoparticles of materials such as CdS and CdSe, and also their properties such as the melting point and the electronic absorption spectra. In Figures 1.4 and 1.5, we show such size effects graphically. It should be noted that even metals show nonmetallic band gaps when the diameter of the nanocrystals is in the 1–2 nm range. Hg clusters show a nonmetallic band gap which shrinks with increase in cluster size. It appears that around 300 atoms are necessary to close the gap. It is also noteworthy that metal particles of 1–2 nm diameter also exhibit unexpected catalytic activity, as exemplified by nanocatalysis by gold particles.

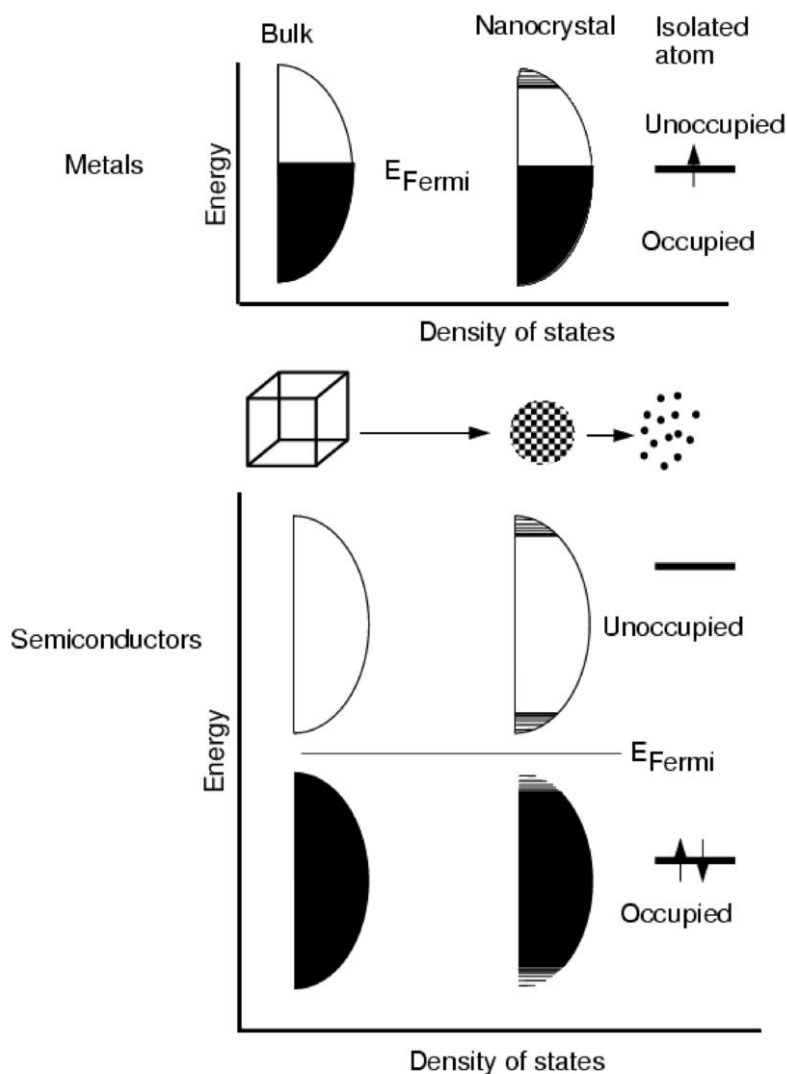


**Fig. 1.2.** Density of states for metal and semiconductor nanocrystals compared to those of the bulk and of isolated atoms [from C. N. R. Rao, G. U. Kulkarni, P. J. Thomas, P. P. Edwards, *Chem-Euro J.*, **2002**, 8, 29.].

## 1.2

### Synthesis and Assembly

The synthesis of nanomaterials and assembling the nanostructures into ordered arrays to render them functional and operational are crucial aspects of nanoscience. The materials/structures include nanoparticles, nanowires, nanotubes,

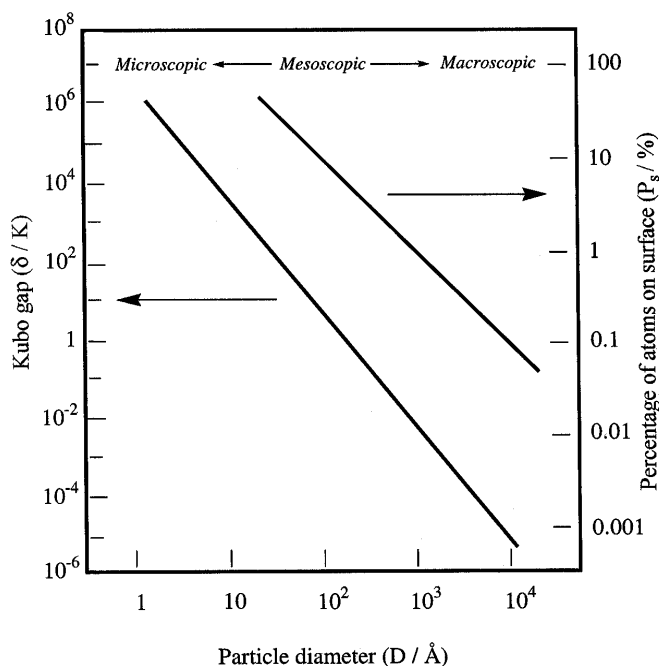


**Fig. 1.3.** A plot of the average electronic energy level spacing (Kubo gap,  $\delta$ ) of sodium as a function of the particle diameter. Also shown is the percentage of sodium atoms at

the surface as a function of particle diameter [From P. P. Edwards, R. L. Johnston and C. N. R. Rao, in *Metal Clusters in Chemistry*, ed. P. Braunstein et al., John Wiley, 1998.].

nanocapsules, nanostructured alloys and polymers, nanoporous solids and DNA chips. What is also noteworthy is that chemists have synthesized molecular entities of nanometric dimensions. In Figure 1.6, we show a two-dimensional crystalline array of thiolized metal nanocrystals to illustrate self-assembly.

### 1.3 Techniques

The emerging nanoworld encompasses entirely new and novel means of investigating structures and systems, besides exploiting the well known microscopic, diffraction and spectroscopic methods. Species as small as single atoms and molecules are manipulated and exploited as switches. Computer-controlled scanning probe microscopy enables a real-time, hands-on nanostructure manipulation. Nanomanipulators have also been designed to operate in scanning and transmission electron microscopes. A nanomanipulator gives virtual telepresence on the

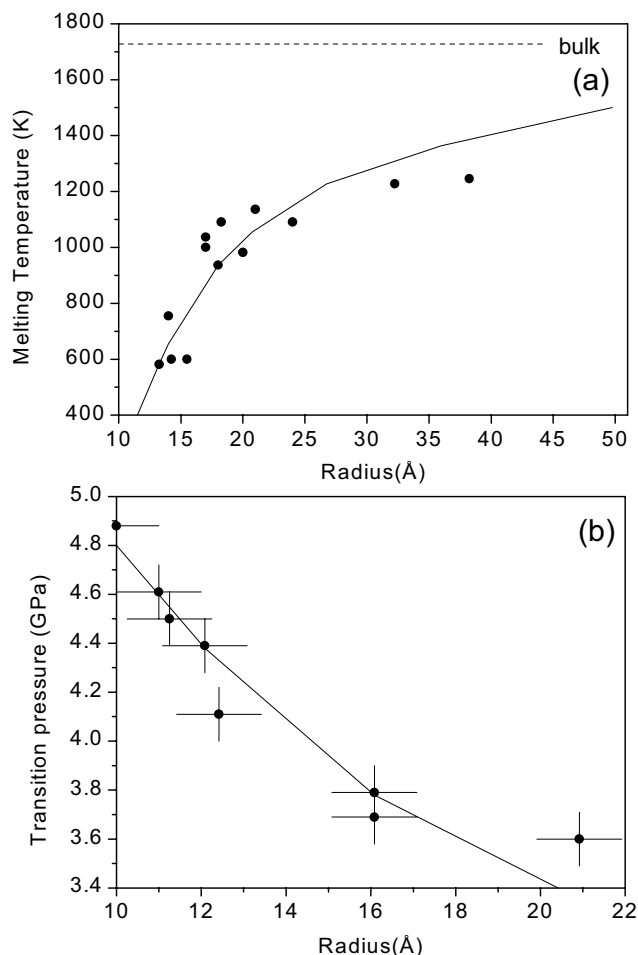


**Fig. 1.4.** (a) Size dependence of the melting temperature of CdS nanocrystals. (b) Size dependence of the pressure-induced wurtzite-rock salt transformation in CdSe nanocrystals [from A. P. Alivisatos, *J. Phys. Chem.*, **1996**, 100, 13226].

surface, with a scale factor of a million to one. Optical tweezers provide another approach to holding and moving nanometer structures, a capability especially useful in investigating the dynamics of molecules and particles. Questions such as, how does a polymer move, generate force, respond to an applied force and unfold, can be answered by the use of optical tweezers. It is noteworthy that the positioning of nanoparticles accurately and reliably on a surface by using the tip of an atomic force microscope as a robot has already been accomplished. Large-scale operations requiring parallel tip arrays are being explored in several laboratories.

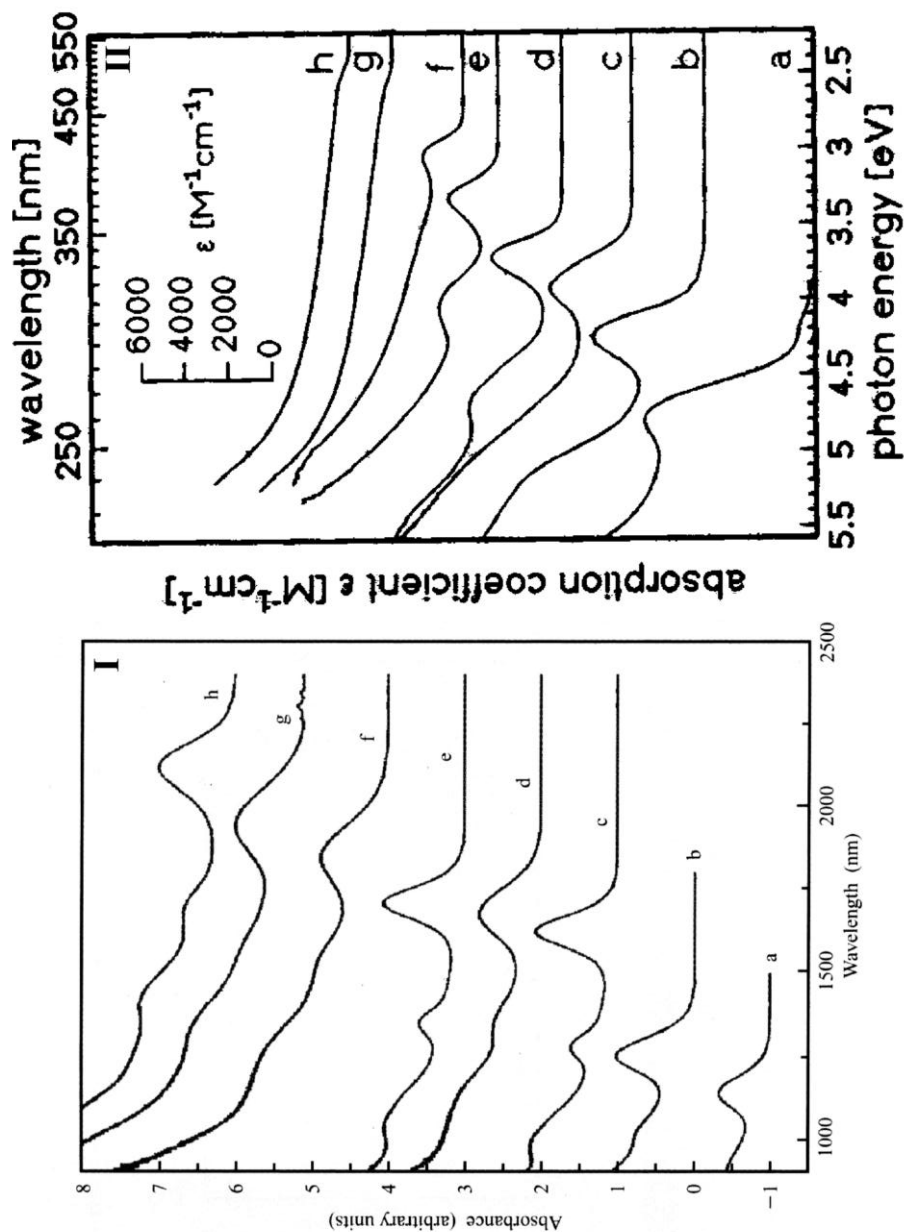
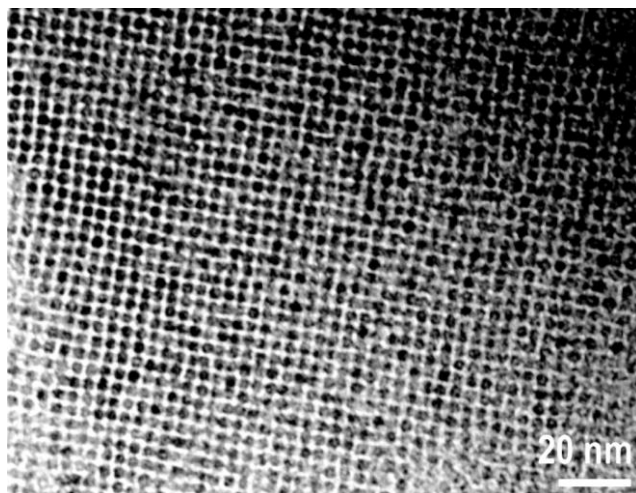


Fig. 1.5. Electronic spectra of (I) PbSe nanocrystals (a. 3.0 nm, b. 3.5 nm, c. 4.5 nm, d. 5.0 nm, e. 5.5 nm, f. 7 nm, g. 8 nm, h. 9 nm) and (II) of CdS nanocrystals (a. 0.64 nm, b. 0.72 nm, c. 0.8 nm, d. 0.93 nm, e. 1.94 nm, f. 2.8 nm, g. 4.8 nm) [from T. Vossmeier et al. *J. Phys. Chem.*, 1994, 98, 7665 and R. W. Murray et al., *IBM J. Res. Dev.*, 2001, 45, 47].





**Fig. 1.6.** Two-dimensional array of thiolized Pd<sub>561</sub>Ni<sub>561</sub> nanocrystals [from P. J. Thomas, G. U. Kulkarni, C. N. R. Rao, *J. Nanosci. Nanotechnol.*, **2001**, *1*, 267].

#### 1.4

#### Applications and Technology Development

Some of the important applications and technologies based on nanomaterials are the following: (i) Production of nanopowders of ceramics and other materials, (ii) nanocomposites, (iii) development of nanoelectrochemical systems (NEMS), (iv) Applications of nanotubes for hydrogen storage and other purposes, (v) DNA chips and chips for chemical/biochemical assays, (vi) gene targeting/drug targeting and (vii) nanoelectronics and nanodevices. The last one, which is probably the most challenging area, includes new lasers, nanosensors, nanocomputers (based on nanotubes and other materials), defect-free electronics for future molecular computers, resonant tunneling devices, spintronics and the linking of biological motors with inorganic nanodevices.

#### 1.5

#### Nanoelectronics

The multidisciplinary area of nanoelectronics has two objectives: (i) utilization of a single nanostructure (e.g. nanocrystal, quantum dot, nanotube) for processing electrical, optical or chemical signals, and (ii) utilization of nanostructured materials involving assemblies of nanostructures for electronic, optoelectronic, chemical and other applications. While it is often difficult to make distinctions between the two, the first category is specifically intended to obtain single-electron devices and the second category is for the purpose of miniaturization in information storage

etc. Typical examples of single nanostructure devices are those employing Coulomb blockade or a single-electron transistor. Arrays of quantum dots, scanning probe tips and nanotubes are examples of the second category. In Coulomb blockade, the addition of a single electron to a nanoparticle of radius  $R$  gives rise to the charging energy,  $W = W(\infty) + [b/R]$  where  $W(\infty)$  relates to the charging energy of the bulk. The minimum voltage,  $V_{\min}$ , required to inject an extra electron into the nanoparticle gives rise to the Coulomb staircase with voltage steps,  $V_{\min} = [W(\infty)/e] + [b/eR]$ . The observation of the staircase provides a direct demonstration of the discrete electronic structure in such finite (nano) systems. In Figure 1.7, we show the  $I$ - $V$  characteristics of an isolated 3.3 nm Pd nanocrystal, exhibiting the Coulomb staircase phenomenon. The dependence of the charging energy on particle size is also shown in Figure 1.7.

## 1.6

### Other Aspects

Consolidated nanostructures employing both ceramic and metallic materials are considered important in creating new generations of ultrahigh-strength, tough structural materials, new types of ferromagnets, strong and ductile cements, and new biomedical prosthetics. Typical of the nanostructured hard materials are Co/WC and Fe/TiC nanocomposites. Nanoparticle-reinforced polymers are being considered for automotive parts. Besides high strength materials, dispersions and powders as well as large bodies of novel morphologies are being produced. Coatings with highly improved features resulting from the incorporation of nanoparticles are being developed.

Nanoelectrochemical systems (NEMS) are likely to augment the already established micro analogue, MEMS. A related aspect pertains to molecular motors. Molecular motors are responsible for DNA transcription, cellular transport and muscle contraction. New fabrication tools enable us to understand and exploit these motors as actuators in nanoelectromechanical systems. These may lead to artificial biological devices that are powered by ATP. Organic chemists are synthesizing molecules (e.g., rotaxanes) capable of various kinds of motions at the nanolevel. Using molecular motors as nanomachines and interfacing them with inorganic energy sources and other nanodevices would be of great interest.

DNA chips and microarrays represent a technology with applications in diagnostics and genetic research. DNA chips and arrays are devices wherein different DNA sequences are arrayed on a solid support, the arrays generally having 100 to 100,000 different pixels (DNA sites) on the chip surface. The chips will be useful in genomic research, drug discovery, forensics and different types of detection and diagnostics. Electronically active DNA microarrays and electronically directed DNA self-assembly technology could be of value in photonic and electronic devices and other areas. Appropriate nanoparticles containing DNA may indeed provide viable means of delivery in the near future. The gene gun is already being used to deliver genetic materials to transfect plant and animal cells.

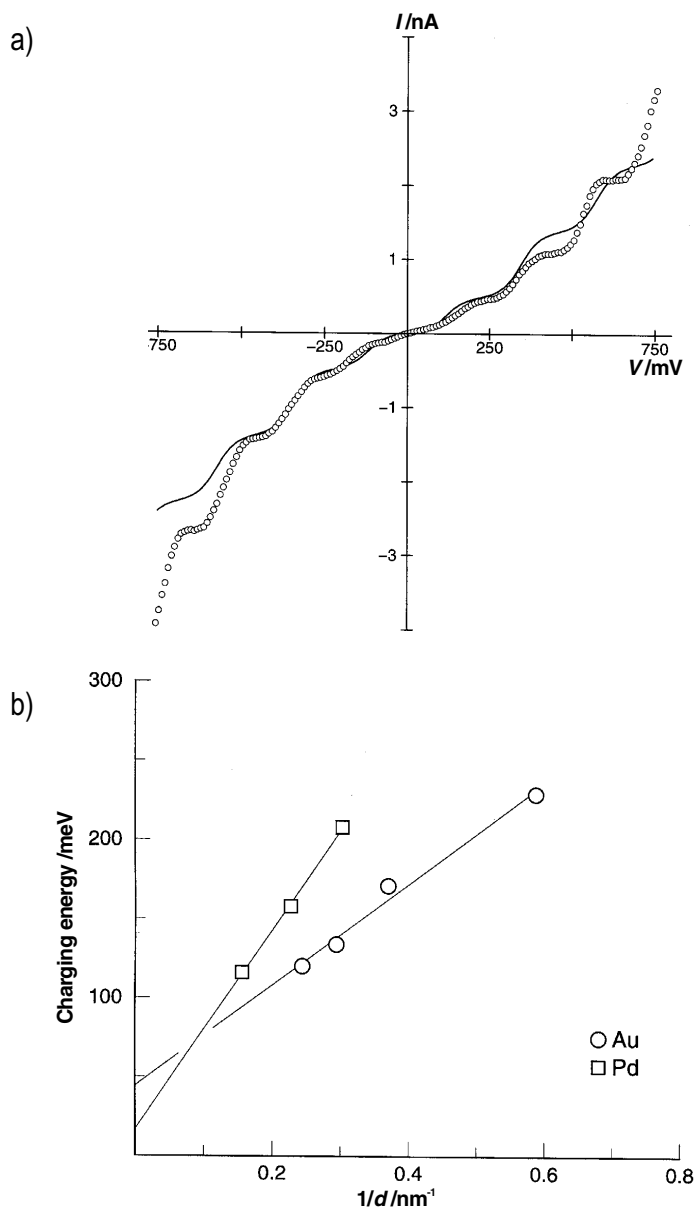


**Fig. 1.7.** (a)  $I$ - $V$  characteristics of an isolated 3.3 nm Pd nanocrystal (dotted line) and theoretical fit (solid line) obtained at 300 K using a semiclassical model. (b) The size dependence of the charging energy [from P. J. Thomas, G. U. Kulkarni and C. N. R. Rao, *Chem. Phys. Lett.*, **2000**, 321, 163.].

Semiconductor nanocrystals are being used as fluorescent biological labels. It is likely that sensors based on nanotechnology will revolutionize health care, climate control and detection of toxic substances. It is quite possible that we will have nanochips to carry out complete chemical analysis. Such nano-total analysis systems will have to employ new approaches to valves, pipes, pumps, separations and detection.

A knowledge of the processes related to nanoscale structures, natural as well as man-made, is useful in understanding transport and other aspects of these materials, and in developing technologies for preventing or minimizing harm to the environment. The use of homogeneous and heterogeneous catalysis (including nanocatalysis) for improving energy efficiency and reducing waste is well documented. The design of environmentally benign nanocomposites, the use of nanoparticles of  $\text{TiO}_2$  and other nanomaterials for environmental cleansing processes and of nano-porous solids for sorption, are examples of the applications of nanotechnology for the protection and improvement of the environment. The use of nanoporous polymers for water purification and purification of liquids by photocatalysis of nanoparticles of  $\text{TiO}_2$  are two other examples.

## 1.7

### Concluding Remarks

The subject of nanomaterials is of great vitality and offers immense opportunities. It is truly interdisciplinary and encompasses chemistry, physics, biology, materials and engineering. Interaction amongst scientists with different backgrounds will undoubtedly create new science, and in particular new materials, with unforeseen technological possibilities. What is noteworthy is that nanotechnology is likely to benefit not only the electronics industry, but also the chemical and space industries, as well as medicine and health care. Chemistry has much to contribute to most aspects of the science and technology of nanomaterials.

### Bibliography

- 1 *Nanostructure Science and Technology*, eds. R. W. SEIGEL, E. HU, M. C. Roco, National Science and Technology Council Report, Kluwer Academic Publishers, Boston 1999.
- 2 M. C. Roco, R. S. WILLIAM, A. P. ALIVISATOS, *Nanotechnology Research Directions*, National Science and Technology Council Report, Kluwer Academic Publishers, Boston 2000.
- 3 Issues in Nanotechnology, *Science*, **2000**, 290, 1523–1555.
- 4 Special topical issue on Nanostructural Systems, *Pure Appl. Chem.*, **2001**, 72, **2002**, 74.
- 5 C. N. R. RAO, A. K. CHEETHAM, J. *Mater. Chem.*, **2001**, 11, 2887.
- 6 J. JORTNER, C. N. R. RAO, *Pure Appl. Chem.*, **2002**, 74, 1491.
- 7 *National Nanotechnology Initiative*, National Science and Technology Council, Washington D.C., June 2002.

## 2

## Strategies for the Scalable Synthesis of Quantum Dots and Related Nanodimensional Materials

*Paul O'Brien and N. Pickett*

## 2.1

### Introduction

At present there is a considerable interest in the potential for use of materials with dimensions that are best defined in terms of nanometers; especially so-called quantum dots as derived from bulk compound semiconducting materials [1–3]. To date almost all work on the synthesis of quantum dots has been carried out in the academic sector, with a strong emphasis on the synthesis of high quality material in small quantity. One product containing quantum dots has to date been marketed, a biological probe formed by binding particles of CdSe to form Qdot™ streptavidin conjugates [4]. However, there is potentially a wide range of applications for such materials which means that the production of quantities of material is becoming an issue of real interest.

The situation is analogous to the development of metal organic precursors for the deposition of compound semiconductors by metal organic chemical vapour deposition (MOCVD). These compounds underwent a period of intense research and development in the last 20 years of the 20<sup>th</sup> century [5]. Although work in this area continues it now underpins a mature technology, although the deposition of oxides is still undergoing active development. In its infancy this aspect of materials chemistry was crucial in delivering new functional devices especially in optoelectronics (e.g. high performance solid-state lasers and LEDs) many of which are in everyday use. It seems probable that the emergence of a materials chemistry for the scalable manufacture of nanodimensional materials will be of similar importance in the first half of the present century.

This chapter will address issues concerned with the synthesis of quantum dots in quantity. Many issues remain ill-defined in this area including the simple problem of defining what will form a proper specification for nanodimensional materials such as quantum dots. A typical material may involve two types of solid-state compound and an apparently ever increasingly complex organic coat used to enhance the stability of the material and the solvents in which it can be dispersed/processed. Again analogies with conventional semiconducting materials can be

made. In this case the specifications for this now singularly important class of materials emerged in the 1930s. It is important for the chemist to remember that the parameters defining the functional properties of such bulk materials: principally mobility and carrier type and concentration are defined by concentrations of impurities or dopants which are very small. The determination of bulk properties from such small concentrations made the initial proper definition of the intrinsic properties of silicon difficult, the history of this problem has been discussed recently [6].

This chapter will be structured as follows:

- The types of nanodimensional materials now routinely prepared, their structures and how these might be defined.
- The emergent uses for nanodimensional materials and how these lead to a market pull for volume manufacture.
- The general methods available for the synthesis of nanodimensional materials.
- The suitability of such methods for scaling.
- Conclusions and perspectives on the future.

In preparing this chapter we have tried to give a perspective on what is an emerging area. Due to constraints of space the referencing has been limited to key papers and indications of a number of major secondary sources are given. Examples have been drawn from the work of one author's own group at Imperial College and latterly in Manchester. The synthesis of nano-dispersed metals and oxides is not considered in detail, although some key references are provided. There are two reasons for omitting metals: Firstly, the problems in scale up are much greater for semiconductors than for metals and hence there is more scope for discussion. Secondly, gold in particular is readily available and widely used in nano-dispersed form [7]. For oxides in terms of well-defined processable nano-materials analogous of quantum dots there are relatively few reports, but for an outstanding example see [8], in contrast crude nanopowders of oxides are commonly available. A very useful review of nanodimensional magnetic materials has just appeared [9].

## 2.2

### Defining Nanodimensional Materials

For the purposes of this article we will limit our discussion to particles defined by a minimum of two dimensions less than 100 nm but usually with 2-dimensions less than 10 nm. Current interest in these materials can principally be traced to work by Luis Brus in the mid-1980s in which he pointed out that the band gap of a simple direct band gap semiconductor such as CdS should be dependent on its size once its dimensions were smaller than the Bohr radius [10]. Experimental work confirmed this suggestion. Initial samples were prepared by low temperature

aqueous precipitations but it was at first surprising to discover that the luminescence of such particles depended markedly on the surface coat. Particles treated with hydroxide were much more efficient than as-prepared particles. The importance of the surface in such materials reflects the relative importance of the surface sites for a typical nanodimension particle around  $4 \text{ nm}^3$  e.g. a few percent of the atoms are found on the surface. Defects tend to anneal to the surface and hence the cores of such small particles are often 'relatively' defect free.

These observations and one further criterion start to define quantum dot systems. The second major possibility is the coating of the central particle with a second material e.g. CdS or ZnS on top of CdSe. When a wider band gap material is coated onto the outside of a narrow band gap material the confinement on the 'core' is enhanced, leading to enhanced optical properties, especially photoluminescence efficiencies.

The above enables us to define the nature of an isolated quantum dot. It will depend on

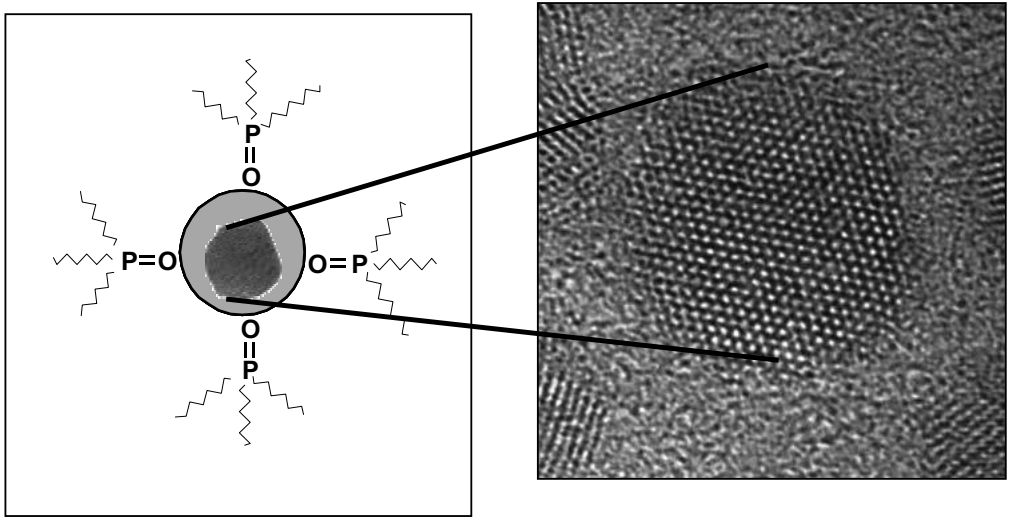
- The nature of the central materials, the core.
- The nature of any subsequent coating 'shell' layer.
- The nature of the final coat on the material, often an organic capping layer.

A typical such material is shown in Figure 2.1. In high quality materials the core of the dot will be a single crystal, the shell epitaxial or close to and the final coat will pacify defects and also confer solubility and or functionality for binding to a substrate or target molecule. However, what is shown in both these schematics and images is a single quantum dot. Each dot is a mesoscopic entity with individual properties, the properties of an ensemble of dots will additionally be determined by the particle size distribution and any differences in morphology within the ensemble. The best quality dots are themselves single crystals, as nicely illustrated by the PbS sample [11] shown in Figure 2.2.

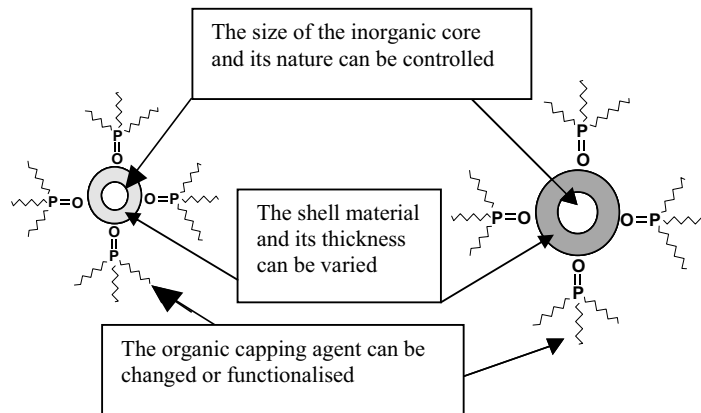
There are as yet no standards defining the properties of such samples; these will clearly need to emerge as these materials become more generally utilised. Such standards will owe more to the definitions of materials and/or polymer science than to the world of the molecule and will include definitions probably statically derived from:

- Size, including aspect ratio.
- The distribution of particle sizes.
- The nature of the core.
- The nature of the shell.
- The nature of the final coat.

The above describe the physical composition of the particle; other properties may define its use, typically quantum efficiency in an optical material and other measures as appropriate, such as coercivity in a magnetic material.



(a)



(b)

**Fig. 2.1.** (a) A ca. 4 nm core-shell dot of CdSe coated with CdS and a TOPO, and a schematic. (b) Anatomy of organically capped quantum dots.

## 2.3

### Potential Uses for Nanodimensional Materials

In nanoparticles derived from semiconductors, once they are below a critical size, their electronic behaviour is governed by quantum physics (hence 'quantum dots'). The absorption of light at one wavelength leads to emission at slightly lower en-



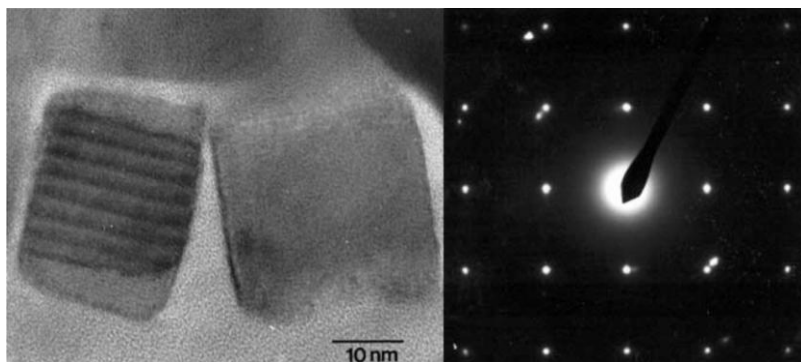


**Fig. 2.2.** Sample of PbS coated with TOPO.

ergy. Such behaviour is usually associated with extremely pure single crystals in bulk semiconductors such as the gallium arsenide or indium phosphide or related alloys used in solid-state lasers. The small shift in the emission is termed a 'Stokes shift'.

The characteristic wavelength of light at which these interactions occur is governed by the size of the particle. This effect could be exploited in:

- Inks and dyes (optical probes in general) with a unique color signature often only visible to the eye when exposed to UV light.
- Functional materials e.g. ones triggered by light to release payloads of proteins or DNA at an exact location in the human body.
- Solar cells probably hybrid organic/inorganic structures.

Leading to market applications in:

- **Security:** Authentication and anti-forgery, specifically the elimination of counterfeit currency, documents, brand name clothing, car parts, etc.  
Overt and covert anti-counterfeiting features – bank notes, paper documents, casino chips and brand protection, i.e. as replacement for specialty conventional (luminescent and fluorescent) dyes in security applications.
- **Life Sciences:** examples include: diagnostics; biological sensors; drug delivery; replacements for luminescent and fluorescent dyes in biological probes for high throughput screening applications.
- **Electronics:** data storage; LEDs; photovoltaics; flat panel displays. The materials are likely to be crucial in the evolution of an electronics industry based on soft materials such as plastics.

These possibilities are summarised schematically in Figure 2.3. Clearly there are a variety of markets in which quantum dots could be used if problems associated with their manufacture could be overcome. The striking sharp photoluminescence spectra of some quantum dots are shown in Figure 2.4 together with pictures of samples taken under UV irradiation.

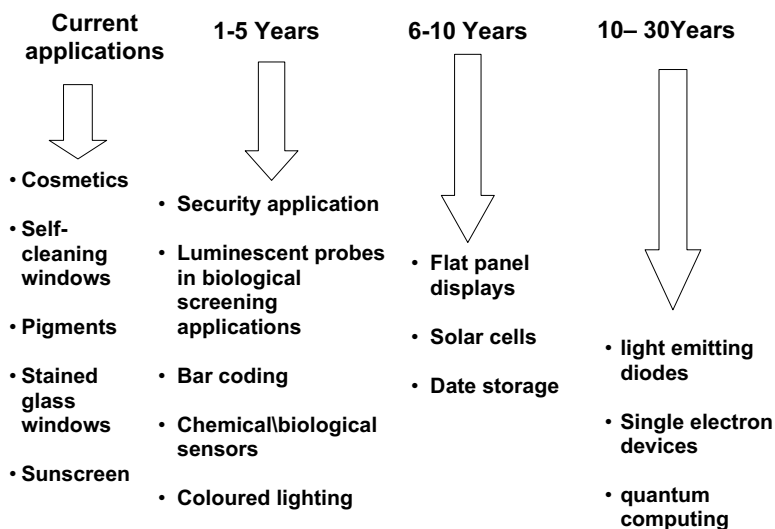


Fig. 2.3. Applications and future markets for nanoparticles and quantum dots.

## 2.4

### The General Methods Available for the Synthesis of Nanodimensional Materials

There is much in common with the synthesis of colloidal materials in the preparation of dispersions of nanodimensional materials. Indeed it is a moot point as to whether such materials are large molecules or small colloidal particles. What probably distinguishes ensembles of quantum dots and related materials from

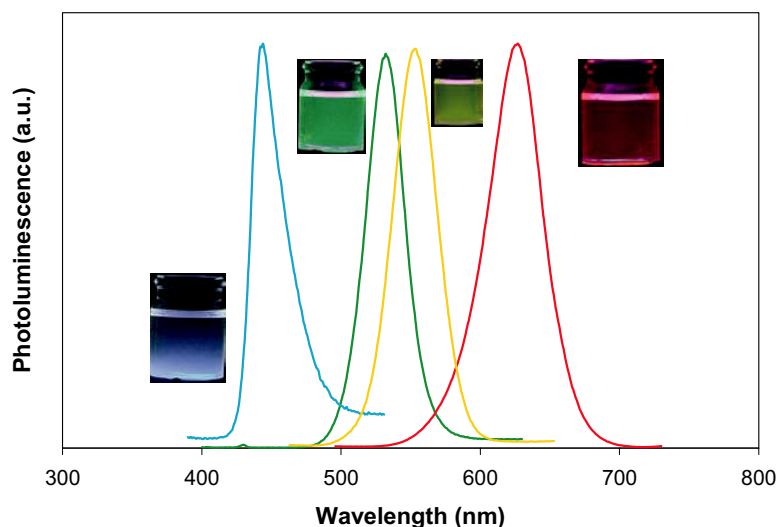
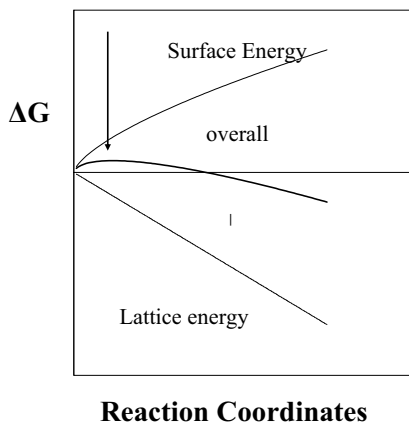


Fig. 2.4. PL spectra and luminescence colors of some CdSe/ZnS core-shell structures.



**Fig. 2.5.** Nucleation and growth.

collections of clusters is that each particle is, in principle, a mesoscopic object with its properties determined by its own nature, i.e. its precise morphology and the number of atomic units from which it is built. It inherently lacks the anonymous nature of a molecule in an assembly.

However there is much that can be learned from colloid chemistry when designing the synthesis of such materials, and it seems colloid chemistry is gaining a new lease of life from a better understanding of the assembly of nanoparticles. Much of the understanding of crystallization is based on the ideas associated with supersaturation. In a typical system undergoing a crystallization process nuclei or small crystallites are generally held to have an unfavorable surface energy compensated by the evolving lattice energy of the solid, Figure 2.5. The situation is different from that in a bulk material as a relatively small percentage of atoms occupy surface sites in a macro or even conventionally termed microscopic particle. It is only when we reach the scale of nanometers that significant numbers of atoms reside at the surface. The majority of routes for the preparation of nanoparticles avoid what might be termed “runaway” into the macroscopic world by using a molecule, ligand, which binds to the surface of the nanoparticle, the growth of particles is further inhibited by e.g. limiting the supply of the constituents forming the material, either by working at high dilution or by controlling their delivery by a chemical decomposition.

These above principles underlie most of the methods for the reproducible syntheses of nanomaterials, the main exception being those reactions which are physically constrained by being carried out in the pore of a solid state material or in a micelle or vesicle. There is a second ramification of the nucleation and growth process that is often used to effect in the reproducible synthesis of uniform assemblies of particles: the temporal separation of the nucleation and growth processes. If nucleation is induced by a perturbation of the system, e.g. a sharp elevation in temperature, and suddenly stopped; this effect is easily achieved by injecting a cold solution of a reactive precursor into a hot solution. Nucleation will occur but the cold solution injected will immediately cool the solution. If this

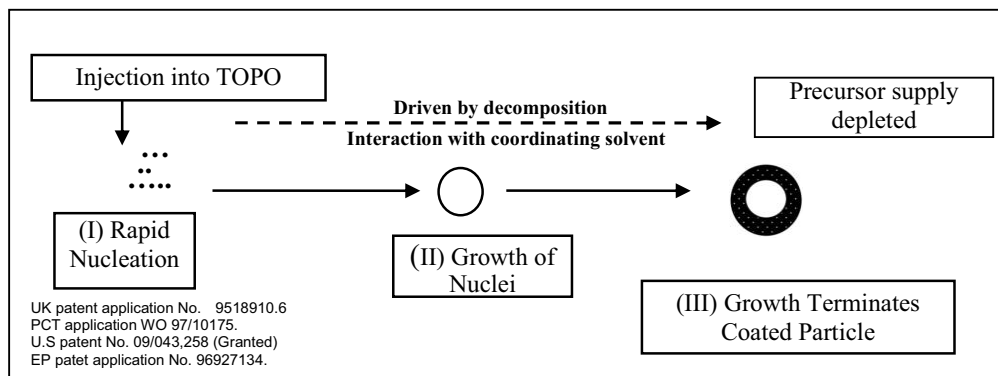


Fig. 2.6. A typical growth process.

cooling is significant, 10 °C or so, it is quite possible for little further nucleation to occur and for the growth process to be dominated by the originally created suite of nuclei growing in concert. This common type of process is generically illustrated in Figure 2.6.

Many specific methods have been reported for the preparation of quantum dots of compound semiconductors and include:

- Precipitative method, usually aqueous and at low temperature.
- Reactive methods in high boiling point solvents, often involving metal organic and or organometallic compounds.
- Hydrothermal and solvothermal methods.
- Vapour phase reactions.
- Reactions in confined solids or constrained on surfaces or involving micelles or confined reaction spaces.

The focus of this article is on the preparation of stable isolated particles and methods suitable for the preparation of such materials will be emphasised. A sound synthetic method will lead to crystalline nanoparticulates of high purity, with a narrow size distribution, that are suitably surface derivatized.

#### 2.4.1

##### Precipitative Methods

This type of method was used by Brus and co-workers in studies on CdS and ZnS [12, 13], which have led to the explosion of interest in solid samples of semiconductors which show quantum confinement effects. They [12] prepared CdS nanoparticles by a process involving the controlled nucleation of CdS in dilute aqueous solutions of cadmium sulfate and ammonium sulfide. The dynamic equilibrium between solvated ions and solid CdS in acetonitrile, as a solvent in the presence of a styrene or maleic anhydride copolymer, allowed the preparation of

stable CdS nanoparticles, with an average size of 3.4 nm or 4.3 nm, respectively [12] ZnS and CdS nanocrystallites have also been synthesised from aqueous and methanolic solutions without an organic capping agent [13].

Henglein and Weller made significant progress [14–16] using CdS colloids prepared by controlled precipitation methods [17–22]. However, to obtain highly monodispersed nanoparticles, post-preparative separation techniques such as size exclusion chromatography [20] and gel electrophoresis have been employed [21]. Gel electrophoresis was found to be superior to other separation techniques.

Weller et al. synthesised nanocrystallites of  $\text{Zn}_3\text{P}_2$  and  $\text{Cd}_3\text{P}_2$  by the injection of phosphine ( $\text{PH}_3$ ) into solutions containing metal salts [18, 23]; control of particle size was achieved by varying the phosphine concentration and the temperature of the reaction. Samples of both  $\text{Zn}_3\text{P}_2$  and  $\text{Cd}_3\text{P}_2$  showed remarkable quantum size effects, as observed by changes in the color of the products. Bulk  $\text{Cd}_3\text{P}_2$  is black whereas a solution containing small nanocrystallites (1.5 nm diameter) is colorless with a maximum in the electronic spectrum at around 310 nm. The color of such  $\text{Cd}_3\text{P}_2$  changes from the black of macrocrystalline (band gap of 0.53 eV) through the visible to white for the 1.5 nm sample (with a band gap of ca. 0.8 eV). Hexametaphosphate was used as a stabiliser to prevent particle aggregation. The sample fluoresced when excited at 300 nm [23].

The relative solubility of inorganic salts can be used to prepare more complex structures by such methods and examples include: CdS/ZnS [24], CdSe/AgS [25] HgS/CdS [26], PbS/CdS [27, 28], CdS/HgS [29], ZnS/CdSe [30] and ZnSe/CdSe [31] particles. The main constraints on the production of such structures involve the relative solubility of the solids and lattice mismatches between the phases. The preparation of “quantum dot quantum well systems” such as CdS/HgS/CdS [32, 33], has also been reported, in which a HgS quantum well of 1–3 monolayers is capped by 1–5 monolayers of CdS. The synthesis grows less soluble HgS on CdS (5.2 nm) by ion-replacement. The solubility products of CdS and HgS are  $5 \times 10^{-28}$  and  $1.6 \times 10^{-52}$  respectively. The authors reported fluorescence measurements in which the band edge emission for CdS/HgS/CdS is shifted to lower energy values with increasing thickness of the HgS well [33].

Other examples of the preparation of semiconductor nanocrystallites by solution methods can be found in the literature [1–3]. Solution methods provide a cheap route to many nanoparticle materials. However, a lack of reaction control can be problematic when larger scale preparations are necessary. Also several important semiconductors are not easily obtained by this preparative method, with some being air and/or moisture sensitive, e.g. GaAs and InSb.

#### 2.4.2

##### Reactive Methods in High Boiling Point Solvents

The routine synthesis of well-defined semiconductor nanocrystallites was really opened up in a landmark paper by Murray, Norris and Bawendi [34]. They reacted solutions of dimethylcadmium ( $(\text{CH}_3)_2\text{Cd}$ ) (in tri-*n*-octylphosphine TOP) and tri-*n*-octylphosphine selenide (TOPSe) in hot tri-*n*-octylphosphine oxide (TOPO) in

the temperature range 120–300 °C. This reaction produced TOPO-capped nanocrystallites of CdSe. The size of the particles is controlled mainly by the temperature of reaction, with larger particles being obtained at higher temperatures. This TOPO method has advantages over previous synthetic methods, including, producing monodispersity ( $\sigma \cong 5\%$ ) and the ability to produce hundreds of milligrams of materials in a single experiment. Alivisatos subsequently used higher temperatures for injection and growth to improve the quality of the material prepared [35]. In a series of recent papers interesting rod and tetrapodal structures have been grown especially in the CdSe system [36]. The method was readily adapted to the production of core-shell structures [37, 38] with materials having high quantum efficiencies being prepared.

In an early paper the use of a single-source precursor, oligomeric  $\text{Cd}(\text{Se}(\text{C}_2\text{H}_5))_2$  [39] was used for the preparation of CdSe in 4-ethylpyridine. Such a compound obviates the need for the use of hazardous compounds such as toxic dimethylcadmium,  $(\text{CH}_3)_2\text{Cd}$ , which are especially toxic at high temperatures. The use of single-molecule precursors, i.e. a single compound containing all elements required within the nanocrystal, such as alkyldiseleno- or alkyledithio-carbamato complexes has been reported [40, 41]. An early example was the synthesis of cubic PbS [42] (see Figure 2.4) and PbSe [43], this work has been emulated and developed recently for the production of various morphologies [44]. Clusters of the general formula  $[\text{M}_{10}\text{Se}_4(\text{SPh})_{16}]^{4-}$  ( $\text{M} = \text{Zn}$  or  $\text{Cd}$  and  $\text{SPh} = \text{phenyl thiolate}$ ) have been used to great effect in the synthesis of nanoparticulates of both the simple and core-shell type [45]; dialkyl-diseleno and dithio-carbamates have also been used to prepare core shell nanoparticles [46].

In devising safer syntheses for nanoparticulates based on the original TOPO type of methodologies it has occurred to more than one group that the use of metal alkyls may not be required [47–49]. In an early experiment cadmium chloride and TOPS were used to prepared CdS. More recently Peng has produced a series of papers in which cadmium salts, especially the acetate, have been used to prepare good quality CdSe [48, 49]. In the most recent report a blend of octadecene and oleic acid was used to produce CdS under conditions in which sulfur was the limiting reagent. Particle size control could be achieved by varying the amount of oleic acid in the reaction mixture. In related work lead-containing materials have been prepared. A recent review of the general area of the synthesis of nanodispersed semiconductors is available [50].

A TOPO-based method has been used [51] by Alivisatos et al. in the synthesis of InP nanocrystals (2–5 nm in diameter). The reaction used  $\text{InCl}_3$  in TOPO followed by addition of  $\text{P}(\text{Si}(\text{CH}_3)_3)_3$ , with annealing of the resulting InP nanocrystals. The band gap for bulk InP is 1.35 eV whereas the InP nanocrystallites produced exhibit values ranging from 1.7 eV to 2.4 eV [51]. InAs has been prepared by a similar method by the dehalosilylation reaction between  $\text{As}[\text{Si}(\text{CH}_3)_3]_3$  and  $\text{InCl}_3$ , surface oxidation did not change the properties of the resulting particles [52]. III/V semiconductors are less ionic in character than their II/VI analogs and thus do not crystallise as readily. Kaner et al. [53] used solid state metathesis involving the reaction of sodium pnictides with group III halides, at high temperatures, in a closed

vessel, to produce III/V nanoparticles. A relatively low temperature method involving similar reactions in organic solvents has been reported for the preparation of GaP and GaAs nanoparticles, using gallium (III) halides and  $(\text{Na/K})_3\text{E}$  ( $\text{E} = \text{P}, \text{As}$ ) [54]. This method avoids the use of hazardous phosphines or arsines. Nanocrystallites of InAs and InP were also synthesised [55] from the reaction of  $\text{InX}_3$  ( $\text{X} = \text{Cl}, \text{Br}, \text{I}$ ) with  $\text{As}(\text{SiMe}_3)_3$  or  $\text{P}(\text{SiMe}_3)_3$ , respectively. Other analogous chemical routes to indium pnictides have also appeared in the literature [55].

GaAs nanocrystallites have been prepared by reacting  $\text{GaCl}_3$  with  $\text{As}(\text{SiMe}_3)_3$  in boiling quinoline, however, as yet unidentified species were found to mask the optical properties of the resulting particles and hence quantum size effects could not be properly determined [56, 57]. The alcoholysis or thermolysis of silylated single molecule precursors is one of several processes used for nanoparticle synthesis of III/V and II/V semiconductor materials. Another preparative method for the syntheses of GaAs [58] and InP [59] is by the methanolysis of organometallic compounds such as  $[\text{Cp}^*(\text{Cl})\text{In}(\mu\text{-P}(\text{SiMe}_3)_2)_2]$ . The chemical route led [60, 61] to bulk, amorphous,  $\text{Cd}_3\text{P}_2$  after rapid flocculation of  $\text{Cd}_3\text{P}_2$  nanoparticles. In order to control the kinetics a single molecule precursor with bulkier substituents was used,  $\text{Cd}[\text{P}(\text{SiPh}_3)_2]_2$  [61, 62]. The methanolysis gave soluble nanoparticles of  $\text{Cd}_3\text{P}_2$  with diameters ranging from 30–40 Å, however, the particles were not crystalline.

Other chemical routes to metal phosphides include phosphinolysis reactions and reactions between metallo-organics and  $\text{P}(\text{SiMe}_3)_3$ ; all involve elimination and condensation processes. Buhro [61] reported the synthesis of several binary phosphide semiconductors along with ternary phases (e.g.  $\text{ZnGeP}_2$ ), using solution-phase metallo-organic routes. A recent review of the preparation of II/V materials has appeared [63].

### 2.4.3

#### Hydrothermal and Solvothermal Methods

An alternative approach to the use of high-temperature solvents, which can be both toxic and expensive, is to use more usual solvents conventionally limited by their rather low boiling points. However, solvents can be used well-above their boiling point at atmospheric pressure if heated in a sealed vessel (an autoclave or ‘bomb’) the autogenous pressure then far exceeds the ambient pressure raising the boiling point of the solvent. Such *solvothermal* reaction conditions are extensively used in the preparation of inorganic solids, especially zeolites [64]. For a comprehensive review of this method for nanoparticles see [65].

A few illustrative examples of this methodology follow. Qian and coworkers [66] have reported wurtzite ZnSe nanoparticles with sizes in the 18 nm range starting from the elements in ethylenediamine ( $T = 120^\circ\text{C}$ ,  $t = 6\text{ h.}$ ) This reaction yields a complex with the formula  $\text{ZnSe}(\text{en})$  where en is ethylenediamine. Seshadri has used toluene as the solvent in a neat preparation of CdSe from cadmium stearate and Se powder [67, 68], tetralin (tetrahydronaphthalene) was added as a reducing agent. Tetralin is aromatized to naphthalene in the presence of Se, producing  $\text{H}_2\text{Se}$

in the process. Monodisperse quantum dots (the particle size distributions have a width that is about 5% of the mean) with good luminescence properties are produced, the only report to date of a solvothermal route to surfactant-capped semiconductor chalcogenide nanoparticles.

$\text{Cu}_{2x}\text{Se}$  particles were obtained by Qian and coworkers [69] starting from  $\text{CuI}$ ,  $\text{Se}$ , and ethylenediamine, with  $T = 90^\circ\text{C}$ ,  $t = 4$  h. The particles are spherical and quite monodisperse. Qian and coworkers have also reported [70] a solvothermal preparation of  $\text{CuInSe}_2$ , obtaining 15 nm particles from  $\text{CuCl}_2$ ,  $\text{InCl}_3$  and  $\text{Se}$  in either ethylenediamine or diethylamine, at  $180^\circ\text{C}$  for 15 h in ethylenediamine, and 36 h for diethylamine.  $\text{CuInSe}_{2x}\text{S}_x$  [71] also has been prepared by Qian and coworkers using  $\text{InCl}_3$ ,  $\text{CuCl}_2$ ,  $\text{S}$  and  $\text{Se}$  with ethylenediamine as the solvent.

Recently microwave-solvothermal reactions and flow-solvothermal reactions have been reported. These methods may be of particular interest in devising scalable synthesis of nanoparticulates. Komarneni et al. [72] have prepared a number of oxide nanoparticles, including 5–20 nm  $\text{MnFe}_2\text{O}_4$ ,  $\text{CoFe}_2\text{O}_4$ ,  $\text{NiFe}_2\text{O}_4$  and  $\text{ZnFe}_2\text{O}_4$  ferrite particles, usually by the reaction of metal nitrates in suitable ammoniacal solution. These solutions are microwaved, typically for around 4 min. In flow-hydrothermal techniques, a preheated solvent is mixed with the reactants just prior to introduction into a heated chamber with a back-pressure regulator. The reactants are pumped using a standard HPLC pump through the system. In this way Poliakoff et al. [73] have prepared  $\text{CeO}_2\text{--ZrO}_2$ . A residence time of 9 s at a (regulated) pressure of 25 MPa was sufficient to yield the product, which comprised nanoparticles with sizes as small as 4 nm. These two methods may well have great promise, not only for scale-up, but also for good monodispersity.

#### 2.4.4

#### Gas-Phase Synthesis of Semiconductor Nanoparticles

Most gas-phase methods of semiconductor nanoparticle synthesis involve atmospheric or low pressure evaporation of either powders or the pre-formed semiconductor, or the co-evaporation of the two elemental components, for example zinc metal and sulfur [74]. However, the use of these techniques usually results in deposits of particles with larger size distributions, in some cases ranging from 10 to 200 nm. Sercel et al. have reported the synthesis of GaAs nanoparticles by using the organometallic precursor trimethylgallium,  $\text{GaMe}_3$ , which on mixing in a furnace flow reactor with arsine gas,  $\text{AsH}_3$ , gives crystalline GaAs particles [75]. These approaches suffer from the problem of particle aggregation due to the absence of a surface passivating (capping) agent. The only report of gas-phase semiconductor nanoparticle synthesis using a capping agent was by Salata et al. who produced PbS and CdS nanoparticles covered with a polymer layer by reacting a polyvinyl alcohol precursor containing  $\text{Pb}(\text{NO}_3)_2$  or  $\text{Cd}(\text{NO}_3)_2$  in the gas phase with  $\text{H}_2\text{S}$  gas [76].

An investigation of the prereactions which occur between  $\text{H}_2\text{S}/\text{H}_2\text{Se}$  and  $\text{Me}_2\text{Cd}/\text{Me}_2\text{Zn}$  when growing II–VI semiconductor films by CVD techniques, showed that the gas-phase reactions result in the formation of chalcogenide de-



posits of ZnS, ZnSe, CdS and CdSe, with the deposits consisting of poorly formed hexagonal phase micro-crystalline material [77–79]. The addition, into the gas phase, of small amounts of pyridine greatly improved the crystallinity exhibited by the particles, while the addition of larger quantities of pyridine retained the improved crystal quality and also led to a decrease in particle size to the range 10–100 nm. Moreover, as the gas phase concentration of pyridine increased particle size decreased. In the case of CdSe a quantization effect was observed by a change in color of the deposit, when  $\text{Me}_2\text{Cd}$  and  $\text{H}_2\text{Se}$  are mixed in the gas phase in the absence of pyridine the deposit is black, when a high concentration of pyridine is present the deposit is a yellowish-red color. For ZnSe when using hydrogen as the carrier gas, instead of helium or argon, with a high gas-phase concentration of pyridine, a relatively narrow particle size distribution (1–5 nm) could be obtained.

#### 2.4.5

#### Synthesis in a Structured Medium

The use of a matrix to define the reaction space is an intrinsically attractive approach to the preparation of large amounts of material which could be deposited from solution or from the vapor phase. A number of matrices have been used including: zeolites [80], layered solids [81], molecular sieves [82–84], micelles/microemulsions [85–89], gels [90–92], polymers [93–97] and glasses [98]. The matrix provides a mesoscopic reaction chamber in which the crystal can only grow to a certain size.

The properties of the nanocrystallites are determined, not only by the confinements of the host material, but also by the properties of the system, which can include a range of factors including the internal/external surface properties e.g. of the zeolite or the lability of a micelle. The particle size is controlled by the system chosen e.g. in zeolites the nanocrystallite diameter is limited by the pore size of the zeolite (typically smaller than 2 nm).

Wang and Herron [80] have studied the optical properties of both CdS and PbS clusters encapsulated in zeolites. The nanocrystallites were prepared in two different zeolites; modernite (unidirectional channels of 7 Å diameter) and zeolite Y (13 Å diameter channels with cages of tetrahedral symmetry interconnected by 8 Å windows, and 5 Å cages interconnected by 3 Å windows). For the preparation of CdS in zeolite Y, the sodium cations in the zeolite were first ion-exchanged with cadmium cations, by treatment with aqueous  $\text{Cd}(\text{NO}_3)_2$  at pH 5. This was followed by passing hydrogen sulfide ( $\text{H}_2\text{S}$ ) gas over the sample [80]. Depending on the loading level of cadmium ions within the zeolite, different sizes of CdS clusters could be obtained. At low loading levels (1:1 metal/sulfide) CdS clusters with an average size less than 13 Å were obtained. These gave an absorption peak at around 280 nm in their optical spectra. When an excess of cadmium was used the individual clusters aggregated into an extended structure, modulated by the internal cavities of the zeolite. These produced optical spectra showing an excitonic shoulder near 350 nm corresponding to CdS clusters of approximately 28 Å in diameter. The small dimensions reported in this work are typical of nanoparticles obtained when zeolites are used as the host structure.

Stable, cubic phase, PbS nanoparticles were prepared in a polymeric matrix by exchanging  $\text{Pb}^{2+}$  ions in an ethylene – 15% methacrylic acid copolymer followed by reaction with  $\text{H}_2\text{S}$  [91]. The size of the PbS nanoparticles was dependent on the initial concentration of  $\text{Pb}^{2+}$  ions with diameters ranging from 13 to 125 Å. The smallest particles (13 Å) are reported to be molecular in nature and exhibit discrete absorption bands in their optical spectra. Two theoretical models, which take into account the effect of nonparabolicity, were proposed in order to explain the observed size-dependent optical shifts for PbS nanocrystallites. The authors reported that the effective mass approximation fails for PbS nanocrystallites.

Steigerwald et al. prepared capped CdSe, ZnS, ZnS/CdSe and CdSe/ZnS nanocrystallites from inverse micellar solutions [30, 99]. Silylchalcogenide reagents were added to micro-emulsions containing the appropriate metal ions. The particle surfaces were subsequently capped; for example with phenyl groups or with other semiconductor materials such as ZnS. Silylorganochalcogenides react readily with metal salts or simple metal alkyls to form metal–chalcogenide bonds [100]. Micelle stabilised CdSe nanocrystallites, with  $\text{Cd}^{2+}$  rich surfaces, react similarly with  $\text{R}[(\text{CH}_3)_3\text{Si}]_2\text{Se}$  to give larger CdSe crystallites encapsulated by a layer of organic ligands (R). These surface passivated crystallites can be isolated as powders, which are soluble in organic solvents such as pyridine.  $^{77}\text{Se}$  NMR spectra of three size distributions of organic-capped CdSe were reported, with each giving different spectra [101], consisting of broad lines corresponding to bulk material along with additional peaks appearing at higher field and becoming more intense with decreasing particle size.

Several types of nanoparticles prepared from synthesis involving biologically related processes, biomimetic, have been reported [102–104]. For example, using empty polypeptide cages found in the iron storage protein ferritin; bio-inorganic nanocomposites of CdS–ferritin can be synthesised [102]. Another approach to nanocrystallite synthesis in a matrix was developed by Choi and Shea [90, 91], who report using porous inorganic–organic xerogel (polysilsesquioxanes) to produce CdS (6 and 9 nm) [90] and chromium particles (1–10 nm) [91]. The chromium precursor used was a zero-valent arene tricarbonyl chromium complex, introduced as a component of the xerogel matrix, which after heating under vacuum produced chromium nanoparticles. By first doping CdS into the starting material two different phases of chromium and CdS are reported to be obtained. Perhaps the most important use of a biological approach to nanoparticle growth is that taken in the commercial sector by Nanomagnetix Ltd. They have used the 8 nm cavity of the iron storage protein ferritin to grow iron oxide for use in magnetic storage devices and hope to fully commercialise the process.

## 2.5

### The Suitability of Such Methods for Scaling

The vast majority of semiconductor nanoparticles are produced, at present, by batch methods in research laboratories in processes which essentially depend on the separation of nucleation and growth. In the semiconductor area high quality

Tab. 2.1. Some typical batch conditions used in the synthesis of nanoparticles.

Material	Precursor (mM)	Solvent system	Approx. [Precursor]/M	[Metal]/M	Ref.
CdSe	Me <sub>2</sub> Cd (13.35) TOPSe (10.00)	TOP 50 g TOPO 50 ml	ca. 0.13	0.13	34
CdSe or CdS	Cd(Se <sub>2</sub> CNMeHex) <sub>2</sub> (1.2) Cd(S <sub>2</sub> CNMeHex) <sub>2</sub> (1.0)	TOP 25 ml TOPO 25 g	ca. 0.06	0.06	42
CdSe or ZnSe	(Li) <sub>4</sub> [Cd <sub>10</sub> Se <sub>4</sub> (SPh) <sub>16</sub> ] (0.28) or (TMA) <sub>4</sub> [Zn <sub>10</sub> Se <sub>4</sub> (SPh) <sub>16</sub> ] (0.20)	HDA 55 g	ca. 0.005	0.02	45
CdS	CdO (0.1) Oleic acid (21.2) Sulfur (0.05)	ODE 4 g	ca. 0.025	0.025	49

TOP: tri-n-octylphosphine

TOPO: tri-n-octylphosphine oxide

HDA: hexadecylamine

ODE: octadecene

materials are likely to be grown at elevated temperatures. The relatively high dilution used in most batch processes in coordinating solvents will make production expensive and of relatively high environmental impact. In Table 2.1 some of the leading methods are compared.

Flow methods have the advantage of the potential for continuous processing but are rare. It has been pointed out that cheap solvents can be used in solvothermal methods [65]. It is clear from the literature that the majority of semiconductor dots and the few being sold are today being made by batch methods based on metal organic or organometallic routes.

A related process in which large quantities of particulates are produced is the manufacture of photographic emulsions. The manufacture involves the reaction of large quantities of material with rapid stirring, this type of method is unlikely to be useful for quantum dots. However the method used does draw our attention to the careful engineering of the manufacturing process. There is little evidence, to date, that serious consideration has been given to the engineering process for the bulk manufacture of quantum dots. In scaling a process the expense of the reagents, their toxicity and environmental impact will all be important factors. In minimising these problems vapor phase synthesis, or spray drying methods, as pioneered by Dobson and co-workers, may well be worth revisiting [76].

## 2.6

### Conclusions and Perspectives on the Future

The synthesis of nanodimensional powders on a large scale remains in its infancy. We can draw inspiration from some of the ingenious processes that have been

developed in closely related fields, perhaps the photographic process is the best example. The need to prepare high quality materials throws into sharp contrast the processing conditions chosen in the electronics industry as compared to biology. The latter tends to work slowly, close to equilibrium and at low temperatures. The electronics industry tends to use high temperature processes close to equilibrium or processes limited by chemical reaction (CVD in its various forms). The reproducible synthesis of well defined nanomaterials spans these two approaches. It seems likely that a modestly high temperature process is most likely to lead to material of the required quality. However, we should not overlook the interesting use of ferritin to produce fully functional magnetic materials. It has been impossible to provide more than an outline of the methods in use in this short chapter. The reader is referred to the many reviews cited for a more comprehensive account. We have tried to give a clear picture of how such processes might be scaled.

What is clear is that there is a major new technology to be developed using such particulates; for example the UK Parliamentary Office of Science and Technology has estimated that in the early part of this century the global market for nanotechnology products will be in excess of £80 bn pa. Those interest in the potential of this area might like to consider the following sources of information: New Dimensions for Manufacturing: A UK Strategy for Nanotechnology: DT and OST June 2002; DTI Nanotechnology 2001, DTI "The International Technology Service Missions on Nanotechnology to Germany and the USA" March 2001, European Commission "Technology Roadmap for Nanoelectronics" November 2000, Luxcapital "Nanotechnology The Nanotech Report: 2001", Red Herring July 17 2000.

### Acknowledgements

Our own work on quantum dots was instigated by Tito Trindade (Universidade Aveiro), principally exploiting carbamate precursors initially developed by Azad Malik, this initial work was ably extended by Mark Green (Oxonica Ltd) and Neerish Revaprasasu (University of Zululand) and is now carried on by the team in the University of Manchester and NanoCo Ltd. Our work has been extensively supported by the EPSRC in the UK and our fruitful collaborations with South Africa have been made possible by the long term support of the Royal Society in London and the NRF in South Africa.

### References

- 1 ALIVISATOS, A. P., *J. Phys. Chem.*, **1996**, 100, 13226.
- 2 GREEN, M., O'BRIEN, P., *Chem Commun.*, **1999**, 2235–2241; PICKETT, N. L., P. O'BRIEN, *The Chemical Record*, **2001**, 1, 467–479; TRINDADE, T., PICKETT, N. L., O'BRIEN, P., *Chem. Mater.*, **2001**, 13, 3843–3858.
- 3 ROGACH, A. L., TALAPIN, D. V., SHEVCHENKO, E. V. et al., *Adv. Funct. Mater.*, **2002**, 12, 653.
- 4 see Q.Dot Corp catalogue available at

- <http://www.qdots.com/new/products/products.html>.
- 5 JONES, A. C., O'BRIEN, P., *The CVD of Compound Semiconducting Materials*, Wiley VCH, Weinheim 1998.
  - 6 CAHN, R. W., *The Coming of Materials Science*, Pergamon Materials Science, Oxford 2001, Ch. 7, p. 256 et seq.
  - 7 for fine examples see the work of BRUS and Schiffrin: KANARAS, A. G., KAMOUNAH, F. S., SCHAUMBURG, K. et al., *Chem. Commun.*, **2002**, 2294; CLARKE, N. Z., WATERS, C., JOHNSON, K. A. et al., *Langmuir*, **2001**, 17, 6048.
  - 8 O'BRIEN, S., BRUS, L., MURRAY, C. B., *J. Am. Chem. Soc.*, **2001**, 123, 12085–12086.
  - 9 HYCON, T., *Chem. Commun.*, **2003**, 927.
  - 10 BRUS, L. E., *J. Chem. Phys.*, **1984**, 80, 4403.
  - 11 Tito Trindade Ph.D. Thesis, Imperial College of Science Technology and Medicine, 1998.
  - 12 ROSSETTI, R., ELLISON, J. L., GIBSON, J. M. et al., *J. Chem. Phys.*, **1984**, 80, 4464.
  - 13 ROSSETTI, R., HULL, R., GIBSON, J. M. et al., *J. Chem. Phys.*, **1985**, 82, 552.
  - 14 HENGLEIN, A., *Chem Rev.*, **1989**, 89, 1861.
  - 15 WELLER, H., *Angew. Chem. Int. Ed. Engl.*, **1993**, 32, 41.
  - 16 WELLER, H., *Adv. Mater.*, **1993**, 5, 88.
  - 17 SPANHEL, L., HAASE, M., WELLER, H. et al., *J. Am. Chem. Soc.*, **1987**, 109, 5649.
  - 18 BARAL, S., FOJTIK, A., WELLER, H. et al., *J. Am. Chem. Soc.*, **1986**, 108, 375.
  - 19 FISCHER, C. H., LILIE, J., WELLER, H. et al., *Ber. Bunsen-Ges. Phys. Chem.*, **1989**, 93, 61.
  - 20 FISHER, C. H., WELLER, H., KATSIKAS, L. et al., *Langmuir*, **1989**, 5, 429.
  - 21 EYCHMULLER, A., KATSIKAS, L., WELLER, H., *Langmuir*, **1990**, 6, 1605.
  - 22 FOJTIK, A., WELLER, H., KOCH, U. et al., *Ber. Bunsen-Ges. Phys. Chem.*, **1984**, 88, 969.
  - 23 WELLER, H., FOJTIK, A., HENGLEIN, A., *Chem. Phys. Lett.*, **1985**, 117, 485.
  - 24 WELLER, H., KOCH, U., GUTIERREZ, M. et al., *Ber. Bunsen-Ges. Phys. Chem.*, **1987**, 91, 88.
  - 25 TALAPIN, D. V., ROGACH, A. L., KORNOWSKI, A. et al., *Nano. Lett.*, **2001**, 1, 207.
  - 26 HÄSSELBARTH, A., EYCHMULLER, A., EICHBERGER et al., *J. Phys. Chem.*, **1993**, 97, 5333.
  - 27 ZHOU, H. S., HONMA, I., KOMIYAMA, H. et al., *J. Phys. Chem.*, **1993**, 97, 895.
  - 28 ZHOU, H. S., SASAHARA, H., HONMA et al., *Chem. Mater.*, **1994**, 6, 1534.
  - 29 EYCHMÜLLER, A., HÄSSELBARTH, A., WELLER, H., *J. Lumin.*, **1992**, 53, 113.
  - 30 KORTAN, A. R., HULL, R., OPILA, R. L. et al., *J. Am. Chem. Soc.*, **1990**, 112, 1327.
  - 31 HOENER, C. F., ALLAN, K. A., BARD, A. J. et al., *J. Phys. Chem.*, **1992**, 96, 3812.
  - 32 EYCHMULLER, A., MEWS, A., WELLER, H., *Chem. Phys. Lett.*, **1993**, 208, 59.
  - 33 MEWS, A., EYCHMULLER, A., GIERSIG, M. et al., *J. Phys. Chem.*, **1994**, 98, 934.
  - 34 MURRAY, C. B., NORRIS, D. J., BAWENDI, M. G., *J. Am. Chem. Soc.*, **1993**, 115, 8706.
  - 35 ALIV, H. T., SHIANG, J. J., KADAVANICH, A. V. et al., *J. Phys. Chem.*, **1995**, 99, 1741.
  - 36 MANNA, L., SCHER, E. C., LI, L.-S. et al., *J. Am. Chem. Soc.*, **2002**, 124, 7136; MANNA, L., SCHER, E. C., ALIVISATOS, A. P., *J. Am. Chem. Soc.*, **2000**, 122, 12700.
  - 37 DABBOUSI, B. O., RODRIGUEZ-VIEJO, J., MIKULEC, F. V. et al., *J. Phys. Chem. B*, **1997**, 101, 9463.
  - 38 PENG, X., SCHLAMP, M. C., KADAVANICH, A. V. et al., *J. Am. Chem. Soc.*, **1997**, 119, 7019.
  - 39 BRENNAN, J. G., SIEGRIST, T., CARROL, P. J. et al., *J. Am. Chem. Soc.*, **1989**, 111, 4141.
  - 40 TRINDADE, T., O'BRIEN, P., *Adv. Mater.*, **1996**, 8, 161.
  - 41 TRINDADE, T., O'BRIEN, P., ZHANG, X., *Chem. Mater.*, **1997**, 9, 523.
  - 42 a) TRINDADE, T., O'BRIEN, P., ZHANG, X. et al., *J. Mater. Chem.*, **1997**, 7, 1011; b) MALIK, M. A., REVAPRASADU, N., O'BRIEN, P., *Chem. Mater.*, **2001**, 13(3); 913–920.
  - 43 TRINDADE, T., MONTEIRO, O. C., O'BRIEN, P. et al., *Polyhedron*, **1999**, 18, 1171.

- 44 LEE, S.-M., JU, Y.-w., CHO, S.-N. et al., *J. Am. Chem. Soc.*, **2002**, 124, 11244.
- 45 CUMBERLAND, S. L., HANIF, K. M., JAVIER, A. et al., *Chem. Mater.*, **2002**, 14, 1576.
- 46 MALIK, M. A., O'BRIEN, P., REVAPRASADU, N., *Chem. Mater.*, **2002**, 14, 2004.
- 47 LAZELL, M. R., O'BRIEN, P., *J. Mater. Chem.*, **1999**, 9, 1381.
- 48 PENG, Z. A., PENG, X., *J. Am. Chem. Soc.*, **2001**, 123, 183; QU, L., PENG, Z. A., PENG, X., *Nanoletters*, **2001**, 333.
- 49 YU, W. W., PENG, X., *Angew. Chem. Int. Ed. Eng.*, **2002**, 41, 2368.
- 50 TRINDADE, T., *Curr. Opin. Solid State Mater. Sci.*, **2002**, 347.
- 51 GUZELIAN, A. A., KATARI, J. E. B., KADAVANICH, A. V. et al., *J. Phys. Chem.*, **1996**, 100, 7212.
- 52 GUZELIAN, A. A., BANIN, U., KADAVANICH, A. V. et al., *Appl. Phys. Lett.*, **1996**, 69, 1432.
- 53 TREECE, R. E., MACALA, G. S., RAO, L. et al., *Inorg. Chem.*, **1993**, 32, 2745.
- 54 KHER, S. S., WELLS, R. L., *Chem. Mater.*, **1994**, 6, 2056.
- 55 WELLS, R. L., AUBUCHON, S. R., KHER, S. S. et al., *Chem. Mater.*, **1995**, 7, 793.
- 56 OLSHAVSKY, M. A., GOLDSTEIN, A. N., ALIVISATOS, A. P., *J. Am. Chem. Soc.*, **1990**, 112, 9438.
- 57 UCHIDA, H., CURTIS, C. J., NOZIK, A. J., *J. Phys. Chem.*, **1991**, 95, 5382.
- 58 BYRNE, E. K., PARKANYI, L. K., THEOPOLD, H., *Science* **1988**, 241, 332.
- 59 DOUGLAS, T., THEOPOLD, K. H., *Inorg. Chem.*, **1991**, 30, 594.
- 60 GOEL, S. C., CHIANG, M. Y., BUHRO, W. E., *J. Am. Chem. Soc.*, **1990**, 112, 5636.
- 61 BUHRO, W. E., *Polyhedron* **1994**, 13, 1131.
- 62 MATCHETT, M. A., VIANO, A. M., ADOLPHI, N. L. et al., *Chem. Mater.*, **1992**, 4, 508.
- 63 GREEN, M., *Curr. Opin. Solid State Mater. Sci.*, **2002**, 355.
- 64 (eds). *Recent Advances in Zeolite Science*, eds. KLINOWSKI, J., BARRIE, P. J., Elsevier, Amsterdam 1990.
- 65 RAJAMATHI, M., SESHADRI, R., *Curr. Opin. Solid State Mater. Sci.*, **2002**, 6, 337.
- 66 ZHAN, J. H., YANG, X. G., ZHANG, W. X. et al., *J. Mater. Res.*, **2000**, 15, 629.
- 67 GAUTAM, U. K., RAJAMATHI, M., MELDRUM, F. et al., *J. Chem. Soc., Chem. Commun.*, **2001**, 629.
- 68 MITCHELL, P. W. D., MORGAN, P. E. D., *J. Am. Ceram. Soc.*, **1974**, 57, 278.
- 69 WANG, W., YAN, P., LIU, F. et al., *J. Mater. Chem.*, **1998**, 8, 2321.
- 70 LI, B., XIE, Y., HUANG, H. et al., *Adv. Mater.*, **1999**, 11, 1456.
- 71 XIAO, J., XIE, Y., XIONG, Y. et al., *J. Mater. Chem.*, **2001**, 11, 1417.
- 72 KOMARNENI, S., D'ARIGO, M. C., LEONELLI, C. et al., *J. Am. Ceram. Soc.*, **1998**, 81, 3041.
- 73 CABAÑAS, A., DARR, J. A., LESTER, E. et al., *J. Chem. Soc., Chem. Commun.*, **2000**, 901-902; CABAÑAS, A., DARR, J. A., LESTER, E. et al., *J. Mater. Chem.*, **2001**, 11, 561-568.
- 74 a) KAITO, C., FUJITA, K., SHIOJIRI, M., *J. Appl. Phys.*, **1996**, 47, 5161; b) KAITO, C., FUJITA, K., SHIOJIRI, M., *J. Crystal Growth*, **1998**, 62, 375; c) KAITO, C., SAITO, Y., *J. Crystal Growth*, **1990**, 99, 743; d) AGATA, M., KURASE, H., HAYASHI, S. et al., *Solid State Commun.*, **1990**, 76, 1061.
- 75 SERCEL, P. C., SAUNDERS, W. A., ATWATER, H. A. et al., *Appl. Phys. Lett.*, **1992**, 61, 696.
- 76 a) SALATA, O. V., DOBSON, P. J., HULL, P. J. et al., *Adv. Mater.*, **1994**, 6, 772; b) SALATA, O. V., DOBSON, P. J., HULL, P. J. et al., *Thin Solid Films*, **1994**, 251, 1.
- 77 PICKETT, N. L., FOSTER, D. F., COLE-HAMILTON, D. J., *J. Mater. Chem.*, **1996**, 6, 507.
- 78 PICKETT, N. L., FOSTER, D. F., COLE-HAMILTON, D. J., *J. Cryst. Growth*, **1997**, 170, 476.
- 79 PICKETT, N. L., LAWSON, S., THOMAS, W. G. et al., *J. Mater. Chem.*, **1998**, 8, 2769.
- 80 WANG, Y., HERRON, N., *J. Phys. Chem.*, **1987**, 91, 257.
- 81 CASSAGNEAU, T., HIX, G. B., JONES, D. J. et al., *J. Mater. Chem.*, **1994**, 4, 189.
- 82 ABE, T., TACHIBANA, Y., UEMATSU, T. et al., *J. Chem. Soc., Chem. Commun.*, **1995**, 1617.
- 83 BRENCHELEY, M. E., WELLER, M. T.,

- Angew. Chem. Int. Ed. Engl.*, **1993**, 32, 1663.
- 84 BLASSE, G., DIRKSEN, C. J., BRENCHLEY, M. E. et al., *Chem. Phys. Lett.*, **1995**, 234, 177.
  - 85 WATZKE, H. J., FENDLER, J. H., *J. Phys. Chem.*, **1987**, 91, 854.
  - 86 STEIGERWALD, M. L., ALIVISATOS, A. P., GIBSON, J. M. et al., *J. Am. Chem. Soc.*, **1988**, 110, 3046.
  - 87 KHAN-LODHI, A., ROBINSON, B. H., TOWEY, T. et al., in *The Structure, Dynamics and Equilibrium Properties of Colloidal Systems*, eds. BLOOR, D. M., WYN-JONES, E., Kluwer Academic Publishers 1990, p. 373.
  - 88 TOWEY, T. F., KHAN-LODI, A., ROBINSON, B. H., *J. Chem. Soc., Faraday Trans.*, **1990**, 86, 3757.
  - 89 KORGEL, B. A., MONBOUQUETTE, G., *J. Phys. Chem.*, **1996**, 100, 346.
  - 90 CHOI, K. M., SHEA, K. J., *J. Phys. Chem.*, **1994**, 98, 3207.
  - 91 CHOI, K. M., SHEA, K. J., *J. Am. Chem. Soc.*, **1994**, 116, 9052.
  - 92 CARPENTER, J. C., LUKEHART, C. M., STOCK, S. R. et al., *Chem. Mater.*, **1995**, 7, 201.
  - 93 WANG, Y., SUNA, A., MAHLER, W. et al., *J. Chem. Phys.*, **1987**, 87, 7315.
  - 94 GAO, M., YANG, Y., YANG, B. et al., *J. Chem. Soc., Chem. Commun.*, **1994**, 2779.
  - 95 NIRMAL, M., MURRAY, C. B., BAWENDI, M. G., *Phys. Rev. B*, **1994**, 50, 2293.
  - 96 TASSONI, R., SCHROCK, R. R., *Chem. Mater.*, **1994**, 6, 744.
  - 97 MOFFITT, M., EISENBERG, A., *Chem. Mater.*, **1995**, 7, 1178.
  - 98 SHINOJIMA, H., YUMOTO, J., UESUGI, N. et al., *Appl. Phys. Lett.*, **1989**, 55, 1519.
  - 99 STEIGERWALD, M. L., ALIVISATOS, A. P., GIBSON, J. M. et al., *J. Am. Chem. Soc.*, **1988**, 110, 3046.
  - 100 STUCZYNSKI, S. M., BRENNAN, J. G., STEIGERWALD, M. L., *Inorg. Chem.*, **1989**, 28, 4431.
  - 101 THAYER, A. M., STEIGERWALD, M. L., DUNCAN, T. M. et al., *Phys. Rev. Lett.*, **1988**, 60, 2673.
  - 102 WONG, K. K. W., MANN, S., *Adv. Mater.*, **1996**, 8, 928.
  - 103 MACKLE, P., CHARNOCK, J. M., GARNER, C. D. et al., *J. Am. Chem. Soc.*, **1993**, 115, 8471.
  - 104 MELDRUM, F. C., HEYWOOD, B. R., MANN, S., *Science* **1992**, 257, 522.

## 3

## Moving Nanoparticles Around: Phase-Transfer Processes in Nanomaterials Synthesis

*M. Sastry*

## 3.1

### Introduction

We are witnessing impressive advances in understanding the unusual physico-chemical and optoelectronic properties of nanomaterials, their synthesis, assembly and packaging for commercial application [1]. One important area of nanotechnology is concerned with the development of reliable processes for the synthesis of nanomaterials over a range of sizes (with good monodispersity) and chemical compositions. Realizing that shape anisotropy could lead to interesting variation in the electronic and catalytic properties of nanoparticles [2, 3], much current research is directed towards development of experimental methods for the synthesis of nanoparticles of varying shapes. Nanorods and nanowires of silver [4, 5]/gold [6–12]/Au-core–Ag-shell [13]/CdSe [14]/tungsten sulfide [15], nanoprisms of silver [16]/gold [17, 18] and CdS [19] are some of the exotic nanocrystalline shapes that may be routinely synthesized in the laboratory today. From a fundamental angle, the ability to control the shape of nanocrystals is particularly exciting and has led to the first observation of two distinct quadrupole plasmon resonance modes in silver nanoprisms [16]. The need to develop eco-friendly synthesis protocols that do away with the use of toxic chemicals has also fuelled research in this direction and bio-related processes that use microorganisms such as bacteria [20–23], fungi [24–27] and actinomycete [28] have been developed to grow nanocrystals of silver and gold both inside and outside the biomass.

Gold nanoparticles have, in particular, been the subject of considerable attention over the ages and enjoy an interesting history dating back to the pioneering work of Faraday on the synthesis of gold hydrosols (gold nanoparticles dispersed in water) [29]. Gold nanoparticles find application in a variety of fields such as catalysis [30], as electron microscopy markers [31] and in DNA sequence determination. It is of little surprise, therefore, that there are many recipes for the synthesis of gold nanoparticles over a range of sizes in an aqueous environment. The procedures for synthesis of gold hydrosols include, (1) reduction of aqueous chloroaurate ions by a variety of reducing agents such as citric acid [33], sodium borohydride [34], and alkaline tetrakis(hydroxymethyl)phosphonium chloride [35]; (2)



radiation-induced reduction of gold ions [36, 37] and (3) sonochemical reduction of gold ions [38], to name just a few. The interested reader is directed to a comprehensive review by Handley that lists at least one dozen protocols for the syntheses of gold hydrosols with particle sizes in the range 10–640 Å.

The synthesis of gold nanoparticles in non-polar organic media is a considerably newer area of research whose origin may be traced to the seminal work of Brust and co-workers [39]. In this report, the authors have demonstrated the phase transfer of chloroaurate ions into toluene using a phase transfer molecule such as tetra-alkylammonium bromide. Thereafter, the gold ions were reduced using sodium borohydride to yield gold nanoparticles of excellent monodispersity capped with alkanethiol molecules. Analogous to the formation of self-assembled monolayers (SAMs) of alkanethiols on gold thin films [40], Brust and co-workers used thiolate chemistry to cap the gold nanoparticles with alkanethiols present in the organic phase during phase transfer and reduction of the gold ions, thus rendering them hydrophobic and soluble in the organic phase [39]. Such surfactant-stabilized gold nanoparticles behave like new compounds and can be easily separated out of solution in the form of a powder and re-dissolved in different organic solvents without significant variation in the particle size distribution. The Brust report has been rapidly followed by publications on the self-assembly on gold and silver nanoparticle surfaces of alkanethiol [41, 42], aromatic thiol [43, 44], alkylamine [45, 46], dialkyl disulfide [47] and thiolated cyclodextrin [48, 49] molecules. Very recently, we have shown in my group that the Brust protocol for the synthesis of hydrophobic metal nanoparticles may be considerably simplified by using a multifunctional molecule, 4-hexadecylaniline [50]. This molecule plays the role of a phase-transfer molecule, reducing and capping agent and results in the one-step synthesis of hydrophobic gold [50] and platinum nanoparticles [51] in a variety of organic solvents. The surface properties of the gold colloids may be tailored by chemisorption of terminally functionalized thiol molecules resulting in a number of interesting applications. One of the exciting areas of research using functionalized colloidal gold particles is the study of the reactivity of monolayer protected colloidal particles (or MPCs as they are termed) [52, 53]. Using a simple place-exchange reaction strategy, Murray and co-workers have demonstrated that alkanethiol derivatized colloidal gold particles in an organic solvent can be poly- $\omega$ -functionalized [54]. This led to the possibility of using the poly-heterofunctionalized colloidal particles as “nanofactories” where the metal core scaffolds support complex organic ligand structures that may include polymeric and hyperbranched domains [54]. Polar terminal functional groups such as carboxylic acid, ammonium ions, sulfonic acid etc. in the monolayers chemisorbed onto the gold particle surface may be used to increase the solubility of the particles in polar solvents such as water, thus enabling the synthesis of water-soluble gold nanoparticles that, like their hydrophobic counterparts, may be dried in the form of a powder and re-dispersed in water and other polar solvents without significant degradation in the particle size and monodispersity [55–57].

The two main approaches for the synthesis of gold nanoparticles, viz. synthesis in water and in non-polar organic solvents, have certain pros and cons that are enumerated below.

### 3.2

#### Water-Based Gold Nanoparticle Synthesis

##### 3.2.1

##### Advantages

1. Water is a good solvent for a number of metal ions as well as a variety of capping molecules. The synthesis involves preparation of an aqueous gold salt solution followed by reduction of the metal ions in a single step. It is therefore considerably simpler than the multi-step Brust protocol [39].
2. No additional stabilization against aggregation of the gold nanoparticles is required – surface bound ions (citrate ions, chloroaurate ions etc.) normally stabilize the nanoparticles electrostatically in solution.
3. Electrostatic layer-by-layer assembly involving, for example, oppositely charged polyelectrolytes/surfactants and nanoparticles may be readily accomplished on suitably functionalized surfaces [58–61].
4. Nanoparticle shape control can be easily effected by using self-assembled structures such as micelles (arising due to spontaneous assembly of suitable surfactants in water) as templates [4–6].
5. Perhaps the biggest advantage of a water-based synthesis procedure is that bioconjugation of the gold and other metal/semiconductor nanoparticles with DNA [32], enzymes [62], antibodies [63] etc. may be easily accomplished.

##### 3.2.2

##### Disadvantages

1. Ionic interactions limit the concentration of metal/semiconductor nanoparticles in the aqueous phase to very dilute levels, a big drawback in biological labeling of the nanoparticles.
2. Control over the particle size and monodispersity in a particular reduction protocol is not very good.
3. The gold nanoparticles do not spontaneously assemble into a close-packed hexagonal arrangement on solvent evaporation.
4. The nanoparticles synthesized in water are not easily separated from solution in the form of a powder that would be readily re-dispersible in water after storage [55–57].

### 3.3

#### Organic Solution-Based Synthesis of Gold Nanoparticles

##### 3.3.1

##### Advantages

1. High degree of control may be exercised over the gold nanoparticle size, monodispersity [34] and chemical nature of the nanoparticle surface (via capping with terminally functionalized thiols, amines, amino acids etc.) [39, 41–57].

2. High concentrations of the gold nanoparticles in solution may be easily prepared.
3. Functionalized gold nanoparticles may be stored as a powder without sintering and irreversible aggregation of the particles.
4. The nanoparticles spontaneously assemble into close-packed, hexagonal monolayers upon solvent evaporation [39, 41, 42, 45, 46]. The collective properties of the nanoparticle assembly may be controlled by varying the interparticle separation via capping with different chain length alkanethiols.

### 3.3.2

#### Disadvantages

1. The procedure is a multi-step one involving, independently, phase transfer of the gold ions followed by their reduction and capping.
2. While close-packed monolayers of the gold nanoparticles may be deposited by solvent evaporation, there is little control over the process of assembly. Furthermore, superlattices of the gold nanoparticles cannot be readily deposited, in contrast with the layer-by-layer assembly that is possible for electrostatically stabilized gold nanoparticles in water.
3. Formation of bioconjugates with the gold nanoparticles is not possible in an organic environment and consequently, biological application of gold nanoparticles becomes difficult.

It is clear that both methods for the synthesis of gold nanoparticles have characteristic advantages. Depending on the particular application of the nanoparticles, the ideal condition would be to somehow marry the two methods and thus maximize their advantages. This may conveniently be done by effecting a *phase transfer* of gold nanoparticles synthesized in one medium (water/organic solvent) to the second medium (organic solvent/water). In addition to maximizing the benefits accruing from a combination of the two syntheses methods, the ability to move nanoparticles across liquid interfaces into environments of specific physicochemical properties to probe, for example, variation in the optical properties of the nanoparticle solution [64] is an attractive feature of phase-transfer protocols. In the remaining part of this chapter, I discuss some of the methods developed to carry out the phase transfer of gold nanoparticles in both directions. The experimental methods are quite general and may be extended to other chemical compositions such as metal sulfide nanoparticles. Examples will also be given wherever possible.

## 3.4

### Moving Gold Nanoparticles Around

#### 3.4.1

##### Phase Transfer of Aqueous Gold Nanoparticles to Non-Polar Organic Solvents

The movement of aqueous gold nanoparticles into non-polar organic solvents requires hydrophobization of the nanoparticles. The many techniques developed to

accomplish phase transfer into organic solvents essentially differ in the nature of the capping molecule employed to hydrophobize the nanoparticles. Possibly the first report on the phase transfer of gold nanoparticles from water to an organic solvent such as butyl acetate was that of Underwood and Mulvaney [64]. In this study, the authors showed that aqueous gold nanoparticles synthesized by the Turkevich method [33] could be quantitatively transferred into butyl acetate by complexation of the particles with a 'comb stabilizer' present in the organic phase [64]. The comb stabilizer used was a co-polymer consisting of a backbone of methyl methacrylate and glycidyl methacrylate with poly(12-hydroxystearic acid) as pendant side chains. Gentle shaking of a biphasic mixture of the gold hydrosol and comb stabilizer in butyl acetate resulted in the emulsification of the gold hydrosol–butyl acetate mixture, this process accelerating the complexation of the polymer with the gold nanoparticle surface. The gold nanoparticles were thereby hydrophobized and were phase transferred to the organic phase. Gold sols possess a lovely pink to ruby red color [64] and therefore, the phase transfer of the gold particles from one phase to another is seen as a dramatic transfer of color between phases.

The focus of the work of Underwood and Mulvaney was to study changes in the optical properties of gold colloids as the refractive index of the organic solution was varied. This was done by preparing the gold sols in solutions consisting of mixtures of butyl acetate and  $\text{CS}_2$  to obtain solutions possessing refractive indices in the range 1.336 (water) to 1.583. Figure 3.1 shows pictures of gold nanoparticles in the different butyl acetate– $\text{CS}_2$  solutions [64]. A clear variation in color with refractive index of the solution is seen and is in quantitative agreement with the Mie theory that is used to understand the optical properties of colloidal solutions [64]. The authors did not perform a detailed characterization of the polymer–gold nanoparticle complex and therefore, little is known of the interaction of the polymer with the particle surface etc.

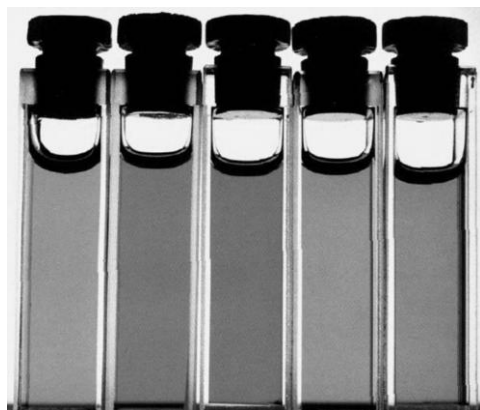


**Fig. 3.1.** Photograph of five sols of colloidal gold prepared in water and in mixtures of butyl acetate and  $\text{CS}_2$ . Refractive indices of the solutions at the absorption band maximum are 1.336, 1.407, 1.481, 1.525 and 1.583 ( $\pm 0.004$ ) respectively. (Reprinted with permission from [64], © 1994, American Chemical Society).

Recognizing that the strong interaction of alkanethiol molecules with gold nanoparticles may be used to hydrophobize gold nanoparticles at the liquid–liquid interface, Rao and co-workers have demonstrated the acid-facilitated phase transfer of aqueous gold and indeed, platinum and silver nanoparticles into organic solvents such as toluene [65, 66]. In a typical experiment, the authors took a mixture of a gold hydrosol and dodecanethiol in toluene. To this biphasic mixture, concentrated HCl was added under stirring. A swift movement of the gold nanoparticles into the organic phase containing the gold nanoparticles was observed, indicating capping of the metal nanoparticles with alkanethiol molecules [65, 66]. The alkanethiol-stabilized colloidal gold, silver and platinum particles transferred to toluene as described above could be self-assembled by solvent evaporation on different substrates yielding close-packed, hexagonal arrays of the nanoparticles [65, 66]. A concentrated solution of the different sized thiol stabilized-gold particles was placed on glass substrates and the particles assembled on the surface. Figure 3.2 shows X-ray diffraction patterns from the different films, the size of the particles is indicated next to the corresponding diffractogram.

The  $d$ -spacings obtained from the low angle peaks (indicated by arrows in Figure 3.2) are also listed in the figure. The low angle diffraction peaks arise from the arrangement of the gold particles in the array formed by solvent evaporation. It is observed that the separation between the clusters decreases as the size of the particles is reduced (Figure 3.2), in accordance with nanoparticle packing considerations. However, the  $d$ -spacing is smaller than that expected from the core + surfactant size considerations indicating some degree of interdigitation of the hydrocarbon chains from neighboring particles in the array [66]. The inset of Figure 3.2 shows the optical absorption spectra recorded from the colloidal gold particles in toluene for gold particles of different sizes. The surface plasmon resonance from the colloidal gold particles centered around 525 nm is clearly seen for the 4.2 nm and 2.1 nm sized particles and the intensity of the resonance is higher for the larger sized particles (Figure 3.2, inset). The resonance could not be detected for the smallest size particles (1.0 nm diameter) and this was attributed to the possibility of the gold particles in this size range being non-metallic [66].

Transmission electron microscopy images recorded from the self-assembled gold nanoparticle monolayer obtained by solvent evaporation are shown in Figure 3.3 [66]. It can be seen that the thiol-derivatized gold nanoparticles self-assemble into nanocrystalline arrays over tens of nanometer length scale. The spacing between the particles is highly regular and roughly 1 nm between the particles. While the larger particles of mean diameter 4.2 nm assembled into regular, close-packed domains, assemblies of smaller particles show a large fraction of voids within the domains [66].

It is known that alkylamine molecules also bind to gold nanoparticles quite strongly through a ‘weak’ covalent bond, as described by Leff, Brandt and Heath [45]. Using a process similar to that adopted for phase transfer of gold nanoparticles with alkanethiols, we have recently demonstrated that octadecylamine molecules present in the organic phase may be used to accomplish the phase transfer of aqueous gold nanoparticles into toluene [67]. Vigorous stirring of a bi-

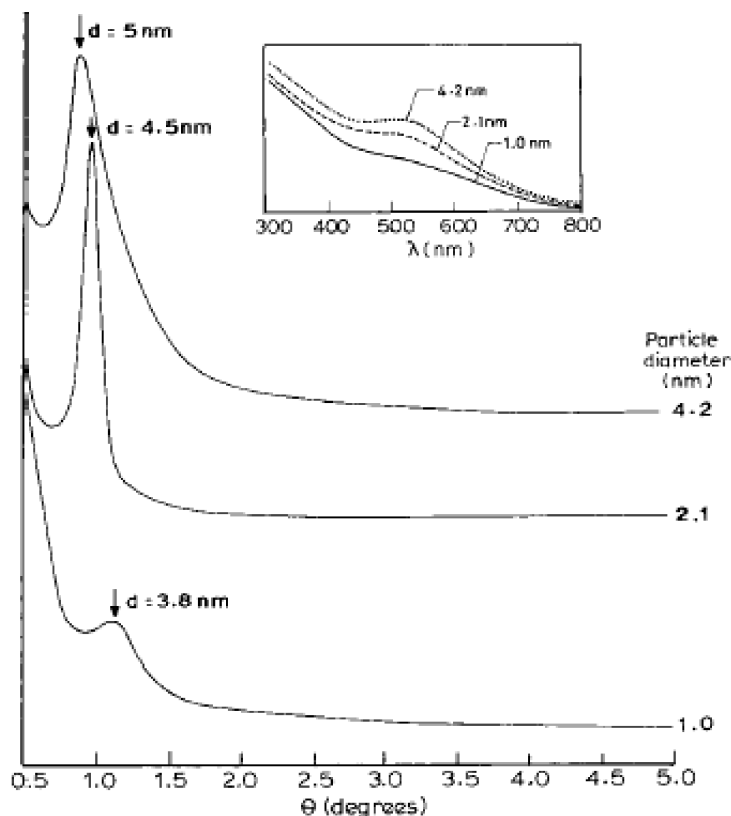


**Fig. 3.2.** XRD patterns from the nanocrystalline arrays of Au particles of different mean diameters (4.2, 2.1, and 1.0 nm). Inset of the figure displays the UV-vis spectra of these particles. (Reprinted with permission from [66], © 1997, American Chemical Society).

phasic mixture containing the gold hydrosol and octadecylamine (ODA) molecules in toluene resulted in the rapid transfer of gold nanoparticles into the organic phase without the use of acid. This is clearly demonstrated in Figure 3.4A that shows a picture of two test-tubes with the biphasic mixture before (test-tube to the right) and after shaking (test-tube to the left). The transfer of the red color from the lower, aqueous phase to the upper, toluene phase is clearly illustrated. UV-vis spectra recorded from the gold hydrosol before (curve 3) and after (curve 1) phase transfer are shown along with the toluene phase after phase transfer (curve 2 in Figure 3.4B). The almost complete disappearance of the gold nanoparticle plasmon resonance in curve 1 indicates facile phase transfer of the gold nanoparticles into toluene. The UV-vis spectrum recorded from the toluene phase after phase transfer of the gold nanoparticles (curve 2) shows a fairly sharp plasmon resonance from the nanoparticles, indicating little aggregation of the particles. Clearly, during

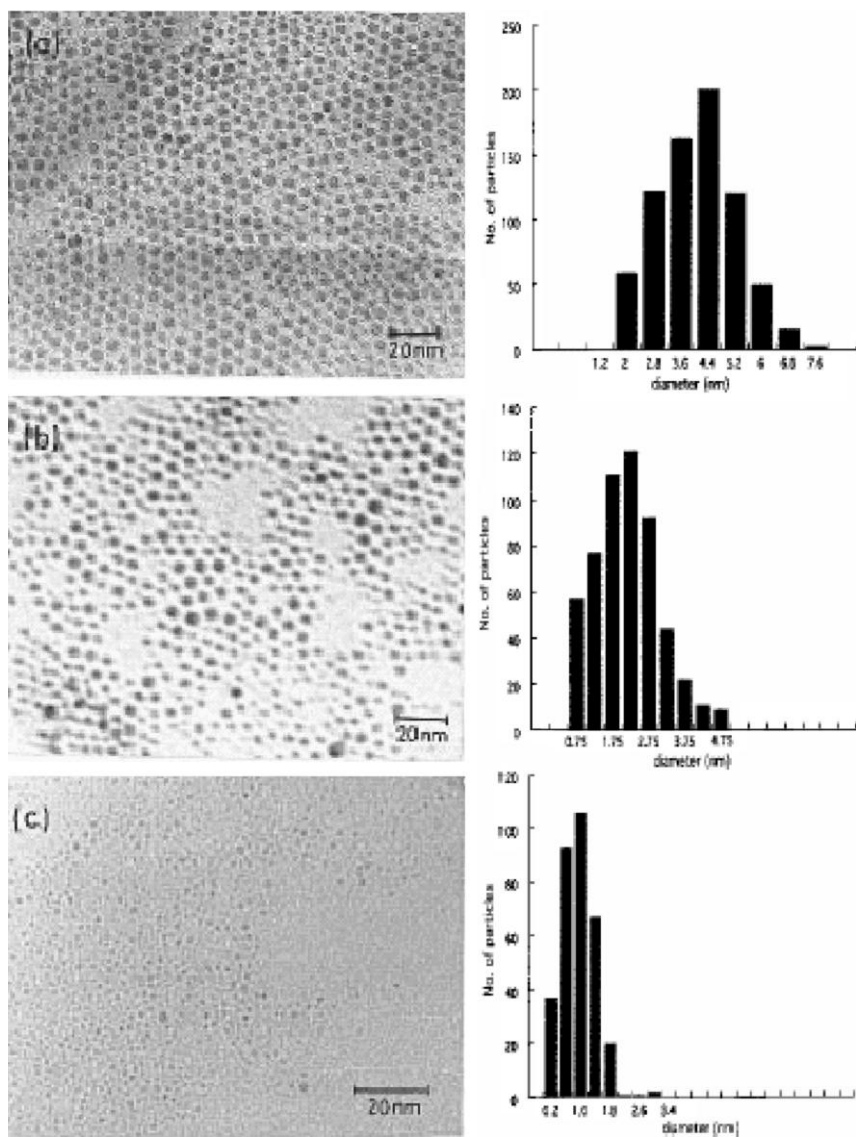


**Fig. 3.3.** TEM images of the thiol derivatized Au nanoparticles. The particle size distributions are shown in the form of histograms alongside the TEM images. The nanoparticles in (a), (b), and (c) were obtained by using 2.2,

2.0, and 1.8 mL of the 25 mM HAuCl<sub>4</sub> solution, respectively. (Reprinted with permission from [66], © 1997, American Chemical Society).

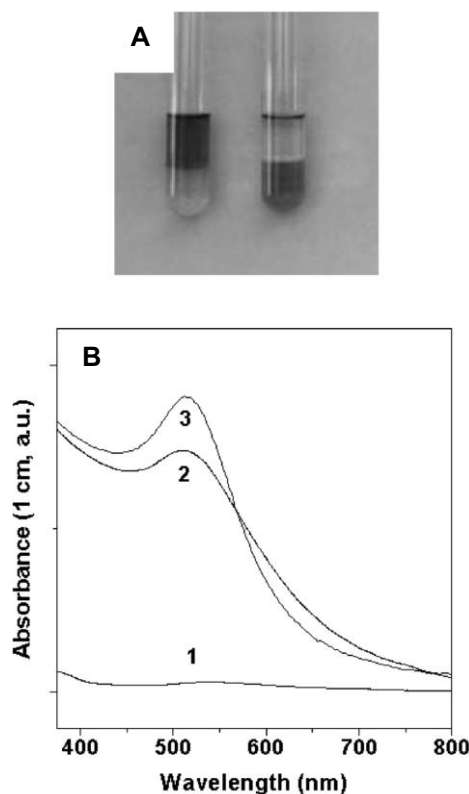


**Fig. 3.4.** (A) Picture showing the two-phase gold hydrosol–ODA containing toluene layers before (test tube on the right) and after (test tube on the left) phase transfer of the gold particles into toluene. (B) UV–vis spectra recorded from the toluene phase (curve 2) and

the aqueous phase before (curve 3) and after (curve 1) phase transfer of the gold colloidal particles into toluene (Figure 3.4A, solutions taken from the test tube on the right).

(Reprinted with permission from [67], © 2001, Elsevier Science).

stirring of the biphasic mixture, the ODA molecules bind to the gold nanoparticles, thereby rendering them hydrophobic and dispersible in the organic phase. The ODA-capped gold nanoparticles could be separated in the form of a dry powder by rotary evaporation of the toluene phase and could be readily redispersed in organic solvents such as chloroform, benzene, carbon tetrachloride etc. [67].

A drop of the toluene phase with the ODA-capped gold nanoparticles was placed on a TEM grid and analyzed after solvent evaporation. Figure 3.5 shows the image obtained wherein a well ordered hexagonal, close-packed configuration of gold nanoparticles can be seen. The ordered domains are not particularly large due to the fact that the monodispersity of the gold particles in the aqueous phase was ca. 15%. It is interesting to observe the separation of the gold nanoparticles into domains based on their size (Figure 3.5).



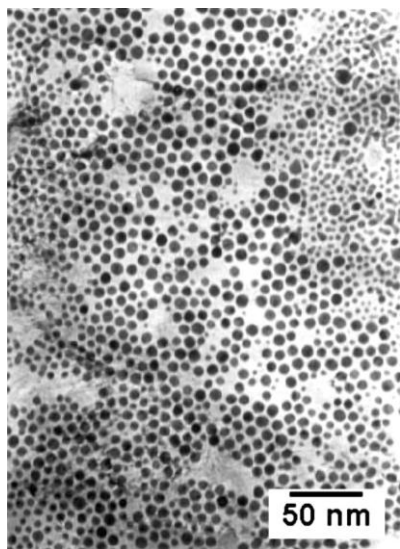


**Fig. 3.5.** TEM micrograph of gold nanoparticles phase transferred into toluene by complexation with ODA molecules and self-assembled by solvent evaporation.

Cyclodextrins (CDs), which are cyclic oligosaccharides consisting of six, seven or eight glucopyranose units ( $\alpha$ -,  $\beta$ - and  $\gamma$ -CDs respectively), are versatile host molecules for 'guests' such as alkanethiols, forming what are known as 'inclusion complexes'. Inclusion complexes of CD and alkanethiols in water have been self-assembled on gold thin films [68] as well as on gold nanoparticles [69]. We have shown recently that gold nanoparticles may be capped with octadecanethiol (ODT) molecules threaded with cyclodextrin and, furthermore, that during vigorous shaking of a biphasic mixture of this hydrosol with chloroform, the gold nanoparticles were rapidly transferred to the organic phase [70]. The inset of Figure 3.6 shows the test tubes before (test tube to the left) and after (test tube to the right) phase transfer of gold nanoparticles capped with inclusion complexes of ODT and CD into chloroform. The process of phase transfer proceeds via detachment of the CD molecules from the alkanethiol molecules capping the gold nanoparticles during stirring of the biphasic mixture. The gold nanoparticles become sufficiently hydrophobic at this stage and are phase transferred into chloroform. The schematics accompanying the picture illustrate the changes occurring in the monolayer of ODT on the surface of the gold nanoparticles during the shaking process leading to hydrophobization of the gold nanoparticles [70].

Just as in the case of gold nanoparticles, appropriate choice of the capping agent for modification of the surface of nanoparticles may be used to accomplish the phase transfer of aqueous silver nanoparticles. Wang, Efrima and Regev have shown that silver nanoparticles can be phase transferred from water to organic solvents by binding the nanoparticles to sodium oleate present in cyclohexane/

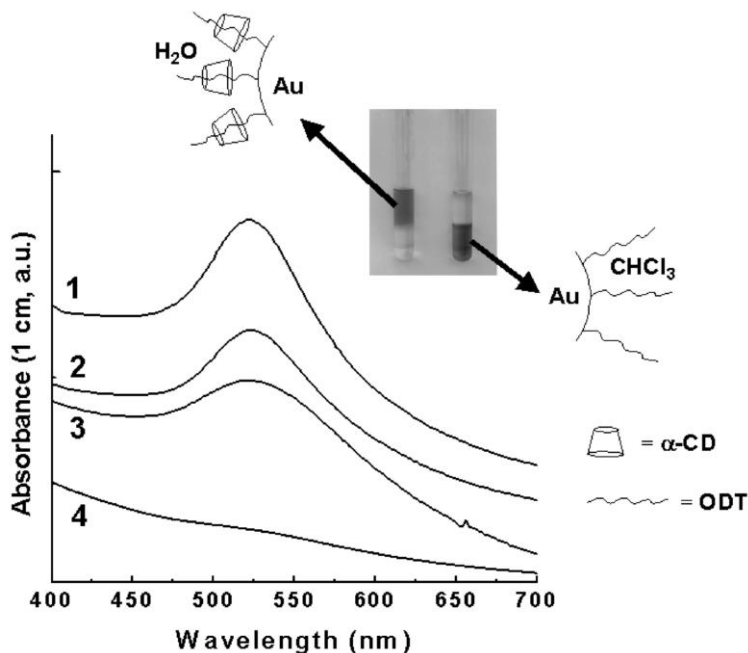


**Fig. 3.6.** UV-vis spectra recorded from the as-prepared gold colloidal solution (curve 1), the gold colloidal solution after capping with  $\alpha$ -CD threaded ODT molecules (curve 2), the chloroform solution after phase transfer of the gold nanoparticles (curve 3), and the aqueous gold colloidal solution after phase transfer of the gold nanoparticles into chloroform (curve 4). The inset is a picture of test tubes containing

solutions of chloroform and  $\alpha$ -CD threaded ODT-capped gold hydrosol before (test tube on the left) and after phase transfer of the gold nanoparticles into chloroform (test tube on the right). The cartoons illustrate the nature of surface modification of the gold nanoparticles in the aqueous phase and in the organic phase. (Reprinted with permission from [70], © 2001, American Chemical Society).

dodecane [71]. Similar to the acid-facilitated phase transfer of gold nanoparticles using alkanethiols [65, 66], the phase transfer of silver particles occurs when a small amount of orthophosphoric/perchloric acid is added to the reaction medium [71]. As observed by other workers, the silver particles assembled into large domains of hexagonally packed nanoparticles [71]. What is interesting about this study is the change in conformation of the surface-bound oleate ions on transfer between the two phases. From FTIR studies, the authors inferred the presence of carboxylate ions on the surface of the silver particles in water that, upon phase transfer into the organic solvent, reversed direction to expose the hydrophobic tails of the oleate molecules towards the solvent. Detailed studies of the position of the double bond in the capping molecule in relation to the carboxylate ions indicated that this factor was crucial for efficient phase transfer of the silver nanoparticles [71].

There is much interest in the synthesis and electronic application of semiconductor nanoparticles, or quantum dots as they are more popularly known [72]. It

is well known that thiols bind to quantum dots of CdS and, therefore, it should be possible to phase transfer aqueous CdS nanoparticles into organic solutions by complexation with alkanethiols and this has been demonstrated by us [73]. The experimental conditions for phase transfer of aqueous CdS into toluene containing octadecanethiol were slightly more stringent than those used for phase transfer of gold nanoparticles. It was observed that pre-formed CdS nanoparticles upon complexation with octadecanethiol molecules at the liquid–liquid interface assembled at the interface and were not transferred to the organic phase [73]. Bubbling  $H_2S$  gas in a biphasic mixture of aqueous  $CdCl_2$  solution and petroleum ether containing octadecanethiol during vigorous stirring resulted in the formation of nanoparticles of CdS capped with the thiol molecules that were rapidly transferred to the organic phase (Figure 3.7A) [73]. The CdS nanoparticle powder was extremely stable and could be readily redispersed in a number of organic solvents such as

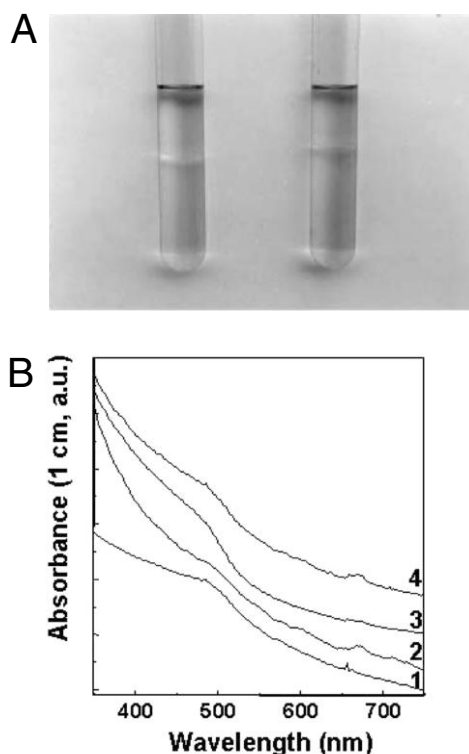


**Fig. 3.7.** (A) Picture showing test tubes containing the biphasic mixture of aqueous CdS and ODT in petroleum ether before (test tube on the left) and after (test tube on the right) phase transfer of the CdS nanoparticles into the organic phase. (B) UV–vis spectra recorded from CdS nanoparticles dispersed in

different solvents. Curve 1: as-prepared CdS nanoparticle solution in water; curve 2: ODT-stabilized CdS nanoparticles in toluene; curve 3: ODT-stabilized CdS in chloroform and curve 4: ODT-stabilized CdS in benzene. (Reprinted with permission from [73], © 2001, American Chemical Society).

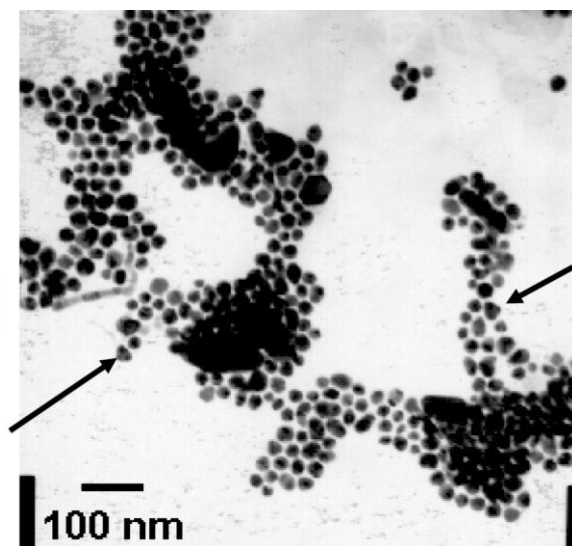


**Fig. 3.8.** TEM picture of CdS quantum dots capped with octadecanethiol molecules and phase transferred into petroleum ether. The arrows in the figure identify some triangular shaped CdS nanoparticles.

chloroform, benzene and toluene without any indication of sintering of the particles (Figure 3.7B) [73]. In the UV-vis spectra of hydrophobized CdS in the different solvents, the onset of absorption occurs at 475 nm and corresponds to a particle size of ca. 6 nm. This size is in good agreement with that determined from TEM studies of CdS nanoparticles transferred into petroleum ether (Figure 3.8). A fairly regular close-packed assembly of the CdS quantum dots can be observed in the TEM micrograph. A number of triangular CdS nanoparticles can also be seen in the figure (identified by arrows).

#### 3.4.2

##### **Transfer of Organically Soluble Gold Nanoparticles to Water**

While many different procedures have been developed for the transfer of aqueous gold nanoparticles into organic solvents, the number of reports on the phase transfer of gold nanoparticles in the reverse direction is much smaller. The key step is to replace the hydrophobic groups bound to the gold nanoparticle surface with polar functional groups, thus rendering the nanoparticles water-soluble. Rotello and co-workers used a place exchange mechanism to functionalize alkanethiol-capped organically soluble gold nanoparticles with carboxylic acid groups [74]. The process is illustrated in Figure 3.9 which depicts replacement of octanethiol molecules bound to the surface of 2 nm diameter gold nanoparticles by 11-thioundecanoic acid. Under the experimental conditions adopted by Rotello et al.,

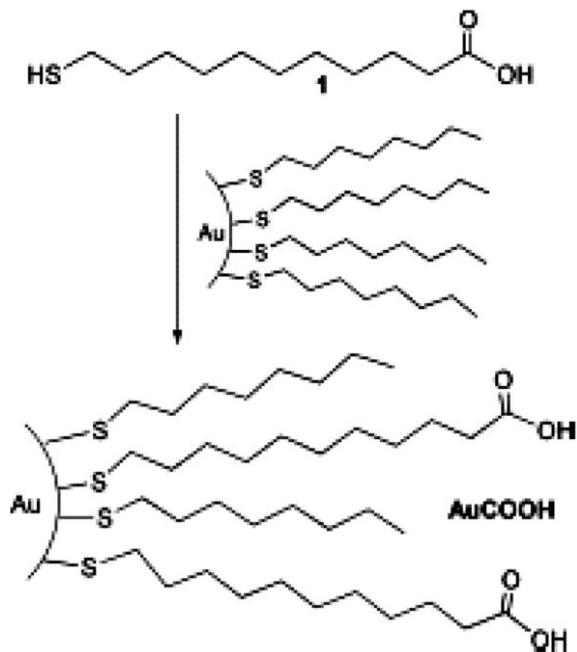


**Fig. 3.9.** Schematic showing the place exchange of octanethiol molecules on the surface of gold nanoparticles by  $\omega$ -thiol carboxylic acid molecules. (Reprinted with permission from [74], © 2000, Royal Society of Chemistry).

the ratio of  $\omega$ -thiol carboxylic acid:octanethiol on the gold nanoparticle surface after place exchange was found to be 1:1. The carboxylic acid derivatized gold nanoparticles were washed with dichloromethane and were found to be soluble in water. One advantage of using carboxylic acid functionality to render the gold nanoparticles water-soluble is that the charge on the nanoparticle surface can be modulated by varying the pH of the gold colloidal solution. Interesting variation in the optical properties of carboxylic acid derivatized gold [44] and silver nanoparticles [75] as a function of solution pH have been studied by us earlier. Rotello and co-workers have shown that as the pH of the gold colloidal solution was reduced below 7, the particles aggregated into close-packed assemblies, the size of the aggregates being largest at the lowest pH value (Figure 3.10).

A more direct method for the phase transfer of gold nanoparticles into water along the lines discussed earlier for phase transfer of aqueous particles into organic solvents involving a biphasic mixture has been demonstrated by Gittins and Caruso [76]. More specifically, Gittins and Caruso showed that gold and palladium nanoparticles synthesized in toluene by the Brust method and stabilized by tetraalkyl ammonium salts could be rapidly and completely phase transferred to water by addition of an aqueous 0.1 M 4-dimethylaminopyridine (DMAP) solution to aliquots of the gold nanoparticles in toluene. As in previous studies (Figures

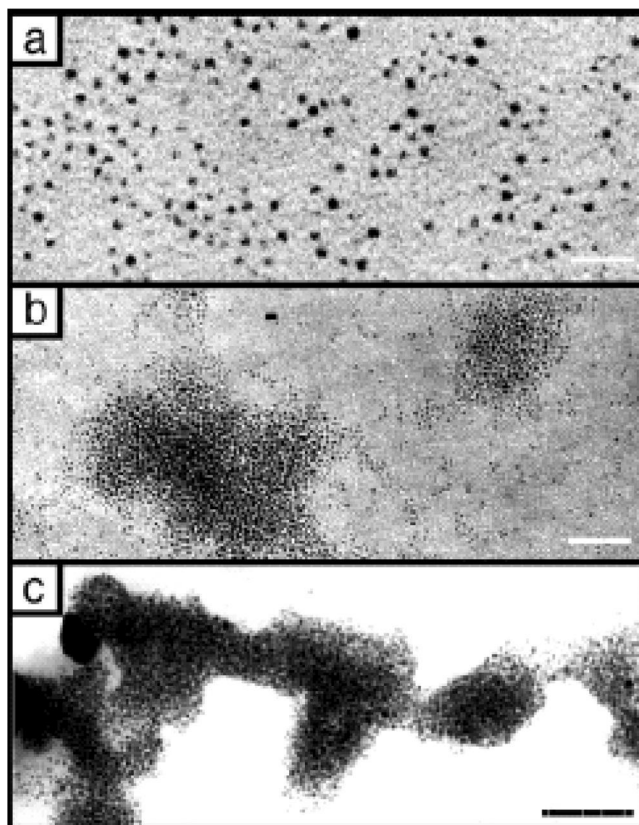


**Fig. 3.10.** TEM micrographs of  $\omega$ -thiol carboxylic acid functionalized gold colloid at (a) pH 10, (b) pH 7, and (c) pH 4. Scale bars represent 10 nm, 25 nm and 50 nm, respectively. (Reprinted with permission from [74], © 2000, Royal Society of Chemistry).

3.4 and 3.6), the process of phase transfer is seen as a transfer of color from the organic phase to the aqueous phase. That the movement of the gold particles between phases was almost 100% can be observed from the UV-vis spectra recorded from toluene before phase transfer (full line, Figure 3.11) and water after phase transfer (dashed line, Figure 3.11). The UV-vis spectra recorded from the two phases are almost identical. There is little broadening of the surface plasmon resonance after phase transfer, indicating no aggregation of the nanoparticles consequent to their movement [76]. The authors have shown that the aqueous gold and palladium solutions were extremely stable with no sign of degradation even after storage for several months [76]. This is graphically illustrated in the TEM micrographs recorded from the gold nanoparticles in the toluene phase (Figure 3.12A) and the aqueous phase one month after phase transfer of the gold nanoparticles

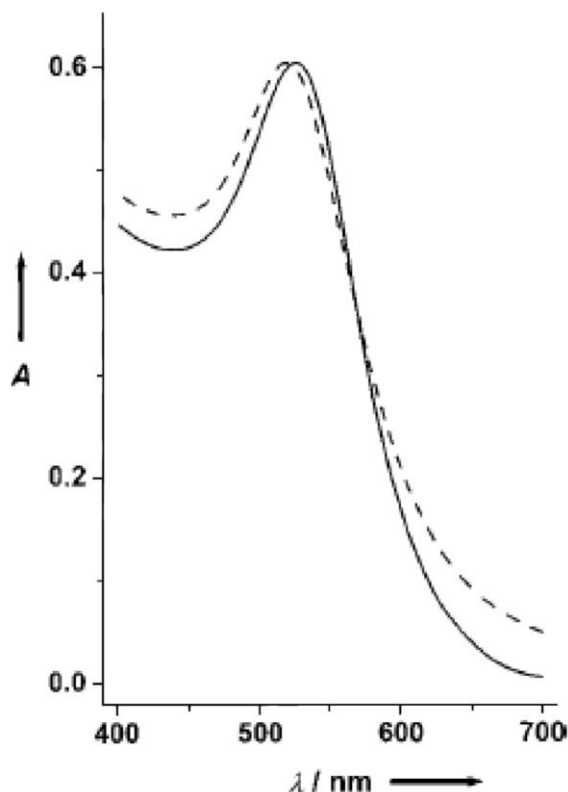


**Fig. 3.11.** UV-vis spectra of a diluted solution of gold nanoparticles in toluene (solid line) and the same sample transferred into an equal volume of 0.1 M DMAP solution at pH 10.5 (dashed line). (Reprinted with permission from [76], © 2001, WILEY-VCH Verlag GmbH).

(Figure 3.12B). A comparison of the two TEM pictures shows that little sintering/aggregation of the gold nanoparticles had occurred after one month of storage.

Gittins and Caruso have speculated on the mode of binding of the DMAP molecules on the gold nanoparticle surface during the phase-transfer process [76]. Based on a series of control experiments, they have proposed a mechanism for the phase transfer as illustrated in Figure 3.13.

Addition of an aqueous DMAP solution to the nanoparticle dispersion in toluene leads to partitioning of the DMAP molecules across the toluene/water boundary as shown in Figure 3.13. The DMAP molecules replace the tetraalkyl ammonium salts and form a labile donor-acceptor complex with the gold atoms on the surface of the nanoparticles through the endocyclic nitrogen atoms. The surface charge on the gold nanoparticles that stabilizes the particles in water arises due to partial



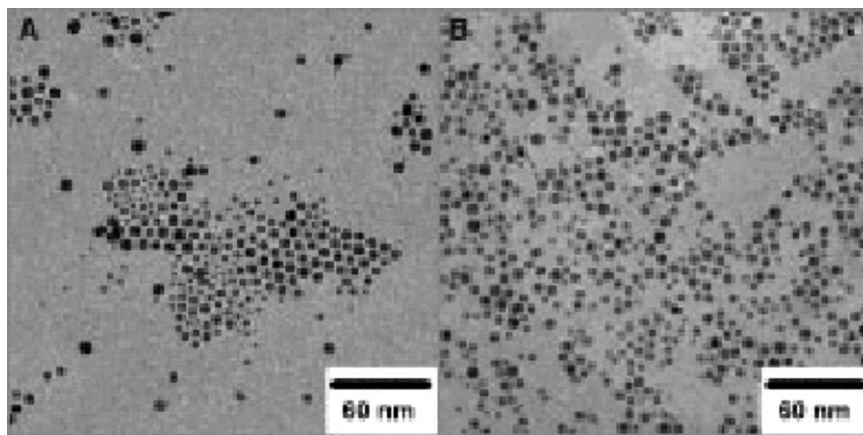


**Fig. 3.12.** Transmission electron micrographs of gold nanoparticles synthesized in toluene (A) and the same sample 1 month after being transferred into water by the addition of DMAP (B). (Reprinted with permission from [76], © 2001, WILEY-VCH Verlag GmbH).

protonation of the exocyclic nitrogens that extend away from the nanoparticle surface towards the solvent (Figure 3.13).

Gittins and Caruso have developed their approach and recently demonstrated the phase transfer of silver, gold, platinum and palladium nanoparticles using a number of exchanging ligands such as mercaptoundecanoic acid (MUA), mecapto-succinic acid etc. [77]. A highlight of the work was the non-specific bioconjugation of the protein, bovine serum albumin (BSA) with MUA-functionalized gold nanoparticles, possibly through electrostatic and hydrogen bonding interactions between the protein and the ionized carboxylate ions on the nanoparticle surface [77].

In a completely different approach, interdigitated bilayers have been used to transfer gold nanoparticles present in non-polar organic solvents to water [78]. Dodecylamine-capped gold nanoparticles dispersed in chloroform were vigorously stirred with an aqueous solution containing the water-soluble surfactant cetyltrimethylammonium bromide (CTAB). During the stirring process, a secondary interdigitated monolayer of CTAB forms on the existing dodecylamine monolayer in contact with the gold nanoparticle surface. This results in significant hydrophilicity of the gold nanoparticles and a consequent phase transfer to the aqueous phase [78].

In conclusion, I have tried to outline the advantages of carrying out the phase transfer of inorganic nanoparticles (gold nanoparticles in particular) from aqueous to non-polar organic environments and vice versa. Various methods in the literature, including work from my group, in this fascinating area have been covered and if there are any omissions, it is unintentional. Future challenges include de-



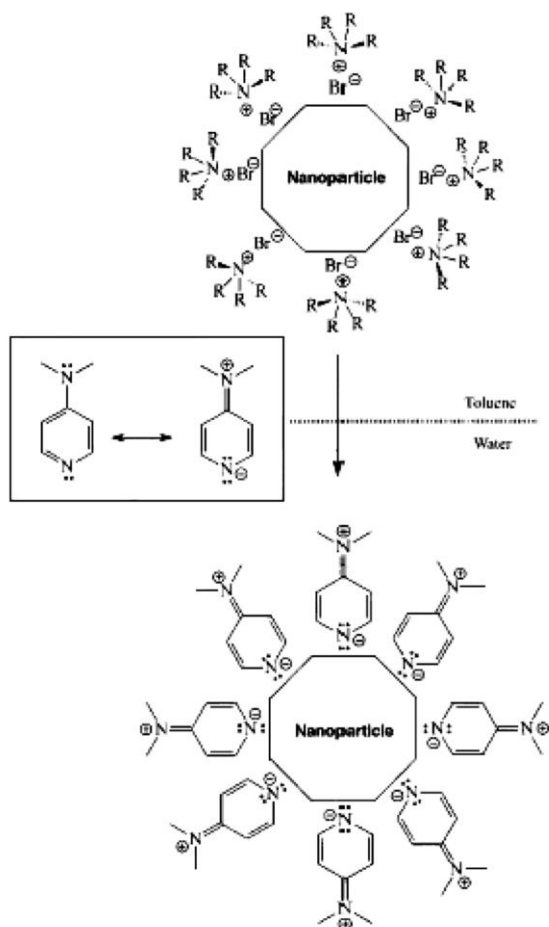


**Fig. 3.13.** Proposed mechanism for the spontaneous phase transfer of gold and palladium nanoparticles from an organic reaction medium (toluene) to water by the addition of DMAP.  $R = C_8H_{17}$ . (Reprinted with permission from [76], © 2001, WILEY-VCH Verlag GmbH).

velopment of strategies to accomplish the phase transfer of nanoparticles with high shape anisotropy and obtaining core-shell structures that can be moved across phase boundaries.

### Acknowledgments

The author wishes to thank his doctoral student, Mr. Ashavani Kumar and his post-doctoral fellow, Dr. Neeta Lala, who carried out much of the experimental

work on nanoparticle phase transfer. Generous funding from the Department of Science and Technology (DST), Government of India, is gratefully acknowledged.

## References

- 1 The September, 2001 issue of *Scientific American* discusses exciting developments in the field of nanotechnology and current/futuristic applications envisaged for nanomaterials.
- 2 T. S. AHMADI, Z. L. WANG, T. C. GREEN et al., *Science*, **1996**, 272, 1924.
- 3 M. A. EL-SAYED, *Acc. Chem. Res.*, **2001**, 34, 257.
- 4 N. R. JANA, L. GEARHART, C. J. MURPHY, *Chem. Commun.*, **2001**, 617.
- 5 S.-W. CHUNG, G. MARKOVICH, J. R. HEATH, *J. Phys. Chem. B*, **1998**, 102, 6685.
- 6 K. ESUMI, K. MATSUHISA, K. TORIGOE, *Langmuir*, **1995**, 11, 3285.
- 7 K. R. BROWN, D. G. WALTER, M. J. NATAN, *Chem. Mater.*, **2000**, 12, 306.
- 8 C. J. JOHNSON, E. DUJARDIN, S. A. DAVIS et al., *J. Mater. Chem.*, **2002**, 12, 1765.
- 9 N. R. JANA, L. GEARHEART, C. J. MURPHY, *J. Phys. Chem. B*, **2001**, 105, 4065.
- 10 S. O. OBARE, N. R. JANA, C. J. MURPHY, *Nano Lett.*, **2001**, 1, 601.
- 11 R. DJALALI, Y. CHEN, H. MATSUI, *J. Am. Chem. Soc.*, **2002**, 124, 13660.
- 12 T. O. HUTCHINSON, Y.-P. LIU, C. KIELY et al., *Adv. Mater.*, **2001**, 13, 1800.
- 13 C. S. AH, S. D. HONG, D.-J. JANG, *J. Phys. Chem. B*, **2001**, 105, 7871.
- 14 X. PENG, L. MANNA, W. YANG et al., *Nature*, **2000**, 404, 59.
- 15 S. I. NIKITENKO, Y. KOLTYPIN, Y. MASTAI et al., *J. Mater. Chem.*, **2002**, 12, 1450.
- 16 R. JIN, Y. CAO, C. A. MIRKIN, K. L. KELLY et al., *Science*, **2001**, 294, 1901.
- 17 N. MALIKOVA, I. PASTORIZA-SANTOS, M. SCHIERHORN et al., *Langmuir*, **2002**, 18, 3694.
- 18 Y. ZHOU, C. Y. WANG, Y. R. ZHU et al., *Chem. Mater.*, **1999**, 11, 2310.
- 19 N. PINNA, K. WEISS, J. URBAN et al., *Adv. Mater.*, **2001**, 13, 261.
- 20 G. SOUTHAM, T. J. BEVERIDGE, *Geochim. Cosmochim. Acta*, **1996**, 60, 4369.
- 21 T. KLAUS-JOERGER, R. JOERGER, E. OLSSON et al., *Trends Biotech.*, **2001**, 19, 15.
- 22 B. NAIR, T. PRADEEP, *Cryst. Growth Des.*, **2002**, 2, 293.
- 23 T. J. BEVERIDGE, R. G. E. MURRAY, *J. Bacteriol.*, **1980**, 141, 876.
- 24 P. MUKHERJEE, A. AHMAD, D. MANDAL et al., *Angew. Chem. Int. Ed. Engl.*, **2001**, 40, 3585.
- 25 P. MUKHERJEE, A. AHMAD, D. MANDAL et al., *Nano Lett.*, **2001**, 1, 515.
- 26 P. MUKHERJEE, S. SENAPATI, D. MANDAL et al., *ChemBioChem*, **2002**, 3, 461.
- 27 A. AHMAD, P. MUKHERJEE, S. SENAPATI et al., *Colloid. Surf. B*, **2003**, 28, 313.
- 28 A. AHMAD, S. SENAPATI, M. I. KHAN et al., *Langmuir*, **2003**, 19, 3550.
- 29 M. FARADAY, *Philos. Trans. R. Soc. London*, **1857**, 147, 145.
- 30 M. HARUTA, T. KOBAYASHI, H. SANO et al., *Chem. Lett.*, **1987**, 405.
- 31 W. BASCHONG, N. G. WRIGLEY, *J. Electron. Microsc. Technique*, **1990**, 14, 313.
- 32 R. ELGHANIAN, J. J. STORHOFF, R. C. MUCIC et al., *Science*, **1997**, 277, 1078.
- 33 J. TURKEVICH, G. GARTON, P. C. STEVENSON, *J. Colloid Sci.*, **1954**, 9, 26.
- 34 D. A. HANDLEY, *Colloidal Gold: Principles, Methods and Applications*, ed. M. A. HAYAT, Academic Press, San Diego, 1989, Vol. 1, Ch. 2.
- 35 D. G. DUFF, A. BAIKER, P. P. EDWARDS, *Langmuir*, **1993**, 9, 2301.
- 36 A. HENGLEIN, *Langmuir*, **1999**, 15, 6738.
- 37 E. GACHARD, H. REMITA, J. KHATOURI et al., *New. J. Chem.*, **1998**, 1257.
- 38 Y. MIZUKOSHI, T. FUJIMOTO, Y. NAGATA et al., *J. Phys. Chem. B*, **2000**, 104, 6028.

- 39 M. BRUST, M. WALKER, D. BETHELL et al., *J. Chem. Soc., Chem. Commun.*, **1994**, 801.
- 40 R. G. NUZZO, D. L. ALLARA, *J. Am. Chem. Soc.*, **1993**, 105, 4481.
- 41 D. V. LEFF, P. C. OHARA, J. C. HEATH et al., *J. Phys. Chem.*, **1995**, 99, 7036.
- 42 R. L. WHETTEN, J. T. KHOORY, M. M. ALVAREZ et al., *Adv. Mater.*, **1996**, 8, 428.
- 43 S. R. JOHNSON, S. D. EVANS, S. W. MAHON et al., *Langmuir*, **1997**, 13, 51.
- 44 K. S. MAYYA, V. PATIL, M. SASTRY, *Langmuir*, **1997**, 13, 3944.
- 45 D. V. LEFF, L. BRANDT, J. R. HEATH, *Langmuir*, **1996**, 12, 4723.
- 46 L. O. BROWN, J. E. HUTCHISON, *J. Phys. Chem. B*, **2001**, 105, 8911.
- 47 L. A. PORTER, D. JI, S. L. WESTCOTT et al., *Langmuir*, **1998**, 14, 7378.
- 48 J. LIU, R. XU, A. E. KAIFER, *Langmuir*, **1998**, 14, 7337.
- 49 J. LIU, S. MENDOZA, E. ROMAN et al., *J. Am. Chem. Soc.*, **1999**, 121, 4304.
- 50 PR. SELVAKANNAN, S. MANDAL, R. PASRICHA et al., *Chem. Commun.*, **2002**, 1334.
- 51 S. MANDAL, PR. SELVAKANNAN, D. ROY et al., *Chem. Commun.*, **2002**, 3002.
- 52 A. C. TEMPLETON, M. J. HOSTETLER, C. T. KRAFT et al., *J. Am. Chem. Soc.*, **1998**, 120, 1906.
- 53 A. C. TEMPLETON, M. J. HOSTETLER, E. K. WARMOTH et al., *J. Am. Chem. Soc.*, **1998**, 120, 4845.
- 54 R. S. INGRAM, M. J. HOSTETLER, R. W. MURRAY, *J. Am. Chem. Soc.*, **1997**, 119, 9175.
- 55 D. E. CLIFFEL, F. P. ZAMBORINI, S. M. GROSS et al., *Langmuir*, **2000**, 16, 9699.
- 56 Y.-S. SHON, W. P. WUELFING, R. W. MURRAY, *Langmuir*, **2001**, 17, 1255.
- 57 PR. SELVAKANNAN, S. MANDAL, S. PHADTARE et al., *Langmuir*, **2003**, 19, 3459.
- 58 R. K. ILER, *J. Colloid Interface Sci.*, **1966**, 21, 569.
- 59 T. CASSAGNEAU, J. H. FENDLER, *J. Phys. Chem. B*, **1999**, 103, 1789.
- 60 M. SASTRY, M. RAO, K. N. GANESH, *Acc. Chem. Res.*, **2002**, 35, 847.
- 61 A. KUMAR, A. B. MANDALE, M. SASTRY, *Langmuir*, **2000**, 16, 6921.
- 62 A. GOLE, C. DASH, V. RAMACHANDRAN, A. B. MANDALE et al., *Langmuir*, **2001**, 17, 1674.
- 63 W. C. W. CHEN, S. NIE, *Science*, **1998**, 281, 2016.
- 64 S. UNDERWOOD, P. MULVANEY, *Langmuir*, **1994**, 10, 3427.
- 65 K. V. SARATHY, G. U. KULKARNI, C. N. R. RAO, *Chem. Commun.*, **1997**, 537.
- 66 K. V. SARATHY, G. RAINA, R. T. YADAV et al., *J. Phys. Chem. B*, **1997**, 101, 9876.
- 67 M. SASTRY, A. KUMAR, P. MUKHERJEE, *Colloid. Surf. A*, **2001**, 181, 255.
- 68 J. YAN, S. DONG, *Langmuir*, **1997**, 13, 3251.
- 69 J. LIU, J. ALVAREZ, A. E. KAIFER, *Adv. Mater.*, **2000**, 12, 1381.
- 70 N. LALA, S. P. LALBEGI, S. D. ADYANTHAYA et al., *Langmuir*, **2001**, 17, 3766.
- 71 W. WANG, S. EFRIMA, O. REGEV, *Langmuir*, **1998**, 14, 602.
- 72 A. P. ALIVISATOS, *Science*, **1996**, 271, 933.
- 73 A. KUMAR, A. B. MANDALE, M. SASTRY, *Langmuir*, **2000**, 16, 9299.
- 74 J. SIMARD, C. BRIGGS, A. K. BOAL et al., *Chem. Commun.*, **2000**, 1943.
- 75 M. SASTRY, K. BANDYOPADHYAY, K. S. MAYYA, *Colloid. Surf. A*, **1997**, 127, 221.
- 76 D. J. GITTINS, F. CARUSO, *Angew. Chem. Int. Ed. Engl.*, **2001**, 40, 3001.
- 77 D. J. GITTINS, F. CARUSO, *ChemPhysChem*, **2002**, 3, 110.
- 78 A. SWAMI, A. KUMAR, M. SASTRY, *Langmuir*, **2003**, 19, 1168.

## 4

## Mesoscopic Assembly and Other Properties of Metal and Semiconductor Nanocrystals

*G. U. Kulkarni, P. J. Thomas, and C. N. R. Rao*

### Abstract

The properties of metal and semiconductor nanocrystals are briefly reviewed. The organization of metal and semiconductor nanocrystals into mesostructures is an important aspect of nanoscience. New methods of nanocrystal synthesis and functionalization relevant to mesoscopic assembly are described, with emphasis on procedures that deal with monodispersed nanocrystals. Programmed assemblies of nanocrystals in one, two and three dimensions are discussed together with attempts to measure the properties of such lattices. Future directions and potential applications of ordered assemblies are indicated.

## 4.1

### Introduction

A nanocrystal is a tiny chunk of the bulk measuring a few nanometers with a finite number of atoms in it. Nanocrystals in the size range 1–50 nm are considered important and are obtainable as sols: a dispersion of a solid in a liquid, also called a colloidal sol. Metal sols possess fascinating colors and have long been used as dyes. That such dyes indeed consist of tiny metal chunks was established as early as 1857 by Faraday [1], but a similar realization in the case of semiconducting nanocrystals had to wait for over a century [2, 3]. Modern techniques of synthesis enable one to obtain sols of metals and semiconductors that can be dried and re-dissolved like water colors. The colloidal particles display a remarkable tendency to remain single-crystalline and are hence named as nanocrystals. Nanocrystals possess high surface area, a large fraction of the atoms in a nanocrystal are on its surface. A small nanocrystal of 1 nm diameter will have as much as 30% of its atoms on the surface, while a larger nanocrystal of 10 nm (~1000 atoms) will have around 15% of its atoms on the surface [4].

An added dimension to research on nanocrystals is their size-dependent properties. The electronic, magnetic and optical properties of a nanocrystal depend on its size [4]. In small nanocrystals, the electronic energy levels are not continuous as

in the bulk but are discrete, due to the confinement of the electron wavefunction to the physical dimensions of the particles [5]. This phenomenon is called quantum confinement and, therefore, nanocrystals are also known as quantum dots. In other words, a small nanocrystal could be a very bad conductor although it is a tiny silhouette of the conducting bulk. Likewise, a tiny nanocrystal of a ferromagnet can be paramagnetic in nature. In the case of semiconductors, besides discretization of levels, the band gap increases due to quantum confinement. In several respects, small nanocrystals behave like molecules. The nanocrystals can be discretely charged with electrons with characteristic charging energies. This means that a nanocrystal carrying an extra electron can exhibit properties different from a neutral species.

The electronic absorption spectrum of metal nanocrystals in the visible region is dominated by the plasmon band. This absorption is due to the collective excitation of the itinerant electron gas on the particle surface and is characteristic of a nanocrystal of a given size. In metal colloids, surface plasmon excitations impart characteristic colors to the metal sols, the beautiful wine-red color of gold sols being well-known [6–8]. The dependence of the plasmon peak on the dielectric constant of the surrounding medium and the diameter of the nanocrystal was predicted theoretically by Mie and others at the turn of the last century [9–12]. The dependence of the absorption band of thiol-capped Au nanocrystals on solvent refractive index was recently verified by Templeton et al. [13]. Link et al. found that the absorption band splits into longitudinal and transverse bands in Au nanorods [6, 7].

In contrast to metals, exciton peaks dominate the absorption of semiconductor nanocrystals. Thus, yellowish CdS, exhibits an excitonic absorption around 600 nm, which gradually shifts into the UV region as the nanocrystal diameters are varied below 10 nm (see Chapter 1). The absorption band can be systematically varied across ranges of a few 100 nm by changing the size of the semiconductor nanocrystal [14–17]. Brus and others proposed an independent theory to describe size quantization effects in semiconductor nanocrystals, based on the effective mass approximation [18, 19] after recognizing the failure of Mie's theory. Since then, theories have grown in sophistication and rigour to include key effects like surface structure and coupling of electronic states [20–22]. However, our understanding of the optical properties of semiconductor nanocrystals is still incomplete and careful experiments on monodisperse nanocrystals are currently being pursued to unravel the mystery [23]. In addition to interesting absorption properties, the semiconductor nanocrystals also exhibit luminescent behaviour [24–27]. The emission from mono-disperse semiconductor nanocrystals such as CdSe is intense, narrow and can be brought about by excitation in a broad range of wavelengths [27]. The emission can be tuned by altering the diameter of the nanocrystal (see Figure 4.1). Further, control over the emission can be exercised by varying the surface structure and controlling the diameter distribution. The above factors have led to the exploration of a wide range of applications for luminescent semiconductor nanocrystals.

The shrinking dimensions of the current microelectronic devices and the realization that current lithographic processes cannot extend to the nanoworld [28] have lent tremendous thrust to research aimed at ordering nanocrystals into functional networks [29–34]. The nanocrystals akin to covalent systems, self-assemble

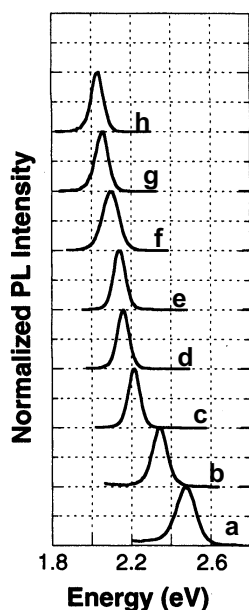


Fig. 4.1. The emission spectra of CdSe nanocrystals of different sizes (a) 2.4 nm; (b) 2.5 nm; (c) 2.9 nm; (d) 3.3 nm (e) 3.9 nm; (f) 4.1 nm; (g) 4.2 nm; (h) 4.4 nm. The change in the emission width is due to decrease in the nanocrystals diameter distribution with increase in diameter (reproduced with permission from [27]).

into ordered arrays in one, two and three dimensions under the right conditions. Lattices of nanocrystals consist of interacting nanocrystals and may exhibit novel properties arising out of such interactions. The ability to engineer such assemblies thus extends the reach of current lithographic techniques and holds promise for a new generation of electronics of the nanoworld [29]. In this context, synthesis and programmed assembly of nanocrystals assumes significance.

In this chapter, we discuss the structure and stability of mesoscopic organizations of nanocrystals in one, two and three dimensions, obtained by using a variety of surfactants. We also examine certain unusual organizations such as clusters of nanocrystals and microcolloidal crystals. Collective properties of nanocrystal organization are presented.

## 4.2

### Synthetic Strategies

#### 4.2.1

##### General Methods

Chemical synthesis of sols of metals and semiconductors results in nanoparticles embedded in a layer of ligands or stabilizing agents, that prevent the aggrega-

tion of particles. The stabilizing agents employed include surfactants such as long chain thiols or amines or polymeric ligands such as polyvinylpyrrolidone (PVP). Reduction of metal salts dissolved in appropriate solvents produces small metal particles of varying size distributions [35–38]. A variety of reducing agents have been employed for the reduction. These include electrides, alcohols, glycols, metal borohydrides and certain specialized reagents such as tetrakis(hydroxymethyl) phosphonium chloride. Si and Ge nanocrystals can be obtained by reduction of  $\text{GeCl}_4$  or silanes with strong reducing agents such as lithium or sodium naphthalide [39–41].

Kinetic control of precipitation (arrested precipitation) is generally used to obtain semiconductor nanocrystals such as CdS [42], CdSe [43], ZnS, HgTe, PbS, CuS,  $\text{Cu}_2\text{S}$ , AgI, ZnO, AgI and  $\text{TiO}_2$  [44–46]. The nanoparticles so obtained possess a broad distribution in diameter. Thermolysis methods involving the decomposition of organometallic precursors in high boiling organic solvents are used to prepare CdSe [47], CdS [47], PbSe [16], InP [17], ZnSe, GaAs, InSb, GaP nanocrystals [45–50]. Reverse micellar methods exploit the “water pools” in water-in-oil mixtures to synthesize nanocrystals and have been successfully utilized in the preparation of Ag, Au, Co, Pt, Co, CdS, CdTe, AgS nanocrystals [51, 52]. The synthesis of nanocrystals at the air–water interface, as in Langmuir–Blodgett films, or at a liquid–liquid interface, is currently attracting wide attention [30, 53, 54]. CdS, PbS and MgS nanocrystals have been prepared by exposing Langmuir–Blodgett films of fatty acids to  $\text{H}_2\text{S}$  [55]. It has been shown recently that films of metal and semiconductor nanocrystals can be prepared using a water–toluene interface [56]. A typical film of Au nanocrystals is shown in Figure 4.2. Traditionally, clusters of controlled sizes have been generated by ablation of a metal target in vacuum followed by mass selection of the plume to yield cluster beams [57, 58]. Such cluster beams could be subjected to in situ studies or be directed on to solid substrates. In order to obtain nanocrystals in solution, Harfenist et al. [59] steered a mass-selected Ag cluster beam through a toluene solution of thiol and capped the vacuum prepared particles.

Colloids of alloys have been made by the chemical reduction of the appropriate salt mixture in the solution phase. In the case of semiconductor nanocrystals, a mixture of salts is subjected to controlled precipitation. Thus, Ag–Pd and Cu–Pd colloids of varying composition have been prepared by alcohol reduction of mixtures of silver nitrate or copper oxide with palladium oxide [60]. Fe–Pt alloy nanocrystals have been made by thermal decomposition of the Fe and Pt acetylacetonates in high boiling organic solvents [61]. Au–Ag alloy nanocrystals have been made by co-reduction of silver nitrate and chloroauric acid with sodium borohydride [62, 63]. Semiconductor nanocrystals of the form  $\text{Cd}_x\text{Mn}_{1-x}\text{S}$ ,  $\text{CdS}_x\text{Se}_{1-x}$  have been obtained by the inverted micelle methods as well as in glasses by sol–gel methods [23, 64]. Alloys of controlled composition are also made by thermal decomposition of carefully chosen precursors, to achieve homogeneity. For example,  $\text{Mn}_2(\text{mSeMe})_2(\text{CO})_8$  was used as selenium source to obtain  $\text{Cd}_{1-x}\text{MnSe}$  nanocrystals [65]. Au–Ag alloying and segregation has been brought about by the use of lasers on Au–Ag layered particles [66, 67].

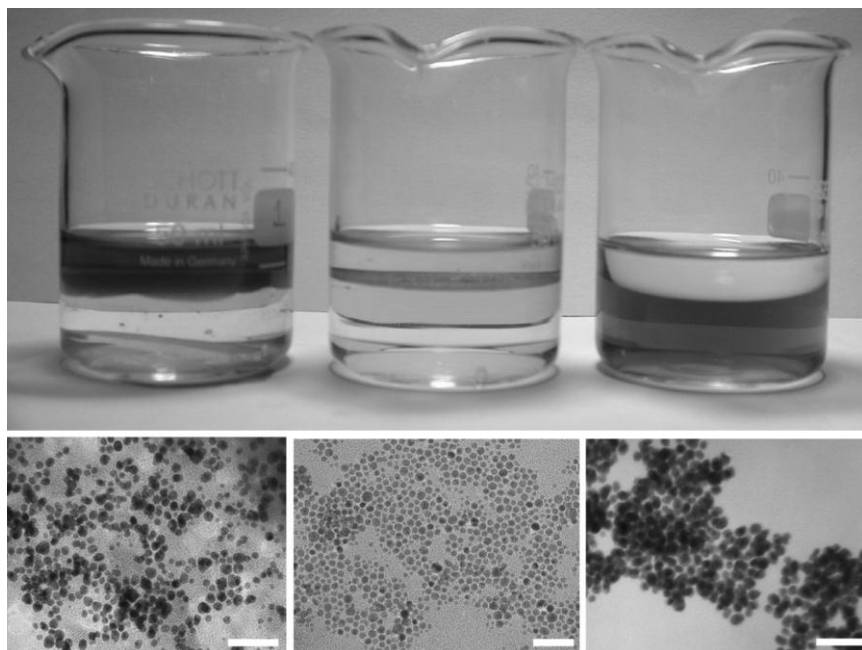


**Fig. 4.2.** Nanocrystalline film of Au formed at the toluene–water interface (middle). Gold is introduced as a toluene solution of  $\text{Au}(\text{PPh}_3)\text{Cl}$  while partially hydrolysed THPC (tetrakis(hydromethylphosphonium)chloride) in water acts as a reducing agent. The film is obtained when the two layers are allowed to stand for several hours. When dodecanethiol

is added to the toluene layer, the film breaks up to form an organosol (left), while mercaptoundecanoic acid added to water produces a hydrosol (right). Shown below are the corresponding TEM images showing nanocrystals. Films of CdS nanocrystals could also be prepared by adopting the same methods. Scale bar 50 nm.

#### 4.2.2

##### Size Control

The successful synthesis of nanocrystals involves three steps nucleation, growth and termination by the capping agent or ligand [35–37]. Though the reaction temperature and reagent concentrations provide a rudimentary control of the three steps, it is often impossible to independently control them and so the obtained nanocrystals usually exhibit a distribution in size. Typically, the distribution is log-normal with a standard deviation of 10% [37]. Given the fact that properties of the nanocrystals are size-dependent, it is significant to be able to synthesize nanocrystals of precise dimensions with minimal size-distributions. This can be accomplished to a limited extent by size selective precipitation, either by centrifugation or by use of a miscible solvent–non-solvent liquid mixture to precipitate the nanocrystals. However, single crystals of large clusters of semiconducting material such as  $\text{Cu}_{147}\text{Se}_{73}(\text{PET}_3)_{22}$  [68],  $[\text{Cd}_{10}\text{S}_4(\text{SPh})_{16}]^{4-}$  [69],  $\text{Cd}_{32}\text{S}_{14}(\text{SC}_6\text{H}_5)_{36}$



DMF<sub>4</sub> [69], Cd<sub>17</sub>S<sub>4</sub>(SCH<sub>2</sub>CH<sub>2</sub>OH)<sub>26</sub> [69], Cd<sub>32</sub>S<sub>14</sub>(SCH<sub>2</sub>CH(CH<sub>3</sub>)OH)<sub>36</sub> [70], Hg<sub>32</sub>Se<sub>14</sub>(SeC<sub>6</sub>H<sub>5</sub>)<sub>36</sub> [71] have been obtained. Solutions of such clusters possess optical properties similar to those of the sols. Schmid [72] and Zamaraev [73] succeeded in preparing truly monodisperse nanocrystals which they called “cluster compounds”. These cluster compounds are like macromolecules with a core containing metal–metal bonds yet are obtainable in definite stoichiometries, typical examples being [Pt<sub>38</sub>(CO)<sub>44</sub>H<sub>2</sub>]<sup>2-</sup> and Au<sub>55</sub>(PPh<sub>3</sub>)<sub>12</sub>Cl<sub>6</sub>. The enhanced stability of Au<sub>55</sub> was recently demonstrated clearly by Boyen et al. [74] who exposed a series of Au<sub>n</sub> nanocrystals to oxidation. These nanocrystals have special stability because they consist of a ‘magic number’ of metal atoms which enables the complete closure of successive shells of atoms in a cubic close packed arrangement. The magic numbers 13, 55, 147, 309 and 561 correspond to the closure of 1, 2, 3, 4 and 5 shells respectively [75]. A schematic illustration of magic nuclearity nanocrystals is shown in Figure 4.3. Since the breakthrough, several magic nuclearity nanocrystals have been prepared including PVP-stabilized Pd<sub>561</sub> nanocrystals [76]. In Figure 4.4, are shown scanning tunnelling and transmission electron microscopic (TEM) images of polymer-protected Pd<sub>561</sub> nanocrystals.

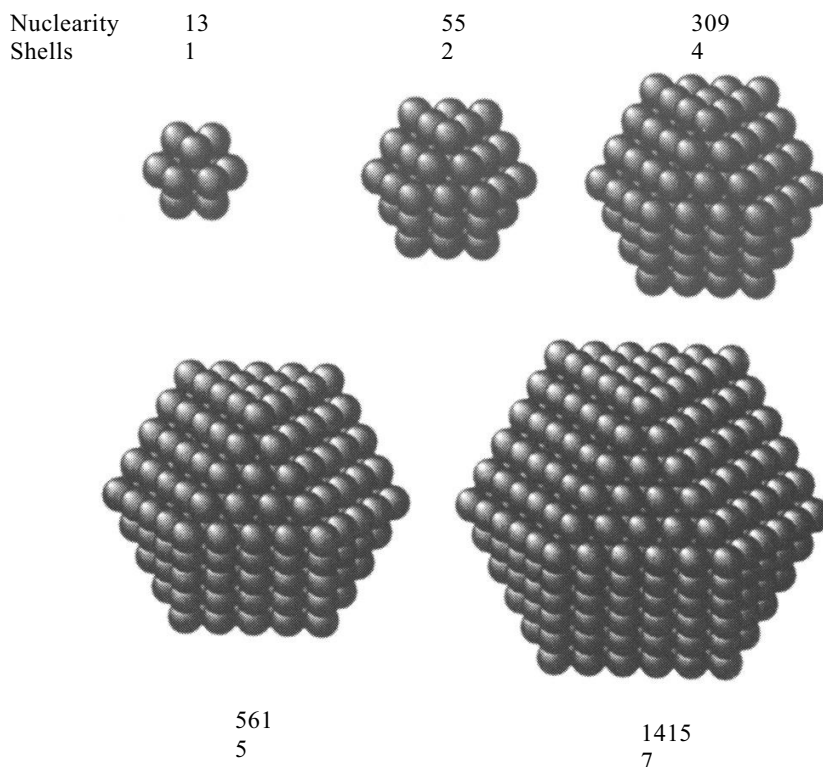
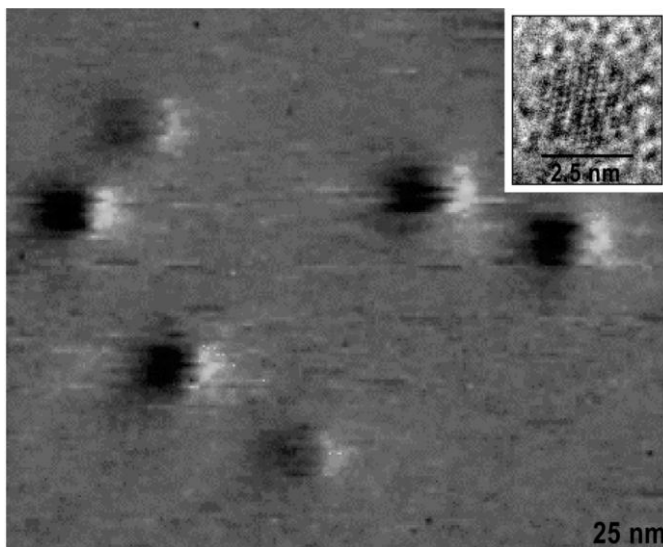


Fig. 4.3. Metal nanocrystals in closed-shell configurations with magic number of atoms.



**Fig. 4.4.** Scanning tunneling microscopy image of polymer-coated  $\text{Pd}_{561}$  nanocrystals. The nanocrystals are seen as fluffy balls against the plane background of the graphite substrate. The inset shows a high-resolution electron micrograph (HRTEM) of an individual

nanocrystal. We see the characteristic 11 [111] fringes in the icosahedral shape measuring 2.5 nm. The diameter estimated from STM is  $\sim 3.4$  nm, the difference being due to the ligand shell.

#### 4.2.3

##### Shape Control

Since the properties of nanocrystals follow from the confinement of the electrons to the physical dimensions of the nanocrystals, it would be interesting to vary the shape of the nanocrystals and study the effect of confinement of electrons in such artificial shapes [77]. For example, it is predicted that light emitted from a nanorod would be linearly polarized along the growth-axis [23]. Such predictions have led to the revival of interest in synthetic strategies yielding non-spherical nanocrystals. Conventional methods such as those due to Turkevich [36] yield, in addition to spherical particles, a mixture of shapes: triangular, teardrop etc., which was then thought of as undesirable. Today, smarter synthetic schemes have been designed which selectively yield nanocrystals in the form of rods, elongated spheres, cubes and hexagons. CdSe nanocrystals in the form of rods, arrows, teardrops and tetrapods have been obtained by careful control of thermolysis conditions such as ratio of surfactants and injection volumes [23, 78]. In Figure 4.5 are shown, TEM micrographs of soluble CdSe nanorods of various aspect ratios. Triangular CdS nanocrystals have been obtained by inverse micelle methods [79]. Large tetrahedral Si nanocrystals as exclusive products have been obtained by careful control of the reducing conditions [80]. TEM images of triangular CdS and tetrahedral Si nano-

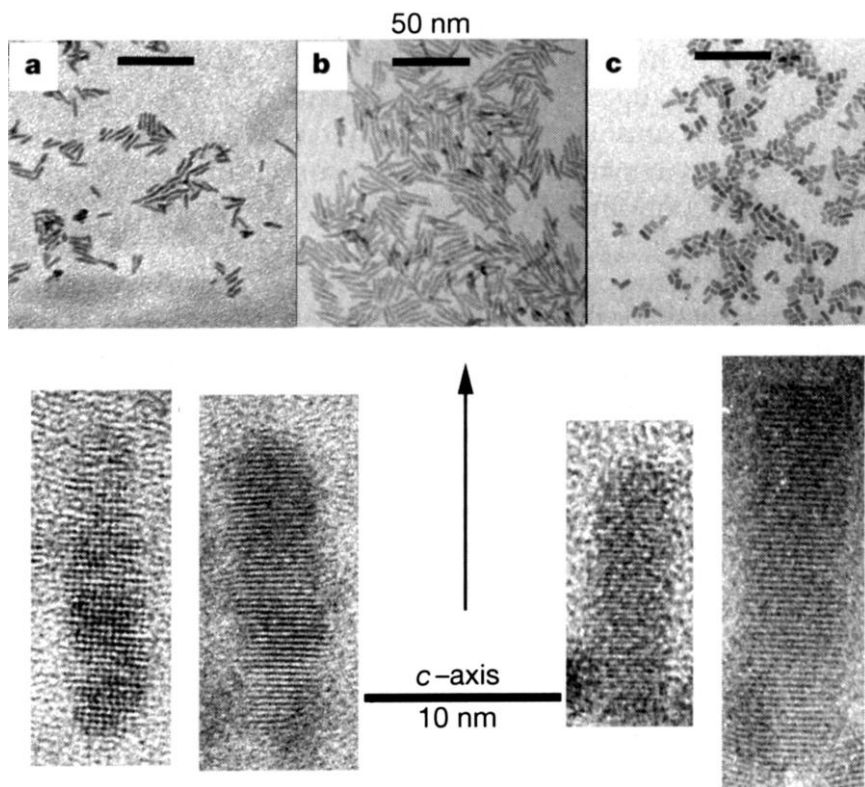


**Fig. 4.5.** (a)–(c) TEM images of different nanorods of CdSe with different sizes and aspect ratios, high resolution TEM images of four nanorods are shown below (reproduced with permission from [78]).

crystals are shown in Figure 4.6. Some shape control has also been demonstrated in the case of CdS and CdTe nanocrystals [81, 82].

#### 4.2.4

##### Tailoring the Ligand Shell

Nanocrystals in their native form are dominated by the surface species, the capping agents employed play a role in determining the property of the nanocrystals [83]. Hence, in addition to controlling the size and the shape of the nanocrystals it is also necessary to tailor its surface with the right capping agent. In addition to traditional capping agents that include ions, surfactants and polymers, a new breed of ligands: dendrimers, hydrogen bonding fragments of protein, DNA and dyes, with pendent thiol groups, as well as silica layers have been used as capping agents [84–86].

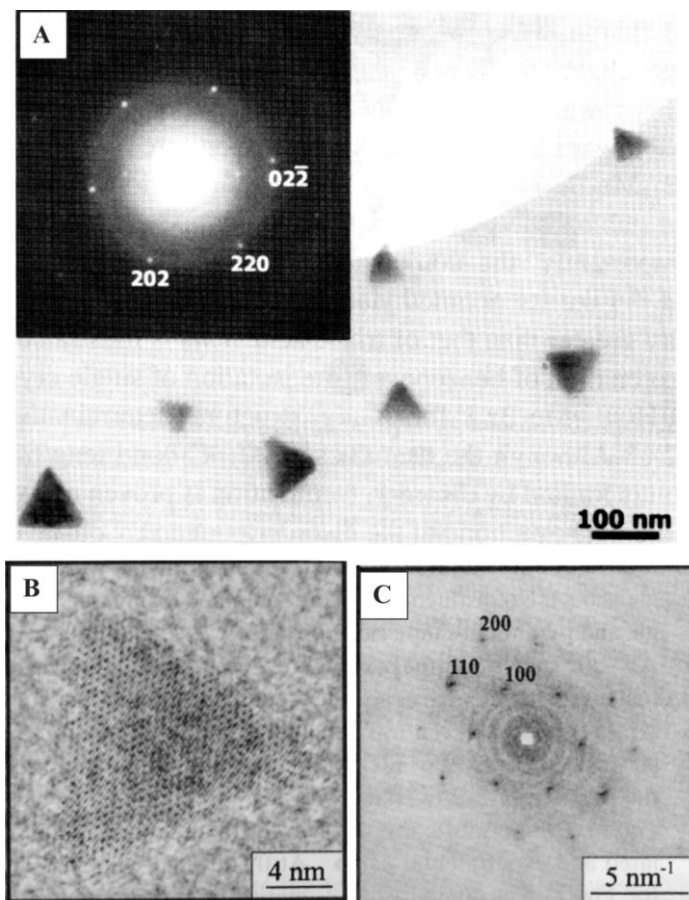


**Fig. 4.6.** (a) TEM micrograph showing tetrahedral Si nanocrystals. The inset shows a selected area electron diffraction pattern typical of a diamond structure. (b) A high resolution TEM image of a triangular CdS nanocrystal. The corresponding power spectrum is in (c). (reproduced with permission from [79, 80]).

In some cases, a layer of a noble metal is used as a buffer between the core nanocrystal and the ligand shell [87]. Thus, a layer of gold lends special stability to Fe nanocrystals and helps prevent oxidation and in preserving the magnetic properties of Fe (see Figure 4.7). A coating of a wider band gap material over a semiconductor nanocrystal aids in lifting the energy of the surface states from in between the highest occupied and the lowest unoccupied levels, thereby enhancing the luminescence efficiency [14, 24]. The lower band gap material acts as a seed for nucleation of the higher band gap material. Thus, core-shell nanocrystals such as CdSe-ZnS, Si-SiO<sub>2</sub>, HgS-CdS, PbS-CdS [45, 46], ZnS-CdSe [88], ZnSe-CdSe [89], CdTe-HgTe nanocrystals have been obtained [90, 91].

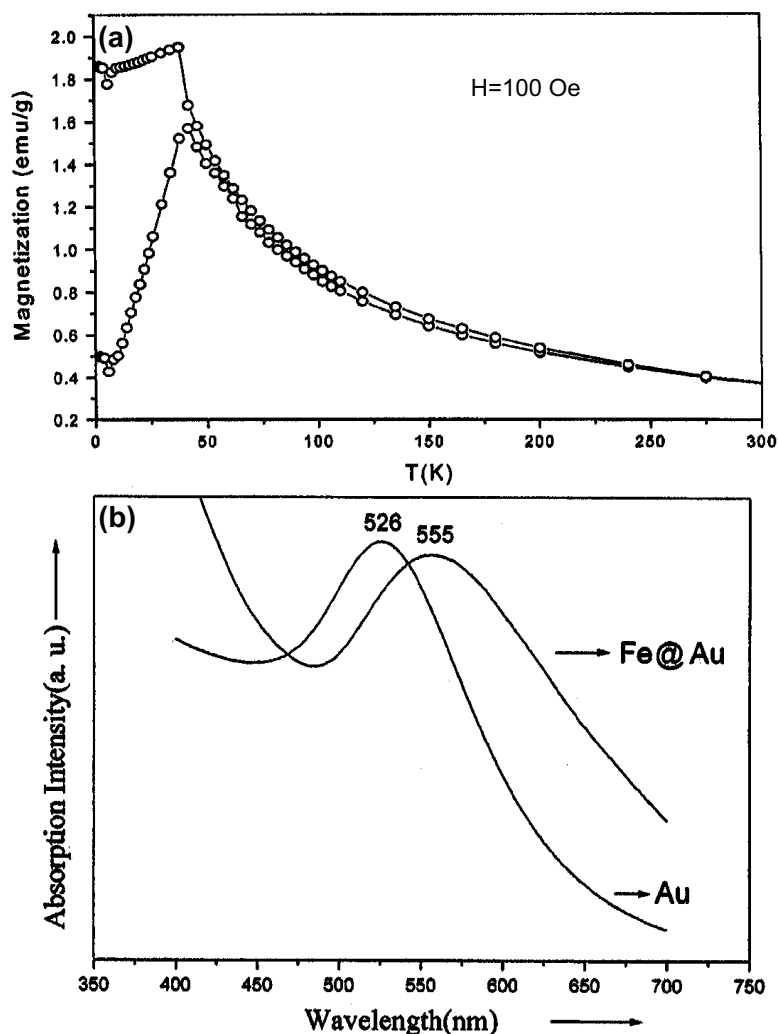


**Fig. 4.7.** (a) Zero field cooled and field cooled magnetization curves for Fe-Au core-shell nanocrystals. The blocking temperature is 42 K. (b) Absorption spectrum showing the Au surface plasmon, shifted due to capping by Fe. For comparison, the spectrum of Au hydrosol is also shown. (reproduced with permission from [87]).

Of special interest with regard to tailoring the ligand shells are reactions that enable the total replacement of one set of ligands with another [92–96]. These reactions also typically enable the transfer of nanocrystals from one phase to another. A novel method of thiol-derivatizing hydrosols of metal sols has been developed by Sarathy et al. [93, 94]. The procedure involves mixing vigorously a hydrosol containing metal particles of the desired size distribution with a toluene solution of an alkane thiol in the presence of a strong acid or reducing agent. The com-

pletion of the derivatization is marked by a vivid interchange of the colors from the aqueous layer to the hydrocarbon layer. The advantage of this method is that well-characterized metal particles can be easily thiol-derivatized in a nonaqueous medium. A variety of hydrosols of Au, Ag and Pt has been thiolized by this procedure. A simple modification of this technique is shown to be effective in the case of CdS nanocrystals [97].

### 4.3

#### Programmed Assemblies

Like molecular systems, nanocrystals capped with suitable ligands spontaneously assemble into ordered aggregates. That such self-assembly can occur through a variety of weak forces is being recognized. Cooperative assemblies of ligated metal and semiconductor as well as of colloidal polymer spheres seem to occur through the mediation of electrostatic and capillary forces [98–100]. The forces that govern the nanocrystal assembly, however, are different in many ways. Surface tension for example, plays an important role [37] because in a nanocrystal, a large fraction of atoms are present at the surface. Surfactant molecules which self-assemble on solid surfaces have proved to be the best means of obtaining ordered arrays of nanocrystals [100].

The way in which the nanocrystals organize themselves depends critically on the core diameter, the nature of the ligand, substrate and even the dispersive medium used [101]. Thiolized metal nanocrystals readily arrange into two-dimensional arrays on removal of the solvent [29]. Using suitable methods, they can also be put into one-dimensional organization in the form of strings or assembled in a stepwise fashion in a three-dimensional superlattice (see Figure 4.8).

#### 4.3.1

##### One-Dimensional Arrangements

Hornayak and coworkers [102] used the ordered channels of porous alumina as templates to obtain linear arrangements of Au nanocrystals. By varying the pore size, the diameter of the nanowire could be controlled. A linear arrangement has also been obtained by coordinating Au particles (~1.4 nm) stabilized with phosphine ligands to single stranded DNA oligonucleotide of the desired length and specific sequence [103, 104]. Liquid crystalline phases of a genetically engineered virus–ZnS nanocrystal hybrid material was used as a template to obtain linear arrays of ZnS nanocrystal aggregates [105]. Similarly, Pt nanocrystals in the form of ribbons have been obtained using a cholesteric liquid crystalline template [106]. Organization of particles in a 1D lattice has met with limited success. Heath and coworkers [107] have fabricated wires of Ag nanocrystals by compressing a dispersion of Ag (4.5 nm) nanocrystals in toluene (Figure 4.9). The wires were one nanocrystal thick, a few nanocrystals wide and extended in length from 20–300 nm. The interwire separation distance and the alignment of the wires could

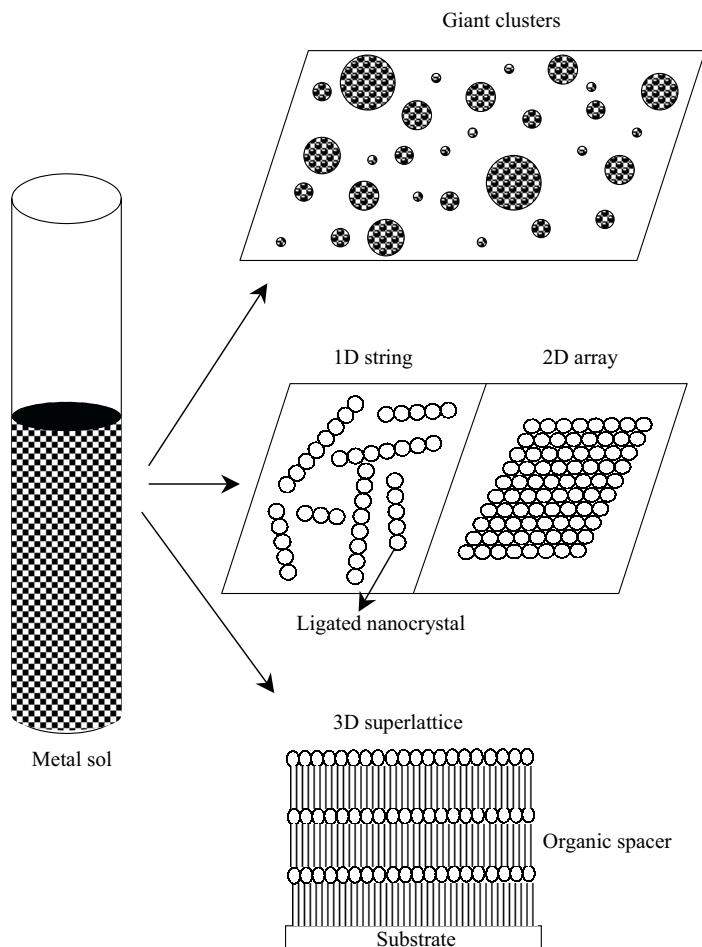


Fig. 4.8. Schematic illustration of the various metal nanocrystal organizations.

be controlled by compressing the film. Based on preliminary experimental observations, it has been suggested that tobacco mosaic virus tubules could serve as templates for the growth of 1D lattice of quantum dots [108].

#### 4.3.2

##### Two-Dimensional Arrays

Ligands based on long chain thiols or phosphines have served as good candidates for assembling monodisperse nanocrystals on a flat substrate. Two-dimensional organizations of a variety of nanocrystals can be brought about by simply evaporating a drop of the sol on a flat substrate.



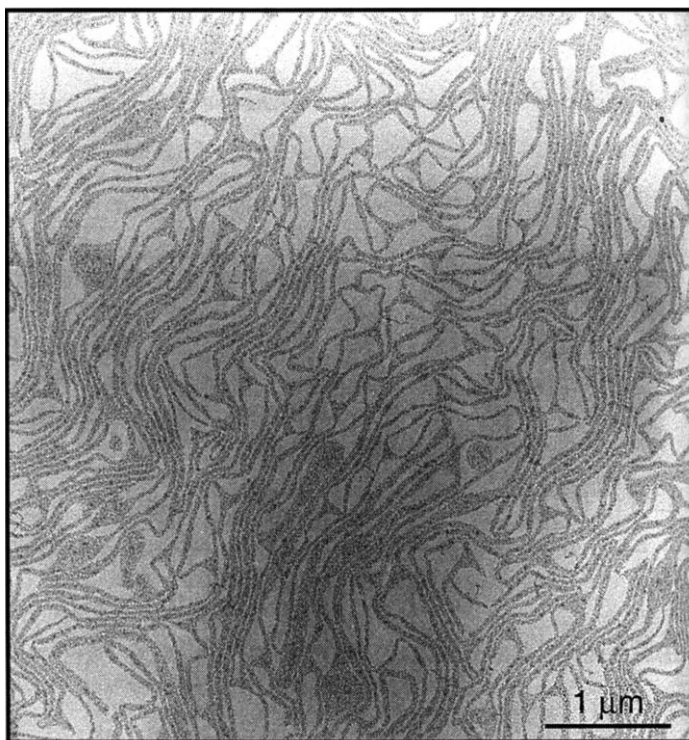


**Fig. 4.9.** TEM image of a continuous stratum structure of compressed LB film of Ag nanocrystals. One-dimensional strings of Ag nanocrystals are clearly seen (reproduced with permission from [107]).

#### 4.3.2.1 Arrays of Metal Nanocrystals

Gold organosols using alkane thiols as surfactants were first prepared by Schiffrin and co-workers [109] by phase transferring gold ions and carrying out reduction in the presence of thiols. Several workers have adopted this procedure to obtain thiolized metal nanocrystals [110–113].

Whetten et al. [111] centrifuged the organosol and separated out fractions containing nanocrystals of different mean sizes, to prepare well-ordered two-dimensional arrays of size-selected Au nanocrystals. Harfenist et al. [59] found that Ag nanocrystals prepared by using a cluster beam, were stable in air and formed extended two-dimensional arrays. In Figure 4.10 is shown a TEM image of a two-dimensional array of dodecanethiol covered Ag nanocrystals obtained by Fitzmaurice and coworkers [112]. The Ag nanocrystals were prepared following the method of Schiffrin and co-workers [109]. Well ordered arrays of magic nuclearity nanocrystals,  $\text{Pd}_{561}$  and  $\text{Pd}_{1415}$ , have been successfully obtained (see Figure 4.11) after replacing their polymer coating by alkanethiols, following the phase transfer method discussed previously [114]. Long chain fatty acids have also been used



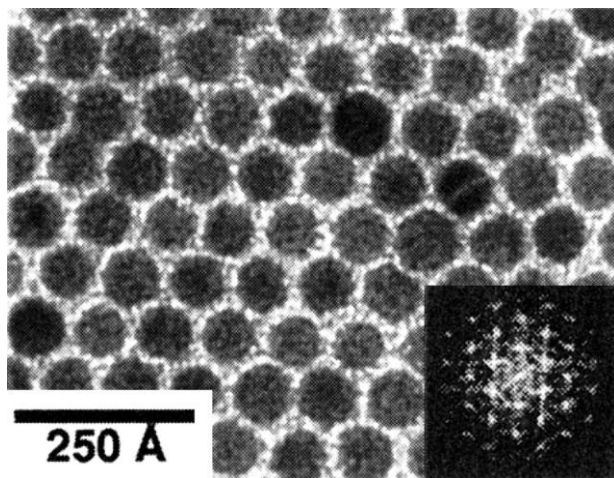


**Fig. 4.10.** Transmission electron micrograph showing hexagonal close-packed Ag nanocrystals (diameter, 7 nm) obtained by evaporating a chloroform dispersion on a

carbon substrate. The average interparticle distance is 1.5 nm. Inset shows the 2D power spectrum of the image (reproduced with permission from [112]).

for ligating and assembling metal nanocrystals. Colloidal dispersion of Co nanocrystals capped with fatty acids were found to self-assemble to yield hexagonally ordered arrays similar to those obtained with alkanethiols [115, 116]. Similarly, Ag nanocrystals capped with fatty acids of appropriate lengths yield cubic or hexagonal close-packed structures [117, 118]. Schmid et al. [119] have reported an ordered two-dimensional array of small  $\text{Au}_{55}$  nanocrystals (diameter  $\sim 1.4$  nm) on a polymer film (see Figure 4.12). At the other end of the size-regime, large Au nanocrystals of 15–90 nm dimensions have also been organized into two-dimensional arrays [120]. Arrays of Au–Ag [62, 63] and Fe–Pt alloy nanocrystals [61] have been obtained. Magic nuclearity  $\text{Pd}_{561}$  nanocrystals, have been exploited to make Pd–Ni core–shell particles with variable Ni loadings [121]. The nanocrystals so obtained possess a core–shell structure, where a Ni layer covers a Pd seed. The magic nuclearity  $\text{Pd}_{561}$  nanocrystals act as high quality seeds and promote the formation of monodisperse Pd–Ni core–shell nanocrystals.

Arrays of  $\text{Pd}_{561}\text{Ni}_n$  ( $n$  upto 10,000 atoms) have been prepared after thiolizing the core–shell nanocrystals as shown in Figure 4.13 [122]. By a simple extension of this technique, arrays of triple layer nanocrystals of the form  $\text{Pd}_{561}\text{Ni}_{3000}\text{Pd}_{1500}$  were also obtained. Methods to organize non-spherical metal nanocrystals into two-dimensional arrays have met with very limited success. Thus, hexagonal Pt as well as elongated silver nanocrystals have been organized into ordered two-dimensional arrays [93, 123]. Interestingly, ordered two-dimensional lattices containing thiolized spherical Au particles of two different sizes have been reported by Kiely et al. (see Figure 4.14) [113], who found that the nanocrystals of different radii follow the

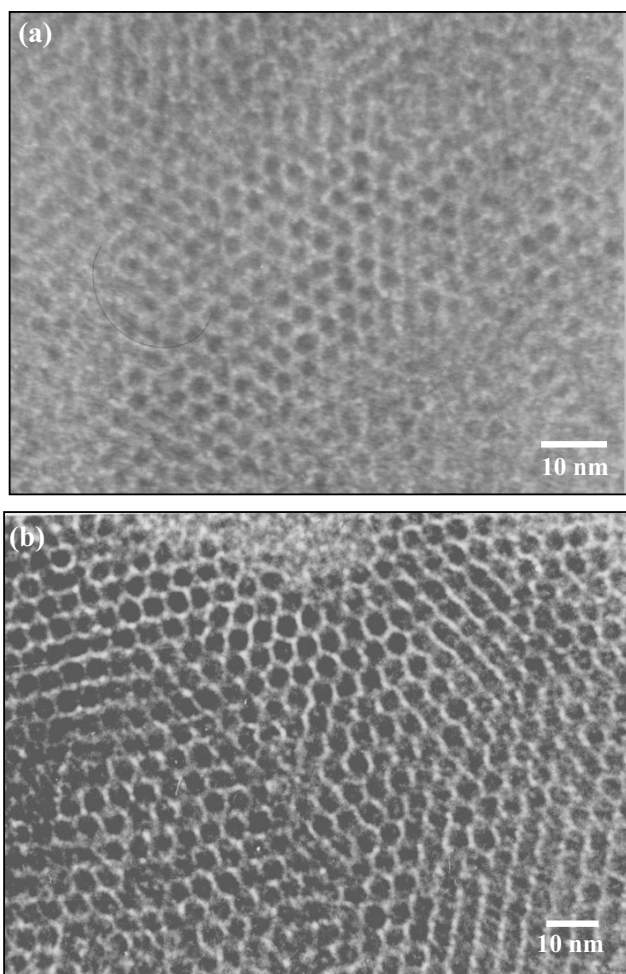


**Fig. 4.11.** TEM micrographs showing hexagonal arrays of thiolized Pd nanocrystals: (a)  $\text{Pd}_{561}$  octanethiol (b)  $\text{Pd}_{1415}$ , octanethiol. Organized arrays of these nanocrystals extend to lengths over several microns.

radius ratio rules formulated for alloying of different metals. Alloy arrays consisting of Au and Ag nanocrystals of different sizes have been made [124].

#### 4.3.2.2 Arrays of Semiconductor Nanocrystals

Bawendi et al. first made monodisperse CdSe nanocrystals by rapid injection of a tri-*n*-octylphosphine (TOP) solution containing dimethylcadmium and tri-*n*-octylphosphine selenide into a hot solution of TOP and TOP oxide [47]. By a simple extension of this technique, CdTe and CdS nanocrystals can also be obtained

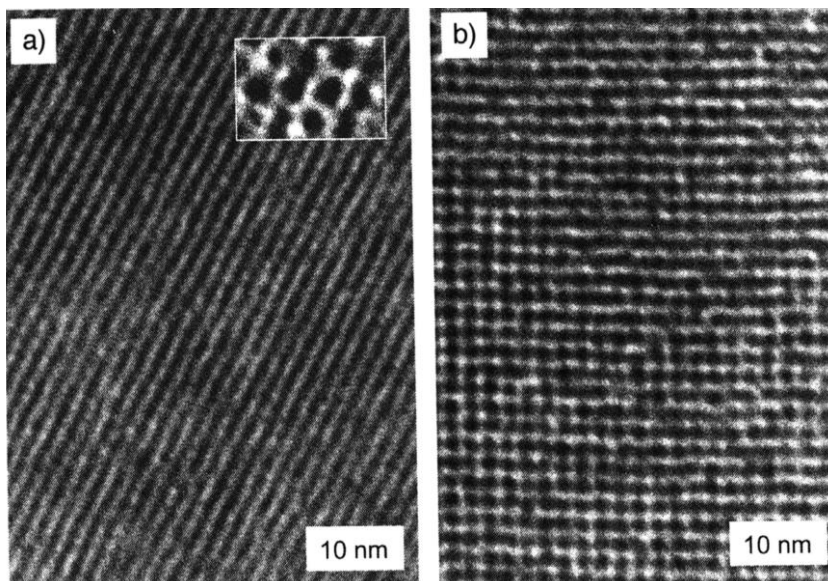


**Fig. 4.12.** TEM images of  $\text{Au}_{55}$  monolayers showing a hexagonal (a) and a cubic (b) structure. The monolayers were prepared on a polyethyleneimine functionalized carbon grid. The magnified inset in (a) shows single clusters in the hexagonal form (reproduced with permission from [134]).

[47]. These nanocrystals could be size-selected to yield monodisperse CdSe nanocrystals [125]. Upon drying on a flat substrate, these CdSe nanocrystals assemble into superlattices that containing several layers of two-dimensionally ordered nanocrystals. TEM images showing the different facets of the two-dimensional layers in these superlattices are shown in Figure 4.15. Hexanethiol capped PbS nanocrystals, prepared by phase transferring Pb ions into an organic medium using hexanethiol, followed by reaction with  $\text{Na}_2\text{S}$  were also organized into two-dimensional lattices (see Figure 4.16) [126, 127]. Motte et al. obtained a hexagonally ordered two-dimensional array of  $\text{Ag}_2\text{S}$  nanocrystals synthesized by the reverse micelle method [64]. Ordered arrays of InP nanocrystals prepared by the thermolysis method have also been obtained [17].

#### 4.3.2.3 Arrays of Oxide Nanocrystals

The very first report of two-dimensional arrays was of  $\text{Fe}_3\text{O}_4$  nanocrystals [128]. Bentzon et al. observed that the ferrofluid obtained by thermolysis of iron pentacarbonyl upon drying (over a period of several weeks) yielded well ordered two-dimensional arrays of  $\text{Fe}_3\text{O}_4$  nanocrystals. Since then, easier methods have been devised to obtain arrays of  $\text{Fe}_3\text{O}_4$  nanocrystals [129]. Two-dimensional arrays of amine-capped metal oxide nanocrystals such as  $\text{Co}_3\text{O}_4$  have been obtained by start-

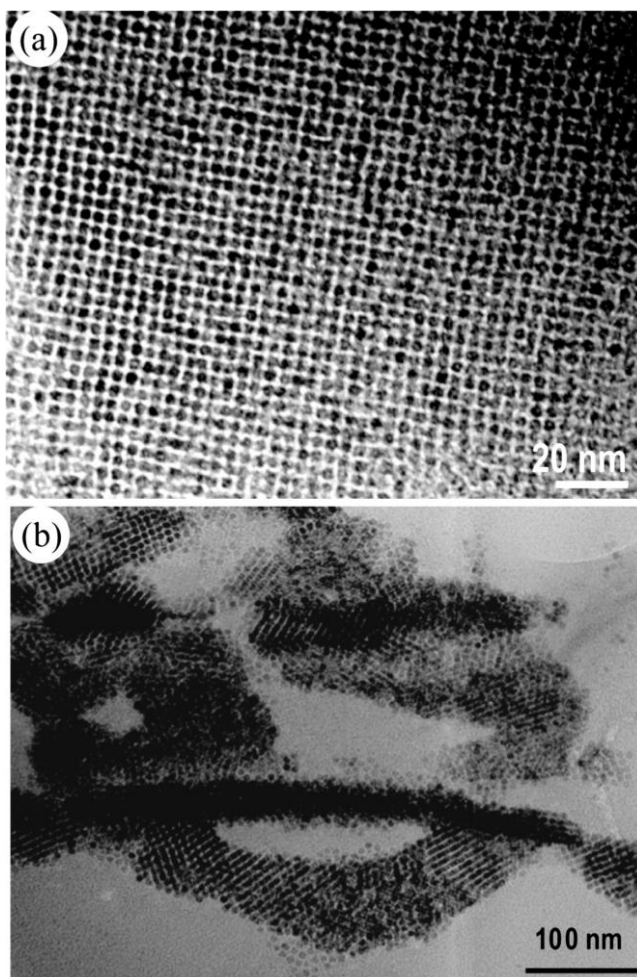


**Fig. 4.13.** TEM image of an ordered array of octanethiol capped (a)  $\text{Pd}_{561}\text{Ni}_{561}$  and (b)  $\text{Pd}_{561}\text{Ni}_{3000}$  nanocrystals. Ni was introduced in the form of its acetate during the reduction process. The nanocrystals were subsequently thiolized.

ing from metal oxide nanocrystals prepared by thermolysis of metal–cupferron complexes [130]. In contrast to metal nanocrystals, attempts to organize non-spherical oxide nanocrystals have met with reasonable success. Thus, tetrahedral  $\text{CoO}$  nanocrystals have been organized into extended two-dimensional arrays [131]. A rectangular superlattice made of prismatic  $\text{BaCrO}_4$  has been observed [132]. More complex arrays such as those consisting of a mixture of nanocrystals of different sizes have been obtained using  $\text{Fe}_3\text{O}_4$  and  $\text{Fe-Pt}$  nanocrystals [133]. The



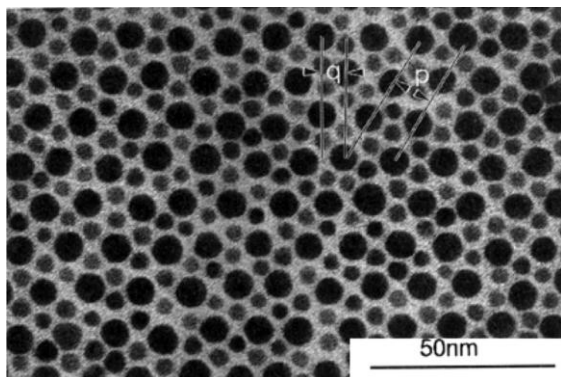


**Fig. 4.14.** A bimodal hexagonal array of Au nanocrystals. The radius ratio of the nanocrystals is 0.58 (reproduced with permission from [113]).

mixed arrays were obtained by evaporating a binary mixture of the metal oxide organosols.

#### 4.3.2.4 Other Two-Dimensional Arrangements

It is possible to obtain micrometer-sized rings of monodisperse nanocrystals, such as  $\text{Ag}_2\text{S}$ , Ag, instead of extended arrays, by varying the solvent evaporation rate and exploiting the resulting fluid instabilities (the Marangoni effect) that occurs during evaporation [134–138]. Neat Au nanocrystals as well as CdSe–ZnS core–shell nanocrystals of various sizes have been organized into two-dimensional lattices using a protein (chaperonin) template [139].

#### 4.3.2.5 Stability and Phase Behaviour of Two-Dimensional Arrays

The nanocrystal organizations mentioned above are mainly entropy-driven. The two lengths involved, the nanocrystal diameter ( $d$ ) and the ligand chain length ( $l$ ) play an important role in deciding the nature of the organization i.e., its orderliness. It has been observed experimentally that for a given diameter of the nanocrystal, the packing changes swiftly as the length of the thiol ligand is increased. The stability diagram in terms of  $d$  and  $l$  shown in Figure 4.17 illustrates that extended close-packed organizations of nanocrystals are found for  $d/l$  values of  $\sim 2$ . Although entropy driven, the above cannot be treated as hard sphere organizations. Based on a study of the effect of the solvent polarity on the self-assembly of ligated metal nanocrystals, Korgel et al. [101, 112] proposed a soft sphere model taking the interparticle interaction into consideration. Accordingly, a ligated nanocrystal allows for penetration of the ligand shell up to its hard sphere limit. In this model, the total potential energy,  $E$ , is considered to be a result of two types of forces between the nanocrystals,

$$E = E_{\text{steric}} + E_{\text{vdW}} \quad (1)$$

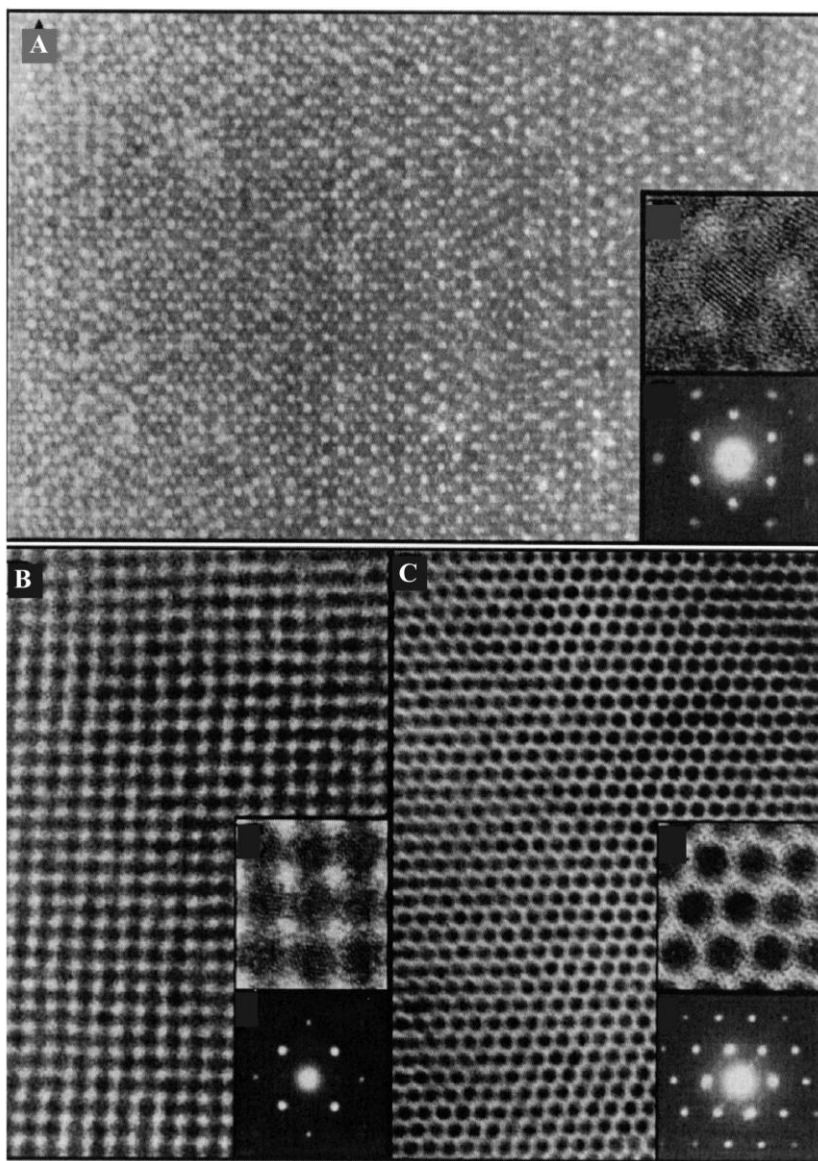


**Fig. 4.15.** Three-dimensional superlattices of 4.8 nm CdSe nanocrystals (a) along  $\langle 100 \rangle$  orientation (b) along  $\langle 101 \rangle$  orientation (c) along  $\langle 111 \rangle$  orientation. High resolution

images as well as a selected area electron diffraction pattern is shown alongside in each case (reproduced with permission from [125]).

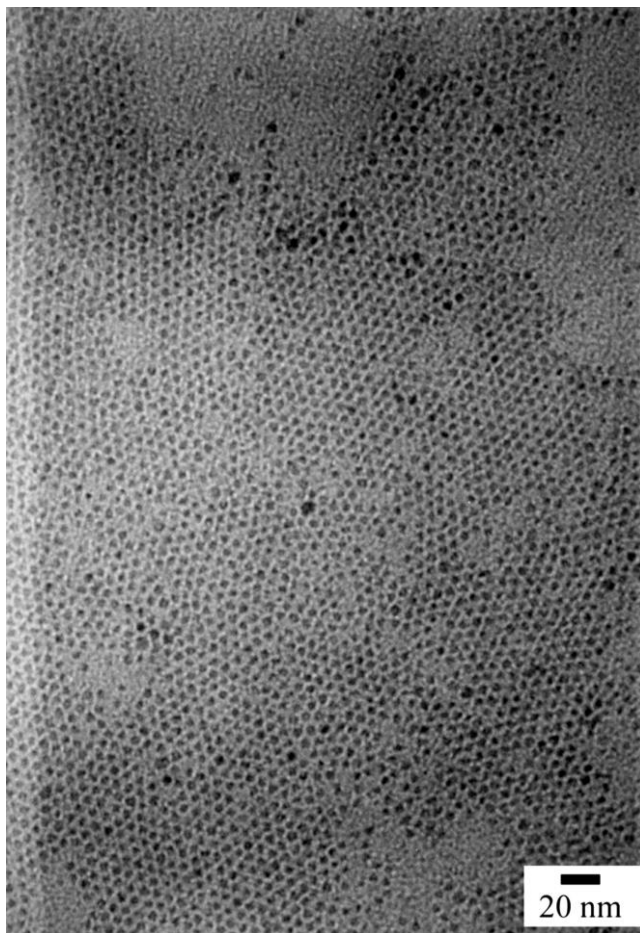


**Fig. 4.16.** TEM micrographs showing hexagonal arrays of hexanethiol capped PbS nanocrystals (unpublished results from our laboratory).

$$E_{\text{vdW}} = \frac{A}{12} \left\{ \frac{d^2}{\tau^2 - d^2} + \frac{d^2}{\tau^2} + 2 \ln \left[ \frac{\tau^2 - d^2}{\tau^2} \right] \right\} \quad (2)$$

$$E_{\text{steric}} = \frac{50dl^2}{(\tau - d)\pi\sigma_a^3} kT e^{-\pi(\tau-d)} \quad (3)$$

The van der Waals interaction due to the polarization of the metal cores constitutes the attractive term and the steric interaction between the thiol molecules on the two surfaces forms the repulsive term, where  $\tau$  is the interparticle distance. The Hamaker constant,  $A$ , for Pd nanocrystals, in toluene for instance, has been estimated to be 1.95 eV [140]. The calculated diameter of the area occupied by the thiol molecule (sa) on the particle surface is 4.3 Å [112]. The total energy is attractive

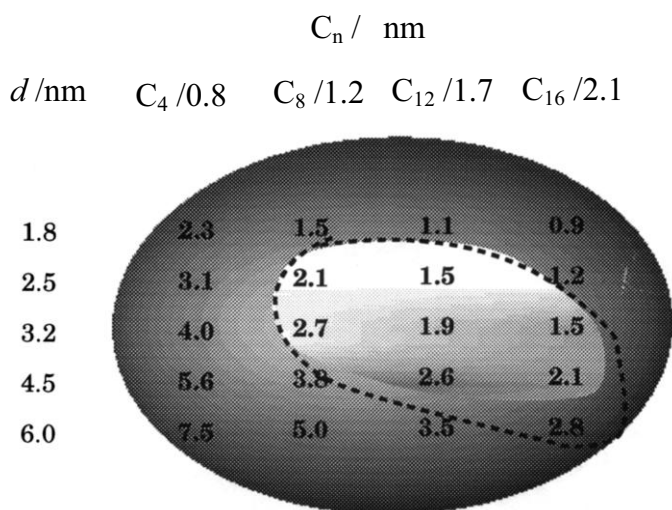


**Fig. 4.17.** The  $d$ - $l$  phase diagram for Pd nanocrystals thiolized with different alkanethiols. The mean diameter,  $d$ , was obtained from the TEM measurements on as-prepared sols. The length of the thiol,  $l$ , is estimated by assuming an all-trans conformation of the alkane chain. The thiol is indicated by the number of carbon atoms,  $C_n$ .

The bright area in the middle encompasses systems that form close-packed organizations of nanocrystals. The surrounding darker area includes disordered or low-order arrangements of nanocrystals. The area enclosed by the dashed line is derived from calculations from the soft sphere model (reproduced with permission from [114]).

over a range of interparticle distances, the magnitude increasing with fall in distance. There could be a range of interparticle distances where the attractive energy from the van der Waals term exceeds the repulsive energy due to the steric factor, giving rise to net stabilization of the two-particle system. This is illustrated in Figure 4.18 in the case of 4.5 nm Pd particles. Stabilization energies of 17 and 2 meV are obtained from the calculation for particles coated with octanethiol and dodecanethiol respectively. When the stabilization energies have moderate values, comparable to the thermal energy of the nanocrystals, ordered organizations can be expected (see the regime shown by dashed line in Figure 4.17). If the  $d/l$  and hence the stabilization energy is not favorable, collapsed monolayers of nanocrystals or loosely packed structures are seen. Clearly, the interdigitation of thiol molecules plays a major role in attributing hardness to the ligated nanocrystal, which in turn decides the nature of the two-dimensional organization. A similar treatment should hold good for other metal and semiconductor nanocrystals.

#### 4.3.3

#### Three-Dimensional Superlattices

Multilayer assemblies using monothiols such as those of CdSe (see Figure 4.15) are generally fragile and are not suited for use in functional devices. One of the



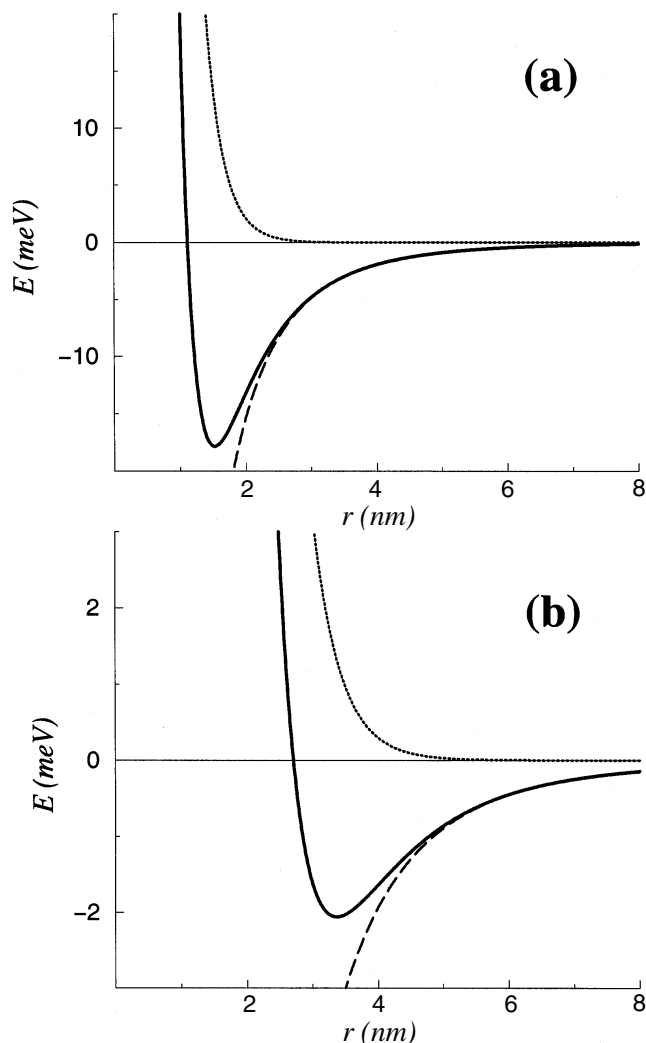


**Fig. 4.18.** Variation of the two components and the total potential energy versus the separation distance between two Pd nanocrystals of 4.5 nm diameter coated with (a) octanethiol (b) dodecanethiol (reproduced with permission from [114]).

means of obtaining robust structures involves multilayer deposition of nanocrystals and has been drawing a great deal of attention over the last few years, since it provides a convenient, low-cost means to prepare ultra-thin films of controlled thickness, suitable for device applications. In a typical experiment, one end of a monolayer forming bifunctional spacer, is tethered to a flat substrate such as gold, aluminum, indium tin oxide or glass, leaving the other end free to anchor nano-

crystals [29, 30]. Subsequent layers can be introduced by dipping the substrate sequentially into the respective spacer molecule solution and the nanocrystal dispersion, with intermediate steps involving washing and drying. The formation of the multilayer assembly can be monitored using a variety of spectroscopy and microscopy tools as illustrated in Figure 4.19. Thus, employing Au substrates and dithiols as spacers, multilayer assemblies of several nanocrystals such as Au or CdS have been accomplished [141]. One such example of layer-by-layer deposition of Pt (5 nm) nanocrystals is shown in Figure 4.19. Brust et al. [142] have reported the formation of multilayers of Au nanoparticles using dithiols. These workers have confirmed the layer-by-layer deposition of particle arrays by employing UV-vis spectroscopy and ellipsometry. Multilayers with CdS nanocrystals prepared by the reverse micelle technique and spaced with alkane were made and measurable photocurrents were generated by these assemblies. Three-dimensional superlattices involving nanocrystals of different metals (e.g. Pt, Au) and of metals and semiconductors (e.g. Au, CdS) have also been prepared and characterized [141]. Such assemblies can be made with polyelectrolytes such as poly(diallyldimethylammonium chloride) (PDDA), Polyethyleneimine (PEI) [143, 144], Poly(allylamine hydrochloride) (PAH) and also polymers such as poly-phenylenevinylene (PPV) [145, 146]. Thus, multilayers such as those of CdTe nanocrystals spaced with PDDA, CdSe spaced with PPV, have been prepared.

#### 4.3.4

#### Superclusters

It has been proposed that self-similarity in metal nanocrystal organization would manifest in the form of a giant cluster whose shape and size are direct consequences of the nanocrystals themselves [147]. The invariance of the shell effects in metal nanocrystals with scaling is shown schematically in Figure 4.20. Thus,  $\text{Pd}_{561}$  nanocrystals would be expected to self-aggregate into a giant cluster of the type  $(\text{Pd}_{561})_{561}$  under suitable conditions. The monodisperse nature of the nanocrystals is thought to be important in assisting the self-aggregation process. Formation of such clusters was observed in the mass spectra of magic nuclearity  $\text{Au}_{55}$  nanocrystals. Secondary ion mass spectrometry indicated the presence of species with large  $m/z$  values and these were attributed to  $(\text{Au}_{13})_{55}$  giant clusters [148]. The giant clusters so obtained have, however, not been isolated or imaged. One such observation was made in the case of  $\text{Pd}_{561}$  nanocrystals where the PVP covered nanocrystals aggregated to form giant clusters [149]. The TEM image in Figure 4.21 is revealing. There are regions where the nanocrystals are densely packed in the form of giant aggregates with estimated nanocrystal nuclearities corresponding to various magic numbers. It is possible that the formation of the giant clusters is facilitated by the polymer shell that encases them. Unlike in the case of Pd nanocrystals coated with alkanethiols, which self-assemble to form ordered arrays, the polymer shell effectively magnifies the facets of the metallic core thereby aiding a giant assembly of the nanocrystals.

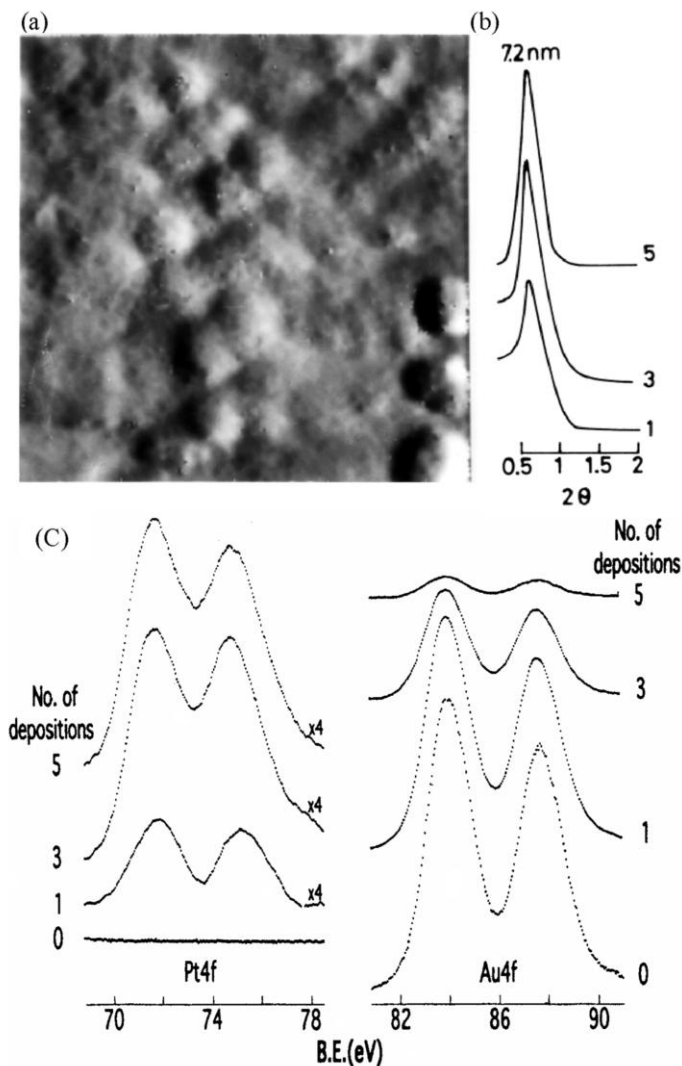


**Fig. 4.19.** Multilayer deposition of Pt (5 nm) nanocrystals on a polycrystalline Au substrate. After each deposition, the structure was characterized by STM, X-ray diffraction and XPS. (a) STM image obtained after the second deposition showing the presence of regular arrays of nanoparticles with an interparticle spacing of 2 nm, extending over 300 nm, corresponding to the size of a typical flat terrace on the substrate. (b) X-ray diffraction pattern of the arrays after the first, third and

fifth depositions exhibiting a low-angle reflection with the  $d$ -spacings reflecting the particle diameter and the interparticle distance. (c) X-ray photoelectron spectra in the Pt(4f) and Au(4f) regions for the 5 nm Pt/Au system. The intensity of the Pt(4f) feature increases with the number of depositions, accompanied by a decrease in the Au(4f) intensity as the substrate gets increasingly shadowed due to the limited escape depth of the photoelectrons.

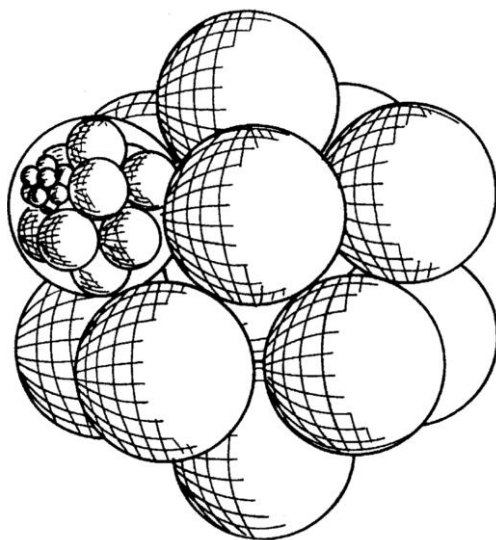


**Fig. 4.20.** Self-similarity: Schematic illustration of the formation of a cluster of metal nanocrystals (super cluster) and a cluster of superclusters. The size effects operating in nanocrystals could be invariant to scaling (reproduced with permission from [147]).

#### 4.3.5

#### Colloidal Crystals

The tendency of monodisperse nanocrystals to arrange into ordered three-dimensional arrays extending to a few microns, has been noticed [150]. Careful tuning of crystallization conditions has yielded crystallites of micrometer dimensions consisting of  $\text{Au}_{55}$  nanocrystals and Fe–Pt alloy nanocrystals (4.5 nm) as shown in Figure 4.22 [151, 152]. Micron-sized crystals consisting of TOPO capped CdSe nanocrystals have previously been obtained by the groups of Bawendi and Weller [125, 153]. However, it was observed that the nanocrystal arrangement in all the above crystallites was polymorphous. It is believed that such crystallites, consisting of ordered nanocrystals, could prove to be the best candidates to study the collective properties of an ensemble of nanocrystals.

#### 4.3.6

#### Nanocrystal Patterning

Creating patterns of nanocrystals on surfaces has attracted wide attention. Such patterned substrates can act as templates to grow nanowires, etch masks to grow nanopillars and quantum dots [154–156]. Other than the layer-by-layer technique mentioned before, simple techniques such as spin coating have been employed to create a nanocrystalline pattern on surfaces [157].

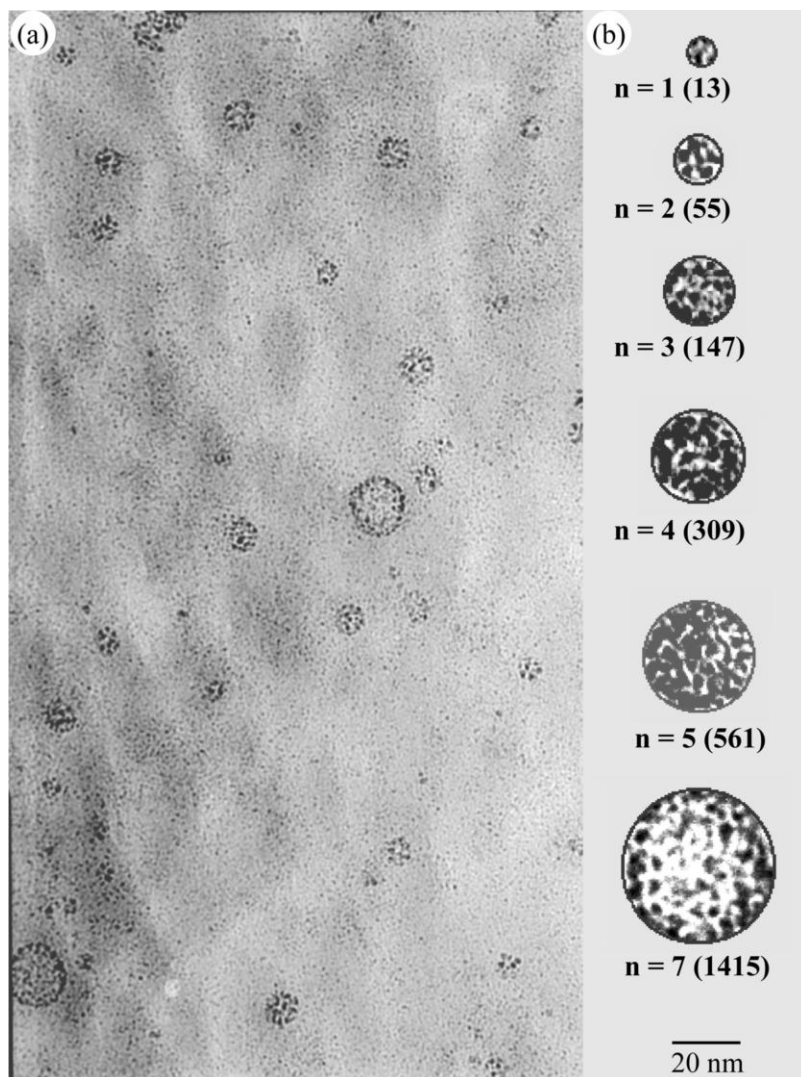


**Fig. 4.21.** TEM micrograph showing the giant clusters comprising Pd<sub>561</sub> nanocrystals. Sample for TEM was prepared by the slow evaporation of a PVP-Pd<sub>561</sub> hydrosol. Giant clusters are enclosed in circles whose diameters correspond to magic numbers. The  $n$  and the numbers in the parenthesis indicate the number of nanocrystals and closed-shells respectively.

In the example shown in Figure 4.23, a direct write lithographic technique, dip pen lithography [158, 159], which relies on a cantilever used for atomic force microscopy (AFM) to write on a substrate to create patterns of Au nanocrystals on mica substrates. Thus, nanocrystals of metals and semiconductors can be patterned into rectangles of varying aspect ratios.

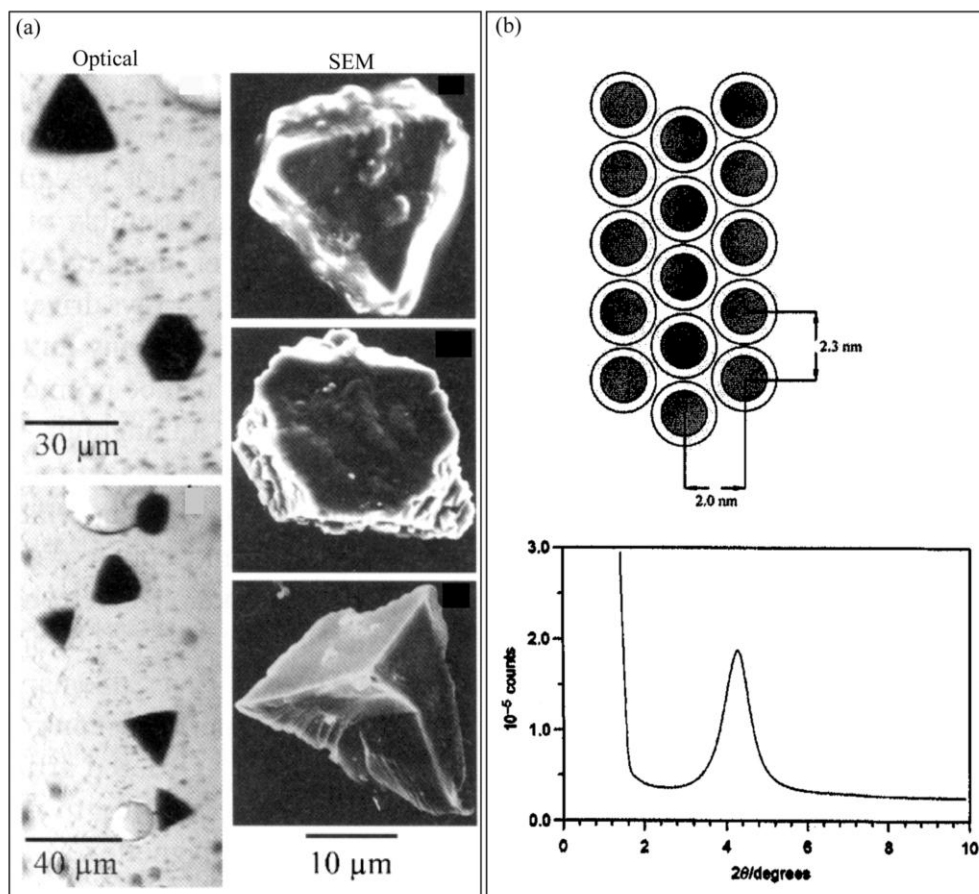


**Fig. 4.22.** Colloidal crystals: (a) from Fe–Pt nanocrystals (b)  $\text{Au}_{55}$  nanocrystals. A schematic illustration of a  $\text{Au}_{55}$  microcrystal along with the corresponding small angle X-ray diffraction pattern is shown alongside (reproduced with permission from [151] and [152]).

#### 4.4

#### Emerging Applications

Several applications have been envisaged for nanocrystals, ranging from simple dyes to magnetic-resonance-imaging contrast agents [160], components of electronic circuitry [33, 161] and magnetic media [115], ingredients in catalyst and sensors, and so on. All the above applications seek to exploit the tunability provided by the size-dependent properties of the nanocrystals [4]. Before we dwell upon collective properties in mesostructures, the case of isolated nanocrystals is briefly discussed.



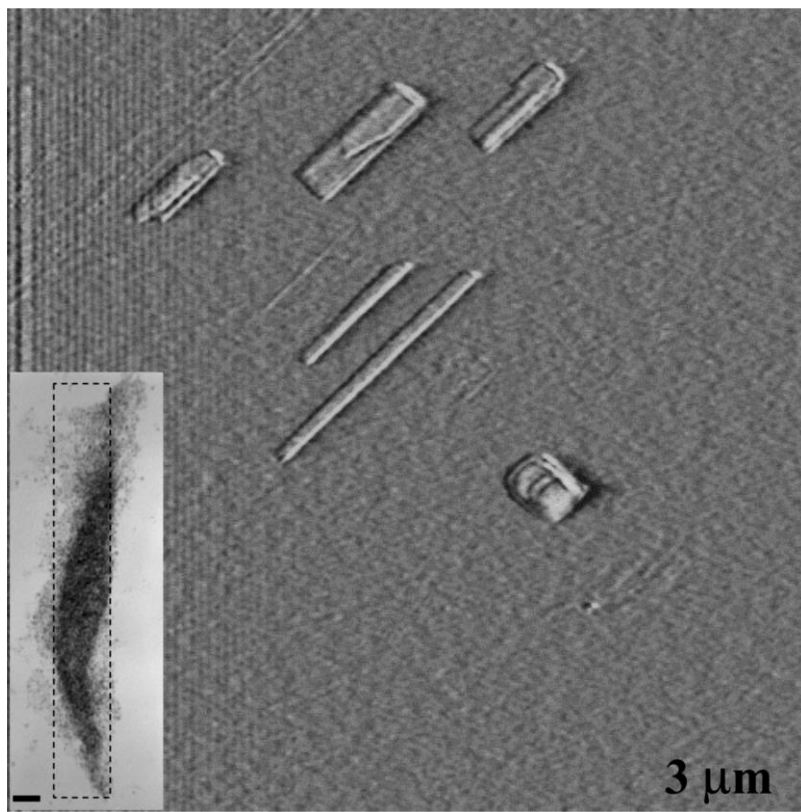


**Fig. 4.23.** Contact AFM scan of a  $9\mu^2$  area on mica substrate showing rectangles of various aspect ratios filled with Au nanocrystals. The patterns were obtained by translating an AFM cantilever dipped in a sol across the surface.

The inset shows a TEM image of a similar pattern on a holey carbon copper grid, the dotted line bounds the area sought to be filled. The scale bar in the inset corresponds to 50 nm.

#### 4.4.1

##### Isolated Nanocrystals

A nanocrystal undergoes a size-induced metal-insulator transition when the diameter of the particles is decreased to below a few nanometers [5, 162, 163]. Scanning tunneling spectroscopy measurements of nanocrystals of various metals have revealed that the nanocrystals of dimensions  $\sim 1$  nm exhibit a definitive band gap (up to 70 meV) that decreases gradually as the volume of the nanocrystal increases [162, 164, 165] (see Figure 4.24). Photoelectron spectroscopic measurements on mass selected  $\text{Hg}_n$  nanoparticles ( $n = 3$  to 250) in the gas phase reveal that the characteristic HOMO–LUMO (s–p) energy gap decreases gradually from  $\sim 3.5$  eV for  $n < 3$  to  $\sim 0.2$  eV for  $n < 250$ , as shown in Figure 4.25. The band gap closure is predicted at  $n \sim 400$ . The change in the electronic structure of the nanocrystal manifests itself in many ways, one example being reactivity [166, 167].

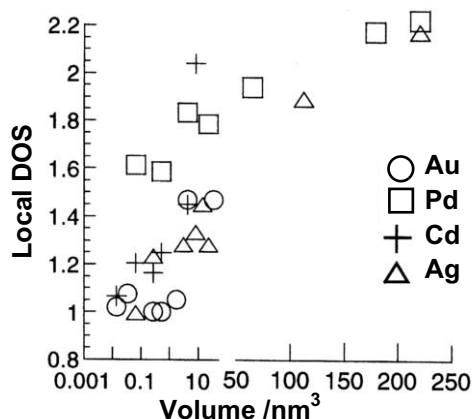


Fig. 4.24. (a) Variation of the nonmetallic band gap with nanocrystal size in metal nanocrystals. The bandgaps were obtained based on scanning tunneling spectroscopic measurements (reproduced with permission from [162]).

The fluorescent properties of semiconductor nanocrystals have drawn wide attention because of their potential use as labels in fluorescence bio-assays [25, 26, 84, 168–170]. When compared to dyes currently in use, the emission from fluorescent nanocrystals is brighter and sharper. Further, the emission can be brought about by excitation over a broad range of wavelengths. It is therefore possible to excite nanocrystals of several different sizes simultaneously with a single source and obtain well resolved emission at different colours. In order that the nano-

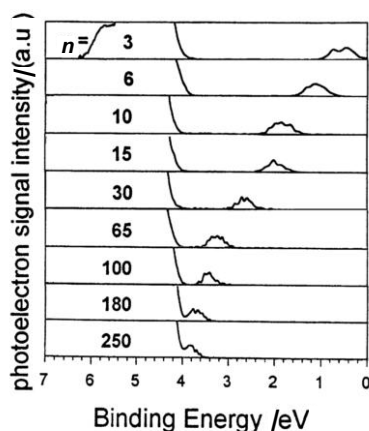


Fig. 4.25. Photoelectron spectra of Hg clusters of varying nuclearity. The 6p feature moves gradually towards the Fermi level, emphasizing that the band gap shrinks with increase in cluster size (reproduced with permission from [165]).



crystals are biocompatible, the nanocrystals need to be water soluble and possess pendant groups at the surface that bind to biomolecules like proteins. These changes can be brought about by tailoring the ligand shell with small DNA fragments or mercapto acids. Several *in vivo* and *in vitro* fluorescence biochemical assays have been carried out with nanocrystalline markers [25, 26, 84, 171]. A few studies have sought to exploit the dependence of the plasmon absorption band on the dielectric constant of the surrounding medium in metal nanocrystals to detect binding events taking place at the ligand shell. Thus, Au nanocrystals could colorimetrically determine the successful hybridization of oligonucleotide strands bound to its surface [99, 103]. It has been proposed that colorimetric sensing of heavy metal ions could be obtained by the use of carboxylic acid terminated bifunctional thiols bound to metal nanocrystals [172, 173]. The changes in the electronic absorption spectra of  $\sim 5$  nm Ag nanocrystals capped with liponic acid, following the addition of the heavy ions,  $\text{Cu}^{2+}$  and  $\text{Fe}^{2+}$  is shown in Figure 4.26. Such a dampening also brings about a change in color. It is apparent that  $\text{Cu}^{2+}$  ions dampen the plasmon band more effectively than  $\text{Fe}^{2+}$ . It is hoped that mesoscale organizations could provide useful substrates consisting of ordered nanocrystals that are required to carry out the above experiments in the solid state.

Nanocrystals are thought of as important in single electron devices, operating at room temperature, such as supersensitive electrometers and memory devices [161, 174]. Capped nanocrystals of both metal and semiconductors by virtue of their size, possess capacitance in the range of aF ( $10^{-18}$  F). Charging a nanocrystal with an extra electron perturbs it to such an extent that the next electron requires an appreciable change in the charging potential. This is often seen as a ‘Coulomb staircase’ in the current–voltage tunneling spectra (see Chapter 1). Indeed, the charging energy varies linearly with the inverse of the diameter of the nanocrystal [175, 176]. The sensitivity of a nanocrystal to single electron charging makes it an ideal candidate for use in single electron transistors and memory devices.

It is well known that in the nanometric domain, the coercivity of magnetic nanocrystals tends to zero [115, 177]. Thus, the nanocrystals behave, as superparamagnets with no associated coercivity or retentivity. The blocking temperature which marks the onset of this superparamagnetism increases with the nanocrystal size. This scenario however changes in the case of interacting nanocrystals, where the interparticle interaction, and hence its magnetic properties, can be tuned by varying the interparticle distance. Thus, lattices of interacting magnetic nanocrystals are considered important in the future magnetic storage devices. Further, the magnetic moment per atom is seen to increase as the size of a particle decreases [178].

Several polymer/polyelectrolyte–nanocrystal hybrid devices have been fabricated seeking to exploit the electro and photoluminescent properties of such material [179–188]. Device fabrication in all these cases is by low-cost self-assembly based techniques. These devices utilize thin films of these hybrids obtained either by multilayer deposition or drop/spin casting methods. Thus, ‘solar cells’ have been made from poly(2-hexylthiophene)–CdSe nanorod multilayers, lasers from drop cast films of CdSe–titania composites and an infrared emitter from multilayers

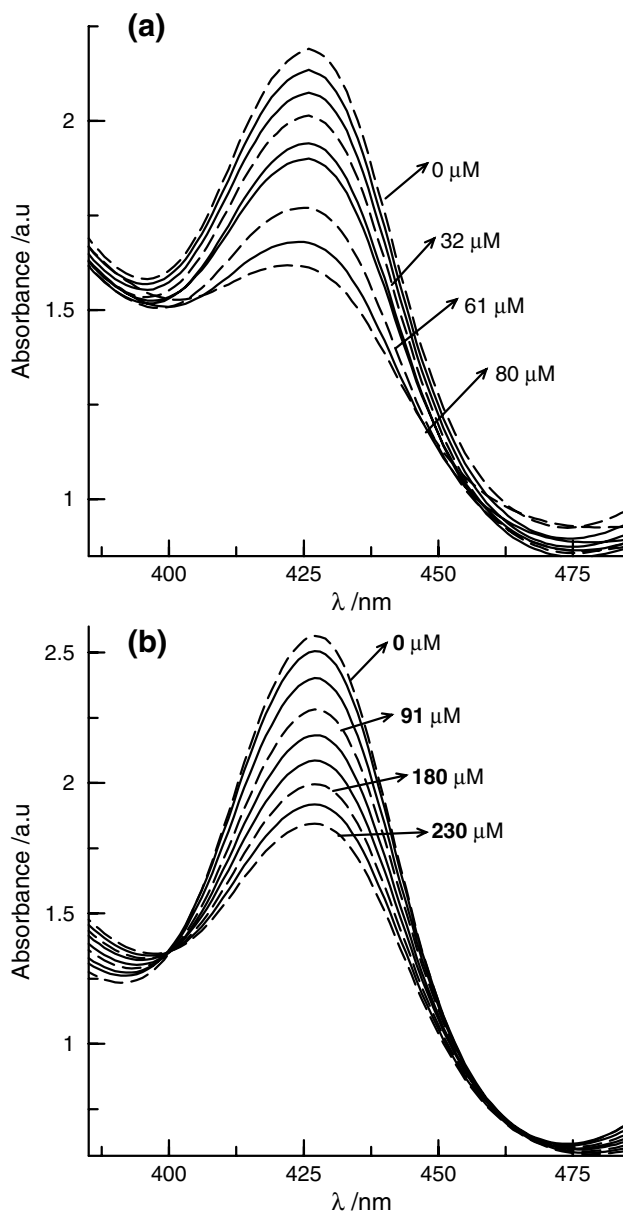


**Fig. 4.26.** Electronic absorption spectra of ~5 nm Ag nanoparticles showing changes accompanying the addition of (a)  $\text{Cu}^{2+}$  and (b)  $\text{Fe}^{2+}$  ions. The concentrations of the ions are indicated.

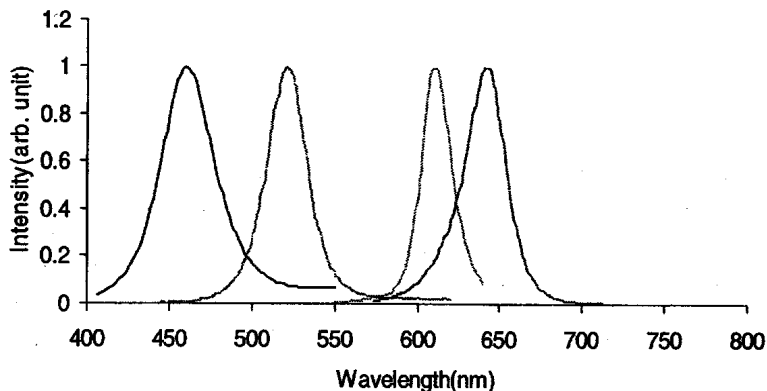


**Fig. 4.27.** Emission spectra of semiconductor nanocrystal polymer composites that were used to make a white light emitting film. (From left) CdS–ZnS core–shell nanocrystals (diameter 3 nm), CdSe–ZnS of diameters 1.3, 2.3, 2.8 nm respectively. The excitation was from a single source (mercury lamp with emission wavelength of 365 nm) (adapted from [187]).

of HgTe and PDDA. White light electroluminescence is seen in multilayers of CdSe–CdS–poly(phenylenevinylene), CdTe–PDDA. White light emission has also been obtained from drop cast films consisting of CdSe–ZnS, CdS–ZnS and poly-laurylmethacrylate (see Figure 4.27). The characteristics of all the above devices can be changed by altering the nanocrystal size.

#### 4.4.2

##### Collective Properties

The fact that the physical properties of nanocrystal organizations can be different from those of the isolated particles is being realized. Pellets of monodisperse nanocrystals, obtained by the use of a bifunctional ligand that binds to more than one nanocrystal or by applying pressure to dried nanocrystalline matter, have been used for electrical transport measurements [189–192]. Pellets made of small Au and Pd nanocrystals exhibit non-metallic behavior with specific conductivities in the range  $10^6 \Omega^{-1} \text{ cm}^{-1}$  [189–191]. The conductivity however increases dramatically with an increase in the diameter of the nanocrystals. An insulator–metal transition has indeed been reported for pellets made of  $\sim 12.5$  nm Au and Ag nanocrystals [192]. Electrical transport measurements on layer-by-layer assemblies of nanocrystals on conducting substrates have been carried out by adopting a sandwich configuration [193–195]. Nanocrystalline films with bulk metallic conductivity have been realized with Au nanocrystals of 5 and 11 nm diameter spaced with ionic and covalent spacers [194, 195]. The conductivity of a monolayered two-dimensional arrays of metal nanocrystals has been studied with patterned electrodes [196–201]. Structural disorder and interparticle separation distance are identified as key factors that determine the conductivity of such layers [196–199].

The conductivity of such layers can be enhanced by replacing alkane thiol with an aromatic thiol in situ [200, 201]. That the interaction energy of nanocrystals in such organizations can be continually varied by changing the interparticle distance was exploited by Heath and co-workers [202, 203], who prepared a monolayer of Ag ( $\sim 3$  nm) nanocrystals at the air–water interface in a LB trough and varied the interparticle distance by applying pressure. A host of measurements including reflectivity and non-linear optical spectroscopic techniques were carried out in situ. This study led to the observation of a reversible Mott–Hubbard metal–insulator transition in the nanocrystal ensemble wherein the coulomb gap closes at a critical distance between the particles. Tunnelling spectroscopic measurements on films of 2.6 nm Ag nanocrystals capped with decanethiol reveal a coulomb blockade behavior attributable to isolated nanocrystals [203]. On the other hand, nanocrystals capped with hexane and pentane thiol exhibit characteristics of strong interparticle quantum mechanical exchange (see Figure 4.28). Similar behavior was observed

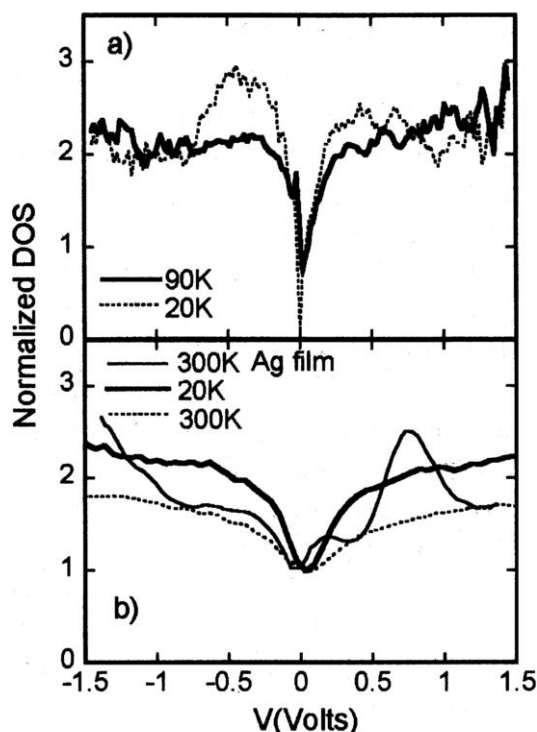


**Fig. 4.28.** Normalized density of states (DOS) measured from arrays of Ag nanocrystals of diameter  $\sim 2.6$  nm capped with (a) decanethiol and (b) hexanethiol at various temperatures. The temperature dependence of DOS near 0 V for decanethiol-capped particles indicates that

the films are non-metallic. In the case of hexanethiol-capped nanocrystals, the DOS around 0 V is temperature independent revealing the metallic nature of the film (reproduced with permission from [203]).

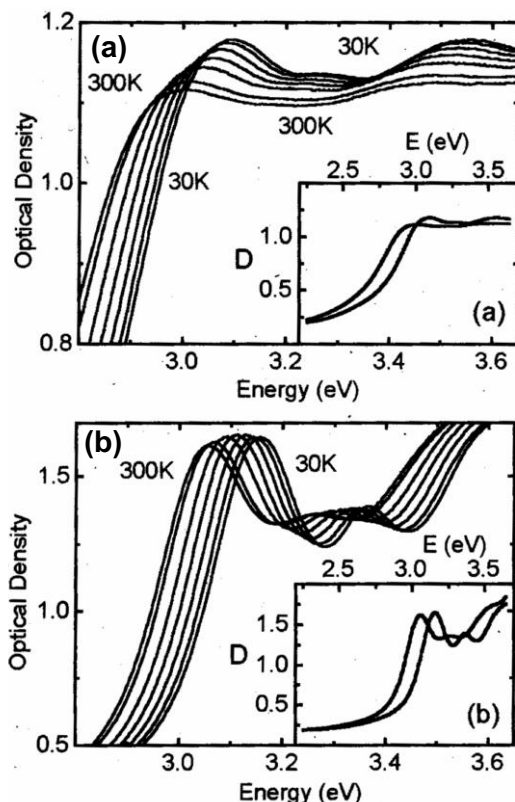


Fig. 4.29. Absorption spectra of thin films of close-packed (a) and isolated (b) CdSe nanocrystals at different temperatures (from right to left curves); 30 K, 80 K, 130 K, 180 K, 230 K, 280 K and 300 K. The insets show the

full-range spectrum of optical density  $D$  for lowest and highest temperatures. A red shift and broadening of the peaks is seen in the case of close-packed films (reproduced with permission from [206]).

in the case of self-assembled two-dimensional arrays of Co nanocrystals and Au nanocrystals [204, 205].

The optical properties of a superlattice of semiconductor nanocrystals are different from those of the individual nanocrystals due to interparticle interactions [32]. Typical spectra showing such a change in the case of CdSe nanocrystals are shown in Figure 4.29. When present in close-packed organization, the absorption spectra of the nanocrystals is broadened and red shifted. This change has been attributed to interparticle dipolar interactions [206]. Bawendi and co-workers have studied such changes in an ensemble of CdSe nanocrystals of different diameters and have obtained evidence for long-range resonance transfer of electronic excitation from smaller to bigger nanocrystals due to dipolar interactions [207]. In a noteworthy experiment, Weller and co-workers, prepared drop cast films of giant CdS clusters of the form  $\text{Cd}_{17}\text{S}_4(\text{SCH}_2\text{CH}_2\text{OH})_{26}$  and  $\text{Cd}_{32}\text{S}_{14}(\text{SCH}_2\text{CH}(\text{CH}_3)\text{OH})_{36}$  with di-

ameters of 1.4 and 1.8 nm respectively. Further, an integrating sphere was used to collect absorption data, thereby virtually eliminating errors from inhomogeneities and size distributions [208]. The experiments due to Weller also support the idea of dipolar interaction leading to the red shift and broadening. The signature of such interactions has also been seen in the case of CdS multilayer deposits [145]. The interparticle interactions, however, could range from weak dipolar interactions to strong exchange interactions based on the interparticle separation. Delocalization of the electronic states of nanocrystals in ensembles due to exchange interactions have been observed in experiments with CdSe nanocrystals. Gaponenko and co-workers have shown that the optical properties of an ensemble of small ( $\sim 1.6$  nm) CdSe nanocrystals are similar to those of bulk CdSe and are due to complete delocalization of the electronic states of individual nanocrystals [209].

Nanocrystals of Co when organized into two-dimensional arrays exhibit a higher superparamagnetic blocking temperature than isolated nanocrystals, i.e., they display a higher resistance to thermal reversal of their spins than when they are isolated [210]. Sun et al. report a lattice of nanocrystals each consisting of a Fe core and a Pt shell prepared by heating Fe–Pt alloy nanocrystals [61]. Following phase segregation, the interaction between the nanocrystals increases, leading to a ferromagnetic film capable of supporting high density magnetization reversal transitions (see Figure 4.30). Exchange spring magnets, nanocomposites that consist

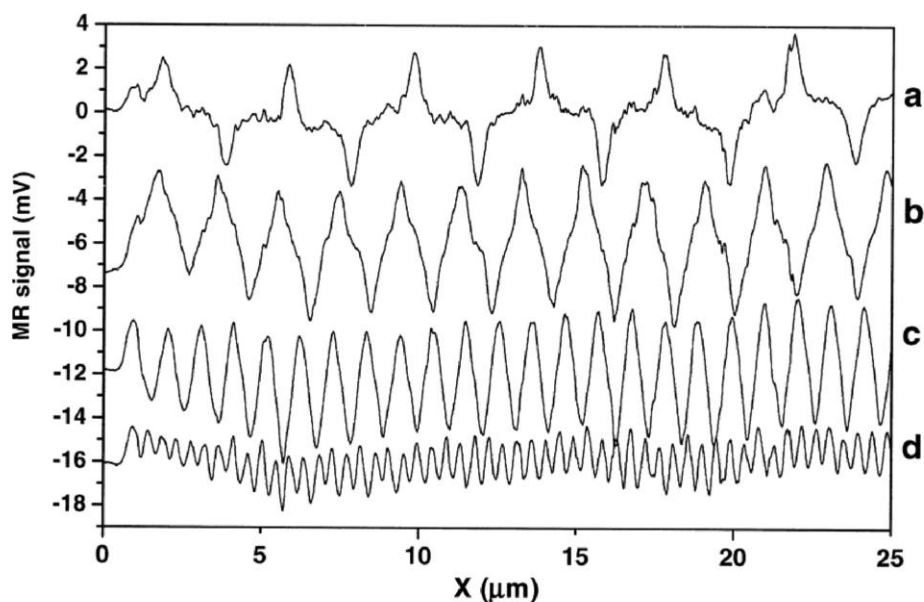


Fig. 4.30. Magnetoresistive (MR) read-back signals from written bit transitions in a array of 4 nm diameter  $\text{Fe}_{48}\text{Pt}_{52}$  nanocrystals. The line scans reveal magnetization reversal transitions at linear densities of (a) 500, (b) 1040, (c) 2140, and (d) 5000 flux changes  $\text{mm}^{-1}$ .

of magnetically hard and soft phases interacting via magnetic exchange coupling, have been made by carefully annealing the mixed nanocrystal array consisting of Fe–Pt and  $\text{Fe}_3\text{O}_4$  [133]. The easy magnetic axis of nanocrystals can be aligned by applying a magnetic field during evaporation of the colloid on a substrate to obtain films with high magnetic anisotropy [211–213].

Thus, ferromagnetic films with parallel anisotropy have been made of superparamagnetic  $\gamma\text{-Fe}_2\text{O}_3$  nanocrystals [211]. By the use of substrate–nanocrystal interactions, films of the same  $\gamma\text{-Fe}_2\text{O}_3$  nanocrystals can be made to exhibit perpendicular anisotropy [212] (see Figure 4.31). The film properties such as coercivity and anisotropy can be tuned by altering the size of the nanocrystals, the film thickness or by suitably doping the nanocrystals with magnetic ions [211–213].

#### 4.4.3

##### Nanocomputing

Ordered arrays of nanocrystals, in principle, could be thought of as arrays of SETs, where the electrostatic interaction between neighboring SETs acts as a wireless communication means. It has been suggested by Korotkov [214] and Lent [215] that simple logical operations can be performed on a circuitry consisting of arrays of SETs in the form of chains or cells with suitable insulating spacers. An electric field applied in one direction polarizes the strings into either the 0 or the 1 state. Lent's scheme, called quantum cellular automata uses, instead, a square cell consisting of five nanocrystals to denote the state of polarization. Preliminary experiments to evaluate the schemes are currently being pursued.

The realization that a self-assembly driven fabrication process is not capable of producing defect-free structures, has fuelled a search for algorithms that can compute even with defective circuitry. Heath and co-workers [216] have developed Teramac, a computer that works despite a high concentration of defects in its bank of microprocessors. A more radical solution called amorphous computing aims to “engineer pre-specified, coherent behavior from the cooperation of large numbers of unreliable parts interconnected in unknown, irregular and time varying ways” [217–219].

#### 4.5

##### Conclusions

Nanocrystals of metal and semiconductors with diameters in the range 1 to 50 nm form a class of materials with unusual properties which are size-dependent. Excellent electrical conductivity that primarily characterizes a metallic state, becomes a rare entity in small nanocrystals ( $< 2$  nm) due to quantum confinement of the electronic states. Similarly, magnetic metals lose much of the coercivity with diminishing size. On the other hand, chemical properties such as reactivity may show up better at smaller sizes due to a greater number of surface bonding sites and other electronic effects. Considering the importance of nanocrystals in tech-

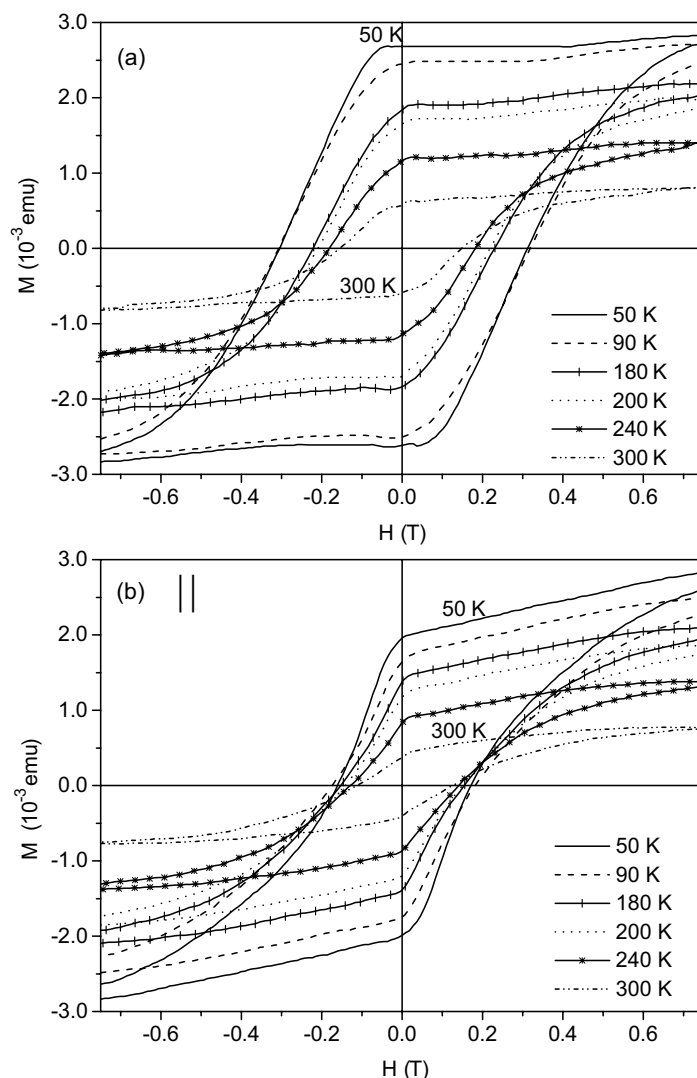


**Fig. 4.31.** Hysteresis loops from a film of  $\gamma$ -Fe<sub>2</sub>O<sub>3</sub> deposited on Si(100) substrates at various temperatures with the substrate held (a) perpendicular and (b) parallel to the applied field direction. The increased coercivity

along the perpendicular direction indicates perpendicular anisotropy caused by orientation of the easy magnetic axis of  $\gamma$ -Fe<sub>2</sub>O<sub>3</sub> nanocrystals perpendicular to the substrate.

nological applications, a large number of synthesis methods have evolved in recent years which include reverse micelle and sonochemical methods as well as laser ablation. Control over size and shape as well as encasing the nanocrystals with ligands of specialized functionalities have become subjects of urgent enquiry. Semiconductor nanocrystals are becoming established as practical alternatives to



fluorescent dyes. Several exploratory devices, whose characteristics are changeable by varying the constituent nanocrystal diameter, have been made. While isolated nanocrystals are interesting by themselves, their organizations, of especially those which are capable of self-assembling into well-ordered arrays, have attracted greater attention. Nanocrystals anchored to fragments of DNA or similar molecules essentially form one-dimensional organizations. When coated with long-chain alkane thiols, nanocrystals exhibit a tendency to assemble into hexagonal arrays on flat substrates. The stability of such a two-dimensional organization depends on the diameter of the nanocrystals and the length of the ligand. Multilayers of nanocrystal arrays can also be made in a programmed way by selecting suitable spacer molecules. However, patterns of nanocrystals can be obtained using scanning probe techniques. Another mesoscale aggregation known is the giant clusters of nanocrystals with definite nuclearities. It would be ideal to grow crystals of nanocrystals, but such efforts have met with only a limited success to date, giving micron-sized crystals. Nanocrystal organizations may exhibit properties very different from those of the individual nanocrystal. They are amenable to unprecedented control over the lattice, the size of the nanocrystal and the interparticle separation, being continuously variable over a range. Exploratory experiments for measuring such collective properties are currently underway in several laboratories around the globe.

## References

- 1 M. FARADAY, *Philos. Trans. R. Soc. London*, 147, 145, 1857.
- 2 C. R. BERRY, *Phys. Rev.*, 161, 848, 1967.
- 3 L. E. BRUS, *J. Chem. Phys.*, 80, 4403, 1984.
- 4 C. N. R. RAO, G. U. KULKARNI, P. J. THOMAS et al., *Chem. Eur. J.*, 29, 27, 2002.
- 5 P. P. EDWARDS, R. L. JOHNSTON, C. N. R. RAO, in *Metal Clusters in Chemistry*, ed. P. BRAUNSTEIN, G. ORO, P. R. RAITHBY, Wiley-VCH, Weinheim 1999.
- 6 S. LINK, M. A. EL-SAYED, *J. Phys. Chem. B*, 105, 1, 2001.
- 7 S. LINK, M. A. EL-SAYED, *Int. Rev. Phys. Chem.*, 19, 409, 2001.
- 8 P. MULVANEY, *Langmuir*, 12, 788, 1996.
- 9 G. MIE, *Ann. Phys.*, 25, 377, 1908.
- 10 G. C. PAPAVALASSILIOU, *Prog. Solid State Chem.*, 12, 185, 1980.
- 11 R. GANS, *Ann. Phys.*, 31, 881, 1911.
- 12 R. GANS, *Ann. Phys.*, 47, 270, 1915.
- 13 A. C. TEMPLETON, J. J. PIETRON, R. W. MURRAY et al., *J. Phys. Chem. B*, 104, 564, 2000.
- 14 S. V. GAPONENKO, *Optical Properties of Semiconductor Nanocrystals*, Cambridge University Press, Cambridge 1998.
- 15 T. VOSSMEYER, L. KATSIKAS, M. GIERSIG et al., *J. Phys. Chem.*, 98, 7665, 1994.
- 16 C. B. MURRAY, S. SUN, W. GASCHLER et al., *IBM J. Res. Dev.*, 45, 47, 2001.
- 17 O. I. MICIC, K. M. JONES, A. CAHILL et al., *J. Phys. Chem. B*, 102, 9791, 1998.
- 18 L. E. BRUS, *J. Chem. Phys.*, 79, 5566, 1983.
- 19 L. E. BRUS, *J. Chem. Phys.*, 80, 4403, 1984.
- 20 P. E. LIPPENS, M. LANNON, *Phys. Rev. B*, 39, 10935, 1989.
- 21 M. V. R. KRISHNA, R. A. FRIESNER, *J. Chem. Phys.*, 95, 8309, 1991.
- 22 S. SAPRA, N. SHANTHI, D. D. SHARMA, *Phys. Rev. B*, 66, 205202, 2002.
- 23 L. MANNA, E. C. SCHER, A. P. ALIVISATOS, *J. Am. Chem. Soc.*, 122, 12700, 2000.
- 24 T. TRINDADE, P. O'BRIEN, N. L. PICKETT, *Chem. Mater.*, 13, 3843, 2001.

- 25 A. J. SUTHERLAND, *Curr. Opin. Solid State Mater. Sci.*, 6, 365, 2002.
- 26 M. BRUCHEZ, JR., M. MORONNE, P. GIN et al., *Science*, 281, 2013, 1998.
- 27 X. PENG, J. WICKHAM, A. P. ALIVISATOS, *J. Am. Chem. Soc.*, 120, 5343, 1998.
- 28 R. F. SERVICE, *Science*, 274, 1834, 1996.
- 29 C. N. R. RAO, G. U. KULKARNI, P. J. THOMAS et al., *Chem. Soc. Rev.*, 29, 27, 2000.
- 30 A. N. SHIPWAY, E. KATZ, I. WILLNER, *ChemPhysChem.*, 1, 18, 2000.
- 31 M. P. PILENI, *J. Phys. Chem. B*, 105, 3358, 2001.
- 32 C. B. MURRAY, C. R. KAGAN, M. G. BAWENDI, *Annu. Rev. Mater. Sci.*, 30, 545, 2000.
- 33 U. SIMON, *Adv. Mater.*, 10, 1487, 1998.
- 34 G. SCHMID, L. F. CHI, *Adv. Mater.*, 10, 515, 1998.
- 35 *Clusters and Colloids: From Theory to Applications*, ed. G. SCHMID, VCH, Weinheim 1994.
- 36 J. TURKEVICH, P. C. STEVENSON, J. HILLIER, *Discuss. Faraday Soc.*, 11, 55, 1951.
- 37 A. I. KIRKLAND, D. E. JEFFERSON, D. G. DUFF et al., *Proc. R. Soc. London Ser. A*, 440, 589, 1993.
- 38 *Physics and Chemistry of Metal Cluster Compounds*, ed. L. J. DE JONGH, Kluwer, Dordrecht 1994.
- 39 R. K. BALDWIN, K. A. PETTIGREW, E. RATAI et al., *Chem. Commun.*, 1822, 2002.
- 40 J. P. WILCOXON, G. A. SAMARA, P. N. PROVENCIO, *Phys. Rev. B*, 60, 2704, 1999.
- 41 A. KORONOWSKI, M. GIERSIG, M. VOGEL et al., *Adv. Mater.*, 5, 634, 1993.
- 42 A. L. ROGACH, A. KORNOWSKI, M. GAO et al., *J. Phys. Chem. B*, 103, 3065, 1999.
- 43 N. HERRON, Y. WANG, H. ECKERT, *J. Am. Chem. Soc.*, 112, 1322, 1990.
- 44 R. ROSSETTI, R. HULL, J. M. GIBSON et al., *J. Chem. Phys.*, 82, 552, 1985.
- 45 A. C. C. ESTEVES, T. TRINDADE, *Curr. Opin. Solid State Mater. Sci.*, 6, 347, 2002.
- 46 M. GREEN, *Curr. Opin. Solid State Mater. Sci.*, 6, 355, 2002.
- 47 C. B. MURRAY, D. J. NORRIS, M. G. BAWENDI, *J. Am. Chem. Soc.*, 115, 8706, 1993.
- 48 S. L. CUMBERLAND, K. M. HANIF, A. JAVIER et al., *Chem. Mater.*, 14, 1576, 2002.
- 49 U. K. GAUTAM, M. RAJAMATHI, F. MELDRUM et al., *Chem. Commun.*, 629, 2001.
- 50 A. A. GUZELIAN, U. BANIN, A. V. KADAVANICH et al., *Appl. Phys. Lett.*, 69, 1432, 1996.
- 51 T. S. AHMADI, L. WANG, A. HENGLEIN et al., *Chem. Mater.*, 8, 428, 1996.
- 52 M. P. PILENI, *J. Phys. Chem.*, 97, 6961, 1993.
- 53 I. MORIGUCHI, F. SHIBATA, Y. TERAOKA et al., *Chem. Lett.*, 761, 1995.
- 54 M. PLATT, R. A. W. DRYFE, E. P. L. ROBERTS, *Chem. Commun.*, 2324, 2002.
- 55 E. S. SMOTKIN, C. LEE, A. J. BARD et al., *Chem. Phys. Lett.*, 152, 265, 1998.
- 56 Unpublished results from the authors laboratory.
- 57 K. SATTLER, J. MHLBACK, E. RECKNAGEL, *Phys. Rev. Lett.*, 45, 821, 1980.
- 58 P. MILANI, S. IANNOTTA, *Cluster Beam Synthesis of Nanostructured Materials*, Springer, Berlin 1999.
- 59 S. A. HARFENIST, Z. L. WANG, R. L. WHETTEN et al., *Adv. Mater.*, 9, 817, 1997.
- 60 H. N. VASAN, C. N. R. RAO, *J. Mater. Chem.*, 5, 1755, 1995.
- 61 S. SUN, C. B. MURRAY, D. WELLER et al., *Science*, 287, 1989, 2000.
- 62 N. SANDHYARANI, M. R. RESHMI, R. UNNIKRISHNAN et al., *Chem. Mater.*, 12, 104, 2000.
- 63 S. T. HE, S. S. XIE, J. N. YAO et al., *Appl. Phys. Lett.*, 81, 150, 2002.
- 64 *Nanoparticles and Nanostructured Films*, ed. J. H. FENDLER, Wiley-VCH, Weinheim 1998.
- 65 F. V. MIKULEC, M. KUNO, M. BENNATI et al., *J. Am. Chem. Soc.*, 122, 2532, 2000.
- 66 Y.-H. CHEN, C.-S. YEH, *Chem. Commun.*, 371, 2001.
- 67 J.-P. ABID, H. H. GIRAULT, P. F. BREVET, *Chem. Commun.*, 829, 2001.
- 68 N. HERRON, J. C. CALABRESE, W. E. FARNETH et al., *Science*, 259, 1426, 1993.

- 69 N. ZHU, D. FENSKE, J. Chem. Soc., Dalton Trans., 1067, 1999; M. BETTENHAUSEN, A. EICHHOFFER, D. FENSKE et al., Z. Anorg. Allg. Chem., 625, 593, 1999.
- 70 T. VOSSMEYER, G. RECK, L. KATSIKAS et al., Science, 267, 1476, 1995.
- 71 S. BEHERENS, M. BETTENHAUSEN, A. C. DEVESON et al., Angew. Chem. Int. Ed. Engl., 35, 221, 1996.
- 72 G. SCHMID, Inorg. Synth., 7, 214, 1990.
- 73 M. N. VARGAFITIK, V. P. ZAGORODNIKOV, I. P. STOLYAROV et al., Chem. Commun., 937, 1985.
- 74 H.-G. BOYEN, G. KASTLE, F. WEIGL et al., Science, 297, 1533, 2002.
- 75 T. P. MARTIN, T. BERGMANN, H. GHILICH et al., J. Phys. Chem., 95, 6421, 1991.
- 76 T. TERANISHI, M. MIYAKE, Chem. Mater., 10, 54, 1998; T. TERANISHI, H. HORI, M. MIYAKE, J. Phys. Chem. B, 101, 5774, 1997.
- 77 S. LINK, M. B. MOHAMED, M. A. EL-SAYED, J. Phys. Chem. B, 103, 3073, 1999.
- 78 X. PENG, L. MANNA, W. YANG et al., Nature, 404, 59, 2000.
- 79 N. PINNA, K. WEISS, H. SACH-KONGEHL et al., Langmuir, 17, 7982, 2001.
- 80 R. K. BALDWIN, K. A. PETTIGREW, J. C. GARNO et al., J. Am. Chem. Soc., 124, 1150, 2002.
- 81 Y. LIU, J. ZHAN, M. REN et al., Mater. Res. Bull., 36, 1231, 2001.
- 82 D. INGERT, M.-P. PILENI, Adv. Mater., 11, 136, 2001.
- 83 P. ZHANG, T. K. SHAM, Appl. Phys. Lett., 81, 736, 2002.
- 84 C. M. NIEMEYER, Angew. Chem. Int. Ed. Engl., 40, 4128, 2001.
- 85 V. CHECHIK, R. M. CROOKS, J. Am. Chem. Soc., 122, 1243, 2000.
- 86 P. MULVANEY, L. M. LIZ-MARZAN, M. GIERSIG et al., J. Mater. Chem., 10, 1259, 2002.
- 87 J. LIN, W. ZHOW, A. KUMBHAR, J. WIEMANN et al., J. Solid State Chem., 159, 26, 2001.
- 88 A. FOJTIK, A. HENGLEIN, Chem. Phys. Lett., 221, 363, 1994.
- 89 A. R. KORTAN, R. HULL, R. L. OPHILA et al., J. Am. Chem. Soc., 112, 1327, 1990.
- 90 S. V. KERSHAW, M. BURT, M. HARRISON et al., Appl. Phys. Lett., 75, 1694, 1999.
- 91 X. PENG, M. C. SCHLAMP, A. V. KADAVANICH, A. P. ALIVISATOS, J. Am. Chem. Soc., 119, 7019, 1997.
- 92 H. HARAI, H. AIZAWA, H. SHIOZAKI, Chem. Lett., 8, 1527, 1992.
- 93 K. V. SARATHY, G. RAINA, R. T. YADAV et al., J. Phys. Chem. B, 101, 9876, 1997.
- 94 K. V. SARATHY, G. U. KULKARNI, C. N. R. RAO, Chem. Commun., 537, 1997.
- 95 D. I. GITTINS, F. CARUSO, Angew. Chem. Int. Ed. Engl., 40, 3001, 2001.
- 96 L. O. BROWN, J. E. HUTCHISON, J. Am. Chem. Soc., 121, 882, 1999.
- 97 A. KUMAR, A. B. MANDALE, M. SASTRY, Langmuir, 16, 9229, 2000.
- 98 A. TERFORT, N. BOWDEN, G. M. WHITESIDES, Nature, 386, 162, 1997.
- 99 C. A. MIRKIN, R. L. LETSINGER, R. C. MUCIC et al., Nature, 382, 607, 1996.
- 100 C. P. COLLIER, T. VOSSMEYER, J. R. HEATH, Annu. Rev. Phys. Chem., 49, 371, 1998.
- 101 B. A. KORGEL, D. FITZMAURICE, Phys. Rev. Lett., 80, 3531, 1998.
- 102 G. L. HORNAYAK, M. KRILL, R. PUGIN et al., Eur. J. Chem., 3, 195, 1997.
- 103 A. P. ALIVISATOS, K. P. JOHNSON, X. PENG et al., Nature, 382, 60, 1996.
- 104 A. KUMAR, M. PATTARKINE, M. BHADBHADRE et al., Adv. Mater., 13, 341, 2001.
- 105 M. MITOV, C. PORTET, C. BOURGERETTE et al., Nature Mater., 1, 229, 2002.
- 106 S.-W. LEE, C. MAO, C. E. FLYNN et al., Science, 296, 892, 2002.
- 107 S. W. CHUNG, G. MARKOVICH, J. R. HEATH, J. Phys. Chem. B, 102, 6685, 1998.
- 108 E. DUJARDIN, C. PEET, G. STUBBS et al., Nanoletters, 3, 413, 2003.
- 109 M. BRUST, M. WALKER, D. BETHELL et al., Chem. Commun., 801, 1994.
- 110 N. SANDHYARANI, T. PRADEEP, Chem. Mater., 12, 1755, 2000.
- 111 R. L. WHETTEN, J. T. KHOURY, M. M. ALVAREZ et al., Adv. Mater., 8, 428, 1996.

- 112 B. A. KORGEL, S. FULLAM, S. CONNOLLY et al., *J. Phys. Chem. B*, **102**, 8379, **1998**.
- 113 C. J. KIELY, J. FINK, M. BRUST et al., *Nature*, **396**, 444, **1998**.
- 114 P. J. THOMAS, G. U. KULKARNI, C. N. R. RAO, *J. Phys. Chem. B*, **104**, 8138, **2000**.
- 115 S. SUN, C. B. MURRAY, *J. Appl. Phys.*, **85**, 4325, **1999**.
- 116 C. PETIT, A. TALEB, M. P. PILENI, *J. Phys. Chem. B*, **103**, 1805, **1999**.
- 117 M. P. PILENI, *New J. Chem.*, **693**, **1998**.
- 118 K. ABE, T. HANADA, Y. YOSHIDA et al., *Thin Solid Films*, **327–329**, 524, **1998**.
- 119 G. SCHMID, M. BÄUMLE, N. BEYER, *Angew. Chem. Int. Ed. Engl.*, **1**, 39, **2000**.
- 120 B. KIM, S. L. TRIPP, A. WEI, *J. Am. Chem. Soc.*, **123**, 7955, **2001**.
- 121 T. TERANISHI, M. MIYAKE, *Chem. Mater.*, **11**, 3414, **1999**.
- 122 P. J. THOMAS, G. U. KULKARNI, C. N. R. RAO, *J. Nanosci. Nanotechnol.*, **1**, 267, **2001**.
- 123 B. A. KORGEL, D. FITZMAURICE, *Adv. Mater.*, **10**, 661, **1998**.
- 124 C. J. KIELY, J. FINK, J. G. ZHENG et al., *Adv. Mater.*, **12**, 639, **2000**.
- 125 C. B. MURRAY, C. R. KAGAN, M. G. BAWENDI, *Science*, **270**, 1335, **1995**.
- 126 S. CHEN, L. A. TRUAX, J. M. SOMMERS, *Chem. Mater.*, **12**, 3864, **2002**.
- 127 Unpublished results from our laboratory.
- 128 M. D. BENTZON, J. VAN WONTERGHEM, S. MORUP et al., *Philos. Mag. B*, **60**, 169, **1989**.
- 129 S. SUN, H. ZENG, *J. Am. Chem. Soc.*, **124**, 8204, **2002**.
- 130 P. J. THOMAS, P. SARAVANAN, G. U. KULKARNI et al., *Pramana*, **58**, 371, **2002**.
- 131 J. S. YIN, Z. L. WANG, *Phys. Rev. Lett.*, **79**, 2570, **1997**.
- 132 M. LI, H. SCHNABLEGGER, S. MANN, *Science*, **402**, 393, **1999**.
- 133 H. ZHENG, J. LI, J. P. LIU et al., *Nature*, **420**, 395, **2002**.
- 134 M. MAILLARD, L. MOTTE, A. T. NGO et al., *J. Phys. Chem. B*, **104**, 11871, **2000**.
- 135 M. MAILLARD, L. MOTTE, M. P. PILENI, *Adv. Mater.*, **16**, 200, **2001**.
- 136 P. C. OHARA, W. M. GELBART, *Langmuir*, **14**, 3418, **1998**.
- 137 T. VOSSMEYER, S.-W. CHUNG, W. M. GELBART et al., *Adv. Mater.*, **10**, 351, **1998**.
- 138 C. STOWELL, B. A. KORGEL, *Nanoletters*, **1**, 595, **2001**.
- 139 R. A. MCMILLAN, C. D. PAAVOLA, J. HOWARD et al., *Nature Mater.*, **1**, 247, **2002**.
- 140 D. BARGEMAN, F. V. V. VADER, *J. Electroanal. Chem.*, **37**, 45, **1972**.
- 141 K. V. SARATHY, P. J. THOMAS, G. U. KULKARNI et al., *J. Phys. Chem. B*, **103**, 399, **1999**.
- 142 M. BRUST, D. BETHELL, C. J. KIELY et al., *Langmuir*, **14**, 5425, **1998**.
- 143 R. BLONDER, L. SHEENEY, I. WILLNER, *Chem. Commun.*, 1393, **1998**.
- 144 Y. LIU, Y. WANY, R. O. CLAUS, *Chem. Phys. Lett.*, **298**, 315, **1998**.
- 145 A. SAMOKHVALOV, M. BERFELD, M. LAHAV et al., *J. Phys. Chem. B*, **104**, 8632, **2000**.
- 146 M. GAO, B. RICHTER, S. KIRSTEIN, *Adv. Mater.*, **9**, 802, **1997**.
- 147 H. G. FRITSCH, H. MULLER, B. FEHRENSSEN, *Z. Phys. Chem.*, **199**, 87, **1997**.
- 148 H. FELD, A. LEUTE, D. RADING et al., *J. Am. Chem. Soc.*, **112**, 8166, **1990**.
- 149 P. J. THOMAS, G. U. KULKARNI, C. N. R. RAO, *J. Phys. Chem. B*, **105**, 2515, **2001**.
- 150 M. MAILLARD, L. MOTTE, A. T. NGO et al., *J. Phys. Chem. B*, **104**, 11871, **2000**.
- 151 G. SCHMID, R. PUGIN, T. SAWITOWSKI et al., *Chem. Commun.*, 1303, **1999**.
- 152 E. SHEVCHENKO, D. TALAPIN, A. KORNOWSKI et al., *Adv. Mater.*, **14**, 287, **2002**.
- 153 D. V. TALAPIN, E. V. SHEVCHENKO, A. KORNOWSKI et al., *Adv. Mater.*, **13**, 1868, **2001**.
- 154 H. AGO, T. KOMATSU, S. OHSHIMA et al., *Appl. Phys. Lett.*, **77**, 79, **2000**.
- 155 Y. CUI, L. J. LAUHON, M. S. GUDISKSEN et al., *Appl. Phys. Lett.*, **78**, 2214, **2001**.
- 156 P. A. LEWIS, H. AHAMED, T. SATO, *J. Vac. Sci. Technol. B*, **16**, 2938, **1998**.
- 157 Y.-K. HONG, H. KIM, G. LEE et al., *Appl. Phys. Lett.*, **80**, 844, **2002**.

- 158 R. D. PINER, J. ZHU, F. XU et al., *Science*, 283, 661, 1999.
- 159 C. A. MIRKIN, S. HONG, L. DEMERS, *ChemPhysChem*, 2, 37, 2001.
- 160 C. R. MARTIN, D. T. MITCHELL, *Anal. Chem.*, 322A, 1998.
- 161 D. L. FELDHEIM, C. D. KEATING, *Chem. Soc. Rev.*, 27, 1, 1998.
- 162 C. P. VINOD, G. U. KULKARNI, C. N. R. RAO, *Chem. Phys. Lett.*, 289, 329, 1998.
- 163 R. BUSANI, M. FOLKER, O. CHESNOVSKY, *Phys. Rev. Lett.*, 81, 3836, 1998.
- 164 M. MIYAKE, T. TORIMOTO, T. SAKATA et al., *Langmuir*, 13, 742, 1997.
- 165 K. RADEMAN, O. D. RADEMAN, M. SCHLAUF et al., *Phys. Rev. Lett.*, 69, 3208, 1992.
- 166 M. VALDEN, X. LAI, D. W. GOODMAN, *Science*, 281, 1647, 1998.
- 167 U. HEIZ, A. SANCHEZ, S. ABBET et al., *J. Am. Chem. Soc.*, 121, 3214, 1999.
- 168 H. MATTOUSSI, J. M. MAURO, E. R. GOLDMAN et al., *J. Am. Chem. Soc.*, 122, 12142, 2000.
- 169 D. GERION, F. PINAUD, S. C. WILLIAMS et al., *J. Phys. Chem. B*, 105, 8861, 2001.
- 170 W. J. PARAK, D. GERION, D. ZANCHET et al., *Chem. Mater.*, 14, 2113, 2002.
- 171 W. C. W. CHAN, S. NIE, *Science*, 281, 2106, 1998.
- 172 Y. KIM, R. C. JOHNSON, J. T. HUPP, *Nanoletters*, 1, 165, 2001.
- 173 S. BERCHMANS, P. J. THOMAS, C. N. R. RAO, *J. Phys. Chem. B*, 106, 4651, 2002.
- 174 Single Charge Tunneling, Coulomb Blockade Phenomena in Nanostructures, ed. H. GRABER, M. H. DEVORET, Plenum, New York 1992, NATO ASI series B294.
- 175 P. J. THOMAS, G. U. KULKARNI, C. N. R. RAO, *Chem. Phys. Lett.*, 321, 163, 2000.
- 176 J. JORTNER, *Z. Phys. D*, 24, 247, 1992.
- 177 C. P. BEAN, J. D. LIVINGSTON, *J. Appl. Phys.*, 30, 1208, 1959.
- 178 VAN DE HEER, P. MILANI, A. CHATELAIN, *Z. Phys. D*, 19, 241, 1991.
- 179 J. NANDA, K. S. NARAYAN, B. A. KURUVILLA et al., *Appl. Phys. Lett.*, 72, 1335, 1998.
- 180 V. L. COLIN, M. C. SCHLAMP, A. P. ALIVISATOS, *Nature*, 370, 354, 1994.
- 181 M. C. SCHLAMP, X. PENG, A. P. ALIVISATOS, *J. Appl. Phys.*, 82, 5837, 1997.
- 182 B. O. DABBOUSI, M. G. BAWENDI, O. ONITSUKA et al., *Appl. Phys. Lett.*, 66, 1316, 1995.
- 183 K. S. NARAYAN, A. G. MANOJ, J. NANDA et al., *Appl. Phys. Lett.*, 74, 871, 1999.
- 184 H.-J. EISLER, V. C. SUNDAR, M. G. BAWENDI et al., *Appl. Phys. Lett.*, 80, 4614, 2002.
- 185 V. C. SUNDAR, H.-J. EISLER, M. G. BAWENDI, *Adv. Mater.*, 14, 739, 2002.
- 186 W. U. HUYNH, J. J. DITTMER, A. P. ALIVISATOS, *Science*, 295, 2425, 2002.
- 187 J. LEE, V. C. SUNDAR, J. R. HEINE et al., *Adv. Mater.*, 12, 1102, 2000.
- 188 M. GAO, C. LESSER, S. KIRSTEIN et al., *J. Appl. Phys.*, 87, 2297, 2000.
- 189 M. BRUST, D. BETHELL, D. J. SCHIFFRIN et al., *Adv. Mater.*, 7, 795, 1995.
- 190 V. TORMA, G. SCHMID, U. SIMON, *ChemPhysChem*, 1, 321, 2001.
- 191 U. SIMON, R. FLESCH, H. WIGGERS et al., *J. Mater. Chem.*, 8, 517, 1998.
- 192 M. ASLAM, I. S. MULLA, K. VIJAYAMOHANAN, *Appl. Phys. Lett.*, 79, 689, 2001.
- 193 R. H. TERRILL, T. A. POSTLEWAITE, C. CHEN et al., *J. Am. Chem. Soc.*, 117, 1237, 1995.
- 194 M. D. MUSICK, C. D. KEATING, M. H. KEEFE et al., *Chem. Mater.*, 9, 1499, 1997.
- 195 Y. LIU, Y. WANG, R. O. CLAUSS, *Chem. Phys. Lett.*, 298, 315, 1998.
- 196 R. PARTHASARATHY, X.-M. LIN, H. A. JAEGER, *Phys. Rev. Lett.*, 87, 186807, 2001.
- 197 J. SCHMELZER, JR., S. A. BROWN, A. WURL et al., *Phys. Rev. Lett.*, 88, 226802, 2002.
- 198 R. C. DOTY, H. YU, C. K. SHIH et al., *J. Phys. Chem. B*, 105, 8291, 2001.
- 199 T. OGAWA, K. KOBAYASHI, G. MASUDA et al., *Thin Solid Films*, 393, 374, 2001.
- 200 R. G. OSIFCHIN, W. J. MAHONEY, J. D. BIELEFELD et al., *Superlattices Microstruct.*, 18, 283, 1995.

- 201 R. G. OSIFCHIN, W. J. MAHONEY, J. D. BIELEFELD et al., *Superlattices Microstruct.*, 18, 275, 1995.
- 202 G. MARKOVICH, C. P. COLLIER, S. E. HENDRICKS et al., *Acc. Chem. Res.*, 32, 415, 1999.
- 203 G. MEDEIROS-RIBEIRO, D. A. A. OHLBERG, R. S. WILLIAMS et al., *Phys. Rev. B*, 59, 1633, 1999.
- 204 A. TALEB, F. SILLY, A. O. GUSEV, F. CHARRA et al., *Adv. Mater.*, 12, 633, 2000.
- 205 T. P. BIGIONI, L. E. HARRELL, W. G. CULLEN et al., *Eur. Phys. J.*, D6, 355, 1999.
- 206 M. V. ARTEMYEV, U. WOGGON, H. JASCHINSKI et al., *J. Phys. Chem. B*, 104, 11617, 1999.
- 207 C. R. KAGAN, C. B. MURRAY, M. G. BAWENDI, *Phys. Rev. B*, 54, 8633, 1996.
- 208 H. DÖLLEFELD, H. WELLER, A. EYCHMÜLLER, *J. Phys. Chem. B*, 106, 5604, 2002.
- 209 M. V. ARTEMYEV, A. I. BIBIK, L. I. GURINOVICH et al., *Phys. Rev. B*, 60, 1504, 1999.
- 210 V. RUSSIER, C. PETIT, J. LEGRAND et al., *Phys. Rev. B*, 62, 3910, 2000.
- 211 A. T. NGO, M. P. PILENI, *J. Phys. Chem. B*, 105, 53, 2001.
- 212 Unpublished results from the authors laboratory.
- 213 A. T. NGO, M. P. PILENI, *Adv. Mater.*, 12, 276, 2000.
- 214 *Molecular Electronics*, ed. J. JORTNER, M. RATNER, Blackwell Scientific, London 1997, IUPAC A 'Chemistry for the 21st Century' monograph.
- 215 A. O. ORLOV, I. AMLANI, G. H. BERSTEIN et al., *Science*, 277, 928, 1997.
- 216 J. R. HEATH, P. J. KUEKES, G. S. SNIDER et al., *Science*, 280, 1717, 1998.
- 217 H. ABELSON, D. ALLEN, D. COORE et al., *Technical Report A. I. Memo 1665*, Massachusetts Institute of Technology, Artificial Intelligence Laboratory, Aug. 1999.
- 218 D. COORE, R. NAGPAL, R. WEISS, *Technical Report A. I. Memo 1614*, Massachusetts Institute of Technology, Artificial Intelligence Laboratory, Oct. 1997.
- 219 H. ABELSON, D. ALLEN, D. COORE et al., *Commun. Assoc. Comp. Mach.*, May 2000.

## 5

**Oxide Nanoparticles***R. Seshadri***Abstract**

Recent developments in the preparation and use of nanoparticulate oxide materials, more specifically isolated nanoparticles of simple and compound oxides, are reviewed. While oxide nanoparticles have been known and studied for many decades, it is only in recent years that methods for their preparation have achieved the level of sophistication which permits monodisperse nanoparticles to be produced in quantity. In addition, it is only in recent years that the notion of capping of oxide nanoparticle surfaces by long-chain surfactants, with the corollary that they become soluble, has taken firm hold. The emphasis is on new routes for the preparation of oxide nanoparticles, and how these could be distinct from those used for metals or chalcogenides. Properties of oxide nanoparticles are discussed with special reference to how they are distinct from the bulk material. Present and possible applications are discussed in context.

Methods of preparation that are encouraging from the viewpoint of scale-up are particularly emphasized. Finally, some important issues in the field are outlined.

## 5.1

**Introduction**

One of Michael Faraday's Bakerian Lectures, published as an article in *Philosophical Transactions of the Royal Society* in 1857 [1] reveals that already in the mid-19th century, a great deal of thought had been devoted to what happens to the properties of materials as their dimensions are made small. Among the materials investigated by Faraday are the now famous gold sols, which he prepared using a variety of means. From the colors that Faraday reports, including ruby red, one infers that he was able to prepare sub-100 nm particles. It would perhaps be proper to describe Faraday as among the first scientists to attempt a systematic study of what today would be called a nanomaterial. Nanomaterials have existed for much longer, an example being Maya blue paint [2], the bright and chemically stable

pigment whose color is believed to arise from the coexistence of metal nanoparticles, oxide superlattices and an organic pigment. Gold colloids find wide use in staining glass, and the nanoparticulate pigment purple of Cassius, obtained by reducing a gold salt using tin (II) chloride is named for the physician Andreas Cassius who died in 1673 [3].

What is then new in the area that it should receive such renewed attention. Firstly, a number of tools, both experimental (exemplified by high-resolution transmission electronic microscopy and scanning tunneling microscopy) and theoretical (exemplified by density functional theory), that permit a much better understanding of these systems have become available. For the first time, researchers in the area can “see” what they are doing. Secondly, in close conjunction with the improved experimental tools are synthetic skills that have been brought to bear upon this area – monodisperse nanoparticles (particularly of metals and chalcogenides), whose surfaces are stabilized by the use of capping agents, have become commonplace in recent years. For chalcogenide nanoparticles, key early studies by the Henglein group in Berlin [4], from Bell laboratories [5], and from the group of Bawendi in MIT [6] have played a role. In the case of metal nanoparticles, the two-phase synthesis of gold nanoparticles by Brust et al. [7] was perhaps the earliest report of well-capped particles. These authors made use of the well-known ability of long chain thiols to form close-packed monolayers on gold surfaces [8] to cap gold nanoparticles. Nanoparticles ensuing from these preparations, unlike the sols of Davy, Faraday and others, are distinct in that they can be precipitated (or collected through evaporation of solvent) and then redissolved. Colloidal sols such as clays in rivers, milk and India ink, once precipitated (or flocculated) cannot be redispersed without great effort [9]. Capped nanoparticles therefore resemble large molecules in their solubility behavior.

Solubility (in the molecular sense, rather than in the sense of forming dispersions and sols) opens up a number of possibilities. The first and perhaps most important, is that it allows size-selective precipitation [10], permitting monodisperse nanoparticles to be prepared. It is only when particles are monodisperse that their size-dependent physical properties can be studied in detail [6]. It is also possible to organize these monodisperse nanoparticles via slow evaporation to yield superlattices [11–13]. Superlattices of nanocrystals can rightly be described as a new class of materials, comprising crystals of crystals as opposed to most crystalline solids which are crystals of atoms [14]. In contrast, naturally occurring opals are crystals of amorphous silica spheres [15].

Oxides, particularly those of the transition metals, display the widest and most fascinating range of properties of any single class of materials. In recent years, oxide materials have been at the heart of many dramatic advances in condensed matter science – layered copper oxides exhibiting high-TC superconductivity readily spring to mind as a good example [16]. Another example is the finding that certain perovskite manganese oxides display dramatic (as large as twelve orders of magnitude) changes in their specific resistivities when subjected to magnetic fields, opening up the new sub-field of colossal magnetoresistance (CMR) [17].



In traditional electronics – LCR circuits, for example – the Ls and the Cs are invariably oxide materials. In the area of integrated semiconductor devices, gate dielectrics [18], dielectrics in dynamic random access memories [19], ferroelectrics in non-volatile memories [20], and decoupling capacitors [21] are all oxide materials. Oxides are also at the heart of many fuel cell [22] and secondary battery materials [23].

Given the importance of oxide materials, it is only natural to ask whether recent understanding regarding the synthesis, properties and applications of capped metal and semiconductor nanoparticles can be extended to oxides.

This review does not concern itself with the vast literature of nanophase materials, which are monolithic materials comprising crystalline grains whose dimensions are in the nanometer range. Such materials are typically prepared using sol–gel and related techniques. This is an older, more mature area that continues to attract a great deal of interest [24].

## 5.2

### Magnetite Particles in Nature

While it was known that many organisms respond to the earth's magnetic field, Blakemore's demonstration in 1975 [25] that certain bacteria found in marine marsh muds tended to rapidly navigate along a specific direction – the local geomagnetic north – was seminal. In addition, Blakemore used transmission electron microscopy to demonstrate that these bacteria contained iron-rich crystals about 100 nm in diameter. Several crystals were found to align themselves into chains along their major axis [Figure 5.1]. Frankel, Blakemore and Wolfe [26] then found that an unclassified magnetotactic spirillum (denoted MS-1) when cultured in solutions containing ferric salts, precipitated uniform single crystals that were shown, by Mössbauer spectroscopy, to be mostly spinel  $\text{Fe}_3\text{O}_4$ . Since these early studies, the importance of magnetotaxis and magnetoreception in a number of organisms, from bacteria through higher vertebrates, continue to be the subject of investigation [27, 28]. It is interesting that the effects of magnetic fields on organisms – described as “a romping ground for quakes and charlatans, dating at least to the French Mesmerists in the late 18th century” [27] should finally find some legitimacy through the discovery that magnetic nanoparticles play a role in magnetotaxis.

Microbial magnetite (and the ferrimagnetic sulfide biomineral greigite  $\gamma\text{-Fe}_3\text{S}_4$ , found in magnetotactic bacteria that grow in marine, sulfidic environments) are fine examples of the control that Nature is able to exert over inorganic crystallizations. The magnetic particles are invariably at the optimal single domain size for the specific mineral. What this means is that each magnetic particle contains only a single magnetic domain. If the particle were smaller or larger, it would not be as effective a magnet. In addition, within the magnetosome, the magnetite (or greigite) crystals are aligned in such a manner that the assembly develops a per-



**Fig. 5.1.** Transmission micrographs of the magnetotactic bacteria *Magnetospirillum magnetotacticum* taken in two different directions. The precise control of both the magnetite nanocrystal shape and size, as well

as the manner in which all the crystals are aligned, provide inspiration to practitioners of oxide nanoparticle preparations. Images kindly provided by Professor R. B. Frankel, California Polytechnic University, San Luis Obispo.

manent magnetic dipole making an effective compass. The natural remnant magnetization of the assembly approaches the saturation magnetization of magnetite [29]. A major concern in the preparation of oxide nanoparticles is to be able to control size and shape very precisely, and, in many cases, to assemble the nanoparticles in a templated manner. Biogenic magnetite provides great inspiration, suggesting what laboratory preparations can aspire to, and providing hints on how these goals could be achieved. Schüler and Frankel [30] have recently reviewed bacterial magnetosomes with reference to their microbiology, biomineralization and applications in biotechnology. Presently, a UK company is exploiting the principles of magnetite biomineralization by using apoferritin protein shells as nanoscale containers within which monodisperse nanoparticles, including nanoparticles of magnetite, can be grown in quantity [31].

Interestingly, the unusual and very specific control over magnetite morphology that Nature (as embodied in magnetotactic bacteria) exercises, has led a team of investigators to suggest that magnetite in certain calcitic globules from the Martian meteorite ALH84001 are actually magnetofossil records of life on Mars [32]. This claim has been disputed [33], based on evidence from electron holography of magnetite nanocrystals from magnetotactic bacteria, and their comparison with the meteoritic magnetite.

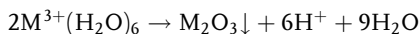
## 5.3

## Routes for the Preparation of Isolated Oxide Nanoparticles

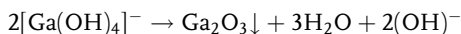
## 5.3.1

## Hydrolysis

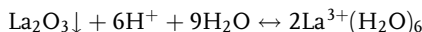
Traditionally, a number of oxide materials have been prepared from aqueous solution using hydrolytic methods. Many of these preparation techniques lend themselves to the preparation of nanoparticles. The term hydrolysis is used in a number of contexts, in most of which it involves breaking up of the water molecule [34]. It is useful to imagine that the hydrolysis of a hydrated trivalent metal ion into an oxide takes place in the following manner:



Such a scheme indicates that the water molecule is decomposed in the process and, in addition, that the formation of an oxide usually requires basic conditions. However, in the preparation of oxides of amphoteric species such as Al(III) or Ga(III), acid hydrolysis could be employed. For example:



An important aspect of such hydrolysis is that not all ions are amenable to it. The alkali, alkaline earth and rare-earth ions, for example, are too stable in solution, and too ionic for hydrolysis to take place. In fact, the hydration reaction is the one that would be favored. For  $La^{3+}$  for example, the equilibrium:



can be shifted completely to the left only at temperatures as high as 1000 K.

Despite these limitations, hydrolytic routes have been the mainstay of many preparations of nanoparticulate oxide materials, particularly of the first row transition metals. It is of interest to note that much of the reported literature on hydrolytic routes concerns aqueous systems and it would not be incorrect to say that much needs to be done on the use of solvents other than water, particularly aprotic solvents, where hydrolysis may be more effective. The use of electrochemistry to assist in hydrolysis is a technique that has found much use in the preparation of transition metal oxide films [35], but its use in the preparation of oxide nanoparticles is not widespread.

Magnetic oxide (typically ferrite spinels or  $\gamma\text{-Fe}_2\text{O}_3$ ) nanoparticles, when dispersed at high concentrations in water or oil, form ferrofluids [36]. Particle sizes in these materials are usually in the 5–15 nm range – small enough that neither magnetic nor gravitational fields should cause their precipitation. The many uses of ferrofluids in magnetic seals, bearings, dampers etc. [36] have resulted in an extensive body of literature on the preparation and properties of dispersions of

magnetic oxide nanoparticles. Many of the preparative routes involve hydrolysis. In many cases, the preparation simply involves raising the pH of a solution of metal ions, taken in the correct proportion, by addition of base. Sorenson, Klabunde and coworkers [37], have made detailed magnetic and Mössbauer studies of  $\text{MnFe}_2\text{O}_4$  nanoparticles prepared by precipitation at high pH followed by digestion. Cabuil and coworkers [38] have shown in the case of the preparation of  $\text{CoFe}_2\text{O}_4$  and  $\gamma\text{-Fe}_2\text{O}_3$  particles that changing the temperature and the nature of the base allows particles of different sizes to be prepared. In addition, they have suggested methods of dispersing the particles in water, through controlling Coulomb repulsion between the particles. The particles can be dispersed in oils by modifying their surfaces with long chain surfactants. Cabuil et al. [39] have also shown that size-selection of particles is possible through control of a combination of surface charge and ionic strength of the dispersing medium. Morales et al. [40] have made a careful study of  $\gamma\text{-Fe}_2\text{O}_3$  nanoparticles, with sizes ranging from 3 to 14 nm, prepared by hydrolytic means (and also by laser pyrolysis of  $\text{Fe}(\text{CO})_5$  in solution). They show that to account for the magnetic properties of the particles, it is necessary to use a model wherein the moments on the surface of the particle are canted.

The use of polar solvents other than water to perform hydrolysis is an exciting prospect. Ammar et al. [41] have demonstrated that glycols (specifically 1,2-propanediol) can be used as a solvent under reflux to hydrolyze a mixture of  $\text{Co}(\text{II})$  and  $\text{Fe}(\text{III})$  salts to obtain equiaxed particles of  $\text{CoFe}_2\text{O}_4$  with an average diameter of 5.5 nm. A combination of Mössbauer spectroscopy, X-ray absorption near-edge structure (XANES) and magnetic measurements suggested that the particles were well-ordered both in terms of being crystalline and having all Co in the divalent state. Rajamathi et al. have been able to capitalize on the unusual properties of glycols – that they are sufficiently polar that they can dissolve metal salts and that they can support hydrolysis and yet they can dissolve long chain surfactants such as amines – in the preparation of n-octylamine-capped 5 nm  $\gamma\text{-Fe}_2\text{O}_3$  nanoparticles [42]. The particles [Figure 5.2] can be dissolved in toluene when a little excess amine is added to the solvent. The particles can be precipitated through addition of a polar solvent such as 2-propanol, and then redissolved in toluene/n-octylamine. Diethylene glycol has also been used as a solvent by Carunto et al. [43] to prepare a number of transition metal ferrites capped by long chain carboxylic acids.

Pileni [44] has reviewed the extensive work from her group on the use of reverse micelles as nanoscale reaction chambers within which nanoparticles can be prepared. In a system of water and surfactant dispersed in oil, under suitable conditions, the water forms spherical droplets of radius  $R_w$  given by:

$$R_w = \frac{3V_{\text{aq}}[\text{H}_2\text{O}]}{\sigma[S]}$$

where square brackets indicate concentration, S refers to surfactant,  $\sigma$  is the area per head group of the surfactant molecule and  $V_{\text{aq}}$  is the volume of a water molecule. By controlling the water and surfactant concentration, the diameter of the water droplet can therefore be controlled. If a nanoparticle is nucleated within the

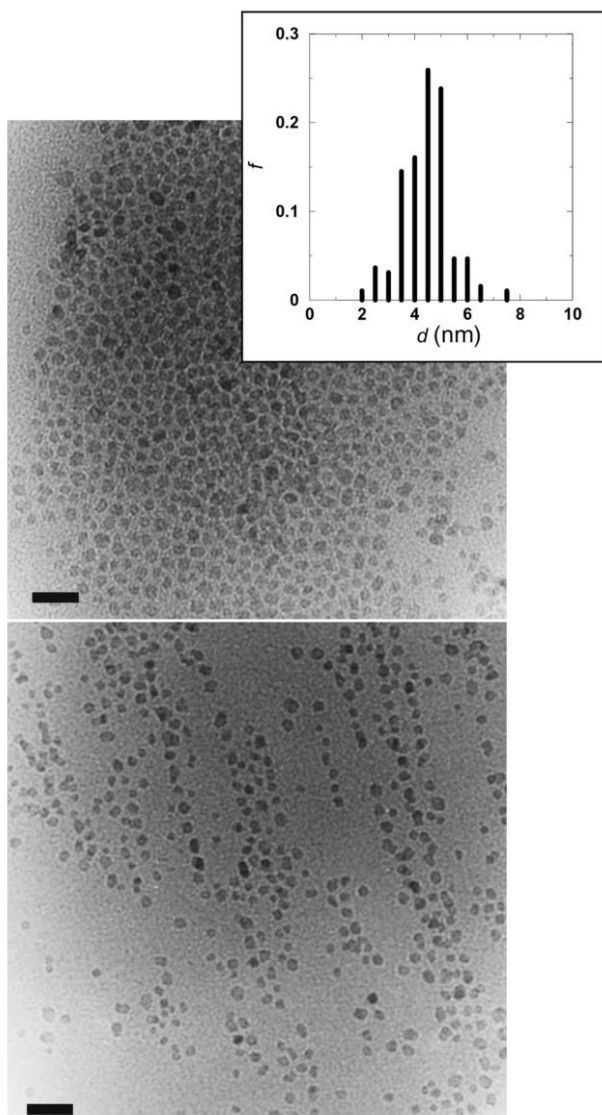


**Fig. 5.2.** Transmission electron micrographs of maghemite  $\gamma\text{-Fe}_2\text{O}_3$  nanoparticles prepared by hydrolysis of Fe(III) salts in refluxing propylene glycol in the presence of amine capping agents. The nanoparticles are soluble in toluene solutions of *n*-octylamine and, as a result, display a tendency for superlattice self-

assembly when concentrated (top) and to form aligned arrays in the direction of the earth's magnetic field when dilute (bottom). The bars are 20 nm. Reproduced from [42] with permission from the Royal Society of Chemistry.

water sphere, its growth is limited by the size constraint of the water droplet. Pillai and Shah [45] have utilized this route to prepare high-coercivity  $\text{CoFe}_2\text{O}_4$  nanoparticles by mixing two water-in-oil microemulsions, one containing metal ions and the other containing base. These authors calcine the particles, so the resulting material is nanophase, rather than nanoparticulate.  $\text{MnFe}_2\text{O}_4$  [46] and  $\text{CoCrFeO}_4$  [47] have been prepared using such reverse-micelle routes by Zhang et al., and characterized by using a combination of magnetization studies and powder neutron diffraction.

Pileni has also pioneered the use of the surfactant-as-reactant approach in the preparation of nanoparticles. For example, in the preparation of  $\text{CoFe}_2\text{O}_4$  nanoparticles with sizes between 2 and 5 nm, instead of preparing inverse-micellar dispersions of the Co and Fe salts, Moumen and Pileni [48] prepared the dodecylsulfonate (DS) analogs  $\text{Fe}(\text{DS})_2$  and  $\text{Co}(\text{DS})_2$ . These were made to form micellar solutions, to raise the pH, aqueous methylamine solution was added. Stirring for 2 h resulted in a magnetic precipitate. Due to the low yield of Fe(II) to Fe(III) oxidation under these conditions, an excess of  $\text{Fe}(\text{DS})_2$  is required.

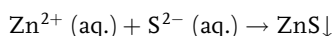
With an increase in concentration of the reactants, there is an increase in particle size. Zinc-doped cobalt ferrite nanoparticles [49] and zinc ferrite [50] have also been prepared using these methods. The 10 nm ferrite nanocrystal ferrofluids prepared using the  $\text{Fe}(\text{DS})_2$  route form deposits with different morphologies when evaporated on oriented graphite substrates [51]. The morphology can be strongly influenced by applying a magnetic field during the evaporation process. Thus magnetic properties of deposits prepared in the presence and absence of a field are quite different.

Hydrolysis can be assisted by using irradiation of the reacting bath with ultrasound. In these sonochemical preparations, acoustic cavitation results in the production of concentrated spots of extremely high temperatures. These “hot spots” accelerate the rate of metal ion hydrolysis. Gedanken and coworkers [52] have prepared  $\text{ZnO}$ ,  $\text{CuO}$ ,  $\text{Co}_3\text{O}_4$  and  $\text{Fe}_3\text{O}_4$  particles by subjecting solutions of the acetates to ultrasound irradiation using a high-intensity horn. Particle morphologies could be altered by using mixtures of water and dimethyl formamide instead of pure water as the solvent. Magnetite nanorods have been prepared by these authors [53] by ultrasonically irradiation of Fe(II) acetate in water in the presence of  $\beta$ -cyclodextrin. The authors suggest that cyclodextrin molecules are acting as size-stabilizing agents.

### 5.3.2

#### Oxidation

Oxides, unlike the other chalcogenides (sulfides, selenides, tellurides), are not associated with an oxide ion source. In other words, while the formation of a sulfide such as  $\text{ZnS}$  can be written:



where the source of the sulfide ion in solution could be  $\text{Na}_2\text{S}$  or thiourea or the like, it is not possible to frame a similar reaction scheme for oxides. On the other hand, it is possible to directly oxidize a metal source in solution. A popular route to this is to use zero-valent carbonyls, for example  $\text{Fe}(\text{CO})_5$ . Decomposing these carbonyls in solvents results in very finely divided metal particles that are easily susceptible to oxidation. In fact, exposing them to an atmosphere of air is usually sufficient to convert the particles to oxides.

Bentzon et al. [11] have prepared iron oxide nanoparticles by decomposing  $\text{Fe}(\text{CO})_5$  in decalin in the presence of oleic acid as the stabilizing ligand. Aging the ferrofluid so formed in air for several weeks results in a mixture of hematite and spinel phases. The fascinating aspect of this work is that it is among the first reports of nanocrystal superlattice formations, and is still only one of few reports on highly coherent oxide nanocrystal superlattices. More recently, Hyeon et al. have prepared monodisperse  $\gamma\text{-Fe}_2\text{O}_3$  nanoparticles in the size range 4–16 nm by decomposing  $\text{Fe}(\text{CO})_5$  complexes in octyl ether at 300 °C in the presence of oleic acid. Oxidation of bcc-Fe to  $\gamma\text{-Fe}_2\text{O}_3$  was achieved by the addition of the organic oxidant  $(\text{CH}_2)_2\text{NO}$ . The resulting capped oxide nanoparticles can easily be redispersed in organic solvents such as hexane or toluene. Particle sizes are altered by varying the ratio of Fe to the capping agent (oleic or lauric acids). The remarkable feature of this preparation is that the as-prepared particles are sufficiently monodisperse that they form nanocrystal superlattices without the need for a size-selection process.

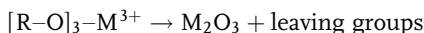
Wagner and coworkers have prepared yttrium oxide [55] and europium-doped yttrium oxide nanoparticles [56] by first reducing rare-earth salts in solution using alkaliides (strong reducing agents that are complexes of crown ethers with alkali metals, and where the anion is a complexed electron) and then oxidizing the rare-earth metal nanoparticle so formed, in aerated water. The white powders were then annealed in air. Some more examples of oxide nanoparticles prepared through direct oxidation will be discussed in the solvothermal methods section.

### 5.3.3

#### Thermolysis

If one starts with a precursor complex wherein the ligands bind to metal ions through oxygen, it could be possible to envisage a decomposition reaction that would leave behind the metal oxide.

For a trivalent ion, such reactions could be generalized as:



Suitable design of the R group (stable leaving groups) would ensure that the reaction proceeds in a facile manner. It should then be possible to carry out such reactions in a suitable high temperature solvent under solvothermal conditions, possibly in the presence of a suitable capping agent.

Rockenberger, Scher and Alivisatos [57] have described the use of cupferron complexes as precursors to prepare transition metal oxide nanoparticles. Cupferron (*N*-phenyl, *N*-nitroso hydroxylamine) forms bidentate, univalent complexes with a number of different transition metals ions. These complexes easily decompose to give the oxide. The authors demonstrated the preparation of  $\gamma$ -Fe<sub>2</sub>O<sub>3</sub>, Cu<sub>2</sub>O and Mn<sub>3</sub>O<sub>4</sub> nanoparticles prepared by injecting octylamine solutions of the corresponding cupferron precursors into refluxing trioctylamine. Size is controlled by controlling the temperature of the reaction. The particles so prepared form stable solutions in solvents such as toluene, from which they can be reprecipitated by the addition of methanol. This work is quite seminal in its generality, and particularly in the manner in which it suggests the search for suitable precursors for the preparation of oxide nanoparticles. Most importantly, it suggests thermolysis as an alternative to hydrolysis which, as pointed out earlier, is simply not viable for a number of metal oxides.

An important contribution to the surface chemistry of metal oxide nanoparticles has been made by Rotello and coworkers [58] who have prepared  $\gamma$ -Fe<sub>2</sub>O<sub>3</sub> nanoparticles by the cupferron decomposition method, and compared the relative efficacies of different long chain surfactants as capping agents. The most stabilizing capping agent (as monitored by ease of redissolution and stability in solution) was obtained by using a two-tailed surfactant (with 12-carbon tails) with the polar part comprising a 1,3-diol.

The thermolysis of Fe(III) hydroxide caprylates in boiling tetralin under argon flow gives  $\gamma$ -Fe<sub>2</sub>O<sub>4</sub> nanoparticles [59]. The surfaces of the nanoparticles could be modified by exchanging the capping caprylate groups with betaine, among other species [60]. Betaine-capped  $\gamma$ -Fe<sub>2</sub>O<sub>3</sub> nanoparticles are reported to have high solubility in water. Using a combination of hydrolysis and oxidation, O'Brien, Brus and Murray [61] have shown that the treatment of a complex alkoxide containing Ba<sup>2+</sup> and Ti<sup>4+</sup>, BaTi(O<sub>2</sub>CC<sub>7</sub>H<sub>15</sub>)[OCH(CH<sub>3</sub>)<sub>2</sub>]<sub>5</sub>, an agent for the MOCVD growth of BaTiO<sub>3</sub>, can be decomposed in diphenyl ether at 140 °C, in the presence of oleic acid as a capping agent, to give nanocrystalline, cubic BaTiO<sub>3</sub> [Figure 5.3]. After cooling to 100 °C, 30% H<sub>2</sub>O<sub>2</sub> is added, and crystallization is induced over a 48 h period. Changing the ratio of capping agent to water, and the amount of peroxide added, permits the size of the particles to be varied. This is perhaps the only report of soluble perovskite oxide nanoparticles and, once again, is a route of great generality and interest. The authors also report using such routes to prepare PbTiO<sub>3</sub> and TiO<sub>2</sub> nanoparticles.

#### 5.3.4

##### Metathesis

In a metathetic reaction, two compounds AB and CD, exchange species to give two new compounds AC and BD. Such routes have been explored in the preparation of nanoparticles. Arnal et al. [62] have reported two non-hydrolytic routes to sol-gel metal oxides, particularly of titanium. The first route involves the reaction of a metal halide with a metal alkoxide:



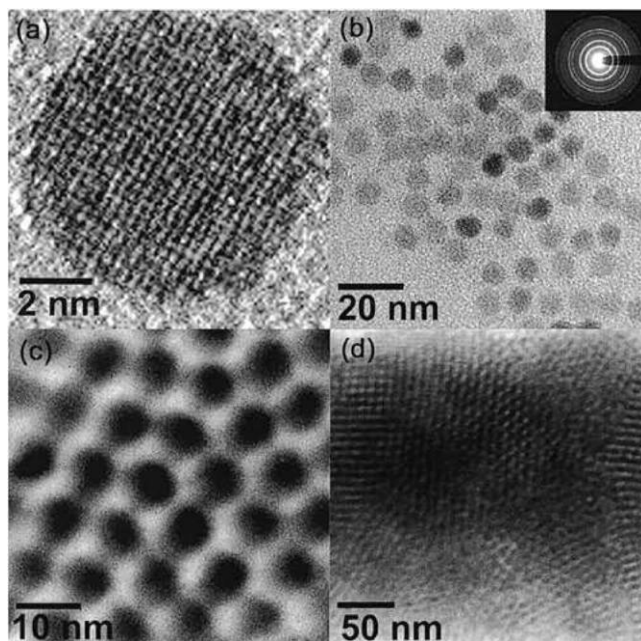
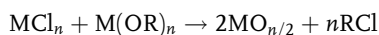
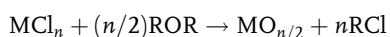


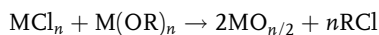
**Fig. 5.3.** Transmission electron micrographs of 8 nm BaTiO<sub>3</sub> nanoparticles prepared by the hydrolysis/oxidation of a Ba–Ti alkoxide precursor. Reproduced from [61] with permission from the American Chemical Society.



and the second route involves the reaction of a metal halide with an ether:



In both reactions, some of the driving force comes from the removal of the volatile product RCl. This first of the two methods has been employed by Colvin and co-workers [63] to prepare capped TiO<sub>2</sub> nanoparticles in refluxing heptadecane with trioctyl phosphine oxide as the capping agent:



The particles formed clear solutions in non-polar solvents, from which they could be precipitated through the addition of a polar solvent such as acetone. When trioctyl phosphine oxide was not taken with the starting materials, insoluble precipitates were obtained.

## 5.3.5

**Solvothermal Methods**

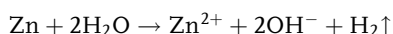
To prepare crystalline oxide materials, high temperatures, associated with the refluxing of reactants in high-boiling solvents, is often called for. There are many problems associated with such solvents, including possible toxicity, expense and their inability to dissolve simple salts. A simple method to circumvent this problem is to use solvothermal methods, employing solvents well above their boiling points in enclosed vessels that support high autogenous pressures. Solvothermal (called hydrothermal when the solvent is water) methods are widespread in their use, particularly in the preparation of crystalline solids, including silicate materials such as zeolites [64].

Recently, Rajamathi and Seshadri [65] have reviewed the uses of solvothermal methods for the preparation of oxide and chalcogenide nanoparticles. For oxide nanoparticles, these methods can involve hydrolysis, oxidation and thermolysis, all performed under hydrothermal or solvothermal conditions. Some of the more striking examples are provided here.

5.3.5.1 **Oxidation**

An unusual reaction reported by Inoue et al. [66] is the direct oxidation of Ce metal in 2-methoxyethanol at temperatures between 200 °C and 250 °C. Most of the product obtained was bulk CeO<sub>2</sub> as a yellow solid, but in addition, they obtained a brown solution of 2 nm CeO<sub>2</sub> nanoparticles. The CeO<sub>2</sub> nanoparticles could be salted out by the addition of NaCl, and redispersed into solution at will. The solutions obeyed the Beer–Lambert law for the concentration dependence of the optical extinction, suggesting that the nanoparticulate dispersion was a genuine solution.

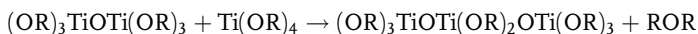
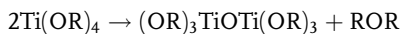
Starting with Zn powder and GaCl<sub>3</sub> in water, Qian and coworkers [67] have used the fact that the oxidation of Zn to Zn<sup>2+</sup> in water is associated with the production of hydroxy ions according to:



The OH<sup>−</sup> ions help in the hydrolysis of Ga<sup>3+</sup>, to eventually give, in the presence of Zn<sup>2+</sup>, the spinel ZnGa<sub>2</sub>O<sub>4</sub>. The authors used a 10–20% over-stoichiometry of Zn and the reaction was carried out at 150 °C for 10 h. 10 nm ZnGa<sub>2</sub>O<sub>4</sub> nanoparticles were obtained. Excess ZnCl<sub>2</sub> formed in the reaction could be washed away with water.

5.3.5.2 **Hydrolysis**

Chemseddine and Moritz [68] have used the polycondensation of titanium alkoxide Ti(OR)<sub>4</sub> in the presence of tetramethylammonium hydroxide, to obtain highly crystalline anatase nanoparticles with different sizes and shapes [Figure 5.4]. A general, stepwise reaction for such polycondensation could be written:



and so on to anatase, though it might not proceed in precisely this manner in the presence of base. The reactions were performed in two steps: First, alkoxide was added to the base at 0 °C in alcoholic solvents in a three-necked flask. The temperature was then raised to reflux. The second stage involved treating the product of the reflux in Ti autoclaves under a saturated vapor pressure of water (2500 kPa) at temperatures between 175 °C and 200 °C for 5 h. The nanocrystals obtained were sufficiently monodisperse that they formed coherent superlattices, as monitored by low-angle powder X-ray diffraction. By using other hydroxides with bulkier alkyl groups (for example, tetrapropylammonium hydroxide) some control over crystallite morphology became possible.

Wu et al. [69] have combined microemulsion and inverse-micelle techniques with hydrothermal techniques in the preparation of rutile and anatase  $\text{TiO}_2$  nanoparticles. They used the system water–cyclohexane–Triton X-100 with n-hexanol as a second emulsifier. The water-filled micellar pockets were acidified (with HCl or  $\text{HNO}_3$ )  $\text{Ti}(\text{OR})_4$  (R = butyl). Treating the system at 120–200 °C for 12–144 h gave anatase particles. When high HCl concentrations were employed, rutile rods were obtained.

Hirano [70] has prepared spinel  $\text{ZnGa}_2\text{O}_4$  nanoparticles by adjusting the pH of Zn and Ga sulfates with  $\text{NH}_3$  to different initial values (varied from 2.5 through 10). The material was heat-treated hydrothermally at temperatures between 150 °C and 240 °C for times between 5 and 50 h. Particle sizes could be varied from 5 to 25 nm.

Cabañas et al. [71] have described the preparation of nanoparticulate  $\text{CeO}_2$ – $\text{ZrO}_2$  solid solutions under *flow-hydrothermal* conditions, wherein the reactants are taken to the final temperature very rapidly in a continuous process. The advantage of performing hydrothermal reactions in such a manner is, firstly, that a large amount of material can be processed, permitting simple scale up. Secondly, the nucleation step can be made very rapid, as a result of the rapid heating. This can help separate nucleation and growth, and can thereby satisfy the famous LaMer criterion [72] for obtaining monodisperse particles. Cabañas and Poliakoff [73] have also prepared a number of spinel ferrite samples in this way, starting from mixtures of different Fe(II) and M(II) acetates (M = Co, Ni, Zn and Co/Ni). Most of the preparations yielded a bimodal distribution of sample sizes, with the smaller samples being about 10 nm in diameter and the larger ones, about 100 nm.

### 5.3.5.3 Thermolysis

Recently, Thimmaiah et al. [74] have extended the thermolytic route to oxide nanoparticles devised by Rockenberger, Scher and Alivisatos [57] to solvothermal conditions. Using solvothermal toluene (typically at 220 °C for 1 h), cupferron precursors of Fe, and Co and Fe are decomposed to obtain sub-12 nm maghemite  $\gamma\text{-Fe}_2\text{O}_3$  nanoparticles and spinel  $\text{CoFe}_2\text{O}_4$  nanoparticles. The reactions do not

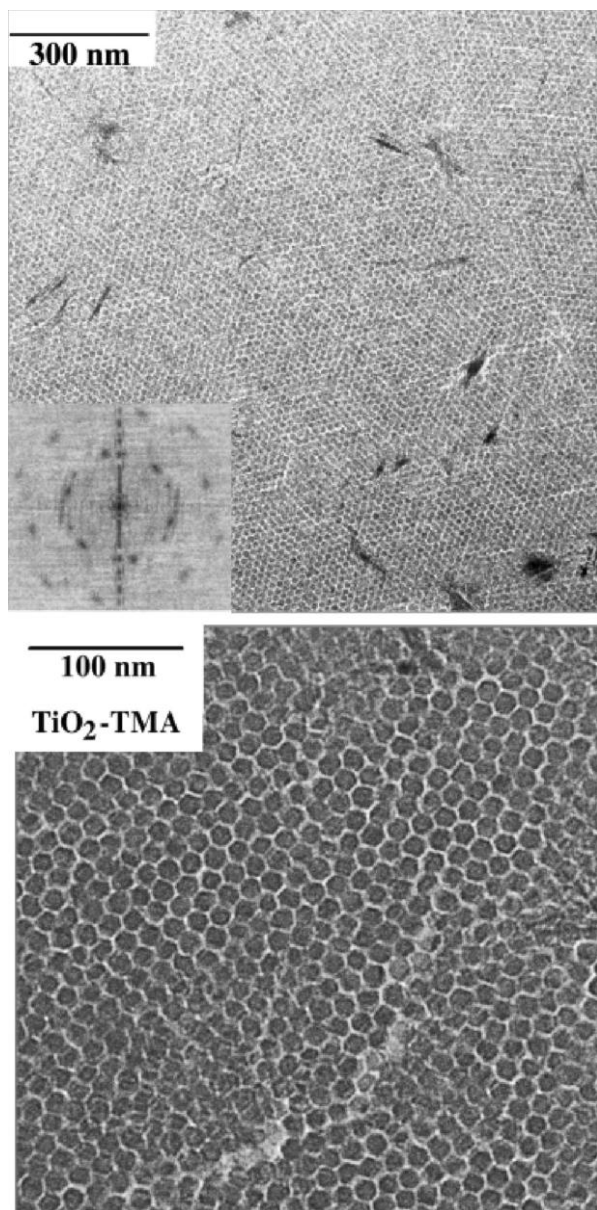


**Fig. 5.4.** Transmission electron micrographs of anatase  $\text{TiO}_2$  nanoparticles prepared by solvothermal treatment of  $\text{Ti}(\text{OR})_4$  after hydrolysis with tetramethylammonium hydroxide. The inset in the upper micrograph displays a Fourier transform with discrete

spots, attesting to the extent of superlattice coherence. The lower, high magnification image shows that the nanocrystals are well-faceted. Reproduced from [68] with permission from Wiley-VCH.

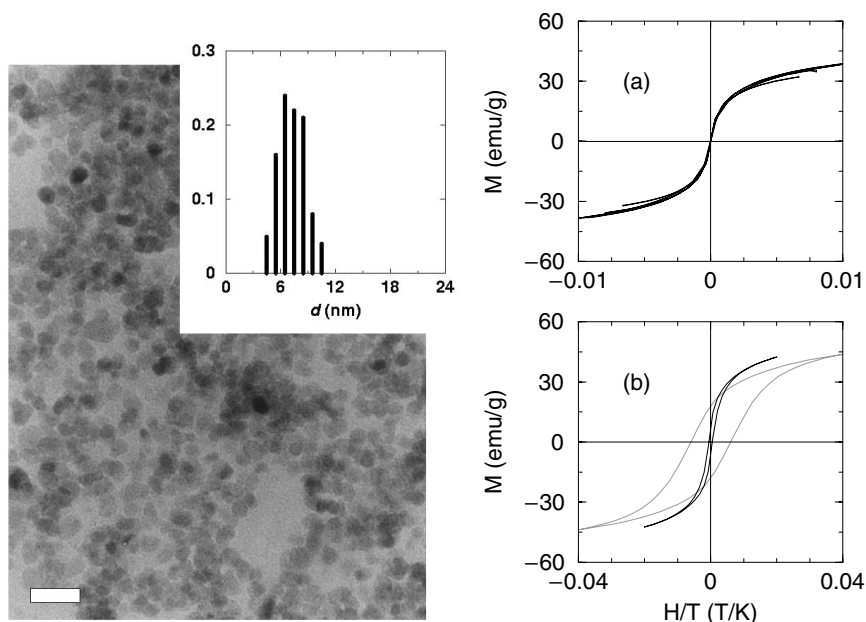


**Fig. 5.5.** Transmission electron micrograph of n-octylamine-capped spinel  $\text{CoFe}_2\text{O}_4$  nanoparticles prepared by the thermolysis of  $\text{Co(II)}$  and  $\text{Fe(III)}$  cupferron precursors in solvothermal toluene. The panels on the right display the magnetic properties of these superparamagnetic particles. (a) is the  $M$  versus  $H/T$  plot for data on a pressed pellet of these nanoparticles taken at temperature of

300, 250, 200, 150 and 100 K. The collapse of all these traces onto a single S-shaped curve indicates superparamagnetic behavior. Only at 50 K and 5 K (black and gray traces in (b)) are the samples “blocked” and hysteretic behavior manifests. Reproduced from [74] with permission from the Royal Society of Chemistry.

work in the absence of long chain amines (n-octylamine and n-dodecylamine) which are added as capping agents. A complete characterization of the magnetic properties of these nanoparticles has been presented by the authors [Figure 5.5]. This is the only report to date of capped oxide nanoparticles prepared by a solvothermal route.

#### 5.4

##### Prospects

As has been emphasized, research on the preparation of oxide nanoparticles is very much an active area that is being pursued across the world. While certain oxide structural classes (such as transition metal spinels) seem easily amenable to being prepared in nanoparticulate form, a number of other oxide materials are not. In particular, few attempts have been made to prepare capped perovskite oxide nanoparticles [61]. While some of the properties of oxide nanoparticles have already

been mentioned alongside their syntheses, some unusual properties and applications call for special mention.

Individual magnetic nanoparticles, apart from displaying superparamagnetic behavior, possess other unusual qualities. Bonet et al. [75] have shown that small ferrite (in the magnetoplumbite structure) nanoparticles can have their magnetic polarizations completely reversed through uniform rotation of their magnetization. The spin precession of the whole particle magnetic moment of 4 nm  $\gamma$ -Fe<sub>2</sub>O<sub>3</sub> nanoparticles has been monitored, using neutron scattering, by Lefmann et al. [76]. These authors find that the precession is coherent since it is associated with the excitation of ferrimagnetism in the nanoparticle.

Oxide nanoparticles, unlike nanoparticles of metals, display an expansion in their lattice parameters in comparison with the bulk. Tsunekawa et al. have examined sub-10 nm CeO<sub>2-x</sub> and sub-100 nm BaTiO<sub>3</sub> nanoparticles using a combination of electron diffraction, X-ray photoelectron spectroscopy and ab initio computer simulations. They find that in the CeO<sub>2-x</sub> system, the lattice expansion arises from a decrease in Ce valence, whilst in the BaTiO<sub>3</sub> system, the decreasing Ti–O covalency with decreasing particle size results in the expanded lattice.

There is continued interest in magnetic oxide nanoparticle assemblies for magnetic data storage. Recent advances in this area have come from the group of Sun, who have prepared magnetite nanoparticles [77] from Fe(II) acetylacetonate in refluxing diphenyl ether in the presence of oleic acid and oleylamine. Precipitation by addition of ethanol gave 4 nm Fe<sub>3</sub>O<sub>4</sub> nanoparticles which could be used to seed the growth of larger Fe<sub>3</sub>O<sub>4</sub> particles (reaching 16 nm). The larger Fe<sub>3</sub>O<sub>4</sub> nanoparticles can be oxidized to  $\gamma$ -Fe<sub>2</sub>O<sub>3</sub> with a distinct powder XRD pattern. The same group [78] have then self-assembled these nanoparticles as well as performed coupled self-assemblies of Fe<sub>3</sub>O<sub>4</sub> nanoparticles with Fe–Pt nanoparticles and then annealed the films to obtain exchange-coupled nanocomposite assemblies.

An interesting and novel application for magnetic nanoparticles is their use as intracellular magnetic labels in nuclear magnetic resonance imaging. The presence of magnetic nanoparticles results in protons in their vicinity relaxing at a much faster rate. Since NMR imaging is based on the rate of magnetic relaxation, there is distinct contrast introduced. Biocompatible dextran-coated nanoparticles have been conjugated with peptides to improve their uptake into target cells. These have then been found to significantly aid the NMR imaging of the cells [79]. Weissleder et al. have also conjugated specific oligonucleotide sequences to magnetic oxide nanoparticles [80]. This results in their being able to employ NMR methods in the rapid detection of DNA sequences that are complementary to the oligonucleotide that is bound to the nanoparticle. In functional magnetic resonance imaging (fMRI) experiments, primates or humans are exposed to some external stimulus while their brains are imaged. This technique has proved invaluable in mapping the brain, in terms of associating region with function. Magnetic nanoparticles (dextran-coated magnetite) have been used to enhance fMRI imaging contrast in the Rhesus brain in experiments that measured photic response [81].

Magnetic oxide nanoparticles are also finding a number of other uses, including in magnetic drug delivery and in hyperthermic cancer therapy. In the former, the

pharmacoactive molecule is bound to a small magnetic particle, and the particle is guided to its in vivo target through the use of magnetic fields. In the latter, cancerous tumors are destroyed by injecting magnetic particles into them and then coupling the particles to a strong radio-frequency magnetic field, resulting in large amounts of heats being delivered locally to, and eventually destroying, the tumor.

While heterogeneous catalysis is a traditional area of chemistry and is not usually classified as an application of nanoparticles, a recent development in cleaner-burning fuels is worth mentioning here. Two major manufacturers of diesel automobiles in Europe, Peugeot–Citroën and Ford, inject sub-10 nm CeO<sub>2</sub> nanoparticles (called by the trade name EOLYS TM, manufactured by the French company Rhodia) into diesel fuel before it is burnt in the engine. This results in an in situ catalyst that not only improves fuel efficiency but also greatly reduces the emission of particulates. Were the particles not sub-10 nm, it would not be possible to make homogeneous dispersions in the diesel fuel. It is expected that more than a million diesel automobiles will incorporate such systems by the year 2005. Another area where large quantities of nanoparticulate oxide materials are expected to be consumed is in the preparation of transparent sunscreens for topical application. Traditionally, sunscreens are applied as opaque creams. The active principle is a ZnO powder that absorbs most of the UV radiation incident upon the skin. There is great interest however, in material that can be sprayed on, and that is invisible. For this, the ZnO particles have to be sub-100 nm.

### Acknowledgments

I thank the office of the Dean of Engineering, UCSB for a seed grant. In writing this review, I have benefited greatly from discussions with Paul O'Brien and his group in Manchester during a recent visit made possible by a grant from the Royal Society of Chemistry. Susanne Stemmer is thanked for inputs on bulk oxide materials. My many coauthors in the area are acknowledged in the papers listed; Michael Rajamathi and Moumita Ghosh are thanked for their help in collating references. Larken Euliss is thanked for critically reading the manuscript.

### References

- 1 M. FARADAY, *Philos. Trans. R. Soc. London*, **1857**, 147, 145–181.
- 2 M. JOSÉ-YACAMÁN, L. RENDÓN, J. ARENAS et al., *Science*, **1996**, 273, 223–225.
- 3 Oxford English Dictionary at <http://dictionary.oed.com/>
- 4 A. FOJTIK, H. WELLER, U. KOCH et al., *Ber. Bunsen-Ges. Phys. Chem.*, **1984**, 88, 969–977.
- 5 M. L. STEIGERWALD, A. P. ALIVISATOS, J. M. GIBSON et al., *J. Am. Chem. Soc.*, **1988**, 110, 3046–3050.
- 6 C. B. MURRAY, D. J. NORRIS, M. G. BAWENDI, *J. Am. Chem. Soc.*, **1993**, 115, 8706–8715.
- 7 M. BRUST, M. WALKER, D. BETHELL et al., *J. Chem. Soc., Chem. Commun.*, **1994**, 801–802.
- 8 R. G. NUZZO, D. L. ALLARA, *J. Am. Chem. Soc.*, **1983**, 105, 4481–4483.



- 9 J. PROST, F. RONDELEZ, Suppl. to *Nature*, **1991**, 350, 11–23.
- 10 A. CHEMSEDDINE, H. WELLER, *Ber. Bunsen-Ges. Phys. Chem.*, **1993**, 97, 636–637.
- 11 M. D. BENTZON, J. VAN WONTERGHEM, S. MØRUP et al., *Philos. Mag. B*, **1989**, 60, 169–178.
- 12 C. B. MURRAY, C. R. KAGAN, M. G. BAWENDI, *Science*, **1995**, 270, 1335–1338.
- 13 R. L. WHETTEN, J. T. KHOURY, M. M. ALVAREZ et al., *Adv. Mater.*, **1996**, 8, 428–433.
- 14 C. P. COLLIER, T. VOSSMEYER, J. R. HEATH, *Annu. Rev. Phys. Chem.*, **1998**, 49, 371–404; R. L. WHETTEN, M. N. SHAFIGULLIN, J. T. KHOURY et al., *Acc. Chem. Res.*, **1999**, 32, 397–406; C. B. MURRAY, C. R. KAGAN, M. G. BAWENDI, *Annu. Rev. Mater. Sci.*, **2000**, 30, 545–610.
- 15 J. V. SANDERS, *Acta Crystallogr. Sect. A*, **1968**, 24, 427–434.
- 16 See for example, R. J. CAVA, *J. Am. Ceram. Soc.*, **2000**, 83, 5–28.
- 17 See for example, J. Z. SUN AND A. GUPTA, *Annu. Rev. Mater. Sci.*, **1998**, 28, 45–78.
- 18 A. I. KINGON, J.-P. MARIA, S. K. STREIFFER, *Nature*, **2000**, 406, 1032–1038.
- 19 J. F. SCOTT, *Annu. Rev. Mater. Sci.*, **1998**, 28, 79–100.
- 20 O. AUCIELLO, J. F. SCOTT, R. RAMESH, *Physics Today*, July **1998**, 22–27.
- 21 D. DIMOS, C. H. MUELLER, *Annu. Rev. Mater. Sci.*, **1998**, 28, 397–419.
- 22 B. C. H. STEELE, A. K. HEINZEL, *Nature*, **2001**, 414, 345–352.
- 23 J.-M. TARASCON, M. ARMAND, *Nature*, **2001**, 414, 359–367.
- 24 H. GLEITER, *Acta Mater.*, **2000**, 48, 1–29.
- 25 R. BLAKEMORE, *Science*, **1975**, 190, 377–379.
- 26 R. B. FRANKEL, R. P. BLAKEMORE, R. S. WOLFE, *Science*, **1979**, 203, 1355–1356.
- 27 J. L. KIRSCHVINK, M. M. WALKER, C. E. DIEBEL, *Curr. Opin. Neurobiol.*, **2001**, 11, 462–467.
- 28 M. M. WALKER, T. E. DENNIS, J. L. KIRSCHVINK, *Curr. Opin. Neurobiol.*, **2002**, 12, 735–744.
- 29 R. E. DUNIN-BORKOWSKI, M. R. MCCARTNEY, R. B. FRANKEL et al., *Science*, **1998**, 282, 1868.
- 30 D. SCHÜLLER, R. B. FRANKEL, *Appl. Microbial Biotechnol.*, **1999**, 52, 464–473.
- 31 <http://www.nanomagnetics.co.uk>
- 32 K. L. THOMAS-KEPRTA, D. A. BAZYLINSKI, J. L. KIRSCHVINK et al., *Geochim. Cosmochim. Acta*, **2000**, 64, 4049–4081.
- 33 P. R. BUSECK, R. E. DUNIN-BORKOWSKI, B. DEVOUARD et al., *Proc. Natl. Acad. Sci. U.S.A.*, **2001**, 98, 13490–13495.
- 34 D. F. SHRIVER, P. W. ATKINS, *Inorganic Chemistry*, 3rd edition., W. H. Freeman and Company, New York.
- 35 G. H. A. THERESE, P. VISHNU KAMATH, *Chem. Mater.*, **2000**, 12, 1195–1204.
- 36 V. CABUIL, *Curr. Opin. Colloid Interface Sci.*, **2000**, 5, 44–48.
- 37 J. P. CHEN, C. M. SORENSON, K. J. KLABUNDE et al., *Phys. Rev. B*, **1996**, 54, 9288–9296.
- 38 S. LEFEBURE, E. DUBOIS, V. CABUIL et al., *J. Mater. Res.*, **1998**, 2975–2981.
- 39 R. MASSART, E. DUBOIS, V. CABUIL et al., *J. Magn. Magn. Mater.*, **1995**, 149, 1–5.
- 40 M. P. MORALES, S. VEINTEMILLAS-VERDAGUER, M. I. MONTERO et al., *Chem. Mater.*, **1999**, 11, 3035–3064.
- 41 S. AMMAR, A. HELFEN, N. JOUINI et al., *J. Mater. Chem.*, **2001**, 11, 186–192.
- 42 M. RAJAMATHI, M. GHOSH, R. SESHADRI, *J. Chem. Soc., Chem. Commun.*, **2002**, 1152–1153.
- 43 D. CARUNTO, Y. REMOND, N. H. CHOU et al., *Inorg. Chem.*, **2002**, 41, 6137–6146.
- 44 M. P. PILENI, *J. Phys. Chem.*, **1993**, 97, 6961–6973; *Langmuir*, **1997**, 13, 3266–3276.
- 45 V. PILLAI, D. O. SHAH, *J. Magn. Magn. Mater.*, **1996**, 163, 243–248.
- 46 C. LIU, Z. J. ZHANG, *Chem. Mater.*, **2001**, 13, 2092–2096.
- 47 C. VESTAL, Z. J. ZHANG, *Chem. Mater.*, **2002**, 14, 3817–3822.
- 48 M. MOUMEN, M. P. PILENI, *Chem. Mater.*, **1996**, 8, 1128–1134; *J. Phys. Chem.*, **1996**, 100, 1867–1873; M.



- MOUMEN, P. BONNEVILLE, M. P. PILENI, *J. Phys. Chem.*, **1996**, *100*, 14410–14416.
- 49 J. F. HOCHÉPIED, Ph. SAINTAVIT, M. P. PILENI, *J. Magn. Magn. Mater.*, **2001**, *231*, 315–322.
- 50 J. F. HOCHÉPIED, P. BONNEVILLE, M. P. PILENI, *J. Phys. Chem.*, **2000**, *104*, 905–912.
- 51 A. T. NGO, M. P. PILENI, *J. Phys. Chem.*, **2001**, *105*, 53–58.
- 52 R. VIJAYA KUMAR, Y. DIAMANT, A. GEDANKEN, *Chem. Mater.*, **2000**, *12*, 2301–2305.
- 53 R. VIJAYA KUMAR, Y. KOLTYPIN, X. N. XU et al., *J. Appl. Phys.*, **2001**, *89*, 6324–6328.
- 54 T. HYEON, S. S. LEE, J. PARK et al., *J. Am. Chem. Soc.*, **2001**, *123*, 12798–12801.
- 55 J. A. NELSON, M. J. WAGNER, *Chem. Mater.*, **2002**, *14*, 915–917.
- 56 J. A. NELSON, E. L. BRANT, M. J. WAGNER, *Chem. Mater.*, **2003**, *15*, 688–693.
- 57 J. ROCKENBERGER, R. C. SCHER, A. P. ALIVISATOS, *J. Am. Chem. Soc.*, **1999**, *121*, 11595–11596.
- 58 A. K. BOAL, K. DAS, M. GRAY, V. M. ROTELLO, *Chem. Mater.*, **2002**, *14*, 2628–2636.
- 59 A. B. BOURLINOS, A. SIMOPOULOS, D. PETRIDES, *Chem. Mater.*, **2002**, *14*, 899–903.
- 60 A. B. BOURLINOS, A. BAKANDRITSOS, V. GEORGAKILAS et al., *Chem. Mater.*, **2002**, *14*, 3226–3228.
- 61 S. O'BRIEN, L. BRUS, C. B. MURRAY, *J. Am. Chem. Soc.*, **2001**, *123*, 12085–12086.
- 62 P. ARNAL, R. J. P. CORRIU, D. LECLERCQ et al., *Chem. Mater.*, **1997**, *9*, 694–698.
- 63 T. J. TRENTLER, T. E. DENLER, J. F. BERTONE et al., *J. Am. Chem. Soc.*, **1999**, *121*, 1613–1614.
- 64 K. BYRAPPA, M. YOSHIMURA, *Handbook of Hydrothermal Technology*, William Andrew Publishing, Norwich, New York 2001.
- 65 M. RAJAMATHI, R. SESHADRI, *Curr. Opin. Solid State Mater. Sci.*, **2002**, *6*, 337–345.
- 66 M. INOUE, M. KIMURA, T. INUI, *J. Chem. Soc., Chem. Commun.*, **1999**, 957–958.
- 67 Y. LI, X. DUAN, H. LIAO, Y. QIAN, *Chem. Mater.*, **1998**, *10*, 17–18.
- 68 A. CHEMSEDDINE, T. MORITZ, *Eur. J. Inorg. Chem.*, **1999**, 235–245.
- 69 M. WU, J. LONG, A. HUANG, Y. LUO et al., *Langmuir*, **1999**, *15*, 8822–8825.
- 70 M. HIRANO, *J. Mater. Chem.*, **2000**, *10*, 469–472.
- 71 A. CABAÑAS, J. A. DARR, E. LESTER et al., *J. Chem. Soc., Chem. Commun.*, **2000**, 901–902; *J. Mater. Chem.*, **2001**, *11*, 561–568.
- 72 V. K. LAMER, R. H. DINEGAR, *J. Am. Chem. Soc.*, **1950**, *72*, 4847.
- 73 A. CABAÑAS, M. POLIAKOFF, *J. Mater. Chem.*, **2001**, *11*, 1408–1416.
- 74 S. THIMMAIAH, M. RAJAMATHI, N. SINGH et al., *J. Mater. Chem.*, **2001**, *11*, 3215–3220.
- 75 E. BONET, W. WERNSDORFER, B. BARBARA et al., *Phys. Rev. Lett.*, **1999**, *83*, 4188–4191.
- 76 K. LEFMANN, F. BØDKER, S. N. KLAUSEN et al., *Europhys. Lett.*, **2001**, *54*, 526–532.
- 77 S. SUN, H. ZENG, *J. Am. Chem. Soc.*, **2002**, *124*, 8204–8205.
- 78 H. ZENG, J. LI, Z. L. WANG et al., *Nature*, **2002**, *420*, 395–398.
- 79 L. JOSEPHSON, C.-H. TUNG, A. MOORE et al., *Bioconjugate Chem.*, **1999**, *10*, 186–191.
- 80 L. JOSEPHSON, J. M. PEREZ, R. WEISSLEDER, *Angew. Chem. Intl. Ed. Engl.*, **2001**, *40*, 3204–3206.
- 81 D. J. DUBOWITZ, K. A. BERNHEIM, D.-Y. CHEN et al., *NeuroReport*, **2001**, *12*, 2335–2340.

## 6

## Sonochemistry and Other Novel Methods Developed for the Synthesis of Nanoparticles

Y. Mastai and A. Gedanken

### Abstract

In this chapter the three synthetic methods that have been developed for the fabrication of nanomaterials in our laboratory will be described. The techniques are sonochemistry, sonoelectrochemistry, and microwave heating. In each category a short introduction to the technique will be presented in which an attempt will be made to interpret why the products produced by this method yield small size particles. In addition, we will report on the various nanosized particles that have been prepared by these methods, and other activities in these three fields related to nanochemistry. It should be mentioned that in 1996 [1a] Suslick and coworkers published an early review on the nanostructured materials generated by ultrasound radiation. Suslick and Price [1b] have also reviewed the application of ultrasound to materials science. Their review [1b] dealt with nanomaterials, but was not directed specifically to this topic. However, the review concentrated only on the sonochemistry of transition metal carbonyls, and catalytic reactions that involve the nanoparticles resulting from their sonochemical decomposition. Grieser and Asokkumar [2] have also written a review on a similar topic. A former coworker, J. J. Zhu, has recently submitted for publication a review article [3], entitled “*Novel Methods for Chemical Preparation of Metal Chalcogenide Nanoparticles*” in which he reviews the same above-mentioned three synthetic methods and their application in the synthesis of nanosized metal chalcogenides. It is for this reason that chalcogenide nanoparticles, their preparation and properties, will not be reviewed in this chapter. We attempt to review all the published literature related to these three synthetic methods published before the beginning of 2003.

### 6.1

#### Sonochemistry

We are all aware of the use of ultrasound radiation in medicine, where it is being used mostly for diagnosis. More recently, however, focused ultrasound radiation is being used to burn cancer cells. Less is known regarding its application in chem-

istry, despite the fact that it has applications across almost the whole breadth of chemistry. The main advantage in conducting sonochemical experiments is that it is cheap to get started in the field, for example, in Romania after Ceaucescu's reign scientists carried out organic reactions using cheap ultrasonic baths as their source of radiation.

Sonochemistry is the research area in which molecules undergo chemical reaction due to the application of powerful ultrasound radiation (20 KHz–10 MHz) [4]. The physical phenomenon responsible for the sonochemical process is acoustic cavitation. Let us first address the question of how 20 kHz radiation can rupture chemical bonds (the question is also related to 1 MHz radiation), and try to explain the role of a few parameters in determining the yield of a sonochemical reaction, and then describe the unique products obtained when ultrasound radiation is used in materials science.

A number of theories have been developed in order to explain how 20 kHz sonic radiation can break chemical bonds. They all agree that the main event in sonochemistry is the creation, growth, and collapse of a bubble that is formed in the liquid.

The first question is how such a bubble can be formed, considering the fact that the forces required to separate water molecules to a distance of two van-der Waals radii, would require a power of  $10^5 \text{ W cm}^{-1}$  [4]. On the other hand, it is well known that in a sonication bath, with a power of  $0.3 \text{ W cm}^{-1}$  [4] water is already converted into hydrogen peroxide. Different explanations have been offered; they are all based on the existence of unseen particles, or gas bubbles, that decrease the intermolecular forces, enabling the creation of the bubble. The experimental evidence for the importance of unseen particles in sonochemistry is that when the solution undergoes ultrafiltration, before the application of the ultrasonic power, there is no chemical reaction and chemical bonds are not ruptured.

The second stage is the growth of the bubble, which occurs through the diffusion of solute vapor into the volume of the bubble. The third stage is the collapse of the bubble, which occurs when the bubble size reaches its maximum value.

From here on we will adopt the hot spot mechanism, one of the theories that explain why, upon the collapse of a bubble, chemical bonds are broken. The theory claims that very high temperatures (5,000–25,000 K) [5] are obtained upon the collapse of the bubble. Since this collapse occurs in less than a nanosecond [5, 6], very high cooling rates, in excess of  $10^{11} \text{ K s}^{-1}$ , are obtained. This high cooling rate hinders the organization and crystallization of the products. For this reason, in all cases dealing with volatile precursors, where gas phase reactions are predominant, amorphous nanoparticles are obtained. While the explanation for the creation of amorphous products is well understood, the reason for the nanostructured products is not clear. One explanation is that the fast kinetics do not permit the growth of the nuclei. If, on the other hand, the precursor is a non-volatile compound, the reaction occurs in a 200 nm ring surrounding the collapsing bubble [7]. In this case, the sonochemical reaction occurs in the liquid phase. The products are sometimes nanoamorphous particles and, in other cases, nanocrystalline. This depends on the temperature in the ring region where the reaction takes place. The

temperature in this ring is lower than inside the collapsing bubble, but higher than the temperature of the bulk. Suslick has estimated the temperature in the ring region as 1900 °C [7]. In short, in almost all the sonochemical reactions leading to inorganic products, nanomaterials were obtained. They varied in size, shape, structure, and in their solid phase (amorphous or crystalline), but they were always of nanometer size.

We cannot mention here how the various parameters: frequencies, power, gas under which the sonication takes place, pressure of the gas, etc. affect the sonochemical yield and rate. We will just mention one important parameter, the temperature. The equation of an adiabatic implosion is

$$T_{\max} = T_0 \{ P_{\text{ex}} (\gamma - 1) / P_{\text{bub}} \}, \quad (1)$$

where  $T_{\max}$  is the temperature reached after the collapse of the bubble,  $T_0$  is the temperature of the sonication bath,  $\gamma = C_p/C_v$ ,  $P_{\text{ex}}$  is the external pressure equal to the sum of the hydrostatic and acoustic pressure, and  $P_{\text{bub}}$  is the pressure of the gas inside the cavity, at the radius at which it collapses. The choice of a non-volatile solvent (such as decalin, hexadecane, isodurene, etc.) guarantees that only the vapors of the solute can be found inside the cavitating bubble. Thus,  $P_{\text{bub}}$  is practically the vapor pressure of the solute, and since it is found in the denominator, lower  $P_{\text{bub}}$  results in higher temperatures and faster reaction rates. The conclusion is that the temperature affects the sonochemical reaction rate in two ways. On the one hand, lower temperatures cause a higher viscosity, which makes the formation of the bubble more difficult, and, on the other hand, the dominant effect is that at lower temperatures, higher rates will be achieved in sonochemical processes. This is why the sonic reaction involving volatile precursors is run at lower temperatures. Apparent negative activation energies were measured for sonochemical reactions.

Our first activity in the field combining sonochemistry and materials science was related to control over the particle size. We have demonstrated in three cases that for gas phase, as well as liquid phase reactions, diluting the precursor's solution decreases the particle size of the product [8–10]. This was illustrated for nanosized Fe [8],  $\text{Fe}_2\text{O}_3$  [9], and for  $\text{GaO}(\text{OH})$  [10]. In the last case, this conclusion was reached by measuring the particle's size from the transmission electron microscopy (TEM) micrograph. For the Fe, and  $\text{Fe}_2\text{O}_3$  nanoparticles it was concluded from indirect magnetic, EPR, and differential scanning calorimetry (DSC) measurements. This is due to the high degree of aggregation that is observed in the TEM picture of these magnetic particles resulting from their strong magnetic interactions.

In the following section we will present the various inorganic systems that have been synthesized in the last few years, and we will then try to emphasize the unique features of sonochemistry, or what can be described by the famous song “anything you can do I (sonochemistry) can do better”. In this section metals will serve as a demonstration of what can be done sonochemically. We will discuss the synthesis of nanometals, colloidal metallic solutions, formation of alloys, the coat-

ing of metallic nanoparticles on surfaces, SAM (self-assembled monolayer coating) on nanosized amorphous metals, and the formation of metal–polymer composites. The next section will be devoted to the sonochemical synthesis of mesoporous materials, and the use of ultrasound for the insertion of nanomaterials into the pores. In the final section we will discuss other important nanomaterials that have been prepared by the sonochemical technique (apart from chalcogenides).

### 6.1.1

#### Sonochemical Fabrication of Nanometals

##### 6.1.1.1 Sonochemical Synthesis of Powders of Metallic Nanoparticles

In addition to the synthesis of the transition metals produced from the corresponding carbonyls (Fe from  $\text{Fe}(\text{CO})_5$  [6, 11], Ni from  $\text{Ni}(\text{CO})_4$  [12], and Co from  $\text{Co}(\text{CO})_3\text{NO}$  [13], other metals have also been synthesized sonochemically. Sonication of aqueous  $\text{Co}^{+2}$  and hydrazine resulted [14] in the formation of anisometric (disk-shaped) cobalt nanoclusters that averaged about 100 nm in width and 15 nm in thickness. Electron diffraction from single particles revealed that they were oriented (001) crystals that conformed to a trigonal or hexagonal unit cell four times the size of the cell adopted by bulk alpha-cobalt. Nanophased particles of metallic copper [15] were formed by the sonochemical reduction of copper (II) hydrazine carboxylate ( $\text{Cu}(\text{N}_2\text{H}_3\text{COO})_2 \cdot 2\text{H}_2\text{O}$ ) in an aqueous solution. When the sonication was carried out under argon a mixture of  $\text{Cu}_2\text{O}$  and metallic copper was obtained. However, sonicating the precursor solution under a mixture of hydrogen and argon yielded pure copper. The particles were obtained as porous materials with diameter 50 nm, smaller than those obtained by the thermal decomposition of the same precursor. A mechanism involving hydrogen radicals as the reducing agent is proposed [15].



In a separate study, nanoparticles of palladium metallic clusters were prepared at room temperature by sonochemical reduction of a 1:2 molar mixture of  $\text{Pd}(\text{O}_2\text{CCH}_3)_2$  and myristyltrimethylammonium bromide,  $\text{CH}_3(\text{CH}_2)_{12}\text{N}(\text{CH}_3) \cdot \text{BrNR}_4\text{X}$ , in THF or MeOH [16]. Apart from its stabilizing effect,  $\text{NR}_4\text{X}$  acts as a reducing agent, probably due to the decomposition that occurs in the liquid-phase region immediately surrounding the collapsing cavity and provides reducing radicals. It is noteworthy that nanosized amorphous Pd is obtained in THF and a crystalline metal in MeOH.

A pioneer in the application of ultrasound to the formation of nanoparticles of noble metals is Y. Maeda. In an earlier study his group [17] synthesized sonochemically metallic nanoparticles of metals such as Ag, Pd, Au, Pt and Rh with a fairly narrow distribution (e.g., about 5 nm for Pd particles obtained from a 1.0 mM Pd(II) solution in polyethylene glycol monostearate solution). They suggested three different reduction pathways under sonication: (i) reduction by H atoms, (ii) reduction by secondary reducing radicals formed by hydrogen abstraction from

organic additives with OH radicals and H atoms, and (iii) reduction by radicals formed from pyrolysis of the additives at the interfacial region between cavitation bubbles and the bulk solution. The reduction of Ag (I) and Pt (II) mainly proceeds through reaction pathway (ii). For Pd (II) and Au (III), the reductions mainly proceed through reaction pathway (iii). The reduction of Rh (III) was not achieved under the same conditions; however, on addition of sodium formate, reduction occurred and the preparation of Rh particles was successful. In another study [18] platinum nanoparticles were prepared sonochemically in an aqueous system in the presence of a surfactant (sodium dodecyl sulfate, SDS). The particles were stable, homogeneously spherical, and relatively monodispersed with an average diameter of 2.6 nm. Reducing species generated near and/or in the hot bubbles would react with the  $\text{PtCl}_4^{-2}$  complexes to form the platinum nanoparticles. Three kinds of reducing species were proposed. Amorphous silver nanoparticles of 20 nm size have been prepared [19] by the sonochemical reduction of an aqueous silver nitrate solution in an atmosphere of argon–hydrogen. The sonochemical reduction occurs through the generation of hydrogen radicals during the sonication process.

The role of the surfactant was further studied in sonochemical reduction [20, 21] processes of Pt (IV) ions in water. It was investigated in the presence of various kinds of surfactants such as sodium dodecylsulfate (SDS) and sodium dodecylbenzenesulfonate (DBS) as anionic surfactants, polyethylene glycol monostearate (PEG-MS) as non-ionic, and dodecyltrimethylammonium chloride (DTAC) and bromide (DTAB) as cationic surfactants. An improved colorimetric determination reveals that Pt (IV) ion is reduced to zero-valent metal in two steps: step (1) Pt (IV) ion to Pt (II) ion, and step (2) Pt (II) ion to Pt (0), and after the completion of step (1), step (2) sets in.

Another Japanese group [22] reported on the preparation of Pd and Pt by sonochemical reduction of solutions containing  $\text{H}_2\text{PtCl}_6$  or  $\text{K}_2\text{PdCl}_4$ . The effect of atmospheric gas on the particle size distribution was investigated. Average diameters and standard deviations of the Pd particles prepared under Ar (Pd/Ar) and  $\text{N}_2$  (Pd/ $\text{N}_2$ ) were found to be  $3.6 \pm 0.7$  nm (Pd/Ar) and  $2.0 \pm 0.3$  nm (Pd/ $\text{N}_2$ ). A smaller and sharper distribution of the particle size was observed for the Pd particles formed under a  $\text{N}_2$  atmosphere. In the case of Pt, a smaller and sharper distribution of the particle size was observed for the particles prepared under a Xe atmosphere. The importance of Xe can be explained in terms of a hot-spot temperature created by acoustic cavitation. Nanosized gold particles were also prepared from gold (III) (tetrachloroaurate (III)) [23]. The Au (III) was reduced in an aqueous solution containing only a small amount of 2-propanol to form colloidal gold nanoparticles. The rates of gold (III) reduction and the sizes of the gold particles formed could be sonochemically controlled by controlling the irradiation parameters such as the temperature of the solution, the intensity of the ultrasound, and the positioning of the reactor. The size of the gold particles depended strongly on the rate of gold (III) reduction, suggesting that this rate affects the initial nucleation of the gold particles. A similar study was published recently by Okitsu et al. [24]. The rates of gold (III) reduction were strongly dependent on the atmosphere, the temperature of the bulk solution, the intensity of the ultrasound, and the dis-

tance of the reaction vessel from the oscillator. For example, the rates of reduction under several atmospheres were in the order:  $\text{CH}_4 = \text{CO}_2 < \text{N}_2 < \text{Ne} < \text{He} < \text{Ar} < \text{Kr}$ , where no reduction proceeded under the  $\text{CH}_4$  and  $\text{CO}_2$  atmospheres. It was clearly seen that the rates of reduction were influenced by the cavitation phenomenon. Upon irradiation, colloidal gold particles having a surface plasmon absorption were formed, although in the absence of any stabilizers for the gold particles. It was found by TEM observation that the average size of the formed gold particles varied from 30 to 120 nm dependent upon the irradiation parameters. The size of the gold particles correlated to the initial rate of gold (III) reduction; the higher the rate of reduction, the smaller the particles.

The magnetic metals were also prepared by a method [25] based on the rapid expansion of supercritical fluid solutions (RESS) coupled with chemical reduction to produce nickel, cobalt, iron, and iron oxide nanoparticles of reasonably narrow size distribution. Under the protection of a polymer stabilization agent, the largely amorphous metal nanoparticles form stable suspensions in room-temperature solvents.

A nonmetallic element, silicon, was prepared sonochemically by reducing tetraethyl orthosilicate (TEOS) with a colloidal solution of sodium. The product was obtained as 2–5 nm sized, highly aggregated particles. The silicon exhibited a luminescence similar to that of porous silicon. This procedure is suggested as a general sonochemical reduction leading to the formation of metallic nanoparticles [26].

#### 6.1.1.2 Sonochemical Synthesis of Metallic Colloids

Although a few of the above-mentioned metallic nanoparticles were formed as colloidal solutions, and since this review is centered on their synthesis, they were included in the previous section. This section is devoted to the unique properties of metallic colloidal solutions prepared sonochemically. A recent survey by Grieser deals with the sonochemical formation of metallic colloids [27]. In the above-mentioned examples noble metal nanoparticles (e.g., Au, Pd, Ag) are obtained by sonicating aqueous solutions of the corresponding salts in the presence of a surfactant, which largely stabilizes the naked colloid. Likewise, a colloidal solution of metallic iron particles (8 nm, average size) has been obtained by sonolysis of  $\text{Fe}(\text{CO})_5$  in the presence of oleic acid [28]. Smaller particles are obtained with poly(vinylpyrrolidone), although in both cases the iron was amorphous and exhibited high magnetism. The sonochemical preparation of magnetic fluids has also been described by other authors [29, 30]. The systems include: (i) a cobalt colloidal solution in decalin stabilized by oleic acid, (ii) a colloidal dispersion of amorphous metallic iron in a polymeric matrix, and (iii) a  $\text{Fe}_2\text{O}_3$  colloidal solution in hexadecane stabilized by oleic acid. For the cobalt colloidal solution uniform acicular-shaped particles were further obtained by an aging process in air (Figure 6.1). The figure demonstrates the conversion of 5–10 nm sized Co particles in a 1  $\mu\text{m}$  sized acicular particle after 1 month of aging under ambient conditions.

Elongated copper nanoparticles were prepared by sonicating the above-mentioned precursor, copper hydrazine carboxylate, in an aqueous solution con-

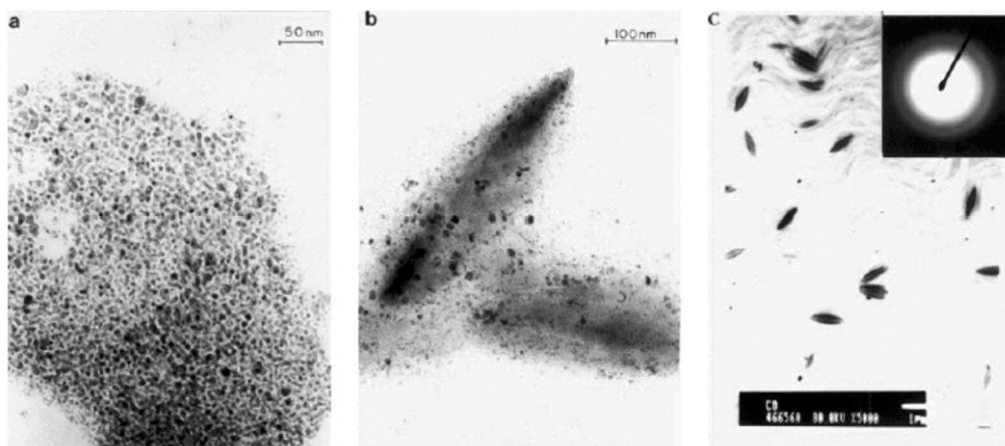


**Fig. 6.1.** TEM micrographs of the cobalt colloidal solution: (a) as prepared fresh, (b) after a week of aging, (c) after a month of aging (inset: ED pattern).

taining a zwitterionic surfactant [31]. In Figure 6.2 the TEM image of the elongated copper nanoparticles surrounded by surfactant molecules is presented. The dimensions of these copper nanoparticles were approximately 500 nm in length and 50 nm in width. In the absence of a surfactant, nanoparticles were spherical in

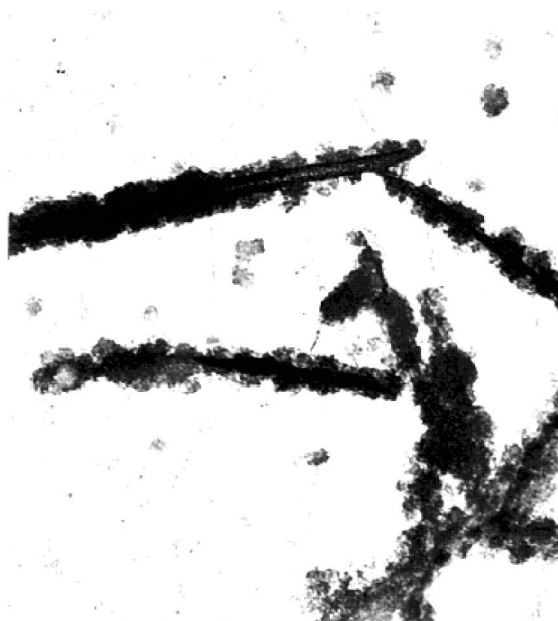


**Fig. 6.2.** Transmission electron micrograph of the elongated copper nanoparticles coated with CTAPTS.



shape, with a diameter of approximately 50 nm. A comparison of the XRD pattern with that obtained for the copper nanoparticles prepared without using a surfactant revealed an elongation taking place along the [111] and [200] planes of the copper nanocrystals.

A comprehensive study on the sonochemical synthesis of colloidal solutions of noble metals was conducted by Grieser and coworkers [32–34]. The 515 kHz ultrasound-initiated reduction of  $\text{AuCl}_4^{-1}$  to Au (0) was examined as a function of the concentration of various surface-active solutes [32]. The amount of  $\text{AuCl}_4^{-1}$  reduced in the presence of ethanol, 1-propanol, and 1-butanol was found to be dependent on the surface excess of the alcohol at the gas/solution interface, i.e., the relative concentration of the alcohol at the gas/solution interface compared to the bulk solution concentration. The efficiency of reduction of  $\text{AuCl}_4^{-1}$  in the presence of the surfactants sodium dodecyl sulfate or octaethylene glycol monododecyl ether was found to be related to the monomer concentration of the surfactant in solution.

The ultrasound irradiation of aqueous solutions of  $\text{PtCl}_6^{-2}$  was found to produce colloidal platinum of about 3 nm in diameter [33]. The presence of aliphatic alcohols significantly enhanced the reduction process. It is shown that the extent of reduction of  $\text{PtCl}_6^{-2}$  in the presence of alcohol is directly related to the Gibbs surface excess of the alcohol at the air–water interface. The significance of this is discussed in relation to ultrasound-induced cavitation in solution. In a recent report Caruso et al. [34] reduced  $\text{AuCl}_4^{-1}$  to colloidal gold in the presence of aliphatic alcohols and sodium dodecyl sulfate in aqueous solutions using 20 kHz ultrasound. The extent of reduction of  $\text{AuCl}_4^{-1}$  was found to be directly dependent on the gas–solution interfacial activity of the solutes used. The diameters of the gold colloids produced were in the size range 9–25 nm. The particle size was dependent on the alcohol concentration in solution and on the hydrophobicity of the alcohol. For a particular alcohol concentration, the greater the hydrophobicity of the alcohol the smaller were the particles obtained. The authors present a detailed mechanism describing the overall sonochemically initiated reduction of  $\text{AuCl}_4^{-1}$  leading to the formation of colloidal gold. Finally, Grieser has also published an early review on sonochemistry in colloidal systems [35].

#### 6.1.1.3 Sonochemical Synthesis of Metallic Alloys

Nanophased amorphous Fe/Co was obtained by sonicating a mixture of  $\text{Fe}(\text{CO})_5$  and  $\text{Co}(\text{CO})_3\text{NO}$  in decalin [36]. The Fe/Co, nanostructured alloys are formed and are non-crystalline by X-ray, neutron, and e-beam diffraction. In a further work, a Fe/Ni alloy was similarly obtained [37]. Remarkably, a 1:1 molar solution of Fe:Ni led to a  $\text{Fe}_{20}\text{Ni}_{80}$  solid composition, which can be attributed to the ratio of the vapor pressure of the two carbonyls in the gas phase of the collapsing bubble. Magnetic susceptibilities of  $\text{Fe}_{40}\text{Ni}_{60}$  and  $\text{Fe}_{60}\text{Ni}_{40}$  indicated blocking temperatures of 35 K and a magnetic particle size of about 6 nm. Thermogravimetric measurements of  $\text{Fe}_{20}\text{Ni}_{80}$  gave Curie temperatures of 322 °C for amorphous and 550 °C for crystallized forms. Differential scanning calorimetry exhibited an endothermic transition at 335 °C from a combination of the magnetic phase transition and alloy crystallization. The  $r$  Mössbauer spectrum of crystallized  $\text{Fe}_{20}\text{Ni}_{80}$  shows a sextet

pattern with a hyperfine field of 25.04 T. A similar study reports on the Co/Ni synthesis, characterization and properties [38].

M50 steel powder has been obtained by sonochemical decomposition of organo-metallic precursors, namely  $\text{Fe}(\text{CO})_5$ ,  $(\text{Et}_x\text{C}_6\text{H}_{6-x})_2\text{Cr}$ ,  $(\text{Et}_x\text{C}_6\text{H}_{6-x})_2\text{Mo}$ , and  $\text{V}(\text{CO})_6$  in decalin [39]. The morphology of the amorphous (as evidenced by X-ray patterns) M50 powder was shown to be a porous coral-like microstructure. The consolidated iron pellet (the consolidation was carried out by vacuum hot press, conditions: 275 MPa, at 700 °C for 1 h) had a density of 100%. The iron sample had a high Rockwell C (RC) hardness of 37 as compared to 4–5 RC for conventional iron. The hardness of the M50 steel sample was 66.3 RC compared with 58–62 for conventional M50 steel after tempering. The authors attribute the extremely high hardness of the consolidated iron to the nanometer size particles, as well as to the low carbon and oxygen contamination.

In a different study [40], argon-saturated aqueous solutions of  $\text{NaAuCl}_4$  and  $\text{PdCl}_2$  or  $\text{K}_2\text{PtCl}_4$  were reduced simultaneously by ultrasound irradiation to prepare noble metal alloy nanoparticles. The Au–Pd nanoparticles exhibited monodispersive distribution (8 nm), and consisted of a gold core and a palladium shell. Au–Pt alloy nanoparticles could not be produced from  $\text{NaAuCl}_4$  and  $\text{K}_2\text{PtCl}_4$  aqueous solutions by either simultaneous or successive reduction.

An aqueous solution of  $\text{AgNO}_3$  in the presence of ammonia and  $\text{Fe}(\text{CO})_5$  was sonicated [41] under a  $\text{H}_2/\text{Ar}$  mixture, yielding a nanostructured homogeneous phase of  $\text{Ag}/\text{Fe}_2\text{O}_3$ . This composite material was further reduced at 300 °C under hydrogen to produce the nanophased Fe/Ag solid mixture. Finally, a ternary nano-sized amorphous alloy, Fe/Ni/Co, was prepared by sonochemical decomposition of solutions of volatile organic precursors,  $\text{Fe}(\text{CO})_5$ ,  $\text{Ni}(\text{CO})_4$ , and  $\text{Co}(\text{NO})(\text{CO})_3$  in decalin, under an argon pressure of 100 to 150 kPa at 273 K [42]. Magnetic measurements indicated that the as-prepared amorphous Fe–Ni–Co alloy particles were super-paramagnetic. The observed magnetization measured up to a field of 1.5 kG of the annealed Fe–Ni–Co samples (75–87 emu  $\text{g}^{-1}$ ) was significantly lower than that for the reported multidomain bulk particles (175 emu  $\text{g}^{-1}$ ), reflecting the ultrafine nature of our sample.

#### 6.1.1.4 Sonochemical Deposition of Nanoparticles on Spherical and Flat Surfaces

Metallic nanoparticles were deposited on ceramic and polymeric particles using ultrasound radiation. A few papers report also on the deposition of nanomaterials produced sonochemically on flat surfaces. Our attention will be devoted to spheres. In a typical reaction, commercially available spheres of ceramic materials or polymers were introduced into a sonication bath and sonicated with the precursor of the metallic nanoparticles. In the first report Ramesh et al. [43] employed the Stober method [44] for the preparation of 250 nm silica spheres. These spheres were introduced into a sonication bath containing a decalin solution of  $\text{Ni}(\text{CO})_4$ . The as-deposited amorphous clusters transform to polycrystalline, nanophasic, fcc nickel on heating in an inert atmosphere of argon at a temperature of 400 °C. Nitrogen adsorption measurements showed that the amorphous nickel with a high surface area undergoes a loss in surface area on crystallization.

The as-deposited amorphous nickel showed a super-paramagnetic behavior, while the polycrystalline nickel on silica was found to be ferromagnetic. FT-IR investigations showed a significant change in the surface silanol composition for the coated and uncoated silica. Ultrasound-driven cavitation desorbs the adsorbed water on silica, making the free silanols available for reaction with nickel species. A positively charged nickel species thus formed could constitute a nucleating site for further aggregation of nickel. An alternate mechanism for the interaction of nickel clusters with the silica surface is proposed, wherein ultrasound irradiation results in the dehydrative condensation of hydrogen-bonded silanols to form siloxane. This is followed by the formation of a bond between nickel and the bridging oxygen of the siloxane group. The surface topography and the adhesion of amorphous and polycrystalline nickel nanoparticles on the surface of silica submicrospheres (200–250 nm) were probed by atomic force microscopy (AFM), and reported in another publication [45]. Probe areas down to  $50 \times 50$  nm in dimension were scanned on a single submicrosphere immobilized in a thermoplastic resin bed. Amorphous nickel particles formed by the aggregation of nickel clusters were soft, experienced poor adhesion to the silica, and caused huge tip-induced particle movements; but polycrystalline nickel nanoparticles in the size range 20–30 nm were hard and adhered strongly to the silica. The stronger adhesion of polycrystalline nickel is explained in terms of a silicate-type impurity phase formed in the nickel–silica interface during crystallization.

Ramesh has extended this study to another magnetic metal, Co. Ferromagnetic cobalt nanoparticles of a size similar to 10 nm well adhered to hard silica microspheres (225–250 nm) were synthesized by the sonochemical decomposition of a volatile organic precursor, cobalt nitrosyl carbonyl  $[\text{Co}(\text{CO})_3\text{NO}]$ , in a suspension of silica in decalin, followed by crystallization of the resultant amorphous product [46]. Silica spheres carrying ferromagnetic cobalt nanocrystals were deposited on a single crystalline silicon [100] substrate by spin coating. The two-dimensional organization of the magnetic microspheres on silicon and the adhesion of cobalt nanoparticles on the surface of microspherical silica have been examined by scanning electron microscopy and atomic force microscopy (AFM), respectively. Two-dimensional arrays of hard spherical particles carrying a nanoprobe hold potential as scanning tip arrays (STA) in force microscopy. Though rigid single molecules of proteins were originally envisioned as suitable probes, the authors suggested the possibility that magnetic nanoparticles could also fit the criteria.

Sonochemistry was also used to deposit Ni on amorphous and crystalline alumina [47]. The study concluded: (1) that amorphous alumina can provide a great number of active sites for reaction with nickel, and can yield a good coating effect in which most of nickel adheres tightly to the alumina surface, while in the case of the crystallized alumina as substrate, most of the nickel particles are distributed in the free space among the alumina submicrospheres. (2) As compared to the unadhered nickel, the adhered nickel has a strong interaction with the alumina core, which can retard the crystallization of elemental nickel and, conversely, promote the formation of the spinel phase  $\text{NiAl}_2\text{O}_4$ . (3) The first stage of the interaction between the nickel and the alumina may be through the isolated hydroxy groups

to form a kind of interface Ni–O–Al bond. The connection positions further become nucleation centers for elemental nickel. After the sample is heated to high temperatures, DRS and IR results showed the diffusion of nickel ions into the vacant tetrahedral sites in alumina. At a higher temperature, an inversion process, the substitution of  $\text{Ni}^{+2}$  ions for part of the  $\text{Al}^{+3}$  at octahedral sites, takes place, resulting finally in the formation of the disordered spinel phase. (4) Magnetization measurements show that the as-prepared sonication products are superparamagnetic due to the ultrafine nature of nickel particles.

In a few studies sonochemistry was used to coat polymers with nanosized particles [48–50]. Of these three reports one [50] dealt with metals, more specifically with noble metals (Pt, Pd, and Au). In this research, metal colloids are adsorbed to the surface of neutral functionalized polystyrene microspheres, PSMS. The authors report on the synthesis and characterization of catalytically important noble monometallic colloids using various chemical and sonochemical methods. These metal colloids are then adsorbed onto suitably functionalized PSMS. The metal-immobilized microspheres are reacted with a linker such as 4-mercaptopbutyl phosphonic acid and subsequently used to grow multilayers.

Lately, we have deposited silver nanoparticles with an average size of 5 nm on the surface of preformed silica submicrospheres with the aid of power ultrasound [51]. Ultrasound irradiation of a slurry of silica submicrospheres, silver nitrate, and ammonia in an aqueous medium for 90 min under an atmosphere of argon to hydrogen (95:5) yielded a silver–silica nanocomposite. By controlling the atmospheric and reaction conditions, we could achieve the deposition of metallic silver on the surface of the silica spheres. Figure 6.3 depicts a silica-coated sphere.

It can be seen that the level of deposition has been improved and we are currently able to create a very smooth coating of a monolayer of nanoparticles on the surface. This was achieved by a gradual reduction of the silver concentration, thus

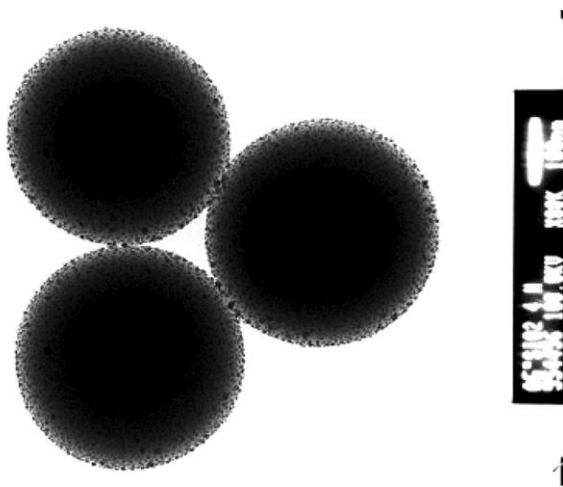


Fig. 6.3. TEM image of silver nanoparticles deposited on silica spheres.

reducing the thickness of the coated layer, as well as the amount of silver found between silica particles rather than on their surface.

Two questions were specifically investigated in these projects. First, the mechanism by which the deposited particles reach and are anchored to the host surface. Secondly, what is the mechanism by which the nanoparticles adhere to the surface, and are not removed, despite the severe stirring caused by the ultrasonic waves? Our answer to the first question involves the formation of shock waves and micro-jets created as after-effects to the collapse of the bubble [1a]. These effects always result when a bubble collapses near a solid surface. These jets, according to our interpretation, push the ultrafine particles towards the solid sphere at very high speeds, and are also known to cause the melting of colliding bodies and their sintering [52]. Once these nanoparticles collide with the surface, chemical bonds or weak interactions keep them on the surface in most cases. AFM studies have demonstrated [45] that the interaction becomes much stronger when the amorphous deposited particles are annealed at their crystallization temperature. The cantilever could scratch and move the particles only for the as-prepared products. Once they were annealed they were unaffected by the cantilever pushing power.

Ulman and coworkers have described in a few papers [53–55] a method by which sonochemically prepared nanoparticles are deposited on a flat surface, usually a silicon wafer. They describe their approach as a “plug and play”, in which sonochemically synthesized amorphous  $\text{Fe}_2\text{O}_3$  nanoparticles are incorporated onto device-quality Si wafers. After annealing the amorphous  $\text{Fe}_2\text{O}_3$  nanoparticles they change their properties from super-paramagnetic to soft ferromagnetic. The samples exhibit multiple light emissions with wavelengths that are crucial for optical fiber communications.

Later, they demonstrate [55] that sonochemically synthesized  $\text{Fe}_2\text{O}_3$  nanoparticles are introduced onto Si from an alcohol suspension. On annealing this sample in ultra-high vacuum, the oxygen atoms change the bonding partner from Fe to Si and desorb as  $\text{SiO}$  at  $750^\circ\text{C}$ . This results in the formation of nanoparticles of Fe on the surface and exhibits ferromagnetic behavior. Deposition of a thin layer (2 nm) of Si onto the sample containing the metallic Fe nanoparticles followed by annealing at  $560^\circ\text{C}$  leads to optically active Si.

Papadimitrakopoulos and coworkers reported on transparent Si/SiO<sub>x</sub> nanocomposite films, spontaneously adsorbed on glass or quartz substrates from their colloidal suspensions via a sonication-assisted oxidation process [56]. Individual nanosilicon particles (ca. 20 nm) appear to cover a significant part of the substrate along with agglomerates of the order of 50–80 nm in thickness. Kinetic studies indicate a rapid initial adsorption that slows down significantly after 3 h.

#### 6.1.1.5 Sonochemical Synthesis of a Polymer-Metal Composite

The use of ultrasound radiation for polymerizing various monomers was reviewed in [1a]. Here we will discuss how ultrasound waves have been used successfully been to embed ultrafine metallic particles in a polymeric matrix. The first report was by Wizel and coworkers [57]. They used ultrasound radiation to prepare a composite material made of polymethylacrylate and amorphous iron nanoparticles.

**Tab. 6.1.** The concentration of iron in polymers prepared by the two methods.

<b>Starting Materials</b>	<b>Fe in starting solution product (%)</b>	<b>Fe in final (%)</b>
Methylacrylate Fe(CO) <sub>5</sub>	0.5	0.56
Methylacrylate (DMF) – 50 mg amorphous Fe	0.3	5.4

Two preparation methods are described [57], in which the monomer, methylacrylate, is the starting material.

In the first, Fe(CO)<sub>5</sub> and distilled methylacrylate were sonicated as a mixture of neat liquids. During the sonication, the glass cell was wrapped in a dark cover to avoid photopolymerization. After 30 min of irradiation (avoiding degradation) at a dry ice–acetone temperature, the solution was treated with cold methanol, precipitating the polymeric product. In the second method, amorphous iron nanoparticles were prepared following Suslick's recipe [6]. The dried amorphous iron powder was introduced into the sonication cell without exposure to air and mixed with a solution of the methylacrylate monomer in *N,N'*-dimethylformamide (DMF). The concentration of the methylacrylate solution in DMF was 5.5 M. 35 ml of this solution was mixed with various amounts of amorphous iron nanoparticles. The amounts of the iron powder were changed from 50 mg to 200 mg. The chemical analysis of polymers prepared by the two methods is presented in Table 6.1.

The percentages presented in Table 6.1 are weight percentages of the iron in the mixture of Fe(CO)<sub>5</sub> and methylacrylate (first row, first column) in the starting solution. The second row presents the weight percent of iron in the starting solution (first column) and in the composite material (second column). The results according to Table 6.1 indicate that it is easier to introduce the iron by starting with amorphous iron as the precursor rather than Fe(CO)<sub>5</sub>. Molecular weights of the polymers are presented in Table 6.2.

When the molecular weight ( $M_w$ ) values of the polymeric composite material are compared with those of the polymeric product obtained from the irradiation of the monomer alone at the same irradiation time and concentration of the monomer, a 20% reduction is detected. This can be ascribed to the influence of the iron on the growth of the polymer. This would mean that the recombination of the iron

**Tab. 6.2.** Molecular weights of polymers obtained from various sonications.

<b>Monomer</b>	<b>Sonication time (min)</b>	<b><math>M_w</math> (g mol<sup>-1</sup>)</b>
Methylacrylate	30	134,000
Methylacrylate in DMF	90	1,760,000
Methylacrylate in DMF containing 50 mg Fe	90	142,000

pentacarbonyl dissociation products disturbs the growth of the polymeric radical. Thus, the dissociation products serve as a quenching agent for the creation of the polymer. The magnetic properties of the composite material are measured and reveal a super-paramagnetic behavior.

Wizel later extended her study and included another metallic nanoparticle, cobalt, and an additional polymer, poly(methylmethacrylate), in her metal-polymer composite research [58]. A significant difference in the solubility of the iron-poly(methylacrylate) and cobalt-poly(methylacrylate) in various solvents was observed. While the iron-poly(methylacrylate) composite (FePMA) and iron-poly(methylmethacrylate) composite (FePMMA) dissolved in chloroform, acetone, and toluene at room temperature, the corresponding cobalt-poly(methylacrylate) composite (CoPMA) was insoluble in these solvents at room temperature. At elevated temperatures (45 °C), dissolution of CoPMA in these solvents was observed. This difference is accounted for by the stronger interaction existing between the cobalt and the surrounding polymer. For iron-poly(methylacrylate) this interaction is weakened due to the formation of an iron complex. The  $M_w$  of the various polymers and composites as a function of the metal-to-monomer weight ratio was measured and reported.

The general features observed are that the molecular weights of the CoPMA are always larger than those of the corresponding FePMA. This comparison is made for equal amounts of starting materials. The second observation is that the larger the amount of the metal, the smaller the molecular weight of the PMA. The opposite is observed for the FePMMA, where a larger molecular weight is obtained for higher amounts of iron clusters. This phenomenon is explained as due to the presence of the oxidized iron, especially  $Fe^{+3}$ . These ions accelerate the polymerization of the methylmethacrylate [59], and a higher amount of metal will favor a higher molecular weight polymer. The presence of oxidized iron is supported by XPS and X-ray absorption near-edge spectroscopy (XANES) measurements. Nano-sized amorphous iron was also imbedded in polystyrene [60] similarly.

A different approach was taken by Kumar and associates [61]. He also embedded metals in polymers, but used as his precursor the polymer and not the monomer. In his first study a composite material containing amorphous Cu nanoparticles and nanocrystalline  $Cu_2O$  embedded in polyaniline matrices was prepared by a sonochemical method. These composite materials were obtained from the sonication of copper (II) acetate when aniline or 1% v/v aniline-water was used as the solvent. Mechanisms for the formation of these products are proposed and discussed. The physical and thermal properties of the as-prepared composite materials are presented. A band gap of 2.61 eV is estimated from optical measurements for the as-prepared  $Cu_2O$  in polyaniline.

In a similar way, well-dispersed nickel nanoparticles in polystyrene were obtained by a sonochemical method [62]. The first step in this synthesis was the preparation of nickel formate, which was prepared according to a previously described method. The preparation of the nickel-polystyrene composite was carried out by the sonochemical method. Typically, 500 mg of nickel formate and 1 g of polystyrene (Aldrich;  $M_w = 350,000$ ) are dissolved in 100 mL of *N,N*-dimethylform-

amide (DMF) and irradiated with a high-intensity ultrasonic horn under 1.5 atm of Ar-H<sub>2</sub> at room temperature for 3 h. The product is washed thoroughly with methanol in an inert glove box and dried overnight in a vacuum. The XRD diffraction indicates that the as-prepared composite material is crystalline. The XRD diffraction patterns match those of metallic nickel. The particle sizes measured from the TEM picture are about 5 nm in diameter and were very well dispersed in the polystyrene. The magnetization measurements established that the as-prepared nanocomposite materials are super paramagnetic due to their small size. The saturation magnetization (30.1 emu g<sup>-1</sup>) and coercivity (5 Oe) of the materials were significantly smaller than those of the bulk nickel, reflecting the nanoparticle nature.

Kitamoto and Abe applied power ultrasonic waves (19.5 kHz, 600 W) to 300 ml of FeCl<sub>2</sub> aqueous solution (pH 7.0) at 70 °C, and succeeded in encapsulating polyacrylate spheres of 250 nm diameter with magnetite ferrite coatings [49]. From TEM observations of the cross sections it was seen that the polymer spheres were covered with uniform columnar crystallites of 30–40 nm in diameter at the bottom and 60–70 nm at the top. The ultrasound waves produce OH groups on the polymer surfaces which work as ferrite nucleation sites; this improves the quality of the ferrite coatings. The ferrite-encapsulated particles will greatly improve the performance of the enzyme immunoassay as a cancer test reagent. The above possible mechanism for the formation of the blue oxide is consistent with explanations in the literature for a sonochemical reaction.

Finally, it should be mentioned that Suslick sonicated the transition-metal carbonyl in a low volatility solvent in the presence of poly(vinylpyrrolidone) and obtained metallic colloids for Fe and Co [63, 64].

#### 6.1.1.6 Sonochemical Synthesis of Nanometals Encapsulated in a Carbon Matrix

The metal particles of an interstitial solid solution of palladium carbide, PdC<sub>x</sub> (0 < x ≤ 0.15), were synthesized [65] at room temperature in an aqueous solution during the reduction of tetrachloropalladate (II) with sonochemically produced organic radicals. The sonochemical reduction was carried out using a 200 kHz ultrasonic generator operating at 200 W (6 W cm<sup>-2</sup>, 65 mL). An aqueous solution of PdCl<sub>2</sub>·2NaCl (1–10 mM, 60 mL) was placed in a cylindrical glass vessel (55 mL), which had a silicon rubber septum for gas bubbling or sample extraction, without exposing the sample to air. The vessel was fixed in a constant position and then irradiated for 1 h under argon at 20 °C. Under experimental conditions, the rate of formation of OH radicals and H atoms in the sonolysis of pure water was estimated to be 20 mM min<sup>-1</sup>.

Organic compounds such as methanol, ethanol, hexanol, isopropanol, *tert*-butyl alcohol, and acetone, were injected into the solution using a microsyringe through the septum just before the irradiation, and acted as accelerators of the reduction of Pd (II).

The number of carbon atoms in the Pd particles was controlled by changing the concentration and the type of organic additives. The mechanism proposed for the PdC formation comprises the following steps: (i) an active Pd cluster is formed



during the synthesis of Pd particles, (ii) organic additives are then adsorbed on the Pd cluster surface, and finally (iii) carbon atoms on the particle surface, which are formed from the catalytic dissociation of the additives, diffuse in the Pd metal lattice.

Similar studies in an organic solvent yielded almost the same product [66]. Nanostructured particles of amorphous carbon-activated palladium metallic clusters have been prepared (in situ) at room temperature by ultrasound irradiation of an organometallic precursor, tris- $\mu$ -[dibenzylideneacetone]dipalladium [ $(\eta\text{-CH=CH-CO-CH=CH-}\eta)_3\text{Pd}_2$ ] in mesitylene. Characterization studies show that the product powder consists of nanosize particles, agglomerated in clusters of approximately 800 Å. Each particle is found to have a metallic core, covered by a carbonic shell that plays an important role in the stability of the nanoparticles. The catalytic activity in a Heck reaction, in the absence of phosphine ligands, has been demonstrated.

Gedanken and his group were searching to replace the  $\text{Ni(CO)}_4$ , which was the source for the preparation of nickel, and is known to be a hazardous material. They found [67] a new precursor for the sonochemical preparation of amorphous nickel,  $\text{Ni(cyclooctadiene)}_2$ , which yielded relatively large (200 nm) amorphous nanoparticles composed of nickel and carbon atoms. Small nickel particles were dispersed all over the particle. When these particles were heated slightly above their crystallization temperature, much smaller particles (5 nm) of encapsulated crystalline nickel in amorphous carbon were obtained. The XPS spectrum reveals that the crystallization process is also accompanied by the reduction of the surface  $\text{Ni}^{+2}$  ions by the amorphous carbon atoms. The DSC measurements substantiate this assumption.

Walter and coworkers [68] intercalated small Pt nanoparticles into graphite using a sonochemical process.  $\text{H}_2\text{PtCl}_6$  was intercalated into natural graphite by applying ultrasound to a mixture of graphite,  $\text{H}_2\text{PtCl}_6$ ,  $\text{CCl}_4$ , and  $\text{SOCl}_2$  for 3 days. X-ray diffraction data showed that the host lattice was partly intercalated by  $\text{H}_2\text{PtCl}_6$ . A mixture consisting of a third and fourth stage together with unreacted graphite was observed. The intercalation compound was suspended in acetone with hydrogen flowing through while the sonication took place for 2 days. Transmission electron microphotographs showed highly dispersed nanoparticles in a narrow size range inside the carbon lattice. X-ray photoelectron spectroscopy gave evidence that these particles are platinum metal ( $\text{Pt(0)}$ ). Particle thickness estimated by X-ray diffraction indicated an average particle thickness of two layers. Selected-area electron diffraction microphotographs showed a pattern that could be hexagonally indexed. A ( $2 \times \alpha$  (graphite)) superstructure was observed for those quasi-two-dimensional aggregates formed by self-organization. This indicates a templating effect due to the carbon lattice.

Iijima and his group used ultrasound radiation to react carbon nanotubes [69]. They sonicated single-wall carbon nanotubes (SWNTs) in a monochlorobenzene (MCB) solution of poly(methyl methacrylate) (PMMA) and were able to react SWNTs with MCB or PMMA chemically. After the SWNTs reacted with these organic materials, they turned into ragged SWNTs (r-SWNTs) with many defects in

the sidewall when burned in oxygen. They consider sonochemistry to be a simple method to functionalize SWNTs.

Nikitenko has succeeded recently in preparing iron nanoparticles that are air-stable [70]. Iron is easily oxidized in ambient conditions, but when it comes to iron nanoparticles they are pyrophoric and burn spontaneously in air. That is why obtaining iron nanoparticles that are air-stable is important. On the other hand, it is known that iron nanoparticles obtained sonochemically from alkane solutions are not stable in contact with air. In his study, Nikitenko prepared coated iron nanoparticles by the sonochemical decomposition of  $[\text{Fe}(\text{CO})_5]$  in diphenylmethane (DPhM), an aromatic solvent with physicochemical properties (m.p. 25 °C, b.p. 265 °C, vapor pressure 1 kPa at 77 °C) that are suitable for sonochemistry. The sonolysis of the neat DPhM forms a polymer-like solid product. It is proposed that small amounts of this product generated in situ would coat the surface of iron nanoparticles formed simultaneously from  $\text{Fe}(\text{CO})_5$ . The as-prepared material contained 17.6 wt% C and 1.5 wt% H. The reaction yield was 53% with respect to iron. The presence of a significant amount of carbon and hydrogen indicates that the as-prepared material contains the sonolytic decomposition products of DPhM. At this stage the as-prepared product is annealed at 700 °C in argon. An air-stable, dark gray magnetic powder is formed as a result of the annealing. The annealed material contains 5.6 wt% C and 0.08 wt% H. The annealed product is air-stable. Its stability in air was checked once a month for the first 6 months after preparation by (1) Mössbauer spectroscopy, (2) XRD, and (3) magnetization measurements. No changes were observed in the measured parameters during this period. The annealed material is ferromagnetic, as follows from the magnetization curve. The saturation magnetization  $M_s$  and coercive force  $H_c$  are 212 emu  $\text{g}^{-1}$  and 40 Oe, respectively. The  $M_s$  value of the material is unexpectedly high and is close to that of bulk bcc Fe (222 emu  $\text{g}^{-1}$ ). The air-stability of the product originates from a  $\text{Fe}_3\text{C}/\text{C}$  layer surrounding the core of the iron nanoparticle.

### 6.1.2

#### Sonochemical Fabrication of Nano-Metallic Oxides

##### 6.1.2.1 Sonochemical Synthesis of Transition Metal Oxides from the Corresponding Carbonyls

Sonication of a decalin solution of  $\text{Fe}(\text{CO})_5$  in air yields amorphous nanoparticles of  $\text{Fe}_2\text{O}_3$  [71]. This paper presents another advantage of using sonochemistry for preparation of an amorphous product. It is well known that, unlike iron, which can be obtained in the amorphous form by the cold quenching technique, amorphous iron oxide cannot be prepared in this way. Higher cooling rates are needed for iron oxides and other metal oxides. This is because the thermal conductivities of metal oxides are usually much lower than those of the metals. This is the reason that glass formers, whose purpose is to prevent crystallization, are added if the quenching method is applied. Amorphous metal oxides can be prepared by rapidly quenching the molten mixture of metal oxides only if a glass former, such as  $\text{P}_2\text{O}_5$ ,  $\text{V}_2\text{O}_5$ ,  $\text{Bi}_2\text{O}_3$ ,  $\text{SiO}_2$ , and  $\text{CaO}$ , is added to the mixture [72–74]. As mentioned above,

the cooling rates obtained during the cavitation collapse are estimated to be greater than  $2 \times 10^9 \text{ K s}^{-1}$ . That is the reason why amorphous iron oxide,  $\text{Fe}_2\text{O}_3$ , can be prepared by sonicating  $\text{Fe}(\text{CO})_5$  in a decalin solution under air without adding any glass former.

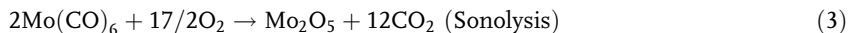
The characterization of an amorphous material is difficult because it lacks characteristic XRD diffractions, so that Auger or Mössbauer spectroscopies are preferred, along with other conventional analytical assays such as spot test and iodometric titration [71]. The  $\text{Fe}_2\text{O}_3$  nanoparticles are converted to crystalline  $\text{Fe}_3\text{O}_4$  nanoparticles when heated to  $420^\circ\text{C}$  under vacuum or when heated to the same temperature under a nitrogen atmosphere. The magnetization of pure amorphous  $\text{Fe}_2\text{O}_3$  at room temperature is very low ( $< 1.5 \text{ emu g}^{-1}$ ) and it crystallizes at  $268^\circ\text{C}$ .

Ultrafine powders of  $\text{Cr}_2\text{O}_3$  and  $\text{Mn}_2\text{O}_3$  have been prepared at room temperature by the sonochemical reduction of aqueous solutions containing  $(\text{NH}_4)_2\text{Cr}_2\text{O}_7$  and  $\text{KMnO}_4$ , respectively [75]. The yield of the sonochemical reduction has been enhanced by raising the reaction temperature or by using a 0.1 M aqueous solution of ethanol. The amorphous powders are nanosized (50–200 nm), and the surface area varies from 35 to  $48 \text{ m}^2 \text{ g}^{-1}$ . The crystallization of amorphous  $\text{Mn}_2\text{O}_3$  and  $\text{Cr}_2\text{O}_3$  could be achieved by heating them at 600 and 900 K, for 4 h, respectively.

Ultrasound irradiation of a slurry of  $\text{Mo}(\text{CO})_6$  in decalin for 3 h under ambient air produces blue-colored,  $\text{Mo}_2\text{O}_5 \cdot 2\text{H}_2\text{O}$  [76]. FT-IR analysis of this material reveals the existence of  $\text{Mo}=\text{O}$  and  $\text{Mo}-\text{O}$  bonds as well as hydrogen-bonded and coordinated water molecules. The amount of water molecules was determined by thermogravimetric analysis. Characterization using powder X-ray diffraction (XRD) and transmission electron microscopy (TEM) with selected area electron diffraction (SAED) shows the amorphous nature of the blue product. The TEM picture shows that the blue oxide is composed of spongy platelet nanoparticles (20 nm in diameter). Heating the initial blue powder at  $300^\circ\text{C}$  for 2 days under an oxygen, hydrogen, and nitrogen atmosphere yields X-ray crystalline  $\text{MoO}_3$ ,  $\text{MoO}_2$ , and a mixture of  $\text{MoO}_3$  and  $\text{MoO}_2$ , respectively. X-ray photoelectron spectroscopy (XPS), along with the potentiometric titration analysis of the blue oxide, confirms the formation of pentavalent molybdenum oxide. UV-visible absorption studies of the blue product demonstrate that the characteristic absorption of the  $\text{Mo}(\text{V})$  ( $d1 - \text{cation}$ ) oxide system and the Mo ions probably consist of two types of coordination symmetry ( $Td$  and  $Oh$ ). Electron paramagnetic resonance (EPR) experimental results revealed an unusual doublet pattern, which is ascribed to superhyperfine coupling of pentavalent molybdenum with a proton of coordinated water. The nanostructured amorphous pentavalent molybdenum oxide (blue oxide) thus formed has also been successfully deposited ultrasonically on Stober's silica microspheres (250 nm). The TEM images of silica-supported blue oxide reveal uniform distribution and the strong adhering nature of the blue oxide. FT-IR spectroscopy illustrated the structural changes that occur when the amorphous  $\text{SiO}_2$  is coated sonochemically with the blue oxide.

The sonochemical oxidation of molybdenum carbonyl would not occur in the bubble, due to its low vapor pressure. Therefore, the sonochemical reaction of

$\text{Mo(CO)}_6$  appears to take place in the interfacial region: Thus, the water molecule formed in the bubble may diffuse into the interfacial region or the water molecules that are available from the atmospheric air, precursor, and solvent, and stabilize the unusual pentavalent molybdenum oxide:



The above possible mechanism for the formation of the blue oxide is consistent with explanations in the literature for a sonochemical reaction.

Magnetite nanorods have been prepared by the sonication of aqueous iron (II) acetate in the presence of  $\beta$ -cyclodextrin [77]. The as-prepared magnetite nanorods are ferromagnetic and their magnetization at room temperature is about  $78 \text{ emu g}^{-1}$ . The particle sizes measured from transmission electron micrographs are about  $48/14 \text{ nm (L/W)}$ . A mechanism for the sonochemical formation of magnetite nanorods is discussed.

Only one report was found that discussed the effect of a magnetic field on sonication and sonication products [78]. The sonochemical irradiation of  $\text{Fe(CO)}_5$  solution in decalin under argon has been carried out with and without an external magnetic field. The sonication cell placed between the poles of a magnetic field of 7 kG which was applied during the sonication. We have already pointed out that this reaction yields amorphous  $\text{Fe}_2\text{O}_3$  [9]. Direct TEM measurements reveal that the sample obtained without a magnetic field consists of sponge-like particles with a mean size of about 25 nm, whereas the sample synthesized in a 7 kG magnetic field consists of highly acicular particles, 50 nm in length and 5 nm in width. Our finding sheds light on the process of particle nucleation during sonication, which cannot be a diffusion-assisted growth because of the very small time scale. We conclude, therefore, that particles are forced to form an acicular entity by direct magnetic interactions. The amorphous nature of the as-prepared substance was verified by X-ray diffraction, selected area electron diffraction, and differential scanning calorimetry. The magnetic moment vs. temperature measurements and Mössbauer spectroscopy reveal a large shift of the blocking temperature of about 70 K toward higher temperatures for the sample obtained in the magnetic field. We attribute the observed shift to the significant enhancement of the particle shape magnetic anisotropy.

#### 6.1.2.2 Sonochemical Synthesis of Ferrites from the Corresponding Carbonyls

It was just a reasonable extension that a mixture of carbonyls would be sonicated under air to yield the corresponding ferrites while the irradiation under argon yielded the metallic alloy [37]. Indeed, nanosized amorphous  $\text{NiFe}_2\text{O}_4$  powder was prepared by sonochemical decomposition of solutions of volatile organic precursors,  $\text{Fe(CO)}_5$  and  $\text{Ni(CO)}_4$  in decalin at 273 K, under an oxygen pressure of 100–150 kPa [79]. The amorphous nature of these particles was confirmed by various techniques. Magnetic measurements, Mössbauer, and EPR spectral studies indi-

cated that the as-prepared  $\text{NiFe}_2\text{O}_4$  ferrite particles were super-paramagnetic. The Mössbauer spectrum of the crystallized sample showed a clear sextet pattern, with hyperfine field values of 500 and 508 kOe for A (tetrahedral) and B (octahedral) sublattices, respectively, of the inverse spinel  $\text{NiFe}_2\text{O}_4$ . Saturation magnetization of the annealed sample ( $25 \text{ emu g}^{-1}$ ) was significantly lower than that for the reported multidomain bulk particles ( $55 \text{ emu g}^{-1}$ ), reflecting the ultrafine nature of the sample. Thermogravimetric measurements with a permanent magnet gave Curie temperatures of  $44^\circ\text{C}$  for amorphous and  $560^\circ\text{C}$  for the crystallized forms.

Another ferrite exhibiting two unique properties was also synthesized sonochemically,  $\text{BaFe}_{12}\text{O}_{19}$  [80]. A solution of  $\text{Fe}(\text{CO})_5$  and barium ethylhexanoate ( $\text{Ba}[\text{OOCCH}(\text{C}_2\text{H}_5)\text{C}_4\text{H}_9]_2$ ) in decane, in stoichiometric ratio, was decomposed by high-intensity ultrasonication. The as-prepared material was an amorphous  $\text{BaFe}_{12}\text{O}_{19}$  precursor in colloidal suspension, where the particles are in the nanometer size regime and are homogeneously distributed. The precursor is extracted from the solution as powder by precipitation or by evaporation and then calcined at low temperature ( $600^\circ\text{C}$ ) to obtain the final  $\text{BaFe}_{12}\text{O}_{19}$  crystalline nanosized powders. The first unique property detected by Shafi was the formation of features such as the *Olympic Rings* on transmission electron micrographs of amorphous  $\text{BaFe}_{12}\text{O}_{19}$  nanoparticles (Figure 6.4). Rings of smaller dimensions trapped inside

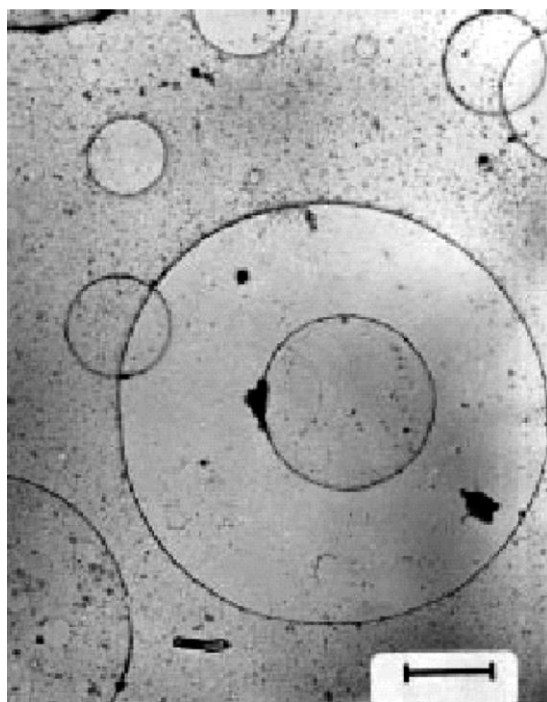


**Fig. 6.4.** TEM micrograph showing the self-organization of super-paramagnetic nanoparticles into submicron size rings the so-called *Olympic Rings* (scale bar is  $0.7 \mu\text{m}$ ).

the larger ones were another unique observation. The intersection of two rings is amazing, as this is in direct contradiction to the proposed mechanism for the ring formation, based on the dry hole formation on an evaporating thin film completely wetted to the substrate. The creation of this unique feature is attributed to the interplay of magnetic forces with the regular particle–substrate interactions. The second detected property was that barium hexaferrite was formed as a colloidal solution without the use of a surfactant.

### 6.1.2.3 Sonochemical Preparation of Nanosized Rare-Earth Oxides

A long list of oxides was prepared sonochemically. Almost all the above-mentioned oxides were synthesized in organic solvents. The other oxides that will be discussed from here on were all prepared in aqueous solutions. Submicron size spheres of silica and alumina prepared by well-known methods were coated sonochemically by nanoparticles of oxides of europium and terbium using the same concentration of ions [81]. We have also used sonochemistry to prepare nanoparticles of silica and alumina doped with the same rare-earth ions for comparison. The highest luminescence intensities were observed for europium and terbium doped in nanoparticles of alumina of dimension 20–30 nm. The intensities are comparable or higher than in commercial phosphors.

The synthesis of the rare-earth oxides was as follows: europium oxide was dissolved in a minimum amount of nitric acid and evaporated to dryness. The dry nitrate was dissolved in 5 mL of water. The required amount of silica microspheres was put in a beaker with 30 mL of water and the europium nitrate solution was added. The sonication was carried out for 1 h in an open beaker kept in an ice bath. 5 mL of 25% aqueous ammonia was added dropwise during the sonication. The resulting product after sonication was washed extensively with water, centrifuged, and dried under vacuum.

The preparation of the europium oxide-doped silica nano-particles (99.0SiO<sub>2</sub>–1.0Eu<sub>2</sub>O<sub>3</sub> mol%) was different. It was also carried out by the hydrolysis of tetraethyl orthosilicate (TEOS) in the presence of H<sub>2</sub>O, ethanol, and a europium nitrate solution. 25% aqueous ammonia was added dropwise during the sonication. In this way, europium oxide incorporated into silica particles was obtained.

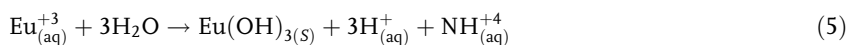
Decay time measurements of Eu<sub>2</sub>O<sub>3</sub>, and Tb<sub>2</sub>O<sub>3</sub> doped and coated on alumina were conducted [82]. The luminescence of the alumina substrate was found to be much shorter than that of the rare-earth oxides. Differences between the decay times of the deposited and doped materials are accounted for by the stronger guest–host interaction and the absence of concentration quenching in the doped material.

In a similar work, ultrasound radiation was used to prepare Eu<sub>2</sub>O<sub>3</sub> doped in zirconia and yttrium-stabilized zirconium (YSZ) nanoparticles [83]. Europium oxide was also coated sonochemically on the surface of submicron spherical zirconia and YSZ, which were fabricated by wet chemical methods. Time decay measurements of the doped and coated materials were conducted using a pulsed laser source. Lifetimes < 1.1 ms radiative lifetime of the Eu<sup>+3</sup> ions were detected for the doped and coated as-prepared materials. When the doped and coated samples were an-

nealed at 700 °C, longer lifetimes were measured. The shorter lifetimes were attributed to concentration quenching.

This series of experiments was continued and we recently deposited sonochemically a nanolayer of  $\text{Eu}_2\text{O}_3$  on submicron-size titania [84]. Ultrasound irradiation of a slurry of titania, europium nitrate, and ammonia in an aqueous medium for 120 min yielded an  $\text{Eu}_2\text{O}_3\text{-TiO}_2$  nanocomposite.

Finally, europium oxide nanorods have been prepared by the sonication of an aqueous solution of europium nitrate in the presence of ammonia [85]. The particle sizes measured from transmission electron micrographs and HRSEM are about  $50 \times 500$  nm ( $W \times L$ ). Sonication of an aqueous solution of europium nitrate in the presence of ammonia results in the precipitation of europium hydroxide: The as-prepared material is europium hydroxide, as confirmed by TGA, DSC, XPS, and Mössbauer spectroscopy measurements, as well as by PXRD of the as-prepared sample assisted by microwave irradiation

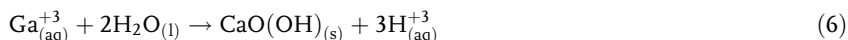


The presence of ammonium ion seems to be important for the formation of particles with morphology usually obtained in the absence of ammonia. In our case this was confirmed by the absence of precipitate after sonicating a solution of europium nitrate without addition of ammonia. Regarding the shape of the as-prepared product, careful examination of TEM, HRSEM, and HRTEM micrographs reveals that the rod-shaped particles of europium hydroxide consist of a few spherical particles aligned in one direction. The formation of europium hydroxide nanorods may be explained as follows. The  $\text{Eu}(\text{OH})_3$  particles formed upon collapse of the bubbles adsorb  $\text{NH}_4^{+}$  ions or ammonia on their surfaces, thus forming a monolayer and fusing them by hydrogen bonding. In this way ammonium ions would be responsible for the observed morphology. This adsorption of  $\text{NH}_4^{+}$  on the surface of the particles is supported by the results of Sherif et al. [86], who showed that ammonium nitrate ( $\text{NH}_4\text{NO}_3$ ) is adsorbed on the surface of the powder after precipitation. We also evoke in the explanation the microjets mentioned above, and due to this very high velocity of liquid jets, the  $\text{Eu}(\text{OH})_3$  nanoparticles are pushed toward each other, forming the nanorods.

#### 6.1.2.4 The Sonochemical Hydrolysis of Group 3A Compounds

A detailed study of the sonochemical hydrolysis of Ga, Al, In and Tl was conducted by sonicating the chloride aqueous solutions of these metals. Unlike the sonication of carbonyls, which resulted in nanophase amorphous products [6, 12], the sonication of inorganic salts such as  $\text{GaCl}_3$ ,  $\text{InCl}_3$ , or  $\text{TlCl}_3$  yields crystalline nanophase products. The sonochemical reaction of an aqueous solution of  $\text{GaCl}_3$  led to the formation of  $\text{GaO}(\text{OH})$  rolled up in a scroll-like layered structure to give cylinders of 80–120 nm diameter and 500–600 nm in length [89]. Small amounts of metallic Ga were incorporated with these tubes. The presence of zero-valent Ga (ca. 1%) was demonstrated by the DSC spectrum, which displayed an endothermic peak at 29.2 °C. The amount of metallic gallium is dependent on the irradiation time:

irradiating the starting solution for 90 min resulted in a DSC signal which was an order of magnitude smaller than that obtained after 6 h of sonication. In a parallel experiment, a 1 M aqueous solution of  $\text{GaCl}_3$  was heated to 300 °C in a high-pressure cell, without sonication. No noticeable powder formation occurred after heating the solution for 4 h. The formation of  $\text{GaO}(\text{OH})$  can occur by reaction (6);



The observation that the pH of the solution changes from 2.37 prior to the sonication to 1.61 at the end of the reaction implies that reaction (6) is the dominant pathway. This reaction is endothermic [90] with an equilibrium constant at 50 °C of ca.  $10^{-3}$ . The high local temperature in the shell surrounding the collapsing bubble constitutes the driving force for the formation of the  $\text{GaO}(\text{OH})$ .

An explanation for the elongated layered structure of the  $\text{GaO}(\text{OH})$  based on cavitation collapse occurring at the solid–liquid boundary has been suggested [89]. The particle size was found to decrease with decreasing concentration of  $\text{GaCl}_3$  due to a reduced amount of reactant at the bubble–liquid interface.

We could not investigate and characterize the sonohydrolytic product of  $\text{AlCl}_3$ , because it is a very hygroscopic product. On the other hand, the products of the sonohydrolysis of  $\text{InCl}_3$  [91], and  $\text{TlCl}_3$  [92], were investigated in great detail, the latter producing inorganic fullerenes (IF) of  $\text{Tl}_2\text{O}$ .

$\text{In}(\text{OH})_3$  nanopowder was prepared via the sonication of an aqueous solution of  $\text{InCl}_3$  at room temperature and at 0 °C. At these temperatures, nonsonicated hydrolysis does not occur. The role of the ultrasound radiation and the mechanism of the reaction are discussed. The proposed mechanism is based on the sonohydrolysis of In (III) ions in the outer ring, and the liquid shell, of the collapsing bubble. The product,  $\text{In}(\text{OH})_3$ , was obtained as needle-shaped particles.

The sonication of an aqueous solution of  $\text{TlCl}_3$  under a flow of argon led to a precipitate, composed of two products. The major product is  $\text{Tl}_2\text{OCl}_2$ , while  $\text{Tl}_2\text{O}$  is obtained in small quantities. The latter has the structure of a multi-shell closed compound. The identification of the inorganic fullerenes in the TEM picture as the thallium (I) oxide is based on SAED measurements. In Figure 6.5 we present a picture of the onion-like IF.

The three-dimensional structure of the IF was demonstrated when the sample was tilted under the electron beam and an identical picture was obtained at all tilting angles (see Figure 2 in [92]). The growth mechanism of both carbon and inorganic fullerenes is not yet fully understood. However, it is believed that the main stimulus for the formation of fullerene-like structures emanates from the large energy associated with the dangling covalent bonds at the edges of the layered structures. The growth conditions of fullerene-like structures, in most cases, are far from equilibrium. The large thermal energies during growth force the nanoclusters of layered materials. We suggest the following mechanism to explain the formation of the closed curved structures. In the first stage,  $\text{Tl}_2\text{O}$  is formed via the sonochemical reduction of the  $\text{Tl}^{+3}$ . It is known that sonohydrolysis of aqueous solutions of metal ions is caused by the high local temper-



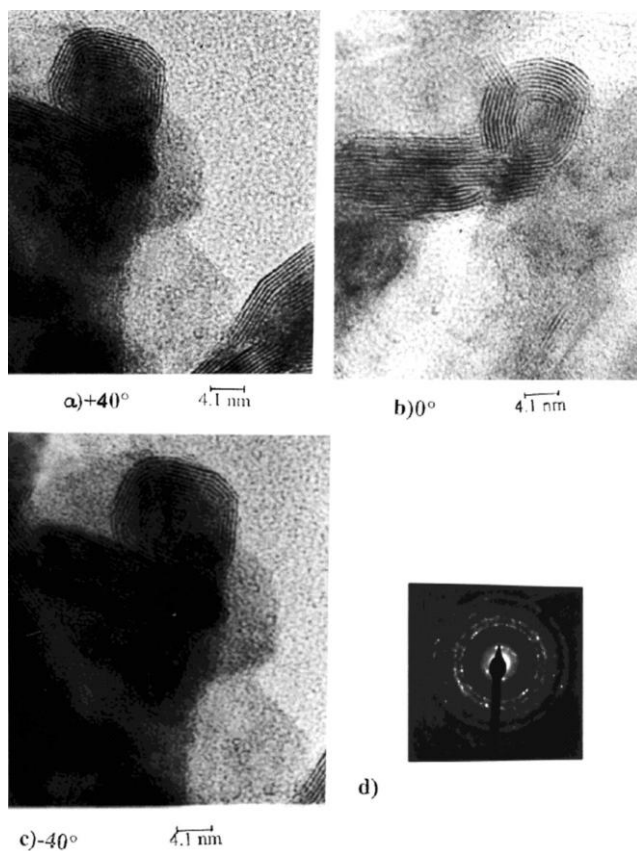


**Fig. 6.5.** TEM image of the as-prepared powder of fullerene-like inorganic  $\text{TiCl}_3$ , at different tilt angles. (a)  $+40^\circ$ , (b)  $0^\circ$ , (c)  $-40^\circ$ , (d) SAED inserted (Scale: 1 cm = 4.1 nm).

atures in or near the cavitation bubbles. If the original  $\text{Ti}_2\text{O}$  particle is planar (two-dimensional), curvature and closure of the fullerene-like structures may occur around the collapsing bubble. The temperature gradient from the bubble surface into the solution should cause a temperature gradient across the particle that causes the curvature. This is helped by the energetics, which favors sheet closure due to bond energy released by eliminating reactive edges in the planar structures.

#### 6.1.2.5 The Sonochemical Synthesis of Nanostructured $\text{SnO}_2$ and $\text{SnO}$ as their Use as Electrode Materials

In recent years there has been an increasing interest in the use of  $\text{SnO}_2$  as an anode material for lithium batteries, starting with the announcement by Fuji Photo Film Celltee Co. Ltd., Japan, about their STALION lithium ion cell. These cells utilized an amorphous tin-based composite oxide as the anode (together with a

$\text{Li}_x\text{CoO}_2$  cathode). It appears that the basic anode process in these cells is lithium insertion into tin oxides, which forms Li–Sn alloys in a matrix of  $\text{Li}_2\text{O}$ . Hence, the reversible process that finally remains is lithium alloying with metallic tin. For this purpose we have prepared  $\text{SnO}_2$ , and later SnO semiconductor nanoparticles. They were synthesized by ultrasonic irradiation of an aqueous solution of  $\text{SnCl}_4$  and azodicarbonamide under ambient air [93]. These nanoparticles are 3–5 nm in size, as calculated using the Debye–Scherrer formula, and as observed by TEM. Electrochemical tests were performed using the  $\text{SnO}_2$  nanoparticles as the electrode materials in nonaqueous Li salt solutions. Amorphous, as well as crystalline, nanoparticles were prepared for this project. The performance of the anode was examined as a function of the crystalline state of the  $\text{SnO}_2$ , as well as the particle size.

These tests clearly indicated that the  $\text{SnO}_2$  particles prepared by sonochemical synthesis have a promising capacity, reversibility, and cycle life in repeated lithium insertion and deinsertion processes. Heat treatment of the sonochemically prepared  $\text{SnO}_2$  nanoparticles had a pronounced effect on their electrochemical behavior. The crystallization of the particles due to the heat treatment increased both the electrode's irreversible and reversible capacities measured during the first lithiation–delithiation cycle. However, while the reversible capacity retention upon cycling of electrodes made of as-prepared  $\text{SnO}_2$  material was good, the capacity of electrodes made of the heat-treated materials degrades upon cycling.

SnO was prepared similarly to the preparation of  $\text{SnO}_2$  [94]. Nanoparticles of SnO were synthesized sonochemically in mildly basic  $\text{SnCl}_2$  solutions. The amorphous product thus obtained could be transformed to a nanocrystalline phase by heating to 200 °C. Composite electrodes comprised (by weight) of 80% SnO, 10% graphite flakes (conductive additive), and 10% polymeric binder (an optimal composition) were tested as anodes for rechargeable Li batteries. Both the amorphous and the nanocrystalline SnO are electrochemically active and can be reduced in nonaqueous Li salt solutions to matrixes of  $\text{Li}_2\text{O}$  and  $\text{Li}_{17}\text{Sn}_4$ . The nanocrystalline SnO was found to be much more effective and a superior anode material to the amorphous and microcrystalline phases, as an active material for electrodes. These electrodes could reach nearly their theoretical capacity ( $= 790 \text{ mA h g}^{-1}$ , SnO) in electrochemical lithiation–delithiation processes versus a Li counter electrode in nonaqueous Li salt solutions. However, there is still a long way to go to the possible use of SnO as an anode material in practical batteries. This is due to its high irreversible capacity ( $\text{Li}_2\text{O}$  formation and surface film precipitation due to reactions of lithium–tin compounds with solution species) and gradual capacity decrease during repeated charge–discharge cycling. Possible reasons for this capacity fading are discussed in [94].

#### 6.1.2.6 The Sonochemical Synthesis of Mesoporous Materials and the Insertion of Nanoparticles into the Mesopores by Ultrasound Radiation

In a recent review article the synthesis of mesoporous (MSP) silica is considered to be one of the four most important discoveries in solid-state and materials science in the last decade [95]. We have summarized our activities in this field in an article

published in Chemistry – A European Journal [96]. We will therefore repeat briefly our early findings and introduce some new results.

The report demonstrates that ultrasound radiation can also be used for the preparation of MSP materials. MSP silica, MCM-41 [97], MSP titania [98], and YSZ (yttria stabilized zirconia) [99] were all prepared by this method. In addition, straight-extended layered mesostructures based on transition metal (Fe, Cr) and rare earth (Y, Ce, La, Sm, Er) oxides were also synthesized sonochemically [100]. The synthetic processes reproduced in most cases the already published sol–gel synthesis [101]. The main advantage of the sonication method is the short irradiation time. In most cases the reaction time was 3 h. The longest sonication period was 6 h. It was applied for the synthesis of MSP YSZ and caused the transformation of the product from a layered to a hexagonal mesostructure due to this prolonged irradiation time. A second advantage of the sonochemical synthesis is that the walls of the sonochemical product were thicker than those obtained conventionally (see Table 1, [97]). The thicker walls are responsible for the MCM-41 obtained sonochemically being more stable than MCM-41 prepared by conventional hydrothermal methods [102]. This was demonstrated when our product was treated with pure water, and its crystallinity changed only a little after heating under reflux for 6 h, and decreased by approximately 65% after heating under reflux for 12 h. In the literature [102] the MCM-41 prepared by using conventional hydrothermal methods became amorphous after refluxing for 12 h.

During the formation of the framework, despite the agitation of the ultrasound, which helps to disperse the small silica oligomers more homogeneously in the mixture, the formation of hot spots within the surfactant–silicate interface may accelerate the silica polymerization, which is slow and rate limiting under normal conditions. Thus, the fabrication of the meso-structure can be achieved more efficiently. On the one hand, acoustic cavitation etches the surfactant–silicate micelles on the surface; this results in a coarse outer surface or even the fragmentation of the micelles. An additional factor is that hot spots accelerate the condensation of surface silanol groups among micelles; in this way ultrasound radiation accelerates the formation of the MCM-41 framework and the growth of particles.

The discovery of MSP materials led immediately to the development of many experimental methods for the deposition of materials, especially catalysts, into the mesopores. We have deposited Mo oxide, and Co/Mo oxides into MCM-41 as well as into the pores of Al-MCM-41 [103]. We have also anchored  $\text{Fe}_2\text{O}_3$  into the mesopores of titania [104]. A large variety of nanoparticles has been introduced into many MSP materials. This work, however, has not been published. In addition to the characterization studies of the composite catalyst-mesoporous product, catalytic studies have also been conducted.

The typical sonochemical reaction is performed as follows: a slurry of the MSP material, for example, Al-MCM-41, in decalin containing dissolved  $\text{Mo}(\text{CO})_6$  and/or  $\text{Co}(\text{CO})_3\text{NO}$ , is sonicated. The sonication is carried out under ambient air at room temperature. The solid product is separated by centrifugation, thoroughly washed with dry pentane, and dried in vacuum at room temperature. The chemical composition of the solid phase was determined by EDAX to probe whether the

transition metal is indeed found in the solid. The kinetics of the decomposition of the carbonyl in the presence of the MSP was faster than in its absence (7 times faster for Al-MCM-41). This is attributed to the large number of bubbles developed due to the solid surface. The amount of  $\text{MoO}_x$  in the solid Al-MCM-41 could reach 67 wt%. However, it was necessary to find the location of the  $\text{MoO}_x$  particles. In other words, to find out whether they have indeed entered the mesopores or can be found outside the pores. This location was determined by mapping the TEM grid employing TEM–EDAX measurements. The data clearly demonstrate [103] that the Mo oxide phase is located inside the support's pores and does not form separate particles up to an  $\text{MoO}_3$  content of about 40–45 wt% upon ultrasonic deposition. High-resolution TEM (HRTEM) pictures [103] reveal that the  $\text{MoO}_3$  deposition does not cause degradation of the Al-MCM-41 hexagonal pore structure. In addition to the EDAX mapping technique, four other methods are used to support these results. In the sample containing 67 wt%  $\text{MoO}_x$ , large amounts of the excess material are found outside the pores. Thus, a monolayer of  $\text{MoO}_x$  particles is strongly anchored to the walls, while the rest are found outside. Considering the surface area of Al-MCM-41 used in the work and an Mo surface concentration of 5 Mo atoms  $\text{nm}^{-2}$ , the geometrical closed, packed monolayer capacity corresponds to 50 wt%  $\text{MoO}_3$ , which is in good agreement with our measurements. XPS measurements proved that chemical bonds are being formed between the silica and the molybdena, forming Si–O–Mo bonds.

The main advantage of using ultrasound for the insertion of nanoparticles into MSP materials is illustrated in Figure 6.6, which compares the normalized surface area (NSA) values obtained by the sonochemical methods with those of other methods such as impregnation and thermal spreading. The NSA is defined as

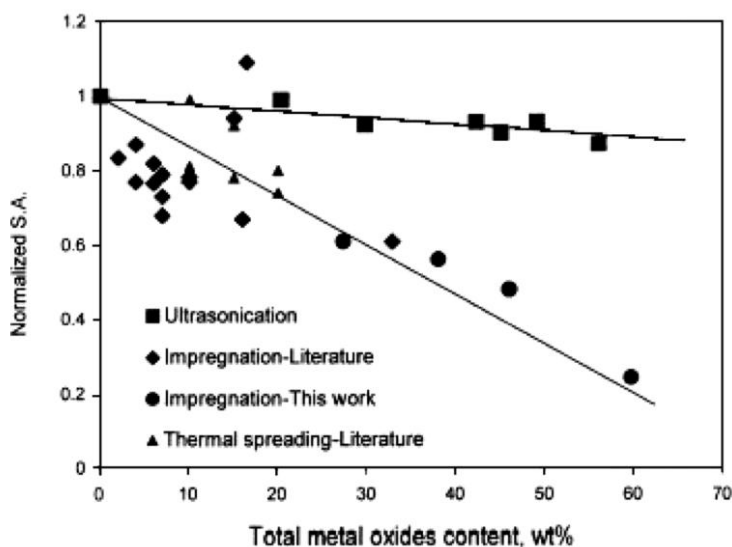


Fig. 6.6. Normalized surface area of MCM-supported catalysts: Mo–, Ni–, and Co(Ni)–Mo catalysts in oxide form.

$$\text{NSA} = \text{SA}_{\text{catalyst}} / (1 - \gamma) \cdot 1 / \text{SA}_{\text{MCM}} \quad (7)$$

where SA is the specific surface area of the parent Al-MCM-41 or the metal oxide/Al-MCM-41 composite, and  $\gamma$  is the weight fraction of metal oxides in the catalyst. In other words, NSA reflects the surface area per gram of MCM. If the active component is distributed at the support surface in the form of a close-packed monolayer of a given thickness (no pore blocking occurs), the NSA decreases only as a result of narrowing of the support pores. For example, for a 45 wt% MoO<sub>3</sub> phase loaded on a wide-pore Al-MCM-41 support, the reduction of pore diameter from 8.3 to 7.7 nm yields an NSA value of 0.93. The results shown in Figure 6.6 speak for themselves, showing that only a slight reduction in the NSA occurs when sonochemistry is used for the insertion of nanoparticles, or in other words, the loading of the MSP by large amounts of nanoparticles reduces the SA only slightly, whereas when other methods are used a considerable reduction in the SA is observed.

The remaining question is what is the role of the ultrasound radiation in the insertion of the nanoparticles into the mesopores? It is clear that the bubble cannot collapse inside the mesopores because the size that the bubble reaches before its collapse is estimated to be about 100  $\mu\text{m}$  [105], while the pore diameter is less than 3 nm. Instead, we propose two possible mechanisms. The first is based on micro-jets and shock waves that result when a bubble collapses near a solid surface. As already explained, near a solid surface the collapse drives high-speed jets of liquid into the surface. Since most of the energy is transferred to the accelerating jet, the jet can reach velocities of hundreds of meters per second. In our case the small nanoparticles are pushed by these jets into the mesopores and, as a result of their reaction with the mesoporous support, are anchored to the inner surface of the mesoporous material. The other possibility is that the solution inside the pores undergoes a chemical reaction initiated by shock waves forming nanoparticles. The nanosized products interact with silanols, forming the chemical bonds described above. The second mechanism sounds a better explanation since it accounts for the homogeneous spreading of the nanoparticles in the pores.

Another active group in this field is that of Chen and Zhang. In their first paper [106] they reported on a sonochemical procedure at room temperature for the preparation of gold nanoparticles loaded in mesoporous silica. They show that the Au nanoparticles, with a mean size of 3–4 nm in diameter and a fairly narrow size distribution, are dispersed uniformly within the pores of the silica host. In a second paper they measured the optical absorption of the Au nanoparticles dispersed within pores of monolithic mesoporous silica after subsequent annealing treatment [107]. Charge transfer at the interfaces between Au nanoparticles and pore walls is introduced qualitatively to discuss the red-shift of Mie resonance absorption band with decreasing the Au particle size. A longer paper [108] gives more details on the sonochemical reduction of chloroauric acid (HAuCl<sub>4</sub>) within the pores of silica. This reduction leads to the insertion of gold nanoparticles into mesoporous silica. The paper also reports on the optical measurements. In another publication related to gold inserted into MSP silica [109], they present an HR-TEM showing nearly

spherical-shaped gold nanoparticles, with a mean diameter of 5.2 nm, located in the pores, most of which are less than 6 nm in diameter. The ultrasonic irradiation time dependence of optical absorption for the soaked porous solid sample, as measured by the variation in absorbance at 310 and 544 nm, indicated the reduction of Au(III) ions, and the nucleation and aggregation of gold nanoparticles within the pores of MSP silica. Additionally, the reaction rates estimated phenomenologically by the absorbance decay at 310 nm for both the porous sample and the corresponding soaking solution, showed the enhancement of the sonochemical reduction rate of Au(III) ions within the pores of mesoporous silica. It is assumed that the extensive liquid–solid interfacial zones in the pores, due to the high specific surface area and great porosity of the mesoporous solid, are the major regions where the efficient sonochemical reduction induced by the cavitation takes place.

In the latest of their publications related to the insertion of gold into MSP silica [110], the same authors discuss the structural changes that the silica skeleton undergoes upon sonication. The structure of mesoporous silica after sonochemical preparation of gold nanoparticles within its pores was studied by a nitrogen adsorption technique. It was shown that the structural parameters, such as specific surface area (SSA), porosity ( $P$ ), and the mean pore diameter ( $l(p)$ ) were increased significantly after ultrasonic irradiation. It is suggested that the collision of Au nanoparticles with the pore walls and localized erosion induced by the asymmetric implosive collapse of cavities on the extensive liquid–solid interface are responsible for the structural change in the mesoporous solid.

One paper by the same group reports on the sonochemical insertion of palladium nanoparticles loaded within mesoporous silica [111]. The formation of Pd nanoparticles (5–6 nm in diameter) was restricted by the coalescence of the sonochemically reduced Pd atoms inside the confined volumes of the porous solid.

One of the most exciting sonochemical preparation procedures of MSP titania did not use any surfactant [112]. Yu and his coworkers used monodispersed  $\text{TiO}_2$  sol particles, which were formed initially by ultrasound-assisted hydrolysis of acetic acid-modified titanium isopropoxide. Then, the mesoporous spherical or globular particles, which have a narrow pore size distribution, were produced by controlled condensation and agglomeration of these sol nanoparticles under high intensity ultrasound irradiation. The mesoporous  $\text{TiO}_2$  has a wormhole-like structure and a lack of long-range order. Nitrogen adsorption results indicate that the mesoporous  $\text{TiO}_2$  retains mesoporosity with a narrow pore size distribution and high surface area to at least 673 K. The thermal stability of mesoporous  $\text{TiO}_2$  is attributed to its thick inorganic walls, consisting of  $\text{TiO}_2$  nanoparticles. A TGA study shows that this synthetic method is environmentally friendly. The photocatalytic activity of mesoporous  $\text{TiO}_2$  for the oxidation of acetone in air was measured. As-prepared mesoporous  $\text{TiO}_2$  has a negligible activity due to its amorphous structure. Calcined mesoporous  $\text{TiO}_2$  shows a better activity than the commercial photocatalyst P25. The reasons for the high activity of mesoporous  $\text{TiO}_2$  are discussed.

In a continuing paper Yu and coworkers reported [113] on the preparation of mesoporous  $\text{TiO}_2$  with a bicrystalline (anatase and brookite) framework, which was synthesized directly under high-intensity ultrasound irradiation. The synthesis was

carried out separately, both with and without the use of a triblock copolymer. Without thermal treatment, mesoporous  $\text{TiO}_2$  was formed by the agglomeration of monodispersed  $\text{TiO}_2$  sol particles. The use of ultrasound irradiation assisted in the formation of the brookite phase. As the content of the brookite phase increased, the pore size and the crystalline sizes of anatase and brookite became larger when the triblock copolymer was used in the synthesis. Both as-prepared samples exhibited better activities than the commercial photocatalyst P25 in the degradation of n-pentane in air. The degradation rate of mesoporous  $\text{TiO}_2$  synthesized in the presence of triblock copolymer was about two times greater than that of P25. The high activities of the mesoporous  $\text{TiO}_2$  with a bicrystalline framework can be attributed to the combined effect of three factors: high brookite content, high surface area, and the existence of mesopores.

Two other MSP oxides were recently reported by Srivastava [114, 115]. Both preparations used the alkoxides of the metals as the inorganic precursor and CTAB as the template. The first report details the preparation of MSP  $\text{SnO}_2$  [114]. The porous tin oxide prepared in this way was used in dye-sensitized solar cells.

The second paper [115] describes the synthesis of mesoporous iron oxide. Iron (III) ethoxide was used as an inorganic precursor and CTAB as an organic structure directing agent. After sonication, the surfactant was removed by calcination and solvent extraction methods. FTIR spectra demonstrated the removal of the surfactant from the pores of the mesoporous iron oxide. The surface area after solvent extraction is found to be  $274 \text{ m}^2 \text{ g}^{-1}$ . The as-prepared amorphous  $\text{Fe}_2\text{O}_3$  shows paramagnetic behavior, but after calcination at  $350^\circ\text{C}$  it changes to  $\gamma\text{-Fe}_2\text{O}_3$  with good magnetic properties. The catalytic activity of mesoporous iron oxide was studied in the reaction of cyclohexane oxidation under mild conditions. The mesoporous  $\text{Fe}_2\text{O}_3$  catalyst showed 36% conversion of cyclohexane into cyclohexanone and cyclohexanol, with a high selectivity. This is the highest conversion percentage ever reported for the oxidation of cyclohexane. The oxidation was conducted under 1 atm of  $\text{O}_2$  at  $70^\circ\text{C}$ .

MSP titania was also used to make electrodes, which were tested in a dye-sensitized solar cell [116]. The short-circuit photocurrent, open-circuit photovoltage and fill factor increased with increasing sintering temperature, having a performance threshold at  $450^\circ\text{C}$ , showing that the more ordered structures are required for high solar cell conversion efficiencies.

Rana [117] has recently demonstrated that ultrasound radiation can be employed for the formation of vesicular mesoporous silica. The dimension of the vesicles ranged from 50–500 nm. If the synthesis is compared with a previous work on the synthesis of MSP silica vesicles [118], the advantages of the sonochemical synthesis are as follows: (1) It employs the commonly used CTAB as a surfactant, instead of Gemini surfactant,  $\text{C}_n\text{H}_{2n+1}\text{NH}(\text{CH}_2)_2\text{NH}_2$ ; (2) the sonochemical reaction takes 1 h as compared with 48 h; (3) the reaction is conducted at  $25\text{--}35^\circ\text{C}$  instead of  $100^\circ\text{C}$ ; and (4) a higher surface area is obtained, 940, as compared with  $280\text{--}520 \text{ m}^2 \text{ g}^{-1}$ . The special role of the bubbles in the formation of the vesicle is also explained.



### 6.1.2.7 The Sonochemical Synthesis of Mixed Oxides

In addition to the above reported synthesis of ferrites our search has revealed that aluminates [119], nickelates [120], and manganates [121], have also been prepared by the sonochemical method. Nanosized nickel aluminate spinel particles have been synthesized [119] with the aid of ultrasound radiation by a precursor approach. Sonicating an aqueous solution of nickel nitrate, aluminum nitrate, and urea yields a precursor which, on heating at 950 °C for 14 h yields nanosized  $\text{NiAl}_2\text{O}_4$  particles with a size of ca. 13 nm and with a surface area of about  $108 \text{ m}^2 \text{ g}^{-1}$ .

Nanostructured  $\text{LaNiO}_3$  was prepared by co-precipitation under ultrasonic radiation [120]. Using various characterization methods and evaluation of catalytic activity, the effects of ultrasound on the structural properties and catalytic activity of  $\text{LaNiO}_3$  were studied. The TEM showed that the ultrasound could cause a decrease in the particle size. The average particle size of  $\text{LaNiO}_3$  prepared by sonochemistry is 20 nm. The specific surface area of  $\text{LaNiO}_3$  is  $11.27 \text{ m}^2 \text{ g}^{-1}$ . Ultrasound could lead to increased surface oxide content and surface crystal oxygen vacancies. The TPR result showed that the  $\text{LaNiO}_3$  prepared by sonochemistry has a lower reduction temperature and a higher ratio of surface oxygen to crystal oxygen. The evaluation of catalytic activity showed that ultrasound could increase the catalytic activity of  $\text{LaNiO}_3$  for NO decomposition.

Lanthanum strontium manganate, known also as LSM, is known for its magnetoresistance properties, and is also used in solid oxide fuel cells (SOFC). Sonochemistry was used for its preparation [121]. Electron magnetic resonance (EMR) spectra of nanosized sonochemically sintered powders of  $\text{La}_{0.7}\text{Sr}_{0.3}\text{MnO}_3$  (annealed,  $T_c = 340 \text{ K}$ ) were studied.

### 6.1.2.8 The Sonochemical Synthesis of Nanosized Hydroxides

The synthesis of nanosized  $\alpha$ -nickel hydroxide has been reported by two groups [122, 123]. The first reported reaction prepared nanosized  $\alpha$ -nickel hydroxide with an interlayer spacing of 7.2 Å. The synthesized hydroxide was found to possess good stability in a KOH medium, and the material might be interesting from the application point of view in secondary alkaline batteries. The second synthesis prepared nanocrystalline  $\alpha$ - $\text{Ni}(\text{OH})_2$  by an ultrasonic precipitation/stirring method [123]. Compared with the sample prepared without ultrasonic stirring, the crystal structure of the  $\alpha$ -phase sample has been changed from the  $\beta$ -phase. The crystalline size of the sample is about 20 nm, which is smaller than the sample produced without ultrasonic stirring (70 nm).

Cobalt hydroxide with an interlayer spacing of 7.53 Å and needle-like morphology has been synthesized with the aid of ultrasound radiation [124]. Characterization methods indicate the formation of  $\alpha$ -cobalt hydroxide. Thermal decomposition of the hydroxide at 300 °C under air or argon yields nanometer-sized oxide particles of  $\text{Co}_3\text{O}_4$  (ca. 9 nm) and  $\text{CoO}$  (ca. 6 nm), respectively.

In a different study [125], an  $\alpha$ -cobalt hydroxide with an interlayer spacing of 12.65 Å was synthesized in sheet shapes with dimensions of 100–120 nm with the



aid of sonication. Acetate anions are intercalated into the interlayer region of the as-prepared  $\alpha$ -cobalt hydroxide in the form of a free ion state.  $\beta$ -Cobalt hydroxide has also been prepared and formed as crystallized thin hexagonal platelets with a diameter of 100 nm. Pure cobalt oxyhydroxide with a particle size of 10–30 nm has also been obtained.

#### 6.1.2.9 Sonochemical Preparation of Nanosized Titania

Because of its many applications, a few attempts are known in which ultrasonic waves have been applied for the synthesis of nanosized titania. Yu and coworkers [126] discovered a novel method for preparing highly photoactive nano-sized  $\text{TiO}_2$  photocatalysts with anatase and brookite phases. The method has been developed by hydrolysis of titanium tetraisopropoxide in pure water or a 1:1 EtOH:H<sub>2</sub>O solution under ultrasonic irradiation; the photocatalytic activity of  $\text{TiO}_2$  particles prepared by this method exceeded that of Degussa P25.

Huang, in a similar reaction [127], found a way to selectively prepare anatase or rutile as well as their mixtures. This was achieved by using various precursors and employing ultrasound irradiation. The products, the particle sizes of which are nanometric (<9 nm), are dependent both upon the reaction temperature and the precursor used; a substantial reduction in reaction time, as well as reaction temperature is observed, as compared to the corresponding hydrothermal processes.

A novel sonochemical method for the direct preparation of anatase nanocrystalline  $\text{TiO}_2$  was reported by Guo et al. [128]. Nanocrystalline  $\text{TiO}_2$  was synthesized by the hydrolysis of titanium tetrabutyl in the presence of water and ethanol under high-intensity ultrasonic irradiation (20 kHz, 100 W cm<sup>-2</sup> at 363 K for 3 h.). The structure and particle sizes of the product were dependent upon the reaction temperature, the acidity of the medium, and the reaction time. The TEM images showed that the particles of  $\text{TiO}_2$  were columnar in shape and the average sizes were ca. 3 nm × 7 nm. The sonochemical formation mechanism of nanocrystalline  $\text{TiO}_2$  is as follows: The hydrolytic species of titanium tetrabutyl in water condensed to form a large number of tiny nuclei, which aggregated to form larger clusters. Ultrasound irradiation generated many local hot spots within the gel, and the crystal structural unit was formed near the hot spots with decrease in the gel nuclei, which led to the formation of nanocrystal particles.

A process has been developed for the formation of titania whiskers and nanotubes with the assistance of sonication [129]. Titanate whiskers are obtained as a slender sheet with length about 1  $\mu\text{m}$  and width 60 nm; arrays of titania whiskers with diameter 5 nm are prepared from the titanate whiskers; titania nanotubes (see Figure 6.7) with diameter about 5 nm, and length 200–300 nm are also synthesized.

The application of ultrasound dramatically increases the rate of exfoliation of  $\text{H}_x\text{Ti}_{2-x/4}\text{O}_4 \cdot y\text{H}_2\text{O}$  in the presence of aqueous tetrabutylammonium (TBA) hydroxide [130]. The effect of ultra sonication power and processing time on particle size distributions are evaluated. Applied powers of 60–300 W and reaction times of 2–30 min effectively reduce the H–Ti particle size to <100 nm. Both particle size distribution analysis and UV–Vis spectroscopy were used to study the effect of the

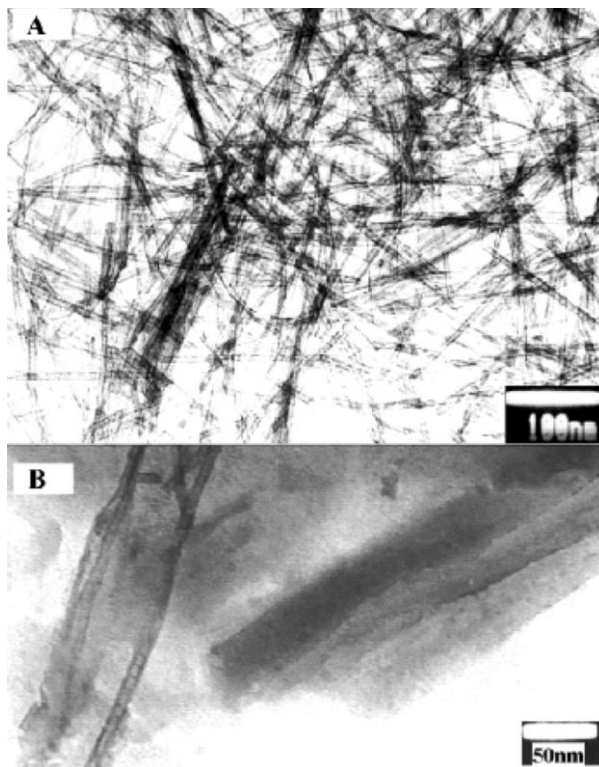


**Fig. 6.7.** TEM images of (a) titania nanotubes, (b) powders obtained by heat-treating sonicated products for 4 h at 110 °C followed by washing with water.

ratio of the TBA ion to exchangeable protons in H-Ti; a minimum ratio of TBA/H greater than or equal to 0.5 is required for rapid exfoliation.

Shafi et al. found that sonochemistry is a fast and efficient technique for coating octadecyltrihydrosilane ( $\text{CH}_3(\text{CH}_2)_{17}\text{SiH}_3$ ) onto titania surfaces [131]. Infrared spectroscopy and thermal analysis confirm that complete coating is achieved after 30 min. Solid-state C-13 NMR spectroscopy establishes the bonding of trihydrosilane to the titania particles. Raman microscopy gives the expected rutile structure and further confirms the presence of an octadecyl monolayer. X-ray diffraction confirms that the rutile structure of the titania particles does not change during sonication. Anatase titania undergoes the same reaction when sonicated in the presence of octadecyltrihydrosilane.

#### 6.1.2.10 The Sonochemical Preparation of Other Oxides

Brij-35 [polyoxyethylene (23) lauryl ether] stabilized palladium nanoparticles, obtained on attempted sonochemical reduction of  $\text{PdCl}_2$ , by sodium sulfite in water

under argon, instantaneously oxidized to PdO [132]. The particles obtained were stable and have a narrow size distribution with an average diameter of 10 nm. PdO nanoparticles were reduced to Pd nanoparticles in an autoclave by treatment with 50 bar hydrogen at 140 °C. The catalytic behavior of the Pd nanoparticles thus obtained is unusual in comparison with conventional Pd catalysts.

Two reports have been published on the sonochemical preparation of nano-sized ceria, CeO<sub>2</sub> [133, 134]. Zhu and coworkers [133] synthesized nanocrystalline ceria (CeO<sub>2</sub>) particles via sonochemical and microwave assisted heating routes from aqueous solutions containing (NH<sub>4</sub>)<sub>2</sub>Ce(NO<sub>3</sub>)<sub>6</sub>, hexamethylenetetramine and poly (ethylene glycol) (PEG *M<sub>w</sub>* = 19,000). Analysis of the results showed that the products had a uniform shape, narrow size distribution, and displayed conspicuous quantum size effects.

In the second synthesis, cerium oxide (CeO<sub>2</sub>) nanoparticles were prepared sonochemically by using cerium nitrate and azodicarbonamide as starting materials, and ethylenediamine or tetraalkylammonium hydroxide as additives [134]. The additives have a strong effect on the particle size and particle size distribution. CeO<sub>2</sub> nanoparticles with small particle size and narrow particle size distribution are obtained by the addition of additives; while highly agglomerated CeO<sub>2</sub> nanoparticles are obtained in the absence of additives. Monodispersed CeO<sub>2</sub> nanoparticles with a mean particle size of ca. 3.3 nm are obtained when tetramethylammonium hydroxide (TMAOH) is used as the additive and the molar ratio of cerium nitrate/azodicarbonamide/TMAOH is 1/1/1. Blue shifts of the absorption peak and the absorption edges of the products are observed in the UV-Vis absorption spectra as a result of the quantum size effect.

A composite material made of zinc oxide and polyvinyl alcohol was prepared by a sonochemical method [135]. Annealing of the composite under air removed the polymer, leaving porous spheres of ZnO. This change was accompanied by a change in the surface area from 2 to 34 m<sup>2</sup> g<sup>-1</sup>. The porous ZnO particles were used as the electrode material for dye-sensitized solar cells (DSSCs). They were tested by forming a film of the doped porous ZnO on a conductive glass support. The performance of the solar cell is reported.

A very unusual and previously unknown oxide of copper, the paramelaconite, Cu<sub>4</sub>O<sub>3</sub>, was synthesized sonochemically in a polyaniline matrix [136]. An aqueous solution of copper (II) acetate and aniline (1:10 molar ratio) is irradiated by ultrasound to produce nanophased Cu<sub>4</sub>O<sub>3</sub> embedded in a polyaniline matrix. The as-prepared Cu<sub>4</sub>O<sub>3</sub>-polyaniline is characterized by X-ray diffraction (XRD), and other methods. The mechanism for the fabrication of Cu<sub>4</sub>O<sub>3</sub>-polyaniline is proposed and discussed. This method is general and works also for the production of nanocrystalline Fe<sub>3</sub>O<sub>4</sub> and Cu<sub>2</sub>O embedded in polyaniline. This technique is also an easy route for the production of other metal oxides embedded in polyaniline.

Amorphous tungsten oxide has been prepared by ultrasound irradiation of a solution of tungsten hexacarbonyl W(CO)<sub>6</sub> in diphenylmethane (DPhM) in the presence of an Ar (80%) and O<sub>2</sub> (20%) gaseous mixture at 90 °C [137]. Heating this amorphous powder at 550 °C under Ar yields snowflake-like dendritic particles consisting of a mixture of monoclinic and orthorhombic WO<sub>2</sub> crystals. Annealing

of the as-prepared product in Ar at 1000 °C leads to the formation of a  $\text{WO}_2$ – $\text{WO}_3$  mixture containing nanorods (around 50 nm in diameter) and packs of these nanorods. Heating the product in air for 3 h leads to triclinic  $\text{WO}_3$  crystal formation, with a basic size of 50–70 nm.

Finally, Vijaykumar et al. reported on a general sonochemical reaction in which metal acetates can be converted to the corresponding metal oxides [138]. The acetates examined in this research were, Zn, Cu, Co, and Fe(II), yielding nanocrystalline  $\text{CuO}$ ,  $\text{ZnO}$ ,  $\text{Co}_3\text{O}_4$ , and  $\text{Fe}_3\text{O}_4$ . The solvents were water and a 10% water–DMF mixture. The diameters of the particles were: 20 nm (length ( $L$ )) and 2 nm (width ( $W$ )), (6), 340 nm (250), 30 nm (20), and 20 nm (8), respectively, when water (water–DMF) is used as the solvent. The results of DRS are analyzed in detail, and the band gap energies for  $\text{CuO}$ ,  $\text{ZnO}$ , and  $\text{Co}_3\text{O}_4$  are seen to be 2.18, 3.35, and 2.26 (3.40) eV, respectively.

#### 6.1.2.11 Sonochemical Synthesis of Other Nanomaterials

Metals, metal oxides, and chalcogenides constitute the main body of the sonochemical research. Only very few other groups of materials have been prepared by using power ultrasound. There may be two reasons for this: first, the difficulty in preparing these materials and, secondly, lack of interest. However, we believe that the first reason can explain why an important material such as GaN, for example, has not been prepared sonochemically.

In this section we will survey briefly other important groups of materials that have been reported as prepared using ultrasonic waves. Only one paper was found describing the preparation of nitrides [139]. This reports on a method for the preparation of nanoparticles of iron nitride powders. Iron nitride particles have been synthesized by two methods. In the first,  $\text{Fe}(\text{CO})_5$  was sonicated in a decane solution under a gaseous mixture of  $\text{NH}_3$  and  $\text{H}_2$  (3.5:1 molar ratio) at ca. 0 °C. The second method was based on nitriding the sonochemically prepared amorphous iron at ca. 400 °C for 4 h under a mixed stream of  $\text{NH}_3$  and  $\text{H}_2$  (3.5:1 molar ratio). Different products were obtained in the two cases. The product of the sonication of  $\text{Fe}(\text{CO})_5$  was amorphous  $\text{Fe}_{2-3}\text{N}$  and a small quantity of iron oxide. The X-ray diffraction patterns in the second case showed  $\text{Fe}_4\text{N}$  as the main product. The magnetic properties of both products were measured. The coercive force  $H_c$  of the  $\text{Fe}_4\text{N}$  is 190 Oe, and the saturation magnetization  $\sigma(s)$ , is 170 emu  $\text{g}^{-1}$ .

More publications were found related to carbides. First, Suslick's early report [64] that certain carbonyls sonicated in a decalin solvent under argon. For Fe and Co, nanostructured metals are formed; for Mo and W, metal carbides (e.g.,  $\text{Mo}_2\text{C}$ ) are produced. Molybdenum carbide was used later as a catalyst. The selectivity and catalytic activity of the Mo and W carbides was examined in the dehydrogenation of alkanes [140]. Another carbide that has already been mentioned is that of Pd [65], which was prepared by Maeda's group. Iron carbide was a byproduct that served as protective layer in Nikitenko's work on air-stable iron nanoparticles [70].

Ultrasonic irradiation (22 kHz, Ar atmosphere) of Th(IV)  $\beta$ -diketonates  $\text{Th}(\text{HFAA})_4$  and  $\text{Th}(\text{DBM})_4$ , where HFAA and DBM are hexafluoroacetylacetone and dibenzoylmethane respectively, causes them to decompose in hexadecane

solutions, forming solid thorium compounds [141]. The first-order rate constants for Th(IV) beta-diketonate degradation were found to be  $(9.30-8) \times 10^{-3}$  for Th(HFAA)<sub>4</sub> and  $(3.80-4) \times 10^{-3} \text{ min}^{-1}$  for Th(DBM)<sub>4</sub>, ( $T = 92^\circ\text{C}$ ,  $I = 3 \text{ W cm}^{-2}$ ). The rate of the sonochemical reaction increased with increasing  $\beta$ -diketonate volatility and decreased with increasing hydrocarbon solvent vapor pressure. Solid sonication products consisted of a mixture of thorium carbide ThC<sub>2</sub> and Th(IV)  $\beta$ -diketonate partial degradation products. The average ThC<sub>2</sub> particle size was estimated to be about 2 nm. ThC<sub>2</sub> formation was attributed to the high-temperature reaction occurring within the cavitating bubble. The thorium  $\beta$ -diketonate partial degradation products were formed in the liquid reaction zones surrounding the cavitating bubbles.

It is more difficult to prepare III–V semiconductors than the II–VI. Two sonochemical investigations reported on the preparation of these materials. The first paper details a safe method for the preparation of transition metal arsenides, FeAs, NiAs, and CoAs [142]. At room temperature, well-crystallized and monodispersed arsenide particles were successfully obtained under high-intensity ultrasonic irradiation for 4 h from the reaction of transition metal chlorides (FeCl<sub>3</sub>, NiCl<sub>2</sub>, and CoCl<sub>2</sub>), arsenic (which is the least toxic arsenic feedstock) and zinc in ethanol. Different characterization techniques show that the product powders consist of nanosize particles. The ultrasonic irradiation and the solvent are both important in the formation of the product.

Another III–V semiconductor was prepared by Li and coworkers [143]. A room temperature sonochemical method for the preparation of GaSb nanoparticles using less hazardous Ga and antimony chloride (SbCl<sub>3</sub>) as the precursors has been described. TEM and SAED results show that the as-prepared solid consists of nanosized GaSb crystals with sizes in the 20–30 nm range. The photoacoustic spectrum result reveals that the GaSb nanoparticles have a direct band gap of about 1.21 eV. On the basis of the control experiments and the extreme conditions produced by ultrasound, an ultrasound-assisted in situ reduction/combination mechanism has been proposed to explain the reaction.

We will conclude this survey of the synthesis of nanomaterials by sonochemical methods by mentioning that the most important material of the last decade, carbon nanotubes, were also synthesized by ultrasound radiation [144]. The carbon nanotube is produced by applying ultrasound to liquid chlorobenzene with ZnCl<sub>2</sub> particles and to *o*-dichlorobenzene with ZnCl<sub>2</sub> and Zn particles. It is considered that the polymer and the disordered carbon, which are formed by cavitation collapse in homogeneous liquid, are annealed by the inter-particle collision induced by the turbulent flow and shockwaves.

## 6.2

### Sonoelectrochemistry

The effect of ultrasound in electrochemistry, i.e. that the application of ultrasonic energy can increase the rate of electrolytic water cleavage, was discovered as early

as 1934. As for the case of sonochemistry, the use of ultrasound in electrochemistry went through a period of neglect until the early 1980s when there was again an upsurge of interest in the field. At present, ultrasound is used in a wide range of electrochemical processes such as: metal plating, deposition of polymers, electro-generation of gases and solids, and electrochemical waste processing.

Ultrasound and electrochemistry provide a powerful combination for several reasons. Ultrasound is well known for its capacity to promote heterogeneous reactions, mainly through increased mass-transport, interfacial cleaning, and thermal effects. Effects of ultrasound in electrochemistry may be divided into several important branches: (1) Ultrasound greatly enhances mass transport, thereby altering the rate, and sometimes the mechanism, of the electrochemical reactions. (2) Ultrasound is known to affect surface morphology through cavitation jets at the electrode–electrolyte interface; it usually acts to increase the surface area. (3) Ultrasound reduces diffusion layer thickness and therefore ion depletion. A comprehensive review of the field has recently been given by Compton et al. [145].

However, it is only recently that the potential benefits of combining sonochemistry with electrochemistry have increasingly been studied. It should be noted that electrochemical methods, mainly electrodeposition, are well established for the preparation of metals and semiconductor nanomaterials (for a review see Mastai et al. [146]).

### 6.2.1

#### Sonoelectrochemical Synthesis of Nanocrystalline Materials

Reisse and co-workers [147–149] were the first to describe a novel device for the production of metal powders using pulsed sonoelectrochemical reduction. This device exposes only the flat circular area at the end of the sonic tip to the electrodeposition solution. The exposed area acts as both cathode and ultrasound emitter, named by Reisse et al. as “sonoelectrode”. A pulse of electric current produces a high density of fine metal nuclei. This is immediately followed by a burst of ultrasonic energy that removes the metal particles from the cathode, cleans the surface of the cathode, and replenishes the double layer with metal cations by stirring the solution. In [145], a list is given of chemically pure fine crystalline powders, mostly metals or metallic alloys, prepared by this method, with particle sizes varying between 10 and 1000 nm depending on deposition conditions.

Powder CdSe nanoparticles prepared by a pulsed sonoelectrochemical technique with a sonoelectrochemical device similar to that described by Reisse, namely the “sonoelectrode”, were reported first by Mastai et al. [150]. In Figure 6.8 we present the experimental set-up for pulsed sonoelectrochemical deposition of CdSe nanoparticles, namely the “sonoelectrode”, and schematics of the sonic and electrochemical waveforms.

In the “sonoelectrode” design, a titanium horn acts both as the cathode and the ultrasound emitter. The electroactive part of the sonoelectrode is the planar circular surface at the bottom of the horn. This sonoelectrode produces a sonic pulse that is triggered immediately following a current pulse. One pulse driver is used to con-

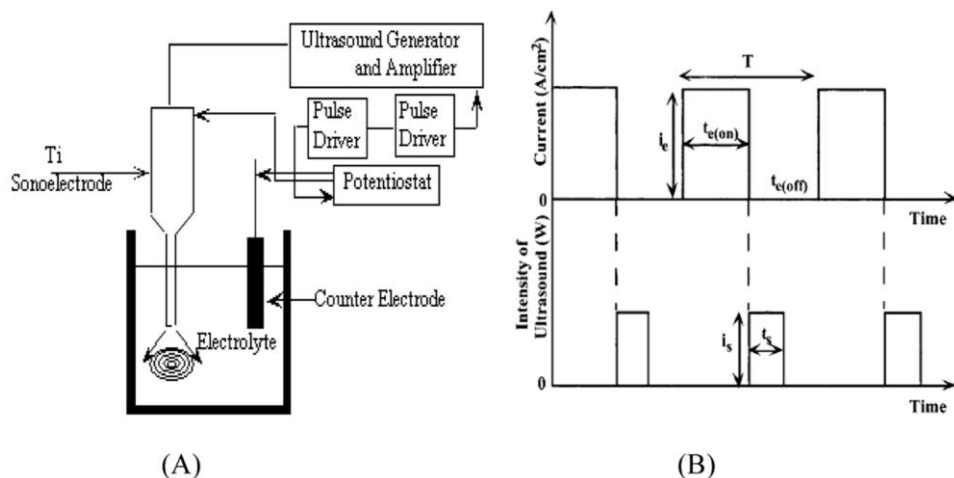


**Fig. 6.8.** Schematic of sonoelectrochemical deposition set-up and the sonic and electrochemical waveforms.

trol a potentiostat and a second controls the ultrasonic processor, which is adapted to work in the pulse mode.

The sonoelectrochemical deposition of CdSe nanoparticles is carried out from an aqueous solution of  $CdSO_4$ , complexed with potassium nitrilotriacetate ( $N(CH_2CO_2K)_3$ ) NTA as a source for Cd, and a selenosulfate solution, ( $Na_2SeSO_3$ ), as source for Se. The CdSe crystal size could be varied from X-ray amorphous up to 9 nm by controlling the various electrodeposition and sonic parameters. The effects of various electrodeposition and sonic parameters on the properties of CdSe nanoparticles are presented in Table 6.3.

**Tab. 6.3.** Effect of various deposition parameters on the CdSe nanoparticles properties in pulsed sonoelectrochemical synthesis.

Variable Parameter	Crystal Size (nm)	Bandgap $E_g$ (eV)
Temperature ( $^{\circ}C$ )		
5	4.5	2.10
25	5.5	2.10
75	6.5	1.93
Ultrasound Intensity (W)		
0	9	1.90
10	10	1.85
60	4	2.15
Continuous ultrasound	Amorphous	–
Current Pulse Width (sec)		
0.68	7	1.95
0.34	5	2.05
0.11	4	2.15

The fundamental basis of the sonoelectrochemical technique to form nanoparticles is massive nucleation using a high current density electrodeposition pulse (ca. 150–300 mA cm<sup>-2</sup>), followed by removal of the deposit from the sonoelectrode by the sonic pulse. Removal of the particles from the electrode before the next current pulse prevents crystal growth. Overall there are many experimental variables involved in sonoelectrochemical deposition: electrolyte composition and temperature, electrodeposition conditions including current density ( $I_e$ ), pulse-on time ( $t_{e(on)}$ ) and ratio between pulse-on time and pulse-off time ( $t_{e(off)}$ ) (the duty cycle); sonic probe conditions: sonic power ( $I_s$ ), sonic pulse parameters,  $t_{s(on)}$  and  $t_{s(off)}$ . The effects of the various sonoelectrochemical parameters on crystal size can be rationalized, in general, as follows:

- *Sonic intensity.* The greater the sonic intensity, the greater will be the efficiency of removal of the deposit and therefore the less chance there will be for crystal growth of existing nuclei. Typically above a certain intensity where all the deposit is removed, further increase in intensity is not expected to affect crystal growth much (in the case of CdSe this maximum sonic intensity is ca. 60 W cm<sup>-2</sup>). Generally long sonic duration ( $t_{s(on)}$ ) resulted in smaller crystal sizes, however, it should be noted that sonoelectrodeposition under continuous ultrasound wave leads to the formation of amorphous materials.
- *Deposition current pulse width.* Quite separately from the sonic wave effects, pulse electrodeposition is well known to result in a smaller crystal-sized deposit. This is particularly pronounced for high current densities, where a high rate of nucleation occurs during each pulse. The shorter the pulse duration ( $t_{e(on)}$ ), the less chance there is of crystal growth occurring by deposition of new material on a previous nucleus. In normal pulse plating, crystal size may or may not increase with the number of pulses, depending on whether each new pulse forms a new nucleus or adds to pre-existing ones. In sonoelectrochemical deposition, where the deposit is removed during each sonic pulse, only new nuclei should be formed, and therefore the crystal size will be smaller with decreasing pulse duration ( $t_{e(on)}$ ).
- *Temperature.* Temperature can affect crystal growth in several ways, all of them resulting in smaller crystal size at lower temperatures. The simplest is that crystal growth is slower at lower temperatures. Within the time between sonic pulses, growth can occur, either by coalescence during the deposition pulse or by migration on the substrate and coalescence at any time. Another effect of temperature is through the thermodynamic instability of very small nuclei below a certain critical size. These nuclei should re-dissolve, but may be stable for long enough to grow larger than the critical size, after which they are thermodynamically stable.

In a series of papers Gedanken and co-workers described the use of a pulse sonoelectrochemical technique for the preparation of nanocrystalline materials. In the first paper [151] in the series, the synthesis of silver nanoparticles of different shapes: spheres, rods, and dendrites, is described. The nanocrystalline Ag de-



posited from an aqueous solution of  $\text{AgNO}_3$  using NTA as a complex agent. The shape of the Ag nanoparticles could be modified as a function of the concentration of  $\text{AgNO}_3$  and NTA in the deposition solutions. In the second paper [152], X-ray amorphous silver nanoparticles were prepared by a pulse sonoelectrochemical method from an aqueous solution of  $\text{AgBr}$  in the presence of gelatin. Finally, it was shown that  $\text{PbSe}$  [153] nanoparticles, ca. 12 nm, could be prepared by a pulse sonoelectrochemical technique from an aqueous solution of sodium selenosulfate and lead acetate. Most recently, Zhu et al. [154] utilized a sonoelectrochemical route for the preparation of uniform silver nanowires of a single crystalline nature. Finally, in a very recent publication, silver nanoparticles were used as a model case to study the processes involved in sonoelectrochemical synthesis of nanoparticles [155]. The authors propose that sonoelectrochemical synthesis is highly affected by the formation of a suspensive electrode. This new model, the suspensive electrode, is based on the concept that the nanoparticles suspended in solution gain the sonoelectrode potential and thus act as part of the electrode. That is to say, during sonoelectrochemical synthesis, a suspension of charged nanosized particles is formed in solution and acts as part of the sonoelectrode.

Hodes et al. [156] demonstrated that the sonoelectrochemical technique could be used to synthesize closed fullerene-like structures of  $\text{MoS}_2$  at room temperature by electrodeposition from a thiomolybdate solution. It should be noted that either electrodeposition or ultrasonic irradiation alone results in X-ray amorphous  $\text{MoS}_2$  products, but the combination of both gives well-crystallized, closed structures of  $\text{MoS}_2$  and  $\text{MoS}_2$  nanotubes. A mechanistic study to explain the formation of the closed curved  $\text{MoS}_2$  structures shows that in the first step amorphous  $\text{MoS}_2$  is formed by electrodeposition onto the sonic probe cathode. At this point the deposit could be spheroidal or planar. Crystallization of the amorphous  $\text{MoS}_2$ , which normally requires high temperatures occurs in the collapse of the cavitation bubbles. The formation of  $\text{MoS}_2$  nanotubes occurs if the bubble collapse occurs at the electrodeposit that is still on the electrode surface. In this case, the effect of the bubble collapse is asymmetric, leading to an asymmetric-shaped product, namely the nanotube.

In conclusion, the combination of electrochemical and sonic processes provides many experimental variables which should allow control of particle size and shape, and will probably be applicable to the formation of closed structures of other layered compounds that can be prepared by electrochemical (and quite likely also chemical) techniques.

### 6.3

#### Microwave Heating

Microwave heating (MWH) is the second method for the fabrication of nanomaterials that will be discussed in this chapter. Microwaves are electromagnetic radiation, whose wavelengths lie in the range 1 mm to 1 m (frequency range 0.3 to 300 GHz). A large part of the microwave spectrum is used for communication

purposes and only narrow frequency windows centered at 900 MHz and 2.45 GHz are allowed for microwave heating purposes. Heating by microwave has been known since the early 1940s and has been used successfully in the food industry. Microwave irradiation as a heating method has found a number of applications in chemistry since 1986, especially in the work of Mingos [157]. Microwaves have been in use for accelerating organic reactions for a quite a while [158, 159]. Microwave synthesis is generally quite fast, simple, and very energy efficient. The exact nature of microwave interaction with reactants during the synthesis of materials is somewhat unclear and speculative [160]. However, transfer of energy from microwaves to the material is believed to occur either through resonance or relaxation, which results in rapid heating. This knowledge is widely used in the discussion of reaction mechanisms. Many successful examples of the applications of MW heating in organic chemistry have been reported [161, 162], although its expansion into the area of inorganic chemistry has been much slower. Only recently has it been noticed that metallic powders can be heated to considerably high temperatures in a microwave oven without arcing [161, 163]. Some metal chalcogenides have been prepared by microwave solid-state reaction [164]. These solid-state reactions do not produce nanoparticles. On the other hand, MW reactions in solutions do yield nanoparticles. The use of MWH in the preparation of solid state inorganic materials has been reviewed recently by the two main contributors to this field, Professor Mingos [159] and Professor K. J. Rao [160]. The preparation of nanoparticles by MWH started only recently. The aim of this section is to review the solution work that has been conducted using a regular domestic microwave oven. We will, therefore, not discuss the many reactions leading to the fabrication of nanomaterials conducted with a microwave plasma. An example of a domestic microwave oven that has been modified for the synthesis of nanomaterials is presented in Figure 6.9.

However, we should mention the pioneering work of Chou and Phillips, where metallic iron and iron oxide particles were produced by injecting ferrocene into the afterglow region of a low-pressure, low-power, plasma, generated using a microwave power source [160]. This gas phase reaction was carried out as part of an attempt to explore the feasibility of using flow-type microwave plasmas for the production of metal nanoparticles.

A short introduction to as to how the irradiated molecule is affected by microwaves is first presented. It is based on the reviews of Rao and Mingos [159, 160].

In general, materials fall into three categories, with respect to their interaction with microwaves [160]: (1) microwave reflectors, typified by bulk metals and alloys, such as brass, which are therefore used in making micro-waveguides; (2) microwave transmitters which are transparent to microwaves, typified by fused quartz, zircon, several types of glass, and ceramics (not containing any transition element), teflon etc.; they are therefore employed for cookware and containers for carrying out chemical reactions in microwaves; and (3) microwave absorbers, which constitute the most important class of materials for microwave synthesis; they take up the energy from the microwave field and heat up very rapidly.

A dielectric material is one that contains either permanent or induced dipoles



Fig. 6.9. A microwave oven with a reflux system.

which, when placed between two electrodes, act as a capacitor [160]. The polarization of dielectrics arises from the finite displacement of charges or rotation of dipoles in an electric field. At the molecular level, polarization involves either the distortion of the distribution of the electron cloud within a molecule, or the physical rotation of molecular dipoles. The latter are particularly significant in the context of microwave dielectric heating. The permittivity of a material,  $\epsilon$ , is a property which describes the charge storing ability of that substance, irrespective of the sample's dimensions. The dielectric constant or relative permittivity is the permittivity of the material relative to that of free space. It is represented in [159] as  $\epsilon_s$ . Compounds, which have large permanent dipole moments, also have large dielectric constants, because the dielectric polarization depends primarily on the ability of their dipoles to reorient in an applied electric field. In the gas and liquid phases the molecules rotate so rapidly that they are normally able to respond to field reverses occurring at  $10^6$  times a second or higher. The permittivity of the material, is frequency-dependent, and, for a polar liquid, generally shows a marked decrease as the frequency of the electromagnetic radiation increases from  $10^6$  (radio frequencies) to  $10^{12}$  Hz (infrared frequencies). For polar molecules with molecular weights less than a few hundred, this relaxation process occurs in the microwave

region, i.e., in the frequency range 300 MHz to 300 GHz. If the frequency of the electromagnetic radiation is in the microwave region ( $\sim 10^9$  Hz) the rotations of the polar molecules in the liquid begin to lag behind the electric field oscillations. The resulting phase displacement  $\delta$ , acquires a component  $I \sin \delta$  in phase with the electric field, and thus resistive heating occurs in the medium. This is described as dielectric loss and causes energy to be absorbed from the electric field. Since the dipoles are unable to follow the higher frequency electric field oscillations, the permittivity falls at the higher frequency and the substance behaves increasingly like a non-polar material.

$$\tan \delta = \epsilon'' / \epsilon' \quad (8)$$

where  $\epsilon'$  is the real part of the dielectric constant and  $\epsilon''$  is the loss factor which reflects the conductance of the material. In his review, Mingos [159] introduces the Debye expression for the complex permittivity and shows how  $\epsilon''$  and  $\epsilon'$  depend on the relaxation time, which is itself dependent on the molecular size and the viscosity of the liquid. Mingos emphasizes that the interaction between the microwave radiation and the polar solvent, which occurs when the frequency of the radiation approximately matches the frequency of the rotational relaxation processes, is not a quantum mechanical resonance phenomenon. Transition between rotational energy levels is not involved and the energy transfer is not a property of a specific molecule, but the result of a collective phenomenon involving the bulk. In the Debye interpretation, the heat is generated by friction forces occurring between the polar molecules whose rotational velocity has been increased by the coupling with the microwave radiation and neighboring molecules. The dielectric heating is a broadband phenomenon and rapid energy transfer occurs even when the frequency of the microwaves and the relaxation frequency are not perfectly matched.

It is worth noting that much of the work for which domestic microwave ovens were used for fabricating nanomaterials concentrated on using ethylene glycol as the solvent. Table 6 in Mingos's review [159] shows that ethylene glycol indeed has a high loss tangent at 2.45 GHz, and when this is coupled with its high boiling temperature (193 °C), this makes it an excellent candidate for dielectric heating and, hence, there is little penetration of microwaves. In large metal samples, as well as in metal films, large electric field gradients occur in the microwave cavity, giving rise to electric discharges. On the other hand, in metal powders no such discharge takes place and, due to eddy currents and localized plasma effects, very rapid heating takes place which may be as high as 100 K s<sup>-1</sup>. Eddy current phenomena arise from the alternating magnetic field associated with microwaves.

### 6.3.1

#### Microwave Synthesis of Nanomaterials

##### 6.3.1.1 Microwave Synthesis of Nanometallic Particles

The first report of a microwave-assisted reaction leading to the formation of nanometallic particles was by Jiang and coworkers [167]. They prepared Au nanopar-

ticles by a microwave high-pressure procedure with alcohol as the reducing agent. The color of colloidal Au nanoparticles is blue-violet. The maximum absorption spectrum of colloidal Au is at 580 nm, and the resonance scattering peak is at 580 nm. Using this method, the colloidal Au solution was very stable and the preparation is described as simple and quick.

Poly(vinylpyrrolidone) (PVP) is a polymer capable of complexing and stabilizing Ag and Au nanoparticles formed through the reduction of  $\text{Ag}^+$  or  $\text{AuCl}_4^-$  ions with *N,N*-dimethylformamide [168]. The reduction is efficiently performed both at reflux and under microwave irradiation, but each of these methods leads to different nanoparticle morphology and colloid stability. The use of microwave irradiation provides an extra degree of control of the reduction process. The use of PVP with different polymer chain lengths leads to particles with similar sizes, though with a different degree of stability. The colloids are also stable in ethanol for months, but only marginally stable in water. Alloys were also prepared by MWH thermal treatment of  $(\eta\text{-C}_2\text{H}_4)(\text{Cl})\text{Pt}(\mu\text{-Cl})_2\text{Ru}(\text{Cl})(\eta^3\text{-}2,7\text{-dimethyloctadienediyl})/\text{Vulcan}$  carbon composites under appropriate oxidizing and reducing conditions. Using microwave dielectric loss heating affords PtRu/Vulcan carbon nanocomposites [169]. This composite consisted of PtRu alloy nanoparticles highly dispersed on a powdered carbon support. Two such nanocomposites containing 16 or 50 wt% total metal and alloy nanoclusters of 3.4 or 5.4 nm average diameter are formed within only 100 or 300 s of total microwave heating.

The polyol reaction was developed by Fivet's group. It was the most popular method for the fabrication of metallic nanoparticles using MWH. In the 1980s, Fievet et al. [170] used ethylene glycol as a solvent and reducing agent for the preparation of submicrometer particles of the transition metals. The mechanism of this reaction is still only poorly understood. It is, however, known that the reduction is based on the decomposition of the ethylene glycol and its conversion to diacetyl. Recently, Tarascon and co-workers [171] demonstrated that in these reactions the temperature is a dominant factor in affecting the reactivity. It is worth mentioning that the preparation of nanophased chalcogenides was also based on the polyol reaction [3].

The noble metals were the favorite metals for demonstrating the usefulness of the microwave operation in conducting the polyol reaction. Among the noble metals platinum was synthesized most frequently. Polymer-stabilized platinum colloids with nearly uniform spherical shape were prepared by Yu and coworkers by microwave dielectric heating [172]. The average diameters of the as-prepared platinum colloids were 2–4 nm with a narrow size distribution in regard to the preparation conditions.

The same group, using the polyol method, have prepared uniform and stable polymer-stabilized colloidal clusters of Pt, Ir, Rh, Pd, Au and Ru by microwave irradiation with a modified domestic microwave oven [173]. The as-synthesized colloidal clusters have small average diameters and narrow size distribution. The microwave method is characterized by rapid and homogeneous heating compared with conventional heating methods, although its thermal effects are similar to those of other heating methods.

Finally, using the polyol reaction and the same reactants as in [172] in a third

paper by this group, they synthesize polymer-stabilized Pt colloids with small particle sizes and narrow size distributions by a continuous microwave synthesis [174]. This synthesis method has good reproducibility for synthesizing uniform metal colloids in bulk amounts.

Komarneni and coworkers [175] conducted a polyol reaction for the preparation of Pt and Ag nanoparticles. The synthesis of the metal nanoparticles [175] was conducted in a double-walled digestion vessel which has an inner liner and a cover made of Teflon PFA and an outer high-strength shell of Ultem polyetherimide. The starting precursors (chloroplatinic acid or silver nitrate) were mixed with ethylene glycol and poly(*N*-vinyl-2-pyrrolidone) of different molecular weights, with and without NaOH, and reacted at 150 °C for 15 min in a microwave system. Large Pt particles 100–400 and 50–150 nm were obtained with PVP molecular weights of 8,000 and 10,000, respectively. Non-uniform Pt particles of <10 nm were crystallized from PVP of 40,000 molecular weight. For the Ag particles strings were obtained. The growth of the Ag metal particles in the form of strings decreased as the molecular weight of the PVP increased. With a PVP molecular weight of 1,300,000 and without NaOH Ag particles of 100 nm were obtained.

In another attempt [176], silver nanoparticles, yellow in color, were prepared by a microwave high-pressure synthetic method, using polyacrylamide as the reducing agent and stabilizer. The maximum absorption peak of colloidal silver is at 421.6 nm, and its strongest resonance scattering peak is at 470 nm. The experimental results showed that the silver nanoparticles are well dispersed and the colloidal solution has good stability. The average diameter of silver nanoparticles is 66 nm. The procedure was rapid and convenient.

Spherical and uniform Pt nanoparticles, 3.5–4.0 nm supported on carbon, were prepared by microwave irradiation [177]. The products exhibited very high electrocatalytic activity in the room-temperature oxidation of liquid methanol. The preparation method was similar to that of Komarneni [175], namely, a polyol reduction. A 100 mL beaker, containing chloroplatinic acid dissolved in an ethylene glycol, KOH solution was added dropwise. Carbon XC-72 was uniformly dispersed in the mixed solution by ultrasound. The beaker was placed in the center of a microwave oven (National NN-S327WF, 2450 MHz, 700 W) and heated for 60 s.

Towards the end of 2002, a paper [178] appeared, claiming to have prepared polychrome silver nanoparticles by a soft solution approach under microwave irradiation from a solution of silver nitrate, AgNO<sub>3</sub>, in the presence of poly (*N*-vinyl-2-pyrrolidone) PVP, without *any other reducing agent*. Different morphologies of silver colloids with lovely colors could be obtained using different solvents as the reaction medium. The influence of the solvent on the morphology of silver was investigated. In a typical procedure, the reaction solutions were prepared by dissolving PVP and AgNO<sub>3</sub> ethanol in a Pyrex flask to obtain a homogeneous reaction mixture, which was placed on the turntable of the microwave oven. The mixture was irradiated discontinuously at a power of 300 W.

#### 6.3.1.2 The Synthesis of Nanoparticles of Metal Oxides by MWH

Similar to sonochemical research, much attention has been devoted to the preparation of nanosized metallic oxides by MWH. When surveying the literature, we

realized that iron oxide was the most popular material to be synthesized by this method.

The first report was by Komarneni and coworkers [179] using a microwave-hydrothermal process to catalyze the synthesis of crystalline oxides such as  $\text{TiO}_2$ ,  $\text{ZrO}_2$  and  $\text{Fe}_2\text{O}_3$ , and binary oxides such as  $\text{KNbO}_3$  and  $\text{BaTiO}_3$ . The importance of this work was that this technique led to fine powders of these materials. The effect of different parameters, such as concentration of chemical species, time and temperature, on the crystallization kinetics of the above phases has been investigated under microwave-hydrothermal conditions using microwaves of 2.45 GHz frequency.

The second work was by Dong et al. [180] who report on the preparation of submicron uniform  $\alpha\text{-Fe}_2\text{O}_3$  by microwave-induced hydrolysis of ferric salts with concurrent dissociation of urea. Although it was not conducted in a domestic MW oven, it is still on our list of references. A mixed solution of  $\text{FeCl}_3$  and  $\text{CO}(\text{NH}_2)_2$  was placed in an Erlenmeyer flask equipped with a reflux condenser. This flask was inserted into a cylindrical resonant cavity. After microwave irradiation (2.4 GHz, 500 W) for a certain period of time, the flask was moved to a homothermal water bath (at  $94^\circ\text{C}$ ) to be aged. Uniform particles of approximately spherical shape with mean diameter 75 nm were obtained. An almost identical paper was published a little later by Li and Wei [181].  $\text{Fe}(\text{NO}_3)_3$  was the iron source instead of the chloride [180]. They conducted the reaction at different pH values. In this way they obtained a larger variety of shapes, including acicular cubic and spherical particles, all in the nanometer range.

Palchik [182] obtained nanosized amorphous iron oxide ( $\text{Fe}_2\text{O}_3$ ) by the pyrolysis of iron pentacarbonyl,  $\text{Fe}(\text{CO})_5$ , in a modified domestic microwave oven in refluxing chlorobenzene as solvent under air. The reaction time was 20 min. Separate particles of iron oxide, 2–3 nm in diameter, were obtained together with aggregated spheres with a diameter of 25–40 nm. Differential scanning calorimetry measurements showed an amorphous/crystalline phase transition at about  $250^\circ\text{C}$ .

A study of microwave effects on the formation of nanoparticles in the hydrolysis reaction of  $\text{FeCl}_3$  with  $\text{NaH}_2\text{PO}_4$  to get spindle-type colloidal hematite particles under microwave radiation, was reported by Han and coworkers [183]. They found that the reaction rate increased greatly, and the reaction conditions, for example, the acidity of the solution, concentration ratio of the components, and the microwave radiation time, had important effects on the nanoparticle formation and their morphology. They discussed the roles of microwaves and the concentration of  $\text{H}_2\text{PO}_4^-$  during the hydrolysis process.

Nanometer-sized quasicubic and spindle  $\alpha\text{-Fe}_2\text{O}_3$  particles were prepared by microwave heating from  $\text{Fe}^{+3}$  salt solutions [184]. The obtained  $\alpha\text{-Fe}_2\text{O}_3$  particles formed by MWH have smaller size and more uniform distribution than with conventional heating. Inorganic ions such as  $\text{H}^+$ ,  $\text{OH}^-$  and  $\text{NaF}$ , were found to affect the precipitating rate of spindle  $\alpha\text{-Fe}_2\text{O}_3$  and accelerate the hydrolysis of ferric ions.

Another research project leading to the formation of amorphous nanoparticles was undertaken by Zhu's group [185]. The product was synthesized by microwave irradiation heating of an aqueous solution containing ferric chloride, polyethylene

glycol-2000, and urea. Amorphous  $\text{Fe}_2\text{O}_3$  nanoparticles of about 3–5 nm in size were obtained.

Komarneni returned to the synthesis of  $\alpha\text{-Fe}_2\text{O}_3$  in 2001 [186]. This time he was interested in this product as a red pigment in porcelains. The methods of preparation were microwave-hydrothermal and conventional-hydrothermal reactions. The precursors were  $\text{FeCl}_3 \cdot 6\text{H}_2\text{O}$  and HCl solutions. The reaction were carried out at 100–160 °C. Acicular and yellow  $\beta\text{-FeOOH}$  (akaganite) particles 300 nm in length and 40 nm in thickness were predominantly formed at 100 °C after 2–3 h, while spherical  $\alpha\text{-Fe}_2\text{O}_3$  particles 100–180 nm in diameter were preferentially formed after 13 h using a conventional-hydrothermal reaction. However, a microwave-hydrothermal reaction at 100 °C led to monodispersed and red  $\alpha\text{-Fe}_2\text{O}_3$  particles 30–66 nm in diameter after 2 h without the formation of  $\beta\text{-FeOOH}$  particles. They investigated the effect of microwave radiation during hydrothermal treatment at 100–160 °C on the formation, yield, kinetics, morphology phase type, and color of  $\alpha\text{-Fe}_2\text{O}_3$ .

Several oxides, including  $\gamma\text{-Fe}_2\text{O}_3$ , and  $\text{Fe}_3\text{O}_4$ , have been prepared recently by the interaction of electromagnetic radiation with a physical mixture of metal nitrates and amides/hydrazides [187]. A judicious choice of such redox mixtures undergoes exothermic reactions when they are coupled with microwave radiation. The coupling of electromagnetic radiation with metal salts and amides/hydrazides depends on the dielectric properties of the individual components in the reaction mixture. This approach has been used to prepare  $\gamma\text{-Fe}_2\text{O}_3$ ,  $\text{Fe}_3\text{O}_4$ ,  $\text{MgCr}_2\text{O}_4$ ,  $\alpha\text{-CaCr}_2\text{O}_4$ , and  $\text{La}_{0.7}\text{Ba}_{0.3}\text{MnO}_3$ .

A microwave hydrothermal route was employed to synthesize various phases of iron oxide powders by using ferrous sulfate and sodium hydroxide as starting chemicals [188]. All the reactions were carried out under the identical microwave hydrothermal conditions of 190 °C, 154 psi, 30 min by varying the molar ratio (MR) of  $\text{FeSO}_4/\text{NaOH}$  (i.e., pH variation) from 0.133 to 4.00 in the solution. It was found that the variation of the molar ratio of  $\text{FeSO}_4/\text{NaOH}$  has a profound effect on the crystallization of various phases of iron oxides under identical processing conditions. The stoichiometric, submicron-sized (0.15–0.2  $\mu\text{m}$ ), spherical agglomerates of  $\text{Fe}_3\text{O}_4$  powders were obtained if the MR of  $\text{FeSO}_4/\text{NaOH}$  was 0.133 ( $\text{pH} \geq 10$ ) was maintained. On the other hand, non-stoichiometric  $\text{Fe}_3\text{O}_4$  powders were obtained for all higher MR of  $\text{FeSO}_4/\text{NaOH}$  between 0.133 and 4.00 ( $6.6 < \text{pH} < 10$ ). However, when the MR of  $\text{FeSO}_4/\text{NaOH}$  was 4.00 ( $\text{pH} \approx 6.6$ ), a varied distribution of shape and size (1–5  $\mu\text{m}$ ) of agglomerates of  $\alpha\text{-Fe}_2\text{O}_3$  powders was produced.

A paper reporting on the microwave-hydrothermal treatment of alcoholic solutions of ferrous chloride ( $\text{FeCl}_2$ ) and sodium ethoxide ( $\text{EtONa}$ ) solutions with a microwave autoclave designed by the authors (the RAMO system) has been published recently [189]. Depending on the initial concentrations, hematite ( $\alpha\text{-Fe}_2\text{O}_3$ ), spinel phase ( $\text{Fe}_{3-x}\text{O}_4$ ) or iron-magnetite ( $\text{Fe}(0)\text{-Fe}_3\text{O}_4$ ) nanocomposites are obtained with a lower grain size than conventional composites. Indeed, X-ray diffraction analysis reveals grain sizes close to 20 nm for magnetite and 60 nm for metallic iron. However, the amount of metal is smaller (close to 11%). Furthermore,



these particles are inert in the ambient atmosphere. Consequently, the RAMO (French acronym of Reactor Autoclave MicroOnde) system appears to provide an efficient source of energy for the rapid production of inert powders of iron, magnetite, and iron–magnetite composites.

Although most of the synthetic work related to iron oxide nanoparticles has concentrated, as we have demonstrated, on  $\text{Fe}_2\text{O}_3$ , and especially on the  $\alpha$ , hematite phase, a few papers also reported on the preparation of magnetite,  $\text{Fe}_3\text{O}_4$ . Submicron-sized (0.15–0.2  $\mu\text{m}$ ) spherical agglomerates of magnetite ( $\text{Fe}_3\text{O}_4$ ) powders have been prepared successfully by microwave hydrothermal (MH) reaction of ferrous sulfate and sodium hydroxide in the temperature range 90–200 °C [190]. This work is closely related to the report of [190]. The Mössbauer spectra of these powders indicated that stoichiometric  $\text{Fe}_3\text{O}_4$  particles are obtained only when the molar ratio of  $\text{Fe}/\text{NaOH} \geq 0.133$  is maintained in the solution. It is observed that the  $\text{Fe}/\text{NaOH}$  ratio is an important parameter for the controlled oxidation of ferrous salts in alkaline media under MH conditions to produce stoichiometric  $\text{Fe}_3\text{O}_4$ . Furthermore, the kinetics of MH synthesis are one order faster than the reported conventional hydrothermal (CH) synthesis. The value of the saturation magnetization  $M = 70 \text{ emu g}^{-1}$  is obtained in the case of stoichiometric  $\text{Fe}_3\text{O}_4$ . However, when ferric salt is treated in an alkaline medium, single-phase  $\alpha\text{-Fe}_2\text{O}_3$  is obtained under the MH conditions of 200 °C (194 psi).

Nanometric ferrites were also prepared by the MWH method. Komarneni [191] has reported on the synthesis of technologically important ferrites such as  $\text{ZnFe}_2\text{O}_4$ ,  $\text{NiFe}_2\text{O}_4$ ,  $\text{MnFe}_2\text{O}_4$ , and  $\text{CoFe}_2\text{O}_4$  by using novel microwave-hydrothermal processing. The precursors, nitrates of zinc, nickel, manganese, or cobalt, were mixed with ferric nitrate and neutralized with ammonia to a specific pH. Nanophase ferrites with high surface areas, in the range of 72–247  $\text{m}^2 \text{g}^{-1}$ , have been synthesized in a matter of a few minutes at temperatures as low as 164 °C. The rapid synthesis of nanophase ferrites via an acceleration of reaction rates under microwave-hydrothermal conditions is expected to lead to energy saving.

Other oxides have also been prepared by the MWH methods. Ceria,  $\text{CeO}_2$ , titania,  $\text{TiO}_2$ , and zirconia,  $\text{ZrO}_2$ , and the tin oxides were the most popular. Zhu's group [134] prepared nanometer-sized  $\text{CeO}_2$  by two methods; sonochemical, and MWH. The precursors were aqueous solutions containing  $(\text{NH}_4)_2\text{Ce}(\text{NO}_3)_6$ , hexamethylenetetramine and poly (ethylene glycol) (PEG  $M_w = 19,000$ ).

The influence of microwave power and reaction time on the formation of  $\text{CeO}_2$  nanoparticles was investigated. When the microwave power is in the range 10% to 40%, the as-prepared  $\text{CeO}_2$  nanoparticles are of similar size and morphology. Violent 'bump' boiling of the solvent occurs when the power is greater than 50%. When the reaction time was less than 5 min, no turbidity was observed and the solution remained transparent. After exposure to microwave irradiation for 8 min the solution became a turbid yellow, indicating the formation of the product. After 10 min, the reaction was complete, and the yield was as high as 90%. If the reaction time was prolonged to 30 min or even longer, the yield did not increase further, and the size and morphology of the  $\text{CeO}_2$  nanoparticles remained almost

unchanged [134]. Narrow size distribution is obtained with an average particle size of 2.8 nm. A communication [192] reporting only on the MWH part of these findings preceded this paper [134].

Nanosized zirconium oxide ( $\text{ZrO}_2$ ) powders were prepared by adding NaOH to a zirconyl chloride aqueous solution under microwave-hydrothermal conditions [193]. The results showed that the tetragonal polymorph increased with increasing NaOH concentration in the starting solution and reached a maximum value by using 1 M  $\text{ZrOCl}_2$ . The authors emphasize the simplicity of the method and that it can lead to powders with desirable characteristics such as very fine size, narrow size distribution, and good chemical homogeneity. The microwave-hydrothermal treatments were conducted at 200 psi for 2 h. The time, pressure, and power were computer controlled. TEM analysis confirmed the effect of concentration on particle size. In particular, the calculated average particle size ranged from 16 ( $\pm 3$ ) to 9 ( $\pm 3$ ) nm, with the  $\text{ZrOCl}_2$  concentration varying from 0.5 M to 1 M. TEM observation of the particles revealed spherical-shaped particles with no agglomeration.

Forced hydrolysis preparation of zirconia sols and powders by microwave heating of zirconium tetrachloride solutions at a temperature of 180 °C led in a few minutes to monodispersed nanoscale zirconia particles [194]. Synthesis was performed using the above-mentioned RAMO system [189]. This process combines the advantages of forced hydrolysis (homogeneous precipitation) and microwave heating (very fast heating rates). Sols are colloidally stable, which means that after 6 months no sedimentation is observed and the size distribution given by photon correlation spectroscopy (PCS) measurements does not change. For all synthesis conditions (with or without HCl, zirconium salt concentration, and synthesis time), zirconia polycrystalline particles were produced. According to the different analyses, these zirconia polycrystalline particles were aggregates of small primary clusters.

Zirconia, and polymer-stabilized tetragonal  $\text{ZrO}_2$  nanopowders with an average size of ca. 2.0 nm have been prepared by microwave heating in an aqueous solution containing  $\text{Zr}(\text{NO}_3)_4 \cdot 5\text{H}_2\text{O}$ , PVA, and NaOH [195]. The photoluminescence of the synthesized  $\text{ZrO}_2$  fine particles has been investigated at two different excitations with an excitation wavelength of 254 nm; three fluorescence emissions at 402 nm, 420 nm, and 459 nm, respectively, could be observed. The PL spectrum obtained at 412 nm excitation exhibited a maximum at 608 nm, with a weak satellite peak at 530 nm. The emissions that appear at short wavelength excitation are ascribed to the near band-edge transitions.

Nanocrystalline  $\text{SnO}_2$  powders of about 3 nm in size have been prepared by a microwave irradiation heating technique from an aqueous solution in the presence of  $\text{SnCl}_4$  and urea [196]. A bandgap estimated to be 4.5 eV is obtained from the optical measurement of the nanoparticles. HRTEM pictures show that the as-prepared  $\text{SnO}$  powders are crystalline with ca. 3 nm particle size, and the particles are held together by an irregular network.

High-purity powders of  $\text{SnO}$  nanocrystallites with crystallite sizes less than 30 nm and surface areas up to 40 m<sup>2</sup> g<sup>-1</sup> have been synthesized by a solution process in which an amorphous oxy-hydroxy precipitate of  $\text{Sn}^{+2}$  is crystallized

with microwave heating [197]. Microwave heating was found to have selectively accelerated SnO crystallization, but not the concurrent  $\text{Sn}^{+2}$  to  $\text{Sn}^{+4}$  oxidation, which otherwise prevails in the conventional thermal heating process. Control studies give a strong indication of a non-temperature effect of the microwave irradiation in the present process.

Microwave-hydrothermal synthesis of titanium dioxide under various reaction conditions was reported by Komarneni [198]. Crystallization of rutile from  $\text{TiOCl}_2$  solutions was found to be extremely rapid. Titanium dioxide, particle size, morphology and polymorph can be controlled by changing various parameters, such as: concentration, pH, pressure (or temperature), time, and anionic species. The main advantages of microwave-hydrothermal processing of  $\text{TiO}_2$  are: (1) rapid heating to required temperature and (2) extremely rapid kinetics of crystallization. Rutile was the only crystalline phase when various concentrations (3 M, and 2 M) of  $\text{TiOCl}_2$  solutions were treated at a variety of pressures (190, 100, 50 and 25 psi) for 2 h. The yield of rutile was 95% at all pressures, which showed that the crystallization of this solution was practically complete. When the  $\text{TiOCl}_2$  was further reduced, a mixture of anatase and rutile phases was obtained.

Another microwave study yielded only the anatase phase [199]. In this work  $\text{TiO}_2$  was synthesized from the alkoxide by the polyol method using various polyols (1,4-butanediol, 1,5-pentanediol, or 1,6-hexanediol) under MW radiation. The authors demonstrated that the crystallite size, which was always less than 10 nm, could be controlled by the quantity of added water and by the nature of the polyol (see Table 1 in [199]).

A group of binary oxide nanophase (titanates and zirconates) materials were prepared using a microwave-assisted soft-chemical route [200].  $\text{BaTiO}_3$ ,  $\text{Ba}_6\text{Ti}_{17}\text{O}_{40}$ ,  $\text{BaZrO}_3$  and  $\text{PbTiO}_3$  were prepared from  $\text{BaCl}_2$  hydrate,  $\text{Pb}(\text{Ac})_2$ ,  $\text{Ti}(\text{OPri})_4$  and  $\text{ZrOCl}_2$ . All reactions were performed in ethylene glycol, which acted both as a solvent and as a growth regulating agent, under atmospheric pressure in a microwave reactor.

The Ni/NiO composite was prepared by using the fast method of microwave-assisted oxidation [201]. Amorphous Ni nanoparticles were used as a precursor, and the oxidizing agent was oxygen. By using vapors of  $\text{H}_2\text{O}_2$ , almost complete oxidation of nickel was achieved.

$\text{CuO}$  nanoparticles with an average size of ca. 4 nm have been successfully prepared by microwave irradiation, using copper(II) acetate and sodium hydroxide as the starting materials and ethanol as the solvent [202]. The as-prepared  $\text{CuO}$  nanoparticles have regular shape, narrow size distribution and high purity. The band gap is estimated to be 2.43 eV according to the results of the optical measurements of the  $\text{CuO}$  nanoparticles.

Before summarizing this section and emphasizing the advantages of using microwave radiation for the synthesis of nanoparticles, we would like to remind the reader that perhaps the largest body of work in this field was conducted in the preparation of nanosized chalcogenides. However, following our own guidelines mentioned above, we have left it to another review [3]. Almost all the authors quoted in this review have mentioned the short reaction time in the microwave

processes as perhaps the biggest advantage. The simplicity of the reaction, whether the reaction vessel is put directly in the microwave oven or hooked up to a reflux system, is that the reaction cell is still very simple and it is easy to assemble the experimental set-up. In almost all his papers Komarnani has pointed out the energy saving in conducting a microwave reaction. MWH is homogeneous: it starts from the inside and progresses towards the glass container, while the opposite is true for conventional heating. Temperature and concentration gradients are avoided in a MW reaction. Whether there is a specific microwave effect, namely a reaction carried out under microwave radiation leading to a different product, compared with the same reaction under *conventional heating*, or not, is not clear. There are a few well known examples showing results different from those obtained by conventional heating [203–205]. However, more detailed kinetic studies have established [206–208] that chemical reactions, which are carried out under MW radiation, are controlled by the same fundamental thermodynamics and kinetics as conventional reactions. The title of [206] is “Specific activation by MW-Myth or Reality”.

In a MWH process one precursor can be heated at much higher heating rates and reach a higher temperature than its surroundings. In this respect it is similar to sonochemistry, where hot spots are formed in the liquid. In the polyol reactions where the first step was the formation of metallic fine particles, we could see the solution of ethylene glycol hot points reaching 600–700 °C. The difference between sonochemistry and MWH is that in the latter method there is no direct contact between the energy source and the solution, while in the sonochemistry the horn is dipped into the solution.

In MWH a reaction can be conducted at temperatures higher than the boiling point of the solvent while employing a simple apparatus. According to Mingos [159], it is possible to increase the temperature of a reaction in common organic solvents up to 100 °C above the conventional boiling point of the solvent.

## Acknowledgements

This work could not have been performed without the help of so many good friends from all around the world. I thank them all without trying to name all of them. I will name however, my coworkers in my laboratory at Bar-Ilan. I would like to thank Dr. X. Cao, Dr. Ziyi Zhong, Dr. Y. Zhao, Dr. S. Ramesh, Dr. M. Shafi, Dr. Arul Dhas, Prof. J. J. Zhu, Dr. Liu Suwen, Dr. R. A. Salkar, Dr. P. Jeevanandam, Prof. X. Tang, Dr. Yanqin Wang, Prof. W. Huang, Prof. Guansheng Peng, Prof. Ynigchun Zhu, Dr. R. Vijayakumar, Dr. Rohit Kumar Rana, Dr. Hong-Liang Li, Dr. Jinping Xiong, Dr. Qiaoling Li, Dr. D. N. Srivastava, Dr. V. Ganesh Kumar, Dr. M. Sivakumar, Dr. Gentao Zhou, Dr. S. Nikitenko, and Dr. Qiu Longhui, my foreign postdoctorate, for adapting rapidly to the Israeli system and enthusiastically conducting innovative research. I also thank my Israeli Ph. D. and M. Sc. students, Dr. Gina Katabi, Dr. Shlomit Wiizel, Dr. Oleg Palchik, Mrs. Tatiana Prozorov, Mr. Ronnen Polsky, Mr. Menachem Motiei, Mrs. Sigalit Avivi (Levi), Mr. Stanislav

Kishinevsky, Mrs. Ayelet Gamili, Haviv Grisaru, Vilas G. Pol, Riki Kerner (Harpeness), Mrs. Alexandra Gabashvili, and Mr. Yaakov David Solomon.

Special thanks are given to Professor Yuri Koltypin, and Dr. Elena Sominska, who helped me in the early stages in switching from spectroscopy to materials science, and liquidating the old equipment. They in turn were helped at the later stages by Dr. Nina Perkas.

This work could not have been accomplished without a few institutions who financed this research. I would like to thank the BSF (Bi-US-Israel Binational Science Foundation), the Israeli Ministry of Science, Culture, and Sport through the Indo-Israeli program in Materials Science (two grants), the Sino-Israeli program in Materials Science, the NEDO Organization, the Israeli Ministry of Science, Culture, and Sport for two Infrastructure Grants, The EC for 4 5<sup>th</sup> Program grants, and 3 INTAS grants, and the Israeli Science Foundation for two equipment grants. I would also like to thank the German BMBF for a DIP (Deutsche-Israel Projects) and a grant provided via the Energy Program.

This review could not have been written without an invitation from Professor S. T. Lee from the City University of Hong Kong for me to spend a short sabbatical at his COSDAF Institute. This invitation enabled this review, and I thank Professor Lee for extending this invitation to me.

## References

- 1 a) K. S. SUSLICK, T. W. HYEON, M. W. FANG, *Chem. Mater.*, **1996**, 8, 2172; b) K. S. SUSLICK, G. J. PRICE, *Annu. Rev. Mater. Sci.*, **1999**, 29, 295.
- 2 M. ASHOKKUMAR, F. GRIESER, *Rev. Chem. Eng.*, **1999**, 15, 41.
- 3 JUN-JIE ZHU, HUI WANG, Novel Methods for Chemical Preparation of Metal Chalcogenide Nanoparticles, in *Encyclopedia of Nanoscience and Nanotechnology*, ed. HARI SINGH NALWA, American Scientific Publishers, New York, 2003.
- 4 T. J. MASON, Sonochemistry, Royal Society of Chemistry, Cambridge, 1990.
- 5 K. S. SUSLICK, S. B. CHOE, A. A. CICHOWLAS et al., *Nature*, **1991**, 353, 414.
- 6 K. S. SUSLICK, R. E. CLINE, D. A. HAMMERTON, *J. Am. Chem. Soc.*, **1986**, 108, 5641.
- 7 K. S. SUSLICK, R. E. CLINE, D. A. HAMMERTON, *J. Am. Chem. Soc.*, **1986**, 108, 5641.
- 8 X. CAO, YU. KOLTYPIN, G. KATABI et al., *J. Mater. Res.*, **1995**, 10, 2952.
- 9 X. CAO, YU. KOLTYPIN, R. PROZOROV et al., *J. Mater. Chem.*, **1997**, 7, 2447.
- 10 S. AVIVI, Y. MASTAI, G. HODES et al., *J. Am. Chem. Soc.*, **1999**, 121, 4196.
- 11 M. W. GRINSTAFF, A. A. CICHOWLAS, S. B. CHOE et al., *Ultrasonics*, **1992**, 30, 168.
- 12 YU. KOLTYPIN, G. KATABI, X. CAO et al., *J. Non Cryst Solids*, **1996**, 201, 159.
- 13 K. S. SUSLICK, M. FANG, M. T. HYEON et al., *Mater. Res. Soc. Symp. Proc.*, **1994**, 351, 443.
- 14 C. P. GIBSON, K. J. PUTZER, *Science*, **1995**, 267, 1338.
- 15 N. A. DHAS, C. P. RAJ, A. GEDANKEN, *Chem. Mater.*, **1998**, 10, 1446.
- 16 N. A. DHAS, A. GEDANKEN, *J. Mater. Chem.*, **1998**, 8, 445.
- 17 K. OKITSU, Y. MIZUKOSHI, H. BANDOW et al., *Ultrason. Sonochem.*, **1996**, 3, S249.
- 18 Y. MIZUKOSHI, R. OSHIMA, Y. MAEDA et al., *Langmuir*, **1999**, 15, 2733.
- 19 R. A. SALKAR, P. JEEVANANDAM, S. T. ARUNA et al., *J. Mater. Chem.*, **1999**, 9, 1333.

- 20 Y. MIZUKOSHI, E. TAKAGI, H. OKUNO et al., *Ultrason. Sonochem.*, **2001**, 8, 1.
- 21 T. FUJIMOTO, Y. MIZUKOSHI, Y. NAGATA et al., *Scr. Mater.*, **2001**, 44, 2183.
- 22 T. FUJIMOTO, S. TERAUCHI, H. UMEHARA et al., *Chem. Mater.*, **2001**, 13, 1057.
- 23 K. OKITSU, A. YUE, S. TANABE et al., *Langmuir*, **2001**, 17, 7717.
- 24 K. OKITSU, A. YUE, S. TANABE et al., *Bull. Chem. Soc. Jpn.*, **2002**, 75, 2289.
- 25 Y. P. SUN, H. W. ROLLINS, R. GUDURU, *Chem. Mater.*, **1999**, 11, 7.
- 26 N. A. DHAS, C. P. RAJ, A. GEDANKEN, *Chem. Mater.*, **1998**, 10, 3278.
- 27 F. GRIESER, *Stud. Surf. Sci. Catal.*, **1997**, 103, 57.
- 28 K. S. SUSLICK, M. M. FANG, T. HYEON, *J. Am. Chem. Soc.*, **1996**, 118, 11960.
- 29 K. V. P. M. SHAFI, S. WIZEL, T. PROZOROV et al., *Thin Solid Films*, **1998**, 318, 38.
- 30 K. V. P. M. SHAFI, A. GEDANKEN, R. PROZOROV, *Adv. Mater.*, **1998**, 10, 590.
- 31 R. A. SALKAR, P. JEEVANANDAM, G. KATABY et al., *J. Phys. Chem. B*, **2000**, 104, 893.
- 32 K. BARBOUR, M. ASHOKKUMAR, R. A. CARUSO et al., *J. Phys. Chem. B*, **1999**, 103, 9231.
- 33 R. A. CARUSO, M. ASHOKKUMAR, F. GRIESER, *Colloid Surf. A*, **2000**, 169, 219.
- 34 R. A. CARUSO, M. ASHOKKUMAR, F. GRIESER, *Langmuir*, **2002**, 18, 7831.
- 35 F. GRIESER, *Stud. Surf. Sci. Catal.*, **1997**, 103, 57.
- 36 K. S. SUSLICK, T. HYEON, M. FANG et al., *Mater. Res. Soc. Symp. Proc.*, **1994**, 351, 201.
- 37 K. V. P. M. SHAFI, A. GEDANKEN, R. B. GOLDFARB et al., *J. Appl. Phys.*, **1997**, 81, 6901.
- 38 K. V. P. M. SHAFI, A. GEDANKEN, R. PROZOROV, *J. Mater. Chem.*, **1998**, 8, 769.
- 39 K. E. GONSALVES, S. P. RANGARAJAN, A. GARCIA RUIZ et al., *J. Mater. Sci. Lett.* **1996**, 15, 1261.
- 40 R. OSHIMA, T. A. YAMAMOTO, Y. MIZUKOSHI et al., *Nanostruct. Mater.*, **1999**, 12, 111.
- 41 S. W. LIU, L. X. YIN, YU. KOLTYPIN et al., *J. Magn. Magn. Mater.*, **2001**, 233, 195.
- 42 K. V. P. M. SHAFI, A. GEDANKEN, R. PROZOROV et al., *J. Mater. Res.*, **2000**, 15, 332.
- 43 S. RAMESH, YU. KOLTYPIN, R. PROZOROV et al., *Chem. Mater.*, **1997**, 9, 546.
- 44 W. STÖBER, A. FINK, E. BOHN, *J. Colloid. Interface Sci.*, **1968**, 26, 62.
- 45 S. RAMESH, Y. COHEN, D. AURBACH et al., *Chem. Phys. Lett.*, **1998**, 287, 461.
- 46 S. RAMESH, Y. COHEN, R. PROZOROV et al., *J. Phys. Chem. B*, **1998**, 102, 10234.
- 47 Z. Y. ZHONG, Y. MASTAI, YU. KOLTYPIN et al., *Chem. Mater.*, **1999**, 11, 2350.
- 48 M. L. BREEN, A. D. DINSMORE, R. H. PINK et al., *Langmuir*, **2001**, 17, 903.
- 49 Y. KITAMOTO, M. ABE, *Nanostruct. Mater.*, **1999**, 12, 41.
- 50 A. DOKOUTCHAEV, J. T. JAMES, S. C. KOENE et al., *Chem. Mater.*, **1999**, 11, 2389.
- 51 V. G. POL, D. N. SRIVASTAVA, O. PALCHIK et al., *Langmuir*, **2002**, 18, 3352.
- 52 S. J. DOKTYCZ, K. S. SUSLICK, *Science*, **1990**, 247, 4946.
- 53 K. PRABHAKARAN, K. V. P. M. SHAFI, A. ULMAN et al., *Adv. Mater.*, **2001**, 13, 1859.
- 54 K. PRABHAKARAN, K. V. P. M. SHAFI, A. ULMAN et al., *Surf. Sci.*, **2002**, 506, L250.
- 55 K. PRABHAKARAN, K. V. P. M. SHAFI, Y. YAMAUCHI et al., *Appl. Surf. Sci.*, **2002**, 190, 161.
- 56 F. PAPADIMITRAKOPOULOS, T. PHELY-BOBIN, P. WISNIECKI, *Chem. Mater.*, **1999**, 11, 522.
- 57 S. WIZEL, R. PROZOROV, Y. COHEN, D. AURBACH et al., *J. Mater. Res.*, **1998**, 13, 211.
- 58 S. WIZEL, S. MARGEL, A. GEDANKEN et al., *J. Mater. Res.*, **1999**, 14, 3913.
- 59 A. DUTTA, P. K. MAHATO, N. N. DASS, *Eur. Polym. J.*, **1991**, 27, 465.
- 60 S. WIZEL, S. MARGEL, A. GEDANKEN, *Polym. Int.*, **2000**, 49, 445.
- 61 R. V. KUMAR, Y. MASTAI, Y. DIAMANT et al., *J. Mater. Chem.*, **2001**, 11, 1209.

- 62 R. V. KUMAR, YU. KOLTYPIN, O. PALCHIK et al., *Appl. Polym. Sci.*, **2002**, 86, 160.
- 63 K. S. SUSLICK, T. HYEON, M. FANG et al., *Mater. Sci. Forum*, **1996**, 225, 903.
- 64 K. S. SUSLICK, T. HYEON, M. M. FANG et al., *Mater. Sci. Eng. A*, **1995**, 204, 186.
- 65 K. OKITSU, Y. MIZUKOSHI, H. BANDOW et al., *J. Phys. Chem. B*, **1997**, 101, 5470.
- 66 N. A. DHAS, H. COHEN, A. GEDANKEN, *J. Phys. Chem. B*, **1997**, 101, 6834.
- 67 Y. KOLTYPIN, A. FERNANDEZ, T. C. ROJAS et al., *Chem. Mater.*, **1999**, 11, 1331.
- 68 J. WALTER, M. NISHIOKA, S. HARA, *Chem. Mater.*, **2001**, 13, 1828.
- 69 A. KOSHIO, M. YUDASAKA, M. ZHANG et al., *Nano Lett.*, **2001**, 1, 361.
- 70 S. NIKITENKO, YU. KOLTYPIN, I. FELNER et al., *Angew. Chem. Int. Ed. Engl.*, **2001**, 40, 4447.
- 71 X. CAO, R. PROZOROV, Y. KOLTYPIN et al., *J. Mater. Res.*, **1997**, 12, 402.
- 72 M. SUGIMOTO, *J. Magn. Magn. Mater.*, **1994**, 133, 460.
- 73 K. TANAKA, K. HIRAO, N. SOGA, *J. Appl. Phys.*, **1991**, 69, 7752.
- 74 M. SUGIMOTO, N. HIRATSUKA, *J. Magn. Magn. Mater.*, **1983**, 31, 1533.
- 75 N. A. DHAS, Y. KOLTYPIN, A. GEDANKEN, *Chem. Mater.*, **1997**, 9, 3159.
- 76 N. A. DHAS, A. GEDANKEN, *J. Phys. Chem. B*, **1997**, 101, 9495.
- 77 R. VIJAYAKUMAR, YU. KOLTYPIN, X. N. XU et al., *J. Appl. Phys.*, **2001**, 89, 6324.
- 78 T. PROZOROV, R. PROZOROV, YU. KOLTYPIN et al., *J. Phys. Chem.*, **1998**, 102, 10165.
- 79 K. V. P. M. SHAFI, Y. KOLTYPIN, A. GEDANKEN et al., *J. Phys. Chem. B*, **1997**, 101, 6409.
- 80 K. V. P. M. SHAFI, I. FELNER et al., *J. Phys. Chem. B*, **1999**, 103, 3358.
- 81 A. PATRA, E. SOMINSKA, S. RAMESH et al., *J. Phys. Chem. B*, **1999**, 103, 3361.
- 82 A. GEDANKEN, R. REISFELD, L. SOMINSKI et al., *Appl. Phys. Lett.*, **2000**, 77, 945.
- 83 A. GEDANKEN, R. REISFELD, E. SOMINSKI et al., *J. Phys. Chem. B*, **2000**, 104, 7057.
- 84 V. G. POL, R. REISFELD, A. GEDANKEN, *Chem. Mater.*, **2002**, 14, 3920.
- 85 V. G. POL, O. PALCHIK, A. GEDANKEN et al., *J. Phys. Chem. B*, **2002**, 106, 9737.
- 86 F. G. SHERIF, F. A. VIA, (Akzo America Inc.), *U.S. Pat.*, 4 764 357, 1988.
- 87 S. AVIVI, Y. MASTAI, G. HODES et al., *J. Am. Chem. Soc.*, **1999**, 121, 4196.
- 88 H. R. CRAIG, S. Y. TYREE, *Inorg. Chem.*, **1969**, 8, 591.
- 89 S. AVIVI, Y. MASTAI, A. GEDANKEN, *Chem. Mater.*, **2000**, 12, 1229.
- 90 S. AVIVI, Y. MASTAI, A. GEDANKEN, *J. Am. Chem. Soc.*, **2000**, 122, 4331.
- 91 J. J. ZHU, Z. H. LU, S. T. ARUNA et al., *Chem. Mater.*, **2000**, 12, 2557.
- 92 D. AURBACH, A. NIMBERGER, E. LEVI et al., *Chem. Mater.*, **2002**, 14, 4155.
- 93 C. N. R. RAO, *J. Mater. Chem.*, **1999**, 9, 1.
- 94 A. GEDANKEN, N. PERKAS, YU. KOLTYPIN et al., *Chem. Eur. J.*, **2001**, 7, 4546.
- 95 Y. WANG, X. TANG, L. YIN et al., *Adv. Mater.*, **2000**, 12, 1137.
- 96 H. X. TANG, S. W. LIU, Y. WANG et al., *Chem. Commun.*, **2000**, 2119.
- 97 Y. Q. WANG, L. X. YIN, O. PALCHIK et al., *Langmuir*, **2001**, 17, 4131.
- 98 Y. WANG, L. YIN, A. GEDANKEN, *Ultrason. Sonochem.*, **2002**, 9, 285.
- 99 C. T. KRESGE, M. E. LEONOWICZ, W. J. ROTH et al., *Nature*, **1992**, 359, 710.
- 100 a) R. RYOO, J. M. KIM, C. H. KO et al., *J. Phys. Chem. B*, **1996**, 100, 17718; b) R. RYOO, S. JUN, *J. Phys. Chem. B*, **1997**, 101, 317.
- 101 M. V. LANDAU, L. VRADMAN, M. HERSKOWITZ et al., *J. Catal.*, **2001**, 201, 22.
- 102 N. PERKAS, Y. WANG, YU. KOLTYPIN et al., *Chem. Commun.*, **2001**, 11, 988.
- 103 K. S. SUSLICK, in *Ultrasound: Its Chemical, Physical and Biological Effects*, ed. K. S. SUSLICK, VCH, Weinheim 1988.
- 104 W. CHEN, W. P. CAI, Z. P. ZHANG et al., *Chem. Lett.*, **2001**, 2, 152.
- 105 W. CHEN, W. P. CAI, G. Z. WANG et al., *Appl. Surf. Sci.*, **2001**, 174, 51.



- 106 W. CHEN, W. P. CAI, C. H. LIANG et al., *Mater. Res. Bull.*, **2001**, 36, 335.
- 107 W. CHEN, W. P. CAI, L. ZHANG et al., *J. Colloid Interface Sci.*, **2001**, 238, 291.
- 108 W. CHEN, W. P. CAI, Z. X. CHEN et al., *Ultrason. Sonochem.*, **2001**, 8, 335.
- 109 W. CHEN, W. P. CAI, Y. LEI et al., *Mater. Lett.*, **2001**, 50, 53.
- 110 J. C. YU, L. Z. ZHANG, J. G. YU, *New J. Chem.*, **2002**, 26, 416.
- 111 J. C. YU, L. Z. ZHANG, J. G. YU, *Chem. Mater.*, **2002**, 14, 4647.
- 112 D. N. SRIVASTAVA, S. CHAPPEL, O. PALCHIK et al., *Langmuir*, **2002**, 18, 4160.
- 113 D. N. SRIVASTAVA, N. PERKAS, A. GEDANKEN et al., *J. Phys. Chem. B*, **2002**, 106, 1878.
- 114 Y. Q. WANG, S. G. CHEN, X. H. TANG et al., *J. Mater. Chem.*, **2001**, 11, 521.
- 115 ROHIT KUMAR RANA, Y. MASTAI, A. GEDANKEN, *Adv. Mater.*, **2002**, 14, 1414.
- 116 S. S. KIM, W. ZHANG, T. J. PINNAVAIA, *Science*, **1998**, 282, 1302.
- 117 P. JEEVANANDAM, Y. KOLTYPIN, A. GEDANKEN, *Mater. Sci. Eng. B*, **2002**, 90, 125.
- 118 X. Y. LIANG, Z. MA, Z. C. BAI et al., *Acta Phys. Chim. Sin.*, **2002**, 18, 567.
- 119 I. SHAMES, E. ROZENBERG, G. GORODETSKY et al., *Appl. Phys.*, **2002**, 91, 7929.
- 120 P. JEEVANANDAM, Y. KOLTYPIN, A. GEDANKEN, *Nano Lett.*, **2001**, 1, 263.
- 121 X. XIA, L. L. SHEN, Z. P. GUO et al., *J. Nanosci. Nanotechnol.*, **2002**, 2, 45.
- 122 P. JEEVANANDAM, Y. KOLTYPIN, A. GEDANKEN et al., *J. Mater. Chem.*, **2002**, 10, 511.
- 123 Y. C. ZHU, H. L. LI, Y. KOLTYPIN, A. GEDANKEN, *J. Mater. Chem.*, **2002**, 12, 729.
- 124 J. C. YU, J. G. YU, W. K. HO et al., *Chem. Commun.*, **2001**, 1942.
- 125 W. P. HUANG, X. H. TANG, Y. Q. WANG et al., *Chem. Commun.*, **2000**, 415.
- 126 L. GUO, X. K. WANG, Z. M. LIN et al., *Chem. J. Chin. Univ.*, **2002**, 23, 1592.
- 127 Y. C. ZHU, H. L. KOLTYPIN, Y. R. HACHOEN et al., *Chem. Commun.*, **2001**, 24, 2616.
- 128 N. SUKPIROM, M. M. LERNER, *Mater. Sci. Eng. A*, **2002**, 333, 218.
- 129 K. V. P. M. SHAFI, A. ULMAN, X. Z. YAN et al., *Langmuir*, **2001**, 17, 1726.
- 130 C. S. S. R. KUMAR, H. MODROW, J. H. HORMES, *Part Part Syst. Char.*, **2002**, 19, 336.
- 131 H. WANG, J. J. ZHU, J. M. ZHU et al., *Phys. Chem. Chem. Phys.*, **2002**, 4, 3794.
- 132 L. X. YIN, Y. Q. WANG, G. S. PANG et al., *J. Colloid Interface Sci.*, **2002**, 246, 78.
- 133 L. X. YIN, Y. Q. WANG, G. S. PANG et al., *J. Colloid Interface Sci.*, **2002**, 246, 78.
- 134 E. V. KUMAR, Y. MASTAI, A. GEDANKEN, *Chem. Mater.*, **2002**, 12, 3892.
- 135 YU. KOLTYPIN, S. I. NIKITENKO, A. GEDANKEN, *J. Mater. Chem.*, **2002**, 12, 1107.
- 136 R. V. KUMAR, Y. DIAMANT, A. GEDANKEN, *Chem. Mater.*, **2000**, 12, 2301.
- 137 YU. KOLTYPIN, X. CAO, R. PROZOROV et al., *J. Mater. Chem.*, **1997**, 7, 2453.
- 138 T. H. HYEON, M. M. FANG, K. S. SUSLICK, *J. Am. Chem. Soc.*, **1996**, 118, 5492.
- 139 S. I. NIKITENKO, P. MOISY, I. A. TCHARUSHNIKOVA et al., *Ultrason. Sonochem.*, **2000**, 7, 177.
- 140 J. LU, Y. XIE, X. C. JIANG, W. HE et al., *J. Mater. Chem.*, **2001**, 11, 3281.
- 141 H. L. LI, Y. C. ZHU, O. PALCHIK et al., *Inorg. Chem.*, **2002**, 41, 637.
- 142 R. KATO, Y. TASAKA, E. SEKRETA et al., *Ultrason. Sonochem.*, **1999**, 6, 185.
- 143 R. G. COMPTON, J. C. EKLUND, F. MARKEN, *Electroanalysis*, **1997**, 9, 509.
- 144 G. HODES, Y. MASTAI, *Electrodeposition of Nanocrystalline Semiconductor Materials*, in *Encyclopedia on Electrochemistry*, Vol. 6: Semiconductor Electrodes and Photoelectrochemistry, ed. S. LICHT, Wiley-VCH, Weinheim, 2001, p. 173.
- 145 J. REISSE, H. FRANCOIS, J. VANDERCAMMEN et al., *Electrochim. Acta*, **1994**, 39, 37.
- 146 A. DURANT, J. L. DELPLANCKE, R. WINAND et al., *Tetrahedron Lett.*, **1995**, 36, 4257.
- 147 J. REISSE, T. CAULIER, C. DECKERKHEER et al., *Ultrason. Sonochem.*, **1996**, 3, S147.



- 148 Y. MASTAI, R. POLSKY, YU. KOLTYPIN et al., *J. Am. Chem. Soc.*, **1999**, 121, 10047.
- 149 J. J. ZHU, S. W. LIU, O. PALCHIK et al., *Langmuir*, **2000**, 16, 6396.
- 150 S. W. LIU, W. P. HUANG, S. G. CHEN et al., *J. Non-Cryst. Solids*, **2001**, 283, 231.
- 151 J. ZHU, S. T. ARUNA, Y. KOLTYPIN et al., *Chem. Mater.*, **2000**, 12, 143.
- 152 J. J. ZHU, Q. F. QIU, H. WANG et al., *Inorg. Chem. Commun.*, **2002**, 4, 242.
- 153 Y. SOCOL, O. ABRAMSON, A. GEDANKEN et al., *Langmuir*, **2002**, 18, 4736.
- 154 Y. MASTAI, M. HOMYONFER, A. GEDANKEN et al., *Adv. Mater.*, **1999**, 11, 1010.
- 155 D. M. P. MINGOS, *Chem. Ind.*, **1994**, 596.
- 156 S. CADDICK, *Tetrahedron*, **1995**, 51, 10403.
- 157 D. M. P. MINGOS, D. R. BAGHURST, *Chem. Soc. Rev.*, **1991**, 20, 1.
- 158 K. J. RAO, B. VAIDHYANATHAN, M. GANGULI et al., *Chem Mater.*, **1999**, 11, 882.
- 159 R. DAGANI, *Chem. Eng. News*, **1997**, 75, 26.
- 160 V. SRIDAR, *Curr. Sci.*, **1998**, 74, 446.
- 161 D. M. P. MINGOS, A. G. WHITTAKER, *J. Chem. Soc., Dalton Trans.*, **1995**, 2073, 1995.
- 162 A. G. WHITTAKER, D. M. P. MINGOS, *J. Chem. Soc., Dalton Trans.*, **1992**, 18, 2751.
- 163 C. GABRIEL, S. GABRIEL, E. H. GRANT et al., *Chem. Soc. Rev.*, **1988**, 27, 213.
- 164 C. H. CHOU, J. PHILLIPS, *J. Mater. Res.*, **1992**, 7, 2107.
- 165 Z. L. JIANG, Z. W. FENG, X. C. SHEN, *Chin. Chem. Lett.*, **2001**, 12, 551.
- 166 I. PASTORIZA-SANTOS, L. M. LIZ-MARZAN, *Langmuir*, **2002**, 18, 2888.
- 167 D. L. BOXALL, G. A. DELUGA, E. A. KENIK et al., *Chem. Mater.*, **2001**, 13, 891.
- 168 a) F. FIEVET, J. P. LAGIER, M. FIGLARZ, *Mater. Res. Bull.*, **1989**, Dec. 29; b) G. VIAU, F. FIEVET-VINCENT, F. FIEVET, *J. Mater. Chem.*, **1996**, 6, 1047; c) G. VIAU, F. FIEVET-VINCENT, F. FIEVET, *Solid State Ionics*, **1996**, 84, 259.
- 169 F. BONET, C. GUERY, D. GUYROMARD et al., *Int. J. Inorg. Mater.*, **1999**, 1, 47.
- 170 W. Y. YU, W. X. TU, H. F. LIU, *Langmuir*, **1999**, 15, 6.
- 171 W. X. TU, H. F. LIU, *J. Mater. Chem.*, **2000**, 10, 2207.
- 172 W. X. YU, H. Y. LIU, *Chem. Mater.*, **2000**, 12, 564.
- 173 S. KOMARNENI, D. LI, B. NEWALKAR et al., *Langmuir*, **2002**, 18, 5959.
- 174 A. M. QIN, Z. L. JIANG, Q. Y. LIU et al., *Chin. J. Anal. Chem.*, **2002**, 10, 254.
- 175 W. X. CHEN, J. Y. LEE, Z. L. LIU, *Chem. Commun.*, **2002**, 2588.
- 176 R. HE, X. QIAN, J. YIN, Z. ZHU, *J. Mater. Chem.*, **2002**, 12, 3783.
- 177 S. KOMARNENI, R. ROY, L. I. QH, *Mater. Res. Bull.*, **1992**, 27, 1393.
- 178 D. C. DONG, P. J. HONG, S. S. DAI, *Mater. Res. Bull.*, **1995**, 30, 531.
- 179 Q. LI, Y. WEI, *Mater. Res. Bull.*, **1998**, 33, 779.
- 180 O. PALCHIK, I. FELNER, G. KATABY et al., *J. Mater. Res.*, **2000**, 15, 2176.
- 181 X. B. HAN, L. HUANG, Z. HUI, *J. Inorg. Mater*, **1999**, 14, 669.
- 182 Z. B. JIA, Y. WEI, H. M. WANG, *J. Inorg. Mater*, **2000**, 15, 926.
- 183 X. H. LIAO, J. J. ZHU, W. ZHONG et al., *Mater. Lett.*, **2001**, 50, 341.
- 184 H. KATSUKI, S. KOMARNENI, *J. Am. Ceram. Soc.*, **2001**, 84, 2313.
- 185 S. S. MANOHARAN, S. J. SWATI, PRASANNA et al., *J. Am. Ceram. Soc.*, **2002**, 85, 2469.
- 186 S. R. DHAGE, Y. B. KHOLLAM, H. S. POTDAR et al., *Mater. Lett.*, **2002**, 57, 457.
- 187 T. CAILLOT, D. AYMES, D. STUERGA et al., *J. Mater. Sci.*, **2002**, 37, 5153.
- 188 Y. B. KHOLLAM, S. R. DHAGE, H. S. POTDAR et al., *Mater. Lett.*, **2002**, 56, 571.
- 189 S. KOMARNENI, M. C. D'ARRIGO, C. LEONELLI et al., *J. Am. Ceram. Soc.*, **1998**, 81, 3041.
- 190 X. H. LIAO, J. M. ZHU, J. J. ZHU et al., *Chem. Commun.*, **2001**, 937.
- 191 F. BONDIOLI, A. M. FERRARI, C. LEONELLI et al., *J. Am. Ceram. Soc.*, **2001**, 84, 2728.
- 192 K. BELLON, D. CHAUMONT, D. STUERGA, *J. Mater. Res.*, **1999**, 16, 2619.

- 193 X. JIANG, F. LI, YADONG LI, *Inorg. Chem.*, **2002**, 41, 3602.
- 194 J. J. ZHU, J. M. ZHU, X. H. LIAO et al., *Mater. Lett.*, **2002**, 53, 12.
- 195 D. S. WU, C. Y. HAN, S. Y. WANG et al., *Mater. Lett.*, **2002**, 53, 155.
- 196 S. KOMARNENI, R. K. RAJHA, H. KATSUKI, *Mater. Chem. Phys.*, **1999**, 61, 50.
- 197 T. YAMAMOTO, Y. WADA, H. YIN et al., *Chem. Lett.*, **2002**, 964.
- 198 O. PALCHIK, J. J. ZHU, A. GEDANKEN, *J. Mater. Chem.*, **2000**, 10, 1251.
- 199 O. PALCHIK, S. AVIVI, D. PINKERT et al., *Nanostruct. Mater.*, **1999**, 11, 415.
- 200 H. WANG, J. Z. XU, J. J. ZHU et al., *J. Cryst. Growth*, **2002**, 244, 88.
- 201 M. M. CHOWDRY, D. M. P. MINGOS, A. J. P. WHITE et al., *Chem. Commun.*, **1996**, 899.
- 202 E. M. GORDON, *Organometallics*, **1993**, 12, 5052.
- 203 M. LARHED, A. HALLBERG, *J. Org. Chem.*, **1996**, 61, 9582.
- 204 R. LAURENT, A. LAPORTERIE, J. DUBAC et al., *J. Org. Chem.*, **1992**, 57, 7099.
- 205 K. D. RANER, C. R. STRAUSS, F. VYSKOC et al., *J. Org. Chem.*, **1993**, 58, 950.
- 206 S. A. GALEMA, *Chem. Soc. Rev.*, **1997**, 26, 233.

## 7

## Solvothermal Synthesis of Non-Oxide Nanomaterials

*Y. T. Qian, Y. L. Gu, and J. Lu*

## 7.1

### Introduction

Inorganic non-oxide materials, such as III–V and II–VI group semiconductors, carbides, nitrides, phosphides, and borides, are traditionally prepared by solid state or gas-phase reactions. They have also been prepared via the pyrolysis of organo-metallic precursors but the products may be amorphous or poorly crystalline and a crystallization treatment at higher temperature is necessary. This treatment, however, may result in the crystalline size being beyond the nanometer scale. Exploration of milder techniques for preparing non-oxide nanomaterials with controlled shapes and sizes is very important for material science.

Hydrothermal synthesis is one of the important methods for producing fine powders of oxides. A hydrothermal system is usually maintained at a temperature beyond 100 °C and the autogenous pressure of water exceeds the ambient pressure, which is favorable for the crystallization of products. Recent research indicates that the hydrothermal method is also a practical means for preparing chalcogenide and phosphide nanomaterials, and hydrothermal treatment is an effective method for passivating porous silicons. Similar to hydrothermal synthesis, in a solvothermal process, a non-aqueous solvent, which is sealed in an autoclave and maintained in its superheated state, is the reaction medium, where the reactants and products are prevented effectively from oxidation and volatilization and the reaction and crystallization can be realized simultaneously. Furthermore, organic solvents may be favorable for the dispersion of non-oxide nanocrystallites and may stabilize some metastable phases.

In this chapter, we briefly review our recent progress in the solvothermal preparation of non-oxide nanomaterials.  $\gamma$ -ray irradiation and room temperature synthesis of chalcogenide nanocrystallites are also briefly described but first we present some progress in hydrothermal synthesis.

In different hydrothermal conditions,  $\text{TiO}_2$  nanocrystallites (anatase and rutile) with nine kinds of morphologies have been prepared [1, 2].  $\text{CdWO}_4$  nanorods [3], which showed very strong photoluminescence at 486 nm ( $\lambda_{\text{ex}} = 253 \text{ nm}$ ) at room temperature, were prepared by a hydrothermal method at 130 °C. Lead tungstate

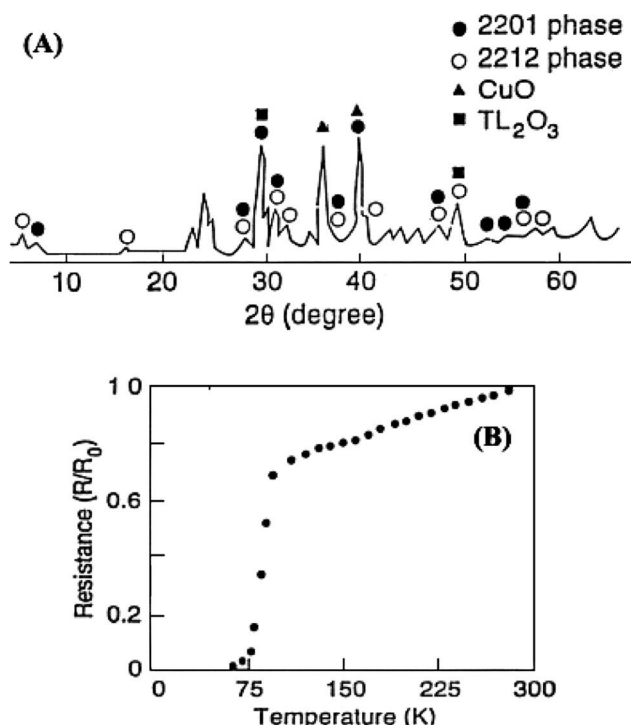


Fig. 7.1. The XRD pattern (A) and the  $R-T$  curve (B) of the Tl-based superconductor prepared by the hydrothermal method.

( $PbWO_4$ ), an important inorganic scintillator, was also hydrothermally synthesized [4]. By using LiOH and  $Nb_2O_5$  as the reactants, 40–100 nm flake-like  $LiNbO_3$  nanocrystallites [5] were prepared.

To avoid the toxicity of thallium oxides in high temperature solid state reactions, a hydrothermal reaction containing  $Tl(NO_3)_3$ , BaO, CuO and  $CaCO_3$  with  $H_2O_2$  at 160 °C was designed and a Tl-based superconductor,  $Tl_2O_3-CaO-BaCu_3O_4$ , with  $T_c$  onset near 95 K and zero resistance at 65 K has been prepared [6]. X-ray diffraction (XRD) studies showed that the products consisted of at least two superconducting phases (2201 and 2212). Figure 7.1 shows the XRD pattern and the  $R-T$  curve of the Tl-based superconductor. As a mixed valent magnetite, cubic perovskite structure  $La_{0.5}Ba_{0.5}MnO_3$  single-crystal nanowires with [110] orientation were grown hydrothermally at 270 °C [7]. They show an enhanced magnetoresistance effect as compared to the bulk crystals.

Fe-passivated porous silicon (PS) with non-degrading photoluminescence (PL) was prepared by treating  $P/P^+$ -type, boron-doped single crystal (111) Si wafers at 140 °C in an aqueous solution with 40 wt% HF and 0.3 M  $Fe(NO_3)_3$  (volume ratio, 7/6) [8, 9]. As shown in Figure 7.2, for freshly prepared samples, the PL peak intensity is 2–2.5 times stronger than that of ordinary PS. Furthermore, unlike

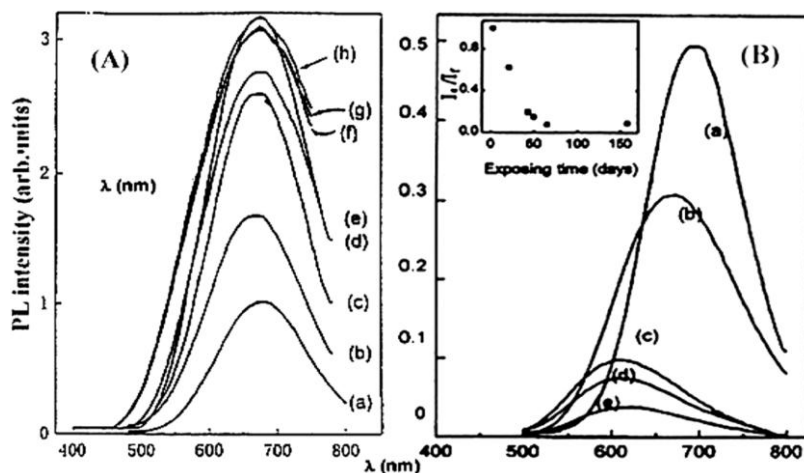


Fig. 7.2. Time evolution of the PS spectra of the Fe-passivated PS (A) and an ordinary PS (B) exposed to ambient air at room temperature for (A) (a) 2 h, (b) 45 days, (c) 75 days, (d) 110 days, (e) 140 days, (f) 170 days, (g) 235 days, (h) 500 days; (B) (a) 0 days, (b) 17 days, (c) 39 days, (d) 50 days, (e) 65 days.

ordinary PS, the PL intensity of the as-prepared PS increases during the first four months and then saturates when exposed to ambient air. No PL degradation was observed for eight months, and the peak position remained unchanged. This PL stability is attributed to the formation of stable Fe–Si bonds on the surface of the PS.

The hydrothermal method has been used to prepare monodispersed ZnS (6 nm) [10] and CdS nanocrystals (16 nm) [11]. By hydrothermal polymerization and simultaneous sulfidation processes, nanocomposites CdS/poly(vinyl acetate) nanorods [12] and nanospheres [13] were synthesized. In aqueous hydrazine solutions, nonstoichiometric metal telluride nanocrystallites such as  $\text{Cu}_{2.86}\text{Te}_2$ ,  $\text{Cu}_7\text{Te}_5$ ,  $\text{Cu}_{2-x}\text{Te}$ , and  $\text{Ag}_7\text{Te}_4$  [14], and cubic  $\text{Co}_9\text{S}_8$  were hydrothermally synthesized [15]. Other transition metal chalcogenides, such as single-molecular-layer  $\text{MoS}_2$  [16] and  $\text{MoSe}_2$  [17] were also prepared under hydrothermal conditions.

As shown in Figure 7.3, novel millimeter-sized tubular crystals of  $\text{Ag}_2\text{Se}$  were grown via a hydrothermal reaction route from  $\text{AgCl}$ , Se and  $\text{NaOH}$  at  $155^\circ\text{C}$  [18]. Similarly,  $\text{CuS}$  millimeter-scale tubular crystals were synthesized at  $185^\circ\text{C}$  [19]. Reacting  $\text{Bi}_2\text{Te}_3$  with  $\text{I}_2$  via an iodine transport hydrothermal method at temperatures ranging from  $190$ – $200^\circ\text{C}$  resulted in  $\text{BiTeI}$  submicrometer hollow spheres with diameters of  $200$ – $300$  nm [20]. The sphere wall is composed of  $\text{BiTeI}$  nanoparticles with average diameter  $5$  nm and thickness about  $10$  nm. The transmission electron microscope (TEM) and high-resolution transmission electron microscope (HRTEM) images of  $\text{BiTeI}$  spheres are shown in Figure 7.4.  $\text{SbSI}$  rodlike crystals [21] and nanorods [22] with diameters of  $20$ – $50$  nm and lengths up to several micrometers were synthesized at about  $200^\circ\text{C}$ .

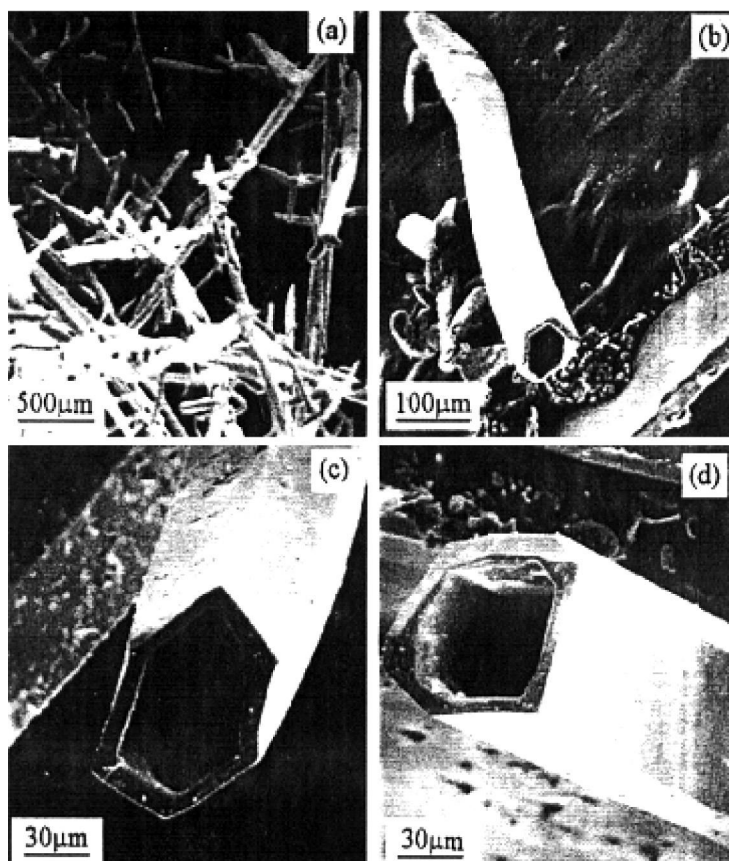


Fig. 7.3. SEM images of the tubular  $\text{Ag}_2\text{Se}$  hydrothermally prepared from  $\text{AgCl}$ ,  $\text{Se}$  and  $\text{NaOH}$  at  $155^\circ\text{C}$ .

A series of ternary sulfides were prepared by hydrothermal methods.  $\text{CdInS}_2$  nanorods ( $20\text{--}25\text{ nm} \times 400\text{--}450\text{ nm}$ ) were prepared by reacting  $\text{CdS}$  nanorods with  $\text{InCl}_3$  and thiourea [23]. Other hydrothermally prepared ternary sulfide nanocrystallites include  $\text{MInS}_2$  ( $\text{M} = \text{Cu}$  [24],  $\text{Ag}$  [25]),  $\text{CuGaS}_2$  [26],  $\text{AgGaS}_2$  ( $6\text{--}12\text{ nm}$ ),  $\alpha\text{-Ag}_9\text{GaS}_6$  [27],  $\text{Ag}_3\text{CuS}_2$  [28],  $\text{PbSnS}_3$  [29], and  $\text{CuFeS}_2$  [30].

Recently,  $\text{InP}$  nanocrystals were synthesized via the hydrothermal reaction of  $\text{InCl}_3 \cdot 4\text{H}_2\text{O}$  and white phosphorus in aqueous ammonia with  $0.01\text{ mol L}^{-1}$  potassium stearate at  $170^\circ\text{C}$  [31]. The XRD pattern can be indexed as the cubic phase. The secondary particles,  $180\text{ nm}$  in size, consisting of fine  $\text{InP}$  nanocrystals,  $15\text{ nm}$  in size, were found from the TEM images (Figure 7.5(a)). Alternatively, using 1,2-dimethoxyethane instead of water as the reaction medium, nanocrystalline  $\text{InP}$   $10\text{ nm}$  in size was synthesized through the solvothermal reaction of anhydrous  $\text{InCl}_3$  and  $\text{Na}_3\text{P}$  at  $150^\circ\text{C}$  [32]. The TEM image is shown in Figure 7.5(b). Obviously, the solvothermal method resulted in better particle morphology. In fact, solvothermal

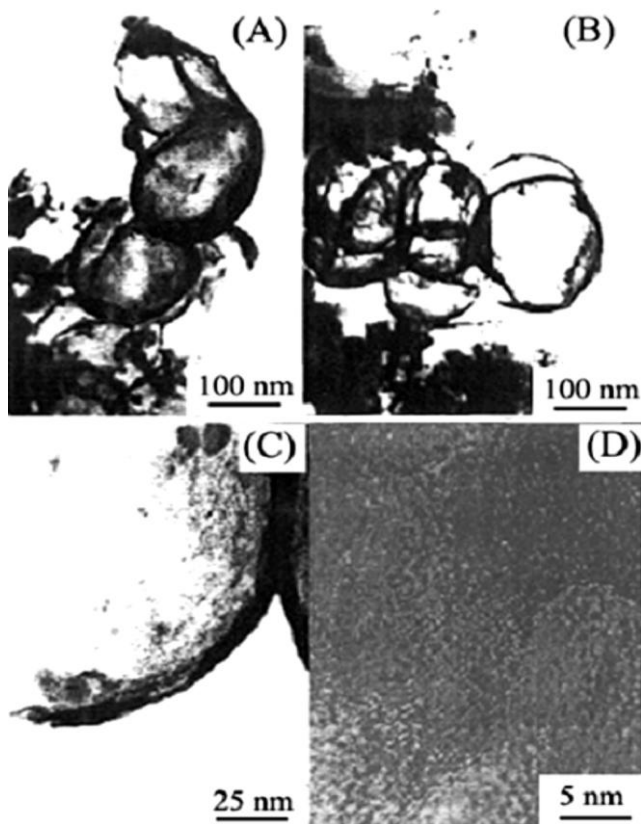


Fig. 7.4. TEM (A, B) and HRTEM (C, D) images of BiTeI spheres.

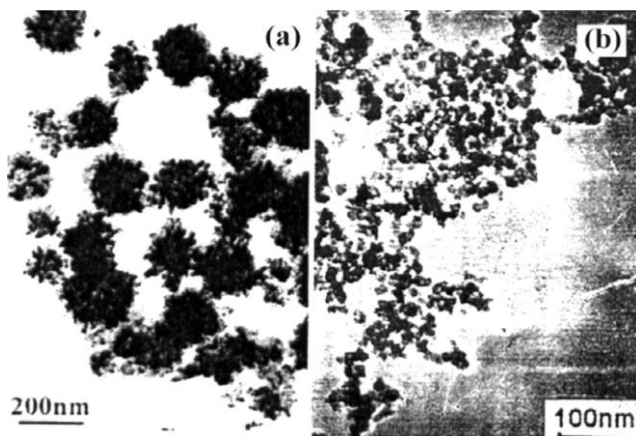


Fig. 7.5. TEM images of InP nanocrystals prepared by hydrothermal (a) and solvothermal (b) methods.



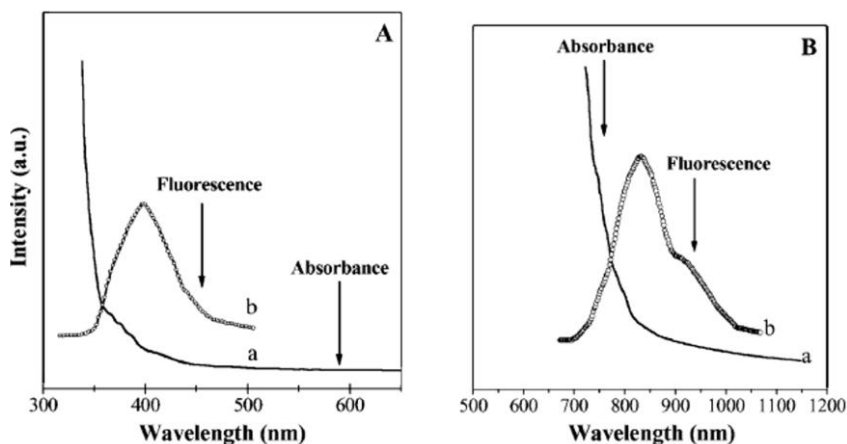


Fig. 7.6. Absorption and photoluminescence (PL) spectra of as-prepared products, GaP nanocrystals (A) and InP nanocrystals (B).

synthesis manifests many advantages over the hydrothermal method for preparing non-oxide materials. For example, it is effective in the preparation of nitride nanomaterials, which commonly cannot be prepared by the hydrothermal method. Recently, quantum-confined 5 nm GaP and 8 nm InP nanocrystals were hydrothermally synthesized at 120–160 °C [33]. As shown in Figure 7.6B an emission peak at 850 nm (1.55 eV) was observed in the photoluminescence spectrum of the as-prepared InP nanocrystals, which revealed the blue shift of the band gap with 0.2 eV, for GaP nanocrystals, an emission peak at 400 nm (3.1 eV) was also found (Figure 7.6A) which shows a pronounced quantum confinement effect.

## 7.2

### Solvothermal Synthesis of III–V Nanomaterials

GaN is a direct band-gap semiconductor, which has potential applications in light-emitting devices in the visible and ultraviolet region. Wurtzite-type GaN was traditionally prepared via a gas-phase reaction in ammonia at 600–1000 °C [34]. It can also be produced via pyrolysis of single source precursors, such as  $[\text{H}_2\text{GaNH}_2]_3$ ,  $\text{Ga}(\text{C}_2\text{H}_5)_3\text{NH}_3$ , which already have a Ga–N bond, followed by treatment at temperatures  $>500$  °C [35]. On the other hand, nitrides of lanthanide or transition metals could be synthesized through a solid-state metathesis reaction (Reaction (1)) [36]:





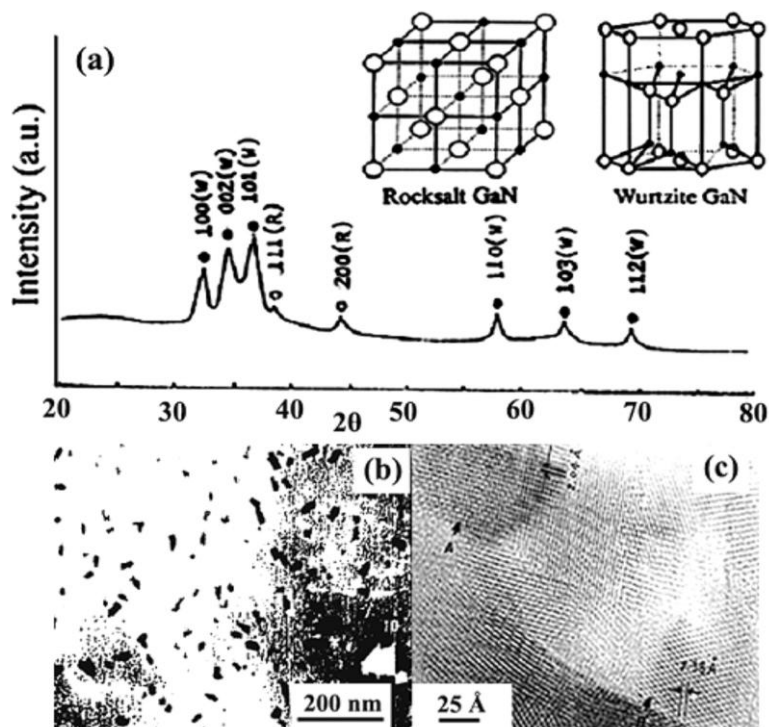
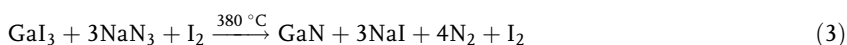


Fig. 7.7. XRD pattern (a), TEM (b) and HRTEM (c) images of the GaN nanoparticles.

However, this solid-state metathesis reaction failed for GaN [37] since  $\text{GaCl}_3$  is hygroscopic at ambient temperature. When the metathesis reaction of  $\text{GaCl}_3$  and  $\text{Li}_3\text{N}$ , Reaction (2), was carried out in benzene at  $280^\circ\text{C}$  under pressure in an autoclave, 30 nm GaN nanocrystallites in  $\sim 80\%$  yield (Figure 7.7(b)) were obtained [38]. As shown in Figure 7.7(a), the XRD pattern indicates that the product consists mainly of wurtzite-type GaN with a small fraction of rocksalt-type GaN [39]. This rocksalt-type phase with a lattice constant  $a = 4.100 \text{ \AA}$ , was observed directly with high-resolution electron microscopy (Figure 7.7(c)). It had been previously observed at ultrahigh pressure (at least 37 GPa) via a pressure-induced phase transition from wurtzite-type GaN [40]; when the pressure was decreased to about 25 GPa, it was transformed into the wurtzite-type GaN again. The size of the as-prepared GaN, 30 nm, is beyond its exciton Bohr diameter (11 nm), therefore, no quantum confinement effect was observed. Using  $\text{I}_2$  as a heat sink and diluting reagents, nanocrystalline GaN was also synthesized from the reaction of  $\text{GaI}_3$  and  $\text{NaN}_3$  (Reaction (3)).



As can be seen in Figure 7.8, the XRD pattern shows that the product is of

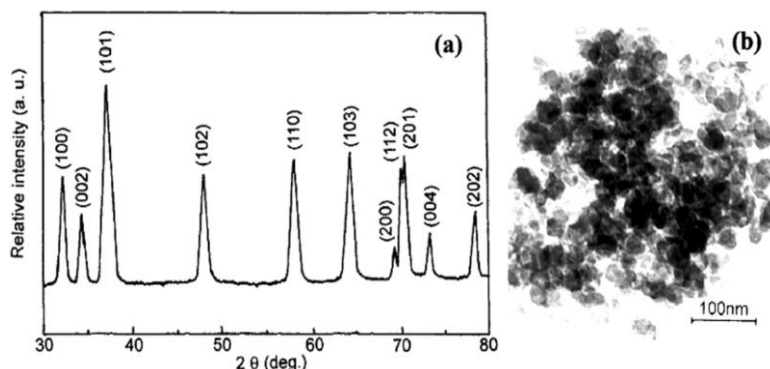
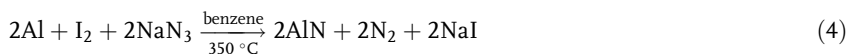


Fig. 7.8. XRD pattern (a) and TEM image (b) of the GaN powders prepared with molar ratios of  $\text{GaI}_3$ ,  $\text{NaN}_3$  and  $\text{I}_2$  of 1/4.5/5.

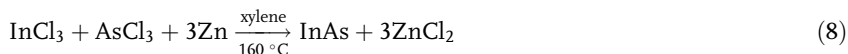
wurtzite-type and the TEM image reveals spherical particles with an average size of 30 nm [41].

AlN nanocrystallites were synthesized via the benzene-solvothermal method [42], from a mixture of aluminum,  $\text{I}_2$ ,  $\text{NaN}_3$  after reacting at 350 °C for 10 h (Reaction (4)).



The XRD pattern (Figure 7.9(a)) of the product can be indexed as the hexagonal AlN, with lattice constants  $a = 3.1175$  and  $c = 4.9813$  Å. TEM (Figure 7.9(b)) shows that the particle sizes range from 5 to 20 nm.

In xylene, 15 nm InAs nanocrystallites (Figure 7.10B) were prepared by zinc co-reduction of  $\text{InCl}_3 \cdot 4\text{H}_2\text{O}$  and  $\text{AsCl}_3$  at 160 °C [43]. The XRD pattern indicates that the products were sphalerite-type cubic InAs (Figure 7.10A). As shown in Reactions (5)–(8), a trace amount of water resulting from the reactants may be helpful to the process.



Compounds containing arsenic are usually very toxic, the order of toxicity being [44]:  $\text{R}_3\text{As}$  ( $\text{R} = \text{H}, \text{Me}, \text{Cl}, \text{etc.}$ )  $> \text{As}_2\text{O}_3$  ( $\text{As (III)}$ )  $> (\text{RAsO})_n > \text{As}_2\text{O}_5$  ( $\text{As(V)}$ )  $> \text{R}_n\text{AsO(OH)}_{3-n} > \text{R}_4\text{As}^+ > \text{As(0)}$ . A safer route reacting  $\text{InCl}_3 \cdot 4\text{H}_2\text{O}$  and  $\text{KBH}_4$  in the presence of arsenic was proposed for the preparation of nanocrystalline InAs [45], see Reaction (9).

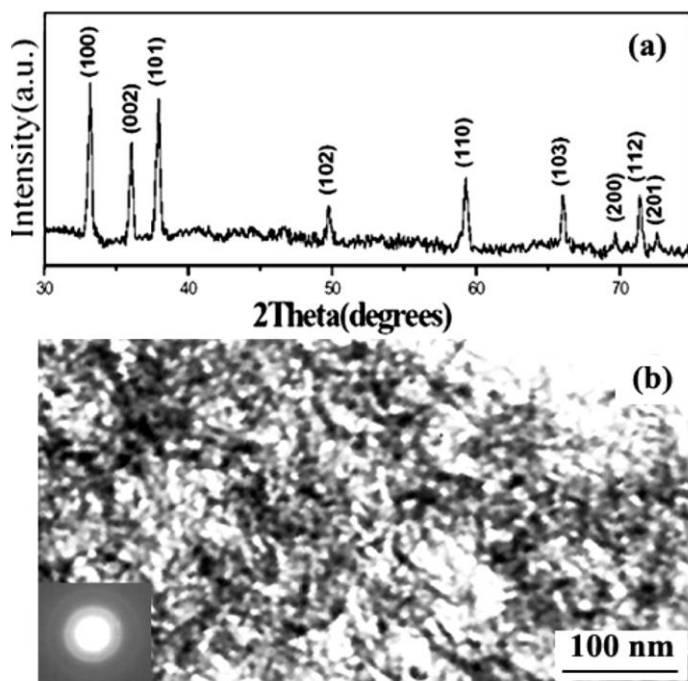
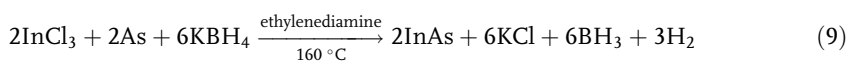
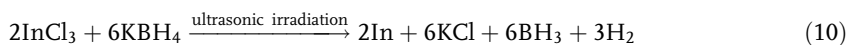


Fig. 7.9. XRD pattern (a) and TEM images (b) of the as-prepared nanocrystalline AlN.



TEM shows that the products are polycrystalline fibers or near-single-crystal whiskers with widths of 15–100 nm and lengths of 150–1000 nm (Figure 7.10E). When the reaction temperature was reduced to 120 °C, which is below the melting point of indium (156.6 °C), spherical InAs nanocrystals of 20–50 nm were obtained (Figure 7.10D). However, there is trace indium co-existing in the products, indicating that the reaction proceeds through a metallic indium intermediate.

Similarly, as shown in Reactions (10) and (11), under high-intensity ultrasonic irradiation, InP nanocrystallites were synthesized in ethanol/benzene mixed solvent at room temperature [46].



The XRD pattern (Figure 7.11(a)) indicates that the product is sphalerite-type cubic InP. The TEM images (Figure 7.11(b)) show that the products are 9 nm spherical

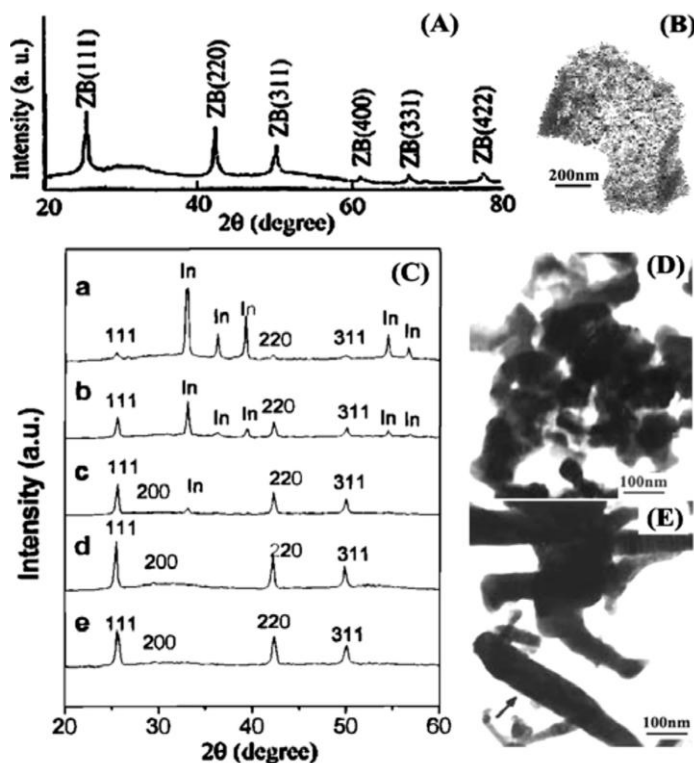


Fig. 7.10. XRD patterns and TEM images of the InAs samples prepared by the solvothermal zinc co-reduction route (A, B) and by the safe low temperature solvothermal route (C, D, E).

(a) 100 °C, before 1 M HCl treatment;  
 (b) 120 °C, before 1 M HCl treatment;  
 (c) 160 °C, before 1 M HCl treatment;  
 (d) 120 °C, after 1 M HCl treatment;  
 (e) 160 °C, after 1 M HCl treatment.

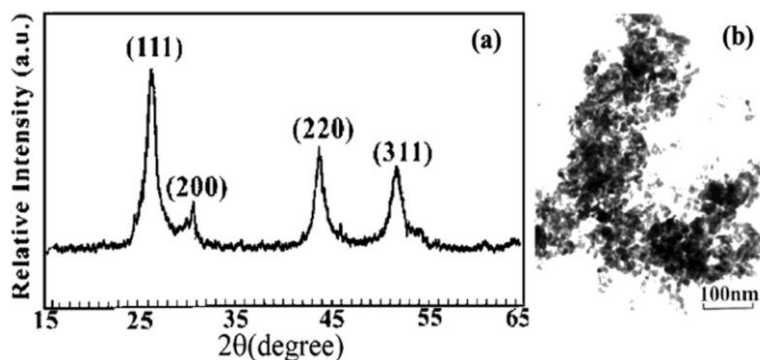


Fig. 7.11. XRD pattern (a) and TEM image (b) of the as-prepared InP nanocrystals.

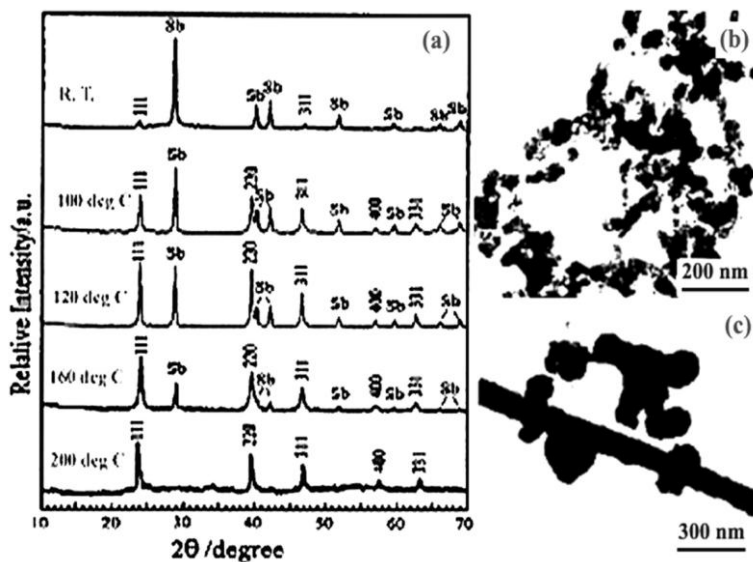
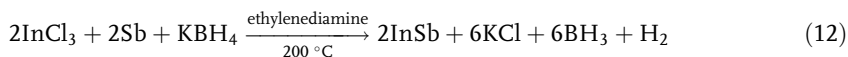


Fig. 7.12. XRD patterns (a) and TEM images (b) and (c) of the InSb nanocrystals prepared by  $\text{NaBH}_4$  reduction of  $\text{InCl}_3$  in the presence of Sb at 100 to 200 °C in ethylenediamine.

grains. Alternatively, from the same reaction, 15–20 nm InP nanocrystals were prepared at about 120 °C in ethylenediamine (en) [47].

A similar reaction was also used to prepare InSb nanomaterials by  $\text{NaBH}_4$  reduction of  $\text{InCl}_3$  in the presence of metallic antimony in en (Reaction (12)).



As shown in Figure 7.12(a), the mean nanocrystalline dimensions of 40 nm are estimated from the half widths of the XRD peaks by the Scherrer equation. Spherical grains of 40–60 nm and rod-like grains with a size of  $120 \times 1500$  nm were found in the TEM images (Figure 7.12(b) and (c)). The reaction also proceeds through an indium intermediate, but a pure phase of nanocrystalline InSb was obtained at 200 °C when  $\text{InCl}_3/\text{Sb} = 4/1$  [48].

Recently, a novel Ullmann-like reaction was designed to prepare one-dimensional InP and GaP nanocrystallites [49] (see Reaction (13)).



As a result of using organic phosphorus starting material, crystal growth was appropriately controlled. Nanowires of sphalerite-type GaP and InP (Figure 7.13) were prepared, suggesting a promising method for the solvothermal synthesis of one-dimensional III–V nanocrystallites.

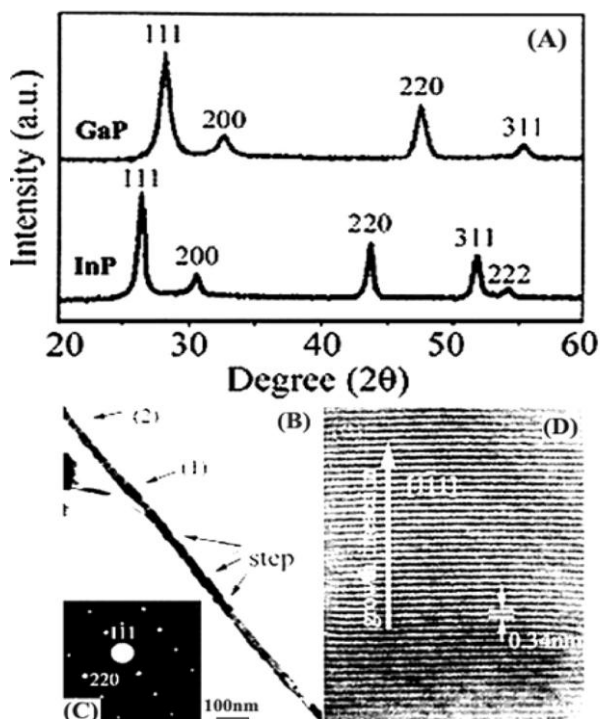


Fig. 7.13. XRD patterns of GaP and InP nanowires (A), TEM (B), ED (insert C) and HRTEM (D) images of InP nanowires prepared by an Ullmann-like reaction.

### 7.3

#### Synthesis of Diamond, Carbon Nanotubes and Carbides

Diamonds were first synthesized through a high-temperature and high-pressure process [50]. Using diamond seeds, micrometer-sized diamonds have been grown in a hydrothermal process at 800 °C and 1.4 kbar [51]. Chemical vapor deposition (CVD) is a low-pressure technique for the preparation of polycrystalline diamonds films using CH<sub>4</sub> or C<sub>2</sub>H<sub>2</sub> as a carbon source [52].

In traditional organic synthesis, the Wurtz reaction:



can be used to link two alkyl groups by forming a C–C single bond. Employing a Wurtz-type reaction coupling alkyl halides with excess metal sodium as both reductant and flux, fine carbon powders containing a trace amount of diamond (yield ~ 2%) (Figure 7.14(c)) were synthesized via a reduction–pyrolysis–catalysis route by reacting CCl<sub>4</sub> with metallic sodium at 700 °C [53]. This temperature is

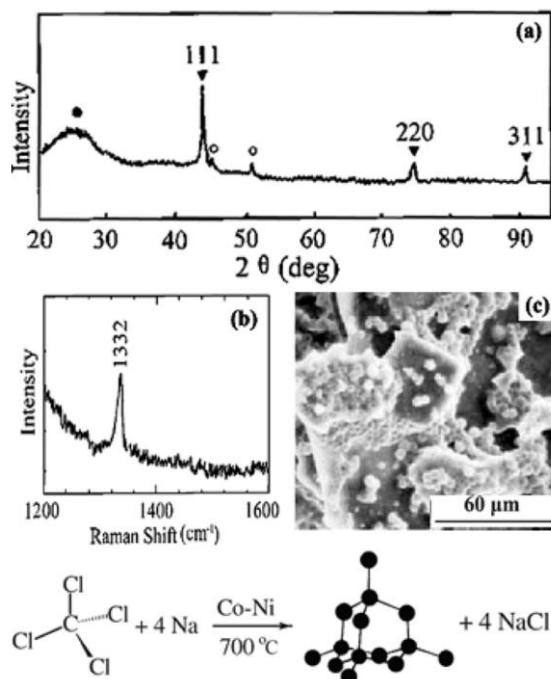
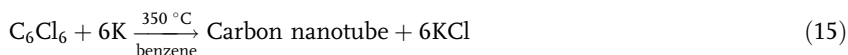


**Fig. 7.14.** XRD pattern (a), Raman spectrum (b) and SEM image (c) of the diamond sample synthesized by the reduction-pyrolysis-catalysis route.

much lower than that of traditional methods. The three strongest diffraction peaks of diamond were found in the XRD pattern (Figure 7.14(a)). The Raman spectrum (Figure 7.14(b)) shows a sharp peak at 1332  $\text{cm}^{-1}$ , which is characteristic of diamond.

Carbon nanotubes are usually prepared by arc-discharge [54], laser evaporation of graphite [55], disproportionation of carbon monoxide [56], and pyrolysis of hydrocarbons [57]. In all these methods, no typical chemical reactions describing the synthetic process of the carbon nanotubes could be given. Since the walls of a carbon nanotube, both the cylindrical stories of a multiwall nanotube, and the planar sheet of a single wall nanotube, are built from a hexagonal lattice of  $\text{sp}^2$  bonded carbon [58], a catalytic-assembly solvothermal route using the planar aromatic hexachlorobenzene ( $\text{C}_6\text{Cl}_6$ ) was developed to prepare multiwalled carbon nanotubes [59], see Reaction (15):



In the reaction, the freshly formed free  $\text{C}_6$  species can assemble into hexagonal carbon clusters, which can grow into nanotubes at the surface of the catalyst par-



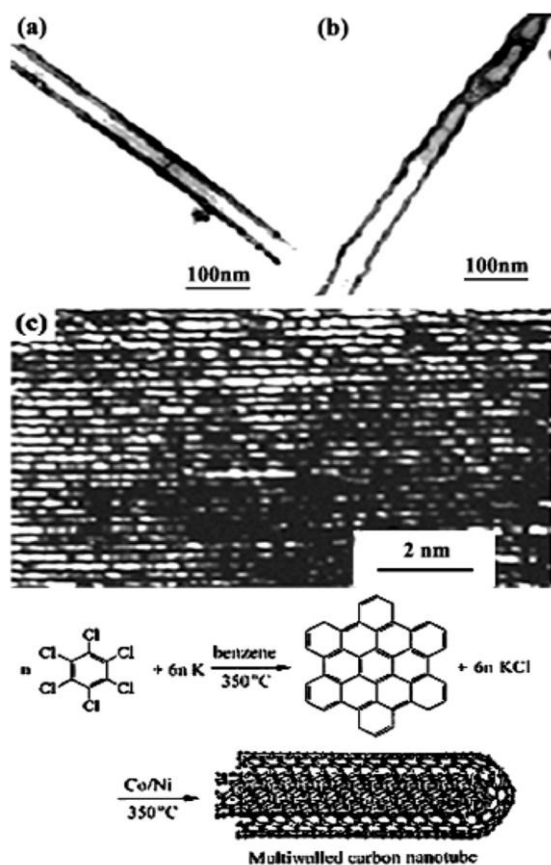
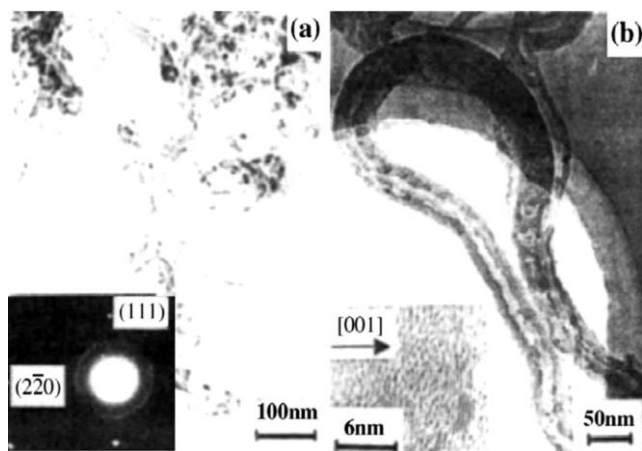


Fig. 7.15. TEM (a) and (b) and HRTEM image (c) of the multiwall carbon nanotubes prepared by a catalytic-assembly solvothermal route.

ticles (Co/Ni). Figure 7.15 shows the TEM and HRTEM images of the as-prepared multiwalled nanotubes. Carbon nanotubes with inner/outer diameter, 5–15 nm/10–35 nm (Figure 7.16(a)) were also prepared using commercial benzene as carbon source and solvent at 480 °C, with micro-size Fe/Ni alloy (46 wt% Ni) as the catalyst [60]. A typical HRTEM image (Figure 7.16(b)) reveals that the nanotube walls are comprised of about 40 graphite monolayers. The least spacing between the lattice stripes is 0.337 nm, which is characteristic of the typical (002) interlayer distance of hexagonal graphite. Tetrachloroethene ( $\text{C}_2\text{Cl}_4$ ) was also used as carbon source for the solvothermal synthesis of carbon nanotubes at 200 °C [61], at the surface of Fe/Au catalyst particles, carbon nanotubes with an inner/outer diameter of 60 nm/80 nm were found, and a Y-junction carbon nanotube was also observed in the TEM images.

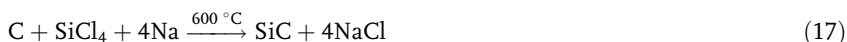
Cubic- or  $\beta$ -SiC nanorods are very attractive semiconductors with potential ap-





**Fig. 7.16.** (a) TEM image of many carbon nanotubes with catalyst in the ends, (insert) SAED pattern of catalyst in the tip of the nanotube, and (b) TEM image of a carbon nanotube of length up to 1.5  $\mu\text{m}$  and (insert) HRTEM image of carbon nanotube.

plications in very-high-speed, high-temperature and high-power devices. The reduction of  $\text{SiCl}_4$  with sodium has already been used to prepare crystalline Si at 375  $^\circ\text{C}$  under high pressure [62]. Ritter [63] has reported a sodium co-reduction of  $\text{SiCl}_4$  and  $\text{CCl}_4$  in a non-polar solvent at 130  $^\circ\text{C}$  to give an amorphous precursor containing Si and C, which required heating at 1450–1750  $^\circ\text{C}$  to form crystalline SiC. When this reaction with excess sodium metal as reductant and flux was carried out in an autoclave at 400  $^\circ\text{C}$  (Reaction (16)),  $\beta$ -SiC nanorods were grown [64]. The TEM images (Figure 7.17(a) and (b)) show that the product consists of nanorods with diameters from 10–40 nm and lengths up to several micrometers. When activated carbon and  $\text{SiCl}_4$  were used as the starting materials (Reaction (17)), nanocrystalline  $\beta$ -SiC was also synthesized at 600  $^\circ\text{C}$  [65]. The TEM images indicate that the SiC powders consist only of spherical particles with an average diameter of 25 nm. Conversely, when using silicon powders and  $\text{CCl}_4$  as the silicon and carbon sources (Reaction (18)), 3C-SiC nanowires (Figure 7.17(c)) of 15–20 nm diameter and length 5–10  $\mu\text{m}$  were prepared through a reduction-carburization route at 700  $^\circ\text{C}$  [66]. In addition, an interesting tubular-like SiC nanowire (Figure 7.17(d)) was also found co-existing in the sample.



TiC nanocrystallites were similarly synthesized at 450  $^\circ\text{C}$  (Reaction (19)).

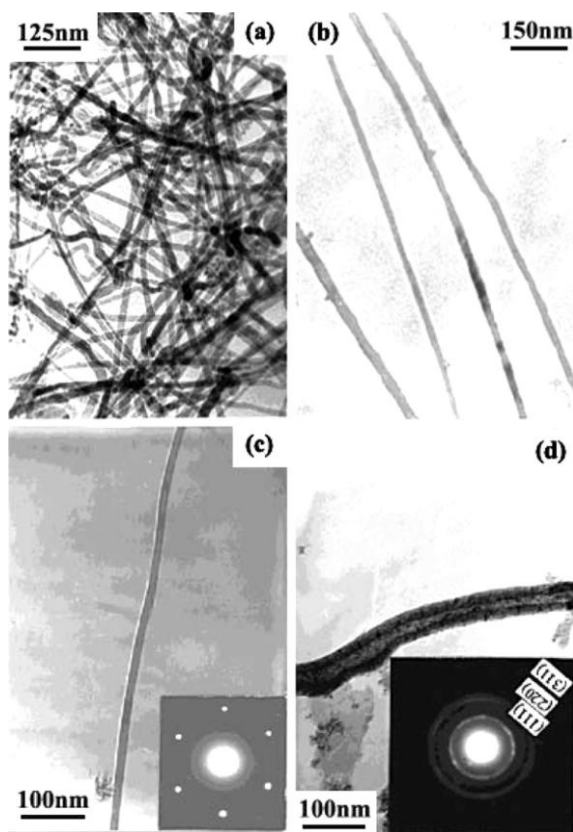


**Fig. 7.17.** (a) and (b) TEM images of SiC nano-wires prepared by sodium co-reduction of  $\text{SiCl}_4$  and  $\text{CCl}_4$  at  $400^\circ\text{C}$ , (c) TEM image of a straight single SiC nanowire and (insert) its ED pattern, and (d) TEM image, and (insert) its ED pattern, of a tubular-like or hollow-structure SiC nano-wire prepared by sodium reduction of  $\text{CCl}_4$  in the presence of silicon powders at  $700^\circ\text{C}$ .



The XRD pattern (Figure 7.18(a)) indicates that the obtained sample is cubic phase TiC, with cell constant  $a = 4.34 \text{ \AA}$ . TEM imaging (Figure 7.18(b)) reveals that it consists of nanoparticles of size 10–20 nm [67]. The co-reduction carburization method may be used to prepare other transition metal carbides. For example, as shown in Reaction (20), nanocrystalline ZrC, size 10–25 nm was synthesized on heating at  $550^\circ\text{C}$  for 12 h [68].



When carbon was used instead of  $\text{CCl}_4$ , 8–12 nm nanocrystalline TiC was also obtained at  $650^\circ\text{C}$  [69].

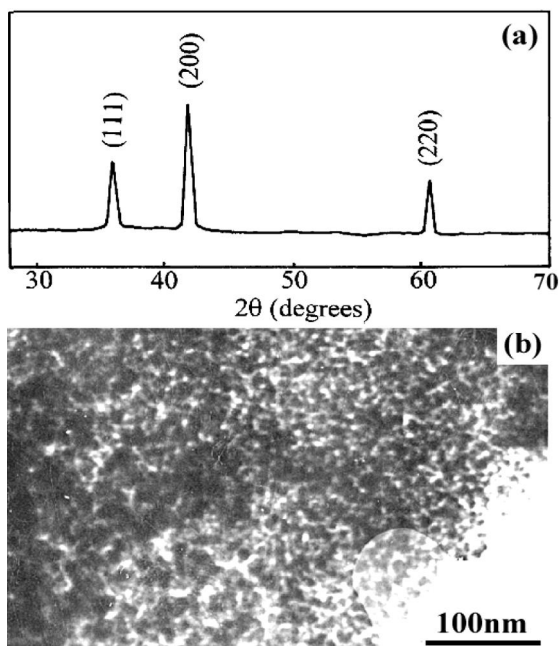


Fig. 7.18. XRD pattern (a) and TEM image (b) of the obtained TiC sample.

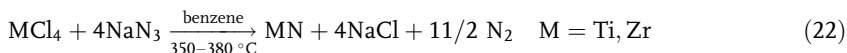
#### 7.4

##### Synthesis of $\text{Si}_3\text{N}_4$ , $\text{P}_3\text{N}_5$ , Metal Nitrides and Phosphides

As shown in Reaction (21), in the liquid–solid reaction of  $\text{CrCl}_3$  and  $\text{Li}_3\text{N}$ , nanocrystalline  $\text{CrN}$  with average particle size of about 25 nm was prepared via a benzene-thermal method in the temperature range 350–420 °C [70]. By using lithium nitride ( $\text{Li}_3\text{N}$ ) instead of explosive  $\text{NaN}_3$ , ultrafine cubic  $\text{ZrN}$  powders of size about 180 nm were prepared in benzene [71].



Nanocrystalline  $\text{TiN}$  of size 50 nm [72] and nanocrystalline  $\text{ZrN}$  of size 10–20 nm [73] were prepared through the benzene-thermal reaction with  $\text{NaN}_3$  (Reaction (22)).



Silicon nitride ( $\text{Si}_3\text{N}_4$ ) is an important material for high-temperature engineering applications due to its chemical stability, high-temperature strength, and excellent creep resistance. A low-temperature preparation of crystalline  $\text{Si}_3\text{N}_4$  has been developed that avoids the elevated temperatures above 1200 °C, which are necessary

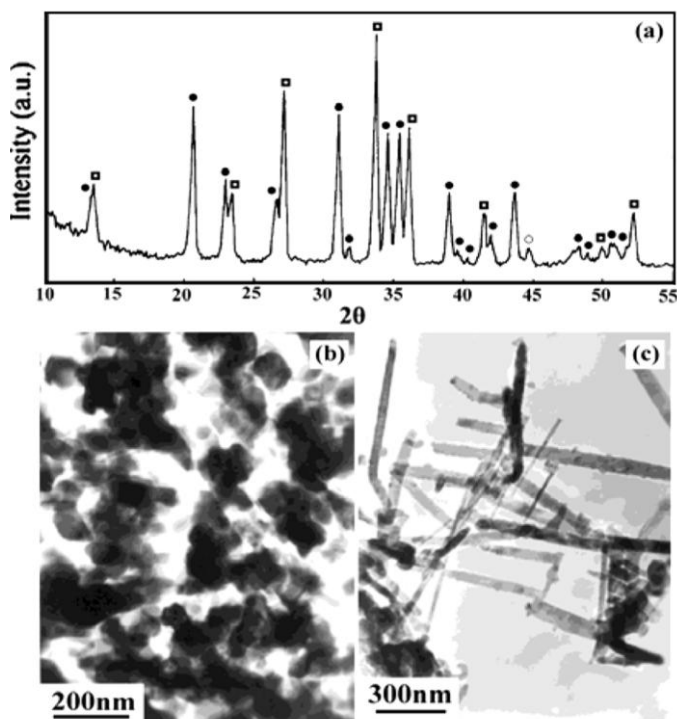
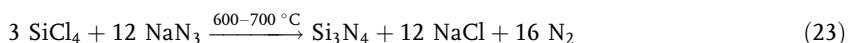


Fig. 7.19. XRD patterns (a) and TEM images of the as-prepared  $\text{Si}_3\text{N}_4$  nanoparticles (b) and nanorods (c). ●,  $\alpha\text{-Si}_3\text{N}_4$ ; ■,  $\beta\text{-Si}_3\text{N}_4$ ; ○,  $\text{Fe}_3\text{Si}$ .

in traditional methods. At 600–700 °C, with excess  $\text{SiCl}_4$  as reactant and solvent, 40–60 nm nanoparticles (Figure 7.19(b)) and 60 × 750 nm nanorods (Figure 7.19(c)) of  $\text{Si}_3\text{N}_4$  were obtained in the same sample (Reaction (23)).



The XRD patterns (Figure 7.19(a)) can be indexed as the hexagonal cell, with lattice parameters  $a = 7.739$ ,  $c = 5.622 \text{ \AA}$  ( $\alpha\text{-Si}_3\text{N}_4$ ).  $\beta\text{-Si}_3\text{N}_4$  was the coexisting phase, with lattice constants  $a = 7.578$ ,  $c = 2.9075 \text{ \AA}$ . The coexisting  $\text{Fe}_3\text{Si}$  may result from the reaction between  $\text{SiCl}_4$  with the surface of the stainless steel reactor [74].

Amorphous phosphorus nitride ( $\text{P}_3\text{N}_5$ ) with flake-like morphology [75] was synthesized from the reaction of  $\text{PCl}_5$  and  $\text{NaN}_3$  in an autoclave at 190–300 °C (Reaction (24)).



When benzene was used as solvent and a hydrogen element source, microtubes, solid balls, hollow balls, and square frameworks (Figure 7.20(a)–(d)) of amorphous

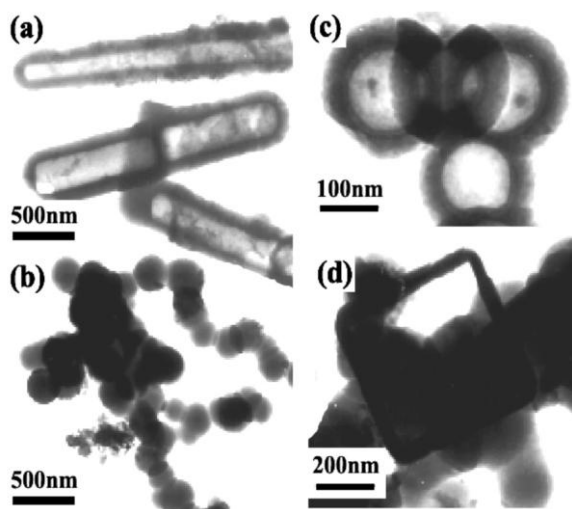
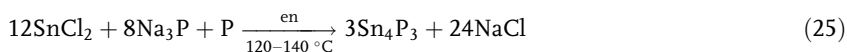


**Fig. 7.20.** TEM images of the amorphous  $\text{HPN}_2$  microtubes (a), solid balls (b), hollow balls (c) and square frameworks (d) prepared at 190–250 °C for 0.5 to 10 days by reacting  $\text{PCl}_5$  with  $\text{NaN}_3$  in benzene.

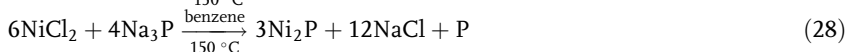
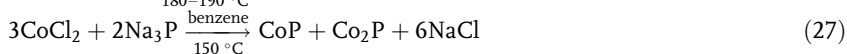
phosphorus nitride imide ( $\text{HPN}_2$ ) were prepared under mild conditions [76]. As an inorganic polymer, amorphous  $\text{HPN}_2$  with these interesting morphologies may see potential uses in industry.

Metal phosphides are made conventionally by direct combination of the elements or by the reaction of highly toxic phosphines with metal or metal hydride via the metal organic chemical vapor deposition or high-temperature self-propagation synthesis route. Based on metathesis reactions, phosphides can be obtained under milder conditions through a solvothermal process. For example, reacting  $\text{SnCl}_2$  with  $\text{Na}_3\text{P}$  synthesized  $\text{Sn}_4\text{P}_3$  nanorods at 120–140 °C (Reaction (25)) using en as the solvent and template [77].



The XRD pattern (Figure 7.21(a)) is indexed as a hexagonal cell with  $a = 3.98$  and  $c = 35.34$  Å. The TEM image (Figure 7.21(b)) indicates that the diameter of the nanorods is about 20 nm and the length up to 400 nm.

As shown in Reactions (26)–(28), similar routes can be used to prepare iron group phosphides.



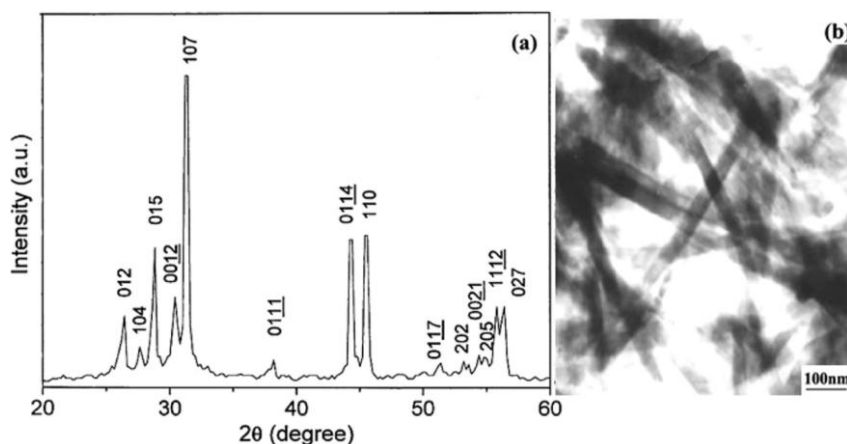
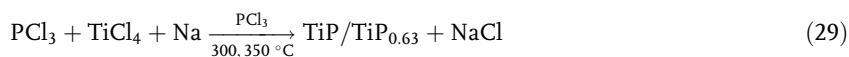


Fig. 7.21. XRD pattern (a) and TEM image (b) of the as-prepared Sn<sub>4</sub>P<sub>3</sub> nanorods.

Figure 7.22 shows the FeP [78], Co<sub>2</sub>P/CoP [79] and Ni<sub>2</sub>P [80] synthesized by solvothermal metathesis reactions.

Metal phosphide nanoparticles of Co<sub>2</sub>P, Ni<sub>2</sub>P and Cu<sub>3</sub>P were also prepared in en at 80–140 °C, when the diamine solvent serves as an N-chelating ligand and reagent for scavenging chlorine from the metal salts [81]. Recently, titanium phosphides were synthesized via solvothermal co-reduction of PCl<sub>3</sub> and TiCl<sub>4</sub> at 300 and 350 °C using metallic sodium as reductant (Reaction (29)) [82].



## 7.5

### Synthesis of BN, B<sub>4</sub>C, BP and Borides

Nanomaterials of boron-containing inorganic compounds and borides have received considerable attention due to their potential application in electronics, op-

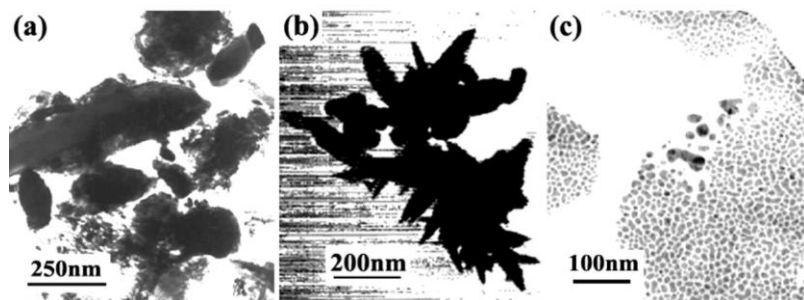


Fig. 7.22. TEM images of FeP (a), Co<sub>2</sub>P/CoP (b) and Ni<sub>2</sub>P (c) prepared by solvothermal metathesis reactions.

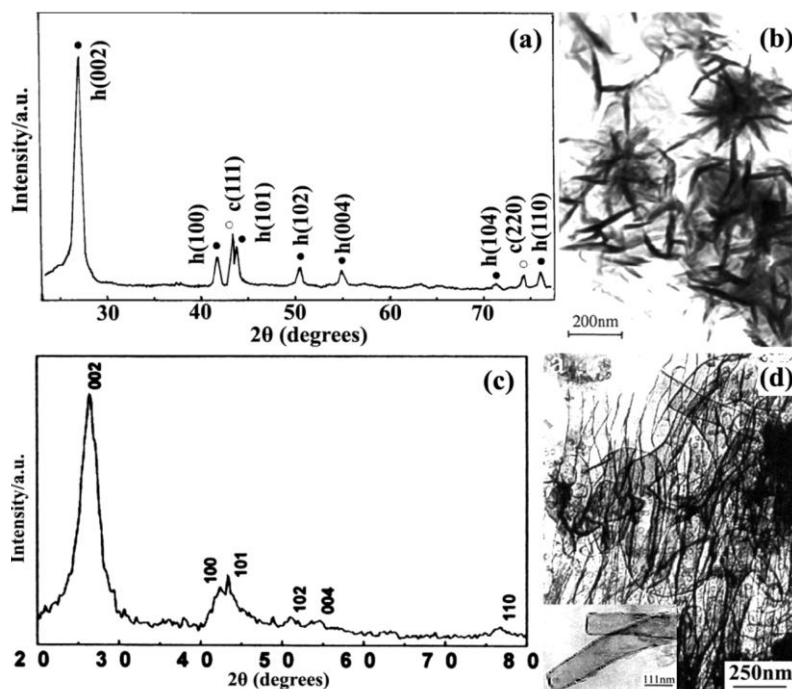
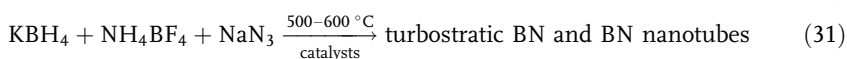


Fig. 7.23. XRD patterns and TEM images of the nanocrystalline BN (a) and (b) and BN nanotubes (c) and (d).

tics, catalysis, and magnetic storage. Unlike the traditional methods, which involve using high temperatures, toxic organometallic precursors, or complicated reactions and post-treatments, the solvothermal method may be a mild synthetic route to these materials.

Cubic BN is widely used in cutting tools and as grinding, and abrasive material. Nanocrystalline BN was prepared by the reaction of  $\text{KBH}_4$  and  $\text{NH}_4\text{Cl}$  at  $650^\circ\text{C}$  [83], Reaction (30). The XRD pattern (Figure 7.23(a)) indicates that the product consists of hexagonal and cubic BN. The TEM image (Figure 7.23(b)) shows the BN powders consist of whisker-like particles with an average size of  $250\text{ nm} \times 10\text{ nm}$ . Cui and co-workers reported that much more of the cubic phase of BN can be obtained via the benzene-thermal reaction of  $\text{BBr}_3$  and  $\text{Li}_3\text{N}$  at about  $450^\circ\text{C}$  [84, 85]. BN nanotubes were prepared via a precursor-pyrolysis route at  $500$  to  $600^\circ\text{C}$  by reacting  $\text{KBH}_4$ ,  $\text{NH}_4\text{BF}_4$  and  $\text{NaN}_3$  in the presence of catalysts (Reaction (31)). Figure 7.23(c) and (d) shows the XRD pattern and TEM image of the as-prepared turbostratic BN and BN nanotubes [86].





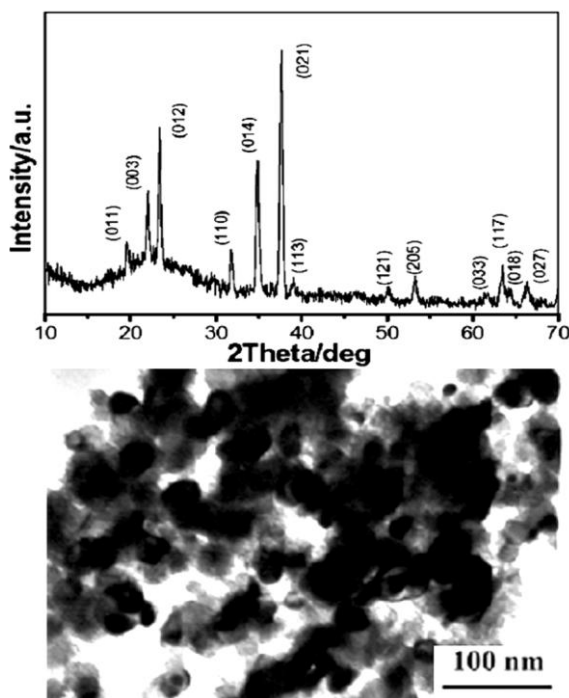
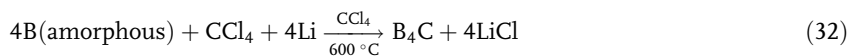


Fig. 7.24. XRD pattern (a) and TEM image (b) of the B<sub>4</sub>C sample prepared by reduction of CCl<sub>4</sub> in the presence of amorphous boron powder at 600 °C.

Boron carbide (B<sub>4</sub>C) is one of the hardest known materials with excellent properties of low density, very high chemical and thermal stability, and high neutron absorption cross-section. Bulk B<sub>4</sub>C is conventionally synthesized by high temperature (up to 2400 °C) reactions, such as the carbothermal reduction of boric acid or boron oxide. Nanocrystalline B<sub>4</sub>C was solvothermally synthesized in CCl<sub>4</sub> at 600 °C (Reaction (32)).



As shown in Figure 7.24, the XRD pattern can be indexed to the hexagonal B<sub>4</sub>C phase with lattice constants  $a = 5.606$  and  $c = 12.089$  Å. The TEM study shows that the B<sub>4</sub>C nanocrystallites are slightly agglomerated, with a particle size of 15–40 nm [87].

Boron phosphide (BP), a semiconductor with an indirect band gap of 2 eV, is one of the most promising high-temperature thermoelectric materials due to its outstanding chemical, mechanical, optical and thermal properties. Traditionally, BP is



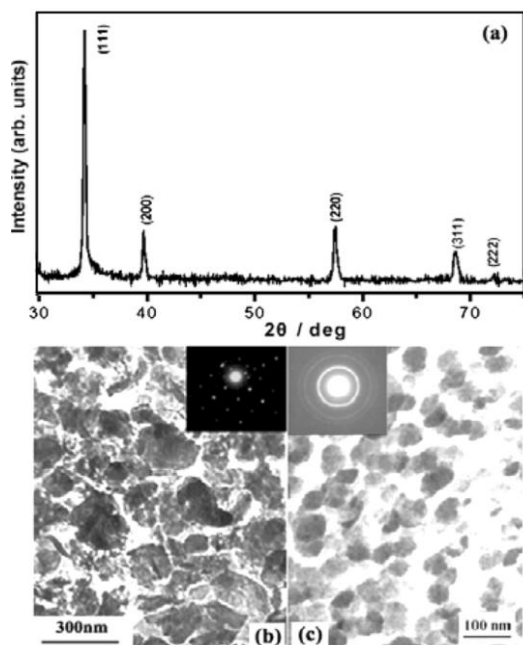
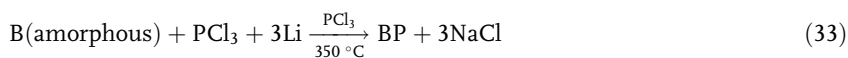


**Fig. 7.25.** XRD pattern and TEM images of the BP samples prepared by reduction of  $\text{PCl}_3$  in the presence of amorphous boron powders at  $350\text{ }^\circ\text{C}$  (a) and (b) and by Na co-reduction of  $\text{PCl}_3$  and  $\text{BBr}_3$  at  $300\text{ }^\circ\text{C}$  in benzene (c).

prepared by various high-temperature reactions (up to  $1000\text{ }^\circ\text{C}$ ). Through metal lithium reduction of  $\text{PCl}_3$  in the presence of amorphous boron powders at  $350\text{ }^\circ\text{C}$  (Reaction (33)), ultrafine cubic BP powders (Figure 7.25(a) and (b)) were synthesized via a benzene-thermal method [88]. When  $\text{BBr}_3$  was used instead of amorphous boron powders (Reaction (34)), nanocrystalline BP powders of about  $30\text{ nm}$  in size (Figure 7.25(c)) were prepared under milder conditions [89].



In a similar way, nanocrystalline  $\text{TiB}_2$  was prepared at  $350\text{ }^\circ\text{C}$  (Reaction (35)).



As shown in Figure 7.26, the XRD pattern can be indexed to the hexagonal cell of  $\text{TiB}_2$ , with lattice constants  $a = 3.027$  and  $c = 3.228\text{ \AA}$ . The TEM image indicates that the particle size is in the range  $15$  to  $40\text{ nm}$  [90].

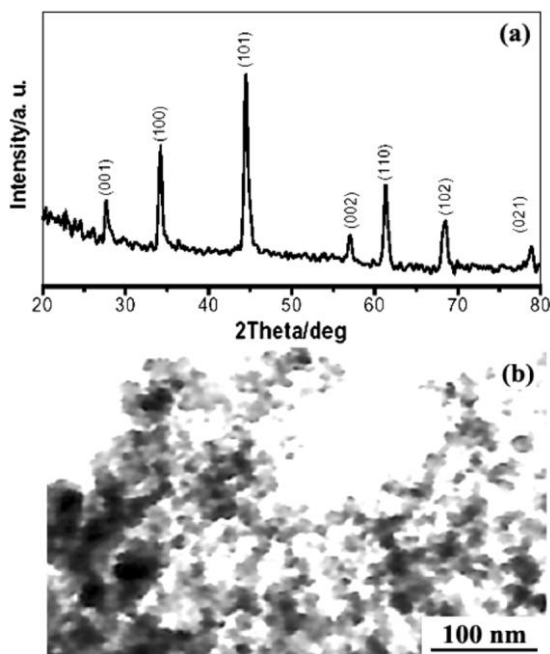


**Fig. 7.26.** XRD pattern (A) and TEM image (B) of the TiB<sub>2</sub> sample prepared by Na reduction of TiCl<sub>4</sub> in the presence of amorphous boron powders at 350 °C.

## 7.6

### Synthesis of One-Dimensional Metal Chalcogenide Nanocrystallites

Morphology control is very important for nanomaterials preparation due to the remarkable properties and potential applications of these materials ranging from microscopy probes to nanoelectronic devices. Therefore, current attention has focused on the development of convenient approaches to the preparation of nanomaterials with controlled shapes and sizes. The solvothermal method has been developed into a practical means of synthesis and controlling the morphology. By designing reactions, choosing solvents, controlling reaction temperatures and so forth, a series of metal chalcogenide nanomaterials, especially those with one-dimensional and special shapes, have been prepared.

Quantum-confined CdS nanowires (Figure 7.27) (4 nm × 150–250 nm) were grown from the decomposition of the precursor, cadmium bis(diethylthiocarbamate), in en at 117 °C for 2 min [91]. Using this synthetic route, CdIn<sub>2</sub>S<sub>4</sub> nanorods were prepared in an en/ethanol mixed solvent at 180 °C (Figure 7.28). The ethanol acts as the transportation reagent for InCl<sub>3</sub> while the en serves as the nucleophile, which causes scission of the thione groups in the cadmium bis(diethylthiocarbamate) molecules and forms inorganic Cd<sub>2</sub>S<sub>2</sub> cores. These newly formed cores as-

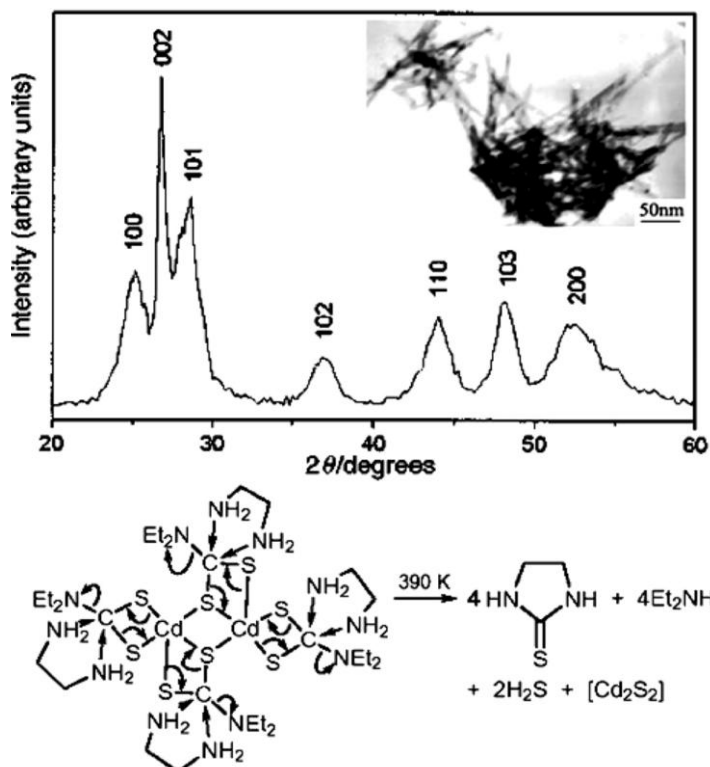


**Fig. 7.27.** XRD pattern, TEM image (insert) of the CdS nanowires prepared by precursor decomposition in organic solvent.

semble into one-dimensional  $[\text{CdS}]_n$  clusters and act as intermediate templates for the subsequent growth of CdS nanorods [92].

Using thiosemicarbamide as the sulfur source, CdS nanowhiskers ( $60 \text{ nm} \times 12 \text{ }\mu\text{m}$ ) were grown via a solvothermal route [93]. Rod-, twinrod- and tetrapod-shaped CdS nanocrystals were obtained from spherical CdS nanocrystals via a solvothermal recrystallization technique [94]. Nanowires of CdS/CdSe core/sheath nanostructure were prepared by treating CdS nanowires with selenium in tributylphosphine at  $100 \text{ }^\circ\text{C}$  [95]. Nanorods of CdE ( $\text{E} = \text{S}, \text{Se}$  or  $\text{Te}$ ) with  $10\text{--}40 \text{ nm}$  diameters and several micrometers in length, were grown by choosing coordinating solvents such as en and 1,6-diaminohexane [96, 97]. When metal salts are used as starting materials, reducing reagents such as metallic sodium or hydrazine may be used as reductants. MSe ( $\text{M} = \text{Zn}$  or  $\text{Cd}$ ) nanorods were prepared at  $80\text{--}100 \text{ }^\circ\text{C}$  in en [98].

By choosing ligand solvents, nanocrystalline CdE can be synthesized by the reactions of  $\text{CdC}_2\text{O}_4$  with E ( $\text{E} = \text{S}, \text{Se}$  or  $\text{Te}$ ) in polyamines such as en, diethylenetriamine and triethylenetetramine. CdS nanorods (Figure 7.29(a)) and nano-

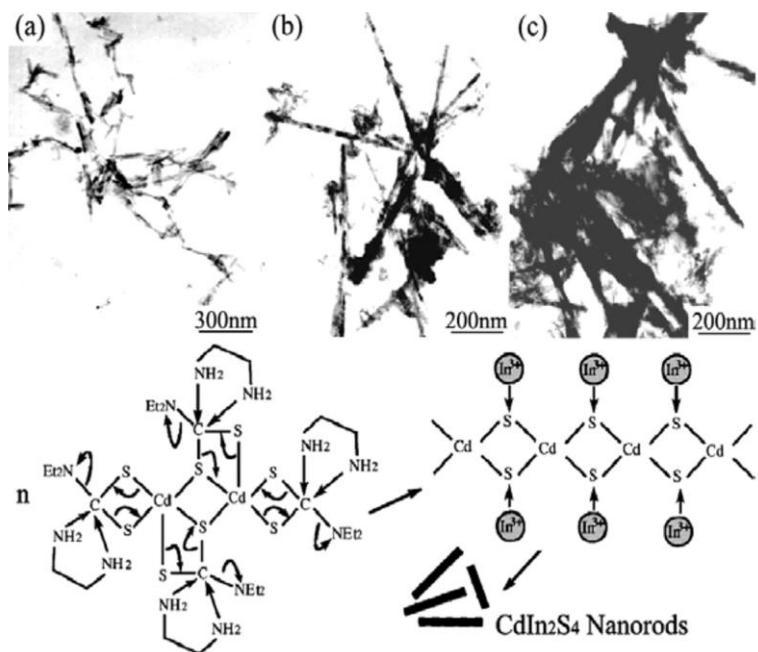


**Fig. 7.28.** TEM images of the  $\text{CdIn}_2\text{S}_4$  nanorods prepared in mixed solvents with different ethanol/ethylenediamine ratios: 1/3 (a), 1/1 (b) and 3/1 (c).

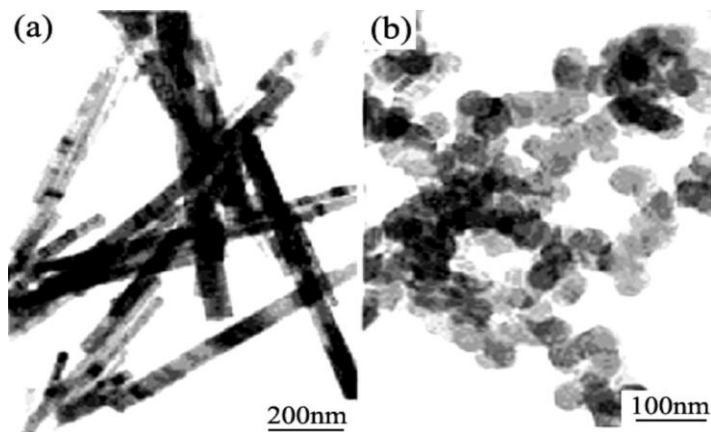


**Fig. 7.29.** TEM images of the  $\text{CdS}$  nanocrystals prepared in different solvents: (a) ethylenediamine, (b) pyridine.

particles (Figure 7.29(b)) were synthesized at 180 °C in en and pyridine, respectively [99].

The en molecules play an important role in controlling the nucleation and growth of the CdS nanorods. As a bidentate ligand, en molecules may react with  $\text{Cd}^{2+}$  ions and form relatively stable complexes. Under appropriate solvothermal conditions, the complexes become unstable and decompose, which results in the formation of CdS nanorods [100]. A mono-dentate ligand, n-butylamine, was found to be a shape controller for nanorods of CdS and MSe ( $\text{M} = \text{Zn}, \text{Cd}$  or  $\text{Pb}$ ) [101]. Similarly, the precursor of  $\text{ZnE(en)}_{0.5}$  ( $\text{E} = \text{S}, \text{Se}$ ) could also form in en which then is converted to ZnSe nanoparticles via pyrolysis in solvothermal conditions [102]. The coordinating ability of the solvent was found to play an important role in the nucleation and growth of nanocrystallites [103].

Polymer-shape-controlled solvothermal synthesis is efficient for fabricating one-dimensional nanomaterials. Using polyacrylamide as growth controller, CdS nanowires with homogeneous size distribution were grown at 170 °C for 10 days in en [104]. As shown in Figure 7.30, the SEM and TEM images show lengths up to 100  $\mu\text{m}$  with diameters of about 40 nm. In the synthetic process,  $\text{Cd}^{2+}$  ions were well distributed in the polymer matrix. The polymer may absorb solvent and form

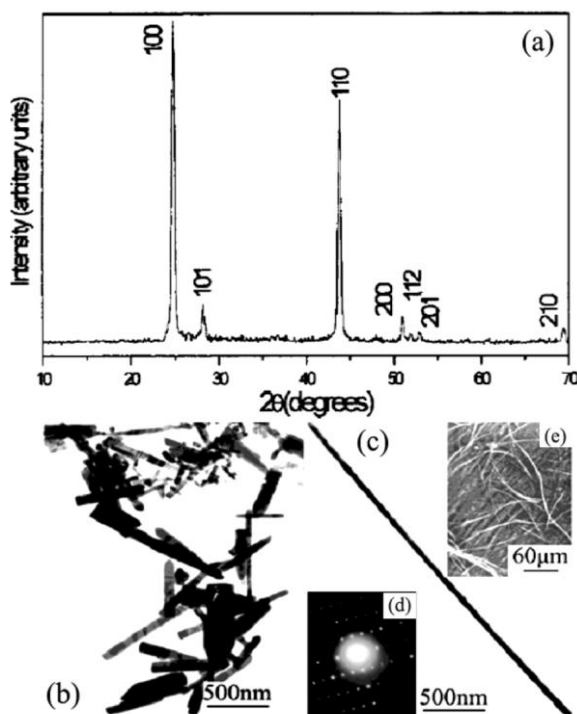


Fig. 7.30. XRD pattern (a), TEM image (b), (c), ED pattern (d) and SEM image (e) of the CdS nanowires prepared by a polyacrylamide-controlled solvothermal method.

a gel with small pores. It was supposed that the growth of CdS nanocrystallites was confined within the pores to form nanowires. Sphalerite-type CdSe nanowires were fabricated through a poly(vinyl alcohol) (PVA) assisted solvothermal reaction at 160–180 °C in en [105]. These as-prepared nanowires exhibit straight or zigzag shapes and most of them are grown with [111] orientation.

Rod-shaped PbS nanocrystals with diameters of 30–160 nm and lengths of up to several micrometers were also prepared by a biphasic solvothermal interface reaction at 140–160 °C [106]. Closed PbS nanowires with regular geometric morphologies (ellipse and parallelogram shape) were prepared with shape control by the polymer poly[*N*-(2-aminoethyl) acrylamide] in en and H<sub>2</sub>O (3:1, v/v) solvent at 110–150 °C [107]. VA group chalcogenides, nanorods or nanowires, were also solvothermally prepared, e.g., Sb<sub>2</sub>E<sub>3</sub> [108, 109], Bi<sub>2</sub>E<sub>3</sub> (E = S or Se) [110, 111, 112] and Bi<sub>3</sub>Se<sub>4</sub> [113].

Interestingly, a novel  $\alpha$ -NiS layer-rolled structure, intermediate between a two-dimensional layered structure and three-dimensional isotropic material, was prepared by adding CS<sub>2</sub> step-by-step to an aqueous ammonia solution containing Ni(NH<sub>3</sub>)<sub>6</sub><sup>2+</sup> ions at about 60 °C [114]. By reacting CS<sub>2</sub> with Ni(NH<sub>3</sub>)<sub>6</sub><sup>2+</sup>, a new complex, Ni(NH<sub>3</sub>)<sub>3</sub>(CS<sub>3</sub>), may form. These complexes orientate and become linked in the least destabilizing mutual arrangement due to the NH–H<sub>2</sub>O hydrogen bonds. These linked complexes decompose on heating to produce the novel structure. The TEM images (Figure 7.31(a) and (b)) show strong contrast between the dark edges and the pale center, indicating the hollow nature of the particles. The contrast at the tip opening is evidence of an open rolled structure, like a broken tube. HRTEM (Figure 7.31(c) and (d)) shows different lattice features in the edge and center parts, indicating a multi-walled structure.

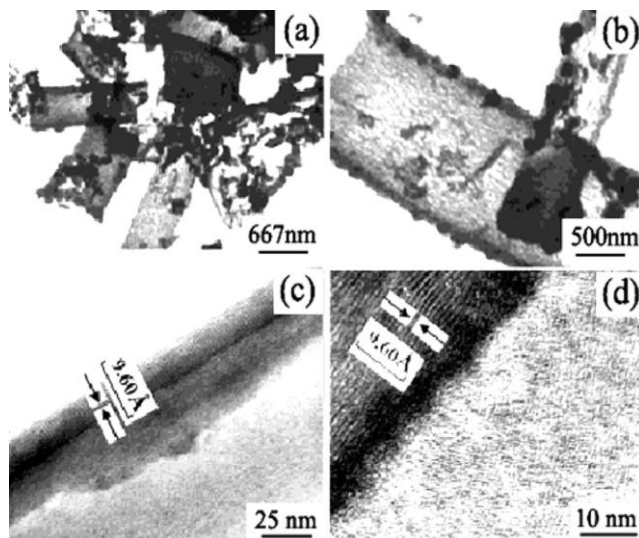


Fig. 7.31. TEM and HRTEM images of the layer-rolled NiS structures.

Reaction temperature and solvent conditions affect the phase transition and morphology of metal chalcogenides. With increasing temperature,  $\text{NiSe}_2$  nanocrystals prepared through solvothermal-reduction at low temperatures transform from an initial filament to a final octahedron [115]. In different solvents, the well-crystallized nickel selenides obtained, such as  $\text{NiSe}_2$ ,  $\text{Ni}_{0.85}\text{Se}$  and  $\text{Ni}_3\text{Se}_2$ , showed different morphologies [116]. The synthesis of  $\text{NiS}$ , using en and hydrazine hydrate as solvent, resulted in a rod-like nanocrystalline product, whereas spherical nanoparticles were obtained in aqueous ammonia [117]. Two different phases of  $\alpha$ - (hexagonal,  $P6_3/mmc$ ) and  $\beta$ - (rhombohedral,  $R3m$ )  $\text{NiS}$  nanocrystals were obtained by hydrazine reduction of  $\text{NiCl}_2 \cdot 6\text{H}_2\text{O}$  in the presence of sulfur at  $110^\circ\text{C}$  in ethanol and pyridine, respectively [118].

The metastable  $\beta$ - and  $\gamma$ - $\text{MnS}$  crystallites were obtained at about  $200^\circ\text{C}$  in tetrahydrofuran and benzene, whereas in water, ammonia liquor, en, the metastable phases converted to the stable phase of  $\alpha$ - $\text{MnS}$  [119]. However, only the stable phase of  $\alpha$ - $\text{MnSe}$  can be obtained by solvothermal reaction at  $190^\circ\text{C}$  in en [120].

In the solvothermal synthesis of the I–III–VI<sub>2</sub> ternary compound semiconductors, organic amines are normally used as solvents for the reactants and as ligands to form metal complexes. In the reaction system  $\text{InCl}_3 \cdot 4\text{H}_2\text{O}$ ,  $\text{CuCl}_2 \cdot 2\text{H}_2\text{O}$  and elemental selenium at  $180^\circ\text{C}$ ,  $\text{CuInSe}_2$  nanowhiskers with widths of 3–6 nm and lengths of 30–80 nm were prepared in en, whereas in diethylamine and pyridine, the product was only spherical nanoparticles [121]. Therefore, bidentate ligands may be more effective than monodentate ligands for directional growth of chalcogenide nanocrystals. Nanorods of  $\text{CuME}_2$  ( $\text{M} = \text{In}$  or  $\text{Ga}$ ,  $\text{E} = \text{S}$  or  $\text{Se}$ ) were also prepared by elemental reactions in en at  $200$ – $280^\circ\text{C}$  [122, 123]. From a stoichiometric mixture of the single-molecule precursors  $\text{M}(\text{S}_2\text{CNET}_2)_3$  ( $\text{M} = \text{In}$ ,  $\text{Cu}$ ,  $\text{Ag}$ ), nanorods of  $\text{MInS}_2$  ( $\text{M} = \text{Cu}$  or  $\text{Ag}$ ) were prepared by removing the thione groups with en solvent at  $195^\circ\text{C}$  [124]. Nanocrystalline  $\text{AgGaS}_2$  and  $\text{AgInS}_2$  with particle sizes ranging from 5 to 12 nm were prepared by reacting  $\text{AgCl}$ , sulfur, elemental gallium or indium in en at  $180$ – $230^\circ\text{C}$  [125].

Some other ternary chalcogenides have also been prepared by the solvothermal method, such as  $\text{Cu}_{5.5}\text{FeS}_{6.5}$  nanotubes [126],  $\text{AgBiS}_2$  nanowhiskers [127],  $\text{Cu}_2\text{SnS}_3$  [128],  $\text{Cu}_2\text{SnSe}_4$  [129],  $\text{CuSbS}_2$  and  $\text{Ag}_3\text{SbS}_3$  [130] nanoparticles.

## 7.7

### Room Temperature Synthesis of Nanomaterials

Room-temperature synthesis of nanomaterials can be realized by designing suitable reactions under some special solution conditions, or with the assistance of additional energy supplies such as  $\gamma$ -ray irradiation and ultrasound.

Traditionally, selenides have been synthesized at high temperature ( $>500^\circ\text{C}$ ) by solid-state reaction [131] or self-propagating synthesis [132]. A high-energy ball milling method at room temperature has also been used [133], however, the product quality was difficult to control. In liquid ammonia, a low-temperature route to selenides was developed [134]. Organometallic precursors have been used to obtain

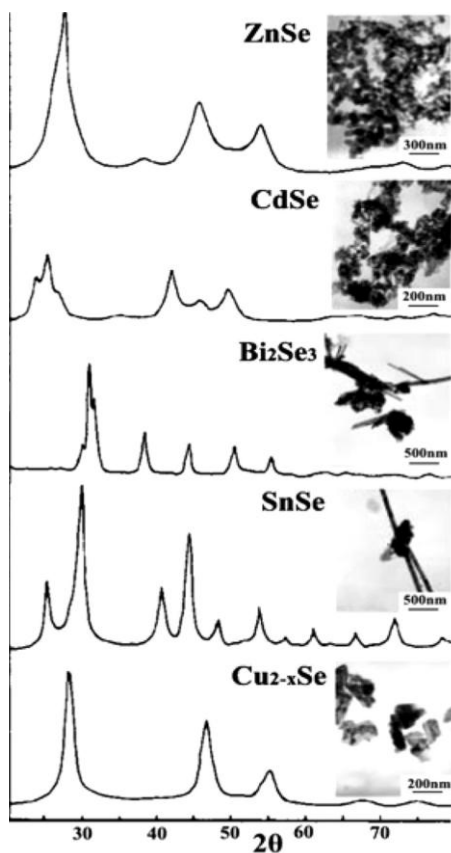


Fig. 7.32. XRD patterns and TEM images of ZnSe, CdSe, Bi<sub>2</sub>Se<sub>3</sub>, SnSe and Cu<sub>2-x</sub>Se nanomaterials prepared in ethylenediamine at room temperature.

selenides, but crystallization-treatment at 250–500 °C was necessary [135]. Therefore, it is necessary to explore a milder and simpler synthetic route for metal selenide nanocrystallites.

By using KBH<sub>4</sub>, nanocrystalline MSe (M = Sn, Bi, Zn, Cd or Cu) (see Figure 7.32) was prepared from mixtures of MCl<sub>n</sub> (SnCl<sub>2</sub>, BiCl<sub>3</sub>, ZnCl<sub>2</sub>, CdCl<sub>2</sub> or CuCl<sub>2</sub>), and elemental selenium at ambient temperature (about 20 °C) and pressure in en [136]. It was supposed that the KBH<sub>4</sub> reduced elemental selenium to Se<sup>2-</sup> ions, which then reacted with metal ions M<sup>n+</sup> to form MSe. A similar process was used to prepare PbSe nanowires from PbCl<sub>2</sub>, elemental selenium and KBH<sub>4</sub> sealed in en at 10 °C for 4 h [137].

Some novel solution routes have been designed for preparing cadmium chalcogenides with special morphologies. By an unusual in-situ source–template–interface method, in which CdCl<sub>2</sub> reacted with H<sub>2</sub>S, generated by adding CS<sub>2</sub> to an



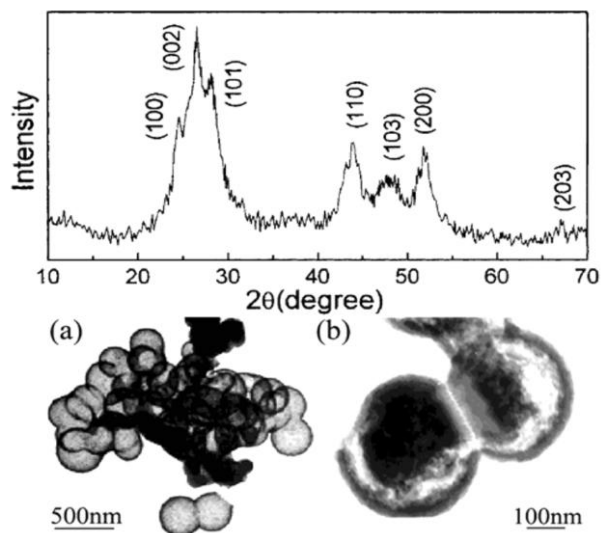


**Fig. 7.33.** XRD pattern and TEM images of the hollow spheres (a) and the peanut-like (b) structures of CdS.

aqueous en solution, forming CdS on the  $\text{CS}_2$ -water interface, hollow spheres [138] and a novel peanut-like structures of CdS [139] were prepared (Figure 7.33) under mild conditions.

Some other nanocrystallites with different morphologies were also prepared by room-temperature processes, such as a novel non-layered compound  $\text{Cu}_{2-x}\text{Se}$  nanotubes (Figure 7.34), CuE and AgE (E = Se or Te) nanocrystallites (nanotubes,

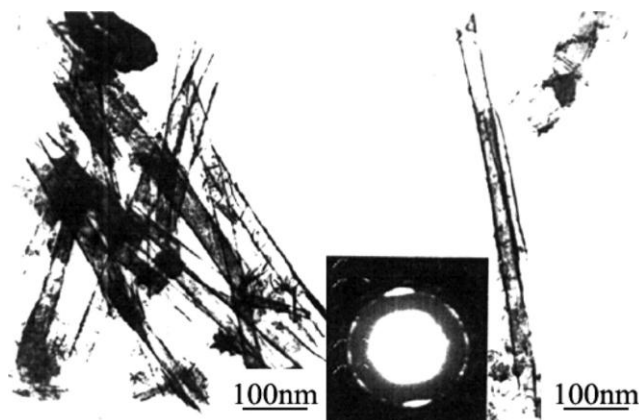


**Fig. 7.34.** TEM and TED images of  $\text{Cu}_{2-x}\text{Se}$  nanotubes from hydrazine,  $\text{CuCl}_2$  and selenium in ethylenediamine at room temperature.

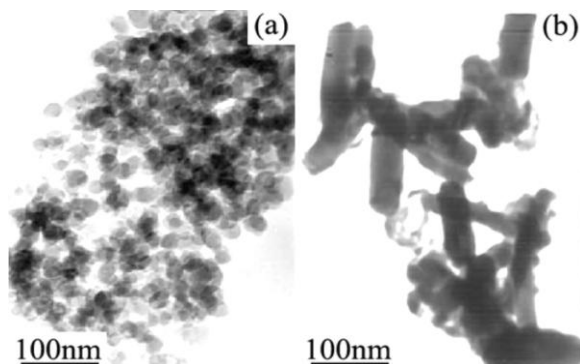


**Fig. 7.35.** TEM images of  $\text{Ag}_2\text{Se}$  (a) and  $\text{Ag}_2\text{Te}$  (b) prepared at room temperature in pyridine and in the mixed solvent of ethylenediamine–hydrazine hydrate, respectively.

nanorods and nanoparticles) [140], rod-like nanocrystalline  $\text{Ag}_2\text{Te}$  (30 nm  $\times$  120 nm, Figure 7.35) [144], and spherical nanoparticles of  $\text{Ag}_2\text{Se}$  ( $\sim 25$  nm) [142].

The  $\gamma$ -ray irradiation synthesis method, which can be carried out at ambient temperature and pressure in aqueous or non-aqueous solutions, has been developed to prepare nanomaterials of metals, alloys, elemental chalcogens, chalcogenide semiconductors and inorganic/polymer nanocomposites.

Nanocrystalline cobalt powders (14–42 nm) were prepared from aqueous ammonia solutions of  $\text{CoSO}_4 \cdot 7\text{H}_2\text{O}$  or  $\text{CoCl}_2 \cdot 6\text{H}_2\text{O}$  and surfactants (polyvinyl alcohol or sodium dodecyl sulfate) at ambient conditions by  $\gamma$ -ray irradiation (a dose rate, 67 Gy  $\text{min}^{-1}$  in a  $^{60}\text{Co}$   $\gamma$ -ray field,  $8 \times 10^6$  eV) [143]. In the process,  $\text{OH}^\cdot$  and  $\text{H}^\cdot$  radicals,  $\text{H}_2\text{O}_2$ ,  $\text{H}_2$ ,  $\text{H}_3\text{O}^+$  and hydrated electrons ( $e_{\text{aq}}^-$ ) may be generated from  $\text{H}_2\text{O}$  upon  $\gamma$ -ray irradiation. The hydrogen radicals and hydrated electrons reduce  $\text{Co}^{2+}$  and  $\text{Co}^+$ , forming metallic cobalt atoms, which then aggregate to give nanoparticles, which are stabilized by the surfactants, and precipitate from the aqueous solution. In a similar way, nanocrystalline Ag [144], Cd [145], Se [146] and ultra-fine Cu–Pd alloy [147] were also prepared by a  $\gamma$ -ray irradiation method.

30 nm PbSe nanoparticles [148] and nanorods (60 nm  $\times$  700 nm) [149] were prepared by a  $\gamma$ -ray irradiation method in en- $\text{H}_2\text{O}$  solution at room temperature. In the process, selenium disproportionates by  $\text{OH}^-$  to form  $\text{Se}^{2-}$  and  $\text{SeO}_3^{2-}$ , followed by co-reduction of the  $\text{Se}^{2-}$  and  $\text{Pb}^{2+}$  by the hydrogen radicals (H) and/or hydrated electrons ( $e_{\text{aq}}^-$ ) forming PbSe. Crystalline CdS, PbS,  $\text{Cu}_2\text{S}$ , and  $\text{Ag}_2\text{S}$  nanoparticles were also prepared in aqueous en media under ambient conditions under  $\gamma$ -ray irradiation [150].

By  $\gamma$ -ray irradiation at room temperature, ZnS nanowires were grown, in which the crystal growth was in situ templated by an inverted hexagonal liquid crystal formed from oligo(ethylene oxide)oleyl ether amphiphiles, n-hexane, n-hexanol/isopropanol (2/1) and water [151]. Nanocrystalline  $\beta$ -ZnS (sphalerite) was prepared in aqueous isopropanol solution [152]. The TEM images (Figure 7.36) indicate that the product from mercaptoethanol is most well dispersed, and that from thiourea

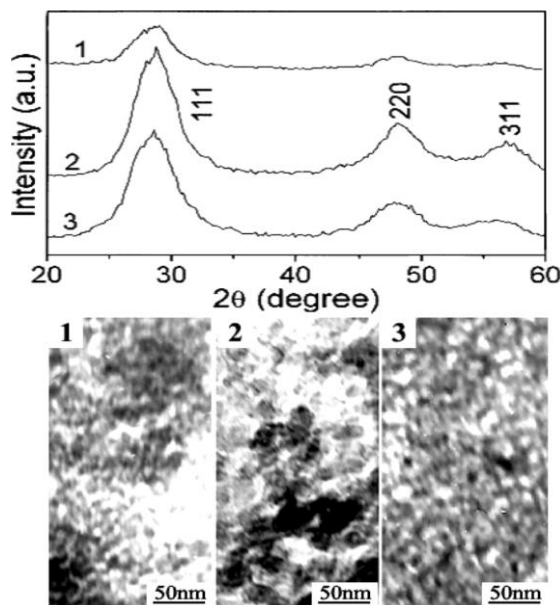


**Fig. 7.36.** XRD patterns and TEM images of nanocrystalline  $\beta$ -ZnS prepared by a  $\gamma$ -irradiation method with different sulfur sources: sodium thiosulfate (1), thiourea (2) and mercaptoethanol (3).

aggregates most heavily. By using  $\text{CS}_2$  as the sulfur source, nanocrystalline CdS of sphalerite and wurtzite structure [153] and nanocrystalline MS ( $\text{M} = \text{Pb}$  or  $\text{Cu}$ ) [154] were prepared. Similarly, when  $\text{NaSeSO}_3$  was used as the selenium source, 10 nm nonstoichiometric  $\text{Cu}_{2-x}\text{Se}$  was obtained [155].

As various organic monomers, such as acrylamide, acrylonitrile, vinyl acetate, maleic acid and styrene, can polymerize at the same time as forming inorganic nanomaterials, various kinds of polymer–inorganic nanocomposites can be prepared at room temperature by a  $\gamma$ -irradiation synthesis method.

The  $\gamma$ -ray irradiation method offers a practical means for fabrication of inorganic/polymer core/sheath nanostructures under ambient conditions. From a heterogeneous system of vinyl acetate monomer,  $\text{CdSO}_4 \cdot 8\text{H}_2\text{O}$  and  $\text{Na}_2\text{SeSO}_3$  in aqueous isopropanol solution, novel nanocables of CdSe-core/poly(vinyl acetate)-sheath were prepared under  $\gamma$ -irradiation at room temperature [156]. As shown in Figure 7.37, the TEM images show that the as-prepared nanocable has an inner diameter as small as 6 nm, an outer diameter of about 80 nm and is some 5  $\mu\text{m}$  in overall length. The image contrast of CdSe and amorphous polymer can be clearly observed. The electron diffraction pattern indicates the crystalline CdSe core. The HRTEM image reveals the lattice fringes of CdSe nanowire and the amorphous polymer sheath, in which plane the intervals of the CdSe area exactly agree with the (200) plane of cubic CdSe. In the synthetic process, the organic monomers may self-organize and build amphiphilic structures with tubule shapes having coelen-

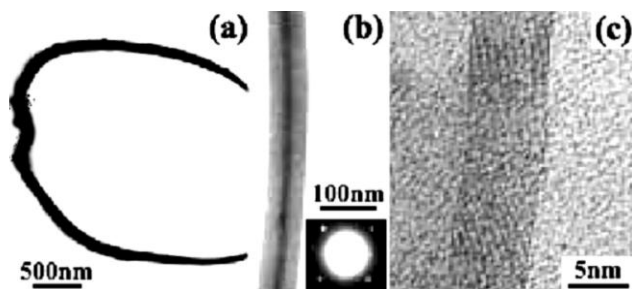


**Fig. 7.37.** Solution route fabricated CdSe-wire/poly(vinyl acetate)-sheath nanocable by  $\gamma$ -irradiation. (a) TEM image at lower magnification; (b) TEM image at higher magnification and inserted ED pattern of the same area; (c) HRTEM image of the nanocable.

terate cavities enveloped by hydrophilic or polar groups of vinyl acetate and co-lenterate walls filled with the monomers. Meanwhile, CdSe is generated in the cavities and proceeds with confined growth into crystalline nanowires, the monomers simultaneously become solidified by  $\gamma$ -ray irradiation polymerization. Therefore, the pre-organized architecture of monomers eventually leads to the core/sheath nanostructures. Similar nanostructures of PbS/poly(vinyl acetate) were also obtained by the  $\gamma$ -ray irradiation method [157].

It is reasonable that, in the synthesis of polymer nanocomposites, the  $\gamma$ -ray irradiation method is convenient for growing nanofibers and nanowires of metal chalcogenides due to the shape-control of the macromolecules formed in situ. Figure 7.38 shows some of the resulting nanofiber-dispersed polymer composites,

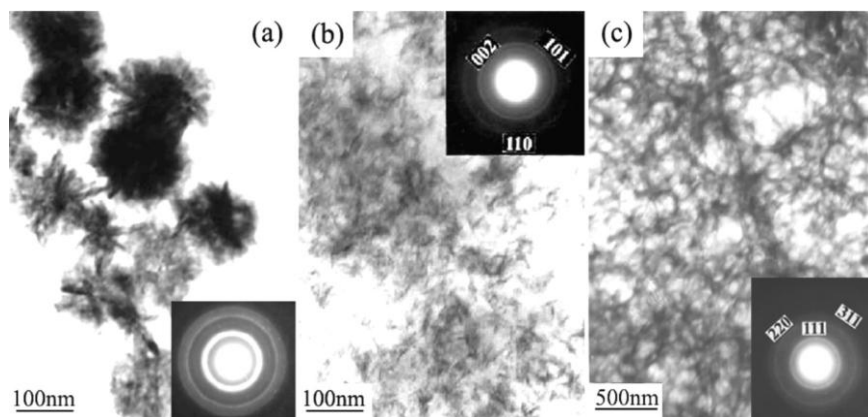


**Fig. 7.38.** TEM images and inserted ED patterns of nanofiber-dispersed polymer composites prepared by a  $\gamma$ -irradiation method. (a) Spherical assembled CdS nanofibers in poly(vinyl acetate); (b) dispersed CdS short nanofibers in poly(styrene-alt-maleic anhydride); (c) very long, entangled CdSe nanofibers in polyacrylamide.

which include spherical assembled CdS nanofibers in poly(vinyl acetate) [158], dispersed CdS short nanofibers in poly(styrene-alt-maleic anhydride) [159] and very long, entangled CdSe nanofibers in a polyacrylamide matrix [160]. Nanocomposites with nanoparticles dispersed in the polymer matrix, such as polyacrylamide/Ag [161], poly(vinyl acetate)/PbS [162], polyacrylamide/CdS [163] and polyacrylonitrile/CdS [164] were also prepared by  $\gamma$ -ray irradiation.

## References

- 1 Y. T. QIAN, Q. W. CHEN, Z. Y. CHEN et al., *J. Mater. Chem.* **1993**, 3 (2), 203–205.
- 2 Q. W. CHEN, Y. T. QIAN, Z. Y. CHEN et al., *Mater. Lett.* **1995**, 22 (1–2), 77–80.
- 3 H. W. LIAO, Y. F. WANG, X. M. LIU et al., *Chem. Mater.* **2000**, 12 (10), 2819.
- 4 C. H. AN, K. B. TANG, G. Z. SHEN et al., *Mater. Lett.* **2002**, 57 (3), 565–568.
- 5 C. H. AN, K. B. TANG, C. R. WANG et al., *Mater. Res. Bull.* **2002**, 37 (11), 1791–1796.
- 6 Q. W. CHEN, Y. T. QIAN, Z. Y. CHEN et al., *Physica C*, **1994**, 224 (3–4), 228–230.
- 7 D. L. ZHU, H. ZHU, Y. H. ZHANG, *Appl. Phys. Lett.* **2002**, 80, 1634.
- 8 Q. W. CHEN, G. ZHOU, J. S. ZHU et al., *Phys. Lett.* **1996**, A224 (1–2), 133–136.
- 9 Y. H. ZHANG, X. J. LI, L. ZHENG et al., *Phys. Rev. Lett.* **1998**, 81 (8), 1710–1713.
- 10 Y. T. QIAN, Y. SU, Y. XIE et al., *Mater. Res. Bull.* **1995**, 30 (5), 601–605.
- 11 Y. F. LIU, J. H. ZHAN, M. REN et al., *Mater. Res. Bull.* **2001**, 36 (7–8), 1231–1236.
- 12 J. H. ZENG, J. YANG, Y. ZHU et al., *Chem. Commun.* **2001**, (15), 1332–1333.
- 13 J. H. ZENG, Y. ZHU, Y. F. LIU et al., *Mater. Sci. Eng.* **2002**, B94 (2–3), 131–135.
- 14 J. YANG, S. H. YU, Z. H. HAN et al., *J. Solid State Chem.* **1999**, 146 (2), 387–389.
- 15 J. H. ZHAN, X. G. YANG, Y. XIE et al., *J. Mater. Res.* **1999**, 14 (11), 4418–4420.
- 16 Y. Y. PENG, Z. Y. MENG, C. ZHONG et al., *J. Solid State Chem.* **2001**, 159 (1), 170–173.
- 17 Y. Y. PENG, Z. Y. MENG, C. ZHONG et al., *Chem. Lett.* **2001**, (8), 772–773.
- 18 J. Q. HU, B. DENG, Q. Y. LU et al., *Chem. Commun.* **2000**, (8), 715–716.
- 19 C. R. WANG, K. B. TANG, Q. YANG et al., *Chem. Lett.* **2001**, (6), 494–495.
- 20 C. R. WANG, K. B. TANG, Q. YANG et al., *J. Mater. Chem.* **2002**, 12 (8), 2426–2429.
- 21 Q. YANG, K. B. TANG, C. R. WANG et al., *J. Cryst. Growth* **2001**, 233 (4), 774–778.
- 22 C. R. WANG, K. B. TANG, Q. YANG et al., *Inorg. Chem. Commun.* **2001**, 4 (7), 339–341.
- 23 J. Q. HU, B. DENG, W. X. ZHANG et al., *Inorg. Chem.* **2001**, 40 (13), 3130–3133.
- 24 J. P. XIAO, Y. XIE, R. TANG et al., *J. Solid State Chem.* **2001**, 161 (2), 179–183.
- 25 J. Q. HU, B. DENG, K. B. TANG et al., *J. Mater. Res.* **2001**, 16 (12), 3411–3415.
- 26 J. Q. HU, B. DENG, C. R. WANG et al., *Solid State Commun.* **2002**, 121 (9–10), 493–496.
- 27 J. Q. HU, B. DENG, K. B. TANG et al., *Solid State Sci.* **2001**, 3 (3), 275–278.
- 28 J. Q. HU, B. DENG, W. X. ZHANG et al., *Int. J. Inorg. Mater.* **2001**, 3 (7), 639–642.
- 29 C. R. WANG, K. B. TANG, Q. YANG et al., *J. Solid State Chem.* **2001**, 160 (1), 50–53.
- 30 J. Q. HU, Q. Y. LU, B. DENG et al., *Inorg. Chem. Commun.* **1999**, 2 (12), 569–571.

- 31 S. WEI, J. LU, L. L. ZENG et al., *Chem. Lett.* **2002**, (10), 1034–1035.
- 32 Y. XIE, W. Z. WANG, Y. T. QIAN et al., *Chin. Sci. Bull.* **1999**, 41 (23), 1964–1968.
- 33 S. M. GAO, J. LU, N. CHEN et al., *Chem. Commun.* **2002**, 3064.
- 34 A. ADDAMIANO, *J. Electrochem. Soc.* **1961**, 108, 1072.
- 35 J. W. HWUANG et al., *Chem. Mater.* **1995**, 7, 517.
- 36 J. B. WILEY, R. B. KANER, *Science* **1992**, 255, 1093.
- 37 J. O. FITZMAUNCE, A. HECTOR, *Polyhedron* **1994**, 13, 235.
- 38 Y. XIE, Y. T. QIAN, W. Z. WANG et al., *Science* **1996**, 272, 1926.
- 39 Y. XIE, Y. T. QIAN, S. Y. ZHANG et al., *Appl. Phys. Lett.* **1996**, 69 (3), 334–336.
- 40 H. XIA, Q. XIA, A. L. ROUFF, *Phys. Rev. B* **1993**, 47, 12925.
- 41 J. Q. HU, B. DENG, W. K. ZHANG et al., *Chem. Phys. Lett.* **2002**, 351 (3–4), 229–234.
- 42 Z. F. LI, Y. L. GU, H. Z. GU et al., unpublished work.
- 43 Y. D. LI, X. F. DUAN, Y. T. QIAN et al., *J. Am. Chem. Soc.* **1997**, 119 (33), 7869–7870.
- 44 W. R. PENROSE, *CRC Crit. Rev. Environ. Control* **1974**, 465.
- 45 Y. XIE, P. YAN, J. LU et al., *Chem. Mater.* **1999**, 11 (9), 2619–2622.
- 46 B. LI, Y. XIE, J. X. HUANG et al., *Ultrasonics Sonochem.* **2001**, 8 (4), 331–334.
- 47 P. YAN, Y. XIE, W. Z. WANG et al., *J. Mater. Chem.* **1999**, 9 (8), 1831–1833.
- 48 J. LU, Y. XIE, X. X. JIANG et al., *Can. J. Chem.* **2001**, 79 (2), 127–130.
- 49 Q. YANG, Y. T. QIAN, unpublished work.
- 50 F. P. BUNDY, H. T. HALL, H. M. STRONG et al., *Nature*, **1955**, 176, 51.
- 51 X. Z. ZHAO, R. ROY, K. A. CHERIAN et al., *Nature* **1997**, 385, 513.
- 52 S. J. HARRIS, *Appl. Phys. Lett.* **1990**, 56, 2298; S. S. LEE, D. W. MINSEK, D. J. VESTYCK et al., *Science*, **1994**, 263, 1596; J. J. WU, F. C. N. HONG, *Appl. Phys. Lett.* **1997**, 70, 185.
- 53 Y. LI AND Y. T. QIAN et al., *Science*. **1998**, 281 (5374), 246–247.
- 54 S. IJIMA, *Nature*, **1991**, 354, 56.
- 55 T. GUO, P. NIKOLAEV, *Chem. Phys. Lett.* **1996**, 260, 471.
- 56 S. HERREYRE, P. GADELLE, *Carbon* **1995**, 33, 234.
- 57 N. M. RODRIGUEZ, *J. Mater. Res.* **1993**, 8, 3233.
- 58 S. IJIMA, T. ICHIHASHI, *Nature*, **1993**, 363, 603.
- 59 Y. JIANG, Y. WU, S. ZHANG et al., *J. Am. Chem. Soc.* **2000**, 122, 12383.
- 60 M. W. SHAO, Q. LI, J. WU et al., *Carbon* **2002**, 40 (15), 2961–2963.
- 61 X. J. WANG, J. LU, Y. XIE et al., *J. Phys. Chem. B* **2002**, 106, 933.
- 62 J. R. HEATH, *Science*, **1992**, 258, 1131.
- 63 J. J. RITTER, *Adv. Ceram.* **1987**, 21, 21.
- 64 Q. Y. LU, J. Q. HU, K. B. TANG et al., *Appl. Phys. Lett.* **1999**, 75 (4), 507–509.
- 65 J. Q. HU, Q. Y. LU, K. B. TANG et al., *Chem. Mater.* **1999**, 11 (9), 2369–2371.
- 66 J. Q. HU, Q. K. LU, K. B. TANG et al., *J. Phys. Chem. B* **2000**, 104 (22), 5251–5254.
- 67 Q. Y. LU, J. Q. HU, K. B. TANG et al., *Chem. Phys. Lett.* **1999**, 314 (1–2), 37–39.
- 68 C. LI, X. G. YANG, Z. Y. ZHAO et al., *Chem. Lett.* **2002**, (11), 1088–1089.
- 69 J. Q. HU, Q. Y. LU, K. B. TANG et al., *Chem. Lett.* **2000**, (5), 474–475.
- 70 X. F. QIAN, X. M. ZHANG, C. WANG et al., *Mater. Res. Bull.* **1999**, 34 (3), 433–436.
- 71 Y. L. GU, F. GUO, Y. T. QIAN et al., *Mater. Lett.* **2003**, 57 (11), 1679.
- 72 J. Q. HU, Q. Y. LU, K. B. TANG et al., *J. Am. Chem. Soc.* **2000**, 83 (2), 430–432.
- 73 J. Q. HU, Q. Y. LU, K. B. TANG et al., *Chem. Lett.* **2000**, (1), 74–75.
- 74 K. B. TANG, J. Q. HU, Q. Y. LU et al., *Adv. Mater.* **1999**, 11 (8), 653.
- 75 Z. Y. MENG, Y. Y. PENG, Z. P. YANG et al., *Chem. Lett.* **2000**, (11), 1252–1253.
- 76 Z. Y. MENG, Y. Y. PENG, Y. T. QIAN, *Chem. Commun.* **2001**, (5), 469–470.
- 77 Y. XIE, H. L. SU, B. LI et al., *Mater. Res. Bull.* **2000**, 35 (5), 675–680.
- 78 Y. L. GU, F. GUO, Y. T. QIAN et al., *Mater. Res. Bull.* **2002**, 37 (6), 1101–1105.
- 79 X. F. QIAN, Y. XIE, Y. T. QIAN et al., *Mater. Sci. Eng.* **1997**, B49 (2), 135–137.

- 80 X. F. QIAN, X. M. ZHANG, C. WANG et al., *Mater. Res. Bull.* **1998**, 33 (5), 669–672.
- 81 Y. XIE, H. L. SU, X. F. QIAN et al., *J. Solid State Chem.* **2000**, 149, 88–89.
- 82 Y. L. GU, L. Y. CHEN, Y. T. QIAN et al., *J. Mater. Sci. Lett.*, in press.
- 83 J. Q. HU, Q. Y. LU, K. B. TANG et al., *J. Solid State Chem.* **1999**, 148 (2), 325–328.
- 84 X. P. HAO, D. L. CUI, G. X. SHI et al., *Chem. Mater.* **2001**, 13 (8), 2457–2459.
- 85 X. P. HAO, M. Y. YU, D. L. CUI et al., *J. Cryst. Growth.* **2002**, 241 (1–2), 124–128.
- 86 L. Q. XU, Y. T. QIAN et al., *Chem. Mater.* **2003**, 15 (13), 2675.
- 87 Y. L. GU, L. Y. CHEN, Y. T. QIAN et al., *J. Am. Ceram. Soc.*, in press.
- 88 Y. L. GU, H. G. ZHENG et al., *Chem. Lett.* **2002**, (7), 724–725.
- 89 Y. L. GU, L. Y. CHEN, Y. T. QIAN et al., *Bull. Chem. Soc. Jpn.*, **2003**, 76 (7), 1469.
- 90 Y. L. GU, Y. T. QIAN, L. Y. CHEN et al., *J. Alloys Compd.*, **2003**, 352 (1–2), 325.
- 91 P. YAN, Y. XIE, Y. T. QIAN et al., *Chem. Commun.* **1999**, (14), 1293–1294.
- 92 J. LU, Y. XIE, G. A. DU et al., *J. Mater. Chem.* **2002**, 12 (1), 103–106.
- 93 J. WU, Y. JIANG, Q. LI et al., *J. Cryst. Growth* **2000**, 235 (1–4), 421–424.
- 94 M. CHEN, Y. XIE, J. LU et al., *J. Mater. Chem.* **2002**, 12 (3), 748–753.
- 95 Y. XIE, P. YAN, J. LU et al., *Chem. Commun.* **1999**, (19), 1969–1970.
- 96 Y. D. LI, H. W. LIAO, Y. DING et al., *Inorg. Chem.* **1999**, 38 (7), 1382–1387.
- 97 Y. D. LI, H. W. LIAO, Y. FAN et al., *Mater. Chem. Phys.* **1999**, 58 (1), 87–89.
- 98 W. Z. WANG, Y. GENG, P. YAN et al., *Inorg. Chem. Commun.* **1999**, 2 (3), 83–85.
- 99 S. H. YU, Y. S. WU, J. YANG et al., *Chem. Mater.* **1998**, 10 (9), 2309–2312.
- 100 J. YANG, J. H. ZENG, S. H. YU et al., *Chem. Mater.* **2000**, 12 (11), 3259–3263.
- 101 J. YANG, C. XUE, S. H. YU et al., *Angew. Chem. Int. Ed. Engl.* **2002**, 41 (24), 4697–4700.
- 102 J. H. ZHAN, X. G. YANG, W. X. ZHANG et al., *J. Mater. Res.* **2000**, 15 (3), 629–632.
- 103 Y. D. LI, Y. DING, Y. T. QIAN et al., *Inorg. Chem.* **1998**, 37 (12), 2844–2845.
- 104 J. H. ZHAN, X. G. YANG, D. W. WANG et al., *Adv. Mater.* **2000**, 12 (18), 1348–1351.
- 105 Q. YANG, K. B. TANG, C. R. WANG et al., *J. Phys. Chem. B* **2002**, 106 (36), 9227–9230.
- 106 M. S. MO, M. W. SHAO, H. M. HU et al., *J. Cryst. Growth* **2002**, 244 (3–4), 364–368.
- 107 D. B. YU, D. B. WANG, Z. Y. MENG et al., *J. Mater. Chem.* **2002**, 12 (3), 403–405.
- 108 J. YANG, J. H. ZENG, S. H. YU et al., *Chem. Mater.* **2000**, 12 (10), 2924–2929.
- 109 D. B. WANG, D. B. YU, M. W. SHAO et al., *Chem. Lett.* **2002**, (10), 1056–1057.
- 110 S. H. YU, L. SHU, J. A. YANG et al., *J. Mater. Res.* **1999**, 14 (11), 4157–4162.
- 111 Q. LI, M. W. SHAO, J. WU et al., *Inorg. Chem. Commun.* **2002**, 5 (11), 933–936.
- 112 H. L. SU, Y. XIE, P. GAO et al., *Chem. Lett.* **2000**, (7), 790–791.
- 113 Y. F. LIU, J. H. ZENG, W. X. ZHANG et al., *J. Mater. Res.* **2001**, 16 (12), 3361–3365.
- 114 X. C. JIANG, Y. XIE, J. LU et al., *Adv. Mater.* **2001**, 13 (16), 1278–1281.
- 115 J. YANG, G. H. CHENG, J. H. ZENG et al., *Chem. Mater.* **2001**, 13 (3), 848–853.
- 116 Z. H. HAN, S. H. YU, Y. P. LI et al., *Chem. Mater.* **1999**, 11 (9), 2302.
- 117 N. CHEN, W. Q. ZHANG, W. C. YU et al., *Mater. Lett.* **2002**, 55 (4), 230–233.
- 118 Z. Y. MENG, Y. Y. PENG, L. Q. XU et al., *Mater. Lett.* **2002**, 53 (3), 165–167.
- 119 J. LU, P. F. QI, Y. Y. PENG et al., *Chem. Mater.* **2001**, 13 (6), 2169–2172.
- 120 T. QIN, J. LU, S. WEI et al., *Inorg. Chem. Commun.* **2002**, 5 (5), 369–371.
- 121 B. LI, Y. XIE, J. X. HUANG et al., *Adv. Mater.* **1999**, 11 (17), 1456–1459.
- 122 Q. Y. LU, J. Q. HU, K. B. TANG et al., *Inorg. Chem.* **2000**, 39 (7), 1606.
- 123 Y. JIANG, Y. WU, X. MO et al., *Inorg. Chem.* **2000**, 39 (14), 2964.
- 124 Y. CUI, J. REN, G. CHEN et al., *Chem. Lett.* **2001**, (3), 236–237.



- 125 J. Q. HU, Q. Y. LU, K. B. TANG et al., *Chem. Commun.* **1999**, (12), 1093–1094.
- 126 Y. Y. PENG, Z. Y. MENG, C. ZHONG et al., *New J. Chem.* **2001**, 25 (11), 1359–1361.
- 127 B. XIE, S. W. YUAN, Y. JIANG et al., *Chem. Lett.* **2002**, (6), 612–613.
- 128 B. LI, Y. XIE, J. X. HUANG et al., *J. Solid State Chem.* **2000**, 153 (1), 170–173.
- 129 B. LI, Y. XIE, J. X. HUANG et al., *Solid State Ionics* **1999**, 126 (3–4), 359–362.
- 130 H. L. SU, Y. XIE, S. K. WAN et al., *Solid State Ionics* **1999**, 123 (1–4), 319–324.
- 131 R. COUSTAL, *J. Chim. Phys.* **1958**, 38, 277.
- 132 I. P. PARKIN, *Chem. Soc. Rev.* **1996**, 25, 199.
- 133 T. OHTANI, M. MOTOKI, *Mater. Res. Bull.* **1995**, 30, 1495.
- 134 G. HENSHAW, I. P. PARKIN, *Chem. Commun.* **1996**, 1095.
- 135 M. L. STEIGERWALD, A. P. ALIVASATOS, J. M. GIBSON, *J. Am. Chem. Soc.* **1988**, 110, 3046; C. B. MURRAY, D. J. NORRIS, M. G. BAWENDI, *J. Am. Chem. Soc.* **1993**, 115, 8706.
- 136 W. Z. WANG, Y. GENG, P. YAN et al., *J. Am. Chem. Soc.* **1999**, 121 (16), 4062–4063.
- 137 W. Z. WANG, Y. T. QIAN et al., *Adv. Mater.* **1998**, 10 (17), 1479.
- 138 J. X. HUANG, Y. XIE, B. LI et al., *Adv. Mater.* **2000**, 12 (11), 808–811.
- 139 Y. XIE, J. X. HUANG, B. LI et al., *Adv. Mater.* **2000**, 12 (20), 1523–1526.
- 140 Y. JIANG, B. XIE, J. WU et al., *J. Solid State Chem.* **2002**, 167 (1), 28–33.
- 141 Y. JIANG, Y. WU, Z. P. YANG et al., *J. Cryst. Growth* **2001**, 224 (1–2), 1–4.
- 142 W. Z. WANG, Y. GENG, Y. T. QIAN et al., *Mater. Res. Bull.* **1999**, 34 (6), 877–882.
- 143 Y. P. LIU, Y. J. ZHU, Y. H. ZHANG et al., *J. Mater. Chem.* **1997**, 7 (5), 787–789.
- 144 Q. YANG, F. WANG, K. B. TANG et al., *Mater. Chem. Phys.* **2002**, 78 (2), 495–500.
- 145 Y. J. ZHU, Y. T. QIAN, M. W. ZHANG et al., *Mater. Trans. JIM* **1995**, 36 (1), 80–81.
- 146 Y. J. ZHU, Y. T. QIAN, H. A. HAI et al., *Mater. Lett.* **1996**, 28 (1–3), 119–122.
- 147 H. R. LIU, Z. C. ZHANG, Y. T. QIAN et al., *Chin. J. Inorg. Chem.* **1999**, 15 (3), 388–392.
- 148 Y. XIE, Z. P. QIAO, M. CHEN et al., *Chem. Lett.* **1999**, (9), 875–876.
- 149 M. CHEN, Y. XIE, J. C. LU et al., *J. Mater. Chem.* **2001**, 11 (2), 518–520.
- 150 M. CHEN, Y. XIE, H. Y. CHEN et al., *J. Colloid Interface Sci.* **2001**, 237 (1), 47–53.
- 151 X. JIANG, Y. XIE, J. LU et al., *Chem. Mater.* **2001**, 13 (4), 1213–1218.
- 152 Z. P. QIAO, Y. XIE, Y. T. QIAN et al., *Mater. Phys. Chem.* **2000**, 62 (1), 88–90.
- 153 Z. P. QIAO, Y. XIE, X. J. LI et al., *J. Mater. Chem.* **1999**, 9 (3), 735–738.
- 154 Z. P. QIAO, Y. XIE, J. G. XU et al., *J. Colloid Interface Sci.* **1999**, 214 (2), 459–461.
- 155 Z. P. QIAO, Y. XIE, J. G. XU et al., *Can. J. Chem.-Revue Canadienne de Chimie* **2000**, 78 (9), 1143–1146.
- 156 Y. XIE, Z. P. QIAO, M. CHEN et al., *Adv. Mater.* **1999**, 11 (18), 1512.
- 157 J. H. ZENG, Y. ZHU, J. YANG et al., *Chem. Lett.* **2001**, (10), 1000–1001.
- 158 Y. XIE, Z. P. QIAO et al., *Nanostructured Mater.* **1999**, 11 (8), 1165–1169.
- 159 M. CHEN, Y. XIE, Z. P. QIAO et al., *J. Mater. Chem.* **2000**, 10 (2), 329–332.
- 160 Z. P. QIAO, Y. XIE, J. X. HUANG et al., *Radiat. Phys. Chem.* **2000**, 58 (3), 287–292.
- 161 Y. J. ZHU, Y. T. QIAN, X. J. LI et al., *Chem. Commun.* **1997**, (12), 1081–1082.
- 162 Z. P. QIAO, Y. XIE, M. CHEN et al., *Chem. Phys. Lett.* **2000**, 321 (5–6), 504–507.
- 163 Z. P. QIAO, Y. XIE, G. LI et al., *J. Mater. Sci.* **2000**, 35 (2), 285–287.
- 164 Z. P. QIAO, Y. XIE, J. G. XU et al., *Mater. Res. Bull.* **2000**, 35 (8), 1355–1360.



## 8

**Nanotubes and Nanowires**

*A. Govindaraj and C. N. R. Rao*

**Abstract**

Carbon nanotubes (CNTs) were discovered as an electron microscopic marvel in 1991. Since then, there has been intense activity related to the synthesis, structure, properties and applications of CNTs. The discovery of CNTs has triggered much research on other one-dimensional nano-objects such as inorganic nanotubes and nanowires. This chapter covers the highlights of the entire variety of nanotubes and nanowires.

**8.1****Introduction**

Diamond and graphite are the two well-known forms of crystalline carbon. Diamond has four-coordinate  $sp^3$  carbon atoms forming an extended three-dimensional network, whose motif is the chair conformation of cyclohexane. Graphite has three-coordinate  $sp^2$  carbons forming planar sheets, whose motif is the flat six-membered benzene ring. The new carbon allotrope, the fullerenes, are closed-cage carbon molecules with three-coordinate carbon atoms tiling the spherical or nearly-spherical surfaces, the best known example being  $C_{60}$ , with a truncated icosahedral structure formed by twelve pentagonal rings and twenty hexagonal rings. Fullerenes were discovered by Kroto et al. [1] in 1985 while investigating the nature of carbon present in interstellar space. The coordination at every carbon atom in fullerenes is not planar, but slightly pyramidalized, with some  $sp^3$  character present in the essentially  $sp^2$  carbons. The key feature is the presence of five-membered rings which provide the curvature necessary to form a closed-cage structure. In 1990, Krätschmer et al. [2] found that the soot produced by arcing graphite electrodes contained  $C_{60}$  and other fullerenes. It was the ability to generate fullerenes in gram quantities in the laboratory, using a relatively simple apparatus, that gave rise to intense research activity on these molecules and caused a renaissance in the study of carbon. Iijima [3] observed in 1991 that nanotubules of graphite were deposited on the negative electrode during the direct current arcing

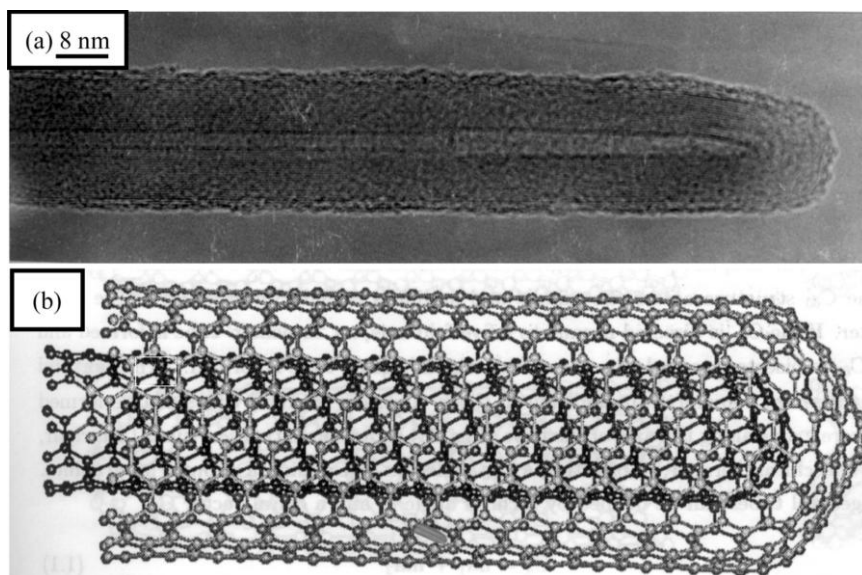


**Fig. 8.1.** (a) A TEM image of a multi-walled carbon nanotube; (b) Minimum energy structure of a double-walled carbon nanotube. Reproduced from ref. [20a], with permission.

of graphite for the preparation of fullerenes. These nanotubes are concentric graphitic cylinders closed at either end due to the presence of five-membered rings. Nanotubes can be multi-walled with a central tubule of nanometric diameter surrounded by graphitic layers separated by  $\sim 3.4 \text{ \AA}$ . Unlike the multi-walled nanotubes (MWNTs), in single-walled nanotubes (SWNTs), there is only the tubule and no graphitic layers. A transmission electron microscope (TEM) image of a MWNT is shown in Figure 8.1(a). In this nanotube, graphite layers surround the central tubule. Figure 8.1(b) shows the structure of a nanotube formed by two concentric graphitic cylinders, obtained by force field calculations. A single-walled nanotube can be visualized by cutting  $C_{60}$  along the center and spacing apart the hemispherical corannulene end-caps by a cylinder of graphite of the same diameter. Carbon nanotubes are the only form of carbon with extended bonding and yet with no dangling bonds. Since carbon nanotubes are derived from fullerenes, they are referred to as tubular fullerenes or bucky tubes.

Ever since the discovery of the carbon nanotubes, several ways of preparing them have been explored. Besides MWNTs, SWNTs have been prepared [4, 5], the various methods including electrochemical synthesis [6] and pyrolysis of precursor molecules [7]. The structure of carbon nanotubes has been extensively investigated by high-resolution electron microscopy [8–10]. The nanotubes, as prepared by arc vaporization of graphite, are closed at either end, but can be opened by various oxidants [11, 12]. There has been considerable success in filling the nanotubes with various materials [13]. Apart from opening and filling, carbon nanotubes have

been doped with boron and nitrogen, giving rise to p-type and n-type materials respectively. By employing carbon nanotubes as removable templates, oxidic, carbidic and other nanostructures have been prepared. One of the recent developments is the synthesis of aligned nanotube bundles for specific applications. A variety of properties and phenomena as well as several applications of carbon nanotubes, some potential and some likely, have been reported. It is no wonder, therefore, that these nanomaterials have elicited such great interest. There have been several review articles, special issues of journals and conference proceedings [14–20] dealing with carbon nanotubes in the literature, together with a book which appeared in 1996 [17]. Some of the reviews present possible technological applications with focus on the electronic properties [19, 20].

Since the discovery of the carbon nanotubes, there has been considerable work on other layered materials such as  $\text{MoS}_2$ ,  $\text{WS}_2$  and BN to explore the formation of nanotubes of these materials. Indeed several of them have been synthesized and characterized [21–23]. Similarly, nanowires of various inorganic materials have also been made [21]. In this chapter, we shall present the various important aspects of carbon nanotubes including their preparation, structure, mechanism of formation, chemical substitution, properties and applications. The methodologies developed for synthesizing nanowires and nanotubes of various inorganic materials as well as their salient features will also be discussed [21–24].

## 8.2

### Carbon Nanotubes

#### 8.2.1

##### Synthesis

##### 8.2.1.1 Multi-Walled Nanotubes

Carbon nanotubes are readily prepared by striking an arc between graphite electrodes in  $2/3$  atm ( $\sim 500$  torr) of helium, considerably higher than the pressure of helium used in the production of fullerene soot. A current of 60–100 A across a potential drop of about 25 V gives high yields of carbon nanotubes. The arcing process can be optimized such that the major portion of the carbon anode is deposited on the cathode in the form of carbon nanotubes and graphitic nanoparticles [25]. Carbon nanotubes have been produced by using plasma arc-jets [26] and in large quantities, by optimizing the quenching process in an arc between a graphite anode and a cooled copper electrode [27]. Scanning tunneling microscope (STM) studies show that the deposition of carbon vapor on cooled substrates of highly oriented pyrolytic graphite gives rise to tube-like structures [28]. Carbon nanotubes are also produced by carrying out electrolysis in molten halide salts with carbon electrodes in an argon atmosphere [29a]. In addition, MWNTs with well-ordered graphitic structures have been synthesized under hydrothermal conditions using a polyethylene and water mixture in the presence of nickel catalyst at around  $800^\circ\text{C}$  under 60–100 MPa pressure [29b]. Besides the conventional arc-

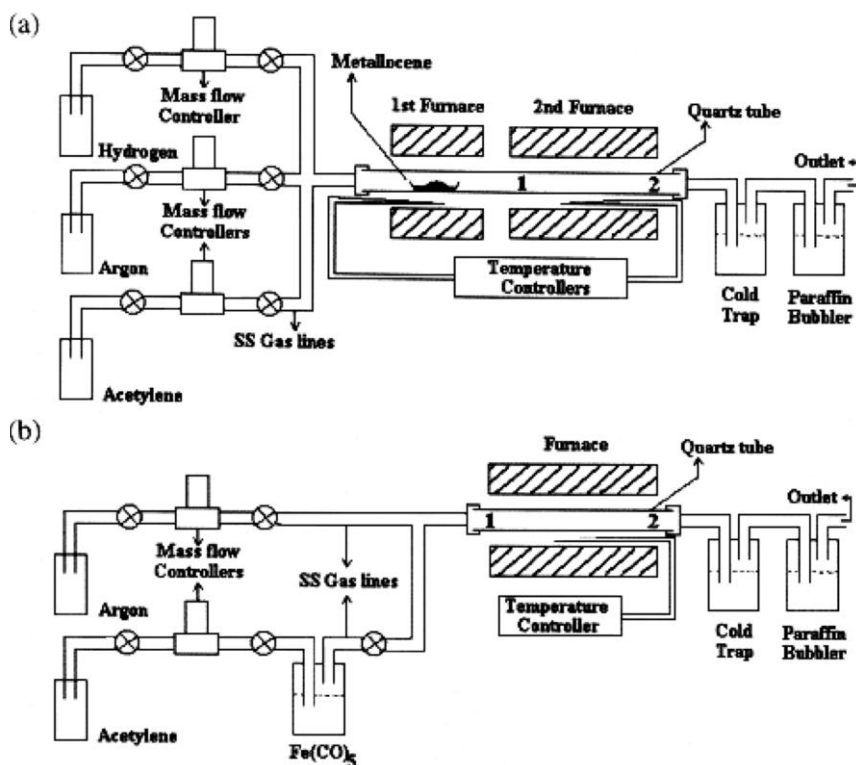
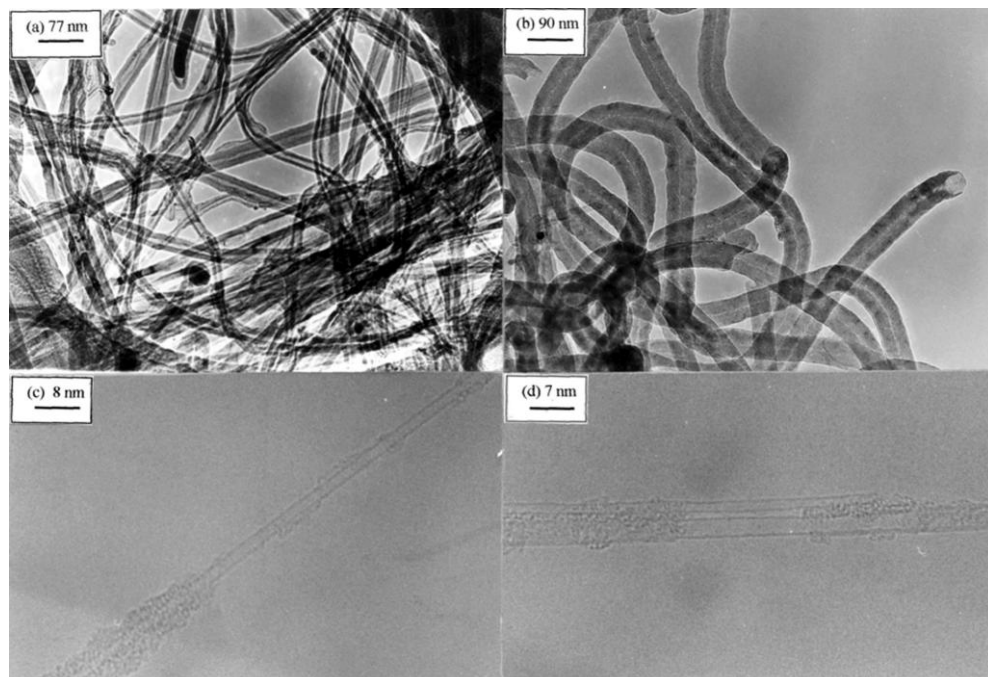


Fig. 8.2. Pyrolysis apparatus employed for the synthesis of carbon nanotubes by pyrolysis of mixtures of (a) metalocene +  $C_2H_2$  and (b)  $Fe(CO)_5$  +  $C_2H_2$ . The numbers 1 and 2 indicated in the figure represent the inlet and outlet, respectively. Reproduced from ref. [44, 45], with permission.

evaporation technique, carbon nanotubes are produced by the decomposition of hydrocarbons such as  $C_2H_2$  under inert conditions at around  $700^\circ C$ , over Fe/graphite [30], Co/graphite [31] or Fe/silica [32] catalysts. The presence of transition metal particles is essential for the formation of nanotubes by the pyrolysis process, and the diameter of the nanotube is determined by the size of the metal particles [33]. Sen et al. [34] prepared carbon nanotubes and metal-filled onion-like structures by the pyrolysis of ferrocene, cobaltocene and nickelocene under reductive conditions, wherein the precursor acts as a source of the metal as well as carbon (Figure 8.2). They also showed that the pyrolysis of benzene or acetylene in the presence of ferrocene or  $Fe(CO)_5$  gives high yields of nanotubes (Figure 8.2), the wall thickness depending on the proportion of the carbon source and the metal precursor [35]. Figure 8.3(a) shows the TEM image of MWNTs obtained by the pyrolysis of mixture of  $C_2H_2$  and ferrocene. Under similar conditions, nickelocene with benzene also gives MWNTs (Figure 8.3(b)).



**Fig. 8.3.** (a) TEM image of MWNTs obtained by pyrolysis of a mixture of  $C_2H_2$  (25 sccm) and ferrocene at  $1100^\circ C$  at 1000 sccm Ar flow. (b) TEM image of MWNTs obtained by pyrolysis of a mixture of nickelocene and benzene at  $900^\circ C$  in 85% Ar and 15%  $H_2$  mixture at a flow rate of 1000 sccm. (c) HREM image of SWNTs obtained by the pyrolysis of nickelocene and  $C_2H_2$  at  $1100^\circ C$  in a flow of Ar (1000 sccm) with  $C_2H_2$  flow rate of 50 sccm. (d) HREM image of SWNTs obtained by the pyrolysis of ferrocene and  $CH_4$  at  $1100^\circ C$  in a flow of Ar (990 sccm) with  $CH_4$  flow rate of 10 sccm. Reproduced from ref. [34, 45], with permission.

### 8.2.1.2 Aligned Carbon Nanotube Bundles

Carbon nanotubes are potential candidates for use as field emitters [36]. Of particular relevance to this application is the synthesis of aligned nanotube bundles. Aligned nanotube bundles have been obtained by chemical vapor deposition (CVD) over transition metal catalysts embedded in the pores of mesoporous silica or the channels of alumina membranes [37, 38]. Terrones et al. [39, 40] prepared aligned nanotubes over silica substrates, laser-patterned with cobalt. Ren et al. [41] employed plasma-enhanced chemical vapor deposition on nickel-coated glass, using acetylene and ammonia mixtures, for this purpose. The mechanism of the growth of nanotubes by this method and the exact role of the metal particles are not clear, although a nucleation process involving the metal particles is considered to be important. Fan et al. [42] have obtained aligned nanotubes by employing CVD on porous silicon and plain silicon substrates patterned with Fe films. The role of the transition metal particles assumes importance in view of the report of Pan et al. [43] that aligned nanotubes can be obtained by the pyrolysis of acetylene over iron/



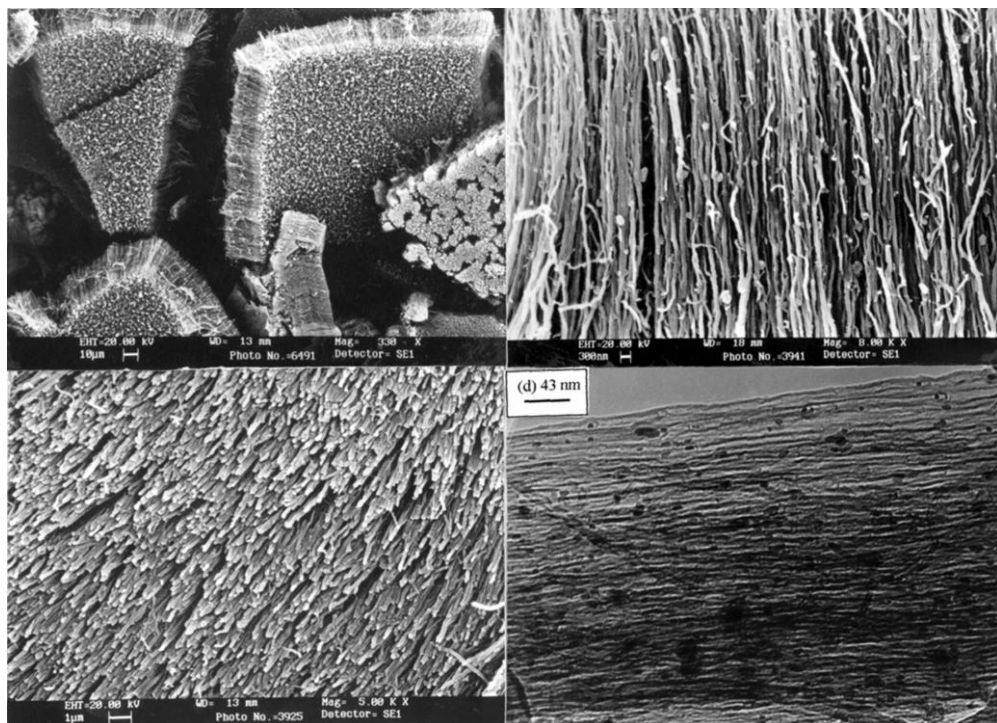


**Fig. 8.4.** SEM image (a) showing the bundles of aligned nanotubes obtained by pyrolysing ferrocene with butane (50 sccm) at 1100 °C in an Ar flow of 950 sccm; (b) and (c) show views of the aligned nanotubes perpendicular to and along the axis of the nanotubes respectively; (d) TEM image of part of an aligned nanotube bundle obtained from the pyrolysis of acetylene (85 sccm) and ferrocene mixture at 110 °C in an Ar flow of 1000 sccm. Reproduced from ref. [45], with permission.

silica catalyst surfaces. In the light of the earlier work on the synthesis of carbon nanotubes by the pyrolysis of mixtures of organometallic precursors and hydrocarbons, [34, 35] one would expect that the transition metal nanoparticles produced in situ in the pyrolysis, may not only nucleate the formation of carbon nanotubes but also align them. This aspect has been examined by carrying out the pyrolysis of metallocenes along with additional hydrocarbon sources, in a suitably designed apparatus (Figure 8.2) [44, 45]. Scanning electron microscope (SEM) images of aligned nanotubes obtained by the pyrolysis of ferrocene are shown in Figure 8.4(a)–(c). The image in Figure 8.4(a) shows larger bundles of aligned nanotubes. The image in Figure 8.4(b) shows the side-view and the image, whereas Figure 8.4(c) shows the top-view of the aligned nanotubes, wherein the nanotube tips are seen. A TEM image of a part of an aligned nanotube bundle obtained from the pyrolysis of acetylene–ferrocene mixture is shown in Figure 8.4(d). The average length of the nanotubes is generally around 60  $\mu\text{m}$  with methane and acetylene. Andrews et al. [46a] have carried out the pyrolysis of ferrocene–xylene mixtures to

obtain aligned carbon nanotubes. Pyrolysis of Fe(II)phthalocyanine also yields aligned nanotubes [46b]. Hexagonally ordered arrays of nanotubes are produced by using alumina templates with ordered pores [47a]. By employing catalytic chemical vapor deposition (CCVD), Mukhopadhyay et al. [47b] have obtained quasi-aligned carbon nanotubes using metal impregnated zeolite templates. The advantage of the precursor method is that the aligned bundles are produced in one step, at a relatively low cost, without prior preparation of substrates. The precursor route to carbon nanotubes has been discussed recently by Rao and Govindaraj [48a].

TEM observations of aligned nanotubes produced by ferrocene + hydrocarbon pyrolysis show the presence of iron nanorods encapsulated inside the carbon nanotubes, the proportion of the nanorods depending on the proportion of ferrocene. Typical TEM images of such nanorods are shown in Figure 8.5(a), (b) and (c). The inset in Figure 8.5(b) shows the selected area electron diffraction (SAED) pattern of the nanorods showing spots due to the (010) and (011) planes of  $\alpha$ -Fe. The high-resolution electron microscope (HREM) image of the iron nanorod shows well-resolved (011) planes of  $\alpha$ -Fe in single-crystalline form. X-ray diffraction studies also show the presence of  $\alpha$ -Fe with a small portion of  $\text{Fe}_3\text{C}$  as the minor phase. In addition to the nanorods, there are iron nanoparticles (20–40 nm diameter) encapsulated inside the graphite layers. Both iron nanorods and nanoparticles are well protected against oxidation by the graphitic layers. The iron nanorods also exhibit a complex behavior with respect to magnetization reversal, showing Barkhausen jumps [48b]. Iron-filled carbon nanotubes could be useful as probes in magnetic force microscopy.

### 8.2.1.3 Single-Walled Carbon Nanotubes

The nanotubes generally obtained by the arc method or hydrocarbon pyrolysis are multi-walled, having several graphitic sheets or layers (Figure 8.1). Single-walled nanotubes (SWNTs) were first prepared by metal-catalyzed dc arcing of graphite rods [4, 5] in a He atmosphere. The graphite anode was filled with metal powders (Fe, Co or Ni) and the cathode was made of pure graphite. SWNTs generally occur in the web-like material deposited behind the cathode. Various metal catalysts have been used to make SWNTs by this route. Dai et al. [49] prepared SWNTs by the disproportionation of CO at 1200 °C over Mo particles of a few nanometers diameter dispersed in a fumed alumina matrix. Saito et al. [50] compared SWNTs produced by using different catalysts and found that a Co or a Fe/Ni bimetallic catalyst gives rise to tubes forming a highway-junction pattern. SWNTs are also prepared by using various oxides  $\text{Y}_2\text{O}_3$ ,  $\text{La}_2\text{O}_3$ ,  $\text{CeO}_2$  as catalysts [51]. The arc discharge technique, though cheap and easy to implement, gives low yields of SWNTs. Journet et al. [52] obtained ~80% yield of SWNTs in the arc, by using a mixture of 1 at.% Y and 4.2 at.% Ni as catalyst. Arc evaporation of graphite rods filled with Ni and  $\text{Y}_2\text{O}_3$  in a He atmosphere (660 torr) gives rise to web-like deposits on the chamber walls near the cathode, consisting of SWNT bundles [45]. HREM images show bundles consisting of 10–50 SWNTs forming highway junctions (Figure 8.6). The average diameter of the SWNTs was around 1.4 nm and the length extended upto 10  $\mu\text{m}$ . SWNTs have been produced in more than 70% yield by the conden-

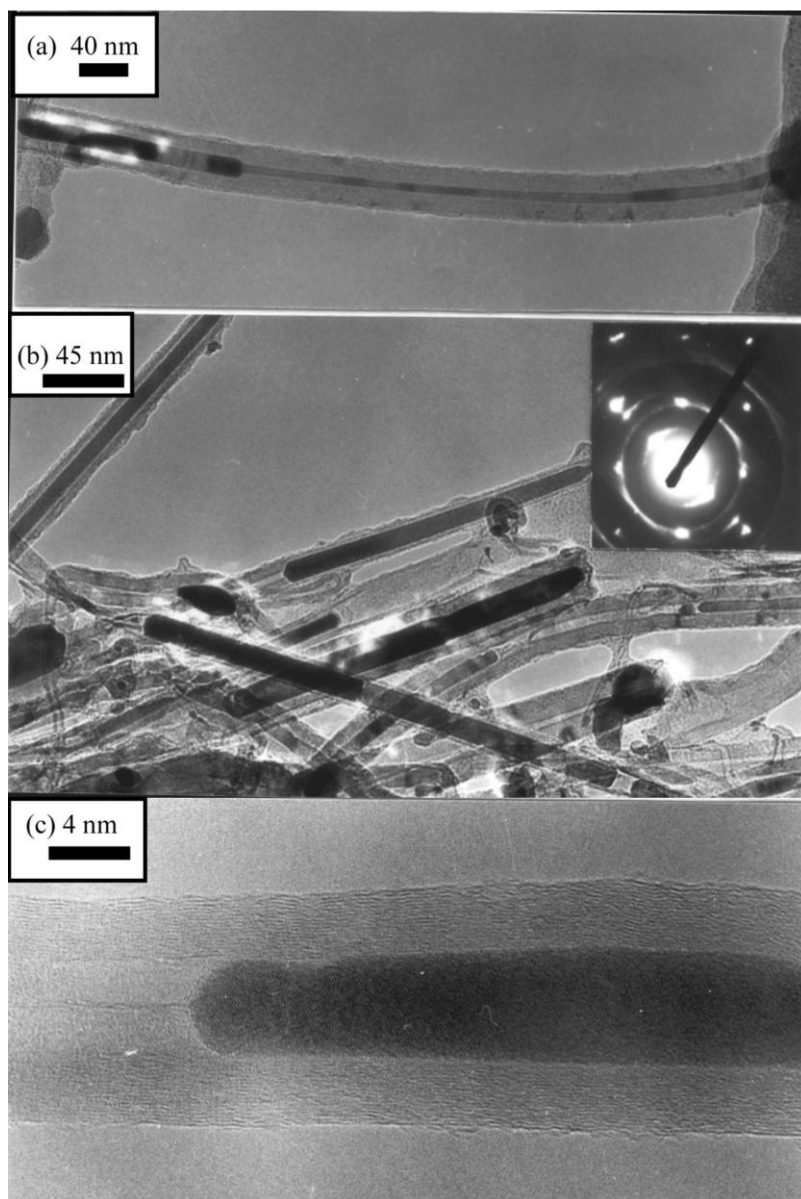


**Fig. 8.5.** (a), (b) TEM images of the iron nanorods encapsulated inside the carbon nanotubes from aligned nanotube bundles. (c) HREM image of a single-crystal iron nanorod encapsulated inside a carbon

nanotube. The inset in (b) represents the selected area electron diffraction (SAED) pattern of an iron nanorod. Reproduced from ref. [45], with permission.



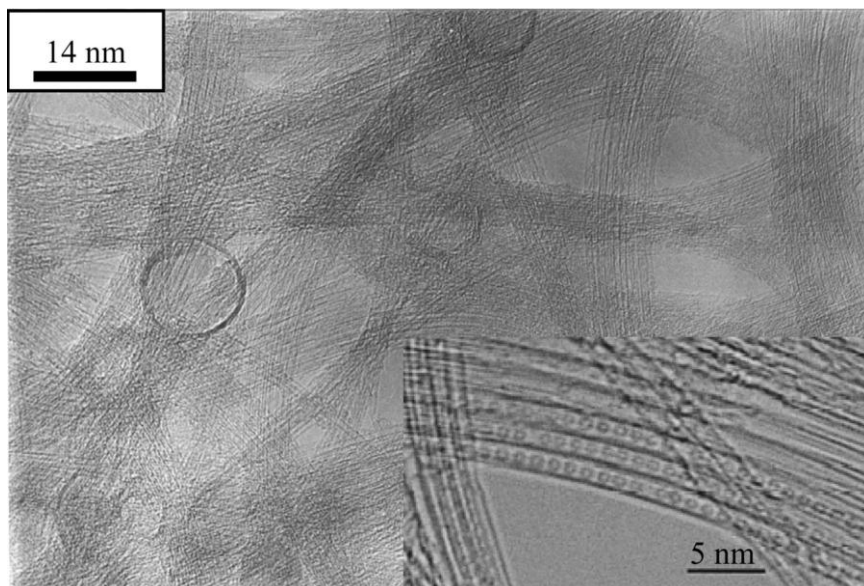


**Fig. 8.6.** HREM image of SWNTs obtained by arcing graphite electrodes filled with Ni and  $Y_2O_3$  under a He atmosphere (660 Torr). Inset: The HREM image of encapsulated fullerenes inside the SWNTs; scale bar is 5 nm. Reproduced from ref. [45], with permission.

sation of a laser-vaporized carbon–nickel–cobalt mixture at 1200 °C [53]. These SWNTs were nearly uniform in diameter and self-assemble into ropes which consist of 100 to 500 tubes in a 2D triangular lattice.

Under controlled conditions of pyrolysis, dilute hydrocarbon–organometallic mixtures yield SWNTs [45, 54]. Pyrolysis of metallocene–acetylene mixtures at 1100 °C yields SWNTs [54, 55], shown in the TEM image in Figure 8.3(c). The diameter of the SWNT in Figure 8.3(c) is 1.4 nm. Figure 8.3(d) shows the SWNTs obtained similarly by the pyrolysis of a ferrocene– $CH_4$  mixture at 1100 °C. It may be recalled that the pyrolysis of nickelocene in admixture with benzene under similar conditions primarily yields MWNTs. The bottom portion of the SWNT in Figure 8.3(c) shows an amorphous carbon coating around the tube, common with such preparations. This can be avoided by reducing the proportion of the hydrocarbon  $C_2H_2$  and mixing hydrogen in the Ar stream. Pyrolysis of acetylene in mixture with  $Fe(CO)_5$  at 1100 °C gives good yields of SWNTs. Pyrolysis of ferrocene–thiophene mixtures also yield SWNTs, but the yield appears to be somewhat low. Pyrolysis of benzene and thiophene along with ferrocene gives a high yield of SWNTs [56].

Laplaze et al. [57] have demonstrated that concentrated solar energy can be employed to vaporize graphite to synthesize SWNTs. Nikolaev et al. [58] have obtained SWNTs using a gas-phase catalytic method involving the pyrolysis of  $Fe(CO)_5$  and CO. The decomposition of CO on a silica-supported Co–Mo catalyst also yields

SWNTs [59]. Colomer et al. [60] obtained SWNTs in high yield by the decomposition of methane over transition metal supported MgO substrates. Flahaut et al. [61] have synthesized SWNTs by passing a  $H_2$ - $CH_4$  mixture over transition metal containing oxide spinels, obtained by the combustion route. The quality of SWNTs has been characterized on the basis of adsorption measurements. Zeolites containing one-dimensional channels have also been investigated for the synthesis of monosized SWNTs [62]. As-prepared SWNTs contain several contaminants such as amorphous carbon and nanometer-size catalyst particles coated with carbon. The amorphous carbon can be burnt away by heating the nanotubes in air at around 300 °C. Bindow et al. [63] use microfiltration to clean SWNTs of the other contaminants. Size exclusion chromatography of the surfactant-stabilized raw SWNTs is also employed to purify the nanotubes from amorphous carbon, metal particles etc [64]. In addition to purification, size separation has also been achieved. Since SWNTs occur as large bundles with lengths of the order of microns, it is desirable to break them from the bundles, for purposes of further manipulation. Liu et al. [65] have employed chemical processing based on ultrasound treatment, wherein the SWNTs in an acidic medium were subjected to sonication so that the bundles break up into open-ended small fragments of 100–300 nm length. The smaller fragments were functionalized.

### 8.2.2

#### Structure and Characterization

Transmission electron microscope observations show that the nanotubes prepared by the arcing process generally consist of multi-layered, concentric cylinders of single graphitic (graphene) sheets. The diameter of the inner tubes is of the order of a few nanometers. The outermost tubes could be as large as 10–30 nm as shown in Figure 8.1(a). During the curling of a graphene sheet into a cylinder, helicity is introduced. Electron diffraction studies establish the presence of helicity, suggesting that the growth of nanotubes occurs as in the spiral growth of crystals. The separation between concentric cylinders in MWNTs is about 3.45 Å, which is close to the separation between the (002) planes of graphite. These are the lowest energy surfaces of graphite with no dangling bonds, so that the nanotubes are in fact the expected structures. In the electron microscope images, one typically observes nanotubes along their lengths, with the electron beam falling perpendicular to the axis of the nanotube. In high-resolution images, it is possible to see spots due to the lattice planes running along the length of the nanotubes. Iijima [66] has published such an image for the (110) planes separated by 2.1 Å. Ring-like patterns are found due to individual tubes comprising cylindrical graphitic sheets which are independently oriented (with no registry between the sheets) with helical symmetry for the arrangement of the hexagons. Graphitic cylinders would have dangling bonds at the tips, but the carbon nanotubes are capped by dome-shaped hemispherical fullerene-type units. The capping units consist of pentagons to provide the curvature necessary for closure. Ajayan et al. [8a] studied the distribution of pentagons at the caps of carbon nanotubes, finding that the caps need not be perfectly conical or hemispherical, but can form skewed structures. The simplest

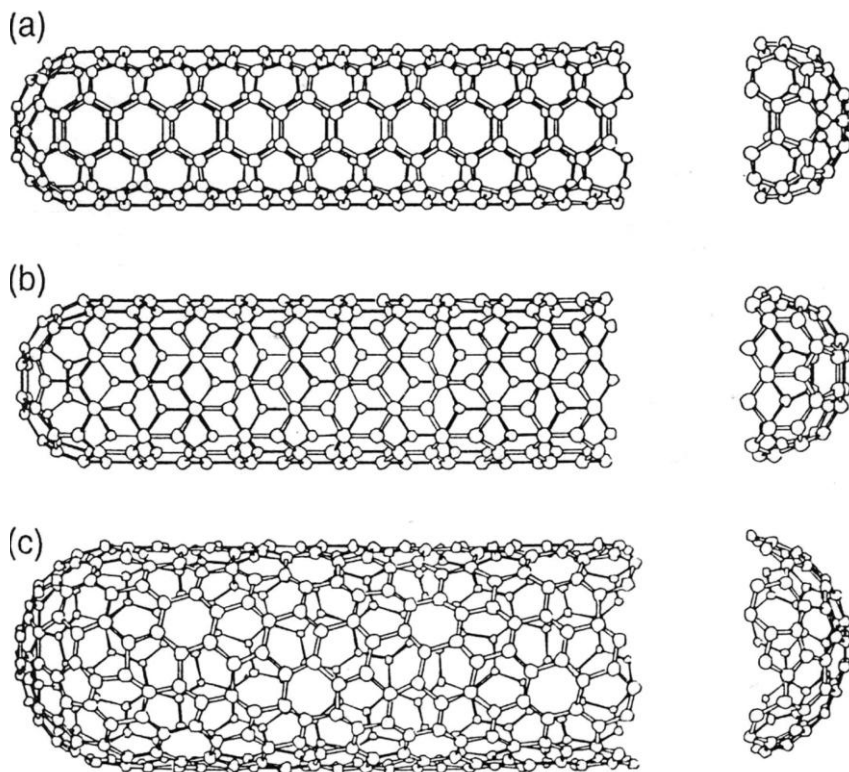


**Fig. 8.7.** Models of (a) armchair, (b) zigzag, and (c) chiral nanotubes. Reproduced from ref. [17], with permission.

possible single-walled carbon nanotube can be visualized by cutting the  $C_{60}$  structure across the middle and adding a cylinder of graphite of the same diameter. If  $C_{60}$  is bisected normal to a five-fold axis, an armchair tube is formed, and if it is bisected normal to a three-fold axis, a zigzag tube is formed. Armchair and zigzag tubes are non-chiral. In addition to these, a variety of chiral tubes can be formed with the screw axis along the axis of the tube. In Figure 8.7 we show the models of the three types of nanotubes formed by bisecting the  $C_{60}$  molecule and adding a cylinder of graphite. Nanotubes can be defined by a chiral angle  $\theta$  and a chiral vector  $C_h$ , given by Eq. (1), where  $a_1$  and  $a_2$  are unit vectors in a 2D graphene lattice and  $n$  and  $m$  are integers.

$$C_h = na_1 + ma_2 \quad (1)$$

The vector  $C_h$  connects two crystallographically equivalent sites on a 2D graphene sheet and the chiral angle is the angle it makes with respect to the zigzag direction, Figure 8.8. A tube is formed by rolling up the graphene sheet in such a way that the two points connected by the chiral vector coincide. A number of possible chiral

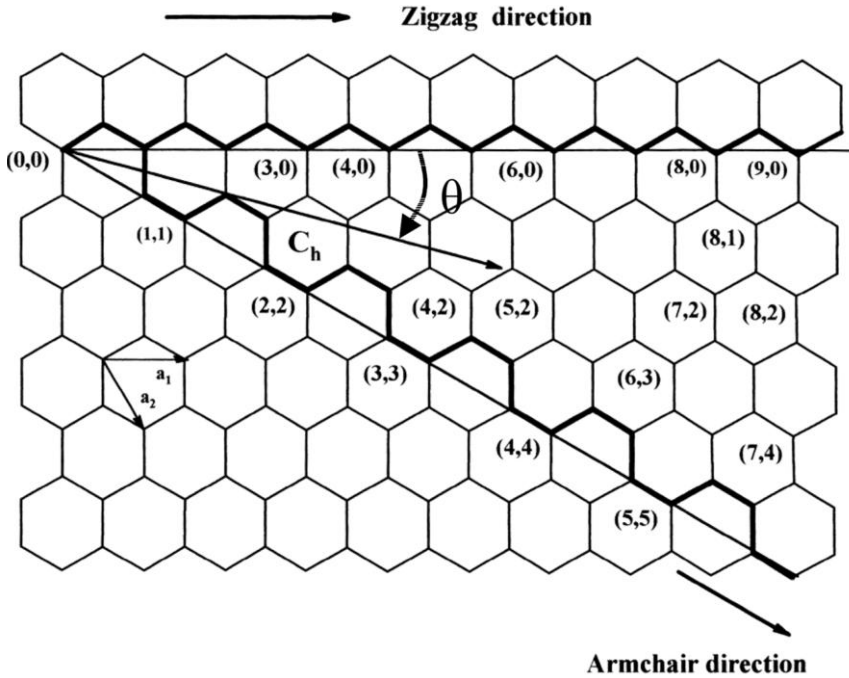


Fig. 8.8. A 2D graphene sheet showing chiral vector  $C_h$  and chiral angle.

vectors can be specified by Eq. (1) in terms of pairs of integers  $(n, m)$ . Many such pairs are shown in Figure 8.8 and each pair  $(n, m)$  defines a different way of rolling up the graphene sheet to form a carbon nanotube of certain chirality. The limiting cases are  $n \neq 0, m = 0$  (zigzag tube), and  $n = m \neq 0$ , (armchair tube). For a carbon nanotube defined by the index  $(n, m)$ , the diameter,  $d$ , and the chiral angle,  $\theta$ , are given by following Eq. (2) and (3) where  $a = 1.42(3)^{1/2}$  and  $0 \leq \theta \leq 30^\circ$ .

$$d = a(m^2 + mn + n^2)^{1/2} / \pi \quad (2)$$

$$\theta = \arctan(-(3)^{1/2}m) / (2n + m) \quad (3)$$

Armchair SWNTs are metals; those with  $n - m = 3k$ , where  $k$  is a nonzero integer, are semiconductors with a tiny band gap; and all others are semiconductors with a band gap that inversely depends on the nanotube diameter [8b, 17, 18]. The MWNTs consist of capped concentric cylinders separated by  $3.45 \text{ \AA}$  (which is slightly larger than the interlayer spacing in graphite) because the number of carbon atoms increases as we go from an inner cylinder to an outer cylinder and it is not possible to maintain perfect ABAB... stacking as in graphite. Thus, an interlayer spacing close to that in turbostratic graphite is observed in MWNTs. In addition to pentagons and hexagons, carbon nanotubes can also have heptagons. Pentagons impart a positive curvature whereas heptagons give rise to a negative

curvature to the otherwise flat graphene sheet made of hexagons. Thus, nanotubes with pentagons and heptagons will have unusual curvatures and shapes. Bent nanotubes arising from the presence of pentagons and heptagons on opposite sides of the tube have been observed [66]. Based on force field calculations, Tersoff and Ruoff [67] suggest that the nanotubes will form cylindrical bundles in a crystal and large tubes will be hexagonal to maximize the van der Waals contact between the tubes. Simulation studies indicate radial p-orbital character and large pyramidalization angles at the sites of local deformation [68].

An interesting observation with SWNTs is the presence of rings in the electron microscopic images [69]. The rings are formed during the ultrasound treatment in an acidic medium, followed by settling of nanotube dispersions on the substrate. Similar ring morphologies are observed in atomic force microscope (AFM) and SEM studies of catalytically produced multi-walled nanotubes [70a]. Huang et al. [70b] have observed “crop circles” of aligned nanotubes in a direction normal to the substrate surface, on pyrolysing Fe(II)phthalocyanine. Yet another important nanostructure discovered recently is the presence of encapsulated fullerenes inside SWNTs, as observed by high resolution TEM [71, 72]. Fullerenes were observed inside the nanotubes after annealing laser-synthesized SWNTs. We present a typical TEM image showing the presence of  $C_{60}$  in SWNTs in Figure 8.6 (inset). Analysis of the size distribution of the encapsulated fullerenes inside arc-produced SWNTs shows that there are indeed significant quantities of fullerenes in the size range  $C_{36}$ – $C_{120}$  in the nanotube capillaries [73].

X-ray diffraction (XRD) measurements have been employed to characterize carbon nanotubes [74, 75]. The XRD patterns of nanotubes show only the ( $hk0$ ) and (001) reflections but no general ( $hkl$ ) reflections. This is the case in turbostratically modified graphites [76]. Warren [77] has suggested special methods for the analysis of the ( $hk0$ ) reflections and such studies support the electron microscopy data in showing that structural correlations exist along the direction perpendicular to the carbon nanotube axis as well as within each individual tube, but not in any combination of these. The correlation lengths obtained from the analysis of the XRD patterns are in the same regime as that from microscopy.

Ebbesen et al. [78] find that the nanotube bundles are self-similar in the sense that large cylindrical bundles comprise smaller ones and the smaller ones are made up of nanotubes and so on. STM has been used to probe the electronic structure of carbon nanotubes deposited on various substrates [81–83]. STM has also been used to probe  $sp^3$  defect structures, closure of the tips and pentagon-induced changes in the electronic structure in carbon nanotubes [84]. Venema et al. [85] have obtained atomically resolved STM images of SWNTs, wherein the chirality of the nanotubes is unambiguously determined, which in turn influences the electronic property of the nanotubes. Raman spectroscopy has provided important insights into the structure of nanotubes. Jishi et al. [86] calculated the Raman-active phonon modes using a zone-folding method for a 2D graphene sheet, and demonstrated that there are 15 allowed Raman modes for each diameter of the tube. The frequency of the allowed mode depends on the tube diameter and the chiral angle, the number of modes being independent of the diameter. Hiura

et al. [87] surprisingly found that the linewidth of phonon peaks in the Raman spectrum was narrow, of the order of  $20 \text{ cm}^{-1}$ . The Raman phonon frequency of nanotubes is softer than that of HOPG, probably due to the curvature of the nanotubes. Softening of phonon modes can be related to the larger  $c$ -axis lattice parameter in the nanotube as compared to graphite. Holden et al. [88] have examined the spectra of single-walled carbon nanotubes produced by using Co catalysts and have compared them with the predictions of Jishi et al. [86]. Studies on SWNTs by Rao et al. [89] reveal many of the characteristic normal modes of an armchair  $(n,n)$  carbon nanotubes and also show a diameter-selective resonance behavior. The resonance results from the one-dimensional quantum confinement of electrons in the nanotubes. Kasuya et al. [90] have provided the first evidence for a diameter-dependent dispersion arising from the cylindrical symmetry of the nanotubes. They carried out Raman scattering studies on SWNTs with mean diameters of 1.1, 1.3 and 2 nm and found size-dependent multiple splitting of the optical phonon peak corresponding to the  $E_{2g}$  mode of graphite. In Figure 8.9, we show typical Raman spectra of laser-synthesized SWNTs. Assignment of bands due to nanotubes of different diameters is indicated in the figure. Polarized Raman

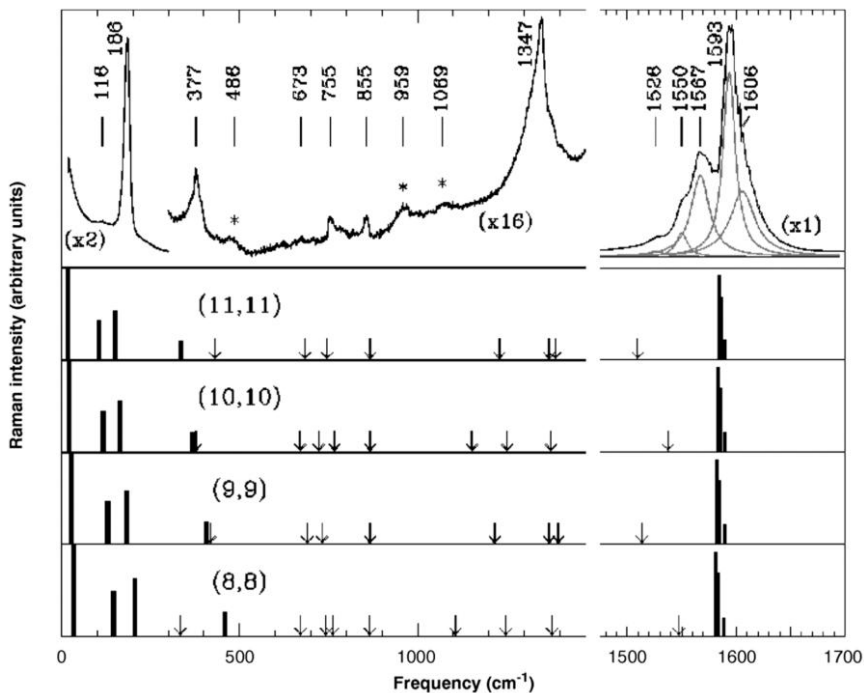


**Fig. 8.9.** Raman spectra showing the diameter-dependent scattering in SWNTs. An asterisk in the spectrum refers to a feature assigned tentatively to second-order Raman

scattering. The four bottom panels show calculated Raman spectra for armchair  $(n,n)$  nanotubes ( $n = 8-11$ ). Reproduced from ref. [89], with permission.



studies on aligned multi-walled carbon nanotubes show a strong dependence of the graphite-like G-band and disorder induced D-band on the polarization geometry [91].

Pressure-induced phase transformations under static and dynamic loading between the many allotropes of carbon like diamond, graphite, C<sub>60</sub> and C<sub>70</sub> and their polymeric and amorphous forms are of academic and practical importance. Pressure-effects on SWNT bundles have been probed by Raman spectroscopy up to a maximum pressure of 25.9 GPa (1 GPa = 10<sup>9</sup> N m<sup>-2</sup>) in a diamond anvil cell [92, 93]. The spectra arising from the radial and tangential modes at 0.1 GPa are similar to those reported earlier at atmospheric pressure [89]. The two dominant radial bands in the spectrum of the sample recorded at 0.1 GPa were at 172 and 182 cm<sup>-1</sup>. For an isolated SWNT, the calculated frequencies of the radial mode  $\omega_R$  [cm<sup>-1</sup>] for a tube of diameter  $d$  [nm] fit to  $\omega_R = 223.75/d$ , irrespective of the nature of the tube [94]. This gives  $\omega_R = 164$  cm<sup>-1</sup> for the (10,10) tube and 183 cm<sup>-1</sup> for the (9,9) tube. The inclusion of van der Waals interaction between the (9,9) tubes shifts the radial mode frequency from 171.8 cm<sup>-1</sup> (for an isolated tube) to 186.2 cm<sup>-1</sup>. This blue shift of 14.4 cm<sup>-1</sup> is due to intertube interaction, and is independent of the tube diameter [95]. Accordingly, the empirical relation for the diameter dependence of the radial mode frequency in a SWNT bundle is given by,  $\omega_R = 14.4 + 209.9/d$ , which retains the  $1/d$  dependence of  $\omega_R$  and reproduces  $\omega_R = 186.2$  cm<sup>-1</sup> for the (9,9) tube [96]. The tangential modes are assigned in terms of the irreducible representations of  $D_{nh}$  ( $D_{nd}$ ) for even  $n$  (odd  $n$ ), with 1531 cm<sup>-1</sup> as  $E_{1g}$ , 1553 and 1568 cm<sup>-1</sup> as  $E_{2g}$ , 1594 cm<sup>-1</sup> with unresolved doublet  $A_{1g} + E_{1g}$  and 1606 cm<sup>-1</sup> with  $E_{2g}$  symmetry [97, 98]. The intensities of the radial modes fall rapidly with increasing pressure, and were not discernible beyond 2.6 GPa, but the features are reversible. The intensities of the tangential modes also decrease with pressure. The modes at  $\omega_T = 1568$  cm<sup>-1</sup> and 1594 cm<sup>-1</sup> show softening between ~10–16 GPa, beyond 16 GPa, the band position increases with pressure. Remarkably, when the pressure is reduced from the highest pressure of 25.9 GPa, the peak positions follow the same trend as in the increasing pressure run. Studies of SWNTs under high pressure confirm the potential of these materials as the strongest ever carbon nanofibers and also their remarkable resilience [96, 99].

### 8.2.3

#### Mechanism of Formation

Several growth models are proposed for the carbon nanotubes prepared by the pyrolysis of hydrocarbons on metal surfaces. Baker and Harris [100] suggested a four-step mechanism. In the first step, the hydrocarbon decomposes on the metal surface to release hydrogen and carbon, which dissolves in the particle. The second step involves the diffusion of the carbon through the metal particle and its precipitation on the rear face to form the body of the filament. The supply of carbon onto the front face is faster than the diffusion through the bulk, causing an accumulation of carbon on the front face, which must be removed to prevent the physical

blocking of the active surface. This is achieved by surface diffusion and the carbon forms a skin around the main filament body, in step three. In the fourth step, overcoating and deactivation of the catalyst and termination of tube growth takes place. Oberlin et al. [101] proposed a mechanism in which bulk diffusion is insignificant and carbon is entirely transported around the particle by surface diffusion. Dai et al. [49] proposed a mechanism wherein carbon forms a hemispherical graphene cap on the catalyst particle and the nanotubes grow from such a yarmulke. The diameter of the nanotube is controlled by the size of the catalytic particle, nanometer size particles yielding SWNTs. A crucial feature of this model is that it avoids dangling bonds at all stages of growth. SWNTs produced by arc vaporization may also be formed by the yarmulke mechanism.

A number of models have been proposed for the growth of MWNTs in the arc. Endo and Kroto [102], based on the observation of  $C_2$  ejection from  $C_{60}$  in mass spectrometry, suggest that tube formation processes are a consequence of the formation of fullerenes. Smalley [103], however, pointed out that only the growth of outer layers of multi-walled tubes would be permitted by such a mechanism. Iijima et al. [104] presented electron microscopy evidence for the open-ended growth of carbon nanotubes and suggested that the termination of incomplete layers of carbon seen on the tube surface may arise because of the extension and thickening of the nanotubes by the growth of graphite islands on the surfaces of existing tubes. The nucleation of pentagons and heptagons on the open tube ends results in a change in the direction of the growing tube and some novel morphologies, including one where the tube turns around  $180^\circ$  during the growth, have been observed. The growth is self-similar and fractal-like with the inner tubules telescoping out of the larger ones, with logarithmic scaling of the size.

Isotope scrambling experiments of Ebbesen et al. [105] show that under the conditions of fullerene formation, the plasma has vaporized atoms of carbon. Based on tube morphologies, a mechanism similar to that of Saito et al. [106], wherein the carbonaceous material reaching the cathode anneals into polyhedral particles, was suggested. Given the right conditions, the tip might open and continue to grow. Such a growth could occur from the outside inwards. Ebbesen et al. [105] suggest the possibility of tubes forming directly from the closing of a large graphene sheet. Such a suggestion gains credence from the simulations of Robertson et al. [107] who have examined the curling and closure of small graphitic ribbons. Amelinckx et al. [108a] introduce the concept of a spatial velocity hodograph to describe the extrusion of a carbon tubule from a catalytic particle. The model is consistent with the observed tubule shapes and explains how spontaneous plastic deformation of the tubule can occur. Amelinckx et al. [108b] propose a model in which the graphene sheets can form both concentric cylinders and scroll-type structures. They also propose that the nanotubes nucleate from a large fullerene type dome. Maiti et al. [109] propose a model wherein nanometer-sized protrusions on the metal particle surface lead to the nucleation of SWNTs.

TEM examination of the carbonaceous products obtained from the pyrolysis of hydrocarbons and organometallic precursors indicates that the size of the catalyst particle plays an important role (see Figure 8.10).



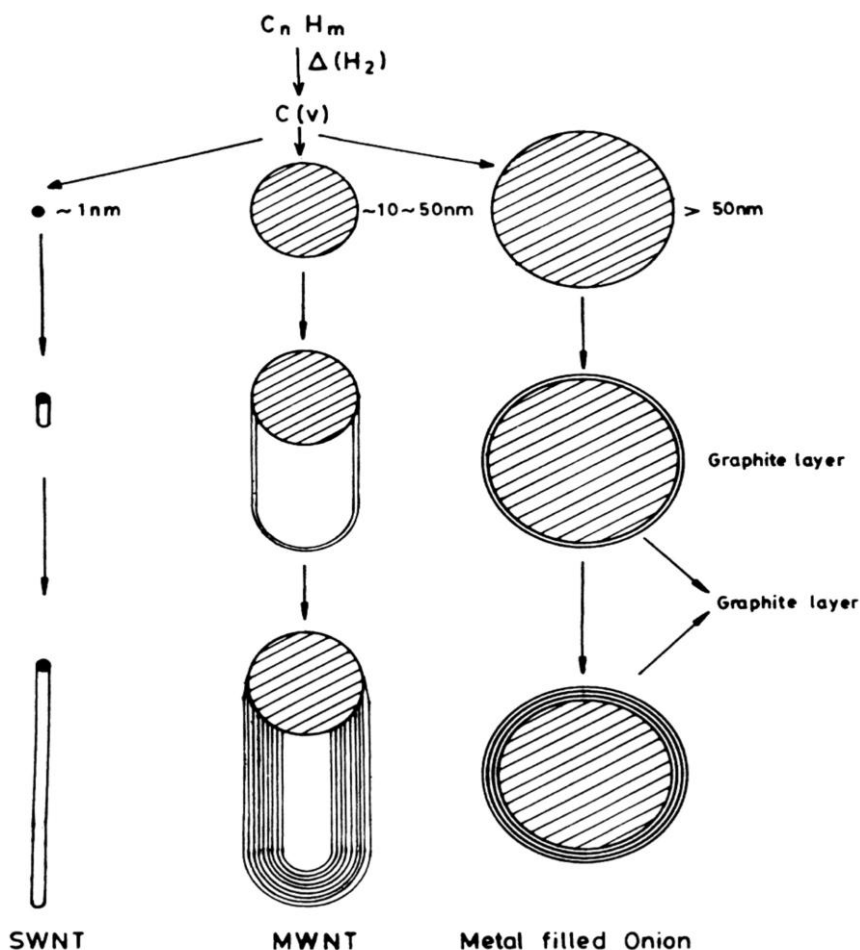


**Fig. 8.10.** Schematic representation of the dependence of the carbon nanostructure obtained by hydrocarbon pyrolysis on the size of the metal nanoparticles. Reproduced from ref. [20a], with permission.

#### 8.2.4

#### Chemically Modified Carbon Nanotubes

##### 8.2.4.1 Doping with Boron and Nitrogen

Since the discovery of carbon nanotubes, there has been immense interest in substituting carbon with other elements. Accordingly, boron-carbon (B-C), boron-carbon-nitrogen (B-C-N) and carbon-nitrogen (C-N) nanotubes have been prepared and characterized. Boron-substitution in the carbon nanotubes gives rise to p-type doping and nitrogen-doped carbon nanotubes correspond to n-type doping. Novel electron transport properties are expected of such doped nanotubes [110].

Boron-doped carbon nanotubes have been synthesized by carrying out the pyrolysis of mixtures of acetylene and diborane and characterized by employing microscopic and spectroscopic techniques [111]. The average composition of these nanotubes is  $C_{35}B$ . B–C–N nanotubes have been prepared by striking an arc between a graphite anode filled with B–N and a pure graphite cathode in a helium atmosphere [112]. B–C–N nanotubes have also been obtained by laser ablation of a composite target containing B–N, carbon, Ni and Co at 1000 °C under flowing nitrogen [113]. Terrones et al. [114] pyrolyzed the addition compound,  $CH_3CN:BCl_3$ , over Co powder at 1000 °C to obtain B–C–N nanotubes. B–C–N as well as C–N nanotubes were prepared by Sen et al. [115] by the pyrolysis of appropriate precursors. Pyrolysis of aza-aromatics such as pyridine over Co catalysts gives C–N nanotubes ( $C_{33}N$  on average). Pyrolysis of the 1:1 addition compound of  $BH_3$  with  $(CH_3)_3N$  produces B–C–N nanotubes. Typical TEM images of a few nanotubes are shown in Figure 8.11, exhibiting bamboo-shaped, nested cone-shaped cross sections as well as unusual morphology, including coiled nanotubes. The composition of the B–C–N nanotubes varies with the preparation. Furthermore, considerable variability exists in the composition in any given batch of B–C, B–C–N or C–N nanotubes obtained by the pyrolysis of precursors.

Aligned carbon nanotubes are considered ideal for field emission properties. The availability of aligned bundles of doped carbon nanotubes may provide further improvement in field-emission characteristics. Nath et al. [116a] have obtained aligned carbon–nitrogen nanotube bundles by the pyrolysis of pyridine over sol-gel derived iron/silica or cobalt/silica substrates. Employing anodic alumina, Sung et al. [116b] synthesized C–N nanotubes by electron cyclotron resonance CVD, using  $C_2H_2$  and  $N_2$ . Suenaga et al. [117] carried out CVD of Ni-phthalocyanine to obtain aligned C–N nanotubes.

Goldberg et al. [118] have employed a method wherein SWNTs were thermally treated with boron trioxide in a nitrogen atmosphere to obtain boron or boron and nitrogen doped SWNTs. EELS analysis showed the boron content to be ~10 at.% in B–C nanotubes. An interesting aspect of the B–C–N nanostructures is that phase separation occurs in which the  $BC_3$  islands segregate in the graphene sheets. Tunneling conductance measurements of doped nanotubes demonstrate acceptor-like states, near the Fermi level, arising out of the  $BC_3$  islands [119]. Efsarjani et al. [120] propose that a nanotube with donor atoms at one side and acceptor atoms on the other can function as a nano-diode. An experimental situation near to this effect is the observation of rectification in a SWNT [121]. The presence of an impurity in one of the segments of a SWNT influences its nonlinear transport behavior.

#### 8.2.4.2 Opening, Filling and Functionalizing Nanotubes

Multi-walled nanotubes are generally closed at either end, the closure being made possible by the presence of five-membered rings. MWNTs can be uncapped by oxidation with carbon dioxide or oxygen at elevated temperatures [74, 122, 123]. High yields of uncapped MWNTs are, however, obtained by boiling them in concentrated  $HNO_3$ . Filling the opened nanotubes with metals has been accomplished. The well-known method [124] involves the treatment of the nanotubes with boiling

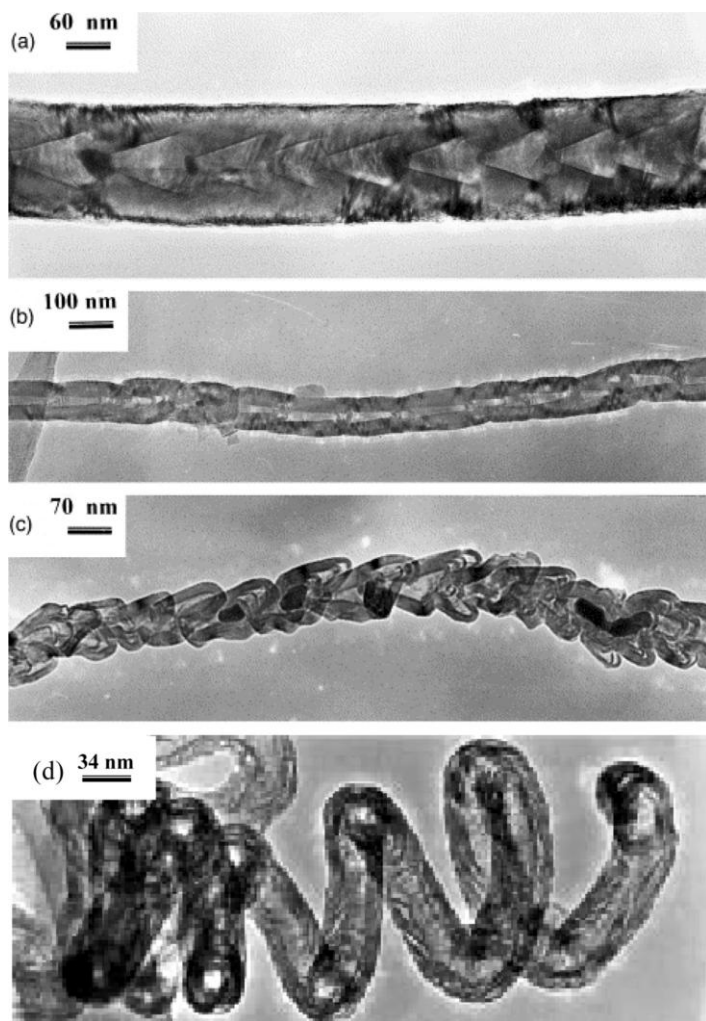


**Fig. 8.11.** TEM images of carbon nanotubes obtained by the pyrolysis of pyridine (flow rate =  $30 \text{ cm}^3 \text{ min}^{-1}$ ) over Fe/SiO<sub>2</sub> substrates at 900 °C for 1.5 h under Ar ( $120 \text{ cm}^3 \text{ min}^{-1}$ ) flow. The nanotubes show (a) bamboo shape, (b) nested cone, and (c) other unusual morphologies. (d) The TEM image of a coiled nanotube obtained by pyridine pyrolysis over Co. Reproduced from ref. [116a], with permission.

HNO<sub>3</sub> in the presence of metal salts such as Ni(NO<sub>3</sub>)<sub>2</sub>. The nanotubes are opened by HNO<sub>3</sub> and filled by the metal salt. On drying and calcination, the metal salt transforms to the metal oxide and reduction of the encapsulated oxide in hydrogen at around 400 °C gives rise to the metal inside the nanotubes. MWNTs have been opened by using a variety of oxidants [125–127] and the opened nanotubes have been filled with Ag, Au, Pd, or Pt by different chemical means, rather than by reduction with hydrogen at high temperatures [127]. By employing in situ tech-

niques in a TEM, Bower et al. [128] observed alkali metal intercalation into the SWNTs. Sealed tube reactions of SWNTs and metal salts are also known to yield metal intercalated SWNTs [129]. In an effort to realize the conversion of  $sp^2$  carbon of nanotubes into  $sp^3$ , Hsu et al. [130] treated potassium intercalated MWNTs with  $CCl_4$  hydrothermally, and obtained crystallization of KCl inside the nanotubes and within the tube walls. Possible ways of closing the nanotubes, opened by oxidants, have been examined [127]. Besides opening, filling and closing nanotubes, highly functionalized MWNTs have been prepared by treatment with acids [127, 131]. SWNTs are readily opened by mild treatment with acids and filled with metals [45, 132]. Acid-treated nanotube surfaces can be decorated by nanoparticles of metals such as Au, Ag or Pt [45, 133].

Chen et al. [134] have derivatized SWNT fragments with halogen and amine moieties in order to dissolve them in organic solvents. Doping has been carried out to modify their electronic properties in the solution phase. Fluorination of SWNTs has been carried out by Mickelson et al. [135]. Fluorinated nanotubes can be solvated in alcohol media and precipitated back by reaction with hydrazine. STM studies of fluorinated SWNTs reveal an interesting banded structure followed by atomically resolved regions, indicating sidewall functionalization [136]. Starting from fluorinated SWNTs, Boul et al. [137] have carried out alkylation by reaction with alkylmagnesium bromides or alkyllithium. Individual SWNTs have been deposited controllably on chemically functionalized nanolithographic templates [138].

### 8.2.5

#### Electronic Structure, Properties and Devices

##### 8.2.5.1 Electronic Structure and Properties

As with the fullerenes, the curvature of the graphitic sheets in the nanotubes would be expected to influence the electronic structure. The electronic properties of perfect MWNTs are rather similar to those of perfect SWNTs, because the coupling between the cylinders is weak in MWNTs. Calculations show that nanotubes may be as good conductors as copper, although a combination of the degree of helicity and the number of six-membered rings per turn around the tube can tune the electronic properties in the metal–semiconductor range [139–141]. Low-temperature STM and scanning tunneling spectroscopy (STS) studies of SWNTs reveal the atomically resolved images of the graphene cylinders and their size-specific transport properties [142, 143], in agreement with theoretical predictions. Collins et al. [144] used STM to explore local electrical characteristics of SWNTs. Well-defined positions where the current changes abruptly from a graphite-like response to a highly nonlinear response, were found, including near-perfect rectification. STM studies conducted in our laboratory in ultra-high vacuum (UHV) show a variable conductivity and gap along the length of the nanotubes. Because of the nearly one-dimensional electronic structure, electron transport in metallic SWNTs and MWNTs occurs ballistically over long nanotube lengths, enabling them to carry high currents with essentially no heating [145, 146]. Phonons also

propagate easily along the nanotube. The measured room temperature thermal conductivity for an individual MWNT ( $>3000 \text{ W m}^{-1} \text{ K}^{-1}$ ) is greater than that of natural diamond and the basal plane of graphite (both  $2000 \text{ W m}^{-1} \text{ K}^{-1}$ ) [147]. Superconductivity has also been observed, but only at low temperatures, with transition temperatures of  $\sim 0.55 \text{ K}$  for  $1.4 \text{ nm}$  diameter SWNTs [148] and  $\sim 5 \text{ K}$  for  $0.5 \text{ nm}$  diameter SWNTs grown in zeolites [149].

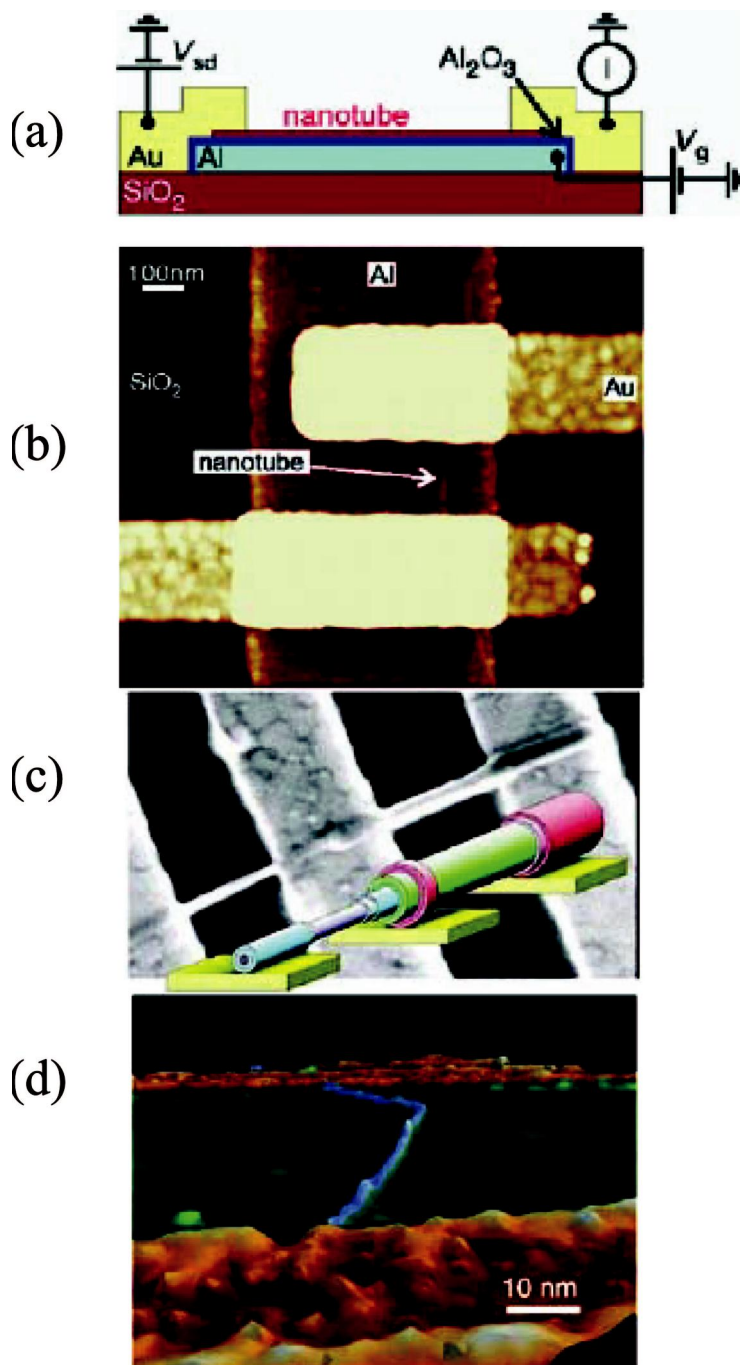
### 8.2.5.2 Electronic and Electrochemical Devices

**Electrochemical Devices** Because of the high electrochemically accessible surface area of porous nanotube arrays, combined with their high electronic conductivity and useful mechanical properties, these materials are attractive as electrodes for devices that use electrochemical double-layer charge injection. Examples include “supercapacitors,” which have giant capacitances in comparison with those of ordinary dielectric-based capacitors, and electromechanical actuators that may eventually be used in robots. Like ordinary capacitors, carbon nanotube supercapacitors [150–152] and electromechanical actuators [153] typically comprise two electrodes separated by an electronically insulating material, which is ionically conducting in electrochemical devices. Because this separation is about a nanometer for nanotubes, as compared with the micrometer or larger separations in ordinary dielectric capacitors, very large capacitances result from the high nanotube surface area accessible to the electrolyte. These capacitances (typically between  $\sim 15$  and  $\sim 200 \text{ F g}^{-1}$ , depending on the surface area of the nanotube array) result in large amounts of charge injection when only a few volts are applied [150–153]. This charge injection can be used for energy storage in nanotube supercapacitors and to provide electrode expansions and contractions that can do mechanical work in electromechanical actuators. The capacitances ( $180$  and  $102 \text{ F g}^{-1}$  for SWNT and MWNT electrodes, respectively) and power densities ( $20 \text{ kW kg}^{-1}$  at energy densities of  $\sim 7 \text{ W h kg}^{-1}$  for SWNT electrodes) [150, 151] are attractive, especially because performance can likely be improved by replacing SWNT bundles and MWNTs with unbundled SWNTs. An extraordinarily short discharge time of  $7 \text{ ms}$  was reported [152] for  $10$  MWNT capacitors connected in series, which operated at up to  $10 \text{ V}$ . Nanotube electromechanical actuators function at a few volts, compared with the  $\sim 100 \text{ V}$  used for piezoelectric stacks and the  $\geq 1000 \text{ V}$  used for electrostrictive actuators. Nanotube actuators have been operated at temperatures up to  $350^\circ\text{C}$ . Operation above  $1000^\circ\text{C}$  should be possible, on the basis of SWNT thermal stability and industrial carbon electrode electrochemical application above this temperature [20b]. From observed nanotube actuator strains that can exceed  $1\%$ , order-of-magnitude advantages over commercial actuators in work per cycle and stress generation capabilities are predicted if the mechanical properties of nanotube sheets can be increased to close to the inherent mechanical properties of the individual nanotubes [20b]. The maximum observed isometric actuator stress of SWNT actuators is presently  $26 \text{ MPa}$  [20b]. This is  $>10$  times the stress initially reported for these actuators and  $\sim 100$  times that of the stress generation capability of natural muscle, and it approaches the stress generation capability of high-

modulus commercial ferroelectrics ( $\sim 40$  MPa). However, the ability to generate stress is still  $>100$  times lower than that predicted for nanotube fibers with the modulus of the individual SWNTs. The success of actuator technology based on carbon nanotubes will depend on improvements in the mechanical properties of nanotube sheets and fibers with a high surface area by increasing nanotube alignment and the binding between nanotubes. The use of nanotubes as electrodes in lithium batteries is a possibility because of the high reversible component of storage capacity at high discharge rates. The maximum reported reversible capacity is  $1000 \text{ mA h g}^{-1}$  for SWNTs that are mechanically milled in order to enable the filling of nanotube cores, as compared to  $372 \text{ mA h g}^{-1}$  for graphite [154] and  $708 \text{ mA h g}^{-1}$  for ball-milled graphite [155].

**Nanometer-Sized Electronic Devices** The possible use of carbon nanotubes in nanoelectronics has aroused considerable interest. Dramatic recent advances have fueled speculation that nanotubes (SWNTs) will be useful for downsizing circuit dimensions. Because of their unique electronic properties, SWNTs can be interfaced with other materials to form novel heterostructures [156]. The simplest device one can imagine with carbon nanotubes is that involving a bend or a kink, arising from the presence of a diametrically opposite pentagon–heptagon pair. The resultant junction connects two nanotubes of different chirality and hence of different electronic structure, leading to the realization of an intramolecular device. Such a device in SWNTs is found to behave like a diode rectifier [157]. Silicon nanowire–carbon nanotube heterojunctions do indeed exhibit a rectification behavior [158].

The current-induced electromigration causes conventional metal wire interconnects to fail when the wire diameter becomes too small. The covalently bonded structure of carbon nanotubes militates against similar breakdown of nanotube wires and, because of ballistic transport, the intrinsic resistance of the nanotube should essentially vanish. Experimental results show that metallic SWNTs can carry up to  $10^9 \text{ A cm}^{-2}$ , whereas the maximum current densities for normal metals are  $10^5 \text{ A cm}^{-2}$  [145, 159]. Unfortunately, the ballistic current carrying capability is less useful for presently envisioned applications because of necessarily large contact resistances. An electronic circuit involving electrical leads to and from a SWNT will have a resistance of at least  $h/4e^2$  or  $6.5 \text{ k}\Omega$ , where  $h$  is Planck's constant and  $e$  is the charge of an electron [160]. Contacting all layers in a MWNT could reduce this contact resistance, but it cannot be totally eliminated. In nanotube field effect transistors (NT-FETs), gating has been achieved by applying a voltage to a submerged gate beneath a SWNT (Figure 8.12(a) and (b)), which was contacted at opposite nanotube ends by metal source and drain leads [161]. A typical nanoelectronic device of NT-FET consists of a semiconducting nanotube, which is on top of an insulating aluminum oxide layer, connected at both ends to a gold electrode. The nanotube is switched by applying a potential to the aluminum gate under the nanotube and aluminum oxide. The transistors were fabricated by lithographically applying electrodes to the nanotubes that were either randomly distributed on a silicon substrate or positioned on the substrate with an atomic





force microscope [162, 163]. A transistor assembled in this way may or may not work, depending on whether the chosen nanotube is semiconducting or metallic, over which the operator generally has no control. It is possible to selectively peel outer layers from a MWNT (Figure 8.12(c)) until a nanotube cylinder with the desired electronic properties is obtained [164], but this process is not yet very reliable and is probably unsuitable for mass production. Research toward nanoscopic NT-FETs aims to replace the source-drain channel structure with a nanotube. A more radical approach is to construct entire electronic circuits from interconnected nanotubes. Because the electronic properties depend on helicity, it should be possible to produce a diode, for example, by grafting a metallic nanotube to a semiconducting nanotube. Such a device has been demonstrated. The bihelical nanotube was not, however, rationally produced; rather, it was fortuitously recognized, in a normal nanotube sample, by its kinked structure (Figure 8.12(d)), which was caused by the helicity change [157]. The development of rational synthesis routes to multiply branched and interconnected low-defect nanotubes with targeted helicity would be a revolutionary advance for nanoelectronics.

With crossed SWNTs, three- and four-terminal electronic devices have been made [165], as well as a nonvolatile memory that functions like an electromechanical relay [166]. For such applications it is important to be able to connect the nanotubes of different diameters and chirality [167]. Complex three-point nanotube junctions have been proposed as the building blocks of nanoelectronics and in this regard Y- and T-junctions have been considered as prototypes [168, 169]. The Y- and T-junctions appear to defy the conventional models in favor of an equal number of five- and seven-membered rings to create nanotube junctions. Instead, the Y- and T-junctions can be created with an equal number of five- and eight-membered rings [169]. However, junctions consisting of crossed nanotubes have been fabricated to study their transport characteristics [165, 170]. Y-junction nanotubes have been produced by using Y-shaped nanochannel alumina as a template [171]. By carrying out a simple pyrolysis of a mixture of nickelocene with thiophene, Y-junction carbon nanotubes have been synthesized recently in good quantities [172]. A TEM image of such Y-junction nanotubes is shown in Figure 8.13(a) and (c). A TEM image revealing the presence of several Y-junction carbon nanotubes is shown in Figure 8.13(b). STM and STS studies of Y-junction carbon nanotubes show interesting diode-like device characteristics at the junctions. The  $I$ - $V$  plot at the junction is asymmetric with respect to bias polarity, unlike that along the arm. Such asymmetry is characteristic of a junction diode and this in

- ← **Fig. 8.12.** Nanoelectronic devices: (a) Schematic diagram [163] for a carbon NT-FET.  $V_{sd}$ , source-drain voltage;  $V_g$ , gate voltage. Reproduced from ref. [163], with permission. (b) Scanning tunneling microscope (STM) picture of a SWNT field-effect transistor made using the design of (a); the aluminum strip is overcoated with aluminum oxide. (c) Image and overlaying schematic representation for the effect of electrical pulses in removing successive layers of a MWNT, so that layers having desired transport properties for devices can be revealed. Reproduced from ref. [164], with permission. (d) STM image of a nanotube having regions of different helicity on opposite sides of a kink, which functions as a diode; one side of the kink is metallic, and the opposite side is semiconducting. The indicated scale bar is approximate. Reproduced from ref. [157], with permission.



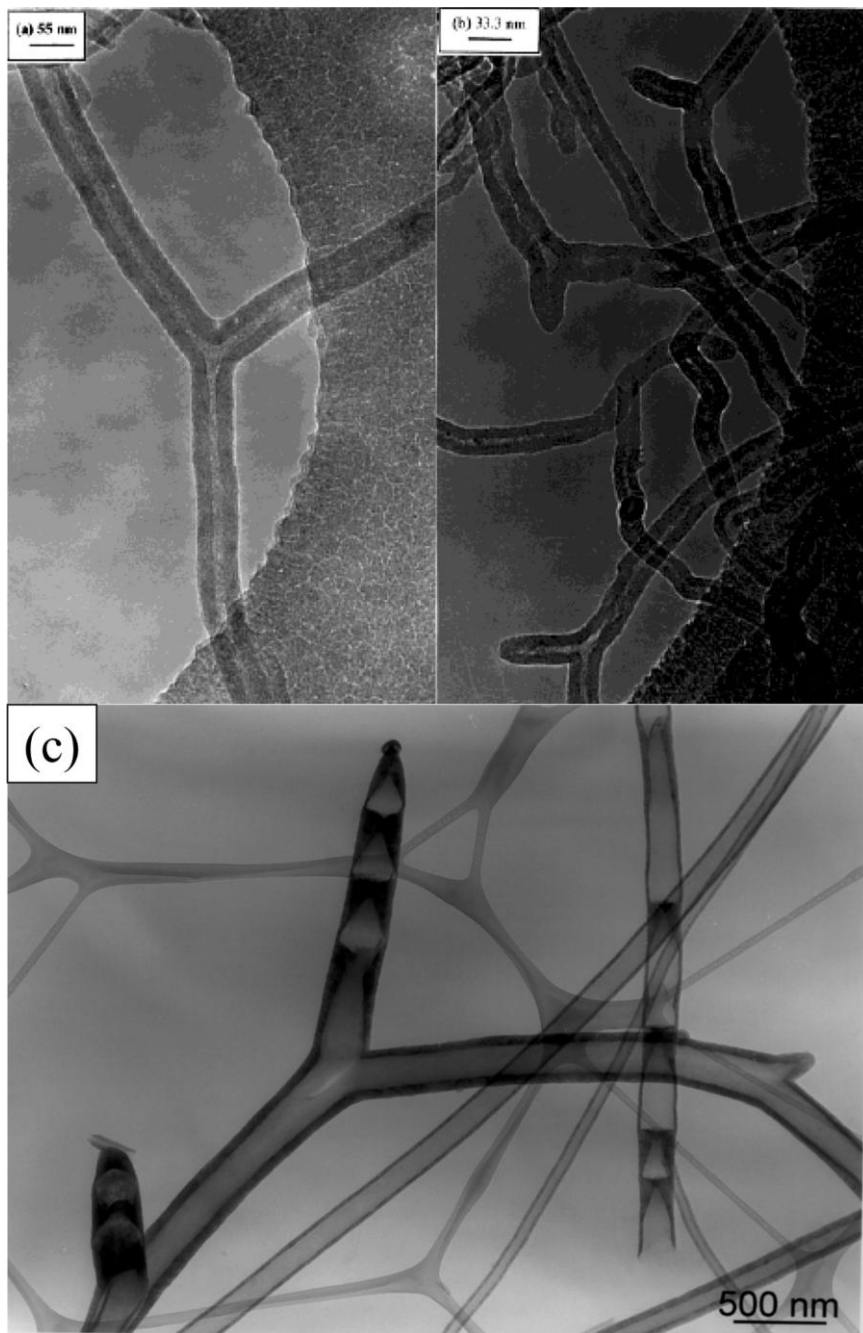


**Fig. 8.13.** TEM images of Y-junction carbon nanotubes obtained by the pyrolysis of nickelocene and thiophene at 1000 °C. Reproduced from ref. [172], with permission.

turn indicates the existence of intramolecular junctions in the carbon nanotubes. The spectrum of interesting findings discussed above opens up the possibility of assembling carbon nanotubes, possessing such novel device-like properties [157, 161, 162, 172] into multi-functional circuits, and ultimately towards the realization of a carbon-nanotube-based computer chip. Rueckes et al. [166] have recently described the concept of carbon-nanotube-based nonvolatile random access memory for molecular computing. The viability of the concept has also been demonstrated. Integrated nanotube devices involving two nanotube transistors have been reported [163, 166], providing visions of large-scale integration. Patterned growth of SWNTs on a 4 in (10 cm) silicon wafer [173] may prove an important step toward integrated nanotube electronics. IBM expects that nanotube electronics will be realized in about a decade [174].

**Sensors and Probes** Possible chemical sensor applications of nonmetallic nanotubes are interesting, because nanotube electronic transport and thermopower (voltages between junctions caused by interjunction temperature differences) are very sensitive to substances that affect the amount of injected charge [175, 176]. The main advantages are the minute size of the nanotube sensing element and the correspondingly small amount of material required for a response. Major challenges remain, however, in making devices that differentiate between absorbed species in complex mixtures and provide rapid forward and reverse responses. Nishijima et al. [177] have developed such a novel microprocess incorporated in a SEM, to attach individual nanotubes to scanning probe microscope tips, which are later used as probes to image biological and industrial specimens. Carbon nanotube scanning probe tips for atomic probe microscopes are commercially available. The cylindrical shape and small tube diameter enable imaging in narrow, deep crevices and improve resolution in comparison to conventional nanoprobe, especially for high sample feature heights [178, 179]. Covalently modifying the nanotube tips, such as by adding biologically responsive ligands, enables the mapping of chemical and biological functions [180]. Nanoscopic tweezers have been made by Kim and Lieber that are driven by the electrostatic interaction between two nanotubes on a probe tip [181]. They attached carbon nanotubes to electrodes fabricated on pulled glass micropipettes. Voltages are applied to the electrodes to achieve closing and opening of the free ends of the nanotubes, to facilitate the grabbing and manipulation of submicron clusters and nanowires. They may be used as nanoprobe for assembly. These uses may not have the business impact of other applications, but they increase the value of measurement systems for characterization and manipulation on the nanometer scale. Arie et al. [182] use Ni<sub>3</sub>C-filled MWNTs as probes in a magnetic force microscope (MFM) and to image magnetic recording media. The resolution, however, needs improvement through the optimization of ferromagnetic particle size, trace height etc. Karl and Tomanek [183] propose a molecular pump based on carbon nanotubes for the transport of atoms. Using SWNTs attached to an AFM cantilever as the probe and atomically flat titanium surfaces on an  $\alpha$ -Al<sub>2</sub>O<sub>3</sub> substrate, Cooper et al. [184] demonstrate an areal data storage density of the order of terabits per square inch. This method

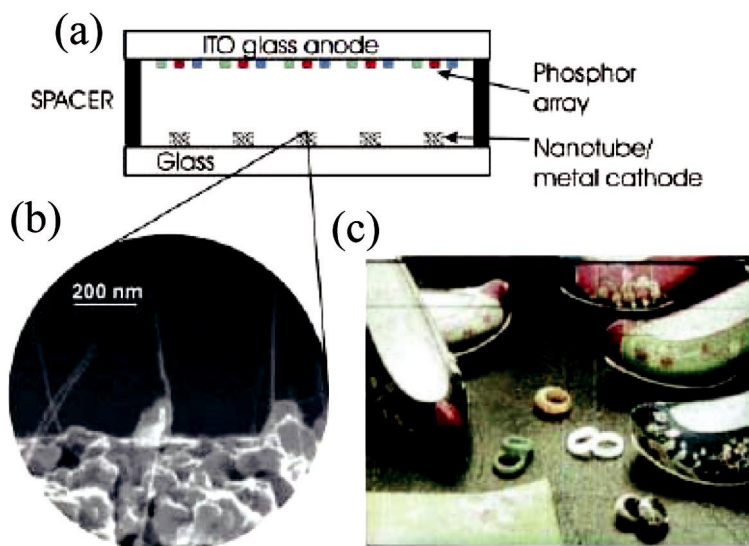


**Fig. 8.14.** (a) Schematic illustration of a flat panel display based on carbon nanotubes. ITO, indium tin oxide. (b) SEM image of an electron emitter for a display, showing well-separated SWNT bundles protruding from the supporting metal base. (c) Photograph of a 5 in (13 cm) nanotube field emission display made by Samsung. Reproduced from ref. [187], with permission.

employs SWNT based lithography which offers sub-10 nm nanofabrication capabilities. In contrast to conventional electronic devices operating on the basis of charge transport, spin-electronic devices operate upon the concept of spin transport.

**Field Emission** Industrial and academic research activity on electronic devices has focused principally on using SWNTs and MWNTs as field emission electron sources [185, 186] for flat panel displays [187], lamps [188], gas discharge tubes providing surge protection [189], and X-rays [190]. A potential applied between a carbon nanotube-coated surface and an anode produces high local fields, as a result of the small radius of the nanofiber tip and the length of the nanofiber. These local fields cause electrons to tunnel from the nanotube tip into the vacuum. Electric fields direct the field-emitted electrons toward the anode, where a phosphor produces light for the flat panel display application (Figure 8.14). However, the complete picture is not nearly so simple. Unlike for ordinary bulk metals, nanotube tip electron emission arises from discrete energy states, rather than continuous electronic bands [191]. Also, the emission behavior depends critically on the nanotube tip structure: Enhanced emission results from opening SWNT [186] or MWNT tips [188]. Nanotube field-emitting surfaces are relatively easy to manufacture by screen-printing nanotube pastes and do not deteriorate in moderate vacuum ( $10^{-8}$  torr). These are advantages over tungsten and molybdenum tip arrays, which require a vacuum of  $10^{-10}$  torr and are more difficult to fabricate [192]. Nanotubes

provide stable emission, long lifetimes, and low emission threshold potentials [185, 188]. Current densities as high as  $4 \text{ A cm}^{-2}$  have been obtained, compared with the  $10 \text{ mA cm}^{-2}$  needed for flat panel field emission displays and the  $>0.5 \text{ A cm}^{-2}$  required for microwave power amplifier tubes [193]. Flat panel displays are one of the more lucrative nanotube applications being developed by industry. However, they are also technically the most complex, requiring concurrent advances in electronic addressing circuitry, the development of low-voltage phosphors, methods for maintaining the required vacuum, spacers withstanding the high electric fields, and the elimination of faulty pixels. The advantages of nanotubes over liquid crystal displays are a low power consumption, high brightness, a wide viewing angle, a fast response rate, and a wide operating temperature range. Samsung has produced several generations of prototypes (Figure 8.14), including a 9 in (23 cm) red–blue–green color display that can reproduce moving images [187].

Aligned carbon nanotubes are considered to be ideal for the purpose because of the high packing density and hence their use as high brightness field emitters. MWNT-based field emission lighting devices have been built and their luminescence characteristics studied [194]. One such field emission lighting device is shown in Figure 8.15. Choi et al. [195a] have assembled a sealed 4.5 in<sup>2</sup> field-emission display device using vertically aligned SWNTs along with organic binders. The display in three primary colors has an emission current of 1.5 mA at  $3 \text{ V } \mu\text{m}^{-1}$ , with a brightness of  $1800 \text{ Cd m}^{-2}$ . Lee et al. [195b] have just shown that aligned nanotube bundles exhibit a high emission current density of around  $2.9 \text{ mA cm}^{-2}$  at  $3.7 \text{ V } \mu\text{m}^{-1}$ . Lovall et al. [196] have investigated the emission properties of SWNT ropes by employing field ion microscopy. The field-emitted electron energy distribution (FEED) of SWNT field emitters shows a large density of states near the Fermi energy. Emission characteristics of CVD produced MWNTs as well as SWNTs have been examined by Groning et al. [197], who obtained an emission site density of  $10000 \text{ emitters cm}^{-2}$  at fields around  $4 \text{ V } \mu\text{m}^{-1}$ . A work function of 5 eV was obtained with MWNTs, and a smaller value with the SWNTs.

The use of dense, quasi-aligned carbon nanotubes produced by the pyrolysis of ferrocene on a pointed tungsten tip exhibit high emission current densities with good performance characteristics [198]. In Figure 8.16(a) we show a typical  $I$ – $V$  plot for the carbon nanotube covered tungsten tip for currents ranging from 0.1 nA to 1 mA. The applied voltage was 4.3 kV for a total current of 1  $\mu\text{A}$  and 16.5 kV for 1000  $\mu\text{A}$ . The Fowler–Nordheim (F–N) plot shown in Figure 8.16(b) has two distinct regions. The behavior is metal-like in the low-field region, while it saturates at higher fields as the voltage is increased. We have obtained a field emission current density of  $1.5 \text{ A cm}^{-2}$  at a field of  $290 \text{ V mm}^{-1}$ , a value considerably higher than that found with planar cathodes. Accordingly, the field enhancement factor calculated from the slope of the F–N plot in the low-field region is also large. The field emission micrographs reveal the lobe structure symmetries typical of carbon nanotube bundles. The emission current is remarkably stable over an operating period of more than 3 h for various current values in the 10–500 mA range. The relative fluctuations decrease with increasing current level, and the emitter can be

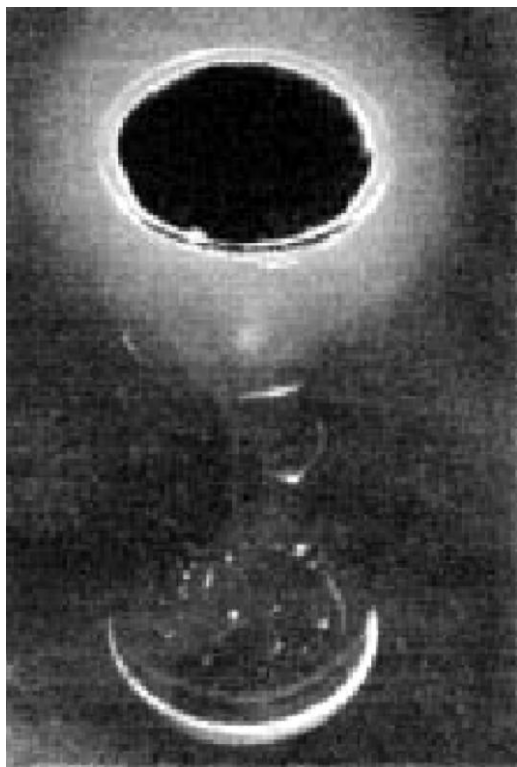


**Fig. 8.15.** A field-emission fluorescent display based on carbon nanotubes. The anode current is 200  $\mu\text{A}$  at a voltage of 10 kV. Reproduced from ref. [194], with permission.

operated continuously at the high current levels for at least 3 h without any degradation in the current.

**Other Properties of Carbon Nanotubes** Optical limiting properties of the carbon nanotubes are considered important for applications involving high power lasers. Optical limiting behavior of visible nanosecond laser pulses in the SWNT suspensions occurs mainly due to nonlinear scattering [199]. Nanotube composites with conducting polymers seem to possess novel electrical and optical properties. Yoshino et al. [200] observed increased conductivity at relatively low nanotube concentrations in the composites and an enhancement of photoconductivity, implying possible use in optoelectronic devices. SWNT-coated molybdenum electrodes appear to be alternatives for gas discharge tubes in advanced telecom networks, due to their lower dc breakdown voltage and higher reliability [189]. Electromechanical actuators based on SWNT-sheets appear to generate stresses higher than natural muscles and higher strains than the ferroelectric counterparts [153]. This behavior of nanotubes may be useful in the direct conversion of electrical energy to mechanical energy, relevant to applications in robotics. Wood and Wagner [201]

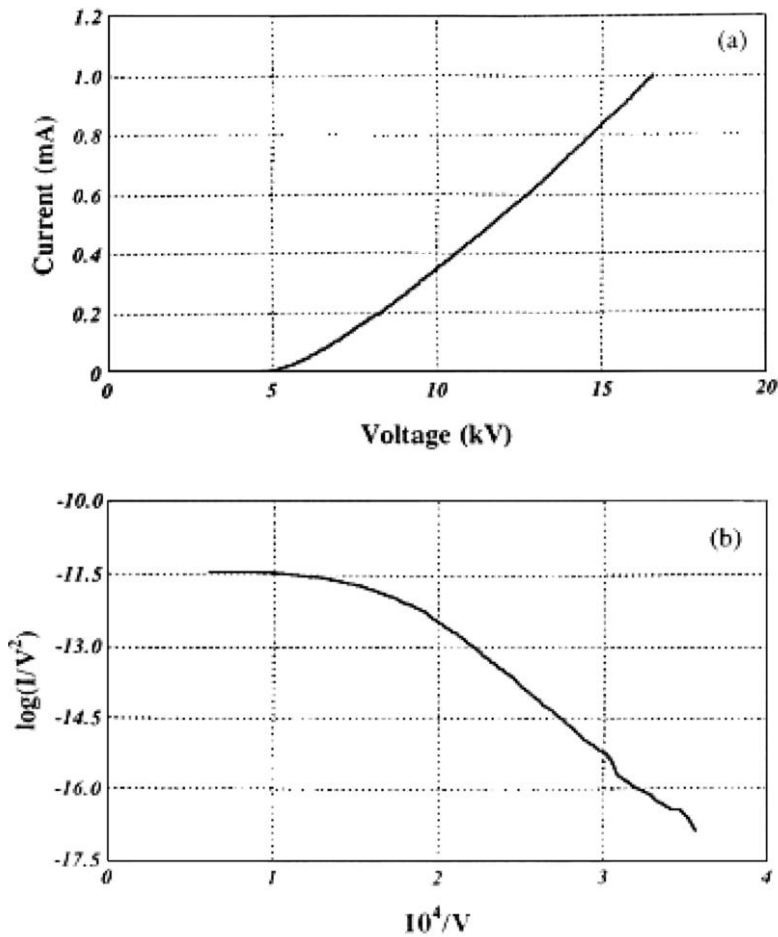


**Fig. 8.16.**  $I$ - $V$  characteristics showing field emission currents in the range 0.1 nA to 1 mA. (b) Fowler-Nordheim plot corresponding to the data in (a). Reproduced from ref. [198], with permission.

observe a significant shift of the peaks in the Raman spectrum of SWNTs upon immersion in liquids. This allows the use of nanotubes as molecular sensors. Kong et al. [176a] have measured the sensitivity of the electron transport properties of SWNTs to gaseous molecules such as  $\text{NO}_2$  or  $\text{NH}_3$ . The nanotubes exhibit faster response and a higher sensitivity than the available solid state sensors at room temperature; there is also good sensor reversibility. Ghosh et al. [176b] have reported that the flow of a liquid on single-walled carbon nanotube bundles induces a voltage/current in the sample along the direction of the flow. They found that the voltage so produced fits a logarithmic velocity dependence over nearly six decades of velocity. The magnitude of the voltage/current depends sensitively on the ionic conductivity and the polar nature of the liquid. Their measurements suggest that the dominant mechanism responsible for this highly nonlinear response should

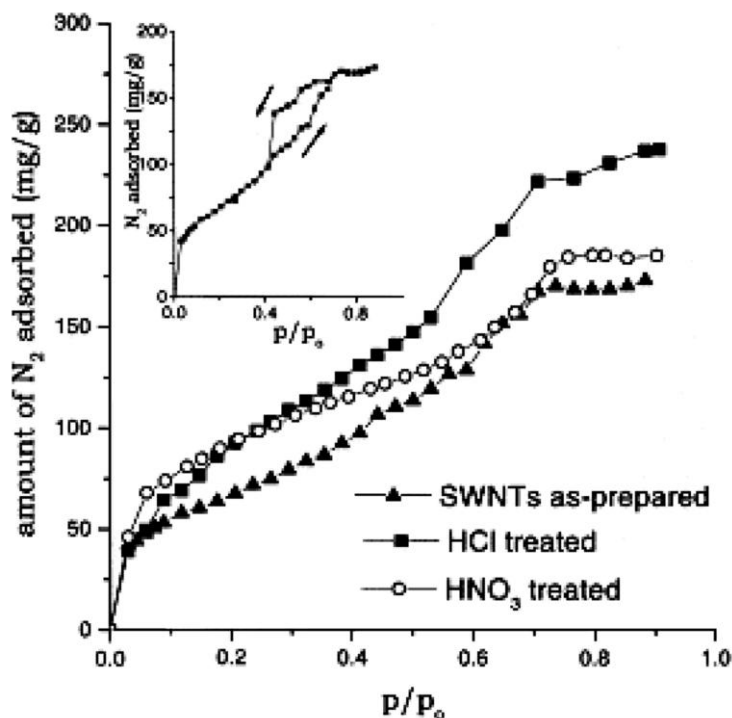


Fig. 8.17.  $N_2$  adsorption isotherms of SWNTs at 77 K; as-prepared ( $\blacktriangle$ ), HCl treated ( $\blacksquare$ ), and  $HNO_3$  treated ( $\circ$ ). Inset: The hysteresis in the adsorption–desorption isotherms for SWNTs. Reproduced from ref. [202], with permission.

involve a direct forcing of the free charge carriers in the nanotubes by the fluctuating Coulombic field of the liquid flowing past it. They propose an explanation based on pulsating asymmetric ratchets. Their work highlights the device potential for nanotubes as sensitive flow sensors and for energy conversion.

SWNTs have nano-sized channels which can facilitate adsorption of liquids or gases. Eswaramoorthy et al. [202] have studied the adsorption properties of SWNTs with respect to methane, benzene and nitrogen. The studies indicate that SWNTs are good microporous materials with a total surface area above  $400 \text{ m}^2 \text{ g}^{-1}$ . In Figure 8.17, we show typical adsorption isotherms for SWNTs. The unique hexagonal packing of the SWNTs in the bundles offers ideal channels, thus allowing the realization of one-dimensional (1D) adsorbates.

**Hydrogen Storage** Carbon nanotubes are considered to be good hosts for hydrogen storage (for example, for fuel cells that power electric vehicles or laptop computers), although there is some controversy about the magnitude of the hydrogen uptake [20a, 203]. However, experimental reports of high storage capacities are so controversial that it is impossible to assess the applications potential [203–207]. Reversible adsorption of molecular hydrogen in carbon nanotubes was first re-



ported by Dillon et al. [208]. These workers measured the hydrogen adsorption capacity of the as-prepared SWNT bundles (0.1–0.2 wt.%) containing unidentified carbonaceous materials as well as large fractions of cobalt catalyst particles (20 wt.%). Composition (H/C) versus pressure isotherms at 80 K ( $-197^{\circ}\text{C}$ ) of as-prepared SWNTs, sonicated SWNTs and a high surface area carbon (Saran) are reported by Ye et al. [207]. These workers find the hydrogen storage capacity in arc-derived SWNTs to be 8.25 wt.% at 80 K and  $\sim 4$  MPa. A hydrogen storage capacity of 4.2 wt.% for SWNTs was reported by Liu et al. [209] at  $27^{\circ}\text{C}$  and 10.1 MPa. The SWNTs used in this study had a large mean diameter of 1.85 nm. Moreover, 78.3% of the adsorbed hydrogen (3.3 wt.%) could be released under ambient pressure at room temperature, while the release of the residual hydrogen (0.9%) required heating of the sample. A comparative study of high-pressure hydrogen adsorption experiments along with electrochemical hydrogen storage has been carried out by Gundiah et al. on various carbon nanotube samples [210]. The carbon samples that they used for hydrogen storage studies are as follows: SWNTs synthesized by the arc-discharge method (as-synthesized), I; SWNTs synthesized by the arc-discharge method (treated with conc.  $\text{HNO}_3$ ), II; MWNTs synthesized by the pyrolysis of acetylene (as-synthesized), III; MWNTs synthesized by the pyrolysis of acetylene (treated with conc.  $\text{HNO}_3$ ), IV; MWNTs synthesized by the arc-discharge method, V; aligned MWNT bundles synthesized by the pyrolysis of ferrocene (as-synthesized), VI; aligned MWNT bundles synthesized by the pyrolysis of ferrocene (treated with acid), VII; aligned MWNT bundles synthesized by the pyrolysis of ferrocene and acetylene (as-synthesized), VIII; and aligned MWNT bundles synthesized by the pyrolysis of ferrocene and acetylene (treated with acid), IX. Figure 8.18(a), shows the plots of hydrogen adsorption versus time for the various carbon nanostructured samples studied by them. By eliminating most of the common errors encountered in these experiments, they achieved a maximum storage capacity of 3.75 wt.% (143 bar,  $27^{\circ}\text{C}$ ) in the case of densely aligned nanotubes, prepared by the pyrolysis of ferrocene–hydrocarbon mixtures. SWNTs and MWNTs (arc-generated) showed a high-pressure hydrogen storage capacity, which is much less than 3 wt.%. In Figure 8.18(b) we show the plots of electrochemical charging capacity of various types of carbon nanotubes. Electrodes made out of aligned MWNTs, clearly demonstrate higher electrochemical charging capacities up to  $1100 \text{ mA h g}^{-1}$  which correspond to a hydrogen storage capacity of 3.75 wt.%. SWNTs and MWNTs (arc-generated), however, show capacity in the range 2–3 wt.%.

### 8.3

#### Inorganic Nanotubes

##### 8.3.1

##### Preliminaries

Several layered inorganic compounds possess structures comparable to the structure of graphite, the metal dichalcogenides (sulfides, selenides, and tellurides),



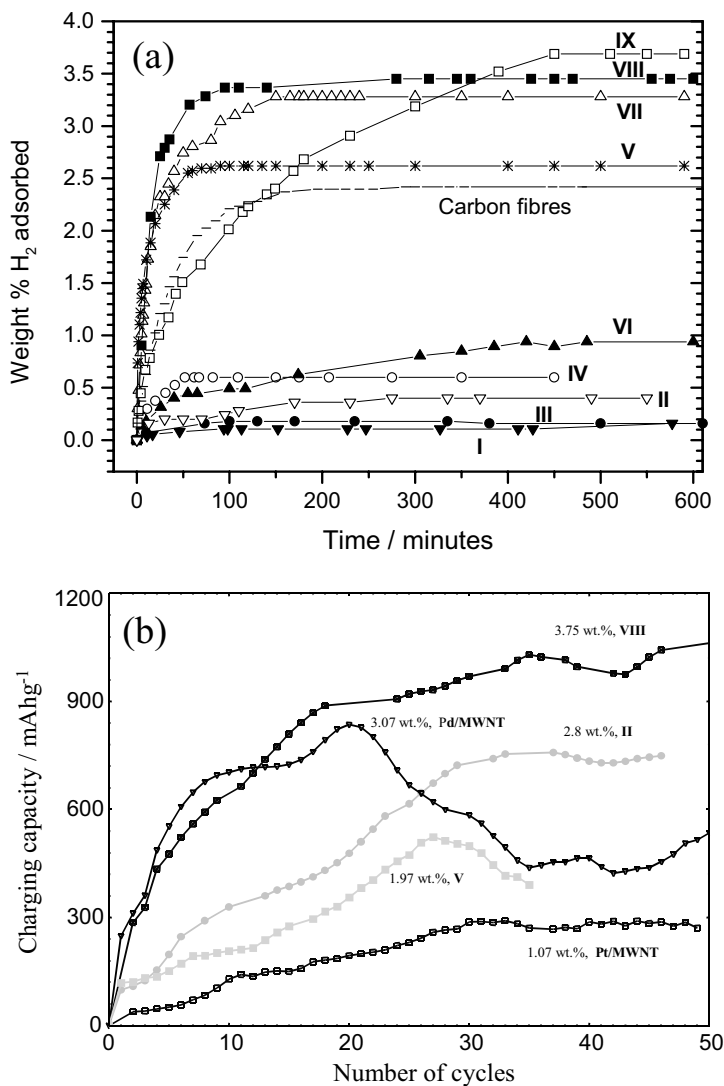


**Fig. 8.18.** (a) Amount of hydrogen adsorbed, in wt%, as a function of time for the various carbon nanostructures (I–IX). The broken curve represents the blank data obtained in the absence of a carbon sample. (b) Plot of the charging capacity against the number of cycles for different carbon nanostructures. Also shown are the corresponding weight percentages of H<sub>2</sub> stored. Reproduced from ref. [210], with permission.

halides (chlorides, bromides, and iodides), oxides, and numerous ternary (quaternary) compounds being important examples. The metal dichalcogenides, MX<sub>2</sub> (M = Mo, W, Nb, Hf; X = S, Se) contain a metal layer sandwiched between two chalcogen layers with the metal in a trigonal pyramidal or octahedral coordination

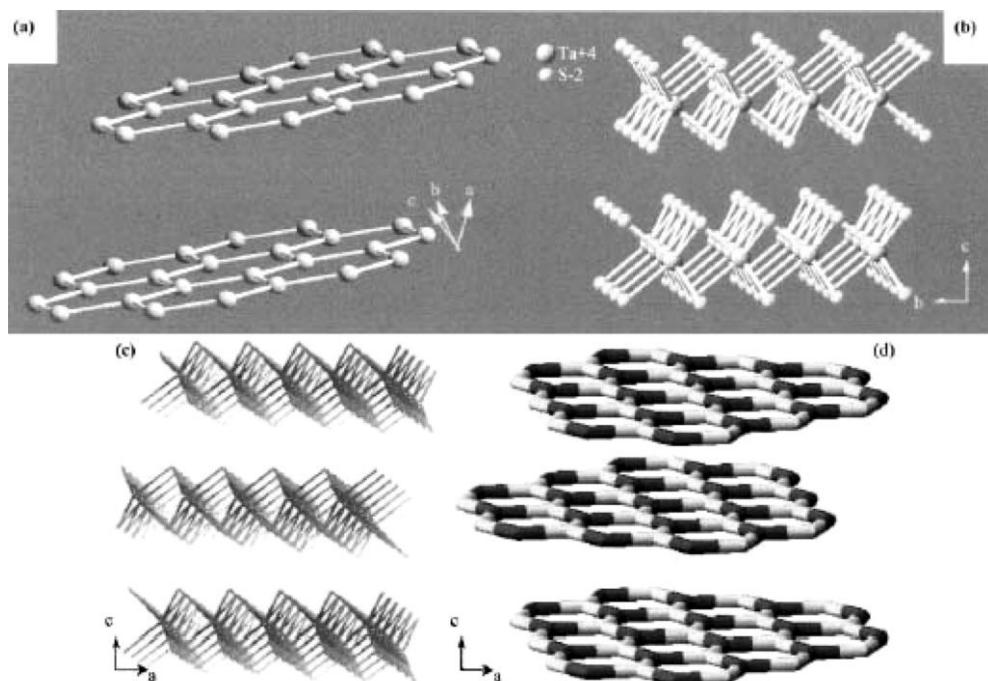


**Fig. 8.19.** Comparison of the structures of (a) graphite and inorganic layered compounds such as (b) NbS<sub>2</sub>/TaS<sub>2</sub>; (c) MoS<sub>2</sub>; (d) BN. In the layered dichalcogenides, the metal is in trigonal prismatic (TaS<sub>2</sub>) or octahedral coordination (MoS<sub>2</sub>). Reproduced from ref. [22], with permission.

mode [211]. The MX<sub>2</sub> layers are stacked along the *c*-direction in ABAB fashion. The MX<sub>2</sub> layers are analogous to the single graphene sheets in the graphite structure (Figure 8.19). However, in contrast to graphite, each molecular sheet consists of multiple layers of different atoms chemically bonded together. When viewed parallel to the *c*-axis, the layers show the presence of dangling bonds due to the absence of an X or M atom at the edges. Such unsaturated bonds at the edges of the layers also occur in graphite. The dichalcogenide layers are unstable towards bending and have a high propensity to roll into curved structures. If the dimensions of the dichalcogenide layers are small, then they form hollow, closed clusters designated as inorganic fullerene-like (IF) structures. Folding in the layered transition metal chalcogenides (LTMCs) was recognized as early as 1979 by Chianelli et al., well before the discovery of the carbon nanotubes [212]. They reported rag-like and tubular structures of MoS<sub>2</sub> and studied their usefulness in catalysis. The observed folded sheets appear as crystalline needles in low magnification transmission electron microscope (TEM) images, and were described as layers that fold onto themselves. These structures indeed represent those of nanotubes. Tenne et al. [213] first demonstrated that Mo and W dichalcogenides are capable of forming

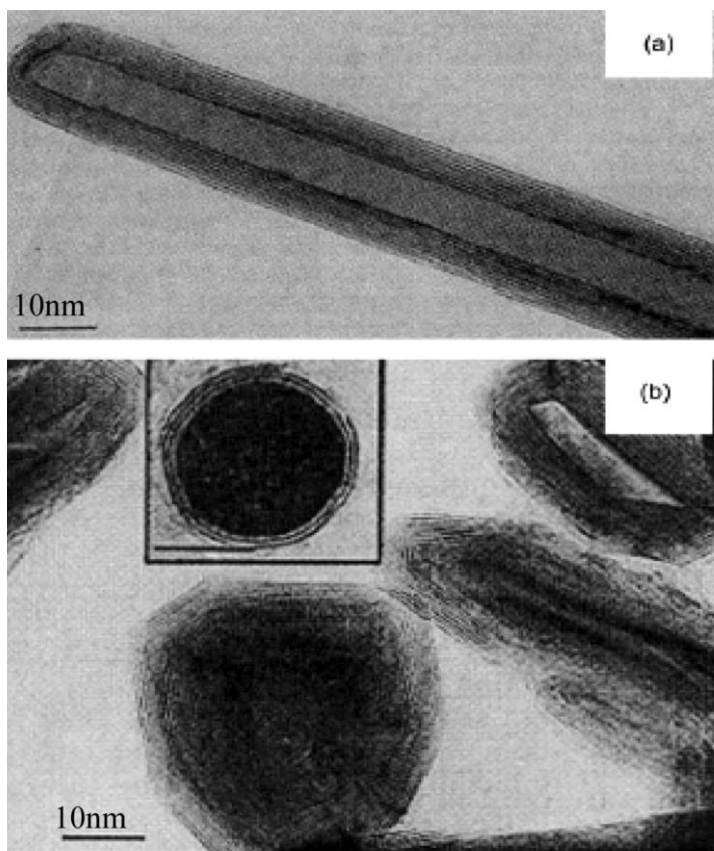


**Fig. 8.20.** TEM images of (a) a multi-walled nanotube of  $\text{WS}_2$  and (b) hollow particles (inorganic fullerenes) of  $\text{WS}_2$ . Reproduced from ref. [213], with permission.

nanotubes (Figure 8.20(a)). Closed fullerene-type structures (inorganic fullerenes) also formed along with the nanotubes (Figure 8.20(b)). The dichalcogenide structures contain concentrically nested fullerene cylinders, with a less regular structure than in the carbon nanotubes. Accordingly,  $\text{MX}_2$  nanotubes have varying wall thickness and contain some amorphous material on the exterior of the tubes. Nearly defect-free  $\text{MX}_2$  nanotubes are rigid as a consequence of their structure and do not permit plastic deformation. The folding of a  $\text{MS}_2$  layer in the process of forming a nanotube is shown in the schematic in Figure 8.21. There has been some speculation on the cause of folding and curvature in the LTMCs. Stoichiometric LTMC chains and layers such as those of  $\text{TiS}_2$  possess an inherent ability to bend and fold, as observed in intercalation reactions. The existence of alternate coordination and therefore of stoichiometry in the LTMCs may also cause folding. Lastly, a change in the stoichiometry within the material would give rise to closed rings. Considerable progress has been made in the synthesis of the nanotubes of

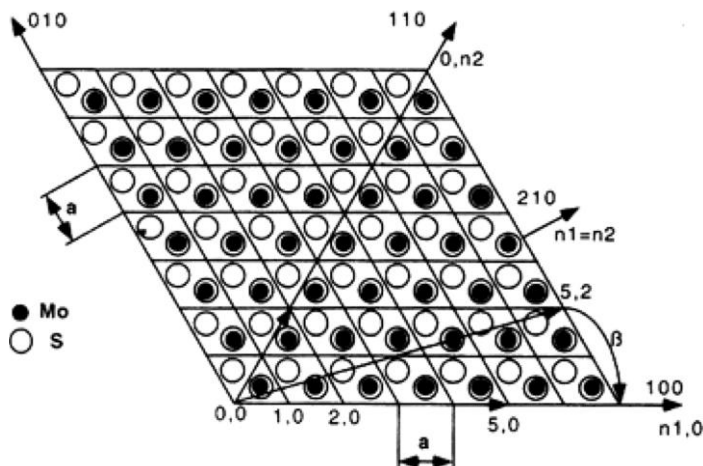


Fig. 8.21. Schematic illustration of the bending of a  $\text{MoS}_2$  layer. Reproduced from ref. [229], with permission.

Mo and W dichalcogenides in the last few years. Detailed studies on the synthesis, structural characterization and applications of these inorganic nanotubes can be found in a series of review articles devoted to this topic [20a, 22–24, 214].

Transition metal chalcogenides possess a wide range of interesting physical properties. They are widely used in catalysis and as lubricants. They have both semiconducting and superconducting properties. With the synthesis and characterization of the fullerenes and nanotubes of  $\text{MoS}_2$  and  $\text{WS}_2$ , a wide field of research has opened up enabling the successful synthesis of nanotubes of other metal chalcogenides. It may be recalled that the dichalcogenides of many of the Group 4 and 5 metals have layered structures suitable for forming nanotubes.

Curved structures are not only limited to carbon and the dichalcogenides of Mo and W. Perhaps the most well-known example of a tube-like structure with diameters in the nanometer range is formed by the asbestos mineral (chrysotil) whose fibrous characteristics are determined by the tubular structure of the fused tetrahedral and octahedral layers. The synthesis of mesoporous silica with well-defined pores in the 2–20 nm range was reported by Beck and Kresge [215]. The synthetic strategy involved the self-assembly of liquid crystalline templates. The pore size in zeolitic and other inorganic porous solids is varied by a suitable choice of the template. However, in contrast to the synthesis of porous compounds, the synthesis of nanotubes is somewhat more difficult.

Nanotubes of oxides of several transition metals, as well as of other metals, have been synthesized by employing different methodologies [24, 216–220]. Silica nanotubes were first produced as a spin-off product during the synthesis of spherical silica particles by the hydrolysis of tetraethylorthosilicate (TEOS) in a mixture of water, ammonia, ethanol and D,L-tartaric acid [216]. Since self-assembly reactions are not straightforward with respect to the desired product, particularly its morphology, templated reactions have been employed using carbon nanotubes to

obtain nanotube structures of metal oxides [217, 218]. Oxides such as  $V_2O_5$  have good catalytic activity in the bulk phase. Redox catalytic activity is also retained in the nanotubular structure. There have been efforts to prepare  $V_2O_5$  nanotubes by chemical methods as well [219].

Boron nitride (BN) crystallizes in a graphite-like structure and can be simply viewed as replacing a C–C pair in the graphene sheet with the iso-electronic B–N pair. It can, therefore, be considered as an ideal precursor for the formation of BN nanotubes. Replacement of the C–C pairs partly or entirely by the B–N pairs in the hexagonal network of graphite leads to the formation of a wide array of two-dimensional phases that can form hollow cage structures and nanotubes. The possibility of replacing C–C pairs by B–N pairs in the hollow cage structure of  $C_{60}$  was predicted [221] and verified experimentally [222]. BN-doped carbon nanotubes have been prepared [112, 115]. Pure BN nanotubes have been generated by employing several procedures, yielding nanotubes with varying wall thickness and morphology [223–225]. It is therefore quite possible that nanotube structures of other layered materials can be prepared as well. For example, many metal halides (e.g.,  $NiCl_2$ ), oxides (e.g.,  $ZnO$ ) and nitrides (e.g.,  $GaN$ ) crystallize in layered structures and nanotubes of such materials have indeed been characterized [226]. Nanotubes of elemental materials such as  $Te$  [227a] and  $Ni$  [227b] have also been prepared. There is considerable interest at present in preparing exotic nanotubes and studying their properties. In this section, we discuss the synthesis and characterization of nanotubes of chalcogenides of  $Mo$ ,  $W$  and other metals, metal oxides, BN and other materials and present the current status of the subject. We briefly examine some of the important properties of the inorganic nanotubes and indicate possible future directions.

### 8.3.2

#### General Synthetic Strategies

Several strategies have been employed for the synthesis of carbon nanotubes [20a]. In addition to arc evaporation and pyrolysis methods, carbon nanotubes have been prepared by laser ablation of graphite, electrochemical and templating (using porous alumina membrane) techniques [228]. The above methods broadly fall into two categories. Methods such as the arc evaporation of graphite employ processes which are far from equilibrium. The chemical routes are generally closer to equilibrium conditions. Nanotubes of metal chalcogenides and boron nitride are also prepared by employing techniques similar to those of carbon nanotubes, although there is an inherent difference in that the nanotubes of inorganic materials such as  $MoS_2$  or BN would require reactions involving the component elements or compounds containing the elements. Decomposition of precursor compounds containing the elements is another possible route.

Nanotubes of dichalcogenides such as  $MoS_2$ ,  $MoSe_2$  and  $WS_2$  are also obtained by employing processes far from equilibrium, such as arc discharge and laser ablation [229]. By far the most successful routes employ appropriate chemical reactions. Thus,  $MoS_2$  and  $WS_2$  nanotubes are conveniently prepared by starting with

the stable oxides,  $\text{MoO}_3$  and  $\text{WO}_3$  [213]. The oxides are first heated at high temperatures in a reducing atmosphere and then reacted with  $\text{H}_2\text{S}$ . Reaction with  $\text{H}_2\text{Se}$  is used to obtain the selenides [230]. Recognizing that the trisulfides  $\text{MoS}_3$  and  $\text{WS}_3$  are likely to be the intermediates in the formation of the disulfide nanotubes, the trisulfides have been directly decomposed to obtain the disulfide nanotubes [231]. Diselenide nanotubes have been obtained from the metal triselenides [232]. The trisulfide route is indeed found to provide a general route for the synthesis of the nanotubes of many metal disulfides such as  $\text{NbS}_2$  [233] and  $\text{HfS}_2$  [234]. In the case of Mo and W dichalcogenides, it is possible to use the decomposition of the precursor ammonium salt, such as  $(\text{NH}_4)_2\text{MX}_4$  ( $\text{X} = \text{S}, \text{Se}$ ;  $\text{M} = \text{Mo}, \text{W}$ ) as a means of preparing the nanotubes [231]. Other methods employed for the synthesis of dichalcogenide nanotubes include hydrothermal methods where the organic amine is taken as one of the components in the reaction mixture.

The hydrothermal route has been used for synthesizing nanotubes and related structures of a variety of other inorganic materials as well. Thus, nanotubes of several metal oxides (e.g.,  $\text{SiO}_2$  [235],  $\text{V}_2\text{O}_5$  [219],  $\text{ZnO}$  [236]) have been produced hydrothermally. Nanotubes of oxides such as  $\text{V}_2\text{O}_5$  are also conveniently prepared from a suitable metal oxide precursor in the presence of an organic amine or a surfactant [237]. Surfactant-assisted synthesis of  $\text{CdSe}$  and  $\text{CdS}$  nanotubes has been reported. Here the metal oxide reacts with the sulfidizing/selenidizing agent in the presence of a surfactant such as Triton X [238, 246].

Sol-gel chemistry is widely used in the synthesis of metal oxide nanotubes, a good example being that of silica [216] and  $\text{TiO}_2$  [239]. Oxide gels in the presence of surfactants or suitable templates form nanotubes. For example, by coating carbon nanotubes (CNTs) with oxide gels and then burning off the carbon, one obtains nanotubes and nanowires of a variety of metal oxides including  $\text{ZrO}_2$ ,  $\text{SiO}_2$  and  $\text{MoO}_3$  [218, 240]. Sol-gel synthesis of oxide nanotubes is also possible in the pores of alumina membranes. It should be noted that  $\text{MoS}_2$  nanotubes are also prepared by the decomposition of a precursor in the pores of an alumina membrane [241].

Boron nitride nanotubes have been obtained by striking an electric arc between  $\text{HfB}_2$  electrodes in a  $\text{N}_2$  atmosphere [242]. BCN and BC nanotubes are obtained by arcing between B/C electrodes in an appropriate atmosphere. A greater effort has gone into the synthesis of BN nanotubes starting with different precursor molecules containing B and N. Decomposition of borazine in the presence of transition metal nanoparticles and the decomposition of the 1:2 melamine-boric acid addition compound yield BN nanotubes [223, 224]. Reaction of boric acid or  $\text{B}_2\text{O}_3$  with  $\text{N}_2$  or  $\text{NH}_3$  at high temperature in the presence of activated carbon, carbon nanotubes or catalytic metal particles has been employed to synthesize BN nanotubes [225]. Goldberger et al. [226b] have synthesized single-crystal GaN nanotubes with inner diameters of 30–200 nm and wall thicknesses of 5–50 nm by employing ‘epitaxial casting’ approach. They used hexagonal ZnO nanowires as templates for the epitaxial overgrowth of thin GaN layers in a chemical vapor deposition system. In a typical experiment they used trimethylgallium and ammonia as precursors with argon or nitrogen as carrier gas and maintained the deposition temperature at

600–700 °C. The ZnO nanowire templates were subsequently removed by thermal reduction and evaporation, resulting in ordered arrays of GaN nanotubes on the substrates.

A wide range of examples of organic templates (organogels) and extensive coverage of the methods for the formation of morphologically interesting inorganic materials were given in a review by Shinkai's group [214]. The organogels present a wider range of morphologies, such as fibrous, tubular, ribbon-like, lamellar, hollow spherical, than have been transcribed so far. These organogels are comprised of an organic liquid and low concentrations (< 0.5 wt.%) of relatively low molecular weight molecules (namely gelators) [243], the morphology of which may be spherical or fibrous. These organogels are usually prepared by heating a mixture of a gelator and solvent until the solid dissolves, upon cooling the solution (sol) thickens to form a gel. The gelation of a number of compounds such as tetraethyl-orthosilicate (TEOS) along with a cholesterol-based gelator, under acidic pH conditions, followed by polycondensation, exhibits a network of fibers with diameter ranging from 50–200 nm [244]. Subsequent drying and calcination steps resulted in silica tubes without the presence of the original organic template.

### 8.3.3

#### Structures

Some of the important inorganic nanotubes synthesized and characterized in the last few years are the following [22]:

*Chalcogenides:* MoS<sub>2</sub>, WS<sub>2</sub>, MoSe<sub>2</sub>, WSe<sub>2</sub>, NbS<sub>2</sub>, NbSe<sub>2</sub>, HfS<sub>2</sub>, ZrS<sub>2</sub>

*Oxides:* TiO<sub>2</sub>, ZrO<sub>2</sub>, VO<sub>x</sub>, SiO<sub>2</sub>, ZnO, Ga<sub>2</sub>O<sub>3</sub>, BaTiO<sub>3</sub>, PbTiO<sub>3</sub>

*Nitrides:* BN, GaN

*Halides:* NiCl<sub>2</sub>

*Metals:* Ni, Cu, Te, Co, Fe

In Figure 8.22 we show the TEM images of MoS<sub>2</sub> nanotubes prepared by the direct thermal decomposition of the ammonium thiomolybdate in H<sub>2</sub> atmosphere (flow) [231]. In addition to providing a direct method for the preparation of dichalcogenide nanotubes [231], the trichalcogenide or the ammonium chalcometallate route also enables the easy synthesis of nanotubes of the other layered dichalcogenides [232–234]. The structure of MoS<sub>2</sub> consists of disulfide layers stacked along the *c*-direction [211]. This implies that the S–S interaction between the MoS<sub>2</sub> slabs is weaker than the intralayer interactions. The S–S interlayer distances are therefore susceptible to distortions during the folding of the layers. This is exemplified by the slight expansion of the *c*-axis (2%) in the MoS<sub>2</sub> nanotubes [229]. High-resolution (HREM) images of the disulfide nanotubes show stacking of the (002) planes parallel to the tube axis. The distance between the layer fringes corresponds to the *d*(002) spacing. In Figure 8.23(a) we show the SEM image of nanotubes of HfS<sub>2</sub> which are quite lengthy, some being more than a micron long. Interestingly, a large proportion of these nanostructures are nanotubes. In Figure 8.23(b) and (c),



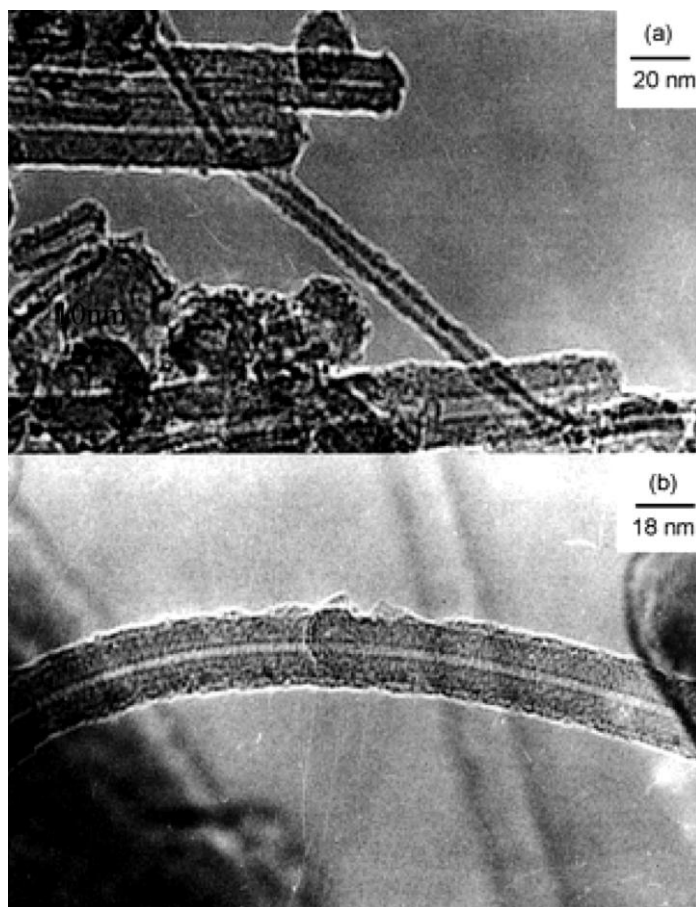


**Fig. 8.22.** (a) Low-resolution TEM images of MoS<sub>2</sub> nanotubes grown by the decomposition of ammonium thiomolybdate; (b) HREM image of the MoS<sub>2</sub> nanotube. Reproduced from ref. [231], with permission.

we show TEM images of these nanotubes. These HfS<sub>2</sub> nanotubes are obtained in good yield by the decomposition of HfS<sub>3</sub> [234]. The HREM image in Figure 8.23(d) shows a considerable number of defects and edge dislocations present along the length of the tube wall. The analysis of the electron diffraction (ED) pattern together with the HREM indicates that the growth axis of the nanotube is perpendicular to the *c*-direction.

Exhaustive studies have been carried out on the synthesis of BN nanotubes and nanowires by various CVD techniques [225]. The methods examined include heating boric acid with activated carbon, multi-walled carbon nanotubes, catalytic iron particles or a mixture of activated carbon and iron particles, in the presence of ammonia. With activated carbon, BN nanowires are obtained as the primary prod-



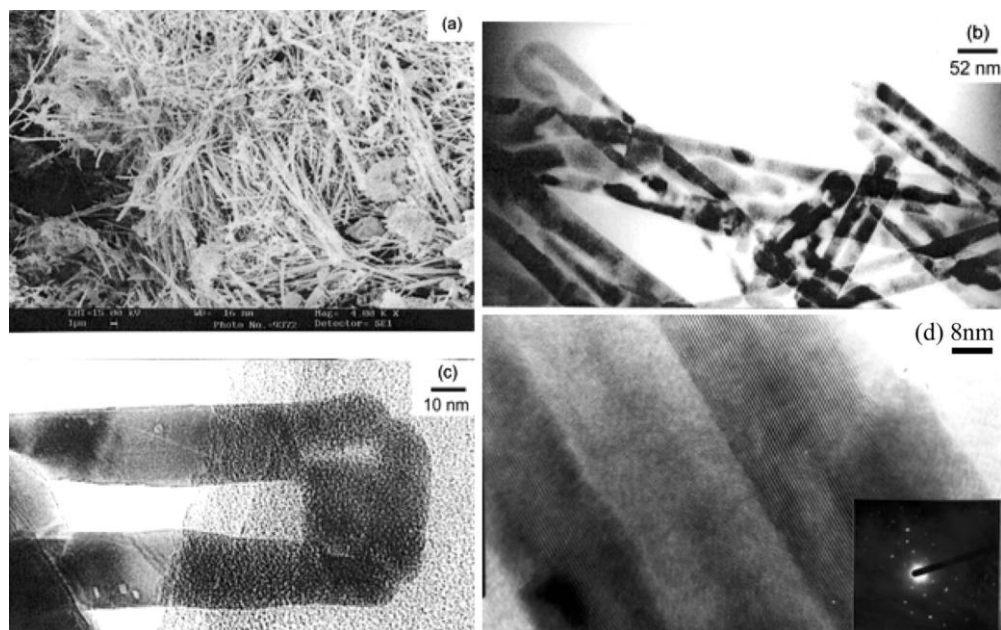


**Fig. 8.23.** (a) SEM image of the  $\text{HfS}_2$  nanostructures; (b) and (c) low-resolution TEM images showing hollow nanotubes. The tube in (c) has a flat tip; (d) HREM image of the  $\text{HfS}_2$  nanotubes, showing a layer separation of  $\sim 0.6$  nm in the walls. Inset shows a typical ED pattern. Reproduced from ref. [234], with permission.

uct. However, with multi-walled carbon tubes, high yields of pure BN nanotubes are obtained as the major product. BN nanotubes with different structures were obtained on heating boric acid and iron particles in the presence of  $\text{NH}_3$ . Aligned BN nanotubes are obtained when aligned multi-walled nanotubes are used as the templates (Figure 8.24).

Needle-shaped  $\text{TiO}_2$  (anatase) nanotubes could be precipitated from a gel containing a mixture of  $\text{SiO}_2$  and  $\text{TiO}_2$  [239]. A mixture of titanium isopropoxide and tetraethylorthosilicate (TEOS) was hydrolyzed and gelled in an incubator, and the gel further heated to  $600^\circ\text{C}$ , resulting in the precipitation of fine  $\text{TiO}_2$  (anatase) crystals. This was further treated with  $\text{NaOH}$  at  $100^\circ\text{C}$  for 20 h to yield the  $\text{TiO}_2$  nanotubular phase. An amorphous  $\text{SiO}_2$ -related phase present in the product was removed by chemical treatment. The nanotubes formed by this method had a diameter of  $\sim 8$  nm and lengths upto 100 nm (Figure 8.25(a)). Much smaller  $\text{TiO}_2$  nanotubes have recently been synthesized by a surprisingly simple procedure.  $\text{TiO}_2$  with anatase or rutile structure was treated with  $\text{NaOH}$  and subsequently with  $\text{HCl}$  [239, 245]. The resulting  $\text{TiO}_2$  nanotubes are 50–200 nm long and their diameter is about 10 nm (Figure 8.25(b)). The HREM image (Figure 8.25(c)) of

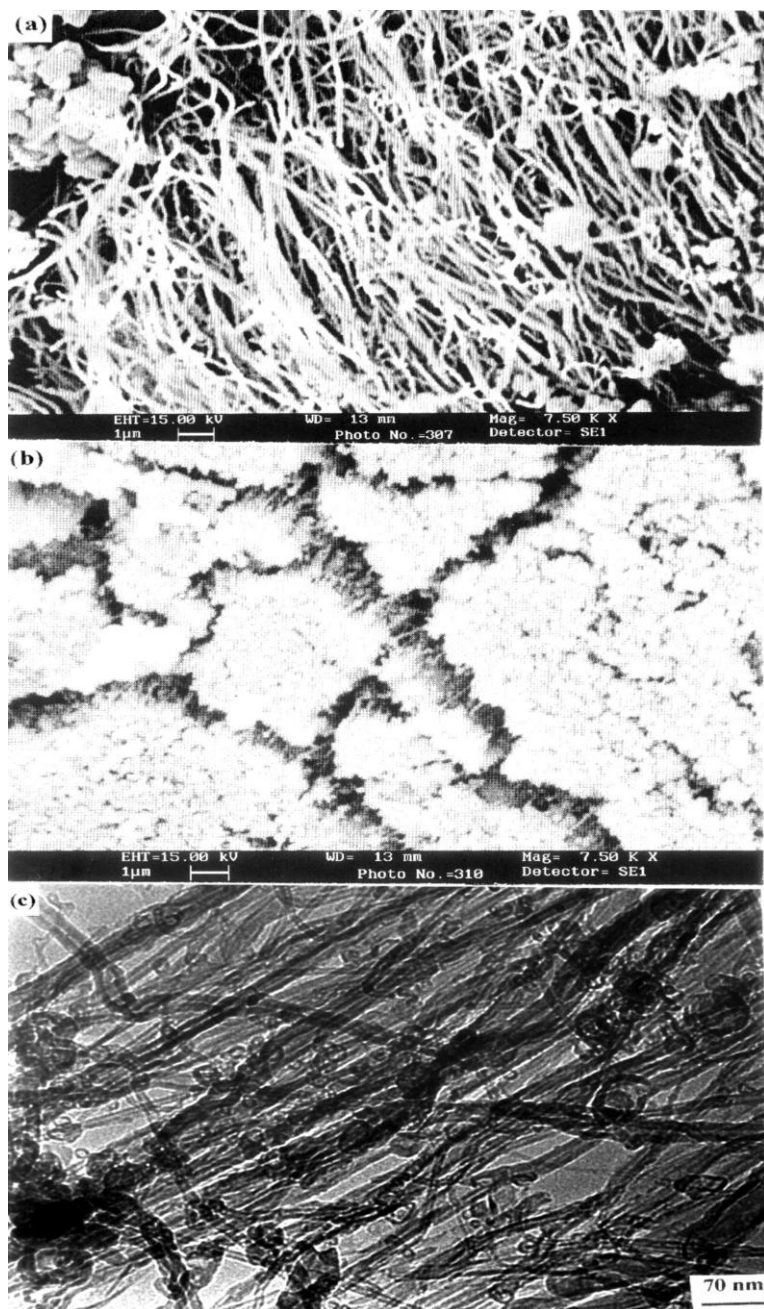


**Fig. 8.24.** SEM and TEM images of aligned BN nanotubes: (a) and (b) give side and top view SEM images, respectively; (c) TEM image of pure BN nanotube. Reproduced from ref. [225], with permission.

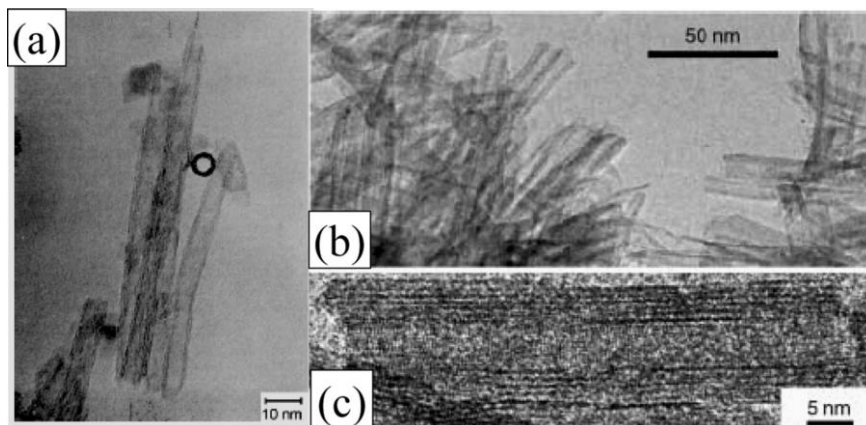


**Fig. 8.25.** (a), (b) TEM images of  $\text{TiO}_2$  nanotubes. (c) HRTEM image of a well developed,  $\sim 50$  nm long nanotube with a diameter of  $\sim 10$  nm. Lattice fringes can be seen. Reproduced from ref. [24, 239], with permission.

such a  $\text{TiO}_2$  nanotube shows that the tubes have an inner core and walls. The presence of lattice fringes indicates the crystalline structure of  $\text{TiO}_2$  nanotubes. Parallel fringes in the walls correspond to a distance of about 7 nm, which can also be detected as a broad reflection by X-ray and electron diffraction.

Nanotubes of II–VI semiconductor compounds such as CdS and CdSe have been obtained by a soft chemical route involving surfactant-assisted synthesis [238, 246]. For CdS nanotubes, the metal oxide was reacted with the sulfidizing reagent in the presence of a surfactant such as Triton 100X in a basic medium. To obtain nanotubes of CdSe, a similar procedure was followed, except that  $\text{NaHSe}$  was used in place of thioacetamide as selenidizing reagent in the presence of a surfactant such as Triton 100X (Figure 8.26). Both the CdSe and CdS nanotubes seem to be polycrystalline, formed by aggregates of nanoparticles [247]. The nanotubes of CdSe, though extended in one direction show quantum confinement and the absorption band is blue-shifted to 550 nm from 650 nm in the bulk sample.

Nesper and co-workers [219, 248] synthesized nanotubules of alkylammonium intercalated  $\text{VO}_x$  by hydrothermal means. The vanadium alkoxide precursor was hydrolyzed in the presence of hexadecylamine and the hydrolysis product (lamellar structured composite of the surfactant and the vanadium oxide) yielded  $\text{VO}_x$  nanotubes along with the intercalated amine under hydrothermal conditions (Figure 8.27(a) and (b)). The interesting feature of this vanadium oxide nanotube is the presence of vanadium in the mixed valent state, thereby rendering it redox-active. The template could not be removed by calcination as the structural stability was lost above  $250^\circ\text{C}$ . Nevertheless, it was possible to partially extract the surfactant under mildly acidic conditions. These workers have later shown that the alkylamine intercalated in the intertubular space could be exchanged with other alkylamines of varying chain lengths as well as  $\alpha,\omega$ -diamines [248]. The distance

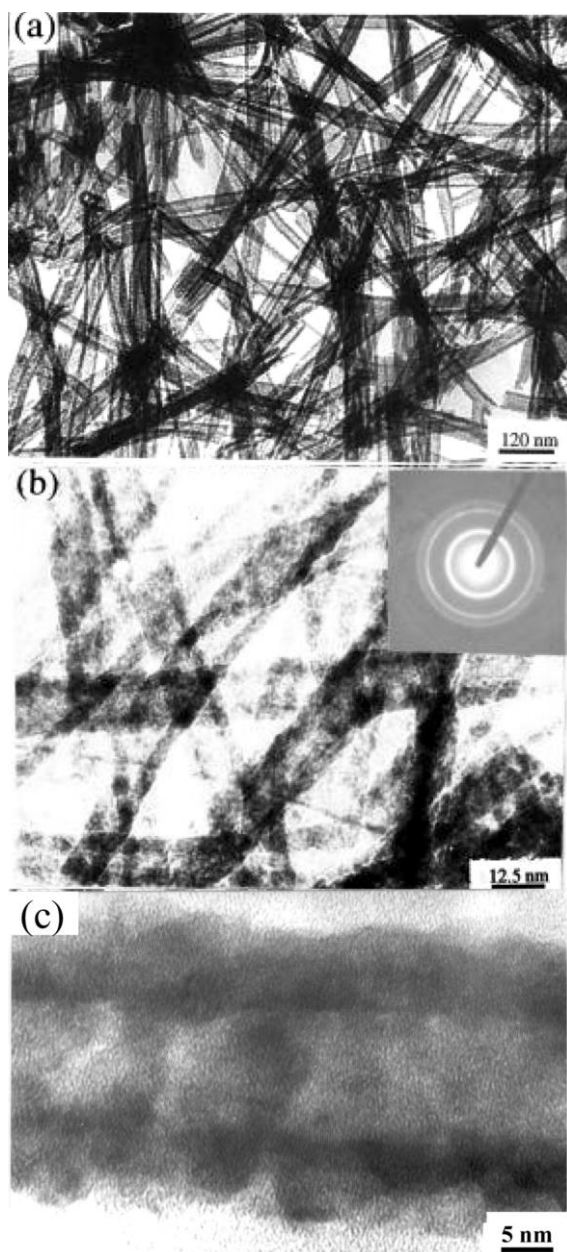


**Fig. 8.26.** (a) and (b) low-resolution TEM images of CdSe nanotubes. Inset shows a typical ED pattern; (c) HREM image of the CdSe nanotube showing walls containing several nanocrystallites. Reproduced from ref. [238, 246], with permission.



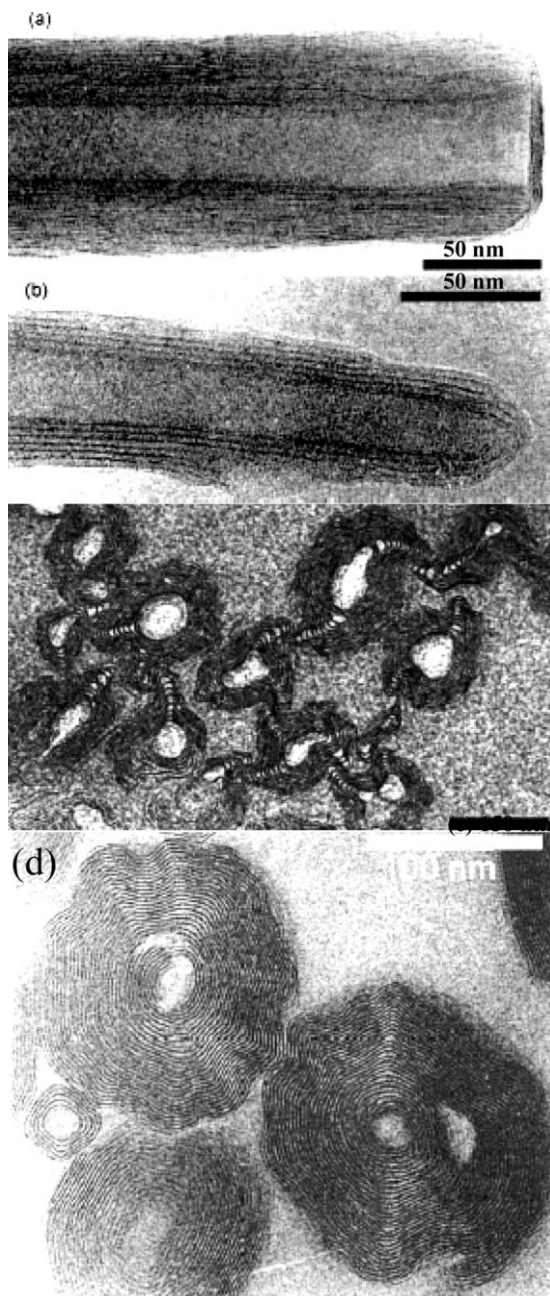


**Fig. 8.27.** TEM images of  $VO_x$  nanotubes with intercalated amine having varying chain lengths; (a)  $C_4VO_x$ -NT; (b)  $C_{16}-VO_x$ -NT. The length of the bar is 50 nm. (c) Cross-sectional TEM images of monoamine-intercalated  $VO_x$  nanotubes showing serpentine-like scrolls.

(d) Cross-sectional TEM images of diamine-intercalated  $VO_x$  nanotubes showing a larger thickness of the tube walls and a smaller inner core. Reproduced from ref. [248], with permission.

between the layers in the  $\text{VO}_x$  nanotubes can be controlled by the length of the  $-\text{CH}_2-$  chain in the amine template.

Most of the  $\text{VO}_x$  nanotubes obtained by the hydrothermal method are open-ended. Very few closed tubes had flat or pointed conical tips. Cross-sectional TEM images of the nanotubular phases show that instead of concentric cylinders, (i.e. layers that fold and close within themselves), the tubes are made up of single or double layer scrolls providing a serpentine-like morphology [248, 249]. The scrolls are seen in the images as circles that do not close (Figure 8.27(c)). Non-symmetric fringe patterns in the tube walls exemplify that most of the nanotubes are not rotationally symmetric and carry depressions and holes in the walls. Diamine-intercalated  $\text{VO}_x$  nanotubes are multilayer scrolls with narrow cores and thick walls, composed of packs of several vanadium oxide layers (Figure 8.27(d)). Many of the nanotubes formed by layered materials show various types of defects. They also exhibit unusual tip structures. The tips are not always spherical in these nanotubes. These aspects are discussed at length by Rao and Nath [22].

#### 8.3.4

#### Useful Properties of Inorganic Nanotubes

The properties and applications of the inorganic nanotubes have not been investigated as extensively as would be desirable. The electronic structures of  $\text{MoS}_2$  and  $\text{WS}_2$  have been examined briefly and the semiconducting nature of the nanotubes confirmed [250, 251a]. It is necessary to investigate the optical, electrical and other properties of the various chalcogenide nanotubes. This is especially true of nanotubes of  $\text{NbS}_2$  and such materials which are predicted to be metallic [251b].  $\text{NbSe}_2$  nanotubes have been found to be metallic at ordinary temperatures, becoming superconducting at lower temperatures [252]. Electronic and optical properties of the BN nanotubes have not yet been investigated in detail. Theoretical calculations suggest BN tubes to be insulating with a wide band gap of 5.5 eV [221].

Like carbon nanotubes, it would be worthwhile to look into the  $\text{H}_2$  storage ability of some of the inorganic nanotubes [253]. The chalcogenide nanotubes with an  $\sim 6 \text{ \AA}$  van der Waals gap between the layers, are potential candidates for storage capacity. It has been shown recently that BN nanotubes can store a reasonable quantity of  $\text{H}_2$  [254]. Multi-walled BN nanotubes have been shown to possess a capacity of 1.8–2.6 wt% of  $\text{H}_2$  uptake under  $\sim 10 \text{ MPa}$  at room temperature. This value, though smaller than that reported for CNTs, nevertheless suggests the possible use of BN nanotubes as a hydrogen storage system.  $\text{MoS}_2$  nanotubes could be electrochemically charged and discharged with a capacity of  $260 \text{ mA h g}^{-1}$  at  $20^\circ \text{C}$ , corresponding to a formula of  $\text{H}_{1.24}\text{MoS}_2$  [255]. The high storage capacity is believed to be due to the enhanced electrochemical–catalytic activity of the highly nanoporous structure. This may find wide applications in high energy batteries.

Mechanical properties of BN nanotubes would be worthy of exploration. Unlike carbon nanotubes, BN nanotubes are predicted to have stable insulating properties

independent of their structure and morphology. Thus, BN tubes can be used as nano-insulating devices for encapsulating conducting materials like metallic wires. Filled BN nanotubes are expected to be useful in nanoscale electronic devices and for the preparation of nano-structured ceramics.

Electrochemical studies have been performed with the alkylammonium intercalated  $\text{VO}_x$  nanotubes [256] as well as Mn intercalated  $\text{VO}_x$  nanotubes [257]. Cyclic voltammetry studies of alkylammonium- $\text{VO}_x$  nanotubes showed a single reduction peak, which broadened, on replacing the amine with Na, with an additional peak. Li ion reactivity has also been tested with Mn- $\text{VO}_x$  nanotubes by reacting with *n*-butyllithium, and it was found that  $\sim 2$  lithiums per V ion are consumed. Electrochemical Li intercalation of Mn- $\text{VO}_x$  nanotubes shows that 0.5 Li ions per V atom were intercalated above 2 V [257]. This observation may be relevant to battery applications.

CNTs have been used as AFM tips and there appears to be every likelihood that extremely narrow structures can be probed [179].  $\text{WS}_2$  could be mounted on the ultrasharp Si tip following a similar methodology. These tips were tested in an AFM microscope by imaging a replica of high aspect ratio, and it was observed that these  $\text{WS}_2$  nanotube tips provide a considerable improvement in the image quality compared to the conventional ultrasharp Si tips [258].

The most likely application of the chalcogenide nanotubes is as solid lubricants. Mo and W chalcogenides are widely used as solid lubricants. It has been observed that the hollow nanoparticles of  $\text{WS}_2$  show better tribological properties and act as a better lubricant compared to the bulk phase in every respect (friction, wear and life-time of the lubricant) [259]. Tribological properties of 2H- $\text{MoS}_2$  and  $\text{WS}_2$  powder can be attributed to the weak van der Waals forces between the layers, which allow easy shear of the films with respect to each other. The mechanism in the  $\text{WS}_2$  nanostructures is somewhat different and the better tribological properties may arise from the rolling friction allowed by the round shape of the nanostructures.

Recently, open-tipped  $\text{MoS}_2$  nanotubes were prepared by the decomposition of ball-milled ammonium thiomolybdate powder under a  $\text{H}_2$ -thiophene atmosphere, and used as catalyst for the methanation of CO with  $\text{H}_2$  [260]. The conversion of CO to  $\text{CH}_4$  was achieved at a much lower temperature compared to polycrystalline  $\text{MoS}_2$  particles, and there was no deterioration even after 50 h of consecutive catalysis cycles. This observation is of importance in the context of energy conversion of global  $\text{CO}_2$ .

Inorganic nanotubes have emerged as a group of interesting materials. Although this area of research started with the layered metal chalcogenides, recent results suggest that other inorganic materials can also be prepared in the form of nanotubes, as typified by the metal oxides. It is likely that many new types of inorganic nanotubes will be made in the near future. These would include metal nanotubes as well as nanotubes of inorganic compounds such as  $\text{MgB}_2$ ,  $\text{GeO}_2$  and GaSe. Theoretical calculations indeed predict a stable nanotubular structure for GaSe [261]. Various layered materials could be explored for this purpose.

## 8.4

### Nanowires

#### 8.4.1

##### Preliminaries

One-dimensional (1D) nanostructures such as nanowires, nanorods and nanobelts, provide good models to investigate the dependence of electronic transport, optical, mechanical and other properties on size confinement and dimensionality. Nanowires are likely to play a crucial role as interconnects and active components in nanoscale devices. An important aspect of nanowires relates to the assembly of individual atoms into such unique 1D nanostructures in a controlled fashion. Excellent chemical methods have been developed for generating zero-dimensional nanostructures (nanocrystals or quantum dots) with controlled sizes and from a wide range of materials (see earlier chapters of this book). The synthesis of nanowires with controlled composition, size, purity and crystallinity, requires a proper understanding of the nucleation and growth processes at the nanometer regime. 1D nanostructures have been fabricated recently using nanolithographic techniques [262], such as electron-beam or focused-ion-beam writing [263], proximal-probe patterning [264] and X-ray lithography [265]. These methods are generally not very cost-effective and rapid for the purpose of making large quantities of the 1D nanostructures based on a broad range of materials. Chemical methods tend to be superior and provide an alternative strategy for generating 1D nanostructures [266]. There are a few reviews dealing with the synthesis, characterization, self-assembly and applications of nanowires [267–269]. Several ways of growing semiconductor nanowires, such as laser ablation, chemical vapor deposition (CVD) and template-assisted growth have been explored. Laser ablation and template-assisted approaches provide large quantities of nanowires, but do not provide control over the composition, size or orientation direction of the nanowires. Chemical methods, include solution and vapor based methods and precursor methods, as well as solvothermal, hydrothermal and carbothermal methods.

#### 8.4.2

##### Synthetic Strategies

One of the aspects of 1D structures relates to crystallization [270], wherein the evolution of a solid from a vapor, a liquid, or a solid phase involves nucleation and growth. As the concentration of the building units (atoms, ions, or molecules) of a solid becomes sufficiently high, they aggregate into small nuclei or clusters through homogeneous nucleation. These clusters serve as seeds for further growth to form larger clusters. Several chemical strategies have been developed for 1D nanowires with different levels of control over the growth parameters [271–277]. These include: (i) the use of the anisotropic crystallographic structure of the solid to facilitate 1D nanowire growth; (ii) the introduction of a solid–liquid interface to



reduce the symmetry of a seed, (iii) the use of templates (with 1D morphologies) to direct the formation of nanowires, (iv) the use of supersaturation control to modify the growth habit of a seed; (v) the use of capping agents to kinetically control the growth rates of various facets of a seed and (vi) self-assembly of 0D nanostructures. They can be usefully categorized into: (1) nanowire growth in the gas phase; (2) solution-based approaches to nanowires.

#### 8.4.2.1 Vapor Phase Growth of Nanowires

Vapor phase growth is commonly used to produce nanowires. Starting with the simple evaporation technique in an appropriate atmosphere to produce elemental or oxide nanowires, vapor–liquid–solid, vapor–solid and other processes are made use of.

**Vapor–Liquid–Solid Growth** The growth of a nanowire via a gas phase reaction involving a vapor–liquid–solid (VLS) process has been extensively studied. Wagner, during his studies on the growth of large single-crystalline whiskers, proposed in the 1960s, a mechanism for the growth via a gas phase reaction involving the so-called vapor–liquid–solid (VLS) process [278]. According to this mechanism, the anisotropic crystal growth is promoted by the presence of a liquid alloy–solid interface. His mechanism was widely accepted and applied to understanding the growth of the nanowires of Si, Ge and others. The growth of Ge nanowire using Au clusters as solvent at high temperature can be explained based on the Ge–Au binary phase diagram as shown in Figure 8.28(b). The Ge and Au will form a liquid alloy when the temperature is higher than the eutectic point (363 °C) as shown in Figure 8.28(a-I). The liquid surface has a large accommodation coefficient and is therefore a preferred deposition site for incoming Ge vapor. After the liquid alloy becomes supersaturated with Ge, Ge nanowire growth occurs by precipitation at the solid–liquid interface (Figure 8.28(a-II, a-III)). A real time observation of Ge nanowire growth conducted in an *in situ* high temperature transition electron microscope shows a sequence of TEM images which directly mirrors the proposed VLS mechanism [279]. This VLS method has been exploited in the past several decades to produce 1–100 μm diameter 1D structures (whiskers). By controlling the nucleation and growth, it is possible to produce semiconductor nanowhiskers (e.g., InAs, GaAs) using organometallic vapor phase epitaxy. There are reports on the VLS growth of elemental semiconductors (e.g., Si and Ge), III–V semiconductors (e.g., GaAs, InP, InAs), II–VI semiconductors (e.g., ZnS, CdS, CdSe), oxides (e.g., ZnO, SiO<sub>2</sub>) [271–273, 277, 279–292]. Lieber and coworkers have developed and optimized a laser ablation based VLS process to produce semiconductor nanowires with many different compositions [273, 277]. TEM studies showed the product obtained after the VLS growth is primarily wire-like structures with remarkably uniform diameters of the order of 10 nm with lengths >1 μm. By knowing the equilibrium phase diagram one can predict the catalyst materials and growth conditions for the VLS approach. By following the VLS approach, Lee and coworkers [293a] have synthesized highly pure, ultra-long and uniform-sized semiconductor nanowires in bulk quantities by employing laser

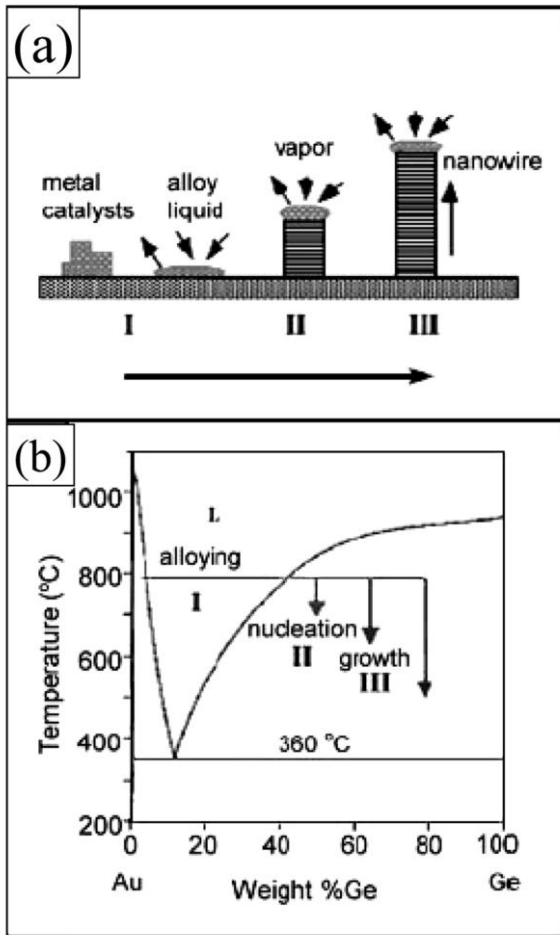


**Fig. 8.28.** (a) Schematic illustration of vapor-liquid-solid nanowire growth mechanism including three stages (I) alloying, (II) nucleation and (III) axial growth. The three stages are projected onto the conventional Au-Ge phase diagram; (b) shows the compositional and phase evolution during the nanowire growth process. Reproduced from ref. [269], with permission.

ablation and thermal evaporation of semiconductor powders mixed with metal or oxide catalysts. The solid target used for laser ablation is made of pure Si powder mixed with metals (Fe, Ni, or Co) and the temperature around the solid target was maintained in the range 1200 to 1400 °C. The temperature of the area around the substrate on which the nanowire grew was between 900 and 1100 °C. The transmission electron microscopy (TEM) investigations showed that Si nanowires obtained by this method were extremely long and highly curved with a typical diameter in the range 20–80 nm (Figure 8.29(a) and (b)). Each wire consisted of an outer layer of Si oxide and a crystalline Si core. A high density of defects, such as stacking faults and micro-twins, has been observed in the crystalline Si core. As

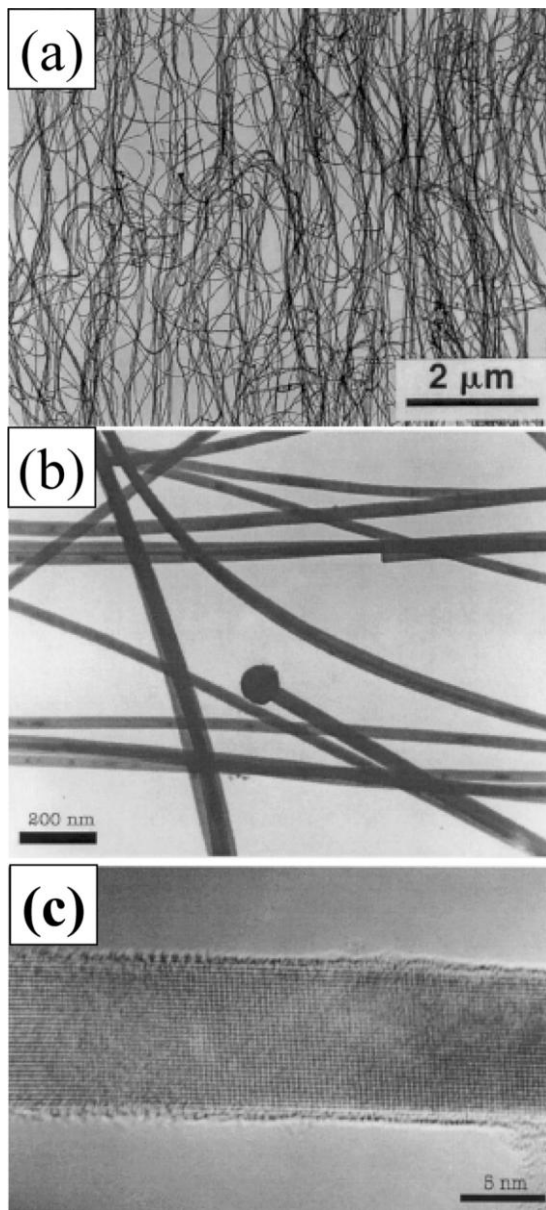
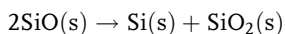
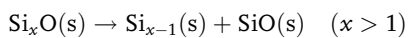


**Fig. 8.29.** (a) TEM micrograph of Si nanowires; (b) the morphology; and (c) a typical HREM image of the Si wires formed in the high temperature zone. Reproduced from ref. [293a], with permission.

identified by electron diffraction and high-resolution transmission electron microscopy (HREM) in Figure 8.29(c), the axis of the nanowires was generally along the  $\langle 112 \rangle$  direction and the  $\{111\}$  surfaces of Si crystalline cores were parallel to the axis of the nanowire.

**Oxide-Assisted Growth** In contrast to the well-established VLS mechanism, Lee et al. have recently proposed a new nanowire growth route called oxide-assisted nanowire growth. They report the synthesis and optical characterization of GaAs nanowires obtained by oxide-assisted laser ablation of a mixture of GaAs and  $\text{Ga}_2\text{O}_3$  [294a]. The GaAs nanowires have lengths up to tens of micrometers and diameter in the range 10–120 nm, with an average of 60 nm. The nanowires have a thin oxide layer covering and a crystalline GaAs core with a  $[111]$  growth direction. The oxide-assisted nanowire growth mechanism was further applied to the production of Si nanowires [293, 295]. The growth of Si nanowires was greatly enhanced when  $\text{SiO}_2$ -containing Si powder targets were used. Wang et al. have synthesized Si nanowires with uniform size by laser ablation of highly pure Si powder targets mixed with  $\text{SiO}_2$  [295a]. A large quantity of Si nanowires was obtained by mixing 30%–70% of  $\text{SiO}_2$  into the Si powder target.  $\text{SiO}_2$  played a crucial role in enhancing the formation and growth of the Si nanowires. In this proposed oxide-assisted growth mechanism, the vapor phase of  $\text{Si}_x\text{O}$  ( $x > 1$ ) generated by thermal evaporation or laser ablation is the key factor.



The Si nanowires synthesized by using different  $\text{SiO}_2$  contents in the targets are similar in structure except that the outer Si-oxide surfaces of the nanowires synthesized from targets with high  $\text{SiO}_2$  content are rough. The diameter of the nanowires measured from the TEM image ranges from 9 to 12 nm. Most nanowires are quasi-aligned. Obviously, the intensity of the cubic Si (111) diffraction ring exhibits a strong texture feature of the Si crystals in the nanowires. This indicates that the crystals in the nanowires should have a similar orientation, i.e., the Si nanowires should have a similar growth direction.

**Vapor–Solid Growth** Besides the VLS mechanism, the classical vapor–solid (VS) method for whiskers growth also merits attention for the growth of nanometer 1D materials [278]. In this process, the vapor is first generated by evaporation, chemical reduction or gaseous reaction. The vapor is subsequently transported and condensed onto a substrate. The VS method has been used to prepare oxide, metal whiskers with micrometer diameters. Hence it is possible to synthesize the 1D nanostructures using the VS process if one can control its nucleation and subsequent growth process. Using the VS method, synthesis of nanowires for oxides of Zn, Sn, In, Cd, Mg and Ga has been attempted. Seo et al. [293c] synthesized single

crystalline gallium phosphide nanowires with mean diameter 40 nm and length up to 300  $\mu\text{m}$  via sublimation of ball-milled gallium phosphide powder. Lee and coworkers [293d] have synthesized large quantities of Si nanowires (6–28 nm diameter,  $\sim 1$  mm in length) by the simple sublimation of SiO powder. The thermal sublimation of SiO powders produced SiO vapor, which underwent a disproportionation reaction, was transported and deposited at  $\sim 930^\circ\text{C}$  to form nanowires containing a crystalline Si core and an amorphous SiO<sub>2</sub> sheath. The axis of the Si nanowires is approximately along the [211] direction. This method has the advantage over the laser-assisted catalytic growth method because it can produce high-purity Si nanowires without any metal contamination. Recently, Ma et al. [294b] have prepared small diameter (1–7 nm) Si nanowires using the above oxide-assisted procedure. They obtained stable, faceted Si nanowire surfaces terminated with hydrogen after removing the SiO<sub>2</sub> sheath by dipping these nanowires in hydrofluoric acid. Scanning tunneling microscopy (STM) of these Si nanowires showed atomically resolved images with two types of nanowire surfaces which they interpreted as hydrogen-terminated Si (111)-(1  $\times$  1) and Si (001)-(1  $\times$  1) surfaces corresponding to SiH<sub>3</sub> on Si (111) and SiH<sub>2</sub> on Si (001), respectively. Interestingly these hydrogen terminated Si nanowire surfaces are more oxidation-resistant than similarly treated Si wafer surfaces. The scanning tunneling spectroscopy (STS) measurements showed that the electronic energy gaps were found to increase with decreasing Si nanowire diameter from 1.4 eV for 7 nm to 3.5 eV for 1.3 nm. Wang et al. reported the synthesis of other nanostructures such as oxide nanobelts by simply evaporating the commercial metal oxide powders at high temperatures [296–298].

**Carbothermal Reactions** It is noteworthy that a variety of oxides, nitrides and elemental nanowires can be synthesized by carbothermal reactions. For example, carbon (activated carbon or carbon nanotubes) in mixture with an oxide produces oxide or suboxide vapor species, which react with other reactants (O<sub>2</sub>, N<sub>2</sub> or NH<sub>3</sub>) to produce the desired nanowires. Thus GaN nanowires are produced by heating a mixture of Ga<sub>2</sub>O<sub>3</sub> and carbon in N<sub>2</sub> or NH<sub>3</sub>. Silicon nanowires can also be made by heating SiO<sub>2</sub> with carbon in a suitable atmosphere.

Yang et al. reported the synthesis of MgO, Al<sub>2</sub>O<sub>3</sub>, ZnO, SnO<sub>2</sub> nanowires via a carbothermal reduction process [299, 300]. Gundiah et al. [301] employed an indirect vapor-phase method via a carbothermal reduction processes, for the synthesis of silicon carbide, silicon oxynitride and silicon nitride nanowires. The simplest method to obtain  $\beta$ -SiC nanowires involves heating silica gel with activated carbon at 1360  $^\circ\text{C}$  in H<sub>2</sub> or NH<sub>3</sub> (Figure 8.30). The same reaction, if carried out in the presence of catalytic iron particles, at 1200  $^\circ\text{C}$  gives  $\alpha$ -Si<sub>3</sub>N<sub>4</sub> nanowires and Si<sub>2</sub>N<sub>2</sub>O nanowires at 1100  $^\circ\text{C}$ . Another method to obtain Si<sub>3</sub>N<sub>4</sub> nanowires is to heat MWNTs with silica gel at 1360  $^\circ\text{C}$  in an atmosphere of NH<sub>3</sub>. In the presence of catalytic Fe particles, this method yields Si<sub>3</sub>N<sub>4</sub> nanowires in pure form. The formation of carbide follows two steps (steps I and II shown below), initially carbon reduces the SiO<sub>2</sub> to the volatile suboxide of silicon and then the formation of carbide follows.

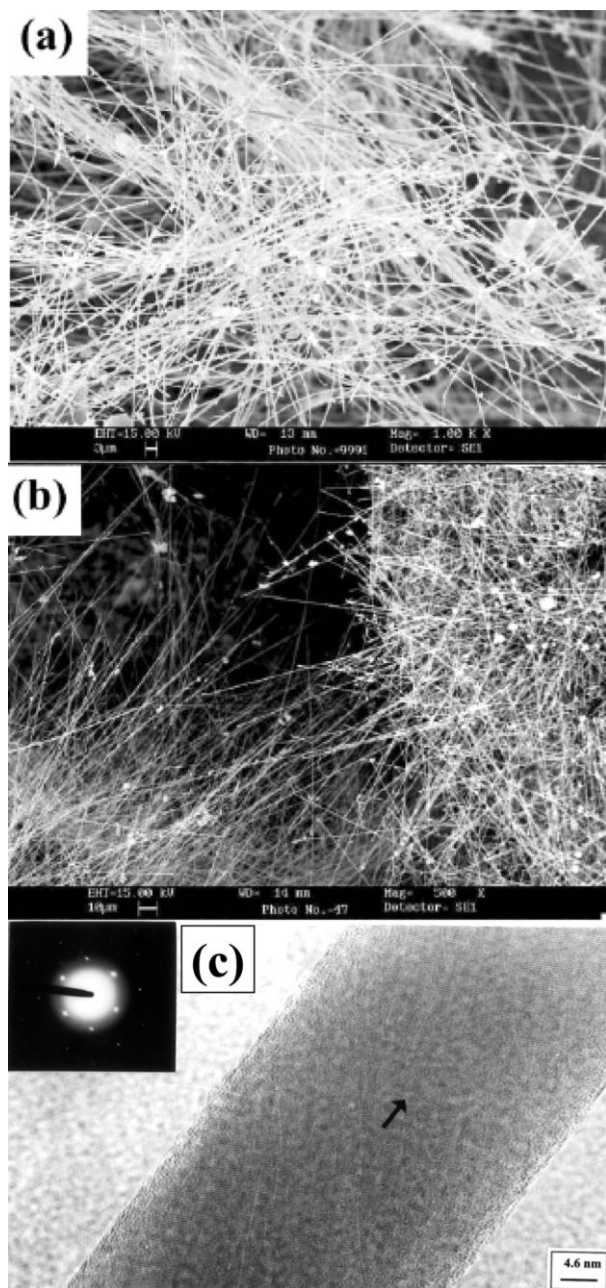


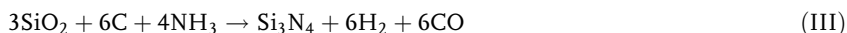
**Fig. 8.30.** SEM images of the  $\beta$ -SiC nanowires obtained by, (a) heating the gel containing the activated carbon and silica at 1360 °C in  $\text{NH}_3$  for 4 h and (b) heating the gel prepared by the reaction of ethylene glycol with citric acid in the presence of TEOS at 1360 °C in  $\text{NH}_3$  for

4 h. (c) HREM image of a  $\beta$ -SiC nanowire prepared by heating the gel containing the activated carbon and silica at 1360 °C in  $\text{NH}_3$  for 7 h. Reproduced from ref. [301], with permission.





Hence, by using the correct carbon source with the silica gel under carbothermal conditions it is possible to obtain nitride or carbide nanowires. With the carbon nanotubes the reaction follows one step (Step III shown below) to produce  $\text{Si}_3\text{N}_4$  nanowires.



The role of the catalytic iron particles in the above reactions is likely to be in facilitating the removal of oxygen from the silica. The iron oxide formed in such a reaction would readily be reduced back to metal particles in the reducing atmosphere. Similarly, Gundiah et al. carried out the conversion of  $\text{Ga}_2\text{O}_3$  powder into nanosheets and nanobelts in addition to nanowires under similar carbothermal conditions [302a]. They were able to prepare different nanostructures of  $\beta\text{-Ga}_2\text{O}_3$  by the reaction of gallium oxide with activated carbon and carbon nanotubes (Figure 8.31(a) and (b)). The flow rate of the Ar gas determines the morphology of the final nanostructures: thin nanowires being favored by a high flow rate of argon whereas at very low flow rates of argon nanobelts of  $\text{Ga}_2\text{O}_3$  were obtained in high yield. The Reaction of  $\text{Ga}_2\text{O}_3$  powder with activated carbon mainly gives rise to nanosheets and nanorods. The procedures employed in this study are attractive since they give high yields of nanowires and nanobelts. The HREM image in Figure 8.31(c) shows that these  $\text{Ga}_2\text{O}_3$  nanowires are single crystalline with the growth direction perpendicular to the (102) planes. Deepak et al. [302b] prepared gallium nitride nanowires by employing several procedures involving the use of carbon nanotube templates or catalytic Fe (Ni) metal particles. These GaN nanowires are single crystalline, with the wurtzite structure, and have high aspect ratios with lengths in the micron range.

#### 8.4.2.2 Other Processes in the Gas Phase

Chen et al. reported the synthesis of another class of semiconductor nanowires of metal silicide systems [303a,b]. In their preparation process, submonolayer amounts of Er deposited onto Si(001) react with the substrate to form epitaxial nanowires of crystalline  $\text{ErSi}_2$ . The  $\text{ErSi}_2$  nanowires so deposited are <1 nm high, a few nanometers wide, close to a micron long, crystallographically aligned to Si <110> directions. Lauhon and co-workers have grown core-shell and core-multishell nanowire heterostructures using a chemical vapor deposition (CVD) method that provides increased control over the structure's composition [304]. Using their technique, the nanowires are grown by gradually building up thin, uniform shells around a nanometre-sized cluster of gold atoms (Figure 8.32). The nanowires had boron-doped silicon shells surrounding intrinsic silicon, as well as silicon wrapped around a silicon oxide core. These nanowires are only 50 nm in diameter, containing a germanium core surrounded by a silicon shell.



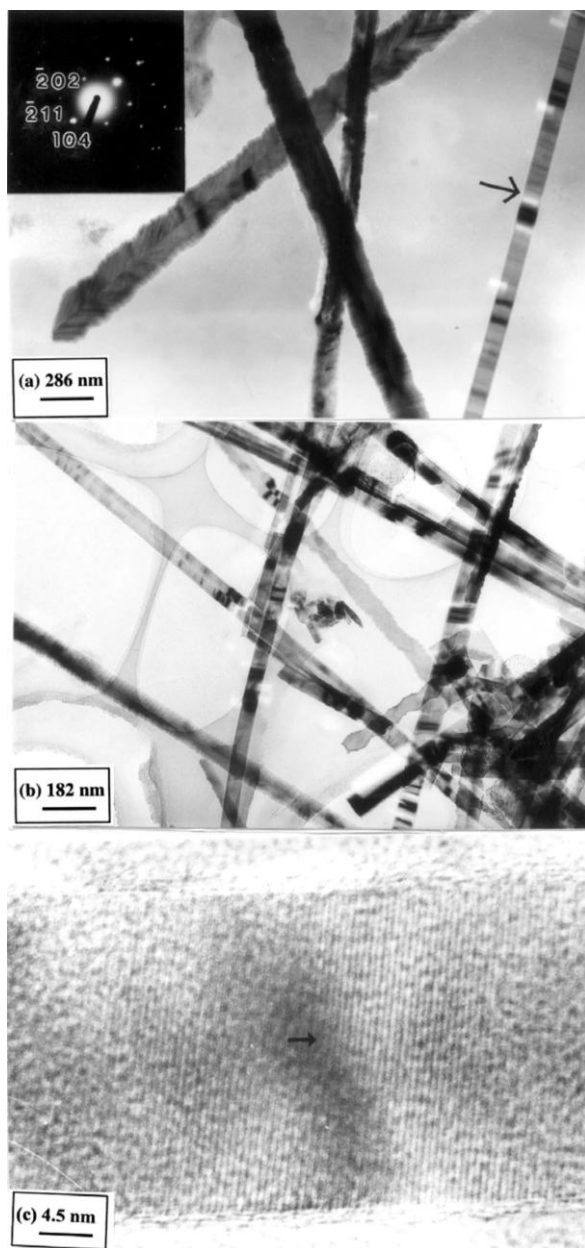
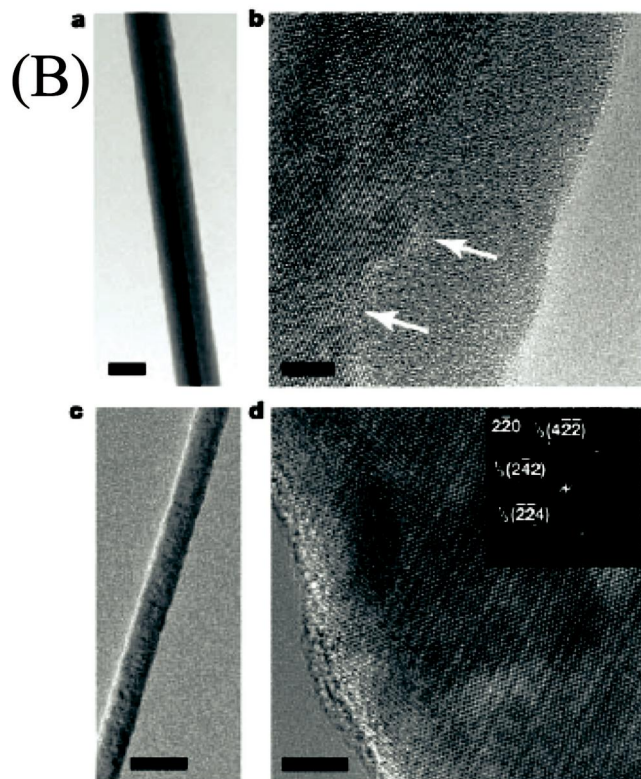
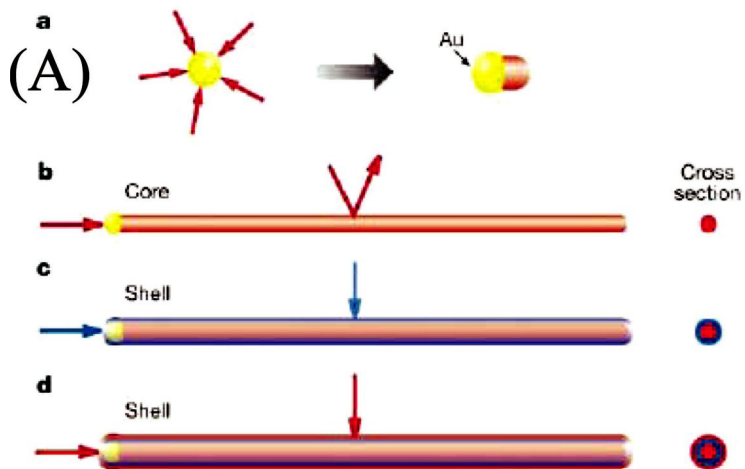


**Fig. 8.31.** Low magnification TEM images of  $\text{Ga}_2\text{O}_3$  nanowires obtained by MWNTs as the source of carbon. (a) At a flow rate of Ar maintained at 40 sccm and the product collected at the inner tube. The arrow shows a nanobelt. Inset is the SAED pattern of the sample. (b) Flow rate of Ar maintained at 80 sccm and the

product collected at the outlet. (c) HREM of a nanowire obtained on the inner tube by using the same procedure on maintaining the flow of the Ar gas at 60 sccm. The arrow indicates the growth direction that makes an angle of  $6^\circ$  with the normal to the  $(\bar{1}02)$  planes. Reproduced from ref. [302a], with permission.



### 8.4.2.3 Solution-Based Growth of Nanowires

This synthetic strategy for nanowires makes use of anisotropic growth dictated by the crystallographic structure of a solid material; or confined and directed by templates; or kinetically controlled by supersaturation; or by the use of appropriate capping agents.

**Highly Anisotropic Crystal Structures by Non-Template Methods** Many solid materials such as polysulphur nitride,  $(\text{SN})_x$ , grow into 1D nanostructures and this habit is determined by the highly anisotropic bonding in the crystallographic structure [305a,b]. Other materials such as selenium [306, 307b], tellurium [308] and molybdenum chalcogenides [309a,b], are also easily obtained as nanowires due to the anisotropic bonding, which makes the crystallization occur along the *c*-axis, favoring the stronger covalent bonds over the relatively weak van der Waals forces between the chains. Molybdenum chalcogenides, with the general formula  $\text{M}_2\text{Mo}_6\text{X}_6$  ( $\text{M} = \text{Li, Na; X} = \text{Se, Te}$ ) contain hexagonally close packed linear chains of formula  $\text{Mo}_6\text{X}_6$ . When dissolved in a highly polar solvent such as dimethylsulfoxide or *N*-methylformamide, they mainly exist as chains of  $\sim 2$  nm diameter. Some chains may aggregate into bundles or fibres with cross sections of  $\sim 1$   $\mu\text{m}$  diameter and lengths up to  $\sim 1$   $\mu\text{m}$ . Yang and co-workers [309a,b] studied the self-organization of these molecular wires ( $\text{Li}_2\text{Mo}_6\text{Se}_6$ ) into mesoscopic bundles in the presence of organic surfactants of opposite charges. By changing the length of the surfactant molecule, the spacing between these inorganic nanowires could be varied in the range 2–4 nm. Xia et al. [307] synthesized a spherical colloidal suspension/dispersion of amorphous (a-) selenium with diameters of  $\sim 300$  nm by refluxing selenious acid and hydrazine at elevated temperatures. After cooling the suspension to room temperature a small amount of selenium dissolved in the solution precipitates out as nanocrystallites of trigonal Se (*t*-Se). During aging of this dispersion in the dark, the a-Se dissolves slowly in the solution and subsequently crystallizes out slowly on a *t*-Se seed. The intrinsic anisotropic nature of *t*-Se building blocks, that is extended, helical chains of Se atoms (Figure 8.33(a)) in the

- ← **Fig. 8.32.** (A) Synthesis of core-shell nanowires by chemical vapor deposition. (a) Gaseous reactants (red) catalytically decompose on the surface of a gold nanocluster leading to nucleation and directed nanowire growth. (b) One-dimensional growth is maintained as reactant decomposition on the gold catalyst is strongly preferred. (c) Synthetic conditions are altered to induce homogeneous reactant decomposition on the nanowire surface, leading to a thin, uniform shell (blue). (d) Multiple shells are grown by repeated modulation of reactants. (B) Si-Si homoepitaxial core-shell nanowires. (a), (b) Diffraction contrast and high-resolution TEM images, respectively, of an unannealed intrinsic silicon core and p-type silicon shell nanowire grown at 450 °C. Crystal facets in the high-resolution TEM image designated by arrows indicate initially epitaxial shell growth at low temperature. Scale bars are 50 nm and 5 nm, respectively. (c), (d) TEM images (analogous to (a) and (b)) of an -Si/p-Si core-shell nanowire annealed at 600 °C for 30 min after core-shell growth at 50 °C. Inset, two-dimensional Fourier transforms of the image depicting the [111] zone axis of the single crystal nanowire. The  $1/3\{422\}$  reflections, although forbidden in bulk silicon, arise as a result of the finite thickness of the nanowire. Scale bar is 50 nm. Reproduced from ref. [304], with permission.

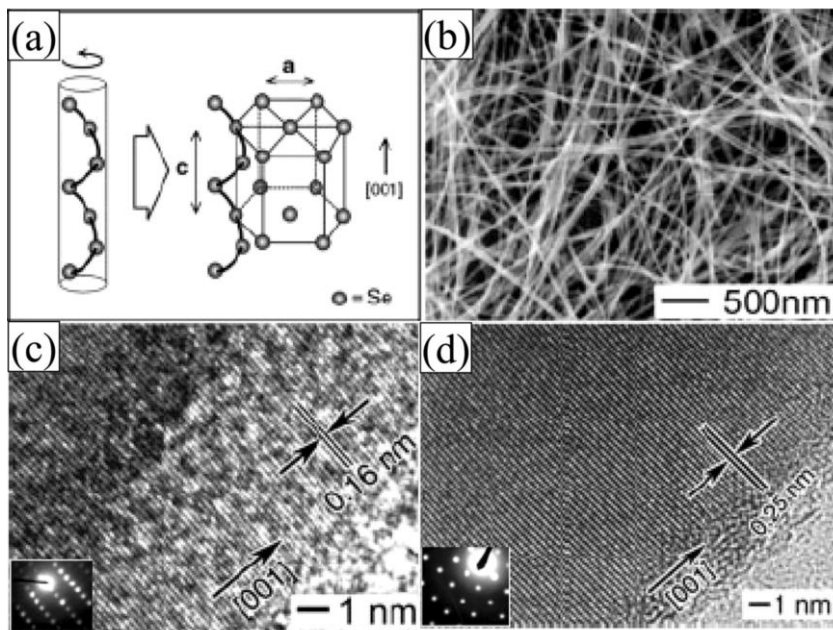


**Fig. 8.33.** (a) An illustration of the crystal structure of *t*-Se composed of hexagonally packed, helical chains of Se atoms parallel to each other along the *c*-axis. (b) Scanning electron microscopy (SEM) image of the T-Se nanowires of 32 nm mean diameter. (c) A high-resolution TEM image recorded from the edge of an individual Se nanowire (inset shows

the ED pattern obtained from the middle portion of the nanowire, confirming the growth direction was along the  $\langle 100 \rangle$  axis) and (d) high-resolution TEM image of an  $\alpha$ -Ag<sub>2</sub>Se nanowire (inset shows the ED pattern corresponding to tetragonal crystal structure). Reproduced from ref. [307, 316b,c], with permission.

trigonal phase assembles (crystallizes) ultimately into nanowires of *t*-Se (Figure 8.33(b)) [307]. Each nanowire is single crystalline, as shown by the high-resolution TEM image (in Figure 8.33(c)) recorded at the edge of a nanowire, showing a well resolved interference fringe spacing, 0.16 nm, that agrees well with the interplanar distance between {003} lattice planes. The electron diffraction pattern (ED) obtained from the middle portion of individual nanowires confirms that the growth direction (inset in Figure 8.33(c)) is along the  $\langle 001 \rangle$  axis. The plausible explanation for the formation of the Se or Te nanowire is that the helical chains (shown as in the schematic Figure 8.33(a)) can be readily packed into a hexagonal lattice through van der Waals interactions. These non-template directed methods are readily extended to a range of other solid materials whose crystallographic structures are characterized by chain-like building blocks [305c–e]. Some other typical examples including SbSI, a ferroelectric and optoelectronic material [309c,d]; K<sub>2</sub>[Pt(CN)<sub>4</sub>], a narrow band gap semiconductor [309e], crystallize in the form of whiskers.

**Template-Based Synthesis** Template directed synthesis represents a convenient and versatile method for generating 1D nanostructures. In this technique, the

template simply serves as a scaffold against which other kinds of materials with similar morphologies are synthesized. In other words, the in situ generated material is shaped into a nanostructure with its morphology complementary to that of the template. These templates could be nanoscale channels within mesoporous materials or porous alumina and polycarbonate membranes. They can be filled using (i) a solution route or (ii) a sol–gel technique or (iii) an electrochemical route to generate 1D nanowires. The produced nanowires can be released from the templates by selectively removing the host matrix [274]. Unlike the polymer membranes fabricated by track etching, porous AAO membranes containing hexagonally packed 2D array of cylindrical pores with a uniform size are prepared using anodization of aluminum foils in an acidic medium (Figure 8.34(a)). Many materials have been fabricated into nanowires using porous anodic alumina membranes (AAM) in a templating process, including various inorganic materials such as Au, Ag, Pt,  $\text{TiO}_2$ ,  $\text{MnO}_2$ ,  $\text{ZnO}$ ,  $\text{SnO}_2$ , electronically conducting polymers: polypyrrole, poly(3-methylthiophene), and polyaniline, and carbon nanotubes [310a]. Figure 8.34(b) shows the highly ordered  $\text{In}_2\text{O}_3$  nanowires uniformly assembled into the hexagonally ordered nanochannels of the AAM by oxidizing the In nanowire arrays electrodeposited in the nanochannels of the AAM [310b]. Figure 8.34(c) shows a TEM image of  $\text{In}_2\text{O}_3$  nanowires after removing the AAM from the  $\text{In}_2\text{O}_3$ /AAM samples by dissolving the AAM in NaOH solution followed by washing several times with distilled water. Besides alumina and polymer membranes, with their high surface areas and uniform pore sizes, mesoporous silica materials (MCM-41 or SBA-15) have been successfully used as templates for the synthesis of polymer and inorganic nanowires [311–315]. Ag nanowires of uniform diameters of 5–6 nm and large aspect ratios between 100 and 1000 are synthesized by  $\text{AgNO}_3$  solution impregnation in SBA-15 or MCM-41 template followed by thermal decomposition. Similarly Ge nanowires have been successfully synthesized within the mesochannels of MCM-41 [315a].

Mesophase structures self-assembled from surfactants (Figure 8.35) provide another class of useful and versatile templates for generating 1D nanostructures in relatively large quantities. It is well known that at critical micellar concentration (CMC) surfactant molecules spontaneously organize into rod-shaped micelles [315c]. These anisotropic structures can be used immediately as soft templates to promote the formation of nanorods when coupled with appropriate chemical or electrochemical reaction. The surfactant needs to be selectively removed to collect the nanorods/nanowires as a relatively pure sample. Based on this principle, nanowires of CuS, CuSe, CdS, CdSe, ZnS and ZnSe have been grown selectively by using surfactants such as Na-AOT or Triton X of known concentrations [238, 246].

The nanowires themselves can be used as templates to generate the nanowires of other materials. The template may be coated onto the nanowire (physically) forming coaxial nanocables [316a], or it may react with the nanowires forming a new material [317a,b]. In the physical (solution or sol–gel coating) approach, the surfaces of the nanowires could be directly coated with conformal sheaths made of a different material to form coaxial nanocables. Subsequent dissolution of the original nanowires could lead to nanotubes of the coated material. The sol–gel



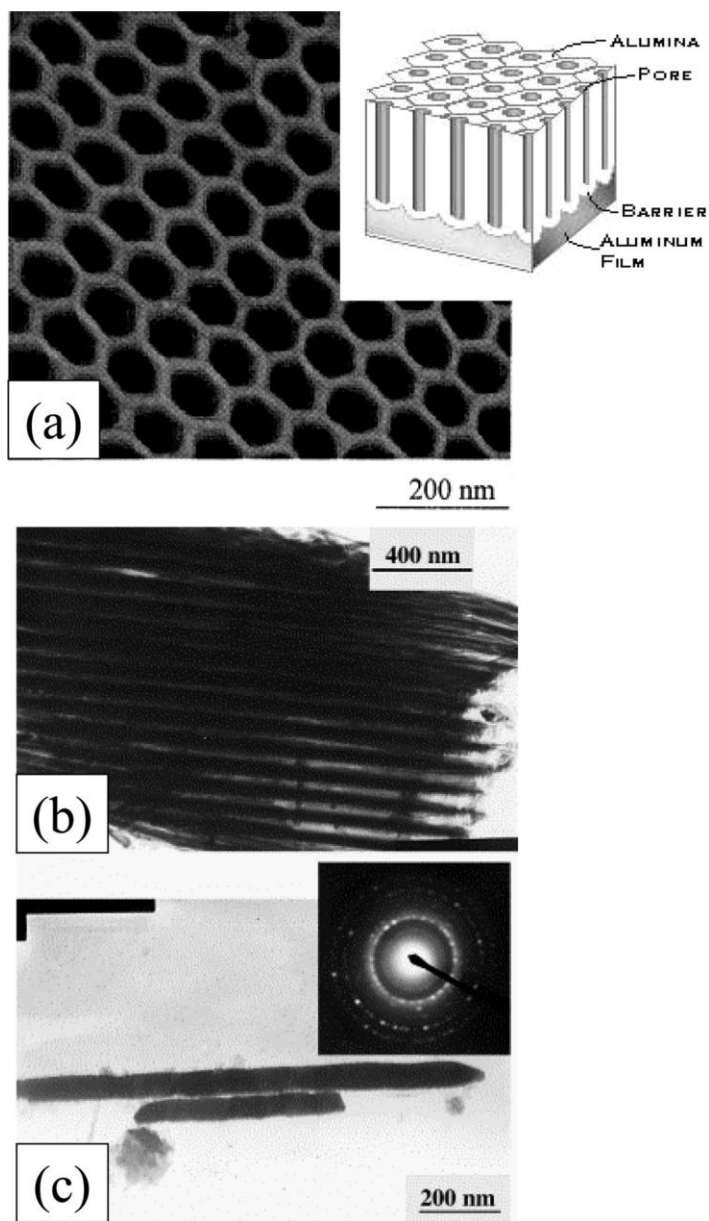


**Fig. 8.34.** TEM micrograph of  $\text{In}_2\text{O}_3$  nanowire arrays embedded in AAM with channel diameters of 60 nm: (a) AFM image of AAO membrane (b)  $\text{In}_2\text{O}_3$ /AAM system. (c)  $\text{In}_2\text{O}_3$  nanowires. Reproduced from ref. [310b], with permission.

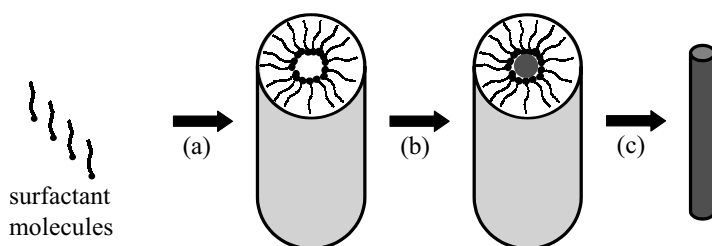


**Fig. 8.35.** Schematic illustrations showing the formation of nanowires by templating against mesostructures which are self-assembled from surfactant molecules; (a) formation of a cylindrical micelle, (b) formation of the desired material in the aqueous phase encapsulated by the cylindrical micelle, (c) removal of the surfactant molecule with an appropriate solvent (or by calcinations) to obtain an individual nanowire.

coating method is a generic route to synthesize coaxial nanocables that may contain electrically conductive metal cores and insulating sheaths [316a]. The thickness of the  $\text{SiO}_2$  sheath could be controlled in the range 2–100 nm by varying the concentration of the precursor and the deposition time. Figure 8.36(a) shows the TEM image of a typical sample of coaxial nanocables, Ag in  $\text{SiO}_2$ , obtained by coating Ag nanowires with silica derived from a sol–gel precursor. Selective removal of the silver core by dissolving in ammonia gives a silica tube as shown in Figure 8.36(b). Single crystalline  $\text{Ag}_2\text{Se}$  (tetragonal) nanowires of diameters less than 40 nm have been successfully synthesized through a novel topotactic reaction wherein *t*-Se single crystalline nanowire templates react with  $\text{AgNO}_3$  solutions at room temperature [317a,b]. The high-resolution TEM image (Figure 8.33(d)) obtained from the edge of an individual nanowire (compared with Figure 8.33(c)) indeed shows the complete conversion of Se nanowire into single crystalline tetragonal  $\text{Ag}_2\text{Se}$  nanowire. The fringe spacing of 0.25 nm corresponds to the interplanar distance of [200], implying the growth direction of this nanowire was  $\langle 100 \rangle$ . Beyond 40 nm diameter the orthorhombic structure becomes more stable. In some other cases this technique, however, intrinsically yields products of a polycrystalline nature.

Template-directed synthesis of metal nanorods covered by carbon and other materials has been reported in the literature [45, 273, 318]. By employing the arc vaporization method, Demoncey et al. [319], have shown the role of sulfur along with the transition metals in the formation of metal-filled MWNTs. Electrolytic formation of carbon-sheathed Sn–Pb nanowires with diameters in the 40–90 nm range has been reported [320]. Sloan et al. [321] find that SWNTs can be filled up to 50% by silver, by employing the  $\text{KCl}$ – $\text{UCl}_4$  and  $\text{AgCl}$ – $\text{AgBr}$  eutectic systems, to produce nanowires. Govindaraj et al. [129], have demonstrated that a variety of metal nanowires of 1.0–1.4 nm diameter can be readily prepared by filling SWNTs, opened by acid treatment. Nanowires of Au, Pt, Pd and Ag have been synthesized by employing sealed-tube reactions as well as solution methods. In addition, incorporation of thin layers of metals in the intertubular space of the SWNT bundles



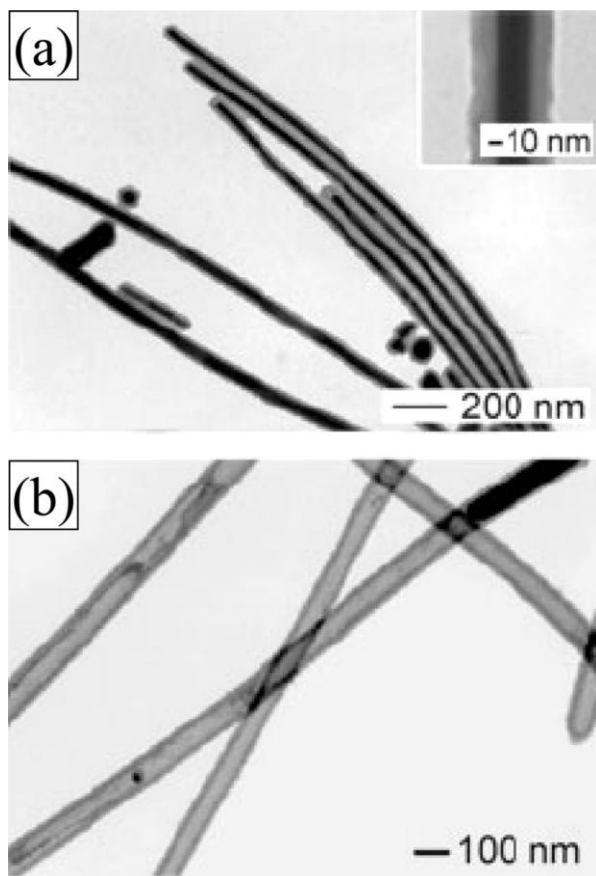


**Fig. 8.36.** (a) TEM image of Ag/SiO<sub>2</sub> coaxial nanocables prepared by coating Ag nanowires with amorphous silica using the sol-gel method. (b) TEM image of silica nanotubes

prepared by selectively dissolving Ag cores of Ag/SiO<sub>2</sub> in ammonia solution (pH 11). Reproduced from ref. [316a], with permission.

has been observed. In Figure 8.37(a), we show a TEM image, which reveals the presence of a large number of gold nanowires obtained from the sealed tube reaction. The image clearly shows extensive filling of SWNT bundles. The length of the gold nanowires is in the range 15–70 nm with diameters in the range 1.0–1.4 nm. In some of the nanowires, however, the metal is single-crystalline, as revealed by the HREM image of Figure 8.37(b). This image reveals the resolved lattice of gold with a spacing of ~0.23 nm, corresponding to the (111) planes. Polycrystalline Au aggregates are transformed into the single crystalline form by annealing. The Au nanowires are decomposed to nanoparticles by electron-beam damage at a temperature of 300–350 °C. Electronic absorption spectra of dispersions of gold nanowires in ethanol show transverse and longitudinal plasmon absorption bands

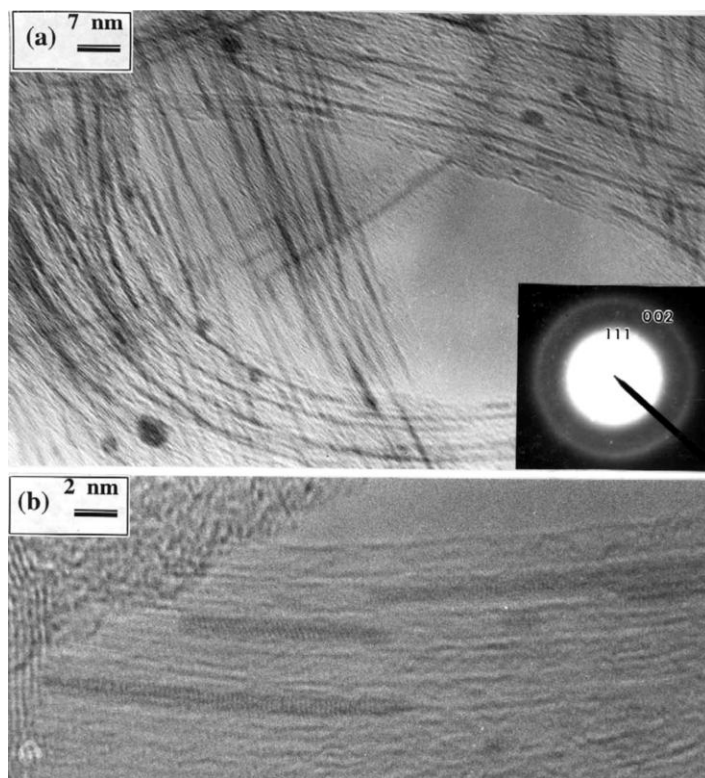


**Fig. 8.37.** (a) TEM image of Au nanowires inside SWNTs obtained by the sealed tube reaction. Inset: A SAED pattern of the nanowires (b) HRTEM image showing the

single crystalline nature of some of the Au nanowires. Lattice planes with  $d_{111} = 2.3 \text{ \AA}$  can be seen. Reproduced from ref. [129], with permission.

[129], with the latter shifting to long wavelengths with the increasing aspect ratio, as predicted by Link et al. [322] Nanowires of bismuth with a diameter of 1 nm have been obtained by filling SWNTs during arc vaporization as well as by a solution method [323]. Interestingly, by employing the anodic aluminum oxide (AAO) templates and organometallic chemical vapor deposition (MOCVD), nickel nanowires of 4 nm diameter have been produced inside the carbon nanotubes [324]. However, the diameter of the AAO templates dictates the diameter of the nanowires, making it difficult to tune the nanowire diameter down to 1 nm. SWNTs with a narrow size distribution seem to have an advantage as ideal templates [323, 325].

**Solution-Liquid-Solid Process** Buhro and coworkers [276], have developed a low temperature solution-liquid-solid (SLS) method for the synthesis of highly crystalline nanowires of III-V semiconductors [276, 327]. In a typical procedure, a metal (e.g., In, Sn, Bi) with a low melting point was used as a catalyst, and the de-

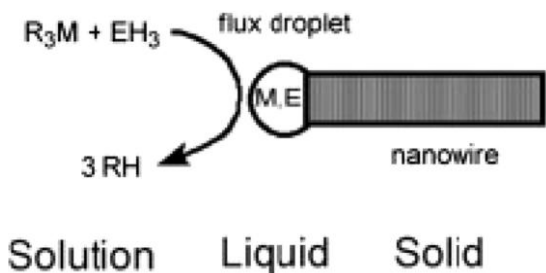


**Fig. 8.38.** (a) Schematic illustration showing the growth of nanowire through the solution–liquid–solid mechanism which is similar to the vapor–liquid–solid process. Reproduced from ref. [280, 333], with permission.

sired material was generated through the decomposition of organometallic precursors. They have grown InP, InAs and GaAs nanowhiskers by low temperature ( $\leq 203^\circ\text{C}$ ) solution phase reactions. The schematic illustration in Figure 8.38 clearly shows the growth of nanowires or whiskers through a solution–liquid–solid (SLS) method. The product was essentially single crystalline whiskers or filaments with dimensions of 10–150 nm and length up to several micrometers. A similar low temperature synthesis route is employed for the catalyzed growth of indium nitride fibres from azido-indium precursors [326]. Highly crystalline InP fibres of diameter 10–100 nm and length 50–1000 nm are grown by the methanolysis of  $\{tert\text{-Bu}_2\text{In}[\mu\text{-P}(\text{SiMe}_3)_2]\}_2$  in aromatic solvent at  $111\text{--}203^\circ\text{C}$  [326, 327a]. The key component of the synthesis was the decomposition of the organometallic precursor which proceeds through a sequence of isolated and fully characterized intermediates to yield a complex  $[tert\text{-Bu}_2\text{In}(\mu\text{-PH}_2)]_3$ ; this complex subsequently underwent alkane elimination to generate the building blocks:  $(\text{InP})_n$  fragments. The fragments dissolved in a dispersion of droplets formed by molten indium, and recrystallized as InP fibers.

Korgel et al. [328a,b], by using the supercritical fluid–liquid–solid (SFSL) approach, have grown bulk quantities of defect-free silicon (Si) and germanium (Ge) nanowires with nearly uniform diameters ranging from 40–50 Å (Si), 50–300 Å (Ge) and with lengths of several micrometers. They used solvent-dispersed, size-monodisperse alkane thiol-capped gold (Au) nanocrystals to direct the Si nanowire growth with narrow wire diameter distributions [328a]. Sterically stabilized Au nanocrystals were dispersed in supercritical hexane with a silicon precursor, diphenylsilane at a temperature of  $500^\circ\text{C}$  and pressure of 270 bar. At this temperature, the diphenylsilane decomposes to Si atoms which dissolve into the sterically stabilized Au nanocrystals until reaching supersaturation, at which point they are expelled from the particle as a thin nanometer-scale wire. This supercritical fluid medium provides the high temperatures necessary to promote Si crystallization.

In addition to these solution routes to elemental and III–V semiconductor nanowires, it has recently been reported that, by exploring the selective capping capabilities of mixed surfactants, it is now possible to extend the well-established

II–IV semiconductor nanocrystal synthesis to the synthesis of semiconductor nanorods [329, 330a], a unique version of nanowires with relatively shorter aspect ratio. Xia and co-workers used a polyol method to generate the Ag nanowires by reducing silver nitrate with ethylene glycol in the presence of polyvinyl pyrrolidone (PVP) [330b–d]. The key to the formation of a 1D nanostructure is the use of PVP as a polymeric capping reagent and the introduction of a seeding step. Silver nitrate reduces in the presence of the seed (Pt, or Ag nanoparticles) to form silver nanoparticles with bimodal size distribution produced via homogeneous and heterogeneous nucleation processes. Ag nanorods grow at the expense of the small Ag nanoparticles, as directed by the capping reagent (PVP). In the presence of PVP, most silver particles can be confined and directed to grow into nanowires of uniform diameter. These nanowires have FCC structure with mean diameter  $\sim 40$  nm.

**Solvothermal Synthesis** Solvothermal methodology has been extensively examined as a possible solution route to semiconductor nanowires and nanorods. In this process, a solvent is mixed with certain metal precursors and possibly crystal growth regulating or templating agents such as amines. This solution mixture was then placed in an autoclave kept at relatively high temperature and pressure to carry out the crystal growth and assembly process. The methodology seems to be quite versatile and has been demonstrated to be able to produce many different crystalline semiconductor nanorods and nanowires [331, 332]. Xia et al. [307] demonstrated a solution-phase approach by refluxing selenious acid and excess hydrazine for the synthesis of uniform nanowires of selenium with lateral dimensions controllable in the range 10–30 nm and with lengths of up to hundreds of micrometers.

#### 8.4.2.4 Growth Control

A significant challenge for the chemical synthesis is how to rationally control the nanostructure assembly so that the size, dimensionality, interfaces and ultimately the 2-D and 3-D superstructures can be tailored to a desired functionality. Many physical and thermodynamic properties are diameter dependent. Yang et al. have used monodispersed Au clusters with sizes 15.3, 20, 25, 29, 52 nm and obtained uniform nanowires with sizes from 23 to 57 nm respectively.

Controlling the growth orientation is important for the applications of nanowires. By applying the conventional epitaxial crystal growth technique to the VLS process, a new vapor–liquid–solid epitaxy (VLSE) technique, has been developed for the controlled synthesis of nanowire arrays. Nanowires generally have preferred growth directions. For example, Si nanowires prefer to grow along the  $\langle 111 \rangle$  direction. Hence if (111) Si wafer is used as substrate, Si nanowires will grow epitaxially and vertically on the substrate [333, 334]. Similarly ZnO nanowires prefer to grow along the  $\langle 001 \rangle$  direction [335].

It is clear from the VLS nanowire growth mechanism that the positions of the nanowires can be controlled by the initial positions of the Au clusters or Au thin films. By creating desired patterns of Au using the lithographic technique it is possible to grow ZnO nanowires of the same designed pattern since they grow

vertically only from the region that is coated with Au and form the designed patterns of ZnO nanowire arrays [333, 334]. Similarly, a network of nanowires with the precise placement of individual nanowires on the substrate with the desired configuration is achieved by the surface patterning strategy [333, 334].

Integration of nanowire building blocks into complex functional networks in a predictable and controlled way is a major scientific challenge. In the very first technique the direct one-step growth process was used [333, 334]. The other technique is to put the nanowire building blocks together into the functional structure to develop a suitable hierarchical assembly. The atomic force microscope has been used to push or deposit the nanotubes into the desired configuration [336]. By using a simple dubbed microfluidic assisted nanowire integration process wherein nanowire solution/suspension was filled in the microchannels formed between poly(dimethylsiloxane) (PDMS) micromold and a flat Si substrate, followed by evaporation of the solvent, nanowire surface patterning and alignment was achieved [337, 338]. Duan has shown by dispersing Si and InP nanowires between the fabricated metal electrode arrays and then by applying a bias (inducing electric field), that it is possible to get alignment of Si and InP nanowires [339]. Kim has used a Langmuir–Blodgett technique to get aligned, high-density nanowire assemblies [340].

#### 8.4.3

#### Properties of Nanowires

Compared with bulk materials, low dimensional nanoscale materials, with their large surface area and possible quantum confinement effect, exhibit distinct electric, optical, chemical and thermal properties. Korgel et al. have shown that the absorption edge of the Si nanowires was strongly blue shifted from the bulk indirect band gap of 1.1 eV [328, 341]. They also observed sharp discrete absorbance features and relatively strong “band edge” photoluminescence. They attribute this observation to a quantum confinement effect as well as to lattice orientation of the nanowires. Lieber et al. studied the fundamental PL properties of individual isolated indium phosphide nanowires [342]. These polarization sensitive measurements reveal a striking anisotropy in the PL intensity recorded parallel and perpendicular to the long axis of the nanowire. This intrinsic anisotropy was used to create polarization-sensitive nanoscale photodetectors, which may be useful in optical switches, high-resolution detectors and integrated photonic circuits.

Huang et al. have demonstrated the room temperature ultra-violet lasing of ZnO nanowires [335]. The observed lasing action in these nanowire arrays without any fabricated mirror indicate these single-crystalline, faceted nanowire arrays can indeed function as natural resonance cavities. This nanowire lasing has been further confirmed with the optical characterization of single ZnO nanowire by near-field scanning microscopy (NSOM) [343]. Semiconductor nanowires have recently been used as building blocks for assembling a range of nanodevices including FETs, p–n diodes, bipolar junction transistors, and complementary inverters [344–348]. The nanotube and nanowires with sharp tips are promising materials for applica-

tions as cold cathode field emission devices. Field emission characteristics of both  $\beta$ -SiC and Si nanowires have been investigated using current voltage measurements and the Fowler–Nordheim equation. These Si and SiC exhibit robust field emission with turn-on fields of 15 and 20 V  $\mu\text{m}^{-1}$ , respectively [286, 349], with current density of 0.01 mA  $\text{cm}^{-2}$ , which are comparable with those of other field emitters like diamond and carbon nanotubes.

## References

- 1 H. W. KROTO, J. R. HEATH, S. C. O'BRIEN et al., *Nature* **1985**, 318, 162–163.
- 2 W. KRATSCHEMER, L. D. LAMB, K. FOSTIROPOULOS et al., *Nature* **1990**, 347, 354–358.
- 3 S. IIJIMA, *Nature* **1991**, 354, 56–58.
- 4 S. IIJIMA, T. ICHIHASHI, *Nature* **1993**, 363, 603–605.
- 5 D. S. BETHUNE, C. H. KIANG, M. S. DE VRIES et al., *Nature* **1993**, 363, 605–607.
- 6 W. K. HSU, J. P. HARE, M. TERRONES et al., *Nature* **1995**, 377, 687.
- 7 M. ENDO, K. TAKEUCHI, S. IGARASHI et al., *J. Phys. Chem. Solids* **1993**, 54, 1841–1848.
- 8 (a) P. M. AJAYAN, T. ICHIHASHI, S. IIJIMA, *Chem. Phys. Lett.* **1993**, 202, 384–388; (b) S. G. LOUIE, *Top. Appl. Phys.* **2001**, 80, 113–145.
- 9 S. IIJIMA, P. M. AJAYAN, T. ICHIHASHI, *Phys. Rev. Lett.* **1992**, 69, 3100–3103.
- 10 V. P. DRAVID, X. LIN, Y. WANG et al., *Science* **1993**, 259, 1601–1604.
- 11 P. M. AJAYAN, T. W. EBBESEN, T. ICHIHASHI et al., *Nature* **1993**, 362, 522–525.
- 12 S. C. TSANG, P. J. F. HARRIS, M. L. H. GREEN, *Nature* **1993**, 362, 520–522.
- 13 S. C. TSANG, Y. K. CHEN, P. J. F. HARRIS et al., *Nature* **1994**, 372, 159–162.
- 14 C. N. R. RAO, R. SESHADRI, A. GOVINDARAJ et al., *Mater. Sci. Eng., R.* **1995**, 15, 209–262; P. M. AJAYAN, *Chem. Rev.* **1999**, 99, 1787–1799.
- 15 Special issue on Carbon Nanotubes, *Appl. Phys. A.* **1998**, 67, 1–119; *Appl. Phys. A.* **1999**, 69, 245–312; Carbon Nanotubes, *J. Mater. Res.* **1998**, 13, 2355–2423; articles in *J. Phys. Chem.* **2000**, 104 and *Physics World*, June **2000**.
- 16 *AIP Conf. Proc.* **1999**, 442.
- 17 M. S. DRESSELHAUS, G. DRESSELHAUS, P. C. EKLUND, in *Science of Fullerenes and Carbon Nanotubes*, Academic Press, San Diego 1996, 756–917.
- 18 Carbon Nanotubes: (special issue), *Acc. Chem. Res.* **2002**, 35, 998–1113.
- 19 M. TERRONES, W. K. HSU, H. W. KROTO et al., *Top. Curr. Chem.* **1999**, 199, 190–234.
- 20 (a) C. N. R. RAO, B. C. SATISHKUMAR, A. GOVINDARAJ et al., *Chem. Phys. Chem.* **2001**, 2, 78–105; (b) R. H. BAUGHMAN, A. A. ZAKHIDOV, W. A. DE HEER, *Science* **2002**, 297, 787–792.
- 21 P. YANG, Y. WU, R. FAN, *Int. J. Nanoscience* **2002**, 1–39.
- 22 C. N. R. RAO, M. NATH, *Dalton Trans.* **2003**, 1–24.
- 23 R. TENNE, *Chem. Eur. J.* **2002**, 8 (23), 5296–5304.
- 24 G. R. PATZKE, F. KRUMEICH, R. NESPER, *Angew. Chem. Int. Ed. Engl.* **2002**, 41, 2446–2461.
- 25 T. W. EBBESEN, P. M. AJAYAN, *Nature* **1992**, 358, 220–222.
- 26 N. HATTA, K. MURATA, *Chem. Phys. Lett.* **1994**, 217, 398–402.
- 27 D. T. COLBERT, J. ZHANG, S. M. MCCLURE et al., *Science* **1994**, 266, 1218–1222.
- 28 M. GE, K. SATTTLER, *Science* **1993**, 260, 515–518.
- 29 (a) W. K. HSU, M. TERRONES, J. P. HARE et al., *Chem. Phys. Lett.* **1994**, 262, 161–166; (b) Y. GOGOTSI, J. A. LIBERA, M. YOSHIMURA, *J. Mater. Res.* **2000**, 15, 2591–2594.

- 30 M. JOSE-YACAMAN, M. MIKI-YOSHIDA, L. RENDON et al., *Appl. Phys. Lett.* **1993**, 62, 202–204.
- 31 V. IVANOV, J. B. NAGY, Ph. LAMBIN et al., *Chem. Phys. Lett.* **1994**, 223, 329–335.
- 32 K. HERNADI, A. FONSECA, J. B. NAGY et al., *Synth. Met.* **1996**, 77, 31–34.
- 33 N. M. RODRIGUEZ, *J. Mater. Res.* **1993**, 8, 3233–3250.
- 34 R. SEN, A. GOVINDARAJ, C. N. R. RAO, *Chem. Phys. Lett.* **1997**, 267, 276–280.
- 35 R. SEN, A. GOVINDARAJ, C. N. R. RAO, *Chem. Mater.* **1997**, 9, 2078–2081.
- 36 W. A. DE HEER, J. M. BONARD, K. FAUTH et al., *Adv. Mater.* **1997**, 9, 87–89.
- 37 W. Z. LI, S. S. XIE, L. X. QIAN et al., *Science* **1996**, 274, 1701–1703.
- 38 G. CHE, B. B. LAXMI, C. R. MARTIN et al., *Chem. Mater.* **1998**, 10, 260–267.
- 39 M. TERRONES, N. GROBERT, J. OLIVARES et al., *Nature (London)* **1997**, 388, 52–55.
- 40 M. TERRONES, N. GROBERT, J. P. ZHANG et al., *Chem. Phys. Lett.* **1998**, 285, 299–305.
- 41 Z. F. REN, Z. P. HUANG, J. W. XU et al., *Science* **1998**, 282, 1105–1107.
- 42 S. FAN, M. C. CHAPLINE, N. R. FRANKLIN et al., *Science* **1999**, 283, 512–514.
- 43 Z. W. PAN, S. S. XIE, B. H. CHANG et al., *Chem. Phys. Lett.* **1999**, 299, 97–102.
- 44 (a) B. C. SATISHKUMAR, A. GOVINDARAJ, C. N. R. RAO, *Chem. Phys. Lett.* **1999**, 307, 158–162; (b) C. N. R. RAO, R. SEN, B. C. SATISHKUMAR et al., *Chem. Commun.* **1998**, 1525–1526.
- 45 C. N. R. RAO, A. GOVINDARAJ, R. SEN et al., *Mater. Res. Innov.* **1998**, 2, 128–141.
- 46 (a) R. ANDREWS, D. JACQUES, A. M. RAO et al., *Chem. Phys. Lett.* **1999**, 303, 467–474; (b) S. HUANG, A. W. H. MAU, T. W. TURNER et al., *J. Phys. Chem. B* **2000**, 104, 2193–2196.
- 47 (a) J. LI, C. PAPADOPOULOS, J. M. XU, M. MOSKOVITS, *Appl. Phys. Lett.* **1999**, 75, 367–369; (b) K. MUKHOPADHYAY, A. KOSHIO, T. SUGAI et al., *Chem. Phys. Lett.* **1999**, 303, 117–124.
- 48 (a) C. N. R. RAO, A. GOVINDARAJ, *Acc. Chem. Res.* **2002**, 35, 998–1007; (b) B. C. SATISHKUMAR, A. GOVINDARAJ, P. V. VANITHA et al., *Chem. Phys. Lett.* **2002**, 362, 301–306.
- 49 H. DAI, A. Z. RINZLER, P. NIKOLAEV et al., *Chem. Phys. Lett.* **1996**, 260, 471–475.
- 50 Y. SAITO, M. OKUDA, T. KOYAMA, *Surf. Rev. Lett.* **1996**, 3, 863–864.
- 51 Y. SAITO, K. KAWABATA, M. OKUDA, *J. Phys. Chem.* **1995**, 99, 16076–16079.
- 52 C. JOURNET, W. K. MASER, P. BERNIER et al., *Nature* **1997**, 388, 756–758.
- 53 A. THESS, R. LEE, P. NIKOLAEV et al., *Science* **1996**, 273, 483–487.
- 54 B. C. SATISHKUMAR, A. GOVINDARAJ, R. SEN et al., *Chem. Phys. Lett.* **1998**, 293, 47–52.
- 55 S. SERAPHIN, D. ZHOU, *Appl. Phys. Lett.* **1994**, 64, 2087–2089.
- 56 H. M. CHENG, F. LI, G. SU, H. Y. PAN et al., *Appl. Phys. Lett.* **1998**, 72, 3282–3284.
- 57 D. LAPLAZE, P. BERNIER, W. F. MASER et al., *Carbon* **1998**, 36, 685–688.
- 58 P. NIKOLAEV, M. BRONIKOWSKI, R. K. BRADLEY et al., *Chem. Phys. Lett.* **1999**, 313, 91–97.
- 59 B. KITTYANAN, W. E. ALVAREZ, J. H. HARWELL et al., *Chem. Phys. Lett.* **2000**, 317, 497–503.
- 60 J. F. COLOMER, C. STEFAN, S. LEFRANT et al., *Chem. Phys. Lett.* **2000**, 317, 83–89.
- 61 E. FLAHAUT, A. GOVINDARAJ, A. PEIGNEY et al., *Chem. Phys. Lett.* **1999**, 300, 236–242.
- 62 H. D. SUN, Z. K. TANG, J. CHEN et al., *Appl. Phys. A* **1999**, 69, 381–384.
- 63 S. BANDOW, A. M. RAO, K. A. WILLIAMS et al., *Phys. Chem. B* **1997**, 101, 8839–8842.
- 64 G. S. DUESBERG, J. MUSTER, V. KRSTIC et al., *Appl. Phys. A* **1998**, 67, 117–119.
- 65 J. LIU, A. G. RINZLER, H. DAI et al., *Science* **1998**, 280, 1253–1256.
- 66 S. IJIMA, *MRS Bull.* **1994**, 19, 43–47.
- 67 J. TERSOFF, R. S. RUOFF, *Phys. Rev. Lett.* **1994**, 73, 676–679.
- 68 D. SRIVASTAVA, D. W. BRENNER, J. D. SCHALL et al., *J. Phys. Chem. B* **1999**, 103, 4330–4337.
- 69 R. MARTEL, H. R. SHEA, Ph. AVOURIS, *J. Phys. Chem. B* **1999**, 103, 7551–7556.



- 70 (a) M. AHLKOG, E. SEYNAEVE, R. J. M. VULLERS et al., *Chem. Phys. Lett.* **1999**, 300, 202–206; (b) S. HUANG, L. DAI, A. W. H. MAU, *J. Mater. Chem.* **1999**, 9, 1221–1222.
- 71 B. W. SMITH, M. MONTHIOUX, D. E. LUZZI, *Nature (London)* **1998**, 396, 323–324.
- 72 B. BURTEAUX, A. CLAYE, B. W. SMITH et al., *Chem. Phys. Lett.* **1999**, 310, 21–24.
- 73 J. SLOAN, R. E. DUNIN-BORKOWSKI, J. L. HUTCHISON et al., *Chem. Phys. Lett.* **2000**, 316, 191–198.
- 74 R. SESHADRI, A. GOVINDARAJ, H. N. AIYER et al., *Curr. Sci. (India)* **1994**, 66, 839–847.
- 75 Y. MURAKAMI, T. SHIBATA, K. OKUYAMA et al., *J. Phys. Chem. Solids* **1993**, 54, 1861–1870.
- 76 W. RULAND, in *Chemistry and Physics of Carbon*, vol 4, ed. P. L. WALKER, Marcel Dekker, New York 1968.
- 77 B. E. WARREN, *Phys. Rev.* **1941**, 59, 693–698.
- 78 T. W. EBBESEN, H. HIURA, J. FUJITA et al., *Chem. Phys. Lett.* **1993**, 209, 83–90.
- 79 Y. ANDO, *Jpn. J. Appl. Phys. Lett.* **1993**, 32, L1342–1345.
- 80 X. K. WANG, X. M. LIN, V. P. DRAVID et al., *Appl. Phys. Lett.* **1993**, 62, 1881–1883.
- 81 Z. ZHANG, C. M. LIEBER, *Appl. Phys. Lett.* **1993**, 62, 2792–2794.
- 82 C. H. OLK, J. P. HAREMANS, *J. Mater. Res.* **1994**, 9, 259–262.
- 83 R. SESHADRI, H. N. AIYER, A. GOVINDARAJ et al., *Solid State Commun.* **1994**, 91, 195–199.
- 84 D. L. CARROLL, Ph. REDLICH, P. M. AJAYAN et al., *Phys. Rev. Lett.* **1997**, 78, 2811–2814.
- 85 L. C. VENEMA, V. MEUNIER, Ph. LAMBIN et al., *Phys. Rev. B* **2000**, 61, 2991–2996.
- 86 R. A. JISHI, L. VENKATARAMAN, M. S. DRESSERHAUS et al., *Chem. Phys. Lett.* **1993**, 209, 77–82.
- 87 H. HIURA, T. W. EBBESEN, K. TANIGAKI et al., *Chem. Phys. Lett.* **1993**, 202, 509–512.
- 88 J. M. HOLDEN, P. ZHOU, X. X. BI et al., *Chem. Phys. Lett.* **1994**, 220, 186–191.
- 89 A. M. RAO, E. RICHTER, S. BANDOW et al., *Science* **1997**, 275, 187–191.
- 90 A. KASUYA, Y. SASAKI, Y. SAITO et al., *Phys. Rev. Lett.* **1997**, 78, 4434–4437.
- 91 A. M. RAO, A. JORIO, M. A. PIMENTA et al., *Phys. Rev. Lett.* **2000**, 84, 1820–1823.
- 92 P. V. TEREDESAI, A. K. SOOD, D. V. S. MUTHU et al., *Chem. Phys. Lett.* **2000**, 319, 296–302.
- 93 A. K. SOOD, P. V. TEREDESAI, D. V. S. MUTHU et al., *Phys. Status Solidi B* **1999**, 215, 393–401.
- 94 S. BANDOW, S. ASAKA, Y. SAITO et al., *Phys. Rev. Lett.* **1998**, 80, 3779–3782.
- 95 U. D. VENKATARAMAN, A. M. RAO, E. RICHTER et al., *Phys. Rev. B* **1999**, 59, 10928–10934.
- 96 J. R. WOOD, M. D. FROGLEY, E. R. MEURS et al., *J. Phys. Chem. B* **1999**, 103, 10388–10392.
- 97 H. D. SUN, Z. K. TANG, J. CHEN et al., *Solid State Commun.* **1999**, 109, 365–369.
- 98 S. A. CHESNOKOV, V. A. NALIMOVA, A. G. RINZLER et al., *Phys. Rev. Lett.* **1999**, 82, 343–346.
- 99 M. J. PETERS, L. E. MCNEIL, J. P. LU et al., *Phys. Rev. B* **2000**, 61, 5939–5944.
- 100 R. T. K. BAKER AND P. S. HARRIS, in *Chemistry and Physics of Carbon*, eds. P. L. WALKER, P. A. THROWER, Marcel Dekker, New York 1978, vol. 14.
- 101 A. OBERLIN, M. ENDO, T. KOYAMA, *J. Cryst. Growth.* **1976**, 32, 335–349.
- 102 M. ENDO, H. W. KROTO, *J. Phys. Chem.* **1992**, 96, 6941–6944.
- 103 R. E. SMALLEY, *Mater. Sci. Eng., B* **1993**, 19, 1–7.
- 104 S. IIJIMA, P. M. AJAYAN, T. ICHIHASHI, *Phys. Rev. Lett.* **1992**, 69, 3100–3103.
- 105 T. W. EBBESEN, J. TABUCHI, K. TANIGAKI, *Chem. Phys. Lett.* **1992**, 191, 336–338.
- 106 Y. SAITO, T. YOSHIKAWA, M. INAGAKI et al., *Chem. Phys. Lett.* **1994**, 204, 277–282.
- 107 D. H. ROBERTSON, D. W. BRENNER, C. T. WHITE, *J. Phys. Chem.* **1992**, 96, 6133–6135.
- 108 (a) S. AMELINCKX, X. B. ZHANG, D. BERNAERTS et al., *Science* **1994**, 265, 635–639; (b) S. AMELINCKX, D.

- BERNAERTS, X. B. ZHANG et al., *Science* **1995**, 267, 1334–1337.
- 109 A. MAITI, C. T. BRABEC, J. BERNHOLC, *Phys. Rev. B* **1997**, 55, R6097–6100.
- 110 Y. MIYAMOTO, A. RUBIO, M. L. COHEN et al., *Phys. Rev. B* **1994**, 50, 4976–4979.
- 111 B. C. SATISHKUMAR, A. GOVINDARAJ, K. R. HARIKUMAR et al., *Chem. Phys. Lett.* **1999**, 300, 473–477.
- 112 O. STEPHAN, P. M. AJAYAN, C. COLLIEX et al., *Science* **1994**, 266, 1683–1685.
- 113 Y. ZHANG, H. GU, K. SUENAGA et al., *Chem. Phys. Lett.* **1997**, 279, 264–269.
- 114 M. TERRONES, A. M. BENITO, C. MANTEGA-DIEGO et al., *Chem. Phys. Lett.* **1996**, 257, 576–582.
- 115 (a) R. SEN, B. C. SATISHKUMAR, A. GOVINDARAJ et al., *Chem. Phys. Lett.* **1998**, 287, 671–676; (b) R. SEN, B. C. SATISHKUMAR, A. GOVINDARAJ et al., *J. Mater. Chem.* **1997**, 7, 2335–2337.
- 116 (a) M. NATH, B. C. SATISHKUMAR, A. GOVINDARAJ et al., *Chem. Phys. Lett.* **2000**, 322, 333–340; (b) S. L. SUNG, S. H. TSAI, C. H. TSENG et al., *Appl. Phys. Lett.* **1999**, 74, 197–199.
- 117 (a) K. SUENAGA, M. YUSADAKA, C. COLLIEX et al., *Chem. Phys. Lett.* **2000**, 316, 365–372; (b) K. SUENAGA, M. P. JOHANSSON, N. HELLGREN et al., *Chem. Phys. Lett.* **1999**, 300, 695–700.
- 118 D. GOLDBERG, Y. BANDO, W. HAN et al., *Chem. Phys. Lett.* **1999**, 308, 337–342.
- 119 D. L. CARROLL, Ph. REDLICH, X. BLASÉ et al., *Phys. Rev. Lett.* **1998**, 81, 2332–2335.
- 120 K. EFSARJANI, A. A. FARAJIN, Y. HASHI et al., *Appl. Phys. Lett.* **1999**, 74, 79–81.
- 121 R. D. ANTONOV, A. T. JOHNSON, *Phys. Rev. Lett.* **1999**, 83, 3274–3276.
- 122 P. M. AJAYAN, T. W. EBBESEN, T. ICHIHASHI et al., *Nature* **1993**, 362, 522–524.
- 123 S. C. TSANG, P. J. F. HARRIS, M. L. H. GREEN, *Nature* **1993**, 362, 520–522.
- 124 R. M. LAGO, S. C. TSANG, K. L. LU et al., *J. Chem. Soc., Chem. Commun.* **1995**, 1355–1356.
- 125 K. C. HWANG, *J. Chem. Soc., Chem. Commun.* **1995**, 173–174.
- 126 H. HIURA, T. W. EBBESEN, K. TANIGAKI, *Adv. Mater.* **1995**, 7, 275–277.
- 127 B. C. SATISHKUMAR, A. GOVINDARAJ, G. N. SUBBANNA et al., *J. Phys. B, Atm. Mol. Opt. Phys.* **1996**, 29, 4925–4936.
- 128 C. BOWER, S. SUZUKI, K. TANIGAKI et al., *Appl. Phys. A* **1998**, 67, 47–52.
- 129 A. GOVINDARAJ, B. C. SATISHKUMAR, M. NATH et al., *Chem. Mater.* **2000**, 12, 202–204.
- 130 W. K. HSU, W. Z. LI, Y. Q. ZHU et al., *Chem. Phys. Lett.* **2000**, 317, 77–82.
- 131 C. N. R. RAO, A. GOVINDARAJ, B. C. SATISHKUMAR, *Chem. Commun.* **1996**, 1525–1526.
- 132 J. SLOAN, J. HAMMER, M. ZWIEFKASIBLEY et al., *Chem. Commun.* **1998**, 347–348.
- 133 B. C. SATISHKUMAR, E. M. VOGL, A. GOVINDARAJ et al., *J. Phys. D, Appl. Phys.* **1996**, 29, 3173–3176.
- 134 J. CHEN, M. A. HAMON, H. HU et al., *Science* **1998**, 282, 95–98.
- 135 E. T. MICKELSON, I. W. CHIANG, J. L. ZIMMERMAN et al., *J. Phys. Chem. B* **1999**, 103, 4318–4322.
- 136 K. F. KELLY, I. W. CHIANG, E. T. MICKELSON et al., *Chem. Phys. Lett.* **1999**, 313, 445–450.
- 137 P. J. BOUL, J. LIU, E. T. MICKELSON et al., *Chem. Phys. Lett.* **1999**, 310, 367–372.
- 138 J. LIU, M. J. CASAVANT, M. COX et al., *Chem. Phys. Lett.* **1999**, 303, 125–129.
- 139 J. W. MINTMIRE, B. I. DUNLAP, C. T. WHITE, *Phys. Rev. Lett.* **1992**, 68, 631–634.
- 140 N. HAMADA, S. SAWADA, A. YOSHIYAMA, *Phys. Rev. Lett.* **1992**, 68, 1579–1581.
- 141 R. SAITO, M. FUJITA, G. DRESSELHAUS et al., *Appl. Phys. Lett.* **1992**, 60, 2204–2206.
- 142 J. W. G. WILDOER, L. C. VENEMA, A. G. RINZLER et al., *Nature* **1998**, 391, 59–62.
- 143 T. W. ODOM, J. L. HUANG, P. KIM et al., *Nature* **1998**, 391, 62–64.
- 144 P. G. COLLINS, A. ZETTL, H. BANDO et al., *Science* **1997**, 278, 100–103.
- 145 W. LIANG, M. BOCKRATH, D. BOZOVIC et al., *Nature* **2001**, 411, 665–669.

- 146 S. FRANK, P. PONCHARAL, Z. L. WANG et al., *Science* **1998**, 280, 1744–1746.
- 147 P. KIM, L. SHI, A. MAJUMDAR et al., *Phys. Rev. Lett.* **2001**, 87, 215502–215502-4.
- 148 M. KOCIK, A. YU. KASUMOV, S. GUÉRON et al., *Phys. Rev. Lett.* **2001**, 86, 2416–2419.
- 149 Z. K. TANG, L. ZHANG, N. WANG et al., *Science* **2001**, 292, 2462–2465.
- 150 K. H. AN, W. S. KIM, Y. S. PARK et al., *Adv. Funct. Mater.* **2001**, 11, 387–392.
- 151 C. NIU, E. K. SICKEL, R. HOCH et al., *Appl. Phys. Lett.* **1997**, 70, 1480–1482.
- 152 C. NIU, J. KUPPERSCHMIDT, R. HOCK, in *Proceedings of the 39th Power Sources Conference* (Maple Hill, NJ, 2000), pp. 314–317.
- 153 R. H. BAUGHMAN, C. CUI, A. A. ZAKIDOV et al., *Science* **1999**, 284, 1340–1344.
- 154 B. GAO, A. KLEINHAMMES, X. P. TANG et al., *Chem. Phys. Lett.* **1999**, 307, 153–157.
- 155 F. SALVER-DISMA, C. LENAIN, B. BEAUDOIN et al., *Solid State Ionics* **1997**, 98, 145–158.
- 156 Y. ZHANG, T. ICHIHASHI, E. LANDREE et al., *Science* **1999**, 285, 1719–1722.
- 157 Z. YAO, H. W. CH. POSTMA, L. BALENTS et al., *Nature* **1999**, 402, 273–276.
- 158 J. HU, M. OUYANG, P. YANG, C. M. LIEBER, *Nature* **1999**, 399, 48–51.
- 159 Z. YAO, C. L. KANE, C. DEKKER, *Phys. Rev. Lett.* **2000**, 84, 2941–2944.
- 160 Z. YAO, C. DEKKER, Ph. AVOURIS, *Top. Appl. Phys.* **2001**, 80, 147–171.
- 161 S. J. TANS, A. R. M. VERSCHUEREN, C. DEKKER, *Nature* **1998**, 393, 49–52.
- 162 R. MARTEL, T. SCHMIDT, H. R. SHEA et al., *Appl. Phys. Lett.* **1998**, 73, 2447–2449.
- 163 A. BACHTOLD, P. HADLEY, T. NAKANISHI et al., *Science* **2001**, 294, 1317–1320.
- 164 P. G. COLLINS, M. S. ARNOLD, Ph. AVOURIS, *Science* **2001**, 292, 706–709.
- 165 M. S. FUHRER, J. NYGARD, L. SHIH et al., *Science* **2000**, 288, 494–497.
- 166 T. RUECKES, K. KIM, E. JOSELUICH et al., *Science* **2000**, 289, 94–97.
- 167 (a) L. CHICO, V. H. CRESPI, L. X. BENEDICT et al., *Phys. Rev. Lett.* **1996**, 76, 971–974; (b) L. KOUWENHOVEN, *Science* **1997**, 275, 1896–1897; (c) P. L. MCEUEN, *Nature (London)* **1998**, 393, 15–17.
- 168 M. MENON, D. SRIVASTAVA, *Phys. Rev. Lett.* **1997**, 79, 4453–4455.
- 169 M. MENON, D. SRIVASTAVA, *J. Mater. Res.* **1998**, 13, 2357–2360.
- 170 J.-C. CHARLIER, *Acc. Chem. Res.* (Special issue) **2002**, 35, 1063–1069.
- 171 J. LI, C. PAPADOPOULOS, J. XU, *Nature (London)* **1999**, 402, 254–255.
- 172 B. C. SATISHKUMAR, P. J. THOMAS, A. GOVINDARAJ et al., *Appl. Phys. Lett.* **2000**, 77, 2530–2532.
- 173 N. R. FRANKLIN, Y. LI, R. J. CHEN et al., *Appl. Phys. Lett.* **2001**, 79, 4571–4573.
- 174 “At IBM, a tinier transistor outperforms its silicon cousins,” *New York Times*, 20 May 2002, p. C4.
- 175 P. G. COLLINS, K. BRADLEY, M. ISHIGAMI et al., *Science* **2000**, 287, 1801–1804.
- 176 (a) J. KONG, N. R. FRANKLIN, C. ZHOU et al., *Science* **2000**, 287, 622–625; (b) S. GHOSH, A. K. SOOD, N. KUMAR, *Science* **2003**, 299, 1042–1044.
- 177 H. NISHIJIMA, S. AKITA, Y. NAKAYAMA, *Jpn. J. Appl. Phys.* **1999**, 38, 7247–7252.
- 178 J. H. HAFNER, C. L. CHEUNG, C. M. LEIBER, *Nature* **1999**, 398, 761–762.
- 179 H. DAI, J. H. HAFNER, A. G. RINZLER et al., *Nature* **1996**, 384, 147–150.
- 180 S. S. WONG, E. JOSELEVICH, A. T. WOOLLEY et al., *Nature* **1998**, 394, 52–55.
- 181 P. KIM, C. L. LIEBER, *Science* **1999**, 286, 2148–2150.
- 182 T. ARIE, H. NISHIJIMA, S. AKITA et al., *J. Vac. Sci. Technol. B* **2000**, 18, 104–106.
- 183 P. KARL, D. TOMANEK, *Phys. Rev. Lett.* **1999**, 82, 5373–5376.
- 184 E. B. COOPER, S. R. MANALIS, H. FANG et al., *Appl. Phys. Lett.* **1999**, 75, 3566–3568.
- 185 W. A. DE HEER, A. CHATELAIN, D. UGARTE, *Science* **1995**, 270, 1179–1180.
- 186 A. G. RINZLER, J. H. HAFNER, P. NIKOLAEV et al., *Science* **1995**, 269, 1550–1553.
- 187 N. S. LEE, D. S. CHUNG, I. T. HAN et

- al., *Diamond Relat. Mater.* **2001**, *10*, 265–270.
- 188 Y. SAITO, S. UEMURA, *Carbon* **2000**, *38*, 169–182.
  - 189 R. ROSEN, W. W. SIMENDINGER, C. DEBBAULT et al., *Appl. Phys. Lett.* **2000**, *76*, 1668–1670.
  - 190 H. SUGIE, M. TANEMURA, V. FILIP et al., *Appl. Phys. Lett.* **2001**, *78*, 2578–2580.
  - 191 J.-M. BONARD, T. STÖCKLI, F. MAIER et al., *Phys. Rev. Lett.* **1998**, *81*, 1441–1444.
  - 192 J.-L. KWO, C. C. TSOU, M. YOKOYAMA et al., *J. Vac. Sci. Technol. B* **2001**, *19*, 23–26.
  - 193 W. ZHU, C. BOWER, O. ZHOU et al., *Appl. Phys. Lett.* **1999**, *75*, 873–875.
  - 194 Y. SAITO, K. HAMAGUCHI, S. UEMURA et al., *Appl. Phys. A* **1998**, *67*, 95–100.
  - 195 (a) W. B. CHOI, D. S. CHUNG, J. H. KANG et al., *Appl. Phys. Lett.* **1999**, *75*, 3129–3130; (b) C. J. LEE, J. PARK, S. Y. KANG et al., *Chem. Phys. Lett.* **2000**, *326*, 175–180.
  - 196 D. LOVALL, M. BUSS, E. GRAUGNARD et al., *Phys. Rev. B* **2000**, *61*, 5683–5691.
  - 197 O. GRONING, O. M. KUTTEL, Ch. EMMENEGGER et al., *J. Vac. Sci. Technol. B* **2000**, *18*, 665–678.
  - 198 R. B. SHARMA, V. N. TONDARE, D. S. JOAG et al., *Chem. Phys. Lett.* **2001**, *344*, 283–286.
  - 199 S. R. MISHRA, H. S. RAWAT, S. C. MEHENDALE et al., *Chem. Phys. Lett.* **2000**, *317*, 510–514.
  - 200 K. YOSHINO, H. KAJII, H. ARAKI, *Fullerene Sci. Technol.* **1999**, *7*, 695–711.
  - 201 J. R. WOOD, H. D. WAGNER, *Appl. Phys. Lett.* **2000**, *76*, 2883–2885.
  - 202 M. ESWARAMOORTHY, R. SEN, C. N. R. RAO, *Chem. Phys. Lett.* **1999**, *304*, 207–210.
  - 203 M. S. DRESSSELHAUS, K. A. WILLIAMS, P. C. EKLUND, *MRS Bull.* **2000**, *24*, 45–50.
  - 204 G. G. TIBBETTS, G. P. MEISNER, C. H. OLK, *Carbon* **2001**, *39*, 2291–2301.
  - 205 M. HIRSCHER, M. BECHER, M. HALUSKA et al., *J. Alloys Compd.* **2002**, *330–332*, 654–658.
  - 206 C. ZANDONELLA, *Nature* **2001**, *410*, 734–735.
  - 207 Y. YE, C. C. AHN, C. WITHAM et al., *Appl. Phys. Lett.* **1999**, *74*, 2307–2309.
  - 208 A. C. DILLON, K. M. JONES, T. A. BEKKEDAHLE et al., *Nature* **1997**, *386*, 377–379.
  - 209 C. LIU, Y. Y. FAN, M. LIU et al., *Science* **1999**, *286*, 1127–1129.
  - 210 G. GUNDIAH, A. GOVINDARAJ, N. RAJALAKSHMI et al., *J. Mater. Chem.* **2003**, *13*, 209–213.
  - 211 (a) P. RATNASAMY, L. RODRIGUES, A. J. LEONARD, *J. Phys. Chem.* **1973**, *77*, 2242–2245; (b) J. A. WILSON, A. D. YOFFE, *Adv. Phys.* **1969**, *269*, 193–335.
  - 212 R. R. CHIANELLI, E. PRESTRIDGE, T. PECORANO et al., *Science* **1979**, *203*, 1105–1107.
  - 213 (a) R. TENNE, L. MARGULIS, M. GENUT et al., *Nature* **1992**, *360*, 444–446; (b) L. MARGULIS, G. SALITRA, R. TENNE et al., *Nature* **1993**, *365*, 113–114; (c) Y. FELDMAN, E. WASSERMAN, D. J. SROLOVITCH et al., *Science* **1995**, *267*, 222–225.
  - 214 K. J. C. VAN BOMMEL, A. FRIGGERI, S. SHINKAI, *Angew. Chem. Int. Ed. Engl.* **2003**, *42*, 980–999.
  - 215 (a) C. T. KRESGE, M. E. LEONOWICZ, W. J. ROTH et al., *Nature* **1992**, *259*, 710–712; (b) J. S. BECK, J. C. VARTULLI, W. J. ROTH et al., *J. Am. Chem. Soc.* **1992**, *114*, 10834–10843.
  - 216 (a) W. STÖBER, A. FINK, E. BOHN, *J. Colloid Interface Sci.* **1968**, *26*, 62–69; (b) M. NAKAMURA, Y. MATSUI, *J. Am. Chem. Soc.* **1995**, *117*, 2651–2652.
  - 217 P. M. AJAYAN, O. STEPHANE, Ph. REDLICH et al., *Nature* **1995**, *375*, 564–567.
  - 218 (a) B. C. SATISHKUMAR, A. GOVINDARAJ, E. M. VOGL et al., *J. Mater. Res.* **1997**, *12*, 604–606; (b) B. C. SATISHKUMAR, A. GOVINDARAJ, M. NATH et al., *J. Mater. Chem.* **2000**, *10*, 2115–2219.
  - 219 M. E. SPAHR, P. BITTERLI, R. NESPER et al., *Angew. Chem. Int. Ed. Engl.* **1998**, *37*, 1263–1265 (*Angew. Chem.* **1998**, *110*, 1339).
  - 220 L. PU, X. BAO, J. ZOU et al., *Angew. Chem. Int. Ed. Engl.* **2001**, *40*, 1490–1493.
  - 221 (a) M. L. COHEN, *Solid State Commun.* **1994**, *92*, 45–52; (b) A. RUBIO, J. L.

- CORKILL, M. L. COHEN, *Phys. Rev. B* **1994**, 49, 5081–5084; (c) Y. MIYAMOTO, A. RUBIO, S. G. LOUIE et al., *Phys. Rev. B* **1994**, 50, 18360–18366.
- 222 (a) K. KOBAYASHI, N. KURITA, *Phys. Rev. Lett.* **1993**, 70, 3542–3544; (b) Z. W. SIEH, K. CHERREY, N. G. CHOPRA et al., *Phys. Rev. B* **1994**, 51, 11229–11232.
- 223 P. GLEIZE, M. C. SCHOULER, P. GADELLE et al., *J. Mater. Sci.* **1994**, 29, 1575–1580.
- 224 (a) O. R. LOURIE, C. R. JONES, B. M. BERTLETT et al., *Chem. Mater.* **2000**, 12, 1808–1810; (b) R. MA, Y. BANDO, T. SATO, *Chem. Phys. Lett.* **2001**, 337, 61–64.
- 225 F. L. DEEPAK, C. P. VINOD, K. MUKHOPADHYAY et al., *Chem. Phys. Lett.* **2002**, 353, 345–352.
- 226 (a) Y. R. HACOEN, E. GRUNBAUM, R. TENNE et al., *Nature* **1998**, 395, 336–337; (a) J. GOLDBERGER, R. HE, Y. ZHANG et al., *Nature* **2003**, 422, 599–602.
- 227 (a) J. BAO, C. TIE, Z. XU et al., *Adv. Mater.* **2001**, 13, 1631–1633; (b) B. MAYERS, Y. XIA, *Adv. Mater.* **2002**, 14, 279–282.
- 228 J. C. HULTEEN, C. R. MARTIN, *J. Mater. Chem.* **1997**, 7, 1075–1087.
- 229 R. TENNE, M. HOMYONFER, Y. FELDMAN, *Chem. Mater.* **1998**, 10, 3225–3238 and references therein.
- 230 (a) M. HERSHFINKEL, L. A. GHEBER, V. VOLTERRA et al., *J. Am. Chem. Soc.* **1994**, 116, 1914–1917; (b) T. TSIRLINA, Y. FELDMAN, M. HOMYONFER et al., *Fullerene Sci. Technol.* **1998**, 6, 157–165.
- 231 M. NATH, A. GOVINDARAJ, C. N. R. RAO, *Adv. Mater.* **2001**, 13, 283–286.
- 232 M. NATH, C. N. R. RAO, *Chem. Commun.* **2001**, 2236–2237.
- 233 M. NATH, C. N. R. RAO, *J. Am. Chem. Soc.* **2001**, 123, 4841–4842.
- 234 M. NATH, C. N. R. RAO, *Angew. Chem. Int. Ed. Engl.* **2002**, 41, 3451–3454.
- 235 A. P. LIN, C. Y. MOU, S. D. LIU, *Adv. Mater.* **2000**, 12, 103–106.
- 236 J. ZHANG, L. SUN, C. LIAO et al., *Chem. Commun.* **2002**, 262–263.
- 237 M. NIEDERBERGER, H.-J. MUHR, F. KRUMEICH et al., *Chem. Mater.* **2000**, 12, 1995–2000.
- 238 C. N. R. RAO, A. GOVINDARAJ, F. L. DEEPAK et al., *Appl. Phys. Lett.* **2001**, 78, 1853–1855.
- 239 T. KASUGA, M. HIRAMATSU, A. HASON et al., *Langmuir* **1998**, 14, 3160–3163.
- 240 C. N. R. RAO, B. C. SATISHKUMAR, A. GOVINDARAJ, *Chem. Commun.* **1997**, 1581–1582.
- 241 C. M. ZELENSKI, P. K. DORHOUT, *J. Am. Chem. Soc.* **1998**, 120, 734–742.
- 242 A. LOISEAU, F. WILLIAME, N. DEMONECY et al., *Phys. Rev. Lett.* **1996**, 76, 4737–4740.
- 243 P. TERECH, R. G. WEISS, *Chem. Rev.* **1997**, 97, 3133–3159.
- 244 Y. ONO, K. NAKASHIMA, M. SANO et al., *Chem. Commun.* **1998**, 1477–1478.
- 245 T. KASUGA, M. HIRAMATSU, A. HOSON et al., *Adv. Mater.* **1999**, 11, 1307–1311.
- 246 A. GOVINDARAJ, F. L. DEEPAK, N. A. GUNARI et al., *Israel J. Chem.* **2001**, 41, 23–30.
- 247 P. V. TEREDESAL, F. L. DEEPAK, A. GOVINDARAJ et al., *J. Nanosci. Nanotechnol.* **2002**, 2, 495–498.
- 248 F. KRUMEICH, H.-J. MUHR, M. NIEDERBERGER et al., *J. Am. Chem. Soc.* **1999**, 121, 8324–8331.
- 249 H.-J. MUHR, F. KRUMEICH, U. P. SCHÖNHOLZER et al., *Adv. Mater.* **2000**, 12, 231–234.
- 250 G. SEIFERT, H. TERRONES, M. TERRONES et al., *Phys. Rev. Lett.* **2000**, 85, 146–149.
- 251 (a) G. SEIFERT, H. TERRONES, M. TERRONES et al., *Solid State Commun.* **2000**, 114, 245–248; (b) G. SEIFERT, H. TERRONES, M. TERRONES et al., *Solid State Commun.* **2000**, 115, 635–638.
- 252 M. NATH, S. KAR, A. K. RAYCHAUDHURI et al., *Chem. Phys. Lett.* **2003**, 368, 690–695.
- 253 (a) H. M. CHENG, Q. H. YANG, C. LIU, *Carbon* **2001**, 39, 1447–1454; (b) P. HOU, Q. YANG, S. BAI et al., *J. Phys. Chem. B* **2002**, 106, 963–966 and references therein.
- 254 R. MA, Y. BANDO, H. ZHU et al., *J. Am. Chem. Soc.* **2002**, 124, 7672–7673.
- 255 J. CHEN, N. KURIYAMA, H. YUAN et al., *J. Am. Chem. Soc.* **2001**, 123, 11813–11814.
- 256 M. E. SPAHR, P. S. BITTERLI, R.

- NESPER et al., *J. Electrochem. Soc.* **1999**, 146, 2780–2783.
- 257 A. DOBLEY, K. NGALA, S. YANG et al., *Chem. Mater.* **2001**, 13, 4382–4386.
- 258 A. ROTHSCHILD, S. R. COHEN, R. TENNE, *Appl. Phys. Lett.* **1999**, 75, 4025–4027.
- 259 L. RAPOPORT, Y. BILIK, Y. FELDMAN et al., *Nature* **1997**, 387, 791–793.
- 260 J. CHEN, S.-L. LI, Q. XU et al., *Chem. Commun.* **2002**, 1722–1723.
- 261 M. CÔTÉ, M. L. COHEN, D. J. CHADI, *Phys. Rev. B* **1998**, 58, R4277–R4280.
- 262 F. CERRINA, C. MARRIAN, *MRS Bull.* **1996**, 21 (December), 56.
- 263 (a) J. M. GIBSON, *Phys. Today* **1997**, October, 56–61; (b) S. MATSUI, Y. OCHIAI, *Nanotechnology* **1996**, 7, 247–258.
- 264 (a) S. H. HONG, J. ZHU, C. A. MIRKIN, *Science* **1999**, 286, 523–525; (b) J. A. DAGATA, *Science* **1995**, 270, 1625 (see reference therein).
- 265 (a) M. D. LEVENSON, P. J. SILVERMAN, R. GEORGE et al., *Solid State Technol.* **1995**, 38, 81–82, 84, 86, 88, 90, 92, 94, 96, 98; (b) P. N. DUNN, *Solid State Technol.* **1994**, 37, 49–50, 52, 58, 61–62.
- 266 Y. XIA, J. A. ROGERS, K. E. PAUL et al., *Chem. Rev.* **1999**, 99, 1823–1848.
- 267 D. ROUTKEVITCH, A. A. TAGER, J. HARUYAMA et al., *IEEE Trans. Electron Devices* **1996**, 43, 1646–1657.
- 268 P. YANG, Y. WU, R. FAN, *Int. J. Nanosci.* **2002**, 1, 1–39.
- 269 Y. XIA, P. YANG, Y. SUN et al., *Adv. Mater.* **2003**, 15, 353–389.
- 270 E. I. GIVARGIZOV, *Highly Anisotropic Crystals*, eds. M. SENECHAL, S. COLLEGE, Reidel, Dordrecht, The Netherlands 1987.
- 271 Y. WU AND P. YANG, *Chem. Mater.* **2000**, 12, 605–607.
- 272 M. H. HUANG, Y. WU, H. FEICK et al., *Adv. Mater.* **2001**, 13, 113–116.
- 273 A. M. MORALES, C. M. LIEBER, *Science* **1998**, 279, 208–211.
- 274 (a) C. R. MARTIN, *Science* **1994**, 266, 1961–1966; (b) D. ALMAWLAWI, C. Z. LIU, M. MOSKOVITS, *J. Mater. Res.* **1994**, 9, 1014–1018.
- 275 W. HAN, S. FAN, W. LI et al., *Science* **1997**, 277, 1287–1289.
- 276 T. J. TRENTLER, K. M. HICKMAN, S. C. GEOL et al., *Science* **1995**, 270, 1791–1794.
- 277 X. F. DUAN, C. M. LIEBER, *Adv. Mater.* **2000**, 12, 298–302.
- 278 R. S. WAGNER, in *Whisker Technology*, ed. A. P. LEVITT, Wiley-Interscience, New York 1970, 47–119.
- 279 Y. WU, P. YANG, *J. Am. Chem. Soc.* **2001**, 123, 3165–3166.
- 280 M. S. GUDIKSEN, C. M. LIEBER, *J. Am. Chem. Soc.* **2000**, 122, 8801–8802.
- 281 C. C. CHEN, C. C. YEH, C. H. CHEN et al., *J. Am. Chem. Soc.* **2001**, 123, 2791–2798.
- 282 X. F. DUAN, C. M. LIEBER, *J. Am. Chem. Soc.* **2000**, 122, 188–189.
- 283 W.-S. SHI, H.-Y. PENG, Y.-F. ZHENG et al., *Adv. Mater.* **2000**, 12, 1343–1345.
- 284 C. C. TANG, S. FAN, M. L. DE LA CHAPELLE et al., *Adv. Mater.* **2000**, 12, 1346–1348.
- 285 G. GU, M. BURGHARD, G. T. KIM, G. S. DUSBERG et al., *J. Appl. Phys.* **2001**, 90, 5747–5751.
- 286 Z. W. PAN, H. L. LAI, F. C. K. AU et al., *Adv. Mater.* **2000**, 12, 1186–1190.
- 287 Y. WU, B. MESSER, P. YANG, *Adv. Mater.* **2001**, 13, 1487–1489.
- 288 M. YAZAWA, M. KOGUCHI, A. MUTO et al., *Adv. Mater.* **1993**, 5, 577–580.
- 289 J. LIU, X. ZHANG, Y. J. ZHANG et al., *J. Mater. Res.* **2001**, 16, 3133–3138.
- 290 K. HIRUMA, M. YAZAWA, T. KATSUYAMA et al., *J. Appl. Phys.* **1995**, 77, 447–462.
- 291 T. SHIMADA, K. HIRUMA, M. SHIRAI et al., *Superlattices Microstruct.* **1998**, 24, 453–458.
- 292 X. F. DUAN, J. F. WANG, C. M. LIEBER, *Appl. Phys. Lett.* **2000**, 76, 1116–1118.
- 293 (a) S. T. LEE, N. WANG, C. S. LEE, *Mater. Sci. Eng. A* **2000**, 286, 16–23; (b) N. WANG, Y. H. TANG, Y. F. ZHANG et al., *Chem. Phys. Lett.* **1999**, 299, 237–242; (c) H. W. SEO, S. Y. BAE, J. PARK et al., *Chem. Commun.* **2002**, 2564–2565; (d) Y. F. ZHANG, Y. H. TANG, C. LAM et al., *J. Cryst. Growth* **2000**, 212, 115–118.
- 294 (a) S. T. LEE, N. WANG, Y. F. ZHANG et al., *MRS Bull.* **1999**, 24, 36–42; (b) D. D. MA, C. S. LEE, F. C. K. AU et al., *Science* **2003**, 299, 1874–1877.

- 295 (a) N. WANG, Y. F. ZHANG, Y. H. TANG et al., *Appl. Phys. Lett.* **1998**, 73, 3902–3904; (b) W.-S. SHI, H.-Y. PENG, N. WANG et al., *J. Am. Chem. Soc.* **2001**, 123, 11095–11096.
- 296 Z. L. WANG, R. P. GAO, Z. W. PAN et al., *Adv. Eng. Mater.* **2001**, 3, 657–661.
- 297 Z. W. PAN, Z. R. DAI, Z. L. WANG, *Science* **2001**, 291, 1947–1949.
- 298 Z. R. DAI, Z. W. PAN, Z. L. WANG, *Solid State Commun.* **2001**, 118, 351–354.
- 299 (a) P. YANG, C. M. LIEBER, *J. Mater. Res.* **1997**, 12, 2981–2996; (b) P. YANG, C. M. LIEBER, US Pat., 5897945, 1999.
- 300 P. YANG, C. M. LIEBER, *Science* **1996**, 273, 1836–1840.
- 301 G. GUNDIAH, G. V. MADHAV, A. GOVINDARAJ et al., *J. Mater. Chem.* **2002**, 12, 1606–1611.
- 302 (a) G. GUNDIAH, A. GOVINDARAJ, C. N. R. RAO, *Chem. Phys. Lett.* **2002**, 351, 189–194; (b) F. L. DEEPAK, A. GOVINDARAJ, C. N. R. RAO, *J. Nanosci. Nanotechnol.* **2001**, 1, 303–308.
- 303 (a) Y. CHEN, D. A. A. OHLBERG, R. S. WILLIAMS, *Mater. Sci. Eng. B* **2001**, 87, 222–226; (b) Y. CHEN, D. A. A. OHLBERG, G. MEDEIROS-RIBEIRO et al., *Appl. Phys. Lett.* **2000**, 76, 4004–4006.
- 304 L. J. LAUHON, M. S. GUDIKSEN, D. WANG et al., *Nature* **2002**, 420, 57–59.
- 305 (a) J. STEJNY, R. W. TRINDER, J. DLUGOSZ, *J. Mater. Sci.* **1981**, 16, 3161–3170; (b) J. STEJNY, J. DLUGOSZ, A. KELLER, *J. Mater. Sci.* **1979**, 14, 1291–1300; (c) A. K. CHEETHAM, P. DAY, *Solid State Chemistry (Compounds)*, Clarendon Press, Oxford 1992, p. 31; (d) *Extended Linear Chain Compounds*, ed. J. S. MILLER, Plenum Press, New York 1982; (e) *Chemistry and Physics of One-Dimensional Metals*, ed. H. J. KELLER, Plenum Press, New York 1977.
- 306 (a) H. R. VAN KRUYT, A. E. VAN ARKEL, *Kolloid-Z.* **1923**, 32, 29–36; (b) A. GUTBIER, *Z. Anorg. Chem.* **1902**, 32, 106–107.
- 307 (a) B. GATES, Y. YIN, Y. XIA, *J. Am. Chem. Soc.* **2000**, 122, 12582–12583; (b) B. GATES, B. MAYERS, B. CATTLE et al., *Adv. Funct. Mater.* **2002**, 12, 219–227.
- 308 B. MAYERS, Y. XIA, *J. Mater. Chem.* **2002**, 12, 1875–1881.
- 309 (a) B. MESSER, J. H. SONG, M. HUANG et al., *Adv. Mater.* **2000**, 12, 1526–1528; (b) J. SONG, B. MESSER, Y. WU et al., *J. Am. Chem. Soc.* **2001**, 123, 9714–9715; (c) C. WANG, K. TANG, Q. YANG et al., *Inorg. Chem. Commun.* **2001**, 4, 339–341; (d) E. I. GERZANICH, V. A. LYAKHOVITSKAYA, V. M. FRIDKIN et al., *Curr. Top. Mater. Sci.* **1982**, 10, 55–190; (e) J. S. MILLER, A. J. EPSTEIN, *Prog. Inorg. Chem.* **1976**, 20, 1–151.
- 310 (a) HUCZKO, *Appl. Phys. A: Mater. Sci. Process.* **2000**, 70, 365–376; (b) M. ZHENG, L. ZHANG, X. ZHANG et al., *Chem. Phys. Lett.* **2001**, 334, 298–302.
- 311 C. G. WU, T. BEIN, *Science* **1994**, 266, 1013–1014.
- 312 M. H. HUANG, A. CHOUDREY, P. YANG, *Chem. Commun.* **2000**, 1063–1064.
- 313 R. ULRICH, A. DU CHESNE, M. TEMPLIN et al., *Adv. Mater.* **1999**, 11, 141–146.
- 314 Z. LIU, Y. SAKAMOTO, T. OHSUNA et al., *Angew. Chem. Int. Ed. Engl.* **2000**, 39, 3107–3110.
- 315 (a) R. LEON, D. MARGOLESE, G. STUCKY et al., *Phys. Rev. B* **1995**, 52, R2285–R2288; (b) N. R. B. COLEMAN, K. M. RYAN, T. R. SPALDING et al., *Chem. Phys. Lett.* **2001**, 343, 1–6; (c) H. RINGSDORF, B. SCHLARB, J. VENZMER, *Angew. Chem. Int. Ed. Engl.* **1988**, 27, 113–158.
- 316 Y. YIN, Y. LU, Y. SUN et al., *Nano Lett.* **2002**, 2, 427–430.
- 317 (a) B. GATES, Y. WU, Y. YIN et al., *J. Am. Chem. Soc.* **2001**, 123, 11500–11501; (b) B. GATES, B. MAYERS, Y. WU et al., *Adv. Funct. Mater.* **2002**, 12, 679–686.
- 318 Y. ZHANG, K. SUENAGA, C. COLLIEX et al., *Science* **1998**, 281, 973–975.
- 319 N. DEMONCY, O. STEPHAN, N. BRUN et al., *Eur. Phys. J. B* **1998**, 4, 147–157.
- 320 W. K. HSU, S. TRASOBARES, H. TERRONES et al., *Chem. Mater.* **1999**, 11, 1747–1751.
- 321 J. SLOAN, D. M. WRIGHT, H. G. WOO et al., *Chem. Commun.* **1999**, 699–700.



- 322 S. LINK, M. B. MOHAMMED, M. A. EL-SAYED, *J. Phys. Chem. B* **1999**, 103, 3073–3077.
- 323 C. H. KIANG, J. S. CHOI, T. T. TRAN et al., *J. Phys. Chem. B* **1999**, 103, 7449–7451.
- 324 B. K. PRADHAN, T. KYOTANI, A. TOMITA, *Chem. Commun.* **1999**, 1317–1318.
- 325 W. K. HSU, W. Z. LI, Y. Q. ZHU et al., *Chem. Phys. Lett.* **2000**, 317, 77–82.
- 326 S. D. DINGMAN, N. P. RATH, P. D. MARKOWITZ et al., *Angew. Chem. Int. Ed. Engl.* **2000**, 39, 1470–1472.
- 327 (a) T. J. TRENTLER, S. C. GOEL, K. M. HICKMAN et al., *J. Am. Chem. Soc.* **1997**, 119, 2172–2181; (b) P. D. MARKOWITZ, M. P. ZACH, P. C. GIBBONS et al., *J. Am. Chem. Soc.* **2001**, 123, 4502–4511; (c) O. R. LOURIE, C. R. JONES, B. M. BARTLETT et al., *Chem. Mater.* **2000**, 12, 1808–1810.
- 328 (a) J. D. HOLMES, K. P. JOHNSTON, R. C. DOTY et al., *Science* **2000**, 287, 1471–1473; (b) T. HENRATH, B. A. KORGEL, *Adv. Mater.* **2003**, 15, 437–440.
- 329 L. MANNA, E. C. SCHER, A. P. ALIVISATOS, *J. Am. Chem. Soc.* **2000**, 122, 12700–12706.
- 330 (a) C. CHAO, C. CHEN, Z. LANG, *Chem. Mater.* **2000**, 12, 1516–1518; (b) Y. SUN, B. GATES, B. MAYERS et al., *Nano Lett.* **2002**, 2, 165–168; (c) Y. SUN, Y. XIA, *Adv. Mater.* **2002**, 14, 833–837; (d) Y. SUN, Y. YIN, B. T. MAY et al., *Chem. Mater.* **2002**, 14, 4736–4745.
- 331 Y. F. LIU, J. H. ZENG, W. X. ZHANG et al., *J. Mater. Res.* **2001**, 16, 3361–3365.
- 332 X. JIANG, Y. XIE, J. LU et al., *Chem. Mater.* **2001**, 13, 1213–1218.
- 333 Y. WU, H. YAN, M. HUANG et al., *Chem. Euro. J.* **2002**, 8, 1260–1268.
- 334 Y. WU, H. YAN, P. YANG, *Top. Catal.* **2002**, 19, 197–202.
- 335 M. HUANG, S. MAO, H. FEICK et al., *Science* **2001**, 292, 1897–1899.
- 336 C. L. CHEUNG, J. H. HAFNER, T. W. ODOM et al., *Appl. Phys. Lett.* **2000**, 76, 3136–3138.
- 337 B. MESSER, J. H. SONG, P. YANG, *J. Am. Chem. Soc.* **2000**, 122, 10232–10233.
- 338 Y. HUANG, X. DUAN, Q. Q. WEI et al., *Science* **2001**, 291, 630–633.
- 339 X. DUAN, Y. HUANG, Y. CUI et al., *Nature* **2001**, 409, 66–69.
- 340 F. KIM, S. KWAN, J. ARKANA et al., *J. Am. Chem. Soc.* **2001**, 123, 4360–4361.
- 341 L. BRUS, *J. Phys. Chem.* **1994**, 98, 3575–3581.
- 342 J. F. WANG, M. S. GUDIKSEN, X. F. DUAN et al., *Science* **2001**, 293, 1455–1457.
- 343 J. C. JOHNSON, H. YAN, R. D. SCHALLER et al., *J. Phys. Chem. B* **2001**, 105, 11387–11390.
- 344 S. W. CHUNG, J. Y. YU, J. R. HEATH, *Appl. Phys. Lett.* **2000**, 76, 2068–2070.
- 345 Y. CUI, C. M. LIEBER, *Science* **2001**, 291, 851–853.
- 346 Y. HUANG, X. DUAN, Y. CUI et al., *Science* **2001**, 294, 1313–1317.
- 347 J. Y. YU, S. W. CHUNG, J. R. HEATH, *J. Phys. Chem. B* **2000**, 104, 11864–11870.
- 348 Y. CUI, X. F. DUAN, J. T. HU et al., *J. Phys. Chem. B* **2000**, 104, 5213–5216.
- 349 X. T. ZHOU, H. L. LAI, H. Y. PENG et al., *Chem. Phys. Lett.* **2000**, 318, 58–62.

## 9

## Synthesis, Assembly and Reactivity of Metallic Nanorods

*C. J. Murphy, N. R. Jana, L. A. Gearheart, S. O. Obare, K. K. Caswell, S. Mann, C. J. Johnson, S. A. Davis, E. Dujardin, and K. J. Edler*

## 9.1

### Introduction

Metal particles with dimensions on the nanometer scale are of great current interest for their unusual properties [1–3]. Fundamentally, the mean free path of an electron in a metal at room temperature is  $\sim 10\text{--}100$  nm, and one would predict that as the metallic particle shrinks to this dimension, unusual effects might be observed [3]. Indeed, gold nanoparticles of diameter  $\sim 100$  nm or less appear red (not gold) when suspended in transparent media [1–3]; and gold nanoparticles of diameter  $\sim 3$  nm are no longer “noble” and unreactive, but can catalyze chemical reactions [4].

The optical properties of silver and gold nanoparticles in the visible region of the spectrum, specifically, absorption and scattering, are exquisitely sensitive to nanoparticle size, shape, aggregation state, and local environment [2, 5–10]. Additionally, molecules adsorbed to the surface of gold and silver nanoparticles undergo surface-enhanced Raman scattering (SERS) effects, due to the coupling of the plasmon band of the irradiated metal (i.e., the collective oscillation of the conduction band electrons upon absorption in the visible for these particular metals, due to their dielectric constant) with the molecules’ electronic states [11, 12]. Thus, one emerging application of metallic nanoparticles is optical sensors, and single-molecule detection via SERS has been reported [8, 9, 11–19].

The aspect ratio of a solid is defined as its length divided by its width; therefore, spheres have an aspect ratio of 1. We define, somewhat arbitrarily, a “nanorod” to be an object with an aspect ratio between 1 and 20, with the short dimension on the  $10\text{--}100$  nm scale, and a “nanowire” to be an object with an aspect ratio greater than 20 (with the short dimension on the  $10\text{--}100$  nm scale) [20]. The extinction spectra (the combination of visible absorption and scattering) of silver and gold nanoparticles are tunable throughout the visible, depending on the aspect ratio [5–10; Figure 9.1].

For nanorods and nanowires, the plasmon band of the metal is split in two: the

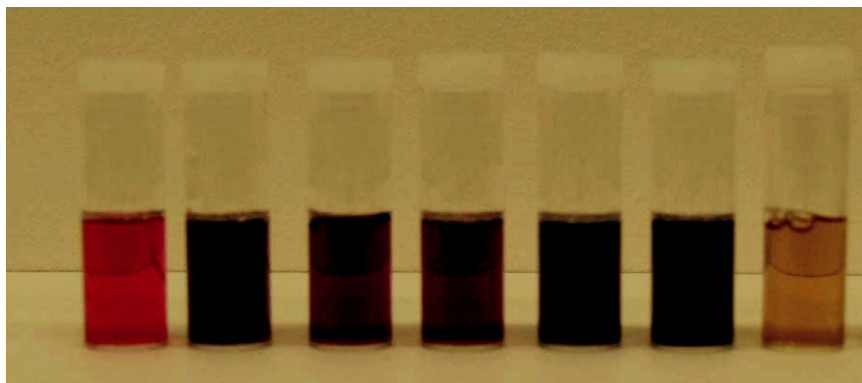


**Fig. 9.1.** Photograph of aqueous solutions of gold nanoparticles of aspect ratio 1 (far left) up to 18 (far right). The short axes of the nanoparticles are 15–30 nm.

longitudinal plasmon band, corresponding to light absorption and scattering along the long axis of the particle, and the transverse plasmon band, corresponding to light absorption and scattering along the short axis of the particle [2, 5–7, 10]. Other nanoparticle shapes are predicted to have other, more complicated extinction spectra [10, 21]. Thus, metallic nanorods and nanowires have tunable optical properties throughout the visible and into the infrared portions of the electromagnetic spectrum, and they are predicted to have enhanced SERS activity compared to spheres [9].

Information technology and storage is another arena for which metallic nanoparticles are of interest. As the size of integrated circuit elements shrinks to the  $\sim 100$  nm scale and below, metallic and semiconducting nanowires of controllable size and ability to be positioned need to be developed [22]. The magnetic domain size in magnetic nanoparticles is of the order of 10 nm, and control of crystal structure and size of the relevant metals and metal alloys (e.g., Fe, Co) on this scale are key to advances in magnetic data storage [23, 24]. Hybrid data storage schemes that rely on melting metallic nanorods to nanospheres in polymer matrices, with subsequent detection of the altered optical properties for “reading” and “writing”, are also being developed [25].

All of the promise of the future technology based on nanometer-scale inorganic solids relies on the production of nanoparticles of controlled size, shape and crystal structure, and further ultimately requires that these nanoparticles be rationally linked to make a working device. Enormous progress has been made in the synthesis of inorganic nanospheres; routinely, at present, control over the diameter of nanoparticles leads to particle size distributions that are within 10% of the mean diameter, and frequently within 5%. Only since the mid-1990s and later have there been good synthetic methods to make nanoparticles of controllable size *and* shape (other than spheres) [3, 20, 22].

## 9.2

**Seed-Mediated Growth Approach to the Synthesis of Inorganic Nanorods and Nanowires**

We have developed a seed-mediated growth approach to make silver and gold nanorods and nanowires of controllable aspect ratio in aqueous solution, at room temperature [20, 26–28]. Our method (Figure 9.2) starts with the reduction of a metal salt in aqueous solution, by a strong reducing agent, to make 3–4 nm metallic “seeds” which are generally spherical. The seed reaction is done in the presence of sodium citrate to prevent the seeds from aggregating and precipitating. The seeds are then added to a “growth” solution that consists of fresh metal salt, and a surfactant, cetyltrimethylammonium bromide, CTAB, that directs the growth of nanoparticles into nanorods and nanowires. Growth is initiated by the addition

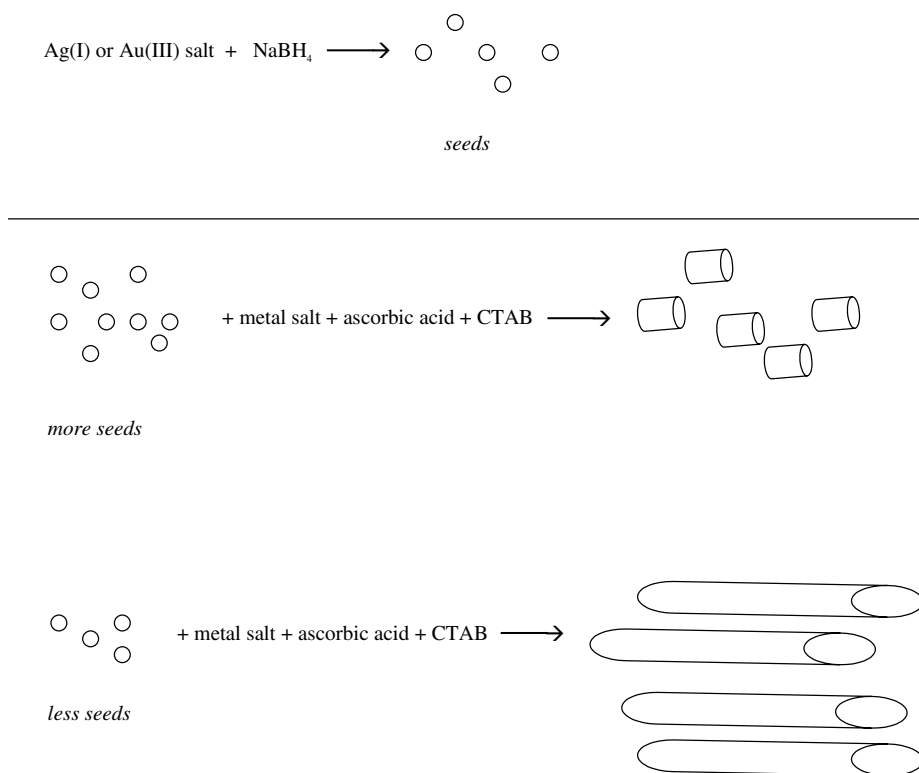


**Fig. 9.2.** Cartoon showing the seed-mediated growth approach to the synthesis of metallic nanorods of controllable aspect ratio. In the first step, metal salts are reduced with sodium borohydride, a strong reducing agent, to metal nanospheres (“seeds”) that are 3–4 nm in diameter. In the subsequent growth steps,

seeds are added to fresh solutions of metal salt in the presence of CTAB, and are reduced with the weak reducing agent ascorbic acid. The ratio of metal seed to salt controls the aspect ratio, fewer seeds leading to longer rod growth.

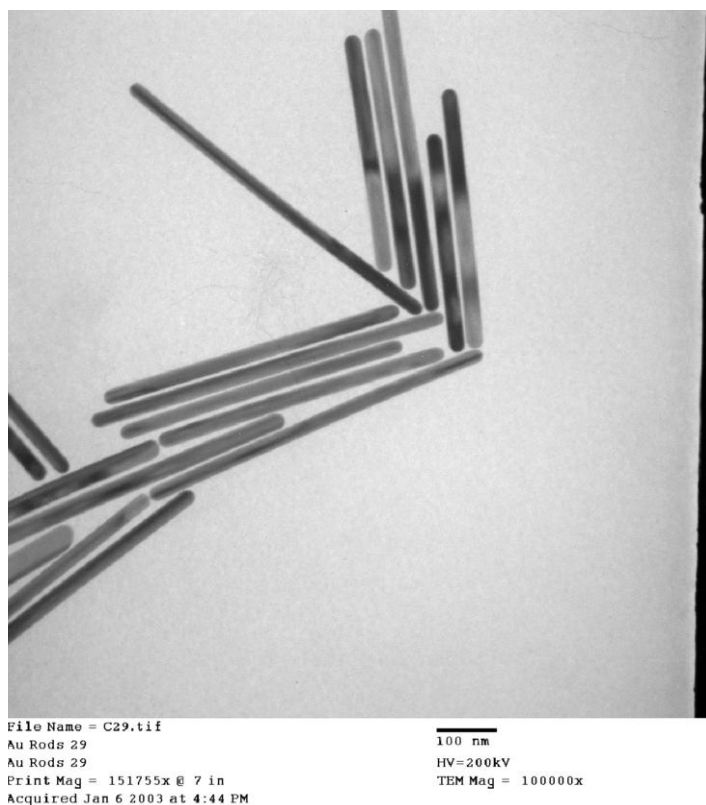


**Fig. 9.3.** Transmission electron micrograph of gold nanorods, prepared by the seed-mediated growth method in water, in the presence of CTAB. Scale bar = 100 nm.

of a weak reducing agent, usually ascorbic acid, that cannot reduce the metal salt on its own (at room temperature). Varying the seed to metal salt ratio controls the aspect ratio of the resulting nanorods. Additionally, one can use short nanorods as “seeds” on which to grow longer nanorods.

Our seed-mediated growth approach has been successful for the synthesis of gold nanorods, with diameters of ca. 20 nm and aspect ratios from 2 to 20, in a controllable fashion (Figure 9.3). For silver, we have been able to make both short nanorods (aspect ratio  $\sim 4$ ) and long nanowires (aspect ratios 50–350); in the case of nanowires the level of control we have is more limited.

Despite the overall simplicity of the seed-mediated growth approach in aqueous solution, there are many complicating factors during the synthetic reactions that can alter the outcome of the reaction. The percent yield of nanorods, compared to spheres, is typically only  $\sim 20\%$ , although with slight changes in reaction conditions, 90% yields have been obtained [29]. Glassware must be rigorously cleaned

with aqua regia. Relatively small changes in the pH of the solution, for example, in the case of silver nanorods, leads to nanowires [26]. Gold, we find, is difficult to make into nanowires, but is relatively easy to make into nanorods, for reasons that are unclear. A few degrees difference in room temperature, as well as the timing of the growth steps, also affects the final product's size and shape. Changing relative concentrations of seed, salt, and surfactant can eliminate nanorods entirely, but produce nanospheres with well-controlled dimensions from 5–40 nm [30]. Also, depending on reaction conditions, it is possible to have seeds promote the formation of more seeds instead of growth [31]!

There is an ever-increasing list of other methods to make inorganic nanorods and nanowires. For example, porous alumina membranes with well-defined nanochannels can be used as hard templates in which to electrochemically deposit metals; the metal forms nanorods dictated by the channel dimensions, and the membrane must of course be attached to the electrode for this to work [5, 6, 19]. Metal nanowires can also be grown via electrodeposition along the step edges of highly-ordered pyrolytic graphite from metal salt in solution, using a scanning tunneling microscope tip to pulse the voltage in “activation”, “nucleation” and “growth” steps [32].

Many methods of producing nonspherical, well-defined nanoparticles of various shapes and sizes use a “soft template” (e.g., microemulsions, polymers, or surfactants) that directs nanoparticle growth, in the absence of preformed seed [24, 33–40]. Some of these preparations are performed at higher temperatures (up to several hundred °C) in organic solvents, with organometallic precursors, while others are simple reductions of metals, or arrested precipitation reactions, in water. Metals, semiconductors, and metal oxides have been made by these soft solution routes [24, 33–40]. Heterogeneous seeded methods, in which the seed is not the same element or compound as the nanostructure grown from it, are also being developed [41, 42], with great success in the case of semiconductor nanowires [41].

Intuitively, one might imagine that the mechanism of anisotropic growth of a nanoparticle in the “soft template” methods would involve physical constraint on the part of the template; for example, that the size and shape of rodlike micellar templates would be mirrored in the size and shape of the resulting nanoparticles made in those matrices. However, it is now more accepted that preferential adsorption of molecules and ions to different crystal faces of the growing nanoparticle leads to different nanoparticle shapes [1, 40, 43–46]. The underlying mechanisms of anisotropic nanoparticle growth are of fundamental interest, but are also of practical interest; for example, poisoning of platinum nanoparticle catalysts by adsorbed sulfur compounds is a problem of great commercial importance, and it has been suggested that the poisoning is due to adsorbate-induced crystal facet changes of the Pt nanoparticle catalyst [47].

In the case of gold nanorods prepared in aqueous solution by the seed-mediated growth method, we have performed high-resolution transmission electron microscopy (HRTEM) and electron diffraction experiments as a function of growth time to crystallographically characterize the nanorods [45]. It is well-known that for the face-centered cubic (fcc) structure of gold, the (111) face is the most stable, close-

packed face, and one might have expected that the surface of the nanorods would consist mostly of this face (e.g., the long sides) and that the dimensions of the nanorods would be limited to the rod-like micelle size of CTAB. But this is not what we have observed [45].

The crystallographic structure and 3-D crystal morphology of individual gold nanorods prepared by seed-mediated sequential growth in the presence of CTAB were determined by selected area electron diffraction (SAED) in combination with HRTEM. At zero degree tilt, not all the rods imaged on the TEM grid showed Bragg diffraction. Of those that did, SAED gave two patterns in equal proportions. Neither pattern could be indexed as a single zone, indicating that the gold nanorods were not single domain crystals. Instead, both patterns consisted of a superposition of two specific crystallographic zones of general form,  $\langle 112 \rangle$  and  $\langle 100 \rangle$  and  $\langle 110 \rangle$  and  $\langle 111 \rangle$ , which were consistent with multiple twinning of a face-centered cubic structure. Both types of composite electron diffraction patterns can be rationalized on the basis that the gold nanorods consist of an elongated variant of a cyclic penta-tetrahedral twin crystal in which five  $\{111\}$  twin boundaries are arranged radially to the direction of elongation. This type of twinning is common in isotropic gold nanoparticles with decahedral ( $D_{5h}$ ) morphology because the interfacial angle between  $\{111\}$  planes ( $70.53^\circ$ ) is close to  $2\pi/5$  ( $72^\circ$ ). In the case of the nanorods, the shape anisotropy originates from a specific elongation along the common  $[110]$  five-fold axis to produce an idealized 3-D morphology based on a pentagonally twinned prism with five  $\{100\}$  side faces and capped at both ends by five  $\{111\}$  faces (Figure 9.4).

The absence of any preferred zone combination in the electron diffraction patterns suggests that the side faces of the nanorods are either not well-developed or consist of two forms, e.g.  $\{100\}$  and  $\{110\}$  with approximately equivalent surface area. HRTEM images of individual gold nanorods (Figure 9.5) show stripe patterns characteristic of the superposition of two diffraction patterns, i.e. a twinned defect structure, consistent with the SAED data.

In our experiments, growth of the isometric twinned “seeds” (diameter 4 nm) in the presence of CTAB results in the initial transformation of ca. 4% of the seeds into short nanorods, while the remaining crystals increase in size to around 17 nm [45]. Once formed, the nanorods grow almost unidirectionally in length when immersed in a fresh reaction solution to produce cylindrical penta-twinned particles with high aspect ratios and variable crystal lengths between 100 and 300 nm. Because the increase in width is minimal, the elongated crystals have a uniform thickness that is determined by the width of the short nanorods formed in the previous stage of the reaction sequence. At the same time, ca. 6% of the 17 nm-sized isometric twins are transformed into a new population of short rod-shaped nanoparticles, while the remaining crystals continue to grow isometrically. Subsequent transfer of the products into fresh reaction solutions reiterates the combination of isometric growth, nanorod elongation and nanorod formation to produce a trimodal distribution in rod widths [45]. The distribution corresponds to three types of nanorods with mean widths of 34, 40 and 58 nm and decreasing aspect ratios with values between 17–20, 8–11, and 2–3, respectively. Each type can be



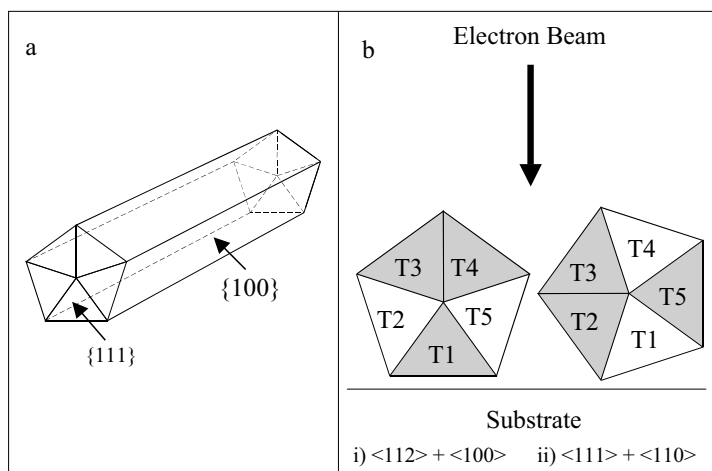


**Fig. 9.4.** Elongated cyclic penta-tetrahedral twin model of gold nanorods, taken from [45]. (a) Idealized 3-D morphology showing {111} end faces and {100} side faces. The common five-fold axis of elongation is [110]. (b) Cross-section of nanorod structure showing arrangement of twins T1 to T5, and possible orientations of domains with respect to the

electron beam. These give rise to superimposed zone combinations of (i)  $\langle 112 \rangle$  and  $\langle 100 \rangle$ , and (ii)  $\langle 110 \rangle$  and  $\langle 111 \rangle$  that are related in the diagram by an anticlockwise rotation of  $18^\circ$  around the five-fold  $\langle 110 \rangle$  central axis. Twin domains in diffraction alignment are highlighted. Reproduced by permission of The Royal Society of Chemistry.

correlated with the widths of the transferred cylindrical, short rod-like or isometric nanoparticles, respectively, which in turn are related to the dimensions and shapes of crystals formed in earlier stages of the sequential process. Isolation of the higher-aspect ratio nanoparticles by centrifugation and precipitation works relatively well [27].

In general, the formation of mixed populations of gold nanoparticles and their associated morphologies and sizes can be rationalized by differences in the delay in the onset of shape anisotropy in the reaction sequence. Clearly, the mechanism responsible for the transformation from isotropic to anisotropic growth of the isometric penta-twinned nanoparticles is not highly competitive, although once achieved, the crystals rapidly elongate along the common [110] axis, suggesting that the process is essentially auto-catalytic. As the unidirectional growth rate is high and the onset of the shape transformation process occurs over an extended reaction period, the nanorods originate at different times to produce a marked variation in the particle lengths. In contrast, the width of each particle increases only slowly, which indicates that the {100} side edges are effectively blocked from further growth compared with the {111} end faces. Previous studies have indicated that the yield of nanorods rises with an increased concentration of CTAB [27], suggesting that CTAB molecules bind more strongly to the side edges than the {111} end faces, with the consequence that the crystal grows preferentially along the [110] direction as the side edges/faces become stabilized. The HRTEM data

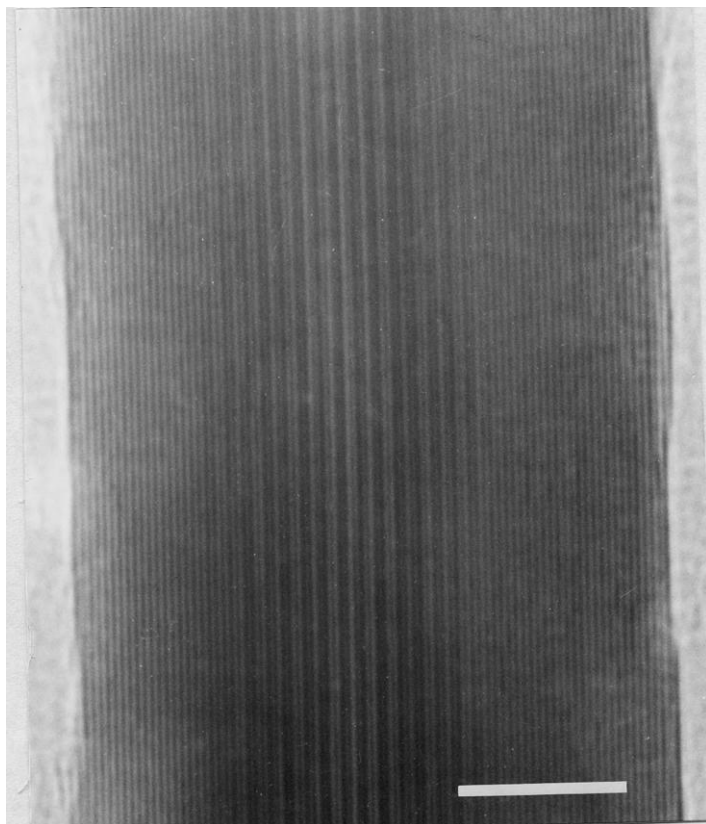


**Fig. 9.5.** High-resolution transmission electron micrograph of a gold nanorod showing the double diffraction pattern, indicating twinning, taken from [45]. Scale bar = 5 nm. Reproduced by permission of The Royal Society of Chemistry.

suggest that this process is not specific enough to produce well-defined {100} side faces, particularly in the initial stages of nanorod formation.

It seems likely that steric and chemical factors play an important role in determining the preferential interactions between the cationic quaternary ammonium headgroups and growth sites on the side edges and faces. One possibility is that surfactant-containing complexes such as  $[\text{AuBrCTA}]^+$  are specifically incorporated into the {100} side edges, whereas non-complexed ion-pairs or  $\text{Au}(0)$  atoms/clusters are added to the {111} end faces. The discrimination between sites could be due to the increased stability of the close-packed {111} surfaces compared with the edge sites, which will contain numerous defects. Moreover, binding of the large  $[\text{NMe}_3]^+$  headgroup of CTAB (diameter = 0.814 nm, area = 0.521 nm<sup>2</sup>) and associated long alkyl chain can be more readily accommodated at the {100} side edges

than within the plane of individual close-packed {111} faces, where the Au–Au spacings are too small to facilitate epitaxy. As the nanorods grow in length, the area of the side faces increases, and this could facilitate the assembly of a bilayer of CTAB molecules at the crystal surface, in which the alkylammonium headgroup points down toward the gold surface, with the long hydrocarbon chain facing the solvent, interdigitating with a second hydrocarbon chain from a second CTAB layer, with the second CTAB's headgroup facing the solvent [46]. In turn, the bilayer would provide additional stabilization and growth inhibition, and this could explain why elongation of the nanorods is rapid once the shape anisotropy has been established, in a “zipping” type of mechanism.

Finally, we note that our proposed mechanism follows a classical description of crystal growth inhibition that involves the preferential attachment of individual molecules to the different crystal faces of the growing nanoparticle. The mechanism does not implicate the involvement of surfactant micelles per se in controlling the shape anisotropy of fcc metallic nanoparticles, as has been previously postulated. Instead, the data indicate that symmetry breaking in fcc metallic structures is an intrinsic structural mechanism (twinning) that is subsequently modulated extrinsically during growth in solution by edge-specific surfactant adsorption. This general conclusion is also being reached by many other research groups [1, 24, 40, 43–45].

### 9.3

#### Assembly of Metallic Nanorods: Self-Assembly vs. Designed Chemical Linkages

While great progress in the synthesis and mechanism of the growth of metallic nanorods has been made, a real challenge in the field is the assembly of nanorods into a functional structure. The researcher faces two general choices in the matter: self-assembly vs. designed assembly. By self-assembly, we mean that the nanorods can be “left to themselves” to order. For example, there is experimental evidence that as one puts lateral pressure on a random “raft” of rods at the air–water interface, nanorods can assemble into ordered rafts [48]. Onsager long ago predicted [49] that increasing the concentration of “hard colloidal” rods in solution would lead to one-dimensional or two-dimensional liquid crystalline ordering, which has been experimentally and theoretically verified [50–55].

By “designed” assembly, we mean that the different crystal faces of the nanorods could be specifically reacted with some reagent to link them in a rational way. This last approach is made difficult by the usual lack of information about the crystal face identity on the ends and edges of nanorods, but progress is being made [1, 24, 40, 45].

In the case of liquid crystalline ordering as a function of nanorod concentration in the self-assembly approach, we have performed TEM, polarizing microscopy, and small angle X-ray scattering experiments to show that gold nanorods of high aspect ratio (13–18) do indeed stack in regular arrays as the concentration increases [55]. The system is not as ideal as the Onsager case, the CTAB outer bilayer

[56] makes our rods “softer” and more highly charged, but nonetheless we do observe concentration-dependent ordering.

In our experiments [55], gold nanorods of aspect ratios 13–18 were concentrated and separated from spherical nanoparticles by centrifugation. Thermogravimetric analysis showed that ~20% of the total mass of the nanorods was associated with the CTAB surfactant. This is significantly larger than that calculated for monolayer coverage (3 wt%) on the basis of particle surface area, and suggests that the nanorods are covered with multiple CTAB layers; indeed, El-Sayed has spectroscopic evidence for CTAB bilayers on gold nanorods [56]. We found that the presence of the surfactant coating was of key importance, not only for hydrophilic stabilization of the nanorods in water but also for controlling long-range self-assembly in concentrated dispersions; we found that the optimum conditions required for in situ liquid crystalline ordering involved redispersing the nanorods in 1–100 mM CTAB. Above this surfactant concentration, the nanorods precipitated instantaneously and were unable to be redispersed to image in the electron microscope. Below this CTAB concentration, nanorods were also unable to be redispersed in water. Although not fully explored, we believe these effects are not simply due to the ionic nature of CTAB, as ~1 mM NaCl precipitates the gold nanorods.

In general, the 18 aspect ratio nanorod solutions were dark brown in color (when concentrated) and had a weak absorbance maximum in the visible at ~530 nm, in addition to a near-infrared absorbance at ~1700 nm [27]. Thin films of the concentrated dispersions supported on glass slides showed iridescent droplets ~0.1 mm in diameter under polarizing light microscopy (Figure 9.6). The observed textures were indicative of localized regions of liquid crystalline ordering and are similar to nematic droplets observed in boehmite nanoneedle solutions [52]. Significantly, the liquid crystalline droplets were stable up to 200 °C in air, after which the surfactant began to degrade, although the nanorods remained unchanged in size and shape. Similar experiments with concentrated surfactant solution alone showed much smaller “speckles” in the polarizing microscope and no liquid crystalline textures.

Small-angle X-ray scattering (SAXS) experiments were undertaken to determine the extent of long-range ordering in concentrated (~5–10 wt% of solids) and diluted (by a factor of ~1000) dispersions of the gold nanorods [55]. The scattering curves show ripples in the scattered X-ray intensity due to particle shape and interparticle interactions. The data were fitted to a model consisting of core-shell cylinders stacked with a Gaussian distribution of interparticle distances using a method of non-linear least-squares fitting. The fitting parameters included the radius of the nanorods, the number of particles in a stack, the width of the Gaussian distribution of interparticle distances in the stack, the surfactant layer thickness and the major radius of the elliptical impurities. Attempts to fit the SAXS data to isolated rods failed; rod stacks were required. The fits suggest that the concentrated solutions contained self-assembled stacks of ca. 200 nanorods, each of which had a surfactant coating 3.9 nm in thickness, consistent with a CTAB bilayer [56]. In contrast, smaller clusters of ~30 rods were present in the more dilute sample. The

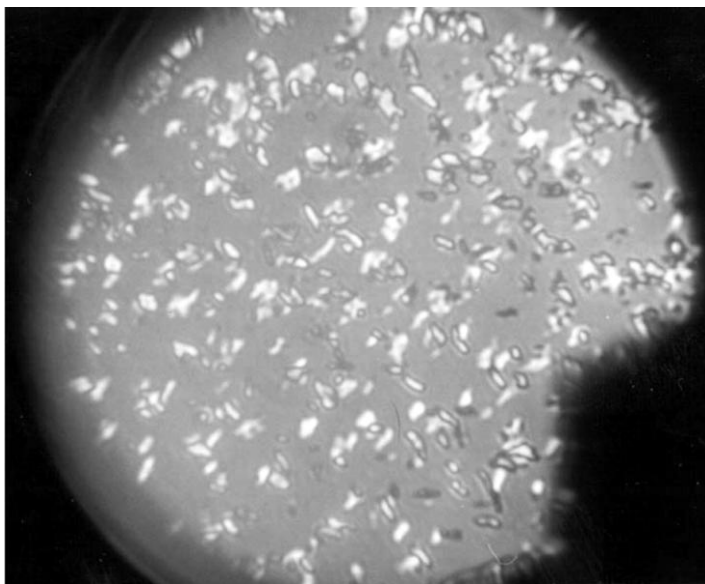


**Fig. 9.6.** Polarizing optical micrograph of a concentrated solution ( $\sim 5\text{--}10\%$  w/w) of aspect ratio 18 gold nanorods in water, taken from [55]. Reproduced by permission of The Royal Society of Chemistry.

width of the Gaussian distribution of spacings between the particle centers was an order of magnitude narrower in the concentrated dispersions compared to the dilute dispersions, consistent with more dense arrays in the concentrated dispersions and a high degree of disorder in the dilute dispersions. No evidence for hexagonal phases was found, under our conditions.

TEM images of air-dried dispersions prepared at low nanorod concentrations ( $<1\%$  by weight, including surfactant) showed mainly discrete nanoparticles (Figure 9.7). Some short-range order involving side-on, end-to-side or end-to-end aggregation was observed, presumably due to capillary forces associated with the drying process [57]. At high nanorod concentrations ( $\sim 5\text{--}10\text{ wt}\%$ ), in contrast, microscopic smectic-like arrays of closely packed nanorods were observed (Figure 9.7). The arrays consisted of nanorods that were aligned parallel to each other in micron-length rows, which in turn were stacked laterally to produce the higher-order superstructure. Such structures were observed predominantly at the edges of dried droplets (apparent by visual inspection of the TEM grid as brown rings), suggesting that capillary forces were responsible for the smectic-like organization [57]. In contrast, other areas of the TEM grid showed a predominance of micrometre-long rows of ordered nanorods (Figure 9.7), which probably correspond more closely to the in situ organization of the nanorods within the concen-

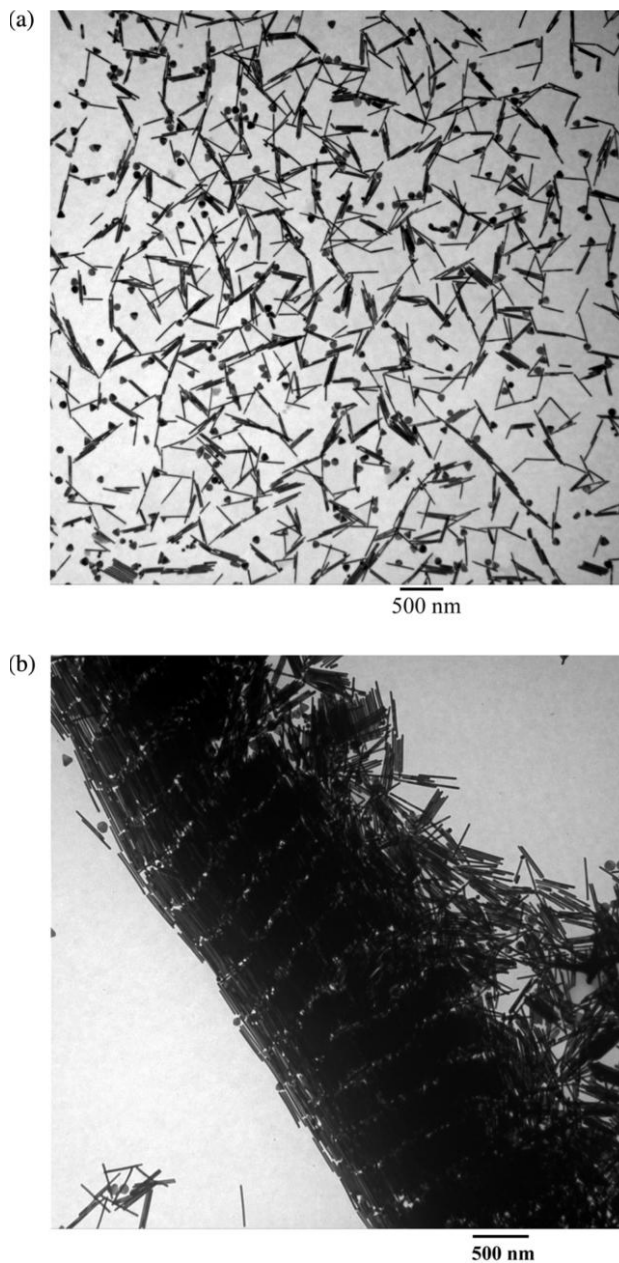


**Fig. 9.7.** Transmission electron micrographs showing concentration dependent ordering of gold nanorods, taken from [55]. (a)  $<1$  wt% showing isolated nanorods; some spherical particles are still present even after centrifugation. (b)  $\sim 5$ – $10$  wt% showing smectic-like arrays, and



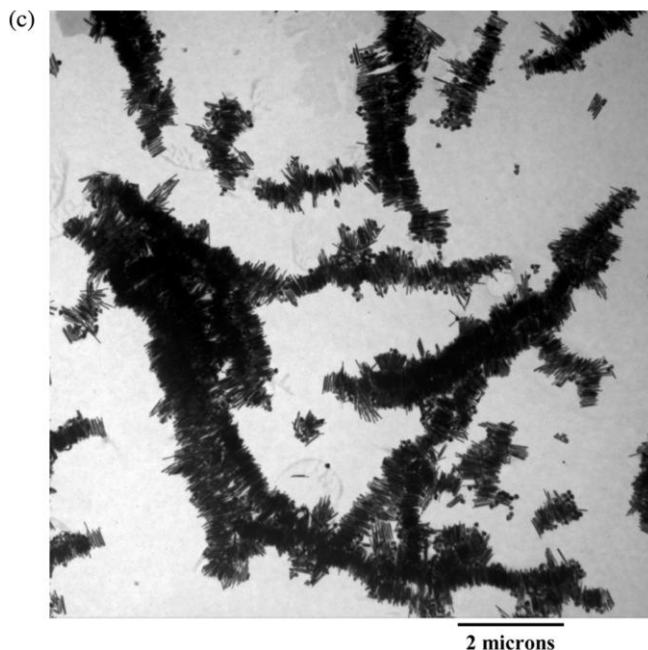


**Fig. 9.7.** (c) ~5–10 wt% showing linear stacks of gold nanorods. Reproduced by permission of The Royal Society of Chemistry.

trated dispersion. We estimate tens of rods assemble in vertical stacks, while ~100 stacks assemble into rows, in reasonable agreement with the SAXS data given the large uncertainties in this fitted parameter. The smectic-like phase presumably arises from secondary ordering of the preformed linear stacks on the TEM grid during drying.

El-Sayed has reported that gold nanorods of aspect ratio 4.6, coated with two different cationic surfactants, assemble into higher-order structures upon concentration from aqueous solution [53]. Our results with higher-aspect ratio nanorods are consistent with this and indicate that surfactant-mediated interactions between gold nanorods of uniform shape and size can give rise to ordered liquid crystalline arrays in concentrated suspensions. Multilayers of surface-adsorbed cationic surfactants such as CTAB can induce a remarkable degree of self-ordering of spherical gold nanoparticles due to a balance between short-range electrostatic repulsion and interchain attraction [58]. Moreover, interdigitation of surfactant chains on specific faces of prismatic nanocrystals can give rise to ordered single chains of other ( $\text{BaCrO}_4$ ) nanoparticles [35] or self-assembled nanocubes of  $\text{Cu}_2\text{O}$  [59]. For the gold nanorods described here, liquid crystalline arrays were only routinely observed in aqueous solutions containing the proper concentration range of CTAB,



suggesting that interactions between surfactant molecules in solution with surface-adsorbed amphiphiles were important aspects of the assembly process. The hydrophilic nature of the gold nanoparticles prior to assembly indicates that the surfactant molecules in the outer layer of the surface coating are oriented with their cationic headgroups exposed to the solvent. However, as the surfactant-coated nanorods approach each other in solution, expulsion of the outermost “cationic head out” CTAB molecules and their associated counterions could result in the formation of hydrophobic nanorods in which the remaining CTAB hydrophobic tails face the solvent; thus, the resulting nanorods spontaneously self-assemble in a side-on fashion to minimize the unfavorable hydrophilic–hydrophobic interactions with water and promote interdigitation of the surfactant tails.

“Designed” assembly of metallic nanorods has been demonstrated recently [60, 61]. In one case [60], metallic nanorods were cross-linked with DNA in a manner analogous to Mirkin’s approach for gold nanospheres [15]. Two different batches of gold nanorods were derivatized with two different DNA sequences, then a third linking DNA strand is added that can hydrogen-bond to both nanorod batches [60]. In this way, the spacing between gold nanorods can be controlled by the length of the DNA linkers. In the other case, gold nanorods derivatized with DNA were bound to a flat gold surface that was patterned DNA, and the assembly was directed by the specific hydrogen-bonding of the DNA [61]. Figure 9.8 shows TEM images of the linked gold nanorods from [60].

Functionalizing the ends only of gold nanorods is possible, if the sides are physically protected from reaction, which could then result in designed end-to-end

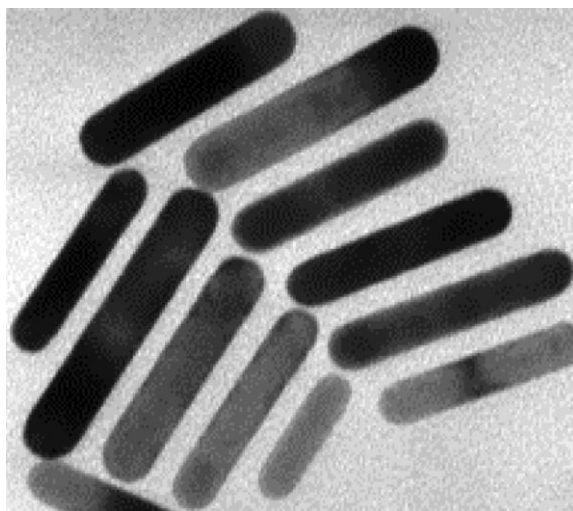


**Fig. 9.8.** Transmission electron micrograph of DNA-linked gold nanorods, taken from [60]. Reproduced by permission of The Royal Society of Chemistry.

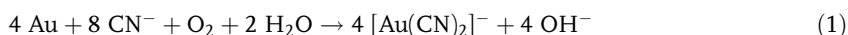
alignment of the rods [61]. It is also possible, however, that the different crystal faces of gold nanorods might react differently with reagents, and also form the basis for rational assembly strategies of gold nanorods.

## 9.4

### Reactivity of Metallic Nanoparticles Depends on Aspect Ratio

Understanding the chemical reactivity of nanoparticles as a function of size and shape is a research area which is likely to lead to many useful and perhaps surprising results. We have already mentioned that gold nanoparticles  $\sim 3$  nm in diameter are no longer “noble” and can catalyze chemical reactions [4]. Poisoning of platinum nanoparticle catalysts by sulfur compounds results in different crystal facets of Pt becoming exposed to the environment, and the subsequent reactivity of the Pt nanoparticles is compromised [47]. We have found that the reactivity of gold with cyanide and persulfate depends on the size and shape of the gold nanoparticles [62].

The reaction of cyanide with gold, in the presence of air and water, produces the gold–cyanide complex ion [63]:



This reaction is the industrially important cyanide process for recovering gold from rocks [63]; in that case, elemental gold is precipitated out by adding Zn dust to reduce the Au(I) back to Au(0).

Gold spheroids have a transverse plasmon band, at  $\sim 530$  nm and a longitudinal plasmon band at 600–1000 nm, depending on the aspect ratio. Various aspect ratio spheroids (aspect ratio 2–5) were used for cyanide dissolution experiments, and all gave similar results; typical results for spheroids of aspect ratio  $2.5 \pm 0.5$  will be described here [62]. Figure 9.9 shows the ultraviolet–visible absorption spectra of the  $2.5 \pm 0.5$  aspect ratio gold spheroids upon reaction with cyanide. In the absence of cyanide, the solution appears violet and has two absorption peaks at approximately 526 nm and 685 nm. Upon addition of cyanide solution to the nanoparticle solution, the absorption spectra changed, depending on the cyanide concentration (Figure 9.9b–g). The violet color gradually turned red from a to d as the cyanide concentration increased; in set e ( $5 \times 10^{-4}$  M cyanide) the solution appeared deep red; and in f and g, it was colorless. For cyanide concentrations below  $2.5 \times 10^{-4}$  M, both of the band positions decreased in absorbance, with the band maximum at 526 nm remaining unchanged and the 685 nm band blue shifting by  $\sim 20$  nm. At  $5 \times 10^{-4}$  M  $\text{CN}^-$  the long wavelength band completely disappeared within 1 min, and the intensity of the 526 nm band decreased by  $\sim 30\%$  within 2 min. At  $10^{-3}$  M  $\text{CN}^-$  only a weak band at 526 nm was observed. As

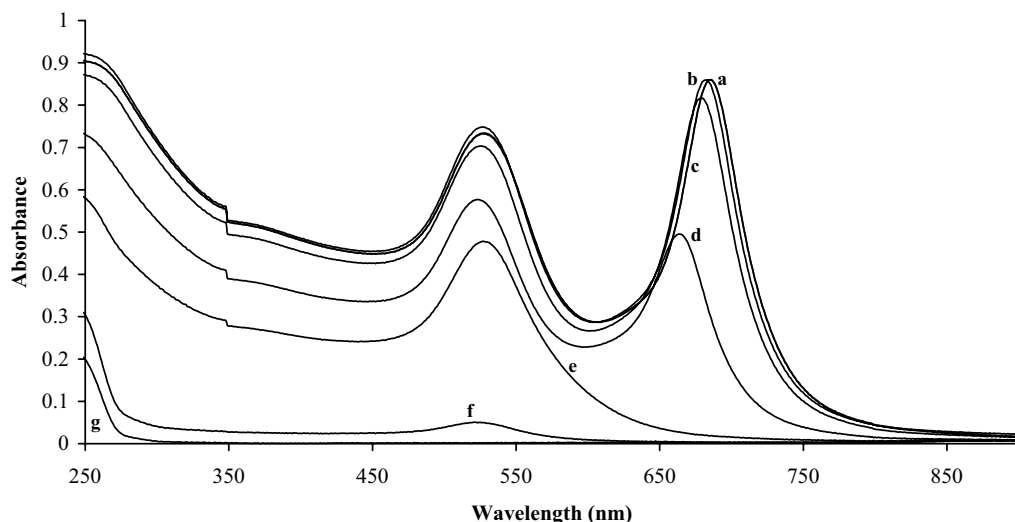
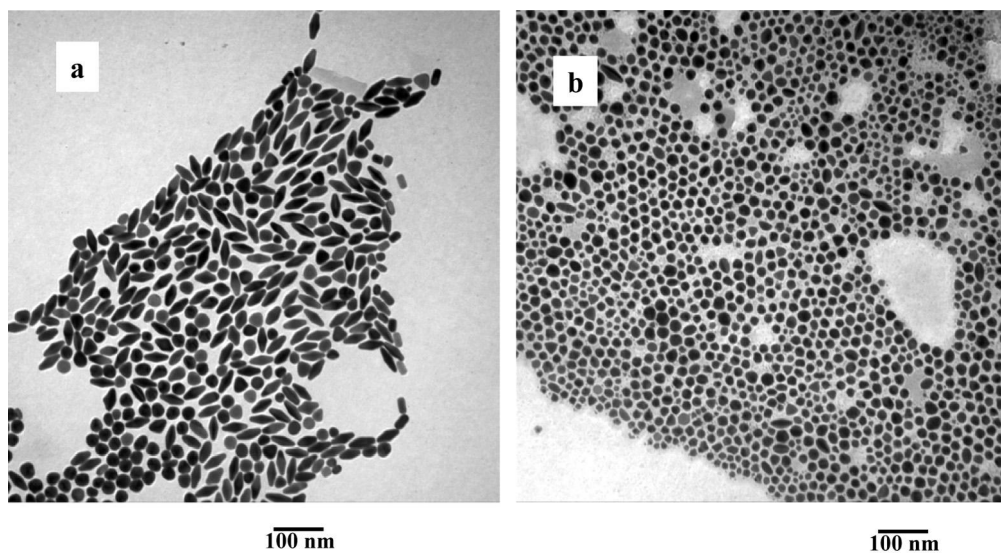


**Fig. 9.9.** UV-visible spectra of  $2.5 \pm 0.5$  aspect ratio gold spheroids with 17 nm short axis ( $2.5 \times 10^{-4}$  M in terms of gold) after 1 h of the addition of various amounts of cyanide solution. a: 0.0 M, b:  $10^{-5}$  M, c:  $10^{-4}$  M, d:  $2.5 \times 10^{-4}$  M, e:  $5 \times 10^{-4}$  M, f:  $10^{-3}$  M, g:  $2.5 \times 10^{-3}$  M sodium cyanide. Reprinted with permission from [62]. Copyright (2002) American Chemical Society.

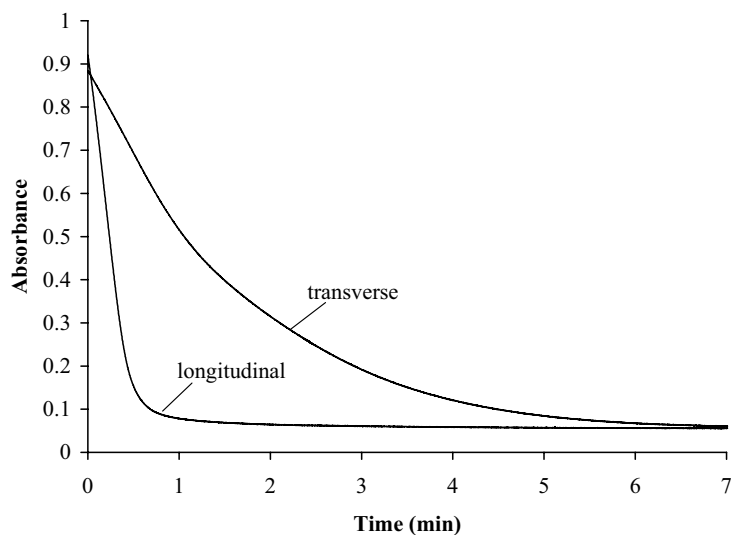
the cyanide concentration was further increased to  $2.5 \times 10^{-3}$  M, this band completely disappeared within 8 min.

Figure 9.10(a) shows the TEM of  $2.5 \pm 0.5$  aspect ratio spheroids (with 17 nm short axis) before  $\text{CN}^-$  addition. The solution also contained a significant amount ( $\sim 40\%$ ) of spheres of similar size ( $\sim 20\text{--}25$  nm). Those spheres contributed only a single absorbance at 526 nm, as they do not have a longitudinal plasmon band. Figure 9.10(b) shows the TEM corresponding to sets e of Figure 9.9. In set e only spheres in the size range 10–25 nm were present in the TEM. In set d (TEM not shown) the percentage of spheroids decreased from 60% to 40%, and size measurement of the spheroids showed that the length decreased but the width remained unchanged. This leads to a reduced average aspect ratio of spheroids from  $2.5 \pm 0.5$  to  $2.0 \pm 0.5$ . In contrast, the spheres present in the solution did not change in size significantly. In sets f only spheres of diameter 2–5 nm ( $\sim 90\%$ ) and 5–15 nm (10%) were observed. In set g no particles were found in the TEM.

Absorbance vs. time (Figure 9.11) (at both the longitudinal and transverse wavelength bands for the spheroids) and successive UV-visible spectra (Figure 9.12) were measured during the dissolution process of the gold spheroids. Figures 9.11 and 9.12 corresponds to set f. The rate of decrease in absorbance is faster for the longitudinal band than the transverse band (Figure 9.11). In the intermediate stage, the longitudinal plasmon band gradually blue shifts with a simultaneous decrease in intensity and finally mixes into the transverse band (Figure 9.12).



**Fig. 9.10.** Transmission electron micrograph of gold spheroids before and 1 h after cyanide treatment. a: no cyanide, b:  $5 \times 10^{-4} \text{ M CN}^-$ . Reprinted with permission from [62]. Copyright (2002) American Chemical Society.



**Fig. 9.11.** Absorbance vs. time plot for cyanide dissolution at wavelengths corresponding to the transverse and longitudinal plasmon bands. Conditions were similar to set 'f' in Figure 9.9. Reprinted with permission from [62]. Copyright (2002) American Chemical Society.

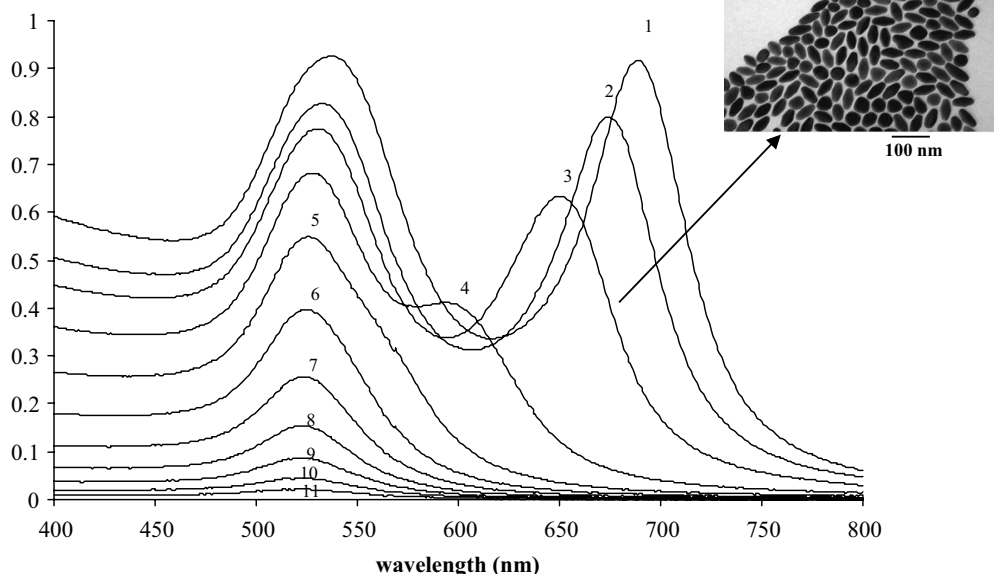
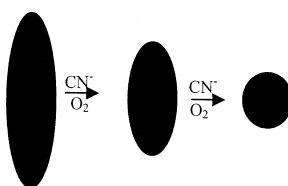


**Fig. 9.12.** Successive UV–visible spectra of gold plasmon bands during cyanide dissolution of set ‘f’. (1) before cyanide addition, (2) after 20 s of cyanide addition and (3 to 10) after 50 s intervals from 2. The inset shows the

TEM of intermediate short spheroids corresponding to spectrum 3 isolated by rapidly centrifuging the particles from reaction mixture. Reprinted with permission from [62]. Copyright (2002) American Chemical Society.

Thus, the apparent transformation of the spheroids to spheres in the presence of cyanide, in air, may be depicted by the following cartoon:



In this cartoon, the width of the nanoparticles does not change, only its length.

The appearance of an intermediate blue shifted longitudinal band also indicates that spheroid dissolution starts at the two ends. The longitudinal band disappears at a faster rate due to the faster dissolution rate of spheroids than spheres. We also isolated the particles at the intermediate stage of cyanide dissolution by rapidly centrifuging the particles and separating them from excess cyanide present in solution before the dissolution reaction could complete. This was performed within 1 min (compared to 5–10 min for the complete reaction). Both TEM and UV–vis

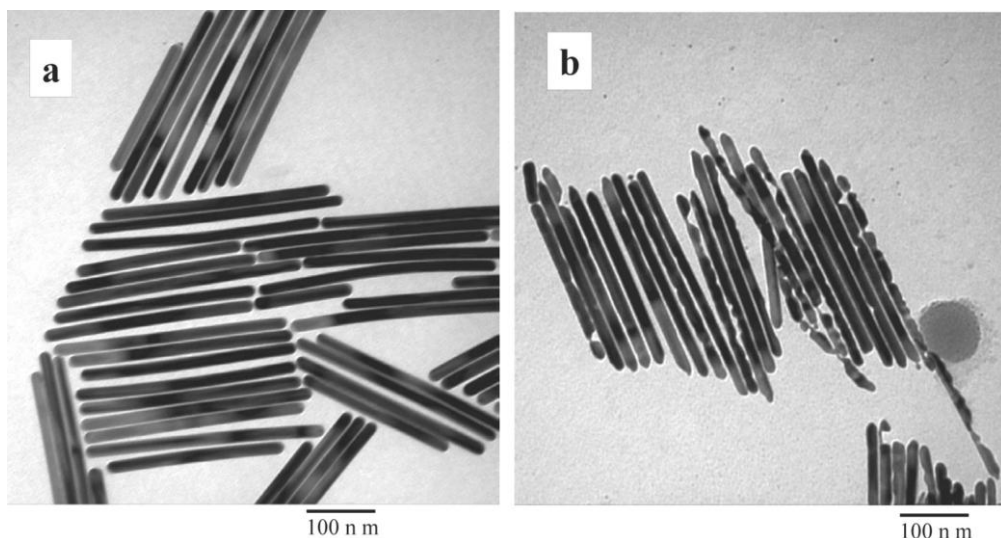


**Fig. 9.13.** Transmission electron micrographs of gold nanorods, aspect ratio 18, before (a) and 24 h after (b) cyanide treatment. Reprinted with permission from [62]. Copyright (2002) American Chemical Society.

spectra indicate that the intermediate particles were smaller 1.8 aspect ratio spheroids (inset of Figure 9.12).

Gold nanorods with 17 nm short axis and aspect ratio of 18 have a weak plasmon band at 503 nm and (presumably) a longitudinal plasmon band beyond  $\sim 2000$  nm. With increasing cyanide concentration the 503 nm band gradually decreased in intensity and finally vanished in  $\sim 60$  min (data not shown). No plasmon band in the 600–1850 nm region was detected at intermediate cyanide concentrations, suggesting that short rods were not intermediates. TEMs of the nanorods showed that they were uniform in shape (Figure 9.13) before reaction with cyanide. At intermediate cyanide concentrations, these higher-aspect ratio nanorods did not decrease in length, but dissolution occurred at many sites along the length of the rod (Figure 9.13), leading to pitted nanorods. At lower cyanide concentrations, many rods remained unchanged and, as the cyanide concentration increased, defective rods increased in number with the increased extent of corrosion. Our results indicate that gold spheroids (aspect ratio 2–5 with 12–30 nm short axis) are more reactive than spheres (20–30 nm) and nanorods (aspect ratio 18 with 16 nm short axis) for reaction with cyanide [62].

For the spheroids, we were able to obtain SERS signals of cyanide, even at concentrations of cyanide too low to show changes in the visible spectra [62]. Thus, it appears that cyanide can adsorb to the surface and yet not immediately react. This is consistent with a purported mechanism of cyanide reaction with gold, in which the adsorbed cyanide ions react to form a protective AuCN layer [62].

The high aspect ratio gold nanorods were not “eaten” from the ends by cyanide, as were their spheroidal counterparts. The topology and chemical potential of edge atoms of spheroids may not favor the formation of stable films of protective AuCN. This may be the reason for enhanced reactivity and anisotropic dissolution of spheroids.

Non-uniform cyanide dissolution of cylindrical nanorods starts at many sites along the length of the nanorod. This may be related to local crystal structures within the rods, which is a twinned defect structure [55]. It is also possible that the CTAB bilayer that is likely to be most strongly bound on the long sides of the nanorods may compete with cyanide for binding and subsequent reaction; thus, the rods are pitted along their long axis due to CTAB pinholes [62]. Statistically, there are many more gold atoms along the long axis of the nanorod than on the end faces, so one might expect dissolution along the long axis of the nanorods to appear there first. Clearly, however, this statistical argument is incorrect for the spheroids of aspect ratios 2–5, which do react from the ends preferentially.

We also examined the dissolution reaction of gold nanospheres, spheroids, and nanorods (aspect ratios 1, 2–5, and 18 respectively) with persulfate, which is thermodynamically a favorable reaction [62]:



Our results, based on UV–vis spectroscopy and TEM [62], indicate that spheroids (aspect ratio 2–5 with 12–30 nm short axis) are more reactive than spheres (20–30 nm) and nanorods (aspect ratio 18 with 16 nm short axis). In the presence of persulfate, spheroids convert to spheres (Figure 9.14), but similar size spheres and rods do not react at all, on the timescale of days. We presume that during the shape transition from spheroid to sphere, a fraction of gold atoms at the spheroid edges oxidize; thus the particle diameter shrinks (~5–10%) after persulfate treatment.

Overall, then, we can conclude that the nanoparticle shape affects its reactivity [62].

## 9.5

### Conclusions and Future Prospects

Metallic nanorods are highly interesting materials from many points of view: as elements in future nanoscale electronic circuits; as sensors; as catalysts; as optical elements in future nanoscale optical devices. Gold and silver nanorods have distinct visible absorption and scattering spectra that are tunable with aspect ratio. Many workers have developed wet synthetic routes to these nanomaterials, with control of aspect ratio a key improvement compared to the synthesis of simple nanospheres. Another key area for which improvements need to be made is the understanding of the atomic arrangements of the different faces of crystalline



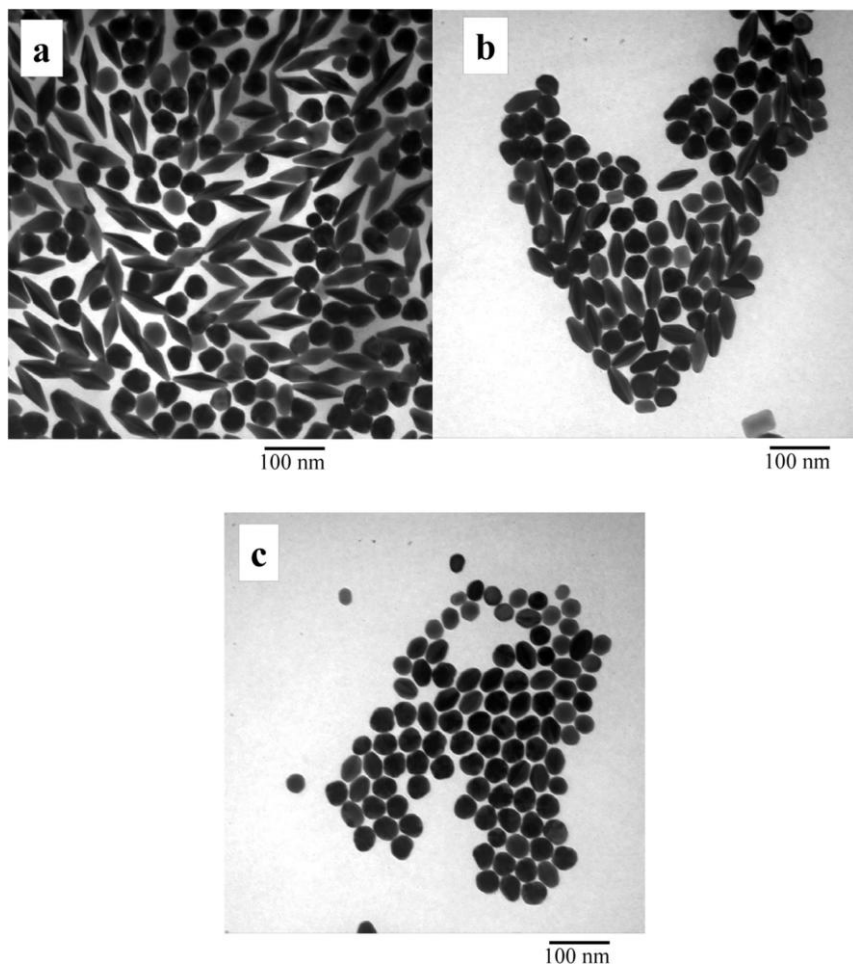


**Fig. 9.14.** Transmission electron micrographs of gold spheroids before (a) and 24 h after (b, c) persulfate treatment: a, no persulfate; b,  $10^{-6}$  M persulfate; c,  $10^{-5}$  M persulfate. Reprinted with permission from [62]. Copyright (2002) American Chemical Society.

nanorods. Assembly of nanorods into organized structures is at a very early stage, but self-assembly into liquid crystalline ordered arrays has been demonstrated. Linkage chemistries to “wire up” the nanorods are being developed, and that endeavor will be greatly aided by better understanding of the chemistry of different crystal faces of the nanorods. Evidence of the different reactivity of the different crystal faces of metallic nanorods, as a function of aspect ratio, is emerging.

## Acknowledgements

We thank the U.S. National Science Foundation (C.J.M.) and the University of South Carolina for support of sabbatical leave for C.J.M. to visit S.M. in Bristol, UK. We also thank the EPSRC, UK for support of a postgraduate studentship to C.J., Dr Igor Dolbina and the other staff on BM26B at the ESRF for assistance in collecting the SAXS data, and the Royal Society for a Dorothy Hodgkin Research Fellowship (K. J. E.).

## References

- MURPHY, C. J. *Science* **2002**, 298, 2139–2141.
- Metal Nanoparticles: Synthesis, Characterization and Applications*, eds. FELDHEIM, D. L., FOSS, C. A., JR., Marcel Dekker, New York 2002.
- EL-SAYED, M. A. *Acc. Chem. Res.* **2001**, 34, 257–264.
- VALDEN, M., LAI, X., GOODMAN, D. W. *Science* **1998**, 281, 1647–1650.
- FOSS, C. A., JR., HORNYAK, G. L., STOCKERT, J. A. et al. *J. Phys. Chem.* **1994**, 98, 2963–2971.
- HORNYAK, G. L., PATRISSI, C. J., MARTIN, C. R. *J. Phys. Chem. B* **1997**, 101, 1548–1555.
- LINK, S., EL-SAYED, M. A. *J. Phys. Chem. B* **1999**, 103, 8410–8426.
- SCHULTZ, S., SMITH, D. R., MOCK, J. J. et al. *Proc. Natl. Acad. Sci. USA* **2000**, 97, 996–1001.
- KOTTMAN, J. P., MARTIN, O. J. F., SMITH, D. R. et al. *Chem. Phys. Lett.* **2001**, 341, 1–6.
- KELLY, K. L., CORONADO, E., ZHAO, L. L. et al. *J. Phys. Chem. B* **2003**, 107, 668–677.
- NIE, S. M., EMORY, S. R. *Science* **1997**, 275, 1102–1106.
- KNEIPP, K., KNEIPP, H., ITZKAN, I. et al. *Chem. Rev.* **1999**, 99, 2957–2976.
- OBARE, S. O., HOLLOWELL, R. E., MURPHY, C. J. *Langmuir* **2002**, 18, 10407–10410.
- LIN, S.-Y., LIU, S.-W., LIN, C.-M. et al. *Anal. Chem.* **2002**, 74, 330–335.
- ELGHANIAN, R., STORHOFF, J. J., MUCIC, R. C. et al. *Science* **1997**, 277, 1078–1080.
- TATON, T. A., MIRKIN, C. A., LETSINGER, R. L. *Science* **2000**, 289, 1757–1760.
- KIM, Y., JOHNSON, R. C., HUPP, J. T. *NanoLett.* **2001**, 1, 165–167.
- THANH, N. T. K., ROSENZWEIG, Z. *Anal. Chem.* **2002**, 74, 1624–1628.
- NICEWARMER-PENA, S. R., FREEMAN, R. G., REISS, B. D. et al. *Science* **2001**, 294, 137–141.
- MURPHY, C. J., JANA, N. R. *Adv. Mater.* **2002**, 14, 80–82.
- JIN, R., CAO, Y. W., MIRKIN, C. A. et al. *Science* **2001**, 294, 1901–1903.
- KOVTYUKHOVA, N. I., MALLOUK, T. E. *Chem. Eur. J.* **2002**, 8, 4355–4363.
- SUN, S., MURRAY, C. B., WELLS, D. et al. *Science* **2000**, 287, 1989–1992.
- PUNTES, V. F., KRISHNAN, K. M., ALIVISATOS, A. P. *Science* **2001**, 291, 2115–2117.
- WILSON, O., WILSON, G. J., MULVANEY, P. *Adv. Mater.* **2002**, 14, 1000–1004.
- JANA, N. R., GEARHEART, L., MURPHY, C. J. *Chem. Commun.* **2001**, 617–618.
- JANA, N. R., GEARHEART, L., MURPHY, C. J. *J. Phys. Chem. B* **2001**, 105, 4065–4067.
- JANA, N. R., GEARHEART, L., MURPHY, C. J. *Adv. Mater.* **2001**, 13, 1389–1393.
- BUSBEE, B. D., OBARE, S. O., MURPHY, C. J. *Adv. Mater.* **2003**, 15, 414–416.
- JANA, N., GEARHEART, L., MURPHY, C. J. *Langmuir* **2001**, 17, 6782–6786.
- JANA, N. R., GEARHEART, L., MURPHY, C. J. *Chem. Mater.* **2001**, 13, 2313–2322.
- WALTER, E. C., MURRAY, B. J., FAVIER,

- F. et al. *J. Phys. Chem. B* **2002**, *106*, 11407–11411.
- 33 AHMADI, T. S., WANG, Z. L., GREEN, T. C. et al. *Science* **1996**, *272*, 1924–1925.
  - 34 TANORI, J., PILENI, M. P. *Langmuir* **1997**, *13*, 639–646.
  - 35 LI, M., SCHNABLEGGER, H., MANN, S. *Nature* **1999**, *402*, 393–395.
  - 36 PENG, X. G., MANNA, L., YANG, W. D. et al. *Nature* **2000**, *404*, 59–61.
  - 37 KWAN, S., KIM, F., AKANA, J. et al. *Chem. Commun.* **2001**, 447–448.
  - 38 PENG, Z. A., PENG, X. G. *J. Am. Chem. Soc.* **2002**, *124*, 3343–3353.
  - 39 SUN, Y., XIA, Y. *Adv. Mater.* **2002**, *14*, 833–837.
  - 40 SUN, Y., XIA, Y. *Science* **2002**, *298*, 2176–2179.
  - 41 HU, J., ODOM, T. W., LIEBER, C. M. *Acc. Chem. Res.* **1999**, *32*, 435–445.
  - 42 YU, H., GIBBONS, P. C., KELTON, K. F. et al. *J. Am. Chem. Soc.* **2001**, *123*, 9198–9199.
  - 43 FILANKEMBO, A., PILENI, M. P. *J. Phys. Chem. B* **2000**, *104*, 5865–5868.
  - 44 MANNA, L., SCHER, E. C., ALIVISATOS, A. P. *J. Cluster Sci.* **2002**, *13*, 521–532.
  - 45 JOHNSON, C. J., DUJARDIN, E., DAVIS, S. A. et al. *J. Mater. Chem.* **2002**, *12*, 1765–1770.
  - 46 YU, S.-H., COLFEN, H., ANTONIETTI, M. *Chem. Eur. J.* **2002**, *8*, 2937–2945.
  - 47 HARRIS, P. J. F. *Nature* **1986**, *323*, 792–794.
  - 48 KIM, F., KWAN, S., AKANA, J. et al. *J. Am. Chem. Soc.* **2001**, *123*, 4360–4361.
  - 49 ONSAGER, L. *Ann. N. Y. Acad. Sci.* **1949**, *51*, 627–659.
  - 50 FRENKEL, D., LEKKERKERKER, H. N. W., STROOBANTS, A. *Nature* **1988**, *332*, 822–823.
  - 51 VAN BRUGGEN, M. P. B., LEKKERKERKER, H. N. W. *Langmuir* **2002**, *18*, 7141–7145.
  - 52 GABRIEL, J.-C. P., DAVIDSON, P. *Adv. Mater.* **2000**, *12*, 9–20.
  - 53 NIKOOBAKHT, B., WANG, Z. L., EL-SAYED, M. A. *J. Phys. Chem. B* **2000**, *104*, 8635–8640.
  - 54 LI, L.-S., WALDA, J., MANNA, L. et al. *NanoLetters* **2002**, *2*, 557–560.
  - 55 JANA, N. R., GEARHEART, L. A., OBARE, S. O. et al. *J. Mater. Chem.* **2002**, *12*, 2909–2912.
  - 56 NIKOOBAKHT, B., EL-SAYED, M. A. *Langmuir* **2001**, *17*, 6368–6374.
  - 57 OLIVER, S. R. J., BOWDEN, N., WHITESIDES, G. M. *J. Colloid Interface Sci.* **2000**, *224*, 425–428.
  - 58 FINK, J., KIELY, C. J., BETHELL, D. et al. *Chem. Mater.* **1998**, *10*, 922–926.
  - 59 GOU, L., MURPHY, C. J. *NanoLetters* **2003**, *3*, 231–234.
  - 60 DUJARDIN, E., HSIN, L.-B., WANG, C. R. C. et al. *Chem. Commun.* **2001**, 1264–1265.
  - 61 MBINDYO, J. K. N., REISS, B. D., MARTIN, B. R. et al. *Adv. Mater.* **2001**, *13*, 249–254.
  - 62 JANA, N. R., GEARHEART, L., OBARE, S. O. et al. *Langmuir* **2002**, *18*, 922–927.
  - 63 GREENWOOD, N. N., EARNSHAW, A. *Chemistry of the Elements*, 2nd edition, Butterworth-Heinemann, Oxford 1997, p. 1175.

## 10

## Oxide-Assisted Growth of Silicon and Related Nanowires: Growth Mechanism, Structure and Properties

*S. T. Lee, R. Q. Zhang, and Y. Lifshitz*

### Abstract

This chapter focuses on the oxide-assisted growth (OAG) of silicon-based nanowires. OAG, invented by the research team of City University of Hong Kong, is different and distinguishable from the conventional metal catalyst vapor–liquid–solid (VLS) growth. The 1D growth is initiated through suboxide droplets which are very reactive to  $\text{Si}_x\text{O}_y$  in the gas phase, and no metal catalyst droplets are needed. The further 1D growth occurs via precipitation of a silicon core encapsulated by a  $\text{SiO}_2$  sheath, which restricts the lateral growth. OAG was found to be a generic method capable of bulk production of a variety of different semiconducting nanowires. We summarize the research efforts at City University of Hong Kong during the past several years. We first describe the discovery of the OAG process, and its distinction from the metal catalyst VLS process as evident from the growth conditions and the structure of the resulting wires. Then we discuss the OAG nucleation and growth process. We follow by showing how we can modify the morphology and size (affecting the properties) of the nanowires by varying growth parameters: (1) morphology control by temperature, (2) diameter control by carrier gas, (3) large-area, aligned, long silicon nanowires (SiNWs) by flow control. Two-dimensional nanostructures, i.e. nanoribbons, have also been fabricated. Hybrid structures, such as nanocables, metalized SiNWs and SiC, were grown by applying multi-step processes, ion implantation and reduction in liquid solutions. The generic nature of the OAG approach was realized in a host of different semiconducting nanowires such as Ge, SiC, GaN, GaAs, and GaP nanowires, as well as ZnO whiskers. The variety of nanowires produced was characterized by different methods including electron microscopy, Raman scattering, photoluminescence, FTIR, field emission, electrical measurements, and scanning tunneling microscopy. The morphology, microstructure, optical, electrical and chemical properties of Si and related nanowires were systematically characterized. The work was supported by modeling efforts which gave additional insight into different aspects of the oxide-assisted nucleation and growth and the resulting properties.

*The Chemistry of Nanomaterials: Synthesis, Properties and Applications, Volume 1.* Edited by C. N. R. Rao, A. Müller, A. K. Cheetham  
Copyright © 2004 WILEY-VCH Verlag GmbH & Co. KGaA, Weinheim  
ISBN: 3-527-30686-2

[www.iran-mavad.com](http://www.iran-mavad.com)

مرجع دانشجویان و مهندسين مواد

## 10.1

### Introduction

The discovery of carbon nanotubes (CNTs) by Iijima [1] in 1991, initiated an intensive study of one-dimensional (1D) nanomaterials including tubes, wires, cables and ribbons in general, and of the fundamental properties and potential applications of carbon nanotubes [2–6] in particular. The interest in CNTs stems from their small diameter (smallest, 4 Å) enabling unprecedented and exciting opportunities for the study of size- and dimensionality-dependent chemical and physical phenomena [7–13]. It is believed that these size effects open the door for many potential applications in nanotechnology, such as high-strength materials [14], electronic components [15], sensors [16, 17], field emitters [18, 19] and hydrogen storage materials [20].

The limitations of carbon nanotubes, such as the selective growth of metallic or semiconducting tubes and the difficulty of achieving controlled doping, motivated the alternative study of conventional one-dimensional (1D) semiconducting materials. These nanowires do not seem to face these problems, which make them much more adaptable for volume fabrication of nanodevices. Silicon nanowires (SiNWs) are of special interest since silicon is the most widely used and studied semiconducting material. In 1998, Lieber et al. [21] and the CityU team [22] independently reported the bulk-quantity synthesis of SiNWs. At CityU, we proposed an oxide-assisted growth (OAG) model to explain the growth of SiNWs [23–28], while Lieber et al. advocated the laser-assisted metal catalyst vapor–liquid–solid (VLS) growth [21]. In contrast to the conventional metal catalyst VLS growth [21], the OAG does not require a catalytic metal nanoparticle tip, thus providing a much “cleaner” method for the 1D material fabrication.

With this OAG approach, highly pure, ultra-long and uniform-sized SiNWs in bulk-quantity could be synthesized by either laser ablation or thermal evaporation of silicon powders mixed with silicon oxide or silicon monoxide only [23–28]. Section 10.2 discusses the physical chemistry aspects of the OAG. Transmission electron microscopic data and theoretical calculations are used to describe the nucleation and the growth of SiNWs via the OAG process.

In further efforts to achieve controlled growth, SiNWs of varying diameter, phase purity, morphology, defect density and doping have been obtained. This was achieved by varying the deposition parameters including growth temperature, carrier gas composition, carrier gas flow, and target composition. Different SiNW diameters were obtained by varying the carrier gas [29]. In contrast to the work of Lieber et al. [30] and Yang et al. [31] (who used metal nanoparticles of uniform size to control the diameter of SiNWs via the laser-assisted catalytic VLS growth) we found that the SiNW diameters had a wide distribution. The OAG method enabled not only fabrication of Si 1D nanostructures of different morphologies [32, 33], but also 2D nanostructures, i.e. silicon nanoribbon [34]. Section 10.3 reviews our work on the control of SiNW structure and size.

Future applications of SiNWs require the production of hybrid structures made

of SiNWs integrated with nanostructures of other materials. We treated this issue by using multistep processes. One example was to grow nanocables. Metallization of the SiNW surfaces is another example of a hybrid configuration. We addressed it by ion implantation of SiNWs with metal ions. An additional route for incorporation of SiNWs with other materials/structures is the transformation of one nanowire to another by chemical reactions. We demonstrate this approach by our work on SiC nanowires. Our works on compound structures are detailed in Section 10.4.

The OAG is a generic method capable of producing different nanostructures from a variety of materials. We have extended the oxide-assisted approach to successfully synthesize a host of semiconducting materials, including Ge [35], GaN [36, 37], GaAs [38, 39], SiC [40], GaP [41], and ZnO (whiskers) [42]. Section 10.5 reviews these works.

The motivation for studying nanoscience and nanotechnology stems from the exciting properties predicted for nanomaterials due to size effects. Section 10.6 details our work on the chemical properties of SiNWs. We first discuss the stability of the hydrogen-terminated SiNWs produced by HF dipping which removes the SiO<sub>2</sub> sheath surrounding the crystalline Si core. This issue is central to the silicon wafer technology. A second study was dedicated to the reduction properties of the SiNWs in liquid solutions containing metal ions. Surface interactions of SiNWs with gases enable their use in chemical sensing. This was demonstrated for ammonia and water vapors in air or nitrogen. The reactivity of SiNWs in a liquid solution can be exploited for their use as templates to grow carbon nanostructures, which is the final topic of this section.

The optical and electrical properties of the nanowires (Section 10.7) have been characterized systematically by Raman scattering, photoluminescence and field emission [43, 44]. Understanding the atomic structure and electronic properties of SiNWs, including the dopant-induced conductivity, is an essential step towards the application of the nanowires. Although the structures and electronic properties of boron-doped silicon wafers have been investigated extensively, the corresponding study for SiNWs is relatively lacking, due to the insulating nature of the oxide sheath on most semiconductor nanowires and the difficulty in dispersing them. We have succeeded in removing the oxide layer of the SiNWs, obtaining atomically resolved STM images of H-terminated surfaces of SiNWs with diameters ranging from 1 to 7 nm. This enabled reliable scanning tunneling spectroscopy (STS) measurements of these wires, from which the electronic density of states and energy band gaps could be derived. The energy band gaps indeed increase from 1.1 eV for a 7 nm diameter SiNW to 3.5 eV for a 1.3 nm diameter SiNW, in accord with theoretical predictions, demonstrating the quantum size effect in SiNWs. In Section 10.7 we review our scanning tunneling microscopy (STM)/STS study on boron-doped and undoped SiNWs [45] and on the quantum size effect in SiNWs as well as our characterization work on other electrical and optical properties of SiNWs.

Modeling of SiNW structures, nucleation and growth processes and properties was done in parallel with the experimental work. The modeling work is most valuable in providing additional insight into the nature of the OAG and in explaining our experimental results. Our modeling efforts are described in Section 10.8.

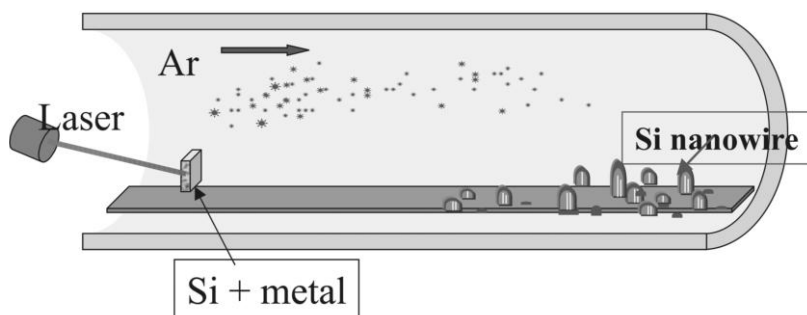


Fig. 10.1. Schematic diagram of metal catalyst VLS growth of SiNWs by laser ablation.

## 10.2

### Oxide-Assisted Nanowire Growth

#### 10.2.1

##### Discovery of Oxide-Assisted Growth [23–25]

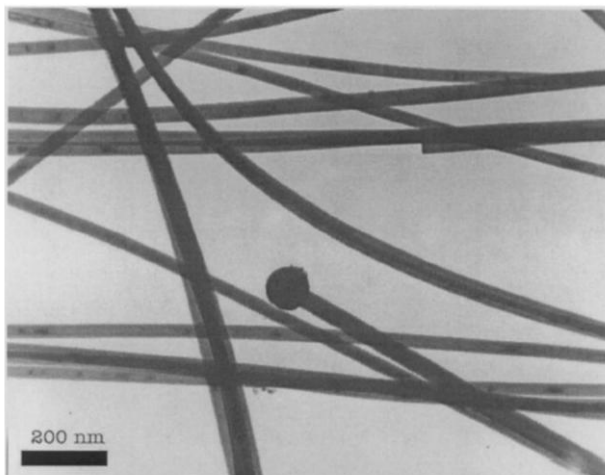
Si nanowires were first produced using the classical metal catalyst VLS approach [21, 22, 46]. Laser ablation of a metal-containing Si target produces metal/metal silicide nanoparticles that act as the critical catalyst needed for the nucleation of SiNWs. The wires grow further by dissolution of silicon in the metallic nano-cap and concurrent Si segregation from the cap. In a typical experiment, an excimer laser is used to ablate the target placed in an evacuated quartz tube filled with an inert gas, e.g. argon [22].

We followed this idea by ablating a solid composite target (Figure 10.1) of highly pure Si powder mixed with metals (Fe, Ni, or Co). The target temperature was 1100–1400 °C and the nanowire growth temperature was selected as 900–1100 °C. Si wires with a typical diameter of 100 nm were formed (see Figure 10.2(a)) in the high furnace temperature zone (around 1100 °C). SiNWs were millimeters long and straight with metallic (Fe) spheres at the wire tip, indicating growth via a metal-catalyst VLS reaction. High-resolution transmission electron microscopy (HRTEM) observations showed that the growth direction of these Si wires was predominantly  $\langle 111 \rangle$  (Figure 10.2(b)). The formation of such Si wires only at the relatively higher temperature was clearly due to the high melting temperature of Fe-silicides, e.g.  $\text{FeSi}_2$ .

Entirely different SiNWs grew in the lower temperature zone ( $\sim 900$  °C) (Figure 10.2(c)). TEM investigations showed that SiNWs obtained in this region were extremely long and highly curved with a typical smaller diameter of  $\sim 20$  nm (see Figure 10.2(c)). Each wire consisted of a crystalline Si core in a sheath of Si oxide. The crystalline Si core had a high density of defects, such as stacking faults and micro-twins. HRTEM and electron diffraction showed that the most frequent axis of the SiNWs was along the  $\langle 112 \rangle$  direction with the  $\{111\}$  surfaces of Si crystalline cores parallel to the nanowire axis [47]. This is in contrast to the  $\langle 111 \rangle$  growth



(a)



(b)

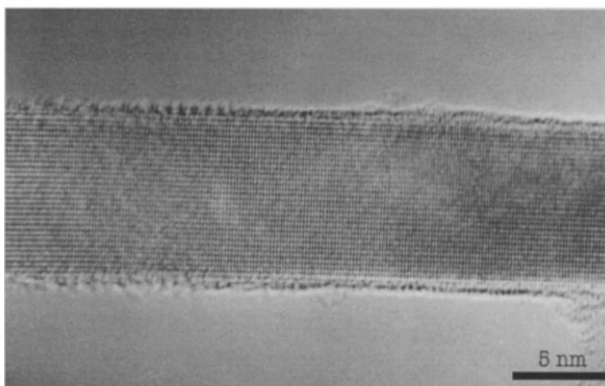


**Fig. 10.2.** TEM images of SiNWs from laser ablation [24]: (a) At high temperature, (1100 °C) note the metallic tip typical for the metal catalyst growth; (b) a typical HRTEM image of SiNWs formed at high temperature (1100 °C); and

direction common for the metal catalyst VLS growth. Most surprisingly, no evidence for metal particles was found either on the SiNWs tips or in the wires themselves, regardless of the metal used in the target (Fe, Ni or Co), in sharp contrast to those SiNWs grown in the high-temperature region. The SiNW tips were generally round and covered by a relatively thick Si oxide layer (2–3 nm) and no other component other than Si or O was detected by electron energy dispersive spectroscopy (EDS). The Si crystal core near the tip contained a high density of stacking faults and micro-twins [27], generally along the nanowire axis in the  $\langle 112 \rangle$  direction.

(c)

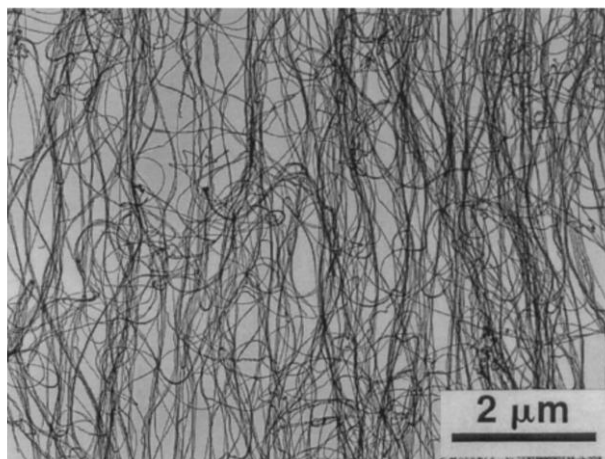


Fig. 10.2. (c) TEM micrograph of Si nanowires formed in the low temperature zone (900 °C).

Similar metal-free SiNWs were obtained for other metal catalysts using laser ablation or even by thermal evaporation (Figure 10.3) of either mixed powders of silicon dioxide and silicon or a pure silicon monoxide powder [23, 24, 27]. The morphology and structure of SiNWs obtained from thermal evaporation of SiO were similar to those grown from a (Si + SiO<sub>2</sub>) solid source. The yield of SiNWs increased with increasing thermal evaporation temperature and pressure (see Figure 10.4). Using highly pure SiO powders, we obtained a high yield of SiNWs at temperatures ranging from 1130 to 1400 °C. This provided the direct evidence for the OAG process. These observations led us to propose that the SiNW growth at lower temperatures was induced by the oxide and not by the metal catalyst. This proposition was further substantiated by the observation that: (1) A limited quantity of SiNWs was obtained by laser ablation of pure Si powders (99.995%) or a high-purity Si wafer. (2) The growth rate of Si nanowires was greatly enhanced when SiO<sub>2</sub> was added to the Si powder targets. The yield of SiNWs produced from SiO<sub>2</sub>-containing Si targets (at 50 wt% SiO<sub>2</sub>) was up to 30 times higher than that from a

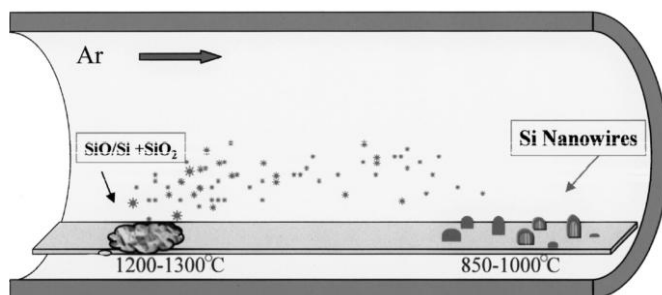


Fig. 10.3. Schematic diagram of oxide-assisted growth of SiNWs by thermal evaporation.

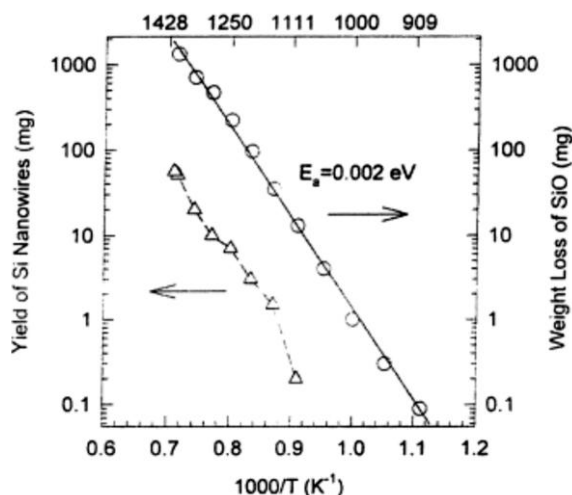


Fig. 10.4. The yield of the Si nanowire product increases with the weight loss of the SiO target temperature when increasing evaporation temperature [24].

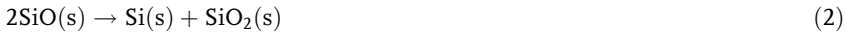
Fe-containing Si target. No nanowires could be obtained using a pure SiO<sub>2</sub> target. We performed several experiments to further understand the nature of this OAG of nanowires. SiNWs could not be formed by ablation of a pure Si target in the absence of a pure metal catalyst. A two-stage experiment was carried out to explore the role of SiO<sub>2</sub> in the nucleation and growth of SiNWs. First, a SiO<sub>2</sub>-containing Si target was laser ablated to form SiNW nuclei. Second, ablation of a pure Si target was attempted for further growth. SiNW growth could be observed only when a SiO<sub>2</sub>-containing Si target was ablated in the second stage. The experiment showed that in the OAG nucleation of a SiNW a pure Si target was not sufficient for the further growth and the oxide was continuously needed throughout the entire SiNW nucleation and growth process. This is in contrast to the metal catalyst VLS mechanism in which the metal catalyst sustains the growth as long as the pure Si supply is maintained.

#### 10.2.2

##### Oxide-Assisted Nucleation Mechanism

We conducted experiments to reveal the nature of the Si core precipitation in the SiO<sub>2</sub> sheath in this new growth process. In these experiments, the vapor phase generated from the mixture of Si and SiO<sub>2</sub> at 1200 °C mainly consisted of Si monoxide [Si(s) + SiO<sub>2</sub>(s) → 2SiO(g), where (s) and (g) represent solid and gas, respectively]. This was proven by the EDS observation that the material collected on the water-cooled Cu finger was Si<sub>m</sub>O<sub>n</sub> ( $m = 0.51, n = 0.49$ ). Si monoxide (SiO) is an amorphous semiconductor of high electrical resistivity, which can be readily generated from the powder mixture (especially in a 1:1 ratio) of Si and SiO<sub>2</sub> by

heating [22, 48]. By heating the SiO sample, Si precipitation was observed. Such precipitation of Si nanoparticles from annealed SiO is quite well known [49]. The precipitation, nucleation and growth of SiNWs always occurred at the area near the cold finger, which suggests that the temperature gradient provided the external driving force for nanowire formation and growth. The nucleation of nanoparticles is assumed to occur on the substrate by decomposition of Si oxide as shown in Eqs. (1) and (2).



Our TEM data suggested that this decomposition results in the precipitation of Si nanoparticles, which are the nuclei of SiNWs, clothed with shells of silicon oxide.

We further initiated theoretical studies to explore the role of the oxide species in the OAG process. The gas-phase composition of silicon oxide clusters evaporated by laser ablation or thermal treatment should be considered to be important in the SiNW synthesis. We first used density functional theory (DFT) calculations to study the nature of the  $\text{Si}_n\text{O}_m$  ( $n, m = 1-8$ ) clusters formed in the gas phase during OAG [50]. Our calculations show that silicon suboxide clusters are the most probable constituent of the vapor, and they have an unsaturated nature and are highly reactive towards bonding with other clusters. Moreover, a silicon suboxide cluster prefers to form a Si-Si bond with other silicon oxide clusters as shown in Figure 10.5 [51], while an oxygen-rich silicon oxide cluster prefers to form a Si-O bond with

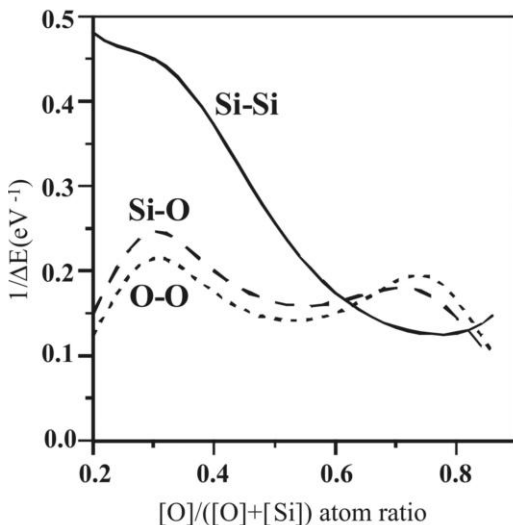


**Fig. 10.5.** The inverse of the energy difference  $\Delta E = \text{LUMO (electron acceptor)} - \text{HOMO (electron donor)}$  and thus the reactivity (proportional to the inverse of the energy difference) for the formation of a Si-Si bond, a Si-O bond, or an O-O bond between two silicon oxide clusters as a function of Si:O ratio [51].

other clusters. Based on these calculations we proposed the following SiNW nucleation scheme [52]: First, a silicon suboxide cluster is deposited on the substrate and some of its highly reactive silicon atoms are strongly bonded to the substrate (silicon) atoms, limiting the cluster motion on the substrate. Non-bonded reactive silicon atoms in the same cluster are now exposed to the vapor with their available dangling bonds directed outward from the surface. They act as nuclei that absorb additional reactive silicon oxide clusters and facilitate the formation of SiNWs with a certain crystalline orientation. The subsequent growth of the silicon domain after nucleation may be crystallographic dependent. Oxygen atoms in the silicon suboxide clusters might be expelled by the silicon atoms during the growth of SiNWs and diffuse to the edge forming a chemically inert silicon oxide sheath [51]. In a certain orientation, e.g. [112], the diffusion might be lower and the high reactive silicon oxide phase can still be exposed to the outside and facilitate the continuous growth of the wire in such a direction. The oxygen-rich sheath formed in other directions may however possess lower reactivity and thus does not favor further stacking of silicon oxide clusters from the gas-phase, leading to growth suppression in such directions. The reactivity of silicon atoms in oxygen-rich clusters becomes very low at a Si:O ratio of 1:2 [51], while the reactivity of oxygen atoms changes to a lesser extent. The overall reactivity for Si:O = 1:2 is low. 1D growth in a specific direction is thus facilitated. In summary, the highly reactive  $\text{SiO}_x$  layer ( $x > 1$ ) at the tip of nanowires acts as a collector for the vaporized silicon oxide, while the outer  $\text{SiO}_2$  layer of the SiNWs stops the diameter growth of the nanowires.

### 10.2.3

#### Oxide-Assisted Growth Mechanism

The Si nanowire growth is determined by four factors: (1) The high reactivity of the  $\text{Si}_x\text{O}$  ( $x > 1$ ) layer on nanowire tips. (2) The  $\text{SiO}_2$  component in the shell, which is formed from the decomposition of SiO and retards the lateral growth of nanowires. (3) defects (e.g. dislocations) in the Si nanowire core. (4) The formation of {111} surfaces, which have the lowest energy among the Si surfaces, parallel to the axis of the growth direction. The first two factors were discussed earlier. As far as the first factor is concerned we would like to add to the previous discussion that the melting temperature of nanoparticles can be much lower than that of their bulk materials. For example, the difference between the melting temperatures of 2 nm Au nanoparticles and Au bulk material is over 400 °C [46, 53]. The materials in the SiNW tips (similar to the case of nanoparticles) may be in or near their molten states, thus enhancing atomic absorption, diffusion, and deposition.

We suggest that the defects of SiNWs are one of the driving forces for the 1D growth. The main defects in Si nanowires are stacking faults along the nanowire growth direction of  $\langle 112 \rangle$ , which normally contain easy-moving 1:6 [112] and non-moving 1:3 [111] partial dislocations, and micro-twins. The presence of these defects at the tip areas should result in the fast growth of Si nanowires, since dislocations are known to play an important role in crystal growth. The SiNW growth

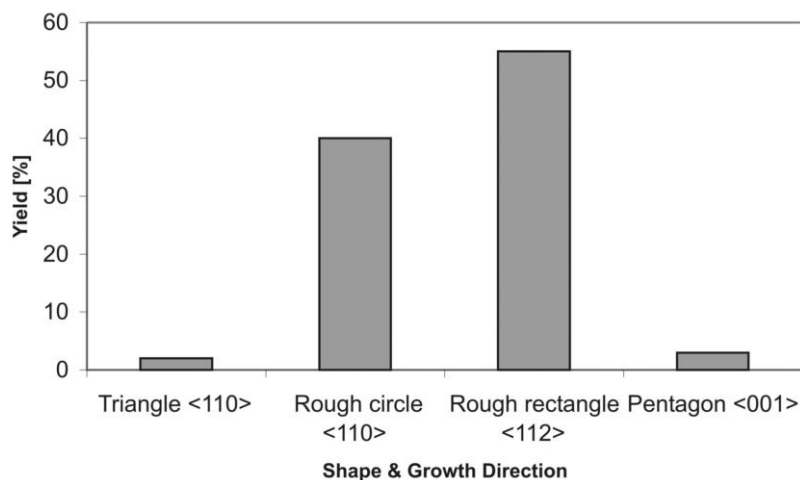


Fig. 10.6. The distribution of shapes, sizes, and growth directions of SiNWs [54].

rate in certain crystallographic directions is enhanced not only by existing dislocations in the growth direction but also by the formation of facets with a low surface energy (Si {111} facets have the lowest surface energy). Figure 10.6 presents the statistical data of SiNW growth directions and shapes derived from the cross-sectional TEM images, showing that SiNWs grown by the OAG technique are primarily oriented in the  $\langle 112 \rangle$  and  $\langle 110 \rangle$  directions, and rarely in the  $\langle 100 \rangle$  or  $\langle 111 \rangle$  directions [54]. The cores of SiNWs are bounded by well-defined low-index crystallographic facets with a variety of shapes that can be circular, rectangular and triangular. We found a correlation between the cross-sectional shape and the growth direction, and proposed a model to explain these findings [55]. We suggest that the SiNW growth direction and cross-section are determined by four factors: (i) the stability of a Si atom occupying a surface site; (ii) the Si {111} surface stability in the presence of oxygen; (iii) the stepped Si {111} surface layer lateral growth process; and (iv) the effect of dislocations in providing perpetuating {111} steps to facilitate SiNW growth. Theoretical evaluation of the SiNW growth along these criteria shows that indeed  $\langle 112 \rangle$  and  $\langle 110 \rangle$  are the preferred wire growth directions, and  $\langle 111 \rangle$  and  $\langle 100 \rangle$  are less likely, in accord with our experimental observations.

#### 10.2.4

#### Comparison between Metal Catalyst VLS Growth and OAG

To end this section we note that the OAG is vastly different from the metal-catalyst VLS growth. The two vary in the growth mechanism, in the growth conditions, in the yield of the grown wires in their abundant growth direction, in their diameters and in the chemical purity. Figure 10.7 compares schematically the two processes

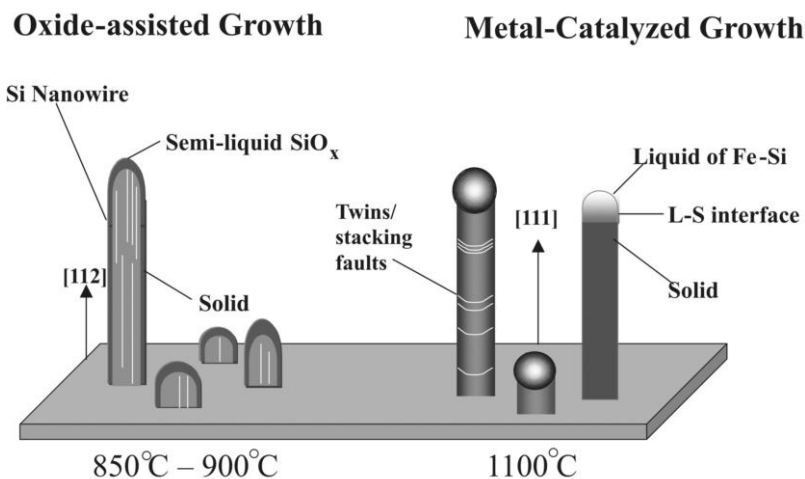


**Fig. 10.7.** Schematic comparison of the laser ablation of SiNWs via metal catalyst (VLS method) and the oxide assisted growth of SiNWs by thermal evaporation.

and Table 10.1 summarizes these differences between metal-free OAG and Fe or Ni catalyst VLS growth under the same conditions. Understandably, in the metal catalyst VLS growth, the characteristics of the grown nanowires depend on the nature of the metal catalyst used. When silane is used with Au nanoparticles, the growth temperature of SiNWs can be as low as 370 °C or close to the eutectic point of Au and Si alloy [56]. Furthermore, our recent work [57] shows that, like silane, SiO or other Si-containing vapor in the presence of Au nanoparticles or films could also decompose and lead to the growth of SiNWs, and the growth temperature was as low as 700 °C. We anticipate that nanoparticles of other kinds of metals can also induce the deposition of SiNWs from SiO vapor, providing the metal can induce SiO decomposition and form a eutectic alloy with Si.

**Tab. 10.1.** OAG versus metal catalyst VLS growth in a 3 in diameter tube.

Property	Oxide-Assisted Growth	Metal Catalyst Growth
Source	SiO; Si + SiO <sub>2</sub>	(Fe or Ni) + Si
Growth temperature	850–900 °C	>1100 °C
Pressure	10–800 Torr	10–800 Torr
Yield	3 mg h <sup>-1</sup>	<0.1 mg h <sup>-1</sup>
Impurity	None	Metal
Tip composition	SiO <sub>x</sub>	Metal
Wire diameter	Typically 2–20 nm	Typically > 10 nm
Growth direction	Mostly <112> & <110>	<111>
Morphologies	Nanowires, nanoribbons, nanochains	nanowires



### 10.3

#### Control of SiNW Nanostructures in OAG

##### 10.3.1

##### Morphology Control by Substrate Temperature

One of the most important issues of nanomaterial growth is the control of the morphology. This can be done by varying different process parameters. The effect of the growth temperature on the structure of the Si nanowires has been studied systematically [32, 33].

The substrate temperature substantially affects the SiNW growth in several ways: (1) determination of the growth process (metal catalyst VLS growth or OAG), (2) determination of the SiNW shape in the growth process itself (e.g. the SiNW diameter), (3) annealing effects that change the structure and morphology of the SiNW after its formation. Examples of these effects were given in our study of SiNWs deposited by laser ablation of a mixture of Si,  $\text{SiO}_x$  and metals (the metallic constituent introduced either intentionally or as impurities or contamination of the system). The study was focused on the nature of the nanostructures produced on the substrate at temperatures ranging from 850 to 1200 °C.

The Si nanostructures produced in this temperature region can be divided to two groups: (1) Region I (1200~1100 °C) forming nanostructures by the metal catalyst VLS process (indicated by the presence of metallic caps), (2) Region II (1100~850 °C) where the OAG process is dominant (the nanostructures do not have metallic caps). HRTEM analysis of samples prepared in region I (temperatures of 1190, 1160, and 1130 °C denoted I1, I2 and I3) and region II (temperatures 1050, 950, and 900 °C denoted II1, II2 and II3) revealed the structure evolution at different temperatures.

In region I the diameter of the SiNWs (all single-crystalline SiNWs) decreases with temperature (200, 80 and 50 nm for 1190, 1160 and 1130 °C respectively) as shown in Figure 10.8. While the first two types of nanowires are straight, continuous ones, the third one has a tadpole-like shape and appears to be broken into short Si rods. The head of the tadpoles is crystalline Si, while the tail of the tadpoles is amorphous  $\text{SiO}_x$ .

In region II the diameter of the Si nanostructures is constant (~20 nm), but their shape changes from tadpole-like through chain-like to wire-like as the temperature decreased from 1050, through 950, to 900 °C respectively. The wires have  $\text{SiO}_x$  caps rather than metallic caps, and are encapsulated in a  $\text{SiO}_2$  sheath, all indicative of an OAG process.

We will now explain these results as a combination of: (1) the dominant growth process (metal-assisted VLS or OAG) and (2) extended annealing of Si nanowires at high temperatures.

Region I is characterized by a metal catalyst VLS growth, as indicated by the metal caps on top of the nanostructures. The diameter of the nanowires in this growth process is determined by the diameter of the liquid alloy droplet at their tips. Metal silicide clusters of different sizes are present in the flowing gas above

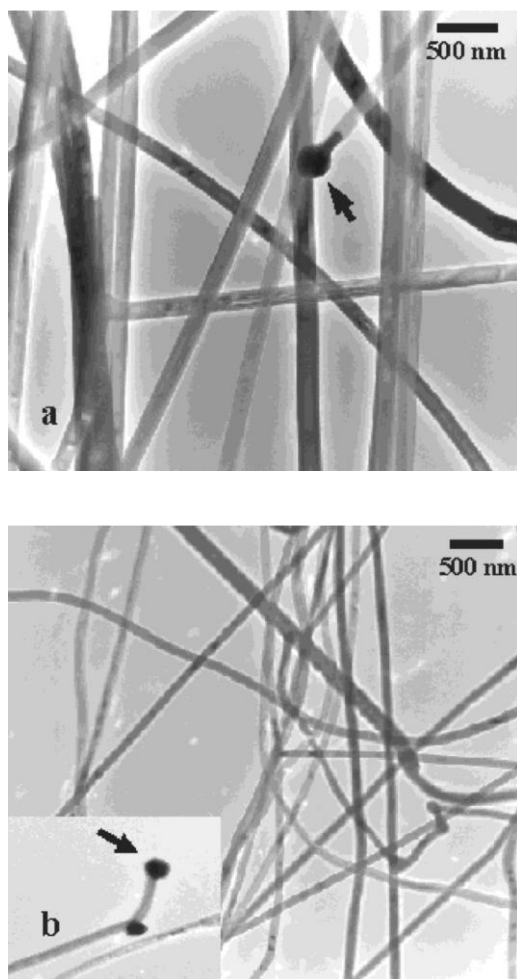


**Fig. 10.8.** Bright-field TEM images showing the typical morphology of Si nanowires grown at: (a) 1190, (b) 1160, and

the substrate, leading to condensation of droplets when the substrate temperature is lower than the melting point of the metal silicide clusters. The melting point of the nanoclusters decreases with decreasing size in the nanometer region. Large droplets will melt and serve as SiNW nucleation sites at higher temperatures than small droplets, explaining the decrease in the SiNW diameter with decreasing temperature. Figure 10.8(d) gives a schematic diagram of the SiNW evolution at different temperatures. The size of the molten droplets decreases with temperature (d1). The droplet absorbs Si-containing clusters from the vapor and becomes supersaturated with Si. The excessive Si precipitates out, resulting in the 1D growth of crystalline SiNWs shown in Figure 10.8(d2) the diameter of which follows that

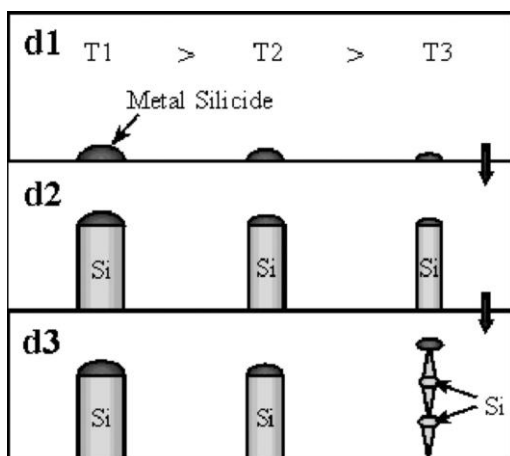
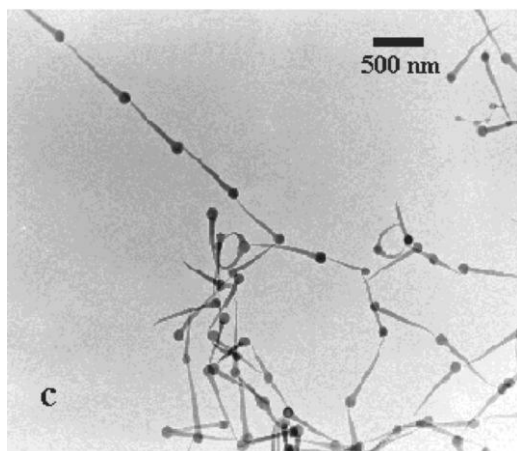


**Fig. 10.8.** (c) 1130 °C. The arrows reveal the metal catalyst present at the tip of the nanowires. The diameter of the Si nanowires can be seen to decrease with decreasing

growth temperature. (d) Diagram showing the morphology evolution of Si nanowires with time in region I: (1) nucleation, (2) growth, and (3) annealing [33].

of the initial droplet. The formation of the SiNWs is restricted to the temperature region for which the temperature is high enough so that the solid particle melts and forms a liquid droplet (lower temperature of region I) on the one hand, and the temperature is low enough to melt and condense from the vapor (upper temperature region) on the other hand. Previous work on Si whiskers revealed that there is a critical whisker diameter at which growth stops completely, due to the Gibbs–Thomson effect [58]. This may be the reason why the smallest nanowires obtained in region I have diameters larger than 50 nm (Figure 10.8). Figure

10.8(d3) shows a spheroidization effect for the smaller diameter nanowires, which is attributed to annealing of the nanowires, as will be described later.

In region II, the OAG region, the diameters of the Si nanowires are quite uniform, irrespective of the substrate temperature. This may be explained by a vapor-solid (VS) process governing the initial nucleation of the OAG rather than a VLS process in which the size of the liquid droplet decreases with decreasing energy, leading to a respective decrease in the SiNW diameter as discussed above (for the metal catalyst growth). This would mean that the small nuclei of crystalline Si nanowires were directly solidified from SiO in the vapor phase. This explanation is, however, not in accord with the formation of a  $\text{SiO}_x$  cap on the top of the SiNW and the alternative proposition that the oxide-assisted nucleation and growth is occurring due to: (1) the lower melting point of  $\text{SiO}_x$  compared to that of  $\text{SiO}_2$ , (2) the high reactivity of the molten  $\text{SiO}_x$  cap to Si-containing clusters in the vapor, and (3) the decomposition of Si suboxide to Si and  $\text{SiO}_2$ . We proposed that the  $\text{Si}_n\text{O}_m$  clusters react with the  $\text{SiO}_x$  cap, the crystalline Si core precipitates below and the excess oxygen diffuses to the sides forming a  $\text{SiO}_2$  amorphous outer layer which solidifies, due to its higher melting point, and limits the further lateral growth of the nucleus. The lateral growth results from the energetically favorable adsorption of vapor clusters by the highly curved  $\text{SiO}_x$  molten tip on the one hand and the lateral restriction imposed by the solid  $\text{SiO}_2$  sheath on the other hand (as shown in Figure 10.9(d2)). The SiNW diameter may be determined not only by the diameter of the initial  $\text{SiO}_x$  droplet, but also by the equilibrium between the condensation and the disproportionation of SiO to Si and  $\text{SiO}_2$  and by diffusion of the excess O to the sides. It is still not completely understood why this equilibrium is not temperature-dependent under our experimental conditions. It could be that the dependence is weak in this limited temperature region and will be revealed if we enlarge this region by using different experimental conditions.

The SiO vapor phase is stable at a high temperature, so that the condensation and disproportionation of the SiO vapor into  $\text{Si} + \text{SiO}_2$  occurs only below a certain substrate temperature (the upper limit of region II). On the other hand, below the lower limit in region II the SiO vapor condenses directly to form SiO solid [59], with no preferential adsorption nor disproportionation, so that the 1D growth is suppressed. This explains why the OAG of SiNWs was restricted to the temperature range 1100–850 °C (region II).

Finally, we discuss the formation of tadpole-like and chain-like Si nanostructures from the metal-catalyst VLS and the OAG (Figures 10.8 and 10.9) processes. Both can be described in terms of a spheroidization mechanism. One-dimensional SiNWs are less stable than the three-dimensional bulk Si, since the wire has a much larger surface area and thus higher surface energy. Annealing of SiNWs for a sufficient time results in spheroidization, as shown schematically in Figure 10.10. The chemical potential of the SiNWs varies with the local curvature so that small variations in their diameter generate a driving force for diffusive transport between different chemical potentials. The Si nanowire would convert into a nanospherical chain first (as shown schematically in Figure 10.10 and experimentally in Figure 10.9(b)). Later, with further diffusion, the inner crystalline Si core

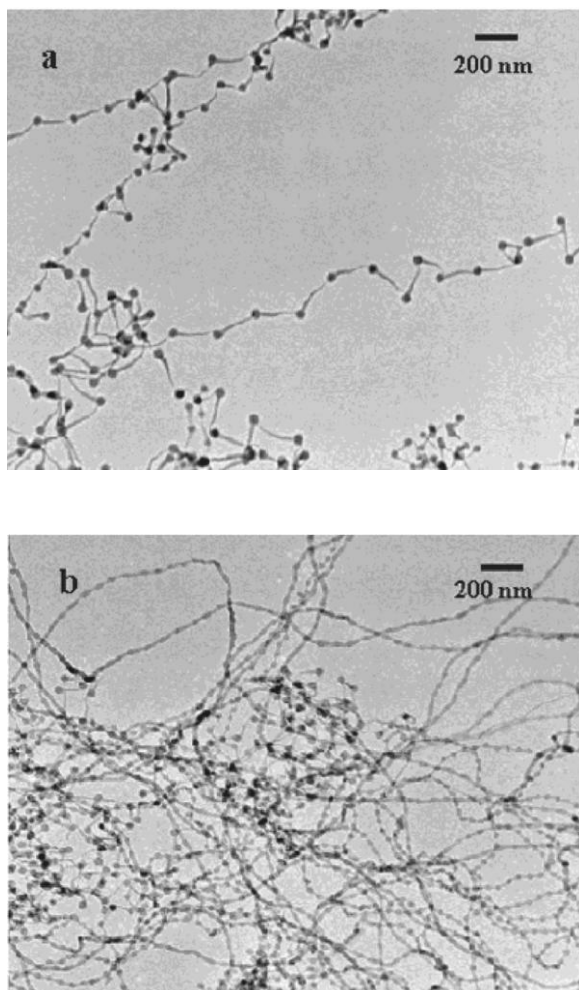


**Fig. 10.9.** Bright-field TEM images showing the typical morphology of Si nanowires grown at: (a) 1050, (b) 950, and

would break up and the spheroidization would become faster due to the larger variations increasing the driving force. The amorphous  $\text{SiO}_x$  nanorods connecting the Si nanospheres then become thinner, and eventually break up. This is why the Si nanosphere chains convert into tadpole-like Si nanorods (as shown schematically in Figure 10.10 and experimentally in Figures 10.9(a) and 10.8(c)). Eventually, the amorphous  $\text{SiO}_x$  tails would disappear and perfect Si/Si oxide spheres might also be formed. Note now the difference between Region I, in which the spheroidization occurs only at the lower temperature (Figure 10.8), and region II, where spheroidization is more significant at higher temperatures (Figure 10.9). In region I the first two SiNWs grown at 1190 and 1160 °C are too thick (200 and 80 nm re-

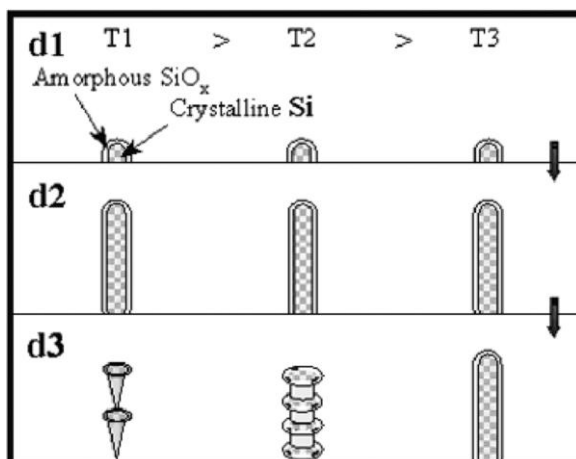
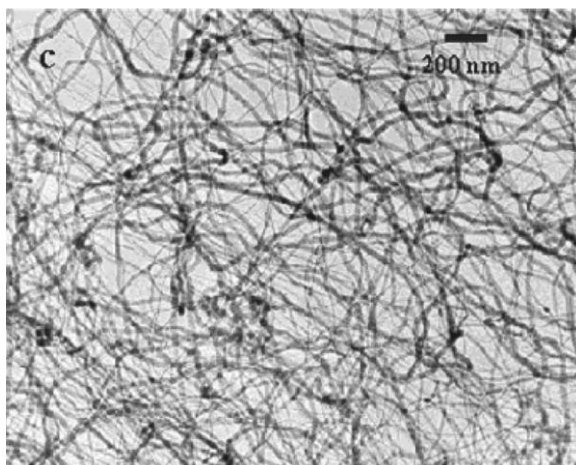


**Fig. 10.9.** (c) 900 °C. The SiNW diameter is independent of the growth temperature. (d) Diagram showing the morphology evolution of Si nanowires with time in region II: (1) nucleation, (2) growth, and (3) annealing [33].

spectively) for spheroidization, which is observed only at the lower temperature of 1130 °C (Si nanowire diameter 50 nm), in spite of the higher diffusion rate at higher temperatures. In region II, however, the SiNW diameter is relatively constant with temperature, so the diffusion rate increases with temperature and the spheroidization becomes more significant at higher temperatures.

We have, until now, discussed the spheroidization process in the context of the formation of different Si nanostructures by varying the substrate temperature at which these structures evolve. One of the structures reported was nanochains of Si

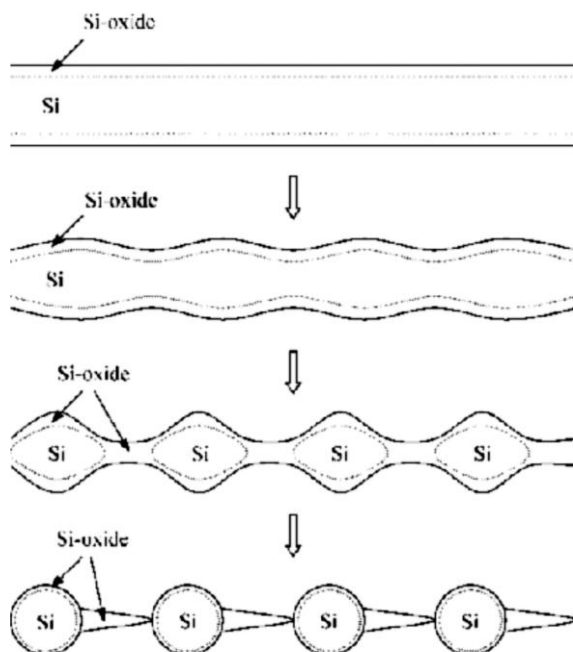


Fig. 10.10. Diagram showing the spheroidization process of one-dimensional Si nanowires [33].

nanospheres enclosed in and linked together to form a chain by  $\text{SiO}_2$ . Similar silicon nanochains (SiNC), this time of boron-doped Si were grown [60, 61] by laser ablation of a compressed target of a mixed powder of  $\text{SiO}$  and  $\text{B}_2\text{O}_3$  at  $1200^\circ\text{C}$ . TEM analysis including imaging (Figure 10.11), diffraction and EDS indeed verifies a structure of nanochains with uniform diameters of the Si nanospheres con-

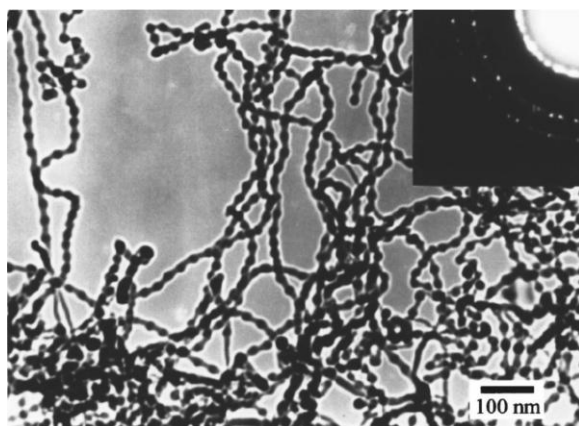


Fig. 10.11. TEM image showing the morphology of Si nanochains.



nected by amorphous  $\text{SiO}_2$ , like a chain of pearls. The SiNC consists of knots and necks with equal distances between them. The average diameters of the knots and necks are 15 and 4 nm, respectively and the thickness of the  $\text{SiO}_2$  sheath surrounding the Si spheres is about 2 nm. The product is uniform with no isolated particles and consisting of 95% SiNC and 5% SiNWs.

To summarize, both the growth process and the morphology of SiNWs can be controlled by the growth temperature. The temperature required for a metal catalyst growth (using iron as the catalyst, for gold the temperature would be much lower) is higher than that required for the OAG. Post-growth annealing results in spheroidization and structural changes which occur faster at higher temperatures. The diameter control by temperature is readily possible for the metal catalyst VLS method but appears to be difficult for the OAG.

### 10.3.2

#### Diameter Control of Nanowires [29]

The motivation for the study of nanomaterials stems from the expected size effects; SiNWs are no exception. This makes the issue of diameter control very important. In a previous section we have shown that the growth temperature affects the diameter of the SiNWs grown by the metal catalyst VLS method but not the diameter of SiNWs grown by the OAG method. Here we show that the SiNW diameter can be affected by the carrier gas used in the growth process.

The SiNWs were synthesized by laser ablation of a target made by compaction of a mixed powder of 90% Si and 10%  $\text{SiO}_2$ . Different carrier gases were used including He,  $\text{N}_2$ , and a mixture of Ar with 5%  $\text{H}_2$ . During growth the carrier gas pressure was about 300 Torr and the flow 50 sccm. The substrate growth temperature was  $\sim 930^\circ\text{C}$ . No deposition was observed at places where the temperature was higher than  $\sim 950^\circ\text{C}$ , while some nanoclusters and amorphous mixtures of Si and oxygen were deposited at lower temperature regions (for  $\text{N}_2$ ). The SiNWs synthesized in He and in Ar (5%  $\text{H}_2$ ) consisted almost entirely of nanowires. Some spherical particles, with diameters ranging from  $\sim 9$  nm to several hundred nm, composed of a mixture of crystalline Si and amorphous Si oxide, were found to coexist with the nanowires grown in a  $\text{N}_2$  atmosphere, and the quantity of the spherical particles was a little less than that of the SiNWs. Most of the SiNWs were smoothly curved with some short straight sections, a few possessed bends and kinks. The SiNWs synthesized in a He atmosphere possessed many more bends and curves.

The diameter distributions of the SiNWs were measured from the TEM micrographs as given in Figure 10.12. The SiNWs (up to several mm long) had a distribution of diameters (Si core plus  $\text{SiO}_2$  sheath) peaked at 13, 9.5 and 6 nm for carrier gas mixtures of He, (5%  $\text{H}_2$  in Ar) and  $\text{N}_2$  respectively. The smallest wires were mixed with spherical particles with diameters ranging from  $\sim 9$  nm to several hundreds of nm. High-resolution TEM images of several SiNWs produced in He, Ar (5%  $\text{H}_2$ ), and  $\text{N}_2$  atmospheres shows that every nanowire consists of a crystalline Si core and an amorphous  $\text{SiO}_2$  sheath. The crystalline Si core has many lat-

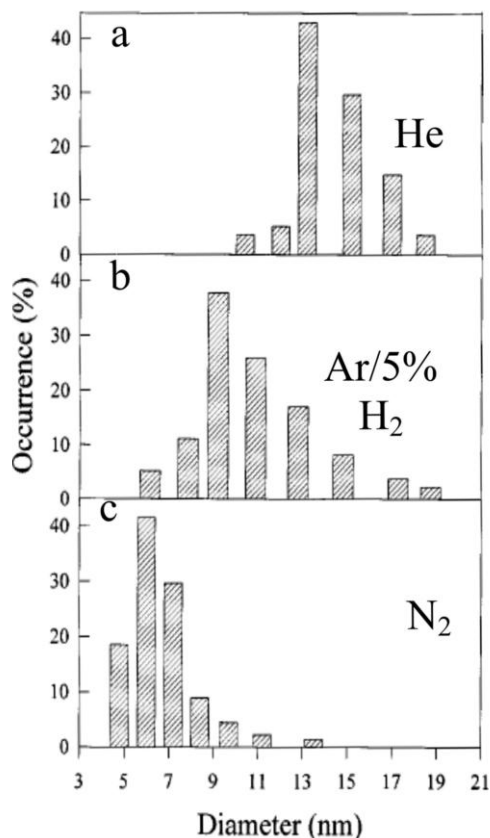


**Fig. 10.12.** Size distribution of SiNWs synthesized by laser ablation using different carrier gases [29]: (a) He, (b) Ar (5% H<sub>2</sub>), and (c) N<sub>2</sub>.

tice defects. The nanowires consisted of only Si and oxygen with no ambient gas atoms, as determined by EDS and XPS.

The mechanism by which the carrier gas affects the growth and diameter of the SiNWs is not clear. We propose that the ambient atoms affect the formation and transport of nanoclusters and the phase separation process at the growth front of SiNWs. We suggest that the dominant effect of the ambient is on the phase separation. First, the thermal conductivity of the ambient affects the cooling rate of the nanoclusters and thus the rate of phase separation. Second, the inert gas atoms are very likely incorporated in the deposited matrix at the growing tips of SiNWs, and their presence would influence the phase separation process, despite their eventual outdiffusion. Helium is smaller, faster moving, and more thermally conducting than N<sub>2</sub>. The collective effect of these processes leads to a slower supply of heat by N<sub>2</sub> and thus faster cooling of nanoclusters. This, in turn, results in faster phase separation and the formation of thinner SiNWs. The fast cooling and elemental

incorporation in the nanoclusters formed in an  $N_2$  environment probably leads to incomplete phase separation and to the formation of the remnant spherical particles. The Ar (5%  $H_2$ ) mixture is suspected to exert an intermediate effect between  $N_2$  and He, thus giving rise to nanowires of intermediate diameters.

### 10.3.3

#### Large-Area Aligned and Long SiNWs via Flow Control [62]

Until now we have discussed the effect of two parameters on the SiNW growth: temperature and carrier gas. Now we show that the carrier gas flow can be exploited as well. In this particular example we use it to grow millimeter-area arrays of highly oriented, crystalline silicon nanowires of millimeter length.

The growth in this particular case was performed by thermal evaporation of  $SiO$  powder. A carrier gas of argon mixed with 5%  $H_2$  was used with a flow of 50 sccm at 400 Torr. The furnace temperature was 1300 °C, while the growth temperature was about 930 °C.

Large area (about 2 mm × 3 mm) of highly oriented, long (up to 1.5–2 cm) nanowires were grown on the surface of the silicon substrate under these conditions, as detected by SEM (Figure 10.13). The thickness of the oriented nanowire product was about 10 μm, as estimated from the cross-sectional image (Figure 10.13(b)) of the sample prepared by focused ion beam cutting. EDX shows that the nanowires are composed of silicon and oxygen with no metal impurities, suggesting an oxide assisted growth. Figure 10.13(c) shows the typical morphology of SiNWs. TEM shows that the SiNWs are quite clean, with very few particles attached to their surfaces, and are relatively homogeneous. The SiNW diameters vary from 18 to 46 nm, and the mean value is about 30 nm.

HRTEM shows the typical SiNW Si core encapsulated by a  $SiO_2$  sheath and the {111} planes of crystalline silicon. The diameters of the crystalline silicon core varied from 13 to 30 nm, and the mean value was about 20 nm. The thickness of the amorphous silicon oxide shell varied from 2 to 10 nm, and the mean value was about 5 nm.

The growth of the oriented SiNWs may be related to the flow of the carrier gas, because it was found that the orientation direction of the SiNWs is parallel to the direction of flow of the carrier gas in the alumina tube. A mechanism for the growth of the oriented silicon nanowires is illustrated below. First, the nucleation of silicon nanowires from silicon oxide ( $SiO_x$ ) vapor started at the proper position on the substrates. Because there was a temperature gradient along the alumina tube, and the planes with the same temperature were perpendicular to the axial direction of the tube, only some particular positions with the appropriate temperature may be suitable for the nucleation of SiNWs [21, 27]. These positions should be located on a line of equal temperature on the substrate and will also be perpendicular to the flow direction of the carrier gas. Once initial nucleation is established, nanowire growth will tend to continue on the substrate. Secondly, the strength of the flow of the carrier gas will force the growing nanowires to grow in

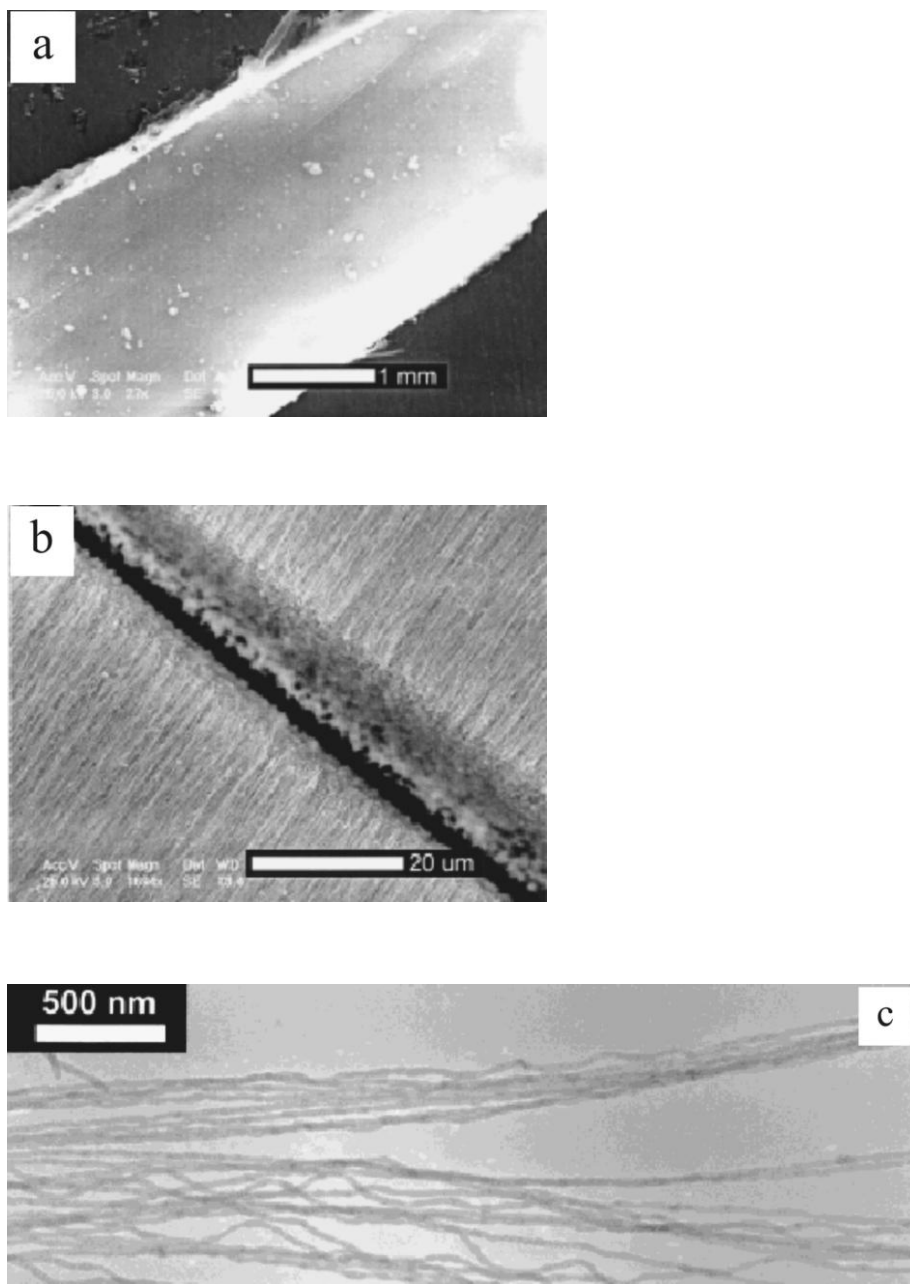


**Fig. 10.13.** (a) SEM image of oriented SiNWs at low magnification; (b) The cross-section of the SiNW in (a) cut by a focused ion beam; (c) TEM image of the oriented silicon nanowires [62].

the direction of the flow. At the same time, overcrowding of the nanowires will limit the possibility of nanowire propagation in other directions [63]. In addition, it was found that a smooth plane substrate is very helpful for oriented growth.

#### 10.3.4

##### Si Nanoribbons

SiNWs are a 1D nanostructure. A distinct feature of the OAG process revealed in our studies is the variety of different configurations it can form. Some were discussed in the previous sections. Now we present an exciting and unexpected 2D configuration, nanoribbons, discovered in the course of studying OAG. A 2D configuration is not expected to exhibit the same magnitude of size effects as a 1D structure, but it may be advantageous in processing and in obtaining signals with more measurable intensities in single object characterization.

The single-crystal silicon nanoribbons were grown by simple thermal evaporation of silicon monoxide (SiO) heated to 1150 °C. No templates or catalysts were used. The nanoribbons have a thickness of only about 10–20 nm (average 15 nm), widths of several hundreds of nanometers (50–450 nm), and lengths of many micrometers [34]. Most of the ribbons have rippling edges (Figure 10.14(a)), and a small portion of the ribbons has smooth edges (Figure 10.14(b)). Due to their small thickness the ribbons seem transparent in TEM imaging (Figure 10.14(b)) using 200 keV electrons. Nanoribbons of different width and morphology have a similar thickness which is constant throughout each individual ribbon. In the typical nanoribbon shown in (Figure 10.14(b)) the thickness is about 14 nm and the width is about 370 nm. The thickness to width ratio of the SiNWs varies from 4 to 22. The rippling and curling features at the edge of most ribbons also confirm that the nanoribbons are quasi-2D structures distinctly different in shape from the 1D SiNWs.

HRTEM imaging of a single nanoribbon revealed that the ribbon has a crystal core nipped by amorphous layers with atomically sharp interfaces. The in-plane layers of the nanoribbon were determined to be silicon (110) facet with a perfect atomic, defect-free, single-crystal structure grown along the  $\langle 111 \rangle$  direction. This direction is different from the predominant  $\langle 112 \rangle$  and  $\langle 110 \rangle$  direction of SiNWs synthesized by the OAG method. It is the same as the most abundant growth direction of Si nanowires synthesized by the metal catalyzed VLS method. The wide part of the ribbon is along the  $\langle 112 \rangle$  direction. The amorphous edges of the ribbon consist of silicon oxide ( $\text{SiO}_x$ ), as determined by EDS and EELS attached to the TEM. The width of the amorphous edge is about 10 nm. Analysis of a number of nanoribbons with different widths shows that the width of the oxide edges varies from 3 to 25 nm, similar to the thickness of the amorphous silicon oxide shell of the nanowires synthesized by OAG. The thickness of the oxide layer covering the flat surfaces of the ribbons is much less than the width of the oxide edges; that is, the thickness of the oxide layers is anisotropic. This result may be understood in terms of the OAG process, in which the silicon oxide shell was formed by the re-

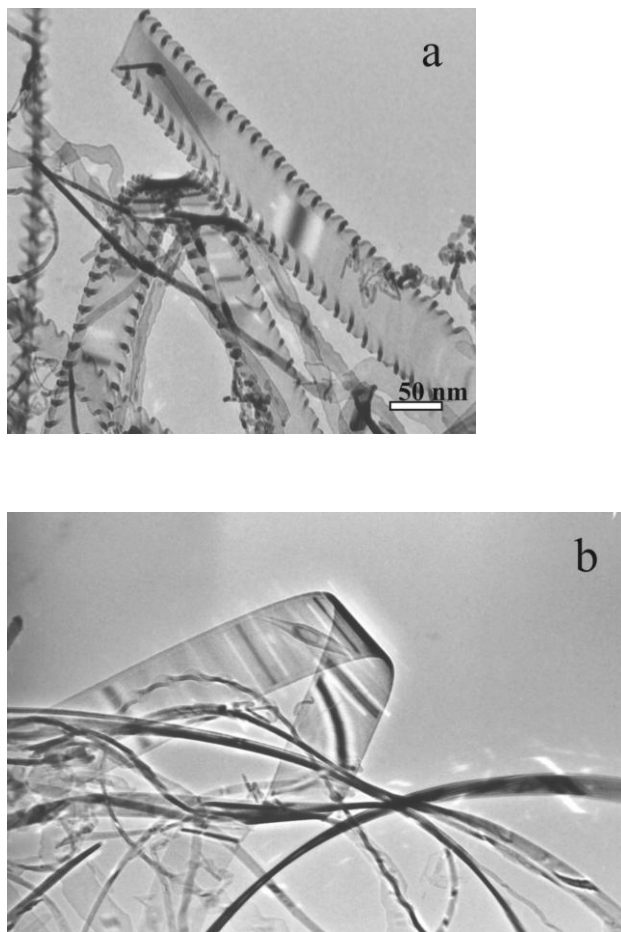


**Fig. 10.14.** TEM images (TEM, Philips CM 20 TEM at 200 kV) of (a) rippling-edge nanoribbons, and (b) a smooth-edge nanoribbon. The thickness of the ribbons is about 14 nm [34].

action of  $\text{SiO} + \text{SiO} = \text{Si} + \text{SiO}_2$ , and subsequently separated from the silicon core during growth. According to this reaction, the amount of segregated silicon oxide is proportional to the amount of silicon at the same place.

The growth of Si nanoribbons cannot be via the twin-plane growth mechanism, (i.e. controlled by a twin plane parallel to the flat surface of the nanoribbons) as suggested for microribbons [64]. A twin-plane mechanism is impossible from crystallographic considerations taking into account the observed structure of the nanoribbons and, indeed, no twins were observed. The precise growth mechanism of the nanoribbons is not yet clear, but it is likely that it is governed by anisotropic

growth kinetics along different crystallographic directions (i.e. two fast growing directions).

#### 10.4

#### Nanowires of Si Compounds by Multistep Oxide-Assisted Synthesis

##### 10.4.1

##### Nanocables [65]

Coaxial three-layer cables offer a potentially simple way of producing nanojunctions. The idea of applying the nanocable configuration was indeed recently reported by Iijima et al. [66]. Such nanocables can be produced by a multistep process. We give as an example a coaxial three-layer nanocable synthesized by combining high-temperature laser ablation of SiC as the first step, and thermal evaporation of SiO at a higher temperature as the second step. Figure 10.15 is a TEM image showing the structure of the nanocables synthesized. Uniform, tens of micrometer long nanocables with diameters smaller than 150 nm were formed. The nanocables were made of: (1) a crystalline Si core with a diameter ranging from 30 to 50 nm, (2) an amorphous SiO<sub>2</sub> interlayer (second layer) 12–23 nm thick, (3) an amorphous carbon sheath (external third layer) 17–31 nm thick. The average dimensions of the nanocable are: core 43 nm in diameter, second layer 16 nm thick, and third layer 24 nm thick. The interfaces between the layers are sharp. Most of the products were nanocables but small amounts of Si and SiC nanowires were also detected.

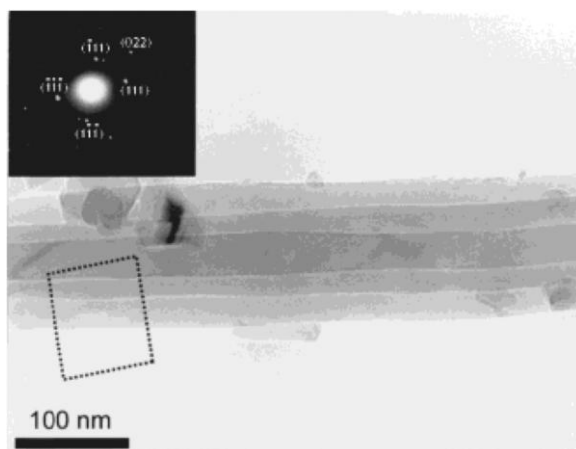


**Fig. 10.15.** A magnified image of the coaxial nanostructure, showing a crystalline core and two additional amorphous layers (a-SiO<sub>2</sub> and a-C). The inset shows the selected area diffraction pattern [65].



## 10.4.2

**Metal Silicide (MS)/SiNWs from Metal Vapor Vacuum Arc Implantation [67]**

A conventional method to produce contacts in the semiconductor industry is ion implantation. The possible advantages of ion implantation for SiNWs are in the control in adding precise (and small) amounts of metal atoms to SiNWs, which might be difficult for bulkier techniques. Here we describe ion implantation of Ni and Co into 20 nm diameter SiNWs produced by thermal decomposition of SiO. The SiNWs were mounted on copper folding grids and directly implanted by metal vapor vacuum arc (MEVVA) implantation with a 5 keV Ni<sup>+</sup> or Co<sup>+</sup> dose of  $1 \times 10^{17} \text{ cm}^{-2}$  at room temperature. The implanted samples were later annealed in argon.

Ni implantation results in the formation a Ni silicide layer on the implanted SiNW surface. The layer contains lots of defects. Rapid thermal annealing (RTA) at 500 °C smoothed the surface of the Ni-implanted SiNWs, which was transformed to a continuous outer layer with a typical thickness of about 8 nm, as shown in Figure 10.16.

The Co-implanted SiNWs surface is much rougher than that of the Ni-implanted surface with isolated CoSi<sub>2</sub> particles 2–40 nm in diameter (Figure 10.17).

The generation of NiSi<sub>2</sub> and CoSi<sub>2</sub> is schematically described in Figure 10.18. Room temperature Ni<sup>+</sup> or Co<sup>+</sup> implantation of the as-grown SiNWs (Figure 10.18(a)) results in the formation of a metal/Si mixture (Figure 10.18(b)). The energy of the ion beam should be optimized (5 keV in the present experiment) to avoid excessive damage of the SiNWs. Post-implantation annealing was found to be efficient in reducing the ion implantation damage. The metal silicides are expected to give an improved electrical conductivity of the SiNWs and provide electrical contacts to the SiNWs. The structure of the MS/SiNWs layer is sensitive to

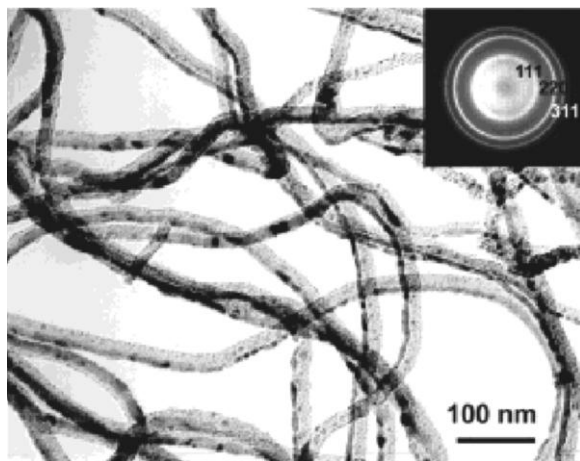


**Fig. 10.16.** Ni implanted SiNWs annealed at 500 °C. The inset shows the TED pattern of the Ni layer [67].

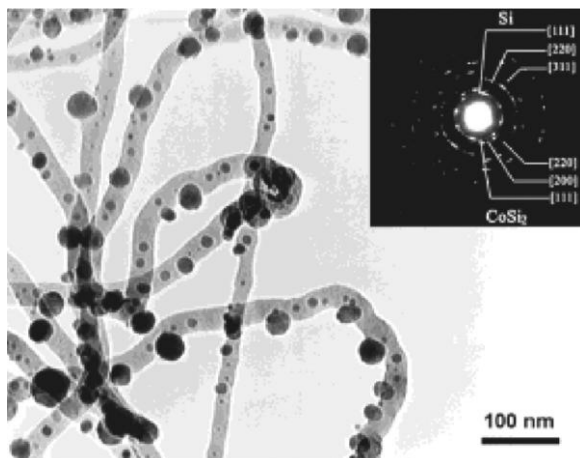


**Fig. 10.17.** Co implanted SiNWs annealed at 900 °C. The inset shows the TED of the Co polycrystals [67].

annealing treatment. Under proper annealing conditions, the MS layer can exhibit a highly oriented relationship to the SiNW core.

#### 10.4.3

#### Synthesis of Oriented SiC Nanowires [68]

One of the fascinating options opened by the OAG method is the possibility of transforming from one type of nanowires to the other. A notable example is the

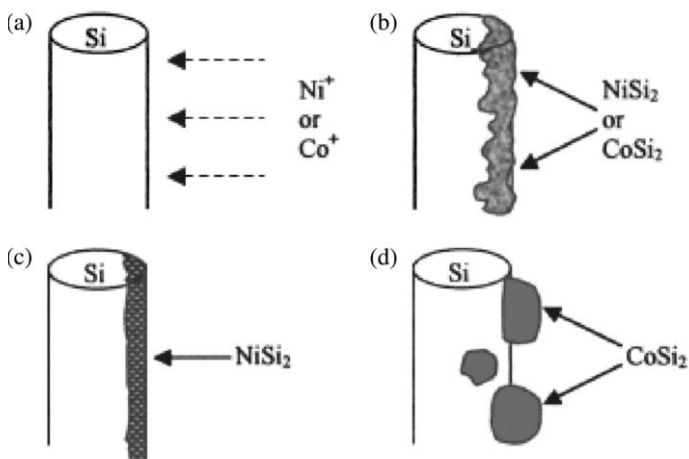


**Fig. 10.18.** The formation mechanism of  $\text{NiSi}_2/\text{Si}$  and  $\text{CoSi}_2/\text{Si}$  on the surface of bare SiNWs [67]. (a) Bare SiNWs implanted with metal ions. (b) Formation of the metal/Si

mixture layer on one side of SiNW. (c) The  $\text{NiSi}_2/\text{Si}$  nanowire after low temperature annealing. (d)  $\text{CoSi}_2$  nanoparticles formed by coarsening at high temperature annealing.

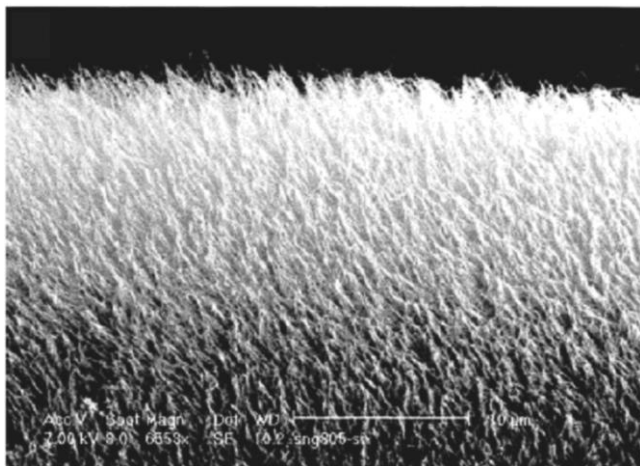


**Fig. 10.19.** SEM images of oriented SiC nanowire array showing high density of well-separated, oriented nanowire tips [68].

synthesis of oriented SiC nanowires by reacting SiO with aligned carbon nanotubes prepared via the established method of pyrolysis of acetylene over film-like iron/silica substrates [69, 70, 71]. Solid SiO powders (purity 99.9%) were placed in a graphite crucible and covered with a molybdenum grid. The highly aligned carbon nanotubes were placed on the molybdenum grid. The crucible was covered with a graphite lid, placed in the hot zone inside the alumina tube, and held in a flowing argon atmosphere (50 sccm) at 1400 °C for 2 h. After reaction, the aligned carbon nanotube arrays were converted to oriented SiC nanowire arrays. These highly oriented SiC nanowires were similar in appearance to the original aligned carbon nanotubes. The bottom end of the nanowire array is composed of a high density of well-separated and highly oriented nanowire tips (Figure 10.19). TEM (Figure 10.20(a)) imaging and diffraction showed that the transformed wires are single crystalline  $\beta$ -SiC with the wire axes along the (111) direction and a high density of stacking faults perpendicular to the wire axis. In contrast to the carbon nanotubes (Figure 10.20(b)) the SiC were full wires and not hollow tubes.

## 10.5

### Implementation of OAG to Different Semiconducting Materials

The OAG method has a general nature and can be applied to a variety of materials other than Si. Based on the OAG method, we have synthesized nanowires of a wide range of semiconducting materials including Ge [35], GaN [36, 37], GaAs [38, 39], GaP [41], SiC [40], and ZnO (whiskers) [42]. The actual OAG process was activated by laser ablation, hot-filament chemical vapor deposition (HFCVD) or thermal evaporation.

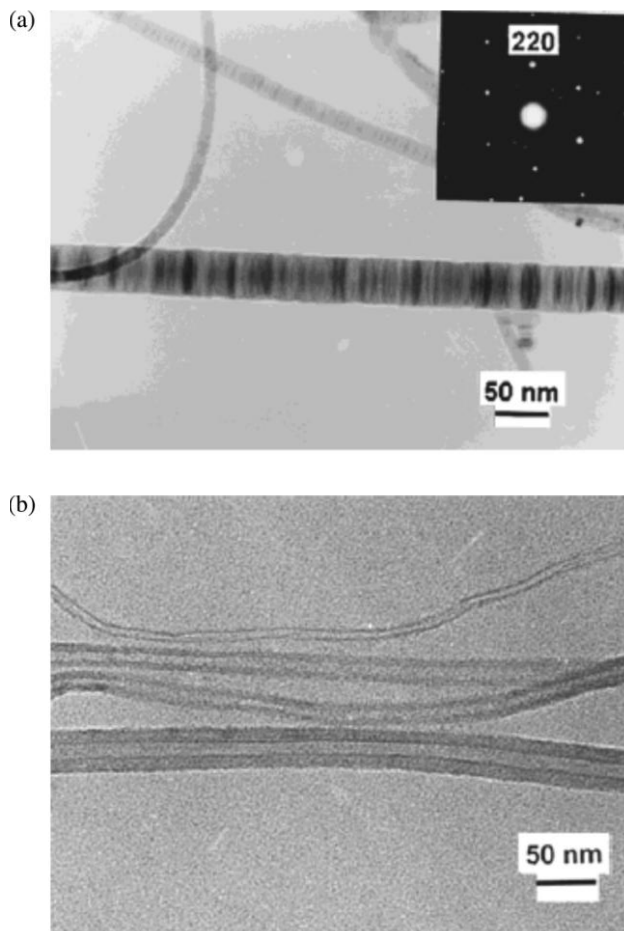


**Fig. 10.20.** (a) TEM image of  $\beta$ -SiC nanowires. The SiC nanowires exhibit a high density of stacking faults perpendicular to the wire axes. The inset shows a selected area electron diffraction pattern of the  $\beta$ -SiC nanowires. (b) TEM image of the initial carbon nanotubes. Note the transition from tubes to filled SiC wires [68].

Similar to the production of Si nanowires, we used laser ablation of a mixed  $\text{GeO}_2/\text{Ge}$  target to synthesize Ge nanowires at 830 °C. In comparison, Morales and Lieber [21] used metal-containing targets for the same purpose. We show that Ge nanowires are obtained by the OAG method in an analogous way to SiNWs. TEM studies (Figure 10.21) show that the structure of the Ge nanowires is similar to that of SiNWs, with a crystalline Ge core and a thick amorphous oxide shell. The diameters of the Ge nanowires in this particular experimental set-up had a larger size distribution than that of SiNWs (ranging from 16 to 370 nm).

Gallium arsenide nanowires with a zinc-blende structure were fabricated by laser ablation of GaAs powders mixed with  $\text{Ga}_2\text{O}_3$  (no metal catalyst used). SEM obser-



**Fig. 10.21.** A TEM image of Ge nanowires and a selected-area electron-diffraction pattern (inset) [35].

vation (Figure 10.22(a)) shows that the product consists of wire-like structures with length up to 10  $\mu\text{m}$  and diameters of the order of 50 nm. The EDX spectrum shown in the inset of this figure demonstrates that the nanowires consist only of gallium, arsenic and oxygen. The silicon signal originates from the silicon substrate. HRTEM, selected-area electron diffraction (SAED) and electron energy-loss spectrometry (EELS) of individual nanowires (Figure 10.22(b)) revealed a zinc-blende GaAs core enclosed in a gallium oxide ( $\text{GaO}_x$ ) sheath. The [111] growth direction of the present nanowires is the same as that of GaAs nanowires grown by a metal-catalyzed VLS process [72]. The diameter of the crystalline GaAs cores range from 10 to 120 nm with the thickness of the outer sheath ranging from 2 to 10 nm. The average diameter of the core was about 60 nm, and the average thickness of the outer sheath was 5 nm. As expected from an OAG process, the crystalline GaAs tip was coated with a thin amorphous layer of  $\text{GaO}_x$ , similar to the  $\text{SiO}_x$  tip of SiNWs, and different from the GaAs nanowires synthesized by the metal catalyzed VLS growth, in which the tips were terminated at metal-alloy nanoparticles [72].

We can thus suggest that the oxide-assisted nucleation and growth of GaAs nanowires advances through the following reactions: (1) laser-induced decomposition of GaAs into Ga and As, (2) reaction of  $4\text{Ga} + \text{Ga}_2\text{O}_3 = 3\text{Ga}_2\text{O}$  in the high-temperature zone, (3) transport of volatile  $\text{Ga}_2\text{O}$  and As to the low-temperature-deposition zone, (4) reaction of  $3\text{Ga}_2\text{O} + 4\text{As} = 4\text{GaAs} + \text{Ga}_2\text{O}_3$  in the low-temperature-deposition zone leading to the nucleation and growth of the GaAs nanowires.

The above model similarly applies to the successful synthesis of GaN and GaP and other binary compounds. Figures 10.23 and 10.24 show the typical HRTEM

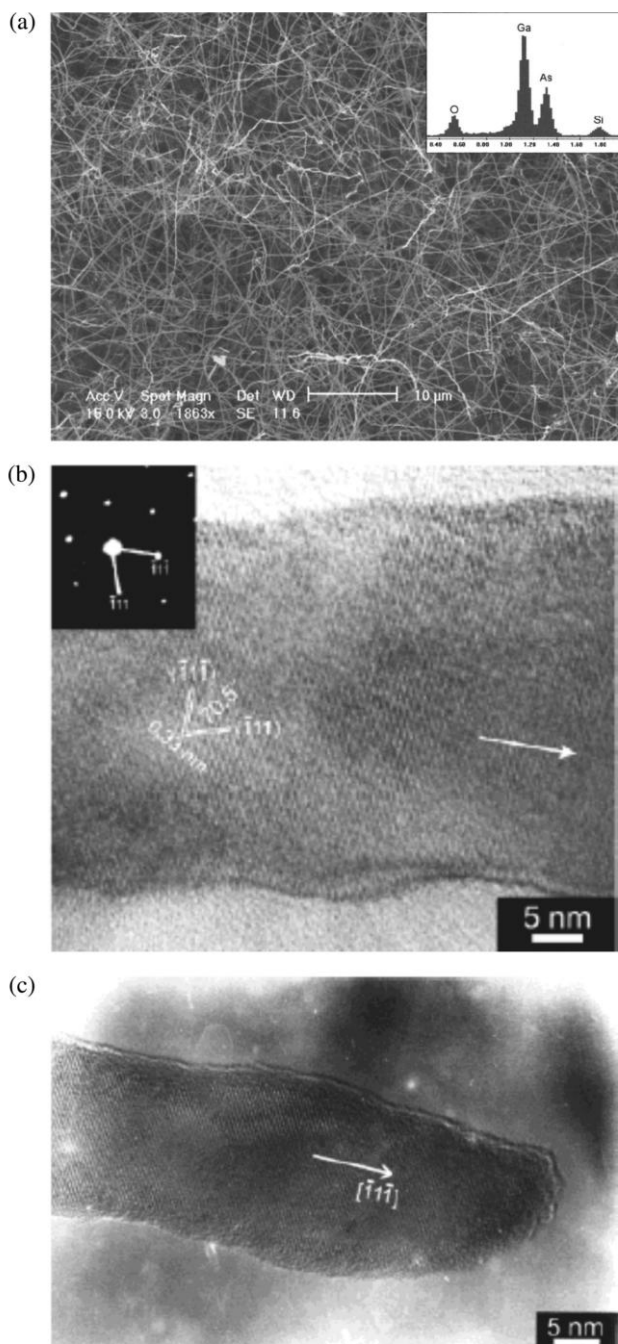


**Fig. 10.22.** (a) A typical SEM image of the GaAs nanowires synthesized by the oxide-assisted method. The EDS in the inset indicates Ga, As, O and Si; (b) a HRTEM image of a GaAs nanowire. The growth axis is close to the  $[\bar{1}\bar{1}\bar{1}]$  direction (white arrow). The

inset is the corresponding ED pattern recorded along the  $[110]$  zone axis perpendicular to the nanowire growth axis; (c) A HRTEM image of the tip of a GaAs nanowire. The growth direction is close to the  $[\bar{1}\bar{1}\bar{1}]$  direction (white arrow) [38].



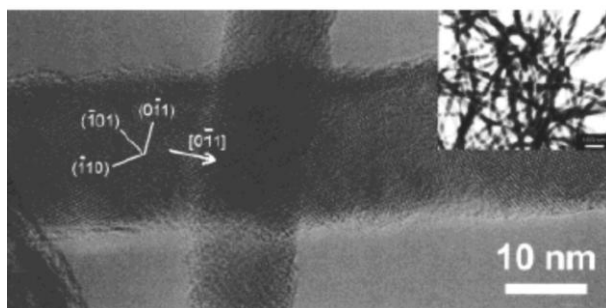


**Fig. 10.23.** A typical HRTEM image of GaP nanowires grown at about 750 °C on a silicon (100) substrate. The growth direction is close to the  $[0\bar{1}1]$  direction. The inset is a TEM image of GaP nanowires [40].

images of GaP and GaN nanowires, respectively. A TEM image of GaP nanowires and a SEM image of GaN nanowires are shown as insets in Figures 10.23 and 10.24, respectively. Again, both kinds of nanowires had a core of crystalline GaP or GaN wrapped in a thin layer of amorphous gallium oxide ( $\text{GaO}_x$ ). The formation of GaP and GaN nanowires is similar to that of GaAs nanowires, replacing As by P and N, respectively. The critical reactions responsible for the formation of GaP and GaN nanowires are,  $3\text{Ga}_2\text{O} + 4\text{P} = 4\text{GaP} + \text{Ga}_2\text{O}_3$  and  $3\text{Ga}_2\text{O} + 4\text{N} = 4\text{GaN} + \text{Ga}_2\text{O}_3$ , respectively.

It is thus obvious that for all the cases described above the oxide reacted with the element to form a volatile oxide. A chemical reaction (oxidation–reduction reaction

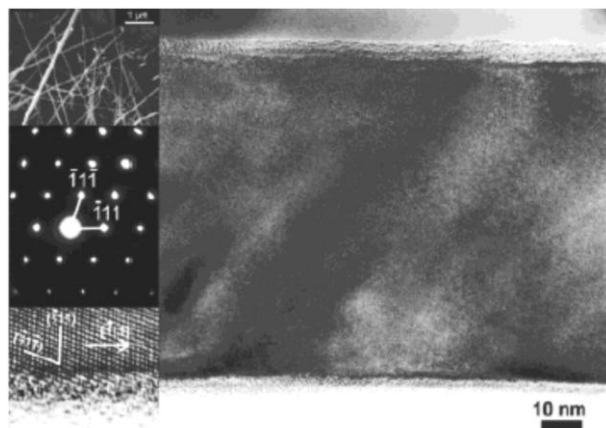


**Fig. 10.24.** A HRTEM image of a GaN nanowire grown at about 900 °C on a silicon (100) substrate. The insets are a SEM image (top), the corresponding ED pattern (middle) recorded along the  $[110]$  zone axis

perpendicular to the nanowire growth axis, and the local enlarged HRTEM image (bottom). The growth direction is along the  $[-111]$  direction (white arrow in bottom inset) [36].



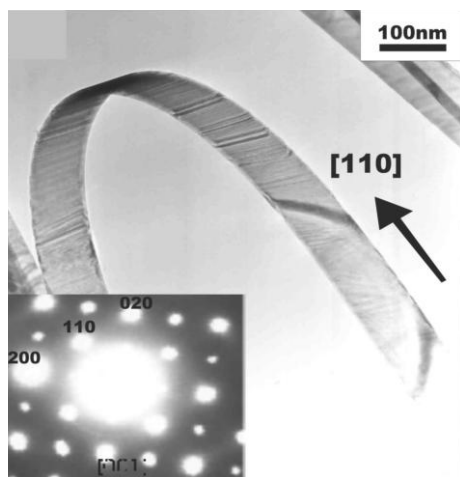


**Fig. 10.25.** TEM image of a single SnO<sub>2</sub> nanoribbon with [110] growth direction, inset showing the SAED pattern along the [001] axis [74].

where the oxide serves as the reactant) induced nucleation and growth of a nanowire embedded in an oxide sheath follow [22–27, 73]. The chemical reaction induced nucleation and growth of nanowires differentiates the OAG from the conventional metal catalyst VLS growth. The oxide-assisted nanowire growth process is free of metal catalysts thus enabling the formation of pure nanowires.

Similar to the growth of silicon nanoribbons, 2D nanostructures of SnO<sub>2</sub> with a ribbonlike morphology were also prepared on a large scale via rapid oxidation of elemental tin at 1080 °C [74]. As shown in Figure 10.25, the as-synthesized SnO<sub>2</sub> nanoribbons were single crystals and had preferred [110] and [203] growth directions. The lengths of the nanoribbons were up to several hundreds of micrometers, and the typical width and thickness were in the range 30–150 nm and 10–30 nm, respectively. Similarly, ZnS nanoribbons were grown (Figure 10.26) with a perfect 2H structure and a [120] growth direction [75].

## 10.6

### Chemical Properties of SiNWs

#### 10.6.1

##### Stability of H-Terminated SiNW Surfaces [76]

Silicon-based technology requires the removal of the surface oxide layer, and the termination and stabilization of the Si surfaces. This is conventionally performed by dipping in HF, which not only removes the oxide layer, but provides H-terminated Si surfaces. Examples of the significance of such a treatment are

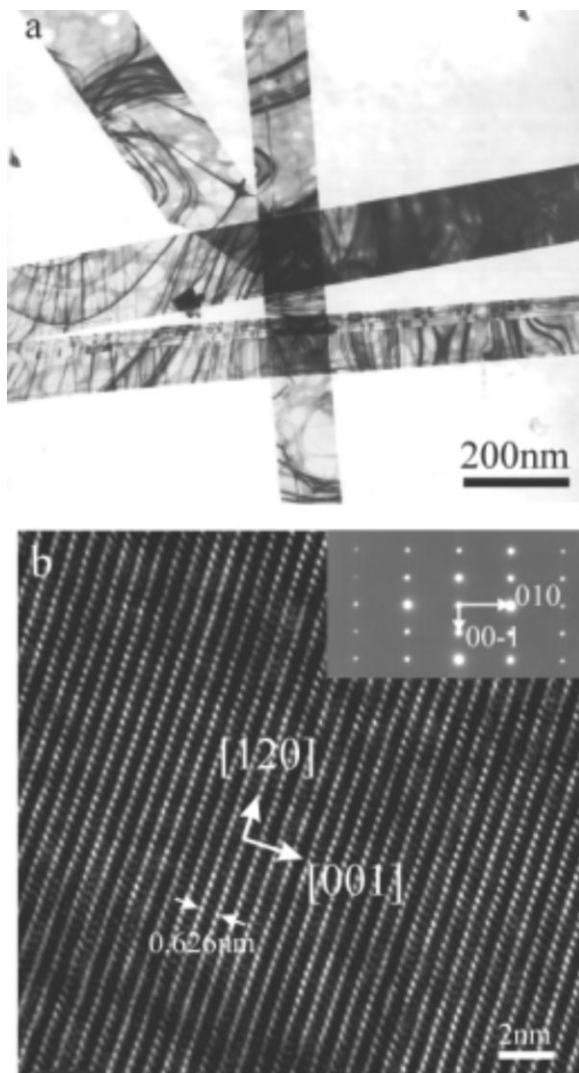


**Fig. 10.26.** (a) Low magnification TEM image and (b) high resolution TEM image and SAED of ZnS nanoribbons [75]. Note the high crystalline quality of the ZnO nanoribbons.

given in the previous and following sections. The stability of the oxide-removed H-terminated Si wafer surfaces has been extensively investigated, and many techniques were developed to suppress its re-oxidation upon exposure to humidity.

These considerations initiated our FTIR study of the nature of the HF-dipped SiNWs and their stability upon exposure to air and to water. The SiNWs had a distribution of diameters from a few nm to tens of nm. The thickness of the oxide layer was about 1/4 to 1/3 of the nominal diameter. Micro ATR-FTIR was used to

monitor the wires (1) as grown, (2) after 5 min immersion in a 5% HF (or DF) solution, (3) upon exposure to air or water for different times, (4) after annealing to different temperatures. We note that the FTIR signals originate mostly from the large-diameter SiNWs (the surfaces of which are larger) and only a small fraction of the signal represents the small-diameter SiNWs. This means that if the stability of SiNW surfaces is size-dependent (as indicated by theoretical calculations, see Section 10.8), this would not be revealed in the experiment.

The as-grown SiNWs clearly show (Figure 10.27) only Si–O vibrations at 1050 and 800  $\text{cm}^{-1}$ . Immersion in HF (Figure 10.27) removes the Si–O related lines and Si–H<sub>x</sub> ( $x = 1, 2, 3$ ) absorption modes appear. These modes can be attributed to mono-hydrides and tri-hydrides on Si(111) and di-hydrides on Si(100) as already

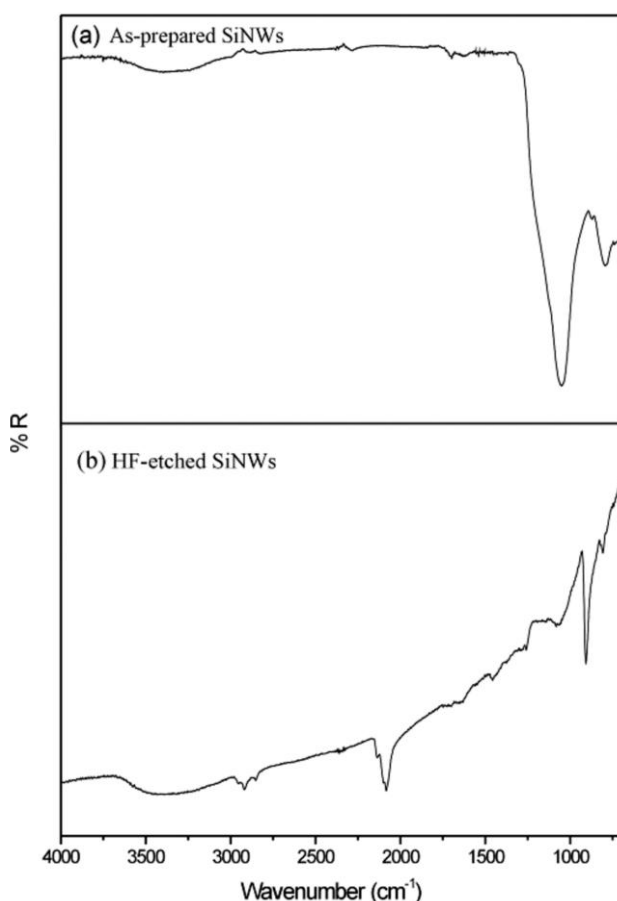


**Fig. 10.27.** ATR-FTIR spectra of (a) as-prepared SiNWs and (b) HF-etched SiNWs in the range 700–4000  $\text{cm}^{-1}$ . Note the removal of the oxide absorption line and the formation of Si–H<sub>x</sub> absorption lines in the etched SiNW [76].

identified for Si wafers. This identification was substantiated by the isotope shift introduced by substitution of hydrogen with deuterium. These results are in accord with atomically resolved STM images of SiNWs described in a later section. Annealing of the SiNWs results in the weakening and disappearance of the trihydride, whereas the monohydride peaks remain strong. The hydrogen is completely removed only at 850 K. Hydrogen is observed on a SiNW surface even 26 days after exposure to air. Si–O bands are however detected 17 h after exposure to air and increase with time while the SiH bands decrease. It is likely that this is a superposition of the incorporation of O in the large-diameter SiNWs while the smaller-diameter (and probably more stable) SiNWs maintain the Si–H signal. It is obvious that the stability of H-terminated SiNW surfaces in water is much lower than in air, and Si–O bands are apparent after immersion in water for 15 min. These results indicate that it is possible to remove the oxide layer from the SiNW surfaces and terminate them by H by immersion in HF, similar to Si wafers. The H-terminated surfaces seem to be stable in air for at least a day, whereas the stability of small-diameter SiNWs, as determined by single-wire STM measurements, seems to be substantially better than that of Si wafers.

#### 10.6.2

##### Reduction of Metals in Liquid Solutions

The reductive deposition of silver and copper ions on (oxygen-removed and hydrogen-terminated) SiNW surfaces in a solution was investigated [76] as an alternative method to ion implantation. The SiNWs surface is indeed capable of reducing silver and copper ions to metal aggregates of various morphologies at room temperature.

Laser ablation was used [22] to produce SiNWs  $\sim 20$  nm in diameter with a polycrystalline silicon core in a thin silicon oxide sheath with  $1/4$ – $1/3$  of the nominal diameter and  $1/3$  of the weight of the SiNW. The oxide layer (which makes the SiNWs surfaces inert) was removed by a 5% HF dip for 5 min resulting in smooth, stable, H-terminated SiNW surfaces [77]. The etched SiNWs were immersed into solutions of silver nitrate and copper sulfate of different concentrations. Silver and copper ions were reduced to metallic aggregates deposited onto the surface of SiNWs. The TEM image of the sample treated with a  $10^{-4}$  M silver nitrate solution (Figure 10.28) shows dark, round silver particles 5–50 nm in diameter. The HF-etched SiNWs treated with  $1.0 \times 10^{-3}$  M copper sulfate show much smaller (a few nm) particles (Figure 10.29) identified by EELS as Cu particles.

The silver metal deposition on SiNWs in different concentrations of silver solution ( $10^{-6}$  to 0.1 M) was studied in detail with SEM, EDS, and XPS. The SEM images show that the morphology of the deposited silver depends on the concentration of silver nitrate. At high concentrations the redox reaction is controlled by the concentration of Ag ions (mass action), so that large quantities of Ag ions in the vicinity of SiNWs are reduced and aggregated as dendrites. At low concentrations, the conditions required for dendrite formation are not reached and silver is de-

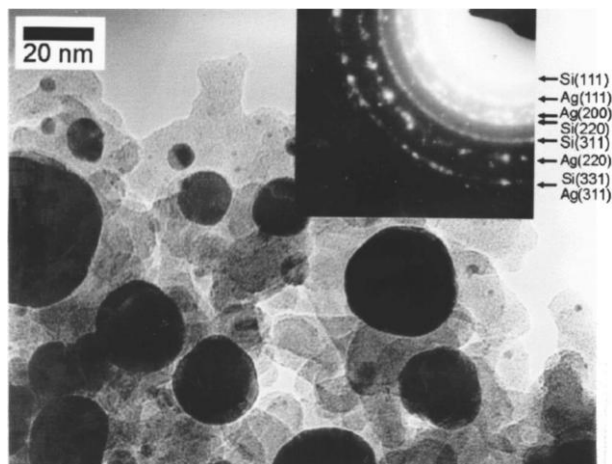


**Fig. 10.28.** A TEM image and the corresponding electron diffraction pattern (inset) of the SiNWs treated by a  $1.0 \times 10^{-4}$  M silver nitrate solution [76].

posited as clusters or small aggregates on the SiNW surfaces. XPS analysis verifies the redox reaction (Figure 10.30). Most of the Si in the initial SiNWs is oxidized (see the Si 2s and Si 2p<sub>3/2</sub> lines in Figure 10.30) and becomes elemental Si after the HF dip that removed the oxygen. The immersion in the Au solution results in the oxidation of Si, which increases with increasing Au concentration, as expected for a redox reaction of the Au ions. The metal concentration in the solution thus controls the size and the morphology of the metal deposited by the SiNWs, from small clusters to dendrites. This can be used for controlled deposition of metal nanoparticles on SiNWs on the one hand and larger self-supported metal configurations on the other hand.

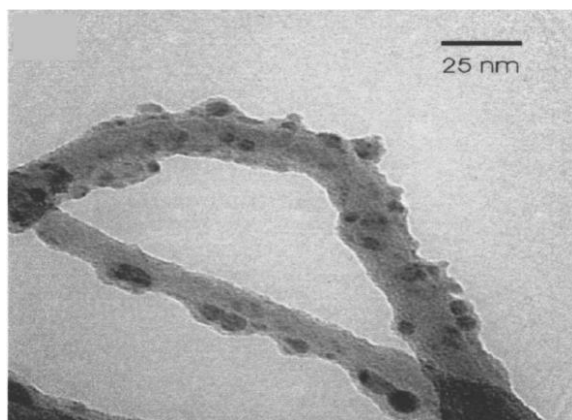


**Fig. 10.29.** A TEM image of the SiNWs treated by a  $1.0 \times 10^{-3}$  M copper sulfate solution [76].

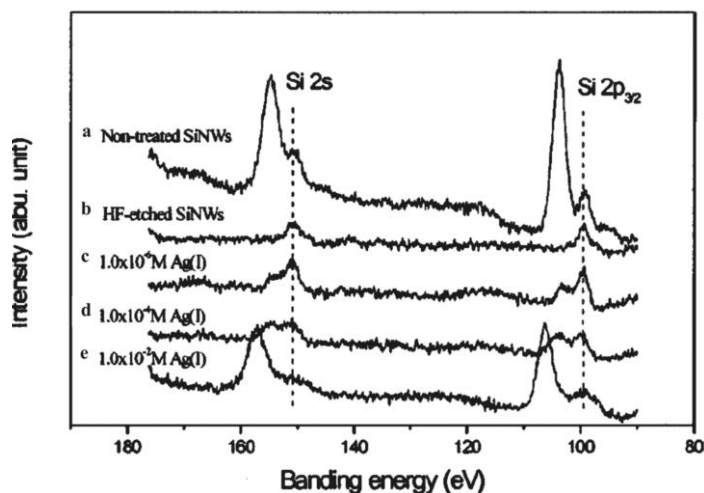


**Fig. 10.30.** Si 2p and 2s core level XPS spectra of (a) untreated SiNWs, (b) HF etched SiNWs, (c)  $1.0 \times 10^{-6}$  M silver nitrate treated SiNWs, (d)  $1.0 \times 10^{-4}$  M silver nitrate treated SiNWs, and (e)  $1.0 \times 10^{-2}$  M silver nitrate treated SiNWs. Note the oxidation of the Si associated with the reduction of the silver ions [76].

### 10.6.3

#### Chemical Sensing of SiNWs [78]

$I$ - $V$  measurements performed on an ensemble of SiNWs with a variety of diameters, growth directions, defect densities etc. are expected to yield only averaged behavior, which is dominated by those wires with the lowest resistivity [as in a parallel configuration of wires (resistors)]. While such ensemble measurements cannot be used to study the electrical conduction properties and mechanisms of nanowires, they can however give rough indications to check a variety of possible applications, one being gas sensing.

We have fabricated bundles of SiNWs of two types: (1) as-grown  $\text{SiO}_2$  sheathed wires, (2) SiNWs dipped in HF to remove the  $\text{SiO}_2$ . Silver contacts were glued to the edges of the bundles and their resistivity was measured at different ambient conditions (vacuum ( $2 \times 10^{-2}$  Torr), air with  $\sim 60\%$  humidity, dry  $\text{N}_2$ ,  $\text{NH}_3:\text{N}_2$  1:1000). The resistivity of the oxide-removed bundles was strongly reduced (by more than three orders of magnitude) upon exposure to humid air and to ammonia, but was hardly changed by exposure to dry nitrogen (Figure 10.31(a)). The process was found to be reversible, i.e. the resistivity increased to the initial value after pumping (Figure 10.31(b)). In contrast, the resistivity of the SiNWs embedded in the  $\text{SiO}_2$  sheath did not change when exposed to different ambient environments.

The gas molecules may affect either the contact resistance across two nanowires or the surface resistance along individual wires, e.g. through charge exchange similar to polycrystalline semiconductor  $\text{SnO}_2$  sensors. This would not happen for  $\text{SiO}_2$  sheathed wires (having a high resistivity) for which gas incorporation has no effect. The chemical sensitivity of HF-etched SiNWs to  $\text{NH}_3$  and water vapor exposure indicate their possible use in gas sensing applications.

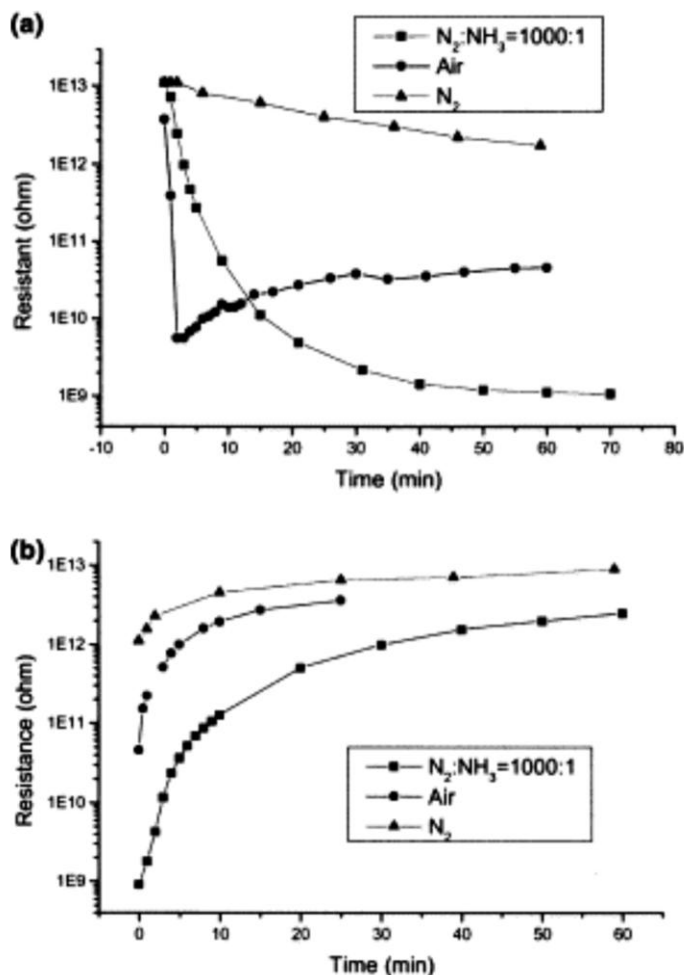


**Fig. 10.31.** Electrical responses with time of the Si nanowire bundle to  $N_2$ , a mixture of  $N_2$  and  $NH_3$  ( $NH_3$  concentration: 1000 ppm), and air with a relative humidity of 60%; (a) when the gases were introduced into the chamber and (b) when the gases were pumped away [78].

#### 10.6.4

#### Use of SiNWs as Templates for Nanomaterial Growth [79]

A novel template effect of SiNWs was discovered accidentally trying to disperse SiNWs in common solvents such as  $CHCl_3$ ,  $CH_2Cl_2$  and  $CH_3I$ . A 15 min bath sonication resulted in a colloidal solution, the products of which were characterized by HRTEM, EELS and Raman. The analysis revealed that under sonication the SiNWs acted as templates on which carbon nanotubes and carbon nano-onions formed (Figure 10.32). Moreover, in addition to these known carbon structures,



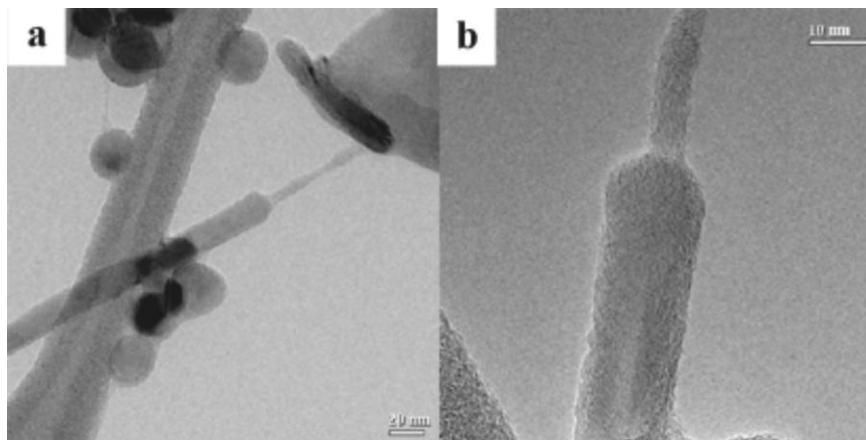


**Fig. 10.32.** Carbon nanotube (thin) grown on the SiNW tips (thick) which serves as a template [79].

nanotubes and nano-onions with plane spacings larger than those of graphite ( $3.5\text{--}5.8\text{ \AA}$ ) were also formed. The latter were interpreted as hydrogenated carbon nanotubes in which hydrogen atoms are bonded between graphitic layers forming  $sp^3$  bonding.

The TEM data indeed verifies that some carbon nanotubes (NTs) and nano-onions (NOs) were attached to the SiNWs (Figure 10.33). We believe that all the NTs and NOs were formed on SiNW templates, since no NT/NO formation was detected in the absence of SiNWs. Moreover, the NT and NO formation occurred only when the oxide layer of the SiNWs was removed by HF dipping (H-terminated SiNWs) but not on as-grown SiNWs with a  $\text{SiO}_2$  sheath.

The template mechanism of the SiNWs is still unclear. We nevertheless believe that the carbon nanostructures result from reactions between the  $\text{SiH}_x$  species on the SiNW surfaces. The substituents of the solvent material are eliminated by the local heating caused by the sonication, giving rise to either C or CH units that wrap around the SiNWs (templating effect). Further sonication causes the SiNWs to shed off the NTs, refreshing the SiNW surfaces for additional templating of new NTs. Prolonged sonication transforms all hydrogenated carbon NTs and NOs to regular carbon structures: hydrogen free CNTs and CNOs.

## 10.7

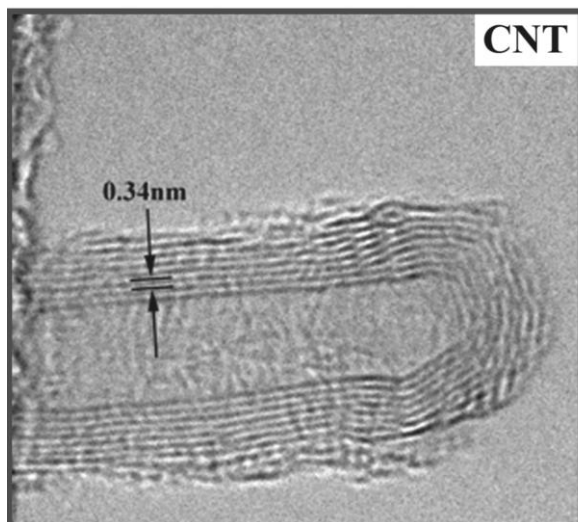
### Optical and Electrical Properties of SiNWs

#### 10.7.1

##### Raman and PL of SiNWs [24]

The Raman spectrum of Si nanowires (Figure 10.34(a)) shows a broad and symmetric peak at  $521\text{ cm}^{-1}$  compared to that of a bulk single crystal Si. The peak

(a)



(b)

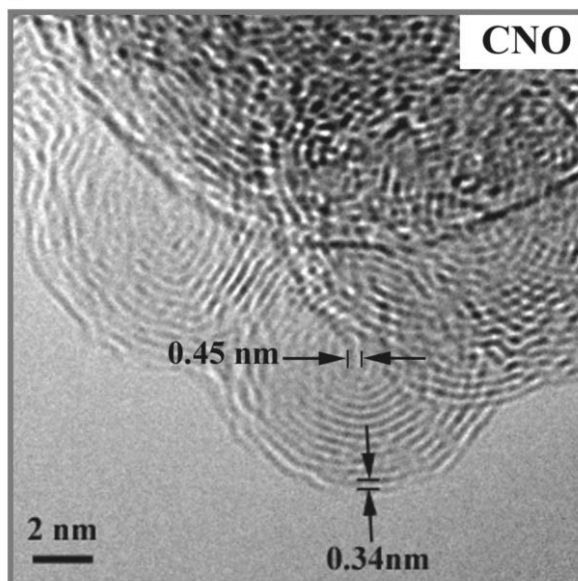


**Fig. 10.33.** High magnifications of (a) carbon nanotube and (b) carbon nano-onion grown on the SiNW template [79].

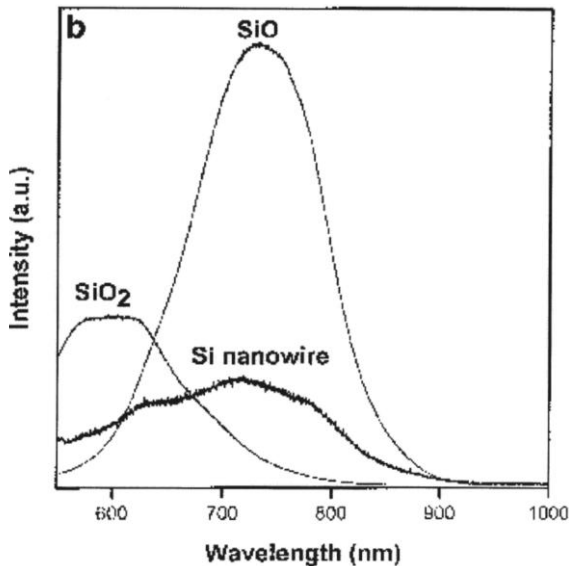
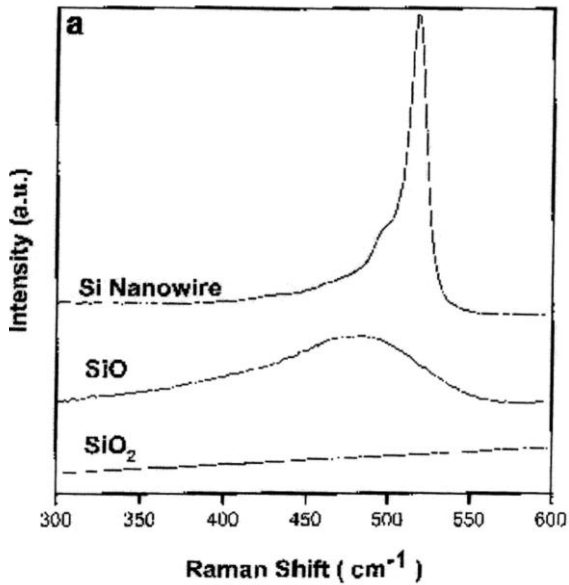


Fig. 10.34. (a) Raman spectra taken from the as-grown Si nanowires, Si monoxide and fully oxidized Si nanowires; (b) PL spectra taken from the as-grown Si nanowires, Si monoxide and fully oxidized Si nanowires [24].

profile may be associated with the effect of the small size of Si nanocrystals or defects. The presence of nonstoichiometric Si suboxide may also contribute to the peak asymmetry. For comparison, the spectrum from a SiO film contains a broad peak at  $480\text{ cm}^{-1}$ , whereas the fully-oxidized SiNWs (prepared by annealing in air) show no Raman scattering (Figure 10.34(a)).

Si monoxide has a strong photoluminescence (PL) at 740 nm, while the oxidized nanowire gives a weak PL peak at 600 nm (Figure 10.34(b)). The PL from the SiNW product is weak and complicated. A typical PL spectrum from SiNWs covers the range 600–800 nm. Clearly, the SiO and Si suboxide components in the nanowires are the main contributors to this spectrum. The SiO generated by thermal evaporation is indeed a mixture of various oxides of Si. Si nanoparticles also coexist with the SiO generated.

### 10.7.2

#### Field Emission from Different Si-Based Nanostructures

It is well known that nanotubes and nanowires with sharp tips are promising materials for application as cold cathode field emission devices. We have investigated the field emission of different nanowire structures. The first is from SiNWS. SiNWs exhibit well-behaved and robust field emission fitting a Fowler–Nordheim (FN) plot. The turn-on field for SiNWs, which is needed to achieve a current density of  $0.01\text{ mA cm}^{-2}$ , was  $15\text{ V }\mu\text{m}^{-1}$  [26]. The field emission characteristics may be improved by further optimization, such as oriented growth or reducing the oxide shell, and may be promising for applications.

The second example of field emission of Si-based nanowires is that of B-doped Si nanochains [80]. The SiNCs were attached onto a Mo substrate by a conductive carbon film. The anode-sample separation ranges from 120 to 220  $\mu\text{m}$ . The turn-on field was  $6\text{ V }\mu\text{m}^{-1}$ , and smaller than that ( $15\text{ V }\mu\text{m}^{-1}$ ) for the SiNWs. The field-emission characteristics of the SiNCs were analyzed according to the FN theory [81]. All the FN curves with different anode-sample separations fall in nearly the same region and have similar “Y” intercepts, showing that the SiNCs are uniformly distributed. A stability test showed no obvious degradation of current density and the fluctuation was within  $\pm 15\%$ , indicating that the B-doped SiNCs are a promising material for field emission applications.

The third example of field emission from Si-based nanowires is from the aligned SiC nanowires. The field emission measurements [68] were carried out in a vacuum chamber at a pressure of  $\sim 5 \times 10^{-7}$  Torr at room temperature. An oriented SiC nanowire array, which was used as the cathode, was stuck to a stainless steel substrate by silver paste with the bottom end of the nanowires facing upward. A copper plate with a diameter of 1 cm, mounted on a precision linear feedthrough, was used as the anode. Field emission current densities of  $10\text{ }\mu\text{A cm}^{-2}$  were observed at applied fields of  $0.7\text{--}1.5\text{ V }\mu\text{m}^{-1}$ , and current densities of  $10\text{ mA cm}^{-2}$  were realized at applied fields as low as  $2.5\text{--}3.5\text{ V }\mu\text{m}^{-1}$ , as shown in Figure 10.35. These results represent one of the lowest fields ever reported for any field-emitting materials at technologically useful current densities. We attributed this emission

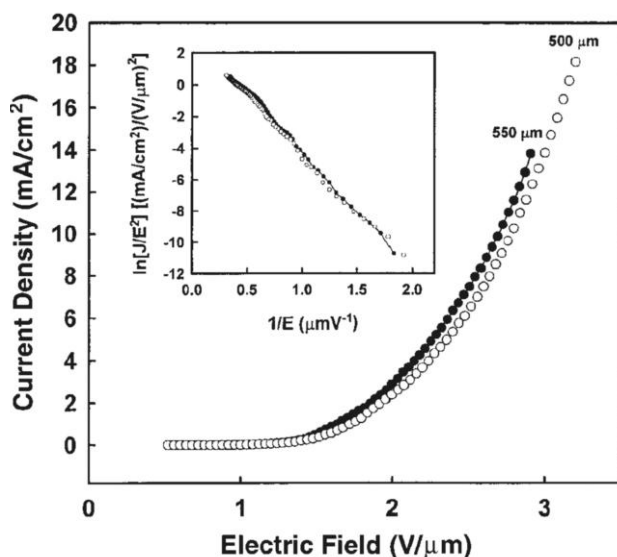


Fig. 10.35. Emission  $J$ - $E$  curves from an oriented SiC nanowire emitter (emitting area  $3.65 \text{ mm}^2$ ). The average turn-on field and threshold field for this sample are about  $0.9 \text{ V mm}^{-1}$  and  $2.7 \text{ V mm}^{-1}$ , respectively.

Inset: Fowler-Nordheim plot. The linearity of these curves indicates that the emission of the oriented SiC nanowires agrees with the properties expected for field emission [68].

behavior to the very high density of emitting tips with a small ratio of curvature at the emitting surface. The fact that when the oriented SiC nanowire array was pressed flat the current density was an order of magnitude lower than for the initial sample under the same electric field strongly supports this point.

### 10.7.3

#### STM and STS Measurements of SiNWs and B-Doped SiNWs

Almost all the characterizations performed by us until now are ensemble characterizations (i.e. probing many nanostructures simultaneously). HRTEM and HRSEM do probe the structure (and elemental composition) of individual nanostructures, but they do not correlate this structure with a specific property. STM and STS measurements are real single-object measurements that reveal the size, shape, and surface atomic structure, as well as the electronic density of states (deduced the  $I$ - $V$  characteristics). The STM/STS measurements offer a way to correlate the electronic properties of SiNWs with the nanostructure size.

STM imaging of SiNWs with atomic resolution requires the complete removal of the oxide layer and the termination of the exposed SiNW surface by hydrogen. This was achieved by HF etching of the SiNWs. Oxide removal and H-termination were confirmed by FTIR measurements and indeed, atomically resolved STM images of SiNWs oriented along the two abundant growth directions ( $[112]$  and  $[110]$ ) were

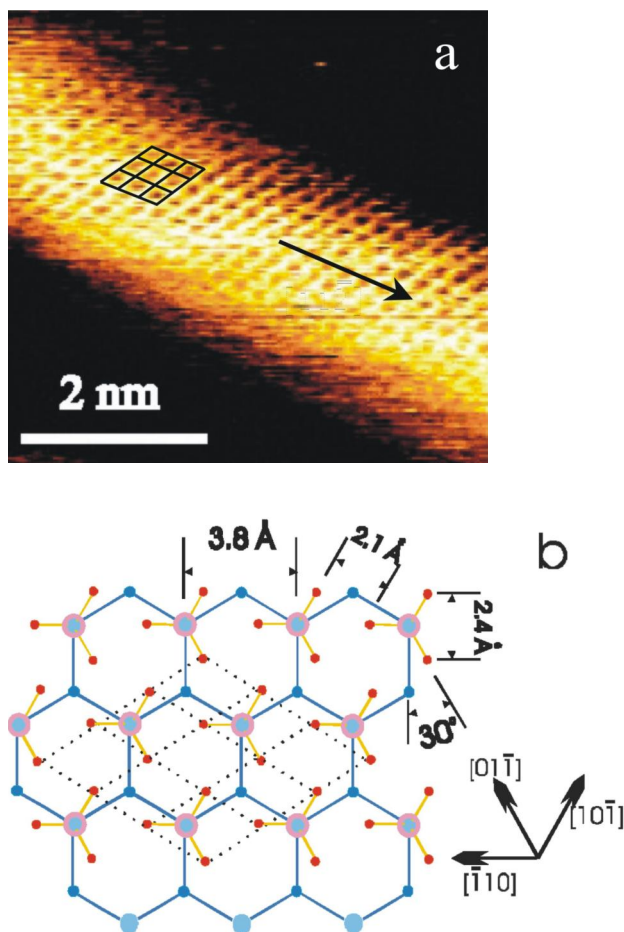


**Fig. 10.36.** STM image and schematic view of a SiNW with Si (111) facet. (a) Constant current STM image of a SiNW on a HOPG substrate. The wire's axis is along the [112] direction, and (b) schematic view of SiH<sub>3</sub> on Si (111) viewed along the [111] direction. Red and

large blue circles represent the H atoms and Si atoms in the SiH<sub>3</sub> radical, respectively. Small blue circles represent Si (111) atoms in the layer below. The crystallographic directions are shown in the inset [82].

obtained (Figures 10.36 and 10.37). The SiNW grown along the [112] direction (Figure 10.36) can be interpreted as a Si(111)-H-terminated surface (tri-hydride). The SiNW grown along the [110] direction (Figure 10.37) is a Si(100)-H-terminated surface (bi-hydride). The later has a hexagonal faceted structure. The removal of the oxide and the formation of the H-terminated facets enabled the performance of reliable STS measurements.  $I$ - $V$  curves and their normalized derivative  $(dI/dV)/(I/V)$  (representing the electronic density of states) of SiNWs with different diameters ranging from 7 nm to 1.3 nm were measured (Figure 10.38(a) and (b)). The

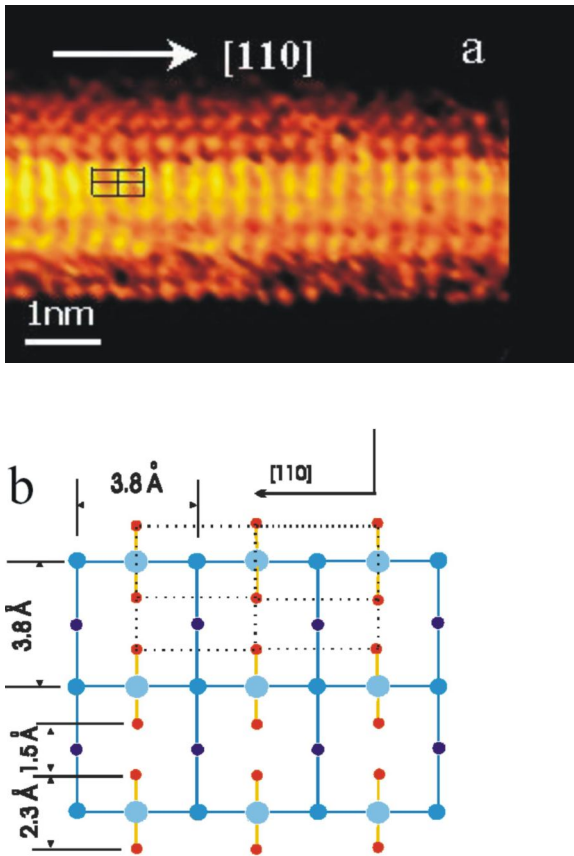


**Fig. 10.37.** STM image and schematic view of a SiNW with Si (001) facet. (a) Constant current STM image of a SiNW on a HOPG substrate. The wire's axis is along the  $[110]$  direction. (b) Schematic view of the dihydride phase on Si (001). Red and large blue circles represent H and Si atoms in the dihydride phase, respectively. Small blue circles correspond to Si atoms on the layers below. The crystallographic directions are shown in the inset [82].

electronic energy bandgaps increase with decreasing SiNW diameter from 1.1 eV for 7 nm to 3.5 eV for 1.3 nm in accord with previous theoretical predictions (Figure 10.38(c)), demonstrating a quantum size effect [82].

STM and STS measurements have been also performed on B-doped and undoped SiNWS [45] produced by OAG [23, 80]. The as-grown sample consisted primarily of SiNWs and nanoparticle chains coated with an oxide sheath. Samples for STM and STS measurements were prepared by dispersing the SiNWs into a suspension, which was then spin-coated onto highly oriented pyrolytic graphite (HOPG) substrates. The presence of nanoparticle chains and nanowires in the B-doped SiNWs sample was observed. Clear and regular nanoscale domains were observed on the SiNW surface, which were attributed to B-induced surface recon-



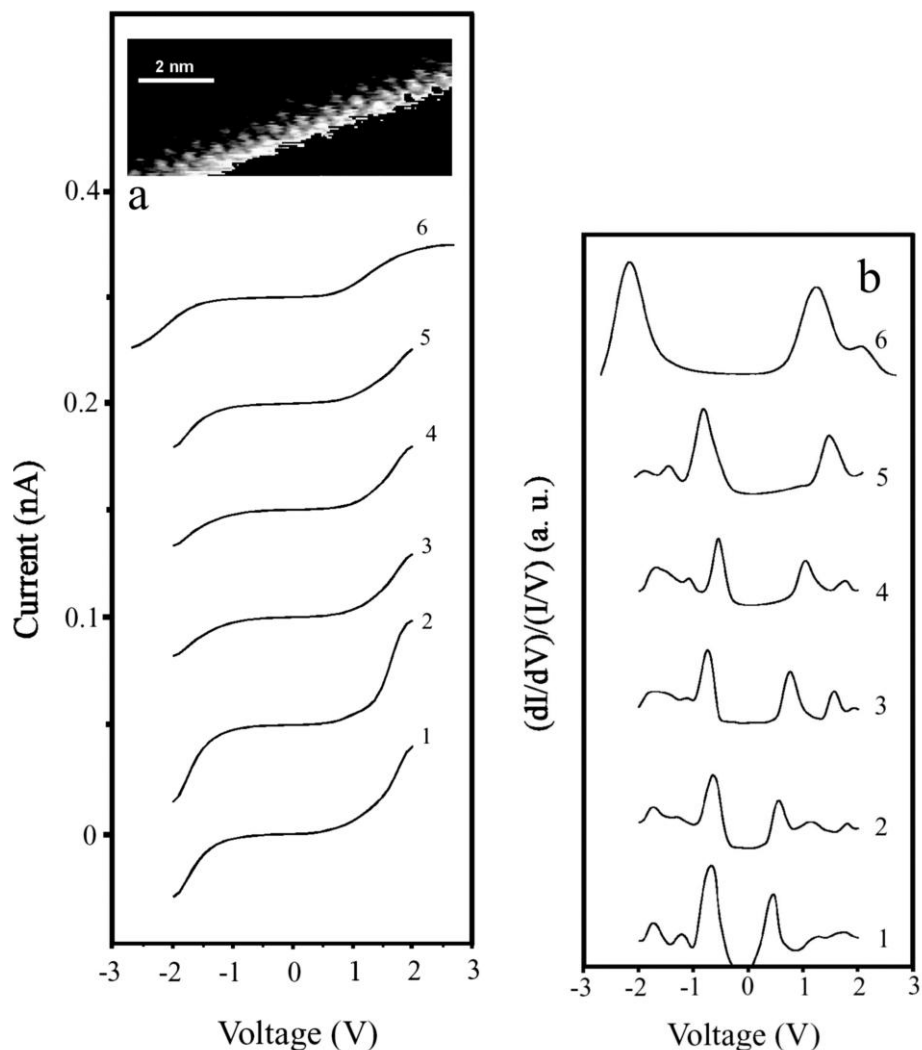


**Fig. 10.38.** Electronic properties of the SiNWs surfaces: (a) Current ( $I$ )–voltage ( $V$ ) curves obtained by STS on six individual SiNWs; the diameter of wires 1 to 6 being 7, 5, 3, 2.5, 2, and 1.3 nm respectively. The inset shows the

atomically resolved STM images of the 1.3 nm wire (6) which is the smallest ever reported. (b) The corresponding normalized tunneling conductances,  $(dI/dV)/I/V$ ; the curves are offset vertically for clarity [82].

struction. STS measurements have provided current–voltage curves for SiNWs, which showed enhancement in electrical conductivity by boron doping.

STM images of several typical SiNWs are shown in Figure 10.39. Figure 10.39(a)–(c) show the images of B-doped SiNWs with different morphologies. Figure 10.39(a) shows a nanoparticle chain with a diameter of 30 nm. The particles in

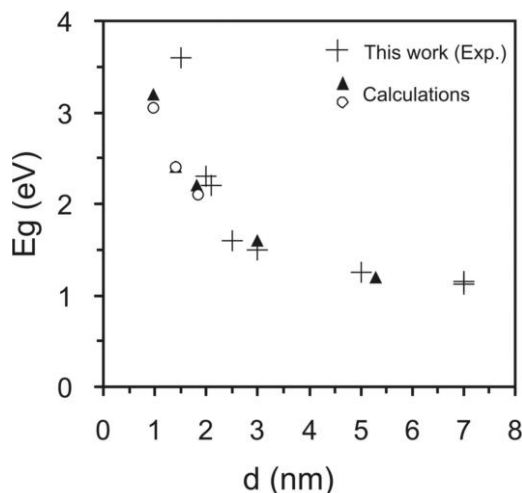


**Fig. 10.38.** (c) Experimental bandgap deduced from 38b versus the diameter of wires 1–6 plus additional three wires not shown in (a) and (b). The references of the calculated bandgaps are found in [82].

the chain are clearly revealed as evenly spaced bright dots of uniform size. Figure 10.39(b) shows a typical straight nanowire, the diameter of which is about 35 nm. Occasionally, sharp images of SiNW of ca. 40 nm in diameter, as shown in Figure 10.39(c), were obtained via air STM. The image reveals clearly resolved rectangular domains of several nanometers in size. These domains are associated with B-induced reconstruction of the silicon surface, and the clear images were made possible by B-enhanced conductivity.

STS measurements have also been performed on the undoped and B-doped SiNWs shown in Figure 10.39. The  $I$ – $V$  and the corresponding differentiated  $dI/dV$  curves of the nanowires reveal several features. First, while the curves for the two B-doped nanowires with different morphologies are quite similar, they are distinctly different from that for the undoped wire. This is because, as far as tunneling from a STM probe is concerned, the particle in the nanochain is the same as any point on a nanowire with a similar doping concentration and oxide sheath. Second, the steeper rise in the  $I$ – $V$  curves and the higher values of  $dI/dV$  for the B-doped SiNWs are consistent with the expected B-induced conductivity enhancement. As  $dI/dV$  values can be regarded as a measure of local density of states (LDOS), the low value between  $-1$  to  $+1$  V in the  $dI/dV$  curve of the undoped wire indicates relatively little LDOS within the gap, while the higher  $dI/dV$  in the same region of the doped wires is in accord with the presence of the B dopants. The minima of the curves are at 0.3 V, indicating that the Fermi level in the B-doped SiNWs lies 0.3 eV closer to the valence band relative to the undoped wire. The position of the Fermi level corresponds to a hole carrier concentration of  $1.5 \times 10^{15} \text{ cm}^{-3}$  in the boron-doped nanowires.

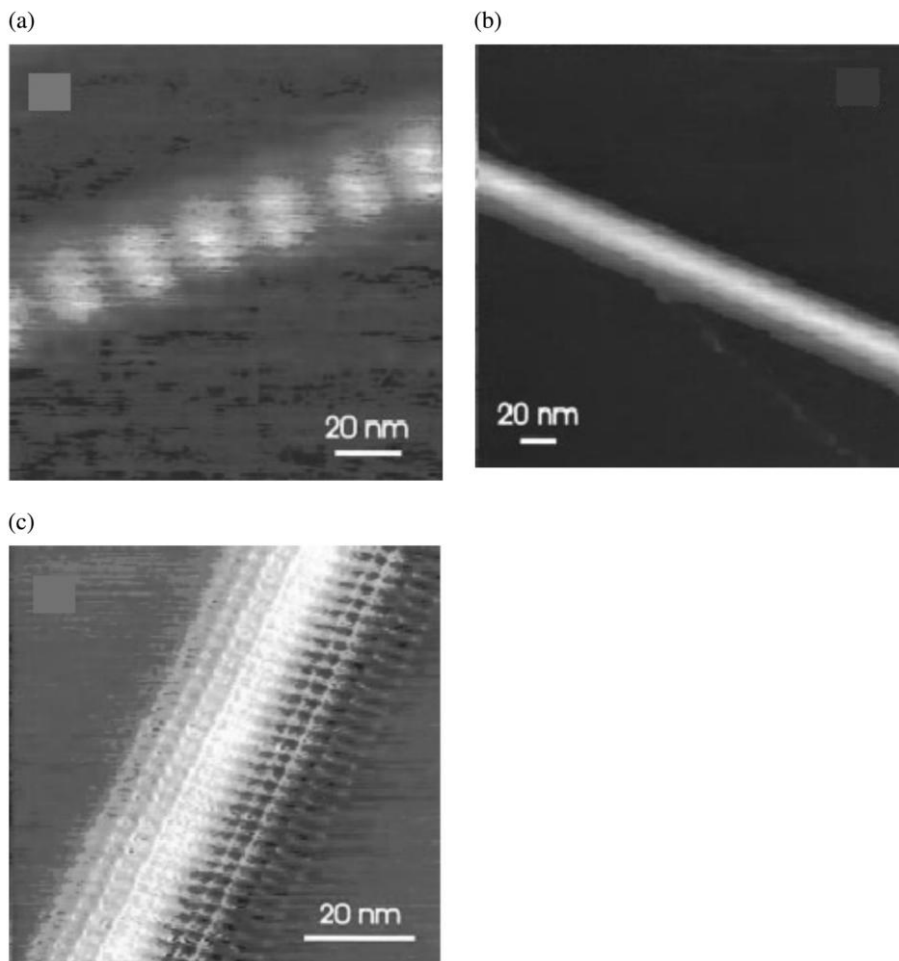


**Fig. 10.39.** STM images of: (a) a B-doped nanoparticle chain, (b) a B-doped straight nanowire, and (c) boron-induced reconstruction of SiNW [45].

#### 10.7.4

##### Periodic Array of SiNW Heterojunctions [83]

The OAG of SiNWs using thermal evaporation of SiO at 1200 °C was studied in detail as previously discussed and the growth at ~900 °C leads to straight, uniform (in diameter) nanowires with a crystalline silicon core embedded in a SiO<sub>2</sub> sheath. STM analysis was performed on such SiNWs that were dipped into HF to remove the oxide sheath and then dispersed on a HOPG substrate and loaded into the

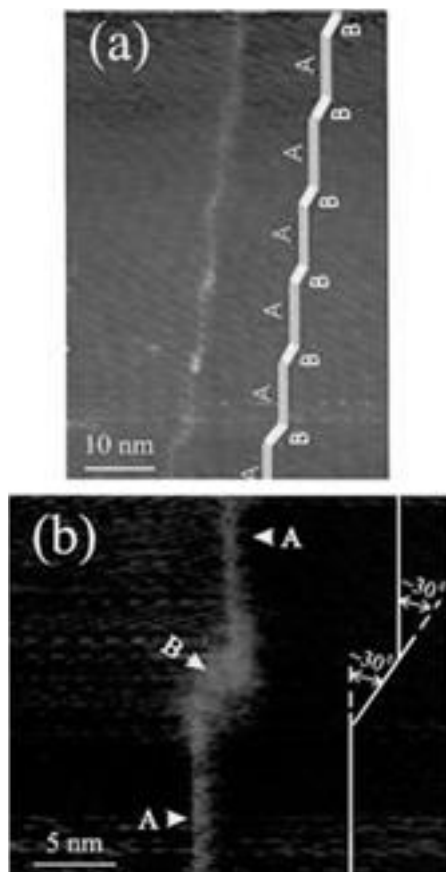


**Fig. 10.40.** STM images of a SiNW showing the periodic array of Si segments: (a) a medium magnification showing six sequences as further illustrated by the schematic sketch denoting segments A ( $\sim 10$  nm long) and B ( $\sim 5$  nm long) and (b) a higher magnification showing an image of a pair of junctions (ABA), also denoting the angle between the segments at  $\sim 30^\circ$  [83].

UHV STM system. Among the less abundant forms of SiNWs,  $\sim 1\%$  have a zigzag shape, composed of many bends or junctions.

Figure 10.40 shows the structure of such a typical zigzag-shaped SiNW with a diameter of 3 nm and a length of several microns. The wire is composed of a periodic array of long ( $\sim 10$  nm) and short ( $\sim 5$  nm) segments, denoted A and B respectively. The angle between the segments is  $\sim 30^\circ$ . The junctions repeat themselves regularly so that the length of the different segments is fairly constant along the entire wire. We have discussed in a previous section the growth directions of SiNWs in the OAG, and have reported that the two most abundant directions are

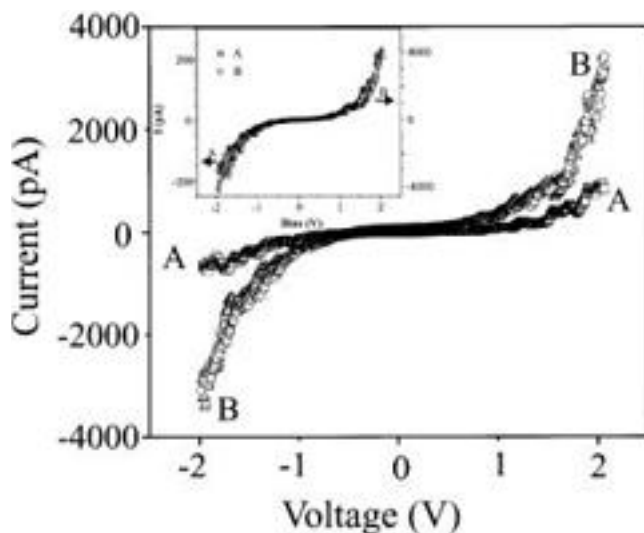


**Fig. 10.41.**  $I$ - $V$  STM curves of segments A and B. Note the significant difference between the two  $I$ - $V$  curves indicating different electronic properties. The inset shows the same  $I$ - $V$  curves for A (squares) and B (circles and triangles) in which the right-hand side scale (for segment B) is the same as in Figure 10.32 but the left-hand side scale (for segment A) was increased (50 pA per bar instead of 1000 pA per bar) until the  $I$ - $V$  curves of the

two segments overlapped. It is evident that the shape of the  $I$ - $V$  curves of the two different segments is similar (the electronic energy gap is almost the same) but the  $I$  values differ by a factor of  $\sim 20$ . The  $I$ - $V$  curve is the same for all A segments or B segments and along each segment. The change from one  $I$ - $V$  curve to the other along the junction (going from A to B or from B to A) is however very sharp [83].

[112] and [110]. We thus speculate that the zigzag shape originates from a periodic transition between two growth directions (which is 30 between [112] and [110] and 35 between [110] and [111]).

STS of these wires performed on several of each segment indicates that the  $I$ - $V$  curves are almost the same along identical segments (i.e. along all As or along all Bs), but very different for the two types of segments as indicated in Figure 10.41. The transition between one type of  $I$ - $V$  curve and the other along the segment interface (junction) is very sharp. We can conclude that periodic arrays of Si intra-molecular junctions were grown in a single SiNW growth process (segmented growth was previously reported by a periodic change in the growth conditions). The difference in the electronic properties of the different segments is unclear at present. Among the possible origins we include: (1) different surface electronic structures, (2) different diameters of the different segments, (3) defect and impurity induced variations, (4) stress effects. The observation of arrays of 66 pairs of junctions per micron indicate that self assembly of SiNWs in the OAG process may be manipulated to grow highly dense devices ( $1.1 \times 10^4$  ABA “transistors” per micron  $\times$  micron).

## 10.8 Modeling

### 10.8.1

#### High Reactivity of Silicon Suboxide Vapor

Silicon oxide is a critical source material in the oxide-assisted growth as described above. It also plays important roles, as is well known, in many fields such as electronics, optical communications, and thin-film technology. Our recent finding of silicon oxide in the synthesis of silicon nanowires, as we reviewed in the previous part of this chapter, would extend further the important new application of silicon oxide.

We have studied the silicon oxide-assisted formation of Si nanostructures based on quantum-mechanical calculations of  $\text{Si}_n\text{O}_m$  ( $n, m = 1-8$ ) clusters [50, 51, 84]. We found that most of the structures contain planar or buckled ring units. Pendent silicon atoms bonded only to a single oxygen atom are found in silicon-rich clusters. Oxygen-rich clusters have perpendicular planar rings, while silicon monoxide-like clusters usually form a large buckled ring. Structures made up of tetrahedrally bonded units are found only in two clusters. Furthermore, the energy gap and net charge distribution for clusters with different Si:O ratios have been calculated. We further found that: (i) the most energetically favorable small silicon oxide clusters have O to Si atomic ratios at around 0.6 (see Figure 10.42); and (ii) remarkably

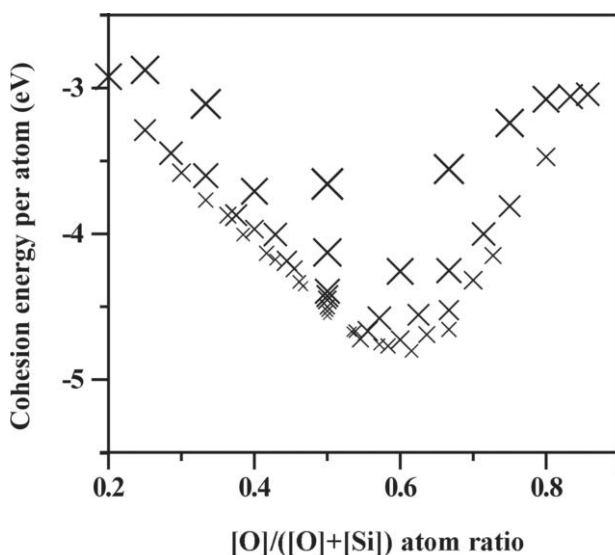
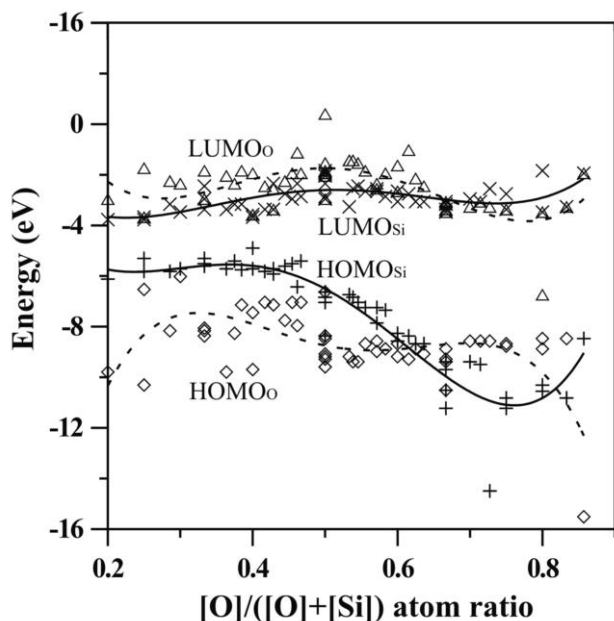


Fig. 10.42. Cohesion energy per atom of  $\text{Si}_n\text{O}_m$  ( $n, m = 1-8$ ) clusters as a function of O ratio based on total energy calculations with B3LYP/3-21G:Si; 6-31G\*:O. The decreasing size of the symbol  $\times$  is related to increasing cluster size ( $n + m$ ) [51].



**Fig. 10.43.** LUMO<sub>Si</sub> ("×"), LUMO<sub>O</sub> ("Δ"), HOMO<sub>Si</sub> ("+" ) and HOMO<sub>O</sub> ("◇") of Si<sub>n</sub>O<sub>m</sub> clusters determined based on the calculations using B3LYP/3-21G:Si; 6-31G\*:O. Their fittings using four-order polynomials are shown with solid curves for LUMO<sub>Si</sub> (upper) and HOMO<sub>Si</sub> (lower) while dashed curves represent LUMO<sub>O</sub> (upper) and HOMO<sub>O</sub> (lower).

high reactivity at the Si atoms exists in silicon suboxide Si<sub>n</sub>O<sub>m</sub> clusters with  $2n > m$  (see Figure 10.43). The results show that the formation of a Si–Si bond is preferred and thus facilitates the nucleation of Si nanostructures when silicon suboxide clusters come together or stack to a substrate. Based on these findings, the mechanism of oxide-assisted nucleation of silicon nanowires has been drawn clearly [52] as we reviewed in Section 10.2.2 of this chapter.

## 10.8.2

### Thermal and Chemical Stabilities of Pure Silicon Nanostructured Materials

For application of the SiNWs in advanced areas, their oxide sheath has to be removed. If the silicon core were not saturated, the stability of the structure would be very poor. Demonstrations of their stability would be useful for understanding the related problems. Other issues of pure silicon nanostructures including the structure and property of the thinnest nanowire and the stability of silicon nanotubes are also interesting. Summarized below are our computational efforts regarding these issues.

#### 10.8.2.1 Structural Transition in Silicon Nanostructures

As is well known, small silicon clusters do not have any structural feature similar to that of bulk silicon (tetrahedral). Between the small silicon clusters and bulk



silicon, there may be structural transition from amorphous to ordered tetrahedral structure. The structural transition to bulk diamond structure in nanosized silicon clusters has been studied by the tight-binding molecular dynamics method combined with a simulated annealing technique [85]. For intermediate-sized clusters (<200 atoms), the energetically favorable structures obtained consist of small subunits like  $\text{Si}_{10}$  and  $\text{Si}_{12}$  (Figure 10.44), qualitatively consistent with the experimental fragmentation behavior of these clusters. For spherical silicon nanocrystals, the surface atoms reconstruct to minimize the number of dangling bonds, forming a continuum surface (Figure 10.45). The large curvature of the continuum surface causes lattice contraction in the nanocrystals. Present calculations predict the lattice contraction versus the particle radius as  $\Delta a = 0.38/R$ , with  $\Delta a$  and  $R$  in Å. By comparing the cohesive energies of the two sorts of structures with the same number of atoms, the structural transition is estimated to occur at about 400 atoms, or 2.5 nm in diameter.

### 10.8.2.2 Thinnest Stable Short Silicon Nanowires

Using a full-potential linear-muffin-tin-orbital molecular-dynamics method, we have studied the geometric and electronic structures of thin short silicon nanowires consisting of tri-capped trigonal prism  $\text{Si}_9$  sub-units and uncapped trigonal prisms, respectively [86]. Comparing to other possible structures, these structures are found to be the thinnest stable silicon nanowires, being in particular much more stable than the silicon nanotubes built analogously to small carbon nanotubes (Figure 10.46). As for their electronic structures, these silicon wires show very small gaps of only a few tenths of an eV between the lowest unoccupied energy level and the highest occupied energy level, and the gaps decrease as the stacked layers increase. The results provide guidance to experimental efforts for assembling and growing silicon nanowires.

### 10.8.2.3 Silicon Nanotubes

In contrast to the synthesis of large quantity of SiNWs, no Si nanotube has ever been observed experimentally, indicating that silicon is an element very different from carbon in forming nanotubular structures although they are in the same group of the Periodic Table. The difficulty in the synthesis of silicon nanotubes is widely attributed to the property of  $\text{sp}^3$  hybridization in silicon. How and to what extent such hybridization affects the tubular structural formation still needs further clarification. To understand the reason(s) for the hitherto unsuccessful synthesis of silicon nanotubes we have studied [87] the differences in the structures and bonding between cubic (diamond-like) and tubular nanostructures of carbon and silicon, and their relative stabilities in terms of their characteristic electronic structures. Our calculated results indicate that when the dangling bonds at the open ends of the tubular structure are properly terminated, Si nanotubes with a severely puckered structure can, in principle, be formed. Such computationally stable, energetically minimized, and geometrically optimized Si nanotube structures may serve as models for the design and synthesis of silicon nanotubes.

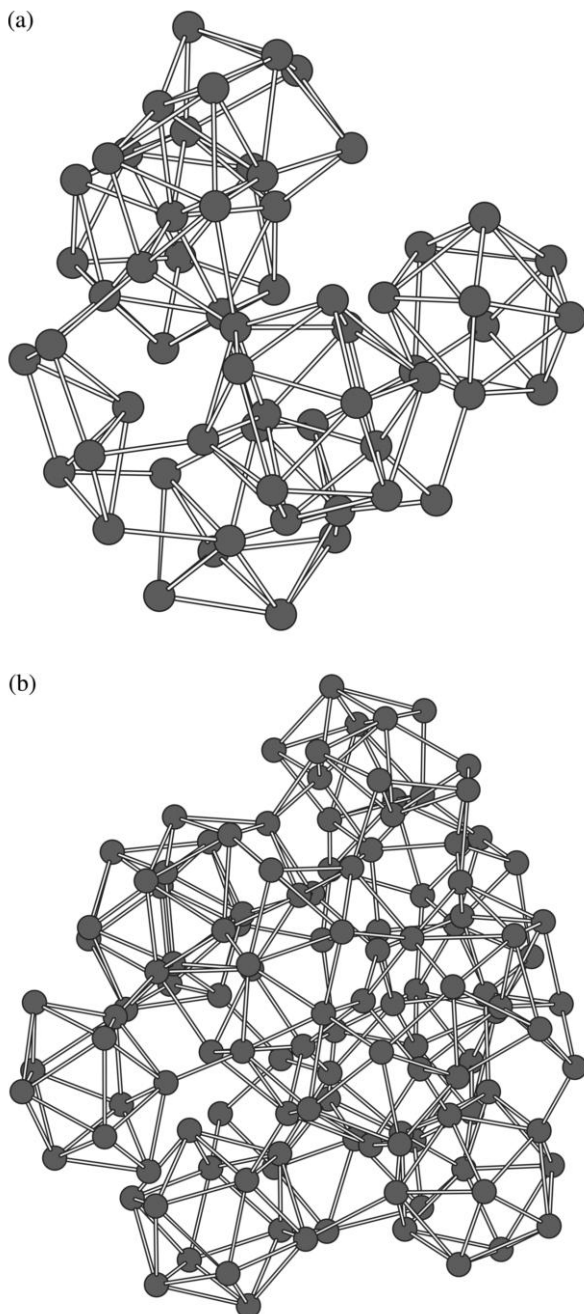


**Fig. 10.44.** Structures of (a) Si<sub>60</sub> and (b) Si<sub>123</sub> after annealing. All bonds below 2.8 Å are drawn out. The structures are fully relaxed, with the root-mean-square force to be 0.015 eV Å<sup>-1</sup> [85].

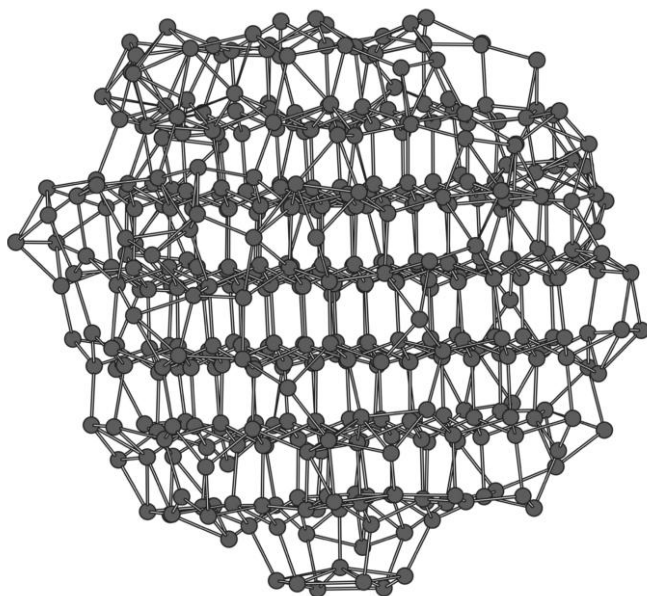


**Fig. 10.45.** Structure of the 417-atom Si nanocrystal with reconstructed surface. All bonds below 2.8 Å are drawn out. The structure is fully relaxed, with the root-mean-square force to be 0.015 eV Å<sup>-1</sup> [85].

### 10.8.3

#### **Thermal and Chemical Stabilities of Hydrogenated Silicon Nanostructures**

As reviewed in Section 10.6, the SiNWs could be etched using HF solution so that the surface oxide sheath is removed and the exposed silicon surface is saturated with hydrogen. The stability of the oxide-removed H-terminated Si wafer surfaces has been investigated and many techniques were invented to suppress its re-oxidation upon exposure to humidity. For the case of nanostructured hydrogenated silicon, its chemical stability would be different from the case of the wafer, as has been demonstrated in our recent computational works. One of our predictions, that the hydrogenated SiNWs possess better stability than that of a silicon wafer, could find a number of supportive evidences from our experiments as described above.

##### **10.8.3.1 Structural Properties of Hydrogenated Silicon Nanocrystals and Nanoclusters**

The structures of hydrogenated Si nanocrystals and nanoclusters were studied using the empirical tight-binding optimizations and molecular dynamics simulations [88]. It was shown that the structural properties of the hydrogen-saturated Si nanocrystals have little size effect, contrary to their electronic properties. The surface relaxation is quite small in the hydrogen-saturated Si nanocrystals, with a lat-

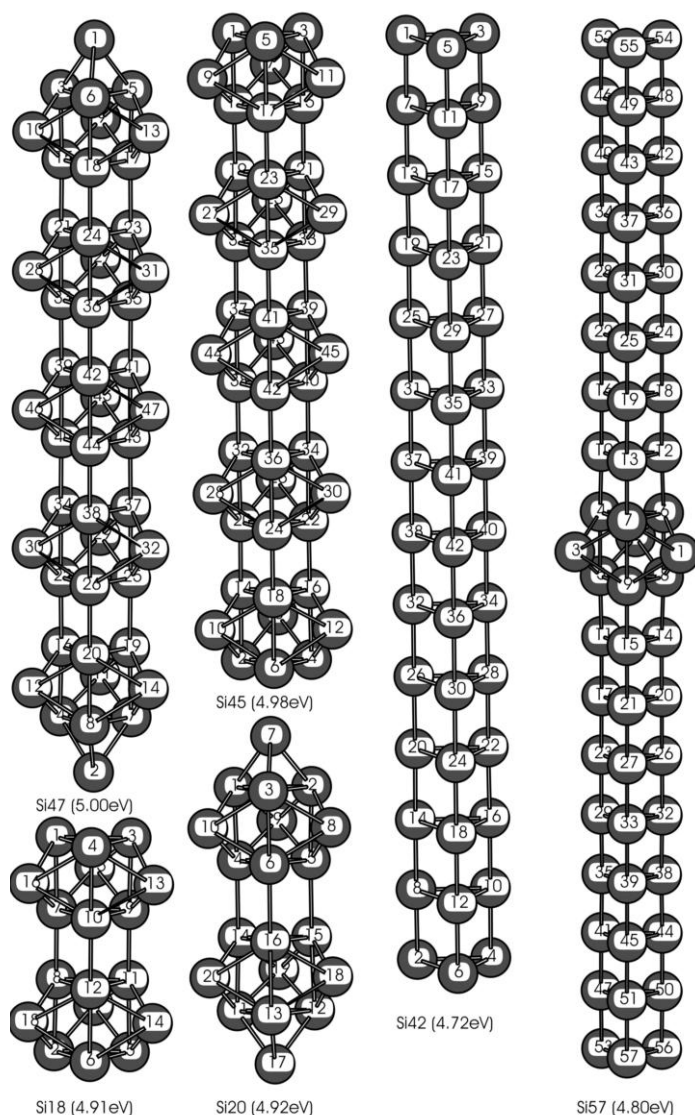


**Fig. 10.46.** Stable structures of some selected Si clusters. Si<sub>18</sub>, Si<sub>20</sub>, Si<sub>45</sub>, and Si<sub>47</sub> correspond to the stacked structures from the tricapped trigonal prisms. Si<sub>42</sub> consists of the trigonal prisms. Si<sub>57</sub> refers to the stacked trigonal

prisms inserted among trigonal prisms by one tricapped trigonal prism. The binding energy per atom is listed below the corresponding structure [86].

tice contraction of 0.01–0.02 Å within the outermost two to three layers. Inside the hydrogenated Si nanocrystals, there is only a very small strain (lattice expansion) of the order of  $10^{-4}$ – $10^{-3}$ , in good agreement with the X-ray diffraction measurement. The fully hydrogenated Si nanocrystals are the most stable structures com-

pared to partially hydrogenated ones. Removal of up to 50% of the total terminating H atoms only causes distortion to the crystal structure, while the tetrahedral structures are retained. By removing more than 70–80% of the total terminating H atoms, the clusters evolve to more compact structures (Figure 10.47).

### 10.8.3.2 Size-Dependent Oxidation of Hydrogenated Silicon Clusters

We have shown explicitly the size-dependent chemical reactivity of hydrogenated silicon clusters towards water [89]. A unique trend of decreasing reactivity with decreasing cluster size has been deduced from reaction energetics, frontier orbital analysis, and chemical reaction rates determined by the transition state theory in conjunction with *ab initio* calculations at Hartree–Fock and Møller–Plesset perturbation levels for water reaction with both dihydride and trihydride silicon configurations, as shown in Figure 10.48. This study indicates the possibility of fabricating stable hydrogenated silicon structures with sizes close to nanometers. We predict that, with the nanosized hydrogenated silicon structures, it is possible to fabricate nonreactive, stable nanodevices.

## 10.9

### Summary

A new method based on OAG has been developed that is capable of producing high-quality and bulk-quantity of various semiconductor nanowires. The presence of oxides in the target is a common and essential ingredient for the synthesis using laser ablation or thermal evaporation, so that the targets are capable of generating semiconductor oxides in the vapor phase. Subsequent decomposition of the vapor phase oxides at high temperature and defect structures play crucial roles in the nucleation and growth of high-quality nanowires. The developed OAG approach has been applied to grow a host of semiconducting nanowires such as Ge, GaN, GaAs, GaP, SiC, ZnO (whiskers), and carbon nanowires, by either laser-ablation, HFCVD or thermal evaporation. Large-area, aligned, and long SiNWs via flow control, and diameter and morphology control by temperature have been achieved. High-quality SiNW-based nanocables and Si nanoribbons using oxide-assisted methods have been additionally grown. Oxide-stripping and hydrogen-termination along with nanowire dispersion enabled the study of SiNW surfaces by STM and STS. The quantum size effect of the SiNW diameter on the electronic bandgap was demonstrated for the first time. The nanochemistry of SiNWs has been investigated by performing surface reactions with Ag and Cu ions on the SiNWs. Nanosized ligated metal clusters on a SiNW surface were realized to achieve good metal–nanowire contact. The surface reactivity of SiNWs was exploited for growing carbon-based nanostructures on a SiNW template (liquid solution) and for chemical sensing in the gas phase. Our synthesized highly-oriented SiC nanowires were shown to be excellent field emitters with large field emission current densities at very low electric turn-on and threshold fields. Modeling of SiNW structures, nu-

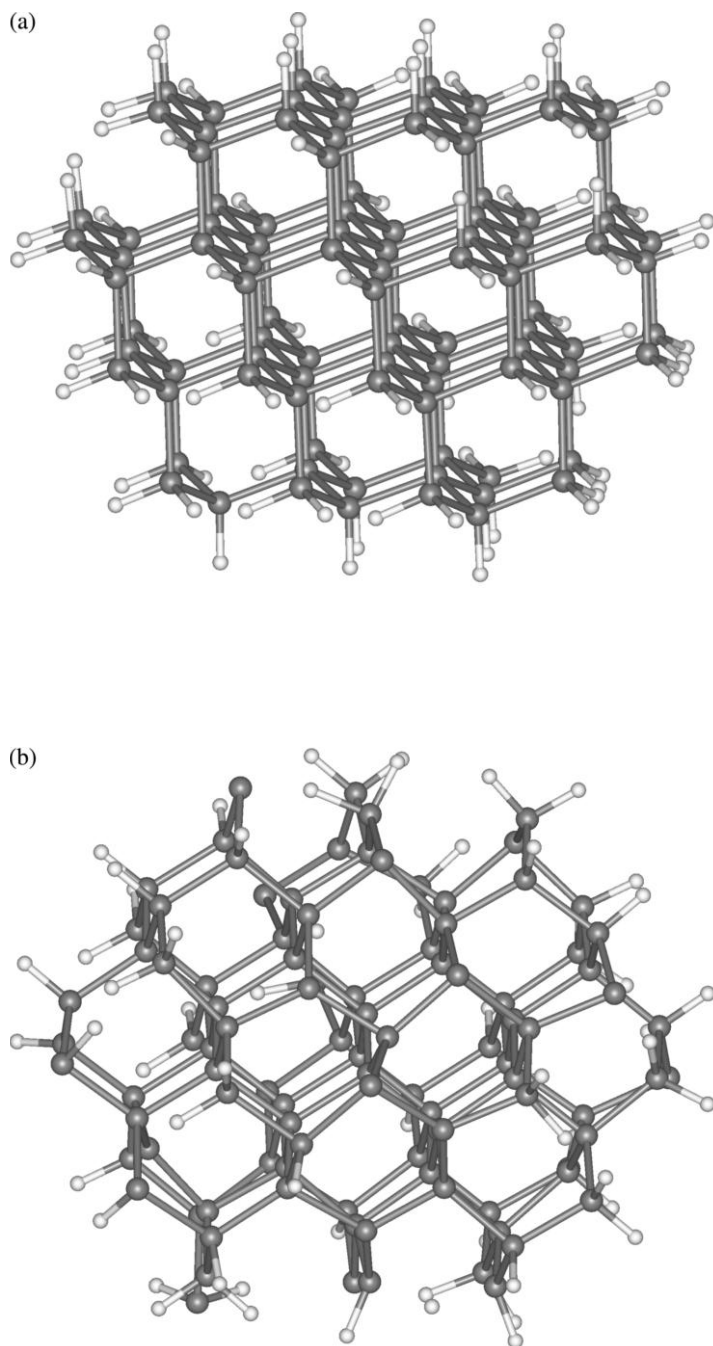


**Fig. 10.47.** Ball-and-stick diagrams of the structures of  $\text{Si}_{100}\text{H}_x$  clusters obtained from simulated annealing. (a) Fully H-saturated  $\text{Si}_{100}\text{H}_{86}$ ; (b)  $\text{Si}_{100}\text{H}_{60}$ ;



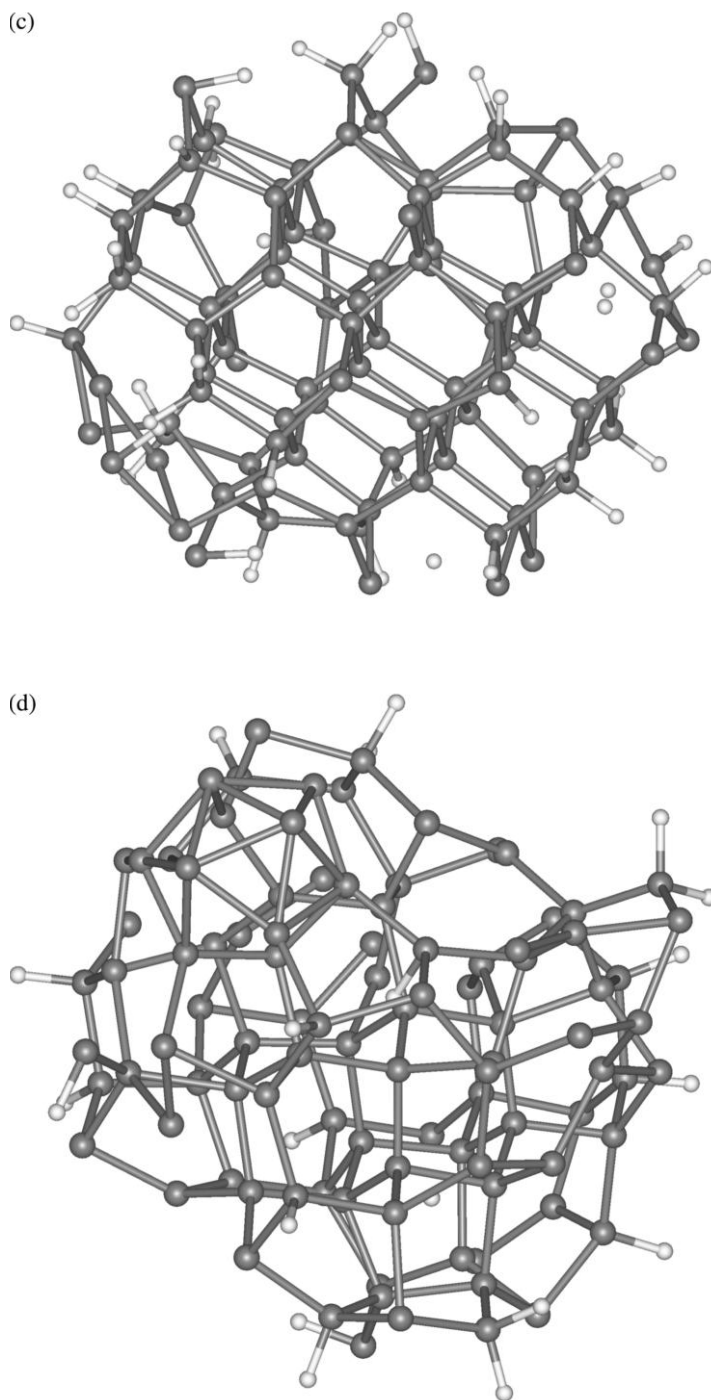
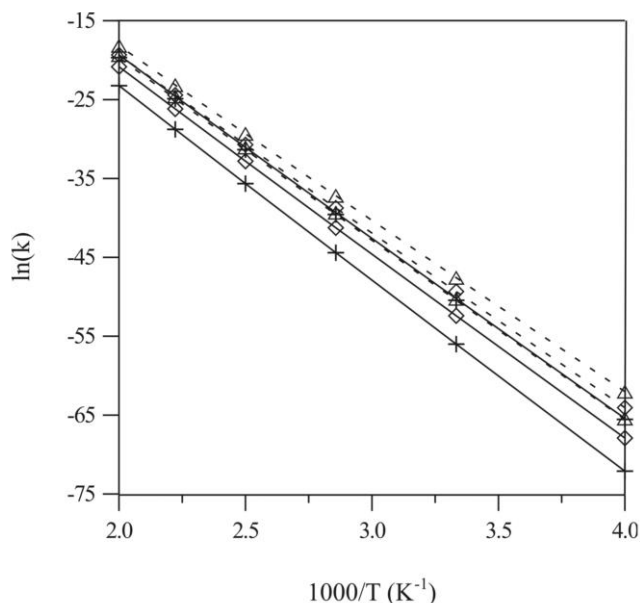


Fig. 10.47. (c)  $\text{Si}_{100}\text{H}_{40}$ ; and (d)  $\text{Si}_{100}\text{H}_{20}$  [87].





**Fig. 10.48.** Calculated total rate constants ( $\text{cm}^3 \text{mol}^{-1} \text{s}^{-1}$ ) at a pressure of 1 atm in a temperature range between 250 and 500 K. Solid lines are those of water reactions on the dihydride configurations:  $\text{Si}_2\text{H}_6\text{-SiH}_2$  ("+" );  $\text{Si}_5\text{H}_{10}\text{-SiH}_2$  ("◇" ); and  $\text{Si}_9\text{H}_{14}\text{-SiH}_2$  ("△" ). Dashed lines are those of water reactions on

the trihydride configurations:  $\text{SiH}_3\text{-SiH}_3$  ("+" );  $\text{Si}_4\text{H}_9\text{-SiH}_3$  ("◇" ); and  $\text{Si}_{10}\text{H}_{15}\text{-SiH}_3$  ("△" ). The inset illustrates the potential energy profile for a representative  $\text{H}_2\text{O}$  reaction with the hydrogenated silicon cluster [89].

cleation and growth processes and properties carried out in parallel with the experimental work is highly valuable in giving additional insight into the nature of the oxide-assisted growth and in explaining our experimental results.

### Acknowledgement

We are grateful to our colleagues (I. Bello, C. S. Lee, D. S. Y. Tong, N. Wang, N. B. Wong), post-doctoral fellows (J. Q. Hu, Y. Jiang, B. X. Li, D. D. D. Ma, Z. W. Pan, H. Y. Peng, W. S. Shi, D. K. Yu), graduate students (F. Au, C. P. Li, X. M. Meng, X. H. Sun, Y. H. Tang), and visiting professors (T. K. Sham, B. K. Teo, D. P. Yu, Y. F. Zhang) to COSDAF for their contributions to the work described in this chapter. The work described herein was supported financially by the Research Grants Council of Hong Kong SAR (Project No. 8730016 (e.g. CityU 3/01C); 9040459; 9040533 (e.g. CityU 1033/00P); 9040633 (e.g. CityU 1011/01P); and 9040746 (e.g. CityU 1138/02P)) and City University of Hong Kong.

## References

- 1 S. IIJIMA, *Nature*, 354, 1991, 56.
- 2 T. W. EBBESEN, *Carbon Nanotubes, Preparation and Properties*, CRC Press, Boca Raton 1997.
- 3 M. DRESSELHAUS, G. DRESSELHAUS, P. EKLUND et al., *Phys. World*, 33, 1998.
- 4 J. W. G. WILDOER et al., *Nature*, 391, 1998, 59.
- 5 P. M. AJAYAN, *Chem. Rev.*, 99, 1999, 1787.
- 6 C. DEKKER, *Phys. Today*, 22, 1999.
- 7 J. W. G. WILDOER, L. C. VENEMA, A. G. RINZLER et al., *Nature*, 391, 1998, 59.
- 8 T. ODOM, J. HUANG, P. KIM et al., *Nature*, 391, 1998, 62.
- 9 L. LANGER, V. BAYOT, E. GRIVEI et al., *Phys. Rev. Lett.*, 76, 1996, 479.
- 10 T. W. EBBESEN, H. LEZEC, H. HIURA et al., *Nature*, 382, 1996, 54.
- 11 A. KASUMOV, I. I. KHODOS, P. M. AJAYAN et al., *Europhys. Lett.*, 34, 1996, 429.
- 12 S. FRANK, P. PONCHARAL, Z. L. WANG et al., *Science*, 280, 1998, 1744.
- 13 A. BATCHTOLD, C. STRUNK, J. P. SALVETAT et al., *Nature*, 397, 1999, 673.
- 14 M. M. J. TREACY, T. W. EBBESEN, J. M. GIBSON, *Nature*, 381, 1996, 678.
- 15 S. J. TANS, R. M. VERSCHUEREN, C. DEKKER, *Nature*, 393, 1998, 40.
- 16 J. KONG et al., *Science*, 287, 2000, 622.
- 17 P. G. COLLINS, K. BRADLEY, M. ISHIGAMI et al., *Science*, 287, 2000, 1801.
- 18 Q. H. WANG et al., *Appl. Phys. Lett.*, 72, 1998, 2912.
- 19 S. FAN et al., *Science*, 283, 1999, 512.
- 20 A. C. DILLON et al., *Nature*, 386, 1997, 377.
- 21 A. M. MORALES, C. M. LIEBER, *Science*, 279, 1998, 208.
- 22 Y. F. ZHANG, Y. H. TANG, N. WANG et al., *Appl. Phys. Lett.*, 72, 1998, 1835.
- 23 S. T. LEE, Y. F. ZHANG, N. WANG et al., *J. Mater. Res.*, 14, 1999, 4503.
- 24 S. T. LEE, N. WANG, C. S. LEE, *Mater. Sci. Eng. A*, 286, 2000, 16.
- 25 S. T. LEE, N. WANG, Y. F. ZHANG et al., *MRS Bull.*, 24, 1999, 36.
- 26 N. WANG, Y. F. ZHANG, Y. H. TANG et al., *Appl. Phys. Lett.*, 73, 1998, 3902.
- 27 N. WANG, Y. F. ZHANG, Y. H. TANG et al., *Phys. Rev. B*, 58, 1998, R16024.
- 28 Y. H. TANG, Y. F. ZHANG, H. Y. PENG et al., *Chem. Phys. Lett.*, 314, 1999, 16.
- 29 Y. F. ZHANG, Y. H. TANG, H. Y. PENG et al., *Appl. Phys. Lett.*, 75, 1999, 1842.
- 30 Y. CUI, L. J. LAUHON, M. S. GUDIKSEN et al., *Appl. Phys. Lett.*, 78, 2001, 2214.
- 31 Y. Y. WU, P. D. YANG, *J. Am. Chem. Soc.*, 123, 2001, 3165.
- 32 H. Y. PENG, N. WANG, W. S. SHI et al., *J. Appl. Phys.*, 89, 2001, 727.
- 33 H. Y. PENG, Z. W. PAN, L. XU et al., *Adv. Mater.*, 13, 2001, 317.
- 34 W. S. SHI, H. Y. PENG, N. WANG et al., *J. Am. Chem. Soc.*, 123, 2001, 11095.
- 35 Y. F. ZHANG, Y. H. TANG, N. WANG et al., *Phys. Rev. B*, 61(7), 2000, 4518.
- 36 W. S. SHI, Y. F. ZHENG, N. WANG et al., *Chem. Phys. Lett.*, 345, 2001, 377.
- 37 H. Y. PENG, X. T. ZHOU, N. WANG et al., *Chem. Phys. Lett.*, 327, 2000, 263.
- 38 W. S. SHI, Y. F. ZHENG, N. WANG et al., *Adv. Mater.*, 13, 2001, 591.
- 39 W. S. SHI, Y. F. ZHENG, N. WANG et al., *Appl. Phys. Lett.*, 78, 2001, 3304.
- 40 W. S. SHI, Y. F. ZHENG, H. Y. PENG et al., *J. Am. Ceram. Soc.*, 83, 2001, 3228.
- 41 W. S. SHI, Y. F. ZHENG, N. WANG et al., *J. Vac. Sci. Technol. B*, 19, 2001, 1115.
- 42 J. Q. HU, X. L. MA, Z. Y. XIE et al., *Chem. Phys. Lett.*, 344, 2001, 97.
- 43 K. W. WONG, X. F. ZHOU, F. C. K. AU et al., *Appl. Phys. Lett.*, 75, 1999, 2918.
- 44 F. C. K. AU, K. W. WONG, Y. H. TANG et al., *Appl. Phys. Lett.*, 75, 1999, 1700.
- 45 D. D. D. MA, C. S. LEE, S. T. LEE, *Appl. Phys. Lett.*, 79, 2001, 2468.
- 46 D. P. YU, Z. G. BAI, Y. DING et al., *Appl. Phys. Lett.*, 72, 1998, 3458.
- 47 N. WANG, Y. H. TANG, Y. F. ZHANG et al., *Chem. Phys. Lett.*, 283, 1998, 368.
- 48 U. SETIOWATI, S. KIMURA, *J. Am. Ceram. Soc.*, 80, 1997, 757; G. HASS,

- C. D. SALZBERG, *J. Opt. Soc. Am.*, **44**, 1954, 18.
- 49 G. HASS, C. D. SALZBERG, *J. Opt. Soc. Am.*, **44**, 1954, 18.
- 50 T. S. CHU, R. Q. ZHANG, H. F. CHEUNG, *J. Phys. Chem. B*, **105**, 2001, 1705.
- 51 R. Q. ZHANG, T. S. CHU, H. F. CHEUNG et al., *Phys. Rev. B*, **64**, 2001, 113304.
- 52 R. Q. ZHANG, T. S. CHU, H. F. CHEUNG et al., *Mater. Sci. Eng. C*, **16**, 2001, 31.
- 53 J. P. BOREL, *Surf. Sci.*, **106**, 1981, 1.
- 54 C. P. LI, C. S. LEE, X. L. MA et al., *Adv. Mater.*, **15**, 2003, 607.
- 55 T. Y. TAN, S. T. LEE, U. GÖSELE, *Appl. Phys. A: Mater. Sci. Process.*, **74**, 2002, 423.
- 56 J. T. HU, T. W. ODOM, C. M. LIEBER, *Acc. Chem. Res.*, **32**, 1999, 435–445.
- 57 S. T. LEE et al., unpublished results.
- 58 E. I. GIVARGIZOV, *J. Cryst. Growth*, **20**, 1973, 217.
- 59 G. HASS, *J. Am. Ceram. Soc.*, **33**, 1950, 353.
- 60 Y. CUI, X. F. DUAN, J. T. HU et al., *J. Phys. Chem. B*, **104**, 2000, 5213.
- 61 Y. H. TANG, Y. F. ZHANG, N. WANG et al., *J. Appl. Phys.*, **85**, 1999, 7981.
- 62 W. S. SHI, H. Y. PENG, Y. F. ZHENG et al., *Adv. Mater.*, **12**, 2000, 1343.
- 63 W. Z. LI, S. S. XIE, L. X. QIAN et al., *Science*, **274**, 1996, 1701.
- 64 R. S. WAGNER, R. G. TREUTING, *J. Appl. Phys.*, **32**, 1961, 2490.
- 65 W. S. SHI, H. Y. PENG, L. XU et al., *Adv. Mater.*, **12**, 2000, 1927.
- 66 Y. ZHANG, K. SUENAGA, C. COLLIEX et al., *Science*, **281**, 1998, 973.
- 67 C. P. LI, N. WANG, S. P. WONG et al., *Adv. Mater.*, **14**, 2002, 218.
- 68 Z. W. PAN, H. L. LAI, F. C. K. AU et al., *Adv. Mater.*, **12**(16), 2000, 1186.
- 69 W. Z. LI, S. S. XIE, L. X. QIAN et al., *Science*, **274**, 1996, 1701.
- 70 Z. W. PAN, S. S. XIE, B. H. CHANG et al., *Nature*, **394**, 1998, 631.
- 71 Z. W. PAN, S. S. XIE, B. H. CHANG et al., *Chem. Phys. Lett.*, **299**, 1999, 9.
- 72 X. DUAN, J. WANG, C. M. LIEBER, *Appl. Phys. Lett.*, **76**, 2000, 1116.
- 73 N. WANG, Y. H. TANG, Y. F. ZHANG et al., *Chem. Phys. Lett.*, **299**, 1999, 237.
- 74 J. Q. HU, X. L. MA, N. G. SHANG et al., *J. Phys. Chem. B*, **106**, 2002, 3823.
- 75 Y. JIANG, X. M. MENG, J. LIU et al., *Adv. Mater.*, **15**, 2003, 323.
- 76 X. H. SUN, H. Y. PENG, Y. H. TANG et al., *J. Appl. Phys.*, **89**, 2001, 6396–6399.
- 77 Y. F. ZHANG, L. S. LIAO, W. H. CHAN et al., *Phys. Rev. B*, **61**, 2000, 8298.
- 78 X. T. ZHOU, J. Q. HU, C. P. LI et al., *Chem. Phys. Lett.*, **369**, 2003, 220.
- 79 X. H. SUN, C. P. LI, N. B. WONG et al., *J. Am. Chem. Soc.*, **124**, 2002, 14856.
- 80 R. H. FOWLER, L. W. NORDHEIM, *Proc. R. Soc. London, Ser. A*, **119**, 1928, 173.
- 81 D. D. D. MA, C. S. LEE, F. C. K. AU et al., *Science*, **299**, 2003, 1797.
- 82 Y. H. TANG, X. H. SUN, F. C. K. AU et al., *Appl. Phys. Lett.*, **79**, 2001, 1673.
- 83 D. D. D. MA, C. S. LEE, Y. LIFSHITZ et al., *Appl. Phys. Lett.*, **81**, 2002, 3233.
- 84 R. Q. ZHANG, T. S. CHU, S. T. LEE, *J. Chem. Phys.*, **114**, 2001, 5531.
- 85 D. K. YU, R. Q. ZHANG, S. T. LEE, *Phys. Rev. B*, **65**, 2002, 245417.
- 86 B. X. LI, R. Q. ZHANG, P. L. CAO et al., *Phys. Rev. B*, **65**, 2002, 125305.
- 87 R. Q. ZHANG, S. T. LEE, C. K. LAW et al., *Chem. Phys. Lett.*, **364**, 2002, 251.
- 88 D. K. YU, R. Q. ZHANG, S. T. LEE, *J. Appl. Phys.*, **92**, 2002, 7453.
- 89 R. Q. ZHANG, W. C. LU, S. T. LEE, *Appl. Phys. Lett.*, **80**, 2002, 4223.

## 11

## Electronic Structure and Spectroscopy of Semiconductor Nanocrystals

*S. Sapra and D. D. Sarma*

## 11.1

### Introduction

There has been a tremendous increase in research in the field of nanocrystals during the past decade [1–7]. Although research on nanocrystals started in the early eighties, the spectacular level of activity was witnessed only in the nineties with the emergence of improved techniques for the synthesis of high quality nanocrystals and better instruments to characterize them. Also, the growing demand from the electronics industry to reduce the size of the integrated circuit chips gave the field of nanotechnology a tremendous boost.

Solid materials can be categorized as metals or semiconductors, depending on their ability to conduct electrical charge. On a microscopic level, this implies that the metal has overlapping valence and conduction bands, allowing the electrons to move freely, and thus giving rise to charge conduction. Semiconductors have fully filled valence bands and the entirely empty conduction band is separated from the valence band by a forbidden range of energies. Thus, conduction in such materials requires a finite energy to promote the electrons from the valence to the conduction band. While metals do not show much change in their electronic properties down to very low sizes, but semiconductors exhibit interesting variations in their properties at sizes of about 10 nm (100 Å) and below. One thing that is most noticeable in the case of semiconductors is the variation of the band gap with a decrease in the size of the nanocrystals below the Bohr exciton radius,  $a_B$ , of the semiconductor. For example, the band gap of CdS, a II–VI semiconductor, can be made to vary more or less continuously from the bulk value of 2.4 eV up to about 4.0 eV observed for a 15 Å nanocrystal by merely tuning the size of the CdS nanocrystals [8]. Other properties such as the melting point also depend strongly on size. For example, while the melting point of bulk CdS is  $\sim 1600^\circ\text{C}$ , 2.5 nm CdS crystallites melt at a temperature as low as  $\sim 400^\circ\text{C}$  [9]. Optical properties such as fluorescence emission are also critically dependent on the size of the nanocrystals. For example, it has been shown that various sized CdSe nanocrystals can fluoresce throughout the visible range of the electromagnetic spectrum [10] with suitable control of the particle size.

The structure of the nanocrystalline materials plays an important role in determining electronic properties. The same material can crystallize in different structures upon size reduction, depending on the reaction conditions. Such structural transformations are discussed in Section 11.2.

As already pointed out, the most direct consequence of a reduction in the nanocrystallite size on the electronic structure of semiconducting materials is a pronounced increase in the band gap due to the quantum confinement effect. While there are several ways to quantitatively understand this phenomenon from a theoretical standpoint, the experimental determination of the band gap variation as a function of size is most directly performed by ultraviolet–visible absorption spectroscopy, with the experimental absorption threshold corresponding to the direct band gap in the material. As the band gap shifts to higher energy, the blue-shift in the absorption edge signals the formation of progressively smaller sized nanocrystals. Therefore, UV–Vis absorption spectroscopy has played an immensely important role in the study of these systems and we discuss the essential aspects in Section 11.3.

The UV–Vis absorption process generates an excited state of the system by generating an electron in the conduction band and a hole in the valence band; this state most often de-excites via a radiative process, giving rise to fluorescence. The emission characteristics depend on various aspects of the electronic structure of the nanocrystallites. Thus, the tuning of the fluorescence wavelength in nanocrystals can be achieved by a variety of methods as discussed in Section 11.4.

A lot of theoretical work has been done in order to explain the size dependent properties of semiconducting nanocrystals. These methods are primarily based on the effective mass approximation, pseudopotential approaches or the tight binding scheme. Each of these methods has certain advantages and disadvantages. We shall explore these methods in some detail in Section 11.5.

Photoemission experiments that probe the electronic structure of the nanocrystals are indispensable if one wishes to gain insight into the electronic structure–property relationship. Though very few studies have been carried out on semiconducting nanocrystalline systems to date, techniques such as photoemission and X-ray absorption spectroscopies are of immense value in probing the electronic structure and also in verifying various theories proposed for the nanocrystals. In Section 11.6 we discuss these spectroscopic studies.

## 11.2

### Structural Transformations

Solids are known to exist in different structural phases depending on the temperature, pressure and other ambient conditions. Semiconductors, especially the group IV, II–VI and III–V that are more covalent than other compounds, prefer tetrahedral coordination around the ions, giving rise to phases such as the zinc blende or the hexagonal phase. Ionic solids are stable in higher symmetry octahe-

dral phases such as the rock salt structure. It is easy to imagine the conversion from tetrahedral coordination to octahedral coordination. Applying pressure to the tetrahedron it can be flattened out to give a square planar structure. Two atoms from the top and bottom can come closer to form an octahedron. Although C and Si, which are highly covalent, would be unstable in octahedral coordination and prefer tetrahedral coordination owing to their  $sp^3$  hybridized orbitals, II–VI and III–V semiconductors, that have some degree of ionicity, can be transformed to the octahedrally coordinated structure by application of pressure. It has been found in the case of CdSe nanocrystallites that the wurtzite nanocrystals are transformed to the rock salt phase by application of 2–9 GPa pressure [2]. Phase transformations from the stable wurtzite phase to the zinc blende structure have been observed in the case of CdS nanocrystals as a function of the nanocrystal size [11]. Figure 11.1 shows the wide angle X-ray diffraction patterns for CdS bulk, and 4.5 nm and 2.2 nm nanocrystals of CdS. The bulk and the larger 4.5 nm nanocrystals exhibit the characteristic wurtzite phase structures, though the pattern for the nanocrystals is broader than that of the bulk. This broadening is exploited to measure the particle size from the X-ray diffraction pattern using the Scherrer formula for spherical particles,

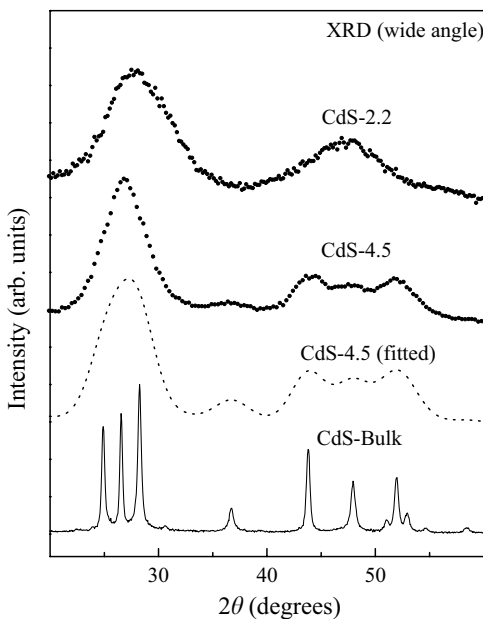


**Fig. 11.1.** X-ray diffraction patterns for bulk CdS, 4.5 nm and 2.2 nm CdS nanocrystals. Also shown is the broadened bulk pattern for spherical CdS nanocrystals of 4.5 nm diameter. Note the change in the structure for the 2.2 nm nanocrystals as seen between  $2\theta$  equal to  $45^\circ$ – $55^\circ$ . Adapted from [11, 99].

$$D = \frac{4}{3} \frac{0.9\lambda}{B \cos \theta}$$

where  $D$ , the diameter of the spherical particles is related to the full-width-at-half-maximum,  $B$ , of the peak centered at  $\theta$  recorded with X-rays of wavelength  $\lambda$ . The broadened pattern is also shown in the figure; the broadening corresponding to 4.5 nm diameter for the particles. The pattern for the 2.2 nm CdS nanocrystals is rather different from the wurtzite structure particularly in the range  $2\theta = 45\text{--}55^\circ$ . It has been suggested that this change in the XRD pattern is due to the presence of a mixture of both the wurtzite and the zinc-blende phases. This structural transformation at small sizes also causes a change in the electronic structure of the nanocrystals. Thus, at small sizes one needs to take into account the structural changes while discussing the electronic properties.

### 11.3

#### Ultraviolet–Visible Absorption Spectroscopy

Band gaps of all semiconducting and insulating materials increase monotonically with decreasing size of the nanocrystallites. However, the band gap increases appreciably only in the domain of extremely small sizes, when the size of the nanocrystals is reduced below the Bohr exciton radius,  $a_B$  of the material. The band gap increase is most easily observed in the UV–Vis absorption spectra as the absorption edge shifts systematically to lower wavelengths. We provide two illustrative examples in Figure 11.2, that shows the absorption spectra for different sizes of (a) ZnS and (b) CdS nanocrystals [11, 12]. For both CdS and ZnS, we observe an increase in the band gap with decreasing size. One can also clearly observe a sharp peak, the excitonic peak, near the absorption edge, particularly in the spectra from the smaller sized nanocrystallites. For example ZnS-1.8, ZnS-2.5 and CdS-2.2 (the numbers here representing the average diameter of the nanocrystallites in nm) exhibit extremely sharp excitonic peaks. Even ZnS-3.5 and CdS-4.5 show the existence of this peak. It is interesting to note, however, that there is no trace of this peak in the room temperature spectra of the corresponding bulk samples shown in Figure 11.2. The exciton binding energy is of the order of a few tens of meV for these bulk solids, which is comparable to the thermal energy at room temperature. Thus, we do not usually observe the excitonic peak for bulk solids at room temperature and one must significantly cool the sample in order to observe the excitonic absorption feature in bulk samples. However, for nanocrystals, the enhanced overlap of the electron and the hole wavefunctions in the spatially confined structure increases the excitonic binding energy, thereby making observation of the excitonic peak possible, even at room temperature. This also explains why the excitonic peak is more clearly observed for small CdS and ZnS nanocrystallites in terms of a progressively increasing excitonic binding energy with decreasing size.



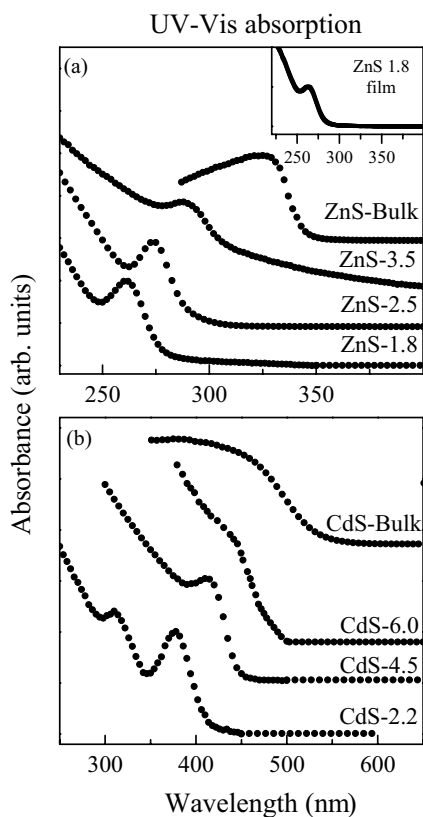


**Fig. 11.2.** UV–Vis absorption spectra of (a) ZnS nanocrystallites of different sizes: 3.5, 2.5 and 1.8 nm diameters in dimethyl formamide solution (inset shows the absorption spectrum of 1.8 nm ZnS nanocrystalline film) and (b)

CdS nanocrystallites of various sizes: 6.0, 4.5 and 2.2 nm diameters. The bulk spectra for the two systems are also shown. Adapted from [11, 99, 100].

It is possible to deduce the size of the nanocrystals from the blue shift in the absorption curves. This is discussed in detail in Section 11.5. Apart from the size of the nanocrystals, the size distribution must be very narrow in order to study any size dependent properties of the nanocrystals. Figure 11.3 shows a typical transmission electron micrograph and the deduced size histogram to illustrate the narrow size distribution for the ZnS-3.5 nanocrystals whose absorption spectrum is shown in Figure 11.2. The UV absorption spectrum can also provide a qualitative indication of the size distribution. For example, the sharp excitonic peak in the absorption spectra in the case of small nanocrystals (see Figure 11.2) is indeed indicative of the narrow size distribution of the nanocrystals in the sample. If the size distribution was broad, there would be a number of exciton peaks appearing at different energies corresponding to different sized nanocrystals and overlapping

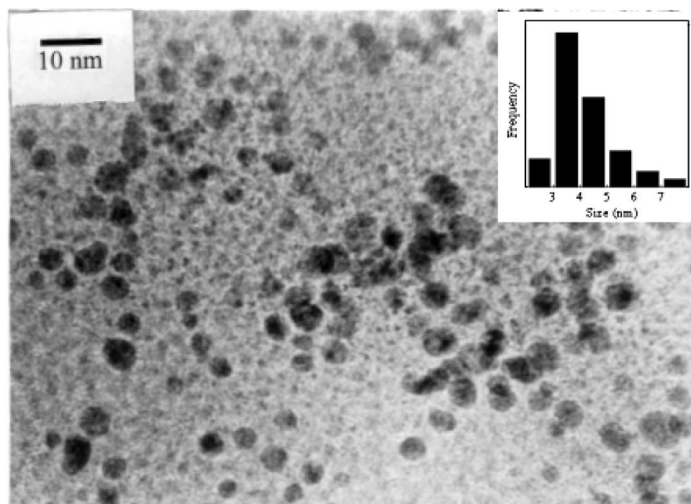


**Fig. 11.3.** Low magnification TEM pictures of ZnS-3.5 showing individual nanocrystallites. Also shown is the histogram for the particle size distribution. Adapted from [11].

with each other and hence we would not observe sharp excitonic features in the absorption spectra, but only a broad and featureless absorption edge.

Besides the monotonic shift in the band gap with size, an interesting observation of a non-monotonic band gap variation was made for Mn-doped CdS nanocrystals [28]. For a fixed Mn composition, the band gap increases with decreasing particle size, as expected on the basis of quantum confinement. However, varying the Mn concentration in a fixed size nanocrystal also results in a small but definite variation of the band gap. The band gap is indeed expected to vary as one goes from CdS to MnS by doping with  $\text{Mn}^{2+}$  ions because the band gaps of the two materials are different; bulk CdS has a 2.4 eV band gap and MnS has a band gap of 3.4 eV [13]. However, the band gap is not found to vary linearly between these two values as a function of  $x$  in  $\text{Cd}_{1-x}\text{Mn}_x\text{S}$ ; instead one notices a minimum in the band gap at about 2–3% Mn doping [28]. This effect is found to be more pronounced for smaller particles and has been ascribed to a stronger hybridization of the host sp bands with the Mn d bands in the case of nanocrystals due to the confinement of the wavefunctions [28].

Interestingly, a reversed type non-monotonic variation in the band gap has been observed with Mn concentration in Mn-doped ZnS nanocrystals [14]. This is shown in Figure 11.4; the main frame shows the UV–Vis absorption spectra and the inset shows an initial increase in the band gap, also seen in the UV–Vis absorption edges, with values of  $x$  in  $\text{Zn}_{1-x}\text{Mn}_x\text{S}$  up to  $x = 6\%$  followed by a decrease on further increase in  $x$ . It is to be noted here that the band gap of ZnS, in contrast to that of CdS, is larger than that in MnS, accounting for the reversed

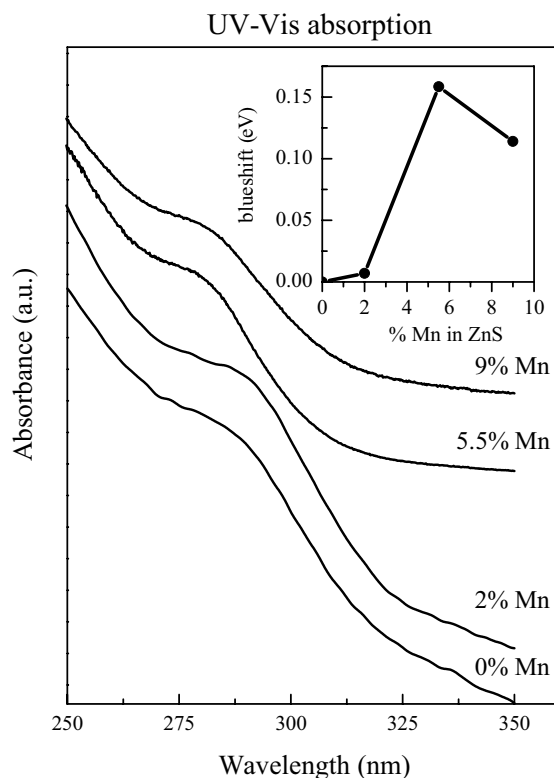


**Fig. 11.4.** UV-Vis absorption spectra of  $\text{Zn}_{1-x}\text{Mn}_x\text{S}$  nanocrystals with varying  $x$ . Notice the change in the band edge with change in the amount of Mn. The inset shows the shift in the band gap with reference to the band gap of undoped ZnS nanocrystals. Adapted from [14, 20].

behavior, though the band gap variation with Mn concentration arises from the interaction of the Mn states with those of the host materials in both cases.

## 11.4

### Fluorescence Spectroscopy

In the absorption process, the electrons are excited across the band gap, from the valence band to the conduction band, by providing an appropriate energy greater than the band gap of the material. These excited electrons must decay back to the valence band by radiative or non-radiative thermal processes. Non-radiative processes are the predominant routes to de-excitation when the electron-phonon coupling is strong. Phonon coupling provides quasi-continuous states which the

electrons can occupy successively to de-excite to the ground state. In the absence of strong phonon coupling, the electrons have to make a radiative transition that often corresponds to energies close to the visible region of the electromagnetic spectrum. This phenomenon, known as fluorescence, can occur in nanocrystals in a variety of ways; for example, the electron–hole recombination can take place by involving the electronic states at the band edge, surface, defect and other trap states, or states on doped impurity atoms, giving rise to fluorescence at different energies for the same material. We shall discuss these different routes in some detail here.

Electrons can de-excite radiatively by making a transition from the bottom of the conduction band (BCB) to the top of the valence band (TVB). This is known as band edge recombination. This leads to an overlap of the fluorescence excitation and emission energies. Such emission has been observed in the case of a number of materials such as CdSe [15] and ZnSe [16]. One such case is illustrated in Figure 11.5 where we show the fluorescence excitation and emission spectra from ZnSe nanocrystallites of approximate diameter 40 Å [17]. By comparing the peaks in the two spectra, one can easily see that there is hardly any shift in the frequency (wavelength) of the light used to excite and the frequency of the emitted radiation. This is easily understood in terms of the absence of any significant trap states; the energy absorbed by the system to create an electron–hole pair will necessarily be

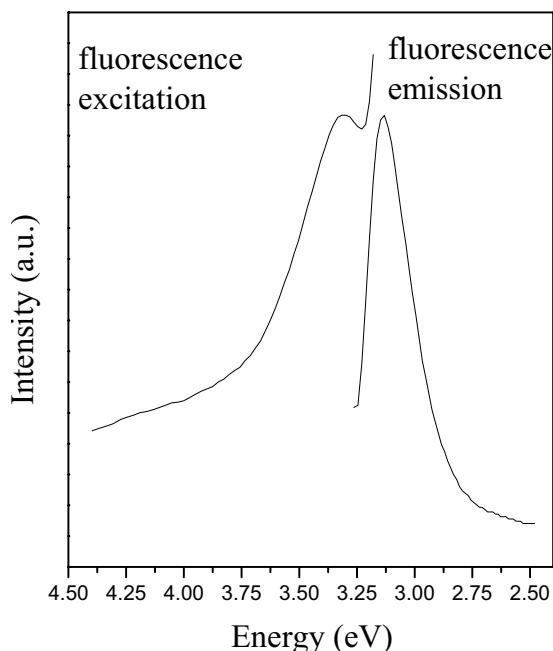


**Fig. 11.5.** Fluorescence excitation and emission spectra of ZnSe nanocrystals showing the band edge emission. Adapted from [17].

equal to the energy emitted, when the electron and the hole recombine without the loss of any energy prior to the emission.

The presence of unquenched dangling orbitals at the surface or any defect states in the bulk, provide traps for the excited electrons and the holes prior to their recombination. These orbitals have their energies in the band gap region, as shall be discussed in greater detail in Section 11.5. Therefore, an electron excited to the conduction band can transfer itself non-radiatively to one of these surface or defect states before making a radiative transition to a lower energy state; likewise, a hole excited in the valence band can move into the defect states depending upon the donor/acceptor character of the defect states. The net result of such non-radiative transfers of electrons and holes to lower energy states prior to radiative recombination is that the emission occurs at energies much lower than the band gap energy of the nanocrystals, in contrast to the band edge recombination considered earlier. This is often referred to as the red-shifted emission in nanocrystals [18]. Figure 11.6 shows the surface or defect state emission from CdS nanocrystals [11]. Evidently, there is a large difference in energies between the peak positions in the excitation and the emission spectra. Such an emission is useful where one requires well separated excitation and emission, as in the case of fluorescent probes. However, such defect states tend to be spread over a wide energy range, leading to

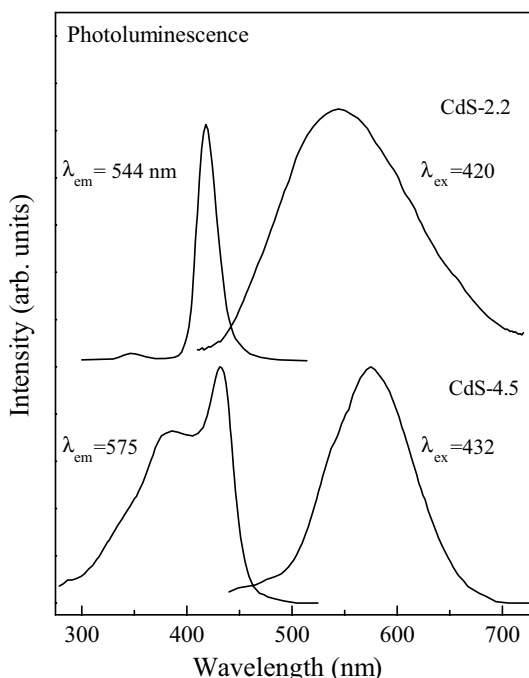
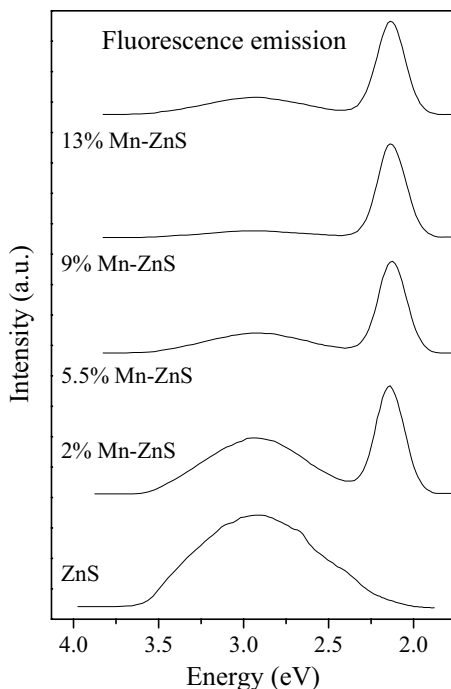


Fig. 11.6. Fluorescence excitation and emission spectra of CdS-2.2 and CdS-4.5 nanocrystals showing the defect state emission. Adapted from [11].

emissions over a range of photon energies, in other words, giving rise to a broad and consequently a low intensity emission. Moreover, it is in general difficult to tailor-make or tune the energies arising from such defect states, rendering it difficult to influence the emission, as required by any specific application, by rational synthesis. Thus, synthesis strategies are often adopted to passivate these dangling bonds, so that the dominant part of the de-excitation process takes place via the band edge recombination, thereby allowing for tuning of the emission characteristics from a nanocrystal sample by tuning the band gap via size-control. Such surface passivation can be achieved by different methods. In one approach, the organic capping agent, that is used to limit the growth of the nanocrystals, is so chosen that it has a strong interaction with the surface states, leading to an effective removal of the surface states from the band gap region. Using cysteine ester, it has been shown [19] that CdS nanocrystals that normally emit in the orange due to such defect states can be made to emit in the blue. Figure 11.5 shows the case of ZnSe with the surface states suitably passivated to give rise to band edge emission. An alternative method to remove the surface states is to overcoat the nanocrystallite with a thin layer of another material of a higher band gap. This has been carried out in the case of CdSe nanocrystals overcoated with a few layers of ZnS [10]. This results in the proper passivation of the trap states giving rise to an enhanced fluorescence compared to CdSe nanocrystals coated with an organic passivating layer.

Another method to induce sharp fluorescence at a chosen energy is to dope impurity ions into the host semiconductor lattice. This results in energy transfer from the band edge to the impurity ion, thus giving rise to fluorescence from the impurity levels. As the energy levels of the impurity ion must be below the bottom of the conduction band for the electron to de-excite into these levels, the emission from impurity levels is, in general, red-shifted with respect to the band edge. The most extensively studied doped systems are those of Mn-doped ZnS [14, 20–34] and Mn-doped CdS [26–28] nanocrystals. Figure 11.7 shows typical fluorescence emission spectra of various percentages of Mn-doped ZnS nanocrystals of 18 Å diameter [20]. The excitation wavelength is 290 nm (4.3 eV). The ZnS surface states, which appear at 440 nm, are almost totally quenched for the 9% Mn-doped ZnS sample and only the Mn d–d orange emission is observed at 590 nm (2.1 eV). The orange emission is slightly weakened at higher temperatures due to exciton–phonon coupling [29]. At temperatures below 50 K the luminescence intensity remains constant indicating a phonon frequency of  $101\text{ cm}^{-1}$  [29]. At room temperature the luminescence efficiency drops to about half the value at 50 K, as studied in a glass matrix, due to phonon coupling [29]. Bhargava et al. concluded that the lifetime of the Mn d–d transition in the case of nanocrystals reduces to the order of a few nanoseconds compared to the bulk material where the transition takes place on a timescale of a few milliseconds [31]. This was attributed to an enhanced overlap of the sp–d exchange interactions between the host bands and the Mn d levels due to the larger overlap of the host sp and Mn d wavefunctions in the confined nanocrystals compared to the bulk material. Bol and Meijerink [34] studied the time resolved fluorescence of Mn-doped ZnS nanocrystals. For a zero time delay they observe only the ZnS defect emission at  $\sim 400\text{ nm}$ , indicating that this



**Fig. 11.7.** Fluorescence emission spectra of 18 Å Mn-doped ZnS nanocrystals. Notice the ratio of orange:blue emission with change in Mn concentration. The excitation energy 4.27 eV (290 nm) corresponds to the band gap of 18 Å ZnS nanocrystals. Adapted from [20].

blue emission is short lived, of the order of nanoseconds. They did not observe the orange emission in this case. However, for time delays as large as 0.5 ms, the only observed emission was that of the Mn d–d transition. There was no blue component in the fluorescence spectrum recorded 0.5 ms after the excitation source was switched off. This indicates that the Mn d–d transition is not a shortlived emission but the timescales for this emission in the bulk and nanocrystalline Mn-doped ZnS are about the same. Further studies on Mn-doped ZnS nanocrystalline samples have established the absence of any Mn-related emission with a decay time in the regime of nanoseconds [24, 25, 34].

It has been found that the emission due to Mn doping can be further tuned by changing the crystal field around the  $\text{Mn}^{2+}$  ions. Instead of the  $\text{S}^{2-}$  ions, as in the case of ZnS, an oxide host can be used to induce a much larger crystal field splitting of the  $t_{2g}$ – $e_g$  levels in  $\text{Mn}^{2+}$  ions, for example by doping  $\text{Mn}^{2+}$  ions in ZnO nanocrystals [20]. In this case, the Mn d–d emission is observed at  $\sim 470$  nm (2.6 eV), representing a blue shift of 0.5 eV compared to the case of Mn emission in Mn-doped ZnS.



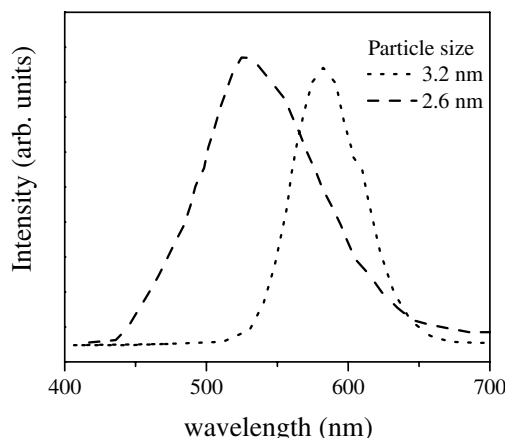


**Fig. 11.8.** Fluorescence emission spectra of Eu-doped ZnS nanocrystals for 2.6 and 3.2 nm nanocrystals. The emission peaks for the  $\text{Eu}^{2+} 4f^6 5d^1 - 4f^7$  transition shift with a change in the nanocrystal size. Adapted from [35].

Another interesting doped system that has been studied is  $\text{Eu}^{2+}$  doped in a ZnS host [35]. As shown in Figure 11.8, the emission from Eu-doped ZnS depends on the size of the ZnS nanocrystal. This is quite intriguing as such an effect has not been observed in the Mn-doped systems. The emission from Eu-doped ZnS has been attributed to the  $4f^6 5d^1(t_{2g}) - 4f^7$  transition [36]. These authors also studied the variation in the fluorescence spectrum as a function of the Eu concentration between 3 and 7% doped in a specific sized nanocrystal. As they did not find any wavelength shift of the emission with changing Eu concentration, they ruled out Eu–Eu exchange interactions as a possible mechanism for the observed shifts in the emission wavelength as a function of the host particle size, shown in Figure 11.8. The host band–Eu band sp–d interaction is also not involved as this, contrary to observation, causes a decrease in the energy of the emission with a decrease in the size of the nanocrystals. The increase in the emission energy has instead been attributed to crystal field effects and phonon coupling. The ground state of  $\text{Eu}^{2+}$  is the  $4f^7 5d^0$  state, while the excited state is the one with an electron in the d level of the  $t_{2g}$  state separated from the higher lying  $e_g$  state by an energy gap of  $10 Dq$ . If the crystal field strength is this high, the  $t_{2g}$  states are pushed to a lower energy; conversely, the  $t_{2g}$  level increases in energy with a decrease in the crystal field strength. For nanocrystals the crystal field strength is a little weaker than in the bulk [33], giving rise to a blue-shift in the emission spectrum. Electron–phonon coupling does not affect the absorption spectrum for particles with sizes less than the wavelength of the light used [37]. However, phonons continue to play an important role in energy relaxation processes [37, 38]. Electron–phonon coupling decreases with decrease in the particle size as the density of states decreases with size [39]. This has been calculated for the case of Eu-doped ZnS using the Huang–Rhys parameter,  $S$  [40]. This parameter is directly proportional to the Stokes shift in the

emission energy

$$\Delta_{\text{Stokes}} \propto S$$

As  $S$  decreases with decreasing particle size, it indicates a decrease in the electron–phonon coupling strength [33]. Therefore, the Stokes shift is smaller for smaller particles, implying that the emission shifts to higher energies for smaller particles. Therefore, both crystal field effects and electron–phonon coupling are responsible for the shifted fluorescence emission wavelength observed in the case of Eu-doped ZnS nanocrystals.

## 11.5

### Electronic Structure Calculations

There has been a huge amount of effort towards understanding the changes in the electronic structure of nanomaterials as one changes the size of the crystallites. Qualitatively, it can be understood as a particle-in-a-box-like problem, where the energy level spacings increase as the box dimensions are reduced due to quantum confinement. This simple idea provides us with the basis of a qualitative understanding of the increase in the band gap with decrease in the particle size. However, a quantitative understanding involves much more elaborate calculations of the band gap of the nanocrystals as a function of their size. There is a fundamental difference between the calculations for the nanocrystals and those for the bulk. In the case of bulk materials, the size of the material can be considered to be infinite for most practical purposes, with the influence of the surface or boundary effects on the electronic structure of the bulk being negligibly small. In the context of a periodic solid, the assumption of an unbounded solid leads to important simplifications in the calculations in terms of a Fourier transform of the real space problem to the momentum space, allowing us to carry out the calculations for the number of orbitals involved inside a single unit cell for a large number of momentum values, providing us with the well-known dispersion relations connecting the energy eigen-values to the momentum vector. Such approaches are detailed in any textbook of solid state physics. In sharp contrast, a nanocrystal is, by definition, bounded on all sides, i.e. the electron propagation is confined in all three dimensions. This implies that the lattice periodicity or the translational invariance is broken in such a finite-sized system and the momentum is no longer a good quantum number to provide a quantum mechanical description of the system. Thus, the electronic structure has to be necessarily evaluated directly in real space. Therefore, such a calculation involves a Hamiltonian matrix with dimension equal to the total number of orbitals in the whole of the nanocrystal. Since, the number of atoms, and therefore also the number of orbitals, in a nanocrystal grows as the cube of the size (say, the diameter of the nanocrystal), the matrix dimension grows very quickly with the size, necessitating highly efficient calculational schemes. The three approaches that have been most used will be discussed in this section.

## 11.5.1

**Effective Mass Approximation**

In the case of solids, the band dispersion describes a complicated dependence of energy on momentum, that usually cannot be described analytically. However, in the case of a semiconductor, the dispersion relations at the top of the valence band (TVB) and at the bottom of the conduction band (BCB), can often be described approximately as parabolic. Therefore, near the band edges, the delocalized electrons or holes, follow a quadratic equation of the form

$$E = \frac{\hbar^2 k^2}{2m^*}$$

where  $m^*$  is the effective mass of the charge carrier (electron or hole). To use the effective mass approximation to describe the band gap variation with size for nanocrystals, one needs to solve the Schrödinger equation for the envelope function  $\psi$ :

$$\left[ -\frac{\hbar^2 \nabla_e^2}{2m_e} - \frac{\hbar^2 \nabla_h^2}{2m_h} - \frac{e^2}{4\pi\epsilon_0\epsilon r_{eh}} + V_0 \right] \psi(r_e, r_h) = E\psi(r_e, r_h) \quad (1)$$

where the subscripts e and h refer to the electron and the hole with  $m$  and  $r$  being the mass and position vector, respectively, and  $r_{eh} = |r_e - r_h|$ .  $\epsilon_0$  and  $\epsilon$  are the permittivity in vacuum and the relative dielectric constant of the material. Using a trial wavefunction the above equation can be solved by approximate methods.

For an infinite potential outside the nanocrystals and zero potential inside, Efros and Efros [41], Brus [42–44] and Kayanuma [45, 46] proposed the following equation for the band gap,  $E_R$ , of a quantum dot of radius  $R$

$$\Delta E_g \equiv E_R - E_g = \frac{\hbar^2 \pi^2}{2R^2} \left[ \frac{1}{m_e} + \frac{1}{m_h} \right] - \frac{1.8e^2}{\epsilon R} - 0.248 E_{Ry}^* \quad (2)$$

where  $E_g$  is the bulk band gap and  $R$  is the radius of the quantum dot. The first term corresponds to the kinetic energies for the non-interacting electron and hole in a spherical box of radius  $R$ . The second term,  $-\frac{1.8e^2}{\epsilon R}$ , arises due to the Coulomb interaction between the electron and the hole, while the third term is due to the spatial correlation between the electron and the hole. The effective Rydberg in meV is defined as:

$$E_{Ry}^* = 13605.8 \frac{1}{\epsilon^2} \left( \frac{m_0}{m_e} + \frac{m_0}{m_h} \right)^{-1} \quad (3)$$

The EMA has been used to calculate the band gap for various semiconducting nanocrystals [47–53]. For larger sizes of nanocrystallites, the infinite potential (IP)-

EMA gives a good description of the band gap variation with size. However, it grossly overestimates the change,  $E_g$ , in the band gap for smaller nanocrystals.

Kayanuma [45] identified two limiting cases depending upon the ratio of the radius of the quantum dot to the Bohr exciton radius,  $a_B$  of the bulk solid. For  $R/a_B \gg 1$ , the exciton can be pictured as a particle moving inside the quantum dot with only a small increment in energy due to the confinement. This is the weak confinement regime. In the strong confinement regime where  $R/a_B \ll 1$ , confinement effects obviously dominate. It was pointed out that in this regime, the electron and the hole should be viewed as individual particles in their respective single particle ground states with little spatial correlation between them as a consequence of the increased kinetic energy term. Kayanuma further found that the strong confinement regime is not only limited to  $R/a_B \ll 1$ , instead confinement effects are seen up to  $R \approx 2a_B$ . This is the regime where the effective mass approximation is relatively more valid, though quantitatively EMA fails to account for the observed changes.

The IP-EMA model essentially neglects any possibility of tunnelling of the wavefunction beyond the surface of the nanocrystals as a consequence of the assumption of a rigid wall (infinite potential), particularly ignoring the role played by the passivating atoms on the surface of the nanocrystals providing a possibility to the electrons and the holes to substantially tunnel outside the nanocrystal. To overcome the shortcomings of the IP-EMA, Kayanuma and Momiji [54] used the finite potential to account for the experimental data for small CdS crystallites. The confining potentials  $\bar{V}_e$ , for the electron and  $\bar{V}_h$  for the hole, satisfy the relation  $E_g + \bar{V}_e + \bar{V}_h = E_g^1$ , where  $E_g^1$  is the band gap energy of the surrounding material. The resulting problem was solved variationally in the Hylleraas coordinate system.

Although the effective mass of the electron is described quite well using a single conduction band, the TVB in these systems is degenerate and the description of the hole effective mass requires a greater number of bands. Therefore, the multi-band EMA (MBEM) theory represents a substantial improvement over the single band, IP-EMA. In CdSe nanocrystals, the size dependences of up to 10 excited states [49, 50] in the absorption spectra are successfully described by the uncoupled MBEM. This includes the valence band degeneracy, but does not couple the valence and conduction bands. Banin et al. [51] have used the MBEM including the valence and the conduction band coupling. They use an eight band Luttinger–Kohn Hamiltonian to calculate the quantum size levels in InAs [51].

Such improvements over the over-simplistic IP-EMA explain the experimental data quite well. However, approaches based on EMA explain the results a posteriori, whereas a theory is required that has predictive capabilities and can be applied to handle new systems.

### 11.5.2

#### Empirical Pseudopotential Method

Another method that has been used to describe the electronic structure of bulk semiconductors is the empirical pseudopotential method [55, 56]. The potential

energy term  $V_p(r)$  in the Hamiltonian

$$H = -\frac{\hbar^2}{2m}\nabla^2 + V_p(r) \quad (4)$$

is the empirically determined pseudopotential

$$V_p(r) = \sum_G [V_s(G)S_s(G) + iV_A(G)S_A(G)] \exp(iGr) \quad (5)$$

where  $V_s$  and  $V_A$  are the symmetric and antisymmetric form factors, respectively. They are determined from the optical absorption data.  $S_s$  and  $S_A$  are the symmetric and antisymmetric structure factors, respectively, determined from the crystal structure of the semiconductor. For a nanocrystal of radius  $R$ , a reasonable assumption is to use the bulk pseudopotential  $V_p(r)$  inside the crystallite and terminate this potential at the edge of the cluster by an infinite potential corresponding to an infinite potential barrier. The Schrödinger equation

$$H\Psi_{n,k}(r) = E_n(k)\Psi_{n,k}(r) \quad (6)$$

is solved at a set of  $k$  points in the Brillouin zone. Due to the finite size of the nanocrystal, the allowed wave vectors are discrete. In the cartesian coordinates, the values of  $k$  are limited to

$$k = \frac{\pi}{\sqrt{3}R} [n_x, n_y, n_z] \quad (7)$$

The solution at these  $k$ -points gives the band structure of the nanocrystals.

Ramakrishna and Friesner [57] calculated the band structure of CdS and GaP nanocrystals up to 30 Å radius in the zinc-blende phase. The calculated variation agrees quite well with the experimental data points. The band gap variation curve in the case of GaP shows a red shifted band gap in the case of very small nanocrystals. This has not yet been experimentally verified.

Recently, Zunger and coworkers [18, 58–63] employed the semi-empirical pseudopotential method to calculate the electronic structure of Si, CdSe [60] and InP [59] quantum dots. Unlike EMA approaches, this method, based on screened pseudopotentials, allows the treatment of the atomistic character of the nanostructure as well as the surface effects, while permitting multiband and intervalley coupling. The atomic pseudopotentials are extracted from first principles LDA calculations on bulk solids. The single particle LDA equation,

$$\left[ -\frac{1}{2}\nabla^2 + V_{\text{nonlocal}}^{\text{ps}}(r) + V_{\text{LDA}}(r) \right] \Psi_i = \varepsilon_i \Psi_i \quad (8)$$

is solved to obtain the electronic structure of a solid. The ionic pseudopotential consists of the non-local part  $V_{\text{nonlocal}}^{\text{ps}}(r)$  and  $V_{\text{LDA}}$  is composed of the local ionic pseudopotential,  $V_{\text{local}}^{\text{ps}}(r)$ , and the screening potential  $V_{\text{HXC}}$  made up of the inter-electron Coulomb (Hartree) and the exchange and correlation (XC) parts. For a given crystal structure, the knowledge of the atomic pseudopotentials allows one to solve Eq. (8). The wave functions are LDA-like while the band structures, effective masses, and deformation potentials matched the experiments. These improvements in the semi-empirical method over the empirical pseudopotential method provide a better description of the electronic structure of the quantum dots. However, the large size of the Hamiltonian does not allow one to calculate the properties of large sized nanocrystals.

### 11.5.3

#### Tight-Binding Method

Within the tight-binding (TB) approach, Slater and Koster [64] described the linear combination of atomic orbitals (LCAO) method as an efficient scheme for calculation of the electronic structure of periodic solids. As this method is computationally much less demanding than other methods such as the plane-wave methods, it has been extensively employed to calculate electronic structures of various metals, semiconductors, clusters and a number of complex systems such as alloys and doped systems. The calculation of the electronic structure requires solving the Schrödinger equation with the TB Hamiltonian given by

$$\mathbf{H} = \sum_{i l_1 \sigma} \varepsilon_{l_1} a_{i l_1 \sigma}^* a_{i l_1 \sigma} + \sum_{ij} \sum_{l_1, l_2 \sigma} t_{ij}^{l_1 l_2} a_{i l_1 \sigma}^* a_{j l_2 \sigma} + \text{h.c.} \quad (9)$$

where the electron with spin  $\sigma$  is able to hop from orbitals labelled  $l_1$  with onsite energies equal to  $\varepsilon_{l_1}$  in the  $i^{\text{th}}$  unit cell to those labelled  $l_2$  in the  $j^{\text{th}}$  unit cell with a hopping strength  $t_{ij}^{l_1 l_2}$ , with the summations  $l_1$  and  $l_2$  running over all the orbitals considered on the atoms in a unit cell, and  $i$  and  $j$  over all the unit cells in the solid.

To calculate the eigenvalue spectra of nanocrystals, we need to know the  $\varepsilon$ 's for the various orbitals and the  $t$ 's for the interactions. These are evaluated by performing a TB-fit, with a prudent choice of the basis orbitals and the interactions, to the band structure of the bulk solid obtained from first principle calculations such as LAPW, LMTO or the pseudopotential methods.

The final results of the electronic structure of the nanocrystals depend on the type of the orbital basis chosen to build the TB Hamiltonian. The first-principle band structure calculation of the bulk material gives a good indication of the choice of the basis set and the interactions. For example, the density of states (DOS) and the partial DOS (PDOS) for the bulk system clearly illustrate the various orbitals involved in bonding at any given energy. The character of various bands in the band dispersions can also be analyzed to obtain similar, but even more detailed information. Thus, one can appropriately select the orbital basis to perform the TB

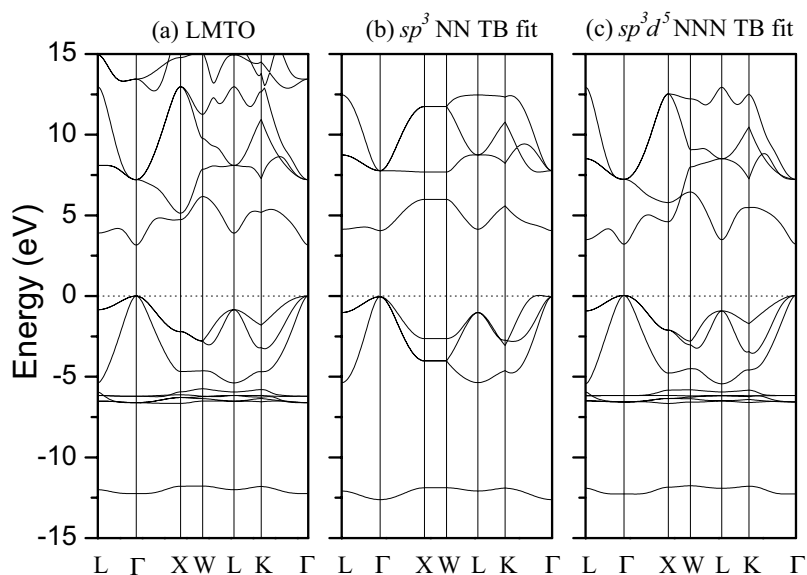


**Fig. 11.9.** (a) LMTO band dispersions, (b)  $sp^3$  nearest neighbor model TB fit and (c)  $sp^3d^5$  next nearest neighbor model TB fit for zinc sulfide in the zinc blende phase. Adapted from [73].

fit of the *ab initio* results. A natural choice for tetrahedrally coordinated semiconductors is the  $sp^3$  orbital basis set. The resulting band dispersions for ZnS within a nearest neighbor TB model are shown in Figure 11.9. Panel (a) shows the LMTO band dispersions and panel (b) shows the TB fitted dispersions with the nearest neighbor  $sp^3$  orbital basis set. From the figure it is clear that one cannot describe even the valence band properly within such a TB model. A careful analysis of the PDOS and fatbands shows that the *d* orbitals also have a non-negligible contribution around the band gap region. Moreover, the crystal orbital Hamiltonian overlap (COHP) can be used to determine the range of interactions between the various ions. It is seen that not only are the nearest neighbor interactions insufficient in the case of II–VI semiconductors but also the next nearest anion–anion interactions are essential. The TB fitted dispersions for the  $sp^3d^5$  orbital model with the cation–anion and anion–anion interactions are shown in Figure 11.9(c). It can be seen here that the  $sp^3d^5$  model with next nearest neighbor interactions provides an excellent description of the electronic structure of ZnS; similar results have been obtained also for other II–VI semiconductors. The TB parameters for the II–VI series obtained from the TB fit are given in Table 11.1. Assuming these parameters to be transferable from the bulk to the nanocrystals, we can use them to calculate the eigenvalue spectrum of the nanocrystals.

The calculation of the eigenvalue spectrum starts with the generation of the nanocrystal in real space by specifying the coordinates of the atoms. The nano-



**Tab. 11.1.** Tight-binding parameters obtained from the least-square-error fit to LMTO band dispersions for the nine II–VI semiconductors in the  $sp^3d^5$  basis with the A–B and B–B interactions. The first row lists the interatomic spacings in Å, the next eight rows contain the onsite energies for all the orbitals, e.g. the row for  $d_c(t_2)$  lists the entries for the  $t_2d$  orbital onsite energies for the cation. The subscript a denotes the anion. The last fifteen rows list the Slater Koster parameters. The last column shows the average value of the Slater Koster parameters multiplied by the square of the cation–anion distance,  $d^2$ .

	ZnS	ZnSe	ZnTe	CdS	CdSe	CdTe	HgS	HgSe	HgTe
$d$ (Å)	2.34	2.45	2.64	2.52	2.62	2.81	2.53	2.63	2.80
$s_c$	2.29	1.40	0.50	1.44	0.83	0.50	−0.85	−0.95	−1.45
$p_c$	9.32	9.21	8.36	8.22	7.80	7.78	8.16	8.35	7.76
$d_c(t_2)$	−6.24	−6.46	−7.26	−7.53	−7.85	−8.46	−6.10	−6.66	−7.27
$d_c(e)$	−6.16	−6.40	−7.21	−7.38	−7.74	−8.39	−6.81	−6.46	−7.18
$s_a$	−10.66	−11.21	−9.82	−10.58	−11.19	−9.70	−11.47	−11.93	−10.45
$p_a$	3.17	2.06	1.12	3.42	2.43	1.06	2.59	1.45	0.72
$d_a(t_2)$	15.31	16.10	13.08	14.32	15.12	13.20	14.72	15.42	12.76
$d_a(e)$	13.63	14.53	12.29	13.16	14.11	11.62	12.92	13.58	11.66
$ss\sigma$	−0.73	−0.74	−0.40	−0.72	−0.50	−0.00	−1.01	−0.88	−0.63
$sp\sigma$	2.57	2.68	2.19	2.12	2.04	2.01	2.05	2.06	1.81
$pp\sigma$	4.95	4.63	3.99	4.40	4.06	3.83	4.16	4.03	3.63
$pp\pi$	−0.88	−0.78	−1.05	−0.44	−0.49	−0.77	−0.48	−0.50	−0.64
$ps\sigma$	−2.11	−1.28	−1.37	−1.41	−1.70	−0.86	−1.00	−0.90	−1.14
$ds\sigma$	−0.67	−1.33	−0.32	−0.73	−0.69	−0.35	−1.17	−1.27	−0.74
$dp\sigma$	0.91	0.84	1.04	0.80	0.67	1.47	0.51	0.93	0.70
$dp\pi$	−0.43	−0.20	−0.10	−0.55	−0.51	−0.17	−0.38	−0.43	−0.37
$ss\sigma(2)$	−0.10	−0.09	−0.06	−0.04	−0.06	−0.01	−0.00	−0.02	−0.03
$sp\sigma(2)$	0.32	0.42	0.00	0.01	0.00	0.30	0.21	0.23	0.26
$pp\sigma(2)$	0.61	0.58	0.50	0.48	0.46	0.37	0.52	0.47	0.38
$pp\pi(2)$	−0.06	−0.02	−0.01	−0.03	−0.018	−0.013	−0.03	−0.02	−0.02
$sd\sigma$	−2.61	−2.87	−2.69	−1.29	−1.44	−1.90	−0.95	−1.47	−1.85
$pd\sigma$	−3.85	−4.19	−3.98	−2.61	−2.64	−3.46	−2.73	−3.06	−3.06
$pd\pi$	2.80	2.81	2.55	2.34	2.49	2.24	2.17	2.31	2.07

crystals are grown one shell after the other. For example, in the case of a zinc blende structure, we start with the central cation surrounded by the four neighboring anions. These four anions are then bonded to twelve cations in the next shell and so on till we reach the desired size of the nanocrystal. Then, the  $\varepsilon$ 's and  $t$ 's are assigned to the various orbitals and pairs of orbitals, respectively, thereby generating the Hamiltonian matrix. The TB-Hamiltonian matrix thus generated is then diagonalized to obtain the eigenvalue spectra. For small sized matrices, direct diagonalization works well, but it becomes progressively more time consuming and eventually almost impossible to diagonalize the Hamiltonian matrix as the size of the nanocrystal grows. Therefore, for larger nanocrystals we revert to more efficient techniques such as the Lanczos algorithm [65]. Calculations for different sized nanocrystal provide us with the dependence of the band gap on size.

Lippens and Lannoo [66] first used the TB method to calculate the variation of band gap with size for CdS and ZnS nanocrystals. They used the  $sp^3s^*$  orbital basis with only the nearest neighbor interactions, as suggested by the work of Vogl et al. [67] for bulk semiconductor materials. The calculations were carried out for clusters ranging in size from 17 atoms (3 shells) to 2563 atoms (15 shells). The surface dangling orbitals which give rise to non-bonded states in the mid-gap region, were removed from the Hamiltonian, as these states make the determination of the band gap difficult. Direct diagonalization for smaller nanocrystals up to 83 atoms and the recursion method for the larger crystallites were used to obtain the TVB and BCB as a function of size. Interestingly, the TVB and BCB do not exhibit a smooth monotonic shift with size. They show a step-like decrease in the energy position of the band edge as the size increases. As alternate shells are composed of cations and anions, the surface shell whose dangling orbitals have been removed is either purely anionic or purely cationic. This change of character of the outermost shell has different effects on determining the TVB and BCB, leading to the step-like variations in these quantities. The subtraction of the TVB energy from that of the BCB gives the band gap of the crystallite. To compare with the experimental results the exciton binding energy needs to be subtracted from the value of the bare band gap obtained from the TB model excluding any excitonic effect. This binding energy is given by the Coulomb term in the EMA equation, Eq. (2). With the  $sp^3s^*$  model, Lippens and Lannoo were able to get a better description of the band gap variation with size compared to the IP-EMA model. However, the results of the  $sp^3s^*$  nearest neighbor TB model underestimate the band gap at all sizes. Following the success of the TB model proposed by Lippens and Lannoo, several researchers have used this scheme. Hill and Whaley employed a time-dependent TB approach to determine the electronic structure of CdS and CdSe nanocrystals [68, 69]. They compared the effect of passivating the CdSe surface with oxygen and removing the dangling orbitals. They also studied the effects of terminating the nanocrystal with a cationic and an anionic surface. Perez-Conde et al. [70, 71] used the  $sp^3s^*$  orbital basis TB method with spin-orbit coupling for CdSe and CdTe nanocrystals. The resulting band gap variation with size obeys a  $1/D^{1.42}$  function rather than the  $1/D^2$  relation expected on the basis of EMA. Recently Allan et al. [72] calculated the quantum confinement effects for zinc blende III–V and group IV semiconducting nanocrystals using the nearest neighbor,  $sp^3d^5s^*$  TB model with the spin-orbit interaction included. Such a model gives a much better description of the bulk semiconductor band structure and thus explains the experimental results for band gap variation more effectively than the  $sp^3s^*$  model.

All the TB models discussed so far are based on the nearest neighbor interactions. Recently, Sapra et al. proposed [73] the  $sp^3d^5$  tight-binding model with cation–anion nearest neighbor and anion–anion next nearest neighbor (NNN) interactions for the  $A^{II}B^{VI}$  semiconductor compounds with  $A = \text{Zn, Cd, Hg}$  and  $B = \text{S, Se, Te}$ . The model was chosen after a careful analysis of the bulk band structures of these compounds obtained from the linearized muffin tin orbital (LMTO) method as described earlier in this section. These calculations were car-

ried out using the same set of TB parameters listed in Table 11.1. This model describes the ab initio band structure better than any of the other TB models containing the  $s^*$  orbital and excluding the next nearest neighbor (NNN) interactions. Thus, this  $sp^3d^5$ -NNN model should be a good starting point for evaluating the electronic structure of nanocrystals. With this model, the authors have calculated the eigenvalue spectra of nanocrystals containing atoms ranging from 17 to 9527 [74, 75]. The dangling orbitals at the surface of the nanocrystals are passivated using a layer of a higher band gap material. It is known from experiments that CdSe surface can be passivated with ZnS overcoating [10]. We illustrate a realization of such a surface passivation by electronic structure calculation in Figure 11.10. The upper panel shows the eigenvalue spectrum of an unpassivated CdS nanocrystallite

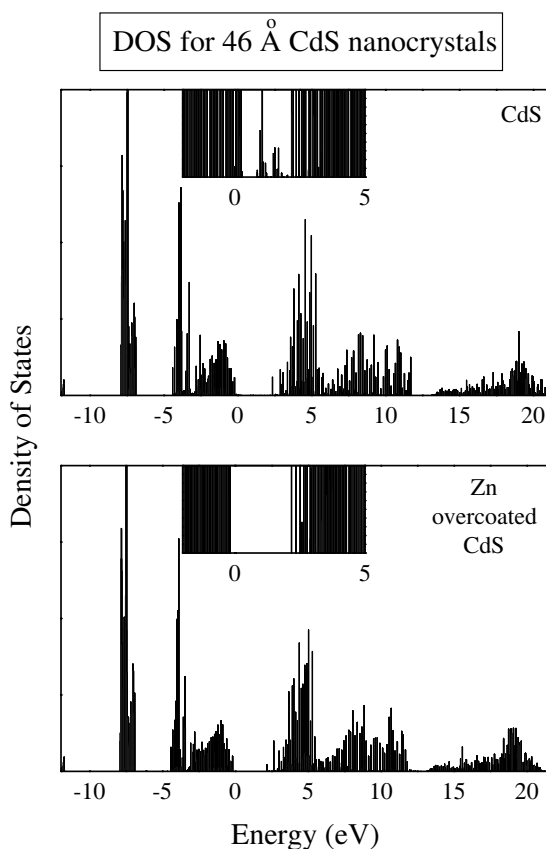


**Fig. 11.10.** Unpassivated and Zn-passivated CdS eigenvalue spectra for 46 Å nanocrystals. Passivation removes the mid-gap states as shown in the inset to the two panels. The zero of energy corresponds to the Fermi energy for bulk CdS. Adapted from [75].

of 46 Å diameter; the corresponding result for a passivated CdS crystallite of the same size is shown in the lower panel. The two results appear essentially the same, suggesting the same gross electronic structures for both systems. When we expand the band gap region, however, some important differences are easily seen, as shown in the insets to the panels. Evidently, the unpassivated cluster (upper panel, inset) shows the presence of many states within the band gap region which cannot be normally seen on the usual scale due to their low intensity. However, these mid-gap states affect the emission properties of the system, as discussed earlier in Section 11.4. Passivating the surface removes these states as shown in the lower panel. While experimentally such passivation provides a convenient way to recover the band gap emission, and therefore the tunability of the emission frequency by controlling the size, as discussed earlier, in the present context it also provides a theoretical handle for proper identification of the band gap by the removal of the unwanted surface states from the mid-gap region.

In Figure 11.11 we show the variation of the band gap with size for the various  $A^{II}B^{VI}$  semiconductors calculated within the  $sp^3d^5$  model [75], along with the results based on the IP-EMA and those from the  $sp^3s^*$  model [76]. The Coulomb term (the third term in Eq. (2)) has been subtracted from each of the calculated band gaps in order to facilitate comparison with the experimental data [8, 12, 16, 77–84, 86–92, 99] that are also plotted in the same figure. Evidently, EMA grossly overestimates the experimentally observed shifts in the band gaps in every case. The results of [75], including the next nearest neighbor interactions (shown by solid lines), are found to describe the experimental data points considerably better than the nearest neighbor  $sp^3s^*$  model (shown by dashed lines in the figure). Sapiro et al. have also used a similar model to calculate the band gap variation in the case of InP nanocrystals [93]. They used the  $sp^3d^5$  orbitals for P atoms and the  $sp^3$  orbitals for In atoms, as the In d orbitals are much lower in energy than the TVB and do not influence the bands close to the band gap region. Here, they needed the In–P, In–In and P–P interactions in order to obtain a good agreement of the ab initio and TB fitted band dispersions. The calculated band gap variation is in excellent agreement with the experimental results.

It has also been possible to calculate the electronic structure of doped semiconductors using the TB method. For example, the variation in the electronic structure of  $Ga_{1-x}Mn_xAs$  has been reported [94] for sizes of particles ranging between 12 and 71 Å for a fixed Mn-doping level of about 6.25%. The authors observed dramatic changes in the electronic structure of the Mn-doped GaAs nanocrystals at sizes smaller than about 30 Å. Figure 11.12 shows the spin resolved electronic density of states for (a) 25.0, (b) 18.5 and (c) 12.1 Å  $Ga_{1-x}Mn_xAs$  nanocrystals. Also shown are the As p (dotted lines in the respective panels) and Mn d (panel d) partial density of states. Here, we notice that the two larger sized nanocrystals have a finite DOS at the Fermi level whereas the 12.1 Å nanocrystals show an insulating behavior. Bulk  $Ga_{1-x}Mn_xAs$  is a known half-metallic ferromagnet [95, 96] and this behavior is observed for the nanocrystals larger than 12 Å i.e. the down-spin channel is insulating whereas the up-spin channel is metallic. Calculations sug-

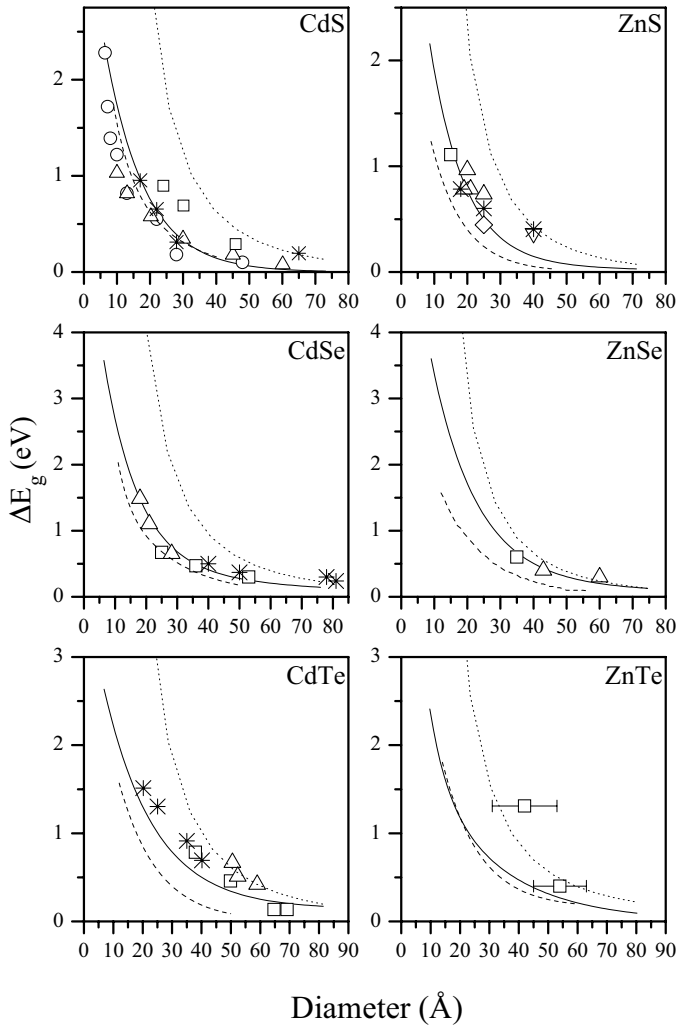


**Fig. 11.11.** The  $sp^3d^5$  TB model with the cation–anion and anion–anion interactions ([75], solid line) compared with the  $sp^3s^*$  TB nearest neighbor model ([76], dashed line), the EMA model (dotted line) and the experimental data points: CdS (○) [77], (△) [78], (\*) [79], (□) [99]; dSe (□) [80], (△) [81], (\*) [82]; CdTe (□) [83], (△) [84], (\*) [85]; ZnS (□) [87], (△) [88], (◇) [89], (○) [90], (\*) [12]; ZnSe (□) [91], (△) [16]; ZnTe (□) [92]. Adapted from [75].

gested a phase transition for nanocrystals of smaller size, whereby the valency of Mn changes from  $Mn^{2+}$  to  $Mn^{3+}$  driving a metal-insulator as well as a magnetic transition. Hanif et al. have reported magnetic behavior in the case of Co-doped CdSe nanocrystals [97], thus experimentally confirming the existence of magnetism in small sized nanocrystals.

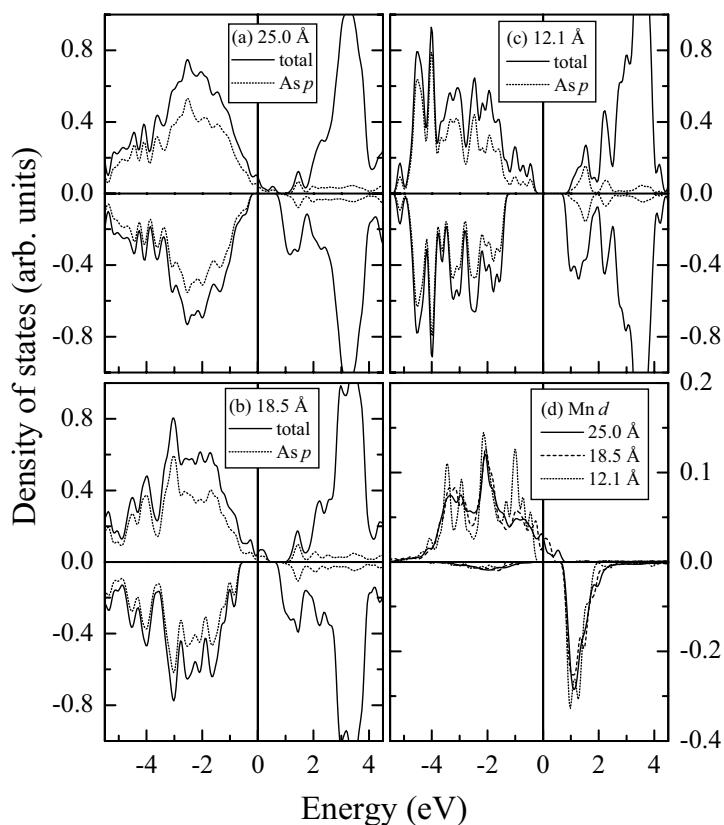


**Fig. 11.12.** Density of states and partial As p density of states for three (Ga, Mn)As finite clusters: (a) 9 shells and 25.0 Å diameter, (b) 7 shells and 18.5 Å diameter, (c) 5 shells and 12.1 Å diameter, and (d) partial Mn d density of states for these three clusters (the Mn d partial DOS has been multiplied by 3 for

clarity). In all the panels, the zero of energy corresponds to the Fermi energy,  $E_F$ , of bulk  $\text{Ga}_{1-x}\text{Mn}_x\text{As}$  with  $x = 0.0625$ ; the individual  $E_F$  is marked with an arrow in each panel. DOS have been broadened by a Gaussian with 0.3 eV FWHM. Adapted from [94].

## 11.6

### Photoemission Studies

The semiconducting nanocrystallites are grown by colloidal chemistry routes and obtained as free standing powders. These nanocrystals are generally coated with a layer of an organic capping agent to arrest their growth. Performing photoemission experiments on these semiconductor nanocrystals is a challenging task as the photoemission process causes charging up of the non-conducting samples due to the continuous removal or emission of electrons. To avoid the problem of charging, various techniques have been employed. For example, Bowen Katari et al. [98] used hexanedithiol as a linker to attach CdSe nanocrystals to gold or aluminum sub-

strates. Hexanedithiol is approximately 10 Å long and thus allows the electrons to tunnel from the metal substrate to the nanocrystals, thus maintaining charge neutrality. A different method to avoid charging was employed by Nanda et al. [99, 100], by mixing nanocrystals with graphite powders to provide a conducting matrix. In some cases, for very large band gap nanocrystals, graphite powder could not remove the charging effect completely. In such cases, a low energy electron flood gun was used to replenish the lost electrons.

### 11.6.1

#### Core Level Photoemission

Detailed investigations on CdS and ZnS nanocrystals have been carried out by different groups [99–101]. Nanda et al. [99, 100] studied various sized nanocrystals of CdS and ZnS capped with thioglycerol. Al-K $\alpha$  radiation ( $h\nu = 1486.6$  eV) was used to probe the electronic structure of these nanocrystals. Figure 11.13 shows the X-ray photoemission (XP) spectra of the Cd 3d regions from bulk and nanocrystalline CdS samples with diameters 2.5 nm (CdS-I) and 4.5 nm (CdS-II). The two spin-orbit components, 3d $_{3/2}$  and 3d $_{5/2}$  are seen in the case of both the nanocrystalline samples and are similar to the bulk spectrum. The peaks in the nano-

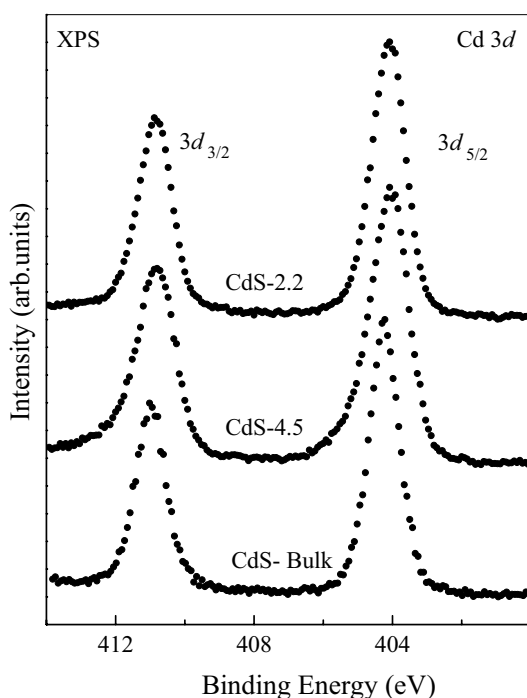
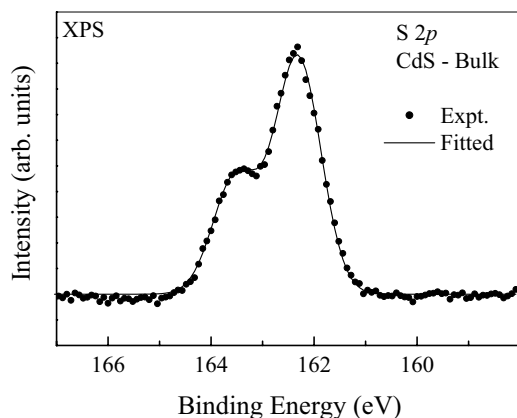


Fig. 11.13. Cd 3d X-ray photoemission spectra for bulk, 4.5 nm and 2.2 nm CdS nanocrystals recorded with an X-ray photon energy of 1486.6 eV (Al-K $\alpha$ ). Adapted from [99].





**Fig. 11.14.** S 2p X-ray photoemission spectrum of bulk CdS recorded with an X-ray photon energy of 1486.6 eV (Al-K $\alpha$ ). Note the spin-orbit split 2p peak which is composed of the  $2p_{3/2}$  and  $2p_{1/2}$  components. Adapted from [99].

crystals are slightly broader and shifted to lower binding energies, which can be attributed to the size distribution of the nanocrystals or a small amount of uncompensated charging. Figure 11.14 shows the S 2p spectrum for bulk CdS. It shows a spin-orbit splitting of 1.2 eV and can be described by two Gaussian functions each with a full width at half maximum (FWHM) of 0.44 eV. The S 2p spectra of nanocrystals are quite complex and clearly cannot be described with only two Gaussian functions as shown in Figure 11.15. A good fit to the experimental spectrum for CdS-I is obtained with a set of three Gaussian doublets with the S  $2p_{3/2}$

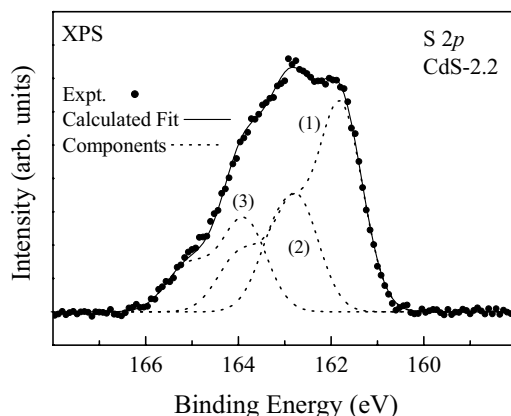


**Fig. 11.15.** X-ray photoelectron spectra of CdS-2.2, shown after the removal of the inelastic background, for (a) S 2p and (b) S 2s core levels. The experimental spectra are shown by solid circles. The dashed lines are the individual sulfur components labelled as 1, 2 and 3, respectively, the solid lines show the overall fit. Adapted from [99].

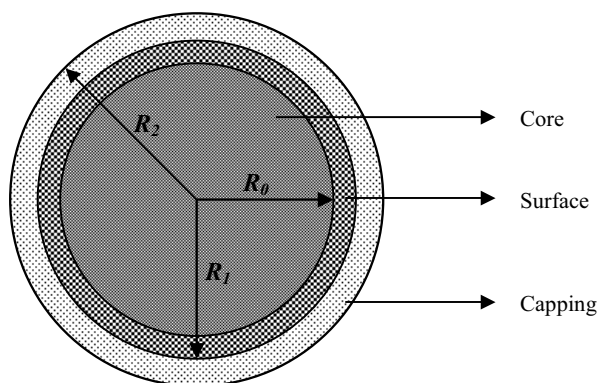


**Fig. 11.16.** Schematic model of a CdS nanocrystallites based on the photoemission core-level analysis.  $R_0$  is the radius of the core,  $R_1$  is the radius of the surface layer, and  $R_2$  is the radius of the capping layer. Adapted from [99].

signal centered at 161.8, 162.9 and 163.9 eV, the spin orbit splitting being the same as for bulk CdS. Similarly, the S 2s spectrum can also be fitted with three Gaussian functions (not shown here) with their energy separations and intensity ratios the same as for the S 2p fitting, establishing the validity of the fitting procedure. The dotted lines in Figure 11.15 are the three fitted Gaussian curves. The individual components centered at 161.8, 162.9 and 163.9 eV were interpreted to arise from three different sulfur species, namely the core (labelled 1), surface (labelled 2) and thiol (labelled 3) sulfur, respectively, based on the binding energies of these species. Using these experimental intensities and with the assumption that the nanocrystals are spherical, it is possible to model the nanocrystal as a layered particle with core, surface and capping layers as shown in Figure 11.16. Analyzing the relative intensities this way, Nanda et al. [99] calculated the thickness of the various shells of the nanocrystals tabulated in Table 11.2 compared with the diameter of the particles determined from X-ray diffraction experiments.

Winkler et al. [101] performed similar studies on CdS nanocrystals of 70, 40 and 27 Å diameter, capped with mercaptopropionic acid, using a synchrotron source.

**Tab. 11.2.** Sizes of the various regions in the nanocrystals, CdS-4.5 and CdS-2.2 obtained from an analysis of the photoelectron intensities. The symbols  $R_0$ ,  $R_1$  and  $R_2$  are the radii of the core, core + surface shell, and core + surface shell + capping layer.

Sample	Core Diam. $2R_0$ (nm)	Surface Layer Diam. $2R_1$ (nm)	Capping Layer Diam. $2R_2$ (nm)	Diam. from Expt. $2R^*$ (nm)
CdS-4.5	4.1	4.4	4.9	4.4
CdS-2.2	2.0	2.3	2.7	2.2

On the synchrotron radiation source they could vary the photon energy to obtain different bulk-to-surface sensitivity ratios, bulk sensitivity being higher for higher photon energies due to an increased mean free path of the electrons [102]. The Cd  $3d_{5/2}$  spectra recorded with highly surface sensitive X-rays ( $h\nu = 445$  eV) revealed two components at 406.1 and 406.6 eV. These two Cd groups are assigned to Cd in the bulk of the nanocrystals and Cd on the surface bonded to sulfur of the capping agent. The S 2p spectra for all three different sized nanocrystals show the three components arising from bulk, surface and capping layer sulfur species. However, there is a fourth component in the case of the smallest sized nanocrystals which has been attributed to the disulfide linkages formed at the surface due to bonding between the capping agent and the surface sulfur atoms. Disulfide linkages are very few in number and can be observed only for very small sized nanocrystals where the surface to bulk ratio is very high. The S 2p spectra for 40 and 70 Å nanocrystals also showed spectral features due to the presence of an oxidized species at a higher binding energy (168.8 eV). In smaller nanocrystals, the number of unsaturated sulfur atoms is less and hence this oxidation is not observed. Annealing leads to minimization of various defects, though it can also give rise to structural and chemical changes. The effect of annealing in ultra-high vacuum conditions, has been closely monitored for the same sized CdS nanocrystals using photoemission spectroscopy [101]. Thermal annealing at 240 °C modifies the surface from being sulfur-terminated at room temperature to a Cd-terminated one. This could be a result of desorption of the capping material at such high temperatures and/or segregation of Cd atoms to the surface from the interior of the nanocrystals.

ZnS passivated InP nanocrystals have been investigated by photoelectron spectroscopy with tunable synchrotron radiation [103]. Following essentially the same ideas presented earlier by Nanda et al. [99, 100], [103] presents a method to characterize the core-shell nature of the nanocrystals and also determine the average thickness of the various layers. Photoelectron spectra were recorded at different photon energies, in order to tune the surface-to-bulk sensitivity ratio via a change in the kinetic energy of the photo-emitted electrons. Surface sensitivity is higher at lower kinetic energies, whereas higher kinetic energies show an enhanced sensitivity towards the atoms deep inside the nanocrystals [102]. The ratio of the core level signals, namely In 3d to Zn 2p levels, increased from 0.06 to 0.15 as the kinetic energy of the emitted photons increased from 87 eV to 247 eV, thus indicating the presence of Zn atoms on the surface and In atoms in the core of the nanocrystals. Using the ratios of the intensities from the In and Zn core levels and the fact that the organic capping layer trioctylphosphine (TOP) caps about 25–50% of the nanocrystal surface, the authors also calculated the size of the different shells. The diameter of the inner core of InP was fixed at 19 Å measured from TEM of InP nanocrystals without the ZnS coverage. The thickness of the ZnS shell and the outer shell of TOP were calculated to be 8.9 Å and 12.3 Å, respectively. A 8.9 Å thick ZnS layer corresponds to 3 monolayer coverage of the InP core by ZnS. The length of the carbon chain in TOP is about 10.5 Å. Hence, this method offers a

good means to determine the average thickness of the nanocrystal shells of different materials.

### 11.6.2

#### Valence Band Photoemission

Colvin et al. [104] were the first to study the valence band photoemission of CdS quantum dots. To avoid charging of the samples, they attached CdS nanocrystals on metal surfaces such as gold (for 38 Å diameter dots) or aluminum (for 24 Å and 70 Å diameter dots). The quantum dots were anchored to the metal surfaces using bifunctional organic groups. The experiments were carried out on a synchrotron source with variable photon energies in the range 20–70 eV. They did not observe any change in the spectra due to the presence of different metals. The metal surfaces are deep inside and the escape depth of electrons for this range of photon energies varies between 10 and 30 Å. In this work, it was found that the top of the valence band of the dots varies as a function of the size in accordance with the theoretical predictions based on the finite potential-EMA model that includes the polarization term as well.

Van Buuren et al. [105] performed photoemission and X-ray absorption experiments on Si nanocrystals to determine the TVB and BCB shifts, respectively, as a function of size. The Si nanocrystals were grown in situ at 1700 °C in an Ar gas buffer of 112 mTorr followed by hydrogen exposure to passivate the surface. The resolution of the photoemission and absorption measurements carried out on a synchrotron radiation source were 0.25 eV and 0.05 eV, respectively. They observed a valence band to conduction band shift ratio of 2:1 for all sizes of Si nanocrystals. This is in agreement with various calculations reported for Si nanocrystals [106].

Soft X-ray emission spectroscopy (SXE) and soft X-ray absorption spectroscopy (SXA) are techniques that also can map out the states in the valence and conduction bands, respectively. Using SXE and SXA, Lüning et al. [107] studied four different sizes of CdS nanocrystallites namely, cadmium thiolate  $\text{Cd}_8(\text{SR})_{16}$ ,  $\text{Cd}_{17}\text{S}_4(\text{SR})_{26}$  (13.5 Å),  $\text{Cd}_{32}\text{S}_{14}(\text{SR})_{36}$  (17.5 Å) and a CdS nanoparticle of 40 Å diameter. Apart from the band gap variation, they also observed a systematic decrease in the band width of the upper part of the valence band, which is mainly comprised of S 3p states; the width decreases from 4.8 eV for CdS bulk to 3.5 eV for Cd thiolate. However, the lower part of the valence band which is derived from the more localized S 3s and Cd 4d states, is hardly affected by size quantization. To determine the shifts in the TVB and BCB, the S 2p core level photoemission spectra for all the nanocrystals were used to calibrate the energy scale internally. The shifts were compared with the IP-EMA, finite potential EMA (FP-EMA) and the  $\text{sp}^3\text{s}^*$  TB model. The FP-EMA gives a good description, with the finite potential barrier adjusted to obtain the best fit to the experimental results but the other two models do not provide good agreement with the experimental results.

Another method to avoid charging of the semiconductor samples is to mix the samples with a conducting matrix such as graphite. Nanda et al. [108] measured

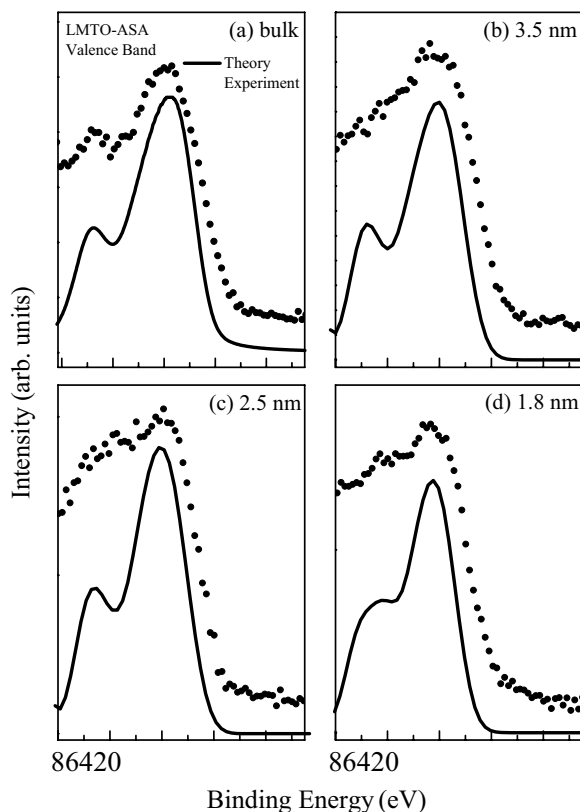


**Fig. 11.17.** Valence band spectra: experimental (solid circles) and calculated spectra (solid line) for (a) bulk ZnS, (b) 3.5 nm nanocrystals, (c) 2.5 nm nanocrystals, and (d) 1.8 nm nanocrystals. The calculated spectra for bulk

ZnS is obtained using the LMT0-ASA method and those for the nanocrystals are from the  $sp^3d^5$  model with nearest neighbor and anion-anion interactions. Adapted from [108].

the valence band photoemission spectra of 1.8, 2.5 and 3.5 nm ZnS nanocrystals dispersed in graphite powder. In the case of excessive charging, the samples were exposed to a low energy electron floodgun. Figure 11.17 compares the experimental density of states (DOS) with the theoretical DOS calculated using the  $sp^3d^5$ -NNN model [75]. The subtle features in the experimental DOS are described reasonably well by the  $sp^3d^5$ -NNN model. The band gap shifts and the change in the spacings between the two peaks are correctly reproduced by this model. The experimentally obtained TVB is subtracted from the experimental value of the band gap measured from absorption experiments in order to estimate the shifts in the BCB. The shifts in the band edges are plotted as a function of size in Figure 11.18. Here also we notice the good agreement between theory and experiment for all sizes. Such excellent agreement is due to the good description of the bulk band structure provided by the  $sp^3d^5$ -NNN model as discussed earlier in Section 11.5.

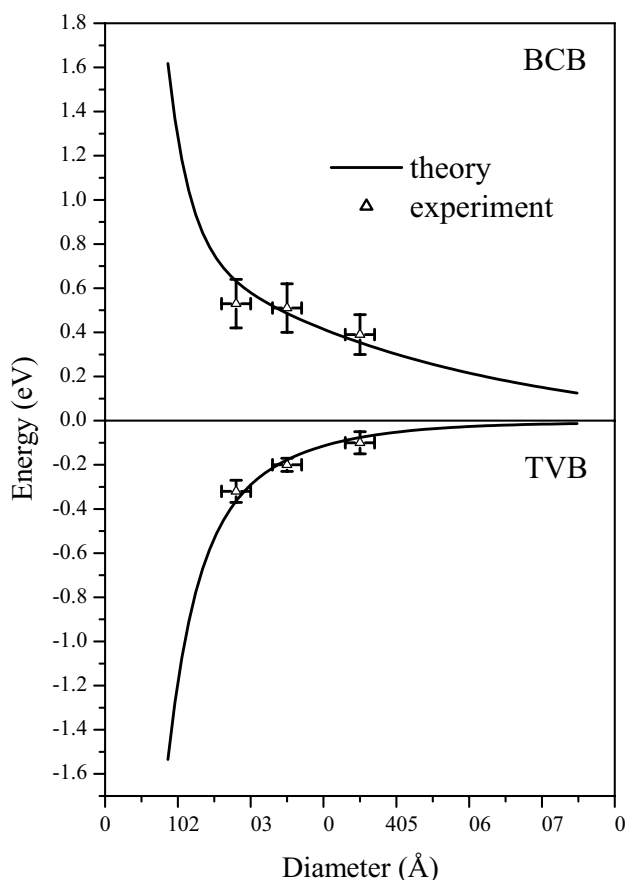


**Fig. 11.18.** Variation of the top of the valence band (TVB) and bottom of the conduction band (BCB) with size as obtained using the  $sp^3d^5$  model with nearest neighbor and anion-anion interactions. The symbols on the TVB variation curve are experimental data points obtained from the photoemission experiments. Those on the BCB curve are obtained after subtraction of the TVB data points from the band gap values obtained from the UV-Vis absorption. Adapted from [108].

## 11.7

### Concluding Remarks

We have reviewed in this chapter the electronic structure and properties of semi-conducting nanocrystals, materials that can be used in the field of nanoelectronics in the near future. Some of these materials already show very interesting properties that can be utilized to make devices and, therefore, it is necessary to have proper experimental and theoretical tools to probe and understand the electronic properties quantitatively.

UV-Vis absorption spectroscopy is the easiest tool available to characterize semi-

conducting nanocrystals. The blue-shift in the band gap reveals the formation of nanocrystals. In conjunction with more accurate approaches to calculate the band gap as a function of the size available these days, it is possible to obtain reliable estimates of the size from the measure of the band gap shift. Also, one can get an estimate of the size distribution from the sharpness of the absorption peak. Fluorescence properties of the nanocrystals can be tuned to obtain emissions at various energies, thus making possible the tunability of the emitted light for a number of applications.

The electronic structure calculation methods discussed here give an overview of the different methods used to study the size dependent electronic properties. The single band IP-EMA method is a simple approach to understand the band gap variation of nanocrystals with size. As the method overestimates the band gap for small sized nanocrystals, improvements in the form of FP-EMA and MBEM have been suggested to get a better agreement between the theoretical results and the experimental data. The pseudopotential techniques provide a very good description of the experimental results. The tight binding methods have found the widest applications in the description of the properties of nanocrystals because of their ease of use. Also, they are computationally less expensive than other methods for large sized nanocrystals. It is found that the  $sp^3d^5$  model with next nearest neighbor interactions included gives the best description of the variation of band gap with size in the case of II–VI semiconductors.

Valence band spectroscopic studies performed on the semiconducting nanocrystals give valuable information about the electronic structure of these materials. The band edges vary with varying nanocrystal size and these can be quantified with the help of the theoretical techniques. The shape of the density of states obtained from the photoemission experiments also changes with the size of the nanocrystals. This has been correlated with the  $sp^3d^5$ -NNN tight binding model, exhibiting an excellent agreement between theory and experiment.

## References

- 1 A. D. YOFFE, *Adv. Phys.*, 50, 1, 2001.
- 2 A. P. ALIVISATOS, *J. Phys. Chem.*, 100, 13226, 1996.
- 3 A. D. YOFFE, *Adv. Phys.*, 42, 173, 1993.
- 4 H. WELLER, *Angew. Chem. Int. Ed. Engl.*, 32, 41, 1993.
- 5 A. HAGFELDT, M. GRATZEL, *Chem. Rev.*, 95, 49, 1995.
- 6 Y. WANG, N. HERRON, *J. Phys. Chem.*, 95, 525, 1991.
- 7 C. B. MURRAY, C. R. KAGAN, M. G. BAWENDI, *Annu. Rev. Mater. Sci.*, 30, 545, 2000.
- 8 J. NANDA, B. A. KURUVILLA, K. V. P. SHAFI et al., in *Physics of Semiconducting Nanostructures*, ed. K. P. JAIN, Narosa Publishers, New Delhi, 1997, p. 25.
- 9 A. N. GOLDSTEIN, C. M. ECHERAND, A. P. ALIVISATOS, *Science*, 256, 1425, 1992.
- 10 B. O. DABBOUSI, J. RODRIGUEZ-VIEJO, F. V. MIKULEC et al., *J. Phys. Chem. B*, 101, 9463, 1997.
- 11 J. NANDA, Ph.D. Thesis, Bangalore, 2000.
- 12 J. NANDA, S. SAPRA, D. D. SARMA et al., *Chem. Mater.*, 12, 1018, 2000.
- 13 J. K. FURDYNA, *J. Appl. Phys.*, 64, R29, 1988.



- 14 S. SAPRA, J. NANDA, A. ANAND et al., *J. Nanosci. Nanotechnol.*, 3, 392, 2003.
- 15 C. B. MURRAY, D. J. NORRIS, M. G. BAWENDI, *J. Am. Chem. Soc.*, 115, 8706, 1993.
- 16 M. A. HINES, P. GUYOT-SIONNEST, *J. Phys. Chem. B*, 102, 3655, 1998.
- 17 S. SAPRA, A. PRAKASH AND D. D. SARMA, unpublished results.
- 18 H. FU, A. ZUNGER, *Phys. Rev. B*, 56, 1496, 1997.
- 19 S. SAPRA, J. NANDA, D. D. SARMA et al., *Chem. Commun.*, 2188, 2001.
- 20 S. SAPRA, R. VISWANATHA, J. NANDA et al., in *Recent Advances in Inorganic Materials*, ed. D. BAHADUR, Narosa Publishers, New Delhi, 2003.
- 21 W. CHEN, R. SAMMYNAIKEN, Y. HUANG, *J. Appl. Phys.*, 88, 5188, 2000.
- 22 W. CHEN, F. SU, G. LI et al., *J. Appl. Phys.*, 92, 1950, 2002.
- 23 B. A. SMITH, J. Z. ZHANG, A. JOLY et al., *Phys. Rev. B*, 62, 2021, 2000.
- 24 W. CHEN, A. G. JOLY, J. Z. ZHANG, *Phys. Rev. B*, 64, 041202(R), 2001.
- 25 M. TANAKA, Y. MASUMOTO, *Chem. Phys. Lett.*, 324, 249, 2000.
- 26 G. CUNIO, T. GACON, J. P. BOILLOT, *J. Phys. Chem. B*, 102, 5257, 1998.
- 27 N. FELTIN, L. LEVY, D. INGERT et al., *J. Phys. Chem. B*, 103, 4, 1999.
- 28 L. LEVY, J. F. HOCHPIED, M. P. PILENI, *J. Phys. Chem.*, 100, 18322, 1996.
- 29 Y. WANG, N. HERRON, K. MOLLER et al., *Solid State Commun.*, 77, 33, 1991.
- 30 A. A. KHOSRAVI, M. KUNDU, B. A. KURUVILLA et al., *Appl. Phys. Lett.*, 67, 2506, 1995.
- 31 R. N. BHARGAVA, D. GALLAGHER, X. HONG et al., *Phys. Rev. Lett.*, 72, 416, 1994.
- 32 K. SOOKLAL, B. S. CULLUM, S. M. ANGEL et al., *J. Phys. Chem. B*, 100, 4551, 1996.
- 33 W. CHEN, R. SAMMYNAIKEN, Y. HUANG et al., *J. Appl. Phys.*, 89, 1120, 2001.
- 34 A. A. BOL, A. MEIJERINK, *Phys. Rev. B*, 58, R15997, 1998.
- 35 W. CHEN, J.-O. MALM, V. ZWILLER et al., *J. Appl. Phys.*, 89, 2671, 2001.
- 36 W. CHEN, J.-O. MALM, V. ZWILLER et al., *Phys. Rev. B*, 61, 11021, 2000.
- 37 S. V. GAPONENKO, *Optical Properties of Semiconductor Nanocrystals*, Cambridge University Press, Cambridge 1998.
- 38 M. NIRMAL, C. B. MURRAY, D. J. NORRIS et al., *Z. Phys. D:At., Mol. Clusters*, 26, 361, 1993.
- 39 J. Z. ZHANG, *Acc. Chem. Res.*, 30, 423, 1997.
- 40 K. HUANG, A. RHYS, *Proc. R. Soc. London, Ser. A*, 204, 406, 1950.
- 41 AL. L. EFROS, A. L. EFROS, *Sov. Phys. Semicond.*, 16, 772, 1982.
- 42 L. E. BRUS, *J. Chem. Phys.*, 79, 5566, 1983.
- 43 L. E. BRUS, *J. Chem. Phys.*, 80, 4403, 1984.
- 44 L. E. BRUS, *J. Phys. Chem.*, 90, 2555, 1986.
- 45 Y. KAYAMMA, *Solid State Commun.*, 59, 405, 1986.
- 46 Y. KAYANUMA, *Phys. Rev. B*, 38, 9797, 1988.
- 47 H. M. SHMIDT, H. WELLER, *Chem. Phys. Lett.*, 129, 615, 1986.
- 48 S. V. NAIR, S. SINHA, K. C. RUSTOGI, *Phys. Rev. B*, 35, 4098, 1987.
- 49 D. J. NORRIS, A. SACRA, C. B. MURRAY et al., *Phys. Rev. Lett.*, 72, 2612, 1994.
- 50 D. J. NORRIS, M. G. BAWENDI, *Phys. Rev. B*, 53, 16338, 1996.
- 51 U. BANIN, C. J. LEE, A. A. GUZELIAN et al., *J. Chem. Phys.*, 109, 2306, 1998.
- 52 G. T. EINEVOLL, *Phys. Rev. B*, 45, 3410, 1992.
- 53 S. V. NAIR, L. M. RAMANIAH, K. C. RUSTOGI, *Phys. Rev. B*, 45, 5969, 1992.
- 54 Y. KAYANUMA, H. MOMIJI, *Phys. Rev. B*, 41, 10261, 1990.
- 55 D. BRUST, J. C. PHILLIPS, F. BASSANI, *Phys. Rev. Lett.*, 9, 94, 1962.
- 56 M. L. COHEN, J. R. CHELIKOWSKY, *Electronic Structure and Optical Properties of Semiconductors*, Springer, Berlin 1989.
- 57 M. V. RAMA KRISHNA, R. A. FRIESNER, *Phys. Rev. Lett.*, 67, 629, 1991.
- 58 A. FRANCESCHETTI, A. ZUNGER, *Phys. Rev. Lett.*, 78, 915, 1997.
- 59 H. FU, A. ZUNGER, *Phys. Rev. B*, 55, 1642, 1997.
- 60 L. W. WANG, A. ZUNGER, *Phys. Rev. B*, 51, 17398, 1995.
- 61 L. W. WANG, A. ZUNGER, *J. Chem. Phys.*, 100, 2394, 1994.

- 62 L. W. WANG, A. ZUNGER, *J. Phys. Chem.*, **94**, 2158, **1994**.
- 63 L. W. WANG, A. ZUNGER, *Phys. Rev. B*, **53**, 9579, **1996**.
- 64 J. C. SLATER, G. F. KOSTER, *Phys. Rev. B*, **94**, 1498, **1954**.
- 65 E. DAGOTTO, *Rev. Mod. Phys.*, **66**, 763, **1994**.
- 66 P. E. LIPPENS, M. LANNOO, *Phys. Rev. B*, **39**, 10935, **1989**.
- 67 P. VOGL, H. P. HJALMARSON, J. D. DOW, *J. Phys. Chem. Solids*, **44**, 365, **1983**.
- 68 N. A. HILL, K. B. WHALEY, *J. Chem. Phys.*, **99**, 3707, **1993**.
- 69 N. A. HILL, K. B. WHALEY, *J. Chem. Phys.*, **100**, 2831, **1994**.
- 70 J.-P. CONDE, A. K. BHATTACHARJEE, *Phys. Rev. B*, **63**, 245318, **2001**.
- 71 J.-P. CONDE, A. K. BHATTACHARJEE, M. CHAMARRO et al., *Phys. Rev. B*, **64**, 113303, **2001**.
- 72 G. ALLAN, Y. M. NIQUET, C. DELERUE, *Appl. Phys. Lett.*, **77**, 639, **2000**.
- 73 S. SAPRA, N. SHANTHI, D. D. SARMA, *Phys. Rev. B*, **66**, 205202, **2002**.
- 74 S. SAPRA, D. D. SARMA, *Proceedings of the 3rd Japan-Korea Joint Workshop on First-Principles Electronic Structure Calculations Oct.–Nov. 2001*, p. 105.
- 75 S. SAPRA, J. NANDA, D. D. SARMA, *Encyclopedia of Nanoscience and Nanotechnology*. Vol X, American Scientific Publishers, **2004**, 1.
- 76 P. E. LIPPENS, M. LANNOO, *Mater. Sci. Eng. B*, **9**, 485, **1991**.
- 77 T. VOSSMEYER, L. KATSIKAS, M. GIERSIG et al., *J. Phys. Chem.*, **98**, 7665, **1994**.
- 78 Y. WANG, N. HERRON, *Phys. Rev. B*, **42**, 7253, **1990**.
- 79 T. TORIMOTO, H. KONTANI, Y. SHIBUTANI et al., *J. Phys. Chem. B*, **105**, 6838, **2001**.
- 80 B. O. DABBOUSI, C. B. MURRAY, M. F. RUBNER et al., *Chem. Mater.*, **6**, 216, **1994**.
- 81 A. L. ROGACH, A. KORNOWSKI, M. GAO et al., *J. Phys. Chem. B*, **103**, 3065, **1999**.
- 82 S. GORER, G. HODES, *J. Phys. Chem.*, **98**, 5338, **1994**.
- 83 Y. MASTAI, G. HODES, *J. Phys. Chem. B*, **101**, 2685, **1997**.
- 84 Y. MASUMOTO, K. SONOBE, *Phys. Rev. B*, **56**, 9734, **1997**.
- 85 H. ARIZPE-CHREZ, R. RAMREZ-BON, F. J. ESPINOZA-BETRIN et al., *J. Phys. Chem. Solids*, **61**, 511, **2000**.
- 86 T. RAJH, O. I. MICIC, A. J. NOZIK, *J. Phys. Chem.*, **97**, 11999, **1993**.
- 87 Y. NAKAOKA, Y. NOSAKA, *Langmuir*, **13**, 708, **1997**.
- 88 R. ROSSETTI, R. HULL, J. M. GIBSON et al., *J. Chem. Phys.*, **82**, 552, **1985**.
- 89 H. INOUE, N. ICHIROKU, T. TORIMOTO et al., *Langmuir*, **10**, 4517, **1994**.
- 90 S. YANAGIDA, T. YOSHIYA, T. SHIRAGAMI et al., *J. Phys. Chem.*, **94**, 3104, **1990**.
- 91 F. T. QUINLAN, J. KUTHER, W. TREMEL et al., *Langmuir*, **16**, 4049, **2000**.
- 92 Y.-W. JUN, C.-S. CHOI, J. CHEON, *Chem. Commun.*, **101**, **2001**.
- 93 S. SAPRA, R. VISWANATHA, D. D. SARMA, unpublished results.
- 94 S. SAPRA, D. D. SARMA, S. SANVITO et al., *Nanoletters*, **2**, 605, **2002**.
- 95 H. OHNO, *Science*, **281**, 951, **1998**.
- 96 H. OHNO, *J. Magn. Magn. Mater.*, **200**, 110, **1999**.
- 97 K. M. HANIF, R. W. MEULENBERG, G. F. STROUSE, *J. Am. Chem. Soc.*, **124**, 11495, **2002**.
- 98 J. E. BOWEN KATARI, V. L. COLVIN, A. P. ALIVISATOS, *J. Phys. Chem.*, **98**, 4109, **1994**.
- 99 J. NANDA, B. A. KURUVILLA, D. D. SARMA, *Phys. Rev. B*, **59**, 7473, **1999**.
- 100 J. NANDA, D. D. SARMA, *J. Appl. Phys.*, **90**, 2504, **2001**.
- 101 U. WINKLER, D. EICH, Z. H. CHEN et al., *Chem. Phys. Lett.*, **306**, 95, **1999**.
- 102 S. HÜFNER, *Photoelectron Spectroscopy: Principles and Applications*, Springer-Verlag, Berlin 1995.
- 103 H. BORCHERT, S. HAUBOLD, M. HAASE et al., *Nanoletters*, **2**, 151, **2002**.
- 104 V. L. COLVIN, A. P. ALIVISATOS, J. G. TOBIN, *Phys. Rev. Lett.*, **66**, 2786, **1991**.
- 105 T. VAN BURREN, L. N. DINH, L. L. CHASE et al., *Phys. Rev. Lett.*, **80**, 3803, **1998**.
- 106 T. VAN BURREN, T. TIEDJE, J. R. DALN, *Appl. Phys. Lett.*, **63**, 2911, **1993**.
- 107 J. LÜNING, J. ROCKENBERGER, S. EISEBITT et al., *Solid State Commun.*, **112**, 5, **1999**.
- 108 J. NANDA, S. SAPRA, D. D. SARMA, unpublished results.

## 12

# Core–Shell Semiconductor Nanocrystals for Biological Labeling

*R. E. Bailey and S. Nie*

### 12.1

#### Introduction

Extensive research in nanomaterials has been mainly directed towards their potential use in microelectronics, optoelectronics, and high-density memory devices [1–10]. Recent progress has also demonstrated that nanostructured materials such as semiconductor quantum dots (QDs) have important applications in biology and medicine [11, 12]. This fusion of nanotechnology and biotechnology is creating a new frontier in which multifunctional or “smart” structures could be designed for disease detection, diagnosis, and treatment [13]. Current efforts in this area have produced biocompatible nanoparticles conjugated to peptides [14], proteins [15–17], and DNA [18, 19]. These nanobioconjugates are useful for homogeneous bioassays [20–22], as multicolor luminescent labels [15–19], as well as for bottom-up assembly of novel materials [23, 24]. For semiconductor nanocrystals, major improvements have occurred in both chemical synthesis [25] and surface conjugation [15, 16], producing large quantities of high-quality and commercially available luminescent nanoparticles.

In this chapter, we discuss core–shell semiconductor quantum dots and their applications in biological labeling (Fig. 12.1). In comparison with organic dyes and fluorescent proteins, semiconductor quantum dots represent a new class of fluorescent labels with unique advantages and applications. For example, the fluorescence emission spectra of quantum dots can be continuously tuned by changing the particle size, and a single wavelength can be used for simultaneous excitation of all different-sized QDs.

### 12.2

#### Optical Properties

In semiconductor nanocrystals, optical absorption and photoluminescence are different from those in traditional, molecular systems. In semiconductors, the absorption of a photon causes a valence band electron to be promoted into the con-

duction band, leaving behind a valence band hole. Once promotion has occurred, the conduction band electron quickly relaxes into the lowest energy conduction band state while the hole moves to the top of the valence band. Holes accumulate in the highest valence band states so that the valence band electrons can cascade down into the lower energy valence states. Photoluminescence arises from the recombination of the conduction band electron with the valence band hole where energy is released in the form of a photon. In the process, the conduction band electron and valence band hole are annihilated. In terms of solid-state physics, it is convenient to refer to this coupled electron–hole pair as a single entity, since one cannot exist without the other if charge neutrality is to be maintained. This pseudoparticle is known as an exciton [8]. In fact, the previous discussion about the electronic properties should be viewed in the light of this pseudoparticle rather than the conduction and valence band electrons only. For simplicity the holes are neglected in the discussion. Since the exciton is composed of an electron and a hole that have opposite charges, a strong coulomb attraction causes them to remain relatively localized within a nanometer-sized crystal. The exciton volume can be calculated for a given material, and quantum confinement occurs when the dimensions of the nanocrystal approach the exciton's Böhr radius.

Although all semiconductors undergo absorption processes, there is a large difference in the luminescence behavior depending on the semiconductor type. Only direct band gap semiconductors exhibit band edge photoluminescence with high quantum efficiencies [26]. This is because in the recombination process both energy and momentum must be conserved. As a result, the following relations must be obeyed:

$$E_{\text{conduction}} - E_{\text{valence}} = h\nu \quad \text{and} \quad \eta k_{\text{valence}} + \eta k_{\text{photon}} = \eta k_{\text{conduction}}$$

Because the photon momentum is negligible compared to the electron crystal momentum, the momentum conservation requirement simplifies to:

$$\eta k_{\text{valence}} \approx \eta k_{\text{conduction}}$$

The result is that optical transitions occur as vertical transitions from the conduction band to the valence band. Examining the  $E$ - $k$  diagram for direct versus indirect band gap materials, one can see that a direct band gap material will accumulate electrons and holes in the region with nearly identical crystal momenta. Conversely, an indirect material will accumulate electrons and holes with a large difference in crystal momentum that cannot be compensated by the emission of a photon. Therefore, the optical transition must be accompanied by the simultaneous release of a lattice phonon in order to conserve momentum. These two particle processes are statistically much less probable than a single particle process, and consequently direct band gap materials such as CdSe are extremely efficient (theoretically 100%) in light emission. By comparison, indirect band gap materials, like silicon, have band edge photoluminescence quantum yields that are 3 to 4 orders of magnitude lower than direct band gap materials. For this reason, optoelectronic

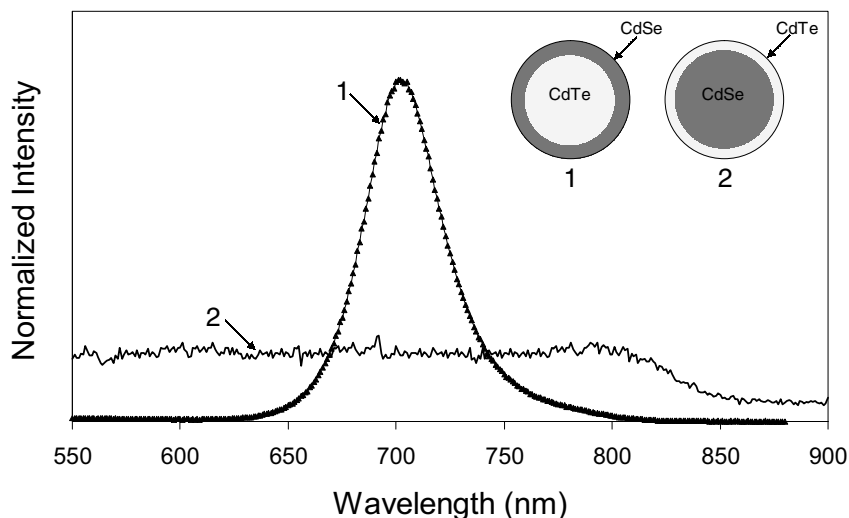


**Fig. 12.1.** Schematic structures of core-shell semiconductor nanocrystals and corresponding photoluminescence spectra.

devices used for light generation are based on direct band gap materials exclusively. Similarly, direct band gap materials must be used to prepare highly luminescent semiconductor nanocrystals. The direct band gap semiconductor cadmium selenide is most frequently used for size-confinement studies [4–7] because of its simple synthesis and efficient photoluminescence properties [4–7].

By examining the absorption spectra of QDs or by simply observing the deeply colored colloids, it is clear that the density of states within their energy levels is very high. In samples of sufficient monodispersity, there are significant fine structures in the absorption spectra (Fig. 12.2). At the absorption onset there is an observable peak followed by several ripples as the absorption increases with energy. This first peak is the first excitonic peak followed by the higher excited excitonic states which are analogous to the first excited and higher excited states in molecular systems. The fact that the absorption coefficient increases towards shorter wavelengths is an important feature for multicolor applications because it allows simultaneous excitation of multicolor dots at a single wavelength. In addition to large molar absorptivity coefficients ( $\sim 10^5$ – $10^6$   $\text{M}^{-1} \text{cm}^{-1}$ ), the emission spectra of core-shell quantum dots are narrow, symmetric (Gaussian in shape), and can span a broad range of wavelengths by a judicious choice of particle size and composition. The width of the emission spectrum is directly related to the sample quality and monodispersity. Typically, room temperature spectra of high quality samples show spectral widths of 25–35 nm (full-width at half maximum or FWHM) due to the finite particle size distribution, whereas the emission spectra of single (CdSe)ZnS QDs are as narrow as 13 nm (FWHM). It has been estimated that single (CdSe)ZnS QDs are  $\sim 20$  times brighter and  $\sim 100$ – $200$  times more stable

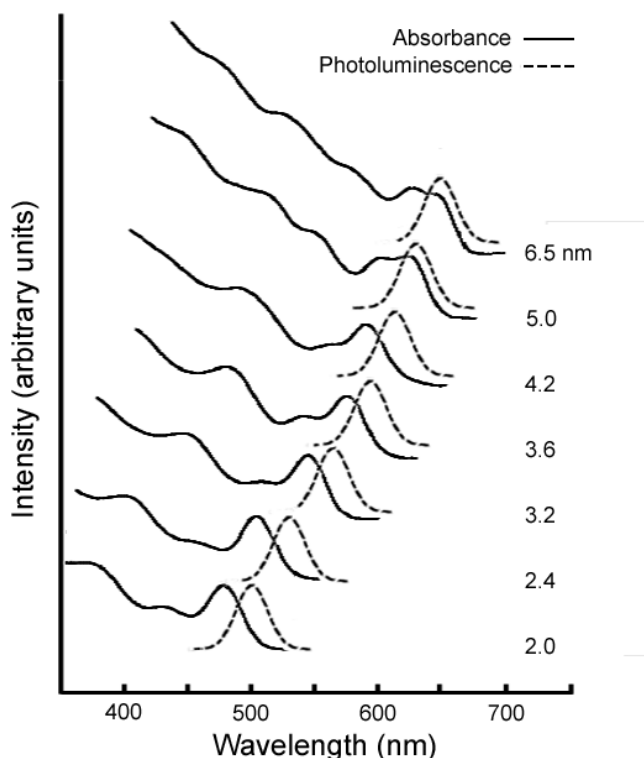


**Fig. 12.2.** Size-dependent absorption and photoluminescence spectra for ZnS-capped CdSe nanocrystals with diameters ranging from 2 to 6.5 nm.

than single Rhodamine 6G molecules [16]. This makes the case that QDs have highly desirable characteristics for fluorescent labeling.

### 12.3

#### Synthesis

The synthesis of nanocrystals from both the II–VI (e.g. ZnS, ZnSe, CdS, CdSe, CdTe and HgS) and III–V (e.g. GaAs, InP and InAs) semiconductor families has long been the subject of study, but until the early 1990s, QDs were usually synthesized in aqueous media using stabilizing agents, similar to the techniques used to produce colloidal gold nanoparticles. Unfortunately, these procedures yielded low-quality QDs with large size variations (relative standard deviation [RSD] > 15%) and very low luminescence quantum yields. These problems made it nearly impossible to resolve the theorized size-dependent properties of the nanocrystals. In 1993, Bawendi and coworkers at MIT reported a high-temperature organo-

metallic procedure to synthesize highly crystalline and nearly monodisperse CdSe QDs [10]. In contrast to previous samples, these nanocrystals had essentially defect-free crystal structures and size variations smaller than 5% but the achieved photoluminescence efficiencies were still relatively low ( $\sim 10\%$ ).

The main cause for such low quantum yields is the imperfect surface structure of the nanocrystals. Low-energy defect states on the particle surface give rise to nonradiative relaxation pathways that degrade the optical properties of the QDs. In 1996, Hines and Guyot-Sionnest reported core-shell nanocrystals in which the CdSe core was coated with a ZnS shell layer which improved the luminescence efficiencies to as high as 50% [27]. The growth of a CdS shell was also found to increase the quantum yield of CdSe nanocrystals [28, 29]. There are several reasons why the surface-capping layer ZnS or CdS has such a beneficial effect on the luminescence efficiency: (i) the shell has similar lattice parameters to the core (since the Zn-S and Cd-S bond lengths are similar to that of Cd-Se); (ii) the shell is capable of crystallizing in the same crystal structure as CdSe (wurtzite structure in this case); and (iii) the shell has a wider bandgap (energy difference between the valence band and the conduction band) than the core. The first two properties work together to minimize lattice mismatch and strain between the core and shell materials, promoting epitaxial growth of the shell, while the latter property shields the core from the outside environment and further confines the exciton to the nanocrystal core.

At present, the successful synthetic procedures are all based on a common theme, with small or incremental variations [10]. Briefly, an appropriate cadmium precursor is combined with the desired chalcogen precursor (sulfur, selenium or tellurium) in a hot coordinating solvent at a sufficiently high temperature to promote fast particle nucleation, followed by a lower temperature growth period. The moderate particle growth rate allows the particle size to be monitored during growth. Once the desired size has been obtained, growth can be terminated by quenching the reaction. Cadmium precursors for synthesizing nanocrystals cores include dimethyl cadmium, cadmium oxide, cadmium carbonate and cadmium acetate, but shell formation is best accomplished using the organometallic reagents dimethyl cadmium and dimethyl or diethyl zinc. Chalcogen species can be either elemental sulfur, selenium or tellurium dissolved in tri-*n*-octyl phosphine (TOP) or tri-*n*-butyl phosphine (TBP) as well as trimethylsilyl reagents of these chalcogens, with either type being equally acceptable for core or shell synthesis. Tri-*n*-octyl phosphine oxide (TOPO) is often used as the main solvent, with the addition of co-solvents such as dodecylamine [30], hexadecylamine [31], and stearic acid [32].

The following procedure describes the synthesis of CdE ( $E = S, Se \text{ or } Te$ ) QD cores whose surface is passivated with TOPO. With the cadmium precursor added to the reaction vessel along with the TOPO, acting as the high-temperature coordinating solvent as well as surfactant, the solution is heated to  $\sim 300\text{--}350^\circ\text{C}$ . At this point, an equimolar amount of chalcogen reagent dissolved in TOP (typical stock solutions are 0.25 M in E) is rapidly injected into the hot solvent. Upon injection, the previously colorless solution rapidly gains color, the sequence of which depends on the type of core material (from colorless to deep yellow for CdS, from



colorless through yellow and red to brown for CdSe, and from colorless through yellow and red to a deep brown for CdTe). Nanocrystal formation is rapid, but lowering the temperature allows the nanocrystals to slowly anneal after formation. The reaction can be monitored by observing the shift in the photoluminescence peak towards longer wavelengths. All manipulations during synthesis must be carried out under an inert atmosphere. Once the QDs have been obtained, subsequent manipulations can be carried out in air, if necessary, without any adverse effects on the optical properties of the nanocrystals. Washing is typically accomplished by dissolving the reaction mixture in chloroform followed by the addition of methanol to precipitate the TOPO-capped QDs out of the colloidal solution. Centrifugation, removal of the supernatant, and redissolving in chloroform can be repeated several times to obtain deeply colored colloidal solutions of TOPO-capped CdE QDs. Size-selective precipitation is unnecessary because the synthesis yields nearly monodisperse populations (ca. 5% RSD). The nanocrystal size can be controlled by varying any one or a combination of parameters: the initial monomer concentration (typically 2.5–50 mM), the initial injection temperature or growth temperature, and the growth time (ranging from minutes to hours, depending on the desired particle size and particular synthetic methods). Periodic injection of additional precursor solutions into the reaction mixture during the growth period can also be used to grow larger nanocrystals.

To increase the photostability and luminescence quantum yields, the nanocrystals can be capped with MS (where M = Zn or Cd) [27, 28]. One route to accomplishing this begins with the CdE cores obtained from the previously described synthesis and, after an annealing period, a solution of MS in TOP is added dropwise (to prevent MS nucleation and promote epitaxial growth) to the reaction mixture. The optimal capping layer thickness is obtained when the luminescence reaches a maximum, as determined during the slow addition process. This step yields high quality and nearly monodisperse TOPO-capped (CdE)MS (core)shell QDs that are soluble in a variety of organic solvents. In order to make these nanocrystals soluble in aqueous media, the QD surface must be linked to molecules with hydrophilic groups, as discussed in the following section.

## 12.4

### Surface Modification and Bioconjugation

Two key issues in utilizing QDs as fluorescent biological labels are (i) making high quality nanocrystals soluble in aqueous media and (ii) choosing an appropriate surface modification technique that enables the nanocrystals to be conjugated to biological macromolecules while avoiding deleterious effects on the optical properties. Several studies, using nuclear magnetic resonance (NMR) spectroscopy and X-ray photoemission spectroscopy (XPS) [33, 34], have probed the nanocrystal surface in order to characterize the QD surface. While the general aspects of the nanocrystal surface properties are held in consensus, details of the exact surface chemistries at play are still under debate. The nanocrystal interior has been well

characterized using transmission electron microscopy and X-ray diffraction, which clearly identifies the crystalline phase and gives strong evidence that the QD surface is faceted rather than smooth [4, 10]. Given the high radius of curvature of the QD surface, the steric hindrance associated with the packing of molecules on the surface is somewhat relaxed, allowing a slightly higher number of surface groups to be attached per unit surface area on the nanocrystalline material as compared to bulk substrates.

Quantum dots synthesized using techniques outlined in Section 12.3 have a capping layer of TOPO molecules strongly coordinated to the surface metal atoms. While TOPO is an ideal capping molecule for maintaining QD solubility and optical properties in organic solvents [36], the extremely hydrophobic nature of this surface requires that they be replaced with molecules containing polar groups that allow the QDs to be transferred into aqueous media. With this purpose in mind, several methods have been designed to prepare water-soluble QDs by displacing the TOPO molecules with a more appropriate layer (Fig. 12.3).

One method involved the use of a siloxane coating for creating water-soluble (CdSe)ZnS [15, 37]. In this case, mercaptopropyltrimethoxysilane (MPS) displaces the TOPO molecules, and a siloxane shell is formed *via* the hydrolysis of the silanol groups under basic conditions. Following the initial shell formation, a mixture of trihydroxysilylpropylmethylphosphonate monosodium salt (TMP) and MPS are added to give the QD surface hydrophilic character and provide surface thiol groups for subsequent bioconjugation. The resulting surface is negatively charged due to the surface phosphonate groups. Alternatively, TMP can be replaced during the second step with poly(ethylene glycol) (PEG)-silane or a mixture of PEG-silane and trimethoxysilylpropyl trimethylammonium chloride in order to obtain a neutral or slightly positively charged surface [38]. Subsequently, the thiol groups can be converted to amine or carboxy groups using standard procedures. These surface groups can be conjugated to biological molecules using an appropriate bifunctional linker and any one of the many well established techniques [39]. These QDs are highly stable against aggregation and show no reduction in the quality of the optical properties. However, it is difficult to scale up this complex procedure which yields only milligram quantities per batch.

A different procedure was reported by Chan and Nie, which involves the adsorption of bifunctional ligands such as mercaptoacetic acid, mercaptosuccinic acid, dithiothreitol, glutathione or histidine directly onto the QD surface [16, 40]. Others have shown that a host of mercapto compounds such as mercaptobenzoic acid, mercaptopropionic acid, mercaptoundecanoic acid, mercaptohexadecanoic acid are also amenable to the same procedure [19, 41]. Essentially, the desired surface molecule is added to TOPO-capped QDs dissolved in chloroform in conjunction with an organic base. The driving force behind this scheme is the high affinity of the thiol or amino groups towards the surface metal atoms which causes the displacement of TOPO molecules on the surface. Within minutes of the addition (carried out at room temperature) the QDs precipitate out of the organic solution and can be isolated and readily redissolved in basic aqueous solution. Although gram quantities of water-soluble QDs can be obtained using this technique, slow

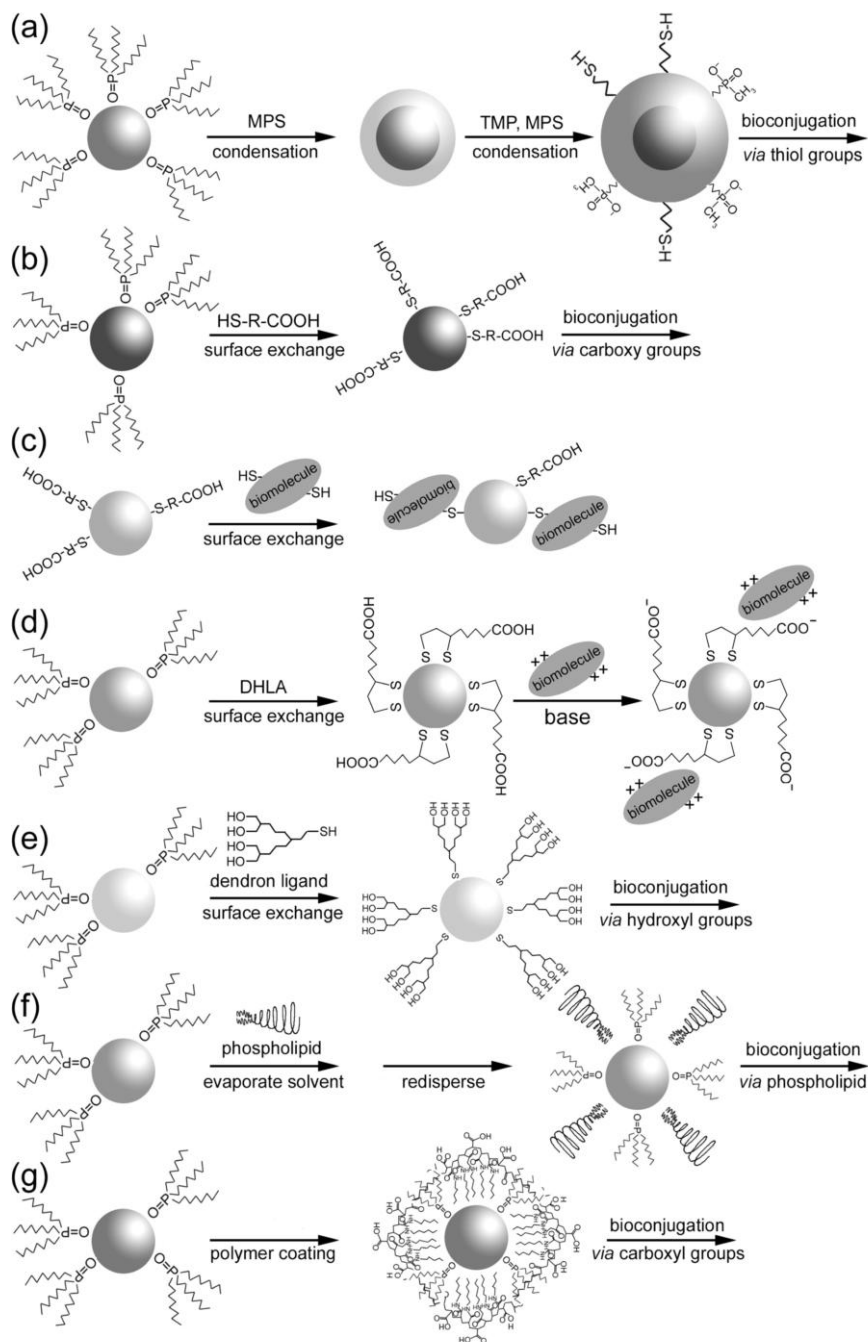


**Fig. 12.3.** Strategies for QD surface modification and bioconjugation: (a) coating quantum dots with a silica shell, (b) direct adsorption of bifunctional linkers, (c) direct adsorption of thiolated biomolecules, (d)

conjugation *via* electrostatic interactions, (e) stabilization and conjugation using organic dendrimers, (f) micellar encapsulation, and (g) polymer coating.

desorption of surface ligands results in aggregation and precipitation of the QDs over a period of several weeks. Also, a reduction in quantum efficiency occurs when using these surface molecules, the extent of which is dependent on the linker used and the chemical environment. In spite of these problems, this simple procedure has allowed the production of fresh batches on an “as-needed” basis. Again, well established protocols can be used for surface bioconjugation.

A variation of this direct adsorption method is to incubate the water soluble QDs with thiol-containing biomolecules, which slowly replace the surface mercapto ligands *via* mass action. This has been demonstrated for DNA [18] and proteins [42] in aqueous solutions as well as for other small biomolecules which can replace the TOPO molecules in polar organic solvents [43]. In fact, in using this thiol-exchange method, Van Orden and coworkers noted that the reduced quantum yield, due to the direct adsorption of mercaptoacetic acid, was completely recovered when thiolated bovine serum albumin (BSA) replaced it on the QD surface. Since this protein-coated surface provides multiple functional groups, it has inherent advantages over the bifunctional linkers in that it is amenable to a wide array of techniques for covalent conjugation to biological molecules and biomaterials.

Several other strategies have been devised in recent years to obtain robust and biocompatible QD capable of long term stability in aqueous solution (Fig. 12.3). Among these, bioconjugation via electrostatic interactions has been used to attach QDs to engineered recombinant proteins. This procedure involves the direct adsorption of dihydrolipoic acid (DHLA) onto the QD surface (leading to negative charges), and then electrostatic self assembly to positively charged proteins [17, 44–46]. A strategy employing hydrophilic organic dendron ligands has been reported by Peng and coworkers [47], and a micellular encapsulation procedure has been described by Dubertret et al. using phospholipids [48]. Importantly, amphiphilic polymer-coated QDs conjugated to streptavidin have become commercially available [49]. These polymer-coated QD bioconjugates are extremely stable against flocculation and highly luminescent. It should be noted that the QD surface modification and bioconjugation in all of these cases results in several macromolecules being attached to one nanocrystal. As a result, the overall size of the QD bioconjugates can be increased 2–3 fold above the original (core)shell nanocrystal.

## 12.5 Applications

Quantum dot bioconjugates have been used for immunoassay [44, 45], FRET-based binding assays [42] and DNA hybridization detection [18, 19, 38]. Nanocrystals are also emerging as a new class of fluorescent labels for targeting cell surface receptors [43] and for *in vivo* targeting and imaging [48, 50]. An important aspect of QD labels is their extremely high photostability, which allows real-time monitoring or tracking of intracellular processes over long periods of time (hours to days) [46]. For example, QD bioconjugates have been injected into *Xenopus* embryos to monitor development to the tadpole stages [48] (Fig. 12.4). The potential for long term

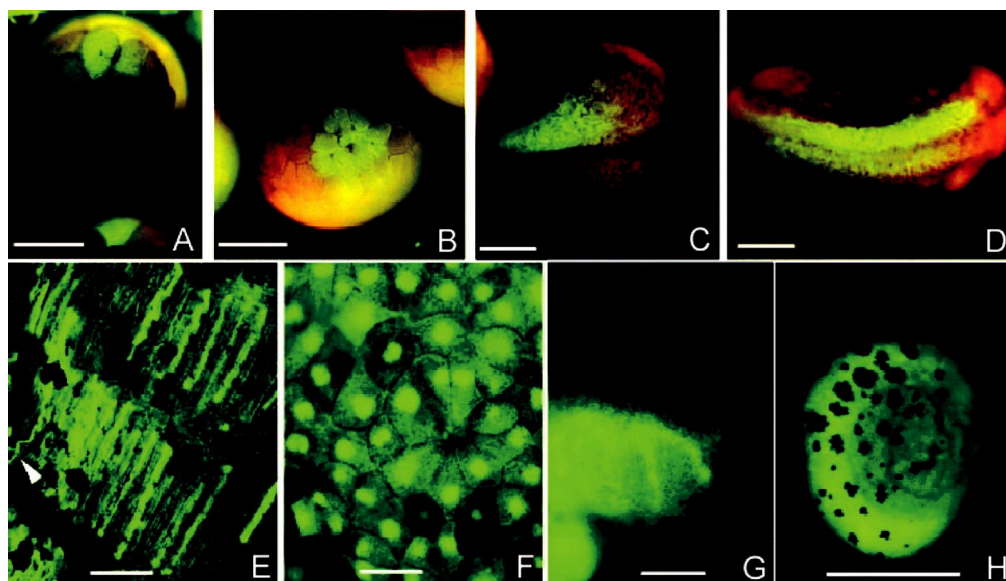


**Fig. 12.4.** QD labeling of *Xenopus* embryos at different stages and specific QD intracellular localizations. (A) Injection of one cell out of an eight-cell-stage embryo resulted in labeling of individual blastomeres. (B) Same embryo shown 1 h later. The daughter cells of the injected blastomere are labeled (C) and at a later stage (D) show two neurula embryos, which were injected into a single cell at the eight-cell-stage in the animal pole. (E)

Intracellular labeling of an axon (arrow) and somites at tadpole stage 40. (F) QDs localized in the nucleus during mid-blastula stages. (G) Labeled neural crest cells migrating into the branchial arches. (H) QD fluorescence observed in the gut of an injected embryo. Bars: (A) to (D), (G), and (H), 0.5 mm; (E) and (F), 30  $\mu$ m. Reproduced with permission from [48].

monitoring applications is enhanced by the inert surface coating, which renders QDs less toxic than organic dyes.

Another key advantage is the use of multicolor nanocrystals to simultaneously image several targets inside living cells or on the cell surface [49]. This is especially useful in the early detection and identification of cancer tumors based on multiple markers. An extension of this type of application is the use of near-infrared (NIR) QDs for in vivo molecular imaging. Similar long-wavelength dyes based on organic NIR fluorophores have been used for tumor imaging in live animals [51, 52]. Recent research has demonstrated that NIR fluorescent nanocrystals having emission wavelengths as long as 850 nm and quantum yields as high as 50% at room temperature can be synthesized and they are compatible with the bioconjugation techniques developed for (CdSe)ZnS QDs. In comparison with carbocyanine and related organic dyes, these NIR QDs are much brighter (higher quantum yields and larger absorption cross-sections) and are much more stable against photo-

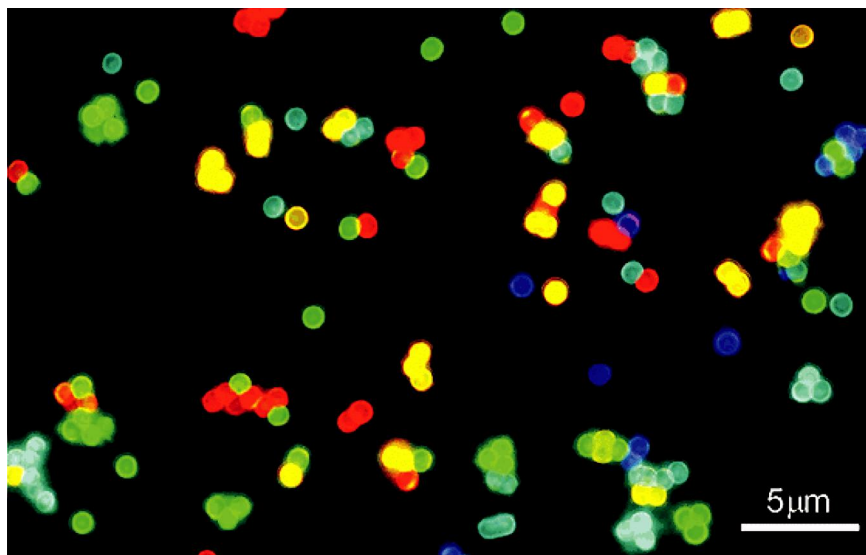


**Fig. 12.5.** Fluorescence micrograph of a mixture of CdSe/ZnS QD-tagged beads emitting single-color signals at 484, 508, 547, 575, and 611 nm. Reproduced with permission from [55].

bleaching [53]. Fluorescence imaging of tissue sections is another area in which multicolor QDs will provide important advantages in reducing analysis time and in expanding the range of detectable biomarkers [54].

Still another application is the use of QD-encoded beads for multiplexed and high-throughput analysis of genes and proteins [55–57] (Fig. 12.5). Polymer microbeads containing populations of multicolor QDs in predetermined color and intensity patterns can serve as a “bar code” identifying the reagent (e.g. proteins, peptides or oligonucleotides) attached to the bead surface. The use of six colors and ten intensity levels can theoretically encode up to one million unique probes. When a target molecule attaches to the surface probe, its presence is detected and identification determined by the specific “bar code” associated with the bead’s spectroscopic signature in combination with the presence of a spectroscopic feature from the target molecule.

Finally, an indirect application involves color-tunable QD-based laser light sources under development [58, 59]. Given the proliferation of laser-induced fluorescence in chemistry and biology, it is reasonable to assume that these unique continuously tunable light sources (the lasing wavelength can be tuned by changing the QD size) will allow laser sources to be produced at any given wavelength. By removing the restraints that have limited the selection of laser wavelengths, these light sources will provide greater flexibility and should allow more economical and more efficient instrumentation.

## Acknowledgement

This work was supported by grants from the National Institutes of Health (R01 GM58173 and R01 GM60562) and the Department of Energy (DOE FG02-98ER14873).

## References

- 1 A. HENGLEIN, *Chem. Rev.* **1989**, 89, 1861–1873.
- 2 G. SCHMID, *Chem. Rev.* **1992**, 92, 1709–1727.
- 3 H. WELLER, *Angew. Chem. Int. Ed. Engl.* **1993**, 32, 41–53.
- 4 A. P. ALIVISATOS, *J. Phys. Chem.* **1996**, 100, 13226–13239.
- 5 A. P. ALIVISATOS, *Science* **1996**, 271, 933–937.
- 6 M. NIRMAL, L. E. BRUS, *Acc. Chem. Res.* **1999**, 32, 407–414.
- 7 W. C. W. CHAN, D. J. MAXWELL, J. X. GAO et al., *Curr. Opin. Biotechnol.* **2002**, 13, 40–46.
- 8 D. L. DEXTER, R. S. KNOX, *Excitons*, Wiley, New York 1965.
- 9 H. JONES, *The Theory of Brillouin Zones and Electronic States in Crystals*, Elsevier, Amsterdam 1975.
- 10 C. B. MURRAY, D. J. NORRIS, M. G. BAWENDI, *J. Am. Chem. Soc.* **1993**, 115, 8706–8715.
- 11 E. KLARREICH, *Nature* **2001**, 413, 450–452.
- 12 P. MITCHELL, *Nat. Biotechnol.* **2001**, 19, 1013–1017.
- 13 C. M. NIEMEYER, *Angew. Chem. Int. Ed. Engl.* **2001**, 40, 4128–4158.
- 14 S. R. WHALEY, D. S. ENGLISH, E. L. HU et al., *Nature* **2000**, 405, 665–668.
- 15 M. BRUCHEZ, JR., M. MORONNE, P. GIN et al., *Science* **1998**, 281, 2013–2015.
- 16 W. C. W. CHAN, S. NIE, *Science* **1998**, 281, 2016–2018.
- 17 H. MATTOUSSI, J. M. MAURO, E. R. GOLDMAN et al., *J. Am. Chem. Soc.* **2000**, 122, 12142–12150.
- 18 G. P. MITCHELL, C. A. MIRKIN, R. L. LETSINGER, *J. Am. Chem. Soc.* **1999**, 121, 8122–8123.
- 19 S. PATHAK, S. K. CHOI, N. ARNHEIM et al., *J. Am. Chem. Soc.* **2001**, 123, 4103–4104.
- 20 R. ELGHANIAN, J. J. STORHOFF, R. C. MUCIC et al., *Science* **1997**, 277, 1078–1081.
- 21 B. DUBERTRET, M. CALAME, A. J. LIBCHABER, *Nat. Biotechnol.* **2001**, 19, 365–370.
- 22 R. A. REYNOLDS, III, C. A. MIRKIN, R. L. LETSINGER, *J. Am. Chem. Soc.* **2000**, 122, 3795–3796.
- 23 C. A. MIRKIN, R. L. LETSINGER, R. C. MUCIC et al., *Nature* **1996**, 382, 607–609.
- 24 A. P. ALIVISATOS, K. P. JOHNSON, X. G. PENG et al., *Nature* **1996**, 382, 609–611.
- 25 Z. A. PENG, X. G. PENG, *J. Am. Chem. Soc.* **2001**, 123, 183–184.
- 26 C. POLLOCK, *Fundamentals of Optoelectronics*, Irwin, USA 1995.
- 27 M. A. HINES, P. GUYOT-SIONNEST, *J. Phys. Chem. B* **1996**, 100, 468–471.
- 28 X. G. PENG, M. C. SCHLAMP, A. V. KADAVANICH et al., *J. Am. Chem. Soc.* **1997**, 119, 7019–7029.
- 29 B. O. DABBOUSI, J. RODRIGUEZ-VIEJO, F. V. MIKULEC et al., *J. Phys. Chem. B* **1997**, 101, 9463–9475.
- 30 D. V. TALAPIN, S. HAUBOLD, A. L. ROGACH et al., *J. Phys. Chem. B* **2001**, 105, 2260–2263.
- 31 D. V. TALAPIN, A. L. ROGACH, A. KORNOWSKI et al., *Nano Lett.* **2001**, 1, 207–211.
- 32 L. QU, Z. A. PENG, X. G. PENG, *Nano Lett.* **2001**, 1, 333–337.
- 33 L. R. BECERRA, C. B. MURRAY, R. G. GRIFFIN et al., *J. Chem. Phys.* **1994**, 100, 3297–3300.
- 34 J. E. B. KATARI, V. L. COLVIN, A. P. ALIVISATOS, *J. Phys. Chem.* **1994**, 98, 4109–4117.



- 35 M. O'NEIL, J. MAROHN, G. MCLENDON, *J. Phys. Chem.* **1990**, 94, 4356–4363.
- 36 J. K. LORENZ, A. B. ELLIS, *J. Am. Chem. Soc.* **1998**, 120, 10970–10975.
- 37 D. GERION, F. PINAUD, S. C. WILLIAMS et al., *J. Phys. Chem. B* **2001**, 105, 8861–8871.
- 38 W. J. PARAK, D. GERION, D. ZANCHET et al., *Chem. Mater.* **2002**, 14, 2113–2119.
- 39 G. T. HERMANSON, *Bioconjugate Techniques*, Academic Press, New York 1996.
- 40 W. C. W. CHAN, T. L. PRENDERGAST, M. JAIN et al., *Proc. SPIE* **2000**, 3924, 2–9.
- 41 J. ALDANA, Y. A. WANG, X. G. PENG, *J. Am. Chem. Soc.* **2001**, 123, 8844–8850.
- 42 D. M. WILLARD, L. L. CARILLO, J. JUNG et al., *Nano Lett.* **2001**, 1, 469–474.
- 43 S. J. ROSENTHAL, I. TOMLINSON, E. M. ADKINS et al., *J. Am. Chem. Soc.* **2002**, 124, 4586–4594.
- 44 E. R. GOLDMAN, G. P. ANDERSON, P. T. TRAN et al., *Anal. Chem.* **2002**, 74, 841–847.
- 45 E. R. GOLDMAN, E. D. BALIGHIAN, H. MATTOUSSI et al., *J. Am. Chem. Soc.* **2002**, 124, 6378–6382.
- 46 J. K. JAISWAL, H. MATTOUSSI, J. M. MAURO et al., *Nat. Biotechnol.* **2003**, 21, 47–51.
- 47 Y. A. WANG, J. J. LI, H. CHEN et al., *J. Am. Chem. Soc.* **2002**, 124, 2293–2298.
- 48 B. DUBERTRET, P. SKOURIDE, D. J. NORRIS et al., *Science* **2002**, 298, 1759–1762.
- 49 X. WU, H. LIU, J. LIU et al., *Nat. Biotechnol.* **2002**, 21, 41–46.
- 50 M. E. ÅKERMAN, W. C. W. CHAN, P. LAAKKONEN et al., *Proc. Natl. Acad. Sci. USA* **2002**, 99, 12617–12621.
- 51 R. WEISSLEDER, C. H. TUNG, U. MAHMOOD et al., *Nat. Biotechnol.* **1999**, 17, 375–378.
- 52 C. BREMER, C. H. TUNG, R. WEISSLEDER, *Nat. Med.* **2001**, 7, 743–748.
- 53 R. E. BAILEY, S. NIE, *J. Am. Chem. Soc.* **2003**, 125, 7100–7106.
- 54 M. DAHAN, T. LAURENCE, F. PINAUD et al., *Opt. Lett.* **2001**, 26, 825–827.
- 55 M. Y. HAN, J. X. GAO, J. Z. SU et al., *Nat. Biotechnol.* **2001**, 19, 631–635.
- 56 N. GAPONIK, I. L. RADTCHENKO, G. B. SUKHORUKOV et al., *Adv. Mater.* **2002**, 14, 879–882.
- 57 D. WANG, A. L. ROGACH, F. CARUSO, *Nano Lett.* **2002**, 2, 857–861.
- 58 V. I. KLIMOV, A. A. MIKHAILOVSKY, S. XU et al., *Science* **2000**, 290, 314–317.
- 59 H. J. EISLER, V. C. SUNDAR, M. G. BAWENDI et al., *Appl. Phys. Lett.* **2002**, 80, 4614–4616.

## 13

## Large Semiconductor Molecules

*J. F. Corrigan and M. W. DeGroot*

## 13.1

## Introduction

The synthesis of large, discrete molecular complexes with several dozen, or indeed several hundred, heavy atoms is currently the focus of numerous research efforts worldwide and recent successful synthetic strategies have intensified efforts in this area. Two primary reasons behind the development of this key area of chemical research are: (i) the *controlled* synthesis of large mixed main group metal semiconductor nanoparticles and nanoclusters leads to a size regime wherein the electronic properties of these molecules no longer resemble those of smaller, discrete molecular units nor do they mimic those of the corresponding bulk materials, and such complexes hold great promise for use in future electronic applications. (ii) The use of discrete 'premixed' binary or ternary clusters, with labile ancillary ligands may afford alternate, low temperature routes to corresponding (and possibly new) solid state materials. The use of preformed molecules in the preparation of solids allows lower reaction temperatures for the formation of solids, thus implying kinetic *versus* thermodynamic control during sample preparation.

Two crucial factors required for the successful development of these applications are the need to synthesize the appropriate nanocluster molecules in such a manner as to have zero size distribution and to be able to structurally characterize the products obtained. The numerous practical applications of binary late-metal chalcogenide semiconductors [1] have spurred the development of chemical methods to access nanometer-sized pieces of these solid materials, where single crystal diffraction can be used to elucidate the three-dimensional structure of the clusters obtained.

The flexibility of chalcogenide ( $E^{2-}$ ) and chalcogenolate ( $RE^-$ ) ligands is demonstrated in their ability to adopt several different bridging coordination modes and to form stable bonds with most transition and post-transition metals [2–9]. This tendency to bridge metals is attributed to the highly polarizable electrons and the anionic nature of these ligands. As a consequence of the bridging ability, binary metal chalcogenides are typically nonmolecular solids, with extensive bonding in one, two, or three dimensions. Access to molecular metal chalcogenide clusters

therefore requires that these interactions be limited via the incorporation of a suitable “surface” on a metal chalcogenide core. This surface is typically formed by the use of heteroligands such as tertiary phosphines or amines or organochalcogenolate anions  $\text{RE}^-$ . These ligands kinetically stabilize the metal chalcogenide cluster core by bonding at the cluster surface, preventing further condensation to bulk materials.

Chalcogenide ligands typically adopt  $\mu_3$ - and  $\mu_4$ - and higher coordination interactions in high nuclearity clusters. The three- and four-coordinate bridging modes are the most common for chalcogenide ligands. The ability to bridge metal centers increases on going down the group from sulfur to selenium to tellurium, and this tendency can be explained as a consequence of the larger ionic radii, and thus larger polarizability of the heavier elements.

The organochalcogenolate ligands ( $\text{RE}^-$ ) constitute a very important ligand type in nanometer-sized metal-chalcogen complexes when used in conjunction with  $\text{E}^{2-}$  ligands. Like their chalcogenide counterparts, they demonstrate a strong tendency to bridge metal centers. The potential to modify the coordinating ability of these ligands by changing the organosubstituent (R) has resulted in these ligands being coined “chalcogenide with a handle” [4]. The most common bonding mode of  $\text{RE}^-$  is the doubly bridging ( $\mu_2$ ) type, which is observed in clusters with thiolate, selenolate, and tellurolate ligands. Triply and higher bridging coordination modes are more common for selenolate and tellurolate ligands than for thiolates, again attributable to the larger size of the heavier chalcogens [2].

In the following sections, an overview of the recent developments in the synthesis of structurally characterized late metal-chalcogen nanocluster semiconductor complexes is given. Relationships and contrasts of the structural and photophysical properties of these molecules compared to solid materials are also discussed. Late metal-chalcogen and -pnictogen clusters typically display condensed core structures, and can thus be contrasted with the more open frameworks observed with the earlier metals [10]. This point is highlighted with the report of the nanometer-sized open iron–selenium framework of  $[\text{Fe}_{20}\text{Se}_{38}]^{18-}$  (1, Figure 13.1) [11].

## 13.2

### Nickel Chalcogenides

The use of trialkylphosphine-selenide and -telluride ligands has been developed for the generation of a series of high nuclearity complexes of nickel-chalcogenides, building upon the successful isolation of lower-nuclearity metal-chalcogen complexes of Cr, Mn, Fe, Co and Pd [12–16]. The reagents  $\text{R}_3\text{P}=\text{E}$  can be viewed as soluble, organometallic sources of elemental chalcogen, where the selenide and (especially) telluride derivatives have sufficiently poor  $\text{E}=\text{P}$  orbital overlap, such that they can act as transfer agents of zerovalent chalcogen [17]. These reagents have been used to transfer selenium or tellurium ligands to zerovalent metals with sufficiently labile ligands (Eq. (1)) [18].

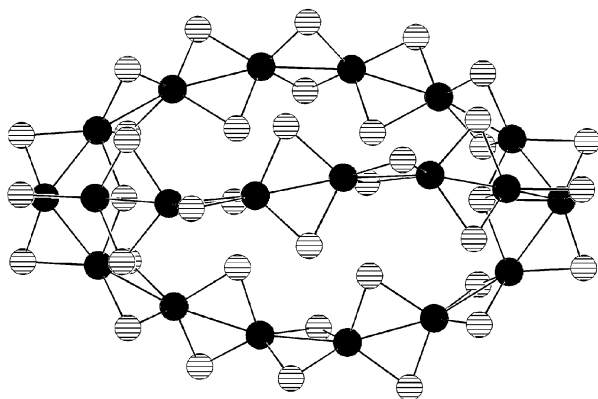
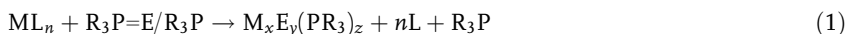


Fig. 13.1. A projection of the open iron–selenium framework in  $[\text{Na}_9\text{Fe}_{20}\text{Se}_{38}]^{9-}$  [11].



Whereas at higher temperatures these reactions typically yield bulk solid M/E materials, similar reactions at room temperature offer a synthetic route to cluster complexes, which are stabilized via the incorporation of ancillary  $\text{PR}_3$  ligands. The isolation and structural characterization of these cluster intermediates has been termed the “molecules-to-clusters-to-solids” pathway [18].

Thus the reaction of  $\text{Ni}(\text{COD})_2$  ( $\text{COD}$  = cyclooctadiene) with  $\text{Et}_3\text{P}=\text{Se}$  in refluxing toluene results in a mixture of  $\text{Ni}_3\text{Se}_2$  and elemental nickel, whereas the molecular complex  $[\text{Ni}_{23}\text{Se}_{12}(\text{PEt}_3)_{13}]$  **2** is isolated in crystalline form from the combination of these reagents under ambient conditions [19]. Cluster **2** is rather unique in that it is best viewed as being comprised of two unrelated fragments (Figure 13.2): the “top” of the cluster is comprised of a Se-rich  $\text{Ni}_{10}\text{Se}_9$  unit with the  $\text{Se}^{2-}$  ligands located on the surface of a nickel-only cluster core (acting as either  $\mu_4$ - or  $\mu_5$ -capping ligands) whereas the “bottom” component of the framework is Ni-rich, consisting of 13 nickel atoms and only three  $\text{Se}^{2-}$  ligands. The metal-rich unit has a central Ni within bonding contact to 12 additional Ni centers, ranging from 2.52 to 2.57 Å. The structural similarities between the “top” half of the cluster and that observed for NiSe and the “bottom” half and that observed for elemental nickel, suggest this cluster may result from an intergrowth of two different cluster types. Thermolysis induced  $\text{PET}_3$  ligand elimination yields however  $\text{Ni}_3\text{Se}_2$ , of which neither substructure is reminiscent.

The heavier congener  $\text{Et}_3\text{P}=\text{Te}$  has been used similarly to access the high-nuclearity nickel telluride cluster  $[\text{Ni}_{20}\text{Te}_{18}(\text{PET}_3)_{12}]$  **3**, the largest structurally characterized Ni/Te cluster, with dimensions in the nanometer size regime [20]. The arrangement of core atoms can be described in terms of a twisted  $\text{Ni}_6$  trigonal prism with a central Te, capped by two Ni atoms (Figure 13.3), with a similar fragment observed in the structure of solid  $\text{Ni}_{1+x}\text{Te}$  [21]. The other twelve Ni atoms are each bonded to four  $\text{Te}^{2-}$  ligands, and further bonded to an ancillary

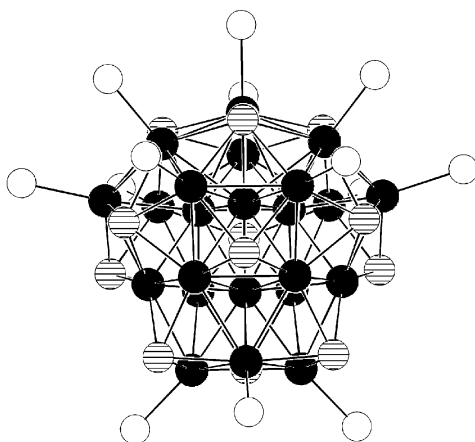


**Fig. 13.2.** The nickel–selenium core in  $[\text{Ni}_{23}\text{Se}_{12}(\text{PEt}_3)_{13}]$  **2** illustrating the Se-rich “top” and Ni-rich “bottom” of the cluster. Surface P atoms are illustrated as open circles [19].

phosphine ligand. These Ni–Te distances vary from 2.45 to 2.90 Å, and can be contrasted with the shorter nickel–selenium distances observed in **2** (2.30–2.48 Å).

The success of this synthetic approach for the delivery of “Te(0)” to the metal centers requires the presence of additional  $\text{PEt}_3$  in the reaction solutions, in order to circumvent the deposition of tellurium metal from the facile reduction of  $\text{R}_3\text{P}=\text{Te}$  to  $\text{R}_3\text{P}$  ( $\text{R}_3\text{P}=\text{Te} \rightleftharpoons \text{R}_3\text{P} + \text{Te}$ ) [17]. In contrast, metal-sulfide clusters are generally not accessible from trialkylphosphine sulfides, due to the inherent strength of P=S bonds, unless more forcing conditions are used [22, 23].

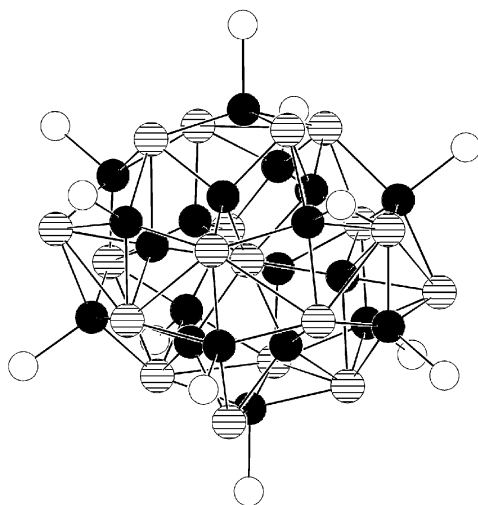


**Fig. 13.3.** A projection of the nickel–tellurium cluster core in  $[\text{Ni}_{20}\text{Te}_{18}(\text{PEt}_3)_{12}]$  **3** [20].

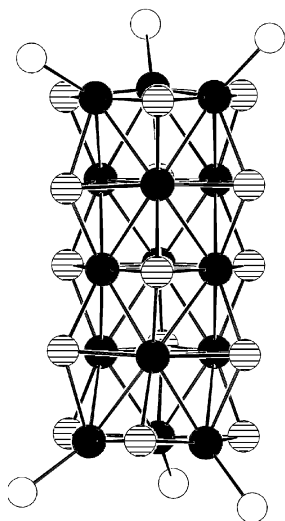


**Fig. 13.4.** The condensed, columnar framework observed in  $[\text{Ni}_{15}\text{E}_{15}(\text{PPh}_3)_6]$  (**4**,  $\text{E} = \text{S}$ ; **5**,  $\text{E} = \text{Se}$ ) illustrating the buildup from  $\text{Ni}_3\text{E}_3$  units [24, 25].

Sodium sulfide,  $\text{Na}_2\text{S}$ , has proven to be an effective reagent for the synthesis of nickel-sulfide clusters, when reacted with phosphine-solubilized  $\text{Ni}(\text{II})$  salts. The nanocluster  $[\text{Ni}_{15}\text{S}_{15}(\text{PPh}_3)_6]$  **4** (Figure 13.4) can be described as a columnar arrangement of triangular  $\{\text{Ni}_3\text{S}_3\}$  stacked units [24]. These units are parallel and staggered with respect to each other, with the sulfide centers acting as both intra- and inter-triangle  $\mu_{3/4}\text{-S}$  bridging ligands, and the oblong cluster is capped at both ends with three  $\text{PPh}_3$  groups. The isostructural  $[\text{Ni}_{15}\text{Se}_{15}(\text{PPh}_3)_6]$  **5** can be prepared from nickel chloride and  $\text{Se}(\text{SiMe}_3)_2$  under room temperature conditions [25]. The reaction between the nickel(II) source and the silylated selenium reagent invariably results in a distribution of products formed, however these provide mechanistic insight into the manner in which the columnar cluster forms. These products include triangular  $[\text{Ni}_3\text{Se}_2\text{X}_2(\text{PR}_3)_4]$  ( $\text{X} = \text{Cl}, \text{SeSiMe}_3$ ), which can be viewed as the building blocks leading to the higher nuclearity complex **5** [26]. Recent theoretical work suggests that continued condensation of such  $\text{Ni}_3$  units to yield clusters  $[\text{Ni}_{3n}\text{Se}_{3n}(\text{PR}_3)_6]$  ( $n = 6\text{--}9$ ) should be accessible [27], consistent with the previous experimental observations [26].

The synthesis and structural characterization of the spherical nanocluster  $[\text{Ni}_{34}\text{Se}_{22}(\text{PPh}_3)_{10}]$  **6** (Figure 13.5) illustrates clearly that nanometer-sized pieces of the binary material can be accessed [28]. Cluster **6** is formed from the reaction of  $\text{NiCl}_2(\text{PPh}_3)_2$  and  $\text{Se}(\text{SiMe}_3)_2$ . The structure of the  $\text{NiSe}$  core in **6** is quite unique with respect to other  $\text{Ni/E}$  clusters, with virtual five-fold symmetry and layers of 5, 10, 10, and 5 nickel atoms. A  $\text{Ni}_4$  unit resides at the center of the molecule. The selenium atoms all act as  $\mu_4$ -capping ligands, save for the two  $\mu_5\text{-Se}$  that cap the top and bottom  $\text{Ni}_5$  pentagons. A similar spherical arrangement of

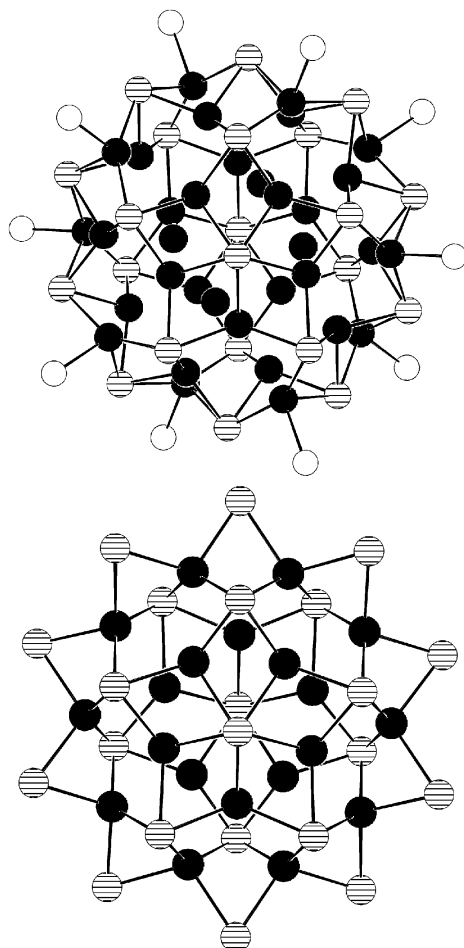


**Fig. 13.5.** The Ni–Se cluster cores in  $[\text{Ni}_{34}\text{Se}_{22}(\text{PPh}_3)_{10}]$  **6** (top) and  $[\text{Ni}_{20}\text{Se}_{12}(\text{SeMe})_{10}]^{2-}$  **7** (bottom) [28, 29].

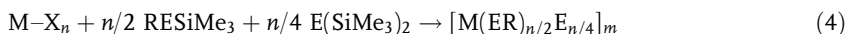
Ni and Se is observed in the structure of the mixed selenide/selenolate cluster  $[\text{Ni}_{20}\text{Se}_{12}(\text{SeMe})_{10}]^{2-}$  (**7**, Figure 13.5) [29]. The cluster contains a  $\text{Ni}_{20}\text{Se}_{12}$  core that is stabilized by surface Me groups bonded to Se centers. The interstitial selenide ligands ( $\text{Se}^{2-}$ ) arise from Se–C bond scission reactions of the  $\text{MeSe}^-$  reagent.

### 13.3 Group XI Chalcogenides

The utility of silylated chalcogen reagents as a soluble delivery source of “ $\text{E}^{2-}$ ” has developed into a powerful method for the generation of nanocluster materials.



Compounds such as  $E(\text{SiMe}_3)_2$  and  $\text{RESiMe}_3$  ( $E = \text{S, Se, Te}$ ) react readily with transition and main group metal salts to form metal chalcogenide or chalcogenolate bonds (Eq. (2)–(4)).



The driving force for the reaction is the thermodynamically favorable formation of an X–Si bond and elimination of  $\text{XSiMe}_3$  (where  $X = \text{halide, OAc, etc.}$ ) [10]. A primary advantage in using silylchalcogen reagents over related alkali-metal chalcogen sources ( $\text{Na}_2\text{S}$ ,  $\text{Li}_2\text{Se}$ , etc.) is the possibility of homogeneous reaction solutions when using the former. This has been of paramount importance for the synthesis and crystallization of  $\text{CuSe}$  and  $\text{AgSe}$  clusters, where the dimensions of the nanometer-sized binary cores overlap with some colloidal systems [30].

### 13.3.1

#### Copper Sulfide and Copper Selenide Nanoclusters

##### 13.3.1.1 Layered $\text{Cu}_2\text{Se}$

Within the copper-chalcogen clusters, the system copper–selenium has proven to offer an incredible wealth of structural types, with cluster sizes ranging from the molecular to the nanoparticle [ $\text{Cu}_{146}\text{Se}_{73}(\text{PPh}_3)_{30}$ ] (**8**, Figure 13.6) [31]. Cluster **8** is prepared from  $\text{CuCl}$ ,  $\text{Se}(\text{SiMe}_3)_2$  and a large excess of  $\text{PPh}_3$  under low temperature conditions [32]. The structure of **8** consists of an overall trigonal prismatic shape, with the Se atoms arranged into three ( $\text{Se}_{21}$ – $\text{Se}_{31}$ – $\text{Se}_{21}$ ) planar layers resembling a hexagonal close-packed (A–B–A) assembly (figure 13.6). This layered arrangement of Se centers is reminiscent of the packing of selenium in the binary  $\text{Cu}_2\text{Se}$ , however the selenium centers in the latter adopt a cubic closest-packed structure [33]. Of the 146 copper atoms in **8**, 120 are located in the tetrahedral holes of the selenium lattice, displaced however to yield variable trigonal or tetrahedral coordination, consistent with the structure of  $\beta\text{-Cu}_2\text{Se}$  [34]. Of the remaining copper centers, 14 are located above and below the deltahedral surfaces of the cluster, and 12 within the central  $\text{Se}_{31}$  layer. The 30  $\text{PPh}_3$  ligands completely envelop the  $\text{Cu}_2\text{Se}$  core. The stoichiometric  $2\text{Cu}:\text{Se}$  ratio in **8** allows for an assignment of +1 to the copper centers, consistent with the non-bonding  $\text{Cu}\cdots\text{Cu}$  distances observed in the structure, and with X-ray photoelectron spectroscopy (XPS) measurements [35]. These XPS measurements also lead to the conclusion that the influence of the  $\text{PPh}_3$  ligands on the electronic properties of the  $\text{Cu}_{146}\text{Se}_{73}$  core is small.

Subsequent to the original report detailing the synthesis of [ $\text{Cu}_{146}\text{Se}_{73}(\text{PPh}_3)_{30}$ ] **8**, the related clusters [ $\text{Cu}_{140}\text{Se}_{70}(\text{PEt}_3)_x$ ] ( $x = 34, 36$ ) have been described [36]. These  $\text{Cu}_{140}\text{Se}_{70}$  systems differ from the structure observed in **8** only at the cluster periphery, specifically at the corners of the triangular prismatic frame. These close structural relationships have been highlighted recently [31].

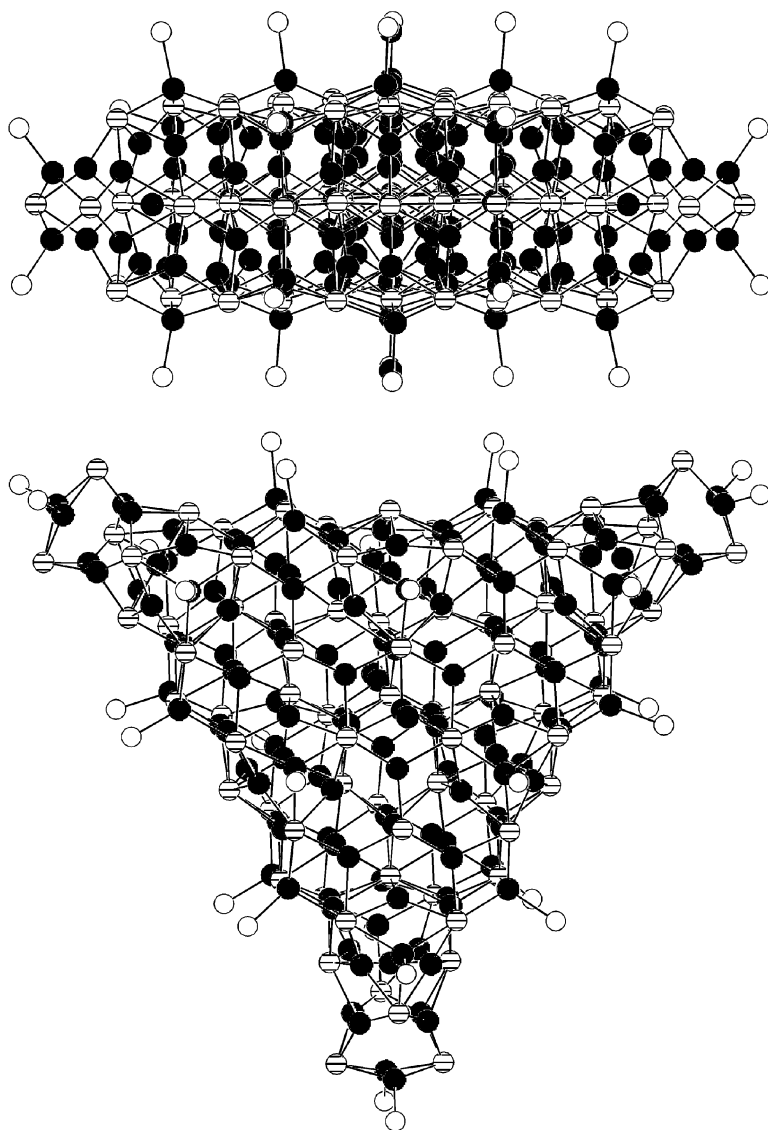


**Fig. 13.6.** Two projections of the cluster  $[\text{Cu}_{146}\text{Se}_{73}(\text{PPh}_3)_{30}]$  **8** illustrating the layered nature of the selenium framework (top) and the overall triangular shape (bottom) of the cluster (carbon atoms not illustrated) [31].

These three  $\text{Cu}_{2x}\text{Se}_x$  ( $x = 70, 73$ ) clusters can thus be described as consisting of  $2.6 \times 2.6 \times 0.9 \text{ nm}^3$  sections of a bulk lattice. Cementing this analogy is a recent report describing the recovery of the cluster  $[\text{Cu}_{70}\text{Se}_{35}(\text{PEt}_3)_{21}]$  **9** from the evaporation of cubic  $\text{Cu}_2\text{Se}$  and its co-condensation with  $\text{PEt}_3$  [37]. This report of

the isolation and structural characterization of nanometer-sized molecular species from the binary material, builds upon previous reports detailing the gas-phase structures of metal-chalcogenide clusters similarly prepared via laser ablation techniques [38]. The layered structure in **9** (Figure 13.7) can also be described as consisting of A–B–A ( $\text{Se}_{10}$ – $\text{Se}_{15}$ – $\text{Se}_{10}$ ) packed layers of selenium, with the copper centers distributed between them and the surface  $\text{PET}_3$  ligands stabilizing the  $\text{Cu}_{70}\text{Se}_{35}$  core. This same arrangement of  $[\text{Cu}_{70}\text{Se}_{35}(\text{PR}_3)_{21}]$  has been reported to form from solution techniques, from the reaction of  $\text{CuOAc}$  and  $\text{Se}(\text{SiMe}_3)_2$  with  $\text{P}^i\text{BuMe}_2$  [39]. Indeed, the dominance of this structural type is demonstrated with the structures of  $[\text{Cu}_{70}\text{Se}_{35}(\text{PR}_3)_x]$  ( $x = 21$ – $24$ ) [31, 40],  $[\text{Cu}_{72}\text{Se}_{36}(\text{PPh}_3)_{20}]$  [41] and  $[\text{Cu}_{73}\text{Se}_{35}(\text{SePh})_3(\text{P}^i\text{Pr}_3)_{21}]$  [36]. Thus the  $\text{Cu}_{70}\text{Se}_{35}$  frame is quite tolerant to variation of the number and types of phosphine ligands. Similarly, the incorporation of 1–3 additional Cu centers occurs with little overall structural change, these additions occurring at the corners of the  $1.6 \times 1.6 \times 0.9 \text{ nm}^3$   $\text{Cu}_{70}\text{Se}_{35}$  trigonal prismatic core. The molecule to solid transition for these megaclusters has also been demonstrated where thermolysis of  $[\text{Cu}_{70}\text{Se}_{35}(\text{PET}_2\text{Ph})_{24}]$  results in a cleavage of the phosphine ligand shell, and the formation of bulk  $\alpha$ - $\text{Cu}_2\text{Se}$ . Evidence has been provided for the intermediate formation of 10 nm particles en route to the solid via this method [42].

### 13.3.1.2 Spherical $\text{Cu}_2\text{E}$

Of particular note is that in the series of copper selenide nanoclusters, there appears to be a definite “transition point” where the  $\text{Cu}_{2x}\text{Se}_x$  clusters no longer exhibit the characteristic layered arrangement present in the clusters  $\text{Cu}_{70}\text{Se}_{35} \rightarrow \text{Cu}_{146}\text{Se}_{73}$ . For the copper selenide clusters synthesized to date, where the number of Cu atoms is less than 60, an arrangement of the  $\text{CuSe}$  core best described as being spherical in nature is typically observed, with experimental evidence for the preferential formation of certain  $\text{Cu}_{2x}\text{Se}_x$  structural motifs [31]. For example, the cluster  $[\text{Cu}_{44}\text{Se}_{22}(\text{PET}_2\text{Ph})_{18}]$  **10** (Figure 13.8) is known, where a non-bonded  $\text{Se}_{22}$  polyhedral arrangement is observed in which the 44 Cu(I) centers are interspersed [43]. The requirement of 18 surface phosphine ligands in **10** can be contrasted with the structure of  $[\text{Cu}_{44}\text{Se}_{22}(\text{P}^n\text{Bu}^i\text{Bu}_2)_{12}]$  in which a similar  $\text{Cu}_{44}\text{Se}_{22}$  core is observed, but with twelve larger surface  $\text{PR}_3$  ligands. A notable effect of the lower phosphine coverage however is the reduced number (12) of copper centers “pulled” out towards the cluster surface versus that in complex **10**, as is commonly observed with these phosphine ligated clusters. A partial listing of “spherical” copper selenide and copper selenide selenolate clusters isolated from  $\text{Se}(\text{SiMe}_3)_2/\text{RSeSiMe}_3$  reagents is given in Table 13.1 [31, 36, 39–41, 43–47].

The number of copper sulfide clusters reported from the reaction of  $\text{CuX}$  and  $\text{S}(\text{SiMe}_3)_2$  is smaller than for the heavier congener selenium, with  $[\text{Cu}_{12}\text{S}_6(\text{PR}_3)_8]$  [48, 49],  $[\text{Cu}_{20}\text{S}_{10}(\text{PRR}'_2)_8]$  ( $\text{R} = \text{R}' = \text{Ph}$ ;  $\text{R} = ^n\text{Bu}$ ,  $\text{R}' = ^i\text{Bu}$ ) [48, 49],  $[\text{Cu}_{24}\text{S}_{12} \cdot (\text{P}^i\text{Pr}_2\text{Me})_{12}]$ ,  $[\text{Cu}_{28}\text{S}_{14}(\text{P}^i\text{Bu}_2\text{Me})_{12}]$  **11** and  $[\text{Cu}_{50}\text{S}_{25}(\text{P}^i\text{Bu}_2\text{Me})_{16}]$  **12** [39] having been reported to date. None of these molecular species displays a clear structural relationship to the binary solid  $\text{Cu}_2\text{S}$ . This is perhaps due to the fact that the “transition point” for these clusters has yet to be reached (vide supra). Coordina-

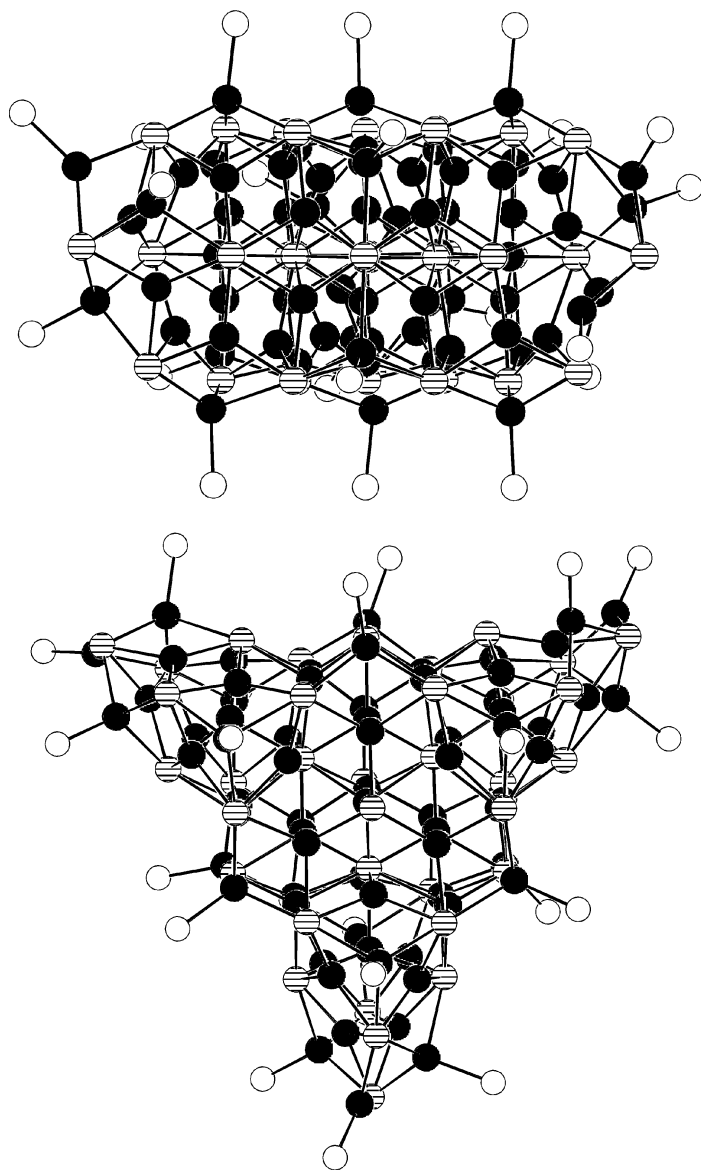


**Fig. 13.7.** Two projections of the cluster  $[\text{Cu}_{70}\text{Se}_{73}(\text{PR}_3)_{21}]$  **9** illustrating the layered nature of the selenium framework (top) and the overall triangular shape (bottom) of the cluster (carbon atoms not illustrated) [37, 39].

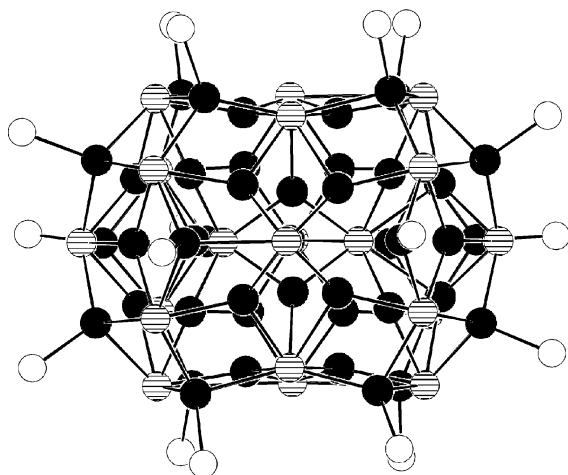


Fig. 13.8. The Cu, Se and P atoms of the cluster  $[\text{Cu}_{44}\text{Se}_{22}(\text{PEt}_2\text{Ph})_{18}]$  **10** [43].

tion environments of the copper centers in these  $\text{Cu}_2\text{S}$  clusters approximate either trigonal planar or linear geometry, while sulfur atoms almost always act as  $\mu_4$  bridges, although additional bridging modes of the sulfur ligands are observed in the larger derivatives **11** ( $\mu_3$ ,  $\mu_5$ ) and **12** ( $\mu_5$ ,  $\mu_6$ ). The higher coordination numbers in **12** are characteristic of  $\text{Cu}_2\text{S}$  phases [50], but its structure is not strongly related to that of the  $\text{Cu}_2\text{S}$  lattice. The structure of the highest nuclearity  $\text{Cu}_2\text{S}$  cluster **12** (Figure 13.9) can be viewed as a condensation of two spherical units, which themselves are clearly structurally related to cluster **11** (Figure 13.9). This description is further supported by contrasting the cylindrical  $0.7 \times 0.7 \times 1.7 \text{ nm}^3$  core in **12**, with the more symmetrical  $0.8 \times 1.2 \times 1.2 \text{ nm}^3$  core observed in the selenide cluster  $[\text{Cu}_{52}\text{Se}_{26}(\text{PPh}_3)_{16}]$  **13** (Figure 13.10) [41]. The absence of highly con-

Tab. 13.1. “Spherical” copper selenium nanoclusters synthesized using silylated chalcogen reagents.

Cluster	Reference	Cluster	Reference
$[\text{Cu}_{20}\text{Se}_{13}(\text{PEt}_3)_{12}]$	40	$[\text{Cu}_{36}\text{Se}_5(\text{SePh})_{26}(\text{dppa})_4]^b$	44
$[\text{Cu}_{25}\text{Se}_4(\text{SePh})_{18}(\text{dppp})_2]^a$	44	$[\text{Cu}_{38}\text{Se}_{13}(\text{SePh})_{12}(\text{dppb})_6]^c$	44
$[\text{Cu}_{26}\text{Se}_{13}(\text{PR}_2\text{R}')_{14-n}]$ ( $n = 0, 4$ )	45	$[\text{Cu}_{44}\text{Se}_{22}(\text{PR}_2\text{R}')_{18-n}]$ ( $n = 0, 6$ )	43
$[\text{Cu}_{29}\text{Se}_{15}(\text{P}^i\text{Pr}_3)_{12}]$	46	$[\text{Cu}_{48}\text{Se}_{24}(\text{Me}_2\text{Ph})_{20}]$	39
$[\text{Cu}_{30}\text{Se}_{15}(\text{PR}_2\text{R}')_{12}]$	46	$[\text{Cu}_{50}\text{Se}_{20}(\text{Se}^t\text{Bu})_{10}(\text{P}^i\text{Pr}_3)_{10}]$	36
$[\text{Cu}_{31}\text{Se}_{15}(\text{SeSiMe}_3)(\text{P}^t\text{Bu}_2\text{Me})_{12}]$	39	$[\text{Cu}_{52}\text{Se}_{26}(\text{PPh}_3)_{16}]$	41
$[\text{Cu}_{32}\text{Se}_{16}(\text{PPh}_3)_{12}]$	41	$[\text{Cu}_{58}\text{Se}_{16}(\text{SePh})_{24}(\text{dppa})_6]^b$	44
$[\text{Cu}_{32}\text{Se}_7(\text{Se}^n\text{Bu})_{18}(\text{P}^i\text{Pr}_3)_6]$	36	$[\text{Cu}_{59}\text{Se}_{30}(\text{PCy}_3)_{16}]$	45
$[\text{Cu}_{36}\text{Se}_{18}(\text{P}^t\text{Bu}_3)_{12}]$	46		

<sup>a</sup> dppp =  $\text{Ph}_2\text{P}(\text{CH}_2)_3\text{PPh}_2$ ; <sup>b</sup> dppa =  $\text{Ph}_2\text{PCCPPH}_2$ ;

<sup>c</sup> dppb =  $\text{Ph}_2\text{P}(\text{CH}_2)_4\text{PPh}_2$

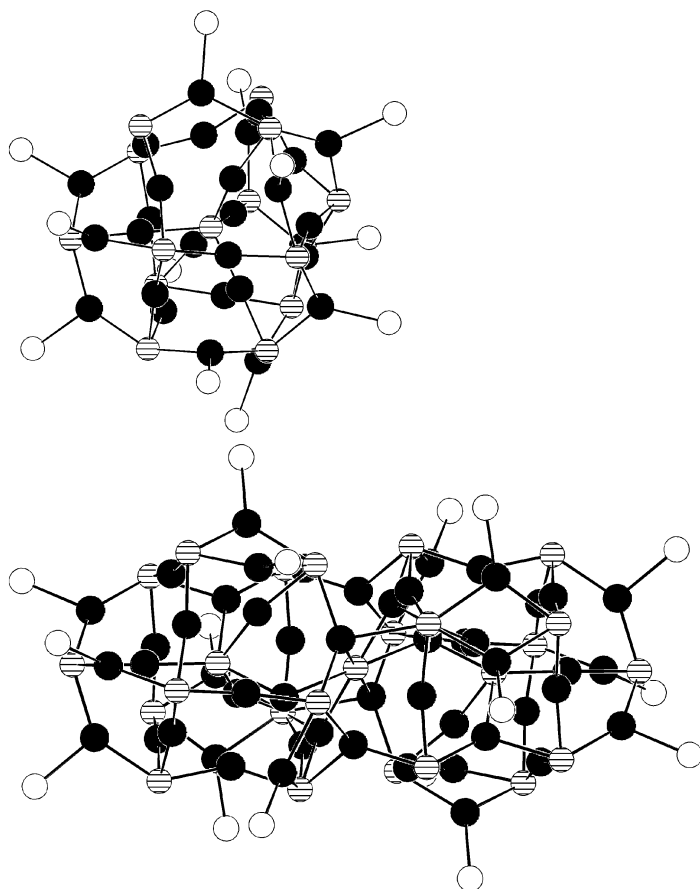


**Fig. 13.9.** An illustration of the copper–sulfur cores observed in  $[\text{Cu}_{28}\text{S}_{14}(\text{P}^t\text{Bu}_2\text{Me})]$  **11** (top) and  $[\text{Cu}_{50}\text{S}_{25}(\text{P}^t\text{Bu}_2\text{Me})_{16}]$  **12** (bottom) illustrating the structural relationships between the two clusters [39].

densed, high nuclearity  $\text{Cu}_2\text{S}$  complexes may stem from the inability of sulfide ligands to adopt the higher coordination modes observed with  $\text{Se}^{2-}$ . This has led to a much larger structural diversity with the latter, as well as the prevalence of the much larger clusters, as described above. Indeed, only with  $[\text{Cu}_{12}\text{E}_6(\text{PR}_2\text{R}')_8]$  ( $\text{E} = \text{S}, \text{Se}$ ) does one observe topologically similar complexes between the two series [31].

The factors controlling the selectivity of cluster formation using  $\text{E}(\text{SiMe}_3)_2$  ( $\text{E} = \text{S}, \text{Se}, \text{Te}$ ) at low temperatures are numerous, and small changes in reaction conditions can have a pronounced effect on product distribution. The products obtained are highly variable and are dependent upon the reaction conditions used. Extensive studies of the synthesis of XI–XVI clusters demonstrate that careful

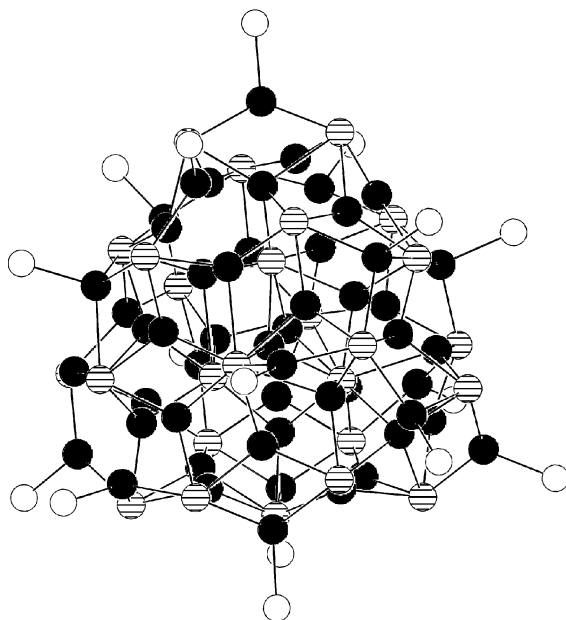


Fig. 13.10. A projection of the copper–selenium core in the cluster  $[\text{Cu}_{52}\text{Se}_{26}(\text{PPh}_3)_{16}]$  **13** [41].

control of the  $\text{M}/\text{E}/\text{PR}_3$  ratio, the nature of the phosphine, and the solvent system can have an incredible effect on the products formed. Thus a comprehensive description of the numerous “CuE nanoclusters” accessed with this methodology is not possible here, however the reader is directed towards a comprehensive and timely review on the subject [31]. Despite the differences observed in both the structures and nuclearities, clusters synthesized via the reaction of Cu(I) salts with  $\text{E}(\text{SiMe}_3)_2$  ( $\text{E} = \text{S}, \text{Se}$ ) have Cu:E ratios that permit a +1 oxidation state to be assigned to the metal centers. This is strictly observed in the  $\text{Cu}_2\text{S}$  clusters and normally holds true for Cu–Se, a consequence of the (relatively) large discrepancies in ionization potentials, electron affinities, and electronegativities of the relevant ions. In the clusters  $[\text{Cu}_{59}\text{Se}_{30}(\text{PCy}_3)_{15}]$  [46] and  $[\text{Cu}_{58}\text{Se}_{16}(\text{SePh})_{24}(\text{dppa})_6]$  ( $\text{dppa} = 1,2$ -bis(diphenyl)phosphinoacetylene) [45] mixed valence copper states of Cu(I)/Cu(II) and Cu(I)/Cu(0), respectively, have however been proposed.

### 13.3.2

#### **$\text{Cu}_{2-x}\text{Te}$ and $\text{Ag}_2\text{Te}$**

Smaller differences in ionization potentials, electron affinities and electronegativities between Cu(I) and  $\text{Te}^{2-}$  (versus S, Se) often results, in addition to stoichiometric CuTe complexes, in the formation of non-stoichiometric “electron-rich” ( $\text{Cu}_{2+x}\text{Te}$ ) and “electron-deficient” ( $\text{Cu}_{2-x}\text{Te}$ ) nanocluster complexes (Table 13.2) [51–56]. If a formal charge of 2– is assigned to the telluride ligands in the latter



**Tab. 13.2.** High nuclearity copper tellurium clusters synthesized using silylated chalcogen reagents.

Cluster	Reference	Cluster	Reference
$[\text{Cu}_{23}\text{Te}_{13}(\text{PR}_3)_{12-n}]$ ( $n = 0, 2$ )	51–5	$[\text{Cu}_{29}\text{Te}_{16}(\text{P}^i\text{Pr}_3)_{12}]$	51
$[\text{Cu}_{24}\text{Te}_{12}(\text{P}^i\text{Pr}_3)_{12}]$	53	$[\text{Cu}_{29}\text{Te}_9(\text{TePh})_{12}(\text{PEt}_3)_8]^-$	55
$[\text{Cu}_{26}\text{Te}_{12}(\text{PEt}_2\text{Ph})_{12}]$	53	$[\text{Cu}_{39}\text{Te}_{16}(\text{TePh})_{11}(\text{PEt}_3)_{13}]$	55
$[\text{Cu}_{26}\text{Te}_{10}(\text{Te}_2)_3(\text{P}^i\text{Bu}_3)_{10}]$	51	$[\text{Cu}_{44}\text{Te}_{23}(\text{PR}_2\text{R}')_{15}]$	53
$[\text{Cu}_{27}\text{Te}_{15}(\text{P}^i\text{Pr}_2\text{Me})_{12}]$	54	$[\text{Cu}_{50}\text{Te}_{17}(\text{TePh})_{20}(\text{PPh}_2\text{Et})_8]^{4-}$	56
$[\text{Cu}_{28}\text{Te}_{13}(\text{Te}_2)_2(\text{PEt}_2\text{Ph})_{10}]$	51	$[\text{Cu}_{58}\text{Te}_{32}(\text{PR}_2\text{R}')_{16-n}]$ ( $n = 0, 2$ )	52, 54

systems, oxidation states of (+1 and +2) and (+1 and 0) respectively must be designated to the copper atoms. Theoretical analyses have shown that in the latter case, as is observed in the cluster  $[\text{Cu}_{26}\text{Te}_{12}(\text{PEt}_2\text{Ph})_{12}]$ , localization of charge creating Cu(0) centers is not possible and the “extra” electrons occupy a valence band comprised of Te(5p) and Cu(4s) orbitals [57]. Close structural similarities between molecular species and bulk materials, such as those observed in the  $\text{Cu}_2\text{Se}$  system, are not found. As previously discussed, strong correlations to the bulk structure for molecular  $[\text{Cu}_2\text{Se}]_n$  clusters do not occur until the number of copper atoms is greater than 59. As the largest copper telluride clusters characterized to date  $[\text{Cu}_{58}\text{Te}_{32}(\text{PR}_2\text{R}')_{16-n}]$  ( $n = 0, 2$ ) [52, 54] do reveal a layered type structure for the 32 Te atoms (14, Figure 13.11), the isolation of larger complexes may yet reveal more pronounced relationships. Interestingly, the telluride cluster 14 is generated using  $\text{BuTeSiMe}_3$  as the source of tellurium, with concomitant Te–C bond cleavage. Typically the copper telluride nanoclusters formed from reactions of phosphine solubilized Cu(I) salts with  $\text{Te}(\text{SiMe}_3)_2$  consist of spherical CuTe cores and the distribution of tellurium centers can be described in terms of deltahedral frameworks, many of which are related to Frank–Kasper polyhedra, as observed in the cluster  $[\text{Cu}_{29}\text{Te}_{16}(\text{P}^i\text{Pr}_3)_{12}]$  (15, Figure 13.11) [55]. Such non-stoichiometric CuTe clusters often display broad intervalence absorption bands in the near IR [53]. The coordination numbers of  $\text{Te}^{2-}$  ligands vary from 4 to 12, with Cu atoms adopting three-coordinate ( $\text{PCuTe}_2$  or  $\text{CuTe}_3$ ) or four-coordinate ( $\text{PCuTe}_3$  or  $\text{CuTe}_4$ ) geometries. A number of clusters containing ditelluride ( $\text{Te}_2^{2-}$ ) ligands have also been isolated from these reactions (Table 13.2).

The limited number of CuTe clusters isolated using the reagent  $\text{Te}(\text{SiMe}_3)_2$  may be due, in part, to the high reactivity and instability of the tellurium source relative to  $\text{Se}(\text{SiMe}_3)_2$ . This may also account for the small size of these clusters, again compared to the selenium and sulfur systems. Conversely, the ability to generate  $\text{Te}^{2-}$  from  $\text{RTe}^-$  reagents may represent a more facile route into higher nuclearity clusters of copper telluride [55]. It has been shown that “low-nuclearity” copper tellurolate complexes can be used in the formation of larger telluride-containing clusters via the elimination of  $\text{TePh}_2$ . The mixed telluride–tellurolate cluster  $[\text{Cu}_{50}(\text{TePh})_{20}\text{Te}_{17}(\text{PPh}_2\text{Et})_8]^{4-}$  is formed from solutions of  $[\text{Cu}_6(\text{TePh})_6(\text{PPh}_2\text{Et})_5]$ , with NMR evidence suggesting the presence of additional intermediate species

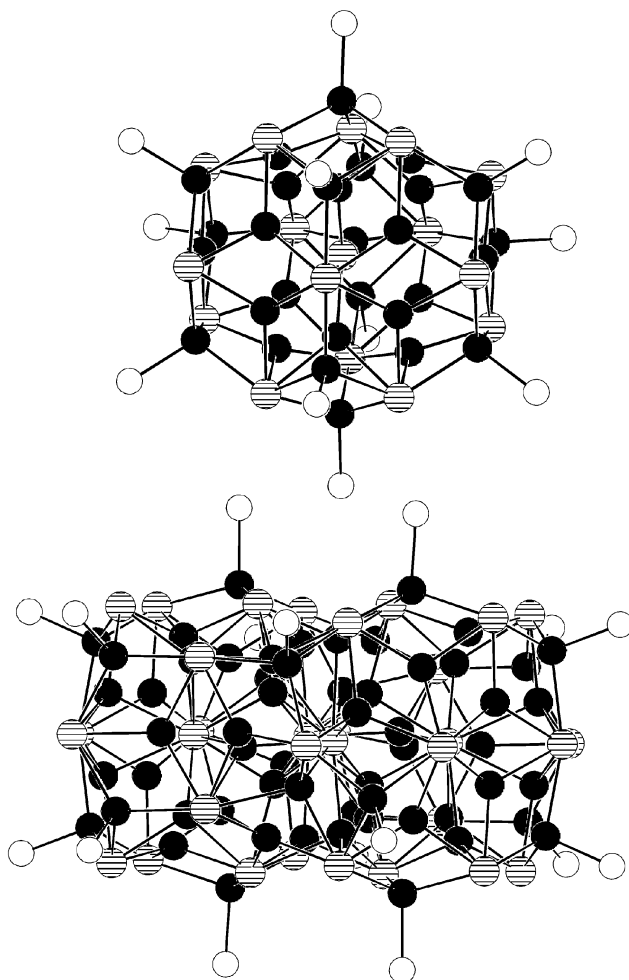


**Fig. 13.11.** Illustrations of the copper, tellurium and phosphorus atoms in the clusters  $[\text{Cu}_{29}\text{Te}_{16}(\text{P}^i\text{Pr}_3)_{12}]$  **15** (top) and  $[\text{Cu}_{58}\text{Te}_{32}(\text{PPh}_3)_{16}]$  **14** (bottom) [52, 55].

[56]. This reaction is driven via the photochemically induced elimination of  $\text{TePh}_2$  from the copper centers, accounting for the presence of the interstitial telluride ligands. The structure of the  $\text{Cu}_{50}$  complex is markedly different from those of  $[\text{Cu}_{58}\text{Te}_{32}(\text{PR}_2\text{R}')_{16-n}]$  **14** synthesized using  $n\text{-BuTeSiMe}_3$  or  $i\text{-BuTeSiMe}_3$ , demonstrating the dependence of cluster geometry on the organo-substituent of the tellurium reagent  $\text{RTeSiMe}_3$ .

Unlike the copper telluride clusters, it has not yet proven possible to generate large silver telluride cluster complexes using a combination of  $\text{R}_3\text{P}$ ,  $\text{Ag-X}$  and  $\text{Te}(\text{SiMe}_3)_2$ . This suggests that the phosphine ligands are unable to kinetically

stabilize such particles and explains the observation that only amorphous binary materials are produced in these reactions [58, 59]. What has proven to be remarkably effective, however, is the combination of both  $\text{PR}_3$  ligands in conjunction with surface tellurolate groups,  $\text{RTe}^-$ . Thus the 4:8:1:2 combination of  $\text{AgCl}$ ,  $\text{PET}_3$ ,  $\text{Te}(\text{SiMe}_3)_2$  and  $\text{PhTeSiMe}_3$  results in the formation of the cluster  $[\text{Ag}_{30}\text{Te}_9 \cdot (\text{TePh})_{12}(\text{PET}_3)_{12}]$  (**16**, Figure 13.12) [58]. Interestingly, the structurally related copper tellurolate complex  $[\text{Cu}_{29}\text{Te}_9(\text{TePh})_{12}(\text{PET}_3)_8]^-$  has been reported, formed from the photochemically induced condensation reaction of two smaller clusters [55]. This  $\text{Cu}_{29}$  cluster and complex **16** represent the only examples with such a demonstrated structural relationship in the  $\text{CuTe}$  and  $\text{AgTe}$  series.

In **16**, the presence of phenyl groups on the twelve tellurium centers of the cluster framework assists in stabilizing the  $\text{AgTe}$  core against further (random) condensation reactions. These  $\text{PhTe}^-$  groups adopt  $\mu_3$ - and  $\mu_4$ -coordination. The order of addition of the silylated reagents does not affect the yield of product produced. As is the case with phosphine ligands in the  $\text{Cu}_2\text{E}$  clusters, modification of the steric and/or electronic properties of the tellurolate groups can also have a marked impact on the structure of the  $\text{AgTe}$  cluster cores. Thus an analogous reaction for the synthesis of **16** substituting  $\text{PhTeSiMe}_3$  with  $(\text{mes})\text{TeSiMe}_3$  ( $\text{mes} = 2,4,6\text{-Me}_3\text{C}_6\text{H}_2$ ) leads to the high yield formation of  $[\text{Ag}_{46}\text{Te}_{17}\{\text{Te}(\text{mes})\}_{12}(\text{PET}_3)_{16}]$  (**17**, Figure 13.12), a cluster with a  $1.6 \times 0.9 \times 0.8 \text{ nm}^3$   $\text{AgTe}$  core [58]. The larger number of interstitial  $\text{Te}^{2-}$  ligands in **17** versus **16** results in the formation of the higher nuclearity complex, although there are structural similarities between the two with respect to the arrangement of  $\text{Ag}$  and  $\text{Te}$  atoms at the cluster surfaces. A +1 oxidation state can be assigned to the silver centers in **16** and **17**, as it can in all silver chalcogenide polynuclear complexes accessed to date.

Other nanometer-sized  $\text{AgTe}$  clusters reported using  $\text{RTe}^-$  ligands in combination with  $\text{PET}_3$  include  $[\text{Ag}_{32}\text{Te}_7(\text{Te}^t\text{Bu})_{18}(\text{PET}_3)_6]$  and  $[\text{Ag}_{48}\text{Te}_{12}(\text{Te}^t\text{Bu})_{24}(\text{PET}_3)_{14}]$  [60]. The latter represents the largest crystallographically characterized silver-tellurium cluster reported to date, however, the oblong  $\text{AgTe}$  core is best described as consisting of two  $\text{Ag}_{24}\text{Te}_{16}$  subunits linked with four  $\mu_3\text{-Te}^t\text{Bu}$  ligands. A related “ $\text{Ag}_{24}\text{Te}_{16}$ ” cluster has yet to be reported. The combination of a bidentate phosphine,  $\text{AgOAc}$  and  $^t\text{BuTeSiMe}_3$  leads to the formation of  $[\text{Ag}_{38}\text{Te}_{13}(\text{Te}^t\text{Bu})_{12}(\text{Ph}_2\text{P} \cdot (\text{CH}_2)_2\text{PPh}_2)_3]$  [61].

### 13.3.3

#### **Ag<sub>2</sub>S**

The rich chemistry of silver thiolate clusters [62] has most recently been complemented via the successful incorporation of sulfide ligands into a preformed  $\text{Ag}_x(\text{SR})_x$  to yield a nanometer-sized cluster complex [63]. As outlined in the previous sections, the formation of nanometer-sized semiconductor metal-chalcogen complexes can only be achieved with the delivery of chalcogenide ions ( $\text{E}^{2-}$ ) during cluster formation. This is of course related to the steric requirements of the chalcogenolate ( $\text{RE}^-$ ) moieties which are thus restricted to the surfaces of the polynuclear frameworks. The nanocluster  $[\text{Ag}_{50}\text{S}_7(\text{SC}_6\text{H}_4^t\text{Bu-4})_{40}]^{4-}$  (**18**, Figure

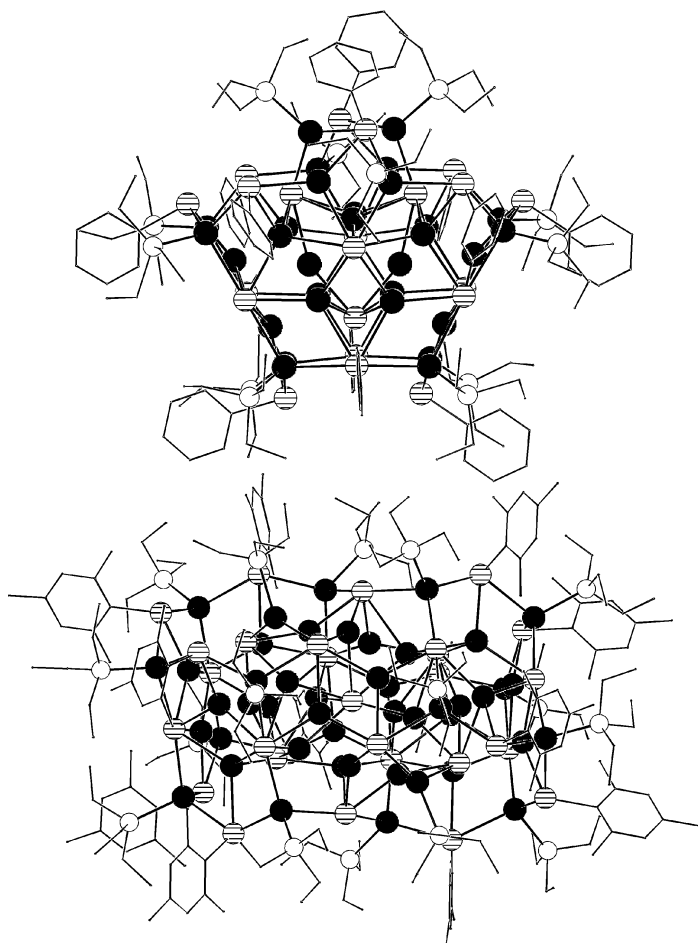


**Fig. 13.12.** The molecular structures  $[\text{Ag}_{30}\text{Te}_9(\text{TePh})_{12}(\text{PEt}_3)_{12}]$  **16** (top) and  $[\text{Ag}_{46}\text{Te}_{17}\{\text{Te}(\text{mes})\}_{12}(\text{PEt}_3)_{16}]$  **17** [58].

13.13) is isolated in 50% yield from the addition of  $\text{CS}_2$  to solutions of an as-yet unidentified silver 4-tertbutylthiolate polynuclear complex. The core of the disc-shaped cluster **18** is asymmetric, with a diameter of 2.0 nm and a maximum thickness  $\sim 0.7$  nm. The oblate nature of the AgS frame may be correlated with the relatively large number of surface thiolate ligands present on such a high nuclearity cluster complex, with a correspondingly low number (seven) of interstitial  $\text{S}^{2-}$  centers. The thiolate ligands bridge 2, 3 and 4 Ag(I) ions.

The possibility of synthesizing silver sulfide nanoclusters, as demonstrated with the formation of **18**, was followed immediately by the report of the isolation and characterization of the mixed silver sulfide–thiolate complex  $[\text{Ag}_{70}\text{S}_{16}(\text{SPh})_{34} \cdot (\text{PhCO}_2)_4(\text{triphos})_4]$  (triphos = 1,1,1-tris[(disphenylphosphino)methyl]ethane) [64]. This cluster is accessed using a combination of  $\text{PhSSiMe}_3$ ,  $\text{S}(\text{SiMe}_3)_2$  and

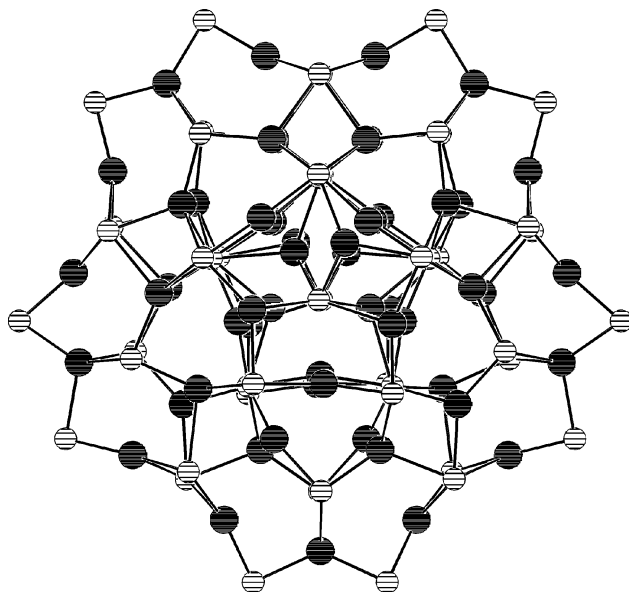
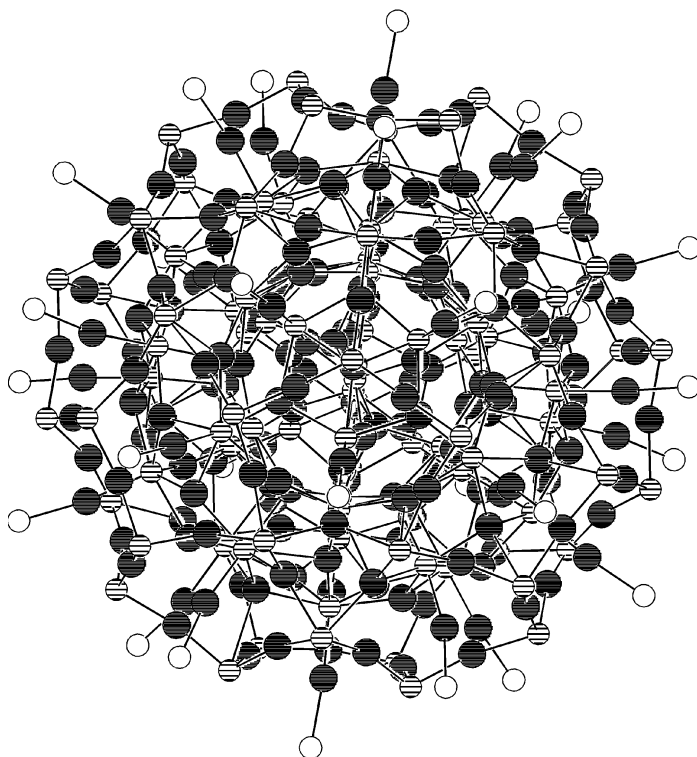


Fig. 13.13. A projection of the silver–sulfur core in the nanocluster  $[\text{Ag}_{50}\text{S}_7(\text{SC}_6\text{H}_4^t\text{Bu-4})_{40}]^{4-}$  **18** [63].

$\text{AgO}_2\text{CPh}$  in the presence of the triphos ligand. The sixteen interstitial sulfide ligands result in a more spherical and condensed silver–sulfur core versus **18**. Whereas in **18** the surface of the cluster contains only thiolate ligands, coverage of the surface of the  $\text{Ag}_{70}$  cluster is achieved with  $\text{PhS}^-$ ,  $\text{PhCO}_2^-$  and phosphine ligands.

Perhaps surprisingly, the synthesis of the nanocluster complex,  $[\text{Ag}_{188}\text{S}_{94}(\text{PR}_3)_{30}]$  (**19**, Figure 13.14,  $\text{R} = \text{Bu}$ ,  $\text{Pr}$ ), arises from the straightforward reaction of  $\text{PR}_3$ -solubilized  $\text{AgO}_2\text{CCF}_3$  with  $\text{S}(\text{SiMe}_3)_2$  [64]. Cluster **19** represents the highest nuclearity semiconductor cluster that has been structurally characterized, and its size can be compared with that of the oxometallate of molybdenum,  $\text{Na}_{48} \cdot [\text{H}_x\text{Mo}_{368}\text{O}_{1032}(\text{H}_2\text{O})_{240}(\text{SO}_4)_{48}]$  [65]. The synthesis and structure of **19** contrast with all other silver–chalcogen nanoclusters in that these invariably require the use of chalcogenolate sources in order to ensure kinetic stabilization of the silver–chalcogenide molecular core (see Sections 13.3.2 and 13.3.4).

The distribution of sulfide ligands in **19** results in a shell-like make up, with a central  $\text{S}_{10}$  non-bonded polyhedron surrounded by  $\text{S}_{34}$  and  $\text{S}_{50}$  polyhedra. The  $\text{Ag}(\text{I})$  centers bonded to the edges of the outer  $\text{S}_{50}$  polyhedron exhibit normal  $\text{Ag-S}$  bonding distances (2.36–2.44 Å), whereas markedly long  $\text{Ag-S}$  contacts are observed for the silver ions at the cluster core (3.33–3.88 Å). The latter have been ascribed to the ionic nature of the  $\text{Ag-S}$  bonds, and compared to the bonding in the ionic conductor  $\text{Ag}_2\text{S}$  [66]. Further advancing this reasoning is the observed occupational site disorder of the  $\text{Ag}^+$  ions in the core center, whereas no disorder



**Fig. 13.14.** An illustration of the spherical silver–sulfur core in the cluster  $[\text{Ag}_{188}\text{S}_{94}(\text{P}^n\text{Pr}_3)_{30}]$  **19** [64].

is present at the cluster periphery. Despite these relationships to the bulk solid, however, the overall arrangement of Ag and S in this  $1.8 \times 1.8 \times 2.0 \text{ nm}^3$  cluster **19** cannot be interpreted as a fragment of the solid  $\text{Ag}_2\text{S}$ . This is unusual in that there are demonstrated structural similarities in the larger copper selenide clusters discussed in Section 13.3.1.1 and in silver selenide systems (see below). To date, no intermediate-sized  $[(\text{Ag}_2\text{S})_x(\text{PR}_3)_y]$  clusters have been reported using the synthetic strategy that leads to **19**.

#### 13.3.4

##### **$\text{Ag}_2\text{Se}$**

The reaction chemistry of Ag(I) salts and  $\text{BuSeSiMe}_3$  complexes in the presence of tertiary phosphine ligands leads to the nanoclusters  $[\text{Ag}_{28}\text{Se}_6(\text{Se}^n\text{Bu})_{16}(\text{Ph}_2\text{P}(\text{CH}_2)_3\text{PPh}_2)_4]$ ,  $[\text{Ag}_{30}\text{Se}_8(\text{Se}^t\text{Bu})_{14}(\text{P}^n\text{Pr}_3)_8]$ ,  $[\text{Ag}_{90}\text{Se}_{38}(\text{Se}^t\text{Bu})_{14}(\text{PEt}_3)_{22}]$ ,  $[\text{Ag}_{112}\text{Se}_{32}(\text{Se}^n\text{Bu})_{48}(\text{P}^t\text{Bu}_3)_{12}]$ ,  $[\text{Ag}_{114}\text{Se}_{34}(\text{Se}^n\text{Bu})_{46}(\text{P}^t\text{Bu}_3)_{14}]$ ,  $[\text{Ag}_{124}\text{Se}_{57}(\text{SeP}^t\text{Bu}_2)_4\text{Cl}_6 \cdot ({}^t\text{Bu}_2\text{P}(\text{CH}_2)_3\text{P}^t\text{Bu}_2)_{12}]$  and  $[\text{Ag}_{172}\text{Se}_{40}(\text{Se}^n\text{Bu})_{92}(\text{Ph}_2\text{P}(\text{CH}_2)_3\text{PPh}_2)_4]$  [67, 68]. The interstitial  $\text{Se}^{2-}$  ligands in these clusters arise from the facile Se–C bond scission

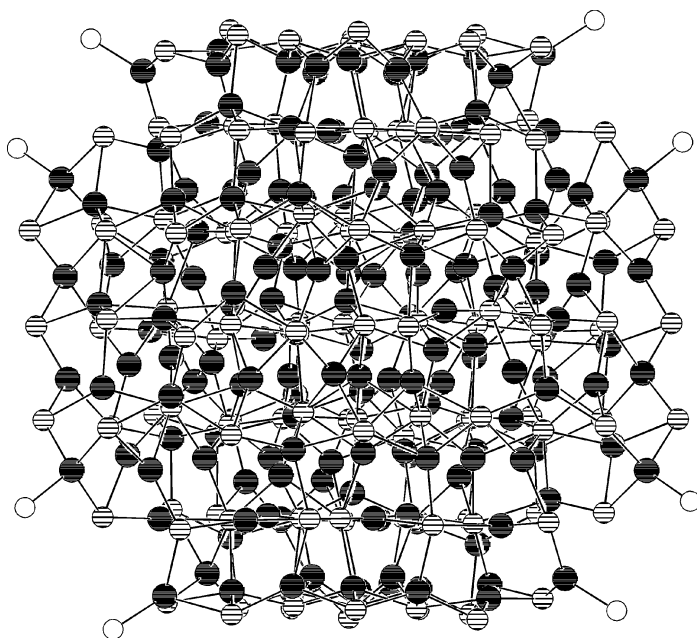
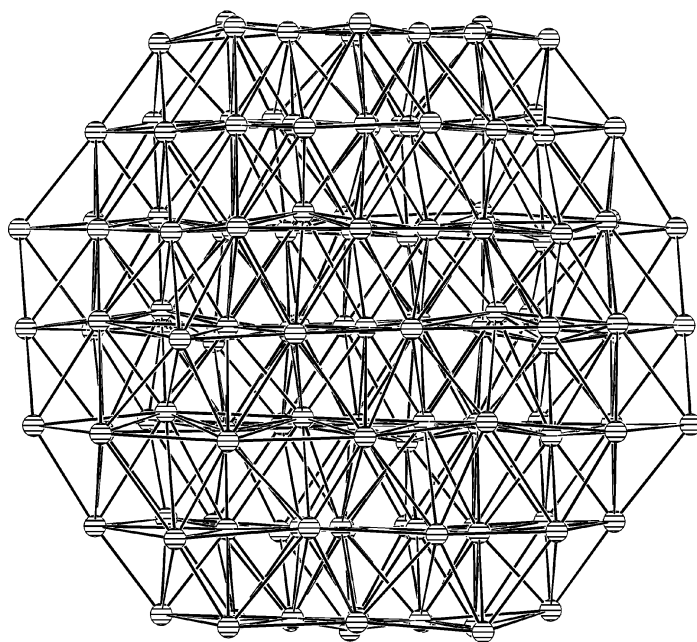


Fig. 13.15. An illustration of the Ag, Se and P positions in the cluster  $[\text{Ag}_{172}\text{Se}_{40}(\text{Se}^n\text{Bu})_{92}(\text{Ph}_2\text{P}(\text{CH}_2)_3\text{PPh}_2)_4]$  **20** [67].

reactions of the BuSe fragments, and this allows for the formation of extremely large Ag–Se frameworks. Although this reactivity limits the number of “low nuclearity” complexes that can be isolated, and thus the amount of information that can be obtained with respect to condensation pathways, it results in a facile route to high nuclearity silver selenide clusters. Also of note is the requirement of acetate salts of silver for the successful isolation of these polynuclear complexes.

The  $2.4 \times 2.4 \times 2.0 \text{ nm}^3$  AgSe cluster core in  $[\text{Ag}_{172}\text{Se}_{40}(\text{Se}^n\text{Bu})_{92}(\text{dppp})_4]$  (dppp = 1,2-bis(diphenylphosphinopropane) **20** (Figure 13.15) represents the largest structurally characterized metal-selenide complex reported to date [67]. As was observed in **19** the distribution of the silver centers in **20** is highly disordered, and as such, the refinement of the X-ray data for **20** was reported to be problematic. In this respect **20** mirrors the structure of solid  $\text{Ag}_2\text{Se}$  where the  $\text{Ag}^+$  cations are also disordered over several sites [66]. The trigonal and tetrahedral coordination geometries favored by the Ag(I) ions in these clusters are also consistent with those observed in the bulk semiconductor. The 40  $\text{Se}^{2-}$  ligands act as  $\mu_5$ ,  $\mu_6$ ,  $\mu_7$  and  $\mu_8$  bridges (Ag–Se = 2.44–3.30 Å) and are arranged with the Se centers of the “BuSe<sup>–</sup> groups to form layered arrangements of selenium corresponding to a distorted cubic-centered structure that is also found in  $\text{Ag}_2\text{Se}$  (Figure 13.16). There are only eight phosphine–silver bonds (four bidentate DPPP ligands) on the surface of cluster **20**, as the 92 butyl chains of the selenolate ligands provide the majority of the stabilization of the silver selenide core.





**Fig. 13.16.** A projection of the (non-bonded) layered  $\text{Se}_{132}$  framework in  $[\text{Ag}_{172}\text{Se}_{40}(\text{Se}^n\text{Bu})_{92}(\text{Ph}_2\text{P}(\text{CH}_2)_3\text{PPh}_2)_4]$  **20** [67].

The “transition point” observed for the Ag–Se nanoclusters, with respect to whether or not a structural relationship to the binary solid is evident, appears to occur for structures with greater than 90 Ag centers. Thus the cluster  $[\text{Ag}_{112}\text{Se}_{32}(\text{Se}^n\text{Bu})_{48}(\text{P}^t\text{Bu}_3)_{12}]$  also displays a layered arrangement of the Se framework, whereas the structure of  $[\text{Ag}_{90}\text{Se}_{38}(\text{Se}^t\text{Bu})_{14}(\text{PEt}_3)_{22}]$  **21** (Figure 13.17) is best described as having a shell-like construction of three Se layers, and an overall torus-shaped cluster core [67]. One should not, however, ignore the influence of the substituents on the surface selenolate ligands and their role in mediating core geometries. The utility of E–SiMe<sub>3</sub> reagents in ensuring the homogeneous conditions necessary for their crystallization, in addition to the relatively ionic bonding (and thus flexible coordination geometries) in the XI–XVI clusters, are both essential in enabling the formation of these unparalleled nanocluster complexes.

### 13.4

#### Group XII-chalogenides and the Quantum Confinement Effect

##### 13.4.1

##### CdS

As described in the previous sections, the vibrant interest in the development of the XI–XVI clusters and nanoclusters may be attributed to the dimensions of the

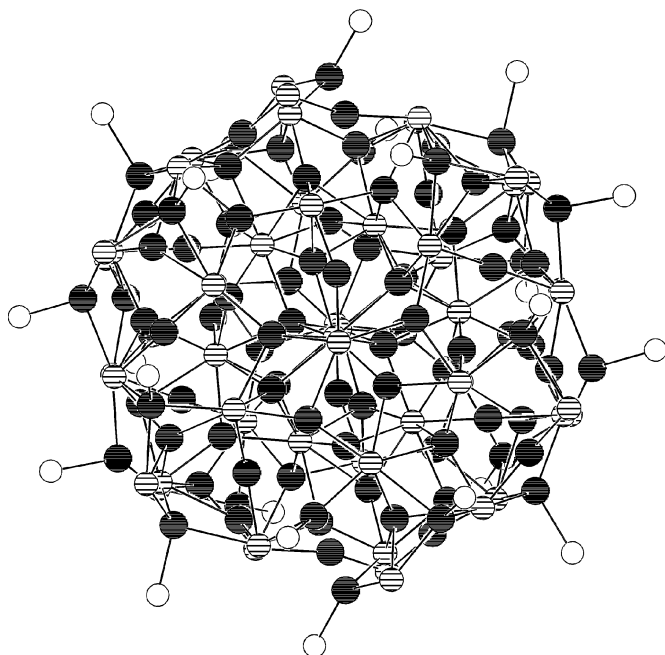


**Fig. 13.17.** An illustration of the silver–selenium core in the nanocluster  $[\text{Ag}_{90}\text{Se}_{38}(\text{Se}^t\text{Bu})_{14}(\text{PEt}_3)_{22}]$  **21** [67].

cluster cores and the often clear transition between those that mimic the structural features observed for the related binary semiconductor and those that do not. For the XII–XVI clusters no such “transition point” need be observed as even the smallest of clusters display a clear structural relationship to the solid materials [10]. The structures observed in the majority of these molecules are best described as being built up from adamantoid and barrelanoid frameworks, the same fundamental units that are observed in the XII–XVI solids. Several larger clusters of the Group XII–XVI elements have been prepared and these structures are based on the fusion of these cages via edge-sharing interactions. This has allowed for a systematic investigation of size–property relationships in these cluster systems.

This fusion principle is illustrated with the isolation of  $[\text{M}_{10}\text{E}_4(\text{SPh})_{16}]^{4-}$  ( $\text{M} = \text{Zn}, \text{Cd}$ ;  $\text{E} = \text{S}, \text{Se}$ ) (**22**, Figure 13.18), formed from the reactions of adamantoid  $[\text{M}_4(\text{SPh})_{10}]^{2-}$  with elemental sulfur or selenium [69]. The neutral analogue  $[\text{Zn}_{10}\text{S}_4(\text{SEt})_{12}(\text{lut})_4]$  ( $\text{lut} = 3,5\text{-lutidine}$ ) has also been reported, where the tetrahedral geometry of the four vertex Zn centers is completed via coordination to the four lutidine molecules [70]. The structurally related, larger cluster  $[\text{Cd}_{17}\text{S}_4(\text{SPh})_{28}]^{2-}$  (**23**, Figure 13.19) was subsequently reported, formed from the reaction of  $\text{Na}_2\text{S}$ ,  $\text{PhS}^-$  and  $\text{Cd}(\text{NO}_3)_2$  [71]. The structure of the nanometer-sized cluster **23** can be described as being built up from four central adamantoid cages (sharing edges and one vertex), capped by four barrelanoid cages. The former are

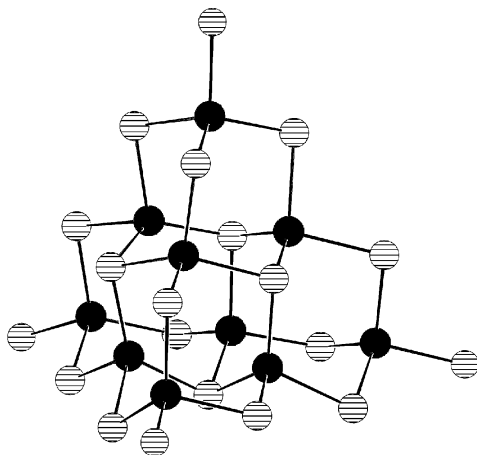


**Fig. 13.18.** An illustration of the adamantoid framework observed in the clusters  $[M_{10}S_4(\mu-E'Ph)_{16}]^{4-}$  **22** ( $M = Zn, Cd, Hg; E = S, Se$ ) [69]. This framework is common to the XII–XVI

clusters  $[M_{10}E_4(\mu-E'R)_{12+n}L_{4-n}]^{n-}$  ( $M = Zn, Cd, Hg; E = E' = S, Se, Te; L = \text{halide, ER, PR}_3, \text{amine; R = alkyl, aryl}$ ) [69, 70, 81, 84, 87, 88].

similar to the structural repeat in the cubic (sphalerite) lattice and the latter the hexagonal (wurtzite) lattice of the XII–XVI metal-chalcogenides. The  $Cd_{17}S$  core observed in **23** has more recently been documented in the “double diamond superlattice” built up of neutral  $[Cd_{17}S_4(SCH_2CH_2OH)_{26}]$  clusters. In the solid state,

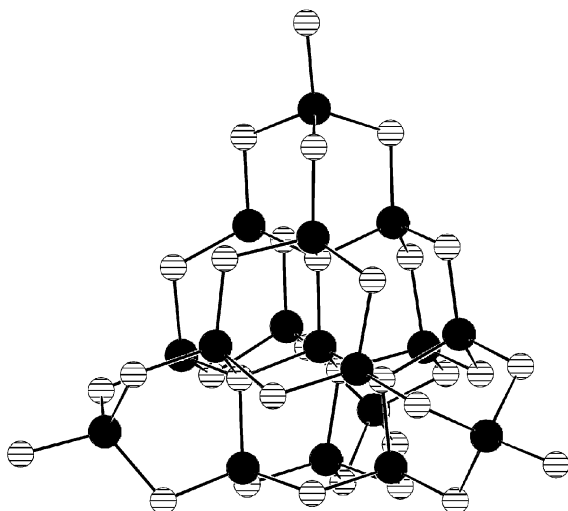


**Fig. 13.19.** A projection of the fused adamantoid/barrelanoid arrangement of Cd and S atoms in the cluster  $[Cd_{17}S_4(\mu-SPh)_{24}(SPh)_4]^{2-}$  **23** [71].

each cluster is bound covalently to its neighbours via sharing of a thiolate ligand at the corners of the tetrahedra, resulting in an extended network [72]. The inter-cluster thiolate bridges are displaced with strong donor solvents, allowing a comparison of the spectral features of molecular “ $\text{Cd}_{17}\text{S}_4(\text{SCH}_2\text{CH}_2\text{OH})_{26}$ ” and the solid network. Although very similar, the UV spectrum of the solid is slightly red-shifted relative to that observed for the individual molecules in solution. Dipole–dipole and electronic interactions between the linked cluster units have been proposed to account for the observed difference [73].

Both solid-state and solution absorption spectra of  $[\text{Cd}_{17}\text{S}_4(\text{SCH}_2\text{CH}_2\text{OH})_{26}]$  display a sharp, discrete maximum ( $\sim 4.3$  eV) that is markedly blue-shifted from the absorption onset of bulk CdS (2.4 eV); this is assigned to the excitonic transition. This transition is observed in the absorption spectra of XII–XVI colloids and clusters as a sharp absorption near the absorption edge, the energy of which is a measure of the size of the “band gap” of the nanoparticles [74]. To this end, UV–visible spectroscopy can be used to demonstrate the effects of quantum confinement in XII–XVI particles of various sizes, highlighted by the systematic shift of the excitonic transition to higher energy with decreasing particle size [75]. As the size of a semiconductor crystal decreases into the nanometer-size regime, a unique situation develops in which the particle size becomes on the order of, or even smaller than, the Bohr radius of the exciton (electron–hole pair). In this circumstance, the exciton must adopt a state of higher kinetic energy to “fit” into such a particle [76]. The result is an increase in the size of the “band gap” (relative to the bulk) and the quantization of energy levels within the bands with decreasing size. Thus the electronic properties of nanometer-sized cluster molecules lie between those of small, molecular species and those of the related XII–XVI solid.

The correlation between the energy of the band gap and the size of the nanoparticle can be described using one of two theoretical models [74, 75, 77]. The first model is a modification of the effective mass approximation, in which the Coulombic interaction between the electron and hole are taken into consideration. In this approach, the valence and conduction bands are assumed to be parabolic near the band gap, yielding Eq. (5) for the difference in energy of the first excited state, relative to the bulk [74]:

$$\Delta E = \hbar^2 \pi^2 / 2R^2 [m_e^{-1} + m_h^{-1}] - 1.786e^2 / \epsilon R \quad (5)$$

The first term is the particle-in-a-box localization energy, which depends quadratically on  $(\hbar^2 \pi^2)$  with a  $1/R^2$  dependence, where  $R$  is the radius of the nanoparticle. The values  $m_e$  and  $m_h$  are the effective masses of the electron and hole respectively. The second term describes the Coulombic interaction of the electron and the hole, where  $e$  is the universal charge and  $\epsilon$  is the dielectric constant of the material in question. Good correlation between theory and experiment has been obtained within this model for larger nanoclusters [78]. In the case of smaller particles, especially those smaller than  $\sim 2$  nm, the lowest excited states are located in a region of the energy band that is no longer parabolic and, as a result, the effective mass approximation breaks down. For these particles a more molecular approach re-

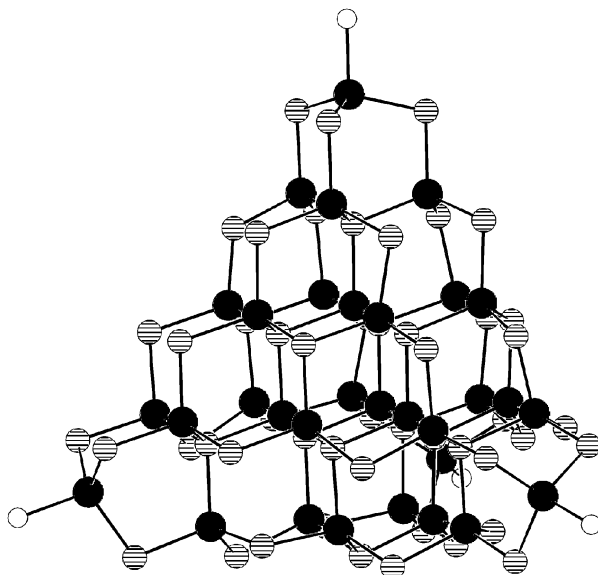


**Fig. 13.20.** An illustration of the core atoms in the clusters  $[\text{Cd}_{32}\text{S}_{14}(\mu\text{-SR})_{36}\cdot\text{L}_4]$  (**24a**:  $\text{R} = \text{Ph}$ ,  $\text{L} = \text{DMF}$ ; **24b**:  $\text{R} = \text{CH}_2\text{CH}(\text{OH})\text{CH}_3$ ,  $\text{L} = \text{H}_2\text{O}$ ) [79, 80].

ferred to as the tight-binding model, which is based upon the linear combination of atomic orbitals, is favored [77].

The study of the optical properties of structurally characterized XII–XVI semiconductor nanoclusters is attractive because the effects of polydispersity are removed, and because they allow the study of the development of bulk properties in the “molecular” size regime. Two independent reports have detailed the synthesis of the clusters  $[\text{Cd}_{32}\text{S}_{14}(\text{SR})_{36}\cdot\text{L}_4]$  **24** (**24a**:  $\text{R} = \text{Ph}$ ,  $\text{L} = \text{DMF}$ ; **24b**:  $\text{R} = \text{CH}_2\text{CH}(\text{OH})\text{CH}_3$ ,  $\text{L} = \text{H}_2\text{O}$ ), the framework of which is illustrated in Figure 13.20 [79, 80]. Complex **24** is a larger homologue of the  $\text{Cd}_{17}$  cluster **23**, and contains 13 fused adamantoid cages, with the four corners of the tetrahedral cluster terminated with the barrelanoid structural unit. Cluster **24a** was isolated by attempting to crystallize the coordinatively unsaturated cluster  $[\text{Cd}_{10}\text{S}_4(\text{SPh})_{12}]$ , which can be generated via the controlled thermolysis of  $[\text{Cd}_{10}\text{S}_4(\text{SPh})_{16}][\text{NMe}_4]_4$ , in donor solvents [79]. Cluster **24b** is obtained directly from the reaction of  $\text{Cd}(\text{ClO}_4)_2$ ,  $\text{H}_2\text{S}$  and  $\text{HSCH}_2\text{CH}(\text{OH})\text{CH}_3$  in basic aqueous solutions, using ion association methods [80].

The effects of quantum confinement in the cadmium sulfide clusters **24** are demonstrated by a blue shift in the lowest-lying transition observed relative to  $\text{CdS}$ , and a marked red-shift relative to the smaller  $\text{Cd}_{17}$  cluster **23**. This change reflects the 1.4 nm size (edge length) of **24** versus 1.1 nm in **23**. Unfortunately, unambiguous assignment of these transitions as arising from the generation of the electron–hole pair is not straightforward as the transitions of the first excited state

become overshadowed by surface (SR) transitions. In cluster **24a** ( $R = \text{Ph}$ ) a  $\lambda_{\text{max}}$  of 358 nm is observed, whereas in **24b** ( $R = \text{CH}_2\text{CH}(\text{OH})\text{CH}_3$ ), a blue shift of the first excitation is observed with  $\lambda_{\text{max}} = 325$  nm. As the  $\text{Cd}_{32}\text{S}_{50}$  cores are identical in the two, this inconsistency must be attributed to the different surface ligands on the clusters, and the mixing of intraligand transitions with the “band gap” absorption [80]. As CdS has a relatively wide band gap (2.4 eV in the bulk), when the particle size is reduced to that of molecular clusters, the transitions of the first excited state become overshadowed by surface (SR) transitions.

CdSe, on the other hand, has a smaller band gap energy (1.7 eV) than CdS, and thus surface ligand transitions are less likely to mask the “band gap” excitation in the absorption spectra of nanoclusters of this material. Recent synthetic success using  $\text{RSeSiMe}_3/\text{E}(\text{SiMe}_3)_2$  reagents has permitted an investigation of the optical properties of a series of CdSe nanoclusters of different sizes that are isostructural with the CdS complexes **22–24**. The position of the first excitation is shifted to lower energy with increasing cluster size for the adamantoid/barrelanoid clusters  $[\text{Cd}_{10}\text{Se}_4(\text{SePh})_{12}(\text{PPr}_3)_4]$  (3.88 eV) [81],  $[\text{Cd}_{17}\text{Se}_4(\text{SePh})_{24}(\text{PPh}_2\text{Pr})_4]^{2+}$  (3.42 eV) [82], and  $[\text{Cd}_{32}\text{Se}_{14}(\text{SePh})_{36}(\text{PPh}_3)_4]$  (3.32 eV) [83]. The  $\text{Cd}_{32}\text{Se}_{50}$  cluster is formed by dissolving the smaller precursor  $[\text{Cd}_{10}\text{Se}_4(\text{SePh})_{12}(\text{PPh}_3)_4]$  in tetrahydrofuran, similar to the methods used for the preparation of  $[\text{Cd}_{32}\text{S}_{14}(\text{SR})_{36}\cdot\text{L}_4]$  **24a** from  $[\text{Cd}_{10}\text{S}_4(\text{SPh})_{12}]$  [79] and  $[\text{Hg}_{32}\text{Se}_{14}(\text{SePh})_{36}]$  from  $[\text{Hg}_{10}\text{Se}_4(\text{SePh})_{12}(\text{PPh}_2\text{Pr})_4]$  [84]. The  $\sim 1.5$  nm size of these monodisperse  $\text{M}_{32}$  nanoclusters overlaps with those reported for small XII–XVI colloids [78]. Surprisingly, the absorption profiles of the CdSe clusters are relatively broad, and if inhomogeneous broadening is a result of size distribution, then particles of a uniform size should negate this effect. The source of this broadening is unclear, however, it is suggested that it may be due to the inhomogeneous distribution of surface coverage by the phenyl ligands [85].

Because of their small size, the number of surface atoms in nanoclusters is a large fraction of the total. As a result, the optical properties of these particles are largely affected by the nature of the surface. It has already been demonstrated above how surface ligand transitions can play a role in the overshadowing of “band gap” absorptions and in the inhomogeneous broadening of absorption spectra. The largest effect of surface states, however, can be observed in the emission spectra using photoluminescence (PL) spectroscopy. The photoluminescence of XII–XVI nanoparticles occurs as one of two types; band edge PL and deep trap PL [86]. Band edge emission occurs due to the recombination of trapped charge carriers from shallow trap states within the particle. This type of emission results in a slight red shift with respect to the absorption maximum, due to the relaxation of the trapped charge carrier into lower lying energy states prior to recombination, and it usually has a narrow line width. Deep trap emission, which is formally forbidden, occurs via the recombination of trapped localized carriers from deep and mid-gap trap states, which are usually hole traps at the surface of the cluster (or colloid). Deep trap emission is characterized by a broad line width, shifted significantly to the red of the excitonic absorption [86].

The PL spectra of the nanoclusters  $[\text{Cd}_{32}\text{Se}_{14}(\text{SePh})_{36}(\text{PPh}_3)_4]$ ,  $[\text{Cd}_{17}\text{Se}_4(\text{SePh})_{24}\cdot$

$(\text{Ph}_2\text{Pr})_4]^{2+}$  and  $[\text{Cd}_{10}\text{Se}_4(\text{SePh})_{12}(\text{PPr}_3)_4]$  exhibit only trapped emission [85]. The clusters can be viewed as having “imperfect” surfaces, which results in the generation of surface trap states. The energy of the trapped emission is independent of the size of the cluster, an effect that is also observed in colloidal samples. This indicates that the nature of the emitting state is similar for all species, also giving strength to the argument that surface states are responsible for this type of emission. The effect of temperature on deep trap emission is such that the intensity of the emission decreases as the temperature increases. This can be explained by non-radiative recombination processes dominating at higher temperatures [86]. The non-radiative relaxation in the CdSe nanoclusters has been attributed to the involvement of a multiphonon relaxation mechanism mediated by low-frequency vibrations of the surface phenylselenolate ligands [85]. The net result is such that, at ambient temperatures, the fast non-radiative decay processes compete with the slower deep-trap radiative recombination from these states, and no emission is observed from these clusters. At lower temperatures, the non-radiative decay processes slow down and the quantum yield of the emission increases dramatically. The quantum yields of these emissions at low temperatures range from 10 to 40%, with lifetimes of 0.8–10  $\mu\text{s}$ . The effect of the chemical make-up of the surfaces of XII–XVI clusters on emission properties is also demonstrated for the adamantoid clusters  $[\text{Cd}_{10}\text{E}_4(\text{EAR})_{12}\text{L}_4]^{n-}$  (Ar = aryl; L =  $\text{PR}_3$ ,  $n = 0$ ; L = halide,  $n = 4$ ) [87, 88].

The phenyl groups bonded to the selenium centers on the surfaces of these  $\text{Cd}_{10}\text{Se}$ ,  $\text{Cd}_{17}\text{Se}$  and  $\text{Cd}_{32}\text{Se}$  clusters are not ideal for passivation of the inorganic core i.e. the elimination of deep-trap surface states. Efficient passivation of nanoparticles is often achieved via the growth of a wide band-gap XII–XVI surface onto a quantum dot seed of another XII–XVI material with a smaller band gap energy. In these “core–shell” particles, the band-edge emission intensities are enhanced markedly relative to those of particles of the core material only [75]. The nanocluster  $[(\text{N},\text{N}'\text{-tmeda})_5\text{Zn}_5\text{Cd}_{11}\text{Se}_{13}(\text{SePh})_6(\text{OC}_4\text{H}_8)_2]$  **25** (Figure 13.21) consists of a  $\text{Cd}_{11}\text{Se}_{13}$  core in which 10 of the  $\text{Se}^{2-}$  ligands are bonded to the five ( $\text{N},\text{N}'\text{-tmeda})\text{Zn}$  sites, located at the cluster surface. Cluster **25** can thus be viewed as the “molecular limit” of core–shell CdSe/ZnSe particles [89]. Consistent with this view is the demonstrated band-edge luminescence observed at room temperature for **25**. It is unclear at present however whether the increased emission quantum yield of **25** versus the CdSe clusters described above is a consequence of efficient surface passivation by ZnSe, or whether it is the absence of phenyl moieties on half of the cluster surface that limits the non-radiative decay efficiencies.

### 13.5

#### Ternary MM'E

In addition to the cage-like cluster molecules  $[\text{Mo}_8\text{Cu}_{12}\text{S}_{28}\text{E}_4]$  (E = O, S) that have been synthesized from the reaction of tetrachalcogenomolybdates with Cu(I) salts [90, 91], alternate synthetic methods have recently led to the isolation of ternary



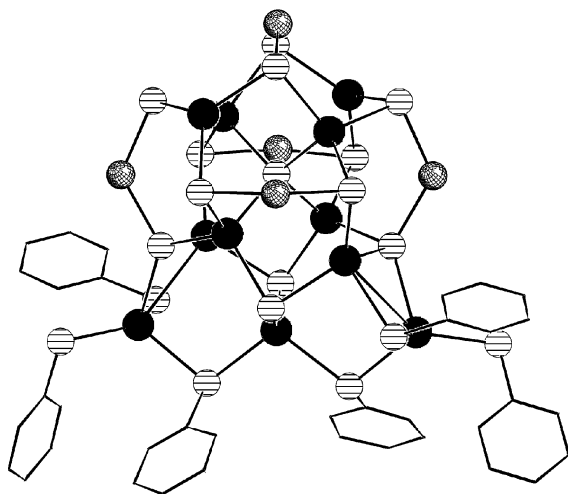


**Fig. 13.21.** A projection of the cluster  $[(N,N'\text{-tmeda})_5\text{Zn}_5\text{Cd}_{11}\text{Se}_{13}(\text{SePh})_6(\text{OC}_4\text{H}_8)_2]$  **25** (Cd atoms are shown as black circles, Zn atoms are illustrated as spheres and Se centers are illustrated as circles with horizontal lines).

Only the carbon atoms of the SePh ligands are illustrated to emphasize the partial coverage of phenyl rings on the cluster surface (see text) [89].

nanoclusters with condensed structural types. The basic principle is to form a metal–trimethylsilylchalcogenolate complex  $\text{M-ESiMe}_3$  where the demonstrated reactivity of the  $-\text{SiMe}_3$  moiety can be exploited to promote the formation of  $\text{M-E-M'}$  bonding interactions. With a suitable designed ancillary ligand sphere, reaction conditions can be controlled to access nanometer-sized  $\text{M}_x\text{M}'_y\text{E}_z$  clusters. The reaction of  $(\text{Pr}_3\text{P})_3\text{Cu-ESiMe}_3$  ( $\text{E} = \text{S}, \text{Se}$ ) with phosphine solubilized  $\text{Hg}(\text{OAc})_2$  leads to the formation of  $[\text{Hg}_{15}\text{Cu}_{20}\text{E}_{25}(\text{PPr}_3)_{18}]$  **26** (**26a**  $\text{E} = \text{S}$ ; **26b**  $\text{E} = \text{Se}$ ; Figure 13.22) in good yields [92, 93]. The “pinwheel”-like structure in **26** displays intimate mixing of the three core elements, with linear and trigonal coordination about the  $\text{Hg}(\text{II})$  centers. Thermal treatment of cluster **26a** results in the formation of Hg metal,  $\text{Pr}_3\text{P}/\text{Pr}_3\text{P}=\text{S}$  and various forms of  $\text{Cu}(\text{I})/\text{Cu}(\text{II})$  sulfides, illustrating the kinetic stabilization of the mixed  $\text{HgCuS}$  core in **26a** with the phosphine ligand shell. The preformed metal–chalcogen bonds in the trimethylsilylchalcogenolate complexes  $(N,N'\text{-tmeda})\text{Zn}(\text{ESiMe}_3)_2$  ( $\text{E} = \text{Se}, \text{Te}$ ) have also been shown to offer a route to the ternary XII–XII'–XVI clusters  $[(N,N'\text{-tmeda})_5\text{Zn}_5\text{Cd}_{11}\text{Se}_{13}(\text{SePh})_6(\text{OC}_4\text{H}_8)_2]$  **25** (Figure 13.21) and the isostructural tellurium complex  $[(N,N'\text{-tmeda})_5\text{Zn}_5\text{Cd}_{11}\text{Te}_{13}(\text{TePh})_6(\text{OC}_4\text{H}_8)]$ , respectively [89].

In certain instances, the direct combination of two metal salts with  $\text{E}(\text{SiMe}_3)_2/\text{RESiMe}_3$  reagents will lead to the isolation of ternary nanocluster complexes. The 1.3 nm cluster  $[\text{Cu}_{11}\text{In}_{15}\text{Se}_{16}(\text{SePh})_{24}(\text{PPh}_3)_4]$  **27** (Figure 13.23) can be described as a combination of adamantane and barrelane cages, as observed in the binary XII–XVI nanoclusters [94]. Unlike the structures of the larger  $\text{Cd}_{17}$  and  $\text{Cd}_{32}$  XII–XVI systems, at the corners of cluster **27** are adamantoid cages, which are con-

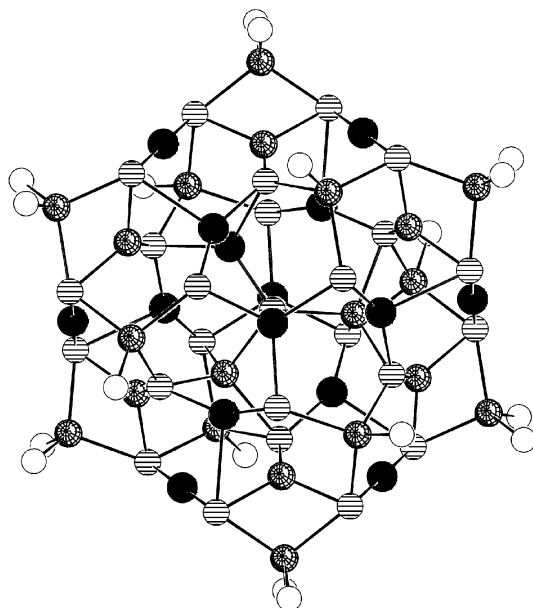


**Fig. 13.22.** An illustration of the core atoms of the ternary cluster  $[\text{Hg}_{15}\text{Cu}_{20}\text{E}_{25}(\text{P}^n\text{Pr}_3)_{18}]$  **26** ( $\text{E} = \text{S}, \text{Se}$ ; Hg atoms are shown as black circles, Cu atoms are illustrated as spheres and E centers are illustrated as circles with horizontal lines) [92, 93].

densed to three inner barrelanoid cages. Four of these  $\text{M}_{10}$  tetrahedral subunits are assembled around a central adamantoid cage to yield the observed structure, with a distribution of the  $\text{In(III)}$  and  $\text{Cu(I)}$  centers throughout the cluster. The tetrahedral framework in **27** contrasts with the spherical binary cores in the system copper-selenium as described in Section 13.3.1.2 and can be attributed to the large number of indium sites in the cluster. The adamantoid structural motif is dominant in the XV–XVI framework solids [95], and is also clearly exhibited in the extended superlattices of  $[\text{In}_{28}\text{Cd}_6\text{S}_{54}]^{12-}$  [96],  $[\text{In}_{16}\text{Cd}_4\text{S}_{35}]^{14-}$  [97] and  $[\text{In}_{16}\text{Cd}_4\text{S}_{33}]^{10-}$  [98], which are built up from these covalently linked semiconductor quantum dot units. These remarkable lattices are formed under solvothermal conditions, by combining commercially available Cd and In sources with elemental sulfur.

### 13.6

#### Metal Pnictides from $\text{E}(\text{SiMe}_3)_3$ Reagents

The demonstrated, rich chemistry that has evolved from the development of the reactions of silylated chalcogen sources  $\text{E}(\text{SiMe}_3)_2$  has yet to be matched with related Group XV reagents. Clear indicators of the utility of these molecules in accessing large, molecular semiconductor clusters have however been reported.

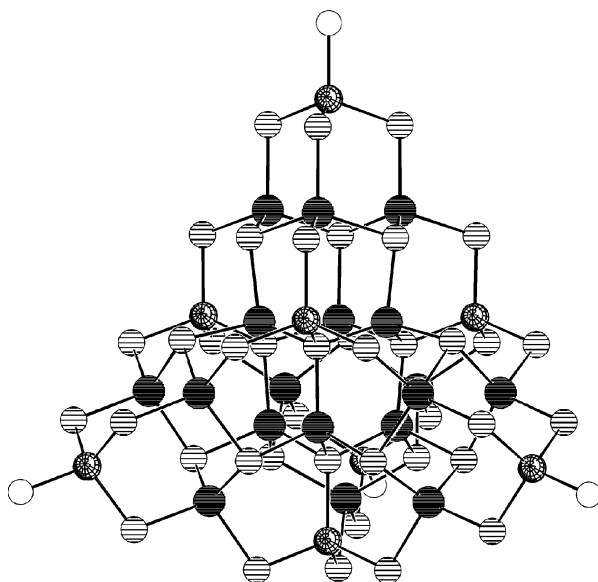


**Fig. 13.23.** The adamnatoid/barrelanoid framework in the ternary cluster  $[\text{Cu}_{11}\text{In}_{15}\text{Se}_{16}(\mu\text{-SePh})_{24}(\text{PPh}_3)_4]$  **27** (In atoms are shown as black circles, Cu atoms are illustrated as spheres and Se centers are illustrated as circles with horizontal lines) [94].

The copper phosphide complex  $[\text{Cu}_{96}\text{P}_{30}\{\text{P}(\text{SiMe}_3)_2\}_6(\text{PEt}_3)_{18}]$  **28** (Figure 13.24) for example is formed from the 10:5:6 reaction of  $\text{CuCl}:\text{PEt}_3:\text{P}(\text{SiMe}_3)_3$  in tetrahydrofuran [99]. The ~3:1 ratio of Cu:P and the A–B–C packing of the phosphide ( $\text{P}^{3-}$ ) centers in **28** enable an analogy to be drawn between this molecular species and the semiconductor  $\text{Cu}_3\text{P}$ , however close structural relationships are not dominant. The Cu(I) ions in **28** lie both within and between the phosphide layers. A similar methodology has also resulted in the formation of the shell-like copper arsenide  $[\text{Cu}_{32}\text{As}_{30}(\text{Ph}_2\text{PCH}_2\text{PPh}_2)_8]$  [57] and palladium arsenide  $[\text{Pd}_{20}\text{As}_{12}(\text{PPh}_3)_{12}]$  nanoclusters using  $\text{As}(\text{SiMe}_3)_3$  [100].

### 13.7

#### Conclusions and Outlook

The wealth of structural chemistry that has appeared over the past several years with metal-chalcogen nanoclusters has permitted the investigation and evaluation of the evolution of the properties of metal-chalcogenides on going from molecular to bulk solid systems. As is clear from the material reviewed in the preceding sections, these nanometer-sized solids continue to hold promise as novel electronic materials or low-temperature precursors to solids, although advanced practical ap-

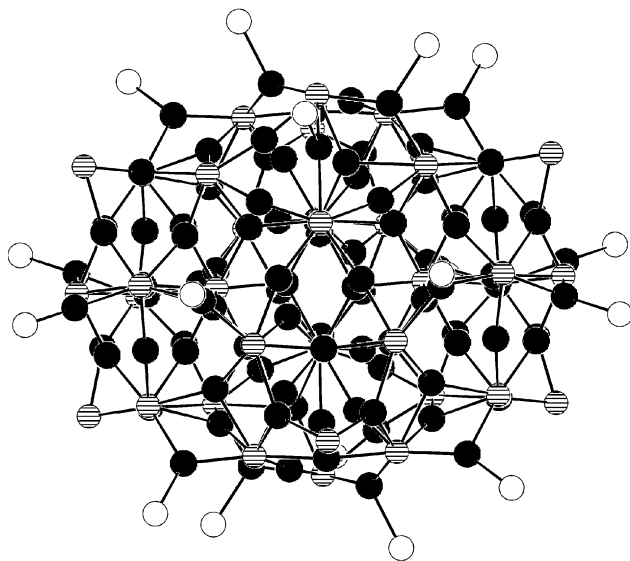


Fig. 13.24. The copper phosphide cluster core in  $[\text{Cu}_{96}\text{P}_{30}\{\text{P}(\text{SiMe}_3)_2\}_6(\text{PEt}_3)_{18}]$  **28** [99].

plications have yet to be realized. The development of synthetic methodologies, especially for Se and Te [3], has occurred in parallel with the availability of more advanced X-ray diffraction instrumentation. This combination will no doubt continue to evolve, with new reagents, more sensitive X-ray detectors and higher intensity X-ray sources, all of which will permit the formation and characterization of new and interesting structural types.

## References

- 1 S. JAIN, M. WILLANDER, R. VAN OVERSTRAETAN, *Compound Semiconductors Strained Layers and Devices*, eds. A. F. W. WILLOUGHBY, R. HULL, Electronic Materials 7, Kluwer Academic, Boston 2000, pp. 214–230.
- 2 J. ARNOLD, *Prog. Inorg. Chem.* **1995**, *43*, 353–417.
- 3 L. C. ROOF, J. W. KOLIS, *Chem. Rev.* **1993**, *93*, 1037–1080.
- 4 I. G. DANCE, *Polyhedron* **1986**, *5*, 1037–1104.
- 5 B. KREBS, G. HENKEL, *Angew. Chem. Int. Ed. Engl.* **1991**, *30*, 769–788.
- 6 I. DANCE, K. FISHER, *Prog. Inorg. Chem.* **1994**, *41*, 637–803.
- 7 A. MÜLLER, E. DIEMANN, *Comprehensive Coordination Chemistry*, Pergamon, Oxford 1987, Vol. 2, Chapter 16.1, pp. 515–558.
- 8 A. MÜLLER, E. DIEMANN, *Adv. Inorg. Chem.* **1987**, *31*, 89–122.
- 9 M. A. ANSARI, J. A. IBERS, *Coord. Chem. Rev.* **1990**, *100*, 223–266.
- 10 M. W. DEGROOT, J. F. CORRIGAN, *Comprehensive Coordination Chemistry II*, Pergamon, Oxford, Vol. 7, Chapter 1.2, eds. M. FUJITA, A. POWELL AND C. CREUTZ, in press.
- 11 J.-F. YOU, G. C. PAPAETHYMIU, R. H. HOLM, *J. Am. Chem. Soc.* **1992**, *114*, 2697–2710.

- 12 B. HESSEN, T. SIEGRIST, T. PALSTRA et al., *Inorg. Chem.* **1993**, 32, 5165–5169.
- 13 M. L. STEIGERWALD, C. E. RICE, *J. Am. Chem. Soc.* **1988**, 110, 4228–4231.
- 14 M. L. STEIGERWALD, T. SIEGRIST, S. M. STUCZYNSKI et al., *J. Am. Chem. Soc.* **1992**, 114, 3155–3156.
- 15 M. L. STEIGERWALD, T. SIEGRIST, S. M. STUCZYNSKI, *Inorg. Chem.* **1991**, 30, 4940–4945.
- 16 J. G. BRENNAN, M. L. STEIGERWALD, T. SIEGRIST et al., *J. Am. Chem. Soc.* **1990**, 112, 9233–9236.
- 17 R. A. ZINGARO, B. H. STEEVES, K. IRGOLIC, *J. Organomet. Chem.* **1965**, 4, 320–323.
- 18 M. L. STEIGERWALD, *Polyhedron* **1994**, 13, 1245–1252.
- 19 J. G. BRENNAN, T. SIEGRIST, Y.-U. KWON et al., *J. Am. Chem. Soc.* **1992**, 114, 10334–10338.
- 20 J. G. BRENNAN, T. SIEGRIST, S. M. STUCZYNSKI et al., *J. Am. Chem. Soc.* **1989**, 111, 9240–9241.
- 21 J. BARSTAD, F. GRONVOLD, E. ROST et al., *Acta Chem. Scand.* **1966**, 20, 2865–2879.
- 22 W. IMHOF, G. HUTTNER, *J. Organomet. Chem.* **1993**, 448, 247–253.
- 23 G. HOGARTH, N. J. TAYLOR, A. J. CARTY et al., *Chem. Commun.* **1988**, 834–836.
- 24 M. HONG, Z. HUANG, H. LIU, *Chem. Commun.* **1990**, 1210–1211.
- 25 D. FENSKE, J. OHMER, *Angew. Chem. Int. Ed. Engl.* **1987**, 26, 148–151.
- 26 D. FENSKE, J. OHMER, J. HACHGENEI et al., *Angew. Chem. Int. Ed. Engl.* **1988**, 27, 1277–1296.
- 27 R. GAUTIER, E. FURET, J. F. HALET et al., *Inorg. Chem.* **2002**, 41, 796–804.
- 28 D. FENSKE, J. OHMER, J. HACHGENEI, *Angew. Chem. Int. Ed. Engl.* **1985**, 24, 993–995.
- 29 D. FENSKE, A. FISCHER, *Angew. Chem. Int. Ed. Engl.* **1995**, 34, 307–309.
- 30 A. MÜLLER, D. FENSKE, P. KOGERLER, *Curr. Opin. Solid State Mater. Sci.* **1999**, 4, 141–153.
- 31 S. DEHNEN, A. EICHHÖFER, D. FENSKE, *Eur. J. Inorg. Chem.* **2002**, 279–317.
- 32 H. KRAUTSCHEID, D. FENSKE, G. BAUM et al., *Angew. Chem. Int. Ed. Engl.* **1993**, 32, 1303–1305.
- 33 K. YAMAMOTO, S. KASHIDA, *J. Solid. State. Chem.* **1991**, 93, 202–211.
- 34 R. M. MURRAY, R. D. HEYDING, *Can. J. Chem.* **1975**, 53, 878–887.
- 35 D. VAN DER PUTTEN, R. ZANONI, *Phys. Lett. A* **1995**, 208, 351–355.
- 36 N. ZHU, D. FENSKE, *J. Chem. Soc., Dalton Trans.* **1999**, 1067–1075.
- 37 N. R. M. CRAWFORD, A. G. HEE, J. R. LONG, *J. Am. Chem. Soc.* **2002**, 124, 14842–14843.
- 38 J. S. MCINDOE, *Transition Met. Chem.* **2003**, 28, 122–131.
- 39 S. DEHNEN, D. FENSKE, *Chem. Eur. J.* **1996**, 2, 1407–1416.
- 40 D. FENSKE, H. KRAUTSCHEID, *Angew. Chem.* **1990**, 29, 1452–1454.
- 41 A. EICHHÖFER, D. FENSKE, *J. Chem. Soc., Dalton Trans.* **1998**, 2969–2972.
- 42 A. EICHHÖFER, E. BECKMANN, D. FENSKE et al., *Israel J. Chem.* **2001**, 41, 31–37.
- 43 S. DEHNEN, D. FENSKE, *Angew. Chem. Int. Ed. Engl.* **1994**, 33, 2287–2289.
- 44 M. BETTENHAUSEN, A. EICHHÖFER, D. FENSKE et al., *Z. Anorg. Allg. Chem.* **1999**, 625, 593–601.
- 45 A. DEVESON, S. DEHNEN, D. FENSKE, *J. Chem. Soc., Dalton Trans.* **1997**, 4491–4498.
- 46 D. FENSKE, H. KRAUTSCHEID, *Angew. Chem. Int. Ed. Engl.* **1990**, 29, 796–798.
- 47 D. FENSKE, *Clusters and Colloids, From Theory to Applications*, VCH, Weinheim 1994, pp. 217–297.
- 48 S. DEHNEN, D. FENSKE, A. C. DEVESON, *J. Cluster Sci.* **1996**, 7, 351–369.
- 49 S. DEHNEN, A. SCHÄFER, D. FENSKE et al., *Angew. Chem. Int. Ed. Engl.* **1994**, 33, 764–768.
- 50 A. F. WELLS, *Structural Inorganic Chemistry*, 5th edition, Clarendon, Oxford 1984, Chapter 25, pp. 1142–1145.
- 51 D. FENSKE, J.-C. STECK, *Angew. Chem. Int. Ed. Engl.* **1993**, 32, 238–242.
- 52 J. F. CORRIGAN, S. BALTER, D. FENSKE, *J. Chem. Soc., Dalton Trans.* **1996**, 729–738.

- 53 A. EICHHÖFER, J. F. CORRIGAN, D. FENSKE et al., *Z. Anorg. Allg. Chem.* **2000**, 626, 338–348.
- 54 D. FENSKE, N. ZHU, J. *Cluster Sci.* **2000**, 11, 135–151.
- 55 M. W. DEGROOT, M. W. COCKBURN, M. S. WORKENTIN et al., *Inorg. Chem.* **2001**, 40, 4678–4685.
- 56 J. F. CORRIGAN, D. FENSKE, *Angew. Chem. Int. Ed. Engl.* **1997**, 36, 1981–1983.
- 57 R. AHLRICHS, J. BESINGER, A. EICHHÖFER et al., *Angew. Chem. Int. Ed. Engl.* **2000**, 39, 3929–3933.
- 58 J. F. CORRIGAN, D. FENSKE, *Chem. Commun.* **1997**, 1837–1838.
- 59 D. FENSKE, J. F. CORRIGAN, *Metal Clusters in Chemistry*, eds. P. BRAUNSTEIN, L. A. ORO, P. R. RAITHBY, Wiley-VCH, Weinheim **1999**, Vol. 3, Chapter 4.2, pp. 1302–1324.
- 60 J. F. CORRIGAN, D. FENSKE, *Chem. Commun.* **1996**, 943–944.
- 61 T. LANGETEPE, D. FENSKE, *Z. Anorg. Allg. Chem.* **2001**, 627, 820–826.
- 62 M. D. JANSSEN, D. M. GROVE, G. VAN KOTEN, *Prog. Inorg. Chem.* **1997**, 46, 97–149.
- 63 K. TANG, X. XIE, Y. ZHANG et al., *Chem. Commun.* **2002**, 1024–1025.
- 64 X.-J. WANG, T. LANGETEPE, C. PERSAU et al., *Angew. Chem. Int. Ed. Engl.* **2002**, 41, 3818–3822.
- 65 A. MÜLLER, E. BECKMANN, H. BÖGGE et al., *Angew. Chem. Int. Ed. Engl.* **2002**, 41, 1162–1167.
- 66 G. A. WIEGERS, *Am. Mineral.* **1971**, 56, 1882–1888.
- 67 D. FENSKE, N. ZHU, T. LANGETEPE, *Angew. Chem. Int. Ed. Engl.* **1998**, 37, 2639–2644.
- 68 D. FENSKE, T. LANGETEPE, *Angew. Chem. Int. Ed. Engl.* **2002**, 41, 300–304.
- 69 I. G. DANCE, A. CHOY, M. L. SCUDDER, *J. Am. Chem. Soc.* **1984**, 106, 6285–6295.
- 70 M. D. NYMAN, M. J. HAMPDEN-SMITH, E. N. DUESLER, *Inorg. Chem.* **1996**, 35, 802–803.
- 71 G. S. H. LEE, D. C. CRAIG, I. MA et al., *J. Am. Chem. Soc.* **1988**, 110, 4863–4864.
- 72 T. VOSSMEYER, G. RECK, L. KATSIKAS et al., *Science* **1995**, 267, 1476–1479.
- 73 H. DÖLLEFIELD, H. WELLER, A. EYCHMÜLLER, *Nanoletters*, **2001**, 1, 267–269.
- 74 L. E. BRUS, *J. Chem. Phys.* **1984**, 80, 4403–4409.
- 75 A. P. ALIVISATOS, *J. Phys. Chem.* **1996**, 100, 13226–13239.
- 76 H. WELLER, *Angew. Chem. Int. Ed. Engl.* **1993**, 32, 41–53.
- 77 P. E. LIPPENS, M. LANNON, *Phys. Rev. B*, **1989**, 39, 10935–10942.
- 78 C. B. MURRAY, D. J. NORRIS, M. G. BAWENDI, *J. Am. Chem. Soc.* **1993**, 115, 8706–8715.
- 79 N. HERRON, J. C. CALABRESE, W. E. FARNETH, Y. WANG, *Science* **1993**, 259, 1426–1428.
- 80 T. VOSSMEYER, G. RECK, B. SCHULZ et al., *J. Am. Chem. Soc.* **1995**, 117, 12881–12882.
- 81 S. BEHRENS, M. BETTENHAUSEN, A. EICHHÖFER et al., *Angew. Chem. Int. Ed. Engl.* **1997**, 36, 2797–2798.
- 82 S. BEHRENS, D. FENSKE, *Ber. Bunsen-Ges. Phys. Chem.* **1997**, 101, 1588–1592.
- 83 S. BEHRENS, M. BETTENHAUSEN, A. C. DEVESON et al., *Angew. Chem. Int. Ed. Engl.* **1996**, 35, 2215–2218.
- 84 A. EICHHÖFER, E. TRÖSTER, *Eur. J. Inorg. Chem.* **2002**, 2253–2256.
- 85 V. N. SOLOVIEV, A. EICHHÖFER, D. FENSKE et al., *J. Am. Chem. Soc.* **2001**, 123, 2354–2364.
- 86 A. EYCHMÜLLER, A. HASSELBARTH, L. KATSIKAS et al., *J. Lumin.* **1991**, 745–749.
- 87 R. D. ADAMS, B. ZHANG, C. J. MURPHY et al., *Chem. Commun.* **1999**, 383–384.
- 88 A. EICHHÖFER, A. AHARONI, U. BANIN, *Z. Anorg. Allg. Chem.* **2002**, 628, 2415–2421.
- 89 M. W. DEGROOT, N. J. TAYLOR, J. F. CORRIGAN, *J. Am. Chem. Soc.* **2003**, 125, 864–865.
- 90 L. JIGUO, X. XIN, Z. ZHONGYUAN et al., *Chem. Commun.* **1991**, 249–250.
- 91 Q. HUANG, Q. WU, T. SHENG et al., *Polyhedron* **1996**, 15, 3405–3410.
- 92 D. T. T. TRAN, N. J. TAYLOR, J. F. CORRIGAN, *Angew. Chem. Int. Ed.* **2000**, 39, 935–937.

- 93 D. T. T. TRAN, L. M. C. BELTRAN, C. M. KOWALCHUK et al., *Inorg. Chem.* **2002**, *41*, 5693–5698.
- 94 A. EICHHÖFER, D. FENSKE, *J. Chem. Soc., Dalton Trans.* **2000**, 941–944.
- 95 C. WANG, X. BU, N. ZHENG et al., *Chem. Commun.* **2002**, 1344–1345.
- 96 W. SU, X. HUANG, J. LI et al., *J. Am. Chem. Soc.* **2002**, *124*, 12944–12945.
- 97 H. LI, J. KIM, T. L. GROU et al., *J. Am. Chem. Soc.* **2001**, *123*, 4867–4868.
- 98 C. WANG, Y. LI, X. BU et al., *J. Am. Chem. Soc.* **2001**, *123*, 11506–11507.
- 99 D. FENSKE, W. HOLSTEIN, *Angew. Chem. Int. Ed. Engl.* **1994**, *33*, 1290–1292.
- 100 D. FENSKE, H. FLEISCHER, C. PERSAU, *Angew. Chem. Int. Ed. Engl.* **1989**, *28*, 1665–1669.

## 14

## Oxomolybdates: From Structures to Functions in a New Era of Nanochemistry

A. Müller and S. Roy

### Abstract

From a unique library containing the molybdenum-oxide based building blocks/fragments under reducing conditions in aqueous solution a huge variety of nano-objects, allowing specific reactions at well-defined positions, can be generated. This enables us to perform a new type of nanochemistry. Examples include the well-known molecular big-wheels of the type  $\{\text{Mo}_{154}\}$  and  $\{\text{Mo}_{176}\}$  and the spherical clusters of the type  $\{\text{Mo}_{132}\}$  and their derivatives. These are considered here in connection with the by far the largest structurally well-characterized cluster  $\{\text{Mo}_{368}\}$ , which contains besides the 368 molybdenum atoms nearly 2000 non-hydrogen atoms, shows positive and negative curvatures, and has the size of hemoglobin and the shape of a lemon. A most recent achievement regarding a unique 'nanosponge'-behaviour of the spherical clusters showing responsive sensing opens new eras of nanochemistry: *nano-spherical-surface*, *nano-porous-cluster*, and *nano-super-supramolecular chemistry*. Historically speaking, after solving the mystery of molybdenum blue solutions, from which the wheel type clusters can be isolated, it became evident that the acquired knowledge could be useful for advancing the frontiers of materials science. Some general aspects of the corresponding chemistry are reviewed here.

## 14.1

### Introduction: Similarities between Nanotechnology in Nature and Chemistry?

*Der chemische Prozeß ist das 'Höchste, wozu die unorganische Natur gelangen kann'.*

G. W. F. Hegel [1]

Nature plays with patterns. Patterning reaches a pinnacle of elegance and intricacy in nanoscopic molecular systems, the most relevant being those found in the biosphere: the variety of specific processes of the living cell are directed by an overwhelming number of nanoscaled structures, for example by the proteins which can act as *carriers*, *fighters*, *administrators*, *food engineers*, *signal receivers* and *transducers*



as well as *transporters*. In this context the question arises as to whether it is possible for chemists/scientists to build up systems with comparable functions that would allow us to speak of *machinery en miniature* in Nature and technology. Remarkably, from aqueous solutions of molybdates under reducing conditions, a huge variety of interesting structures can be obtained which offer a unique substance library and show really remarkable functionalities, even the phenomenon of cation transport through pores and of modelling cell response. These nanoscaled systems emerge by linking well-defined preformed building blocks under the canopy of *self-assembly* processes, which are unique regarding the overwhelming variety obtainable. A textbook example is the generation of the tobacco mosaic virus (TMV) in two phases [2]. In the first phase, the large protein building blocks are generated using encrypted genetic information and these in the second phase become linked to form the complete viral shell entity.

## 14.2

### Sizes, Shapes, and Complexity of Nano-objects are Determined by the Nature and Variety of the Constituent Building Blocks

In inorganic polyoxometalate systems, especially in solutions of molybdates under reducing conditions, a ‘virtual library’ of well-defined linkable building blocks exists, which can be connected under suitable conditions to form a plethora of sophisticated nanostructures. For instance, *two or three identical well-defined building blocks* or fragments, each comprising 17 molybdenum atoms, become linked to form the two different nanostructures shown in Figure 14.1 [3a,b]. All such cluster species, emerging via self-assembly and woven from well-defined building blocks

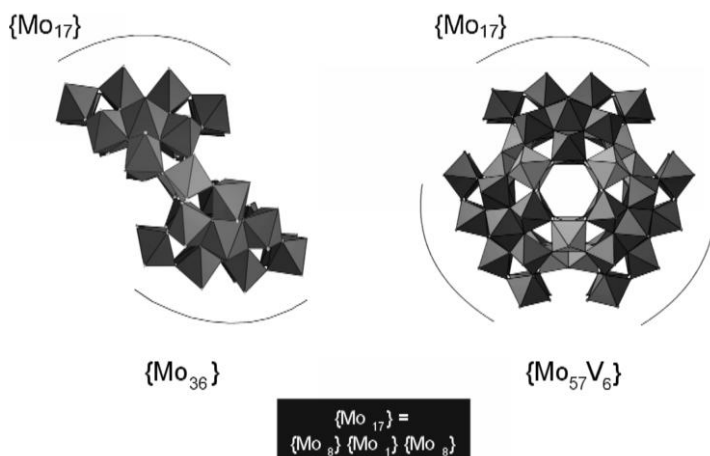


**Fig. 14.1.** Two relatively large clusters with different structures formed by the same  $\{Mo_{17}\}$  building block: Two or three of these  $\{Mo_{17}\}$  building blocks are linked in different modes by different linkers to form different clusters.

of molybdenum and oxygen atoms, the most important of which are collected in Table 14.1, show the following characteristics:

- All listed clusters contain the fundamental pentagonal  $\{(Mo)Mo_5\}$  building block, comprising a central pentagonal bipyramidal  $\{MoO_7\}$  group with six surrounding edge-sharing  $\{MoO_6\}$  octahedra. These can occur in very different environments.
- The units are, for example, central to the construction of spherically shaped entities with positive curvatures. (Note that even the famous so-called bucky-ball  $\{C_{60}\}$  fullerene molecule contains 12 pentagonal 'units'.) However, for the generation of more complex patterns, including negative as well as positive curvatures, that is showing symmetry breaking, a rather large number of negative and positive vertices with polygons of different kinds, for example including heptagons, is necessary [4].

The highly symmetric  $[(pent)_{12}(link)_{30}]$  type spherical clusters, such as the  $\{Mo_{132}\}$  type nanospheres (Figure 14.2, right), are comprised of 12 pentagonal  $\{(Mo)Mo_5\}$  groups (pent) connected by 30  $\{Mo_2\}$  groups acting as linkers (link) [3]. The cluster type  $\{Mo_{132}\}$  also has an interesting stoichiometric aspect in the sense that it can be formally written as  $\{Mo_{132}\} \equiv \{Mo_{11}\}_{12} \equiv \{(Mo)Mo_5Mo_5'\}_{12}$  [5] (see below). The number *twelve*, an emblem of icosahedral symmetry, is significant in the context of two Platonic solids: the icosahedron and dodecahedron, the latter having 12 faces, the former 12 vertices. Interestingly, the aforementioned  $\{Mo_{11}\}$  unit, like its smaller counterpart  $\{(Mo)Mo_5\}$ , also shows a five-fold symmetry axis which is necessary for the construction of spherical entities with icosahedral symmetry, be it a  $\{Mo_{132}\}$  type nanosphere or a spherical virus. The presence of the related 14 and 16  $\{Mo_{11}\}$  groups in wheel-shaped  $\{Mo_{154}\}$  ( $\equiv \{Mo_{11}\}_{14}$ ) and  $\{Mo_{176}\}$  ( $\equiv \{Mo_{11}\}_{16}$ ) type clusters (Table 14.1), respectively, also reveals the central role of the pentagonal building blocks. The two different types of  $\{Mo_{11}\}$  building blocks can be distinguished easily as a lower symmetry (that is,  $C_s$ ) is observed in the wheel-shaped clusters resulting from the displacement of one of the  $\{MoO_6\}$  octahedra (see Figures 14.3 and 14.4).

The structure of the  $\{Mo_{368}\}$  type cluster [4], the largest inorganic species known to date and also obtained from a special type of molybdenum blue solution, presents us with a paradigm shift with respect to symmetry breaking and changing curvatures in the nanocosmos. The phenomenon of symmetry breaking is visible at the surface due to the abundance of different large local symmetry areas as well as the presence of negative curvatures in between positive curvatures (see Figures 14.5 and 14.6). The structure of this cluster can be considered as a hybrid between the wheel- and ball-type clusters. The hybrid character is, in the terminology of ref. [5], manifested by the occurrence of 24  $C_5$ -type  $\{Mo_{11}\}$  groups of the ball-type clusters together with the related 16  $C_s$ -type  $\{Mo_{10}\}$  groups of the wheel-type clusters which correspond to the abundant  $\{Mo_{11}\}$  groups with only one  $MoO_6$  octahedron less (see [4]).

**Tab. 14.1.** The nanocosmos of molybdenum oxide clusters formulated according to metal-based building blocks especially  $\{(\text{Mo})\text{Mo}_5\}$ . This important unit which is found in all molybdenum-based nanoarchitectures (Figure 14.3), has a pentagonal  $\{\text{MoO}_7\}$  bipyramid in the centre while the Mo atoms in all other building blocks, like  $\{\text{Mo}_1\}$  or  $\{\text{Mo}_2\}$ , have Mo in an octahedral environment. Building blocks, like  $\{\text{Mo}_1\}$ , can show different ligand dispositions. (References are based mainly on our earlier reviews.)

Cluster	Figure	Formulation Based on Largest Building Blocks	Smaller Building Blocks of the Larger Groups	Associated Counterions/Ligands	References
$\{\text{Mo}_{36}\}$	–	$\{\text{Mo}_{17}\}_2\{\text{Mo}_1\}_2$	$\{\text{Mo}_{17}\} = \{(\text{Mo})\text{Mo}_5\}_2\{\text{Mo}_1\}_5^{**}$		7
$\{\text{Mo}_{57}\text{M}_6\}$	14.1	$\{\text{Mo}_{17}\}_3\{\text{Mo}_2\}_3\text{M}_6$ ( $\text{M} = \text{Fe}^{\text{III}}, \text{V}^{\text{IV}}$ )	$\{\text{Mo}_{17}\} = \{(\text{Mo})\text{Mo}_5\}_2\{\text{Mo}_1\}_5^{**}$		3a
$\{\text{Mo}_{63}\text{M}_6\}$	–	$\{\text{Mo}_{17}\}_3\{\text{Mo}_2\}_3\{\text{Mo}_1\}_6\text{M}_6^{**}$	$\{\text{Mo}_{17}\} = \{(\text{Mo})\text{Mo}_5\}_2\{\text{Mo}_1\}_5^{**}$		3a
$\{\text{Mo}_{146}\}$	14.8	$\{\text{Mo}_8\}_{16}\{\text{Mo}_2\}_9$	$\{\text{Mo}_8\} = \{(\text{Mo})\text{Mo}_5\}_2\{\text{Mo}_1\}_2$	$16 \text{ SO}_4^{2-}, 16 \text{ K}^+$	10
$\{\text{Mo}_{154}\}$	–	$\{\text{Mo}_8\}_{14}\{\text{Mo}_2\}_{14}\{\text{Mo}_1\}_{14}$	$\{\text{Mo}_8\} = \{(\text{Mo})\text{Mo}_5\}_2\{\text{Mo}_1\}_2$		3a, 3b, 6
$\{\text{Mo}_{176}\}$	14.4	$\{\text{Mo}_8\}_{16}\{\text{Mo}_2\}_{16}\{\text{Mo}_1\}_{16}$	$\{\text{Mo}_8\} = \{(\text{Mo})\text{Mo}_5\}_2\{\text{Mo}_1\}_2$		3a, 6
$\{\text{Mo}_{248}\}$	14.9	$\{\text{Mo}_8\}_{16}\{\text{Mo}_2\}_{16}\{\text{Mo}_1\}_{16}\{\text{Mo}_{36}\}_2$	$\{\text{Mo}_{36}\} = \{(\text{Mo})\text{Mo}_5\}_2\{\text{Mo}_1\}_2$		3a, 12a
$\{\text{Mo}_{75}\text{V}_{20}\}$	–	$\{(\text{Mo})\text{Mo}_5\}_{10}\{\text{Mo}_5\}_2\{\text{Mo}_{5/2}\}_2\text{V}_{20}$	$\{\text{Mo}_{5/2}\} = 5[\text{Mo}_x] \text{ (} x = 0.2-0.8 \text{)}$		3a
$\{\text{Mo}_{102}\}$	–	$\{(\text{Mo})\text{Mo}_5\}_{12}\{\text{Mo}_1\}_{30}$		$10 \text{ SO}_4^{2-}, 10 \text{ Na}^+$	***
$\{\text{Mo}_{132}\}$	14.2	$\{(\text{Mo})\text{Mo}_5\}_{12}\{\text{Mo}_2\}_{30}$		$12 \text{ CH}_3\text{COO}^-$	***
$\{\text{Mo}_{72}\text{M}_{30}\}$	14.2, 14.11	$\{(\text{Mo})\text{Mo}_5\}_{12}\text{M}_{30}$ (for example with $\text{M} = \text{Fe}^{\text{III}}$ )		$30 \text{ CH}_3\text{COO}^-$	3a
$\{\text{Mo}_{368}\}$	14.5	$\{(\text{Mo})\text{Mo}_5\}'_8\{(\text{Mo})\text{Mo}_5\}''_{32}\{\text{Mo}_2\}'_{16}\{\text{Mo}_2\}''_8\{\text{Mo}_2\}'''_8\{\text{Mo}_1\}_{64}$		$12 \text{ CH}_3\text{COO}^-$	3a, 14
				$48 \text{ SO}_4^{2-}$	4

\* Exist with different metal centres.

\*\* Other possible tilings:  $\{\text{Mo}_{17}\} = \{\text{Mo}_8\}_2\{\text{Mo}_1\}$  and

$\{\text{Mo}_8\} = \{(\text{Mo})\text{Mo}_5\}\{\text{Mo}_1\}_2$ .

\*\*\* A. Müller, S. Q. N. Shah, H. Bögge et al., Thirty Electrons

“Trapped” in a Spherical Matrix: A Molybdenum Oxide-Based

Nanostructured Keplerate Reduced by 36 Electrons, *Angew. Chem. Int.*

*Ed. Engl.* **2000**, 39, 1614–1616.

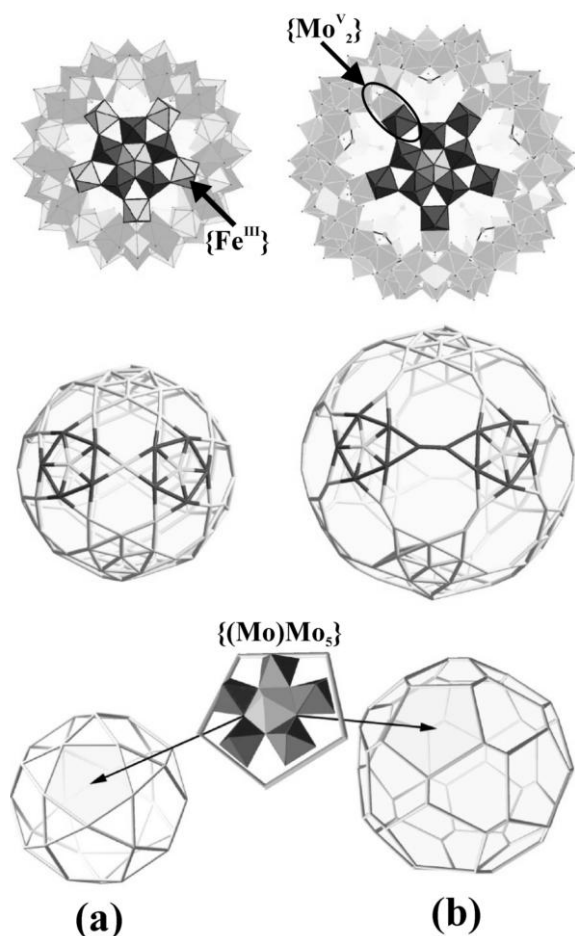


**Fig. 14.2.** “Sizing” the nanospheres is possible. Top: polyhedral representations of the cluster type  $[(\text{pent})_{12}(\text{link})_{30}] \equiv \{(\text{Mo})\text{Mo}_5\}_{12}\{\text{link}\}_{30}$  (linkers:  $\{\text{Mo}^{\text{V}}_2\}$  and  $\{\text{Fe}^{\text{III}}\}$  type units, indicated by arrows) showing a size-comparison of the two clusters  $\{\text{Mo}_{72}\text{Fe}_{30}\}$  (a) and  $\{\text{Mo}_{132}\}$  (b). Middle: size-comparison of the two clusters via wire-frame representation of the metal skeletons. Note in (a) the size-‘shrinking’ as the dinuclear  $\{\text{Mo}^{\text{V}}_2\}$

of (b) is replaced by the mononuclear  $\{\text{Fe}^{\text{III}}\}$  linker and the increase in ‘pore size’ on moving from a  $\{\text{Mo}_3\text{Fe}_3\text{O}_6\}$  ring of the  $\{\text{Mo}_{72}\text{Fe}_{30}\}$  cluster (a) to an  $\{\text{Mo}_9\text{O}_9\}$  ring of the  $\{\text{Mo}_{132}\}$  cluster (b). Bottom: structures only formed by the linkers: the icosidodecahedron with 12 pentagons and 20 triangles formed by  $\{\text{Fe}_{30}\}$  (a) and the (distorted) truncated icosahedron with 12 pentagons and 20 hexagons formed by  $\{\text{Mo}^{\text{V}}_2\}_{30}$  (b).

An imminent question in this context might be: what leads to the development of such positive and negative curvatures in the nanoscopic landscape of a cluster? Without doubt, the presence of a large number of building blocks in the reaction medium is a reason for the emergence of such complex architectures showing

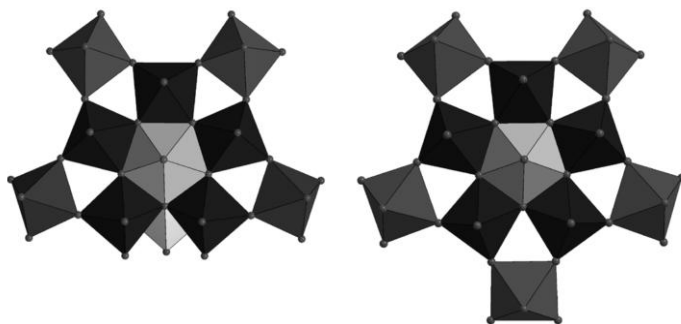


**Fig. 14.3.** Two “pentagonal”  $\{\text{Mo}_{11}\}$  units with the central  $\{(\text{Mo})\text{Mo}_5\}$  building block. One finds the more symmetric ( $C_5$ ) unit (right) in the spherical type cluster  $\{\text{Mo}_{132}\}$  and the less symmetric ( $C_s$ ) (left) with one shifted  $\{\text{MoO}_6\}$  octahedron (light grey) in the wheel type clusters (cf. Table 14.1 and Figure 14.4).

symmetry breaking. But still the question remains: how can such a structure be produced or how can a large number of building blocks be generated in solution? It is known that the largest cluster in acidified molybdate solution is, in the absence of a reducing agent, the “rather small”  $\{\text{Mo}_{36}\}$  type anion [3a, 4, 6, 7] which starts growing under reducing conditions. (Note that this is even larger than the largest discrete silicate ion.) An increase in negative charge, due to reducing conditions, not only prevents uncontrolled linking, but also initiates further protonation which is a prerequisite for further growth [4]. The increase in negative charge in the present case is also supported by the abundance of  $\text{SO}_4^{2-}$  ligands coordinated to the intermediates and the final cluster species. Another important aspect is the related coordination ability:  $\text{SO}_4^{2-}$  is a moderately strong ligand and therefore favors an increase in the number of building blocks which might be coordinated or non-coordinated. In the presence of much weaker coordinating ligands, such as  $\text{Cl}^-$  or  $\text{ClO}_4^-$  ions, in cases where  $\text{HClO}_4$  or  $\text{HCl}$  is used as acidification agent instead of  $\text{H}_2\text{SO}_4$ , the  $\{\text{Mo}_{368}\}$  cluster is not formed, “only” pure molybdenum oxide-based  $\{\text{Mo}_{154}\}$  or  $\{\text{Mo}_{176}\}$  wheel-type species, i.e. without  $\text{Cl}^-$  or  $\text{ClO}_4^-$  ligands, are formed. For the present purpose it is important to note that the coordination ability of the  $\text{SO}_4^{2-}$  ligand is ideal, as it is not too strong (as would be the case for  $\text{PO}_4^{3-}$  where all units would be coordinated) and not too weak [4].

### 14.3

#### Nanoscaled Clusters with Unusual Form–Function Relationships

Let us continue our tour of sophisticated nanostructures by giving some striking examples of the multifaceted form–functionality correlation principles involved. The following parent cluster types will be considered (here we refer to earlier published reviews):

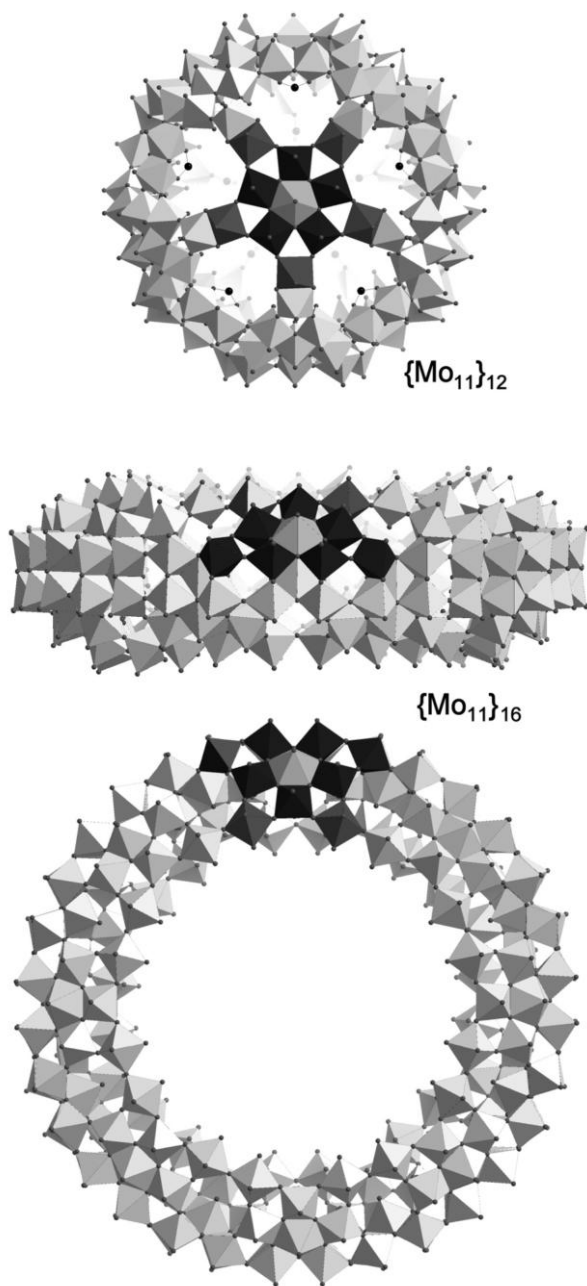


**Fig. 14.4.** Our spherical and wheel-shaped clusters show a remarkably similar (formal)  $\{\text{Mo}_{11}\}_n$  stoichiometry: comparison of the structures of the  $\{\text{Mo}_{11}\}_{12}$  (top) and  $\{\text{Mo}_{11}\}_{16}$  clusters (middle and bottom, with side and top view, respectively). ( $\{\text{Mo}_{11}\}$  units highlighted).

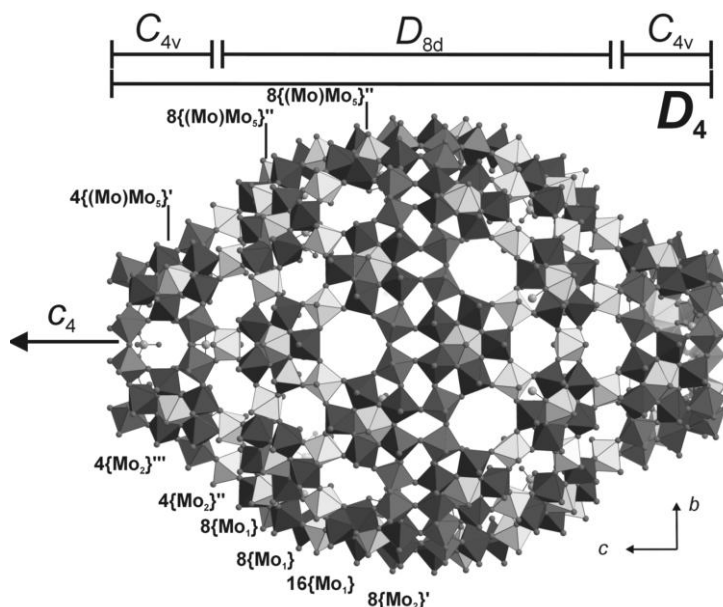
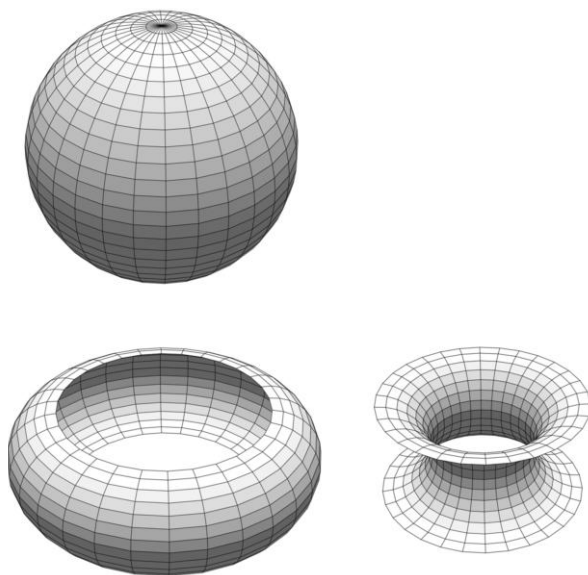


Fig. 14.5. An exciting molecular blue ‘nanolemon’: the  $[H_x Mo_{368} O_{1032} (H_2O)_{240} (SO_4)_{48}]^{48-}$  cluster anion in polyhedral representation showing large areas of different local symmetry based on the different abundant basic building blocks  $\{Mo_1\}$ ,  $\{Mo_2\}$ , and  $\{(Mo)Mo_5\}$ .

1. Wheel-shaped clusters of the type  $\{Mo_{154}\}$  and  $\{Mo_{176}\}$  [3, 6] with large central cavities that can be easily modified by means of simple well-known chemical reactions (see Figure 14.4).
2. Spherical-shaped clusters of the type  $[(pent)_{12}(link)_{30}]$  [3, 5, 8] with nanoscaled tunable cavities and tunable pores (see Figure 14.2).
3. Torus-shaped clusters of the type  $\{Mo_{57}M_6\}$  [3a] with potential functional indentations on the cluster surface (see Figure 14.1 right).

The *giant wheel molybdenum-oxide based anions* can be considered as objects which show a variety of nanoscale structural functionalities (“nanostructured landscape”) not only allowing reactions at a variety of well-defined centres/groups but also offering the option of acting as potential nano-reactors or -containers. Some relevant reactions are:

- The substitution of  $H_2O$  ligands coordinated to the molybdenum centres of  $\{Mo_{154}\}$  by ambivalent and/or multivalent ligands, for example the amino acid cystine can be coordinated to the inner wall of the cluster cavity and hence creates hydrophobic and hydrophilic surroundings with different functionalities (see Figure 14.7) [9].



**Fig. 14.6.** Forms with positively and negatively curved surfaces: the sphere (top) and the outer part of a torus (bottom left) are examples of surfaces exhibiting positive curvatures, the saddle (bottom right) and the inner part of the torus (bottom left) representing negative curvatures.

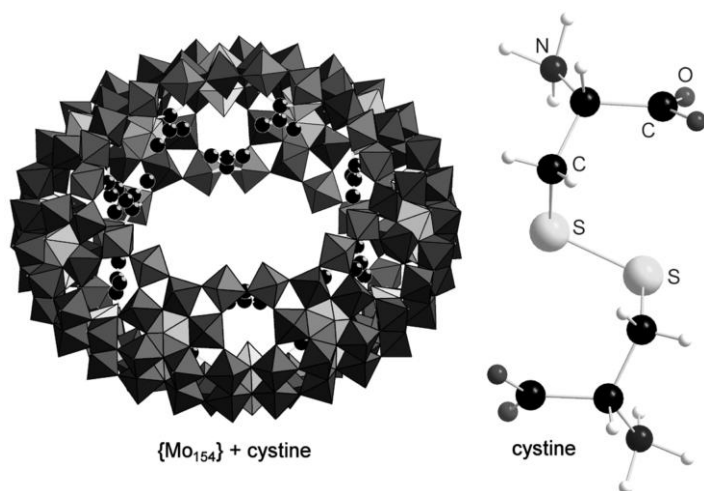


**Fig. 14.7.** Endohedral functionalization of the inner surface of a wheel-shaped  $\{Mo_{154}\}$  type nanocluster by cystine ligands (polyhedral representation, carboxylate group in ball-and-stick).



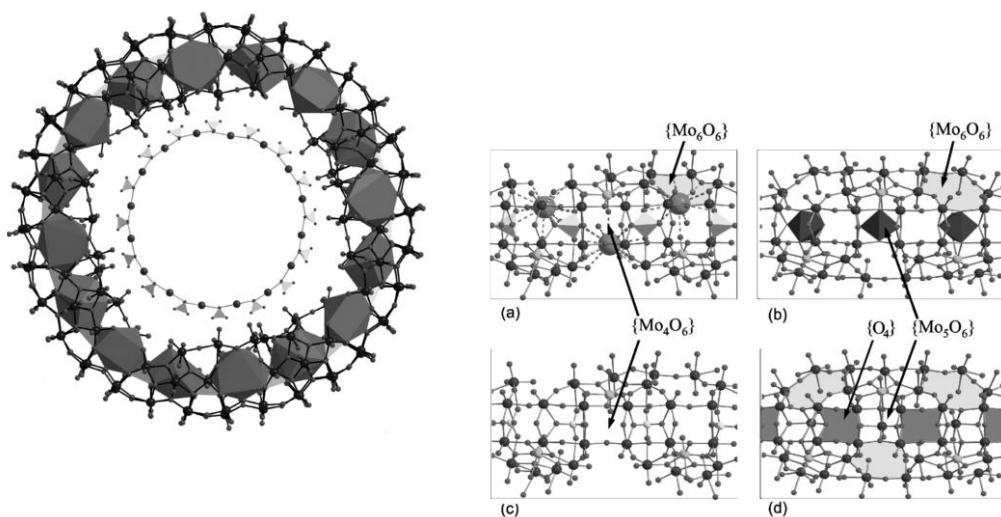


**Fig. 14.8.** Left: structure of  $[\text{Mo}^{\text{VI}}_{114}\text{Mo}^{\text{V}}_{32}\text{O}_{429}(\text{H}_2\text{O})_{50}(\text{KSO}_4)_{16}]^{30-}$  cluster anion and separately of the integrated  $[\text{KSO}_4]_{16}$  ring on a smaller scale in the centre (top view) in crystals of  $\text{K}_{14}\text{Na}_{16}[\text{Mo}^{\text{VI}}_{114}\text{Mo}^{\text{V}}_{32}\text{O}_{429}(\text{H}_2\text{O})_{50} \cdot (\text{KSO}_4)_{16}] \cdot \text{ca. } 500 \text{ H}_2\text{O}$  in ball-and-stick representation showing the  $\text{KO}_{11}$  units in polyhedral representation to demonstrate the overall K environment (see [10] for further details). Right ((b), (d)): demonstration of the multitude of adjacent receptors (forming a zigzag ring) for  $16 \text{ K}^+$  ( $\{\text{Mo}_6\text{O}_6\}$

receptors (light gray, indicated by an arrow in (a) and (b)) and  $16 \text{ SO}_4^{2-}$  ions (sites between  $\{\text{Mo}_5\text{O}_6\}$  compartments schematically emphasized in gray, indicated by an arrow and  $\{\text{O}_4\}$  in (d)); furthermore, the change from the “classical”  $\{\text{Mo}_2\text{Mo}_8\text{Mo}_1\}_n$  type ((b), (d)) [6] to the  $\{\text{Mo}_2\}_{n-x}\{\text{Mo}_8\}_n$  type ((a), (c)) ring structure with the change of the  $\{\text{Mo}_5\text{O}_6\}$  [6] to the  $\{\text{Mo}_4\text{O}_6\}$  unit by a release of  $\{\text{Mo}_1\}$  is demonstrated ( $\{\text{Mo}_1\}$  dark gray octahedra in (b);  $\text{SO}_4^{2-}$  light gray tetrahedra,  $\text{K}^+$  emphasized in (a) as large gray spheres).

- The (larger) hexadecameric  $\{\text{Mo}_{176}\}$  type cluster also shows a similar variety of functionalities and even a manifold of  $(16 + 16)$  non-equivalent (formal) receptor sites for cations as well as anions allowing, for example, the formation of a novel extremely complex supramolecular host–guest system while integrating  $16 \text{ K}^+$  and  $16 \text{ SO}_4^{2-}$  ions, thus leading to the formation of an unusual encapsulated 64-membered zigzag ring system (see Figure 14.8) [10].
- Paramagnetic metal centres like  $\text{Cu}^{2+}$  ions can be incorporated into the cavities spanned by four O atoms and having the appropriate size, for example in case of the  $\{\text{Mo}_{154}\}$ -type rings. This type of reaction can lead to the formation of nano-objects with unique neutral magnetic properties [11].
- The “addition” of two neutral  $\{\text{Mo}_{36}\}$ -type ‘hub-caps’ to the surface inside the cavity of the  $\{\text{Mo}_{176}\}$ -type wheel leads to the formation of a  $\{\text{Mo}_{248}\}$  cluster and corresponds to a nucleation process under boundary conditions [3a] (see Figure 14.9). This reaction can be regarded as a model for both *crystal growth*, especially for the related *initial nucleation* process, which is still not clearly understood, and also for *metal-centre uptake* processes in biological systems. In particular, such

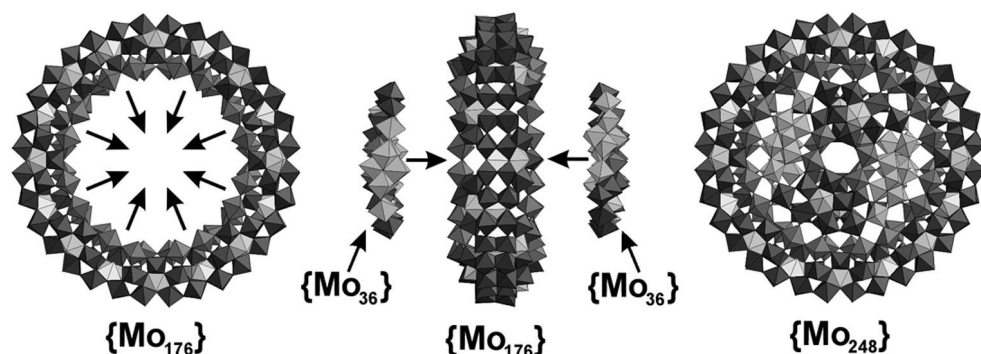


Fig. 14.9. Addition of two  $\{Mo_{36}\}$  'hub-caps' to the inner surface of the  $\{Mo_{176}\}$  type wheel leading to the formation of the  $\{Mo_{248}\}$  cluster.

growth processes might be allied to *biomineralization processes in compartments*. In this context the molybdenum-atom uptake of the Mo storage protein of the  $N_2$ -fixing microorganism *A. vinelandii* is worth mentioning. According to our preliminary results the inorganic nucleus corresponds to a rather large polyoxomolybdate.

- The nucleophilic  $\{Mo_6O_6\}$  type hexagonal ring-shaped sites act as (formal) receptors for cations, for example protonated urea guests [12b], to some extent a comparable situation to the above-mentioned case of the integrated 16  $K^+$  [10]. In the urea case this can be used to decrease the negative charge thereby nicely facilitating chain formation [12b], a fact which shows perspectives for related *nano-, supramolecular-, and solid-state chemistry*.

In the case of the *spherical nano-objects* (Table 14.1), formed by 12 pentagonal  $\{(Mo)Mo_5\}$  units linked by 30 mono- or dinuclear linkers, there is, for each species, a nanoscaled capsule cavity and 20 size-tunable specific nanopores of the type  $\{M_nO_n\}$  (for example with  $n = 6$  or 9), which can act as substrate specific receptors [8]. The cavity can even house smaller polyoxometalates, like different Keggin ions, to form a supramolecular nanocomposite of a unique kind (see Figure 14.10) [13]. Some typical interesting reactions are:

- The replacement of the 30 diamagnetic  $\{Mo_2\}$ -type linkers of the spherical  $\{Mo_{132}\}$ -type clusters by 30 paramagnetic centres like  $Fe^{III}$  leads to the emergence of unusual molecular nanoantiferromagnets of the type  $\{Mo_{72}Fe_{30}\}$  (see Figures 14.2 and 14.11) [14].
- The neutral spherical nano-objects of the type  $\{Mo_{72}Fe_{30}\}$  can be crosslinked in a solid-state reaction, even at room temperature (!), to form layers by following an elementary inorganic condensation reaction, known already for the formation of polycations like those of  $Fe^{III}$  in aqueous solution. The rapid loss of water molecules from the freshly filtered crystals, comprising discrete spheri-

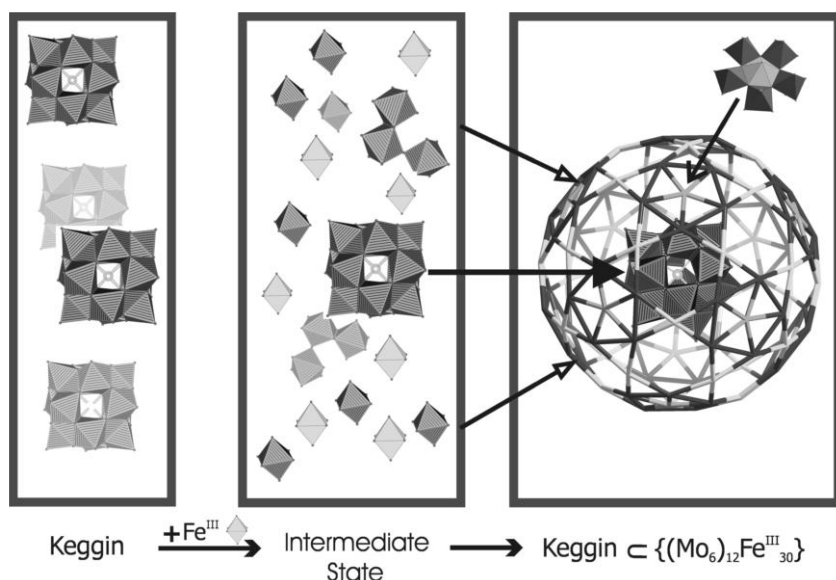


**Fig. 14.10.** Reaction scheme showing the decomposition of a part of the Keggin anions  $\{\text{PMo}_{12}\text{O}_{40}\}^{3-}$  (left, polyhedral representation) in the presence of  $\text{Fe}^{3+}$  ions, leading finally to the formation of the  $\{[(\text{Mo})\text{Mo}_5]_{12}[\text{Fe}]_{30}\}$  type cage (wireframe representation of the capsule)

which has one of the remaining non-decomposed Keggin anions encapsulated (polyhedral representation) thereby forming the unusual supramolecular species with core–shell topology: guest  $\subset$  [(pent)<sub>12</sub>(link)<sub>30</sub>].

cal clusters, leads to their approach which is a condition for their covalent linking (see Figure 14.12) [15]. The possibility of forming a related one-dimensional chain (paramagnetic Keplerate “necklaces”) from similar spherical nanospheres in a room-temperature reaction also exists [16].

- It is even possible to ‘kick out’, like soccer balls, the neutral giant molybdenum oxide spheres, for example the  $\{\text{Mo}_{72}\text{Fe}_{30}\}$  ones, into the gas phase using all matrix-assisted laser desorption and ionization (MALDI) methods. It is important that the clusters range from dimers to pentamers (see Figure 14.13) [17].

A further fascinating point refers to the possibility of performing different types of reactions inside the cavities of such spherical clusters at well-defined sites, which can be hydrophilic or hydrophobic. Here we describe for the first time an example, the details of which have, as yet, not been published: the reaction of  $\{[(\text{Mo}^{\text{VI}})\text{Mo}_5]_{12}[\text{L}]_{30}\}^{42-}$  ( $\text{L} = \{\text{Mo}_2\text{O}_4(\text{CH}_3\text{COO})\}^+$ ) with phosphate and molybdate in aqueous solution at different pH values demonstrates that, after replacement of the acetate ligands, the cluster shows in its cavity a pH-dependent nucleation process in the presence of molybdate. This leads to the formation of new P–O–Mo bonds at low pH, a situation comparable to the formation of the  $[\text{PMo}_{12}\text{O}_{40}]^{3-}$  Keggin anion at low pH values [18] (see also Figure 14.14).

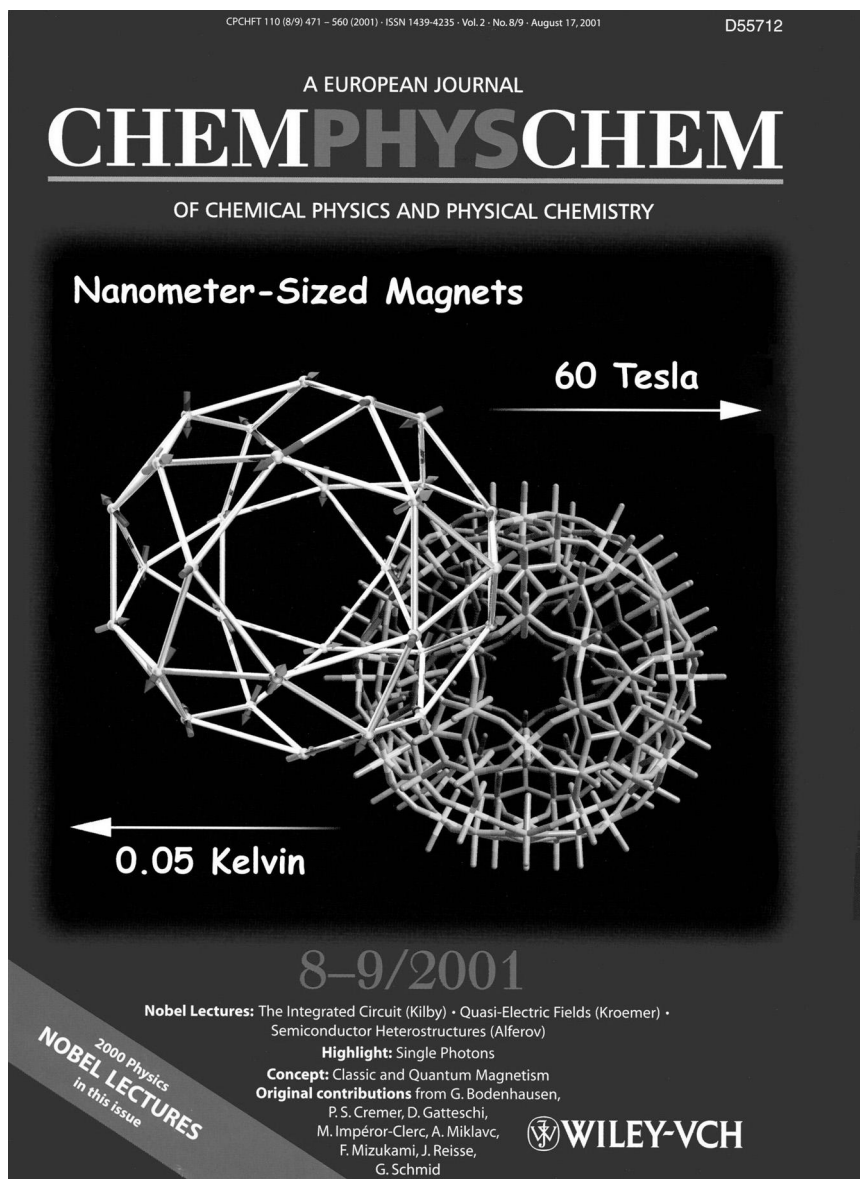


**Fig. 14.11.** Nanomagnet as a classical magnet en miniature on the cover-page of *ChemPhysChem*. The  $\{(\text{Mo})\text{Mo}_5\}_{12}\{\text{Fe}\}_{30}$  cluster (see also Figure 14.2) in two representations, including one showing the orien-

tation of the spins at the  $\text{Fe}^{\text{III}}_3$  triangles was, because of its unusual properties, studied at very low temperature (there it still behaves as a classical magnet) and extremely high magnetic field strength.

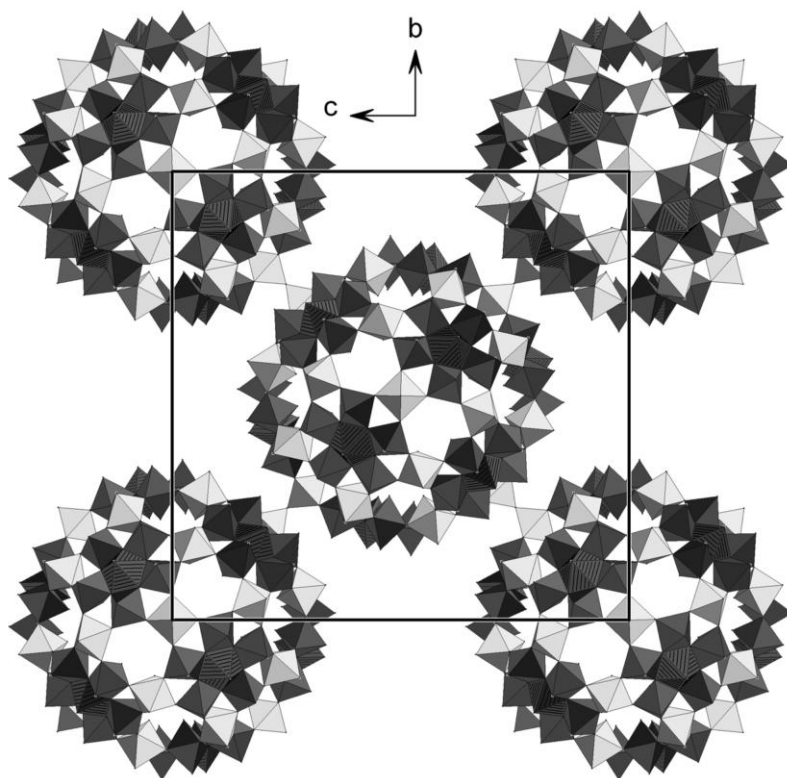


**Fig. 14.12.** Crosslinking neutral spherical nanoclusters of the type  $[(\text{Mo})\text{Mo}_5]_{12}[\text{Fe}^{\text{III}}]_{30}$  via  $\text{FeO}_6$  octahedra sharing corners, leads to the formation of a layered structure based on an unusual solid-state reaction at room temperature.

All these spherical clusters can be described, as mentioned above, as  $[(\text{Mo})\text{Mo}_5]_{12}(\text{link})_{30}$ . It was suggested to call them ‘Keplerates’ because of their striking similarity to a fragment of Kepler’s early speculative model of the universe, as described in his opus *Mysterium Cosmographicum* (see Figure 14.15). The related Keplerate type chemistry is especially interesting for mathematicians [3c]. Furthermore, these clusters also show, topologically speaking, a similarity to spherical viruses (Figure 14.16).

#### 14.4

#### Perspectives for Materials Science and Nanotechnology: En Route to Spherical-Surface, Nanoporous-Cluster, and Super-Supramolecular Chemistry including the Option of Modelling Cell Response

The clusters described above are interesting for materials science and nanotechnology aspects because of their *stability*, *size*, *solubility* (in several solvents), *giant*

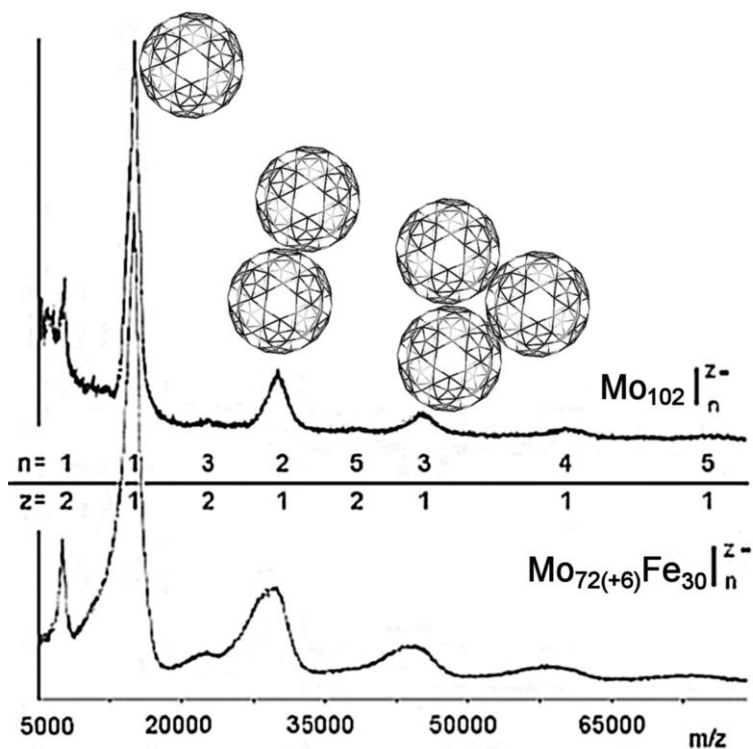


Fig. 14.13. Unique nanocluster aggregates in the gas phase: MALDI mass spectra showing the neutral clusters of the type  $\{\text{Mo}_{72}\text{Fe}_{30}\}$  and  $\{\text{Mo}_{102}\}$  and their oligomers.

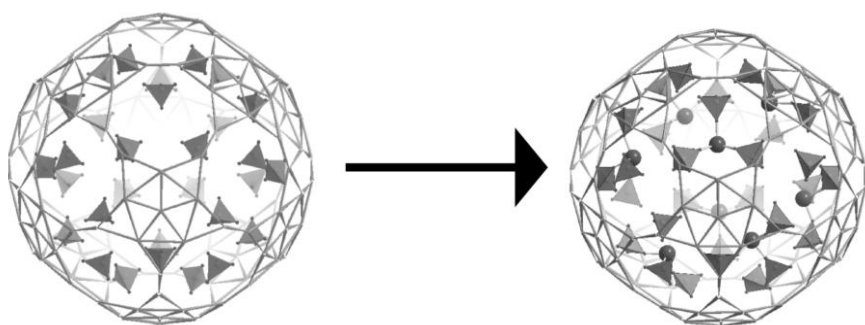


Fig. 14.14. pH controlled nucleation in nanoscaled cluster cavities: the cluster  $\{[(\text{Mo}^{\text{VI}})\text{Mo}^{\text{VI}}_5]_{12}[\text{L}]_{30}\}$  with  $\text{L} = \text{phosphate}$  (gray tetrahedra left) shows in the presence of

molybdate in solution and by lowering the pH to nearly 2 a 'nucleation' process inside the cluster cavities with the formation of P-O-Mo bonds (new  $\{\text{MoO}_3\}$  units gray spheres).



D 3461

# ANGEWANDTE CHEMIE

A Journal of the  
Gesellschaft  
Deutscher Chemiker

INTERNATIONAL EDITION

**1998  
37/24**



**Review:** Dynamic Behavior of Reactive Intermediates  
**Highlights:** Crystallography of Mid-Sized Molecules • Methane Oxidation

Index Issue

 **WILEY-VCH**

ACIEF5 37 (24) 3329–3516 (1998) · ISSN 1433–7851 · Vol. 37 · No. 24 · January 4, 1999

**Fig. 14.15.** Nano- and macrocosmos/universe similarities: schematic representation of the  $\{\text{Mo}_{132}\}$  type cluster on the cover-page of *Angew. Chem.*, highlighting its similarity to Kepler's early model of the universe and

"abundance" of related icosahedra in both cases. Important: it was the starting point for the consideration of Keplera type nanochemistry from a topological point of view (see [3c]).

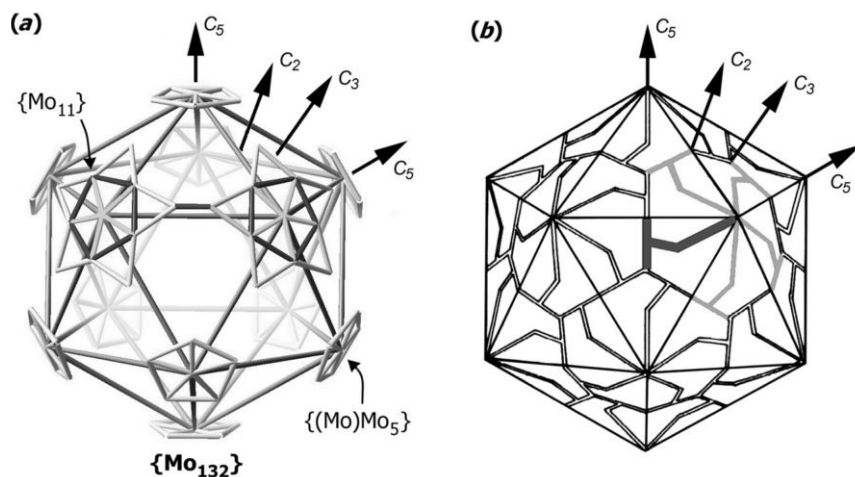


**Fig. 14.16.** Nanoscaled systems of the biosphere and of chemistry show the same topology: schematic representation of the icosahedron spanned by the 12 centres of the  $\{(Mo)Mo_5\}$  units of the  $\{Mo_{132}\}$  type cluster (a) and of the satellite tobacco necrosis virus (STNV) with the triangulation number  $T = 1$

(see for example [3a]) highlighting one of the 60 protomers (dark gray) (b). Two  $\{Mo_{11}\}$  units in (a), each formed by the  $\{(Mo)Mo_5\}$  groups and the five related Mo centres of the five neighbouring  $\{MoV_2O_4\}^{2+}$  linkers, are highlighted.

cavities, ‘nanosized’ changeable pores, unique surfaces, unusual electronic structures, and last but not least abundance of magnetic centres in a variety of topologies. Moreover, most of the clusters, especially the spherical ones, can be manipulated whilst keeping the robust nanoscopic oxomolybdate skeleton intact. Encapsulation of the giant clusters with surfactant molecules allows one to produce LB films and monolayers. Some of these even form a new type of vesicle perhaps with the option of getting information about the structure of liquid water. A summary of these and other relevant aspects is presented in Table 14.2; for further details see the collection of papers in [19].

A recent challenge in nanotechnology is to mimic the material constructions and molecular-recognition-type responsive sensing of biological systems. Intracellular response to extracellular signals involves signal transduction via molecular recognition of the specific receptors on the cell surface, which can trigger enzymatic reactions in the cell. Such a “cognitive isomorphism” on a molecular level, a rare phenomenon in classical chemistry, is, for example, of immense importance for understanding the complex dynamics of ‘uptake and release’ of substrates in general.

The nanoball of the type  $\{Mo_{132}\}$  shows such molecule-response activity. It can be compared to a ‘nanosponge’ with a multitude of open pores accessible for a specific substrate, for example, guanidinium cation guests in the case of  $\{Mo_{132}\}$



**Tab. 14.2.** Nanoscaled polyoxometalate clusters for materials science problems.

Topics/Keywords	Characteristics	References
LB films	Based on encapsulation of $\{\text{Mo}_{132}\}$ with cationic surfactants	19c
Monolayers	Based on encapsulation of $\{\text{Mo}_{132}\}$ with cationic surfactants	19c
Liquid crystals	Based on encapsulation of $\{\text{Mo}_{154}\}$ with cationic surfactants	19g
Hybrid materials with silica and carbon tubes	Based on integration of $\{\text{Mo}_{154}\}$ and $\{\text{Mo}_{132}\}$ clusters	19f, 19h
Nanoporous clusters with cavities	Ball-shaped clusters with pores are highly selective for cations and allow the incorporation of clusters and important aggregates, for example of water molecules including those with electrolytes	8, 13, 21*
Nanoreactors	Wheel-shaped clusters show functionalities and especially nucleation processes inside their central nanoscaled cavity	3a**
Soft matter: aggregates, vesicles, colloids	Giant clusters show hierarchic patterning in solution and lead to a new type of vesicles	19j, 19k, 19l
Clusters as magnets	$\{\text{Mo}_{75}\text{V}^{\text{IV}}_{20}\}$ with 10 $\text{V}^{\text{IV}}$ triangles linked $\{\text{Mo}_{72}\text{Fe}^{\text{III}}_{30}\}$ is a model for a classical magnet $\{\text{V}^{\text{IV}}_{15}\}$ shows a layered magnetic structure	3a, 3c, 14***

\* A. Müller, B. Botar, H. Bögge et al., A Potassium Selective 'Nanosponge' with Well Defined Pores, *Chem. Commun.* **2002**, 2944–2945.

\*\* A. Müller, S. Q. N. Shah, H. Bögge et al., Molecular Growth from a  $\text{Mo}_{176}$  to a  $\text{Mo}_{248}$  cluster, *Nature* **1999**, 397, 48–50.

\*\*\* Several sophisticated physical studies of the  $\text{V}_{15}$  cluster have been published, for example: I. Chiorescu, W. Wernsdorfer, A. Müller et al., Butterfly Hysteresis Loop and Dissipative Spin Reversal in the  $S = 1/2$ ,  $\text{V}_{15}$  Molecular Complex, *Phys. Rev. Lett.* **2000**, 84, 3454–3457; B. Barbara, I. Chiorescu, W. Wernsdorfer et al., The  $\text{V}_{15}$  Molecule, a Multi-Spin Two-Level System: Adiabatic LZS Transition with or without Dissipation and Kramers Theorem, *Progr. Theor. Phys. Suppl.* **2002**, 145, 357–369.

(Figure 14.17). The suction of substrates into this 'nanosponge', while simultaneously closing the pores, essentially triggers a restructuring of the incarcerated solvent molecules, a situation formally comparable to the mentioned intracellular response to an extracellular stimulus. Moreover, as different types of substrates can interact with different types of capsule pores, i.e. on a specific spherical nanosurface, the situation might be noted as the beginning of an era of *nanoscaled spherical-surface chemistry*. Additionally, since the pore sizes of the clusters can be varied and

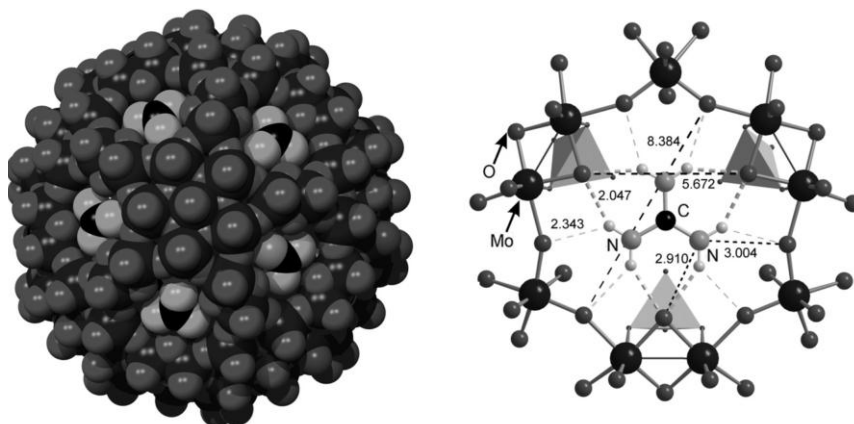


**Fig. 14.17.** The 20 pores of a spherical nanocluster of the type  $\{\text{Mo}_{132}\}$  can be closed through substrate uptake. Right: one  $\{\text{Mo}_9\text{O}_9\}$  pore with encapsulated guanidinium cations in ball-and-stick representation ( $\text{PO}_2\text{H}_2^-/\text{SO}_4^{2-}$

ligands shown as tetrahedra). Left: space-filling model of the cluster with inserted guanidinium cations (only  $\text{CN}_3^+$  part shown). Closing the pores leads to a structural reorganization of the encapsulated water molecules.

show correspondingly different reactivities, we can also refer to a new type of *nanoporous-cluster chemistry* and, because of the large number of receptors involved (20 in the case of icosahedral spheres), to a *super-supramolecular chemistry*. In this connection recent unpublished  $^1\text{H}$  NMR investigations have revealed that the uptake and release of ‘guanidinium’ substrates in solution by the ‘nanosponge’ shows an interesting temperature dependence corresponding to an open-and-shut process [20].

An aspect of particular relevance refers to the exciting problem of the structure of liquid water. The closing of the cluster’s ‘nanowindow’ leads, in the case of the  $\{\text{Mo}_{132}\}$  cluster, to the reorganization of the internal  $\text{H}_2\text{O}$  molecules into a giant and structurally well-defined  $(\text{H}_2\text{O})_{100}$  cluster which can perhaps be considered as a snapshot of liquid water (see [8, 21] and Figures 14.18 and 14.19). (The endohedral clusterization of water molecules upon substrate uptake into the pores formally corresponds to the cellular response to an extracellular stimulus on the cell surface.) Our special endohedral clusterization of water molecules would certainly have pleased both Plato and Archimedes as the water cluster can be formally (!) arranged in shells showing a larger and smaller dodecahedron, each composed of a  $(\text{H}_2\text{O})_{20}$  segment and one rhombicosidodecahedron  $(\text{H}_2\text{O})_{60}$  [8, 21]. This example shows that with the present nanocontainers, available for the encapsulation of segments of different kinds of (macroscopic) substances and even rather large molecular systems, problems of tremendous importance for contemporary nanoscience can be solved. Even perhaps the liquid water problem which has been characterized as “*The most important problem in science that hardly anyone wants to solve*” [22].

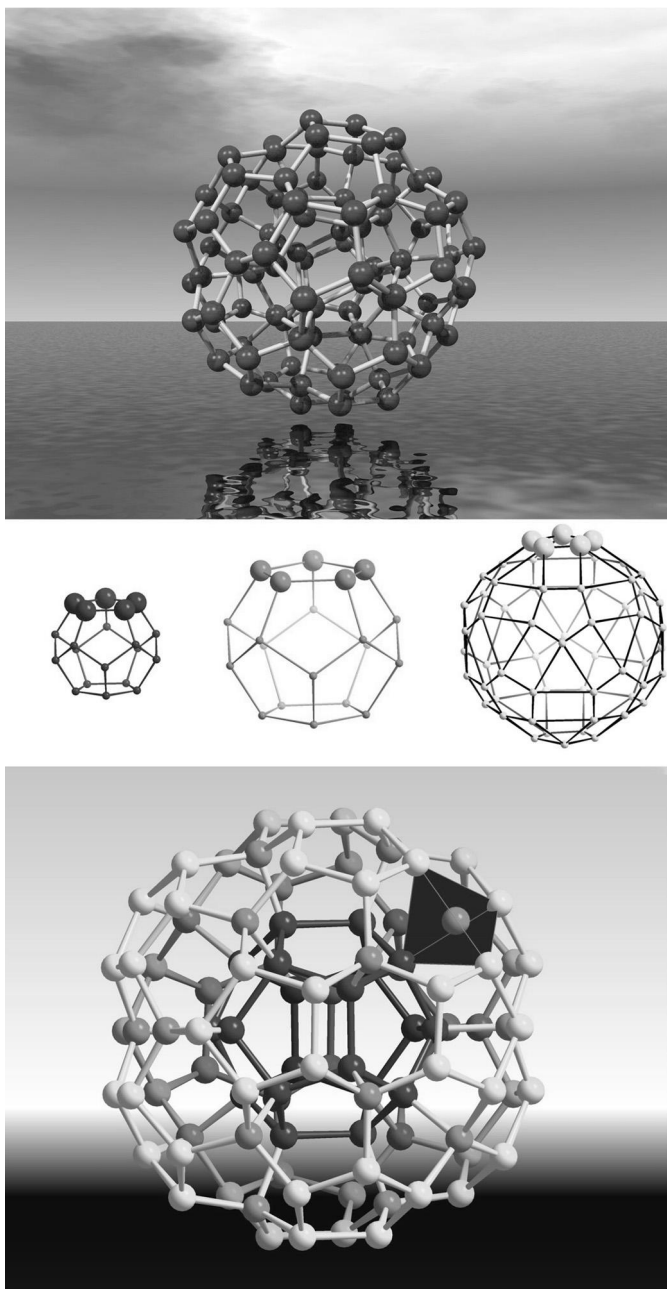


**Fig. 14.18.** A nanodrop of water found in the cavity of a  $\{\text{Mo}_{132}\}$  cluster (top) and the hierarchical structure of the  $(\text{H}_2\text{O})_{100}$  assembly showing two Platonic (a larger and a smaller  $(\text{H}_2\text{O})_{20}$  dodecahedron) and one  $(\text{H}_2\text{O})_{100}$  Archimedean solid in a formal consideration (middle). One tetrahedrally coordinated O atom as in liquid water is also emphasized (bottom).

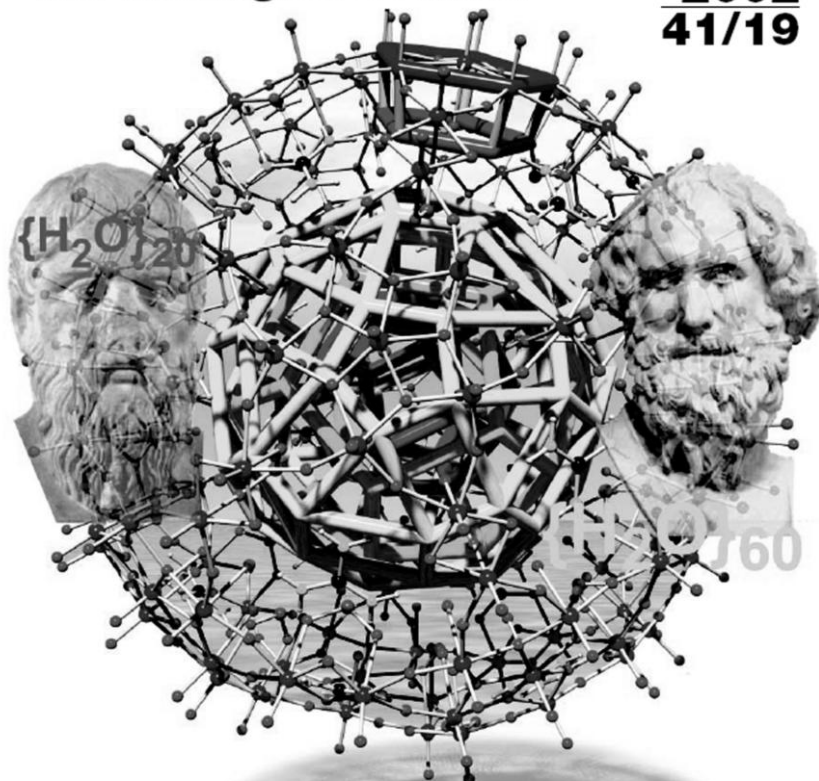
# ANGEWANDTE CHEMIE

A Journal of the  
Gesellschaft  
Deutscher Chemiker

INTERNATIONAL EDITION

**2002**  
**41/19**

ANGEWANDTE CHEMIE INTERNATIONAL EDITION 2002, Number 19, Pages 0000-0000



**WILEY-VCH**

Reviews: Lanthanide Complexes in Asymmetric Synthesis •  
Metalloid Aluminum and Gallium Clusters  
Highlights: Carbohydrate Arrays • Metal-Free Aziridination

ACIEF 5 41 (19) 0000-0000 (2002) · ISSN 1433-7851 · Vol. 41 · No. 19 · October 4, 2002

**Fig. 14.19.** A result of modern nanochemistry: (formally) in the form of shells, that is two Plato and Archimedes look pleased viewing the nanodrop of water  $\{H_2O\}_{100}$  inside a molybdenum-oxide 'nanosponge' occurring  $(H_2O)_{20}$  dodecahedra and a rhombicosidodecahedron  $(H_2O)_{60}$ . Note, as in liquid water all  $O \cdots O$  distances are of the order of 2.7 Å.

## Acknowledgments

We thank Dr. H. Bögge (Bielefeld) for his collaboration. The financial support of the Deutsche Forschungsgemeinschaft, the Fonds der Chemischen Industrie, the Volkswagenstiftung, and the European Commission is gratefully acknowledged. S. R. thanks the Graduiertenkolleg 'Strukturbildungsprozesse', Bielefeld University, for a fellowship.

## References

- 1 Cited according to A. ANZENBACHER, *Einführung in die Philosophie*, Herder, Freiburg 1992, p. 87.
- 2 (a) L. STRYER, *Biochemistry*, Freeman, New York 1988; see also: (b) H. G. SCHLEGEL, *Allgemeine Mikrobiologie*, Thieme, Stuttgart, 7. Auflage, 1992.
- 3 (a) A. MÜLLER, P. KÖGERLER, C. KUHLMANN, A Variety of Combinatorially Linkable Units as Disposition: From a Giant Icosahedral Keplerate to Multi-Functional Metal-Oxide Based Network Structures, *Chem. Commun.* **1999**, 1347–1358 and literature cited therein; (b) A. MÜLLER, S. ROY, En Route from the Mystery of Molybdenum Blue via Related Manipulable Building Blocks to Aspects of Materials Science, *Coord. Chem. Rev.* in press; (c) A. MÜLLER, P. KÖGERLER, A. W. M. DRESS, Giant Metal-Oxide-Based Spheres and Their Topology: From Pentagonal Building Blocks to Keplerates and Unusual Spin Systems, *Coord. Chem. Rev.* **2001**, 222, 193–218 and literature cited therein.
- 4 A. MÜLLER, E. BECKMANN, H. BÖGGE et al., Inorganic Chemistry Goes Protein Size: A Mo<sub>368</sub> Nano-Hedgehog Initiating Nanochemistry by Symmetry Breaking, *Angew. Chem. Int. Ed. Engl.* **2002**, 41, 1162–1167.
- 5 A. MÜLLER, P. KÖGERLER, H. BÖGGE, Pythagorean Harmony in the World of Metal Oxygen Clusters of the {Mo<sub>11</sub>} Type: Giant Wheels and Spheres both Based on a Pentagonal Type Unit, *Struct. Bonding* **2000**, 96, 203–236 and literature cited therein.
- 6 A. MÜLLER, C. SERAIN, Soluble Molybdenum Blues – “des Pudels Kern”, *Acc. Chem. Res.* **2000**, 33, 2–10 and literature cited therein.
- 7 (a) A. MÜLLER, H. REUTER, S. DILLINGER, Supramolecular Inorganic Chemistry: Small Guests in Small and Large Hosts, *Angew. Chem. Int. Ed. Engl.* **1995**, 34, 2328–2361 and literature cited therein; (b) A. MÜLLER, F. PETERS, M. T. POPE et al., Polyoxo-metalates: Very Large Clusters – Nanoscale Magnets, *Chem. Rev.* **1998**, 98, 239–271 and literature cited therein.
- 8 A. MÜLLER, E. KRICKEMEYER, H. BÖGGE et al., Changeable Pore Sizes Allowing Effective and Specific Recognition by a Molybdenum-Oxide Based “Nanosponge”: En Route to Sphere-Surface and Nanoporous-Cluster Chemistry, *Angew. Chem. Int. Ed. Engl.* **2002**, 41, 3604–3609.
- 9 A. MÜLLER, S. K. DAS, C. KUHLMANN et al., On the Option of Generating Novel Type Surfaces with Multiphilic Ligands within the Cavity of a Giant Metal-Oxide Based Wheel Type Cluster: Chemical Reactions with Well-Defined Nanoobjects, *Chem. Commun.* **2001**, 655–656.
- 10 A. MÜLLER, L. TOMA, H. BÖGGE et al., Synergetic Activation of “Silent Receptor” Sites Leading to a New Type of Inclusion Complex: Integration of a 64-Membered Ring Comprising K<sup>+</sup> and SO<sub>4</sub><sup>2-</sup> Ions into a Molybdenum Oxide-Based Nanoobject, *Chem. Commun.* **2003**, 2000–2001.
- 11 A. MÜLLER, E. KRICKEMEYER, H. BÖGGE et al., “Nanoobjects” by Self-

- Assembly Concomitant with Modifications under Alterable Boundary Conditions: Incorporation of Paramagnetic Metal Centers ( $\text{Cu}^{2+}$ ) in Ring-Shaped Molybdenum-Oxide Based Clusters, *Angew. Chem. Int. Ed. Engl.* **2001**, 40, 4034–4037.
- 12 (a) A. MÜLLER, S. Q. N. SHAH, H. BÖGGE et al., Molecular Growth from a  $\text{Mo}_{176}$  to a  $\text{Mo}_{248}$  Cluster, *Nature* **1999**, 397, 48–50; (b) A. MÜLLER, S. ROY, M. SCHMIDTMANN et al., Urea as “Deus ex Machina” in Giant Molybdenum Blue Type Cluster Synthesis: An Unusual Hybrid Compound with Perspectives for Related Nano, Supramolecular and Extended Structures, *Chem. Commun.* **2002**, 2000–2002.
  - 13 A. MÜLLER, S. K. DAS, P. KÖGERLER et al., A New Type of Supramolecular Compound: Molybdenum-Oxide-Based Composites Consisting of Magnetic Nanocapsules with Encapsulated Keggin-Ion Electron Reservoirs Cross-Linked to a Two-Dimensional Network, *Angew. Chem. Int. Ed. Engl.* **2000**, 39, 3413–3417.
  - 14 (a) A. MÜLLER, M. LUBAN, C. SCHRÖDER et al., Classical and Quantum Magnetism in Giant Keplerate Magnetic Molecules, *ChemPhysChem. (Concepts)* **2001**, 2, 517–521; see also: (b) A. MÜLLER, S. SARKAR, S. Q. N. SHAH et al., Archimedean Synthesis and Magic Numbers: “Sizing” Giant Molybdenum-Oxide-Based Molecular Spheres of the Keplerate Type, *Angew. Chem. Int. Ed. Engl.* **1999**, 38, 3238–3241; (c) D. GATTESCHI, R. SESSOLI, A. MÜLLER et al., in *Polyoxometalate Chemistry: From Topology via Self-Assembly to Applications*, eds. M. T. POPE, A. MÜLLER, Kluwer, Dordrecht **2001**, p. 319.
  - 15 A. MÜLLER, E. KRICKEMEYER, S. K. DAS et al., Linking Icosahedral, Strong Molecular Magnets  $\{\text{Mo}^{\text{VI}}_{72}\text{Fe}^{\text{III}}_{30}\}$  to Layers – A Solid-State Reaction at Room Temperature, *Angew. Chem. Int. Ed. Engl.* **2000**, 39, 1612–1614.
  - 16 A. MÜLLER, S. K. DAS, M. TALISMANOVA et al., Paramagnetic Keplerate “Necklaces” Synthesized by a Novel Room-Temperature Solid-State Reaction: Controlled Linking of Metal-Oxide-Based Nanoparticles, *Angew. Chem. Int. Ed. Engl.* **2002**, 41, 579–582.
  - 17 A. MÜLLER, E. DIEMANN, S. Q. N. SHAH et al., Soccer-Playing Metal Oxide Giant Spheres: A First Step Towards Patterning Structurally Well Defined Nano-Object Collectives, *Chem. Commun.* **2002**, 440–441.
  - 18 A. MÜLLER, S. K. DAS, E. BECKMANN et al., unpublished results.
  - 19 (a) D. G. KURTH, P. LEHMANN, D. VOLKMER et al., Surfactant-Encapsulated Clusters (SECs):  $(\text{DODA})_{20}(\text{NH}_4)[\text{H}_3\text{Mo}_{57}\text{V}_6(\text{NO})_6\text{O}_{183} \cdot (\text{H}_2\text{O})_{18}]$ , a Case Study, *Chem. Eur. J.* **2000**, 6, 385–393; (b) D. G. KURTH, D. VOLKMER, M. RUTTORF et al., Ultrathin Composite Films Incorporating the Nanoporous Isopolyoxomolybdate “Keplerate”  $[(\text{NH}_4)_{42}[\text{Mo}_{132}\text{O}_{372}(\text{CH}_3\text{COO})_{30} \cdot (\text{H}_2\text{O})_{72}]]$ , *Chem. Mater.* **2000**, 12, 2829–2831; (c) D. G. KURTH, P. LEHMANN, D. VOLKMER et al., Biologically Inspired Polyoxometalate–Surfactant Composite Materials. Investigations on the Structures of Discrete, Surfactant-Encapsulated Clusters, Monolayers, and Langmuir–Blodgett Films of  $(\text{DODA})_{40}(\text{NH}_4)_2 \cdot [(\text{H}_2\text{O})_n \subset \text{Mo}_{132}\text{O}_{372}(\text{CH}_3\text{CO}_2)_{30} \cdot (\text{H}_2\text{O})_{72}]$ , *J. Chem. Soc., Dalton Trans.* **2000**, 3989–3998; (d) F. CARUSO, D. G. KURTH, D. VOLKMER et al., Ultrathin Molybdenum Polyoxometalate–Polyelectrolyte Multilayer Films, *Langmuir* **1998**, 14, 3462–3465; (e) D. VOLKMER, A. DU CHESNE, D. G. KURTH et al., Toward Nanodevices: Synthesis and Characterization of the Nanoporous Surfactant-Encapsulated Keplerate  $(\text{DODA})_{40}(\text{NH}_4)_2[(\text{H}_2\text{O})_n \subset \text{Mo}_{132}\text{O}_{372}(\text{CH}_3\text{COO})_{30}(\text{H}_2\text{O})_{72}]$ , *J. Am. Chem. Soc.* **2000**, 122, 1995–1998; (f) S. POLARZ, B. SMARSLY, C. GÖLTNER et al., The Interplay of Colloidal Organization and Oxo-Cluster Chemistry: Polyoxometalate–Silica Hybrids – Materials with a Nanochemical Function, *Adv. Mater.* **2000**, 12, 1503–1507; (g) S. POLARZ, B.

- SMARLY, M. ANTONIETTI, Colloidal Organization and Clusters: Self-Assembly of Polyoxometalate-Surfactant Complexes towards Three-Dimensional Organized Structures, *ChemPhysChem*. **2001**, 2, 457–461; (h) L. AN, J. M. OWENS, L. E. McNEIL et al., Synthesis of Nearly Uniform Single-Walled Carbon Nanotubes Using Identical Metal-Containing Molecular Nanoclusters as Catalysts, *J. Am. Chem. Soc.* **2002**, 124, 13688–13689; (i) D. GATTESCHI, L. PARDI, A. L. BARRA et al., Layered Magnetic Structure of a Metal Cluster Ion, *Nature* **1991**, 354, 463–465; (j) T. LIU, Supramolecular Structures of Polyoxomolybdate-Based Giant Molecules in Aqueous Solution, *J. Am. Chem. Soc.* **2002**, 124, 10942–10943; (k) T. LIU, A. MÜLLER et al., Self-Assembly in Aqueous Solution of Wheel-Shaped Mo<sub>154</sub> Oxide Clusters into Vesicles, *Nature* **2003**, in press; (l) A. MÜLLER, E. DIEMANN, C. KUHLMANN et al., Hierarchic Patterning: Architectures Beyond ‘Giant Molecular Wheels’, *Chem. Commun.* **2001**, 1928–1929.
- 20** A. MÜLLER, S. ROY, A. MIX et al., unpublished results.
- 21** A. MÜLLER, H. BÖGGE, E. DIEMANN, Structure of a Cavity Encapsulated Nanodrop of Water, *Inorg. Chem. Commun.* **2003**, 6, 52–53.
- 22** C. H. CHO, S. SINGH, G. W. ROBINSON, Liquid Water and Biological Systems: The Most Important Problem in Science that Hardly Anyone Wants to Solve, *Faraday Discuss.* **1996**, 103, 19–27.



## 15

**Nanostructured Polymers***S. Ramakrishnan***Abstract**

During the latter half of the 20th century, polymer chemists have successfully developed the necessary tools to control various molecular structural parameters in synthetic macromolecules, such as their molecular weight and polydispersity, regio- and stereo-regularity, topology of repeat unit connectivity, such as in the case of dendrimers, and to a limited extent even copolymer sequence distribution. However, the control over the next level of organization, namely chain conformation and the subsequent packing of chains in the macroscopic dimension, has proven to be a far more difficult task. Control of molecular organization in the nanometer dimensions and subsequent organization of these nanoscale entities could be one way to define nanostructured polymers. An alternative way to perceive this class of materials would be to disregard molecular-level structural order present in the sub-nanometer dimension and focus only on the generation of well-controlled nanometer-size polymeric objects, such as nanospheres, nanocapsules, nanofibres, nanotubes, etc. In this chapter I shall deal with both these aspects separately, and highlight, using recent examples, the various approaches that have been used to achieve this objective.

## 15.1

**Introduction**

Efforts at controlling molecular ordering at smaller and smaller dimensions are driven, on the one hand, by the immense potential technological implications and, on the other, by the desire to emulate the sheer beauty and elegance with which nature is able to control hierarchical structural organization, which spans over very wide length scales. Nanostructural control in synthetic polymeric systems implies the control of structure and dimension in the 1–100 nm size domain, although slightly larger sizes, up to several microns, have also often been included within this category. In synthetic polymeric systems, control of nanostructure has been achieved via two distinct approaches: one using *block copolymers* and the other



using *surfactants*. A number of reviews that discuss different aspects of both approaches to the generation of polymeric nanostructures have appeared recently [1–14]. Block copolymers form nanometer-size aggregates of various sizes and shapes, due to the intrinsic property of structurally dissimilar macromolecular segments to phase separate in bulk. They also form a variety of mesophases, ranging from micellar aggregates to more complex bicontinuous gyroid phases, when dissolved in an appropriate solvent (or solvent mixture), which functions as a *block-selective* solvent, i.e. a medium that serves as a good solvent for one block and a poor solvent for the other. Utilizing these phase-separated morphologies, in conjunction with domain-specific crosslinking strategies, a wide range of polymeric nanostructures have been generated. The second approach is based on the utilization of the rich variety of aggregate morphologies formed by surfactants. Here again, approaches either rely on direct fixation by polymerization of ordered nanometer-size phases formed by appropriately designed polymerizable surfactants, or they utilize selective partitioning of monomers within specific domains followed by polymerization to generate structures that mirror the original surfactant aggregate morphology. Both approaches, using block copolymers and surfactants, have received considerable attention during the past decade and will form the bulk of the discussions that follow.

Block copolymers, as will become evident, form one of the main underlying structural motifs in a variety of strategies to prepare nanostructured polymeric systems. This being the case, the first part of this chapter will discuss the underlying principles behind the preparation of block copolymers, together with a brief introduction to living polymerization methods, which are the most important synthetic tool for the generation of block copolymers. Different strategies for utilizing bulk phase-separated morphologies to generate nanostructures, ranging from nanofibers, nanotubes and nanochannels, will be highlighted. Similarly, approaches that utilize block-selective solvents to generate a rich variety of lyotropic phases, and approaches for their permanent fixation to generate macromolecular objects such as nanospheres and nanobubbles, will be discussed. Towards the end, exciting developments in surfactant-based strategies for the preparation of hollow nanospheres and nanoporous polymeric systems will be described.

## 15.2

### Macromolecular Structural Control

Unlike the organization of small molecules into crystalline lattices, polymeric molecules typically do not organize in an orderly fashion to form a macroscopic solid. This is due to the innumerable conformations of similar energies which long polymer chains can adopt. In turn, this leads to a topologically heterogeneous collection of molecular entities that cannot readily organize into a typical crystalline molecular solid. The problem is further compounded by yet another intrinsic constraint while dealing with synthetic polymers, which is the molecular structural heterogeneity that arises from the distribution of molecular weight (chain lengths),

structural irregularities due to regio- and stereochemical complexities, and monomer sequence distribution in the case of copolymers (polymers that contain more than one type of monomer unit). During the last few decades, many of these issues have been addressed to varying levels of perfection by clever manipulation of catalyst structure, polymerization temperature and other reaction conditions. Of these different structural heterogeneities, control of two factors, more than any other, has been crucial for the development of nanostructured polymers. These are: (i) the precise control of length of the polymer chain and, (ii) the generation of block copolymers, in which two (or more) types of monomers (repeat units) are sequence-segregated along the polymer backbone. Control of both these features has become possible because of the development of a special type of polymer-forming process termed “living polymerization” [15–17].

### 15.2.1

#### Living Polymerization

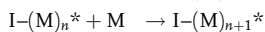
Living polymerizations are limited to the realm of chain-growth polymerizations, in which a monomer is transformed to a polymer by a reactive species (an initiator, I) via a kinetic chain reaction (Scheme 15.1). An intrinsic limitation of a typical chain-growth process, such as free-radical polymerization, is the occurrence of termination reactions that lead to the formation of *dead chains*, chains that are incapable of further growth.

Furthermore, as both the initiation and the termination processes often occur during the entire polymerization time period, one is typically left to contend with a statistical distribution of chain lengths. One strategy to overcome this limitation, is to develop a chain polymerization process wherein there are no chemically (mechanistically) feasible termination pathways, while at the same time ensuring that much of the initiation process takes place over a relatively short time duration in comparison to the polymer chain growth period. The former criterion ensures that no dead chains are formed during the polymerization, while the latter ensures that all chains have grown to essentially the same length (added on the same number of monomer units) at any given time during the polymerization. In as far as

#### Initiation

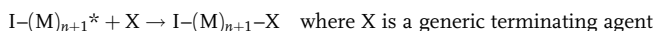


#### Propagation



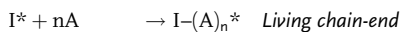
\* signifies active chain-ends

#### Termination

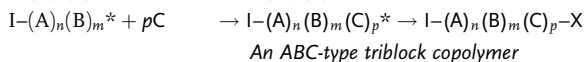
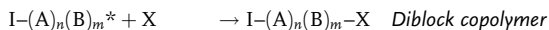


Dead chain

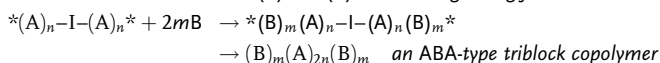
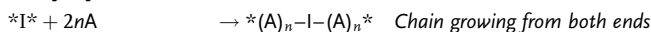
**Scheme 15.1.** Typical chain polymerization process depicting the various steps of the polymerization.



*Willful termination*



*Use of di-functional initiator*



**Scheme 15.2.** Block copolymer preparation via living polymerization methods.

structural control of the polymer chain is concerned the first feature ensures that the growing polymer chain-ends remain *living*, i.e., *active*, and are capable of adding on further monomer units to increase their chain length. This is a particularly important feature of living polymerization that enables the preparation of *block copolymers*. For instance, after complete consumption of one type of monomer, say monomer A, addition of the second monomer B, would lead to the generation of AB type diblock copolymers (Scheme 15.2).

By slight alterations in either sequence of monomer addition and/or utilization of bifunctional initiators, which generate polymer chains that grow in a living fashion at both ends, one can readily prepare other important types of block copolymers, such as ABC or ABA type triblock copolymers. It is evident that inability to retain chain-end activity in every single polymer chain will result in contamination of the block copolymer with homopolymer molecules resulting from the dead chains. Among the first living polymerization approaches was anionic polymerization, which is a chain polymerization process that uses carbanions (like, *sec*-butyl lithium) as initiators. This process works most efficiently with monomers, such as styrene, vinyl pyridine, butadiene, isoprene, etc., providing a very high level of control over molecular weight and polydispersity, as well as enabling the preparation of well-defined block copolymers. Anionic living polymerization has been the workhorse for the preparation of a wide range of block copolymers [15, 18, 19] which have been utilized in the generation of nanostructured polymers.

Other living polymerization approaches that have been extensively investigated include living cationic polymerization [20], group-transfer polymerization [21], iniferter-based (initiator-chain transfer-terminator) approaches [22] and, more recently, stable radical-mediated free-radical polymerization [16], atom-transfer radical polymerizations (ATRP) [17] and reversible addition–fragmentation–chain transfer (RAFT) polymerization [16]. Most of the latter living polymerization routes are based on radical chain propagation, and rely primarily on curtailing the radical–radical termination processes by effecting a drastic reduction in the concentration of *active* growing radical sites. In essence, this is achieved by trapping or transforming *active* growing free-radical sites to *dormant* ones, in a rapid equilibrium

process, utilizing suitable agents. The extraordinary attention that these *living*, or more appropriately termed “*controlled radical polymerizations*” (as the “true livingness” criteria is not rigorously obeyed by these approaches), have gained during the last decade is because of their relative simplicity and unparalleled functional group tolerance that make them uniquely versatile [16]. Further discussions of living polymerization routes are outside the scope of this chapter and interested readers may refer to the review articles that have appeared recently [16–22].

The standard molecular structural parameters that one would like to control in block copolymer structures, especially in the context of polymeric nanostructures, are the *relative size* and *nature* of the blocks. The relative size implies the length of the block (or degree of polymerization, i.e., the number of monomer units contained within the block), while the nature of the block requires a slightly more elaborate description that includes its solubility characteristics, glass transition temperature ( $T_g$ ), relative chain stiffness, etc. Using standard living polymerization methods, the size of the blocks is readily controlled by the ratio of the monomer concentration to that of the initiator. The relative sizes of the blocks can thus be easily fine-tuned very precisely; to date the best control of these parameters in block copolymers is achieved using anionic polymerization. The nature of each block, on the other hand, is controlled by the selection of the monomer; for instance, styrene would provide a relatively stiff (hard) block while isoprene would provide a soft one. This is a consequence of the very low  $T_g$  of polyisoprene compared to that of polystyrene, which in simplistic terms reflects the relative conformational stiffness of the polymer chain.

To summarize, it is evident that control of the length and nature of the blocks in block copolymers is readily achieved using living polymerization methods. Newer living polymerization methods based on free-radical chain growth, although effective in generating block copolymers, have yet to attain the precision that the more traditional anionic polymerization approach has achieved. The relatively wider distribution of block lengths, and homopolymer contamination, are the two main factors, wherein the newer methods often fail to meet the stringent molecular structural criteria that are often key to the development of nanostructured polymeric materials. Despite this drawback, these newer routes are likely to play a crucial role in the future development of nanostructured polymeric materials because of the significantly wider range of functional block copolymers that they can access.

### 15.3

#### Polymer Conformational Control

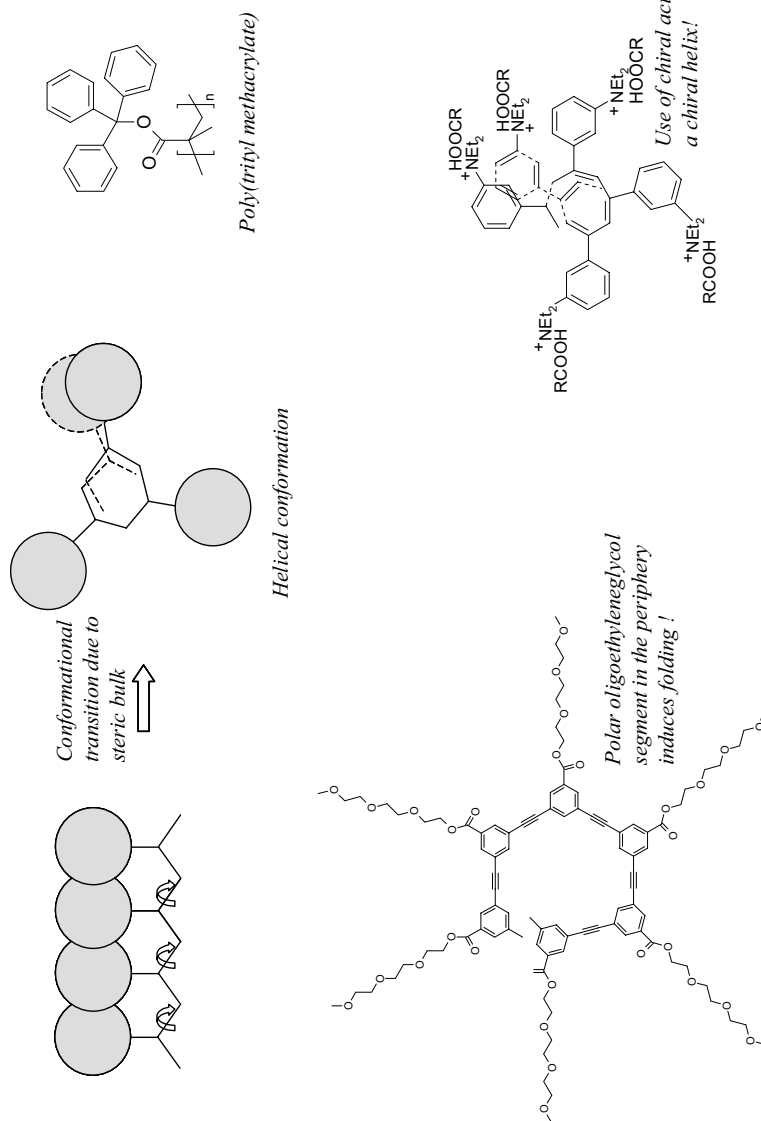
Although conformational control of synthetic macromolecules is a daunting proposition, given the enormous entropy cost that has to be borne, approaches to achieve this are being actively researched. Typically, synthetic polymer chains adopt a random coil conformation in solution, unlike biological macromolecules which

often adopt well-defined secondary structures by virtue of specific intra-chain interactions that help overcome the entropic penalty associated with such structure generation. Control of secondary structures of synthetic macromolecules in solution could be one approach to creating well-defined nanometer-size entities that could further organize to generate hierarchically ordered macroscopic systems [23]. Although this approach, via the utilization of conformationally controlled macromolecular entities for the generation of nanostructured polymeric materials, is in its infancy, precisely directed folding of synthetic macromolecules, in itself, has generated a lot of interest among chemists, physicists and theoreticians alike, because of the elegant parallel in biology [24, 25]. Hence, I have chosen to include a short discussion on this topic with the conviction that, in the near future, the polymer nanostructuring repertoire will be more heavily reliant on these pre-folded macromolecular entities.

At the two extreme ends of the flexibility spectrum are polymer chains that are very rigid rod-like macromolecules with limited conformational freedom, and those that are very flexible chains and can adopt a wide range of randomly coiled conformations. The majority of polymers have conformational properties that lie in between these extremes. Conformational restrictions can be introduced into macromolecules either by way of *steric* or *bond angle* constraints or through specific *intra-chain inter-segment interactions* that stabilize certain conformations over the others. A few examples of macromolecules that adopt preferred conformations by virtue of some of these constraints are depicted in Figure 15.1. In the case of steric constraint, the bulkiness of the side group imposes a helical motif to the backbone, which provides the maximum possible volume for the accommodation of the bulky substituent. Examples of such a system are poly(tritylmethacrylate), polychloral, etc. [25]. Bond angle constraint comes into operation most effectively in cases where the backbone is relatively rigid with very limited conformational freedom, such as in the case of poly(*meta*-phenylene ethynylene) [24] and *cis*-poly(phenylacetylene) [26]. Additional coercions, such as solvophobic effects and salt-formation, have been utilized to effect folding into helical motifs. Other examples of conformationally rigid polymers that adopt helical conformations include, poly(isocyanide)s, poly(isocyanate)s etc. [25].

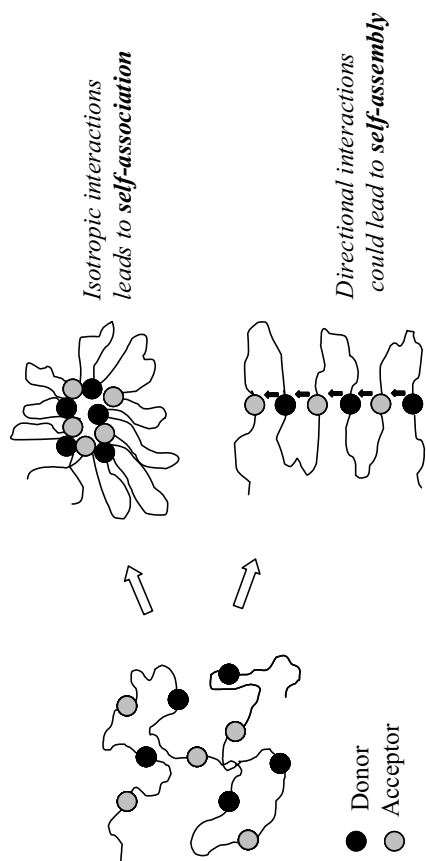
Imposition of conformational restrictions through specific *inter-segment intra-chain interactions*, often aided by restricted rotational freedom, is the approach that nature has chosen to *fold* biological macromolecules. Like in proteins, efforts that use H-bonding to effect folding of synthetic macromolecules have led to several interesting systems that are now often clubbed under a newly coined term: *foldamers* [27]. The general problem of folding of conformationally flexible macromolecules may be simplified by a schematic depiction of the macromolecule as containing well-defined and equally-spaced segments along the polymer backbone that interact strongly with each other (Figure 15.2).

A straightforward consequence of such strong interactions (in the absence of inter-chain interactions, such as in very dilute solutions) would be aggregation (or clustering) of these segments, a situation that can be termed *self-association*. Such a

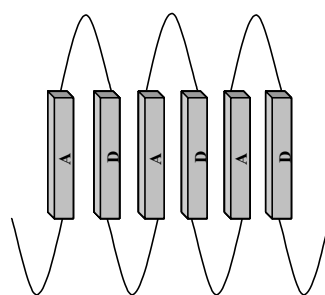


Bond angle constraint aided by solvophobic effect  
**Fig. 15.1.** Examples of polymers with conformational restriction due to steric and bond angle constraints.

Bond angle constraint aided by electrostatic interactions



### Directed versus undirected collapse



*A schematic representation of the folded structure of the polymer*

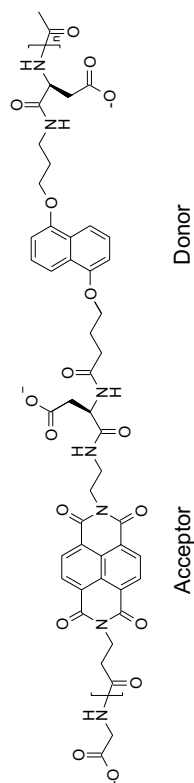


Fig. 15.2. Self-association versus self-assembly.

situation arises in polysoaps, a specific class of macromolecules that possess equally spaced ionic moieties that tend to cluster in hydrophobic solvents, in a situation akin to aggregation of surfactants to form micelles [28]. Since, in the case of polysoaps, the surfactant molecules are strung together to form a single polymer chain, the aggregation is present even at very dilute polymer concentrations, unlike the case of simple surfactants which exhibit a critical micelle concentration (CMC). Effective strategies to *fold* synthetic macromolecules, therefore, will need to preclude such aggregation, which occurs due to the isotropic nature of the interaction between the segments. Instead, by the introduction of a strong directionality to the interaction between the equi-spaced units along the polymer chain, the chains can be made to *fold* (see Figure 15.2). For instance, a design wherein the interacting segments along the polymer backbone are flat disk-like aromatic units (with high aspect ratio) could lead to the generation of a folded structure that results from stacking of the disk-like segments. Such a directional aggregation could be termed *intra-chain self-assembly*. An interesting example of such an assembly was recently demonstrated in H-bonded polymeric systems based on disk-shaped units [29]. A few other examples of such assembly that utilize other types of interactions, such as donor–acceptor interactions,  $\pi$ -stacking interactions and solvophobic effects, often in tandem, have been reported in oligomeric systems [30].

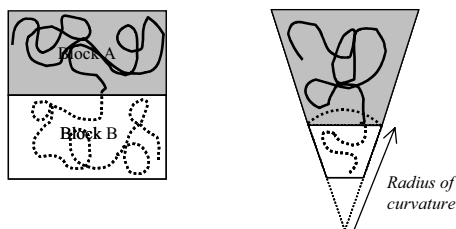
To summarize, folding synthetic macromolecules into topologically well-defined molecular entities remains a major challenge. The significant strides that have been taken in supramolecular science [31], which deals with the assembly of small molecules using a variety of non-covalent interactions, would serve as an ideal launching pad for the development of precisely folded macromolecules. It is evident that several weak interactions will need to work in tandem to overcome the entropic penalty that accompanies the folding process. Several steps have been taken in the right direction and many more are needed before we can accomplish even a small fraction of what nature has perfected.

#### 15.4

#### Morphology of Block Copolymers

The majority of polymers are immiscible and, in bulk, they phase separate to form domains of varying sizes and shapes, depending on their relative volume fraction. This happens because of the very low entropy of mixing in the case of large polymeric molecules. Therefore, unless there is a large favorable enthalpic contribution, *most polymers do not form molecularly miscible systems*. The same is true for block copolymers, in which the length of each block exceeds a certain critical value. As mentioned earlier, block copolymers are systems wherein two (or more) different types of homopolymers are linked to each other at the chain end(s); diblock copolymers, represented as  $(A)_m-(B)_n$ , are systems in which two homopolymers are linked to each other at one end, while triblock copolymers, represented as  $(A)_m-(B)_n-(C)_p$ , are systems in which one central homopolymer block is linked at either end with two other homopolymers. The values  $m$ ,  $n$  and  $p$ , represent the





$$f = V_A/V_B = \quad 1.0 \quad > 1.0$$

**Fig. 15.3.** Schematic depiction of the geometric arguments for prediction of block copolymer morphology. (Adapted from [1].)

number of monomer repeat units of A, B, and C in the respective block segments. Depending on the relative volume fractions of the two blocks, diblock copolymers can form a variety of phase-separated morphologies ranging from spherical dispersions of one phase in the other, to more complex morphologies such as bi-continuous structures [32]. Unlike in polymer blends, in block copolymers each polymer chain traverses across the boundary between the domains formed by the two phases. This being the case, the shape and size of the domains are directly dictated by the relative sizes of the blocks, say A and B in a simple diblock copolymer. Simple geometric arguments based on the volume ratio of the two blocks,  $f = V_A/V_B$ , can be used to explain the formation of the various types of morphologies (Figure 15.3) [1]. For instance, if the volume ratio is 1, then lamellar domains are mostly formed, which produce planar interfaces (curvature radius  $R = \infty$ ). On the other hand, when the volume ratio deviates from one, a decrease in the curvature radius of the interface occurs, finally leading to the formation of spherical domains dispersed in the dominant (by volume) continuous phase (Figure 15.4). Though the exact nature of the intermediate phases is not readily apparent from these simple geometric arguments, application of differential geometry leads to good predictions of the topologies and symmetries of the superlattices that are formed. Apart from the classical morphologies such as spheres, cylinders and lamellae, other more complex bicontinuous morphologies, such as the gyroid phase, have also often been observed in diblock copolymers (Figure 15.4). The simplistic geometric approach, however, glosses over one important molecular feature,  $\chi$ , the Flory–Huggins interaction parameter, which provides an estimate of the repulsive interaction between the two polymer blocks, i.e., the extent to which polymer molecules of one block dislike being surrounded by molecules of the other. Theoretical phase diagrams of block copolymers that include this interaction parameter have been calculated using self-consistent mean field theory [34]. As seen from Figure 15.4, apart from the volume fraction of the block ( $f_{PI}$  in this case), it is apparent that both the  $\chi$ -parameter and the total chain length, defined by  $N$ , the total number of repeat units in the copolymer chain, play a critical role in governing the morphology of the domains.

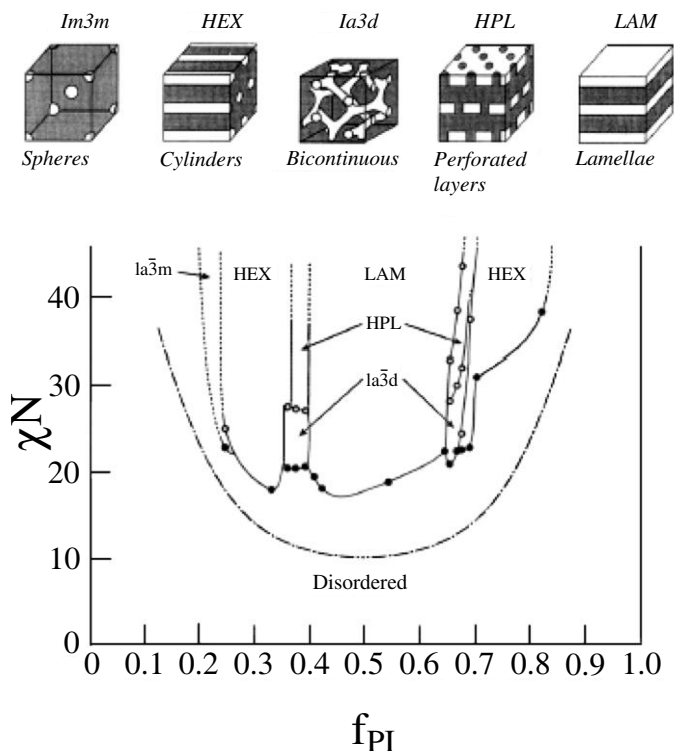


**Fig. 15.4.** Various morphologies observed in phase-separated diblock copolymers, along with the experimental phase portrait for PI-*b*-PS diblock copolymer. (Reprinted with permission from *Macromolecules*, **1995**, 28, 8796 [33]. © 1995 American Chemical Society.)

## 15.5

### Nanostructures Based on Bulk Phase Separation

Selective fixation of one of the domains in any of the morphologies formed by block copolymers, either by polymerization or by photo-crosslinking, is an elegant way to generate nanostructures. Utilizing such a concept, several types of nanosize objects, such as nanospheres, nanofibres and nanotubes etc., have been successfully prepared. A schematic representation of this general methodology is shown in Figure 15.5.

One of the very early examples of this concept for the generation of nanospheres utilized a diblock copolymer-poly(styrene)-*block*-poly(4-vinyl pyridine), labeled PS-*b*-P4VP [35]. Using a diblock copolymer with a higher weight-fraction of PS (>75 wt%), solvent cast films were shown to contain spherical micellar aggregates with a P4VP core embedded in a PS matrix, as confirmed by TEM studies. Exposure of these films to vapors of 1,4-dibromobutane (DBB), caused crosslinking of the PVP

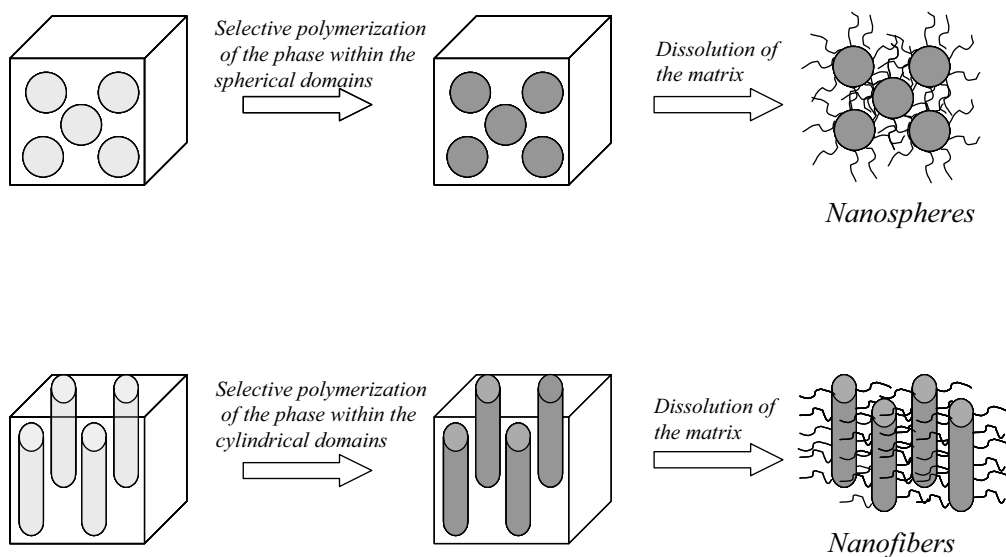


**Fig. 15.5.** Schematic depiction of the generalized strategy for preparation of polymeric nanostructures via bulk phase-separated block copolymers.

cores via quaternization of the pyridine rings. Dispersion of the core-crosslinked nanospheres was achieved by dissolution of the PS matrix in a solvent such as THF. TEM observations of the nanospheres obtained from these solutions clearly confirmed the existence of stabilized micellar aggregates. These early studies clearly demonstrated the feasibility of structural fixation in bulk phase-separated block copolymers.

More recently, Liu and coworkers have carried out extensive studies, wherein they utilize the photodimerization of the cinnamoyl units contained within one of the blocks in a variety of diblock copolymers to generate nanostructures [2] (Figure 15.6). Using a diblock copolymer, polystyrene-*block*-poly(2-cinnamoyl ethyl methacrylate), abbreviated as PS-*b*-PCEMA (labeled S750-C107), in which the PS block has 750 repeat units and the PCEMA block 107 repeat units, films were cast from a toluene solution. The films, when thermally annealed over extended periods form completely equilibrium phase-separated morphologies. The volume fraction of the PS block in this case being significantly higher than that of PCEMA, the equilibrium morphology consists of cylinders of PCEMA embedded in a PS matrix (Figure 15.7a). Photo-crosslinking of the cinnamoyl units in the PCEMA cylinders and subsequent dissolution of the PS matrix, using a solvent such as THF, led to the generation of *nanofibers* of ~50 nm diameter and about 20  $\mu\text{m}$  length [36]. A TEM image (Figure 15.7b) of such nanofibers confirms the existence of very long fibers that are, in effect, crosslinked *nanosize molecular objects*. The term *molecular object* is used here to signify that the crosslinking process has arrested the conformational freedom, which is an essential feature of macromolecular species. It is

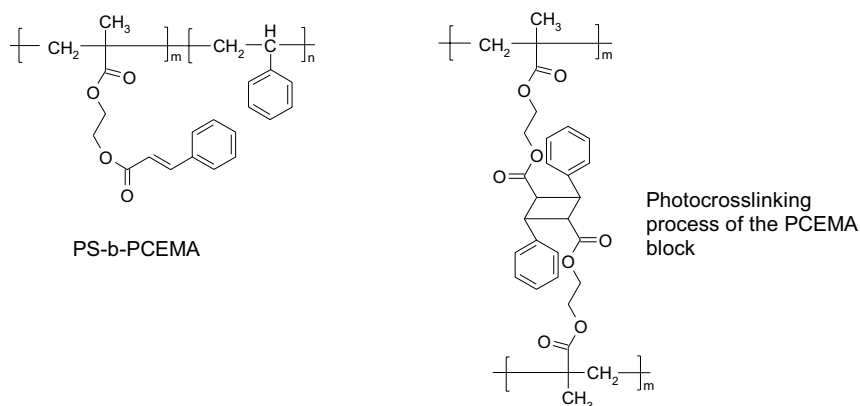


Fig. 15.6. Structure of Liu's block copolymers and photocrosslinking process.

important to recall, however, that these fibers consist of a crosslinked PCEMA core from which emanate numerous PS chains (termed *hairy fibers*), the extent of whose protrusion into the medium depends on the degree to which these chains are solvated in the dispersing solvent. The existence of such a core-shell structure in these fibers was confirmed from TEM studies of selectively stained samples (see inset in Figure 15.7b). These nanofibers, due to their very high aspect ratio, were shown to exhibit interesting lyotropic liquid crystalline properties similar to those exhibited by rigid-rod macromolecules such as KEVLAR [37]. The possibility of transforming these into carbon nanofilaments, by subsequent pyrolysis, opens up some exciting possibilities for preparing carbon filaments of precisely controllable diameters. One important feature of such an approach is that the diameter of the

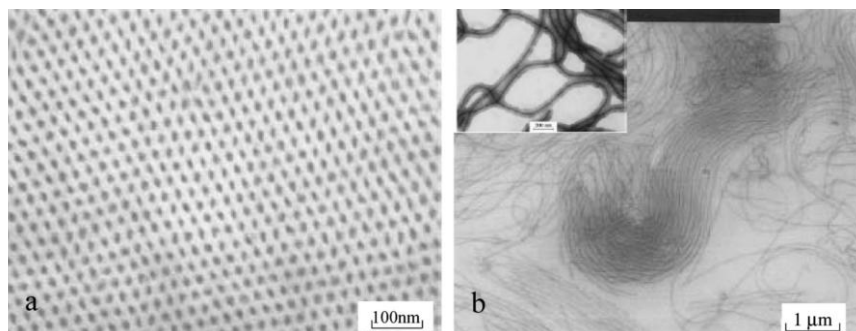


Fig. 15.7. TEM pictures showing a cross-sectional view of the bulk film confirming the formation of cylindrical domains perpendicular to the film plane (a) and that of the nanofibers after crosslinking (b). (Reprinted with permission from *Macromolecules*, **1996**, 29, 5508.

© 1996 American Chemical Society [36].) Inset in (b) a close-up view showing the core-shell morphology of similar fibers. (Reprinted with permission from *Chem. Eur. J.*, **1999**, 5, 2740 [37].)

fiber is often directly controlled by the molecular weight of the diblock copolymer, and therefore can be fine-tuned at will.

Using a similar strategy with an  $(A)_m-(B)_n-(C)_p$  type triblock copolymer, but with an additional feature of being able to transform (or degrade) the core block, Liu and coworkers reported the preparation of *nanotubes* [38, 39]. An interesting example is based on a triblock copolymer, poly(*n*-butyl methacrylate)-*block*-poly(2-cinnamoyloxyethyl methacrylate)-*block*-poly(*tert*-butyl methacrylate), labelled B1270-C190-tB270, containing 1270, 190 and 270 repeat units within each of the respective blocks, generated an equilibrium phase-separated morphology, in which cylinders containing concentric layers of a PtBA core and PCEMA shell are present [39]. These cylinders are embedded in the majority PBA phase (Figure 15.8). Photo-crosslinking of the PCEMA block enabled the fixation of the cylindrical structures, wherein the cylindrical shell is crosslinked. Dissolution of the majority PBA phase in a suitable medium disperses the nanocylinders. The core of these cylinders, which is made up of PtBA is then hydrolyzed using a mild two-step process (*tert*-butyl ester is first transformed to the trimethylsilyl ester and then hydrolysed) to generate a poly(acrylic acid) (PAA) core, which when dried collapses on to the inner walls of the cylindrical shell to generate *nanotubes*. An interesting feature of the PAA chains is that their conformation is very pH and ionic strength dependent; a feature that has been utilized to prepare nanoporous membranes having tunable permeability, as will be seen later.

The formation of cylindrical domains of one block in a matrix of another, in diblock copolymers, has also been exploited for the generation of nanochannels in thin film membranes [40, 41]. Using diblock copolymers of PtBA-*b*-PCEMA, but this time with a larger volume fraction (ca. 74 vol%) of the photo-crosslinkable PCEMA block, Liu et al, prepared thin polymer films containing a densely packed array of nanocylinders (diameter  $\sim 22$  nm) [40]. As expected, in these cases the PCEMA block forms the continuous phase with nanocylinders of the hydrolyzable PtBA blocks forming a densely packed array. Typically, thick films (or disks of ca. 1–4 mm thick) of these diblock copolymers were solvent cast and further thermally annealed for extended periods to enable the formation of the equilibrium morphologies. Very thin sections, with thickness ranging from 50 nm to 2  $\mu$ m, then need be microtomed to generate membranes that contain the PtBA cylinders oriented perpendicular to the membrane surface. The existence of such regularly packed cylindrical domains in these thin sections was confirmed by TEM studies. Photo-crosslinking of the majority continuous PCEMA phase, followed by mild selective hydrolysis of the *tert*-butyl groups in the PtBA block, generates hexagonally arranged nanochannels across an insoluble polymer film (Figure 15.9).

It must be recognized that these channels are not empty but have poly(acrylic acid) (PAA) chains tethered to their inner walls. However, since the relative volume occupied by these chains is significantly lower than the parent PtBA, these channels are rendered substantially porous. A very interesting feature of these porous membranes is the “*chemical valving effect*”, wherein the relative permeability of the membranes was shown to vary by almost two orders of magnitude as a function of pH, with the lowest permeability being witnessed at a pH of 3 [41]. The explana-

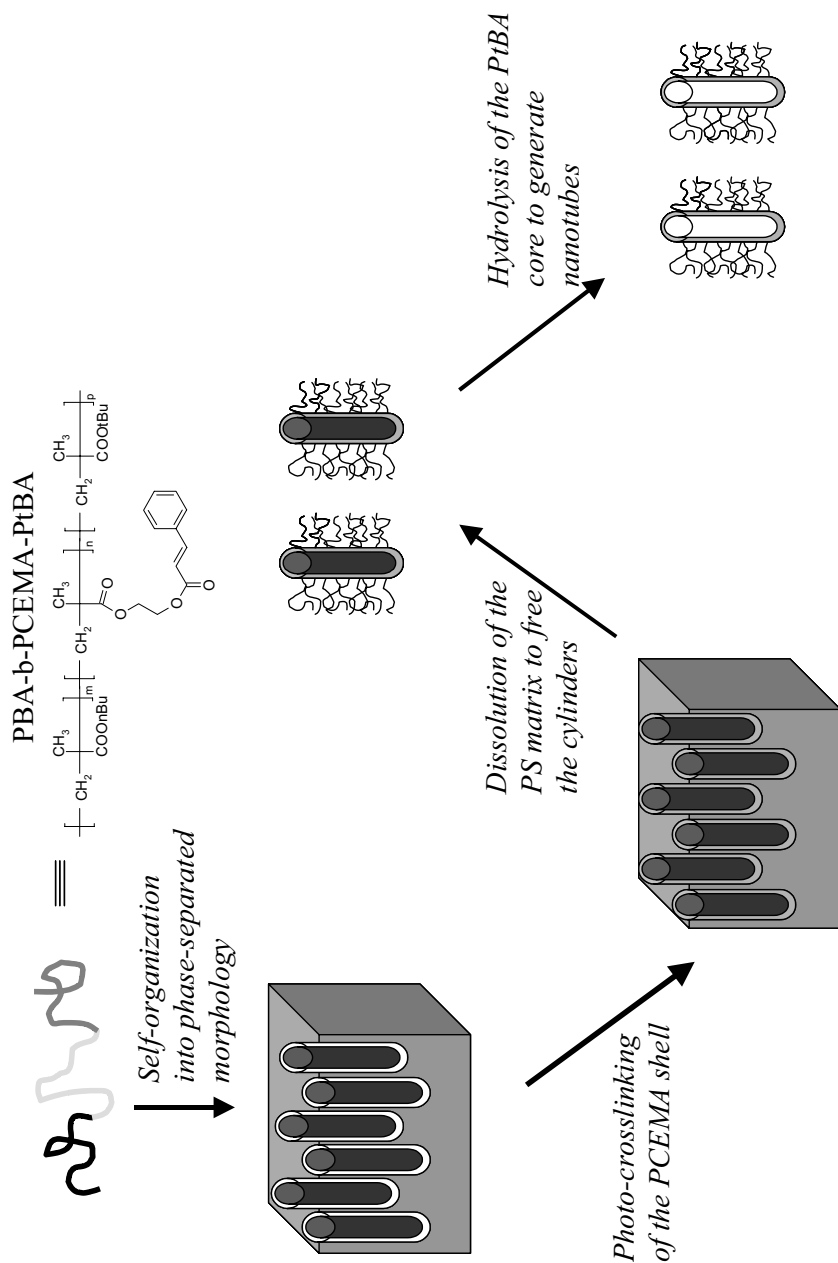


**Fig. 15.8.** Schematic depiction of the approach to generate nanotubes using triblock copolymers. (Adapted from [39].)

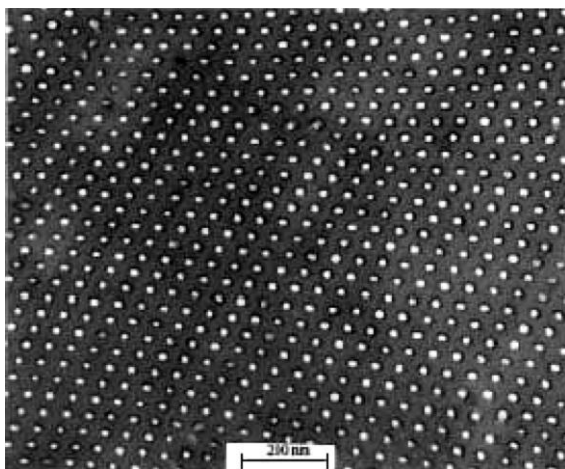


**Fig. 15.9.** TEM image of a small area of 50 nm thick PAA-*b*-PCEMA film generated by crosslinking the PCEMA matrix followed by hydrolysis of the PtBA domain. (Reprinted with permission from *Macromolecules*, **1997**, 30, 1851. © 1997 American Chemical Society [40].)

tion provided for this behaviour is based on the state of ionization of the carboxylic acid groups on the PAA chains. At pH 3, they exist in the carboxylic acid form, wherein they are intricately H-bonded to form a network that has very low permeability to water. However, at a higher pH of 12, the carboxylate ions formed are readily solvated by water, and thereby enhanced permeability to water is observed. It is anticipated that such nanoporous membranes with tunable porosity could be useful as templates for semiconductor nanofabrication, for controlled drug delivery applications as well as in sensing devices.

Direct formation of well-ordered nanoporous thin-film coatings has also been demonstrated by an innovative utilization of cylindrical domain formation in thin block copolymer films, followed by selective removal of the cylindrical phase by photo-degradation. It is anticipated that a well-ordered array of pores on an appropriate substrate could serve as a lithographic template or as scaffolds for periodic assembly of nanosize electronic materials. For such applications, it is very important to ensure that the cylinders are oriented perpendicular to the film surface. Although, such perpendicular orientation of cylinders in block copolymer films has been attained by application of an electric field [42, 43], a more elegant approach uses the intrinsic entropy-driven alignment on a specifically pre-formed neutral surface [44]. In one study, poly(styrene)-*block*-poly(methylmethacrylate), PS-*b*-PMMA (containing 30 vol% PMMA) was deposited as very thin films (50 nm) on a silicon substrate previously coated with a random copolymer of PS and PMMA [45]. The random copolymer coating renders the substrate neutral and ensures the formation of cylindrical domains of PMMA normal to the film surface upon thermal annealing. Deep-UV irradiation of the films causes the PMMA chains to de-

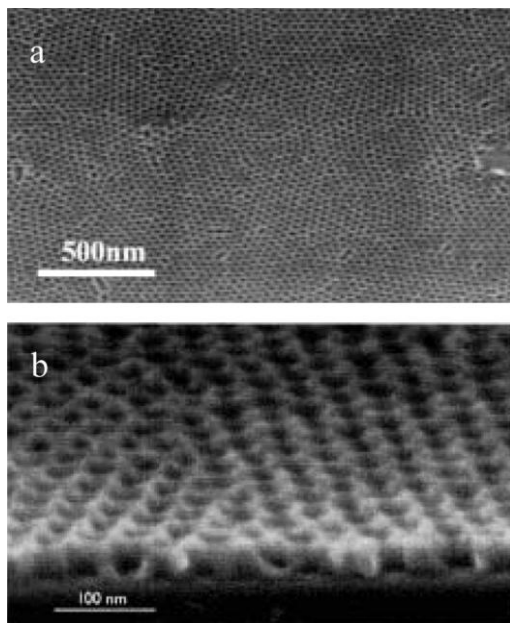


**Fig. 15.10.** FESEM image of a thin film of PS-b-PMMA after removal of the PMMA block from within the cylinders. (a) Shows top view and (b) shows a cross-sectional view. (Reprinted with permission from *Adv. Mater.*, **2000**, 12, 787 [45].)

grade via chain-scission (PMMA is a well-known deep-UV negative photoresist material), while the PS phase becomes insoluble due to the occurrence of cross-linking. Exploiting this diametrically opposite behaviour of the PMMA and PS phases to photo-exposure, an array of circular holes axially extending across the entire thickness of the films was readily prepared after selective removal of the photodegraded PMMA phase by aqueous etching. Figure 15.10, which shows the FESEM pictures of these etched films, clearly confirms the formation of uniform pores (ca. 20 nm in diameter) and the cross-sectional view shows that the pores stretch axially across the film thickness.

More recent studies have shown that the pore size can be varied by changing the molecular weight of the block copolymer (while maintaining the same relative volume fractions of the two blocks), while the optimum thickness for attaining narrow pore-size distribution is ca. 40 nm; at higher thickness the distribution broadens [46]. These investigations clearly demonstrate the potential of block copolymer based strategies to generate patterns that go much beyond the length scales typically achievable via the conventional lithographic techniques.

Bicontinuous morphologies, such as the gyroid phase, formed by block copolymers are particularly interesting for generating nanoporous high surface area materials for potential applications as membrane reactors. Hashimoto et al., used



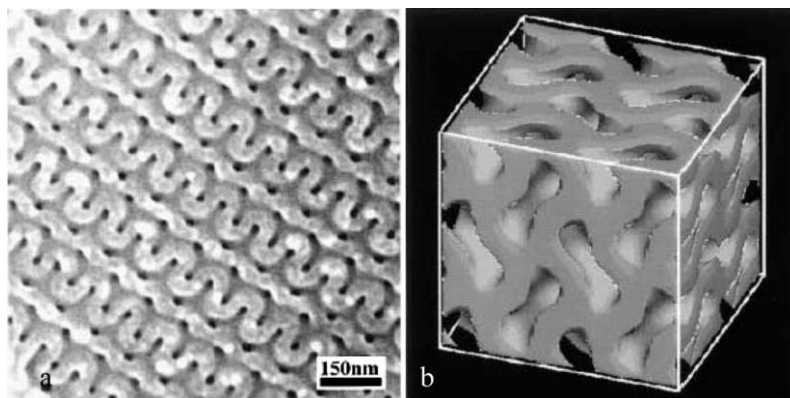


**Fig. 15.11.** SEM micrograph showing the bicontinuous nanochannels in a PS matrix (a) and a computer graphics 3D view of the double gyroid network (b). (Reprinted with permission from *Langmuir*, **1997**, 13, 6869. © 1997 American Chemical Society [47].)

poly(styrene)-*block*-poly(isoprene), abbreviated as PS-*b*-PI ( $\sim 0.5$  wt% of PI), along with PS homopolymer (such that the net PS vol% is ca. 66%) to prepare films that exhibited a bicontinuous morphology [47]. Selective and complete removal of the PI phase was achieved by ozonolysis, leaving behind bicontinuous nanochannels with diameters in the range 20 to 30 nm (Figure 15.11). This kind of structure has a very high internal surface area, which when suitably functionalized, could be potentially useful as a membrane nanoreactor with catalytic activity. To this end Hashimoto et al. have carried out nonelectrolytic Ni-plating of the nanochannels retaining the porous channel structure, albeit with a considerable narrowing of the pores [47]. These preliminary studies clearly demonstrate the potential of such systems for generating very high surface area porous supports for anchoring catalytic sites.

## 15.6

### Nanostructures Based on Lyotropic Mesophases

Lyotropic mesophases refer to self-assembled aggregate structures that are formed when molecular species are dissolved in a solvent, typically requiring a certain threshold concentration. In the previous section I dealt with the generation and fixation of nanostructured morphologies in bulk phases of block copolymers, which were formed due to the mutual immiscibility of the block segments. In this section I shall discuss approaches that utilize block copolymers that contain blocks with distinctly different solubility characteristics. Diblock copolymers when dissolved in a solvent, which is a good solvent for only one of the blocks, a so-called *block-selective* solvent, form a variety of aggregate morphologies including spherical

micelles, vesicles, cylindrical micelles etc. [48]. Thus diblock copolymers, which contain a hydrophilic block and a hydrophobic one, behave like simple surfactants and form a rich variety of structures in aqueous media, ranging from simple spherical micelles to more complex phases, such as the bicontinuous phases. Micelles formed by block copolymers differ from those formed by simple surfactants, both in terms of their significantly larger sizes and their higher stability (less dynamic).

The majority of the efforts to generate nanostructures utilizing phase-separated block copolymers in the bulk have focused on the cylindrical domains, while only limited effort has been made to utilize other morphologies. Efforts to use lyotropic mesophases formed by block copolymers, in this sense, complement those utilizing the bulk phase-separated systems, since the major focus of research based on lyotropic systems has been towards utilization of spherical aggregates for the generation of nanospheres, nanocapsules, etc. The general scheme for the preparation of various types of nanoparticles is depicted in Figure 15.12. Spherical aggregates, made up of a core containing the insoluble segment and a shell formed by the soluble block, are formed when diblock copolymers are dissolved in a block-selective solvent. Structural fixation, either by polymerization or crosslinking, can be done specifically within the core or the shell to generate *core-crosslinked* or *shell-crosslinked micelles*, respectively.

As with phase separation of block copolymers in bulk, the nature and size of the aggregates formed in a block-selective solvent depends on the relative sizes of the two blocks as well as the overall molecular weight of the diblock copolymer. In

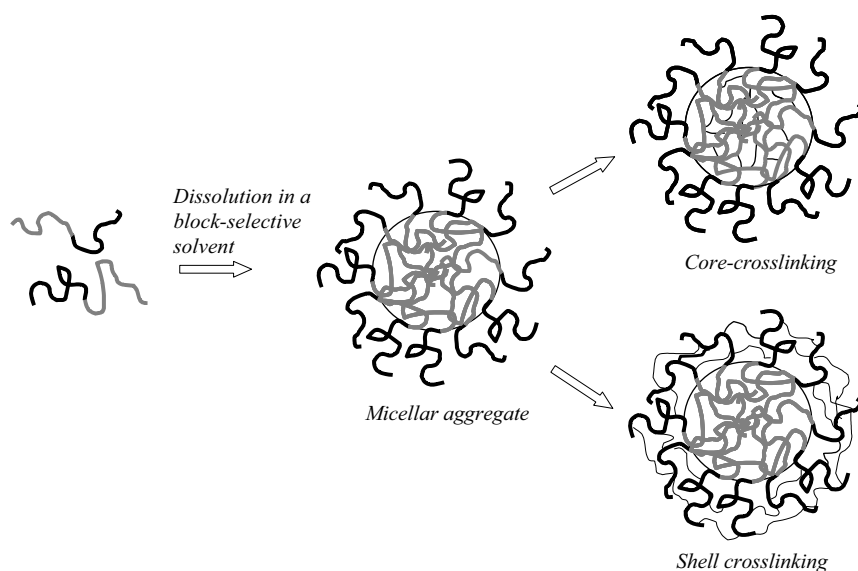


Fig. 15.12. Generalized scheme for preparing core-crosslinked and shell-crosslinked nanospheres using block copolymers.

general, diblock copolymers with a short soluble block and a long insoluble block tend to form crew-cut micelles, vesicles, cylinders or donuts, while when the relative block lengths are just reversed spherical micellar aggregates (star micelles) are formed [48]. In lyotropic systems, one other tunable parameter is the nature of the solvent, increasing the concentration of the block-selective solvent relative to the mutual solvent, which dissolves both the blocks, favors the formation of vesicles and cylinders. Thus, lyotropic systems offer a greater degree of control than bulk systems and, furthermore, are more adaptable for larger scale preparation of nanosize polymeric objects. Additionally, shell-crosslinked systems are more readily achieved using lyotropic systems, but this would require the use of triblock copolymers, if it were to be achieved based on bulk phase-separated morphologies.

### 15.6.1

#### Core-Crosslinked Systems

Early efforts to freeze the spherical aggregates of block copolymers in solution by core-crosslinking often led to the formation of insoluble products due to micelle fusion during the crosslinking process. Using diblock copolymers of poly(polystyrene)-*block*-poly(2-cinnamoyl ethyl methacrylate), PS-*b*-PCEMA, Liu and coworkers prepared core-crosslinked *hairy nanospheres*, via the photo-crosslinking of the PCEMA core [49]. More interestingly, they also prepared water soluble nanospheres using poly(2-cinnamoyl ethyl methacrylate)-*block*-poly(acrylic acid), PCEMA-*b*-PAA [50]. Spherical micelles having a PCEMA core and a PAA shell were formed by dissolution of the diblock copolymer in DMF–water mixtures, and photo-crosslinking of the core generated *water dispersible nanospheres* which were shown to be stable even in the presence of DMSO, a mutual solvent for both the blocks, confirming the enhanced stability derived from the crosslinking process. Typical hydrodynamic radii  $R_h$ , of these nanospheres ranged from ca. 40 to 60 nm. The lightly crosslinked hydrophobic cores are readily swollen in suitable media and can act as scavengers of organic compounds from water. Their studies demonstrated that while the uptake capacity for organic compounds from water was limited in the unswollen state, the use of a small amount of an organic co-solvent, like DMSO or acetone, led to a drastic increase in the uptake capacity [50]. The potential for these nanospheres to take up organic guest species into the hydrophobic cores, makes them potentially useful candidates for water clean-up operations (oil spill) as well as for drug delivery applications.

With the object of increasing the uptake capacity of nanospheres, specifically designed diblock copolymers, that contain one block made up of a random copolymer of CEMA and 2-octanoyl ethyl methacrylate, OEMA, and the other of PAA, were used [51]. To increase the porosity of the crosslinked core, the spherical micelles were prepared in the presence of the homopolymer, POEMA that co-dissolved in the hydrophobic core during micellization (Figure 15.13). Photo-crosslinking of the core, followed by extraction of the porogen, POEMA, using an organic solvent generated the *porous nanospheres*, whose perylene uptake capacity was shown to be significantly higher than the identical nanospheres prepared in

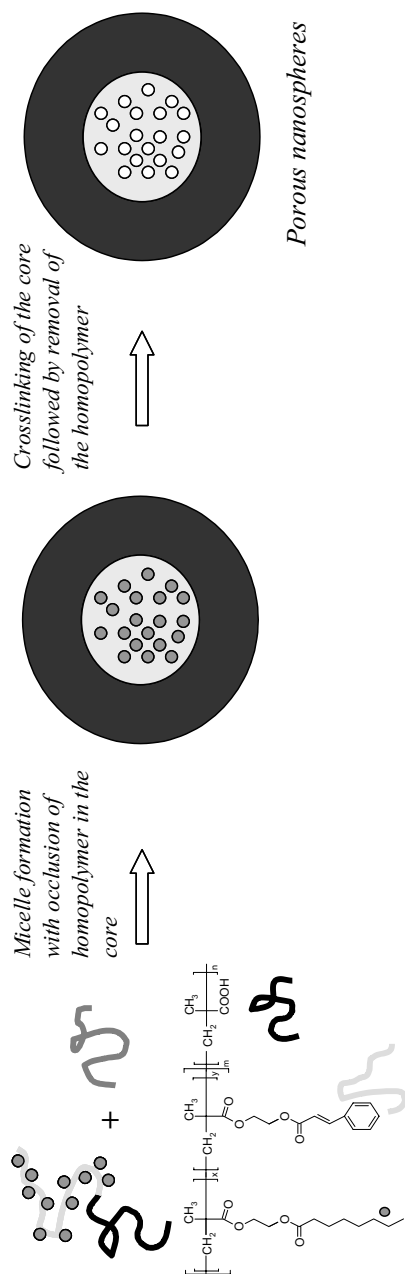


Fig. 15.13. Schematic depiction of generation of porous nanospheres with increased host uptake capacity.

the absence of the porogen [51]. More recently, by the use of core segments, which contain repeat units that incorporate thymine groups, nanospheres with very high affinity for adenine (which was used as the porogen during the micelle preparation) were prepared. The porous nanospheres generated after removal of the adenine porogen exhibited very high affinity and uptake rates for adenine, paving the way for possible utilization of such specifically imprinted nanospheres as micro-extractors [52].

### 15.6.2

#### Shell-Crosslinked Systems

As depicted in Figure 15.12, shell-crosslinked micellar systems are formed by crosslinking the solvent-soluble block, which forms the shell of the micellar aggregates, by using appropriate chemical strategies. Unlike the core-crosslinked micelles, these systems offer several advantages in terms of both structural and functional control: (i) the core of these structures being un-crosslinked exhibits higher mobility as well as greater swellability and thereby should possess greater host-uptake capability; (ii) control of the thickness as well as the extent of crosslinking of the shell-layer can be readily achieved by variation of the block copolymer structure, which in turn can control functional parameters, like permeability and maximum core-swellability; (iii) by selection of the core segment that can be chemically degraded, its role can be reduced to that of a scaffold for the generation of empty crosslinked polymeric shells i.e. *nanocapsules*.

The early efforts to generate shell-crosslinked systems utilized a diblock copolymer, poly(styrene)-*block*-poly(4-vinyl pyridine), abbreviated PS-*b*-P4VP, wherein the P4VP block was partially quarternized using 4-chloromethyl styrene, which functioned as the potentially crosslinkable site [53]. Micellar aggregates containing a PS core and a P4VP shell were formed in aqueous-THF and the shell was crosslinked by a free-radical-initiated polymerization (using an appropriate water-soluble photo-initiator) of the styrene units present in the shell-region (Figure 15.14). AFM and dynamic light scattering (DLS) studies clearly demonstrated that the size of such crosslinked micelles is readily controlled by the relative sizes of the two blocks;  $R_h$  by DLS was shown to increase from 7 to 10 to 15 nm, when the styrene:vinyl pyridine ratio in the diblock copolymer was increased from 1:2 to 1:1.2 to 1.9:1, respectively [53].

In an effort to develop alternative strategies that permit greater control over some critical molecular properties of the crosslinked shell, such as the crosslink density and shell composition, Wooley and coworkers utilized poly(styrene)-*block*-poly(acrylic acid), PS-*b*-PAA diblock copolymers [54]. These diblock copolymers formed micelles containing a PS core and PAA shell; the shell was then crosslinked using diamines, such as diamino(oligoethylene oxide), via an amidation reaction, via a process similar to that shown in Figure 15.16, see next section. By varying the length and the relative amount of the oligoethylene oxide segment in the crosslinker, the crosslink density and hence the permeability characteristics of the shell layer are readily modulated. In the context of the utilization of these

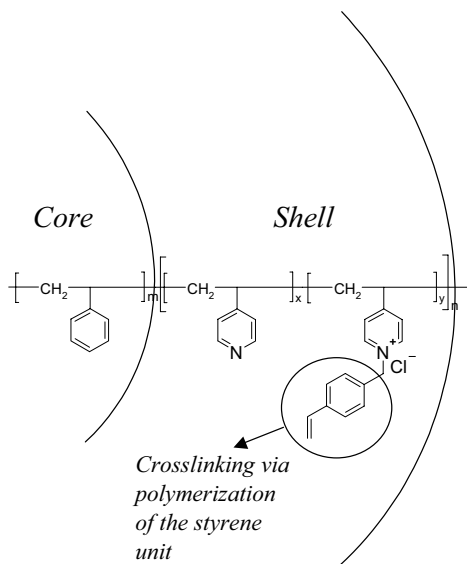


**Fig. 15.14.** Shell-crosslinking strategy using partially quaternized PS-*b*-P4VP diblock copolymer micelles.

nanoparticles for drug delivery applications, it is essential that the diffusion characteristics of various types of molecules be understood. Using special NMR methods, it was shown that hydrophobic guest molecules reside within the core, while amphiphilic molecules reside at the core-shell interface [55]. More importantly, it was also established that, at higher crosslink densities, the shell hinders the diffusion of the host into the core, suggesting that chemical tuning of the shell characteristics clearly provides a handle for control of release rates of encapsulated molecules [56].

One of the very important reasons for generating water-soluble nanospheres is their relevance to biological applications. Most systems discussed thus far contain a hydrophobic core and a crosslinkable hydrophilic shell and hence inclusion of hydrophilic guest species within the core would clearly be difficult. To overcome this problem, Butun et al. utilized a specifically designed diblock copolymer wherein the core-forming block is one whose water-solubility is modulated by varying the temperature; at higher temperatures of ca. 60 °C the block is insoluble in water while at 25 °C it becomes water-soluble [57]. Thus, utilizing a diblock copolymer, poly[2-(dimethylamino)ethyl methacrylate]-*block*-poly(N-morpholinoethyl methacrylate), abbreviated as PDAEMA-*b*-PMEMA, in which the PDAEMA block is partially quaternized, they prepared micellar aggregates in water at 60 °C. The PMEMA block is water insoluble at this temperature and forms the core of the micelle, while the partially quaternized PDAEMA block forms the shell. Cross-linking the shell region is achieved at 60 °C by quaternization using an  $\alpha,\omega$ -diiodo(oligoethylene oxide). Cooling the shell-crosslinked micellar solution to

25 °C, re-hydrates the core causing a small increase in the size from 28 to 30 nm. That crosslinking has indeed occurred is confirmed by the very existence of aggregates at 25 °C, as in its absence the diblock copolymers are completely soluble at this temperature. Tunability of the solubility of the PMEMA block in water arises from the fact that its lower critical solution temperature (LCST) lies between 25 and 60 °C. This reversible hydration of the core could be a very useful feature to trigger release of occluded guest molecules from the core interior. More recently, utilizing a similar methodology, zwitterionic shell-crosslinked systems have also been prepared wherein the core and shell domains contain amine and carboxylic acid groups, respectively, or vice versa. Such systems exhibit an isoelectric point, at a pH wherein the crosslinked micelles (~40 nm) become electrically neutral and precipitate out in water; addition of acid or base causes complete redissolution of these nanospheres [58].

One of the drawbacks of most approaches described thus far for the preparation of shell-crosslinked systems, is that the crosslinking of the micellar aggregates has to be carried out under very dilute conditions in order to prevent inter-micellar crosslinking. An interesting approach to overcoming this problem was developed by Butun et al., using a triblock copolymer, poly(ethylene oxide)-*block*-poly[2-(dimethylamino)ethyl methacrylate]-*block*-poly(N-morpholinoethyl methacrylate), abbreviated as PEO-b-PDAEMA-b-PMEMA [59]. Just as in the simple diblock copolymer PDAEMA-b-PMEMA, the micelles formed at 60 °C contain a PMEMA core and a PDAEMA shell, but this time an added steric protection is provided by the PEO corona, which forms the outermost layer in an onion-like layered micelle (Figure 15.15). This outermost PEO layer prevents the occurrence of inter-micellar

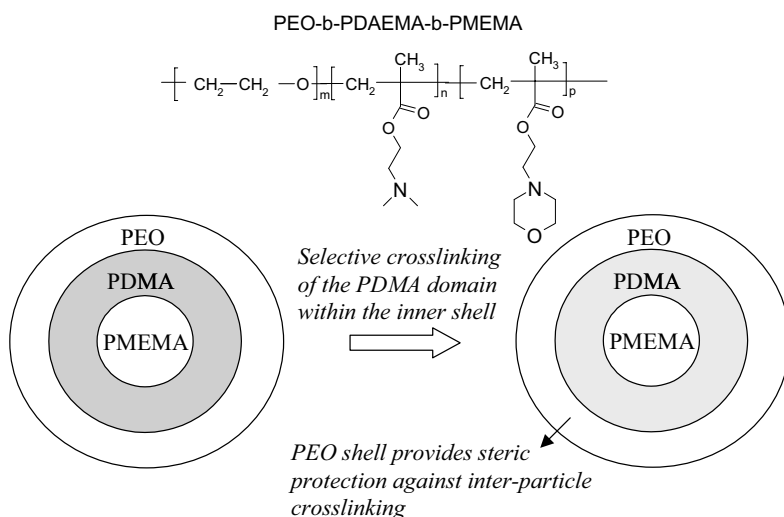


**Fig. 15.15.** Steric protection strategy using PEO-b-PDAEMA-b-PMEMA triblock copolymer for preparing core-crosslinked nanospheres using high solids content. (Adapted from [59].)

crosslinking during the crosslinking process, even at a very high solids content of  $\sim 10$  wt%. Control experiments using the simple diblock copolymer, PDAEMA-*b*-PMEMA lead to the formation of crosslinked gels at such high concentrations, clearly demonstrating the efficacy of the steric stabilization affected by the PEO layer.

### 15.6.3

#### Nanocages

Extending the approach even further, diblock copolymers, poly(isoprene)-*block*-poly(acrylic acid), abbreviated PI-*b*-PAA, were used to prepare shell-crosslinked nanospheres, utilizing diamino(oligoethylene) glycols as crosslinkers [60]. By selective oxidative degradation of the PI-core by ozonolysis and subsequent removal of the degraded products, the contents of the core were emptied to generate *nanocages* (Figure 15.16). The average hydrodynamic diameter of the nanoparticles in solution, as determined by DLS, increased from ca. 27 nm to about 133 nm, after the core-degradation. This rather counter-intuitive enhancement is readily explained, based on the fact that the crosslinked hydrophilic shell-layer acts as a hydrogel and undergoes swelling (and expansion) as the empty inner core fills up with water. A smaller diameter of 75 nm for the nanocages, measured by TEM in the dry state, as compared to the DLS measurement in water, serves to confirm the swelling-induced increase in the size of the nanocages. Use of a much longer crosslinker having 70 ethylene oxide repeat units, leads to the formation of a much more loosely crosslinked shell-layer, which undergoes a significantly larger extent

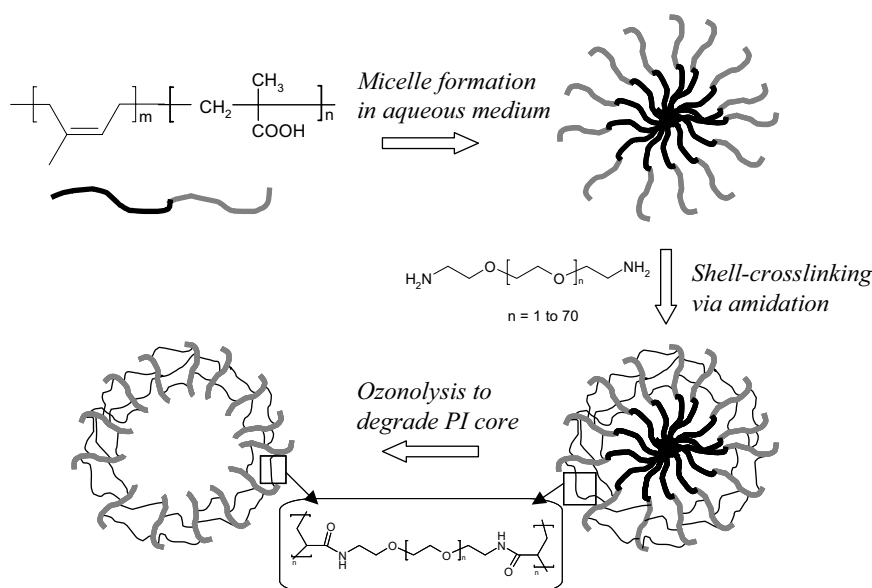


Fig. 15.16. Schematic depiction of the formation of nanocages. (Adapted from [60].)



of swelling, thereby generating nanocages of larger dimension. Nanocages utilizing other hydrolytically degradable core segments such as poly(caprolactone), PCL, have also been prepared by using diblock copolymers containing a PCL block and a poly(acrylic acid) block, which was crosslinked by using a diamine via an amidation process. The biodegradable PCL core of the parent nanospheres could also serve as a potential reservoir for controlled drug release applications [60].

Apart from the approach described above, wherein solid core-shell aggregates are shell-crosslinked followed by core degradation to generate hollow liquid-filled nanocapsules, hollow structures can also be directly generated from certain amphiphilic diblock copolymers of modest molecular weights ( $\sim 4000$ ). Poly(ethylene oxide)-*block*-poly(ethylene) ( $\text{PEO}_{40}\text{-b-PE}_{37}$ ) spontaneously organizes into a variety of structures, such as spherical and rod-like micelles and bilayer vesicles [61]. These vesicular structures, with typical bilayer thickness of about 8 nm, are much more robust than those formed from simple low molecular weight surfactants. Release of entrapped guest species was shown to be much slower in these systems compared to the standard liposomes, confirming the relatively lower segment mobility of the bilayer structure. Further experiments with poly(ethylene oxide)-*block*-poly(butadiene) ( $\text{PEO}_{26}\text{-b-PB}_{46}$ ) permitted free-radical initiated crosslinking via polymerization of the olefinic sites in the butadiene segment, to permanently lock-in the vesicular membrane capsule [62]. Elegant experiments were done to probe the efficacy of the crosslinking process, and these clearly demonstrated a dramatic increase, by several orders of magnitude, in both the elastic modulus and the rupture strength of the bilayer membrane upon crosslinking. Utilizing a mixture of the saturated diblock copolymer ( $\text{PEO}_{40}\text{-b-PE}_{37}$ ) and  $\text{PEO}_{26}\text{-b-PB}_{46}$  in various ratios, the crosslinking density, and thereby the elastic modulus and rupture strength of the membrane, were fine-tuned [62].

Another interesting and novel vesicular architecture was recently reported by Shen and Eisenberg using PS-*b*-PAA, wherein equi-spaced concentric bilayers build-up an onion-like vesicular structure, with overall diameters exceeding 1  $\mu\text{m}$  [63]. As many as 6 concentric bilayers, of thickness  $\sim 22$  nm and inter-layer spacing of about 60 nm, were clearly visible in some cases (Figure 15.17). Similar multi-layer vesicular structures with no space between the layers, so-called solid onion-type vesicles, were formed when quaternized PS-*b*-P4VP block copolymers were used. In contrast to the regular liquid-filled vesicles this type of layered vesicle, which has liquid chambers between the layers, could find some potential use in controlled-release applications as the overall diffusion rates will be governed by the number of bilayer shells that the encapsulated species will need to cross before reaching the bulk phase. It must be added that although these vesicles are not stabilized by polymerization or crosslinking, their stability is significantly greater than those formed by simple surfactants, due to the polymeric nature of the diblock copolymer amphiphile.

It is evident from the discussions so far that block copolymer-based strategies to construct structurally fixed nanosize objects provide ample opportunities to modulate the final size, shape and properties of the nanostructures. Much of the fine-tuning is done at the stage of the design and synthesis of the diblock copolymers.

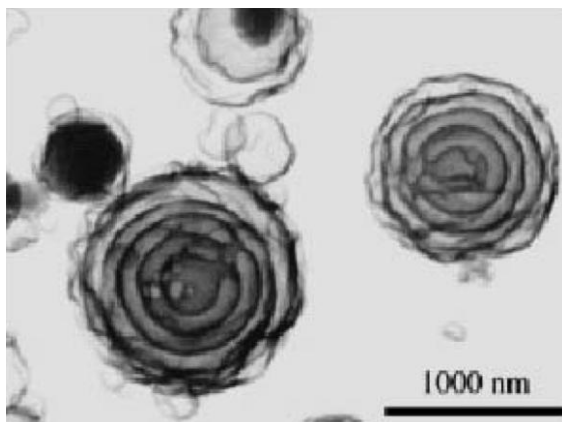


**Fig. 15.17.** TEM picture of the onion-type multiplayer vesicles. (Reprinted with permission from *Angew. Chem. Int. Ed. Engl.*, **2000**, 39, 3310 [63].)

By judicious choice of the structure and relative sizes of the block segments, a wider range of nanostructures have become accessible in a relatively short time-span.

## 15.7

### Rod-Coil Diblock Copolymers

Block copolymers, wherein both blocks consist of polymer chains that adopt a random coil conformation, are by far the most thoroughly investigated systems and, as seen in the earlier section, they have been extensively utilized to prepare a variety of nanostructures. However, in most of these systems there is little if any molecular order within the nanosize objects they help to generate. Replacing one of the blocks by a relatively stiff rod-like segment generates systems that are termed *rod-coil diblock* copolymers [64]. Strongly interacting and often crystallizable rod-segments could provide an additional driving force for the microphase separation in terms of the enthalpic contribution. Another important factor that is distinct in rod-coil systems is the stiffness asymmetry (or stiffness contrast) between the two blocks, which leads to an increase in the Flory-Huggins  $\chi$ -parameter. This in turn can induce phase separation at relatively smaller block lengths (degree of polymerization) when compared to simple coil-coil diblock copolymers, thereby permitting the formation of much smaller domain sizes. Furthermore, because the rods form orientationally ordered domains, it has been possible to generate polar ordering in bulk systems utilizing this approach. Thus, the final morphology that results from rod-coil block copolymers is often governed by the competition between the microphase separation of the rod and coil segments, and the tendency for the rods to form anisotropic orientationally ordered domains.

Some of the early efforts to understand rod–coil block copolymers were based on rigid segments that were made up of  $\alpha$ -helices formed by polypeptides, conjugated chains or thermotropic mesogens [65]. Most of the earlier systems contained poly-disperse blocks of both the rigid and coil segments, and were less amenable to discrete nanostructured phase separation. One of the first efforts to prepare rod–coil block copolymers with precisely controlled size of the rod-segment, utilized a molecularly exact mesogenic segment built from biphenyl units, while the coil segment consisted of a poly(isoprene) segment, whose molecular weight was varied (3200, 4200 and 5400), leading to rod–coil systems with the volume fraction of the rod ( $f_{\text{rod}}$ ) decreasing from 0.36 to 0.30 to 0.25, respectively (Structure A, in Figure 15.18). Thin films of these rod–coil diblock copolymers exhibit nanophase separation forming rod-rich and coil-rich domains with dimensions less than 10 nm. With decreasing volume fraction of the rod segment, continuous strip-like domains break up to form discrete aggregates. Electron tomography studies proved to be particularly useful in establishing the nature of the packing across the film thickness. A schematic depiction of the packing of the strips that measure 6–7 nm in width (approximately the molecular length of the rod segment) is shown in Figure 15.19. The strips were shown to pack in layers parallel to the film plane in the manner shown; the order in which the block copolymer domains assemble is a consequence of the need to minimize the extent of stretching that the coils must sustain in order to ensure uniform filling of the available space (uniform segment density across the domain). As the volume fraction of the rod segment decreases to 0.25, small disk-like aggregates are formed that form close-packed hexagonal superlattices (Figure 15.19).

It was argued that the formation of aggregates with an intrinsically self-limited size could be possible if steric constraints were built into the block copolymer design. Increasing the cross-sectional area of the coil block is one possible approach to bring about the formation of such a *self-limiting nanoaggregate*. Incorporation of another block of poly(styrene) to generate rod–coil triblock copolymers, in which the coil block consists of two blocks, one a poly(styrene) block (semiflexible) and the other a poly(isoprene) block (flexible), proved to be one such approach (Structure B in Figure 15.18) [68]. What distinguishes this particular study from many of the earlier efforts is that it dealt with macromolecules having relatively small sizes of each block. The triblock copolymer consisted of PS and PI segments, each having an average of just 9 repeat units, that was linked to a trimeric biphenyl segment. Films cast from this rod–coil block copolymer generated *mushroom-shaped nanostructures* (Figure 15.20a), which lacked a center of inversion. Each of these aggregates was estimated to contain about 100 molecules. Thus, the origin of these self-limiting aggregates is believed to be the interplay between the crystallization tendency of the biphenyl segments, the coil entropy of the flexible PI coil segment and the steric repulsion of the semiflexible PS segments. One of the most interesting features of these structures was the macroscopic layer-wise self-assembly of these mushroom-shaped nano-aggregates, even in the bulk film [68]. Using a series of such triblock copolymers with varying sizes of the coil diblock, a clear linear relationship between the layer periodicity and the extended average size of the

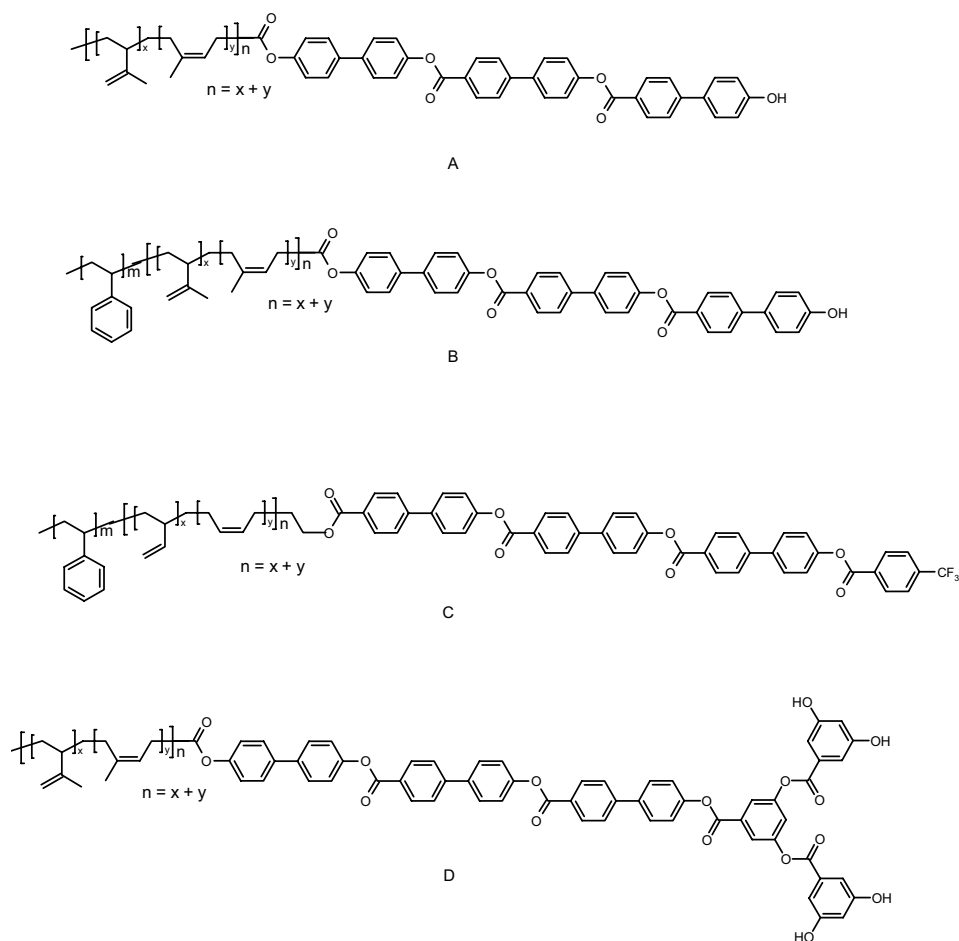


**Fig. 15.18.** Structures of a few representative rod-coil block copolymers that have been investigated.

molecule offered evidence for the formation of mushroom-shaped nano-aggregates [69].

If indeed supramolecular clusters are formed spontaneously in bulk films of appropriately designed rod-coil systems, by inclusion of appropriate reactive units it should be possible to convert these into *molecular objects* by crosslinking, while maintaining the precise size and shape of the cluster. In order to test this hypothesis, rod-coil triblock copolymers, with structures similar to those described previously, but with a few modifications to enable crosslinking, were prepared. Stupp and coworkers replaced the poly(isoprene) block with a poly(butadiene) (PB) block (which contains both 1,2- and 1,4-linked repeat units), which is known to undergo thermal crosslinking at high temperatures [70]. Additionally, the phenolic OH

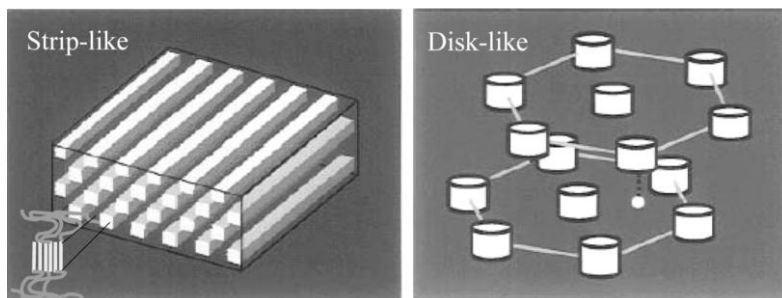


**Fig. 15.19.** Schematic depiction of the packing of strip-like and disk-like domains formed by the rod segments. (Reprinted with permission from *Macromolecules*, **1997**, 30, 2110. © 1997 American Chemical Society [67].)

group was replaced by a benzoate derivative possessing a  $\text{CF}_3$ - group at its terminus (molecule C in Figure 15.18). Thin films of this triblock copolymer were shown to contain similar mushroom-shaped nano-aggregates, but with significantly smaller sizes, roughly ca. 20–23 molecules per aggregate. Heating these films to  $250^\circ\text{C}$ , the temperature at which these materials form a thermotropic liquid crystalline phase, for prolonged periods (20 h) under inert atmosphere led to the fixation of these aggregates by a crosslinking process via the olefinic sites in the PB block. Interestingly, after thermal crosslinking the films were readily soluble in organic solvents and GPC analysis confirmed the formation of macromolecular objects that were the result of stitching together ca. 20 triblock copolymer molecules. The polydispersity values obtained from GPC were also very low, ca. 1.1.

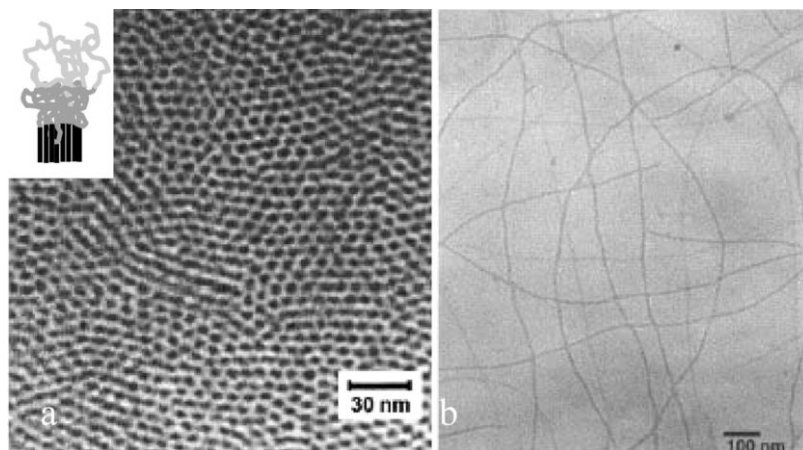


**Fig. 15.20.** TEM picture of the mushroom-shaped aggregate (a) (inset shows a schematic depiction of the aggregate) and of the nano-ribbons (b). ((a) Reprinted with permission from *Macromolecules*, **2000**, 33, 3550. © 2000 American Chemical Society [69], and (b) from *J. Am. Chem. Soc.*, **2001**, 123, 4105. © 2001 American Chemical Society [71].)

Among several triblock copolymer systems, wherein only the terminal group of the rod segment was changed, keeping all other structural features the same, it is surprising that only the  $\text{CF}_3$ -terminated system generated macromolecular objects with precisely controlled size having a very narrow size distribution. All other triblock systems either generated insoluble bulk-crosslinked material or soluble systems with much larger aggregate size and very broad size distributions (polydispersity  $> 8$ ). This suggests that only in the case of the  $\text{CF}_3$ -terminated derivative, was successful steric isolation of the coil PB segment during the crosslinking process achievable. Interestingly, none of the dimensions of the aggregate varied significantly after the crosslinking process; the average diameter of the aggregate was ca. 2 nm, while the thickness of the layers formed when these objects were packed was about 8 nm. Most importantly, films cast from solutions of the *cross-linked macromolecular objects* retained identical packing to those prepared directly from the nascent triblock copolymers, confirming that little change had occurred to the size and structure of the nano-aggregate upon crosslinking [70].

It is clear that while dealing with relatively smaller molecules, small changes in the molecular structure can lead to dramatic differences in the nature and size of the supramolecular aggregates formed. Terminating the rod-segment with a *dendron* (a branched segment) as in molecule D (in Figure 15.18), led to an unprecedented gelation in organic solvent at concentrations as low as 0.2 wt% [71]. By varying the length of the biphenyl segment and the functionality at the termini, it was established that the strongest gel was formed when 4 biphenyl segments were present in the rod-segment which at the same time possesses at least four hydroxy groups that enable the formation of an H-bonded structure. TEM pictures clearly established the formation of nanoribbons with aspect ratios as high as 1000 (Figure 15.20b). From the width of the nanoribbon (ca. 6.5 nm) and its thickness (2 nm), it is clear that bimolecular packing resulting from H-bonding between the terminal dendrons could explain the formation of such nanostructures. Changing the size of the coil segment, either by significantly increasing or decreasing its length, led to either simple precipitation without gel formation or complete absence of gelation. This suggests that an optimum balance of rod-coil size was critical for the generation of nanoribbons [71]. More recently, these nanoribbons have been used to scaffold polystyrene that was prepared by polymerization of the gel formed by dissolution of the dendron rod-coil system in styrene monomer. The most interesting aspect of this study was that, despite the very low concentrations of the nanoribbons ( $\sim 1$  wt%), the entire solid polystyrene sample exhibited birefringence, suggesting the enormous contact surface area between the nanoribbons and the matrix [72].

One of the major motivations for the study of nano-aggregate formation, either in bulk or in solution, is because it provides an opportunity to construct macromolecular objects with dimensions significantly larger than molecular dimensions, and therefore would pave the way to further organize them well into the macroscopic domain. Thus, this serves as a step-wise approach to organizing macromolecules in the bulk phase, with a control over the molecular organization at each step along the way. The fixation of the mushroom-shaped supramolecular ag-

gregates, and their further organization in the bulk, clearly stands out as a fine example of one such approach. An alternative approach using significantly higher molecular weight polymers, wherein the rod-block is made up of a conjugated segment and the coil block is made up of poly(styrene) has recently been demonstrated [73, 74]. Unlike in most cases discussed so far, where using a block selective solvent that dissolves the coil-block generated the nanostructures, the prime driving force being the aggregation (crystallization) of the rod segment, Jenekhe et al. showed that utilizing a solvent that solubilized the rod-segment could lead to the formation of rather unexpected hollow spherical aggregates [73]. Rod-coil block copolymers, thus present unique opportunities that combine both the possibilities of generation and fixation of nano-size molecular objects while at the same time permitting the retention of ordered domains within these structures.

## 15.8

### Nanostructures from Polymerized Surfactant Assemblies

The approaches to the preparation of nanostructured polymeric materials discussed thus far have focused on the use of block copolymers as the basic molecular entity. The domain sizes have typically been varied from ca. 10 nm to tens of  $\mu\text{m}$ . To access even smaller nanostructures, one will need to exploit aggregates formed from small molecules. Surfactants are one of the most extensively studied systems, which are known to form a variety of organizes (Figure 15.21), typically when dissolved in water, due to the presence of both hydrophobic and hydrophilic molecular segments. Reverse micelles and inverted mesophases are formed when they are dissolved in a hydrocarbon solvent, in most cases requiring small amounts of water to aid the aggregate formation. Surfactant molecules, when appropriately modified to include a polymerizable group, either within the hydrocarbon tail or as a part of the hydrophilic head group, or even as a counter-ion, could serve as a very useful approach to the generation of very small nano-size structures of various sizes and shapes, ranging from a few nanometers to 100s of nanometers. Polymerization of surfactant assemblies has been extensively studied for over two decades. The early efforts focused largely on the more stable assemblies, like vesicles, lipid microtubules and other lamellar bilayer assemblies, and the objectives then were largely focused on stabilizing vesicular structures by polymerization, primarily for use as drug-carriers [75]. One of the overriding problems of structural fixation of the geometrically more complex and relatively less stable nonlamellar phases is the retention of the original phase structure during and after polymerization. Thus, it was only more recently that fixation of a variety of other nonlamellar phases, such as the hexagonal and the bicontinuous cubic phases was successfully established. My review of this approach will focus only on some of the more recent approaches that deal with the polymerization of the more complex structures for the generation of nanostructured polymeric structures. Readers may refer to several reviews that deal with this broad area of polymerizable surfactants in order to gain a better insight into the evolution of this field [10–12, 75].

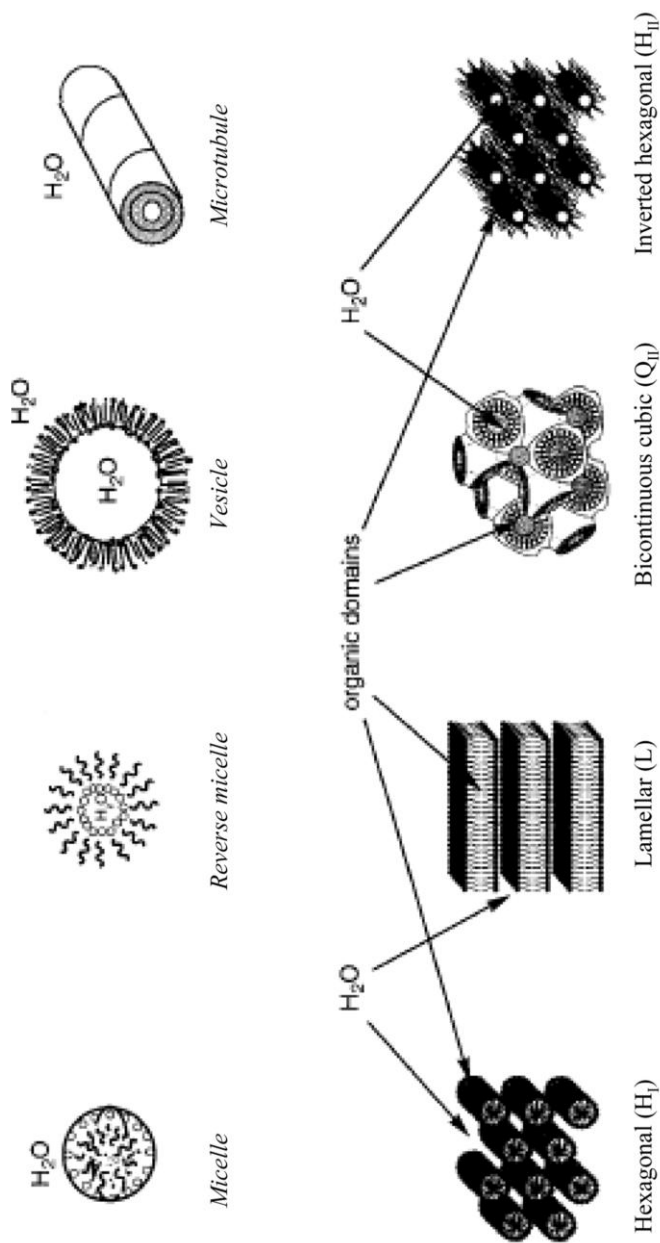


**Fig. 15.21.** Various types of aggregates that could be formed by surfactants. (Reprinted with permission from *Acc. Chem. Res.*, 2001, 34, 973. © 2001 American Chemical Society [10].)



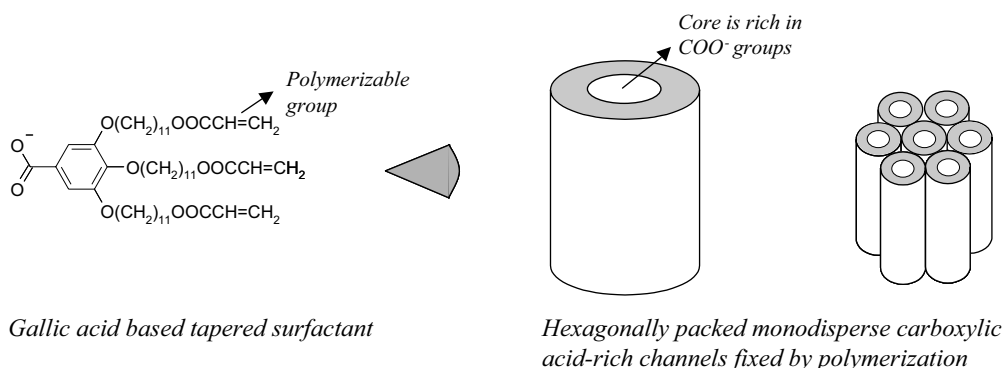


**Fig. 15.22.** Schematic depiction of inverted hexagonal (H<sub>II</sub>) phase formed by tapered surfactants.

The polymerization of nonlamellar phases, such as the hexagonal (both normal H<sub>I</sub> and the inverted H<sub>II</sub>) and the bicontinuous cubic phase has been achieved only recently. Using specially designed surfactants that have a tapered shape, with the hydrophilic head group at the tip of the wedge (Figure 15.22), Lin and coworkers demonstrated the formation of the H<sub>II</sub> in the presence of a small amount (5 to 20 wt%) of water [76]. Polymerization resulted in freezing this structure to generate a robust organic network possessing hexagonally packed channels, typically of about 1.5 nm in diameter, and an inter-channel spacing of about 4 nm. The particularly interesting feature of this approach is the presence of a very high density of functionality (–COOH groups in this case) within the inner walls of the nanochannels that could be potentially useful as catalysts or catalyst-anchoring sites. Elaboration of this theme has led to the incorporation of functionality such as sulfonic acid groups as well as several transition metals, some of which have been shown to exhibit excellent catalytic properties [10]. The use of these nanoporous functional-group-rich structures to generate functional inorganic nanomaterials, such as CdS etc., has also been reported [77].

A particularly interesting study that exemplifies the effect of nano-confinement is one where poly(phenylene vinylene) PPV, a luminescent polymer, was incorporated into the channels formed from these polymerized hexagonal phases [78]. These hexagonal PPV nanocomposites exhibited a significant enhancement in the photoluminescence quantum yields, from ca. 25 to 80%. The origin of this enhancement is ascribed to the prevention of the formation of poorly emissive inter-chain excitonic species as a result of the confinement of the PPV chains into well-defined and well-separated nanochannels. An important feature of these nanocomposites was that they could be readily processed into thin films and fibres and, more importantly, macroscopic alignment of the channels encapsulating the PPV chains led to polarized emission [79].

The generation of nanoporous polymeric materials with controllable pore dimensions serves as an alternative to the inorganic counterparts, as in zeolites. The

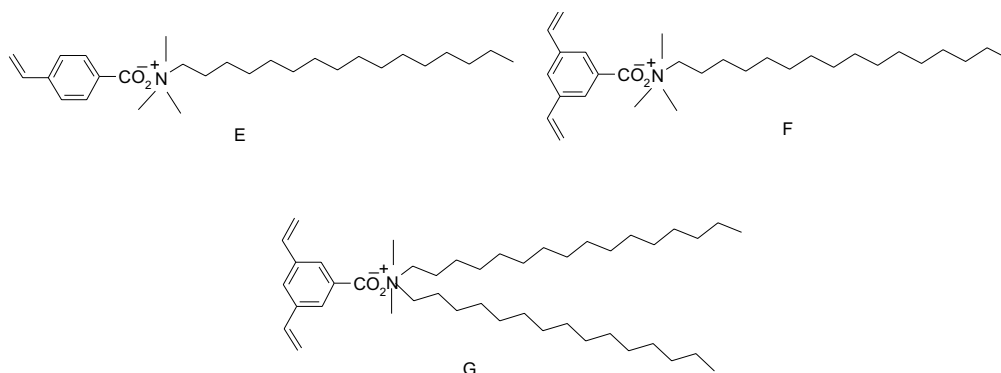


Fig. 15.23. Structures of counter-ion polymerizable surfactants.

added advantage of polymer-based organic nanoporous structures is their versatility in terms of functional group incorporation, which in turn should prove valuable for heterogeneous catalysis. With this objective, the bicontinuous cubic phase (1a3d, gyroid symmetry) formed using a glycerol-based nonionic surfactant was polymerized with retention of morphology [80].

A slightly different and interesting approach is one wherein the polymerizable group does not form an integral part of the surfactant but is the counter-ion. The earliest demonstration of such approaches led to the generation of “ghost vesicles” by Regen and co-workers, in which the hydrocarbon tails were removed after polymerization of the counter-ion, a diallylammonium group [81]. More recently, Kline polymerized highly entangled rod-like micellar aggregates prepared from cetyl trimethylammonium vinyl benzoate, Figure 15.23E [82]. The particularly interesting feature of this approach is that the polymer is formed at the interfacial regions and the long hydrocarbon tails merely serve as a template to hold the nanostructure in place and can be removed after polymerization. Recently, we have gone a few steps further and prepared surfactants that have crosslinkable counter-ions, such as divinyl benzoate (Figure 15.23F). Polymerization of various aggregate structures based on these amphiphiles lead to the *permanent fixation* of the aggregate morphology. Using two-tail analogues (Figure 15.23G), vesicles that are enveloped on either side by a crosslinked macromolecular sheath were prepared. These cross-linked vesicular structures were shown to be stable to lysis in the presence of excess of CTAB and their stability could be varied by varying the extent of cross-linkable surfactant in mixed vesicular formulations containing both vinyl and divinyl benzoate surfactants [83].

In the context of utilizing surfactant assemblies for building nanostructured polymeric materials, one other approach that deserves mention is the polymerization of standard monomers partitioned into the hydrophobic regions of surfactant aggregates: one in particular that has received a lot of attention is *vesicle templating* [84]. The basic idea in this approach is to generate vesicles using appropriate surfactants and then to solubilize standard monomers, such as styrene, within the

hydrophobic bilayer regions of the vesicular structure without disrupting the aggregate morphology. Polymerization of the monomer is then expected to produce polymer chains that weave through the bilayer structure, lending enhanced stability to the vesicles. Although this concept was presented and attempted almost 20 years ago [85], the recent surge of interest in developing structurally fixed nanostructures has spurred a revival of this idea. Kaler and coworkers, recently utilized equilibrium vesicles formed by using a combination of anionic and cationic surfactants, such as cetyltrimethylammonium toluene sulfonate (CTAT) and sodium dodecylbenzene sulfonate (SDBS) for the inclusion of monomers, such as styrene and divinyl benzene (DVB) [86]. By varying the ratio of CTAT to SDBS, up to 10 wt% of styrene was taken up by the vesicular aggregates without disruption of their structure. Polymerization of the embedded monomers leads to a dramatic enhancement of the vesicle stability, as shown by lysis experiments. Typical sizes of these vesicles are ca. 60 nm in diameter and the thickness of the bilayer shell is around 10 nm.

In a similar study, Meier and coworkers utilized simple kinetically stabilized vesicles prepared by sonication of a cationic surfactant, like dimethyldioctadecyl ammonium bromide (DODAC), which was then swollen with the monomer, butyl methacrylate, and the crosslinker, 1,2-di(methacryloyloxy)-ethane [87]. Polymerization of the methacrylate monomers, led to the generation of shell-stabilized hollow polymeric nanospheres (Figure 15.24). More recently, Sauer and Meier have extended this approach of vesicle templating, using *tert*-butyl acrylate and a hydrophilic crosslinker, ethylene glycol dimethacrylate (EGDMA), to generate pH-responsive nanocapsules [88]. Selective hydrolysis of the *tert*-butyl groups after polymerization led to the generation of a polyelectrolyte, poly(acrylic acid), whose conformation is known to be very pH-dependent, thus leading to dramatic changes in the dimensions of the capsules as a function of pH.

One of the hotly debated issues in the context of this approach is the retention of the original structure and the homogeneous distribution of the polymer chains

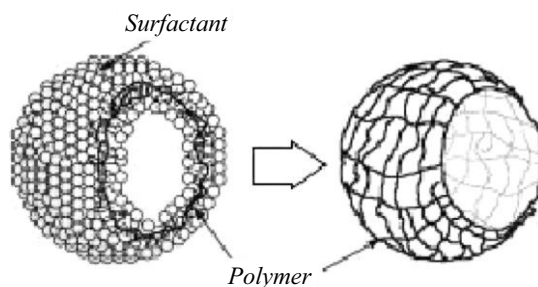


**Fig. 15.24.** Schematic depiction of the polymerization of monomers within the vesicle bilayer leading to the formation of hollow nanospheres. (Reprinted with permission from *Langmuir*, **1998**, 14, 1031. © 1998 American Chemical Society [87].)

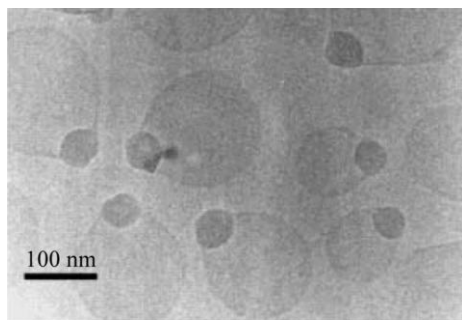


**Fig. 15.25.** Cryo-TEM showing the formation of parachute-like vesicles along with a putative mechanism for their formation. (Reprinted with permission from *Adv. Mater.*, **2000**, 12, 1291 [84].)

within the bilayer membrane after the polymerization of the occluded monomer. Jung et al. have contested this aspect, and in their studies have clearly demonstrated the phase separation of the polymer particle within the vesicular bilayer, forming what they term as “parachute-like vesicles” [89]. It is evident that the miscibility of the monomer in the hydrophobic bilayer region does not guarantee the miscibility of the polymer formed and therefore, more often than not one expects that, as the polymerization proceeds, collapse of the polymer chain will occur, leading to nucleation and precipitation of the polymer. The precipitated polymer particle can either be excluded from the bilayer or remain within it: both situations are seen to happen from cryo-TEM observations, that show the presence of free polymer particles as well as polymer particles within the vesicular bilayer generating parachute-like structures (Figure 15.25). In cases where such phase-separation is not seen, it has been argued that this is because the monomer, such as butyl methacrylate, generates polymers that remain soluble in the bilayer medium [87]. One approach that Jung and coworkers have adopted to overcome the problem of phase-separation, is to utilize a polymerizable surfactant along with the monomer: in this way, as the polymerization proceeds, the polymer chain attaches the surfactant molecules along the way, preventing phase-separation [90]. Although, this approach was shown to be successful, it takes away one of the most important advantages, namely the avoidance of using synthetically complex surfactant molecules.

It is clear that the approach of utilizing other types of surfactant aggregate mor-

phologies to selectively partition monomers into well-defined regions of controllable size and shape offers an attractive yet simple route to the generation of nanostructured polymeric materials. The advantages are obvious, in that it utilizes standard commercially available surfactants and monomers and, therefore, unlike the approaches that use more complex polymerizable designer surfactants, these are more readily accessible and scalable. However, while they present exciting prospects, they raise several difficult problems too. The primary issues that remain to be addressed are: (i) detailed understanding of factors that govern destabilization of the aggregate structures in the presence of the monomers; (ii) discerning the factors that enable retention of the surfactant aggregate morphology during the polymerization; and (iii) evolving strategies, based on selection of the monomer (comonomer, if necessary), monomer concentration, polymerization temperature etc., to enable retention of the aggregate morphology by design. Research in these directions should enable creative utilization of the rich morphological features of surfactant assemblies for generation of nanostructured polymeric systems with a wide range of structures and function.

## 15.9

### Summary and Outlook

The confluence of innovative synthetic methodologies, sophisticated characterization techniques and potential technological utility has brought about the sudden surge in research activity pertaining to nanostructural control in polymeric systems. In this chapter, I have tried to present various facets of nanostructural control in polymeric systems, beginning with control of polymer structure and conformation, and ending with polymerization within spatially restricted domains, such as those formed by surfactant assemblies. In selecting such a broad canvas, I have knowingly forsaken the ability to cover any of the subtopics in great detail. As this book attempts to cover several wide-ranging topics, only one of which is dedicated to polymeric nanostructures, I have chosen to provide the reader with a flavor of the various approaches that have been used to generate nanostructured polymeric systems. For exhaustive reviews concerning each of these sub-areas, interested readers may consult many recent in-depth reviews to which I have made reference. I have also left out a few topics that, in principle, merit mention, such as nanostructured polymeric materials as templates for the preparation of inorganic materials, nanostructured inorganic solids as templates for polymerization, surface patterning of polymeric materials using techniques such as soft-lithography etc., all of which could be brought under the larger umbrella of nanostructured polymers. While the emphasis of the chapter has been on various approaches to the building of nanostructures, details of property evaluation, which in many cases is still in its infancy, may have been a little underplayed.

Block copolymers are clearly going to be the materials for which an increasing number of nanostructuring strategies will be developed. The tremendous advances

that have been made in living polymerization methodologies during the last decade, especially those based on free-radical polymerizations, will open up the arena to a much wider range of functional monomers than was ever possible during the anionic polymerization era. In spite of the relatively poorer control over the molecular weight (and polydispersity), the simplicity of many of these controlled free-radical polymerizations and their unparalleled tolerance to functional groups, will serve to propel these approaches to the fore, as the method of choice for generating nanostructured polymeric materials. Conjugated polymers have seen a resurgence of activity due to many new exciting properties, such as photoluminescence, electroluminescence, lasing etc. By virtue of being intrinsically rigid rod-like entities, block copolymers based on conjugated polymers will continue to provide exciting prospects for the development of nanostructured systems with novel and exciting properties. Bicontinuous morphologies, using such conjugated rod-coil block copolymers, for instance, could serve as ideal systems for photovoltaic applications.

Polymerization of pre-organized entities, be it surfactant assemblies or block copolymer assemblies, is clearly an elegant way to construct permanent macromolecular objects, with wide-ranging sizes and shapes. Although impressive strides have been taken in this approach, the basic building blocks, both block copolymers and polymerizable surfactants, are still expensive and difficult to access. In this context, the confinement of simple monomers, by selective partitioning within selected domains of surfactant assemblies and their subsequent polymerization, offers unique opportunities that could combine both the richness of structural variety and simplicity. Clearly greater understanding of the fundamental factors that govern the selective partitioning of monomers and retention of morphology after polymerization is needed before this approach becomes mature and of wider utility.

The richness and excitement of understanding and applying the fundamental principles that govern organization from the atomic scale to the macroscopic one, specifically in relation to polymeric systems, is what I hope this chapter will have conveyed. It is evident that many milestones, such as the structural control of polymer molecules using “living” polymerization methods, methodologies for block copolymer preparation with precisely controllable block sizes, predictable control of morphological features in block copolymer systems etc., have been crossed. Armed with these successes, scientists are now free to explore and exploit the structural and functional variety to create new polymeric systems with potentially exciting properties, both the *expected* and the *as yet unseen*.

## Acknowledgements

The help of many of my students and coworkers, G. Padmanaban, Geeta Kheter Paul and Arun Prasath, in retrieving references and figures is gratefully acknowledged.

## References

- 1 S. FORSTER, T. PLANTENBERG, *Angew. Chem. Int. Ed. Engl.*, **41**, 688, (2002).
- 2 G. LIU, in *Handbook of Nanostructured Materials and Nanotechnology*, ed. H. S. NALWA, Academic Press, New York 2000, Vol. 5, Chapter 9, p. 475.
- 3 T. LIU, C. BURGER, B. CHU, *Prog. Polym. Sci.*, **28**, 5, (2003).
- 4 G. LIU, *Curr. Opin. Colloid Interface Sci.*, **3**, 200, (1998).
- 5 M. SHIMOMURA, T. SAWADAISHI, *Curr. Opin. Colloid Interface Sci.*, **6**, 11, (2001).
- 6 C. G. CLARK, K. L. WOOLEY, *Curr. Opin. Colloid Interface Sci.*, **4**, 122, (1999).
- 7 S. I. STUPP, P. OSEANAR, in *Synthesis of Polymers*, ed. A. D. SCHLUTER, Wiley-VCH, Weinheim 1999, Chapter 15, p. 513.
- 8 S. A. MILLER, J. H. DING, D. L. GIN, *Curr. Opin. Colloid Interface Sci.*, **4**, 338, (1999).
- 9 W. MEIER, *Chem. Soc. Rev.*, **29**, 295, (2000).
- 10 D. L. GIN, W. GU, B. A. PINDZOLA et al., *Acc. Chem. Res.*, **34**, 973, (2001).
- 11 D. F. O'BRIEN, B. A. ARMITAGE, A. BENEDICTO et al., *Acc. Chem. Res.*, **31**, 861, (1998).
- 12 B. A. ARMITAGE, D. E. BENNETT, H. G. LAMPARSKI et al., *Adv. Polym. Sci.*, **126**, 53, (1996).
- 13 K. L. WOOLEY, *J. Polym. Sci., Polym. Chem.*, **38**, 1397, (2000).
- 14 W. MEIER, *Curr. Opin. Colloid Interface Sci.*, **4**, 6, (1999).
- 15 R. P. QUIRK, D. J. KINNING, L. J. FETTERS, in *Comprehensive Polymer Science*, ed. S. L. AGGARWAL, Pergamon Press, London 1989, Vol. 7, p. 1.
- 16 C. J. HAWKER, A. W. BOSMAN, E. HARTH, *Chem. Rev.*, **101**, 3661, (2001).
- 17 M. KAMIGAITO, T. ANDO, M. SAWAMOTO, *Chem. Rev.*, **101**, 3689, (2001).
- 18 N. HADJICHRISTIDIS, M. PITSIKALIS, S. PISPAS et al., *Chem. Rev.*, **101**, 3747, (2001).
- 19 H. L. HSIEH, R. P. QUIRK, *Anionic Polymerization: Principles and Practical Applications*, Marcel Dekker, New York 1996.
- 20 M. SAWAMOTO, T. HIGASHIMURA, in *Encyclopedia of Polymer Science and Technology*, 2nd edition (suppl.), Wiley, New York 1990, p. 399.
- 21 O. W. WEBSTER, *J. Polym. Sci., Part A: Polym. Chem.*, **38**, 2855, (2000).
- 22 T. OTSU, *J. Polym. Sci., Part A: Polym. Chem.*, **38**, 2121, (2000).
- 23 M. MUTHUKUMAR, C. K. OBER, E. L. THOMAS, *Science*, **277**, 1225, (1997).
- 24 For an excellent review on foldamers, see D. J. HILL, M. J. MIO, R. B. PRINCE et al., *Chem. Rev.*, **101**, 3893, (2001).
- 25 T. NAKAMOTO, Y. OKAMOTO, *Chem. Rev.*, **101**, 4013, (2001).
- 26 K. MAEDA, S. OKADA, E. YASHIMA et al., *J. Polym. Sci., Part A: Polym. Chem.*, **39**, 3180, (2001).
- 27 S. H. GELLMAN, *Acc. Chem. Res.*, **31**, 173, (1998).
- 28 Y. MORISHIMA, in *Functional Monomers and Polymers*, 2nd edition, eds. K. TAKEMOTO, R. M. OTTENBRITE, M. KAMACHI, Marcel Dekker, New York 1997, p. 455.
- 29 J. H. K. K. HIRSCHBERG, L. BRUNSVELD, A. RAMZI et al., *Nature*, **407**, 167, (2000).
- 30 R. S. LOKEY, B. L. IVERSON, *Nature*, **375**, 303, (1995); A. J. ZYCH, B. L. IVERSON, *J. Am. Chem. Soc.*, **122**, 8898, (2000).
- 31 J.-M. LEHN, *Supramolecular Chemistry: Concepts and Perspectives*, VCH, Weinheim 1995.
- 32 F. S. BATES, G. H. FREDRICKSON, *Phys. Today*, **32**, (1999).
- 33 A. K. KHANDPUR, S. FORSTER, F. S. BATES et al., *Macromolecules*, **28**, 8796, (1995).
- 34 M. W. MATSEN, F. S. BATES, *Macromolecules*, **29**, 1091, (1996).
- 35 K. ISHIZU, T. FUKUTOMI, *J. Polym. Sci., Part C: Polym. Lett.*, **26**, 281, (1988).

- 36 G. LIU, L. QIAO, A. GUO, *Macromolecules*, 29, 5508, (1996).
- 37 G. LIU, J. DING, L. QIAO et al., *Chem. Eur. J.*, 5, 2740, (1999).
- 38 S. STEWART, G. LIU, *Angew. Chem., Int. Ed. Engl.*, 39, 340, (2000).
- 39 X. YAN, F. LIU, L. ZHAO et al., *Macromolecules*, 34, 9112, (2001).
- 40 G. LIU, J. DING, A. GUA et al., *Macromolecules*, 30, 1851, (1997).
- 41 G. LIU, J. DING, T. HASHIMOTO et al., *Chem. Mater.*, 11, 2233, (1999).
- 42 K. AUMNDSON, E. HELFAND, X. QUAN et al., *Macromolecules*, 27, 6559, (1994).
- 43 T. L. MORKVED, M. LU, A. M. URBAS et al., *Science*, 273, 931, (1996).
- 44 E. HUANG, L. ROCKFORD, T. P. RUSSELL et al., *Nature*, 395, 757, (1998).
- 45 T. THRUN-ALBRECT, R. STEINER, J. DEROUCHÉY et al., *Adv. Mater.*, 12, 787, (2000).
- 46 K. W. GUANNI, C. T. BLACK, S. H. I. YEUNG, *Adv. Mater.*, 14, 120, (2002).
- 47 T. HASHIMOTO, K. TSUTSUMI, Y. FUNAKI, *Langmuir*, 13, 6869, (1997).
- 48 L. ZHANG, A. EISENBERG, *J. Am. Chem. Soc.*, 118, 3168, (1996).
- 49 A. GOU, G. LIU, J. TAO, *Macromolecules*, 29, 2487, (1996).
- 50 F. HENSELWOOD, G. LIU, *Macromolecules*, 30, 488, (1997).
- 51 F. HENSELWOOD, G. LIU, *Macromolecules*, 31, 4213, (1998).
- 52 J. ZHOU, Z. LI, G. LIU, *Macromolecules*, 35, 3690, (2002).
- 53 K. B. THURMOND II, T. KOWALEWSKI, K. L. WOOLEY, *J. Am. Chem. Soc.*, 118, 7239, (1996).
- 54 H. HUANG, T. KOWALEWSKI, E. E. REMSEN et al., *J. Am. Chem. Soc.*, 119, 11653, (1997).
- 55 A. H. BAUGHER, J. M. GOETZ, L. M. McDOWELL et al., *Biophys. J.*, 75, 2574, (1998).
- 56 J. SCHAEFER, H. HUANG, K. L. WOOLEY, *Polym. Prepr.*, 40(1), 460, (1999).
- 57 V. BUTUN, N. C. BILLINGHAM, S. P. ARMES, *J. Am. Chem. Soc.*, 120, 12135, (1998).
- 58 V. BUTUN, A. B. LOWE, N. C. BILLINGHAM et al., *J. Am. Chem. Soc.*, 121, 4288, (1999).
- 59 V. BUTUN, X.-S. WANG, M. V. DEPAZ BANEZ et al., *Macromolecules*, 33, 1, (2000).
- 60 H. HUANG, E. E. REMSEN, T. KOWALEWSKI et al., *J. Am. Chem. Soc.*, 121, 3805, (1999).
- 61 B. M. DISCHER, Y. Y. WON, D. S. EGE et al., *Science*, 284, 1143, (1999).
- 62 B. M. DISCHER, H. BERMUDEZ, D. A. HAMMER et al., *J. Phys. Chem.*, 106, 2848, (2002).
- 63 H. SHEN, A. EISENBERG, *Angew. Chem., Int. Ed. Engl.*, 39, 3310, (2000).
- 64 S. I. STUPP, *Curr. Opin. Colloid Interface Sci.*, 3, 20, (1998).
- 65 J. T. CHEN, E. L. THOMAS, C. K. OBER et al., *Science*, 273, 343, (1996).
- 66 L. H. RADZIŁOWSKI, S. I. STUPP, *Macromolecules*, 27, 7747, (1994).
- 67 L. H. RADZIŁOWSKI, B. O. CARRAGHER, S. I. STUPP, *Macromolecules*, 30, 2110, (1997).
- 68 S. I. STUPP, V. LEBONHEUR, K. WALKER et al., *Science*, 276, 384, (1997).
- 69 M. U. PRALLE, C. M. WHITAKER, P. V. BRAUN et al., *Macromolecules*, 33, 3550, (2000).
- 70 E. R. ZUBERAV, M. U. PRALLE, L. S. LI et al., *Science*, 283, 523, (1999).
- 71 E. R. ZUBERAV, M. U. PRALLE, E. D. SONE et al., *J. Am. Chem. Soc.*, 123, 4105, (2001).
- 72 E. R. ZUBERAV, M. U. PRALLE, E. D. SONE et al., *Adv. Mater.*, 14, 198, (2002).
- 73 S. A. JENEKHE, X. L. CHEN, *Science*, 279, 1903, (1998).
- 74 S. A. JENEKHE, X. L. CHEN, *Science*, 283, 372, (1999).
- 75 H. RINGSDORF, B. SCHLARB, J. VENZMER, *Angew. Chem. Int. Ed. Engl.*, 27, 113, (1988).
- 76 R. RESEL, G. LEISING, P. MARKART et al., *Macromol. Chem. Phys.*, 20, 1128, (2000).
- 77 D. H. GRAY, D. L. GIN, *Chem. Mater.*, 10, 1827, (1998).
- 78 R. C. SMITH, W. M. FISCHER, D. L. GIN, *J. Am. Chem. Soc.*, 119, 4092, (1999).
- 79 E. ZOJER, P. MARKART, E. J. W. LIST et al., *Synth. Met.*, 102, 1270, (1999).
- 80 W. SRISIRI, A. BENIDICTO, D. F.



- O'BRIEN et al., *Langmuir*, 14, 1921, (1998).
- 81 S. L. REGEN, J.-S. SHIN, J. F. HAINFELD et al., *J. Am. Chem. Soc.*, 106, 5756 (1984).
- 82 S. R. KLINE, *Langmuir*, 15, 2726, (1999).
- 83 K. P. GEETA, S. RAMAKRISHNAN, *Langmuir*, to be submitted.
- 84 D. H. W. HUBERT, M. JUNG, A. L. GERMAN, *Adv. Mater.*, 12, 1291, (2000).
- 85 J. MURTAGH, J. K. THOMAS, *Faraday Discuss. Chem. Soc.*, 81, 127, (1986).
- 86 J. D. MORGAN, A. JOHNSON, E. W. KALER, *Langmuir*, 13, 6447, (1997).
- 87 J. HOTZ, W. MEIER, *Langmuir*, 14, 1031, (1998).
- 88 M. SAUER, W. MEIER, *Chem. Commun.*, 55, (2001).
- 89 M. JUNG, D. H. W. HUBERT, E. VAN VELDHOVEN et al., *Langmuir*, 16, 3165, (2000).
- 90 M. JUNG, I. DEN OUDEN, A. MONTOLYA-GINI et al., *Langmuir*, 16, 4185, (2000).

## 16

## Recent Developments in the Chemistry and Chemical Applications of Porous Silicon

*J. M. Schmeltzer and J. M. Buriak*

## 16.1

### Introduction

Porous silicon is a fascinating derivative of bulk crystalline silicon that has inspired an enormous body of research since the first reports of this material [1, 2]. Early developments of this highly resistive silicon were applied for dielectric isolation, including isolation by porous oxidized silicon (IPOS) and silicon-on-insulator (SOI) technologies [3]. Interest in porous silicon has literally exploded since the seminal paper outlining room temperature photoluminescence from this material was published in 1990 [4]. This interest, once largely confined to the electrical properties of porous silicon, has now expanded to include the optical, chemical, and physical characteristics as well. More importantly, work of the past several years has seen the birth of a number of novel and exciting applications based upon porous silicon. Great strides have been taken in understanding the formation and behavior of porous silicon [5]; nonetheless, much work still remains to elucidate the details and specifics of its properties and reactivity.

The aim of this chapter is to describe the most recent advances and discoveries in the chemistry of porous silicon. A brief introduction to the formation and chemical functionalization of this substance is given, followed by discussion of several emerging technologies founded upon porous silicon, including chemical analyses, biological implants, and biochemical sensors. Lesser consideration is given to physical and electronic applications since they lie mostly beyond the scope of this book and have been previously reviewed elsewhere [5, 6]. Investigations into the chemical and biochemical activities of porous silicon are ongoing and continue to develop new uses and improve extant applications for this material.

## 16.2

### Preparation and Characterization of Porous Silicon Substrates

Porous silicon is comprised of interconnected zero-dimensional nanocrystallites and one-dimensional nanowires produced through the chemical [7], photochemi-

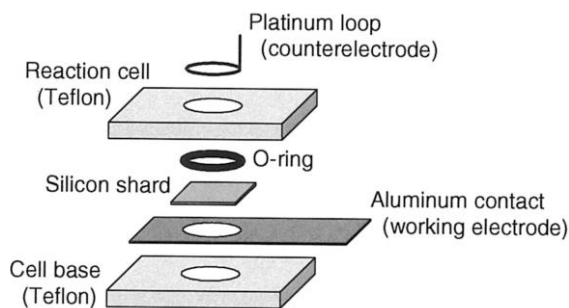
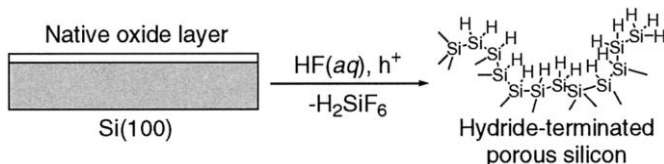


**Fig. 16.1.** Etching cell used for the electrochemical preparation of porous silicon [10]. The liquid-tight well fashioned by the assembly of this cell contains the etching solution directly above the flat silicon substrate. Anodization is accomplished using an aluminum contact for the working electrode

and a platinum wire loop (immersed in the liquid etchant) for the counterelectrode. This particular cell is bored with holes in the electrode and the base to allow characterization of the porous silicon specimen with transmission FTIR spectroscopy directly within the etching cell.

cal [8], or electrochemical [9] etching of flat, single-crystal silicon with fluoride solutions. Although chemical (“stain”) etching of flat silicon is easily accomplished owing to its open-circuit, relatively simple experimental apparatus, porous silicon prepared in this fashion exhibits substantial variability in its properties from sample to sample. Galvanostatic anodization of flat silicon is the method most often employed to fabricate porous silicon since greater reliability and selectivity in the product can be achieved. Aqueous HF in ethanol is the etchant chiefly used; the ethanol is added as a surfactant to reduce the surface tension of the etching solution and to enable full wetting of the silicon substrate. Anodization is completed at room temperature in open air within a fluoride-resistant (e.g. Teflon) reaction cell (Figure 16.1) [10], eliminating the need for complex, inert atmosphere set-ups and illustrating the relative ease of synthesis for this material.

The mechanism of electrochemical etching to produce porous silicon has been studied by a number of researchers [11–13]. Although it is certain that several different reactions are occurring simultaneously, anodic etching of crystalline silicon ultimately leads to oxidation and dissolution of the surface to silicon hexafluoride (Scheme 16.1). Under these conditions, Si–Si bonds are electrochemically activated and react with fluoride ions to form soluble, molecular perfluoro species; solvation of these silicon fluorides by the etching medium yields a physically irregular, high area porous silicon matrix. Visual indicators for the anodization are the appearance



**Scheme 16.1**

of colours within the etching solution (known as Fabry–Pérot fringes) and the evolution of dihydrogen gas, the reduction product, from the platinum loop cathode. Despite preparation in air, the surface of freshly etched porous silicon is hydride-terminated and not oxide-terminated, resulting in a hydrophobic and chemically homogeneous interface. Like flat crystalline silicon, hydride-passivated porous silicon oxidizes readily under ambient conditions to form a thin, insulating oxide overlayer, demonstrating a common reactivity for these two materials. However, porous silicon has a number of novel properties that distinguish it from its parent substrate, illustrating the unique nature of the silicon nanocrystallites and making this material a new, possibly complementary component for silicon-based technologies.

The physical and chemical properties of porous silicon can be characterized by a variety of analytical techniques. Electron and scanning probe microscopies are employed to directly image the structural elements of the silicon matrix and acquire information regarding size, shape, and orientation of the nanocrystalline domains. The dimensions of the silicon nanocrystallites ( $10^0$ – $10^1$  nm) are well within the resolution of transmission electron microscopy (TEM) [14]; however, the inherent fragility of these domains requires exceptional caution in the preparation of microscopy samples. Tightly controlled ion milling is the most successful means of preparing exceptionally thin specimens without inflicting significant damage to the nanocrystalline structure. Imaging with scanning electron microscopy (SEM) can provide a pseudo-three-dimensional perspective of the surface topography and reveal details about the size and extent of the pores (Figure 16.2). Compared to TEM, relatively little specimen preparation is needed; typically, only an ultrathin layer of carbon or gold is used to ensure strong contrast and mini-

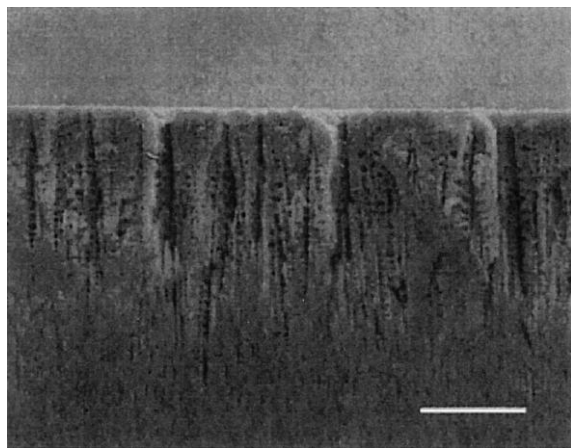


**Fig. 16.2.** Cross-sectional SEM of porous silicon prepared from n-type (P-doped, 0.75–0.95  $\Omega$  cm) Si(100). The directionality of the pores illustrates the anisotropy of the etch. Etching was accomplished with 49% HF(aq)/

EtOH (1:1 v:v) at  $+77.2 \text{ mA cm}^{-2}$  for 1 min; the scale bar is 10  $\mu\text{m}$ . (Reprinted with permission from [29]. Copyright 2002 American Chemical Society. H. C. Choi is gratefully acknowledged for this micrograph.)

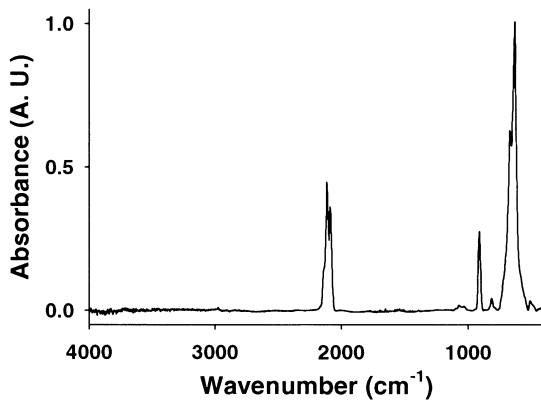


**Fig. 16.3.** Transmission FTIR spectrum of freshly etched, hydride-terminated porous silicon. The sharp, tripartite band centered at  $2100\text{ cm}^{-1}$  is assigned to the stretching modes of mono- ( $\text{SiH}$ ), di- ( $\text{SiH}_2$ ), and trihydride ( $\text{SiH}_3$ ) moieties comprising the surfaces of the nanocrystallites. Silicon hydride bending modes appear below  $1000\text{ cm}^{-1}$ . Silicon oxide, which absorbs near  $1100\text{ cm}^{-1}$ , is conspicuously absent.

mize specimen charging. When used in conjunction with ancillary techniques such as energy dispersive X-ray (EDX) analysis and electron energy loss spectroscopy (EELS), chemical microanalysis of minute regions of the porous substrate can be completed. Atomic force microscopy (AFM) and scanning tunneling microscopy (STM) can be used to physically image porous silicon surfaces to atomic-scale lateral resolution [15]; however, the dimensions of the scanning probe tip often exceed those of the porous matrix, resulting in distortion of the vertical scale. Using gas adsorption, an approximation of the specific surface area of porous silicon can be achieved through Brunauer–Emmett–Teller (BET) analysis [16]; values ranging from less than  $10^0\text{ m}^2\text{ g}^{-1}$  for macroporous silicon to nearly  $10^3\text{ m}^2\text{ g}^{-1}$  for microporous substrates have been estimated. These expansive values for surface area confirm the vast extent of porosity that is indigenous to this material; moreover, characterization of these extensive surfaces can be accomplished with population-dependent spectroscopic methods such as FTIR (Figure 16.3) [17] and nuclear magnetic resonance (NMR) [18, 19] spectroscopies that are normally inaccessible to flat substrates with relatively low area. Other techniques used to identify the chemical nature of porous silicon include X-ray photoelectron spectroscopy (XPS) [20] and secondary ion mass spectrometry (SIMS) [21], utilized respectively for the analysis of surface groups in the upper porous regions and groups throughout the full thickness of the material.

The physical properties of porous silicon can be specifically varied by systematically changing the chemical reagents and electrochemical parameters of the etching procedure. The complex nanoscale architecture of porous silicon depends largely upon the doping of the single-crystal precursor, ranging from a sponge-like morphology typically produced from lightly-doped p-type substrates to a more columnar structure usual for n-type precursors [22]. Effects of fluoride concentration,

current density, anodization time, and illumination of the etching reaction, upon the morphology of porous silicon have also been examined [9]. A range of pore sizes, total porosities, and surface areas are readily accessible through different etching conditions, demonstrating the ability to fabricate porous silicon matrices with particular dimensions [23]. The anisotropic nature of the anodic etch tends to result in the unidirectional formation of pore structures, although some lateral etching does occur (Figure 16.2); this is attributed to the different kinetic reactivities of the silicon crystal faces, which exhibit unequal rates of dissolution under these reaction conditions. Control over the formation of these pore channels, along with regulation of the substrate thickness and the size distribution of the silicon nanocrystallites, is imperative for the fabrication and optimization of devices and physical applications based upon porous silicon.

The dimensions of the silicon nanocrystallites are also believed to play an integral role in the luminescent properties of porous silicon [6]. The origin of photoluminescence, still under investigation, is hypothesized to manifest from the nanocrystalline domains where quantum confinement of charge carriers occurs [4]. Recombination of these confined electron-hole pairs (excitons) releases energy in the visible spectrum; the color of the emission depends upon the sizes of these domains and shifts from red to blue as the diameters of the nanocrystallites decrease. In contrast to flat single-crystal silicon, which emits light only weakly ( $<0.001\%$ ) in the infrared owing to its indirect bandgap [24], nanocrystalline porous silicon luminesces with much greater efficiency, exhibiting emission quantum yields up to several percent and functioning more like a direct bandgap semiconductor (Figure 16.4) [25]. The large fraction of silicon surface atoms, however, suggests that surface states may greatly affect the luminescence behavior of this material. Oxidation or conversion of the native hydride surface to other groups often results in changes to the photoluminescence intensity and wavelength, thus supporting this hypothesis [26, 27]. Dependence upon interfacial parameters has also been reported for the electroluminescence of porous silicon induced by formic acid/sodium formate [28]. Just as for physical applications, effective and efficient optoelectronic devices based upon porous silicon require strict control over the substrate properties.

### 16.3

#### Surface Chemistry of Porous Silicon Surfaces

Ongoing investigations into the chemistry of porous silicon surfaces seek to develop methods for the preparation of chemically functional interfaces that protect the underlying silicon nanocrystallites from degradation without changing or annihilating their intrinsic behavior. The native, hydride-terminated surface is only metastable under ambient conditions and oxidation of freshly prepared porous silicon commences within minutes when exposed to air. While surface oxide can suitably passivate the nanocrystalline silicon and stabilize its photoluminescence, the electrically insulating and structurally defective character of this oxide layer

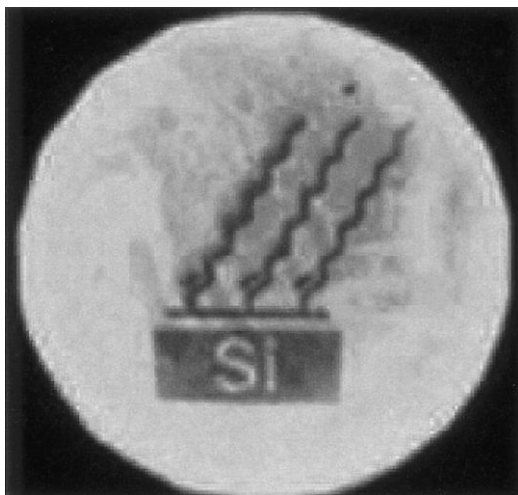


**Fig. 16.4.** Photoluminescent porous silicon patterned with chemically bound dodecenyl groups. Illumination of the substrate with UV light (365 nm) induces orange photoluminescence from the unfunctionalized (hydride-

terminated) regions and diminished, red-shifted emission from the chemically modified areas. Photopatterning was accomplished via light-promoted hydrosilylation of 1-dodecyne with hydride-terminated porous silicon.

poses a major obstacle to the development of electronic devices based upon this material. Furthermore, excessive or uncontrolled oxidation may deleteriously and irreversibly alter the useful, inherent properties of the nanocrystallites, compromising their integrity and drastically limiting their utility for other technological applications. Thus, the desire for greater control over the interfacial properties of porous silicon has redirected focus from the oxide layer to exploitation of the chemistry of the freshly etched hydride surface to synthesize covalently bonded organic monolayers [29]. Passivation of porous silicon with organic moieties imparts resistance to oxidation and gives some regulation over the stability of this material [30]. Additionally, such groups can be readily manipulated through the expansive resources of organic and organometallic chemistry, leading to the synthesis of derivatized surfaces exhibiting distinct chemical activities [31–33]. The tunable reactivity and durability of organically-passivated nanocrystalline silicon offer the incorporation of stability, selectivity, and recognition into porous silicon, expanding its usefulness from optoelectronic applications to analytical and chemical devices as well [34].

Beyond the motivation to fabricate working systems from functionalized porous silicon, there is also more fundamental interest in the reactions of its surfaces. Because the vast surface of nanocrystalline silicon contains a large fraction of the total atoms, the composition and environment of the silicon interface are believed to affect greatly the physical, chemical, and electronic properties of the material. In particular, functionalization of porous silicon with certain organic groups is known to diminish photoluminescence [27]; however, the mechanism of quenching has

not yet been fully elucidated, allowing only approximate comparisons of quenching efficiencies to be made. The effects of surface chemistry upon the physical morphology of the nanocrystalline architecture, the breadth and depth of porosity, the magnitude of surface area, and the electronic character of the porous silicon also remain to be more completely investigated. By establishing how various functionalization reactions and surface terminations affect the material properties, more precise control of the surface states can be achieved with minimal damage or transformation of the silicon nanocrystallites. Research into the mechanisms of these reactions may yield new insight into the general nature of semiconductor interfaces and reveal additional strategies for the functionalization of these surfaces.

Progress in the synthesis of stable, functional materials has generated, within the past decade, a number of wet chemical methods for the modification of porous silicon surfaces [22, 35]. In particular, the formation of organic monolayers bound via Si-C bonds has garnered more attention in recent years owing to the low polarity and kinetically inert nature of these largely covalent linkages [29, 36–38]. Advances in the chemistry of hydride-terminated nanocrystalline silicon for the preparation of such monolayers have resulted in a plethora of reactions, including thermal [20, 39, 40], chemical [21, 41–47], electrochemical [48–51], and photochemical [52, 53] methods, that are capable of producing selectively functionalized materials upon demand (Figure 16.5). Some of these methods are adapted from similar reactions known for molecular silicon compounds [54], illuminating some parallels between the chemistries of solution-phase hydrosilanes and solid-state, hydride-terminated surfaces. Others are developed from procedures known to functionalize flat, single-crystal silicon surfaces [55–62], illustrating reactions that may proceed on all varieties of hydride surface, regardless of morphology or orientation. Several of these reactions have no known molecular or flat-surface analogs, instead employing reactive properties unique to nanocrystalline silicon to drive the formation of surface bonds. While earlier strategies for the derivatization of porous silicon focused upon the reactions of hydride and oxide surfaces to form Si-O bonds [22], interest in this approach has generally waned owing to the generally inferior stability of these monolayers and the relatively narrow range of functionalities that can be imparted to the silicon surfaces.

Preparation and analysis of porous silicon substrates functionalized with organic monolayers can be readily accomplished by a variety of procedures using equipment and techniques familiar to most chemists. The native material can be handled in air for brief periods without significant oxidation and contamination, but porous silicon keeps much longer when maintained under inert atmosphere. Most manipulations and chemical treatments can be completed using straightforward Schlenk and glovebox practices. The high surface area of porous silicon permits characterization by reliable, convenient analytical tools such as transmission FTIR, diffuse reflectance infrared Fourier transform (DRIFT), solid-state NMR, and X-ray photoelectron spectroscopies. In fact, owing to its relative ease of characterization, porous silicon may serve as a 'test bed' for chemical reactions to be attempted upon flat silicon substrates. A host of functional groups have been successfully incorpo-



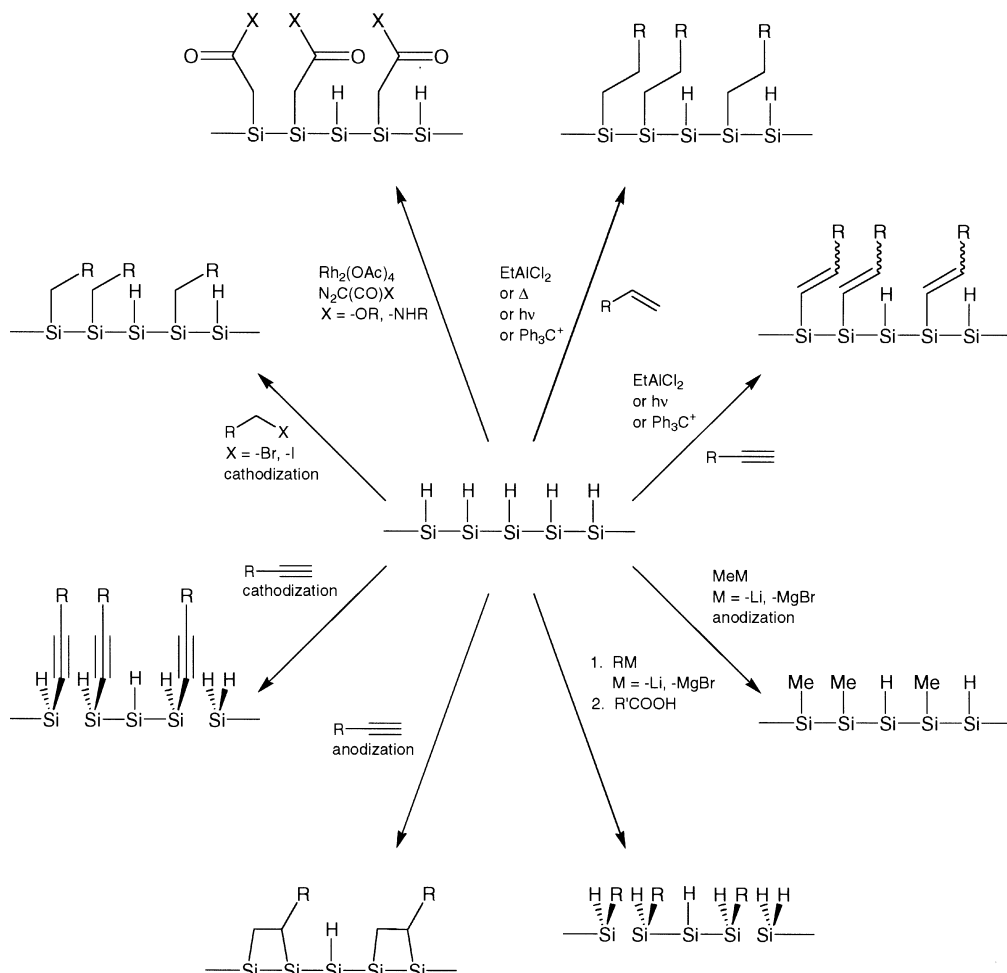
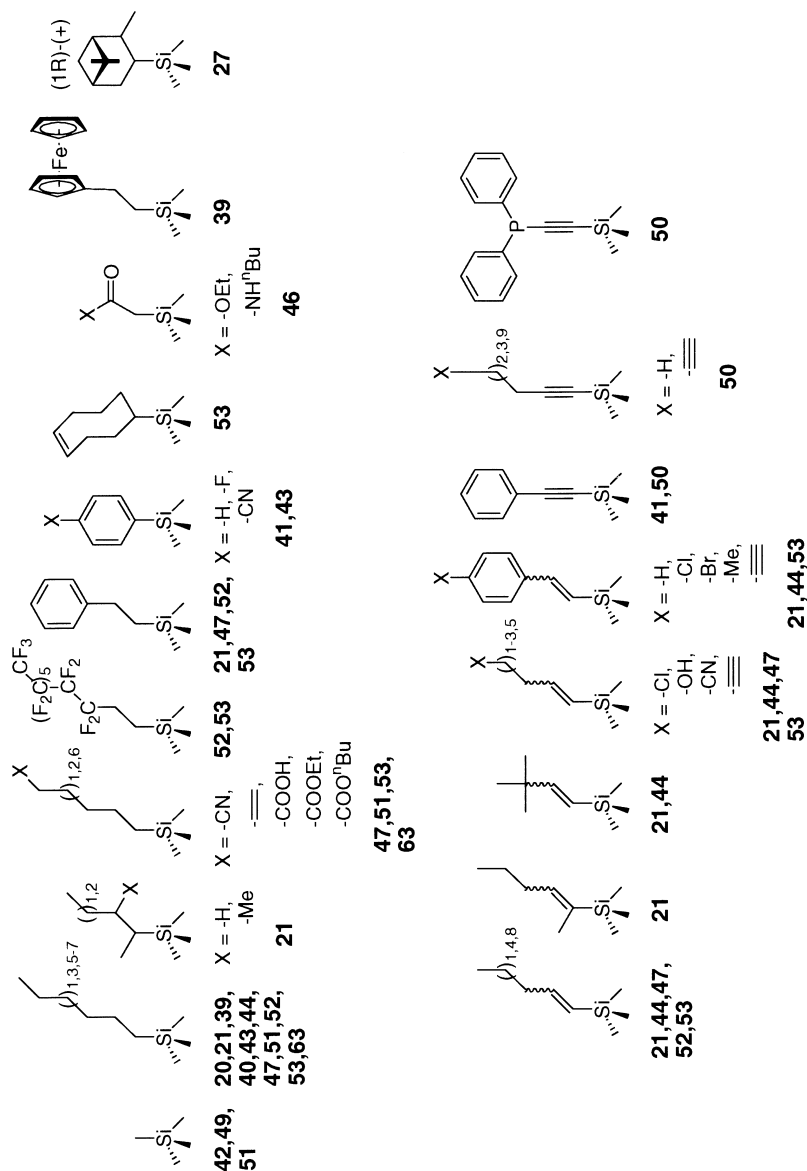


**Fig. 16.5.** Synthetic methods employed for the functionalization of hydride-passivated porous silicon with monolayers bound via Si–C bonds. Derivatization has been accomplished through the cleavage of Si–Si surface bonds as well as by the reaction of Si–H groups.

rated into porous silicon substrates (Figure 16.6), demonstrating the ability to tailor surfaces for particular reactivity or interaction. Numerous studies of the stability of functionalized surfaces have shown repeatedly that the steric, hydrophobic organic monolayers protect the underlying material from the oxidation and degradation inflicted by long-term storage in air, exposure to boiling organic solvents and basic aqueous solutions, and even full immersion and incubation in simulated biological media. In contrast, hydride-terminated porous silicon corrodes quickly or dissolves completely under these chemically demanding conditions. Although these mono-



layers serve to shield the nanocrystallites from chemical attack, the organic surfaces themselves are not necessarily inert and can react further; this may be especially useful for the synthesis of functional interfaces that cannot be prepared directly at the silicon surface due to competitive oxidation or other undesired side reactions. As the chemistry of silicon surfaces continues to advance, it is expected that additional methods for the preparation of stable monolayers will be discovered, contributing further to the technological development of porous silicon and to more complete understanding of its fundamental properties and reactivity.

## 16.4

### Chemical Applications Based on Porous Silicon

The native properties of high surface area, luminescence, tunable biostability, and reactive surface chemistry identify porous silicon as a potentially useful substrate for a variety of tasks. Presented below are several uses that have been developed by exploiting the chemical reactivity or changes effected by chemical interactions with the nanocrystallites. These applications range from use as a material or structural implant to use as a sensor or analytical support.

#### 16.4.1

##### Bioactive Porous Silicon

Silicon is an attractive choice as a biomaterial because of its relative abundance, semiconducting properties, and well-established practices for processing and modification. Bionic sensory and motor implants based on silicon could function as electronic devices activated by the body's own neural network [64]. Direct interfacing of silicon to biological systems without destruction of its electronic properties or induction of cellular death is thus a key step toward the realization of these bionic devices. Flat, unetched bulk silicon is known to be largely bioincompatible and thus unsuitable for in vivo applications. In contrast, porous silicon was found to demonstrate bioactivity through the crystallization and growth of hydroxyapatite films directly upon its surface (Figure 16.7) [65]. Since the publication of this report and subsequent works [66, 67], additional research into this aspect of porous silicon has investigated the effects of surface terminations on biocompatibility. It was demonstrated that an alkenyl monolayer interface renders the silicon surface bioinert [30, 68]; neither hydroxyapatite deposition nor dissolution of the dodecyl-functionalized porous silicon in simulated body fluid (SBF) was observed. By altering the surface chemistry of nanocrystalline silicon, the bioactivity of this material can be modestly controlled. Encouraged by these promising findings, other groups are investigating porous silicon for real-world biochemical applications.

Ji et al. have adapted soft lithographic microcontact printing [69, 70] with specific etching procedures to produce patterned porous silicon substrates for the spatially-controlled deposition of calcium phosphate [71]. Calcification, confirmed

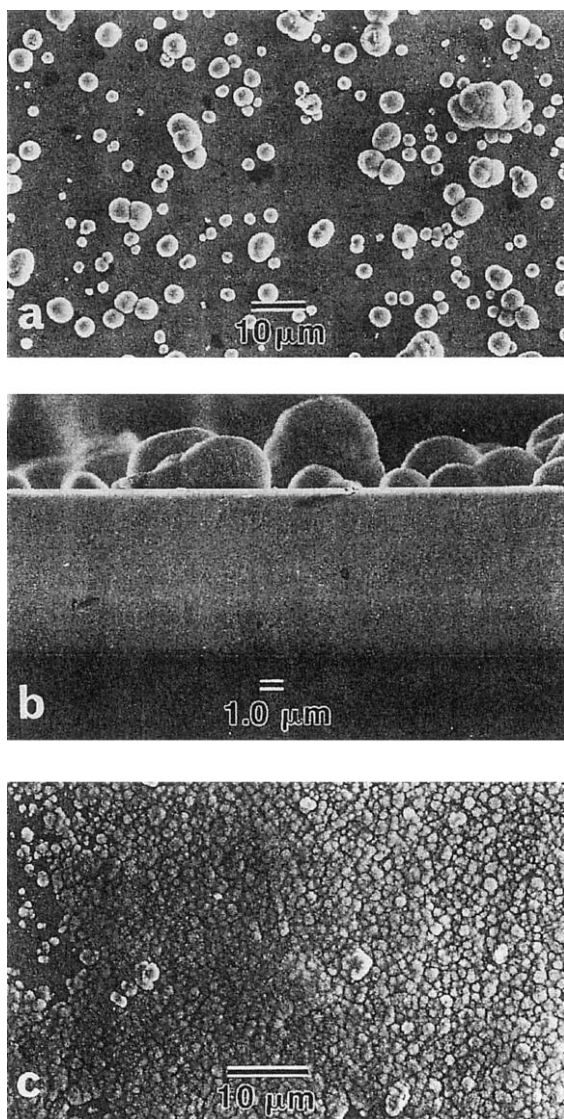


**Fig. 16.7.** SEM micrographs of hydroxyapatite spherulites deposited upon porous silicon substrates from SBF. (a) Deposition upon anodized region after 7 days exposure to SBF. (b) Cross-section of substrate shown in (a). (c) Deposition adjacent to anodized region after 6 days exposure to SBF. (L. T. Canham is thanked for permission to reprint this figure.)

by energy-dispersive spectroscopy (EDS), was observed to proceed almost exclusively upon the porous regions for brief exposures (30 min) to SBF under cathodic conditions (Figure 16.8), although deposition across the entire surface during extended treatments (2 h) was also reported. Variation in the size, shape, and density

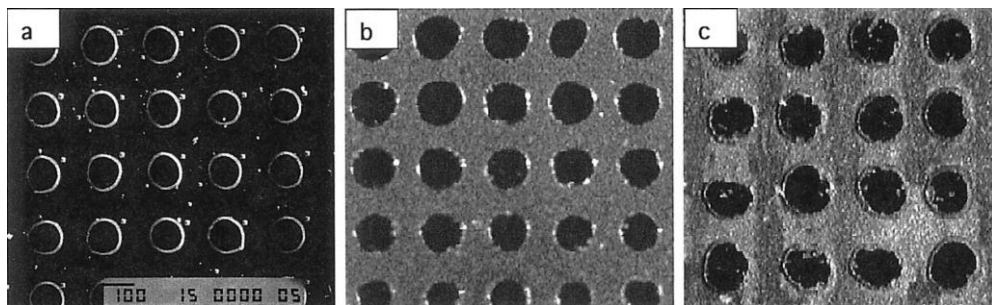


**Fig. 16.8.** Images of patterned silicon substrates. (a) SEM image of 100  $\mu\text{m}$  wide  $\text{SiO}_2$  mesas on silicon. (b) Optical image of (a) after anodic etching of the silicon surface. (c) Optical image of (b) after cathodization in

SBF for 30 min. (Reprinted with permission from [71]. Copyright 2002 Wiley-VCH. J. L. Coffe is thanked for permission to reprint this figure.)

of the patterned features can be achieved simply by changing the aspect of the lithographic stamp, allowing flexibility in the directed growth of hydroxyapatite upon porous silicon. Additional collaboration between Canham and Coffe has resulted in the preparation of transition metal complex-doped hydroxyapatite/silicon systems that are potentially capable of *in vivo* delivery of anti-tumor agents and nucleotide partners [72, 73]. Immersion of porous silicon substrates in SBF containing Ru(II) species produced calcium phosphate films doped with metal complex, confirmed by photoluminescence spectroscopy and fluorescence microscopy. Diffusion of the metal complex from the hydroxyapatite matrix was observed upon heating to 130  $^{\circ}\text{C}$ , releasing submicromolar concentrations of Ru(II) as determined by spectrophotometry. Incorporation of anti-cancer agents such as *cis*-platin and related Pt(II) complexes into hydroxyapatite films was also accomplished, shown through SIMS and EDS. Increasing the concentration of Pt(II) in the SBF medium resulted in higher dopant levels; however, the thickness of hydroxyapatite deposits decreased on average, suggesting that the metal complex may inhibit diffusion and nucleation of the solvated apatite precursors upon the silicon surface. At equivalent concentrations, doping of hydroxyapatite/porous silicon with the more steric carboplatin species was less efficient than *cis*-platin, further supporting a complex-inhibitive mechanism. Diffusion rates of Pt(II) complexes to the surrounding medium upon thermal annealing were discovered to depend largely upon the initial loading concentrations and comparatively little upon the ligands. These results indicate that a variety of platinum- and other metal-based drugs and biomolecules could be dispensed from these hydroxyapatite–silicon structures, limited primarily by the amount of compound that can be precipitated within the calcium films. Future work is expected to focus upon the development of these undoped and metal complex-doped hydroxyapatite–silicon composites, as well as biodegradable porous silicon itself, for connective tissue grafts and drug delivery implants.

The bioactivity of porous silicon toward living cellular systems is also under investigation. Efforts have been made by Bayliss, Buckberry, and their collabo-

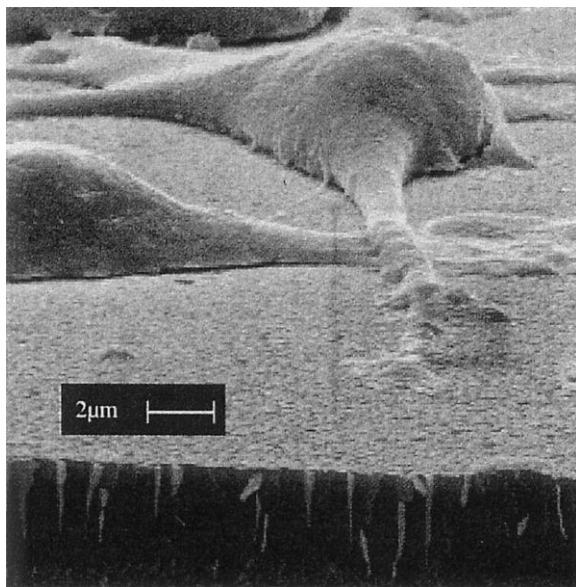


**Fig. 16.9.** SEM image of B50 neuron 72 h after deposition on porous silicon. (S. C. Bayliss is thanked for permission to reprint this figure.)

rators to directly culture cells upon porous silicon and explore this material's biocompatibility beyond the scope of inorganic biological materials [74–79]. Seeding of porous silicon surfaces with Chinese hamster ovary cells was confirmed by optical and rapid SEM after 24 h exposure. Despite their rapid degradation under ambient conditions, these cells persistently remained attached to the substrates, even after diligent rinsing, indicating that the cells adhered in some capacity to the silicon surfaces. Growth over one week of rat neuronal (B50) cells directly upon the porous silicon surface (Figure 16.9) without an intermediate biochemical layer was confirmed by confocal microscopy of dye-viability assays. In contrast, significantly lesser populations of viable neurons were counted for seeded poly-silicon and bulk silicon substrates, highlighting the bioactive nature of porous silicon. Porous silicon treated with tissue culture media containing hydroxyapatite precursors showed no deposits of hydroxyapatite, suggesting that inhibitors within the culture sera may allow the selective deposition of cells without concurrent formation of potentially destabilizing phosphate films. Toxic effects from the silicon structure or its possible degradation products (silicone, silane) upon the adhered cells were not evident. Attachment of primary rat hepatocytes to oxidized porous silicon was demonstrated by Chin et al. [80]. Cell deposition was confirmed from media containing adhesive protein sera and/or collagen additives; adhesion of the hepatocytes to porous silicon was also seen in the absence of protein binding species, but only with substantially lesser coverage. No change in the physical morphology of the porous substrate occurred upon treatment with these biological media,



showing the adhesion of these cells to be most likely derived from chemical factors. The long-term culture of hepatocytes on porous silicon closely resembled that from tissue culture polystyrene, evidenced by comparison of their viable populations and productions of albumin and urea.

These studies of cell growth upon porous silicon indicate that the fabrication of bioactive silicon implants may be achieved in the near future. The coupling of cellular and tissue structures to the optoelectronic properties of porous silicon may allow the implantation of biocompatible, intelligent, and fully integrated devices for controlled release of drugs, diagnostics of bodily functions, and replacement of failed bodily processes. The interfacing of neural cells (substantia nigra) to silicon-based electronics may be the next step in this area of research [81].

#### 16.4.2

#### Micro Enzyme Reactors ( $\mu$ IMERS) and Total Analysis Systems ( $\mu$ TAS)

For separation- and catalysis-based technologies, interfacial characteristics are critical. There has been considerable research to understand the effects of different surface terminations on non-specific binding of biological molecules, such as proteins, to surfaces based on thiol-on-gold self assembly [82]. It is expected that the results of these studies can be generalized to silicon-based monolayers; thus, tailoring of the nanocrystalline porous silicon interface will allow versatility and optimization of properties for specific applications. This desire for control over surface chemistry has extended to size as well. Interest in the miniaturization of analytical substrates and the conservation of analyte samples has driven the development of compact integrated platforms for biochemical analysis. Recent work from Bengtsson et al. outlined the use of high-aspect ratio porosified silicon enzyme microreactors with immobilized glucose oxidase and trypsin reagents [83]. Colorimetric assay and mass spectrometry of the trypsin digests were used to assess the catalytic turnovers of these  $\mu$ IMERS; the greatest activity was measured for silicon substrates that had been etched to form porous layers of equal thickness throughout the full length of the microreactor channels (Figure 16.10). In contrast, non-porous substrates functionalized with these enzymes, lacking the expansive surface area of the etched, porous reactors, show substantially smaller turnover numbers, as evidenced by preceding work [84–87]. The inferior performance of  $\mu$ IMERS with variable porous layer thicknesses was ascribed to the relatively inefficient transport properties of the inhomogeneous pore morphology of these systems; the smaller, incongruous sizes of such pores hinder the diffusion of chemical substrates into the enzyme-derivatized material and thus limit the efficiency of these microreactors. In addition to etching conditions, variation in the dimensions of the microreactor channels and walls was also found to affect catalytic turnover; however, thicker porous layers did not generally increase enzymatic activity, suggesting the existence of an optimal thickness. Although the physical attributes of these systems and their effects upon enzymatic activity have been investigated, the surface chemistry remains to be more fully researched. In other work, development of reliable and stable immunoassays based upon antibody-modified porous silicon

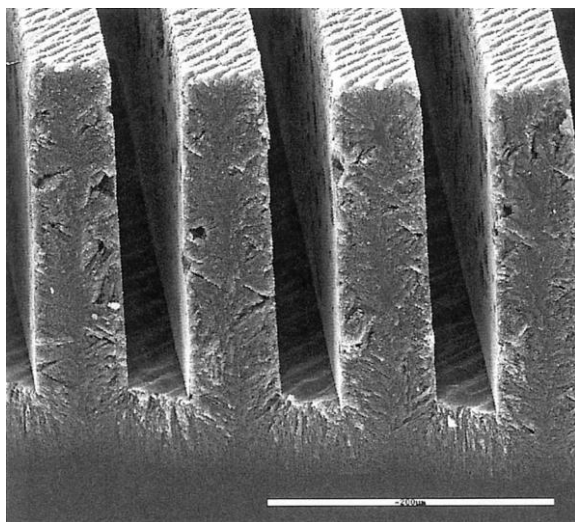


**Fig. 16.10.** SEM image of microreactor cross-section after anodization ( $+50 \text{ mA cm}^{-2}$  for 10 min) to form the porous silicon layer. The scale bar is 200  $\mu\text{m}$  in length. (T. Laurell is thanked for permission to reprint this figure.)

microchips was reported by Yakovleva et al. [88]. Detection limits of  $\text{ng L}^{-1}$  levels of labeled atrazine were established for several types of immuno surfaces, offering this material as a sensitive and durable substrate for  $\mu\text{TAS}$  sensing. Appropriation of free-standing porous silicon for physical applications in  $\mu\text{TAS}$  such as micro-sieves has also been proposed [89].

#### 16.4.3

##### Porous Silicon Sensors

The development of sensors based upon porous silicon materials has proceeded in recent years, seeking to fashion these readily abundant and easily modified substrates into inexpensive and reliable detection devices. Efforts in this area, particularly those of the Sailor group and its collaborators, have focused upon changes in the optical reflectivity of porous silicon substrates when exposed to biomolecular [90–93] or chemical [94–96] analytes (Figure 16.11). Diffusion of gaseous species into porous silicon has been shown to effect changes in the refractive index of this material, shifting the wavelengths of the Fabry–Pérot fringes when probed with laser interferometry (Figure 16.12). Gao et al. have examined the shifts induced by the adsorption of ethanol vapor onto oxidized porous silicon by measuring the change in reflectance at a fixed laser wavelength [97, 98]; the difference in reflectivity between the exposed substrate and the untreated material was directly correlated to the concentration of the vapor. Concentrations as low as 250 ppb were detected by laser interferometry of these porous silicon sensors. The substrates



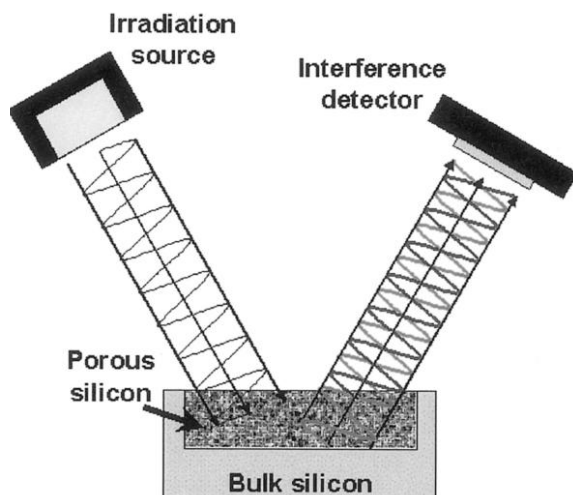


**Fig. 16.11.** Schematic of a porous silicon optical interferometric sensor [90]. Reflection of light from the porous surface and the porous-bulk interface yields an interference spectrum. Adsorption of species into the

silicon matrix alters the refractive property of the porous layer, resulting in shifts in these interference patterns that can be detected and measured.

continued to respond even after cycling several times between ethanolic and ambient air, showing the reversible adsorption of the vapor and demonstrating the reusability of these devices. Sensor response depended greatly upon the etching conditions and the wavelength of the laser source, offering the opportunity to diversify or tune these experimental parameters to detect a variety of gaseous agents.

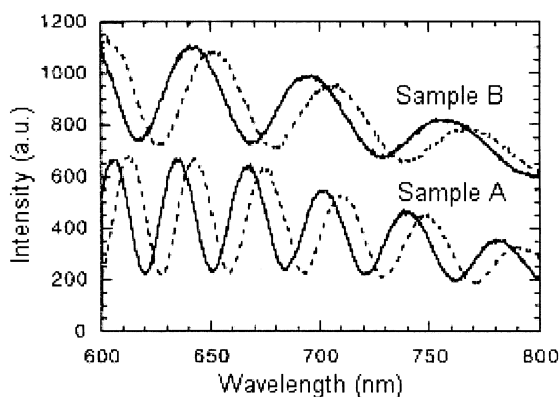


**Fig. 16.12.** Reflectance spectra from porous silicon samples with different thicknesses (A and B) before (solid curves) and after (dashed curves) exposure to 1.7% ethanol in air. The wavelength of detection is 687 nm. (M. J. Sailor is thanked for permission to reprint this figure.)

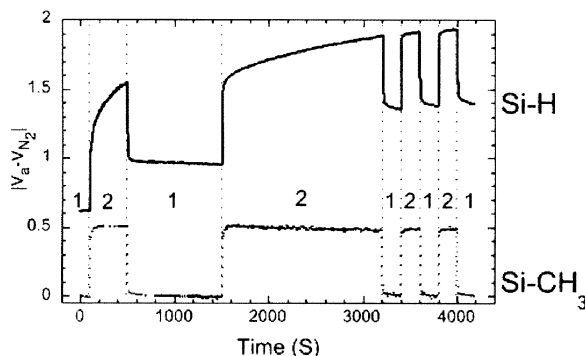


**Fig. 16.13.** Photodiode voltage differences induced by response of porous silicon sensors (unfunctionalized, hydride-terminated and methyl-terminated surfaces) to pure dinitrogen (1) and 2.4% methyl ethyl ketone (MEK) in dinitrogen (2). Sensor response is indicated by a sudden increase in the potential difference. Exposure to the organic analyte induces an obvious, reversible change in potential. The

methyl-terminated sensor, however, exhibits greater reproducibility (constant difference) in its response over time, illustrating the relative stability of this functionalized sensor against the unfunctionalized substrate. (Reprinted with permission from [99]. Copyright 2001 American Chemical Society. M. J. Sailor is also thanked for permission to reprint this figure.)

Derivatization of the porous silicon surface can also affect the sensory properties [99]. Porous silicon oxidized thermally or by treatment with ozone yielded hydrophilic surfaces that exhibited greater affinity for polar vapors such as ethanol and methyl ethyl ketone (MEK). Conversely, porous silicon modified with hydrophobic methyl groups responded more actively to nonpolar, gaseous hexane, although this affinity was lesser in magnitude than those of the oxidized surfaces. However, the durability imparted to the silicon by functionalization with methyl species exceeded those for the unfunctionalized and oxidized materials, seen in the greater reproducibility in reflectivity measurements of the sensor over time (Figure 16.13). Chemical derivatization of porous silicon with other surface groups may lead to sensors that show further selectivity and discrimination for a greater range of analytes.

Detection via reflectance quenching was also reported by the adsorption of organic vapors onto porous silicon “smart dust” particles [100]. Detection of ethanol, acetone, and toluene was accomplished from a distance of 20 m. Interference from water vapor, an object of concern for chemical sensing in ambient environments, was not seen in these experiments; as observed in previous work (*vide supra*), the hydrophobicity of freshly prepared “smart dust” effectively prevented water from penetrating the porous matrix. This standoff detection may be particularly useful in the direct recognition of harmful industrial chemicals (e.g. HF vapors [95]) or the indirect detection of fluorophosphonate nerve agents [96], where analysis can be accomplished at a safe distance. Additionally, “smart dust” may function not only as a remote sensing material but also as an agent in high-throughput screenings and assays, as shown by Bhatia and Sailor [100]. Masked anodic etching of

crystalline silicon with a specific variable current was employed to prepare regions of porous silicon multilayers that were then galvanically detached from the underlying semiconductor bulk and ground to optically active particles similar to rugate filters. The populations and wavelengths of the reflectivity peaks of these porous silicon particles could be varied and shifted by changing the magnitude and periodicity of the etching current, demonstrating the potential to produce millions of encoded substrates. Encoded particles treated with rat albumin could be identified from an antibody-incubated mixture of coded specimens by coupling fluorescence spectra, which clearly showed the interaction of the albumin-treated substrates with tagged antibodies, to optical spectra that expressed the characteristic combination of reflectivity peaks. The relative sharpness of peaks, near-IR range of reflective wavelengths, and biocompatibility of “smart dust” offers this material as an alternative to other substrates (e.g. CdSe particles) which may be toxic or relatively unstable for in vivo and medical diagnostic applications.

Evolution of reflectivity signals over time has been used to temporally resolve the constituents of a binary vapor mixture [102]. Since the studied solvents (ethanol and acetone) have identical refractive indices, changes in the optical reflectance of porous silicon exposed to these vapors were shown to depend upon the rates of diffusion and adsorption of these species into the material. Time-resolved refractometry revealed that an equimolar mixture of acetone and ethanol vapors exhibited markedly different condensation within porous silicon than did the pure mixture constituents (Figure 16.14). This method is comparable to gas chromatography in that the vapor mixture interacts with the matrix in a manner dependent upon the physical properties of its components, but the porous silicon device

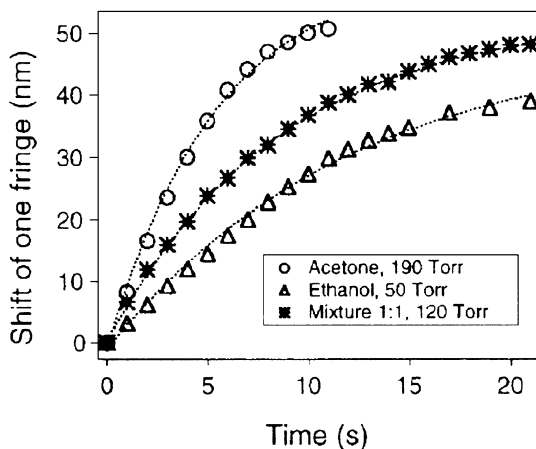


**Fig. 16.14.** Wavelength shift of a single Fabry–Pérot fringe as a function of exposure time to organic vapors. As the fraction of acetone was increased, greater and more rapid shifts in the reflectance spectrum were measured. (M. J. Sailor is thanked for permission to reprint this figure.)

bears the distinct advantage of acting simultaneously as separator and detector. Similarly, simultaneous separation and detection of bovine serum albumin (BSA) was demonstrated using porous silicon prepared through an asymmetric electrochemical etching process, resulting in a gradient of porosities [103]. By measuring changes in effective optical thickness of porous silicon samples treated with buffered (pH 4) solutions of BSA, penetration of the BSA into the pores could be identified. Changes in EOT were observed only at regions of the substrate where the pores were large enough to admit BSA into the porous structure; the dimensions of these pores were confirmed by AFM and SEM measurements. No penetration was measured for BSA solutions at higher pH (7.2), attributed to the electrostatic repulsion between the negatively charged protein and the inherently negative oxide-covered porous silicon. Thus, pH-gating may be used in conjunction with porosity to contain or exclude proteins and other biomolecules from porous silicon. Related research has further investigated time-resolved detection of other gaseous organics [104] as well as interferometric sensing of endocrine disruptors [105].

Besides examining changes in optical reflectivity, detection of chemicals with porous silicon has also been investigated by quenching of its visible photoluminescence. Content et al. discovered irreversible quenching of the porous silicon photoluminescence by nitroaromatics [106]. The efficiency of quenching was established to depend upon the vapor pressures of the analytes with nitrobenzene extinguishing photoluminescence more completely than either dinitrotoluene (DNT) or trinitrotoluene (TNT). When comparing approximately equal concentrations of analytes, however, exposure to DNT and TNT showed greater diminution in the silicon photoluminescence. These losses were attributed largely to chemical oxidation of the porous silicon surface. Detection limits of 2 ppb for DNT and 1 ppb for TNT could be established, compared to 400 ppm for benzene. Selective detection of DNT and TNT was accomplished by examining the photoluminescence quenching inflicted by the  $\text{NO}_2$  [107] produced from catalytic oxidation. The relatively low concentrations of DNT and TNT required for detection, upon oxidation, produced levels of  $\text{NO}_2$  that were below the sensing limit; hence, only trace photoluminescence reduction was measured from these catalyzed vapors. To contrast, the greater concentration required for nitrobenzene produced higher levels of  $\text{NO}_2$  that quenched photoluminescence nearly equally to the unoxidized organic vapor. This result offers discrimination between these species through the comparison of their catalyzed and uncatalyzed quenching efficiencies. Chan et al. have developed a sensor that exploits changes in the photoluminescence of porous silicon multilayers upon adsorption of Gram-negative bacteria [108, 109]. Exposure of a porous microcavity resonator functionalized with a bacterial binding agent to *Escherichia coli* resulted in a photoluminescence redshift of several nanometers (Figure 16.15). Other Gram-negative bacterial strains induced similar shifts; however, exposure to Gram-positive species did not affect the photoluminescence spectra. The change in refractive index of the silicon microcavity upon binding of the bacteria was proposed to induce photoluminescence shifts in a similar fashion to changes measured for optical reflectance. Photolumi-

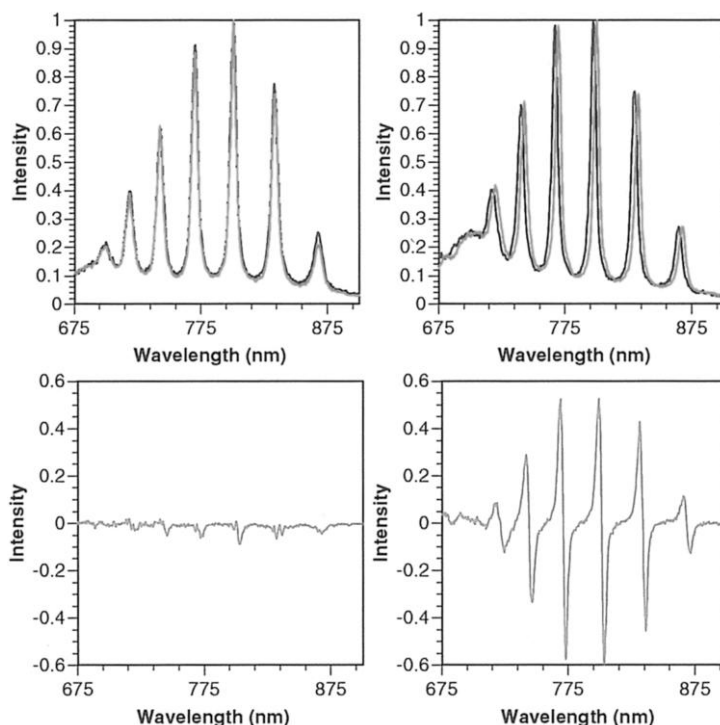


**Fig. 16.15.** Photoluminescence spectra of derivatized porous silicon microcavity sensors treated with *B. subtilis* (Gram-(+), left spectra) or *E. coli* (Gram-(−), right spectra) lysates. In the top two spectra, the dark lines correspond to measurements before treatment with the bacteria; the grey spectra are those obtained after treatment. The bottom two spectra plot

the difference in photoluminescence afforded by the bacterial treatment; the sensory response for the Gram-negative bacteria is clearly evident. (Reprinted with permission from [108]. Copyright 2001 American Chemical Society. B. L. Miller is also thanked for permission to reprint this figure.)

nescence studies of microcavities have also been used for solvent sensing and assessment of solvent penetration [110, 111].

Sensing of analytes via changes in both photoluminescence and reflectivity has been combined in an electronic nose [112]. Experiments completed with both oxidized porous silicon substrates and metal oxide sensors revealed that the former required only seconds after response to return to the signal baseline, whereas the latter required over 15 min. By measuring both photoluminescence and reflectance intensities for an array of substrates exposed to a mixture of organic vapors, the nose was able to discriminate the analyte constituents. Discrimination indices calculated for several gaseous mixtures that were analyzed with porous silicon sensors matched closely to values measured for sensing with metal oxides, establishing this silicon nose to be a viable instrument for the analysis of vapor mixtures. In comparison to existing metal oxide-derived noses, however, devices constructed from porous silicon may be fabricated more cheaply and may almost certainly be

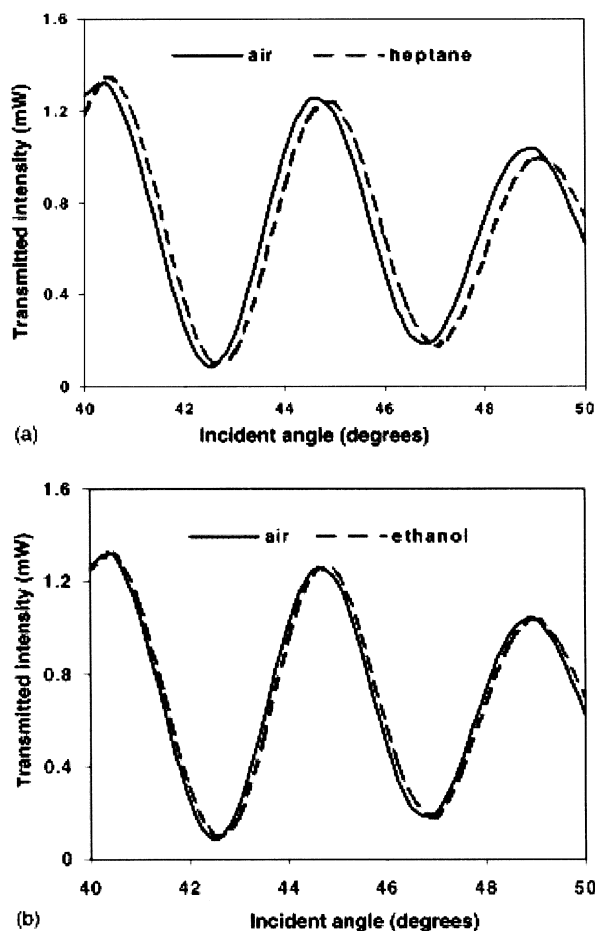


**Fig. 16.16.** Polarization interference spectra of porous silicon exposed to heptane and ethanol vapors (both 2.0% in air). The solid curve represents the measurements made in solvent-free air; the dashed line indicates measurements from substrates exposed to the organic analytes. (M. J. Sailor is thanked for permission to reprint this figure.)

more easily integrated to other, larger-scale silicon processing technologies. Additional work on the sensing capabilities of porous silicon has employed polarization interference [113]. Sailor and Fainman reported shifts in polarization interference measurements upon exposure of porous silicon to concentrations of ethanol or heptane vapors. The deeper, more complete penetration of heptane into the hydrophobic, hydride-terminated surface yielded a greater change in the interference spectrum than with ethanol (Figure 16.16). As shown for time-resolved refractometry [102], a mixture of the two vapors could be distinguished from the pure compounds, showing a shift in magnitude intermediate to those from its constituents. Similar to the mechanism of optical reflectivity, these shifts were attrib-

uted to changes in the refractive index of the porous silicon upon adsorption of the analyte. Sensors employing this transduction scheme exhibited reversible behavior with these particular analytes, but detection was limited to concentrations at the parts per thousand level. Sensing based upon the birefringent properties of porous silicon has also been studied [114] as well as light-addressable potentiometric sensors (LAPS) fashioned from this material [115, 116].

These fascinating results clearly point to the incredible promise of porous silicon for sensing applications. It is expected that future work will continue to improve selectivity and discrimination for singular analytes from complex mixtures. To realize success in this endeavor, interfacial tailoring must enable the detection of a great range of gaseous species and should permit recycling of sensors through stabilization of the surface, particularly under biological conditions.

#### 16.4.4

##### Explosive Porous Silicon

Recent work by Mikulec et al. [117] has exploited an unusual property of porous silicon and used this material as an explosive matrix for atomic emission spectroscopy. Freshly prepared, hydride-terminated substrates soaked in aqueous solutions of  $\text{Gd}(\text{NO}_3)_3$  were detonated with mechanical or electrical triggers in a flashy, exothermic reaction not unlike the combustion of black powder (Figure 16.17). The estimated high ( $\sim 2000$  K) local temperature created by the explosion was employed to generate emission spectra for alkali metals and heavy metals deposited upon the substrates from solution or suspension. Detonation was completed for a range of porous specimens and did not depend upon either the crystalline identity of the precursor or the morphology of the etched material; however, oxidized substrates exhibited a lesser propensity to explode. The intensity of the explosion was



**Fig. 16.17.** Photograph of the bright flash from explosion of porous silicon treated with  $\text{Gd}(\text{NO}_3)_3$ . Detonation was provided from a transformer (upper right). (M. J. Sailor is thanked for permission to reprint this figure.)

controlled, in part, by variation of the etching conditions and the nitrate treatment. Explosion of porous silicon by condensation of dioxygen within the pores has also been reported [118]. Hydride-passivated porous silicon cooled below 90 K was spontaneously exploded upon saturation with dioxygen gas. Detonation of dioxygen-saturated, oxide-terminated substrates could also be induced through illumination with UV light or by weak impact. Such an explosion was calculated to occur within 1  $\mu\text{s}$ , rivaling many conventional strong munitions, and to expend nearly 12 kJ  $\text{g}^{-1}$ , exceeding the release of TNT (4.2 kJ  $\text{g}^{-1}$ ). The intensity of the explosion was sufficient to annihilate the underlying bulk silicon to micron-sized powder. It has been proposed that the explosion is “sparked” when condensed dioxygen reacts with dangling silicon bonds to yield highly reactive, oxidizing species, specifically hydroxyl, oxygen, and hydrogen radicals. The rapid exothermic chain reactions of these radicals with silicon surface atoms result in the uncontrolled oxidation and consequent detonation of the porous silicon. Besides atomic emission, applications that could use this explosive property include microchip arrays for elemental analysis, propulsive devices for microelectromechanical systems (MEMS), power sources for electronic systems, and self-destructing computer circuits for the preservation of commercial and national securities.

#### 16.4.5

#### Desorption/Ionization on Silicon Mass Spectrometry (DIOS-MS)

Matrix-assisted laser/desorption ionization mass spectrometry (MALDI-MS), introduced in the 1980s, is widely employed in mass measurements of organic and biological macromolecules such as proteins, polymers, and drug candidates [119, 120]. In this technique, an analyte is dispersed within an organic matrix exhibiting high UV absorptivity and this is then irradiated with a UV laser source. Energy accumulated from the laser pulse by the matrix is transferred to the incorporated analyte; this exchange induces vaporization and ionization of the dispersed molecules which are then detected and measured by time-of-flight (TOF) mass spectrometry. In contrast to direct desorption/ionization methods from matrix-less surfaces that may yield a plethora of fragmented ion products from a single analyte, MALDI-MS is considered a “soft” ablation technique in that the energy transfer is indirect and relatively gentle, substantially reducing the extent of ion degradation and simplifying the interpretation of the mass spectra [121–126]. Furthermore, its sensitivity to femtomolar and attomolar levels of analytes and its tolerance for mixtures and biological contaminants afford the characterization of minimal sample sizes of only modest purity. Characterization of masses to nearly 200,000 Da in size is possible; however, spectrometry of low-mass analytes is generally not feasible with this method owing to concurrent ablation of the organic matrix with the cocrystallized analyte. The resultant mass spectrum may exhibit substantial complexity in the low-mass region due to interference of matrix fragment signals with those of the ionized analyte. To fully optimize this spectrometric method for specimens of masses less than 1000 Da, the implementation of an inert and nonablative matrix is imperative.



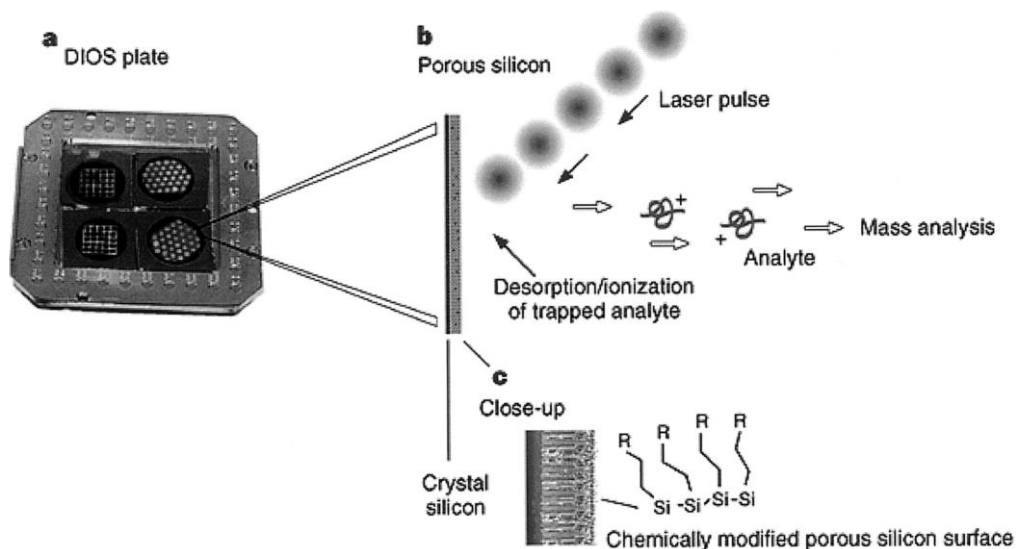


**Fig. 16.18.** DIOS-MS using porous silicon. (a) Four porous silicon substrates mounted upon a MALDI spectrometer plate. (b) Desorption/ionization of deposited analytes. (c) Cross-

section of chemically functionalized DIOS-MS substrate. (Reprinted with permission from [127]. Copyright 1999 Nature Publishing Group.)

Desorption/ionization on silicon mass spectrometry (DIOS-MS), introduced by Buriak and Siuzdak in 1999 [127], employs porous silicon prepared by anodization of high-purity, single-crystal bulk silicon to contain and energize a variety of low-molecular weight species for mass analysis (Figure 16.18). Similar to MALDI-MS, DIOS-MS utilizes a pulsed UV laser to vaporize and ionize the analyte for detection; in contrast to MALDI-MS, however, DIOS-MS requires no added matrix to effect specimen desorption/ionization. It was proposed that the high ultraviolet absorptivity, immense surface area, and substantial thermal conductivity of porous silicon serve to efficiently transfer laser energy to the adsorbed analyte molecules. Furthermore, analyses of mass spectra of a range of compounds revealed no conclusive evidence for ablation or ionization of the porous silicon substrate itself. When compared to spectra measured from MALDI-MS, those of DIOS-MS revealed little to no interference in the low-mass range, permitting quicker and more complete analysis of specimen peaks in this region (Figure 16.19). Additionally, post-source decay (PSD) analysis of targets, generally impossible to realize in MALDI-MS owing to the matrix interference, was readily accomplished with DIOS-MS. This technique detected even to the attomole level with resolution equivalent to MALDI-MS and ranged from under 200 Da to over 12,000 Da in mass. Sensitive and accurate measurements could even be completed from analytes dispersed and dried from saturated salt solutions, indicating that DIOS-MS demonstrates excellent tolerance for contaminants. The time needed to prepare DIOS-MS specimens is comparatively low since no organic matrix is used, requir-

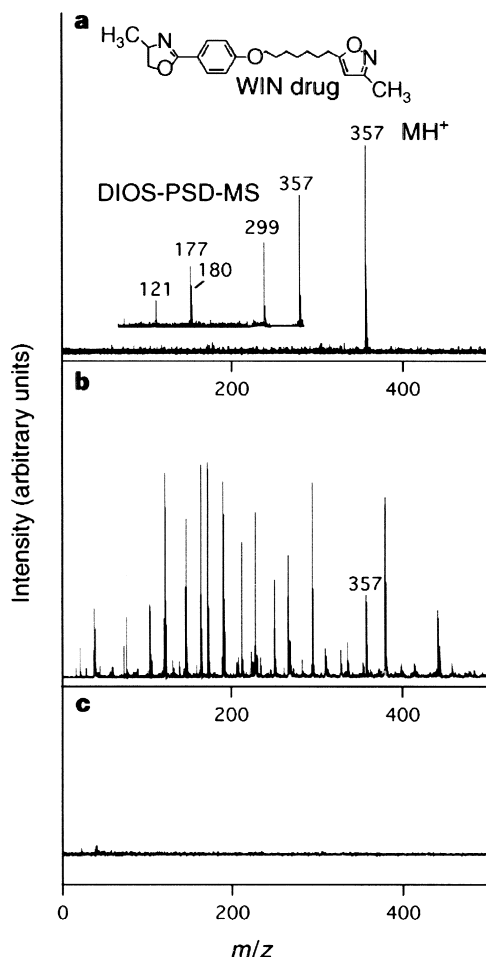


**Fig. 16.19.** Mass spectrometry of WIN antiviral drug. (a) DIOS-MS spectrum of WIN deposited upon porous silicon. Inset: DIOS-PSD-MS spectrum of WIN. (b) MALDI-MS spectrum of WIN dispersed in  $\alpha$ -cyano-4-hydroxycinnamic acid (HCCA). (c) Attempted

desorption/ionization from WIN deposited upon gold MALDI plate, illustrating the necessity of the matrix for successful spectrometry. (Reprinted with permission from [127]. Copyright 1999 Nature Publishing Group.)

ing only the time to prepare the porous silicon, within minutes, or to acquire a previously etched substrate from storage. Chemical modifications of the substrates can stabilize the surfaces against degradation and modulate the interfacial properties to control deposition, desorption, and ionization of target analytes. Considering the availability of reactions for the modification of porous silicon surfaces, tailoring a DIOS-MS substrate for the optimal characterization of a particular analyte could well be accomplished through chemical manipulation.

Since this initial report, a number of research groups have published improvements and modifications for this analytical technique to include a wider range of analytes, experimental conditions, and theoretical considerations of the desorption/ionization mechanism [128–133]. Effects of anodization parameters, pre-, and post-etching treatments of porous silicon substrates upon DIOS-MS performance were reported by Shen et al. [134], showing that a wide range of etching conditions may be utilized without adversely affecting spectrometric activity. Little dependence of DIOS-MS upon the silicon precursor, etchant solution, or electrochemical variables was observed. However, “double etching” of DIOS-MS substrates, soaking of oxidized porous silicon in aqueous HF, was generally found to improve DIOS-MS performance despite requiring greater laser fluence, particularly for larger analyte concentrations and for silicon substrates that had been aged in air. It was also observed that porous silicon samples stored in ethanol for 1 day prior to use in DIOS-MS tended to show lower intensities in light-mass background peaks, improving the detection and assignment of analyte fragments in the lower mass range. Research from Bohn and Sweedler employed porous silicon substrates prepared from electroless  $\text{H}_2\text{O}_2$ –metal–HF (HOME-HF) etching to better understand the factors that govern analyte desorption and ionization [135]. Variation in either photoluminescence of porous silicon or the irradiation wavelength of the laser source was not observed to affect DIOS-MS of peptides; however, DIOS-MS substrates of large pore size typically generated mass spectra with greater reproducibility and higher quality than did specimens with smaller pores (Figure 16.20). As reported above, it was found that storage of freshly prepared porous silicon substrates in methanol before use produced spectra with enhanced peak intensity and little noise, reaffirming this post-etching treatment as an effective method for improving DIOS-MS performance (Figure 16.21). The hydrophobic nature of unfunctionalized hydride-terminated porous silicon tends to restrict diffusion of hydrophilic, aqueous-derived analytes into the porous structure; considering this, it was believed that the methanol treatment wets the pores and facilitates inclusion of the analyte within the silicon matrix. The inferior performance of oxidized substrates was justified by acknowledging the different thermal properties of the oxide overlayer, which may hinder the energy transfer from the laser pulse to the adsorbed analyte. Mass spectrometry of analytes deposited upon porous GaAs or porous GaN was unsuccessful, implying that only porous silicon may have the optimum combination of crucial properties to support direct desorption/ionization of specimens with low fragmentation.

In mechanistic considerations of the desorption/ionization process, comparisons of DIOS-MS to surface-assisted laser-desorption ionization mass spectrometry (SALDI-MS) have been outlined by Alimpiev et al. [136]. DIOS-MS of adsorbed diethylamine was reported both from anodically etched porous silicon and from ion-etched roughened silicon substrates (Figure 16.22). These results suggest that desorption/ionization may require not porosity, but perhaps only surface roughness. No spectra were obtained from flat polished crystalline silicon surfaces. In contrast to the negative findings from porous GaAs and GaN [135], mass spectra could also be obtained from ion-etched highly oriented pyrolytic graphite (HOPG).

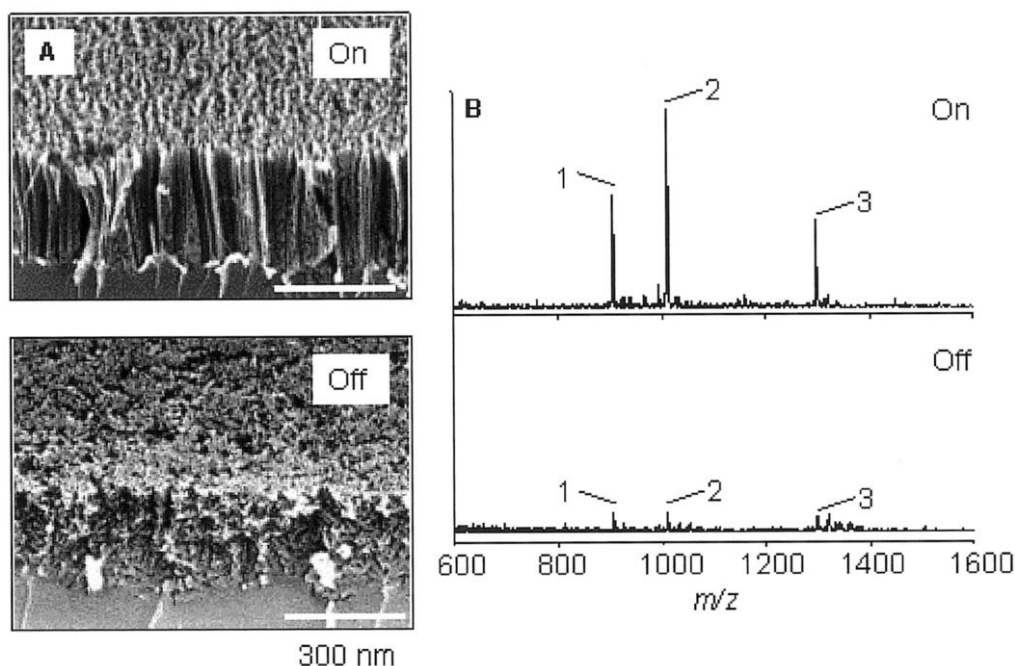


**Fig. 16.20.** (A) Cross-sectional SEM images on and off Au-patterned regions of porous silicon illustrating the difference in substrate porosity. The upper micrograph shows the substrate with larger pores. (B) DIOS-MS

spectra of a three-peptide mixture on and off patterned regions. (Reprinted with permission from [135]. Copyright 2001 American Chemical Society. J. V. Sweedler is also thanked for permission to reprint this figure.)

It was suggested that the surface roughness plays a key role in facilitating charge separation upon the substrate, which activates dispersed analytes for desorption/ionization. A porous substructure, however, seems to function in some additional capacity; the peak intensities of the mass spectrum from porous silicon measured substantially greater than those from the other two surfaces. It was proposed that diffusion from the porous substructure may serve to resupply the surface after a laser pulse, increasing the absolute intensity of mass peaks and improving the signal-to-noise ratio of the analysis. Desorption/ionization from porous silicon was also accomplished by irradiation with an infrared (IR) laser source (IR-DIOS-MS) (Figure 16.23), supporting a mechanism consistent with the heating-induced desorption of preformed surface ions. This mode of DIOS-MS succeeded only for cooled specimens and apparently yielded finer results when water and acetic acid vapors were deliberately leaked into the instrument chamber. The effects of low temperature and vapors suggest that IR-DIOS-MS may proceed through a physisorbed solvent matrix that absorbs IR radiation and accommodates complete transfer of energy to the dissolved analyte.

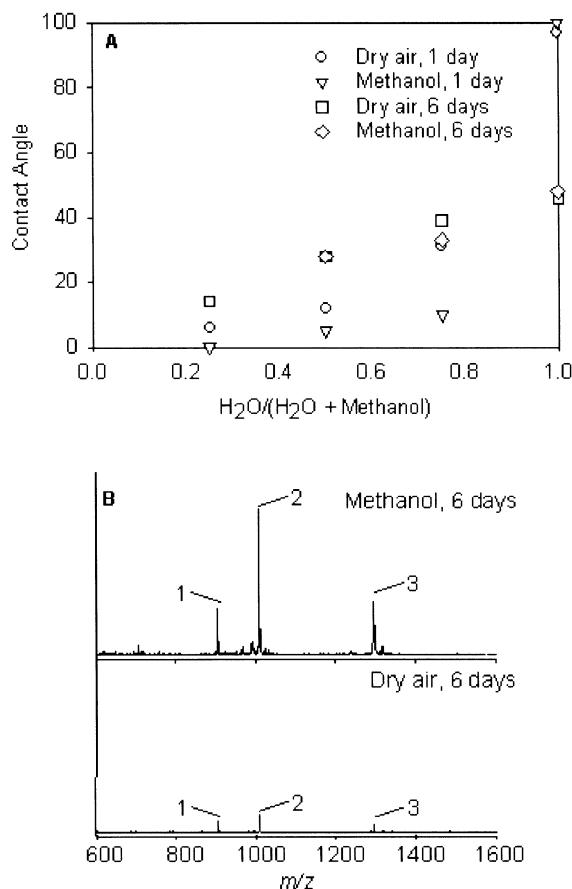


**Fig. 16.21.** (A) Contact angle goniometry of porous silicon substrates stored in dry air and methanol for 1 day and 6 days. Solvents used for goniometry range from 0–75% methanol in ultrapure water (x-axis). On average, silicon substrates stored for longer periods exhibited lower contact angles, representative for

hydrophilic surfaces. (B) DIOS-MS spectra of a three-peptide mixture (same as that analyzed in Figure 16.20) from porous silicon substrates stored for 6 days. (Reprinted with permission from [135]. Copyright 2001 American Chemical Society. J. V. Sweedler is also thanked for permission to reprint this figure.)

The advances of DIOS-MS since its earliest work promise the reliable measurement of low-molecular weight species in tandem with, and possibly without, MALDI-MS. Additionally, the well-established integration of devices upon silicon chips offer the ability to fashion samples capable of supporting multiple analyses in series or parallel, confining all characterizations of biological or chemical species to a lone substrate. It is clear that surface termination and bound functionalities are important not only for analysis but also for recycling the porous silicon chip for multiple uses.

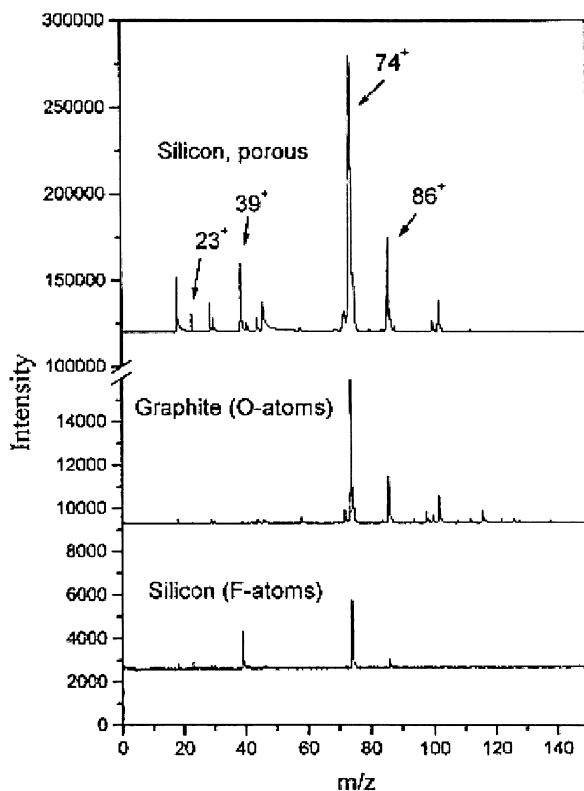


Fig. 16.22. DIOS-MS spectra of diethylamine measured from porous silicon (top),  $F^-$ -etched roughened silicon (bottom), and  $O^-$ -etched roughened HOPG (middle).

## 16.5

### Conclusion

The most recent advances in the chemistry of porous silicon and its applications for chemical systems show that this material is a compatible substrate for a wide variety of analytical and physiological pursuits. The combination of luminescence, surface area and porosity, chemical reactivity, and other novel properties designate porous silicon as a versatile component for optoelectronics, bionics, and sensors, among other devices. Essential to the success of these devices is precise and deliberate control over the interfacial chemistry of this material. Through selective organic and inorganic chemistry at the surface, modulation of the nanocrystallite properties can be achieved for the design and implementation of chemically durable and intelligent substrates.

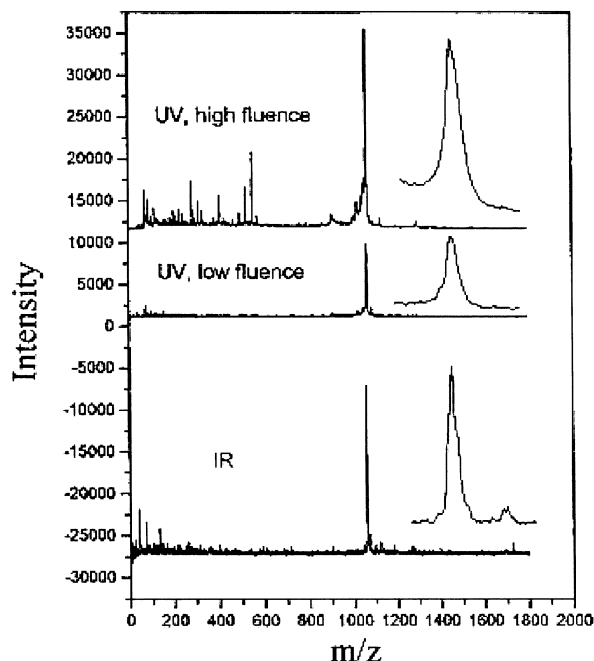


Fig. 16.23. DIOS-MS spectra of bradykinin from UV and IR laser sources. Insets: Expanded  $m/z = 1061$  peak of bradykinin.

## Acknowledgments

Support from the Purdue Research Foundation is acknowledged. J. M. B. is a Research Fellow of the Alfred P. Sloan Foundation (2000–2002), a Cottrell Teacher-Scholar of Research Corporation (2000–2002), and a Camille and Henry Dreyfus Foundation Teacher-Scholar (2002–2004).

## References

- 1 UHLIR, A., JR. *Bell. System Tech. J.* **1956**, 35, 333.
- 2 TURNER, D. R. *J. Electrochem. Soc.* **1958**, 105, 402.
- 3 BONDARENKO, V. P.; YAKOVITSEVA, V. A., in *Properties of Porous Silicon*, ed. CANHAM, L. T., INSPEC, London 1997, p. 343.
- 4 CANHAM, L. T. *Appl. Phys. Lett.* **1990**, 57, 1046.
- 5 *Properties of Porous Silicon*, ed. CANHAM, L. T., INSPEC, London 1997.
- 6 CULLIS, A. G.; CANHAM, L. T.; CALCOTT, P. D. *J. J. Appl. Phys.* **1997**, 82, 909.
- 7 COFFER, J. L., in *Properties of Porous Silicon*, ed. CANHAM, L. T., INSPEC, London 1997, p. 23.
- 8 NOGUCHI, N.; SUEMUNE, I. *Appl. Phys. Lett.* **1993**, 62, 1429.

- 9 HALIMAOU, A., in *Properties of Porous Silicon*, ed. CANHAM, L. T., INSPEC, London 1997, p. 12.
- 10 LEE, E. J.; BITNER, T. W.; HA, J. S. et al. *J. Am. Chem. Soc.* **1996**, *118*, 5375.
- 11 LEHMANN, V.; GÖSELE, U. *Appl. Phys. Lett.* **1991**, *58*, 856.
- 12 ZHANG, X. G. *J. Electrochem. Soc.* **1991**, *138*, 3750.
- 13 SMITH, R. L.; COLLINS, S. D. *J. Appl. Phys.* **1992**, *71*, R1.
- 14 CULLIS, A. G.; CANHAM, L. T.; WILLIAMS, G. M. et al. *J. Appl. Phys.* **1994**, *75*, 493.
- 15 YU, T.; LAIHO, R.; HEIKKILÄ, L. *J. Vac. Sci. Technol. B* **1994**, *12*, 2437.
- 16 HERINO, R.; BOMCHIL, G.; BARLA, K. et al. *J. Electrochem. Soc.* **1987**, *134*, 1994.
- 17 GROSAN, A.; ORTEGA, C., in *Properties of Porous Silicon*, ed. CANHAM, L. T., INSPEC, London 1997, p. 145.
- 18 CHANG, W. K.; LIAO, M. Y.; GLEASON, K. K. *J. Phys. Chem.* **1996**, *100*, 19653.
- 19 PETIT, D.; CHAZALVIEL, J.-N.; OZANAM, F. et al. *Appl. Phys. Lett.* **1997**, *70*, 191.
- 20 BOUKHERROUB, R.; MORIN, S.; WAYNER, D. D. M. et al. *Chem. Mater.* **2001**, *13*, 2002.
- 21 BURIK, J. M.; STEWART, M. P.; GEDERS, T. W. et al. *J. Am. Chem. Soc.* **1999**, *121*, 11491.
- 22 SONG, J. H.; SAILOR, M. J. *Comments Inorg. Chem.* **1999**, *21*, 69.
- 23 HÉRINO, R., in *Properties of Porous Silicon*, ed. CANHAM, L. T., INSPEC, London 1997, p. 89.
- 24 FAUCHET, P. M. *J. Lumin.* **1996**, *70*, 294.
- 25 COLLINS, R. T.; FAUCHET, P. M.; TISCHLER, M. A. *Phys. Today* **1997**, *50*, 24.
- 26 LI, K.-H.; TSAI, C.; CAMPBELL, J. C. et al. *J. Electron. Mater.* **1994**, *23*, 409.
- 27 BURIK, J. M.; ALLEN, M. J. *J. Lumin.* **1999**, *80*, 29.
- 28 CHOI, H. C.; BURIK, J. M. *Chem. Mater.* **2000**, *12*, 2151.
- 29 BURIK, J. M. *Chem. Rev.* **2002**, *102*, 1271.
- 30 CANHAM, L. T.; REEVES, C. L.; NEWBY, J. P. et al. *Adv. Mater.* **1999**, *11*, 1505.
- 31 KIM, N. Y.; LAIBINIS, P. E. *J. Am. Chem. Soc.* **1999**, *121*, 7162.
- 32 PIKE, A. R.; LIE, L. H.; EAGLING, R. A. et al. *Angew. Chem. Int. Ed. Engl.* **2002**, *41*, 615.
- 33 HART, B. R.; LÉTANT, S. E.; KANE, S. R. et al. *Chem. Commun.* **2003**, 322.
- 34 STEWART, M. P.; BURIK, J. M. *Adv. Mater.* **2000**, *12*, 859.
- 35 SAILOR, M. J.; LEE, E. J. *Adv. Mater.* **1997**, *9*, 783.
- 36 BURIK, J. M. *Adv. Mater.* **1999**, *11*, 265.
- 37 BURIK, J. M. *Chem. Commun.* **1999**, 1051.
- 38 STEWART, M. P.; BURIK, J. M. *Comments Inorg. Chem.* **2002**, *23*, 179.
- 39 BATEMAN, J. E.; EAGLING, R. D.; WORRALL, D. R. et al. *Angew. Chem. Int. Ed. Engl.* **1998**, *37*, 2683.
- 40 BATEMAN, J. E.; EAGLING, R. D.; HORROCKS, B. R. et al. *J. Chem. Phys. B* **2000**, *104*, 5557.
- 41 SONG, J. H.; SAILOR, M. J. *J. Am. Chem. Soc.* **1998**, *120*, 2376.
- 42 SONG, J. H.; SAILOR, M. J. *Inorg. Chem.* **1999**, *38*, 1498.
- 43 KIM, N. Y.; LAIBINIS, P. E. *J. Am. Chem. Soc.* **1998**, *120*, 4516.
- 44 BURIK, J. M.; ALLEN, M. J. *J. Am. Chem. Soc.* **1998**, *120*, 1339.
- 45 HOLLAND, J. M.; STEWART, M. P.; ALLEN, M. J. et al. *J. Solid State Chem.* **1999**, *147*, 251.
- 46 SAGHATELIAN, A.; BURIK, J.; LIN, V. S. Y. et al. *Tetrahedron* **2001**, *57*, 5131.
- 47 SCHMELTZER, J. M.; PORTER, L. A., JR.; STEWART, M. P. et al. *Langmuir* **2002**, *18*, 2971.
- 48 VIEILLARD, C.; WARNTJES, M.; OZANAM, F. et al. *Proc. Electrochem. Soc.* **1996**, *95*, 250.
- 49 OZANAM, F.; VIEILLARD, C.; WARNTJES, M. et al. *Can. J. Chem. Eng.* **1998**, *76*, 1020.
- 50 ROBINS, E. G.; STEWART, M. P.; BURIK, J. M. *Chem. Commun.* **1999**, 2479.
- 51 GURTNER, C.; WUN, A. W.; SAILOR, M. J. *Angew. Chem. Int. Ed. Engl.* **1999**, *38*, 1966.
- 52 STEWART, M. P.; BURIK, J. M. *Angew. Chem. Int. Ed.* **1998**, *37*, 3257.
- 53 STEWART, M. P.; BURIK, J. M. *J. Am. Chem. Soc.* **2001**, *123*, 7821.



- 54 *The Chemistry of Organosilicon Compounds*, eds. RAPPAPORT, Z.; APELOIG, Y., John Wiley & Sons, Chichester 1998, Vol. 2.
- 55 LINFORD, M. R.; CHIDSEY, C. E. D. *J. Am. Chem. Soc.* **1993**, *115*, 12631.
- 56 LINFORD, M. R.; FENTER, P.; EISENBERGER, P. M. et al. *J. Am. Chem. Soc.* **1995**, *117*, 3145.
- 57 SIEVAL, A. B.; DEMIREL, A. L.; NISSINK, J. W. M. et al. *Langmuir* **1998**, *14*, 1759.
- 58 TERRY, J.; LINFORD, M. R.; WIGREN, C. et al. *Appl. Phys. Lett.* **1997**, *71*, 1056.
- 59 TERRY, J.; LINFORD, M. R.; WIGREN, C. et al. *J. Appl. Phys.* **1999**, *85*, 213.
- 60 CICERO, R. L.; LINFORD, M. R.; CHIDSEY, C. E. D. *Langmuir* **2000**, *16*, 5688.
- 61 BOUKHERROUB, R.; MORIN, S.; BENSEBAA, F. et al. *Langmuir* **1999**, *15*, 3831.
- 62 DE VILLENEUVE, C. H.; PINSON, J.; BERNARD, M. C. et al. *J. Phys. Chem. B* **1997**, *101*, 2415.
- 63 BOUKHERROUB, R.; WAYNER, D. D. M.; LOCKWOOD, D. J. et al. *J. Electrochem. Soc.* **2001**, *148*, H91.
- 64 CANHAM, L.; ASTON, R. *Phys. World* **2001**, *14*, 27.
- 65 CANHAM, L. T. *Adv. Mater.* **1995**, *7*, 1033.
- 66 CANHAM, L. T.; NEWBY, J. P.; REEVES, C. L. et al. *Adv. Mater.* **1996**, *8*, 847.
- 67 CANHAM, L. T.; REEVES, C. L.; LONI, A. et al. *Thin Solid Films* **1997**, *297*, 304.
- 68 CANHAM, L. T.; STEWART, M. P.; BURIK, J. M. et al. *Phys. Status Solidi A* **2000**, *182*, 521.
- 69 XIA, Y.; WHITESIDES, G. M. *Angew. Chem. Int. Ed. Engl.* **1998**, *37*, 550.
- 70 SIRBULY, D. J.; LOWMAN, G. M.; SCOTT, B. et al. *Adv. Mater.* **2003**, *15*, 149.
- 71 JI, J.; LI, X.; CANHAM, L. T. et al. *Adv. Mater.* **2002**, *14*, 41.
- 72 LI, X.; COFFER, J. L.; CHEN, Y. et al. *J. Am. Chem. Soc.* **1998**, *120*, 11706.
- 73 LI, X.; ST. JOHN, J.; COFFER, J. L. et al. *Biomed. Microdevices* **2000**, *2*, 265.
- 74 BAYLISS, S.; BUCKBERRY, L.; HARRIS, P. et al. *Thin Solid Films* **1997**, *297*, 308.
- 75 BAYLISS, S. C.; HARRIS, P. J.; BUCKBERRY, L. D. et al. *J. Mater. Sci. Lett.* **1997**, *16*, 737.
- 76 BAYLISS, S. C.; BUCKBERRY, L. D.; FLETCHER, I. et al. *Sens. Actuators, A* **1999**, *74*, 139.
- 77 BAYLISS, S. C.; HEALD, R.; FLETCHER, D. I. et al. *Adv. Mater.* **1999**, *11*, 318.
- 78 MAYNE, A. H.; BAYLISS, S. C.; BARR, P. et al. *Phys. Status Solidi A* **2000**, *182*, 505.
- 79 BAYLISS, S. C.; BUCKBERRY, L. D.; HARRIS, P. J. et al. *J. Porous Mater.* **2000**, *7*, 191.
- 80 CHIN, V.; COLLINS, B. E.; SAILOR, M. J. et al. *Adv. Mater.* **2001**, *13*, 1877.
- 81 FAN, Y. W.; CUI, F. Z.; HOU, S. P. et al. *J. Neurosci. Methods* **2002**, *120*, 17.
- 82 SIGAL, G. B.; BAMDAD, C.; BARBERIS, A. et al. *Anal. Chem.* **1996**, *68*, 490.
- 83 BENGTSOON, M.; EKSTRÖM, S.; MARKOVARGA, G. et al. *Talanta* **2002**, *56*, 341.
- 84 LAURELL, T.; DROTT, J.; ROSENGREN, L. et al. *Sens. Actuators B* **1996**, *31*, 161.
- 85 DROTT, J.; ROSENGREN, L.; LINDSTRÖM, K. et al. *Thin Solid Films* **1998**, *330*, 161.
- 86 BENGTSOON, M.; EKSTRÖM, S.; DROTT, J. et al. *Phys. Status Solidi A* **2000**, *182*, 495.
- 87 BENGTSOON, M.; DROTT, J.; LAURELL, T. *Phys. Status Solidi A* **2000**, *182*, 533.
- 88 YAKOVLEVA, J.; DAVIDSSON, R.; LOBANOVA, A. et al. *Anal. Chem.* **2002**, *74*, 2994.
- 89 TJERKSTRA, R. W.; GARDENIERS, J. G. E.; KELLY, J. J. et al. *J. Microelectromech. Systems* **2000**, *9*, 495.
- 90 LIN, V. S.-Y.; MOTESHAREI, K.; DANCIL, K.-P. S. et al. *Science* **1997**, *278*, 840.
- 91 JANSHOFF, A.; DANCIL, K.-P. S.; STEINEM, C. et al. *J. Am. Chem. Soc.* **1998**, *120*, 12108.
- 92 DANCIL, K.-P. S.; GREINER, D. P.; SAILOR, M. J. *J. Am. Chem. Soc.* **1999**, *121*, 7925.
- 93 TINSLEY-BOWN, A. M.; CANHAM, L. T.; HOLLINGS, M. et al. *Phys. Status Solidi A* **2000**, *182*, 547.
- 94 SNOW, P. A.; SQUIRE, E. K.; RUSSELL, P. St. J. et al. *J. Appl. Phys.* **1999**, *86*, 1781.
- 95 LÉTANT, S. E.; SAILOR, M. J. *Adv. Mater.* **2000**, *12*, 355.

- 96 SOHN, H.; LÉTANT, S.; SAILOR, M. J. et al. *J. Am. Chem. Soc.* **2000**, 122, 5399.
- 97 GAO, J.; GAO, T.; SAILOR, M. J. *Appl. Phys. Lett.* **2000**, 77, 901.
- 98 GAO, J.; GAO, T.; LI, Y. Y.; *Langmuir* **2002**, 18, 2229.
- 99 GAO, T.; GAO, J.; SAILOR, M. J. *Langmuir* **2002**, 18, 9953.
- 100 SCHMEDAKE, T. A.; CUNIN, F.; LINK, J. R. et al. *Adv. Mater.* **2002**, 14, 1270.
- 101 CUNIN, F.; SCHMEDAKE, T. A.; LINK, J. R. et al. *Nature Mater.* **2002**, 1, 39.
- 102 LÉTANT, S. E.; SAILOR, M. J. *Adv. Mater.* **2001**, 13, 335.
- 103 COLLINS, B. E.; DANCIL, K.-P. S.; ABBI, G. et al. *Adv. Funct. Mater.* **2002**, 12, 187.
- 104 ALCOCK, P.; SNOW, P. A. *J. Appl. Phys.* **2001**, 90, 5052.
- 105 RYU, C.-S.; CHO, S. M.; KIM, B.-W. *Biotechnol. Lett.* **2001**, 23, 653.
- 106 CONTENT, S.; TROGLER, W. C.; SAILOR, M. J. *Chem. Eur. J.* **2000**, 6, 2205.
- 107 HARPER, J.; SAILOR, M. J. *Anal. Chem.* **1996**, 68, 3713.
- 108 CHAN, S.; HORNER, S. R.; FAUCHET, P. M. et al. *J. Am. Chem. Soc.* **2001**, 123, 11797.
- 109 CHAN, S.; FAUCHET, P. M.; LI, Y.; ROTHBERG, L. J. et al. *Phys. Status Solidi A* **2000**, 182, 541.
- 110 MULLONI, V.; PAVESI, L. *Appl. Phys. Lett.* **2000**, 76, 2523.
- 111 GABURRO, Z.; DALDOSSO, N.; PAVESI, L. et al. *Appl. Phys. Lett.* **2001**, 78, 3744.
- 112 LÉTANT, S. E.; CONTENT, S.; TAN, T. T. et al. *Sens. Actuators, B* **2000**, 69, 193.
- 113 LIU, R.; SCHMEDAKE, T. A.; LI, Y. Y. et al. *Sens. Actuators, B* **2002**, 87, 58.
- 114 GROSS, E.; KOVALEV, D.; KÜNZNER, N. et al. *J. Appl. Phys.* **2001**, 90, 3529.
- 115 YOSHINOBU, T.; ECKEN, H.; POGHOSSIAN, A. et al. *Sens. Actuators, B* **2001**, 76, 388.
- 116 YOSHINOBU, T.; ECKEN, H.; ISMAIL, A. B. Md. et al. *Electrochim. Acta* **2001**, 47, 259.
- 117 MIKULEC, F. V.; KIRTLAND, J. D.; SAILOR, M. J. *Adv. Mater.* **2002**, 14, 38.
- 118 KOVALEV, D.; TIMOSHENKO, V. Y.; KÜNZNER, N. et al. *Phys. Rev. Lett.* **2001**, 87, 068301.
- 119 STUMP, M. J.; FLEMING, R. C.; GONG, W.-H. et al. *Appl. Spectrosc. Rev.* **2002**, 37, 275.
- 120 COHEN, L. H.; GUSEV, A. I. *Anal. Bioanal. Chem.* **2002**, 373, 571.
- 121 ZENOBI, R. *Chimia* **1997**, 51, 801.
- 122 ZHAN, Q.; WRIGHT, S. J.; ZENOBI, R. *J. Am. Soc. Mass Spectrom.* **1997**, 8, 525.
- 123 HRUBOWCHAK, D. M.; ERVIN, M. H.; WOOD, M. C. et al. *Anal. Chem.* **1991**, 63, 1947.
- 124 VARAKIN, V. N.; LUNCHEV, V. A.; SIMONOV, A. P. *High Energy Chem.* **1994**, 28, 406.
- 125 WANG, S. L.; LEDINGHAM, K. W. D.; JIA, W. J. et al. *Appl. Surf. Sci.* **1996**, 93, 205.
- 126 POSTHUMUS, M. A.; KISTEMAKER, P. G.; MEUZELAAR, H. L. C. et al. *Anal. Chem.* **1978**, 50, 985.
- 127 WEI, J.; BURIK, J. M.; SIUZDAK, G. *Nature* **1999**, 399, 243.
- 128 THOMAS, J. J.; SHEN, Z.; CROWELL, J. E. et al. *Proc. Nat. Acad. Sci. USA* **2001**, 98, 4932.
- 129 ZOU, H.; ZHANG, Q.; GUO, Z. et al. *Angew. Chem. Int. Ed. Engl.* **2002**, 41, 646.
- 130 THOMAS, J. J.; SHEN, Z.; BLACKLEDGE, R. et al. *Anal. Chim. Acta* **2001**, 442, 183.
- 131 KRUSE, R. A.; RUBAKHIN, S. S.; ROMANOVA, E. V. et al. *J. Mass Spectrom.* **2001**, 36, 1317.
- 132 ZHANG, Q.; ZOU, H.; GUO, Z. et al. *Rapid Commun. Mass Spectrom.* **2001**, 15, 217.
- 133 LAIKO, V. V.; TARANENKO, N. I.; BERKOUT, V. D. et al. *Rapid Commun. Mass Spectrom.* **2002**, 16, 1737.
- 134 SHEN, Z.; THOMAS, J. J.; AVERBUJ, C. et al. *Anal. Chem.* **2001**, 73, 612.
- 135 KRUSE, R. A.; LI, X.; BOHN, P. W. et al. *Anal. Chem.* **2001**, 73, 3639.
- 136 ALIMPIEV, S.; NIKIFOROV, S.; KARAVANSKII, V. et al. *J. Chem. Phys.* **2001**, 115, 1891.

## 17

**Nanocatalysis***S. Abbet and U. Heiz*

## 17.1

**Introduction**

The term “catalysis” was introduced in 1836 by Berzelius in order to classify certain types of chemical reactions whose progress is affected by additional substances which are not part of the reaction products [1]. Since then, a molecular understanding of catalytic processes has been emerging, notably with the introduction of model catalysts (metal surfaces or metal particles supported on oxide surfaces) [2]. However, most catalysts in use today were discovered by trial and error, by “shaking and baking” metals and ceramics and then seeing how the results affect the reactions and their products. As we enter the nano-age, another approach is appearing. Indeed, nanotechnology, being defined as the creation of functional materials, devices, and systems through the control of matter at a scale of nanometers, as well as the exploitation of novel properties and phenomena developed at that scale [3, 4], the catalysts of the nano-age, called nanocatalysts, are shaped atom-by-atom. Different approaches can be used to build nanocatalysts: these are self-assembly, nanolithography or nanoarchitecturing by using the building blocks of nanotechnology, which are nanocrystals, nanofilms, nanowires, and clusters [5].

Here we define nanocatalysis when two important conditions are fulfilled [6]. First, the valence electrons of the active part of a nanocatalyst are highly confined, leading to physical and chemical properties non-scalable from the bulk properties. This condition is true for clusters/particles of the nanometer length scale or smaller. Second, nanocatalysts are designed in a controlled manner. The exploration of materials properties in the non-scalable regime has profound consequences. Atomic clusters, e.g., exhibit unique size-dependent electronic [7, 8], magnetic [9, 10], and chemical properties [11] that differ from those of bulk materials. In contrast to supported particles of larger size or extended solid surfaces, small clusters adsorbed at specific sites of a support material change their intrinsic properties to a large extent, in particular when charging of the cluster occurs. Nanocatalysts exhibit remarkable quantum size effects and structural fluxionality. This opens new avenues for atom-by-atom design of nanocatalysts whose chemical activity, specificity, and selectivity can be tuned by controlling the cluster size,

through the incorporation of impurity atoms, and via manipulation of the strength of the cluster–support interaction, the degree of charging of the cluster, and by changing their magnetic properties. In a completely different approach catalytic reactions can be induced by nanodevices, where the energy of the localized electrons inducing the reaction can be tuned by changing the potential of the device. An example is the use of an STM tip in close contact with the reactants. In this chapter we present some studies on model systems for nanocatalysts. With such systems the complexity of working nanocatalysts can be reduced and in many cases simple reaction steps can be identified. It has to be pointed out that in this chapter we use the expression “catalysis” when a chemical reaction is catalyzed by a nanoscale system. We are aware, however, that none of the systems/methods presented here have been tested to withstand the harsh conditions of real catalysis. We feel, however, that such studies are extremely important for developing guiding principles in nanocatalysis.

## 17.2

### Chemical Reactions on Point Defects of Oxide Surfaces

In a recent review, Pacchioni presents a detailed classification of point defects at the surfaces of oxide materials [12]. He describes at least four major kinds of irregularities: low-coordinated sites, divacancies, impurity atoms and surface vacancies. The last category includes cation vacancies, usually called V centers, as well as oxygen vacancies, which are called color centers or F centers (from the German word for “color”: “Farbe”). In a broader sense, an F center is defined as an electron trapped in an anion vacancy and was first introduced to explain chemical- and radiation-induced coloration of alkali halides. In bivalent oxides, like MgO and CaO, two types of F centers exist. The vacancy containing two electrons is called the F center and the one containing only one electron is labelled as the  $F^+$  center. In both vacancies the electrons are confined by the Madelung potential of the crystal. Thus, in a first approach, the  $F/F^+$  centers can be described as two/one electrons moving in quantum box of nanometer length scale; i.e.  $F/F^+$  centers are systems with highly confined electrons and with our definition they are examples of nanocatalysts.

The unique chemical activity of F centers has been demonstrated recently. In a combined theoretical and experimental study, it was shown that the heterolytic decomposition of methanol on MgO thin films is catalyzed by surface oxygen vacancies [13]. In these films the oxygen vacancies are generated by changing the preparation method [14], e.g. the Mg evaporation rate and the oxygen background pressure. In this way, two kinds of films are prepared: defect-poor (Mg evaporation rate:  $0.3\text{--}0.5\text{ ML min}^{-1}$ ,  $O_2$  background:  $5 \cdot 10^{-7}$  Torr) and defect-rich (Mg evaporation rate:  $2\text{--}5\text{ ML min}^{-1}$ ,  $O_2$  background:  $10^{-6}$  Torr) films. Both films are annealed to 1200 K and 840 K for 10 min, respectively. Auger electron spectroscopy (AES) measurements show a one-to-one stoichiometry for magnesium and oxygen and the absence of any impurity [15]. Typical thicknesses are about 10 monolayers,

as determined by AES peak intensities [15] and by X-ray photoemission (XPS), using the intensity attenuation of the Mo 3d core level with increasing film coverage [16]. Both films have also been studied by electron energy loss spectroscopy [16]. In contrast to defect-poor films, which are characterized by a loss at about 6 eV in the EEL spectra (Figure 17.1a, in good agreement with previous studies on MgO(100) single crystals [17]), the EEL spectra of defect-rich films exhibit characteristic losses between 1 and 4 eV, lying within the MgO band gap (Figure 17.1a). Similar loss structures have been observed before [18], and according to first-principle calculations using large cluster models, they have been attributed to transitions characteristic for neutral surface F centers in various coordinations on flat terraces, at steps and at kinks [19]. The density of these oxygen vacancies is estimated to be larger than  $5 \times 10^{13} \text{ cm}^{-2}$ .

The interaction of methanol with the defect-poor and defect-rich films was studied using thermal desorption spectroscopy (TDS) (Figure 17.1c). For both films the desorption of physisorbed methanol at around 180 K is most dominant. On the defect-poor films small amounts of chemisorbed methanol desorb up to around 350 K. On defect-rich films the desorption of chemisorbed methanol evolves in three distinct peaks at 200 K, 260 K, and 340 K. A small reproducible feature is observed at around 500 K. Most importantly,  $\text{H}_2$  desorbs at 580 K only on defect-rich films. The corresponding infrared spectra taken at 90 K (insets of Figure 17.1c) confirm the presence of mainly physisorbed  $\text{CH}_3\text{OH}$  with the typical vibrational band for the OH group at  $3285 \text{ cm}^{-1}$ , bands of the symmetric C–H stretching ( $2930 \text{ cm}^{-1}/2828 \text{ cm}^{-1}$ ) and the C–H bending ( $1475 \text{ cm}^{-1}$ ) modes of the  $\text{CH}_3$  group, as well as the C–O vibrational mode at  $1080 \text{ cm}^{-1}/1050 \text{ cm}^{-1}$ . For defect-poor films most of the intensity of the vibrational bands disappears between 180 K and 200 K, consistent with the desorption observed at 180 K in the TDS. Up to temperatures of about 400 K small bands are observed for the  $\text{CH}_3$ – and C–O bands. Their intensity decreases with temperature. These bands are attributed to chemisorbed methanol. As for the defect-rich films, the evolution of the IR spectra with temperature is consistent with the corresponding TDS. Physisorbed methanol desorbs before 200 K (disappearance of the OH band), and the more intense vibrational features of chemisorbed methanol are unambiguously detected up to 360 K. At higher temperatures a clear peak is observed at  $1070\text{--}1085 \text{ cm}^{-1}$  [13]. It is interesting to note that the disappearance of this band correlates with the desorption of  $\text{H}_2$  from the surface at around 580 K and therefore this peak is attributed, in accordance with the theoretical studies, to a proton trapped in the cavity of an F center. The calculations show that F centers easily dissociate methanol giving a  $\text{CH}_3\text{O}$  group and an  $\text{H}^+$  ion adsorbed into the F center. This adsorbed proton is strongly bound as the dissociation of a neutral H atom,  $\text{Fs}/\text{H}^+ \rightarrow \text{Fs}^+ + \text{H}^+$ , costs 4.1 eV. This represents a crude estimate of the barrier to be overcome in order to observe  $\text{H}_2$  desorption from the surface. Once the H atom is detached from the F center it will rapidly diffuse on the surface. In fact, the binding of an H atom to an  $\text{O}_{5c}$  ion on a terrace is about 0.5 eV. Diffusion will eventually lead to recombination with a second H to form  $\text{H}_2$ ;  $\text{H}_2$  is weakly bound to the MgO terrace sites and at 580 K will immediately desorb. The adsorbed hydrogen gives rise to vibrations

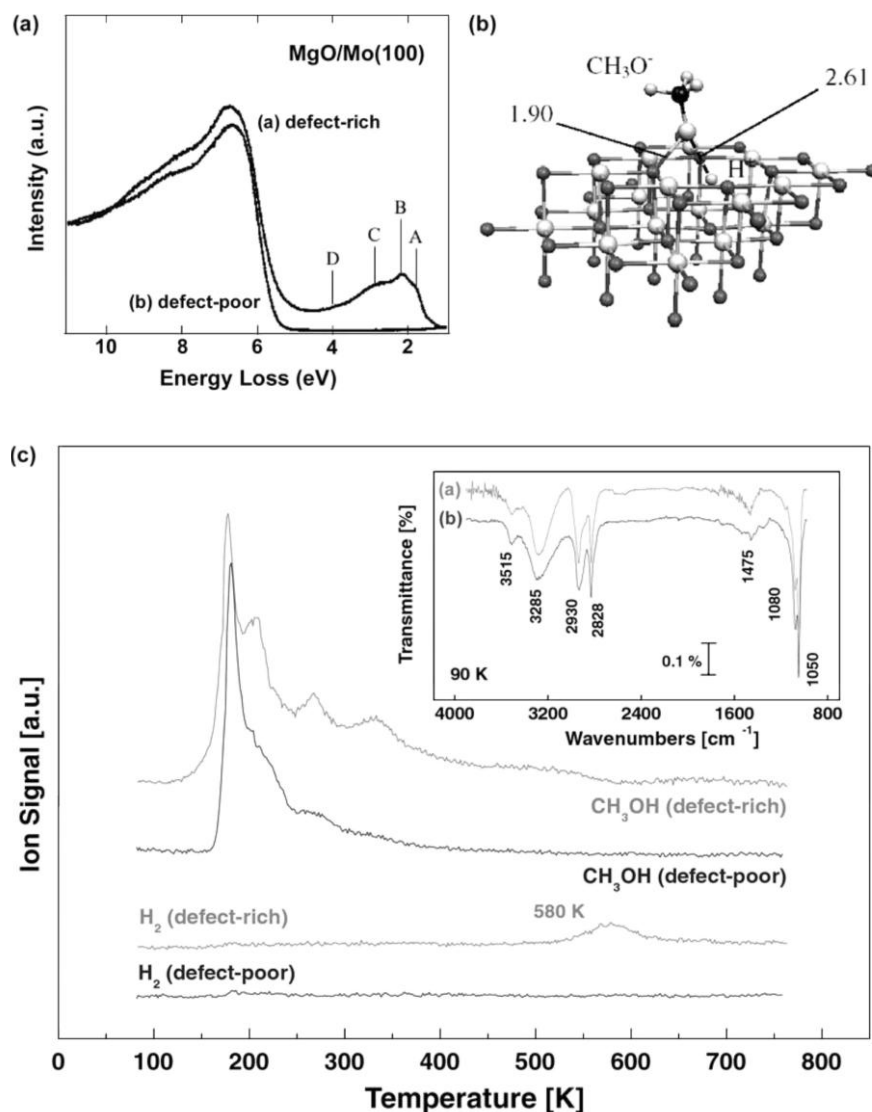


**Fig. 17.1.** (a) EEL spectra of thin defect-poor and defect-rich MgO(100) films grown on Mo(100) under different experimental conditions (see text). A to D are losses, which are attributed theoretically to transitions characteristic of neutral F centers on MgO. (b) Model of an oxygen vacancy at a terrace of a MgO(100) surface with chemisorbed  $\text{CH}_3\text{OH}$

( $\text{CH}_3\text{O}^- - \text{H}^+$ ). (c) Thermal desorption spectra of  $\text{CH}_3\text{OH}$  and  $\text{H}_2$  on defect-poor and defect-rich MgO(100) films. Note the desorption of  $\text{H}_2$  at 580 K for defect-rich films. The insets show FTIR spectra recorded at 90 K for adsorbed  $\text{CH}_3\text{OH}$  on both defect-poor and defect-rich films.

of strong intensity at  $830\text{--}950\text{ cm}^{-1}$  when isolated, and to an intense band at  $1030\text{ cm}^{-1}$  in the chemisorbed complex shown in Figure 17.1b. Therefore the stable species is assigned to H atoms incorporated into oxygen vacancies.

In conclusion, this combined experimental and theoretical study of methanol adsorbed on MgO films with different defect density allows one to better identify the surface sites responsible for the MgO reactivity. On the inert terrace sites only physisorption is observed. Molecular chemisorption, activation and heterolytic dissociation occur on irregular sites. The low-coordinated Mg–O pairs of ions located at edges and steps can lead to strongly activated and even dissociated methanol molecules. Adsorption of  $\text{CH}_3\text{O}^-$  and  $\text{H}^+$  fragments seems to be preferred over dissociation into  $\text{CH}_3^+$  and  $\text{OH}^-$  units. All these species are stable on the surface for temperatures up to 350 K and account for the TDS spectra of the defect-poor films. On defect-rich films (F centers) the O–H bond is selectively dissociated, resulting in the observed desorption of  $\text{H}_2$  at high temperature. Thus, these oxygen vacancy centers, called F centers, act as nanocatalysts.

### 17.3

#### Chemical Reactions and Catalytic Processes on Free and Supported Clusters

##### 17.3.1

##### Catalytic Processes on Free Metal Clusters

Free clusters are ideal model systems to probe the influence of their intrinsic, size-dependent properties on the catalytic activity due to the lack of any support interactions. Free clusters are prepared from cluster sources [20] and only very low densities are obtained. They are highly unstable under normal conditions and, even under UHV conditions, exothermal catalytic reactions may lead to fragmentation without the presence of a buffer gas. Thus, free clusters may not become relevant for industrial applications. Nevertheless, they are important vehicles to gain a fundamental understanding of nanocatalysis.

The following method is often used for producing free clusters. The material of interest is evaporated by means of intense laser pulses [21], electrical discharges [22] or highly energetic inert ions [23]. A buffer gas thermalizes the ultra-hot plasma or supersaturated atomic gas produced. The mixture expands through a nozzle into the vacuum upon supersonic expansion. By this process, the clusters formed are cooled to cryogenic temperatures and generate well-defined molecular beams of neutral and charged clusters. The reactivity of the clusters can then be studied by various experimental techniques, including fast flow reactor kinetics in the post-vaporization expansion region of a laser evaporation source [24, 25], ion flow tube reactor kinetics of ionic clusters [26, 27], ion cyclotron resonance [28, 29], guided-ion-beam [30], and ion-trap experiments [31–33]. Which of these techniques is applied depends on the charge state of the reactants (neutral, cationic, anionic), on whether the clusters are size-selected before the reaction zone, on single or multiple collisions of the clusters with the reactants, on the pressure of a

buffer gas if present, and on the temperature and collision energy of the reactant molecules.

A representative experimental set-up may be described in the following way [31]. The cluster anions are produced by a sputter source and are extracted into a helium-filled quadrupole, where they are cooled to room temperature and collimated to the axis of the ion optics. A second quadrupole selects a single cluster size. The cluster ions are then transferred with a quadrupole ion guide into an octopole ion trap, which can be continuously cooled from  $T_T = 350$  to 20 K. The potentials on the entrance and exit lenses can be switched in order to fill the trap, store the ions in the trap, and finally extract product ions for mass analysis. Through collisions with a buffer gas (helium or argon) in the trap, the clusters are thermalized within a few milliseconds. Different reactants, can be added to the ion trap under known partial pressures  $p_R$ . Typically the number of reactant molecules is orders of magnitude higher than the number of clusters and thus it can be taken as constant. After reaction time  $t_R$ , the charged products are extracted from the trap and are analyzed by a quadrupole mass spectrometer as a function of  $t_R$ ,  $p_R$ , and  $T_T$ .

With such experimental techniques the interaction of reactants, e.g. CO and O<sub>2</sub> molecules, or even complete catalytic cycles have been observed on small Au<sub>*n*</sub><sup>−</sup> anions [33, 34]. By varying the reaction temperatures and measuring the kinetics of the processes, the energetics of complete reaction mechanisms could be obtained and compared with ab initio simulations [32, 35]. The reactivity of Au<sub>2</sub><sup>−</sup> toward O<sub>2</sub> or CO, as well as the coadsorption of both molecules, revealed an interesting and unexpected selectivity. O<sub>2</sub> only reacts with even-*n* Au<sub>*n*</sub><sup>−</sup> clusters, while odd-*n* clusters and Au<sub>16</sub><sup>−</sup> are inert. In addition, the reactive clusters adsorb just one O<sub>2</sub> molecule. The relative reactivities correlate well with measured electron affinities of neutral clusters, suggesting a mechanism involving the adsorption of O<sub>2</sub> as a one-electron acceptor [36, 37]. The reactivity of gold cluster anions with CO also shows a distinct size-selectivity, although less pronounced than that with O<sub>2</sub> [38]. In this reaction, the most reactive cluster sizes are Au<sub>11</sub>, Au<sub>15</sub>, and Au<sub>19</sub>. Most reactive cluster sizes readily adsorb several CO molecules in the saturation limit. The full geometric coverage, e.g. one CO per surface gold atom, is, however, never reached. On real catalysts and single crystals competitive adsorption is usually observed, meaning that in many examples CO poisons the active catalysts. This is not true for small Au<sub>*n*</sub><sup>−</sup> clusters. In contrast, for distinct cluster sizes cooperative adsorption is observed, where the presence of preadsorbates enhances the adsorption probability of subsequent adsorbates. As examples, for Au<sub>3</sub><sup>−</sup> preadsorbed CO enables the adsorption probability of O<sub>2</sub>, Au<sub>2</sub><sup>−</sup> is inert for the adsorption of CO at around room temperature, the presence of preadsorbed O<sub>2</sub>, however, makes the adsorption possible at this temperature [33]. A similar effect is observed for Au<sub>10</sub><sup>−</sup>, where O<sub>2</sub> enhances the adsorption of CO by a factor of more than 5. Finally, Au<sub>6</sub><sup>−</sup> reveals even an enhanced cooperative adsorption with increasing numbers of adsorbate molecules [34].

Let us now turn our attention to Au<sub>2</sub><sup>−</sup> where a full catalytic cycle could unambiguously be observed by measuring the kinetics of the process at different



temperatures [32]. At room temperature oxygen reacts by a straightforward association reaction mechanism with the dimer anion, as determined from the measured product ion concentration as a function of the reaction time, and the negative dependence of the reaction rate with temperature:



As mentioned above no adsorption of CO is observed at around room temperature. When both reactants,  $\text{O}_2$  and CO, are introduced into the ion trap, the reaction kinetics of  $\text{Au}_2^-$  changes drastically, as seen by the offset in the  $\text{Au}_2^-$  signal. This offset increases when the partial pressure of CO is augmented. In addition, at temperatures below 200 K the intermediate with the stoichiometry  $\text{Au}_2(\text{CO})\text{O}_2^-$  could be isolated (Figure 17.2A-b). The ion stoichiometry clearly shows that CO and  $\text{O}_2$  are able to coadsorb onto an  $\text{Au}_2^-$  dimer. From the kinetics of all observable ions,  $\text{Au}_2^-$ ,  $\text{Au}_2\text{O}_2^-$ , and  $\text{Au}_2(\text{CO})\text{O}_2^-$ , measured under a multitude of different reaction conditions the catalytic conversion of CO to  $\text{CO}_2$  could unambiguously be detected. The reaction mechanism that fulfills all the prerequisites and fits all kinetic data measured under all the different reaction conditions could be described by the reaction equations below:



By studying the kinetics as a function of concentration and temperature (Figure 17.2B) some important findings were obtained. (1) Undoubtedly  $\text{O}_2$  adsorption precedes CO adsorption in the catalytic reaction. This is, furthermore, supported by the reaction kinetics of  $\text{Au}_2^-$  when only  $\text{O}_2$  or CO is present in the trap: The adsorption of  $\text{O}_2$  is faster by at least a factor of 10 than the adsorption of CO molecules [39]. (2) These experiments revealed that varying the oxygen partial pressure inside the trap mainly affects the pseudo-first order rate constant  $k_1$ , such that  $k_1$  increases linearly with increasing  $p(\text{O}_2)$  and, to a smaller extent, the rate constant  $k_4$ , which was attributed to the higher abundance of  $\text{Au}_2(\text{CO})\text{O}_2^-$ . (3) An increase in the carbon monoxide partial pressure results, at room temperature, in an increasing back pseudo-first order reaction rate  $k_2$  (Eq. (2)), i.e. the  $\text{Au}_2^-$  offset is increasing. Resolving the kinetics at lower temperature, 190 K, reveals a clearly positive dependence of  $k_4$  (Eq. (2c)) on  $p(\text{CO})$ , also correlated to the  $\text{Au}_2^-$  offset. (4) Finally, with decreasing temperature the final equilibrium concentration of  $\text{Au}_2(\text{CO})\text{O}_2^-$  increases, whereas the  $\text{Au}_2\text{O}_2^-$  concentration decreases (Figure 17.2B). This is consistent with the decreasing rate constants  $k_1$ ,  $k_2$ , and  $k_3$  with increasing temperature and this negative temperature dependence is indicative of barrierless reaction steps, explained in the framework of the Lindemann theory [39, 40]. Most importantly, however,  $k_4$  increases with increasing temperature. Hence, an activation barrier is involved in the corresponding reaction (2c).

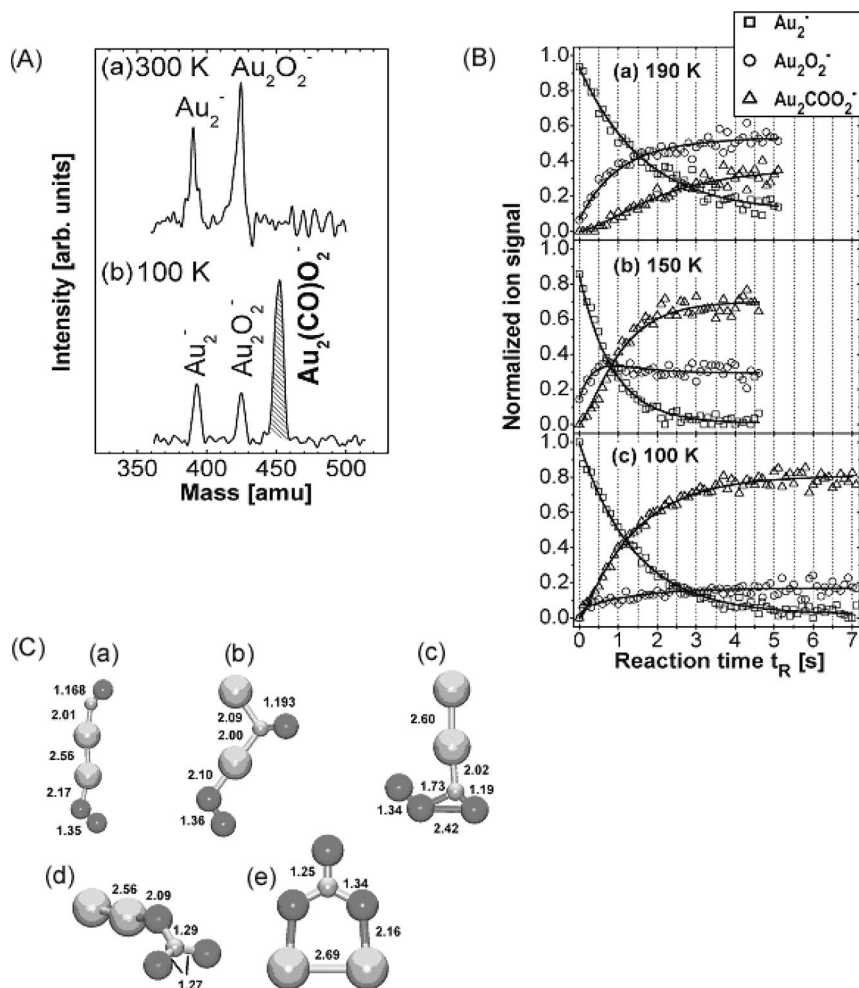


**Fig. 17.2.** (A) Mass spectra of product ion distributions analyzed after trapping  $Au_2^-$  for 500 ms inside the octopole ion trap filled with 0.02 Pa  $O_2$ , 0.05 Pa CO, and 1.23 Pa He. (a) At a reaction temperature of 300 K only  $Au_2^-$  and  $Au_2O_2^-$  are detected. No further ion signals are observed at temperatures above 200 K. Cooling further reveals an additional ion signal appearing at the mass of  $Au_2(CO)O_2^-$ . Mass spectrum (b) shows the ion distribution at 100 K. (B) Product ion concentrations as a function of reaction time for three different reaction temperatures. (a)  $T_T = 190$  K;  $p(O_2) = 0.06$  Pa;  $p(CO) = 0.07$  Pa;  $p(He) = 1.0$  Pa. (b)  $T_T =$

150 K;  $p(O_2) = 0.04$  Pa;  $p(CO) = 0.04$  Pa;  $p(He) = 1.0$  Pa. (c)  $T_T = 100$  K;  $p(O_2) = 0.02$  Pa;  $p(CO) = 0.03$  Pa;  $p(He) = 1.0$  Pa. Open symbols represent the normalized experimental data. The solid lines are obtained by fitting the integrated rate equations of the catalytic reaction cycle (see text) to the experimental data. (C) Five optimized structures (a)–(e) of  $Au_2CO_3^-$ , with bond lengths in Å. The relative stability of these structures is shown in Table 17.1. (a), (b), (c), and (e) are planar, and the two carboxen species (d) and (e) have  $C_{2v}$  symmetry.

**Tab. 17.1.** The relative stability, vertical electron detachment energy, binding energy of CO (with O<sub>2</sub> preadsorbed) and binding energy of O<sub>2</sub> (with CO preadsorbed) for the five structures (a)–(e) of Au<sub>2</sub>CO<sub>3</sub><sup>−</sup>, shown in Figure 17.2C.

Structure	$\Delta E$ (eV)	VDE (eV)	BE(CO) (eV)	BE(O <sub>2</sub> ) (eV)
(a)	2.80	2.82	0.93	1.34
(b)	2.94	3.32	0.78	1.20
(c)	2.82	3.82	0.91	1.32
(d)	0	4.67	3.72	4.14
(e)	1.04	3.38	2.69	3.10

Further details of the reaction mechanism were obtained by complementary theoretical simulations [35] revealing that the bonding of O<sub>2</sub> to Au<sub>2</sub><sup>−</sup> is characterized by partial electron transfer (0.4 e) from the metal cluster to the antibonding  $\pi$ -orbital of the oxygen molecule, making the oxygen molecule a superoxo-like species. The binding energy is 1.39 eV. The molecular adsorption is clearly favored energetically over dissociative adsorption. In agreement with the experimental findings, the molecular binding is a non-activated process, i.e. a barrierless reaction channel exists for the approaching oxygen molecule, leading to the described configuration. The binding energy of CO to Au<sub>2</sub><sup>−</sup> is 0.91 eV. The stronger binding of O<sub>2</sub> to Au<sub>2</sub><sup>−</sup> explains the observation that high CO partial pressures are required before CO adsorption can compete with O<sub>2</sub> adsorption as the first reaction step.

Five structures corresponding to the mass of the complex Au<sub>2</sub>(CO)O<sub>2</sub><sup>−</sup> predicted theoretically, and the pertinent structural and energetic information are given in Figure 17.2C and Table 17.1. Structures (a) and (b) correspond to molecular co-adsorption of CO and O<sub>2</sub> to Au<sub>2</sub><sup>−</sup>. From the two molecularly co-adsorbed species, CO can readily (without barrier) bind to the end of the Au–Au axis (structure (a)) whereas a barrier of 0.2 eV was found for CO association from the gas phase to the Au–Au bridging site of structure (b). The barrier for forming (b) from (a) via diffusion of CO from the end of the complex to the Au–Au bridge is high, of the order of 0.9 eV. In both structures (a) and (b) the O–O bond is activated to a value typical of a superoxo-species (about 1.35 Å). Structure (c) is close to the stability of structure (a). It contains a reacted O–O–C–O group bound to the Au<sub>2</sub> axis via the carbon atom. The O–O bond is activated to a superoxo-state, and this species bears some resemblance to the gold-peroxyformate complex identified in the early experiments on gold atoms in cryogenic CO/O<sub>2</sub> matrices [41]. The formation of this species was investigated via two routes: (i) a Langmuir–Hinshelwood (LH) mechanism that involves diffusion of CO from the bridging position in structure (b), (ii) an Eley–Rideal (ER) mechanism where CO(g) approaches the preformed Au<sub>2</sub>O<sub>2</sub><sup>−</sup>. The LH mechanism has a high activation barrier of 1.1 eV, and since the barrier is of the order of the activation energy for CO desorption from structure (b) (1 eV), formation of (c) from (b) is unlikely. Interestingly, mechanism (ii) does not involve an activation barrier.

By far the most stable structures corresponding to the mass of Au<sub>2</sub>(CO)O<sub>2</sub><sup>−</sup> are

the two carbonate species (d) and (e). Structure (e) requires a preformed  $\text{Au}_2\text{O}_2^-$  where the molecular axes of  $\text{Au}_2$  and  $\text{O}_2$  lie parallel to each other. Since this structure of  $\text{Au}_2\text{O}_2^-$  is 1 eV less stable than the ground state discussed above (the binding energy of oxygen in this configuration is 0.39 eV vs. the optimal binding energy of 1.39 eV) it is unlikely to be formed and consequently structure (e) does not play a relevant role in the catalytic cycle. On the other hand, formation of the most stable structure (d) by an ER mechanism with  $\text{CO(g)}$  inserting in the middle of the O–O bond in  $\text{Au}_2\text{O}_2^-$  has a barrier of only 0.3 eV, which is easily overcome under the experimental conditions. The absence of the complex  $\text{Au}_2\text{C}_2\text{O}_4^-$  in the experimental mass spectrum, as well as the calculated high barriers for CO diffusion along the Au–Au axis justify the considerations of only ER mechanisms for the final reaction step Eq. (2c). It is also worth noting that further intermediates such as  $\text{Au}_2\text{O}^-$  and  $\text{Au}_2\text{CO}_2^-$  are not observed experimentally. This leads to only two possible scenarios for the final reaction step (2c): ER reactions of  $\text{CO(g)}$  with structures (c) or (d), and the reaction proceeds to completion releasing two  $\text{CO}_2$  molecules. The formation of  $\text{CO}_2$  from the reaction between  $\text{CO(g)}$  and structure (c) (Figure 17.2C) involves a low barrier of 0.3 eV, resulting in the formation of a metastable  $\text{Au}_2\text{CO}_2^-$  complex, where  $\text{CO}_2$  is bound to  $\text{Au}_2$  via the carbon atom. However, the large heat of reaction (4.75 eV) from the formation of the first  $\text{CO}_2$  molecule is much more than that needed to overcome the binding energy (0.52 eV) of the remaining  $\text{CO}_2$  to  $\text{Au}_2^-$ , readily facilitating its desorption from the metal cluster. The second scenario involves two branches [35]. First, thermal dissociation of  $\text{CO}_2$  from the carbonate (d) is endothermic by 1.12 eV but produces highly reactive  $\text{Au}_2\text{O}^-$  which reacts without barrier with  $\text{CO(g)}$  to produce  $\text{CO}_2$ . Second, ER reaction of  $\text{CO(g)}$  with (d) to produce  $\text{CO}_2$  involves a modest barrier of 0.5 eV but readily releases two  $\text{CO}_2$  molecules since the remaining  $\text{Au}_2\text{CO}_2^-$  configuration, where  $\text{CO}_2$  is bound to  $\text{Au}_2$  via one of the oxygen atoms, is unstable. This is the more likely branch to occur in the experiments (100–300 K) described above. Thus, these studies showed that both experimental and theoretical results prove the existence of the full catalytic cycle.

In another example [42, 43] it was demonstrated that gas-phase platinum cluster anions,  $\text{Pt}_n^-$  ( $n = 3-7$ ) efficiently catalyze the oxidation of CO to  $\text{CO}_2$  in the presence of  $\text{N}_2\text{O}$  or  $\text{O}_2$  near room temperature in a full thermal catalytic reaction cycle. At the end of the process the intact cluster is regenerated and each step is exothermic and occurs rapidly at thermal energies. In these experiments the  $\text{Pt}_n^-$  clusters produced are first thermalized by collisions with a buffer gas. When either  $\text{O}_2$  or  $\text{N}_2\text{O}$  is introduced downstream in the flow tube,  $\text{Pt}_n\text{O}^-$  and  $\text{Pt}_n\text{O}_2^-$  ions are formed in rapid exothermic reactions [44]. With the introduction of CO into the gas cell the  $\text{Pt}_n^-$  clusters reappear, as observed with mass spectrometry. From these experiments it was concluded that neutral  $\text{CO}_2$  is stoichiometrically formed on the clusters according to the scheme in Figure 17.3a and that negligible fragmentation occurs for the metal cluster with  $n \geq 4$ . Further experiments revealed that, at low energies, the cross-section approaches the calculated collision limit, meaning that the reactions are quite efficient. When  $\text{Pt}_n\text{O}_2^-$  ions are selected initially, sequential loss of oxygen atoms is observed, forming two  $\text{CO}_2$  products, as

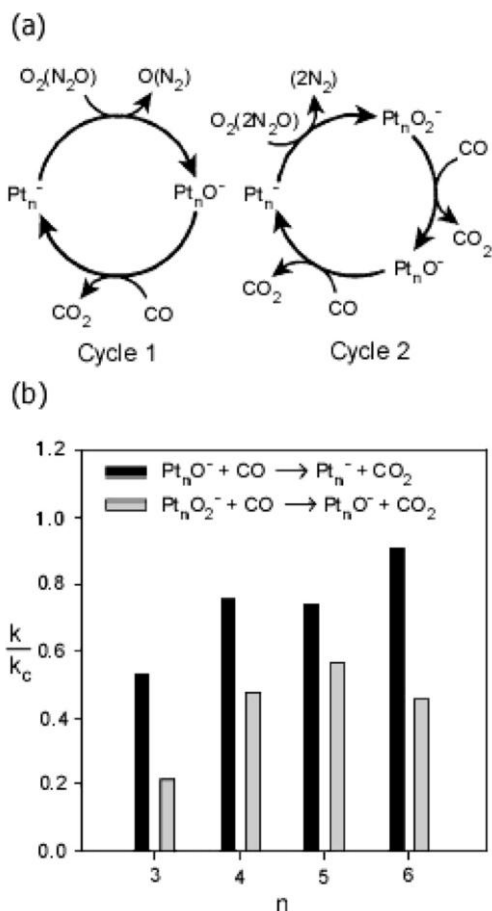


**Fig. 17.3.** (a) Catalytic cycles observed for the oxidation of CO to  $\text{CO}_2$  by  $\text{N}_2\text{O}$  or  $\text{O}_2$  using gas-phase platinum cluster anions as the model catalysts. (b) Relative reaction efficiencies for the conversion of CO to  $\text{CO}_2$  by  $\text{Pt}_n\text{O}_m^-$  clusters of various compositions.

shown by CO pressure dependence studies. This observation implies that  $\text{O}_2$  is dissociatively adsorbed on the metal cluster as oxygen atoms, rather than chemisorbed or physisorbed as molecular  $\text{O}_2$ . Two other observations support this conclusion. (1)  $\text{Pt}_n\text{O}_2^-$  ions produced by reaction of the bare cluster with either  $\text{O}_2$  or  $\text{N}_2\text{O}$  show the same reactivity; (2) collision-induced dissociation of  $\text{Pt}_n\text{O}_2^-$  shows loss of oxygen atoms with no  $\text{O}_2$  loss. The regeneration of  $\text{Pt}_n^-$  ions at low energies proves that a full catalytic oxidation cycle can be completed at near room temperature, in either a single-step or a two-step process. Figure 17.3b shows the measured reaction efficiencies for the oxidation of the first CO molecule by  $\text{Pt}_n\text{O}^-$  or  $\text{Pt}_n\text{O}_2^-$  ( $n = 3-6$ ). The reaction efficiencies for a single collision are greater than

40% for  $n \geq 4$ ; so only a few collisions would be required for complete conversion. From this it was concluded that at near room temperatures the gas-phase metal cluster anions are better catalysts than the supported catalysts used in current technology for automotive catalytic converters. These need to be heated to high temperatures: on platinum surfaces, temperatures of 400–500 K are typically required for oxidation of CO [45].

Both examples revealed unique and size-dependent catalytic properties of very small metal clusters. As mentioned in the introduction, gas phase clusters will probably never be important in real catalysis, however, such small clusters can be stabilized on support materials so they may become relevant for future applications.

### 17.3.2

#### Chemical Reactions and Catalytic Cycles on Supported Clusters

##### 17.3.2.1 Single Atoms on Oxide Surfaces

F centers can act as nanocatalysts, however few reactions are catalyzed by oxygen vacancies because only two confined electrons at the same energy level are present. In order to change these two parameters (number of confined electrons and energy levels) without modifying the size of the quantum box, the F center can be decorated with metal atoms to produce a third kind of nanocatalyst: supported atoms on oxide surfaces.

The metal atoms are produced by a recently developed high-frequency laser evaporation source [15]. The positively charged ions are guided by home-built ion optics through differentially pumped vacuum chambers and are size-selected by a quadrupole mass spectrometer (Extrel Merlin System; mass limits: 1000, 4000, 9000 u). In these experiments it is important to deposit only 0.5–0.8% of a monolayer of atoms ( $1 \text{ ML} = 2.25 \times 10^{15} \text{ clusters cm}^{-2}$ ) at 90 K with low kinetic energy in order to land them isolated on the surface and to prevent agglomeration on the defect-rich MgO films. The presence of isolated atoms is confirmed experimentally and theoretically. Experimentally, nickel atoms, dimers and trimers are used as it is well known that they form stable metal carbonyls. This carbonyl formation of small deposited  $\text{Ni}_n$  ( $n = 1-3$ ) was studied by exposing the deposited clusters to carbon monoxide. Mass spectrometry experiments showed that the nuclearity of the formed  $\text{Ni}_n$  carbonyls ( $n = 1-3$ ) is not changed. The absence of, for example,  $\text{Ni}_2(\text{CO})_x$  and  $\text{Ni}_3(\text{CO})_x$  after deposition of Ni atoms directly excludes agglomeration, whereas the absence of  $\text{Ni}(\text{CO})_4$  after depositing  $\text{Ni}_2$  excludes fragmentation of the cluster, relevant for the experiments described in the next section [46]. Second, Monte Carlo simulations revealed that under such experimental conditions, e.g. cluster flux ( $\sim 10^9 \text{ cm}^{-1}$ ), cluster density ( $\sim 10^{13} \text{ cm}^{-1}$ ), and defect density ( $\sim 5 \cdot 10^{13} \text{ cm}^{-1}$ ) on the MgO(100) films less than 10% of the atoms coalesce when migrating to the trapping centers [47].

To characterize the model catalysts in detail it is, however, necessary to identify the adsorption sites of the clusters. One possibility is to study the adsorption of probe molecules on the deposited clusters by means of thermal desorption (TDS)

and Fourier transform infrared (FTIR) spectroscopies. As an example [48], CO desorbs from the adsorbed Pd atoms at a temperature of about 250 K, which corresponds to a binding energy,  $E_b$ , of about  $0.7 \pm 0.1$  eV. FTIR spectra suggest that at saturation two different sites for CO adsorption exist on a single Pd atom. The vibrational frequency of the most stable, singly adsorbed CO molecule is  $2055 \text{ cm}^{-1}$ . Density functional cluster model calculations have been used to model possible defect sites at the MgO surface where the Pd atoms are likely to be adsorbed. CO/Pd complexes located at regular or low-coordinated O anions of the surface exhibit considerably stronger binding energies,  $E_b = 2\text{--}2.5$  eV, and larger vibrational shifts than were observed in the experiment. CO/Pd complexes located at oxygen vacancies (F or  $F^+$  centers) are characterized by much smaller binding energies,  $E_b = 0.5 \pm 0.2$  or  $0.7 \pm 0.2$  eV, which are in agreement with the experimental value. Such comparisons therefore identify adsorption sites of the clusters on the MgO surface, particularly in the examples shown below these trapping centers are shown to be oxygen vacancies.

After characterizing this type of nanocatalyst consisting of metal atoms trapped on oxygen vacancies, simple reactions like acetylene polymerization or CO oxidation can be studied by means of temperature programmed reaction studies and infrared spectroscopy.

For the cyclotrimerization on Ag, Pd and Rh atoms and the CO oxidation on Pd atoms the nanocatalysts were exposed at 90 K, using a calibrated molecular beam doser, to about 1 Langmuir (L) of acetylene or 1 L of  $^{18}\text{O}_2$  and  $^{13}\text{CO}$ , respectively. In a temperature programmed reaction (TPR) study, catalytically formed benzene ( $\text{C}_6\text{H}_6$ ), butadiene ( $\text{C}_4\text{H}_6$ ) and butene ( $\text{C}_4\text{H}_8$ ) or  $^{13}\text{C}^{18}\text{O}^{16}\text{O}$  molecules were detected by a mass spectrometer and monitored as a function of temperature. It is interesting to note that the reactants ( $^{13}\text{CO}$ ,  $^{18}\text{O}_2$ ,  $\text{C}_2\text{H}_2$ ) are only physisorbed on the MgO and desorb at temperatures lower than 150 K in all three cases, e.g. before the reaction takes place. In addition, the interactions of the product molecules with the model catalysts are weak, as described in [48, 49]. The thermal stabilities of the deposited Pd and Rh atoms were investigated by using Fourier transform infrared spectroscopy and the probe molecule, CO. It was found that Pd starts to migrate at around 300 K [48], whereas Rh is stable up to 450 K [50].

Surprisingly, and in contrast to single crystal studies [51], a single Pd atom already catalyzes the cyclotrimerization reaction and the benzene molecule ( $\text{C}_6\text{H}_6$ ) desorbs at 300 K (Figure 17.4a). No other product molecules of the polymerization reaction (e.g.  $\text{C}_4\text{H}_6$ ,  $\text{C}_4\text{H}_8$ ) are observed. Thus this model catalyst is highly selective for the polymerization reaction. We note that on a clean MgO(100) surface no products are formed (Figure 17.4a). This surprising result can be rationalized by studying theoretically a Pd atom adsorbed on different MgO sites represented by a cluster of ions embedded in an array of point charges. First a Pd atom was adsorbed on a five-coordinated oxygen ion on the MgO(001) terrace,  $\text{O}_{5c}$ , the binding energy is about 1 eV. It was found that indeed the  $\text{Pd}(\text{C}_4\text{H}_4)$  complex is formed but the third acetylene molecule is not bound to the complex and therefore this configuration is catalytically inactive. Other bonding sites for the adsorption of Pd atoms are considered. On four-coordinated step or three-coordinated corner oxygen

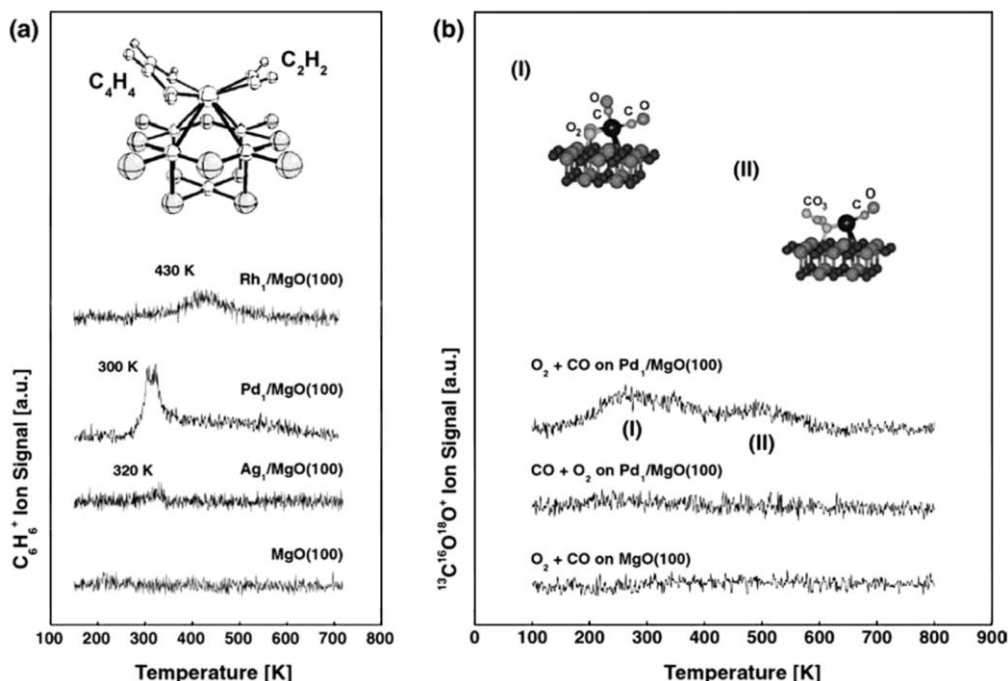


**Fig. 17.4.** (a) Temperature programmed reaction spectra of  $C_6H_6$  formed on Ag, Pd, and Rh atoms deposited on defect-rich MgO thin films grown on Mo(100) surfaces. As comparison the same experiment was performed on a clean defect-rich MgO film. The calculated transition state of the cyclo-trimerization reaction on Pd atoms adsorbed

on an F center of the MgO(100) surface is also shown. (b) TPR spectra of  $CO_2$  from a defect-rich MgO thin film and deposited Pd atoms after exposure to  $O_2$  and CO (lower and upper spectrum) as well as from deposited Pd atoms after exposure to CO and  $O_2$ . Calculated transition states of the two observed mechanisms (I) and (II) are also depicted.

sites,  $O_{4c}$  and  $O_{3c}$ , respectively, the Pd atom binds slightly more strongly with an energy of 1.2–1.5 eV, in addition, the atom is more reactive. However, on both  $O_{3c}$  and  $O_{4c}$  sites the third  $C_2H_2$  molecule is only weakly bound or even not bound to the  $Pd(C_4H_4)$  surface complex, with the binding energy less than the activation energy of the formation of  $C_6H_6$ . Thus, Pd atoms adsorbed on  $O_{nc}$  sites cannot explain the observed activity. This is consistent with the results of the study on the adsorption properties of CO on  $Pd_1/MgO$  [48], where the experimental results were rationalized in terms of Pd atoms, which are stabilized on oxygen vacancies (F centers) in neutral or charged states, F or  $F^+$ , respectively. The interaction of a Pd atom with the F center is much stronger, 3.4 eV, which makes these centers good candidates for Pd binding. On  $F^+$  centers binding energies of about 2 eV have been computed [48]. The presence of trapped electrons at the defect site results in a more efficient activation of the supported Pd atom. In fact, the complex  $(C_4H_4)(C_2H_2)/Pd_1/F_{5c}$ , Figure 17.4a, shows a large distortion and a strong inter-



action of the third  $C_2H_2$  molecule. These results indicate that F and  $F^+$  centers can act as basic sites on the MgO surface and turn the inactive Pd atom into an active catalyst. Notice that the supported Pd atoms on defect sites not only activate the cyclization reaction, but also favor benzene desorption, as shown by the very small  $(C_6H_6)/Pd_1/F_{5c}$  adsorption energy. The complete reaction path for this specific nanocatalyst has been calculated [52]. The first barrier of the reaction path is that for the formation of the intermediate  $Pd(C_4H_4)$  and is only 0.48 eV. The formation of the  $C_4H_4$  intermediate is thermodynamically favorable by 0.82 eV. On  $(C_4H_4)/Pd_1/F_{5c}$  the addition of the third acetylene molecule is exothermic by 1.17 eV, leading to a very stable  $(C_4H_4)(C_2H_2)/Pd_1/F_{5c}$  intermediate (Figure 17.4a). To transform this intermediate into benzene one has to overcome a barrier of 0.98 eV. The corresponding energy gain is very large, 3.99 eV, and mainly related to the aromaticity of the benzene ring. Once formed,  $C_6H_6$  is so weakly bound to the supported Pd atom that it immediately desorbs. Thus, the reaction on  $Pd/F_{5c}$  is rate limited in the last step, the conversion of  $(C_4H_4)(C_2H_2)$  into  $C_6H_6$ . This is different from the Pd(111) surface where the rate determining step for the reaction is benzene desorption. The calculations are consistent with the experimental data. In fact, on  $Pd_1/F_{5c}$  the computed barrier of 0.98 eV corresponds to a desorption temperature of about 300 K, as observed experimentally, Figure 17.4a. On Pd(111) surfaces, the bonding of benzene is estimated to be  $\approx 1.9$  eV. This binding is consistent with a desorption temperature of 500 K as observed for a low coverage of  $C_6H_6$  on Pd(111) [53].

The electronic structure of palladium atoms,  $4d^{10}5s^0$ , is unique and may be responsible for this specific catalytic property for the acetylene cyclotrimerization. This raises the question as to whether other transition metal atoms are also reactive for this reaction. Results are shown for deposited Rh ( $4d^85s^1$ ) and Ag ( $4d^{10}5s^1$ ) atoms. Ag atoms are almost unreactive (Figure 17.4a), on supported Rh atoms, however, benzene is formed and desorbs at around 430 K (Figure 17.4a).

For CO oxidation, it was first verified that the clean MgO(100) thin films are inert; e.g., no  $^{13}C^{16}O^8O$  was formed in a one-heating-cycle experiment after adsorbing  $^{18}O_2$  and  $^{13}C^{16}O$  (Figure 17.4b) or vice versa [54]. When Pd atoms are trapped on the  $F_{5c}$ s, preadsorption of oxygen and subsequent saturation of CO leads to the formation of carbon dioxide, with desorption peaks at 260 K and around 500 K (Figure 17.4b). The existence of two desorption peaks in the TPR spectrum (Figure 17.4b) suggests the presence of two different reaction mechanisms. Note that preadsorption of  $^{13}CO$  suppresses the catalytic process as it poisons the nanocatalyst (Figure 17.4b). Ab initio calculations showed that a single Pd atom binds strongly to the oxygen vacancy (binding energy of 3.31 eV), with a small amount of charge (0.15 e) transferred to the adsorbed atom. In comparison, the binding energy of Pd atoms to terrace oxygen sites is only 1.16 eV. The enhanced binding to the  $F_{5c}$  is also reflected in the corresponding bonding lengths of 1.65 and 2.17 Å for  $MgO(F_{5c})-Pd$  and  $MgO-Pd$ , respectively. Binding of two CO molecules saturates the  $MgO(F_{5c})-Pd$  system; occupying the  $MgO(F_{5c})-Pd$  system with three CO molecules leads to spontaneous (barrierless) desorption of one of the molecules. In the most stable configuration the two CO molecules are not

equivalent; one CO binds on top and the second adsorbs on the side of the Pd atom (this top-side geometry is similar to that shown in Figure 17.4bI but without the O<sub>2</sub>), and the total binding energy of the two CO molecules is 1.62 eV. To study the oxidation mechanisms of CO on MgO(F<sub>5c</sub>)–Pd the system was optimized first with coadsorbed O<sub>2</sub> and two CO molecules. Two stable geometric arrangements were found, with the most stable one shown in Figure 17.4bI where the CO molecules bind in a top-side configuration and the O<sub>2</sub> is adsorbed parallel to the surface on the other side of the Pd atom. The adsorbed O<sub>2</sub> molecular bond is stretched and activated (1.46 Å compared to the calculated gas-phase value of 1.25 Å). In addition, a stable carbonate complex Pd(CO<sub>3</sub>)(CO) was found (Figure 17.4bII), whose binding energy is 4.08 eV larger than the aforementioned Pd(CO)<sub>2</sub>(O<sub>2</sub>) complex. These complexes were identified by comparison of calculated and spectroscopically measured CO vibrational frequencies [55]. Two reaction mechanisms are proposed corresponding to the two CO<sub>2</sub> peaks observed experimentally (Figure 17.4b). At low temperatures the two relevant precursors are shown in Figures 17.4bI and 17.4bII. Corresponding to the CO<sub>2</sub> desorption peak at 260 K, the following reaction mechanism is proposed. In a competitive process, CO desorbs or is oxidized upon heating. The theoretically estimated activation energies of the two processes are 0.89 eV for desorption and 0.84 eV for oxidation. Formation of CO<sub>2</sub> at higher temperatures (corresponding to desorption at around 500 K, Figure 17.4b) involves decomposition of the Pd(CO<sub>3</sub>)(CO) carbonate complex (Figure 17.4bII). This mechanism is observed in molecular dynamics simulations where the temperature is controlled to 500 K by Langevin dynamics.

### 17.3.2.2 Size-Selected Clusters on Oxide Surfaces

By decorating F centres with atoms, it is possible to increase the number of confined electrons whilst modifying the size of the quantum box only slightly. By using size-selected clusters instead of atoms, the confinement of the valence electrons is subtler and the examples presented below reveal the possibility for tuning the efficiency and selectivity of chemical reactions atom by atom by simply changing cluster size or doping the cluster with impurity atoms. Furthermore, a comparison of the experimental results with first-principles theoretical simulations provides insights into the physical factors and microscopic mechanisms that govern nanocatalysis.

The metal clusters are produced by the same high-frequency laser evaporation source used to produce metal atoms. In this source a cold He pulse (40 K) thermalizes the laser-produced plasma [15]. Subsequent supersonic expansion of the helium–metal vapor leads to cold clusters with a narrow kinetic energy distribution ( $E_{\text{kin}} \leq 0.2 \text{ eV atom}^{-1}$ ). The positively charged clusters guided by ion optics through differentially pumped vacuum chambers and size-selected by a quadrupole mass spectrometer (Extrel Merlin System; mass limit: 1000, 4000, 9000 u) are then deposited with low kinetic energy ( $<0.2 \text{ eV atom}^{-1}$ ) onto MgO/Mo(100) thin films, under these conditions the clusters ‘softland’ on the substrate. In fact, when exploring chemical or catalytic properties of nanoassembled materials consisting of small monodispersed clusters on surfaces the key challenge is to preserve the

identity of the cluster upon deposition. Upon impact a redistribution of the total energy of the cluster takes place. In the deposition process this energy consists of the cluster's kinetic and internal energy, the binding energy between cluster and substrate and an eventual Coulomb energy between the cluster ion and an induced image charge (metal) or surface charge density (dielectric) on the support. The amount of this energy is decisive for the degree of melting, disordering, fragmentation, implantation or rebounding of the cluster. The cluster-surface and Coulomb interactions are given intrinsically by the chosen cluster and support materials, whereas the internal and kinetic energies can be changed to a large extent by the experimental conditions. 'Softlanding' is defined as a collision outcome allowing plastic deformation of the cluster but not fragmentation and implantation into the substrate [56]. Molecular dynamic studies [57–59] have shown that cluster implantation occurs at about  $1 \text{ eV atom}^{-1}$  kinetic energy of the cluster, regardless of the cluster-substrate system. Consequently, this value represents the upper kinetic energy limit for softlanding conditions. Softlanding of size-selected  $\text{Si}_{30}$  and  $\text{Si}_{39}$  clusters on  $\text{Ag}(111)$  was observed in recent low-temperature STM experiments performed at kinetic energy well below the softlanding limit and without rare buffer layers, i.e. under the same experimental conditions as the experiments shown below [60]. Finally, to prepare cluster-assembled nanocatalysts, less than 0.5% of a ML of size-selected clusters ( $1 \text{ ML} = 2 \times 10^{15} \text{ clusters cm}^{-2}$ ) are deposited at 90 K, in order to land them isolated on the surface and to prevent agglomeration of the cluster on the surface. Under these experimental conditions, the landing and the migration and trapping of the clusters on the surface was investigated with Monte Carlo simulations [47]. These simple calculations show that the preparation of samples with monodispersed clusters is possible only when a small number of clusters is deposited. In order to prepare clusters on identical adsorption sites it is therefore essential to use support materials with low defect densities for systems with a strong cluster-support interaction or use surfaces with high defect densities when the cluster-support interaction is weak. The deposition of the clusters on defects is additionally favored by the recently discovered "funnel" effect [10]; ab initio calculations revealed that clusters are attracted, e.g. by F centers, well before landing on the surface.

**Changing catalytic efficiency atom-by-atom: oxidation of carbon monoxide on pure and strontium-doped gold nanocatalysts** In the first example we focus on gold nanocatalysts, which led recently to most remarkable and rather surprising findings. More specifically, low adsorption energies and high activation barriers for dissociation of small molecules on extended gold surfaces are responsible for the nobleness of gold as a bulk material [61]. Nanosize particles of gold, however, show high and rather unusual catalytic reactivity [62, 63]. While the novel heterogeneous catalysis by nanosize gold aggregates supported on oxides is of great significance, the processes underlying the catalytic activity of gold in reduced dimensions and the reaction mechanisms are not yet understood and still represent an enigma in catalysis. In the following these issues are addressed theoretically and experimentally through investigations of the low temperature combustion of CO on size-

selected gold clusters,  $\text{Au}_n$  ( $n \leq 20$ ), and strontium-doped gold clusters,  $\text{SrAu}_n$  ( $n \leq 20$ ), supported on defect-poor and defect-rich  $\text{MgO}(100)$  films [6, 14].

Subsequent to verification that oxidation of CO does not occur on bare MgO substrate films (with and without defects), the catalyzed combustion of CO by nanosize gold and strontium-doped gold clusters adsorbed on the two different MgO films was studied by temperature programmed reaction (TPR) experiments. Isotopically labeled  $^{18}\text{O}_2$  and  $^{13}\text{CO}$  were used to disentangle the  $\text{CO}_2$  production on the cluster from an eventual catalytic oxidation of CO involving oxygen atoms from the MgO substrate. Indeed, the  $^{13}\text{CO}$  molecule is exclusively oxidized by  $^{18}\text{O}_2$  since only the  $^{13}\text{C}^{16}\text{O}^{18}\text{O}$  isotopomer is detected. Furthermore, the experiments revealed that the pure gold clusters up to the heptamer are inert for the oxidation of CO and that the low temperature ( $T < 250$  K) combustion of CO is most effective for  $\text{Au}_8$ . By doping gold clusters with strontium the number of gold atoms in the smallest catalytically active cluster size is reduced to just three. In addition, these results revealed that, e.g.  $\text{Au}_8$ , the smallest active cluster size, becomes inert when it is deposited it on defect-poor films. This indicates that substrate defects are important when trying to understand the factors, which govern the chemical properties of nanoscale, supported clusters (Figure 17.5A).

Let us first turn our attention to the reaction mechanism and role of defect sites in the case of  $\text{Au}_8$ . When first deposited on  $\text{MgO}(100)$  films with a vanishing number of F centers the catalytic activity observed experimentally during one heating cycle reveals a very small combustion of CO at temperatures between 150 and 250 K (Figure 17.5A-d). Surprisingly, the CO combustion on  $\text{Au}_8$  at 250 K increases dramatically when depositing the octamer on defect-rich MgO-films (Figure 17.5A-e). This particular behavior pertains even after several reaction cycles up to temperatures of 350 K. It indicates that the model catalyst is thermally stable and the reaction heat of the combustion of CO does not change the cluster's structure, an important issue when using  $\text{Au}_8$  as a real catalyst. Evaluating the area of the TPR signal yields the production of about one  $\text{CO}_2$  molecule per  $\text{Au}_8$  cluster. To explore the energetics and reaction mechanisms underlying the above observations extensive ab initio simulations were performed [14, 64]. Figure 17.5B summarizes the energetics and atomic configurations of the initial, transition, and final states proposed for the combustion of CO at 140 K and 250 K catalyzed by  $\text{Au}_8$  clusters adsorbed on  $\text{MgO}(\text{F}_{5c})$ . Both  $\text{O}_2$  and CO adsorb on the  $\text{Au}_8$  cluster supported on the  $\text{MgO}(100)$  surface (with or without  $\text{F}_{5c}$  defects). However, the observed single sharply peaked stretching frequency of adsorbed CO with  $\nu_a = 2102$   $\text{cm}^{-1}$  compared to  $\nu_a = 2143$   $\text{cm}^{-1}$  for the free  $^{12}\text{C}^{16}\text{O}$  molecule, implies a single adsorption site on the cluster and a rather minor influence of adsorption on the internal structure and bonding of the molecule. Indeed, it is found that in the optimal adsorption configuration CO binds on-top of an Au atom of the upper triangular facet of the adsorbed  $\text{Au}_8$  cluster (see Figures 17.5B-d,f, initial state) with  $d(\text{CO}) = 1.14$  Å (compared to 1.13 Å in the free molecule) and  $d(\text{AuC}) = 1.92$  Å. On the other hand, an  $\text{O}_2$  molecule may readily adsorb at several sites, both on the upper Au<sub>3</sub> facet (Figure 17.5B-d) and at the interface between the adsorbed gold cluster and the underlying magnesia surface (Figure 17.5B-f). In all cases the ad-

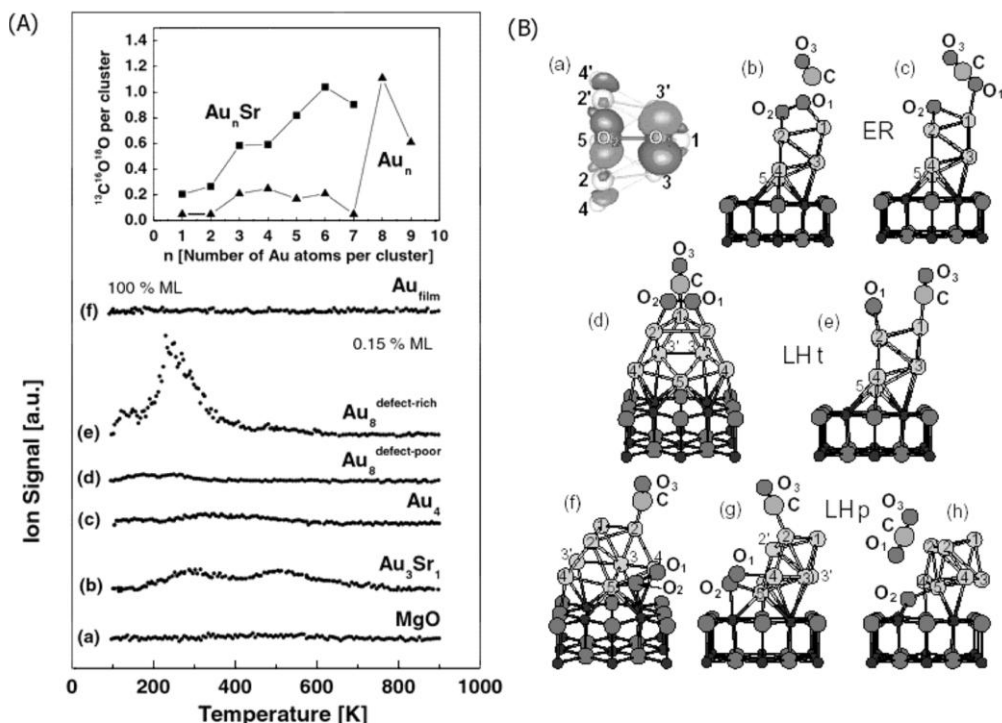


**Fig. 17.5.** (A) TPR spectra of  $\text{CO}_2$  from a defect-rich  $\text{MgO}$  thin film (a), various pure and mixed  $\text{Au}_n$  and  $\text{Au}_n\text{Sr}$  clusters (b)–(e) as well as from a thin  $\text{Au}$  film grown on a defect-rich  $\text{MgO}$  thin film (f). The reactivity expressed as the number of  $\text{CO}_2$  molecules formed per

cluster is shown for cluster sizes up to  $\text{Au}_9$ . (B) Calculated snapshots of three different reaction mechanisms (ER, LHt, LHp) for the oxidation of  $\text{CO}$  on  $\text{Au}_8$  adsorbed on an F center of a  $\text{MgO}(100)$  surface.

sorbed molecule is found to be activated to a peroxo  $\text{O}_2^*$  molecular state with a weakened highly stretched intramolecular bond length (1.41 Å–1.46 Å) compared to that in the free molecule (1.24 Å). The activation of the adsorbed oxygen molecule involves occupation of the antibonding  $\pi_{||}^*$  molecular orbital (i.e., the molecular oxygen  $\pi_g^*$  orbital oriented parallel to the adsorbing surface), which hybridizes with the orbitals of neighboring gold atoms of the partially negatively charged adsorbed gold cluster (Figure 17.6a).

The two reaction pathways, which may mainly contribute to the observed oxidation of  $\text{CO}$  are of the Langmuir–Hinshelwood (LH) type. For the formation of  $\text{CO}_2$  at 140 K the two reactants are initially coadsorbed on the triangular top facet of the  $\text{Au}_8$  cluster, with the distance between the carbon atom and one of the peroxo oxygens in this local minimum state equal to 3.11 Å ( $d(\text{CO}_1)$  (Figure 17.5B-d; initial state); in the following this LH top-facet reaction mechanism is labeled LHt. Through mapping of the potential energy surface along the C– $\text{O}_1$  reaction coordinate (via total relaxation of the system with the variable C– $\text{O}_1$  distance as a con-

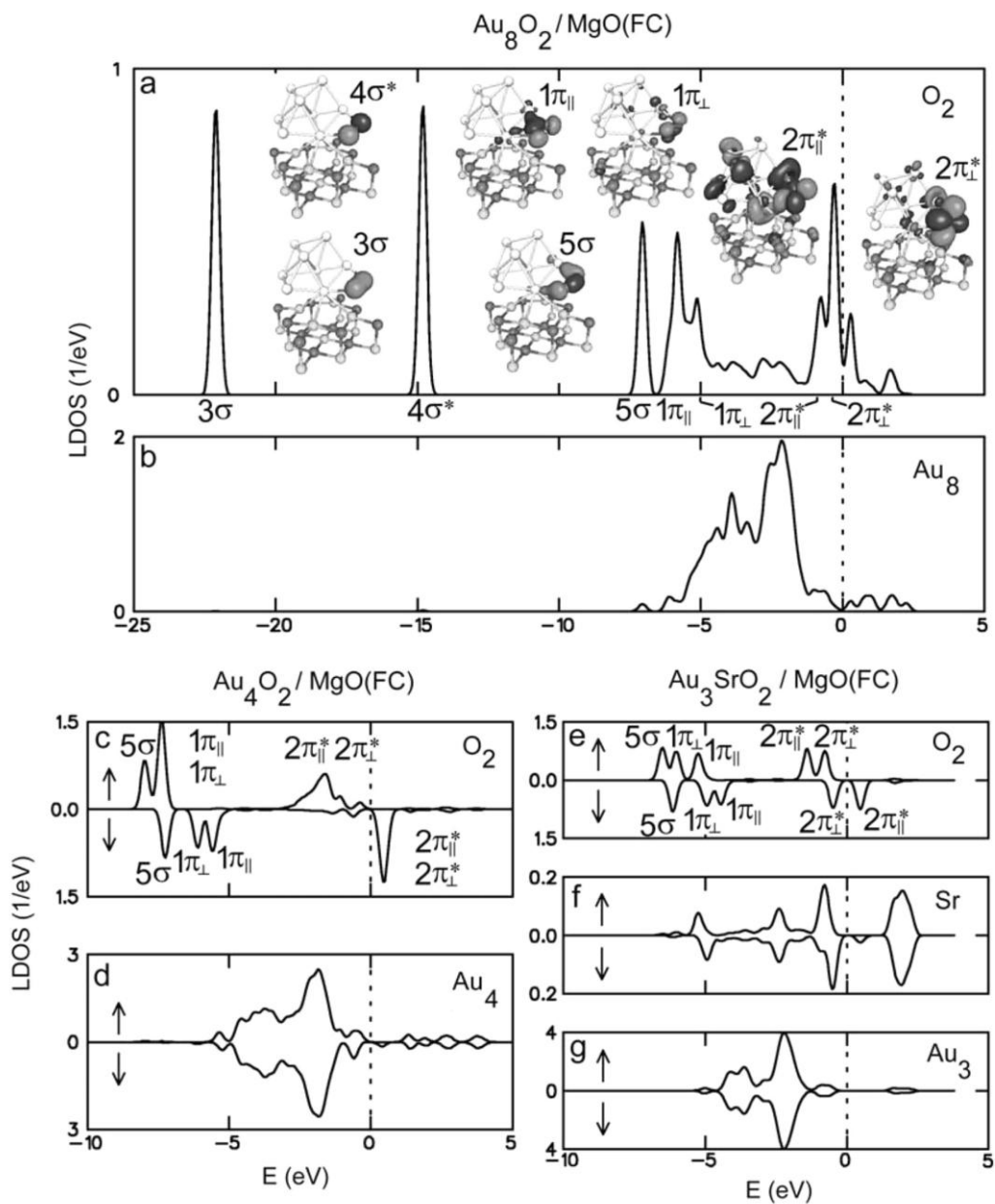


**Fig. 17.6.** Local density of states of spin-up and spin-down electronic states (LDOS) of the nanocatalysts  $\text{Au}_8$ ,  $\text{Au}_4$ , and  $\text{Au}_3\text{Sr}$  adsorbed on F centers of a  $\text{MgO}(100)$  surface projected on the oxygen (a), (c), (e) and on the metal part (b), (d), (f), (g).

straint) a rather low energy barrier  $\Delta E_b(\text{LHt}) = 0.1 \text{ eV}$  occurring at  $d(\text{CO}_1) \approx 2.0 \text{ \AA}$  is determined for the LHt oxidation channel with the end product of a weakly adsorbed carbon dioxide molecule ( $\sim 0.2 \text{ eV}$ ). The total exothermicity of the reaction  $\text{MgO}(\text{F}_{5c})/\text{Au}_8 + \text{O}_2(\text{g}) + \text{CO}(\text{g}) \rightarrow \text{MgO}(\text{F}_{5c})/\text{Au}_8\text{O} + \text{CO}_2(\text{a})$  is  $\sim 4.8 \text{ eV}$  and it is  $\sim 5 \text{ eV}$  when the  $\text{CO}_2$  product is desorbed, here (g) and (a) denote gas phase and adsorbed molecules, respectively. This LHt low-temperature oxidation mechanism was found by these studies (with similar energetics) for reactions on the gold cluster deposited on either a defect-free  $\text{MgO}(100)$  surface or one containing an  $\text{F}_{5c}$ , and both are expected to be relatively insensitive to the  $\text{Au}_n$  cluster size, correlating with the experimental results. As aforementioned, the higher temperature channel is strongly enhanced for  $\text{Au}_8$  supported on a defect-rich  $\text{MgO}(100)$  support (compare the  $\text{CO}_2$  signals at  $\sim 240 \text{ K}$  in Figures 17.5A-d,e). This trend correlates with the simulations of a LH-periphery (LHp) reaction mechanism, starting with the CO adsorbed on the top-facet of the  $\text{Au}_8$  cluster and the peroxo  $\text{O}_2^*$  molecule bonded to the periphery of the interfacial layer of the cluster (Figure 17.5B-f/g; initial state), where the distance between the C atom and the oxygen marked  $\text{O}_1$  is  $d(\text{CO}_1) = 4.49 \text{ \AA}$ ). Indeed, mapping of the potential energy surface along the C– $\text{O}_1$  reaction coordinate revealed, for  $\text{MgO}(\text{F}_{5c})/\text{Au}_8$ , a rather broad reaction barrier  $\Delta E_b(\text{LHp}) \sim 0.5 \text{ eV}$  at  $d(\text{CO}_1) \sim 2.0 \text{ \AA}$  (Figure 17.5B-g), while for the defect-free substrate a significantly higher barrier was found,  $\Delta E_b(\text{LHp}) \sim 0.8 \text{ eV}$ ; the reaction product is shown in Figure 17.5B-h for the  $\text{MgO}(\text{F}_{5c})/\text{Au}_8$  catalyst. Another reaction path was found theoretically, starting from the optimal configuration of  $\text{O}_2^*$  adsorbed on the  $\text{MgO}(\text{F}_{5c})/\text{Au}_8$  catalyst. A gas phase CO molecule brought to the vicinity of the peroxo molecule reacts spontaneously (without an energy barrier) forming a carbon dioxide molecule weakly bound to the catalyst. This Eley–Rideal (ER)-type reaction mechanism corresponds to a low temperature generation of (weakly adsorbed)  $\text{CO}_2$  through direct reaction of gaseous CO with a preadsorbed peroxo  $\text{O}_2^*$  molecule. This reaction channel can occur even at  $90 \text{ K}$ , i.e. during the initial dosing stage in the experiment.

The catalytic behavior can be further changed by cluster size and impurity doping. To understand the origin of this size-dependent and element-specific behavior the atomic structure and the electronic spectra of these model catalysts were studied by extensive first-principles simulations, and the optimized structures of  $\text{Au}_8$  (with two relevant isomers),  $\text{Au}_4$ , and  $\text{Au}_3\text{Sr}$  adsorbed on  $\text{MgO}(\text{F}_{5c})$  are shown in Figure 17.7, before (a to d) and after (e to h)  $\text{O}_2$  adsorption. As shown above these clusters bind to the  $\text{MgO}(\text{F}_{5c})$  surface quite strongly (calculated binding energy of  $2.65 \text{ eV}$  to  $4.06 \text{ eV}$ ), and their binding is significantly enhanced (typically by about  $2 \text{ eV}$ ) due to the F center defects. These high binding energies and the “anchoring” effect by the F centers correlate well with the observed thermal stability of the supported clusters in the TPR experiments. Another important finding pertains to the charge state of the adsorbed clusters: in particular, our calculations predict that the interaction with the surface is accompanied by charge transfer [14] of  $0.5 \text{ e}$ ,  $0.3 \text{ e}$ , and  $0.3 \text{ e}$  to the adsorbed  $\text{Au}_8$ ,  $\text{Au}_4$  and  $\text{Au}_3\text{Sr}$  clusters, respectively.

Binding and activation of molecular  $\text{O}_2$  by the model catalyst are necessary elementary steps in the CO oxidation process [65, 66], and thus understanding the



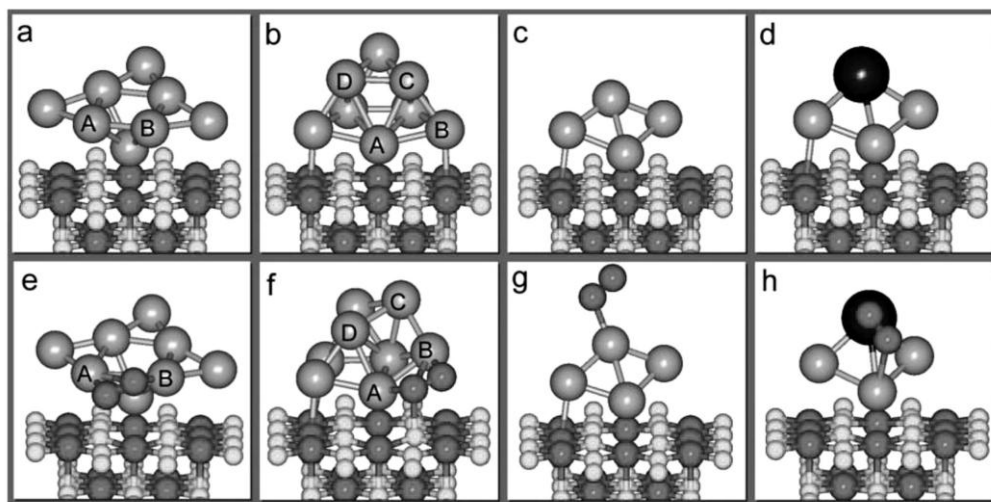


**Fig. 17.7.** The optimized atomic structures of nanocatalysts comprised of  $\text{Au}_8$  (a,b),  $\text{Au}_4$  (c),  $\text{Au}_3\text{Sr}$  (d) clusters adsorbed at an F center of a  $\text{MgO}(100)$ . For  $\text{Au}_8$  two relevant isomers, separated by an energy difference of 0.29 eV are shown. The optimal adsorption geometries of the  $\text{O}_2$  molecule to these nanocatalysts are shown in panels (e) to (h).

structural, dynamical, electronic and compositional factors that govern these processes is the key to elucidation of the observed size-dependent activity of the  $\text{Au}_n/\text{MgO}(\text{F}_{5c})$  model catalysts. Indeed, these first-principles simulations show that the binding energy of  $\text{O}_2$  to the supported  $\text{Au}_n$  clusters and the degree of O–O bond activation are strongly dependent on the cluster size (see below). In contrast, the adsorption energy of CO to the supported clusters is relatively insensitive to the cluster size, and it is higher than that of oxygen (0.7–1.0 eV per CO molecule, depending on coverage). Consequently, in the following the adsorption and activation of  $\text{O}_2$  by the supported gold nanoclusters is studied in more detail, to illustrate the aforementioned nanocatalytic factors that govern this key reaction step.

1. *Structural Dynamical Fluxionality:* The capability of small clusters to exhibit several structural forms (isomers) of comparable energies, and to interconvert between such isomers at finite temperature, is one of the hallmarks of cluster science. This unique structural variability may influence the chemical reactivity of nanocatalytic systems in two main ways. First, at finite temperature, the model catalyst (and in particular the cluster component) will form an equilibrium ensemble of coexisting structural configurations, with various isomers exhibiting different chemical reactivities. This is illustrated here via the two structural isomers of the  $\text{Au}_8$  cluster with the two-layered one (Figure 17.7b), which is thermodynamically less stable (by 0.29 eV) than the quasi-planar isomer (Figure 17.7a), showing a higher energy gain upon oxygen adsorption (0.47 eV compared to 0.28 eV for the latter isomer). Second, and most important, is the structural dynamic fluxionality of clusters in the course of reactions, that expresses itself in the ability



of a given structural isomer to dynamically adapt its structure so as to allow the reaction to evolve on the most favorable free-energy path. Such fluxional propensity is illustrated in Figures 17.7b and 17.7f where the more reactive two-layered  $\text{Au}_8$  cluster is shown to undergo a large structural transformation upon adsorption of molecular oxygen at the “periphery site”; i.e., the approximate bi-capped octahedral geometry (Figure 17.7b) is transformed to a bi-capped trigonal prism (Figure 17.7f). Note, that the structural fluxionality is essential for the reaction to occur, since it was found that constraining the cluster to maintain its original geometry (Figure 17.7b) prevents the adsorption and activation of  $\text{O}_2$ .

**2. Electronic Size Effects:** Understanding the size-dependent electronic structure of the  $\text{Au}_n/\text{MgO}(\text{F}_{5c})$  model catalysts, which is fundamental for elucidation of their atom-by-atom controlled reactivity, is facilitated by analysis of the spectra of the local density of electronic states (LDOS) projected on the oxygen molecule and on the metal cluster; a similar analysis is often employed in the context of the interaction of adsorbates with extended surfaces [67]. Figure 17.6a shows the LDOS projected on the  $\text{O}_2$  molecule which is adsorbed at the periphery site (Figure 17.5B-f) of the more reactive isomer of the  $\text{Au}_8/\text{MgO}(\text{F}_{5c})$  model catalyst. All the prominent peaks of the LDOS spectrum in Figure 17.6a can be unambiguously assigned to orbitals of (free) molecular oxygen origins. In addition, these states overlap with the entire d-band of the  $\text{Au}_8$  cluster (shown in Figure 17.6b) in the range  $-7 \text{ eV} \leq E \leq E_F$ , where  $E_F$  is the Fermi energy. Bonding of the oxygen molecule to the gold octamer involves mainly hybridization of the  $5\sigma$ ,  $1\pi_{||}$ , and  $1\pi_{\perp}$  oxygen states with the gold d-band (Figure 17.6b). Most importantly, the full spin-manifold of the antibonding  $2\pi^*$  states of  $\text{O}_2$  is located below  $E_F$ , resulting in strong activation of the  $\text{O}_2$  molecule through occupation of the antibonding orbitals. This leads to weakening of the O–O bond that is reflected in a significant increase in its length (1.43 Å in Figure 17.7f) compared to that of the free molecule (1.25 Å). Accompanying the activation process is a change in the spin state of the molecule from a triplet state in the gas phase to a peroxo-like adsorbed state with a zero net spin.

A drastically different scenario is found for the interaction of  $\text{O}_2$  with the smaller gold cluster,  $\text{Au}_4/\text{MgO}(\text{F}_{5c})$ , where molecular oxygen adsorbs in an “on-top” configuration, with one of the oxygen atoms binding to a single gold atom (Figure 17.7g). This system exhibits rather weak binding of the molecule to the metal cluster (0.18 eV), an almost unperturbed O–O bond length (1.28 Å), and a spin-splitting of the oxygen-projected LDOS spectrum (see Figure 17.6c). The weak binding is attributed to the narrower d-band of the adsorbed  $\text{Au}_4$  cluster compared to that of  $\text{Au}_8$  (see Figures 17.6b and 17.6d), with a consequent lack of overlap between the states at the bottom of the d-band of the gold cluster (Figure 17.6d) and the molecular oxygen states with energies  $E < -5 \text{ eV}$ . Moreover, the spin-down antibonding  $2\pi^*_{\perp}$  and  $2\pi^*_{||}$  orbitals of the adsorbed oxygen molecule are now located above  $E_F$  (unlike the case of the larger cluster, compare Figures 17.6c and 17.6a) which results in no activation of the molecule by the adsorbed  $\text{Au}_4$  cluster.

**3. Impurity-doping Effects:** Finally, we address the possibility of enhancing the

catalytic activity of a nanocluster by designed incorporation (doping) of an impurity, demonstrated here by the catalyzed oxidation of CO on  $\text{Au}_3\text{Sr}/\text{MgO}(\text{F}_{5c})$ . The LDOS spectra projected onto the oxygen molecule, the Sr atom, and the  $\text{Au}_3$  part of the metal cluster, are displayed in Figures 17.6e, 17.6f, and 17.6g, respectively. Doping by a single impurity atom changes significantly the bonding and activation of  $\text{O}_2$  compared to the pure gold tetramer,  $\text{Au}_4$ , case; the bonding of  $\text{O}_2$  is mainly to the strontium atom of the  $\text{Au}_3\text{Sr}$  cluster (Figure 17.7h), and it is characterized by a substantially higher adsorption energy (1.94 eV compared to 0.18 eV for the configuration shown in Figure 17.7g) and a significant activation of the O–O bond that is reflected in an increased bond length of 1.37 Å. This activation is due to occupation of the spin-down  $2\pi^*_{\perp}$  oxygen orbital (compare Figures 17.6e and 17.6c where, in the latter that corresponds to the pure cluster, this state contributes to the peak just above  $E_F$ ), resulting in a superoxo-like state of the adsorbate. Bonding of the oxygen molecule to  $\text{Au}_3\text{Sr}/\text{MgO}(\text{F}_{5c})$  occurs via resonances formed between the Sr states in the energy intervals 5–6 eV and 0–1 eV below  $E_F$ , with the spin-up  $1\pi_{\parallel}$  and  $2\pi^*_{\perp}$  states, as well as with the spin-down  $1\pi_{\perp}$  and  $2\pi^*_{\perp}$  orbitals, of the adsorbed activated  $\text{O}_2$ .

#### Changing catalytic selectivity atom-by-atom: polymerization of acetylene on palladium nanocatalysts

Another important factor in catalysis is the selectivity of a catalytic reaction. So far, however, information on the atom-by-atom evolution of this astonishing catalytic selectivity is still lacking. In this example we illustrate such a size-dependent selectivity with the polymerization of acetylene on palladium nanocatalysts [49]. This reaction over supported Pd particles reveals a direct correspondence between reactivities observed on model systems and the behavior of industrial catalysts under working conditions [68]. In ultra high vacuum (UHV) [69] as well as under high pressure, large palladium particles of typically thousands of atoms show an increased selectivity for the formation of benzene with increasing particle size [68]. In contrast, small palladium particles of typically hundreds of atoms are less selective for the cyclotrimerization and catalyze butadiene and butene as additional products [68].

The TPR spectra of the different products of the polymerization of acetylene on small supported, monodispersed palladium clusters are shown in Figure 17.8. Striking atom-by-atom size-dependent reactivities and selectivities are observed. Only the three reaction products  $\text{C}_6\text{H}_6$ ,  $\text{C}_4\text{H}_8$ , and  $\text{C}_4\text{H}_6$  are detected. Remarkably, no  $\text{C}_3\text{H}_n$ ,  $\text{C}_5\text{H}_n$  and  $\text{C}_8\text{H}_n$  are formed, indicating the absence of C–C bond scission, as already observed on Pd single crystals [70] and Pd particles [68]. Up to  $\text{Pd}_3$ , only benzene is catalyzed, reflecting a high selectivity for the cyclotrimerization of acetylene.  $\text{Pd}_n$  ( $4 \leq n \leq 6$ ) clusters reveal a second reaction channel by catalyzing in addition the formation of  $\text{C}_4\text{H}_6$ , which desorbs at around 300 K. The third reaction product,  $\text{C}_4\text{H}_8$ , desorbing at a rather low temperature of 200 K, is clearly observed for  $\text{Pd}_8$ . For this cluster size the abundance of the three reaction products is similar. For even larger clusters ( $13 \leq n \leq 30$ ) the formation of  $\text{C}_6\text{H}_6$  increases with cluster size, whereas the conversion of acetylene to  $\text{C}_4\text{H}_8$  reaches a maximum for  $\text{Pd}_{20}$ . Note that  $\text{Pd}_{30}$  selectively suppresses the formation of  $\text{C}_4\text{H}_6$ . (The peak in

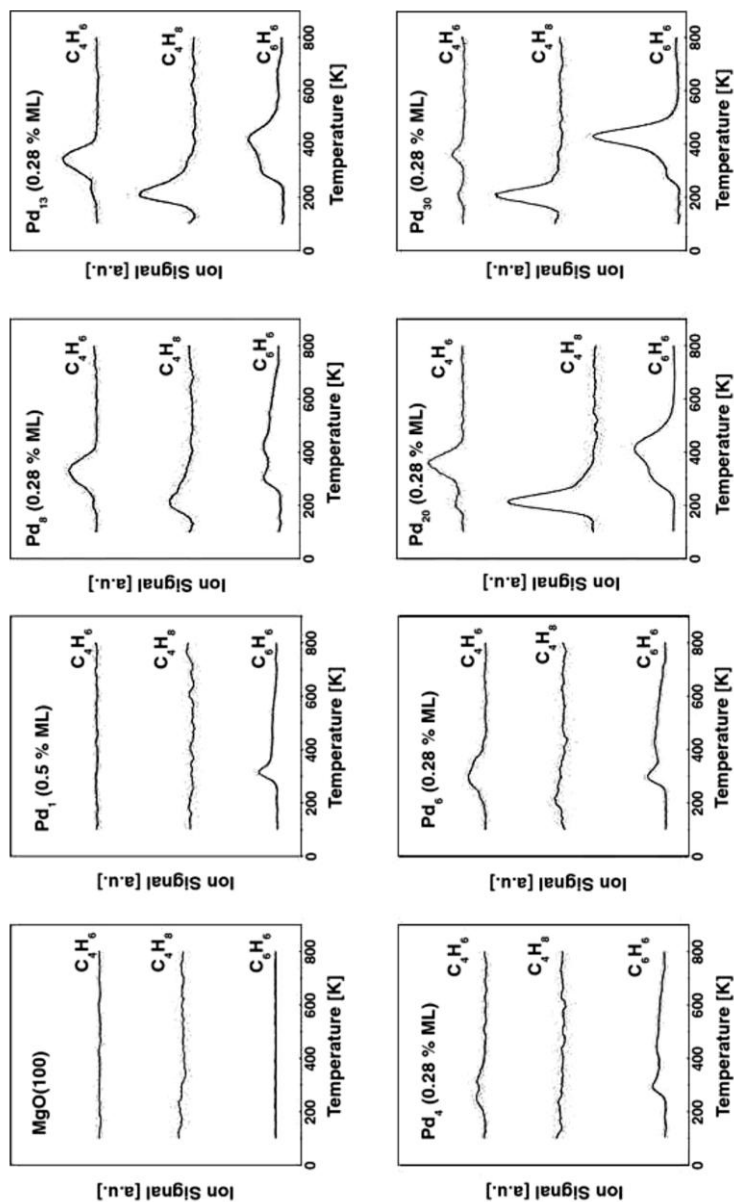
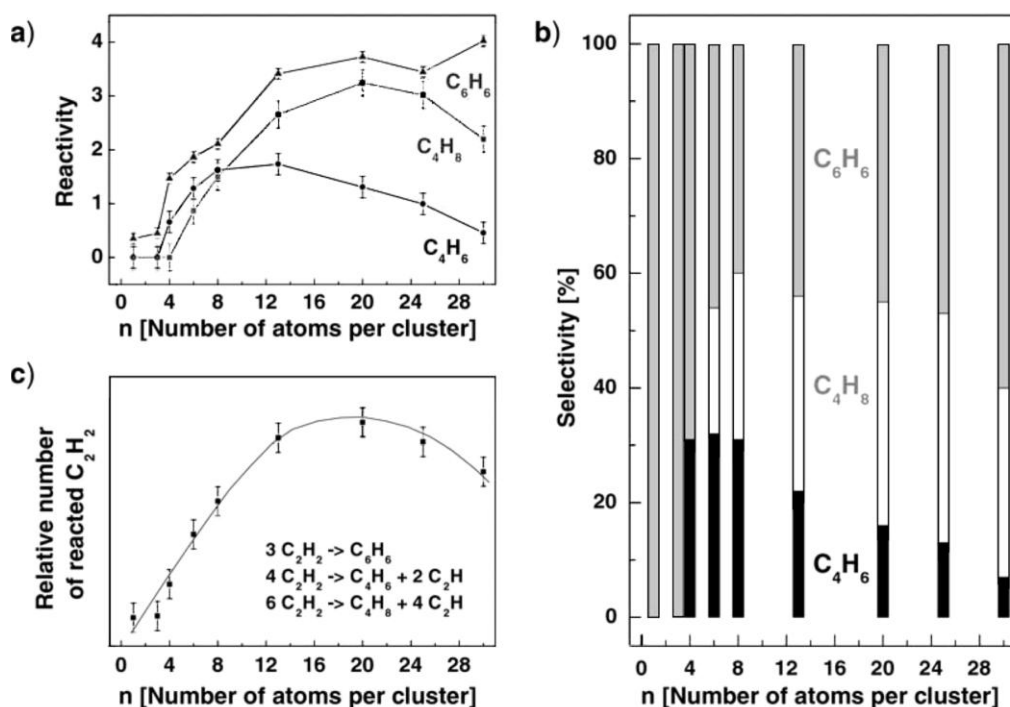


Fig. 17.8. TPR spectra of the catalytic formation of C<sub>6</sub>H<sub>6</sub>, C<sub>4</sub>H<sub>6</sub>, and C<sub>4</sub>H<sub>8</sub> for a defect-rich MgO thin film, Pd<sub>1</sub>, Pd<sub>4</sub>, Pd<sub>6</sub>, Pd<sub>8</sub>, Pd<sub>13</sub>, Pd<sub>20</sub>, and Pd<sub>30</sub>. The relative ion intensities are corrected with the relative detection efficiencies of the experiment and scale with the number of product molecules formed per cluster.

the TPR spectrum of  $C_4H_6$  at 200 K is part of the fragmentation pattern of  $C_4H_8$ .) For  $Pd_{20}$  the experiments were repeated in the presence of  $D_2$  [49];  $D_2$  was exposed prior and after  $C_2H_2$ . The results clearly indicate that no product containing deuterium is formed. Consequently  $D_2$  is not involved in the polymerization reaction. However, the presence of  $D_2$  opens a new reaction channel, the hydrogenation of acetylene. In addition,  $D_2$  blocks the active sites on the palladium clusters for the polymerization, as the formation of the products is slightly reduced when exposing  $D_2$  prior to  $C_2H_2$ . On  $Pd(111)$ , pre-dosing with  $H_2$  completely suppresses the cyclotrimerization but enhances the hydrogenation of acetylene to form ethylene [53].

The relative ion intensities of the products in the TPR spectra scale with the product formation by the model catalysts. By integrating the total area of the TPR spectra shown in Figure 17.8, the number of catalytically produced benzene, butadiene and butene molecules per cluster is obtained and illustrated in Figure 17.9a. Figure 17.9b shows the selectivities  $S$  for the formation of the products  $P_1(C_6H_6)$ ,  $P_2(C_4H_6)$ , and  $P_3(C_4H_8)$  for different cluster sizes calculated from, e.g.:

$$S(P_1) = (\text{number of } P_1 \text{ per cluster} / \text{number of } \sum P_n \text{ per cluster}) * 100 \quad [\%]$$



**Fig. 17.9.** Reactivity (a) (expressed as the number of product molecules per cluster) and selectivity (b) (expressed as the relative amount in %) of the polymerization of  $C_2H_2$

on size-selected  $Pd_n$  ( $n = 1-30$ ) deposited on defect-rich MgO thin films. Also shown is the relative number of reacted  $C_2H_2$  as a function of cluster size.

The striking atom-by-atom size-dependent selectivity for the polymerization of acetylene is summarized as follows:  $C_6H_6$  is catalyzed with a selectivity of 100% on cluster sizes up to  $Pd_3$ . The selectivity for  $C_4H_6$  reaches a maximum for  $Pd_6$  (~30%) and the production of  $C_4H_8$  is most efficient (~40%) for  $Pd_{20-25}$ . If one assumes stoichiometric reactions, as indicated in Figure 17.9c, and estimates the relative number of  $C_2H_2$  from Figure 17.9a one observes a proportional increase in acetylene with the number of palladium atoms per cluster up to  $Pd_{13}$ . Surprisingly, at this cluster size the surface-to-bulk ratio as well as the coordination number of Pd in the cluster changes as at this size one Pd atom sits completely in the cluster. In addition, according to the free stoichiometric chemical reactions, each reaction requires a minimum number of Pd atoms, which are 3, 4, and 6. The experimental results are surprisingly consistent, that is  $C_4H_6$  is formed for  $Pd_n$  with  $n \geq 4$  and  $C_4H_8$  for cluster sizes with  $n \geq 6$ .

Analyzing the products formed on small size-selected  $Pd_n$  ( $1 \leq n \leq 30$ ) clusters deposited on MgO(100) thin films indicates that the surface intermediate  $C_4H_4$  is produced efficiently on all cluster sizes. Thus at least two acetylene molecules are adsorbed in a  $\pi$ -bonded configuration at the initial stage of the reaction [71]. The observed size-dependent selectivity may then be understood by regarding the influence of the cluster size to steer the reaction either towards the cyclotrimerization to form  $C_6H_6$  or towards a direct hydrogen transfer from adsorbed  $C_2H_2$  to the  $C_4H_4$  intermediate to catalyze the formation of  $C_4H_6$  or  $C_4H_8$ , respectively. Cyclotrimerization is generally observed when a third acetylene molecule is adsorbed in a  $\pi$ -bonded configuration, which results in a change from sp-hybridization towards  $sp^2$ -hybridization [72]. This bonding configuration leads to a weak activation of the C–H bond, in analogy to ethylene [73]. The hydrogenation of the  $Pd_n(C_4H_4)$  metallocycle, on the other hand, is favored by the adsorption of di- $\sigma/\pi$  bonded acetylene to three Pd atoms, effecting a more efficient activation of the C–H bond, in analogy to ethylene [73].

For Pd atoms adsorbed on defect sites the  $Pd(C_4H_4)$  intermediate is formed with an energy gain of around 2 eV. A third adsorbed  $C_2H_2$  molecule is purely  $\pi$ -bonded (Figure 17.4a) and the activated acetylene molecule reacts with the intermediate to form benzene with a total exothermicity of about 7 eV. The weakly bound  $C_6H_6$  (0.3 eV) then desorbs at low temperature from the nanocatalyst [71]. A second reaction channel, the formation of butadiene,  $C_4H_6$ , opens for  $Pd_4$ . This channel reveals highest selectivity for  $Pd_6$ , in this case a third  $C_2H_2$  molecule can bind in a di- $\sigma/\pi$  bond configuration to three Pd atoms. The charge transfer from the substrate to the cluster further enhances the activation of the C–H bonds. For even larger cluster sizes the adsorption of two di- $\sigma/\pi$ -bonded  $C_2H_2$  molecules becomes possible and opens up the third reaction path, the formation of  $C_4H_8$ . In our experiments this is clearly observed for  $Pd_8$ . Purely geometrical arguments (possible adsorption of two di- $\sigma/\pi$ -bonded  $C_2H_2$  molecules close to the  $C_4H_4$  intermediate) suggest that this third channel is more pronounced for the larger clusters, and indeed our results show maximal  $C_4H_8$  formation for cluster sizes of 20–25 Pd atoms. For the largest clusters of the measured range, e.g.  $Pd_{30}$ , the increased number of metal–metal bonds and the concomitant delocalization of the charge transferred from the substrate to the cluster results in less charge density available

for the activation of the C–H bond [74]. Consequently, the cyclotrimerization becomes again more efficient than the hydrogenation of the  $C_4H_4$  intermediate. Going to even larger particles or to Pd(111) single crystals the cyclotrimerization to benzene is selectively catalyzed.

### 17.3.3

#### Turn-Over Frequencies of Catalytic Reactions on Supported Clusters

The examples presented above showed that size-selected clusters on surfaces reveal remarkable size-effects, however, they have been studied so far only by one-cycle experiments. Thus an experimental proof that these systems are active for catalytic processes, e.g. several cycles of a catalytic reaction are promoted without destruction of the catalyst, is still missing. In the following we present an experimental scheme to study catalytic processes of clusters on surfaces with high sensitivity and we report turn-over frequencies TOFs for the oxidation of CO on size-distributed supported Pd clusters.

##### 17.3.3.1 A Newly Designed Pulsed Valve for Molecular Beam Experiments

To study catalytic processes of clusters on surfaces with high sensitivity, a newly designed pulsed valve with excellent pulse-to-pulse stability, in combination with absolutely calibrated mass spectrometry, was used to determine turn-over frequencies [75].

A systematic view of the relevant elements is depicted in Figure 17.10. The deposited clusters can be exposed to different reactant gases by two kinds of valves. First, they can be exposed isotropically to e.g.  $O_2$  by a commercial, ultra-high vacuum (UHV) compatible, variable leak valve. Second, reactant molecules (e.g. CO) can be introduced via a pulsed molecular beam produced by a piezo-electric driven, pulsed valve. This pulsed valve has a high pulse-to-pulse stability (time profile), and allows the study of catalytic processes on supported clusters at relatively high pressures (up to  $10^{-2}$  mbar). Furthermore, a stainless steel tube is attached to the pulsed nozzle in order to collimate the molecular beam and to expose the reactant molecules to the substrate only. The pulse duration at the position of the sample can, in principle, be varied from 1 ms up to continuous operation. For the experiments described below a constant pulse duration of about 100 ms was used. The repetition rate of the pulsed valve can be up to 100 Hz. The experiments were carried out at 0.1 Hz; the 10 s interlude allows the reactant gas to be pumped completely.

After ejecting the CO molecule to the substrate at a constant isotropic pressure of  $O_2$  ( $5 \times 10^{-7}$  mbar), the resulting product molecules ( $CO_2$ ) were detected by an absolutely calibrated quadrupole mass spectrometer. The differentially pumped, computer-controlled mass spectrometer (Balzers QMG 421) is mounted in line-of-sight with the sample. At the entrance, near the ionizer of the quadrupole mass spectrometer, a skimmer with an opening of 3 mm is mounted. The skimmer is biased to  $-150$  V in order to prevent electron-stimulated desorption induced by emitting electrons from the ionizer of the mass spectrometer. After amplifying

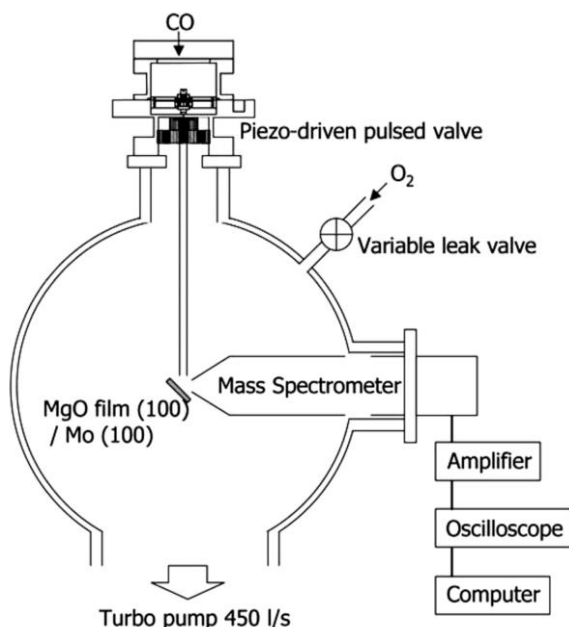


**Fig. 17.10.** Experimental scheme of the relevant elements for performing pulsed molecular beam experiments showing the UHV chamber with the pulsed piezo-electric valve, the variable leak valve and the absolutely calibrated mass spectrometer. The cluster

sample is mounted on the vertical axis of the chamber by an  $x, y, z$ -manipulator. The signal is amplified by a multichannel plate and the preamplifier of the mass spectrometer and subsequently recorded by a digital oscilloscope interfaced to a PC.

the ion current with a multichannel plate detector, the output of the preamplifier (Balzers, EP 112) is recorded and averaged by a digital oscilloscope (Tektronix TDS320) interfaced to a personal computer.

The turn-over frequencies for the oxidation of CO on size-distributed  $\text{Pd}_x$  clusters ( $x = 55 \pm 25$ ) are measured in the following way: On a freshly prepared  $\text{MgO}(100)$  thin film, 1% ML ( $1 \text{ ML} = 2.2 \times 10^{15} \text{ cm}^{-2}$ ) of Pd clusters were deposited. The coverage of the clusters is known with high precision as the cluster current is integrated during deposition. The vacuum chamber is then filled with a given partial pressure of  $\text{O}_2$  ( $1 \times 10^{-8} \text{ mbar} < p_{\text{oxygen}} < 2 \times 10^{-6} \text{ mbar}$ ), resulting in an isotropic  $\text{O}_2$  exposure on the cluster sample. The pulsed valve is then turned on and operated at 0.1 Hz. For each pulse the sample is first dosed with a strongly anisotropic CO pulse from the highly directed molecular beam; the maximal, effective pressure on the sample is  $2 \times 10^{-4} \text{ mbar}$ ; subsequently the sample is exposed to the isotropic contribution of backscattered reactant molecules. The anisotropic and isotropic contributions can easily be disentangled by first putting the sample in front of the mass spectrometer and then taking the sample out of this position. As expected the isotropic contribution is smaller and time delayed ( $\sim 10$

ms). For each pulse the product molecule,  $\text{CO}_2$ , can then be detected by the mass spectrometer.

More important is the evaluation of the integral of the  $\text{CO}_2$  pulse. The mass spectrometer was calibrated by measuring the reflected CO from the MgO substrate of a known pulse from the piezo-electric valve. The error of this measurement is estimated to be about 10%. As the cluster density on the surface (see above) is also known, turn-over frequencies (TOF) for the oxidation of CO can be extracted by simply calculating the ratio of the total number of  $\text{CO}_2$  formed and the number of clusters on the surface times the pulse duration.

### 17.3.3.2 Size-Distributed Clusters on Oxide Surfaces

So far, it has been an open question as to whether such small clusters on surfaces indeed remain stable after a single catalytic reaction, a necessary condition in catalysis. These transient molecular beam experiments (carried out under the conditions described above) on palladium nanocatalysts, which are formed by depositing 1% ML (1 ML =  $2.2 \times 10^{15}$  atoms  $\text{cm}^{-2}$ ) of mass-distributed  $\text{Pd}_x$  clusters ( $x = 55 \pm 25$ ) on a MgO(100)/Mo(100) thin film indeed reveal first that the nanocatalysts are active for at least 1 h (longest period of the performed experiments) at around room temperature and second that during this period the formation of  $\text{CO}_2$  is nearly constant. In these experiments no  $\text{CO}_2$  could be detected on clean MgO(100) thin films. In detail, Figure 17.11 shows the evolution of the  $\text{CO}_2$  pulses for various sample temperatures and for a constant, isotropic oxygen background pressure ( $5 \times 10^{-7}$  mbar). Below  $\sim 250$  K, no  $\text{CO}_2$  formation is observed. At 269 K, a small narrow  $\text{CO}_2$  pulse is detected. For all temperatures only a single, averaged  $\text{CO}_2$  pulse (30 samples) from an extended series is shown. The intensity of this peak increases up to about 408 K, where it reaches the maximal value. The intensity decreases for higher temperatures and disappears at 709 K. At 307 K, a broad second, delayed peak (between 2 s and 4 s) is detected. This second peak is also present at 327 K and 356 K, however it shifts towards shorter times. In addition, the width clearly decreases with temperature [75]. The turn-over frequencies (TOFs) as a function of temperature are obtained by integrating the  $\text{CO}_2$  pulses and dividing the obtained value by the number of deposited clusters and the width of the CO pulses (reaction time). For this procedure the mass spectrometer has been calibrated using the procedure described above and taking the different sensitivities for CO and  $\text{CO}_2$  into account. The number of deposited clusters was obtained by integrating the measured ion cluster current over the deposition time. This procedure results in accurate TOFs for size-selected and mass-distributed clusters. The absolute TOFs [number of  $\text{CO}_2$  molecules/number of Pd atoms  $\times$  s] for the present study are displayed in the inset of Figure 17.11. The maximal TOF of the size-distributed Pd clusters is  $18 \pm 8$ . The maximal TOF of palladium model catalysts consisting of larger Pd particles (2.8 nm and 13 nm in diameter) on MgO(100) show much lower values (0.12), these TOFs, however, were measured under steady-state conditions [76]. Pd model catalysts consisting of similar sized Pd particles on  $\text{SiO}_2$  revealed higher TOFs (20–2000) when measured at high pressures (1.5 Torr) [77]. The asymmetrical shape of the temperature dependent



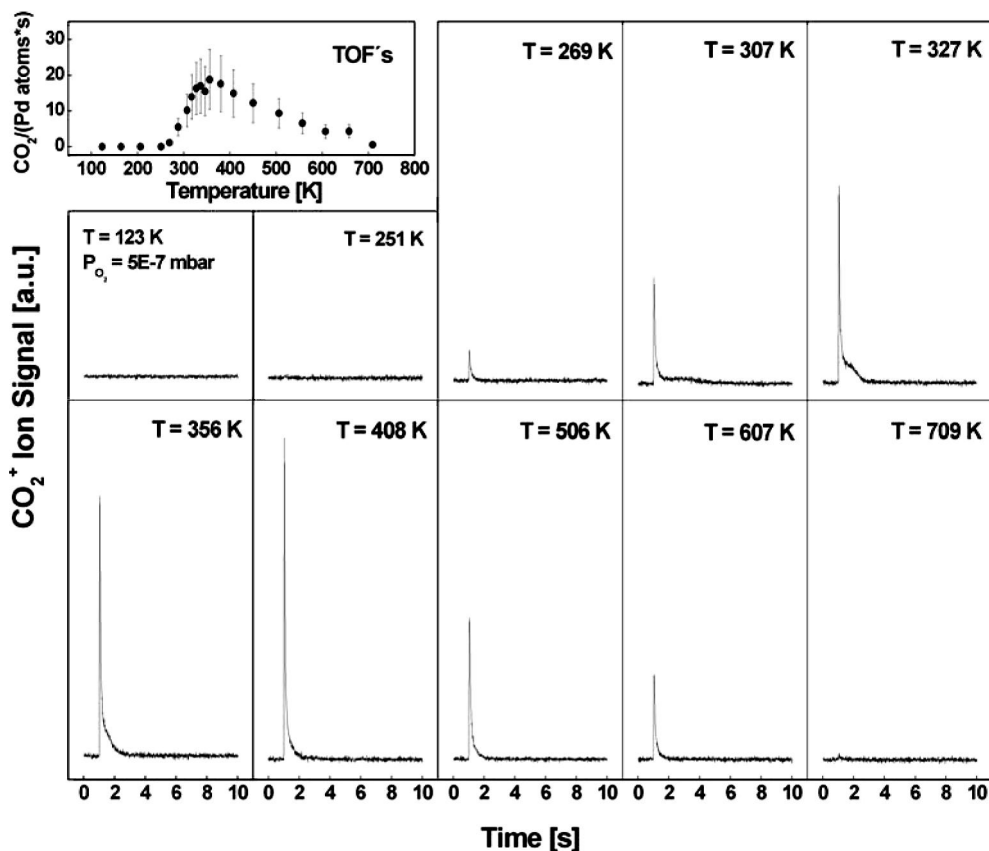


Fig. 17.11. The formation of  $\text{CO}_2$  at various reaction temperatures and at a constant  $\text{O}_2$  pressure of  $5 \times 10^{-7}$  mbar. The TOFs shown in the inset are obtained by integrating the  $\text{CO}_2$  peaks and normalizing with the cluster density.

curve is comparable to the curves measured on single crystals and model catalysts, but interestingly the maximum is shifted by 100 K to lower temperatures. In fact, the nanocatalysts consisting of small Pd clusters reveal maximal TOF at around 380 K whereas on single crystals or model catalysts maximal reactivity is observed at around 500 K. Such a shift in temperature was also observed for small unsupported Pt clusters, where the CO oxidation was studied in the gas phase and compared to real catalysts [30]. Below 380 K, the TOFs decrease because on the one hand the activation energy for the  $\text{CO}_2$  formation is not reached and on the other hand CO coverage is important (enhanced CO sticking coefficient at low temperature) and blocks oxygen adsorption. In contrast, above 380 K the smaller TOFs can be explained by the low CO coverage (decreased CO sticking coefficient at high temperatures). The observed decrease may also partly be explained by cluster diffusion.

## 17.4

**Chemical Reactions Induced by Confined Electrons**

In the examples described above single chemical bonds of reactants and products are activated, dissociated and formed by interacting with the electronic states of confined valence electrons of nanoscale systems such as point defects, free or supported atoms or clusters. In a completely different approach single chemical bonds are manipulated by nanoscale devices. Such a device can be a scanning tunneling microscope (STM) where tunneling electrons resonate with single electronic states of molecules to induce chemistry by making and breaking bonds [78]. These two methods for doing chemistry on the nanoscale differ completely. In the first example confinement is achieved by the system (point defects, atoms, clusters) itself and in the best case it may act as a real nanocatalyst. The second method uses a nanoscale device, which can be applied to non-localized systems to induce chemistry on the nanoscale.

The use of nanoscale devices for inducing chemical reactions was first introduced by the group of Somorjai in 1994, when a platinum–rhodium tip of a STM operating inside an atmospheric-pressure chemical reactor cell was used to locally rehydrogenate carbonaceous fragments deposited on the (111) surface of platinum [79]. Recently the groups of Rieder (FU-Berlin) [80] and Ho (Cornell) [81] used a tip of an STM as a local electron source to induce bond-selected chemistry with a spatial resolution on the atomic scale ( $\sim 1 \text{ \AA}$ ). With the same device the induced changes can be imaged with similar spatial resolution. The sharp metal tip of an STM is held in close proximity to a conducting surface. The tip is then positioned above a selected bond of a reactant molecule and by applying different bias voltages the energy of the tunneling electrons is tuned to resonate with single bonds. At a tip–surface distance of about  $6 \text{ \AA}$  this process is dominant and the overlap of the wavefunctions of the tip and the reactant molecule is negligible. In such a way a chemically bound CO molecule on Cu(111) could e.g. be transferred to and from the tip reversibly [82] or in another example tunneling-electron-stimulated desorption of H atoms from a Si(100)– $2 \times 1$  surface could be successfully used for nanopatterning [83]. They observed that for localized and controlled reactions the energies of the tunneling electrons ought to be below 1 eV (for bias voltages below 1 V). For example, the dissociation of a single O<sub>2</sub> molecule on Pt(111) is confined to the molecule if the bias is less than 0.5 V [84]. However, when the bias is increased to 1.0 V, molecules as far away as 100 Å are also dissociated, even though the electrons are confined to atomic dimensions. The detailed mechanism for this non-local effect is not yet understood. In general, they conclude that for bias voltages larger than 2.5 V non-local chemistry is dominant, whereas for voltages up to about 1–2 V local, single-molecule chemistry takes place.

The Cornell group studied the local dissociation of a chemisorbed, single O<sub>2</sub> molecule on Pt(111) in great detail. Obviously this system is of relevance in catalysis. It is known that oxygen adsorbs molecularly on Pt(111) at temperatures below 100 K [85]. When the temperature is increased to about 150 K, some of the O<sub>2</sub> molecules desorb and the remaining molecules dissociate and recombine and de-

sorb at about 600 K. The bonding configurations of molecular and atomic oxygen on Pt(111) could be detected by low-temperature STM (8–350 K) [84, 86]. The thermodynamically stable atomic O resides in face-centered cubic (fcc) 3-fold hollow sites; O atoms on the hexagonal close-packed (hcp) sites are metastable and can only be created nonthermally by irradiation with electrons or photons [86]. No molecules are observed at (100) steps. They then studied the dissociation of  $O_2$  induced by tunneling electrons on the bridge and 3-fold hollow sites of Pt(111) [84]. The adjacent atoms of the underlying Pt atoms on the (111) surface are determined to be 2.77 Å; the observed separation of the two  $O_2$  molecules is 5.54 Å. The STM tip was then positioned about 6 Å above one of the molecules and a voltage pulse of 0.3 V and 100 ms duration was applied. The sudden change in the tunneling current (12.5 nA) indicates the moment of dissociation. The image taken after the dissociation showed the two O products, one on the hcp site and the other on the fcc site, as well as the other  $O_2$  molecule, which is not perturbed. The two O products are found to be within two lattice constants of the original molecule and one to three lattice constants apart. Approximately 1.1 eV of energy per O atom is dissipated upon dissociation through substrate excitations. The rates of energy dissipation and scattering with the corrugated potential of the surface limit the range of motion of the products [87]. Ho et al. studied the mechanisms and the dynamics of single-bond dissociation by measuring the dissociation rate as a function of bias voltage and tunneling current and by theoretical modeling of the data [84]. The dissociation rate reveals a power law dependence on the tunneling current. They propose a mechanism based on inelastic vibrational excitations of an adsorbed molecule by the tunneling electrons [88–90]. In this process tunneling electrons inelastically scatter from an adsorbed molecule and transfer energy to the vibrational modes of the molecule. For the dissociation of  $O_2$  an energy barrier of 0.35–0.38 eV needs to be overcome via one or multiple vibrational excitations in the ground electronic state. Such a vibrational ladder climbing process requires one or multiple inelastic scatterings. For a 0.4 V bias used in the reported experiment, the  $O_2$  molecule can be dissociated with a single inelastic scattering event, leading to a linear dependence of the dissociation rate with the current. However, at least two scatterings are required for 0.3 V bias, and the discrete nature of the vibrational levels requires three scatterings for 0.2 V bias. As the vibrational relaxation rate is greater than the excitation rate, the most probable path to dissociation is the one with the minimum relaxation probability, which is clearly the path with the fewest transitions. For 0.4 V bias, the bound-to-continuum transition corresponds to a single excitation to overcome the dissociation barrier of 0.35–0.38 eV. Finally it is interesting to calculate the electrical energy for this example to dissociate a single  $O_2$  molecule. At a voltage of 0.3 V, a current of 12 nA and a pulse duration of 30 ms an energy of  $1.1 \times 10^{-10}$  J is used. For the dissociation of 1 mol  $O_2$  this corresponds to  $6.5 \times 10^{10}$  kJ mol<sup>-1</sup>!

The dissociation of  $O_2$  is the rate-determining step in the catalytic oxidation of CO on metal surfaces, thus Ho et al. showed in another experiment [91] that bond-selected chemistry can even be used to induce this catalytic reaction. After preparing oxygen atoms by dissociating single  $O_2$  molecules with tunneling electrons, as

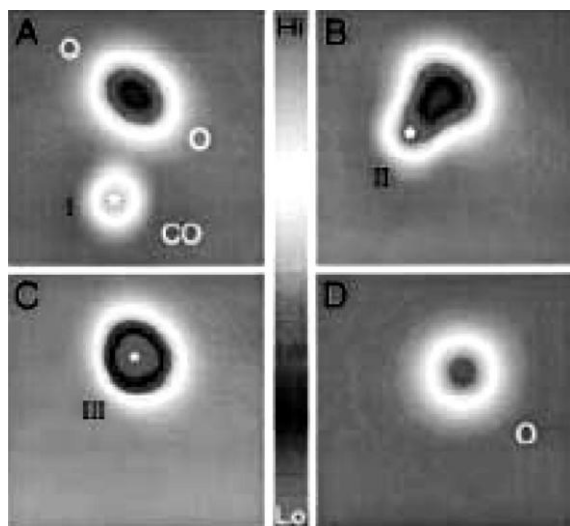


**Fig. 17.12.** STM topographical images showing the manipulation of a CO molecule toward two O atoms coadsorbed on Ag(110) at 13 K. (A) A single CO molecule and two O atoms. (B) The CO was moved toward the O atoms. (C) The CO was moved to the closest distance from the two O atoms to form the O–CO–O complex. (D) Remaining O atom after tip-induced oxidation of CO.

described above, they exposed the surface at 13 K to a small amount of CO. The adsorbed reactants and products were then imaged by STM before during and after manipulation with the STM tip and reaction of a CO with one of the two O atoms (Figure 17.12). The CO and O atoms are imaged as depressions (Figure 17.12a). The CO was moved toward the O atoms by repeatedly applying sample bias pulses over the CO (from Figure 17.12a to Figure 17.12b) since the CO does not always move towards the O atoms. However, they succeeded in eventually forming the O–CO–O complex (Figure 17.12c). As the CO approaches the O atoms, the composite images (Figure 17.12b/c) show increasing depressions. With an additional sample bias pulse over the CO in the complex, they induced the formation of CO<sub>2</sub> and the product quickly desorbed, leaving the remaining O atom on the surface (Figure 17.12d). From the spatial distribution of inelastic electron tunneling spectroscopy (STM-IETS) [92] intensity they conclude that the CO in the complex is between the two Ag atoms along the [001] direction and that the CO may be tilted by the repulsive interaction between the O atom of CO and adsorbed O atoms, as suggested for a transition state in CO oxidation on the Ru(0001) surface [93]. The Ho group illustrated another oxidation pathway by direct transfer of a CO molecule from the tip to an adsorbed O atom. In this experiment [91] the CO-terminated tip was positioned over one of the O atoms. They applied a +470 mV pulse with the feedback turned off and a re-scan of the same area showed the remaining O atom on the surface after CO<sub>2</sub> formation.

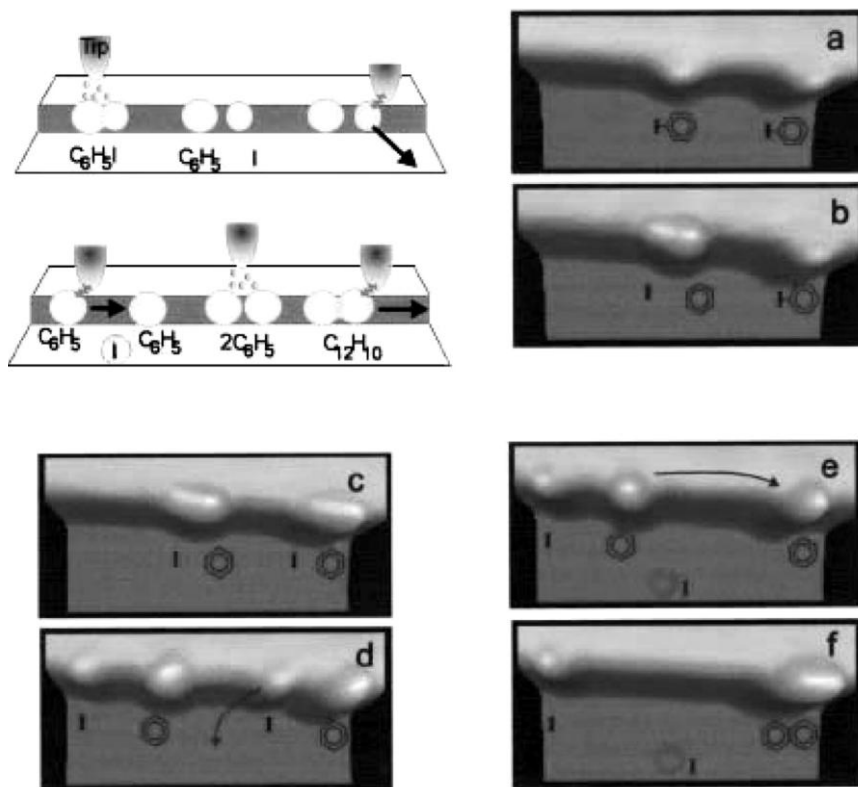


**Fig. 17.13.** Schematic illustration and STM images of the STM tip-induced synthesis steps of biphenyl molecule from iodobenzene. (a) Two iodobenzene molecules adsorbed at a Cu(111) step edge. (b), (c) Iodine is abstracted from both molecules by applying a voltage pulse. (d) Iodine atoms and phenyl molecules are separated by lateral manipulation. (e) An iodine atom is removed onto the lower terrace. (f) The two phenyl molecules are moved together.

In another example Rieder's group induced all the elementary steps of the Ullmann synthesis [94], the formation of biphenyl from iodobenzene on copper, on individual molecules with an STM in a controlled step-by-step manner utilizing a variety of manipulation techniques [80]. Two reactant molecules are shown in Figure 17.13a. The first reaction step is the separation of iodine from iodobenzene by using tunneling electrons (Figure 17.13b,c). After dissociation, iodine was moved to terrace sites of the copper surface by lateral manipulation (Figure 17.13d). One chemisorbed phenyl reactant was then moved close to another phenyl by soft lateral manipulation [95] (Figure 17.13e). Finally the two phenyls were brought together by molecular excitation by inelastic tunneling (Figure 17.13f). Successful chemical association was then verified by pulling the synthesized molecule by its front end with the STM tip.

## 17.5

## Conclusions

The term nanocatalysis was introduced by Somorjai in 1994 when he used confined electrons of an STM tip to induce an electrochemical process. Earlier experiments on free clusters pointed towards the possibility of using small clusters with intrinsically confined valence electrons as catalysts to tune the properties atom-by-atom. These two completely different pioneering ideas have become further sophisticated during the last few years. It has become possible to use size-selected clusters on surfaces to catalyze simple chemical reactions and to tune the catalytic properties with size as well as using the tip of an STM to control every step of a chemical reaction on a local scale. With these examples a deeper understanding of nanocatalytic factors is now emerging and such studies will have profound impact on the catalysis of systems at the ultimate size limit.

## Acknowledgements

This work was supported by the Deutsche Forschungsgesellschaft (DFG). S.A. acknowledges the Swiss National Science Foundation and the Alexander von Humboldt Foundation for financial support.

## References

- 1 BERZELIUS, J. J. *New Philos. J.* **1836**, XXI, 223.
- 2 ERTL, G.; FREUND, H.-J. *Phys. Today* **1999**, 52, 32–38.
- 3 <http://itri.loyola.edu/IWGN.Research.Directions/>, eds. ROCO, M. C., WILLIAMS, R. S., ALIVISATOS, P. 1999.
- 4 Special nanotechnology issue, *Sci. Am.* **2001**, 285, 38–56 (see RAUKES, M. p 48–57; WHITERIDES, G. M., SAVE, J. C. p 38–56).
- 5 HEIZ, U.; SCHNEIDER, W.-D. *Crit. Rev. Solid State Mater. Sci.* **2001**, 26, 251–290.
- 6 HÄKKINEN, H.; ABBET, S.; SANCHEZ et al. *Angew. Chem.* **2003**, in press.
- 7 KNIGHT, W. D.; CLEMENGER, K.; DE HEER, W. et al. *Phys. Rev. Lett.* **1984**, 52, 2141.
- 8 SCHUMACHER, E.; BLATTER, F.; FREY, M. et al. *Chimia* **1988**, 42, 357–376.
- 9 BILLAS, I. M. L.; CHATELAIN, A.; DEHEER, W. A. *Science* **1994**, 265, 1682.
- 10 MOSELER, M.; HÄKKINEN, H.; LANDMAN, U. *Phys. Rev. Lett.* **2002**, 89, 176103.
- 11 KALDOR, A.; COX, D.; ZAKIN, M. R. *Adv. Chem. Phys.* **1988**, 70, 211.
- 12 PACCHIONI, G. *Surf. Rev. Lett.* **2000**, 7, 277.
- 13 DI VALENTIN, C.; DEL VITTO, A.; PACCHIONI, G. et al. *J. Phys. Chem. B* **2002**, 106, 11961.
- 14 SANCHEZ, A.; ABBET, S.; HEIZ, U. et al. *J. Phys. Chem. A* **1999**, 103, 9573–9578.
- 15 HEIZ, U.; VANOLLI, F.; TRENTO, L. *Rev. Sci. Instrum.* **1997**, 68, 1986.
- 16 HEIZ, U.; SCHNEIDER, W.-D. *J. Phys. D: Appl. Phys.* **2000**, 33, R85–R102.
- 17 HE, J.-W.; MØLLER, P. L. *Chem. Phys. Lett.* **1986**, 129, 13.
- 18 PETERKA, D.; TEGENKAMP, C.; SCHRÖDER, K. M. et al. *Surf. Sci.* **1999**, 431, 146–155.
- 19 ILLAS, F.; PACCHIONI, G. *J. Chem. Phys.* **1998**, 108, 7835.

- 20 DEHEER, W. A. *Rev. Mod. Phys.* **1993**, 65, 611–676.
- 21 DIETZ, T. G.; DUNCAN, M. A.; POWERS, D. E. et al. *J. Chem. Phys.* **1981**, 74, 6511–6512.
- 22 SIEKMANN, H. R.; LÜDER, C.; FÄHRMANN, J. et al. *Z. Phys. D. – At., Mol. Clusters* **1990**, 20, 417–420.
- 23 KELLER, R.; NÖHMEIER, F.; SPÄDTKE, P. et al. *Vacuum* **1984**, 34, 31.
- 24 COX, D. M.; REICHMAN, K. C.; TREVOR, D. J. et al. *J. Chem. Phys.* **1988**, 88, 111.
- 25 PARKS, E. K.; KLOTZ, T. D.; RILEY, S. J. *J. Chem. Phys.* **1990**, 92.
- 26 REN, X.; HINTZ, P. A.; ERVIN, K. M. *J. Chem. Phys.* **1993**, 99, 3575.
- 27 LEUCHTNER, R. E.; HARMS, A. C.; CASTELMAN JR., A. W. *J. Chem. Phys.* **1990**, 92, 6527.
- 28 JIAO, C. Q.; FREISER, B. S. *J. Phys. Chem.* **1995**, 99, 10723.
- 29 ALFORD, J. M.; WEISS, F. D.; LAAKSONEN, R. T. et al. *J. Phys. Chem.* **1986**, 90, 4480.
- 30 SHI, Y.; ERVIN, K. M. *J. Chem. Phys.* **1998**, 108, 1757–1760.
- 31 SOCACIU, L. D.; HAGEN, J.; HEIZ, U. et al. *Chem. Phys. Lett.* **2001**, 340, 282.
- 32 SOCACIU, L. D.; HAGEN, J.; BERNHARDT, T. M. et al. *J. Am. Chem. Soc.* **2003**, 125, 10437–10445.
- 33 HAGEN, J.; SOCACIU, L. D.; ELIJAZYFER, M. et al. *Phys. Chem. Chem. Phys.* **2002**, 4, 1707.
- 34 WALLACE, W. T.; WHETTEN, R. L. *J. Am. Chem. Soc.* **2002**, 124, 7499.
- 35 HÄKKINEN, H.; LANDMAN, U. *J. Am. Chem. Soc.* **2001**, 123.
- 36 COX, D. M.; BRICKMAN, R.; CREEGAN, K. et al. *Z. Phys. D. – At., Mol. Clusters* **1991**, 19, 353–355.
- 37 COX, D. M.; BRICKMAN, R. O.; CREEGAN, K. et al. *Mater. Res. Soc. Symp. Proc.* **1991**, 206, 43–48.
- 38 WALLACE, W. T.; WHETTEN, R. L. *J. Phys. Chem. B* **2000**, 104, 10964.
- 39 HAGEN, J.; SOCACIU, L. D.; ELIJAZYFER, M. et al. *Chem. Phys. Phys. Chem.* **2002**, 4, 1707–1709.
- 40 STEINFELD, J. I.; FRANCISCO, J. S.; HASE, W. L. *Chemical Kinetics and Dynamics*, 2nd edition, Upper Saddle River, N J 1999. Prentice Hall.
- 41 HUBER, H.; MCINTOSH, D.; OZIN, G. A. *Inorg. Chem.* **1977**, 16, 675.
- 42 ERVIN, K. M.; GRUSHOW, A. *J. Chem. Phys.* **1997**, 106, 9580–9593.
- 43 ERVIN, K. M. *Int. Rev. Phys. Chem.* **2001**, 20, 127.
- 44 HINTZ, P. A.; ERVIN, K. M. *J. Chem. Phys.* **1995**, 103, 7897.
- 45 CAMPBELL, I. M. *Catalysis at Surfaces*; Chapman & Hall, London 1988.
- 46 HEIZ, U. *Appl. Phys. A* **1998**, 67, 621–626.
- 47 ABBET, S.; JUDAI, K.; KLINGER, L.; HEIZ, U. *Pure Appl. Chem.* **2002**, 74, 1527.
- 48 ABBET, S.; RIEDO, E.; BRUNE, H. et al. *J. Am. Chem. Soc.* **2001**, 123, 6172–6178.
- 49 ABBET, S.; SANCHEZ, A.; HEIZ, U. et al. *J. Catal.* **2001**, 198, 122–127.
- 50 JUDAI, K.; WÖRZ, A. S.; ABBET, S. et al. *J. Phys. Chem. B* **2003**, 107, 9377–9387.
- 51 ORMEROD, R. M.; LAMBERT, R. M. *J. Phys. Chem.* **1992**, 96, 8111–8116.
- 52 FERRARI, A. M.; GIORDANO, L.; ABBET, S. et al. *J. Phys. Chem. B* **2002**, 106, 3173.
- 53 TYSOE, W. T.; NYBERG, G. L.; LAMBERT, R. M. *J. Chem. Soc., Chem. Commun.* **1983**, 623–625.
- 54 HEIZ, U.; SANCHEZ, A.; ABBET, S. et al. *Eur. J. Phys. D* **1999**, 9, 35.
- 55 ABBET, S.; HEIZ, U.; HÄKKINEN, H. et al. *Phys. Rev. Lett.* **2001**, 86, 5950–5953.
- 56 HARBICH, W., in *Metal Clusters at Surfaces*, ed. MEIWES-BROER, K.-H., Springer Series in Cluster Physics, Berlin 2000.
- 57 CLEVELAND, C. L.; LANDMAN, U. *Science* **1992**, 257, 355.
- 58 CHENG, H.-P.; LANDMAN, U. *Science* **1993**, 260, 1304–1307.
- 59 CHENG, H.-P.; LANDMAN, U. *J. Phys. Chem.* **1994**, 98, 3527.
- 60 MESSERLI, S.; SCHINTKE, S.; MORGENSTERN, K. et al. *Surf. Sci.* **2000**, 465, 331–338.
- 61 HAMMER, B.; NORSKOV, J. K. *Nature* **1995**, 376, 238–240.
- 62 HARUTA, M. *Catal. Today* **1997**, 36, 153–166.
- 63 HARUTA, M. *Appl. Catal. A* **2001**, 222, 427.

- 64 HÄKKINEN, H.; LANDMAN, U. *Phys. Rev. B* **2000**, 62, R2287.
- 65 ALLERS, K.-H.; PFNÜR, H.; FEULNER, P. et al. *J. Chem. Phys.* **1994**, 100, 3985.
- 66 EICHLER, A.; HAFNER, J. *Phys. Rev. B* **1999**, 59, 5960.
- 67 SCHEFFLER, M.; STAMPFL, C., in *Electronic Structure*, eds. HORN, K., SCHEFFLER, M., Elsevier, Amsterdam 1999, Vol. 2.
- 68 ORMEROD, R. M.; LAMBERT, R. M. *J. Chem. Soc., Chem. Commun.* **1990**, 1421–1423.
- 69 HOLMBLAD, P. M.; RAINER, D. R.; GOODMAN, D. W. *J. Phys. Chem. B* **1997**, 101, 8883–8886.
- 70 PATTERSON, C. H.; LAMBERT, R. M. *J. Phys. Chem.* **1988**, 92, 1266–1270.
- 71 ABBET, S.; SANCHEZ, A.; HEIZ, U. et al. *J. Am. Chem. Soc.* **2000**, 122, 3453–3457.
- 72 PACCHIONI, G.; LAMBERT, R. M. *Surf. Sci.* **1994**, 304, 208–222.
- 73 FAHMI, A.; VAN SANTEN, R. A. *J. Phys. Chem.* **1996**, 100, 5676–5680.
- 74 BURKART, S.; BLESSING, N.; GANTEFÖR, G. *Phys. Rev. B* **1999**, 60, 15639–15642.
- 75 JUDAI, K.; ABBET, S.; WÖRZ, A. S. et al. *Int. J. Mass Spectrom.* **2003**, 229, 99–106.
- 76 BECKER, C.; HENRY, C. R. *Surf. Sci.* **1996**, 352, 457.
- 77 SANTRA, A. K.; GOODMAN, D. W. *Electrochim. Acta* **2002**, 47, 3595.
- 78 HO, W. *Acc. Chem. Res.* **1998**, 31, 567.
- 79 MCINTYRE, B. J.; SALMERON, M.; SOMORJAI, G. A. *Science* **1994**, 265, 1415.
- 80 HLA, S.-W.; BARTELS, L.; MEYER, G.; RIEDER, K.-H. *Phys. Rev. Lett.* **2000**, 85, 2777.
- 81 LEE, H.-J.; HO, W. *Science* **1999**, 286, 1719.
- 82 BARTELS, L.; MEYER, G.; RIEDER, K.-H. *Appl. Phys. Lett.* **1997**, 71, 213.
- 83 AVOURIS, P. *Acc. Chem. Res.* **1995**, 28, 95.
- 84 STIPE, B. C.; REZAEI, M. A.; HO, W. et al. *Phys. Rev. Lett.* **1997**, 78, 4410.
- 85 GLAND, J. L.; SEXTON, B. A.; FISHER, G. B. *Surf. Sci.* **1980**, 95, 587.
- 86 STIPE, B. C.; REZAEI, M. A.; HO, W. *J. Chem. Phys.* **1997**, 107, 6443.
- 87 WAHNSTROM, G.; LEE, A. B.; STROMQUIST, J. *J. Chem. Phys.* **1996**, 105, 326.
- 88 GAO, S.; PERSSON, M.; LUNDQVIST, B. I. *Solid State Commun.* **1992**, 84, 271.
- 89 GAO, S.; PERSSON, M.; LUNDQVIST, B. I. *Phys. Rev. B* **1997**, 55, 4825.
- 90 WALKUP, R. E.; NEWNS, D. M.; AVOURIS, P. *Phys. Rev. B* **1993**, 48, 1859.
- 91 HAHN, J. R.; HO, W. *Phys. Rev. Lett.* **2001**, 87, 166102–166101.
- 92 STIPE, B. C.; REZAEI, M. A.; HO, W. *Science* **1998**, 280, 1732–1735.
- 93 ZHANG, C.; HU, P.; ALAVI, A. J. *Am. Chem. Soc.* **1999**, 121, 7931.
- 94 ULLMANN, F.; MEYER, G. M.; LOEWENTHAL, O. et al. *Justus Liebig's Ann. Chem.* **1904**, 331, 38.
- 95 MEYER, G.; BARTELS, L.; ZÖPHEL, S. et al. *Phys. Rev. Lett.* **1997**, 78, 1512.



## 18

## Nanoporous Materials

A. K. Cheetham and P. M. Forster

## 18.1

## Introduction

The scope of this chapter concerns crystalline inorganic and hybrid inorganic–organic materials that exhibit periodic porosity in the nanometer range. The prototypic systems of the inorganic class are the aluminosilicate zeolites, which have regular channels with diameters that range between approximately 0.3 and 1.0 nm. Such channels are able to accommodate relatively small inorganic and organic molecules, thereby facilitating a wide range of commercial applications as well as fundamental studies of molecules in confined spaces. We shall explore the growing chemical and structural diversity of such materials. Amorphous materials, such as activated carbons, which exhibit nanoporosity on a similar length-scale, will not be discussed. Nor shall we cover mesoporous silicas and related materials, since they are non-crystalline.

There has been an enormous growth in the chemical diversity of open-framework and nanoporous materials\* during the last 20 years [1]. Prior to the early 1980s, when the nanoporous aluminum phosphates were first reported by Flanigen and co-workers [2], the aluminosilicate zeolites and closely related systems represented the predominant class of nanoporous materials with three-dimensional crystalline structures. The extent of the change during recent years can be judged from the fact that as many as 35 elements of the main block and the transition series are now known to participate as major components of such frameworks, and the number is increasing rapidly. Most are based upon oxygen-containing materials, especially phosphates, but there is a growing list of examples based upon other chemistries, such as oxyfluorides [3], nitrides [4], sulfides [5], and halides [6]. The range of systems has also increased in another sense: whereas the zeolites and early  $\text{AlPO}_4$ s were based entirely upon corner-sharing tetrahedra,

\*There is much inconsistency in the literature regarding the use of the terms “open-framework” and “nanoporous”. Here, we use open-framework to refer to materials with open

architectures, and use nanoporous to refer specifically to materials where porosity has been demonstrated through surface area or ion exchange experiments.

e.g.  $\text{SiO}_4$ ,  $\text{AlO}_4$  etc., many of the newer architectures involve other types of polyhedra such as octahedral  $\text{XO}_6$ , pentacoordinated  $\text{XO}_5$ , or pyramidal  $\text{XO}_4$  or  $\text{XO}_3$  units. These exciting developments will gradually have an impact on the applications of such materials. The traditional applications of aluminosilicate zeolites lie in the areas of ion-exchange, separations and catalysis [7], but the new generation of materials offers a wider range of chemical and physical properties that are only just beginning to be explored.

Two other developments have further enhanced the scope of crystalline nanoporous materials during the last decade. One is the discovery of the so-called mesoporous materials at Mobil in 1992 [8]. The essence of Mobil's discovery is that self-assembling organic molecules, such as surfactants or block copolymers, can be used to create silicas with porosity on the 2–30 nm scale. This class of materials is often referred to as the M41S family. Their porosity is periodic, but the silica walls of the materials remain amorphous. The concept has been extended to other types of materials, such as metals [9], oxides [10], and phosphates [11], and other classes of self-assembling organics, such as block copolymers [12], have also been used. These fascinating materials have interesting properties and are beginning to be exploited for a diverse range of application, including catalysis, low- $\kappa$  dielectrics, and lasers. We shall not cover this area in the present chapter since it has recently been reviewed in some detail [13].

The second area that has exploded during the last decade concerns materials that involve open-frameworks that are constructed from both inorganic and organic components; we shall refer to them collectively as hybrid materials and will cover them in two separate sections. The first will examine the so-called coordination polymers [14] in which molecular coordination compounds are connected by organic linkers to form chains, sheets or 3-D networks. The second class involves extended metal–oxygen–metal networks that are decorated by organic ligands; we shall refer to these as hybrid metal oxides.

## 18.2

### Stability of Open-Framework Materials

The open frameworks of zeolites are slightly less stable than the corresponding condensed structures [15, 16] into which they will transform during severe thermal treatment. Nevertheless, the difference in energy between  $\alpha$ -quartz, the most stable polymorph of silica, and siliceous faujasite, one of the most open and least stable, is only about  $15 \text{ kJ mol}^{-1}$ . The extensive occurrence of aluminosilicate zeolites and their widespread utility in industry therefore depend heavily upon both the strengths of their T–O bonds (e.g.  $\text{Si–O} \sim 466 \text{ kJ mol}^{-1}$ ), which render them stable with respect to framework rearrangement. The challenge with many of the newer materials is that their stability with respect to transformation into alternative condensed structures is considerably lower and they frequently collapse on dehydration or other means of activation. It is for this reason that only a small subset of the many open-framework families of materials can be rendered truly nanoporous,

and even fewer have found applications in processes that require porosity. These exceptions include SAPO-34, an aluminum phosphate with the chabazite structure that is being exploited for the conversion of methanol to olefins [17] and the titanosilicate, TS-1, which is very effective for selective oxidations using hydrogen peroxide [18]. Attempts to make nanoporous transition metal phosphates, for example, have led to the discovery of many new open-frameworks, e.g. V-P-O [19], Fe-P-O [20], and Co-P-O [21], but, as is the case with most non-silicate materials, the poor thermal stability of these systems leads, in most cases, to the collapse of the pore structures on activation. The nickel phosphates, which are stable to around 500 °C, represent a notable exception and exhibit a wide range of interesting properties [22].

### 18.3 Aluminosilicate Zeolites

The aluminosilicate zeolites, of general formula  $A_{x/n}[\text{Si}_{1-x}\text{Al}_x\text{O}_2] \cdot n\text{H}_2\text{O}$  where A is typically a cation of valence  $n$ , or a protonated or quaternary organic amine, was the first class of nanoporous materials to be recognized. They occur quite extensively in nature, and synthetic examples were made as early as the mid-19th century [23]. Such has been the rate of development in this area during the second half of the 20th century that as many as 133 different architectures are now known [24], all of which are based upon vertex-sharing  $\text{SiO}_4$  and  $\text{AlO}_4$  tetrahedra, as in the example of faujasite shown in Figure 18.1. Their nomenclature is often confus-

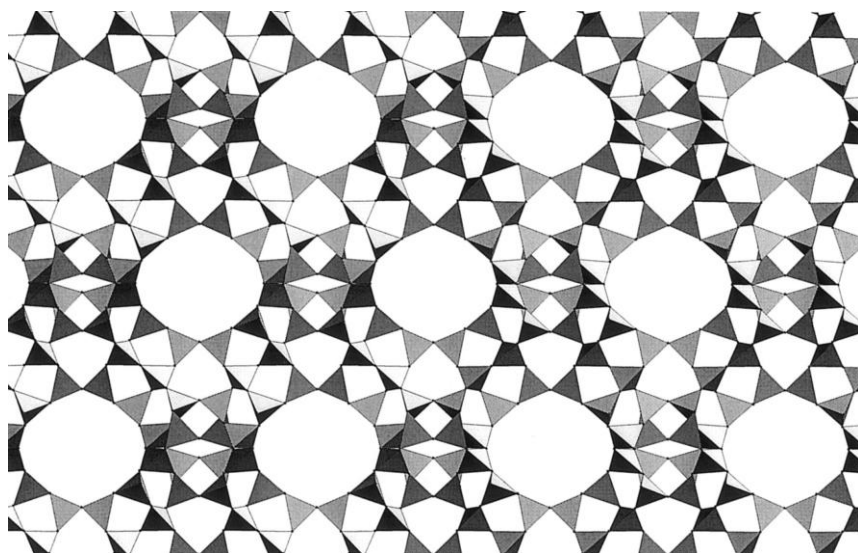


**Fig. 18.1.** The zeolite faujasite.  $\text{SiO}_4$  tetrahedra are represented in gray, and water molecules and extra-framework cations have been omitted for clarity.

**Tab. 18.1.** Examples of nanoporous aluminosilicates, giving the three letter IZA designations and a brief description of the pore systems.

<b>System</b>	<b>Pore System</b>
Sodalite family (SOD) (e.g. mineral and synthetic sodalites)	3-dimensional; 6-ring channels
Zeolite A family (LTA) (e.g. zeolites A, ZK-4; no mineral analogue)	3-dimensional; 8-ring channels
Chabazites (CHA) (e.g. mineral chabasites, SSZ-13)	3-dimensional; 8-ring channels
ZSM-5 (MFI) (e.g. mineral murataite, silicalite)	2-dimensional; 10-ring channels
Ferrierites (FER) (e.g. mineral and synthetic ferrierites)	2-dimensional; 10 & 8-ring channels
Faujasites (FAU) (e.g. mineral faujasite, zeolites LSX, X, Y, US-Y)	3-dimensional; 12-ring channels

ing, in spite of the fact that the International Zeolite Association has assigned a three letter code to each structure type, since many materials are more commonly known by acronyms chosen by the laboratory in which they were discovered. Pore sizes range from about 0.2 nm in the case of sodalites (SOD), in which the largest channel has rings containing 6 Si/Al sites (i.e. 6-rings), to about 1 nm in so-called UTD-1 which has a 14-ring channel [25]; some common examples are given in Table 18.1. The majority of the systems with large channels contain rings with even numbers of T sites ( $T = \text{Si, Al}$ ), e.g. 8-, 10-, 12- or 14-rings, but a recent X-ray diffraction study found both 7- and 9-rings in the high silica zeolite, SSZ-23 [26].

Industrial interest in these materials has been driven by their excellent ion-exchange properties in the hydrated state, and by the exciting adsorption and catalytic properties exhibited by their dehydrated forms. Indeed, it is for this reason that many of the most eye-catching synthetic discoveries have been made in industrial laboratories, such as those of Mobil, Union Carbide (now UOP), British Petroleum and Exxon. Table 18.2 summarizes some of the most important actual and prospective applications. Commercial production of zeolites was approximately one million tons in 1999, most of which was accounted for by the applications in catalytic cracking, xylene isomerization, and detergency. This pattern is gradually changing, however, as new applications are developed.

Hydrated, low-silica zeolites, such as natural clinoptilolite (HEU) and phillipsite (PHI), and synthetic sodium zeolite A (LTA), are used widely for ion-exchange applications, where their high cation content leads to high exchange capacities. In the case of detergency, for example, the sodium form of zeolite A is used to remove magnesium and calcium from hard water. The higher affinity of the zeolite for  $\text{Ca}^{2+}$  and  $\text{Mg}^{2+}$  versus  $\text{Na}^{+}$  is an important consideration in the choice of this material. Other factors, such as cost and good kinetics, are also important. Dehydrated forms of the large pore, low-silica zeolites, such as zeolite X (FAU), are used in adsorption and separation applications, including non-cryogenic air separation (Li-zeolite X). The interaction between undercoordinated cations and sorbate molecules is a crucial feature of such processes. In air separation, for example, it is the

**Tab. 18.2.** Some important applications of aluminosilicate zeolites and other nanoporous materials.

**Well-established:**

- Ion-exchange using hydrated zeolites
  - Detergency (e.g. zeolites Na-A and Na-P)
  - Water softeners
  - Animal feeds
  - Radwaste remediation (e.g. Cs, Sr with clinoptilolite)
- Molecular sieving using dehydrated zeolites
  - Air separation ( $N_2$  from  $O_2$  with Li-LSX)
  - Drying agents (e.g. double glazing, a/c)
  - Sulfur removal from natural gas
  - Separation of HFCs (CFC substitutes)
- Catalysis with dehydrated zeolites
  - Catalytic cracking (gasoline production) – zeolite-Y derivatives
  - Xylene isomerization (for polyesters) – H-ZSM-5
  - Butene isomerization – H-FER
  - Methanol to gasoline – H-ZSM-5
  - Phenol to hydroquinone – Titanosilicates
  - Denox reactions – Cu-ZSM-5, Co-FER

**Future possibilities include:**

- Hydrogen storage
- Nano-composites for optoelectronics
- Sensors using zeolite thin films
- Stereo-selective polymerization
  - Contrast enhancement in MRI (e.g. Gd-Y)
  - Ship-in-bottle synthesis
  - Zeolite nanocrystals for delivery systems

affinity of the lithium for the dinitrogen molecule, which has a quadrupolar moment that is three times bigger than that of dioxygen, that provides the basis for the separation [27]. The low-silica materials are relatively unstable at high temperatures, so materials with high Si/Al ratios are preferred for catalytic applications. These include high-silica FAUs, such as ultrastabilized Y, and ZSM-5. Most of the catalytic processes are based upon acid catalyzed reactions in which the exchangeable cation of the zeolite is replaced by a proton that provides Brønsted acidity. In addition, the shape and size of the zeolite cavities leads to selectivity in the reaction, hence the term “shape-selective catalysts”. This is the case in the hydrocarbon cracking catalysts used in gasoline manufacture and the isomerization catalysts used in *p*-xylene production for polyester manufacture. In xylene production, it is the small size of the zeolite channels that favors the *p*-isomer over the *o*- and *m*-xylenes. Some of the new titanosilicates, such as ETS-1 (MFI), which contains framework titanium, exhibit redox activity and are being used for partial oxidation reactions involving phenols and hydrogen peroxide [18].

Naturally occurring zeolites normally have quite low Si/Al ratios, typically three or less, and it is often quite easy to make synthetic analogues of these materials

under hydrothermal conditions. For example, synthetic analogues of the mineral faujasite (FAU) can be made from reaction between sodium silicate and sodium aluminate under basic conditions at 60–150 °C. Variations in the temperature, charge-compensating cation, time of reaction, and the pH, amongst other variables, yield a variety of low-silica, aluminosilicate zeolites, though all such reactions are carried out under basic conditions. Post-synthesis modifications, such as steaming or treatment with silicon tetrachloride, have been developed to increase the Si/Al ratios of these materials. A major breakthrough in respect of the direct synthesis of high-silica materials took place in the 1970s with the development of synthetic routes involving the hydroxides of quaternary organic amines in place of the normal inorganic base. These organic amines, which normally play the role of template molecules or structure-directing agents, are incorporated into the final product where they replace the usual charge-compensating cations. They play two important roles: (i) the size and shape of the quaternary amine can lead to the creation of new pore structures which cannot be made in other ways; (ii) the large sizes of these cations, when compared with traditional metallic cations, means that they can only compensate for a relatively low framework charge, thus leading to the formation of high Si/Al materials. The organic cation can normally be removed from the zeolite by calcination, leaving behind the acid form of the zeolite (see above). A classical example is zeolite ZSM-5, which is made in the presence of tetramethylammonium cations, TMA [28]. Curiously, over 20 years after its synthesis in the laboratory, a natural analogue of ZSM-5, known as mutinaite, has recently been discovered [29]; its Si/Al ratio, equal to 7.6, is the highest found in any natural zeolite.

In addition to the aluminosilicates, some obvious synthetic analogues, such as borosilicates, gallosilicates and ferrisilicates, have also been explored. The borosilicates are more difficult to prepare, probably because the much smaller boron, with its tendency towards planar, three-fold coordination, is not an obvious substitute for the role of aluminum. Gallium and iron(III) materials, though, are well known and usually have properties similar to those of the aluminosilicates. There is evidence, however, for some unique behavior with gallosilicates, as in their ability to catalyze cyclization reactions and activate methane [30]. Other silicate-based systems include the titanosilicates, mentioned earlier, and some recently discovered vanadium silicates that show excellent thermal stability and can potentially be activated for catalysis [31].

Another interesting development has been the direct synthesis of pure silica materials with no exchangeable cations. The synthesis of the silica polymorphs, which include silicalite (MFI) [32] and siliceous ferrierite (FER) [33], may still require template molecules or structure-directing agents, and there is an interesting question as to how the charge of the quaternary amine is compensated in the absence of framework aluminum. Since they are completely ordered (once the organic has been removed), they provide excellent vehicles for detailed characterization by  $^{17}\text{O}$  and  $^{29}\text{Si}$  NMR studies [34], as well as for computer simulation studies [35]. They are also very interesting candidates in the context of low-dielectric materials for integrated circuit manufacturing [36] since they can be made defect free

and have up to nearly 50% pore volume. The pure silica zeolite polymorphs have remarkable stability and in some cases will survive calcination at 1000 °C.

## 18.4

### Open-Framework Metal Phosphates

#### 18.4.1

#### Aluminum Phosphates

The extensive development of nanoporous aluminosilicates has led to the search for new families of three-dimensional open frameworks. The aluminophosphates ( $\text{AlPO}_4$ ) were considered first since they are isoelectronic with  $\text{SiO}_2$  and can be regarded as the III–V analogues. Several allotropic forms of  $\text{AlPO}_4$  corresponding to condensed silica polymorphs are known, e.g. berlinite, which is analogous to  $\alpha$ -quartz. In such materials, aluminum and phosphorus are observed in tetrahedral coordination, as in the silicas. From these considerations, Flanigen and co-workers at Union Carbide Corporation discovered a new generation of nanoporous aluminophosphate materials,  $\text{AlPO}_4\text{-}n$  ( $n$  refers to a structural type), in the early 1980s [2]. These materials, and related ones made subsequently, are the subject of this section.

The synthetic procedure is similar to that used for zeolites: the aluminophosphates are prepared hydrothermally under autogeneous pressure in the temperature range 100–250 °C. They are typically obtained from a mixture of aluminum oxyhydroxide or alkoxide and phosphoric acid in water, leading to the formation of an aluminophosphate gel. An amine or quaternary ammonium salt, which plays a templating or structure-directing role, is then added to the mixture. The crystallisation time depends on multiple variables such as temperature, reactant composition, and structural type, and ranges from several hours up to several weeks. The pH of the reaction, which is less than that observed in zeolite synthesis, varies within the range from 3 to 10 and goes towards neutral values at the end of the reaction. The organic molecule, which is trapped within the pores, plays a critical role in producing the open framework, and in the absence of such a molecule, only dense  $\text{AlPO}_4$  or  $\text{AlPO}_4 \cdot n\text{H}_2\text{O}$  hydrates are formed. The thermal stability of the open-framework solids is similar to that obtained for zeolites and the template can often be removed by calcination in air at 500–600 °C. In the  $\text{AlPO}_4\text{-}n$  series, the Al/P ratio is 1 and the frameworks are electrostatically neutral. A typical example,  $\text{AlPO}_4\text{-}5$  [37], is shown in Figure 18.2.

Elements with different valences can be incorporated into  $\text{AlPO}_4$  frameworks in order to modify the chemical properties for catalysis, ion-exchange and so on. In this respect, Union Carbide researchers synthesized several new series of materials, in particular the silicoaluminophosphates ( $\text{SAPO-n}$ ) [38], metalaluminophosphates ( $\text{MePO-n}$ ) and metalsilicoaluminophosphates ( $\text{MeAPSO-n}$ ) [39]. The strategy was first to explore the divalent cations of the periodic table which can adopt tetrahedral coordination (e.g.  $\text{Me} = \text{Mg}^{2+}$ ,  $\text{Mn}^{2+}$ ,  $\text{Fe}^{2+}$ ,  $\text{Co}^{2+}$  and  $\text{Zn}^{2+}$ ). The

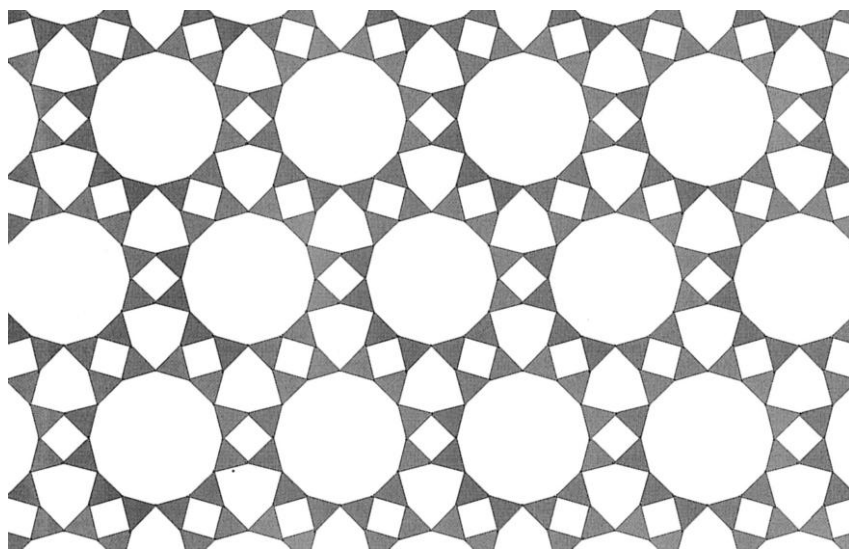


**Fig. 18.2.** The aluminophosphate AlPO-5.  $\text{AlO}_4$  and  $\text{PO}_4$  tetrahedra, which are strictly alternating, are represented in gray, and water molecules have been omitted for clarity.

weakly acidic pH used in the reaction prevents the precipitation of the metals into hydroxides or oxides and facilitates their partial incorporation into the inorganic framework. These phases have framework compositions of general formula  $(\text{Si}_x\text{Me}_w\text{Al}_y\text{P}_z)\text{O}_2$ , where  $x$  varies from 0 to 0.20 and  $w$  from 0 to 0.25. The silicon substitutes preferentially at the phosphorus site whereas the metal substitutes exclusively for the aluminum. The introduction of these elements renders the frameworks negative and therefore requires charge-compensating cations, as in the aluminosilicate zeolites. When these cations are protons, the materials exhibit acid catalytic properties that vary as a function of the structural type and the nature of the substituting element [40].

From the structural point of view, the microporous aluminophosphate-based compounds include more than 40 different framework types. As in the zeolites, the three-dimensional structure is delimited by channels and cavities where the templating agent is located. However, there are some differences compared with the topologies encountered in the zeolite family. The majority of the aluminophosphate-based solids exhibit networks with alternating Al and P on tetrahedral sites. This rule limits the structural possibilities because rings must be formed by even numbers of T atoms, thus preventing the occurrence, for example, of 5-ring units. Thus, no  $\text{AlPO}_4$  exists with the MFI type structure, which contains 5-ring units.

The occurrence of coordination numbers greater than four for the aluminum is another feature of the phosphate-based solids in comparison with the zeolites. For example, in some phases aluminum adopts five-fold (trigonal bipyramidal) or six-fold (octahedral) coordination. In these cases, anionic species such as hydroxy or



water groups complete the coordination sphere of the aluminum, leading to connection modes already encountered in mineral aluminophosphates in which  $\text{AlO}_n$  polyhedra may share corners or edges through Al–O–Al linkages. It can also result in the formation of odd-numbered rings. The channel size appears to be limited as a consequence of the increase of the aluminum coordination, which thus seems to be a drawback for producing large pores.

Several studies have explored the use of non-aqueous solvents, mainly alcohols (butanol, triethylene glycol, etc.), for the synthesis of open framework aluminum phosphates [41]. Better crystallization is generally observed, which is helpful for X-ray structural characterization. In many cases, low-dimensional AlPOs [42, 43] have been obtained, corresponding to several series of layered and chain solids, with P:Al ratios ranging from 4:3 to 2:1, in which the interlamellar or interchain space is occupied by organic cations. In a recent examination of the formation of aluminophosphates under non-aqueous conditions, Ozin and co-workers [44] have suggested that intermediates based upon one-dimensional chains could be involved in the crystallization of two-dimensional porous layers and finally the three-dimensional open framework materials. We shall show in the following sections that the versatility of aluminum phosphates in terms of dimensionality is a common feature of systems that are prone to form open-framework architectures. The other feature is the P:Al ratio, which often differs from unity in phases obtained from non-aqueous solvents. All of the  $\text{AlO}_4$  tetrahedra share their vertices, but this is not the case for the phosphate groups, some of which exhibit terminal P–OH bonds giving rise to an interrupted framework.

The use of fluoride in phosphate synthesis was first used by Kessler and co-workers [45, 46]. When fluorine is present in the final structure, it can adopt specific configurations in which certain  $\text{AlPO}_4$  structural types are essentially preserved. For example, in  $\text{AlPO}_4\cdot 5$  (AFI) [47] the fluorine is located in the 4-ring columns between two 4-rings. It is linked to two aluminum atoms with rather long distances (Al–F 0.219 nm). Similarly, in the aluminophosphate analogues of zeolites chabazite (CHA) and gismondine (GIS), two fluorines bridge two aluminum atoms across the 4-ring units, rendering them octahedrally coordinated rather than tetrahedrally coordinated as in the aluminosilicate forms. The most exciting feature of the fluorine method is its use in the synthesis of new aluminophosphate architectures incorporating fluorine atoms into the open framework. Two situations are found for the fluorine. First, it seems to stabilize the double 4-ring cage (D4R), i.e. a cube in which the corners are occupied by  $\text{TO}_4$  tetrahedra. The occurrence of this octameric unit is found in aluminophosphates such as  $\text{AlPO}_4\cdot 16$  (AST) [48] synthesized in the presence of hydrofluoric acid. This building unit has also been prepared as an isolated cluster in Mu-1 [49] and as linear chains in Mu-3 [50].

Alternatively, fluorine can participate more directly in the coordination sphere of the metal and increase the coordination number from V to VI. Studies performed by Férey and co-workers [51, 52] in Le Mans gave rise to a new series of oxyfluorinated phosphates called ULM-*n*. In this family, the basic building unit can be either tetramers, as is usually found in the crystal chemistry of phosphates [53],

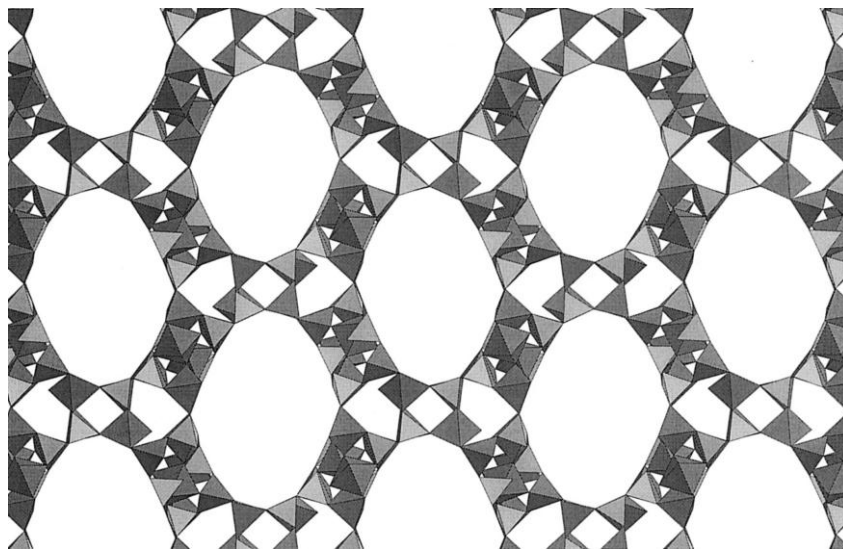


**Fig. 18.3.** The gallophosphate ULM-5. Gallium polyhedra are shown in gray and  $\text{PO}_4$  tetrahedra are represented in light gray. Water molecules and the organic template have been omitted for clarity.

or hexamers. For the tetramers, the connection of the metal atom is via fluorine corner- or edge-sharing. The hexameric unit is quite common in fluorinated materials. It is composed of a central Al octahedron linked to two Al trigonal bipyramids, via fluorine. This trimer is capped by three phosphate groups. The connection of these hexamers generates different packing structures, such as ULM-3 or ULM-4 where the channels are delimited by 10-rings windows. The hexameric unit can be found with other building blocks, such as the D4R cage in ULM-5 (Figure 18.3) [54]. The other feature of fluorinated materials is that fluorine in the framework creates anchoring points for the N–H groups of the amines as a result of strong hydrogen bonding.

#### 18.4.2

#### Phosphates of Gallium and Indium

In the mid-1980s, research was extended to microporous phosphates in which other elements completely replace the aluminum. For example, Parise [55–56] described the synthesis of several gallophosphates which are related to the  $\text{AlPO}_4$ -*n* family. There is now a vast family of such materials, some of which exhibit unique topologies. The gallium can be found in 4-, 5- and 6-fold coordination, as in the aluminum compounds, though there is a general trend for the coordination numbers to be higher than with Al.

The use of fluoride in the synthesis of open-framework GaPOs has been ex-

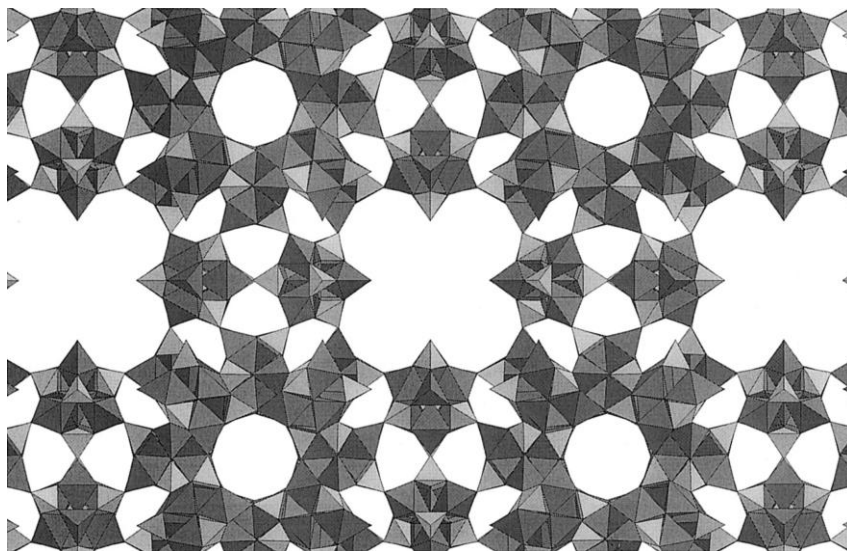


**Fig. 18.4.** The gallophosphate cloverite. Gallium polyhedra are shown in gray and  $\text{PO}_4$  tetrahedra are represented in light gray. Water molecules and the organic template have been omitted for clarity.

tremely productive. The most striking example was the discovery of cloverite (Figure 18.4) [57] a gallophosphate with extra large pore openings comprising 20  $\text{TO}_4$  units and a three-dimensional channel system similar to that in faujasite-type zeolites. The expected pore size is 1.32 nm, but the effective diameter is limited by the presence of terminal hydroxy groups pointing towards the centers of the channels.

The aluminum and gallium phosphates confirm that it is possible to produce open, three-dimensional architectures with metallic atoms in four-, five- or six-fold coordination. Indium, therefore, represents an interesting case since, by comparison with the smaller Al or Ga, which can adopt three types of coordination, it is only expected to occur with octahedral coordination. This has been confirmed in several examples. In the first report of an organically templated indium phosphate, Haushalter [58] described a new open-framework,  $\text{H}_3\text{NCH}_2\text{CH}_2\text{NH}_3$   $[\text{In}_2(\text{HPO}_4)_4]$ , obtained with ethylenediamine. This work was followed by several other examples incorporating various amine molecules, including a pillared layer structure obtained with imidazole [59]. As with the aluminum and gallium phosphates, the use of fluoride has yielded interesting results with indium.

#### 18.4.3

##### **Tin(II) Phosphates and Antimony(III) Phosphates**

Since the first report in 1997 [60], a large number of tin(II) phosphate frameworks with different dimensionalities have been reported. Tin(II) is mainly found in

three-fold coordination, connected to three phosphorus atoms via bridging oxygens located at the vertices of a trigonal pyramid; the lone pair occupies the fourth vertex of a hypothetical tetrahedron. For three-dimensional systems based on the alternation of  $\text{PO}_4$  tetrahedra and  $\text{SnO}_3$  trigonal pyramids, this yields a framework of general formula  $[\text{Sn}_4\text{P}_3\text{O}_{12}]^-$  with pores in which the organic amine species are occluded [61]. The channels found to date include both 8- and 12-rings, but the effective size for accessibility is smaller than anticipated due to the hindrance of the lone pair of electrons pointing towards the centers of the channels. In the oxophosphate phase,  $\text{SnOPO-1}$  [62], the Sn:P ratio is 2:1 and tin atoms are connected together via a common oxygen atom which coordinates three tin atoms. In a system with a Sn:P ratio of 3:2, the presence of both trigonal pyramidal  $\text{SnO}_3$  and square pyramidal  $\text{SnO}_4$  units also results in Sn–O–Sn linkages [63]. As in the AlPO systems, monomeric, chain, layered and 3-D structures have also been observed, and there is evidence that a simple tetramer,  $\text{Sn}_2\text{P}_2\text{O}_8$ , may be a fundamental building unit in many of these structures [64].

The discovery of the tin(II) phosphate family led to the search for other systems containing lone pair cations, such as antimony(III). This indeed has turned out to be feasible, and an extensive range of antimony(III) phosphates and fluorophosphates has been discovered [65]. As with the tin compounds, the structures appear to be open but the presence of lone pairs protruding into the cavities reduces their porosity.

#### 18.4.4

#### Transition Metal Phosphates

Following the successful introduction of transition metals into the zeolitic AlPOs and GaPOs and the parallel discovery of open framework solids with polyhedral coordinations larger than four, it was natural that workers in this field should attempt to synthesize open-framework transition metal phosphates. The presentation will follow a chronological sequence.

##### 18.4.4.1 Molybdenum and Vanadium Phosphates

By using hydrothermal techniques in combination with large removable cations, Haushalter et al. [66] successfully prepared some MoPOs with open frameworks. Typical reactions involved a molybdenum source ( $\text{MoO}_3 + \text{Mo}$  or  $\text{MoCl}_5$ ), phosphoric acid and an organic cationic template heated in an autoclave between 200 and 400 °C. Several open framework solids were synthesized in this way by changing the nature of the template; they contain a variety of cluster units, such as tetramers and octamers, but have relatively poor thermal stability [67, 68].

Vanadium phosphates were made in an analogous manner by Haushalter and Férey. The association of different vanadium valence states (V, IV, III) with their various polyhedra (tetrahedra, square pyramids, distorted and regular octahedra) leads to a very large diversity for the interesting structures. Some eye-catching results originate from this research, including the first evidence of an inorganic double helix in  $[(\text{CH}_3)_2\text{NH}_2]\text{K}_4[\text{V}_{10}\text{O}_{10}(\text{H}_2\text{O})_2(\text{OH})_4(\text{PO}_4)_7] \times 4\text{H}_2\text{O}$  [69] and the

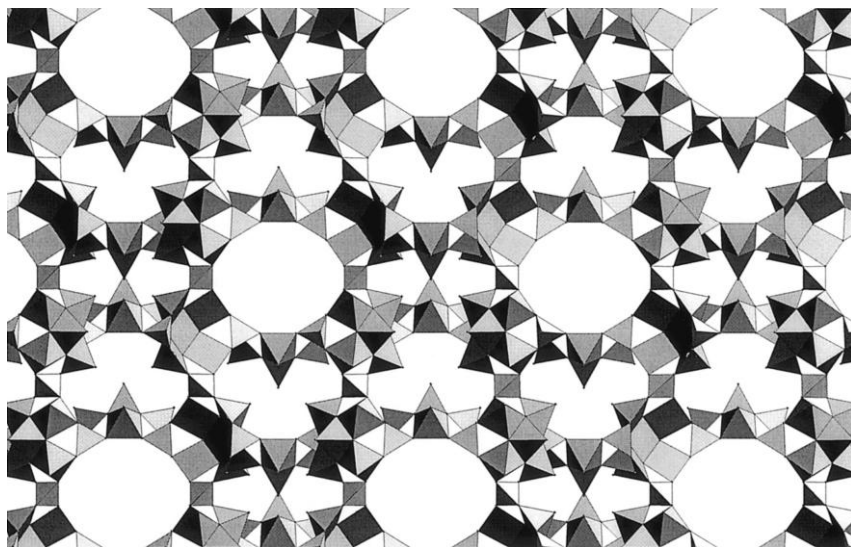


**Fig. 18.5.** The vanadium phosphate  $\text{Cs}_3[\text{V}_5\text{O}_9(\text{PO}_4)_2]$ . Vanadium polyhedra are shown in gray and  $\text{PO}_4$  tetrahedra are represented in light gray. Water molecules have been omitted for clarity.

existence of giant voids in the two square pyramidal-tetrahedral framework vanadium phosphates  $\text{Cs}_3[\text{V}_5\text{O}_9(\text{PO}_4)_2] \times \text{H}_2\text{O}$  and  $[\text{HN}(\text{CH}_2-\text{CH}_2)_3\text{NH}]\text{K}_{1.35}[\text{V}_5\text{O}_9(\text{PO}_4)_2] \times \text{H}_2\text{O}$  [70]. The former (Figure 18.5) contains units already encountered in molecular chemistry with the famous vanadium clusters described by Müller [71]. This material is made from a continuous framework composed of  $\text{V}_5\text{O}_9$  clusters bridged by phosphate into a 3D fcc lattice. Large, roughly cubic cages (1.4 nm in diameter) are connected by 12-ring windows (0.73 nm free diameter). The system is particularly noteworthy as one of the few transition metal phosphates that dehydrates without pore collapse.

All of the above compounds are oxides. The application of the fluorine route already described for AlPOs and GaPOs has shown that it is also possible to obtain open framework structures with fluoride in the VPOs. This led to the discovery by Riou and Férey [72] of the first open-framework fluorovanado(V)phosphate, ULM-7 or  $(\text{H}_3\text{N}(\text{CH}_2-\text{CH}_2)\text{NH}_3)[(\text{V}^{\text{V}}\text{O}_2)_2(\text{PO}_4)\text{F}]$ , in which the building units are  $\text{V}_2\text{P}$  trimers. Vanadium exhibits both octahedral and square pyramidal coordination, and fluoride ion is shared between them. The three-dimensional network generated by corner-sharing of these trimers, exhibits 10-membered rings occupied by diprotonated amines.

#### 18.4.4.2 Iron Phosphates

In the mineral kingdom, iron phosphates are among the most important materials besides silicates and aluminates. The most striking example of an open framework

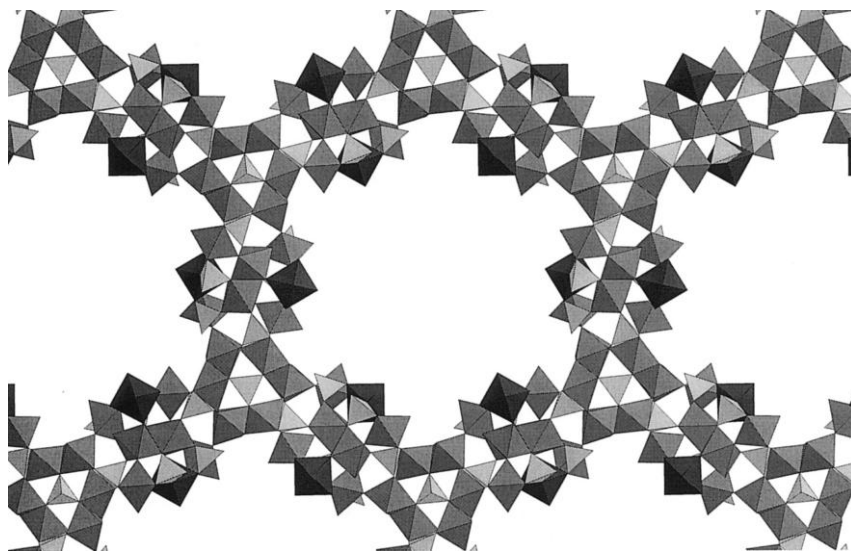


**Fig. 18.6.** The iron phosphate mineral cacoenite.  $\text{FeO}_6$  octahedra are shown in gray and  $\text{AlO}_4$  and  $\text{PO}_4$  tetrahedra are represented in light gray. Water molecules are omitted for clarity.

iron phosphate is provided by the mineral cacoenite [73],  $[\text{AlFe}_{24}(\text{OH})_{12}(\text{PO}_4)_{17} \cdot (\text{H}_2\text{O})_{24}] \cdot 51\text{H}_2\text{O}$ , (Figure 18.6) which contains cylindrical tunnels occupied by water molecules, with a free diameter of 1.42 nm. The first synthetic analogues, those of the minerals hureaulite and alluaudite, were described by Cheetham et al. in 1986 [74] and opened the way for synthetic open-framework iron phosphates whose applications in catalysis could be very important. For example, dense iron phosphates are used as the selective catalysts during the oxidative dehydrogenation of isobutyric acid into methacrylic acid.

Paradoxically, and at variance with the other families, the first synthetic, open-framework iron phosphates containing organic cations in the pores were not pure oxides, but oxide-fluorides obtained by using the fluorine route already described. The first of them, ULM-12 or  $\text{N}_2\text{C}_6\text{H}_{14}[\text{Fe}_4(\text{PO}_4)_4(\text{H}_2\text{O})_3\text{F}_2]$ , was discovered in 1996 [75]. Other oxyfluorinated compounds followed in large numbers, but the first all oxide homologues were synthesized in 1997 by Lii in Taiwan [76].

The main interest in the fluoroferric phosphates concerns their magnetic properties. Despite the existence of isolated clusters linked by phosphate groups, three-dimensional magnetic ordering takes place in the range 15–40 K, with either antiferro- or ferrimagnetic properties. They open the way to a new class of open framework solids that combine the well known sieving properties with magnetic properties; these might be used for magnetic separation if the ordering temperatures reached are sufficiently high.



#### 18.4.4.3 Cobalt(II) and Manganese Phosphates

Cobalt(II) has a special place in the open framework family because it is one of the few transition metal cations that easily exhibits tetrahedral coordination, in addition to five and sixfold ones. Moreover, magnetic couplings can give rise to interesting magnetic properties, similar to those described above for iron. Furthermore, it is well known that Co doping enhances the catalytic performance of certain zeolites and related compounds. For instance, CoAPO-5 and CoAPO-11 have been used for the autoxidation of cyclohexane [77] and *p*-cresol [78].

Recently, a substantial effort was made to synthesize pure cobalt phosphates with an open framework, using either inorganic or organic templates. The first success [79] concerned the pseudo-tetragonal three-dimensional  $\text{CoPO}_4 \cdot 0.5\text{C}_2\text{H}_{10}\text{N}_2$ . The framework consists of three systems of channels with eight-membered windows limited by Co and P tetrahedra in strict alternation. The dimensions are  $0.39 \times 0.47 \text{ nm}^2$ , and the compound becomes antiferromagnetic at 2 K. The three-dimensional character exists only with ethylenediamine. As soon as the length of the carbon chain increases (e.g. 1,3-diaminopropane and 1,4-diaminobutane), the solids become two dimensional [80] with planes built up from corner sharing trans chains of  $\text{Co}^{2+}$  tetrahedra linked by phosphate groups.

Subsequently, Stucky's group [81], being aware that the tremendous success with the aluminophosphate system was in part due to the initial recognition of structural analogies between  $\text{AlPO}_4$  and  $\text{SiO}_2$ , sought to determine if the same analogies also exist between cobalt phosphates and aluminosilicate minerals. This design approach led them to characterize, using alkali ( $\text{M} = \text{Na}, \text{K}, \text{Rb}$ ) and  $\text{NH}_4^+$  ions, chiral tetrahedral  $\text{MCoPO}_4$  cobalt phosphates. They exhibit either the zeolite Li-ABW structure type with  $\text{NH}_4^+$  and Rb, or a hexagonal structure, intermediate between the ABW and tridymite structures, with Na, K, and  $\text{NH}_4^+$ . The latter shows 6-ring channels. This paper clearly shows the difficulty of the corresponding chemistry and underlines the drastic influence of pH and the nature of the solvent on the synthesis of the desired products. Despite the usually antiferromagnetic behavior of these  $\text{CoPO}_4$  materials, the sodium compound is ferromagnetic at 2 K.

Manganese phosphates with an open framework are very scarce, but the chemistry of new phases in this area is emerging with some recent reports of organically-templated, layered manganese phosphates [82, 83] and a three-dimensional system with narrow channels,  $\text{NH}_4\text{MnPO}_4$ , which orders ferromagnetically at  $\sim 17 \text{ K}$  [84].

#### 18.4.4.4 Copper and Nickel Phosphates

While open-framework copper phosphates have proven difficult to prepare using conventional hydro/solvothermal reactions, Hwu and coworkers have developed a novel approach using molten salt fluxes to synthesize several microporous copper phosphates. Examples have been prepared with salt occupying relatively large channels in several different structure types [85, 86], including homochiral single crystals [87]. In at least one of these compounds, the salt can be replaced with water (except for some  $\text{Cs}^+$  cations necessary for charge balance), resulting in an

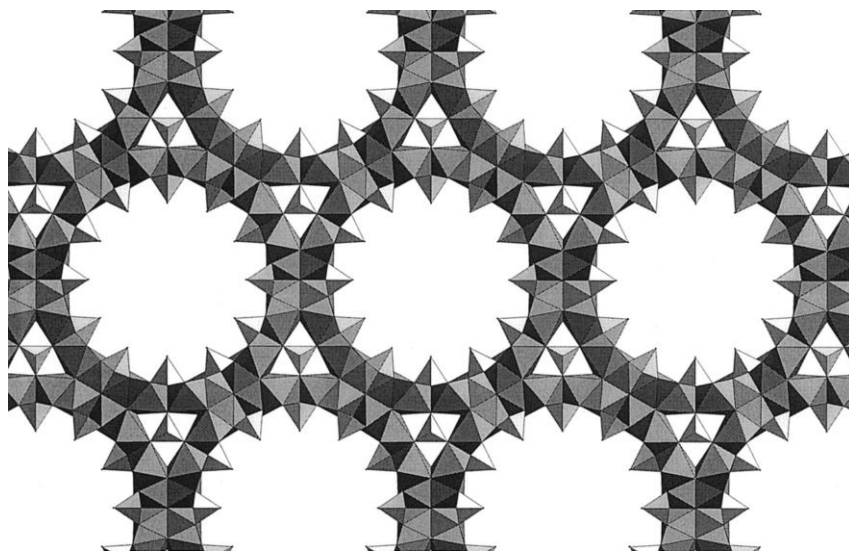


**Fig. 18.7.** The nickel phosphate VSB-1.  $\text{NiO}_6$  octahedra are shown in gray and  $\text{PO}_4$  tetrahedra are represented in light gray. Water molecules, extra-framework cations, and partial occupancy are omitted for clarity.

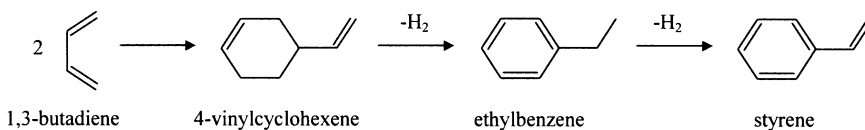
apparently porous material [85]. These materials demonstrate that compounds with very open architectures may be prepared through high temperature reactions, offering materials scientists an alternative tool for the synthesis of porous compounds.

Recent work in Versailles and Santa Barbara has led to the synthesis of several nanoporous nickel(II) phosphates. A zeolitic nickel(II) phosphate, VSB-1 (Versailles/Santa Barbara-1), was prepared under simple hydrothermal conditions [22] and has a unidimensional pore system delineated by 24  $\text{NiO}_6$  and  $\text{PO}_4$  polyhedra with a free diameter of approximately 0.9 nm (Figure 18.7). It becomes microporous on calcination in air at 350 °C, yielding BET surface areas up to 160 m<sup>2</sup> g<sup>-1</sup>, and is stable in air to approximately 500 °C. The surface area appears low compared with aluminosilicate zeolites, but the density of VSB-1 is twice that of a zeolite and the channel walls are particularly thick. VSB-1 can be prepared in both ammonium and potassium forms, and exhibits ion-exchange properties that lead, for example, to the formation of the lithium and sodium derivatives. Other cations (e.g. Mn, Fe, Co, and Zn) can be substituted for Ni in VSB-1, up to a level as high as 30 atomic%. The parent compound shows canted antiferromagnetic order at  $T_N = 10.5$  K with  $\theta = -71$  K; on doping with Fe,  $T_N$  increases to 20 K and  $\theta$  decreases to  $-108$  K.

The catalytic properties of VSB-1 turn out to be very interesting. In terms of acid



catalysis, which is widely found with the aluminosilicate zeolites, VSB-1 shows little reactivity. However, it exhibits excellent stability and high selectivity (>80%) for the dehydrocyclodimerization of 1,3-butadiene to ethylbenzene (see scheme below) [88]. The catalytic performance is ascribed to the bifunctional role of VSB-1, i.e. the dehydrogenation ability of Ni species and the concentration effect of the nanoporous structure. The absence of acidity is a virtue in this case because it suppresses the formation of oligomeric products.



Synthesis under alkaline rather than acidic conditions yields a second NiPO (designated VSB-5) that is quite different from VSB-1 in a number of respects [89]. The unit cell is again hexagonal, but the composition is quite different ( $\text{Ni}_{20}[(\text{OH})_{12}(\text{H}_2\text{O})_6][(\text{HPO}_4)_4(\text{PO}_4)_8] \cdot 12\text{H}_2\text{O}$ ) and the BET surface area is much higher ( $500 \text{ m}^2 \text{ g}^{-1}$ ). Like VSB-1, it is stable in air to approximately  $500^\circ\text{C}$ , but the framework is neutral and there are no exchangeable cations. Catalytic measurements with VSB-5 reveal both the high activity and the basic character of the catalyst. For example, it functions as an excellent partial hydrogenation catalyst, converting butadiene selectively into butenes rather than butane. It also exhibits excellent affinity for adsorbing hydrogen, with evidence from neutron scattering for a direct Ni–hydrogen interaction [90].

In spite of their highly open structures, both materials may be synthesized without structure directing agents. Since most transition metal phosphates containing template molecules typically cannot be calcined without pore collapse, template-free synthesis appears to be the most promising direction for the formation of new porous materials. The exciting properties observed in the VSB family are likely glimpses of what may occur in other transition metal phosphate systems once thermal stability problems are overcome.

#### 18.4.4.5 Zirconium and Titanium Phosphates

With tetravalent cations, synthesis often leads to two-dimensional phosphates, as is clearly shown by the work of Clearfield on the zirconium phosphates [91]. However, the fluorine route has very recently led to the first zirconium phosphates with three-dimensional open framework structures [92, 93]. For example,  $[(\text{enH}_2)_{0.5}] \cdot [\text{Zr}_4\text{}_2(\text{PO}_4)_2(\text{HPO}_4)\text{F}] \cdot \text{H}_2\text{O}$  exhibits eight-membered tunnels formed by strict Zr–P alternation. The Zr octahedra are of two types:  $\text{ZrO}_6$  and  $\text{ZrO}_5\text{F}$ , the Zr–F bond being terminal. The same method, applied to titanium, very recently led [94] to a mixed valence fluorinated titanium phosphate with seven-membered channels. In a non-fluorinated medium, a new phosphate,  $\rho\text{-TiP}$ , has been also found [95], with three types of tunnels (4-, 6-, 8-membered rings).

## 18.5

## Chalcogenides, Halides, Nitrides and Oxides

## 18.5.1

## Sulfides and Selenides

The known classes of open-framework materials are overwhelmingly dominated by oxide or mixed oxide/fluoride matrices. In 1989, however, Bedard and co-workers of UOP [96] proposed to extend this class of materials to metal sulfide compounds. Metals exhibiting tetrahedral coordination in sulfides were considered first in order to imitate the crystal chemistry of the zeolites and nanoporous aluminophosphates. In the original paper, only germanium (IV) and tin (IV) sulfides were described, but the preparation of antimony (III) [97] and indium (III) [98] sulfides was subsequently reported by Parise. These compounds are obtained under hydrothermal conditions in a similar way to zeolites and other derivatives. The reaction is carried out with a mixture of metal sulfide (or metal + sulfur) and an amine or quaternary alkylammonium species that is heated at temperatures from 25 to 18 °C for several days. In some preparations, the organic template is used in the carbonate or hydrogenosulfide ( $\text{HS}^-$ ) form, rather than the hydroxide; this appears to give rise to a mineralizer effect. By changing the nature of the organic species, new open-frameworks have been isolated and different configurations of building units have been observed, depending on the elements.

The reaction of germanium sulfide with organic amines frequently leads to the formation of amine germanium sulfides containing clusters of  $[\text{Ge}_4\text{S}_{10}]^{4-}$  which may be found isolated or in low-dimensional compounds such as DPA-GS-8 [99]. This kind of tetrameric unit is quite common in germanium sulfide chemistry and is related to the structure of adamantane. The four germanium atoms are tetrahedrally coordinated by sulfur atoms and are connected by corner-sharing. This unit can be viewed as a tetrahedron in which germanium occupies each corner and is reminiscent of the tetrahedral units  $[\text{SiO}_4]^{4-}$  observed in silicates. The production of three-dimensional networks is carried out by using an additional metal that furnishes the connection between the  $\text{Ge}_4\text{S}_{10}$  adamantine units. The utilization of several metals, including Mn, Fe, Co, Ni, Cu, Zn, and Ga [96, 100], has been reported. Yaghi and co-workers [101] have proposed an alternative route for the synthesis of these sulfides. They can crystallize from the diffusion of an aqueous solution containing the 3d metal into a solution of a  $\text{Ge}_4\text{S}_{10}[\text{amine}]$  complex at room temperature. In the case of copper(I), for example, the  $\text{Ge}_4\text{S}_{10}$  tetrahedral clusters are bridged by the Cu(I) cations which can be in linear 2-fold coordination ( $\text{CuS}_2$ ) or trigonal planar 3-fold coordination ( $\text{CuS}_3$ ).

Little is known about the properties and potential applications of the open-framework chalcogenides, though Jiang et al. [102, 103] have recently described the adsorption and spectroscopic properties of some of the layered tin sulfides belonging to this family of materials.

## 18.5.2

**Halides**

In 1997, Martin and Greenwood [104] introduced a new generation of microporous compounds utilizing halides as replacements for the normal oxygen or chalcogenide anions. New materials were formed from metal halides such as zinc dichloride and copper chloride; Zn and Cu are both known to exhibit tetrahedral geometries with chlorine. Three compounds, named CZX-*n*, have been synthesized under solvothermal conditions (160 °C) in benzene. The framework of CZX-1 is isostructural with the aluminosilicate sodalite (SOD), while CZX-2 and CZX-3 adopt new framework topologies. All three structures are based on  $\text{ZnCl}_4$  and  $\text{CuCl}_4$  tetrahedra sharing corners, as in the aluminosilicate zeolites, and the organic molecules are trapped in the micropores. One interesting property of these microporous halides is their high capacity to adsorb methanol into the framework. They can adsorb up to three equivalents per framework unit, but the addition of more methanol results in dissolution of the structure and the formation of a colloidal solution.

## 18.5.3

**Nitrides**

The existence of condensed framework structures based upon ceramic nitrides, e.g. the silicon nitrides of composition  $\text{Si}_3\text{N}_4$ , led to the idea that the synthesis of open-framework nitrides might also be feasible. The first success in this area was the preparation of the phosphorus nitride,  $\text{Zn}_7[\text{P}_{12}\text{N}_{24}]\text{Cl}_2$ , by Schnick in 1992 [105]. This was achieved by means of a high temperature (7–800 °C) solid state reaction between  $\text{ZnCl}_2$  and  $\text{HPN}_2$ , and yielded a small pore open-framework with the sodalite structure. A similar reaction, in which a source of oxygen ( $\text{OP}(\text{NH}_2)_3$ ) was also included in the reaction mixture, has more recently led to the discovery of a phosphorus oxonitride with the same structure [106]. The preparation of open-framework silicon nitrides requires more severe conditions, but Schnick successfully achieved this objective in 1997 with the synthesis of the small pore, zeolitic  $\text{Ba}_2\text{Nd}_7\text{Si}_{11}\text{N}_{23}$  [107]. In this instance, reaction between the metals and silicon imide,  $\text{Si}(\text{NH})_2$ , under a nitrogen atmosphere in an RF furnace operating at temperatures between 900 and 1650 °C, was necessary. By analogy with the progress in other areas, it seems probable that much milder reaction conditions will be necessary if the preparation of large pore nitrides is to be achieved.

## 18.5.4

**Binary Metal Oxides**

Whereas the development of crystalline, open-frameworks based upon silicates, phosphates and related materials has progressed at an ever increasing pace, the synthesis of simple binary oxides with periodic open structures has been less suc-

cessful to date. An obvious exception to this generalization, however, is the case of  $\text{MnO}_2$ , which is known to exhibit small channels up to about 0.7 nm in diameter in the minerals hollandite, cryptomelane, and todorokite. Synthetic analogues of these minerals have been made [108, 109] in the presence of metallic cations (M) such as  $\text{Mn}^{2+}$ ,  $\text{Ni}^{2+}$ ,  $\text{Cu}^{2+}$  and  $\text{Zn}^{2+}$ . They are based upon a structural principle in which octahedral  $\text{MnO}_6$  units share edges and the metallic cations occupy the channels, and correspond to a stoichiometry of  $\text{M}_x\text{MnO}_2 \cdot n\text{H}_2\text{O}$  in the as-synthesized form. As a consequence, these are mixed valence materials with a manganese oxidation state typically in the range 3.5–3.8, and they show a variety of interesting electronic, magnetic, and catalytic properties. A small concentration of manganese vacancies is often observed, and a limited amount of manganese substitution is also possible. The water of hydration can be removed at temperatures up to about 500 °C, yielding nanoporous materials which will adsorb small organics such as cyclohexane.

The existence of these stable, open-frameworks in the specific case of manganese is presumably related to the high ligand field stabilization energy associated with the  $t_{2g}^3$  electronic configuration of  $\text{Mn}^{4+}$ . This should render the materials kinetically stable with respect to their collapse into more condensed phases. It is also, no doubt, the reason why it has been possible to make stable mesoporous phases based upon  $\text{MnO}_2$ , and indeed to remove the surfactant templates in order to access their microporosity [110].

#### 18.5.5

##### Sulfates

Given the many examples of open-framework metal phosphates, it is not surprising that sulfates are now being explored as possible open-framework materials. Synthesis strategies suitable for preparing open-framework materials are still being proposed [111], but hydro/solvothermal conditions similar to those used to make phosphates are currently being employed. Although open-framework materials with three-dimensional architectures have not yet been prepared, one- and two-dimensional examples of V [112], Fe [113, 114], Cd [115], La [116], and U [117] sulfates have now been synthesized. Each of these examples incorporates the same types of amine molecules commonly used to template metal phosphates, suggesting that porous materials may be achievable. Interesting polyhedral networks are also possible. Rao and coworkers, for example, have discovered an iron fluorosulfate [114] exhibiting a distorted Kagome lattice. This relatively rare example exhibits magnetic hysteresis at low temperatures, which has not previously been observed for undistorted examples.

#### 18.6

##### Hybrid Nanoporous Materials

The rapid and eye-catching developments in the area of nanoporous inorganic materials over the last decade have been paralleled by work on systems in which

organic moieties are introduced into open-framework architectures. These are different from the materials discussed previously in that the organic molecule is now a part of the framework rather than simply occupying space in a pore system. A major research theme in this field concerns *coordination polymers*, which we define as extended arrays composed of metal atoms or clusters bridged by polyfunctional organic molecules. Initial strategies focused on using rigid organic linkers to connect individual metal ions or clusters into extended networks, but more recent efforts have clearly shown that flexible linkers can also be used to great effect. The development of the coordination polymer area can be traced back to the work of Gravelleau, Garnier and Hardy in Poitiers in the late 1970s, in which zeolitic materials exhibiting ion-exchange properties were made by linking hexacyanoferrates units with (tetrahedrally coordinated)  $\text{Zn}^{2+}$  cations [118]. Charge balance is provided by sodium ions. The concept gained fresh impetus in 1994/5 with the work of Robson [119] and Moore [120], who used rigid organic building blocks (e.g. porphyrins) to construct three-dimensional networks with the topologies of known structure types such as PtS and  $\text{ThSi}_2$ . Much work in this area has been devoted to crystal engineering, or the ability to rationally tailor reaction conditions and organic ligands to generate a predetermined network [121], often related to a classical, high-symmetry inorganic structure [122].

A second class of materials contains infinite metal–oxygen–metal (M–O–M) arrays as a part of their structures. Some of this work can trace its roots to a strategy that was originally used by Alberti to increase the inter-layer spacing in layered compounds [123]. The approach took advantage of monophosphonates, which acted as spacers between the layers, albeit with no bonding connection between them. In order to build open, three-dimensional frameworks, Johnson and Jacobson, showed that it is possible to create connections between the layers by using diphosphonates [124]. It is now known that hybrid frameworks can be made not only with layered metal oxide structures, but also with systems in which the metal–oxygen–metal (M–O–M) linkages are one- or three-dimensional. We shall collectively refer to this class of materials as *hybrid metal oxides*. These two classes of hybrid materials are discussed below in separate sections.

### 18.6.1

#### Coordination Polymers

Robson [119] chose as a geometrical/topological model one of a number of simple three-dimensional nets such as diamond,  $\alpha$ -Po, and PtS, and then tried to devise ways of chemically linking together the building blocks with a functionality and a stereochemistry appropriate to the chosen parent net. Using this approach, he linked metalloporphyrins like  $\text{Cu(II)(tcp)}$  or  $\text{Cu(II)(tpp)}$  via Cu(I) complexes to generate open frameworks in which the tunnels were occupied by disordered molecules of solvent. The first success of Lee and Moore [120] concerned  $[\text{Ag}(\text{TCB})(\text{CF}_3\text{SO}_3)]$  (TCB = 1,3,5-tricyanobenzene). TCB has threefold symmetry and its terminal nitrogens serve as ligating groups for the soft Ag(I) cation. The combination of TCB and Ag(I) triflate leads to a honeycomb lattice in which tri-

coordinated Ag links three TCB units with dimensions of ca 1 nm to form cavities, in the centers of which are the triflate anions. The layers are stacked in an ABCABC manner.

A similar methodology was developed simultaneously by Yaghi. In this instance, he used 4,4'-bipyridine as the organic component, using the two nitrogens of the molecule for ligation. This led to three-dimensional compounds with interpenetrating subnetworks; the cations used were  $\text{Cu}_2\text{Cl}_2$  dimers, Cu and Ag [125]. It is noteworthy that the cavities generated in this family of compounds accommodate either solvent molecules or exchangeable anions, at variance to the situation in zeolites. However, the vast majority of cyano- or amino-based coordination polymers do not remain crystalline after solvent removal.

In terms of stability, carboxylates and phosphonates have proven to be the most useful coordinating groups for hybrid systems. Indeed, many examples remain crystalline following solvent removal, often yielding high surface areas. Yaghi and coworkers have prepared several structures based on zinc and aromatic carboxylic acids [126], including a zinc 1,4-benzenedicarboxylate compound, MOF-5 (MOF = metal organic framework) [127]. This structure, illustrated in Figure 18.8, consists of  $\text{Zn}_4\text{O}(\text{OOC-R})_6$  clusters where six carboxylate groups coordinate to four tetrahedral zinc atoms surrounding a central oxygen atom. This arrangement, known in molecular form from coordination chemistry [128], may be pictured as an octahedron of carboxylate groups. The bifunctional 1,4-benzenedicarboxylate serves to bridge these clusters into a three-dimensional *fcc* framework with comparable pore volume and adsorption-desorption characteristics to the zeolite faujasite. The structural versatility possible in coordination polymer systems has been dramatically illustrated by the synthesis of 16 variations [129] of the MOF-5 structure type, with cavities ranging from 0.38 to 2.88 nm, simply by changing the dicarboxylate used in the synthesis. These structures show promising methane adsorption characteristics, and have recently been investigated for hydrogen storage [130]. Similarly, Williams and coworkers prepared a related porous structure [131] based on Cu(II) dimers linked by 1,3,5-benzenetricarboxylate. The channels contain water bound to Cu sites that can be reversibly exchanged with amines and thus might find applications in catalysis, separations or chemical sensing. Kim et al. produced a homochiral compound by using only one enantiomer of a chiral coordination complex to build a porous framework [132]. This material shows selectivity in both adsorption and catalysis based on chirality and may find applications in enantiomer-specific separations or catalysis. Finally, the squarate ion, has recently been used (with Co(II) and other metals) to create architectures that are remarkably similar to that of zeolite sodalite [133].

One remarkable aspect of many of these materials, as well as the hybrid metal oxide materials discussed in the next section, is that templates are rarely used in their synthesis. Instead, the open architectures are a consequence of interactions between the organic and inorganic groups. One notable exception is an open-framework zinc oxalate where the organic template, guanadinium, occupies a system of channels in the structure [134].

Many intriguing coordination polymers prepared in the last decade utilized flex-

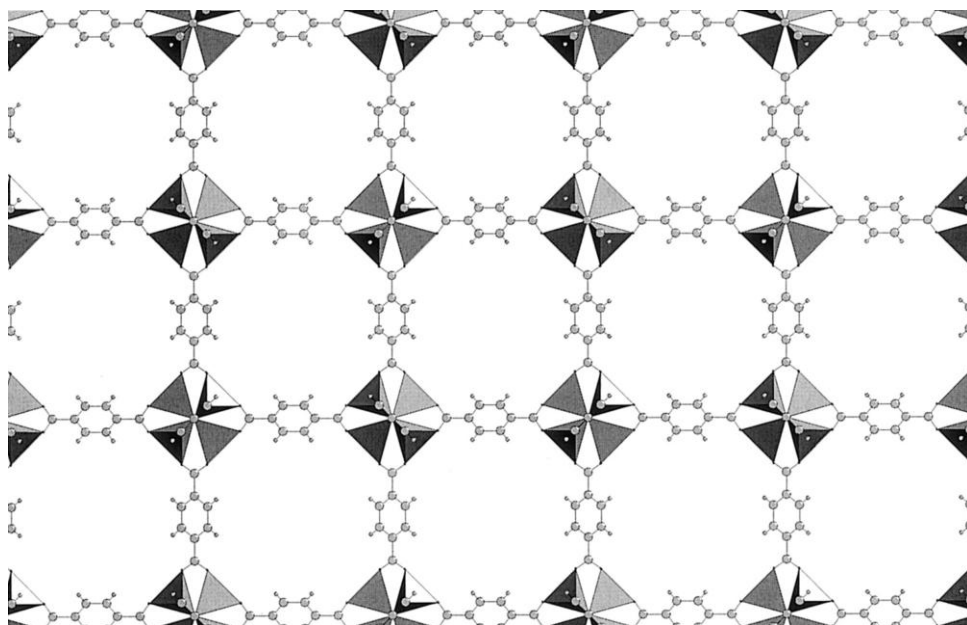


**Fig. 18.8.** The zinc terephthalate hybrid polymer MOF-5.  $\text{ZnO}_4$  tetrahedra are shown in gray and carbon and hydrogen atoms are drawn as gray spheres. Solvent molecules are omitted for clarity.

ible diphosphonates in combination with transition metals. Two of the most spectacular examples from this field are  $[\text{M}(\text{O}_3\text{PCH}_2\text{NH}(\text{C}_2\text{H}_4)_2\text{NHCH}_2\text{PO}_3)] \cdot \text{H}_2\text{O}$  ( $\text{M} = \text{Mn}, \text{Co}$ ) and  $[\text{NH}_4]_4[(\text{V}^{\text{IV}}\text{O})_3(\text{O}_3\text{PCH}_2\text{PO}_3)_4(\text{H}_2\text{O})_4] \cdot 4\text{H}_2\text{O}$ . The first [135] is made from tetrameric  $\text{Co}_2\text{P}_2$  entities linked by  $\text{CH}_2\text{NH}(\text{C}_2\text{H}_4)_2\text{NHCH}_2$  groups in three directions. The long connections between the tetramers lead to very large, ellipsoidal 44-membered rings ( $0.47 \times 1.8 \text{ nm}^2$ ) containing water molecules. The second [136], using vanadium, leads to clover-like windows in which ammonium ions and water molecules lie. Such an approach, successful with 3d transition metals, is also valuable for lanthanides [137]. For example, a whole series of lanthanide phosphonates has recently been characterized. Some of these materials involve vertex-sharing chains of  $\text{LnO}_n$  polyhedra, in which case they formally belong to the hybrid metal oxides category described in the next section.

Several drawbacks to the coordination polymer approach exist. First, their thermal stability is relatively low (typically losing crystallinity below  $300^\circ\text{C}$ ). Secondly, organic molecules do not normally communicate magnetic interactions efficiently enough to prepare magnetic materials with ordering temperatures sufficiently high to be useful. Recently, Veciana and coworkers demonstrated that organic radicals could be used to improve the strength of coupling between  $\text{Cu}^{2+}$  centers in an open-framework coordination polymer [138]. While the ordering temperature is relatively low because their material is two-dimensional, it remains to be seen if

this strategy can push magnetic ordering to reasonable temperatures when three-dimensional compounds are prepared.

### 18.6.2

#### Hybrid Metal Oxides

It is reasonable to expect that both the thermal stability and magnetic ordering temperatures in hybrid systems may be improved by synthesizing materials with extended M–O–M arrays. In other words, as the connectivity between transition metals through oxygen increases, hybrid metal oxides should assume properties closer to transition metal oxides and further from purely organic polymers. In this section, we focus exclusively on transition metal systems, since their parent oxides have the most exciting properties [139].

The earliest examples of such materials are the pillared layered structures, consisting of metal–oxygen sheets connected via diphosphonate bridges [140]. Porous materials may be synthesized by combining both a rigid diphosphonate (such as biphenylenebis(phosphonate)) and phosphite, where the average pore size may be adjusted by varying the ratio of acids used in the synthesis. One important advantage of this approach is that materials with pores between the ranges covered by crystalline zeolites and mesopores may be prepared. The relatively small crystallite sizes and their tendency to grow as flat plates allows the synthesis of materials with both nano- and mesoporosity. Because of their tunable pore sizes, aptitude for functionalization, and moderately high thermal stability, these materials may find similar applications to those of zeolites.

Polyoxometalate chemistry has been used to prepare a number of new metal oxygen arrays. For example, many new molybdenum oxygen structures [141] have been generated with diamines playing a similar charge balancing and templating role as in aluminosilicate chemistry. Jacobson and coworkers have prepared several transition metal–vanadate hybrid materials [142] with open architectures and reversible hydration/dehydration [143]. However, for the later transition metals, such architectures are less likely due to the difficulty in maintaining high oxidation states in hydro/solvothermal reactions.

More recently, several groups, particularly those of Férey and Cheetham, have focused on metal carboxylates as a promising family for synthesizing novel hybrid metal oxides. Férey and coworkers have used hydrothermal synthesis to prepare the first vanadium carboxylate,  $V(OH)(1,4\text{-benzenedicarboxylate})$  [144]. The structure consists of a 1D chain of octahedral  $V^{3+}$  bridged in four directions by the dicarboxylate to create large channels. Despite having only 1D M–O–M connectivity, long-range antiferromagnetic ordering is observed at 95 K. Along with an isostructural  $Cr^{3+}$  analog [145], these materials may be dehydrated to show zeolitic porosity with BET surface areas as high as  $1500\text{ m}^2\text{ g}^{-1}$ .

Livage and Férey used the flexible,  $\alpha,\omega$ -dicarboxylate succinic acid to prepare several structures, MIL-9 [146] and MIL-16 [147], with two dimensional Co–O–Co sheets. Nickel succinate [148] (Figure 18.9) provides a striking example of this new class of hybrid materials with a honeycomb framework based on a three-



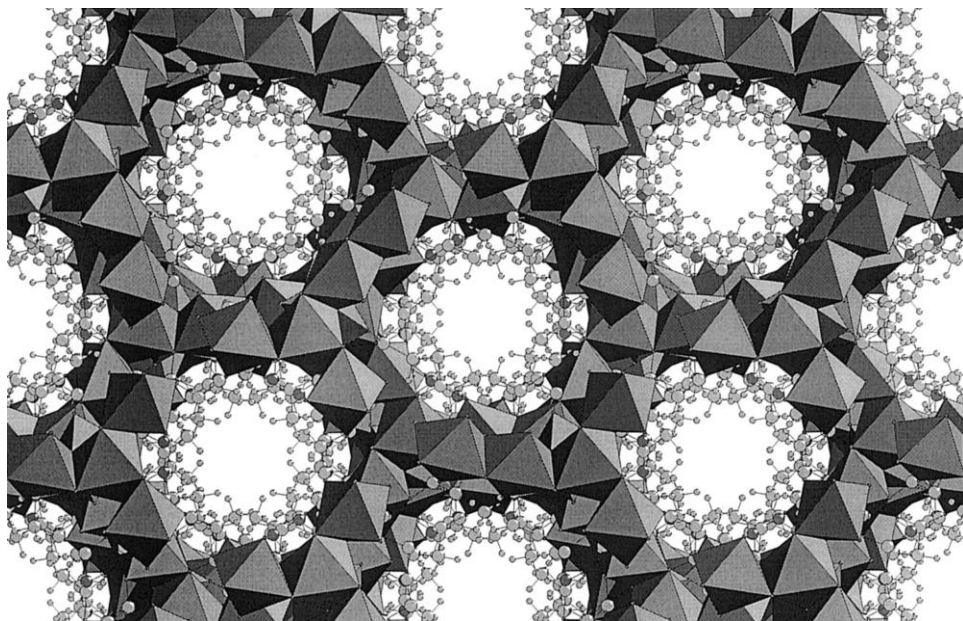


**Fig. 18.9.** The hybrid metal oxide nickel succinate.  $\text{NiO}_6$  octahedra are shown in gray, oxygen atoms are drawn as dark gray spheres, and carbon and hydrogen atoms are drawn as light gray spheres.

dimensional network of edge- and vertex-sharing  $\text{NiO}_6$  octahedra. The methylene groups of the succinates create a very hydrophobic channel system, quite unlike those found in traditional zeolitic materials. Nickel succinate retains its crystal structure up to 400 °C, as verified by in situ XRD and TGA studies, supporting expectations of improved thermal stability for hybrid systems with 3D M–O–M connectivity.

Recent work has offered several insights as to why these materials exhibit higher M–O–M dimensionality than is typically found in hybrid carboxylate systems. Livage and Férey observed that the use of hydrothermal synthesis favors increased condensation of cobalt centers, resulting in the higher M–O–M dimensionality than phases obtained through reactions near room temperature [149]. More recent systematic studies in the cobalt succinate system have further clarified this result [150]. Forster et al. demonstrated that five unique cobalt succinate structures could be synthesized using identical starting mixtures by varying only the temperature. The resulting series of cobalt succinates show a progressive decrease in water content with increasing temperature, as would be expected based on entropic considerations. Octahedral coordination is maintained by increased sharing of carboxylate oxygen atoms between cobalt centers, resulting in the 2D M–O–M materials seen at higher temperatures. This trend may be seen in Table 18.3.

Based on these and other structures, Forster and Cheetham have proposed that

**Tab. 18.3.** Data for the five cobalt succinates synthesized using one specific starting mixture heated to different temperatures.

Synthesis Temp./°C	Phase	H <sub>2</sub> O/ Co <sup>2+</sup> *	Co <sup>2+</sup> / COO <sup>-</sup>	Co <sup>2+</sup> / 10 <sup>3</sup> Å <sup>3</sup>	Dimensionality <sup>†</sup>
60	Co(H <sub>2</sub> O) <sub>4</sub> (C <sub>4</sub> H <sub>4</sub> O <sub>4</sub> ) <sub>2</sub> ·	4(4)	1	4.74	1(0)
100	Co(H <sub>2</sub> O) <sub>2</sub> (C <sub>4</sub> H <sub>4</sub> O <sub>4</sub> ) <sub>2</sub>	2(2)	2	5.50	1(0)
150	Co <sub>4</sub> (H <sub>2</sub> O) <sub>2</sub> (OH) <sub>2</sub> (C <sub>4</sub> H <sub>4</sub> O <sub>4</sub> ) <sub>3</sub> ·2H <sub>2</sub> O	1( $\frac{1}{2}$ )	2.67	7.28	2(2)
190	Co <sub>6</sub> (OH) <sub>2</sub> (C <sub>4</sub> H <sub>4</sub> O <sub>4</sub> ) <sub>5</sub> ·2H <sub>2</sub> O	$\frac{1}{3}$ (0)	2.8	8.05	3(2)
250	Co <sub>5</sub> (OH) <sub>2</sub> (C <sub>4</sub> H <sub>4</sub> O <sub>4</sub> ) <sub>4</sub>	0(0)	3	8.88	3(2)

\*The first number in the H<sub>2</sub>O/Co<sup>2+</sup> column refers to total water content, the second in parentheses refers to water molecules coordinated to cobalt centers. <sup>†</sup>The first number in the Dimensionality column refers to the total dimensionality, the second to the dimensionality of the M–O–M framework.

positional flexibility for coordinating oxygen atoms is also critical in determining the overall M–O–M dimensionality of hybrid metal oxides [151]. This is a consequence of the requirement of oxygen atoms to be in very specific locations to satisfy the coordination requirements of stable transition metal–oxygen networks. Based on this supposition, simple, monofunctional organic molecules would in fact be more likely to form materials with extended M–O–M connectivity than polyfunctional ones. The existence of three-dimensional zeolite-like phosphonates such as  $\beta$ -Cu(O<sub>3</sub>PCH<sub>3</sub>) [152], Zn(O<sub>3</sub>PC<sub>2</sub>H<sub>4</sub>NH<sub>2</sub>) [153] and  $\beta$ -Al<sub>2</sub>(CH<sub>3</sub>PO<sub>3</sub>)<sub>3</sub>·H<sub>2</sub>O [154], supports this. One surprising result from this area has been the discovery of a remarkable antimony(III) methylphosphonate nanotube structure [155]. Even more surprising is the recent discovery by Forster and Cheetham of a number of open-framework formats [151, 156], acetates [151] and other monocarboxylates [157] with two- and three-dimensional M–O–M networks. For example, Figure 18.10 shows the structure of an open-framework nickel formate. These monocarboxylates are synthesized under virtually identical conditions as the polycarboxylate hybrid metal oxides.

Several drawbacks limit the utility of the hybrid metal oxides prepared to date. Firstly, it has proven extremely difficult to create materials with porosity as high as is in coordination polymers. This is especially true in the case of materials with two- and three-dimensional M–O–M frameworks. Secondly, while some examples of these materials have relatively high magnetic ordering temperatures, there are still no examples that order at or above room temperature. However, there do not appear to be any fundamental reasons why these difficulties cannot be overcome.

## 18.7

### Conclusions

The field of nanoporous materials has emerged as one of the most exciting and diverse areas of nanomaterials. The discoveries of the last decade have demon-

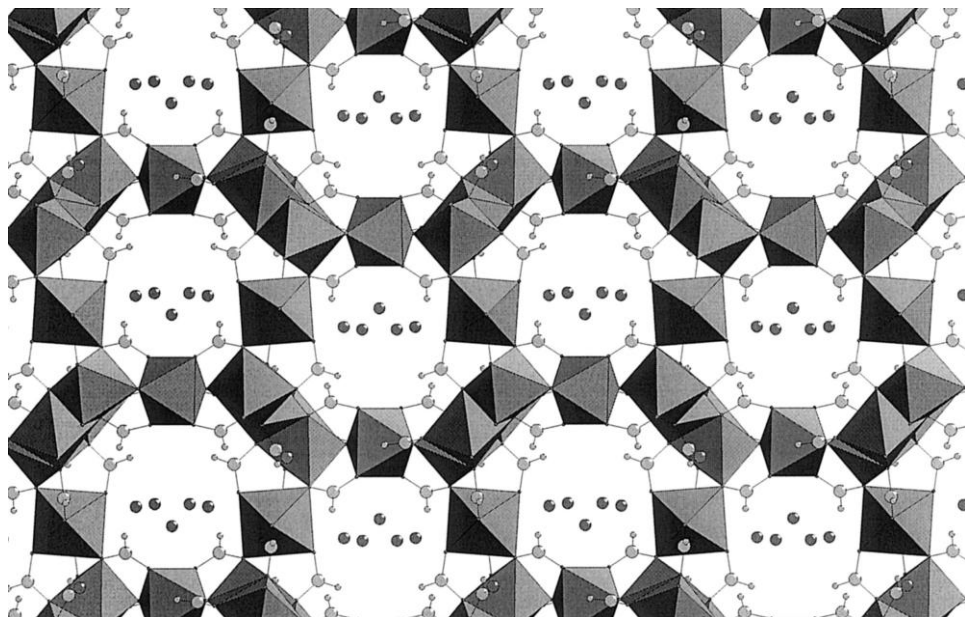


**Fig. 18.10.** A hybrid metal oxide form nickel formate.  $\text{NiO}_6$  octahedra are shown in gray, carbon and hydrogen atoms are drawn as gray spheres, and non-coordinated water molecules occupying the cavities are shown in dark gray.

strated that, far from being limited to aluminosilicates and closely related materials, open-framework solids can be made with a rich diversity of chemistries. The developments in the transition metal area, for example, mean that it is now possible to contemplate the creation of nanoporous solids that exhibit some of the interesting and useful properties that are found with condensed transition metal compounds, e.g. ferromagnetism, metallic conductivity, and perhaps even superconductivity. The recent focus on hybrid materials has also extended the scope dramatically, and led to exciting new possibilities in terms of both materials design and novel applications. The story would not be complete without a mention of some of the parallel developments in the organic area. Nanoporous organics have been known for many decades in the context of gas clathrates, but many other classes are now known. They include the channel-structured cyclodextrins, in which hydrogen bonding plays a crucial role, and the calixarenes. It is also recognized that pore formation is important in the functionality of ion channel proteins [158], and that proteins can be further functionalized for the design of sensors [159]. This is undoubtedly a very rich field in which many other exciting discoveries will be made in the future.

## References

- 1 A. K. CHEETHAM, G. FÉREY, T. LOISEAU, *Angew. Chem. Intl. Ed. Engl.* **1999**, 38, 4000; W. T. A. HARRISON, *Curr. Opin. Solid State Mater. Sci.* **2002**, 6, 407.
- 2 S. T. WILSON, B. M. LOK, C. A. MESSINA et al., *J. Am. Chem. Soc.* **1982**, 104, 1146.
- 3 G. FÉREY, *J. Fluorine Chem.* **1995**, 72, 187; *C. R. Acad. Sci. Séries C* **1998**, 1, 1.
- 4 S. HORSTMANN, E. IRRAN, W. SCHNICK, *Angew. Chem. Intl. Ed. Engl.* **1997**, 36, 1992, and references therein.
- 5 R. L. BEDARD, S. T. WILSON, L. D. VAIL et al., *Stud. Surf. Sci. Catal.* **1989**, 49A, 375; J. B. PARISE, *Science* **1991**, 251, 293; H. LI, A. LAINE, M. O'KEEFE et al., *Science* **1999**, 283, 1145.
- 6 J. D. MARTIN, K. B. GREENWOOD, *Angew. Chem. Intl. Ed. Engl.* **1997**, 36, 2072.
- 7 M. E. DAVIS, *Chem. Eur. J.*, **1997**, 3, 1745 and references therein.
- 8 C. T. KRESGE, M. E. LEONOWICZ, W. J. ROTH et al., *Nature* **1992**, 359, 710.
- 9 G. S. ATTARD, P. N. BARTLETT, N. R. B. COLEMAN et al., *Science*, **1997**, 278, 838.
- 10 Q. S. HUO, D. I. MARGOLESE, U. CIESLA et al., *Nature* **1994**, 368, 317.
- 11 U. CIESLA, S. SCHACHT, G. D. STUCKY et al., *Angew. Chem. Eng. Ed. Engl.* **1996**, 35, 541.
- 12 D. Y. ZHAO, J. L. FENG, Q. S. HUO et al., *Science* **1998**, 279, 548.
- 13 J. Y. YING, C. P. MEHNERT, M. S. WONG, *Angew. Chem. Eng. Ed. Engl.* **1999**, 38, 56.
- 14 S. R. BATTEN, R. ROBSON, *Angew. Chem. Eng. Ed. Engl.* **1998**, 37, 1461.
- 15 I. PETROVIC, A. NAVROTSKY, M. E. DAVIS et al., *Chem. Mater.* **1993**, 5, 1805.
- 16 N. J. HENSON, J. D. GALE, A. K. CHEETHAM, *Chem. Mater.* **1994**, 6, 1647.
- 17 B. V. VORA, T. L. MARKER, P. T. BARGER et al., in Fourth International Natural Gas Conversion Symposium, M. DE PONTES, R. L. ESPINOZA, C. P. NICOLAIDES, J. H. SCHOLTZ, M. S. SCURRELL (Eds.), Elsevier, Amsterdam, *Stud. Surf. Sci. Catal.* **1997**, 107, 87.
- 18 T. TARAMASSO, G. PEREGO, B. NOTARI, *US Pat.* 4,410,501, 1983; B. NOTARI, *Adv. Catal.* **1996**, 41, 253; R. J. SAXTON, *Top. Catal.*, **1999**, 43, 9.
- 19 V. SOGHOMANIAN, Q. CHEN, R. C. HAUSHALTER et al., *Science*, **1993**, 259, 1596; T. LOISEAU, G. FÉREY, *J. Solid State Chem.* **1994**, 111, 416.
- 20 D. R. CORBIN, J. F. WHITNEY, W. C. FULTZ et al., *Inorg. Chem.* **1986**, 25, 2280; H. M. LIN, K.-H. LIU, W.-C. JIANG et al., *Chem. Mater.* **1999**, 11, 519.
- 21 J. CHEN, R. H. JONES, S. NATARAJAN et al., *Angew. Chem. Intl. Ed. Engl.* **1994**, 33, 639; P. FENG, X. BU, S. H. TOLBERT et al., *J. Am. Chem. Soc.* **1997**, 119, 2497.
- 22 N. GUILLLOU, Q. GAO, M. NOGUES et al., *C. R. Acad. Sci. Paris*, **1999**, 2, 387.
- 23 H. DE SAINTE CLAIRE DEVILLE, *C. R. Acad. Sci.* **1862**, 54, 324.
- 24 C. BAERLOCHER, W. M. MEIER, D. H. OLSEN, *Atlas of Zeolite Framework Types*, 5th edition, Elsevier, London 2001.
- 25 C. C. FREYHARDT, M. TSAPATSIS, R. F. LOBO et al., *Nature*, **1996**, 381, 295.
- 26 M. A. CAMBLOR, M.-J. DIAZ-CABANAS, J. PEREZ-PARIENTE et al., *Angew. Chem. Intl. Ed. Engl.* **1998**, 37, 2122.
- 27 T. R. GAFFNEY, *Curr. Opin. Solid State Mater. Sci.* **1996**, 1, 69.
- 28 G. T. KOKOTAILO, S. L. LAWTON, D. H. OLSON et al., *Nature* **1978**, 272, 437.
- 29 E. GALLI, G. VEZZALINI, S. QUARTIERI et al., *Zeolites* **1997**, 19, 323.
- 30 P. VAREY, *Chem. Eng.-London*, **1991**, 491, 13; Y. J. LI, J. N. ARMOR, *J. Catal.* **1994**, 145, 1.
- 31 X. Q. WANG, L. M. LIU, A. J. JACOBSON, *J. Am. Chem. Soc.* **2002**, 124, 7812.
- 32 H. VAN KONINGSVELD, J. C. JANSSEN, H. VAN BEKKUM, *Zeolites* **1990**, 10, 235.
- 33 A. KUPERMAN, S. NADIMI, S. OLIVER et al., *Nature* **1993**, 365, 239.
- 34 A. K. CHEETHAM, L. M. BULL, N. J. HENSON, *Stud. Surf. Sci. Catal.* **1997**, 105, 2267; L. M. BULL, A. K. CHEETHAM, *Stud. Surf. Sci. Catal.* **1997**, 105, 471; L. M. BULL, A. K.

- CHEETHAM, T. ANUPOLD et al., *J. Am. Chem. Soc.* **1998**, 120, 3510.
- 35 N. J. HENSON, J. D. GALE, A. K. CHEETHAM, *Chem. Mater.* **1994**, 6, 1647.
- 36 C. M. JIN, J. D. LUTTMER, D. M. SMITH et al., *MRS Bull.* **1997**, 22, 39.
- 37 J. M. BENNETT, J. P. COHEN, E. M. FLANIGEN et al., *ACS Symp. Ser.*, **1983**, 218, 109.
- 38 B. M. LOK, C. A. MESSINA, R. L. PATTON et al., *J. Am. Chem. Soc.* **1984**, 106, 6092.
- 39 E. M. FLANIGEN, B. M. LOK, R. L. PATTON et al., *Pure Appl. Chem.* **1986**, 58, 1351.
- 40 E. M. FLANIGEN, R. L. PATTON, S. T. WILSON, *Stud. Surf. Sci. Catal.* **1988**, 37, 13.
- 41 R. E. MORRIS, S. J. WEIGEL, *Chem. Soc. Rev.* **1997**, 26, 309.
- 42 R. H. JONES, J. M. THOMAS, R. XU et al., *J. Chem. Soc., Chem. Commun.* **1990**, 1170.
- 43 R. H. JONES, J. M. THOMAS, R. XU et al., *J. Chem. Soc., Chem. Commun.* **1991**, 1266.
- 44 S. OLIVER, A. KUPERMAN, G. A. OZIN, *Angew. Chem. Int. Ed. Engl.* **1998**, 37, 46.
- 45 H. KESSLER, *Stud. Surf. Sci. Catal.* **1989**, 52, 17.
- 46 H. KESSLER, *Mater. Res. Soc. Symp. Ser.* **1991**, 233, 47.
- 47 S. QIU, W. PANG, H. KESSLER et al., *Zeolites* **1989**, 9, 440.
- 48 C. SCHOTT-DARIE, J. PATARIN, P. Y. LE GOFF et al., *Microporous Mater.* **1994**, 3, 123.
- 49 K. KALLUS, J. PATARIN, B. MARLER, *Microporous Mater.* **1996**, 7, 89.
- 50 P. REINERT, J. PATARIN, T. LOISEAU et al., *Microporous Mesoporous Mater.* **1998**, 22, 43.
- 51 T. LOISEAU, G. FÉREY, *Chem. Commun.* **1992**, 1197.
- 52 G. FÉREY, *J. Fluorine Chem.* **1995**, 72, 187; *C. R. Acad. Sci. Sér. C*, **1998**, 1, 1.60.
- 53 F. C. HAWTHORNE, *Z. Kristallogr.* **1990**, 192, 1.
- 54 T. LOISEAU, G. FÉREY, *J. Solid State Chem.* **1994**, 111, 403.
- 55 J. B. PARISE, *Inorg. Chem.* **1985**, 24, 4312.
- 56 J. B. PARISE, *Chem Commun.* **1985**, 606.
- 57 M. ESTERMANN, L. B. MCCUSKER, C. BAERLOCHER et al., *Nature* **1991**, 352, 320.
- 58 S. S. DHINGRA, R. C. HAUSHALTER, *Chem. Commun.* **1993**, 1665.
- 59 A. M. CHIPPINDALE, S. J. BRECH, A. R. COWLEY et al., *Chem. Mater.* **1996**, 8, 2259.
- 60 S. NATARAJAN, M. P. ATTFIELD, A. K. CHEETHAM, *Angew. Chem. Int. Ed. Engl.* **1997**, 36, 978.
- 61 S. NATARAJAN, A. K. CHEETHAM, *Chem. Commun.* **1997**, 1089.
- 62 S. NATARAJAN, A. K. CHEETHAM, *J. Solid State Chem.* **1997**, 134, 207.
- 63 S. NATARAJAN, S. AYYAPPAN, A. K. CHEETHAM et al., *Chem. Mater.* **1998**, 10, 1627.
- 64 S. AYYAPPAN, A. K. CHEETHAM, S. NATARAJAN et al., *J. Solid State Chem.* **1998**, 139, 207.
- 65 B. A. ADAIR, G. DÍAZ DE DELGADO, J. M. DELGADO et al., *Angew. Chem.* **2000**, 39, 745.
- 66 R. C. HAUSHALTER, L. A. MUNDI, *Chem. Mater.* **1992**, 4, 31.
- 67 R. C. HAUSHALTER, K. G. STROHMAIER, F. W. LAI, *Science* **1989**, 246, 1289.
- 68 L. A. MUNDI, L. YACULLO, R. C. HAUSHALTER, *J. Solid State Chem.* **1991**, 95, 283.
- 69 V. SOGHOMANIAN, Q. CHEN, R. C. HAUSHALTER et al., *Science* **1993**, 259, 1596.
- 70 M. I. KAHN, L. M. MEYER, R. C. HAUSHALTER et al., *Chem. Mater.* **1996**, 8, 43.
- 71 A. MÜLLER, K. HOVEMIEIR, R. ROHLFING, *Angew. Chem., Int. Ed. Engl.* **1992**, 31, 1192.
- 72 D. RIOU, G. FÉREY, *J. Solid State Chem.* **1994**, 111, 422.
- 73 P. B. MOORE, J. SHEN, *Nature* **1983**, 306, 356.
- 74 D. R. CORBIN, J. F. WHITNEY, W. C. FULTZ et al., *Inorg. Chem.* **1986**, 25, 2279.
- 75 M. CAVELLEC, D. RIOU, C. NINCLAUS et al., *Zeolites* **1996**, 17, 250.
- 76 K.-H. LIU, Y.-F. HUANG, V. ZIMA et al., *Chem. Mater.* **1998**, 10, 2599 and refs therein.

- 77 S. S. LIN, H. S. WENG, *Appl. Catal. A*, **1993**, 105, 289.
- 78 J. DAKKA, R. A. SHELDON, *The Netherlands Pat.* 9,200,968, 1992.
- 79 J. CHEN, R. H. JONES, S. NATARAJAN et al., *Angew. Chem. Int. Ed. Engl.* **1994**, 33, 639.
- 80 J. R. D. DeBORD, R. C. HAUSHAETER, J. ZUBIETA, *J. Solid State Chem.* **1996**, 125, 270.
- 81 P. FENG, X. BU, S. H. TOLBERT, G. D. STUCKY, *J. Am. Chem. Soc.* **1997**, 119, 2497 and references therein.
- 82 J. ESCOBAL, J. L. PIZARRO, J. L. MESA et al., *Chem. Mater.* **2000**, 12, 376.
- 83 K. O. KONGHAUG, H. FJELLVÅG, K. P. LILLERUD, *J. Solid State Chem.* **2001**, 156, 32.
- 84 S. NEERAJ, M. L. NOY, A. K. CHEETHAM, *Solid State Sci.* **2002**, 4, 397.
- 85 Q. HUANG, M. ULUTAGAY, P. A. MICHENER et al., *J. Am. Chem. Soc.* **1999**, 121, 10323.
- 86 Q. HUANG, S.-J. HWU, X. MO, *Angew. Chem. Int. Ed. Engl.* **2001**, 40, 1690.
- 87 Q. HUANG, S.-J. HWU, *Inorg. Chem.* **2003**, 42, 655.
- 88 J.-S. CHANG, S.-E. PARK, Q. GAO et al., *Chem. Commun.* **2001**, 859.
- 89 N. GUILLLOU, Q. GAO, P. M. FORSTER et al., *Angew. Chem.* **2001**, 40, 2831.
- 90 P. M. FORSTER, J. ECKERT, J.-S. CHANG et al., *J. Am. Chem. Soc.* **2003**, 125, 1309.
- 91 A. CLEARFIELD, *Comments Inorg. Chem.* **1990**, 10, 89; A. CLEARFIELD, *Curr. Opin. Solid State Mater. Sci.* **1996**, 1, 268.
- 92 E. KEMNITZ, M. WLOKA, S. I. TROJANOV et al., *Angew. Chem. Int. Ed. Engl.* **1996**, 35, 2677.
- 93 M. WLOKA, S. I. TROJANOV, E. KEMNITZ, *J. Solid State Chem.* **1998**, 135, 293.
- 94 C. SERRE, G. FÉREY, *Compt. Rend. Acad. Sci. Ser. II C* **1999**, 2, 85.
- 95 A. I. BORTUN, S. A. KHAINAKOV, L. N. BORTUN et al., *Chem. Mater.* **1997**, 9, 1805; M. A. SALVADO, P. PERTIERRA, S. GARCIA-GRANDA et al., *Eur. J. Solid State Inorg. Chem.* **1997**, 34, 1237.
- 96 R. L. BEDARD, S. T. WILSON, L. D. VAIL et al., *Stud. Surf. Sci. Catal.* **1989**, 49A, 375.
- 97 J. B. PARISE, *Chem. Commun.* **1990**, 1553.
- 98 C. L. CAHILL, Y. KO, J. B. PARISE, *Chem. Mater.* **1998**, 10, 19.
- 99 D. M. NELLIS, Y. KO, K. TAN et al., *Chem. Commun.* **1995**, 541.
- 100 C. L. BOWES, A. J. LOUGH, A. MALEK et al., *Chem. Ber.* **1996**, 129, 283.
- 101 O. M. YAGHI, Z. SUN, D. A. RICHARDSON et al., *J. Am. Chem. Soc.* **1994**, 116, 807.
- 102 T. JIANG, A. LOUGH, G. A. OZIN et al., *J. Mater. Chem.* **1998**, 8, 721.
- 103 T. JIANG, A. J. LOUGH, G. A. OZIN et al., *Chem. Mater.* **1995**, 7, 245.
- 104 J. D. MARTIN, K. B. GREENWOOD, *Angew. Chem. Int. Ed. Engl.* **1997**, 36, 2072.
- 105 W. SCHNICK, J. LÜCKE, *Angew. Chem. Int. Ed. Engl.* **1992**, 31, 213.
- 106 N. STOCK, E. IRRAN, W. SCHNICK, *Chem., Eur. J.* **1998**, 4, 1822.
- 107 S. HORSTMANN, E. IRRAN, W. SCHNICK, *Angew. Chem. Int. Ed. Engl.* **1997**, 36, 1992.
- 108 Y.-F. SHEN, R. N. DeGUZMAN, R. P. ZERGER et al., *Stud. Surf. Sci. Catal.* **1993**, 83, 19, and references therein.
- 109 S. L. SUIB, L. E. ITON, *Chem. Mater.* **1994**, 6, 429.
- 110 Y.-G. YIN, W.-Q. XU, R. DeGUZMAN et al., *Inorg. Chem.* **1994**, 4384.
- 111 A. CHOUDHURY, J. KRISHNAMOORTHY, C. N. R. RAO, *Chem. Commun.* **2001**, 2610.
- 112 G. PAUL, A. CHOUDHURY, R. NAGARAJAN et al., *Inorg. Chem.* **2003**, 42, 2004.
- 113 G. PAUL, A. CHOUDHURY, C. N. R. RAO, *Chem. Mater.* **2003**, 15, 1174.
- 114 G. PAUL, A. CHOUDHURY, C. N. R. RAO, *Chem. Commun.* **2002**, 1904.
- 115 G. PAUL, A. CHOUDHURY, C. N. R. RAO, *J. Chem. Soc., Dalton Trans.* **2002**, 3859.
- 116 Y. XING, Z. SHI, G. H. LI et al., *J. Chem. Soc., Dalton Trans.* **2003**, 940.
- 117 A. J. NORQUIST, P. M. THOMAS, M. B. DORAN et al., *Chem. Mater.* **2002**, 14, 5179.
- 118 P. GRAVEREAU, M. GARNIER, A. HARDY, *Acta Crystallogr., Sect. B* **1979**, 35, 2843.
- 119 B. F. ABRAHAMS, B. F. HOSKINS, D. M. MICHAEL et al., *Nature* **1994**, 369, 727.



- 120 D. VENKATARAMAN, S. LEE, J. ZHANG et al., *Nature* **1994**, 371, 591; D. VENKATARAMAN, G. B. GARDNER, S. LEE et al., *J. Am. Chem. Soc.* **1995**, 117, 11600.
- 121 B. MOULTON, M. J. ZAWOROTKO, *Chem. Rev.* **2001**, 101, 1629.
- 122 M. EDDAUDI, D. B. MOLER, H. L. LI et al., *Acc. Chem. Res.* **2001**, 34, 319.
- 123 G. ALBERTI, U. CONSTANTINO, S. ALLULLI et al., *Inorg. Nucl. Chem.* **1978**, 40, 1113.
- 124 J. W. JOHNSON, A. J. JACOBSON, W. M. BUTLER et al., *J. Am. Chem. Soc.* **1989**, 111, 381; G. HUAN, J. W. JOHNSON, A. J. JACOBSON, *Chem. Mater.* **1990**, 2, 91; G. HUAN, J. W. JOHNSON, A. J. JACOBSON, *J. Solid State Chem.* **1990**, 89, 220; G. HUAN, J. W. JOHNSON, A. J. JACOBSON, *Chem. Mater.* **1992**, 4, 661.
- 125 O. M. YAGHI, D. A. RICHARDSON, G. LI et al., *Mater. Res. Soc. Symp. Proc.* **1994**, 371, 15.
- 126 M. EDDAUDI, H. LI, O. M. YAGHI, *J. Am. Chem. Soc.* **2000**, 122, 1391.
- 127 H. LI, M. EDDAUDI, M. O'KEEFFE et al., *Nature*, **1999**, 402, 276.
- 128 W. CLEGG, D. R. HARBRON, C. D. HOMAN et al., *Inorg. Chim. Acta* **1991**, 186, 51.
- 129 M. EDDAUDI, J. KIM, N. ROSI et al., *Science* **2002**, 295, 469.
- 130 J. ECKERT, O. M. YAGHI, to be published.
- 131 S. S.-Y. CHUI, S. M.-F. LO, J. P. H. CHARMANT et al., *Science*, **1999**, 283, 1148.
- 132 J. SOO SEO, D. WHANG, H. LEE et al., *Nature*, **2000**, 404, 982.
- 133 S. NEERAJ, M. L. NOY, C. N. R. RAO et al., *Solid State Sci.* **2002**, 4, 1231.
- 134 R. VAIDHYANATHAN, S. NATARAJAN, A. K. CHEETHAM et al., *Chem. Mater.* **1999**, 11, 3636.
- 135 R. LADUCA, D. ROSE, J. R. D. DEBORD et al., *J. Solid State Chem.* **1996**, 123, 408 and references therein.
- 136 D. RIOU, O. ROUBEAU, G. FÉREY, *Microporous Mesoporous Mater.* **1998**, 23, 23.
- 137 F. SERPAGGI, G. FÉREY, *J. Mater. Chem.* **1998**, 8, 2749.
- 138 D. MASPOCH, D. RUIZ-MOLINA, K. WURST et al., *Nature Mater.* **2003**, 2, 190.
- 139 C. N. R. RAO, B. RAVEAU, *Transition Metal Oxides*, 2nd edition, Wiley-VCH, Weinheim 1998.
- 140 A. CLEARFIELD, *Chem. Mater.* **1998**, 10, 2801.
- 141 P. J. HAGRMAN, D. HAGRMAN, J. ZUBIETA, *Angew. Chem. Int. Ed. Engl.* **1999**, 38, 2638.
- 142 L. M. ZHENG, X. Q. WANG, Y. S. WANG et al., *J. Mater. Chem.* **2001**, 11, 1100; J. DO, A. J. JACOBSON, *Inorg. Chem.* **2001**, 40, 2468.
- 143 L. M. ZHENG, T. WHITFIELD, X. WANG et al., *Angew. Chem. Int. Ed. Engl.* **2000**, 39, 4528.
- 144 K. BARTHELET, J. MARROT, D. RIOU et al., *Angew. Chem. Int. Ed. Engl.* **2002**, 41, 281.
- 145 C. SERRE, F. MILLANGE, C. THOUVENOT et al., *J. Am. Chem. Soc.* **2002**, 124, 13519.
- 146 C. LIVAGE, C. EGGER, M. NOGUES et al., *J. Mater. Chem.* **1998**, 8, 2743.
- 147 C. LIVAGE, C. EGGER, G. FÉREY, *Chem. Mater.* **2000**, 11, 1546.
- 148 P. M. FORSTER, A. K. CHEETHAM, *Angew. Chem. Int. Ed. Engl.* **2002**, 41, 457.
- 149 C. LIVAGE, C. EGGER, G. FÉREY, *Chem. Mater.* **2001**, 13, 410.
- 150 P. M. FORSTER, A. R. BURBANK, C. LIVAGE et al., submitted.
- 151 P. M. FORSTER, Z. YANG, A. K. CHEETHAM, submitted.
- 152 J. LeBIDEAU, C. PAYEN, P. PALVADEAU et al., *Inorg. Chem.* **1994**, 33, 4885.
- 153 S. DRUMEL, P. JANVIER, D. DENIAUD et al., *Chem. Commun.* **1995**, 1051.
- 154 K. MAEDA, J. AKIMOTO, Y. KIYOZUMI et al., *Chem. Commun.* **1995**, 1033.
- 155 B. A. ADAIR, N. GUILLLOU, M. ALVAREZ et al., *J. Solid State Chem.* **2001**, 162, 347.
- 156 P. M. FORSTER, Z. YANG, A. K. CHEETHAM, submitted.
- 157 P. M. FORSTER, Z. YANG, A. K. CHEETHAM, *Solid State Sci.* in press.
- 158 K. K. TAI, S. A. N. GOLDSTEIN, *Nature* **1998**, 391, 605.
- 159 O. BRAHA, S. CONLAN, S. CHELEY et al., *Nature*, **1999**, 398, 686.

## 19

# Photochemistry and Electrochemistry of Nanoassemblies

*P. V. Kamat*

### 19.1

#### Metal and Semiconductor Nanostructures

Semiconductor and noble metal nanoclusters in the nanometer size regime display many interesting optical, electronic and chemical properties that are size-dependent (see for example, [1–13]). Such nanoscale materials have potential applications in developing new catalysts [14, 15], nanosensors [16–18], and optoelectronic nanodevices [12, 19–23]. Increasing interest in nanotechnology has induced a burst of research activity in the area of synthesis and organic functionalization of metal nanoparticles. The size and shape dependent optical and electronic properties of metal nanoparticles make an interesting case for photochemists and photobiologists to exploit their role in light induced chemical reactions [24].

Nanoparticles are the building blocks of future nanodevices as they can be assembled as two- and three-dimensional nanostructures using self-assembled, layer-by-layer assembly and electrophoretic deposition techniques [25]. By controlling the preparative conditions of metal or semiconductor colloid precursors and functionalization of these particles with redox or photoactive molecules, it is possible to tailor the properties of these nanostructures. For example, thin metal oxide films cast on conducting glass electrodes exhibit interesting photochromic, electrochromic, photocatalytic and photoelectrochemical properties that are inherited from native colloids [26]. This chapter presents an overview of photochemical and electrochemical aspects of native and functionalized semiconductor and metal nanostructures. The discussion on the hybrid assemblies should provide a broad basis for designing new generation nanodevices.

### 19.2

#### Photoinduced Charge Transfer Processes in Semiconductor Nanoparticle Systems

The multidisciplinary research of semiconductor nanoclusters has witnessed exceptional growth during the past decade. By making use of the principles of pho-



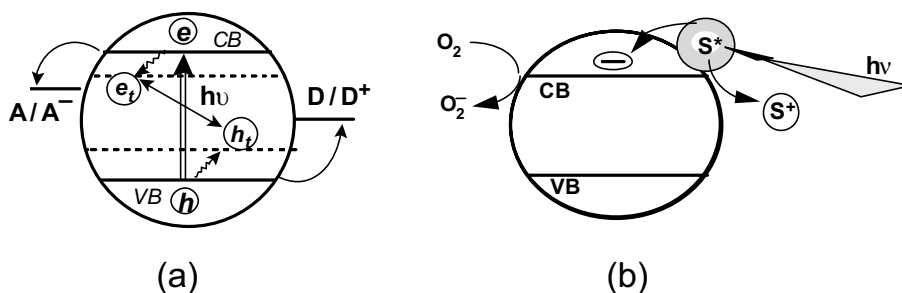


**Fig. 19.1.** Photoinduced charge transfer processes in semiconductor nanoclusters. (a) Under bandgap excitation and (b) sensitized charge injection by exciting adsorbed sensitizer (S). CB and VB refer to the conduction and valence bands of the semiconductor and  $e_t$  and  $h_t$  refer to trapped electrons and holes, respectively.

toelectrochemistry, different semiconductor nanoparticle systems have been employed in the direct conversion of light energy into chemical or electrical energy. Basic understanding of the nanostructured semiconductor systems is important for establishing their practical use in photochemical solar cells, electrochromic devices, sensors, and photocatalytic degradation of organic contaminants.

The participation of a semiconductor nanoparticle in a photocatalytic process can be either direct or indirect as illustrated in Figures 19.1(a) and 19.1(b), respectively. Charge separation in semiconductor particles occurs when they are subjected to bandgap excitation. The photogenerated electrons and holes are capable of oxidizing or reducing the adsorbed substrates (Figure 19.1(a)). Alternatively the semiconductor nanoclusters also promote a photocatalytic reaction by acting as a mediator for the charge transfer between two adsorbed molecules (Figure 19.1(b)). This process, which is commonly referred to as photosensitization, is extensively used in photoelectrochemistry and imaging science. In the first case, the bandgap excitation of a semiconductor particle is followed by charge transfer at the semiconductor/electrolyte interface. However, in the second case, the semiconductor nanoparticle quenches the excited state by accepting an electron and then transfers the charge to another substrate (e.g., adsorbed oxygen) or to a collecting electrode surface to generate photocurrent. The energy of the conduction and valence bands of the semiconductor and the redox potential of the adsorbed molecule control the reaction course of the surface photochemical reaction.

The  $\text{TiO}_2$  photocatalyst has been the popular choice of most of the published photocatalysis work. Its large bandgap energy (3.2 eV) necessitates UV-excitation to induce charge separation within the particle. In aqueous solutions the holes are scavenged by surface hydroxy groups to generate  $\cdot\text{OH}$  radicals which then promote the oxidation of organics [27–31]. The  $\cdot\text{OH}$  radical mediated oxidation has been successfully employed in the mineralization of several chemical contaminants. Interestingly, the electron scavenging becomes a rate limiting factor in such oxidation processes [32–38]. Alternative methods have also been suggested to promote the charge separation by applying an electrochemical bias to a  $\text{TiO}_2$  particulate film

electrode [36]. On the other hand, both reductive and oxidative steps can be beneficially used to degrade aromatic compounds such as trinitrophenol [39].

Obtaining insight into charge transfer processes is important in order to improve the photoconversion efficiencies in semiconductor-based nanoassemblies. The principles and mechanism of photocatalytic reactions in advanced oxidation processes can be found in earlier review articles [40–42]. Technological advances in this area have already led to the product development for a variety of day-to-day operations. Commercialization of products such as self-cleaning glass, disinfectant tiles and filters for air purification demonstrate the initial success of nanosystems for environmental applications [43].

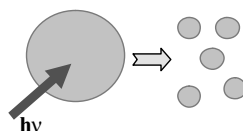
### 19.3

#### Photoinduced Transformations of Metal Nanoparticles

Noble metals in bulk are photoactive only to a small extent, as in the case of photoemission from silver electrodes [44]. The nanoparticles of noble metals on the other hand exhibit increased photochemical activity because of their high surface/volume ratio and unusual electronic properties. For example, Henglein and co-workers [45, 46] reported photochemical dissolution of Ag colloids when photoejected electrons were scavenged by species such as  $N_2O$ . The photochemical activity of metal nanocluster systems can be visualized under two different scenarios (Figure 19.2): (i) Direct excitation of the metal nanoparticles, and (ii) indirect excitation achieved via a surface bound fluorophore or a dye molecule. Furthermore, metal nanoparticles are known to assist photocatalytic reactions by promoting interfacial redox processes. Optical properties of metal colloids, morphological changes under light irradiation and excited state interaction with photoactive molecules have been the subject of many recent investigations [3, 13, 24, 47–51].

The electronic excitation associated with direct excitation of the metal nanoclusters has been probed by pump–probe spectroscopy. In contrast to the bulk metal property, colloidal metals (e.g., gold) have been shown to be photolu-

**Morphological changes  
(Electron ejection,  
fragmentation and melting)**



**Energy and/or electron  
transfer between excited  
fluorophore and metal core**

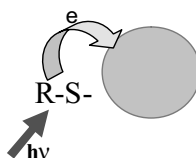


Fig. 19.2. Photoinduced transformations in pristine and functionalized gold nanoparticles.

minescent [52–54]. For example, gold nanorods exhibit an enhancement of  $10^6$  in the photoemission yield as compared to the bulk metal [53]. Many interesting nonlinear optical phenomenon [55, 56] as well as surface enhanced Raman scattering effects [57–64] have been observed with silver and gold nanoparticles. Examples discussed in the following sections highlight laser induced processes in gold and silver nanoparticles.

### 19.3.1

#### Transient Bleaching of the Surface Plasmon Band

The visible absorption bands of the gold ( $\sim 530$  nm) and silver ( $\sim 380$  nm) colloids make them ideal candidates to probe the optical effects using transient absorption [65–67] and transient grating spectroscopy [68]. Optical limiting and nonlinear optical properties of metal colloids have also been explored recently [55, 56, 68, 69]. When the metal colloids are excited with a short laser pulse, a prompt bleaching of the plasmon band is observed within the laser pulse duration. The difference absorption spectrum of gold colloids shown in Figure 19.3 exhibits an intense bleaching of the surface plasmon band at 520 nm. The plasmon band of metal nanoparticles, as explained on the basis of Mie theory, involves dipolar oscillations of the free electrons in the conduction band that occupy energy states immediately above the Fermi level [50, 70]. Once these electrons are excited by a laser pulse, they do not oscillate at the same frequency as that of the unexcited electrons, thus resulting in a decrease of the plasmon absorption band. These aspects have been addressed in recent spectroscopic investigations [65, 68, 71, 72]. The recovery of the plasmon band on the picosecond timescale arises from the electron–phonon and phonon–phonon relaxation. Similar transient bleaching has also been observed for silver nanoparticles [66, 73] and bimetallic particles [74–76].

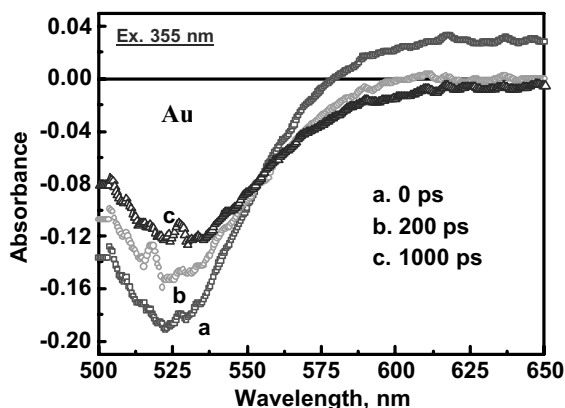


Fig. 19.3. Time-resolved difference absorption spectra recorded following 355 nm laser pulse (pulse width 20 ps) excitation of 0.12 mM Au colloidal suspension. (From [24].)

The bleaching recovery of the pristine Au colloids consists of a fast ( $\tau = 2.5$  ps) and a slow process ( $\tau > 50$  ps) [71]. The slower component of the recovery had a lifetime of 170 ps. These fast and slow recoveries correspond to the relaxation of “hot” electrons via electron–phonon coupling and phonon–phonon relaxation of the lattice, respectively. Dumping thermal energy into the solvent causes the dielectric of the surrounding medium to change, which in turn, influences the plasmon resonance frequency of the metal nanoclusters.

### 19.3.2

#### Laser Induced Fusion and Fragmentation of Metal Nanoclusters

Silver and gold nanoparticles show significant photoactivity under high intensity UV and visible irradiation. These nanoparticles undergo morphological changes under laser irradiation [73, 77–82]. Whereas photofragmentation and photofusion processes are found to be biphotonic and require high intensity laser excitation, simple shape changes can occur even at low intensity excitation [83].

The morphological changes caused by the 532 nm laser pulse irradiation of thionicotinic acid-capped gold nanoparticle samples are shown in transmission electron microscopy (Figure 19.4). Native gold colloids prepared by the citric acid reduction method are nearly spherical in shape with a particle diameter of 15–20 nm. Surface neutralization of citrate-stabilized gold nanoparticles with thiol readily yields clustered aggregates with broad absorption in the infrared. The purple colored gold colloidal solution turns blue if one adds small amounts of thionicotinamide (TNA). The transmission electron micrograph of TNA-capped gold nanoparticles (Figure 19.4A) shows the presence of cluster islands, each consisting of several nanoparticles that are in close contact. After 1 min laser pulse irradiation (532 nm, 10 Hz, 1.5 mJ) the aggregate sample transforms to form large size spherical particles (Figure 19.4B). Pumping the laser pulses (532 nm) for a longer duration (15–30 min) results in the fragmentation of these fused particles (Figure 19.4C).

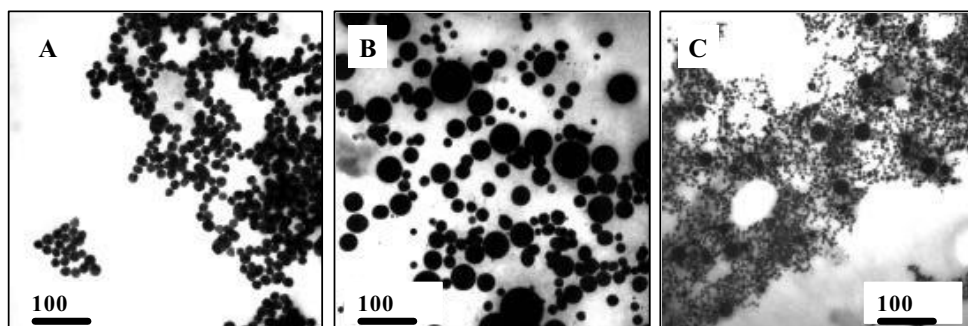


**Fig. 19.4.** Thionicotinamide capped gold nanoparticles (A) before, (B) after 1 min and (C) after 30 min of 532 nm laser excitation. (From [78].)

The photofusion phenomenon occurs as a result of the melting of gold nanoparticle aggregates to form larger spherical particles during laser irradiation. As the gold particles are repeatedly bombarded with laser pulse, the temperature of these particles increases leading to melting. Theoretical calculations have predicted a rise in temperature up to 2500 K during laser excitation [84]. Similar laser induced fusion is not seen in uncapped gold colloids because the individual particles are well separated and the heat gained from laser excitation is quickly dumped into the surrounding aqueous medium ( $< 200$  ps) [72, 85, 86].

### 19.3.3

#### Photoinduced Energy and Electron Transfer Process between Excited Sensitizer and Metal Nanocore

Researchers have often used functional groups such as thiols, amines, or silanes to attach electroactive or photoactive molecules to the gold surface [87–91]. The ability of gold surfaces to bind with specific functional groups makes them potentially useful in the development of biological probes [92–95], photonic materials [96], and chemical sensors [18, 97]. An inorganic–organic hybrid probe also offers the possibility of using complementary sensing via fluorescence spectroscopy and electron microscopy. Since fluorescence spectroscopy is a very sensitive technique, fluorophore bound gold nanoparticles are useful probes for biomolecular labeling (e.g., as immunoprobes) [21, 92, 94]. An example of binding a pyrenemethylamine probe molecule to a gold nanocluster is shown in Figure 19.5. The charge transfer interaction between the gold nanoparticle and pyrenemethylamine results in highly fluorescent hybrid material that can be used for sensing applications [98].

Assembling fluorophore–metal nanoparticle superstructures as a two- or three-dimensional architecture provides routes to design novel materials with tailored electrical [99], optical [100–102], lithographic [63, 103–107], sensing [18, 108–112],

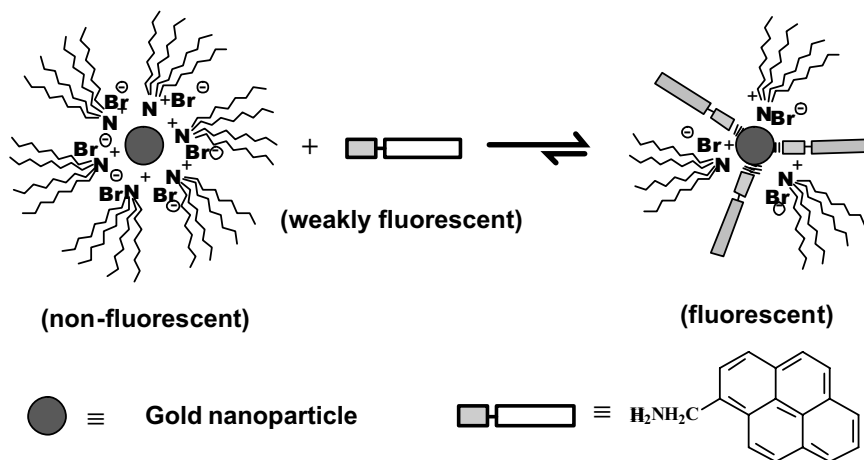


Fig. 19.5. Binding of fluorophore molecules to metal nanoparticles.

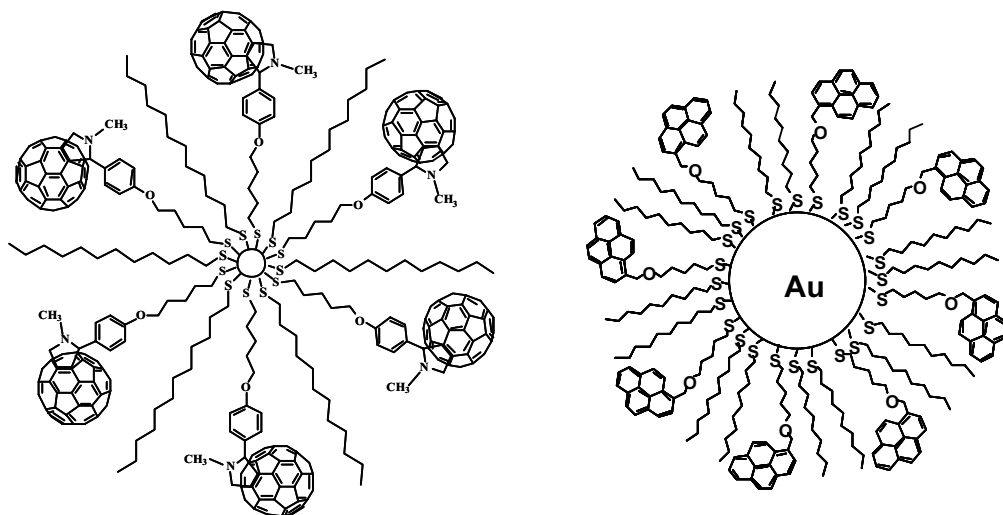


Fig. 19.6. Functionalization of gold nanoparticles with thiol derivatives of fullerene and pyrene.

and photochemical [113–118] properties. In order to meet the practical challenges that lie ahead we need to understand surface interactions at the molecular level and develop strategies for refining properties of nanoparticle superstructures.

Photoinduced electron transfer and energy transfer in a number of donor–acceptor systems have been extensively studied with an aim to mimic natural photosynthesis, by converting the charge-separated state into chemical or electrical energy [119, 120]. By suitably assembling these systems on a metal surface one can find ways to utilize the separated charge in such molecular assemblies. Demonstration of such a concept is made using self assembled monolayers (SAMs) of photoactive molecules on gold electrodes [108, 114, 118, 121–130]. Direct binding of a fluorophore to the metal surface often results in the quenching of excited states [49, 91, 128, 131]. Both energy-transfer and electron-transfer processes are considered to be major deactivation pathways for excited fluorophores on metal surfaces. Examples of gold nanoparticles functionalized with thiol-derivatized fullerene and pyrene are presented in Figure 19.6.

Recent transient absorption spectroscopy experiments have related the excited-state quenching of the surface-bound fluorophores to an electron transfer process in the pyrene thiol-bound gold (Au–SR–Pyrene) nanoassemblies [132]. The interesting redox property of thiol-capped gold nanoparticles renders them to hold the charge in a quantized fashion [133–136]. In the example of Au–SR–Pyrene, the ability of the gold nanocore to accept charge from the excited pyrene makes the charge separation possible. It is interesting to note that this charge separation is sustained for several microseconds before undergoing recombination. The ability of gold nanoparticles to participate in photoinduced electron transfer reactions demonstrates the possibility of employing fluorophore-bound gold nanoparticles as light-harvesting assemblies.

## 19.4

## Electrochemistry of Semiconductor Nanostructures

## 19.4.1

## Nanostructured Metal Oxide Films

Semiconductor nanoparticles exhibit an interesting property of storing electrons and holes at trap sites. This redox property opens the way to modulate charging of these particles using an electrochemical bias. Efforts have been made in the past to investigate electrochemically induced chromic effects in  $\text{WO}_3$  nanoparticle suspensions [137] and films [138–144]. Nanoparticles of  $\text{SnO}_2$ ,  $\text{TiO}_2$ , and  $\text{WO}_3$  are readily assembled as three-dimensional arrays on conducting glass electrodes. These highly porous nanostructured thin films undergo color changes under applied potential.

The presence of alkali metal ions is crucial for the stabilization of excess charge trapped within the nanoparticles. Intercalation of metal ions within the nanoparticle thus becomes a limiting factor as the rate of transport of these ions becomes slower in thicker metal oxide films. This in turn controls the rate of coloration and recovery of the electrochromic effects. Limited efforts have also been made to employ mixed  $\text{TiO}_2/\text{WO}_3$  [145],  $\text{WO}_3/\text{V}_2\text{O}_5$  [146], and  $\text{WO}_3/\text{MoO}_3$  [147] systems to enhance the efficiency of electrochromic effects. The beneficial aspect of these nanostructured semiconductor films in electrochromic devices is yet to be explored in a systematic way.

Figure 19.7 shows the absorption changes in nanostructured  $\text{WO}_3$  films at different applied negative potentials. At positive potentials (0 V or higher), no change in the absorption is seen, but with increasing negative potentials an increase in the IR absorption is observed. Switching the electrode to positive bias can reverse the blue color observed in these films. At potentials more negative than  $-1.2$  V the color changes to brown.

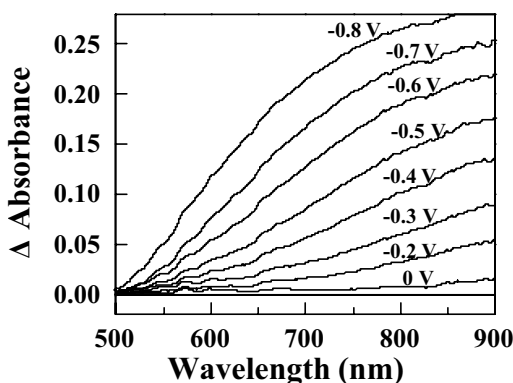
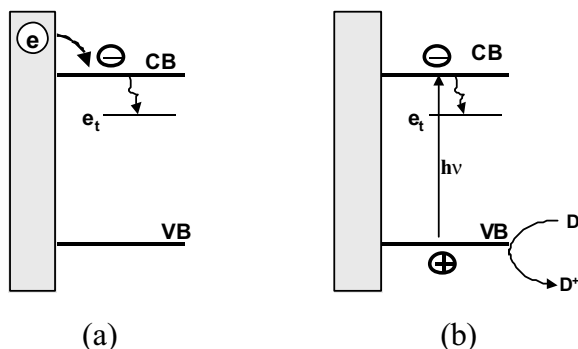


Fig. 19.7. Dependence of electrochromic effect of  $\text{WO}_3$  particulate film on the charging potentials. (From [143]. Reprinted with permission from the American Chemical Society.)



**Fig. 19.8.** (a) Electrochemically induced and (b) photoinduced charge separation and electron trapping processes leading to color changes in metal oxide semiconductor nano-

crystallites. CB and VB refer to conduction and valence bands of the semiconductor,  $e_t$  refers to surface traps and D refers to a hole scavenger.

The onset potential at which the electrochromic effect is observed corresponds to the flat band potential of the corresponding semiconductor and is dependent on the pH of the medium. With increasing pH the onset of the electrochromic effect was found to shift to more negative potentials [148, 149]. By monitoring the optical absorbance, Fitzmaurice and his coworkers [148–152] have determined the flat-band potentials of nanostructured films of  $\text{TiO}_2$  and GaAs and the extinction coefficient of the trapped electrons. On the other hand  $\text{ZnO}$  [153],  $\text{SnO}_2$  [154], and  $\text{CdS}$  [155] films exhibit bleaching at potentials more negative than the flat band potential.

As confirmed from the spectroelectrochemical study of  $\text{TiO}_2$  particulate films [148, 149], the inherent semiconductor properties such as trapping of electrons at the defect sites is responsible for the coloration effects (Figure 19.8). Electrochemical and photoelectrochemical approaches have supported this mechanism for coloration in  $\text{WO}_3$  colloids [137] and nanostructured films [143]. The net color change was found to be spectrally similar whether one employed direct bandgap excitation of  $\text{WO}_3$  nanoparticles or subjected them to a negative electrochemical bias.

#### 19.4.2

##### Nanostructured Oxide Films Modified with Dyes and Redox Chromophores

Oxide nanoparticles (e.g.  $\text{SnO}_2$  or  $\text{TiO}_2$ ) can be modified with dyes and electroactive molecules that have been functionalized with reactive groups such as carboxylic acid or phosphonate. These functional groups chemically bind to the oxide surface, thus creating a semiconductor–organic dye assembly. One can also use electrostatic interactions to bind the cationic or anionic dye molecules to the particle surface of  $\text{SnO}_2$  or  $\text{TiO}_2$ . Close packing of dye molecules often lead to aggregation effects on the surface of these particles. The schematic diagram presented in



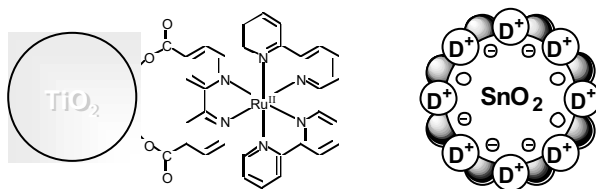


Fig. 19.9. Binding of redox chromophores to oxide nanoparticles via charge transfer and electrostatic interactions.

Figure 19.9 illustrates the principle of surface modification of oxide nanoparticles with dyes. Dyes that absorb in the visible and/or IR region become colorless (or change to another color) upon undergoing reduction (or oxidation) under the influence of an electrochemical bias. The feasibility of this concept has already been demonstrated in our laboratory by binding a thiazine dye to nanostructured  $\text{SnO}_2$  film [156]. Reverse electrochromism obtained using such dye systems provides an alternate approach to conventional oxide-based electrochromic devices.

This approach can be extended to bind redox chromophores directly to a nanostructured semiconductor film and induce color changes under applied potentials (Figure 19.10). The oxide nanoparticles in the film merely act as a high surface area support for anchoring these molecular assemblies and stabilizing the redox species. As a result of such high coverage one can achieve 2–3 order of magnitude enhancement in the color changes associated with the oxidation or reduction of an adsorbed molecular monolayer. For example, a phosphonate linkage has been used to bind viologen compounds to nanostructured  $\text{TiO}_2$  films and construct electrochromic windows [157, 158]. Under an applied negative bias the viologens are reduced to develop a blue coloration. Long term stability and high coloration efficiencies ( $\sim 200 \text{ cm}^2 \text{ C}^{-1}$ ) have been reported in these studies.

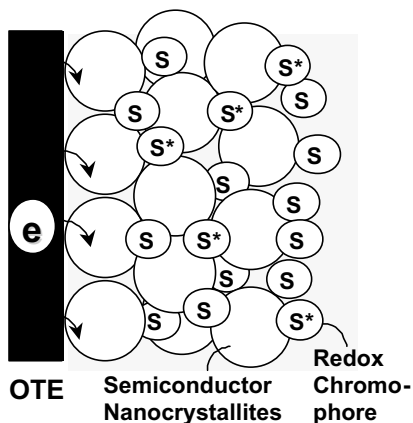


Fig. 19.10. Schematic diagram of nanostructured-semiconductor-redox chromophore assembly for electrochromic applications.

Nanocrystalline  $\text{TiO}_2$  thin films on conductive glass electrodes have been modified with monolayers of different electrochromic moieties (mono-, di- and trimeric  $N,N'$ -dialkyl- or diphenyl-4,4'-bipyridinium salts) functionalized with  $\text{TiO}_2$  anchoring groups such as benzoate, salicylate, phosphonates [159, 160]. The type of anchoring group and the viologen moiety influenced the electrochemically active coloring centers on  $\text{TiO}_2$ . The transmittance changes from 79 to 11% in less than 1 s indicating the fast response time of these electrodes [160]. An attempt has also been made to prepare electrochromic material by electropolymerizing  $N,N'$ -bis[*p*-(trimethoxysilyl)benzyl]-4,4'-bipyridinium dichloride ( $\text{BPQ}^{2+} \cdot 2\text{Cl}^-$ ) on top of a reductively conducting film of tungsten trioxide [161]. The resulting composite film responds to a potential step from 0.9 to  $-0.65$  V by turning from colorless to blue in two steps: the absorbance due to one-electron reduction of each monomer unit in poly( $\text{BPQ}^{2+}$ ) increases quickly (in  $<4$  s), and is followed by a slower development of the absorbance due to the  $\text{WO}_3$  reduction ( $>1$  min). Metal hexacyanoferrates constitute another class of redox species that can be coupled with semiconductor nanostructures for designing electrochromic hybrid assemblies. For example  $\text{TiO}_2$ -metal hexacyanoferrate has recently been shown to possess excellent electrochromic properties [162].

#### 19.4.3

##### Photocurrent Generation

The nanostructured films of semiconductor oxides ( $\text{SnO}_2$ ,  $\text{TiO}_2$ ,  $\text{ZnO}$ ) when used as photoanodes in a photoelectrochemical cell, respond to the UV light by generating photocurrent. One way to extend their photoresponse is to modify the semiconductor surface with sensitizing dyes that absorb strongly in the visible. This approach of light energy conversion is similar to plant photosynthesis, in which chlorophyll act as light absorbing antenna molecules. In other words, the dye modified semiconductor films (see for example, Figure 19.9) provide an efficient method to mimic the photosynthetic process. The high porosity and strong surface bonding property of the nanostructured semiconductor films facilitate surface modification with organic dyes and organometallic complexes such as bis(2,2'-bipyridine)(2,2'-bipyridine-4,4'-dicarboxylic acid)ruthenium(II). The nanostructured  $\text{TiO}_2$  films modified with a ruthenium complex exhibit photoconversion efficiencies of about 10% [163], which is comparable to that of amorphous silicon-based photovoltaic cells.

When the dye modified semiconductor electrode is illuminated with visible light the sensitizer molecules absorb light and inject electrons into the semiconductor (e.g.,  $\text{TiO}_2$ ) particles. These electrons are then collected at the conducting glass surface to generate anodic photocurrent. The redox couple (e.g.,  $\text{I}_3^-/\text{I}^-$ ) present in the electrolyte quickly regenerates the sensitizer. By choosing an appropriate sensitizer it is possible to tune the photoresponse of these nanostructured semiconductor films. For example, sensitizing dyes such as chlorophyll *a* and chlorophyll *b*, [164, 165] squaraines [166] and oxazines [156] can extend the photoresponse of  $\text{SnO}_2$  films to the red-infrared region. Ru(II) polypyridyl complex modified  $\text{TiO}_2$

nanostructured films exhibit photon conversion efficiency of nearly 90% under optimized light-harvesting conditions [163]. A detailed discussion on the semiconductor nanostructure based photochemical solar cells can be found elsewhere [167–169].

## 19.5 Electrochemistry of Metal Nanostructures

Unlike bulk films, metal nanoparticles exhibit an unusual property of quantized double layer charging effects [170]. However, relatively little work has been carried out to date to elucidate the electrochemical behavior of metal nanoparticles. It is evident from electrochemical [20, 134], photochemical [132], and spectroelectrochemical [171] experiments that metal nanoparticles possess a unique property of storing electrons. For example, charge storage within the gold nanocore causes a large build-up of capacitance of the Helmholtz and diffuse double layer. As demonstrated earlier [172], the excess electron density remains mainly on the metal islands because the Helmholtz capacitance of the metal–solution interface is much higher than the space charge capacity of the semiconductor nanoparticle, even under accumulation.

Engineering of the nanocluster surfaces with photoactive molecules has potential applications in designing electrochromic devices of nanometric dimension. Controlled charging of an Au nanoassembly has enabled us to modulate the excited state interaction between the gold nanocore and a surface-bound fluorophore. A bifunctional surface-linking molecule such as mercaptopropionic acid is useful to link the gold nanoparticle to the  $\text{TiO}_2$  surface (thiol group on to gold and carboxylic group on to  $\text{TiO}_2$ ). Fluorophore functionalized electrodes can be prepared by immersing a  $\text{TiO}_2$  modified conducting electrode (referred to as OTE, optically transparent electrode) into the THF solution containing gold nanoparticles that were previously functionalized with mercaptopropionic acid and pyrene thiol ( $\text{Ac-S-(Au)-SR-Py}$ ) [171]. The pyrene functionalized electrode (referred to as OTE/ $\text{TiO}_2/\text{Ac-S-(Au)-S-Py}$ ) exhibits weak emission with a maximum around 395 nm. The decreased singlet lifetime as well as formation of the oxidation product, pyrene cation radical in the  $\text{Au-SR-Py}$  assembly, indicates the ability of gold nanoparticles to accept electrons from excited pyrene [132]. Since the oxidation potential of excited pyrene is around  $-1.5$  V versus NHE one can expect an energetically favorable electron transfer of electrons to gold nanoparticles ( $E_F = 0.5$  V).

Spectroelectrochemical experiments carried out using a thin layer electrochemical cell, show the emission spectra of OTE/ $\text{TiO}_2/\text{Ac-S-(Au)-S-Py}$  electrode at different applied potentials (Figure 19.11). As the electrode is biased to negative potentials one observes an increase in the emission yield. It is important to note that the overall shape of the emission band essentially remains the same. This, in turn, suggests that the photoactive species that contribute to the emission remain unperturbed. At potentials more negative than  $-1.0$  V, the quenching of the excited fluorophore by the gold nanocore is suppressed and the emission reaches

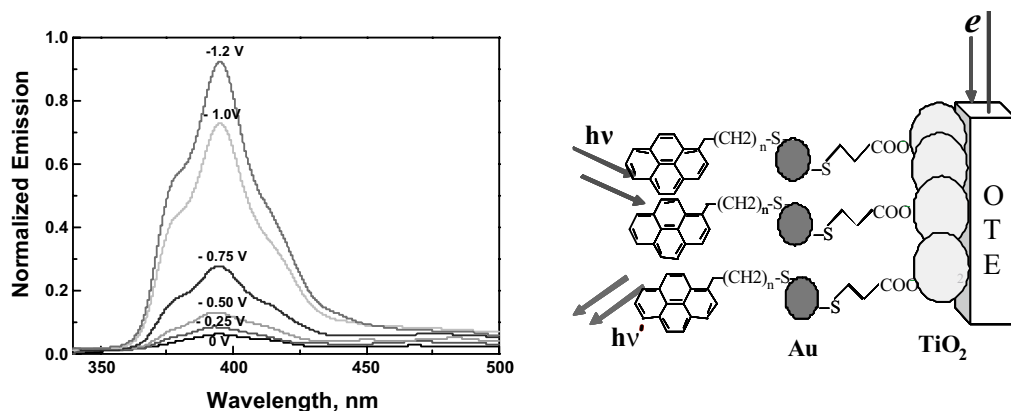


**Fig. 19.11.** Emission spectra (left) of OTE/TiO<sub>2</sub>/OOCS-(Au)-S-Pyrene electrode (right) at different applied potentials. (From [171]. Reprinted with permission from John Wiley Interscience.)

a plateau. Thus, more than 90% of the quenched emission can be restored by charging the gold nanoparticle with an externally applied electrochemical bias. The quantized charging effects studied with organic-capped gold nanoparticles suggest that the potential shift amounts to about 0.1 V per accumulated electron [134]. The electron transfer from excited pyrene molecules to gold nanocore experiences a barrier as we charge them with negative electrochemical bias.

## 19.6

### Semiconductor–Metal Nanocomposites

By designing semiconductor–metal composite nanoparticles it is possible to improve the catalytic properties of photocatalysts (Figure 19.12). Contact of metal

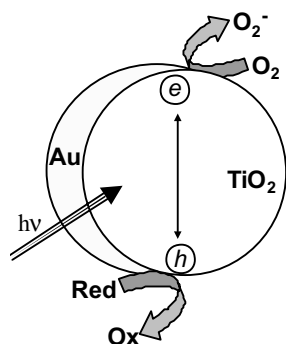


**Fig. 19.12.** Interfacial charge transfer processes in a metal–semiconductor nanoparticle.

with the semiconductor indirectly influences the energetics and interfacial charge transfer processes in a favorable way. The deposition of a noble metal on semiconductor nanoparticles is an essential factor for maximizing the efficiency of photocatalytic reactions [173]. It is normally assumed that the noble metal (e.g., Pt) acts as a sink for photoinduced charge carriers and promotes interfacial charge transfer processes. However, recent studies have presented a more complex reaction mechanism dictating the redox processes in semiconductor–metal systems [174].

### 19.6.1

#### Improving the Efficiency of Photocatalytic Transformations

It has been shown that the photocatalytic electron transfer processes at the semiconductor interface can be greatly enhanced by depositing a noble metal on the semiconductor particle [175–179]. The photogenerated holes are capable of oxidizing thiocyanate ions at the semiconductor interface [180]. The thiocyanate radicals  $((\text{SCN})_2^{\cdot-})$  generated in the photocatalytic oxidation can be conveniently monitored from its absorbance at 480 nm [180–183].

By employing a 337 nm pulsed laser as the excitation source for exciting  $\text{TiO}_2$  colloids and initiating the redox reactions at the interface one can monitor the interfacial hole transfer process (reactions (1) and (2)).



Since the formation of  $(\text{SCN})_2^{\cdot-}$  radicals immediately after the laser pulse excitation represents the quantitative estimate of the hole oxidation process, we monitored maximum absorbance at 480 nm at different  $\text{TiO}_2\text{:Au}$  ratios. (The  $\text{TiO}_2\text{:Au}$  ratio was varied by varying the gold concentration during sample preparation.) Figure 19.13 shows the dependence of  $(\text{SCN})_2^{\cdot-}$  yield on the gold shell concentration. In the absence of gold capping,  $\text{TiO}_2$  colloids generate  $(\text{SCN})_2^{\cdot-}$  radicals with a quantum yield of 0.09. At low concentrations of gold we see an increase in the efficiency of the oxidation process. For a  $[\text{Au}]:[\text{TiO}_2]$  ratio of 0.17 we see more than 40% enhancement in the oxidation efficiency ( $\Phi(\text{SCN})_2^{\cdot-} = 0.13$ ). As we further increase the Au concentration the efficiency of thiocyanate oxidation at gold-capped  $\text{TiO}_2$  nanoparticles decreases. Inability of the photogenerated holes to reach the electrolyte interface as well as increased absorption by the gold are the likely reasons for observing lower  $(\text{SCN})_2^{\cdot-}$  yield at higher capping concentrations of gold.

On the other hand, when low concentrations of metal are used to cap the semiconductor core we can expect the outer layer to be discontinuous. Such a configuration of core shell particles (i.e. small metal islands deposited on the  $\text{TiO}_2$  core) provides a favorable geometry for facilitating the interfacial charge transfer under UV irradiation. It should be noted that, a new band appears at 390 nm in the case of  $\text{TiO}_2/\text{Au}$  nanoparticles as the transient absorption corresponding to  $(\text{SCN})_2^{\cdot-}$

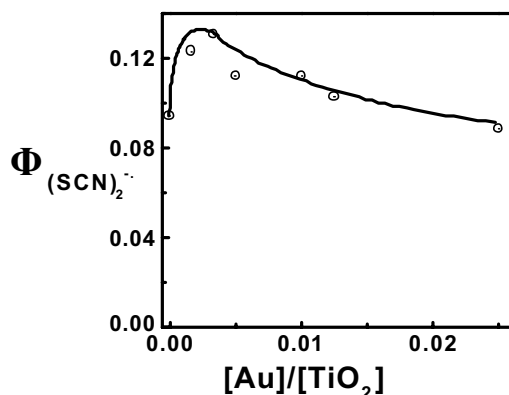


**Fig. 19.13.** Dependence of  $(\text{SCN})_2^{\bullet-}$  yield on the concentration of gold cap. The maximum absorbance at 480 nm was used to determine the quantum yield of oxidation process using

benzophenone carboxylate as actinometry reference. (From [82]. Reprinted with permission from the American Chemical Society.)

decays. As confirmed from the pulse radiolysis experiments [183], the 390 nm absorption band represents complexation between  $(\text{SCN})_2^{\bullet-}$  radicals and the gold surface which results in the oxidation of the gold layer.

#### 19.6.2

##### Fermi Level Equilibration

Metal islands or nanoparticles deposited on a semiconductor surface undergo Fermi level equilibration following charging with photogenerated electrons. The effect of Fermi level equilibration is predominantly seen when the metal deposits consist of small islands or small particles. Unlike the ohmic contact observed in bulk metals, the nanoparticles retain the charge before transferring them to the redox species. During extended UV-photolysis, electron-capture by metal islands of Ag, Au and Cu becomes inhibited as their Fermi level shifts close to the conduction band of the semiconductor. Pt on the other hand acts as an electron sink and fails to achieve Fermi level equilibration.

Semiconductor nanoparticles such as  $\text{TiO}_2$  and  $\text{ZnO}$  store electrons following bandgap excitation. Since the Fermi level of gold ( $E_F = +0.5$  V vs. NHE) is more positive than the conduction band energy of  $\text{TiO}_2$  and  $\text{ZnO}$  ( $E_{CB} = -0.5$  V vs. NHE at pH 7), we expect a quick distribution of electrons between excited semiconductor and metal nanoparticles. The electrons transferred to a gold nanoparticle increase the electron density within the nanoparticle, thus shifting the Fermi-level towards more negative potentials. The transfer of electrons to metal continues until the Fermi level equilibrates with the conduction band edge of the semiconductor (Figure 19.14).

By employing  $\text{C}_{60}/\text{C}_{60}^-$  as a probe-redox couple it is possible to estimate the apparent Fermi levels of  $\text{TiO}_2$  and  $\text{TiO}_2/\text{Au}$  nanoparticles [184]. The particle size of

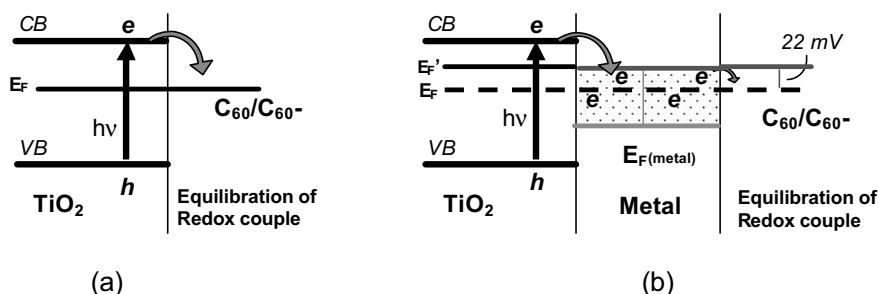


**Fig. 19.14.** Charge distribution between  $TiO_2$  and gold nanoparticles leading to equilibration with a  $C_{60}/C_{60}^-$  redox couple: (a) In the absence and (b) in the presence of metal nanoparticles.  $E_F$  and  $E_F'$  refer to the Fermi level of  $TiO_2$  before and after attaining the equilibration.

the metal particle also influences the shift in the Fermi level of the composite. For example, the Fermi level shift observed with 5 nm Au nanoparticles was  $-40$  mV as compared to  $-22$  mV for 8 nm Au nanoparticles in the Au- $TiO_2$  nanocomposite system. The shift of Fermi level to more negative potentials is indicative of increased charge storage and improved charge separation in semiconductor-metal composite systems. These results, in turn, elucidate the indirect role of noble metals towards improving the charge separation as well as promoting interfacial charge transfer kinetics in semiconductor assisted photocatalysis.

Photoelectrochemical studies [185, 186], carried out by depositing gold nanoparticles on nanostructured  $TiO_2$  films exhibit enhanced photocurrent generation. Improved interfacial charge transfer at the semiconductor/electrolyte interface resulted in nearly 5 times enhancement of photocurrent generation and a shift in the apparent flat band potential. Although the  $TiO_2$ -Au interface may offer many complex scenarios, the photoelectrochemical and photocatalytic measurements support the argument that the metal nanoparticle deposition facilitates charge (electron) stabilization in nanostructured semiconductor films and promotes interfacial redox processes.

## 19.7

### Concluding Remarks

The photochemical properties of various nanoassemblies discussed in this chapter highlight the ways in which the metal and semiconductor nanoparticles interact with light. Furthermore, one can fine tune these responses by subjecting nanostructures to an externally applied electrochemical bias. The ability to functionalize these nanoparticles with photoactive molecules has opened new avenues to utilize these nanoassemblies in light energy conversion and catalytic applications. By suitably modulating the fluorescence of the surface bound fluorophore these

nanoassemblies can be tuned to design sensors, display devices and biological probes. Molecular architecture of inorganic and organic hybrid structures will in future play a crucial role in tailoring the requirements of new generation nanodevices.

### Acknowledgement

The author acknowledges the support of the U.S. Department of Energy (DOE), Office of Science, and Basic Energy Sciences. This is contribution NDRL No. 4446 from the Notre Dame Radiation Laboratory.

### References

- 1 A. HENGLEIN, Physicochemical properties of small metal particles in solution: "Microelectrode" reactions, chemisorption, composite metal particles, and the atom-to-metal transition. *J. Phys. Chem.* **1993**, 97, 5457–5471.
- 2 P. MULVANEY; M. GIERSIG; A. HENGLEIN, Electrochemistry of multilayer colloids: Preparation and absorption spectrum of gold-coated silver particles. *J. Phys. Chem.* **1993**, 97, 7061–7064.
- 3 A. HENGLEIN, Electronics of colloidal nanometer particles. *Ber. Bunsenges. Phys. Chem.* **1995**, 99, 903–13.
- 4 Y. WANG; N. HERRON, X-ray photoconductive nanocomposites. *Science* **1996**, 273, 632–634.
- 5 P. V. KAMAT, *Composite Semiconductor Nanoclusters – Physical, Chemical and Catalytic Aspects.*, P. V. KAMAT AND D. MEISEL, Editors. 1997, Elsevier Science: Amsterdam. p. 237–259.
- 6 M. NIRMAL; B. O. DABBOUSI; M. G. BAWENDI; J. J. MACKLIN; J. K. TRAUTMAN; T. D. HARRIS; L. E. BRUS, Fluorescence intermittency in single cadmium selenide nanocrystals. *Nature* **1996**, 383, 802–804.
- 7 M. P. PILENI, Optical properties of nanosized particles dispersed in colloidal solutions or arranged in 2D or 3D superlattices. *New J. Chem.* **1998**, 693–702.
- 8 A. HENGLEIN, Radiolytic Preparation of Ultrafine Colloidal Gold Particles in Aqueous Solution: Optical Spectrum, Controlled Growth, and Some Chemical Reactions. *Langmuir* **1998**, 14, 6738–6744.
- 9 N. TOSHIMA; T. YONEZAWA, Bimetallic nanoparticles – novel materials for chemical and physical applications. *New Journal of Chemistry* **1998**, 22, 1179–1201.
- 10 S. LINK; M. A. EL-SAYED, Size and temperature dependence of the plasmon absorption of colloidal gold nanoparticles. *J. Phys. Chem. B* **1999**, 103, 4212–4217.
- 11 S.-H. KIM; G. MEDEIROS-RIBEIRO; D. A. A. OHLBERG; R. STANLEY WILLIAMS; J. R. HEATH, Individual and Collective Electronic Properties of Ag Nanocrystals. *J. Phys. Chem. B* **1999**, 103, 10341–10347.
- 12 P. GOMEZ-ROMERO, Hybrid organic-inorganic materials – In search of synergic activity. *Advanced Materials* **2001**, 13, 163–174.
- 13 M. A. EL-SAYED, Some interesting properties of metals confined in time and nanometer space of different shapes. *Accounts of Chemical Research* **2001**, 34, 257–264.
- 14 B. C. GATES, Supported Metal-Clusters – Synthesis, Structure, and Catalysis. *Chemical Reviews* **1995**, 95, 511–522.
- 15 J. M. THOMAS; B. F. G. JOHNSON; R. RAJA; G. SANKAR; P. A. MIDGLEY,



- High-Performance Nanocatalysts for Single-Step Hydrogenations. *Acc. Chem. Res.* **2003**, 36, 20–30.
- 16 M. LAHAV; A. N. SHIPWAY; I. WILLNER, Au-nanoparticle-bis-bipyridinium cyclophane superstructures: assembly, characterization and sensoric applications. *Journal of the Chemical Society-Perkin Transactions 2* **1999**, 1925–1931.
  - 17 D. J. MAXWELL; J. R. TAYLOR; S. M. NIE, Self-assembled nanoparticle probes for recognition and detection of biomolecules. *Journal of the American Chemical Society* **2002**, 124, 9606–9612.
  - 18 G. BAUER; F. PITTNER; T. SCHALKHAMMER, Metal nano-cluster biosensors. *Mikrochim. Acta* **1999**, 131, 107–114.
  - 19 J. J. HICKMAN; D. OFER; P. E. LAIBINIS; G. M. WHITESIDES; M. S. WRIGHTON, Molecular self-assembly of 2-terminal, voltammetric micro-sensors with internal references. *Science* **1991**, 252, 688–691.
  - 20 S. CHEN; R. S. INGRAM; M. J. HOSTETLER; J. J. PIETRON; R. W. MURRAY; T. G. SCHAAFF; J. T. KHOURY; M. M. ALVAREZ; R. L. WHETTEN, Gold Nanoelectrodes of Varied Size: Transition to Molecule-Like Charging. *Science* **1998**, 280, 2098–2101.
  - 21 R. ELGHANIAN; J. J. STORHOFF; R. C. MUCIC; R. L. LETSINGER; C. A. MIRKIN, Selective Colorimetric Detection of Polynucleotides Based on the Distance-Dependent Optical Properties of Gold Nanoparticles. *Science* **1997**, 277, 1078–1081.
  - 22 G. MARKOVICH; C. P. COLLIER; S. E. HENRICH; F. REMACLE; R. D. LEVINE; J. R. HEATH, Architectonic Quantum Dot Solids. *Acc. Chem. Res.* **1999**, 32, 415–423.
  - 23 I. WILLNER; B. WILLNER, Molecular and biomolecular optoelectronics. *Pure Appl. Chem.* **2001**, 73, 535–542.
  - 24 P. V. KAMAT, Photophysical, photochemical and photocatalytic aspects of metal nanoparticles. *J. Phys. Chem. B* **2002**, 106, 7729–7744.
  - 25 L. LIZ-MARZAN; P. V. KAMAT, *Nanoscale Materials*. Boston: Kluwer Academic/Plenum Publishers. 499 **2003**.
  - 26 P. V. KAMAT; D. MEISEL, eds. *Semiconductor Nanoclusters-Physical, Chemical and Catalytic Aspects*. Studies in Surface Science and Catalysis. Elsevier Science: Amsterdam. 474 **1997**.
  - 27 B. KRAEUTLER; C. D. JAEGER; A. J. BARD, Direct observation of radical intermediates in the radical formation by electron spin resonance. *J. Am. Chem. Soc.* **1978**, 100, 4903–4905.
  - 28 M. ANPO; T. SHIMA; Y. KUBOKAWA, ESR and photoluminescence evidence for the photocatalytic formation of OH<sup>•</sup> radicals on small TiO<sub>2</sub> particles. *Chem. Lett.* **1985**, 1799–1802.
  - 29 R. F. HOWE; M. GRAETZEL, EPR observation of trapped electrons in colloidal TiO<sub>2</sub>. *J. Phys. Chem.* **1985**, 89, 4495–4499.
  - 30 O. I. MICIC; Y. ZHANG; K. R. CROMACK; A. D. TRIFUNAC; M. C. THURNAUER, Photoinduced hole transfer from TiO<sub>2</sub> to methanol molecules in aqueous solution studied by electron paramagnetic resonance. *J. Phys. Chem.* **1993**, 97, 13284–13288.
  - 31 O. I. MICIC; Y. ZHANG; K. R. CROMACK; A. D. TRIFUNAC; M. C. THURNAUER, Trapped holes on TiO<sub>2</sub> colloids studied by electron paramagnetic resonance. *J. Phys. Chem.* **1993**, 97, 7277–7283.
  - 32 H. GERISCHER; A. HELLER, The role of oxygen in photooxidation of organic molecules on semiconductor particles. *J. Phys. Chem.* **1991**, 95, 5261–5267.
  - 33 C. M. WANG; A. HELLER; H. GERISCHER, Palladium catalysis of O<sub>2</sub> reduction by electrons accumulated on TiO<sub>2</sub> particles during photoassisted oxidation of organic compounds. *J. Am. Chem. Soc.* **1992**, 114, 5230–5234.
  - 34 H. GERISCHER; A. HELLER, Photocatalytic oxidation of organic molecules at TiO<sub>2</sub> particles by sunlight in aerated water. *J. Electrochem. Soc.* **1992**, 139, 113–118.
  - 35 M. W. PETERSON; J. A. TURNER; A. J. NOZIK, Mechanistic studies of the photocatalytic behavior of TiO<sub>2</sub>.

- Particles in a photoelectrochemical slurry cell and the relevance to photodetoxification reactions. *J. Phys. Chem.* **1991**, 95, 221–225.
- 36 K. VINODGOPAL; S. HOTCHANDANI; P. V. KAMAT, Electrochemically assisted photocatalysis.  $\text{TiO}_2$  particulate film electrodes for photocatalytic degradation of 4-chlorophenol. *J. Phys. Chem.* **1993**, 97, 9040–9044.
  - 37 J. M. KESSELMAN; A. KUMAR; N. S. LEWIS, *Fundamental photoelectrochemistry of  $\text{TiO}_2$  and  $\text{SrTiO}_3$  applied to environmental problems*, in *Photocatalytic Purification and Treatment of Water and Air*, D. F. OLLIS AND H. AL-EKABI, Editors. 1993, Elsevier Science Publishers B. V.: Amsterdam. p. 19–37.
  - 38 J. M. KESSELMAN; G. A. SHREVE; M. R. HOFFMANN; N. S. LEWIS, Flux-matching condition at  $\text{TiO}_2$  photoelectrodes: Is interfacial electron transfer to  $\text{O}_2$  rate-limiting in the  $\text{TiO}_2$ -catalyzed degradation of organics? *J. Phys. Chem.* **1994**, 98, 13385–13395.
  - 39 D. SCHMELLING; K. A. GRAY; P. V. KAMAT, Role of reduction in the photocatalytic degradation of trinitrotoluene. *Environ. Sci. Technol.* **1996**, 30, 2547–2555.
  - 40 P. V. KAMAT, Photochemistry on nonreactive and reactive (semiconductor) surfaces. *Chem. Rev.* **1993**, 93, 267–300.
  - 41 M. R. HOFFMANN; S. T. MARTIN; W. CHOI; D. W. BAHNEMANN, Environmental applications of semiconductor photocatalysis. *Chem. Rev.* **1995**, 95, 69–96.
  - 42 N. SERPONE, Relative phototonic efficiencies and quantum yields in heterogeneous photocatalysis. *J. Photochem. Photobiol., A: Chem.* **1997**, 104, 1–12.
  - 43 A. FUJISHIMA; K. HASHIMOTO; T. WATANABE,  *$\text{TiO}_2$  photocatalysis. Fundamentals and Applications*. Tokyo, Japan: Bkc, Inc. 176 **1999**.
  - 44 J. K. SASS; R. K. SEN; E. MEYER; H. GERISCHER, Tunneling processes at highly doped  $\text{ZnO}$ -electrodes in aqueous electrolytes. Part II. Electron exchange with the valence band. *Surf. Sci.* **1974**, 44, 515.
  - 45 P. MULVANEY; T. LINNERT; A. HENGLEIN, Surface chemistry of colloidal silver in aqueous solution: Observations on chemisorption and reactivity. *J. Phys. Chem.* **1991**, 95, 7843–7846.
  - 46 T. LINNERT; P. MULVANEY; A. HENGLEIN, Photochemistry of colloidal silver particles: The effects of  $\text{N}_2\text{O}$  and adsorbed  $\text{CN}^-$ . *Ber. Bunsenges. Phys. Chem.* **1991**, 95, 838–841.
  - 47 D. CAHEN; G. HODES, Molecules and electronic materials. *Adv. Mater.* **2002**, 14, 789–798.
  - 48 M. BRUST; C. KIELY, Some recent advances in nanostructure preparation from gold and silver particles: a short topical review. *Colloid Surface A* **2002**, 202, 175–186.
  - 49 P. AVOURIS; B. N. J. PERSSON, Excited States at Metal Surfaces and Their Nonradiative Relaxation. *J. Phys. Chem.* **1984**, 88, 837–848.
  - 50 U. KREIBIG; M. VOLLMER, *Optical Properties of Metal Clusters*. Berlin: Springer **1995**.
  - 51 M.-P. PILENI, The role of soft colloidal templates in controlling the size and shape of inorganic nanocrystals. *Nature Materials* **2003**, 2, 148–150.
  - 52 J. P. WILCOXON; J. E. MARTIN; F. PARSAPOUR; B. WIEDENMAN; D. F. KELLEY, Photoluminescence from nanosize gold clusters. *J. Chem. Phys.* **1998**, 108, 9137–9143.
  - 53 M. B. MOHAMED; V. VOLKOV; S. LINK; M. A. EL-SAYED, The ‘lightning’ gold nanorods: fluorescence enhancement of over a million compared to the gold metal. *Chemical Physics Letters* **2000**, 317, 517–523.
  - 54 T. HUANG; R. W. MURRAY, Visible Luminescence of Water-Soluble Monolayer-Protected Gold Clusters. *J. Phys. Chem. B* **2001**, 105, 12498–12502.
  - 55 T. SATO; T. ICHIKAWA; T. ITO; Y. YONEZAWA; K. KADONO; T. SAKAGUCHI; M. MIYA, Nonlinear optical properties of silver sols prepared by photoreduction method. *Chem. Phys. Lett.* **1995**, 242, 310–314.

- 56 L. FRANÇOIS; M. MOSTAFAVI; J. BELLONI; J.-F. DELOUIS; J. DELAIRE; P. FENEYROU, Optical Limitation induced by Gold Clusters. 1. Size Effect. *J. Phys. Chem. B* **2000**, *104*, 6133–6137.
- 57 P. C. LEE; D. MEISEL, Adsorption and surface-enhanced Raman of dyes on silver and gold sols. *J. Phys. Chem.* **1982**, *86*, 3391–3395.
- 58 R. G. FREEMAN; M. B. HOMMER; K. C. GRABAR; M. A. JACKSON; M. J. NATAN, Ag-Clad Au nanoparticles: Novel aggregation, optical and surface-enhanced Raman scattering properties. *J. Phys. Chem.* **1996**, *100*, 718–724.
- 59 S. J. OLDENBURG; S. L. WESTCOTT; R. D. AVERITT; N. J. HALAS, Surface enhanced Raman scattering in the near infrared using metal nanoshell substrates. *J. Chem. Phys.* **1999**, *111*, 4729–4735.
- 60 A. M. MICHAELS; J. JIANG; L. BRUS, Ag Nanocrystal Junctions as the Site for Surface-Enhanced Raman Scattering of Single Rhodamine 6G Molecules. *J. Phys. Chem. B* **2000**, *104*, 11965–11971.
- 61 S. J. OLDENBURG; S. L. WESTCOTT; R. D. AVERITT; N. J. HALAS, Surface enhanced Raman scattering in the near infrared using metal nanoshell substrates. *J. Chem. Phys.* **1999**, *111*, 4729–4735.
- 62 C. D. KEATING; K. K. KOVALESKI; M. J. NATAN, Heightened electromagnetic fields between metal nanoparticles: Surface enhanced Raman scattering from metal-cytochrome c-metal sandwiches. *J. Phys. Chem. B* **1998**, *102*, 9414–9425.
- 63 J. C. HULTEEN; D. A. TREICHEL; M. T. SMITH; M. L. DUVAL; T. R. JENSEN; R. P. VAN DUYN, Nanosphere lithography: Size-tunable silver nanoparticle and surface cluster arrays. *J. Phys. Chem. B* **1999**, *103*, 3854–3863.
- 64 M. C. CHEN; S. D. TSAI; M. R. CHEN; S. Y. OU; W. H. LI; K. C. LEE, Effect of silver-nanoparticle aggregation on surface-enhanced Raman-scattering from benzoic-acid. *Phys. Rev. B* **1995**, *51*, 4507–4515.
- 65 J. Z. ZHANG, Ultrafast studies of electron dynamics in semiconductor and metal colloidal nanoparticles: Effect of size and surface. *Acc. Chem. Res.* **1997**, *30*, 423–429.
- 66 S. LINK; M. A. EL-SAYED, Spectral Properties and Relaxation Dynamics of Surface Plasmon Electronic Oscillations in Gold and Silver Nanodots and Nanorods. *J. Phys. Chem. B* **1999**, *103*, 8410–8426.
- 67 J. HODAK; A. HENGLEIN; G. V. HARTLAND, Photophysics of Nanometer Sized Metal Particles: Electron-Phonon Coupling and Coherent Excitation of Breathing Vibrational Modes. *J. Phys. Chem. B* **2000**, *104*, 9954–9965.
- 68 E. J. HEILWEIL; R. M. HOCHSTRASSER, Nonlinear spectroscopy and picosecond transient grating study of colloidal gold. *J. Chem. Phys.* **1985**, *82*, 179–183.
- 69 O. A. AKTSIPETROV; P. V. ELYUTIN; A. A. FEDYANIN; A. A. NIKULIN; A. N. RUBTSOV, Second-harmonic generation in metal and semiconductor low-dimensional structures. *Surface Science* **1995**, *325*, 343–355.
- 70 G. MIE, *Ann. Physik B* **1908**, *25*, 377.
- 71 T. S. AHMADI; S. L. LOGUNOV; M. A. EL-SAYED, Picosecond dynamics of colloidal gold nanoparticles. *J. Phys. Chem.* **1996**, *100*, 8053–8056.
- 72 J. HODAK; I. MARTINI; G. V. HARTLAND, Ultrafast study of electron-phonon coupling in colloidal gold particles. *Chem. Phys. Lett.* **1998**, *284*, 135–141.
- 73 P. V. KAMAT; M. FLUMIANI; G. HARTLAND, Picosecond dynamics of Silver nanoclusters. Photoejection of electrons and fragmentation. *J. Phys. Chem. B* **1998**, *102*, 3123–3128.
- 74 J. HODAK; A. HENGLEIN; M. GIERSIG; G. V. HARTLAND, Laser-Induced Inter-Diffusion in AuAg Core-Shell Nanoparticles. *J. Phys. Chem. B* **2000**, *104*, 11708–11718.
- 75 S. LINK; Z. L. WANG; M. A. EL-SAYED, Alloy Formation of Gold-Silver Nanoparticles and the Dependence of the Plasmon Absorption on Their Composition. *J. Phys. Chem. B* **1999**, *103*, 3529–3533.
- 76 P. V. KAMAT; M. FLUMIANI; A.

- DAWSON, Metal-metal and metal-semiconductor composite nanoclusters. *Colloids and Surfaces A. Physicochemical and Engineering Aspects* **2002**, *202*, 269–279.
- 77 A. TAKAMI; H. YAMADA; K. NAKANO; S. KODA, The size reduction of silver particles in aqueous solution by laser irradiation. *Jap. J. Appl. Phys.* **1996**, *35*, L781–L783.
  - 78 H. FUJIWARA; S. YANAGIDA; P. V. KAMAT, Visible laser induced Fusion and fragmentation of thionicotinamide capped gold nanoparticles. *J. Phys. Chem. B* **1999**, *103*, 2589–2591.
  - 79 S. LINK; C. BURDA; M. B. MOHAMED; B. NIKOOBAKH; M. A. EL-SAYED, Laser photothermal melting and fragmentation of gold nanorods: Energy and laser pulse-width dependence. *J. Phys. Chem. A* **1999**, *103*, 1165–1170.
  - 80 Y. NIIDOME; A. HORI; T. SATO; S. YAMADA, Enormous size growth of thiol-passivated gold nanoparticles induced by near-IR light. *Chem. Lett.* **2000**, 310–311.
  - 81 S. LINK; Z. L. WANG; M. A. EL-SAYED, How Does a Gold Nanorod Melt? *J. Phys. Chem. B* **2000**, *104*, 6767–6772.
  - 82 A. DAWSON; P. V. KAMAT, Semiconductor-metal nanocomposites. Photo-induced fusion and photocatalysis of gold-capped  $\text{TiO}_2$  ( $\text{TiO}_2/\text{Au}$ ) nanoparticles. *J. Phys. Chem. B* **2001**, *105*, 960–966.
  - 83 R. C. JIN; Y. W. CAO; C. A. MIRKIN; K. L. KELLY; G. C. SCHATZ; J. G. ZHENG, Photoinduced conversion of silver nanospheres to nanoprisms. *Science* **2001**, *294*, 1901–1903.
  - 84 A. TAKAMI; H. KURITA; S. KODA, Laser-induced size reduction of noble metal particles. *J. Phys. Chem. B* **1999**, *103*, 1226–1232.
  - 85 S. L. LOGUNOV; T. S. AHMADI; M. A. EL-SAYED; J. T. KHOURY; R. L. WHETTEN, Electron dynamics of passivated gold nanocrystals probed by subpicosecond transient absorption spectroscopy. *J. Phys. Chem. B* **1997**, *101*, 3713–3719.
  - 86 B. SHANGHAVI; P. V. KAMAT, Interparticle electron transfer in metal/semiconductor composites. Pico-second dynamics of CdS capped gold nanoclusters. *J. Phys. Chem. B* **1997**, *101*, 7675–7679.
  - 87 A. C. TEMPLETON; D. E. CLIFFEL; R. W. MURRAY, Redox and fluorophore functionalization of water soluble, tioponin-protected gold clusters. *J. Am. Chem. Soc.* **1999**, *121*, 7081–7089.
  - 88 D. FITZMAURICE; S. N. RAO; J. A. PREECE; J. F. STODDART; S. WENGER; N. ZACCHERONI, Heterosupramolecular Chemistry: Programmed Pseudorotaxane Assembly at the surface of a nanocrystal. *Angew. Chem. Int. Ed. Engl.* **1999**, *38*, 1147–1150.
  - 89 W. HAN; S. LI; S. M. LINDSAY; D. GUST; T. A. MOORE; A. L. MOORE, Stable binding of isothiocyanatoporphyrin molecules to Au(111): An AFM study. *Langmuir* **1996**, *12*, 5742–5744.
  - 90 N. R. JANA; T. PAL; T. K. SAU, Nanoparticle induced fluorescence quenching. *Rad. Phys. Chem.* **1997**, *49*, 127–130.
  - 91 O. V. MAKAROVA; A. E. OSTAFIN; H. MIYOSHI; J. R. NORRIS; D. MEISEL, Adsorption encapsulation of fluorescent probes in nanoparticles. *J. Phys. Chem. B* **1999**, *103*, 9080–9084.
  - 92 J. F. HAINFELD; F. R. FURUYA, A 1.4 nm Gold cluster covalently attached to antibodies improves immunolabeling. *J. Histochem. Cytochem.* **1992**, *40*, 177–184.
  - 93 C. A. MIRKIN; R. L. LETSINGER; R. C. MUCIC; J. J. STORHOFF, A DNA-based Method for Rationally Assembling Nanoparticles into Macroscopic Materials. *Nature* **1996**, *382*, 607–609.
  - 94 S. RIBRIOUX; G. KLEYMANN; W. HAASE; K. HEITMANN; C. OSTERMEIER; H. MICHEL, Use of Nanogold- and Fluorescent-labeled Antibody Fv Fragments in Immunocytochemistry. *J. Histochem. Cytochem.* **1996**, *44*, 207–213.
  - 95 R. D. POWELL; C. M. R. HALSEY; J. F. HAINFELD, Combined fluorescent and gold immunoprobes: Reagents and methods for correlative light and electron microscopy. *Microscopy Research and Technique* **1998**, *42*, 2–12.

- 96 R. C. HAYWARD; D. A. SAVILLE; I. A. AKSAY, Electrophoretic assembly of colloidal crystals with optically tunable micropatterns. *Nature* **2000**, *404*, 56–59.
- 97 D. AHERNE; S. NAGARAJA RAO; D. FITZMAURICE, Programming a Gold Nanocrystal to Recognize and Selectively Bind a Molecular Substrate in Solution. *J. Phys. Chem. B* **1999**, *103*, 1821–1825.
- 98 K. GEORGE THOMAS; P. V. KAMAT, Making Gold Nanoparticles Glow. Enhanced emission from a Surface Bound Probe. *J. Am. Chem. Soc.* **2000**, *122*, 2655–2656.
- 99 M. BRUST; D. BETHELL; C. J. KIELY; D. J. SCHIFFRIN, Self-assembled gold nanoparticle thin films with nonmetallic optical and electronic properties. *Langmuir* **1998**, *14*, 5425–5429.
- 100 A. ISHIDA; Y. SAKATA; T. MAJIMA, Surface plasmon excitation of a porphyrin covalently linked to a gold surface. *J. Chem. Soc., Chem. Comm* **1998**, 57–58.
- 101 J. P. NOVAK; L. C. BROUSSEAU; F. W. VANCE; R. C. JOHNSON; B. I. LEMON; J. T. HUPP; D. L. FELDHEIM, Nonlinear optical properties of molecularly bridged gold nanoparticle arrays. *J. Am. Chem. Soc.* **2000**, *122*, 12029–12030.
- 102 D. G. WALTER; D. J. CAMPBELL; C. A. MIRKIN, Photon-gated electron transfer in two-component self-assembled monolayers. *Journal of Physical Chemistry B* **1999**, *103*, 402–405.
- 103 S. E. HENRICHs; J. L. SAMPLE; J. J. SHIANG; J. R. HEATH; C. P. COLLIER; R. J. SAYKALLY, Positive and Negative Contrast Lithography on Silver Quantum Dot Monolayers. *J. Phys. Chem. B* **1999**, *103*, 3524–3528.
- 104 T. R. JENSEN; M. D. MALINSKY; C. L. HAYNES; R. P. VAN DUYN, Nanosphere Lithography: Tunable Localized Surface Plasmon Resonance Spectra of Silver Nanoparticles. *J. Phys. Chem. B* **2000**, *104*, 10549–10556.
- 105 R. D. PINER; J. ZHU; F. XU; S. H. HONG; C. A. MIRKIN, “Dip-pen” nanolithography. *Science* **1999**, *283*, 661–663.
- 106 C. L. HAYNES; R. P. VAN DUYN, Nanosphere Lithography: A Versatile Nanofabrication Tool for Studies of Size Dependent Nanoparticle Optics. *J. Phys. Chem. B* **2001**, *105*, 5599–5611.
- 107 A. IVANISEVIC; C. A. MIRKIN, “Dip-Pen” nanolithography on semiconductor surfaces. *Journal of the American Chemical Society* **2001**, *123*, 7887–7889.
- 108 M. VALINA-SABA; G. BAUER; N. STICH; F. PITTNER; T. SCHALKHAMMER, A self assembled shell of 11-mercaptopendecanoic aminophenylboronic acids on gold nanoclusters. *Mat. Sci. Eng C – Biomimetic and Supramol. Syst.* **1999**, *8–9*, 205–209.
- 109 K. V. GOBI; F. MIZUTANI, Efficient mediatorless superoxide sensors using cytochrome c-modified electrodes: surface nano-organization for selectivity and controlled peroxidase activity. *J. Electroanal. Chem.* **2000**, *484*, 172–181.
- 110 I. WILLNER; V. PARDO-YISSAR; E. KATZ; K. T. RANJIT, A photoactivated ‘molecular train’ for optoelectronic applications: light-stimulated translocation of a beta-cyclodextrin receptor within a stoppered azobenzene-alkyl chain supramolecular monolayer assembly on a Au-electrode. *J. Electroanal. Chem.* **2001**, *497*, 172–177.
- 111 R. A. REYNOLDS; C. A. MIRKIN; R. L. LETSINGER, A gold nanoparticle/latex microsphere-based colorimetric oligonucleotide detection method. *Pure and Applied Chemistry* **2000**, *72*, 229–235.
- 112 L. M. DEMERS; C. A. MIRKIN; R. C. MUCIC; R. A. REYNOLDS; R. L. LETSINGER; R. ELGHANIAN; G. VISWANADHAM, A fluorescence-based method for determining the surface coverage and hybridization efficiency of thiol-capped oligonucleotides bound to gold thin films and nanoparticles. *Analytical Chemistry* **2000**, *72*, 5535–5541.
- 113 M. BRUST; P. M. BLASS; A. J. BARD, Self-assembly of photoluminescent copper(I)-dithiol multilayer thin films and bulk materials. *Langmuir* **1997**, *13*, 5602–5607.

- 114 M. LAHAV; T. GABRIEL; A. N. SHIPWAY; I. WILLNER, Assembly of Zn(II)-porphyrin-bipyridinium dyad and Au-nanoparticle superstructures on conductive surfaces. *J. Am. Chem. Soc.* **1999**, 121, 258–259.
- 115 M. LAHAV; E. KATZ; A. DORON; F. PATOLSKY; I. WILLNER, Photochemical imprint of molecular recognition sites in monolayers assembled on Au electrodes. *J. Am. Chem. Soc.* **1999**, 121, 862–863.
- 116 H. IMAHORI; M. ARIMURA; T. HANADA; Y. NISHIMURA; I. YAMAZAKI; Y. SAKATA; S. FUKUZUMI, Photoactive Three-Dimensional Monolayers: Porphyrin-Alkanethiolate-Stabilized Gold Clusters. *J. Am. Chem. Soc.* **2000**, 122, 335–336.
- 117 H. IMAHORI; H. NORIEDA; H. YAMADA; Y. NISHIMURA; I. YAMAZAKI; Y. SAKATA; S. FUKUZUMI, Light-Harvesting and Photocurrent Generation by Gold Electrodes Modified with Mixed Self-Assembled Monolayers of Boron-Dipyrin and Ferrocene-Porphyrin-Fullerene Triad. *J. Am. Chem. Soc.* **2001**, 123, 100–110.
- 118 J. HU; J. ZHANG; F. LIU; K. KITTREDGE; J. K. WHITESELL; M. A. FOX, Competitive photochemical reactivity in a self-assembled monolayer on a colloidal gold cluster. *J. Am. Chem. Soc.* **2001**, 123, 1464–1470.
- 119 D. GUST; T. A. MOORE; A. L. MOORE, *Acc. Chem. Res.* **1993**, 26, 198.
- 120 P. V. KAMAT; S. BARAZZOUK; S. HOTCHANDANI; K. GEORGE THOMAS, Nanostructured Thin Films of C<sub>60</sub>-Aniline Dyad Clusters. Electrodeposition, Charge Separation and Photoelectrochemistry. *Chem., Euro. J.* **2000**, 6, 3914–3921.
- 121 S. E. CREAGER; D. M. COLLARD; M. A. FOX, Mediated electron transfer by a surfactant viologen bound to octadecanethiol on gold. *Langmuir* **1990**, 6, 1617–1620.
- 122 D. AMIHOOD; E. KATZ; I. WILLNER, Organization of Au colloids as monolayer films onto ITO glass surfaces: Application of the metal colloid films as base interfaces to construct redox-active monolayers. *Langmuir* **1995**, 11, 1313–1317.
- 123 T. AKIYAMA; H. IMAHORI; A. AJAWAKOM; Y. SAKATA, Synthesis and self assembly of porphyrin-linked Fullerene on gold surface using S–Au linkage. *Chem. Lett.* **1996**, 907–908.
- 124 H. IMAHORI; T. AZUMA; A. AJAWAKOM; H. NORIEDA; H. YAMADA; Y. SAKATA, An investigation of photocurrent generation by gold electrodes modified with self-assembled monolayers of C<sub>60</sub>. *J. Phys. Chem. B* **1999**, 103, 7233–7237.
- 125 F. ARIAS; L. A. GODINEZ; S. R. WILSON; A. E. KAIFER; L. ECHEGOYEN, Interfacial hydrogen bonding. Self-assembly of a monolayer of a fullerene-crown ether derivative on gold surfaces derivatized with an ammonium-terminated alkanethiolate. *J. Am. Chem. Soc.* **1996**, 118, 6086–6087.
- 126 A. BADIA; S. SINGH; L. DEMERS; L. CUCCIA; G. R. BROWN; R. B. LENNOX, Self-assembled monolayers on gold nanoparticles. *Chem., Euro. J.* **1996**, 2, 359–363.
- 127 S. R. JOHNSON; S. D. EVANS; S. W. MAHON; A. ULMAN, Alkanethiol Molecules Containing an Aromatic Moiety Self-Assembled onto Gold Clusters. *Langmuir* **1997**, 13, 51–57.
- 128 T. PAGNOT; D. BARCHIESI; G. TRIBILLON, Energy transfer from fluorescent thin films to metals in near-field optical microscopy: Comparison between time-resolved and intensity measurements. *Appl. Phys. Lett.* **1999**, 75, 4207–4209.
- 129 O. ENGER; F. NUESCH; M. FIBBIOLI; L. ECHEGOYEN; E. PRETSCH; F. DIEDERICH, Photocurrent generation at a fullerene self-assembled monolayer-modified gold electrode cast with a polyurethane membrane. *J. Mater. Chem.* **2000**, 10, 2231–2233.
- 130 N. TERASAKI; T. AKIYAMA; S. YAMADA, Preparation and photoelectrochemical properties of a self-assembled monolayer of a ruthenium tris(2,2'-bipyridine)-viologen 1:2 linked compound. *Chem. Lett.* **2000**, 668–669.

- 131 K. SAITO, Quenching of excited J aggregates on metals by surface plasmon excitations. *J. Phys. Chem. B* **1999**, *103*, 6579–6583.
- 132 B. I. IPE; K. GEORGE THOMAS; S. BARAZZOUK; S. HOTCHANDANI; P. V. KAMAT, Photoinduced Charge Separation in a Fluorophore-Gold Nanoassembly. *J. Phys. Chem. B* **2002**, *106*, 18–21.
- 133 J. F. HICKS; A. C. TEMPLETON; S. CHEN; K. M. SHERAN; R. JASTI; R. W. MURRAY; J. DEBORD; T. G. SCHAAFF; R. L. WHETTEN, The Monolayer Thickness Dependence of Quantized Double-Layer Capacitances of Monolayer-Protected Gold Clusters. *Anal. Chem.* **1999**, *71*, 3703–3711.
- 134 S. CHEN; R. W. MURRAY, Electrochemical Quantized Capacitance Charging of Surface Ensembles of Gold Nanoparticles. *J. Phys. Chem. B* **1999**, *103*, 9996–10000.
- 135 W. P. MCCONNELL; J. P. NOVAK; L. C. BROUSSEAU III; R. R. FUERER; R. C. TENENT; D. L. FELDHEIM, Electronic and Optical Properties of Chemically Modified Metal Nanoparticles and Molecularly Bridged Nanoparticle Arrays. *J. Phys. Chem. B* **2000**, *104*, 8925–8930.
- 136 J. LI; Y. YAMADA; K. MURAKOSHI; Y. NAKATOA, Sustainable metal nanocontacts showing quantized conductance prepared at a gap of thin metal wires in solution. *Chem. Commun.* **2001**, 2170–2171.
- 137 I. BEDJA; S. HOTCHANDANI; P. V. KAMAT, Photoelectrochemistry of quantized WO<sub>3</sub> colloids. Electron storage, electrochromic, and photoelectrochromic effects. *J. Phys. Chem.* **1993**, *97*, 11064–11070.
- 138 C. M. LAMPERT, Electrochromic materials and devices for energy efficient windows. *Solar Energy Mater.* **1984**, *11*, 1–27.
- 139 T. OI, *Ann. Rev. Mater. Sci.* **1986**, *16*, 185.
- 140 C. G. GRANQVIST, Electrochromic tungsten oxide films: Review of progress. *Solar Energy Mater. Solar Cells* **2000**, *60*, 1993–1998.
- 141 C. G. GRANQVIST, Progress in electrochromics: tungsten oxide revisited. *Electrochim Acta* **1999**, *44*, 3005–3015.
- 142 S. H. LEE; H. CHEONG, M.; C. E. TRACY; A. MASCARENHAS; A. W. CZANDERNA; S. K. DEB, Electrochromic coloration efficiency of  $\alpha$ -WO<sub>3</sub>-y thin films as a function of oxygen deficiency. *Appl. Phys. Lett.* **1999**, *75*, 1541–1543.
- 143 S. HOTCHANDANI; I. BEDJA; R. W. FESSENDEN; P. V. KAMAT, Electrochromic and photoelectrochromic behavior of thin WO<sub>3</sub> films prepared from quantum size colloidal particles. *Langmuir* **1994**, *10*, 17–22.
- 144 I. BEDJA; S. HOTCHANDANI; R. CARPENTIER; K. VINODGOPAL; P. V. KAMAT, Electrochromic and photoelectrochemical behavior of thin WO<sub>3</sub> films prepared from quantized colloidal particles. *Thin Solid Films* **1994**, *247*, 195–200.
- 145 S. HASHIMOTO; H. MATSUOKA, J. *Electrochem. Soc.* **1991**, *138*, 2403.
- 146 N. OZER; C. M. LAMPERT, Electrochromic performance of sol-gel deposited WO<sub>3</sub>-V<sub>2</sub>O<sub>5</sub> films. *Thin Solid Films* **1999**, *349*, 205–211.
- 147 S. PAPAETHIMIOU; G. LEFTHERIOTIS; P. YIANOULIS, Study of electrochromic cells incorporating WO<sub>3</sub>, MoO<sub>3</sub>, WO<sub>3</sub>-MoO<sub>3</sub> and V<sub>2</sub>O<sub>5</sub> coatings. *Thin Solid Films* **1999**, *344*, 183–186.
- 148 B. O'REGAN; M. GRAETZEL; D. FITZMAURICE, Optical Electrochemistry. 2. Real-time spectroscopy of conduction band electrons in a metal oxide semiconductor electrode. *J. Phys. Chem.* **1991**, *95*, 10525–10528.
- 149 B. O'REGAN; M. GRAETZEL; D. FITZMAURICE, Optical Electrochemistry I: Steady-state spectroscopy of conduction band electrons in a metal oxide semiconductor electrode. *Chem. Phys. Lett.* **1991**, *183*, 89–93.
- 150 G. REDMOND; D. FITZMAURICE; M. GRAETZEL, Effect of surface chelation on the energy of an intraband surface state of a nanocrystalline TiO<sub>2</sub> film. *J. Phys. Chem.* **1993**, *97*, 6951–6954.
- 151 G. REDMOND; D. FITZMAURICE, Spectroscopic determination of flatband potentials for polycrystalline



- TiO<sub>2</sub> electrodes in nonaqueous solvents. *J. Phys. Chem.* **1993**, 97, 1426–1430.
- 152 L. BUTLER; G. REDMOND; D. FITZMAURICE, Preparation and spectroscopic characterization of highly confined nanocrystallites of GaAs in Decane. *J. Phys. Chem.* **1993**, 97, 10750–10755.
  - 153 G. REDMOND; A. O'KEEFE; C. BURGESS; C. MACHALE; D. FITZMAURICE, Spectroscopic determination of flat-band potential of transparent nanocrystalline ZnO films. *J. Phys. Chem.* **1993**, 97, 11081–11086.
  - 154 I. BEDJA; S. HOTCHANDANI; P. V. KAMAT, Preparation and characterization of thin SnO<sub>2</sub> nanocrystalline semiconductor films and their sensitization with bis(2,2'-bipyridine)(2,2'-bipyridine-4,4'-dicarboxylic acid)ruthenium complex. *J. Phys. Chem.* **1994**, 98, 4133–4140.
  - 155 C. LIU; A. J. BARD, Effect of excess charge on band energetics (optical absorption edge and carrier redox potentials) in small semiconductor particles. *J. Phys. Chem.* **1989**, 93, 3232–3237.
  - 156 D. LIU; P. V. KAMAT, Electrochemically active nanocrystalline SnO<sub>2</sub> films. Surface modification with thiazine and oxazine dye aggregates. *J. Electrochem. Soc.* **1995**, 142, 835–839.
  - 157 R. CINNSEALACH; G. BOSCHLOO; S. N. RAO; D. FITZMAURICE, Colored electrochromic windows based on nanostructured TiO<sub>2</sub> films modified by adsorbed redox chromophores. *Sol. Energy Mater. Sol. Cells* **1999**, 57, 107–125.
  - 158 R. CINNSEALACH; G. BOSCHLOO; S. N. RAO; D. FITZMAURICE, Electrochromic windows based on viologen-modified nanostructured TiO<sub>2</sub> films. *Sol. Energy Mater. Sol. Cells* **1998**, 55, 215–223.
  - 159 P. BONHOTE; E. GOGNIAT; F. CAMPUS; L. WALDER; M. GRAETZEL, Nanocrystalline electrochromic displays. *Displays* **1999**, 20, 137–144.
  - 160 F. CAMPUS; P. BONHOTE; M. GRAETZEL; S. HEINEN; L. WALDER, Electrochromic devices based on surface-modified nanocrystalline TiO<sub>2</sub> thin-film electrodes. *Solar Energy Mater. and Solar Cells* **1996**, 56, 281–297.
  - 161 N. LEVENTIS; Y. C. CHUNG, Preparation And Characterization Of Tungsten Trioxide Dibenzy Viologen Polymer Bilayer Electrochromic Films. *J. Mater. Chem.* **1993**, 3, 833–839.
  - 162 N. R. DE TACCONI; K. RAJESHWAR; R. O. LEZNA, Preparation, photoelectrochemical characterization, and photoelectrochromic behavior of metal exacyanoferrate-titanium dioxide composite films. *Electrochim Acta* **2000**, 45, 3403–3411.
  - 163 M. K. NAZEERUDDIN; A. KAY; I. RODICIO; B. R. HUMPHRY; E. MUELLER; P. LISKA; N. VLACHOPOULOS; M. GRAETZEL, Conversion of light to electricity by cis-X<sub>2</sub>bis(2,2'-bipyridyl-4,4'-dicarboxylate)ruthenium(II) charge-transfer sensitizers (X = Cl<sub>2</sub>, Br<sub>2</sub>, I<sub>2</sub>, CN<sub>2</sub>, and SCN<sub>2</sub>) on nanocrystalline TiO<sub>2</sub> electrodes. *J. Am. Chem. Soc.* **1993**, 115, 6382–90.
  - 164 I. BEDJA; S. HOTCHANDANI; R. CARPENTIER; R. W. FESSENDEN; P. V. KAMAT, Chlorophyll *b* modified nanocrystalline SnO<sub>2</sub> semiconductor thin film as a photosensitive electrode. *J. Appl. Phys.* **1994**, 75, 5444–5456.
  - 165 S. HOTCHANDANI; P. V. KAMAT, Modification of electrode surface with semiconductor colloids and its sensitization with chlorophyll *a*. *Chem. Phys. Lett.* **1992**, 191, 320–326.
  - 166 S. HOTCHANDANI; S. DAS; K. GEORGE THOMAS; M. V. GEORGE; P. V. KAMAT, Interaction of semiconductor colloids with J-aggregates of squaraine dye and its role in sensitizing nanocrystalline semiconductor films. *Res. Chem. Intermed.* **1994**, 20, 927–938.
  - 167 A. HAGFELDT; M. GRAETZEL, Light-induced redox reactions in nanocrystalline systems. *Chem. Rev.* **1995**, 95, 49–68.
  - 168 P. V. KAMAT, *Electron Transfer Processes in Nanostructured Semiconductor Thin Films*, in *Nanoparticles and Nanostructural Films*, J. H. FENDLER, Editor. 1998, Wiley-VCH: New York. p. 207–233.



- 169 D. CAHEN; M. GRAETZEL; J. F. GUILLEMOLES; G. HODES, *Dye Sensitized Solar Cells: Principles of Operation*, in *Electrochemistry of Nanomaterials*, G. HODES, Editor. 2001, Wiley-VCH Verlag GmbH: Weinheim. p. 201–228.
- 170 A. C. TEMPLETON; W. P. WUELFING; R. W. MURRAY, Monolayer protected cluster molecules. *Acc. Chem. Res.* **2000**, *33*, 27–36.
- 171 P. V. KAMAT; S. BARAZZOUK; S. HOTCHANDANI, Electrochemical Modulation of Fluorophore Emission at a Nanostructured Gold Film. *Angew. Chem. (Int. Ed.)* **2002**, *41*, 2764–2767.
- 172 A. WOOD; M. GERSIG; P. MULVANEY, Fermi Level Equilibration in Quantum Dot-Metal Nanojunctions. *J. Phys. Chem. B* **2001**, *105*, 8810–8815.
- 173 A. J. BARD, Design of semiconductor photoelectrochemical systems for solar energy conversion. *J. Phys. Chem.* **1982**, *86*, 172–177.
- 174 V. SUBRAMANIAN; E. E. WOLF; P. V. KAMAT, Influence of Metal/Metal – Ion Concentration on the Photocatalytic Activity of TiO<sub>2</sub>–Au Composite Nanoparticles. *Langmuir* **2003**, *19*, 469–474.
- 175 A. HELLER, Optically transparent metallic catalysts on semiconductors. *Pure Appl. Chem.* **1986**, *58*, 1189–1192.
- 176 Y. NOSAKA; Y. ISHIZUKA; H. MIYAMA, Separation mechanism of a photo-induced electron-hole pair in metal-loaded semiconductor powders. *Ber. Bunsenges. Phys. Chem.* **1986**, *90*, 1199–1204.
- 177 Y. CHEN; Z. WEI; Y. CHEN; H. LIN; Z. HONG; H. LIU; Y. DONG; C. YU; W. LI, Metal-semiconductor catalyst: Photocatalytic and electrochemical behavior of Pt–TiO<sub>2</sub> for the water-gas shift reaction. *J. Mol. Catal.* **1983**, *21*, 275–289.
- 178 Y. NAKATO; H. TSUBOMURA, The photoelectrochemical behavior of an n-TiO<sub>2</sub> electrode coated with a thin metal film, as revealed by measurements of the potential of the metal film. *Isr. J. Chem.* **1982**, *22*, 180–183.
- 179 N. R. DE TACCONI; J. CARMONA; K. RAJESHWAR, Chemically modified Ni/TiO<sub>2</sub> nanocomposite films. Charge transfer from photoexcited TiO<sub>2</sub> particles to hexacyanoferrate redox centers within the film and unusual photoelectrochemical behavior. *J. Phys. Chem. B* **1997**, *101*, 10151–10154.
- 180 P. V. KAMAT, Photoelectrochemistry in particulate systems. 3. Phototransformations in the colloidal TiO<sub>2</sub>-thiocyanate system. *Langmuir* **1985**, *1*, 608–611.
- 181 D. BEHAR; P. L. T. BEVAN; G. SCHOLES, Pulse radiolysis of aqueous thiocyanate solutions. Nature of the intermediate transient species. *J. Phys. Chem.* **1972**, *76*, 1537–1542.
- 182 DUONGHONG, D., J. RAMSDEN, AND M. GRAETZEL, Dynamics of interfacial electron-transfer processes in colloidal semiconductor systems. *J. Am. Chem. Soc.*, **1982**, *104*, 2977–85.
- 183 A. DAWSON; P. V. KAMAT, Complexation of Gold Nanoparticles with Radiolytically Generated Thiocyanate Radicals ((SCN)<sub>2</sub><sup>•-</sup>). *J. Phys. Chem. B* **2000**, *104*, 11842–11846.
- 184 M. JAKOB; H. LEVANON; P. V. KAMAT, Charge Distribution between UV-Irradiated TiO<sub>2</sub> and Gold Nanoparticles. Determination of Shift in Fermi Level. *Nano Lett.* **2003**, *3*, 353–358.
- 185 N. CHANDRASEKHARAN; P. V. KAMAT, Improving the Photoelectrochemical Performance of Nanostructured TiO<sub>2</sub> Films by Adsorption of Gold Nanoparticles. *J. Phys. Chem. B* **2000**, *104*, 10851–10857.
- 186 V. SUBRAMANIAN; E. WOLF; P. V. KAMAT, Semiconductor-Metal Composite Nanostructures. To What Extent Metal Nanoparticles (Au, Pt, Ir) Improve the Photocatalytic Activity of TiO<sub>2</sub> Films? *J. Phys. Chem. B* **2001**, *105*, 11439–11446.

## 20

**Electrochemistry with Nanoparticles***S. Devarajan and S. Sampath***Outline**

This chapter is organized into sections corresponding to various electrochemical characteristics of nanometallic particles. The introduction gives a brief idea of the basics of colloids together with related literature. Subsequently, the electrochemistry with nanoparticles and ensembles of nanoelectrodes is explained followed by the electrochemical coulomb staircase behaviour of monolayer-protected nanometallic clusters. The investigation of nanoparticles using techniques based on combinations of different spectroscopic and electrochemical techniques is then reviewed. Sensors and electrocatalysis form the next sections and finally a summary and perspectives are given.

**20.1****Introduction**

Small metallic particles have been the subject of scientific and technological interest since the time of Faraday when he proposed that the ruby red color of gold colloid is the consequence of its small particle size [1]. A large number of theoretical and experimental studies have been carried out to understand the basic characteristics of the optical, electronic, chemical and mechanical properties of metallic nanoparticles [2–17]. Mie has made seminal contributions to quantitatively correlate the changes in the optical properties with the variation in the size of the particles [2]. The size-dependent properties have given rise to enormous applications that have emerged in the last few decades. Data storage, sensing devices, catalysis, biological interfaces, quantum level phenomena, nanoelectromechanical devices and nanotribology are some of the areas where the impact has already been very substantial.

Electrochemistry has been inherently associated with nanoscience, particularly when the stability and the assembly of the particles are probed using the so-called ‘bottom up’ chemical approach. The stability of colloids is related to the repulsive forces when the double layers around them overlap with each other. Low electrolyte

concentration coupled with high diffuse layer potential is essential for good stability. The spherical electrical double layer around the particles determines the extent and the nature of the chemistry as well as the electron transfer processes involving colloids. The double layer theories developed by Helmholtz, Grahame, Stern, Gouy and Chapman to understand the interfaces of an electronic conductor/liquid electrolyte are used to build models to explain colloidal behavior.

Most of the electrochemical phenomena occur in size regimes that are very small. The effects of size on diffusion kinetics, electrical double layer at the interface, elementary act of charge transfer and phase formation have recently been reviewed by Petri and Tsirlina [12]. Mulvaney has given an excellent account of the double layers, optical and electrochemical properties associated with metal colloids [11]. Special emphasis has been given to the stability and charge transfer phenomenon in metal colloid systems. Willner has reviewed the area of nanoparticle-based functionalization of surfaces and their applications [6–8]. This chapter is devoted to electrochemistry with nanoparticles. One of the essential requirements for electrochemical studies is that the material should exhibit good conductivity. This includes two classes of materials namely, semiconductors and metals. There have been excellent reviews on electrochemistry with semiconductor nanoparticles [18–20]. Here, we confine ourselves to electrochemical studies with metallic nanoparticles.

## 20.2

### Preparation of Nanostructures

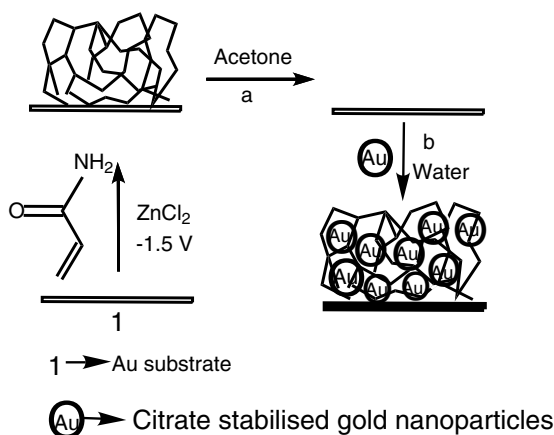
Electrochemical studies with nanosized particles require them to be accessible to the electrode surface where the potential can be controlled. This can be accomplished either by using the metallic colloid along with an inert, planar electrode or by attaching the nanoparticle onto a conducting matrix. Both these methods have been demonstrated in the literature [21–25]. In this section, some of the anchoring methods that are available for this purpose are briefly explained. A few other methods of preparation are explained wherever appropriate.

Transparent, conducting indium tin oxide (ITO) electrodes are widely used to generate assemblies for simultaneous electrochemical and spectroscopic measurements [26]. Oxide surfaces such as ITO and silica are generally functionalized with amino- or mercaptosilanes that can further be used to attach metallic particles [23, 24, 27, 28]. Molecules containing carboxylic acid groups are also frequently used to functionalize titania and alumina surfaces [29, 30]. Gold is one of the most extensively studied electrode materials for anchoring various molecules. The procedure involves the assembly of a base monolayer consisting of bifunctional groups where one of them is sulfur or nitrogen based so that the metal–sulfur/nitrogen interaction takes place spontaneously [31]. The other end of the functionalized molecule is used to attach the nanoparticles. Electrophoretic deposition is also reported to form an assembly of particles on conducting matrices [32]. Bharathi and Lev demonstrated the electrochemical deposition of gold particles from an

aminosilane-stabilized gold sol onto planar electrodes [33]. This involves the stabilization of metal nanoparticles in an aminosilane matrix that is simultaneously hydrolyzed to form a sol. The sol is then electrolysed to give a coating of silane-stabilized metallic particles on a conducting substrate.

Musick and co-workers have prepared nanoelectrodes [34], which are derived from self-assembled monolayers of colloidal gold on glass surfaces. The base monolayer for colloidal gold deposition is formed by the silanization of glass surfaces with amino- or mercaptosilane groups. Further functionalization is carried out by two different methods. One involves the stepwise assembly of Au nanoparticles cross-linked with bifunctional groups, which gives good control over the number of layers of deposited gold. The second procedure involves the electroless deposition of gold on gold nanoparticles using  $\text{NH}_2\text{OH}$  and  $\text{Au}^{3+}$  ions as initiators for the process. Electrochemical potential control has also been shown to assist in varying the rate of Au monolayer formation and interparticle spacing, thus giving a good handle on the morphology of the surface [35]. These electrodes can also be characterized by several different techniques such as optical spectroscopy, AFM and electrochemistry. Such electrodes exhibit conductivities and electrochemical properties comparable to macroelectrodes and also have advantages in terms of ease of preparation and ability to control the geometric shape [34]. Electrodes prepared using a layer-by-layer growth technique show a transition from micro-electrode array type of voltammetry to the usual reversible behavior observed at a bulk, planar gold electrode, depending on the number of metallic layers [34]. The active electrochemical area of these surfaces is larger than the geometric area due to the roughness associated with the nanocrystalline phases [34]. Microband electrodes can also be fabricated using this method and they are found to exhibit almost ideal microelectrode behavior [34].

Another novel way of encapsulating gold particles into an electropolymerized matrix has been developed by Willner and co-workers [36]. This involves the use of hydrogels based on polyacrylamide that exhibit reversible swelling and shrinking properties. The swelling is accomplished in the presence of a citrate-stabilized gold colloid while the shrinking property is brought about by the use of acetone as the solvent. Gold particles stabilized by citrate molecules have a high hydrogen bonding potential and hence the particles get trapped in the acrylamide matrix while the shrinking mechanism is operative. The method is described in Scheme 20.1. The extent of incorporation of gold particles varies as a function of the number of swelling–shrinking (breathing) cycles. This is confirmed by following the charge transfer resistance using impedance measurements in the presence of a ferrocyanide/ferricyanide ( $\text{Fe}(\text{CN})_6^{3-/4-}$ ) redox couple. The enhanced conductivity due to gold particle incorporation is shown in the form of a decreased charge transfer resistance as a function of the number of breathing cycles. Bard and co-workers [37] reported the preparation of gold nanoparticles at the tip end of glass micropipettes and used it for scanning electrochemical microscopy (SECM) studies. Shao and co-workers [38] developed a method based on a laser-based micropipette puller to prepare nanometer-sized electrodes and used them in sensing applications. Other techniques to form nanostructures include Langmuir–Blodgett



**Scheme 20.1.** Method for the assembly of Au-Nanoparticle-containing electropolymerized hydrogels by the 'breathing technique'. First the hydrogel is electropolymerized, then the nanoparticles are introduced by (a) shrinking

the gel in acetone and (b) re-swelling the gel in a nanoparticle-containing solution. Steps (I) and (II) may be repeated to increase the nanoparticle concentration in the gel. (Adapted from *Chem. Commun.*, **2000**, 1025).

assembly, electrostatic or covalent ordering, use of polymers, and patterning based on biomolecules such as DNA etc. [39]. Carbon is an important substrate for many applications related to the use of nanoparticles, especially in electrocatalysis [40a]. Electrodeposition of metal particles on carbon surfaces is one of the ways of producing uniformly dispersed catalytic particles [40b–e]. Another method involves the adsorption of metal salts on the substrate and then reducing them chemically [41a]. Nanoparticles containing more than one metal component have been synthesized using stabilizers such as functionalized silanes, citrate, polyvinyl alcohol and thiols [41b–g]. Metal nanowires and their arrays have been prepared by an electrodeposition technique [41h]. The metallic nanowires composed of molybdenum, copper, nickel, gold and palladium are electrodeposited selectively on basal plane oriented pyrolytic graphite (HOPG) electrodes. The electrochemically decorated nanowires are found to be 500  $\mu\text{m}$  long, hemicylindrical and polycrystalline in nature. The nanowires can also be lifted off the HOPG surface and this property makes them amenable for sensing applications.

### 20.3

#### Electrochemistry with Metallic Nanoparticles

Studies of the interaction of colloidal metal particles with macroelectrodes are essential for an understanding of properties such as the redox potential of the nanometallic particles in the presence of a particular environment. This information will be useful in extending the conventional electrochemical treatment to colloidal systems.

Bard and co-workers have reported on the attainment of equilibrium between the nanosized particles and an electrode in the presence of a redox mediator [25a]. The study refers to the production of a mediator (methyl viologen radical cation) that reduces water in the presence of colloidal gold and platinum metal catalyst. An electrochemical model based on the assumption that the kinetic properties are controlled by the half-cell reactions is proposed to understand the catalytic properties of the colloidal metals. The same authors have used 15 nm electrodes to detect single molecules using scanning electrochemical microscopy (SECM) [25b]. A Pt–Ir tip of nm size diameter is used along with a ferrocene derivative in a positive feedback mode of SECM. The response has been found to be stochastic and Faradaic currents of the order of pA are observed.

The possibility of constructing electrochemical interfaces with tunable kinetic barriers has recently been reported [42]. A planar gold electrode is modified with a hydrolyzed mercaptosilane sol to yield a surface with high blocking properties. The barrier properties are demonstrated using a freely diffusing  $[\text{Fe}(\text{CN})_6]^{3-/4-}$  redox couple in the solution phase. Different loading of the metallic particles is achieved by immersing the silane-modified electrode in citrate-stabilized gold sol for varying periods of time. The barrier properties of the resulting surfaces are different, depending on the extent of metal loading.

Henglein and co-workers [43–46] have developed a radiolytic method to deposit excess electrons onto colloidal metal particles in aqueous solutions. These excess electrons can then be used to initiate electrochemical reactions on the surface of the colloidal particle. This mechanism has been utilized to deposit metals such as gold, cadmium, lead and indium on silver nanoparticles. The Ag nanoparticles behave like ‘microelectrodes’ in solution. They become charged via the electron transfer of free radicals that are generated in situ in the solution by radiolysis. The nanoparticles can store a large number of excess electrons and can be used to reduce different metals on their surface. A similar concept has been used to polarize a nanocapacitor consisting of a metal (Au) core with a semiconducting ( $\text{SnO}_2$ ) shell [47]. Since there is a large difference in the Fermi-energy level of the core and the conduction band energy of the shell, mobile electrons remain trapped within the core for long periods of time. The charge can be stored for up to 10 h in the Au core in the absence of oxygen but when  $\text{O}_2$  is introduced into the system, there is a slow discharge of electrons at the gold/ $\text{SnO}_2$  interface. Charging and discharging processes in aqueous solutions have been monitored by observing changes in the surface plasmon position [47].

The corrosion behavior of supported and unsupported iron nanoparticles has been followed by Ponder and co-workers [48]. The material referred to as ‘ferragels’ is found to be stable in air and the electrochemical behavior is observed to be similar to that of iron filings. Gold nanoparticle enhanced microchip capillary electrophoresis has been developed by Pumera and co workers [49a]. This has resulted in achieving a good selectivity of solutes and an increase in the efficiency of separation. The walls of a microchannel are coated with a polymer [poly(diallyl-dimethylammonium chloride)] and subsequently with citrate-stabilized gold nanoparticles. The separation of aminophenol is demonstrated using this material. Voltammetry

and scanning tunneling microscopy have been used to characterize platinum nanoparticles of various crystallographic faces [49b]. The surface morphology of platinum on carbon used for enantioselective hydrogenation is related to the various sorption processes based on electrochemical data.

### 20.3.1

#### Monolayer-Protected Nanoclusters

Since the pioneering work of Schiffrin and co workers [50], the synthesis and characterization of isolable, capped metallic clusters has gained considerable interest. Murray introduced the term 'monolayer-protected clusters (MPCs)', otherwise known as 3-D self assembled monolayers (3-D SAMs) on metallic particles [51]. The synthesis procedure involves the phase transfer of a metal ion to an organic phase where it is reduced in the presence of a capping agent. The solvent can then be evaporated to obtain the solid particles that are soluble in various solvents. This procedure has also been extended to alloy nanoparticles such as Au/Ag, Au/Cu, Au/Ag/Cu, Au/Pt, Au/Pd, and Au/Ag/Cu/Pd stabilized with thiol molecules [41b–d]. These clusters have been characterized by various techniques including UV–Vis absorbance, IR, NMR, DSC, TEM, STM/AFM and XRD. The MPCs are soluble nanoelectrodes that exhibit various unusual electrochemical properties when compared to functionalized planar electrodes. Murray and co-workers have contributed enormously to the understanding of the electrochemistry of  $\omega$ -functionalized and unfunctionalized alkanethiolate stabilized Au-cluster compounds [52–59]. Functional groups such as anthraquinone (AQ), ferrocene (Fc), phenothiazine, arenes, esters, acids, alcohols and dithiols of different chain lengths have been incorporated into alkanethiolate modified Au-clusters using the place exchange method [52]. The place exchange method offers an advantage in retaining the core size of the metallic particles while simultaneously allowing other functionalities to be incorporated on the cluster. Clusters functionalized with redox active substituents exhibit unusual multi-electron transfer reactions [52].

Ferrocene (Fc) functionalized MPCs show similar electrochemical activity in both dissolved and adsorbed forms [52]. The voltammetry on glassy carbon electrodes shows symmetric peaks with a peak separation of 15 mV. The charge under the peak reveals partial monolayer coverage of adsorbed clusters. Rotating disk electrochemistry (RDE) experiments have been carried out in  $\text{CH}_2\text{Cl}_2$  solutions containing Au clusters functionalized with mixed monolayers of octanethiolate and  $\omega$ -ferrocenyloctanethiolate ligands of different molar ratios. The voltammograms exhibit an Fc oxidation wave with a limiting current that is mass transport controlled. Analysis of the RDE wave leads to the number of electrons involved in the reaction ( $n$ ) being equal to 1 (Figure 20.1). The NMR and the diffusion coefficient measurements lead to the number of ferrocene units per cluster being largely dependent on the fraction of  $\omega$ -ferrocenyloctanethiolate ligands used to prepare the cluster. This implies that the Fc sites are not strongly electronically coupled. The reaction can, however, be thought of as successive electron transfers, independent

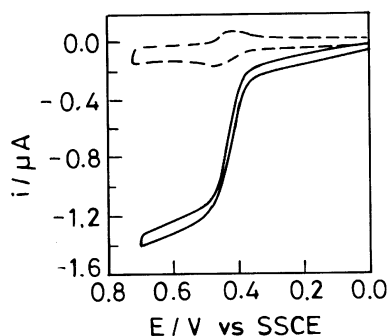


**Fig. 20.1.** Cyclic voltammograms at  $5 \text{ mV s}^{-1}$  for  $1 \mu\text{M}$  Fc containing MPC (average 9 Fc per cluster) in  $0.1 \text{ M}$  tetrabutylammonium perchlorate ( $\text{Bu}_4\text{ClO}_4$ )/ $\text{CH}_2\text{Cl}_2$  at a stationary (---) and rotated (—, 1600 rpm) glassy carbon disk electrode. (Adapted from *J. Am. Chem. Soc.*, **1996**, 118, 4212).

of one another. Further, the consequence of heavy functionalization is observed in a multi-electron transfer process and in the present case, a 15 electron reaction is observed and is unusual for any non-polymeric molecule. Similar results have been obtained with anthraquinone (AQ)-modified clusters where the MPCs contain as many as 25 anthraquinone sites per cluster [57]. Such redox-modified cluster molecules hold great promise as multi-electron donor/acceptor reagents and catalysts. Mediated electrocatalysis has been demonstrated using AQ functionalized MPCs [57, 60]. AQ moieties bound to Au clusters show sixfold higher catalytic efficiencies in the reduction of dinitrocyclohexane (DNC) than freely diffusing anthraquinone molecules in solution. The exact reason for this observation is presently unclear but the authors speculate that the multi-electron transfer sites may lead to successive electron transfers to the once reduced DNC molecule leading to an enhanced activity.

The preparation and electrochemical characterization of  $\text{C}_{60}$ -functionalized gold nanoparticles has been reported by Fujihara and Nakai [51g]. The preparation involves the place exchange of fullerene-appended thiol molecules with octanethiol molecules on the gold surface. Octanethiol-modified planar gold electrodes when immersed in a solution of  $\text{C}_{60}$ -functionalized gold particles, give an assembly of the  $\text{C}_{60}$  molecules on the surface. The electrochemistry of this nanoparticle-coated fullerene-based assembly shows two well-defined redox waves corresponding to  $\text{C}_{60}/\text{C}_{60}^{\cdot-}/\text{C}_{60}^{2-}$  systems. The same authors [61] prepared further electroactive tetrathiafulvalene-derivatized gold nanoparticles using a similar methodology. The functionalized particles are observed to show reversible voltammetric behaviour. Redox-active biferrocene-functionalized gold and palladium MPCs have been prepared and electrodeposited on ITO, GCE and metal electrode surfaces [62–64]. The clusters undergo two-step oxidation reactions in aprotic solvents and the second oxidation reaction is reported to result in the electrodeposition of the Au clusters. Strong inter-cluster attractive interactions are the driving force for the deposition.



The electrochemical characteristics of anthraquinone-derivatized Au clusters prepared by an electroreduction method are similar to those observed on a planar surface. However, the double layer capacitance values reveal that it is possible to control the charging phenomenon stepwise when multiple redox activity is present.

The incorporation of polar ligands such as nitrothiophenyl moieties (NTP) in hexanethiolate-stabilized gold MPCs by the place exchange method leads to an increase in the observed double layer capacitance [65]. The value increases from 0.61 aF for hexane thiolate protected gold clusters (HT-MPCs) to 0.73 aF for nitrophenyl incorporated ones (HT + NTP-MPCs). The HT + NTP-MPCs exhibit two well-defined reversible voltammetric waves corresponding to the reduction of NTP moiety in aprotic media while planar gold electrodes modified with NTP do not exhibit these features. Water soluble tiopronin-based MPCs have been prepared and used for further place exchange with other functionalities such as viologen. Capacitance values as high as 4.5 aF have been observed for tiopronin MPCs in aqueous solutions containing  $\text{NH}_4\text{PF}_6$  as supporting electrolyte [66]. The carboxylic acid functional groups available on tiopronin MPCs can be titrated as weak acids that would lead to charge repulsion effects [67]. Polyethylene glycol attached MPCs have been reported to show ionic conductivities when lithium salts are dissolved in the matrix [68]. The ionic conductivity is found to be higher than the corresponding polymer–lithium salt composites. The same group has recently reported a novel method to prepare a molecular melt of a few nm sized quantum dots [69]. The PEG-based quantum dots are also able to dissolve lithium salts. Dry films of arenethiolate or alkanethiolate protected MPCs show electronic conductivity as governed by electron tunneling through the thiolate ligands. The current–potential curves under high potential gradients show characteristics of hopping type conductivity [70]. A tunneling constant ( $\beta$ ) of 1.2 per Å is obtained that is similar to 2-D SAMs on planar electrodes.

### 20.3.2

#### Nanoelectrode Ensembles

Martin and co-workers have extensively studied the preparation of templated electrodes using microporous membranes and their electrochemical behavior [71–80]. The process involves the synthesis of a desired material within the pores of a uniform membrane. This has been shown to be a very general procedure for the preparation of ensembles of a variety of electrode materials [71, 76, 78, 79, 81]. The availability of membranes with high monodispersity allows the preparation of uniform nanostructures. Track etched plastic/mica-based filtration membranes and microporous alumina have been used as templates for a long time [74, 77–79, 82]. ‘Nanochannel glass’ is a novel type of membrane introduced recently [83]. This is formed by heating and drawing glass capillaries until the desired pore size is obtained. Pore sizes of the order of 17 nm with pore densities as high as  $3 \times 10^9$  pores  $\text{cm}^{-2}$  have been achieved. Highly ordered arrays with excellent monodispersity can be fabricated using this method. Many metals such as copper, platinum

Tab. 20.1. Characteristics of membranes.

Pore diameter (nm)	Pore density (cm <sup>-2</sup> )	Distance between pores (μm)	Fractional pore area <sup>1</sup>	Fractional electrode area <sup>2</sup>
10	6 × 10 <sup>8</sup>	0.2	0.00047	0.00094
30	6 × 10 <sup>8</sup>	0.2	0.0042	0.0042

<sup>1</sup> Determined from electron micrographs of membrane.<sup>2</sup> Determined electrochemically.(Adapted from *Electroanalytical Chemistry Series*, Vol. 21, eds. A. J. Bard,

I. Rubinstein, 1999, Marcel Dekker, NY, pp. 1–74).

and nickel have been electrodeposited using the ‘nanochannel’ glass membranes. Other templates that have been reported include synthetic lipids, peptides and mesoporous molecular sieves [84–88].

Polycarbonate membranes having uniform pore diameter of 10 or 30 nm with an average distance between the pores of 0.2 μm have been used by Martin and co workers [71]. The characteristics of the membranes used are given in Table 20.1. Electroless silver coating on these membranes is achieved with the use of a sensitizer, Sn<sup>2+</sup>. Briefly, the process involves the immersion of the membrane in the SnCl<sub>2</sub> salt solution. Subsequently, when the membrane is immersed into silver nitrate solution, Ag<sup>+</sup> ions are reduced while Sn<sup>2+</sup> ions are oxidized. When the metallic silver-coated surface is immersed in to an Au plating bath, Ag is galvanically displaced by Au and the pore walls become coated with Au particles. This plating process is continued until nanowires of gold are obtained in the pores of the membrane. Nanoelectrode ensembles (NEEs) are obtained by removing the gold coating from one side of the membrane that exposes the gold nanodisks at pre-determined distances based on the properties of the membrane. The same authors have also demonstrated that the diameter of the microtubules (electrodes) can be controlled by carefully manipulating the deposition rate [5].

Electrochemistry with the NEEs has been carried out both in the base supporting electrolyte and in the presence of redox couples [71, 89]. The double layer charging currents for different NEEs are observed to be smaller than those on planar surfaces of the same geometric area (Figure 20.2). The nature of the voltammograms observed on the NEEs for redox reactions depends on the diffusion characteristics that in turn will be dictated by the size and the distance between the nanoelectrodes [71, 90–92]. The voltammograms depicted in Figure 20.2 are based on the complete overlap of the diffusion profiles leading to planar diffusion. There are certain points that should be highlighted at this juncture. First, the concentrations of both the electroactive species as well as the supporting electrolyte are low. Second, it is found that the uncompensated resistance does not distort the voltammograms in spite of the mM concentrations of the supporting electrolyte used. Third, the experimental voltammograms, uncorrected for the background currents, agree well with the simulated data where only Faradaic currents are used. This is due to the fact that the charging currents of the nanoelectrode ensemble are much smaller than the planar macroelectrode of the same geometric area. The im-

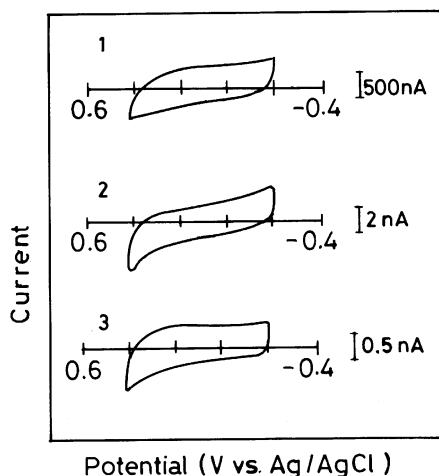


**Fig. 20.2.** Background cyclic voltammograms in 50 mM sodium nitrate at  $100 \text{ mV}^{-1}$  for (1) a gold macrodisk electrode, (2) a 30 NEE (30 electrode NEE), and (3) a 10 NEE. The geometric area for all electrodes was  $0.079 \text{ cm}^2$ . (Adapted from *Anal. Chem.*, **1995**, 67, 1920).

plications are directly observed in the signal to noise ratio (S/N) being larger on the NEEs than on the planar electrodes. The consequence of the S/N being high is exemplified in the lower detection limit of the electroactive analytes [71].

The flux being very large in the case of NEEs as compared to the macroelectrode means that the NEEs will be more sensitive to the kinetics of electron transfer than the macroelectrodes [71]. The flux is related to the square root of the scan rate. The consequence is seen in the larger scan rate ( $10^6$  times) required to obtain the same kinetic information on a macroelectrode than on a 10-electrode-based NEE, where the flux is  $10^3$  times larger than the corresponding macroelectrode [71]. An interesting observation on NEEs is the effect of supporting electrolyte concentration on the shape and the reversibility of the voltammetric response [71]. The peak currents decrease while the peak potential separation ( $\Delta E_p$ ) increases for a ferrocene-based redox couple, as the concentration of supporting electrolyte is increased (Figure 20.3). Different supporting electrolytes such as  $\text{NaNO}_3$ ,  $\text{NaClO}_4$ ,  $\text{Na}_2\text{SO}_4$ ,  $\text{ZnSO}_4$ ,  $\text{KNO}_3$  and  $(\text{C}_2\text{H}_5)_4\text{NClO}_4$  are observed to show this effect. The effect is reversible and very reproducible. Additionally, the effect is independent of the membranes used to prepare the NEEs. According to the authors, the reason for this observation is not very clear at present but is being explored.

The minimum detection limit in the voltammetric analysis on NEEs should be smaller than the value observed on the macroelectrodes, based on their fractional electrode area. Indeed, detection limits of several nM for analytes such as [(trimethylamino)methyl]ferrocene ( $\text{TMAFc}^+$ ) are observed with NEEs while the same species on a macroelectrode could be detected only to a minimum of several  $\mu\text{M}$  [71] (Figure 20.4). Membranes with Au nanotubules are shown to function as

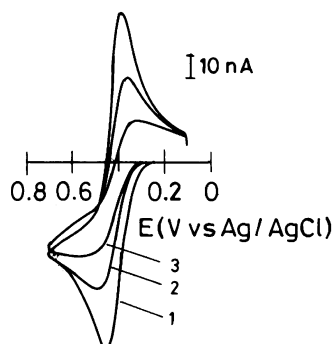


**Fig. 20.3.** Cyclic Voltammograms illustrating the effect of supporting electrolyte concentration at a 10 NEE for  $5 \mu\text{M}$  TMAFc<sup>+</sup> in aqueous NaNO<sub>3</sub> at concentrations of (1) 1; (2) 10 and (3) 100 mM. Scan rate,  $100 \text{ mV s}^{-1}$ . (Adapted from *Anal. Chem.*, **1995**, 67, 1920).

electrochemically switchable ion exchangers. The authors refer to these materials, based on their property to separate molecules as a function of size, as ‘molecular filters’ [93, 94].

The selective ion transport phenomenon using NEEs is exemplified in a simple experiment where a membrane separates two different solutions in a U-tube cell

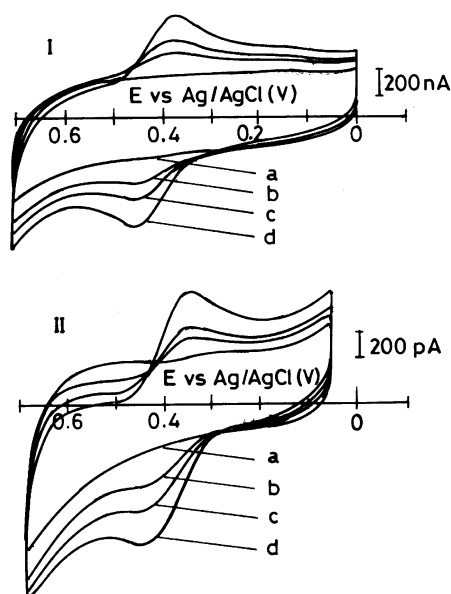


**Fig. 20.4.** Cyclic voltammograms at  $100 \text{ mV s}^{-1}$  in aqueous TMAFc<sup>+</sup> at (I) a gold macrodisk electrode in 50 mM sodium nitrate and (II) a 10 NEE in 1 mM sodium nitrate. TMAFc<sup>+</sup> concentrations correspond to (a) 0.5

$\mu\text{M}$ ; (b)  $7.8 \mu\text{M}$ ; (c)  $15.6 \mu\text{M}$  and (d)  $31.2 \mu\text{M}$  for I and (a) 0.5 nM; (b) 7.8 nM; (c) 15.6 nM and (d) 31.2 nM for II, respectively. Electrode geometric areas in both cases are  $0.079 \text{ cm}^2$ . (Adapted from *Anal. Chem.*, **1995**, 67, 1920).

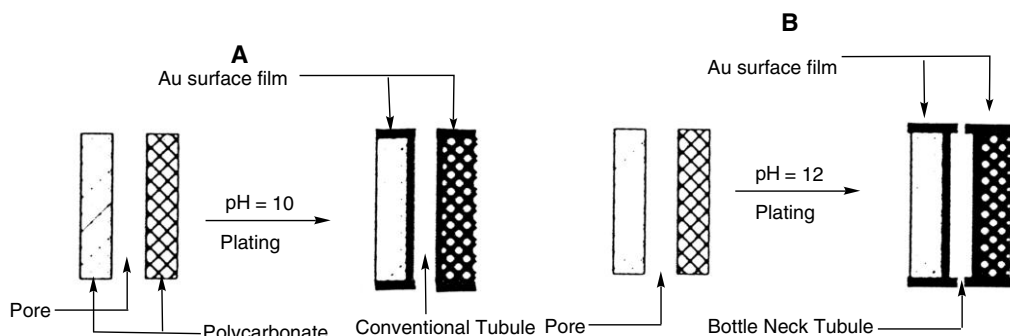


**Fig. 20.5.** Schematic illustrations of shapes of the Au nanotubule obtained by carrying out electroless Au plating at (A) pH 10 and (B) pH 12. The higher pH causes bottleneck tubules. The tubules plated at the lower pH also have some of this bottleneck character. Hence the

depictions in both (A) and (B) are approximate and serve to illustrate the conceptual differences between the two types of nanotubules investigated. (Adapted from *Electroanalytical Chemistry Series*. Vol 21. eds. A. J. Bard, I. Rubinstein. 1999. Marcel Dekker, NY.

[75]. One side is filled with 1 mM KCl while the other side is filled with either 0.5 mM solution of a cationic dye, methylene blue or 1 mM of  $\text{KMnO}_4$  solution. In the former case, the transport is observed from one half of the cell to the other while the latter does not penetrate through the membrane. This is clear evidence to show that the membranes transport a large cation while a small anion does not pass through. This cation permselectivity or charge based selectivity is further explored by potentiometry [75]. The authors go on to demonstrate that the selectivity towards cations or anions can be controlled by the potential applied to the membrane [75].

The size-based selective separation has been in use in the form of dialysis for a long time. The nanofiltration membranes demonstrated here combine both size and chemical transport selectivity and are selective for the particular separation involved. The tubules are prepared as 'bottleneck tubules' as shown in Figure 20.5. The diameter of the tubule may be manipulated, depending on the preparation conditions, resulting in applications based on size-based separations, pH switchable ion-transport selectivity, manipulation of potential dependent fluxes etc. [75, 95, 96].

Wang and co-workers have reported the preparation of NEEs by assembling monolayers of mercaptopropyltrimethoxysilane on ITO substrates followed by immersion in a colloidal gold sol for different periods of time [97, 98]. By controlling the time of immersion, the concentration of active sites or nanoelectrodes on the surface can be tuned.

## 20.4 Single Electron Events

The transfer of single electrons across nanosized particles has been a subject of intensive research in the recent past [99]. Most of the studies tap into the quantum

properties of nanoparticles through the use of scanning tunneling microscopy (STM). Weaver and Gao have reported the sequential electron transfer kinetics for solution phase Pt-carbonyl clusters and correlated this phenomenon to the bulk metal/vacuum interface [100]. The use of electrochemistry to follow the discrete charging events that occur at a metal/solution interface is of recent origin [101, 102].

Fan and Bard described the observation of single electron processes with nanometer-sized Ir–Pt electrodes using SECM [101]. The schematic diagram illustrating the technique is given in Figure 20.6. A pair of electrodes with radii 2.5 and 3.2 nm were used in a solution containing 1  $\mu\text{M}$  ( $\text{Cp}_2\text{FeTMA}^{+1/2+}$ ) [(trimethylammonio)methyl] ferrocene or 10  $\mu\text{M}$   $\text{Fe}(\text{CN})_6^{3-/4-}$  redox couple. Well-resolved staircase-shaped current–potential traces are obtained in the low bias region where the electron transfer is kinetically controlled (Figure 20.7). A step-width of  $(60 \pm 6)$  mV is observed for the  $\text{Cp}_2\text{FeTMA}^{+/2+}$  couple and it is found to be independent of the data-sampling rate, scan rate of the voltammetric experiment and the concentration of the redox couple used. The step height observed is of the order of 60 aA ( $1 \text{ aA} = 10^{-18} \text{ A}$ ) with some variation. The calculated capacitance

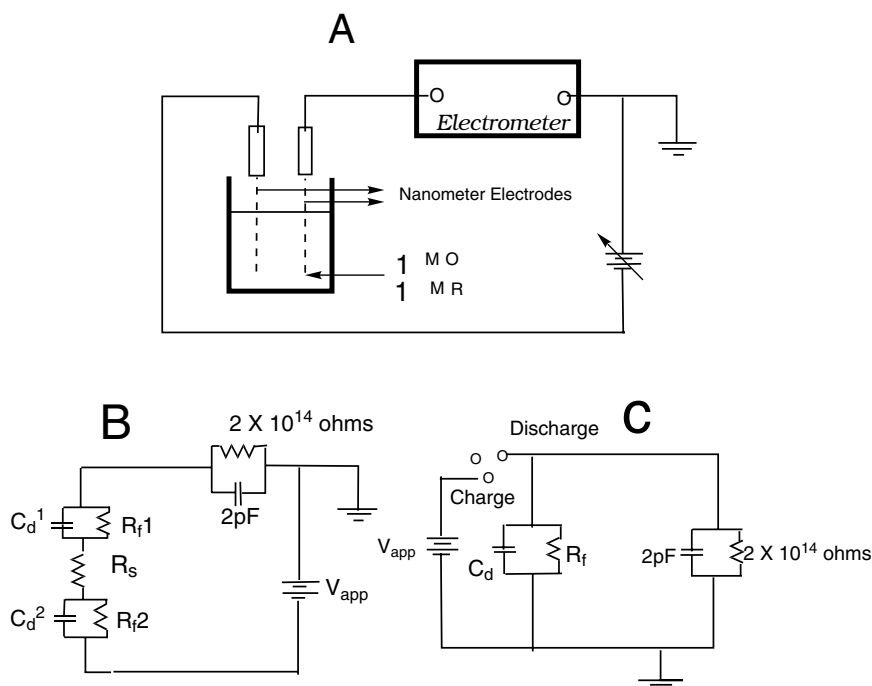


**Fig. 20.6.** Experimental set-up for the current or voltage measurements. (B) Schematic representation of two (electrode/solution) interfaces coupled in series through the solution.  $C_d$  double-layer capacitance;  $R_f$  Faradaic impedance of each interface;  $R_s$ ,

solution resistance;  $V_{app}$ , voltage source. The electrometer has an input impedance of  $\sim 2 \times 10^{14} \Omega$  and a shunt capacitance of 2 pF. (C) Schematic representations of the experimental set-up for the coulostatic experiment. (Adapted from *Science*, **1997**, 277, 1791).

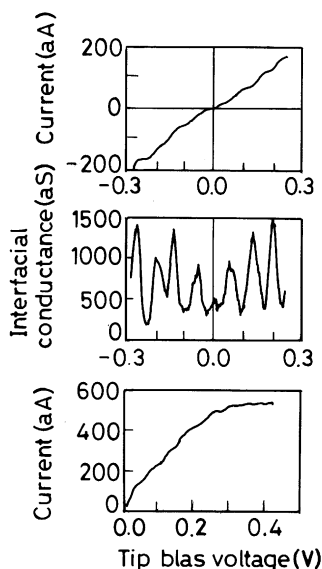


**Fig. 20.7.** (Top) Experimental  $i$ - $V$  characteristics of a two-interface system consisting of a pair of electrodes with radii 2.5 and 3.2 nm immersed in a deaerated solution containing  $1 \mu\text{M}$  each of  $\text{Cp}_2\text{FeTM}^+$ ,  $\text{Cp}_2\text{FeTM}^{2+}$ ,  $\text{NH}_4^+$

and  $\text{SO}_4^{2-}$  and  $2 \mu\text{M}$   $\text{PF}_6^-$ . (Middle) The corresponding differential conductance  $(di/dV)$ - $V$  plot. (Bottom)  $i$ - $V$  curve taken to more positive potentials. (Adapted from *Science*, **1997**, 277, 1791).

values  $[(2.4 \pm 0.2) \times 10^{-18} \text{ F}]$  based on the experimental data match with the expected capacitance for an electrode of radius 2.8 nm, assuming a double layer capacitance of  $10 \mu\text{F cm}^{-2}$ . Higher bias voltages lead to diffusion-controlled currents, as expected for a redox process on a small electrode. The  $\text{Fe}(\text{CN})_6^{3-/4-}$  redox couple yields a step width of  $(70 \pm 1) \text{ mV}$  and a step height of  $<7 \text{ aA}$  though the concentration of the electroactive species is 10 times larger than that of the ferrocene couple. The differences observed with the two redox couples are reported to be consistent with the predictions of the semi-classical coulomb staircase model [103]. The step height, as a first approximation, is proportional to the charge transfer resistance ( $R_{\text{ct}}$ ) associated with the redox couple at the interface. The heterogeneous electron transfer rate constant ( $k_s$ ) for the  $\text{Fe}(\text{CN})_6^{3-/4-}$  system has been observed to be two orders of magnitude smaller than that of the  $\text{Cp}_2\text{FeTMA}^{+/2+}$  couple. The authors also demonstrated a coulometric type experiment for the same system where the discharge potential of the working electrode is followed with respect to a large quasi-reference electrode [101]. The nanoelectrode is biased by about 85 mV for 30 to 60 s in a solution containing the  $\text{Fe}(\text{CN})_6^{3-/4-}$  redox couple. The bias voltage is switched off, and the discharge potential is followed with time using a high input impedance electrometer. A staircase-like behaviour in the potential decay is observed when the discharge time exceeds 200 s. The temporal relation of the voltage of the electrochemical system,  $V_{\text{corr}}$ , can be

represented by:

$$V_{\text{corr}} = n(t)e/C + \text{terms independent of } n(t)$$

where  $n$  is the discrete number of electrons gained by the electrode during the discharge process and  $C$  is its capacitance. The change in  $n(t)$  is quantized and hence this relationship conveniently describes the discontinuous jump in  $V_{\text{corr}}$  during an electron transfer event.

Murray has demonstrated that soluble metallic clusters exhibit coulomb staircase-type behaviour [102]. The ionic space charge formed around the dissolved MPCs is reported to contribute to its capacitance, upon charging of the metal core. It is well known that small metal particles exhibit double layer charging (capacitive charging) properties in liquid electrolytes [104]. The sub-attofarad capacitance associated with the MPCs leads to charging of the tiny capacitor by single electron processes in potential intervals of  $\Delta V$  that surpass  $k_B T$  where  $k_B$  is the Boltzmann constant and  $T$  is the temperature [102, 105].

In general, currents observed at rotating microdisk electrodes in the double layer region are typically small and potential independent when the solution does not contain any redox-active component. However, the situation is different in the case of MPCs stabilized with mixed thiols wherein one of the components is electro-active. Voltammograms obtained at GC and Pt rotating disk electrodes in electrolytes containing gold MPCs stabilized with octane thiol and ferrocenyl octanethiol result in noticeable curvature in the potential regions more negative and positive than that of Fc oxidation (Figure 20.1). This is attributed to the charging of the double layer at the metal cluster. The variation in current with potential ( $\Delta i/\Delta E$ ) being proportional to (angular velocity,  $\omega$ )<sup>1/2</sup> leads to the conclusion that the double layer charging of the clusters is under hydrodynamic mass transport control. The MPCs, hence, act as diffusing, molecule-sized “nanoelectrodes” [52, 106].

Further evidence that the double layer charging occurs as a series of discrete one-electron processes is obtained from DPV and CV measurements carried out at a Pt electrode in a solution containing highly monodisperse (1.64 nm diameter) hexanethiolate stabilized 3-D SAMs [102]. They exhibit a series of well-resolved multiple current peaks over a wide potential range. The spacing between the peaks is a sensitive indicator of the particle size as well as the capacitance of the cluster. This can be summed up by the expression,  $\Delta V = e/C$  [102], where  $\Delta V$  is the spacing between consecutive peaks,  $e$  is the electronic charge and  $C$  the capacitance of the cluster. This report is one of the first to show the phenomenon of “Coulomb staircase charging” (later christened ‘quantized double layer charging’ (QDL)) of ensembles of clusters at a metal/solution interface under ambient conditions. The authors have invoked the concept of separately coexisting configurations of solution/metal cluster/Pt electrode junctions to explain the electrochemical charging phenomenon. Monodispersity of the nanoparticles is a key factor in the observation of this phenomenon [105, 107]. Techniques such as fractionation, annealing and separation using high pressure liquid chromatography (HPLC) have been used to obtain very uniform sized particles [102, 105, 107].



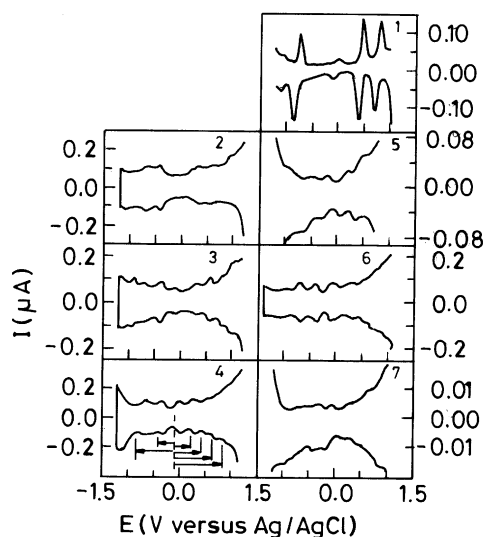


**Fig. 20.8.** Differential pulse voltammograms for 2,3,4-butanethiolate (C4) and 1,5,6,7-hexanethiolate (C6) Au MPCs as a function of uniform core size, in 0.05 M  $\text{Hex}_4\text{NClO}_4$ /toluene/acetonitrile (2/1 v:v), at  $9.5 \times 10^{-3} \text{ cm}^{-2}$  Pt electrode; DC potential scan  $10 \text{ mV s}^{-1}$ , pulse amplitude  $50 \text{ mV}$ . Concentrations

are: (2) 14 kD, 0.086 mM; (3) 22 kD, 0.032 mM; (4) 28 kD, 0.10 mM; (1) 8 kD, 0.30 mM; (5) 22 kD, 0.10 mM; (6) 28 kD, 0.1 mM and (7) 38 kD, 0.10 mM. Arrows at lower left indicate  $\Delta E$  potential steps used. (Adapted from *Science*, **1998**, 280, 2098).

Murray and co-workers have also demonstrated that the variation in Au-core sizes leads to a transition from metal-like double layer capacitive charging for larger sized particles to redox-like charging for smaller particles ranging between 1.1 nm and 1.9 nm diameter [105] (Figure 20.8). Gold particles stabilized with short chain alkanethiolate monolayers have been used in this study. The capacitance of the clusters is calculated using the concentric sphere capacitance model:

$$C_{\text{CLU}} = 4\pi\epsilon_0\epsilon(r/d)(r + d)$$

where  $C_{\text{CLU}}$  represents the capacitance of the cluster,  $\epsilon_0$  is the permittivity of free space and  $\epsilon$  is the monolayer static dielectric constant,  $r$  is the radius of the cluster and  $d$  is the length of the stabilizing ligand [108]. The cluster capacitance increases with increasing core diameter and decreases with decreasing monolayer chain length [108]. Smaller particle size leads to wider spacing between current peaks at values close to the potential of zero charge of the MPCs. The wider spacing corresponds to an electrochemical band gap and is observed to be consistent with the optical band gap of the MPCs (0.4 to 0.9 eV) [105]. The double layer charging peaks of small metal clusters are found to be analogous to current peaks seen in redox reactions. The charging process is generally fast and hence the currents are determined by the Nernst equation coupled with mass transport [109]. Each metallic core is associated with a formal potential at which QDL events occur and is

given by,

$$E_{Z/(Z-1)} = E_{PZC} + (Z - 1/2)e/C_{CLU}$$

where  $E_{PZC}$  is the potential of zero charge of the cluster at  $Z = 0$ ,  $Z > 0$  implies oxidation and  $Z < 0$ , reduction of the metal core [108]. Plots of peak potential (determined from DPV) vs. the charge state (referred to as 'Z-plots') are linear and the slopes are used to determine the capacitance of the clusters. Another important observation is that the capacitance of these clusters seems relatively insensitive to the solvents employed to carry out the experiments [108].

The metal clusters need not be freely diffusing in the bulk of the solution in order to observe QDL effects. Multilayers of MPC clusters attached to an Au substrate by means of ligand/metal ion/ligand linkers also show the staircase charging phenomenon [110]. The HT/mercaptohexanoic acid MPCs or mixed HT/Mercaptoundecanoic acid MPCs anchored to gold substrate through carboxylate/metal ion bridges show well-defined single electron charging of their double layers in  $CH_2Cl_2$  solutions. The charging peak currents, being proportional to the scan rate, imply that the MPCs are surface confined. It is observed that the capacitance does not vary much whether the MPCs are freely diffusing or immobilized on the surface. DPV studies show similar variations in the capacitance as a function of applied voltage. Layer by layer growth of assemblies comprising polymer-gold MPCs also show QDL effects [111]. The QDL effects are not confined to non-aqueous media. The MPC films assembled on gold surfaces through a dithiol linker also show charging effects in aqueous media [112–115]. Initial experiments indicate that MPC-modified electrodes should be immersed in solutions of hexanethiol to block voids on the electrode surface in order to observe quantized double layer charging. Once the electrode is fully covered, charging effects are observed in aqueous solutions. The reasons for the above observation is that in organic solvents,  $C_{El} < C_{SAM}$  where  $C_{El}$  is the capacitance of the bare electrode and  $C_{SAM}$  is the double layer capacitance on the electrode with adsorbed MPCs. Therefore, the electrode double layer capacitance is governed by the MPCs and quantized charging effects are observed on as-prepared MPCs. In aqueous solutions, on the other hand,  $C_{El} > C_{SAM}$  and hence the electrode double layer charging is through the bare Au surface that shows the classical double layer charging of the electrode. Therefore, the voids should be filled with low dielectric molecules like HT in order to observe quantized charging effects. The effect of using organic molecules to fill the voids can be mimicked by using supporting electrolytes containing hydrophobic anions [113, 114]. Rectification observed with these systems, however, depends strongly upon the electrolyte used. Hydrophobic anions such as  $PF_6^-$ ,  $ClO_4^-$  and  $BF_4^-$  induce rectification. These anions are thought to expel water molecules from the electrode interface by binding strongly to the positively charged Au MPCs at positive potentials and hence  $C_{El} < C_{SAM}$ . At negative potentials however, the binding is disfavored leading to  $C_{El} > C_{SAM}$ , thus revealing featureless characteristics in the negative potential regime. Capacitance values obtained in aqueous media are larger than those determined for the same sample in

organic media (1.05 aF in aqueous media vs. 0.75 aF in organic solvents such as  $\text{CH}_2\text{Cl}_2$ ) [113]. The binding of  $\text{PF}_6^-$  on the surface-immobilized MPCs probably increases the effective dielectric constant and hence the capacitance. Rectification is induced only in the presence of specific soft, hydrophobic anions, as mentioned earlier, and to a small extent in the presence of soft cations such as (tetramethylammonium, TMA) $^+$  and (tetraethylammonium, TEA) $^+$ . In effect, both hydrophobic and electrostatic forces play a significant role in ion binding.

Other metallic clusters that have been demonstrated to show the QDL effect are palladium [116, 117], silver [118] and copper [119]. Palladium MPCs capped with mixed monolayers of hexanethiolate/dodecanethiolate and ferrocene thiolate ligands are prepared in a manner similar to that employed for gold MPCs. The DPV studies exhibit a quantized charging effect but the current peaks are not as well defined as those observed for Au-MPCs. Capacitance values of the order of 0.35 aF are obtained, indicating smaller core sizes or thicker monolayer dielectrics [116]. Fresh copper nanoparticles show the QDL effect and the aged particles behave like semiconductors due to the formation of the oxide film [119].

An important observation related to the QDL effects is that the MPCs can be electrolytically charged to controllable potentials [120]. The pattern and the height of the current peaks can be used to estimate the number of electrons (or holes) stored on the cluster. The charged MPCs are stable for several hours in the solution phase and the interesting fact is that these particles retain most of their charge when isolated in the dry form. Some charge is lost during this process due to several factors, but the remaining charge is reasonably stable. These charged clusters thus hold great promise as oxidizing and reducing agents. Charging the MPCs at positive potentials results in increased solubility in polar solvents. Thus, a substituent effect can be incorporated by electrochemical tuning of the clusters. Preliminary experiments have indicated that they can be used to carry out redox reactions with electron acceptor or donor molecules like ethylferrocene (EtFc) and 7,7,8,8-tetracyanoquinodimethane (TCNQ) respectively. A small amount of these charged clusters is added to a solution of EtFc or TCNQ and the subsequent electron transfer reactions can be monitored like any regular potentiometric titration [120]. Differently charged MPC clusters can also undergo electron transfer reactions with each other. These mixed valent solutions follow the Nernstian behavior as given by:

$$E = E_{\text{MPC}}^0 - 0.059 \log\{[N_z]/[N_{z-1}]\}, \quad \text{where } E_{\text{MPC}}^0 = E_{\text{PZC}} + [z - (1/2)]e/C_{\text{clu}}.$$

Thus, the electronic charges associated with double layer charging of MPCs have numerous redox-like formal potentials that can be taken to a desired charge state [120].

The dynamics of self-exchange between the MPCs is probed by linking them through carboxylate-metal ion-carboxylate bridges [121] on an electrode surface. The diffusion-like electron transport in multilayer films is used to obtain information on the nanoparticle-nanoparticle electron transfer dynamics. Potential step experiments that give an idea of the rate of electron hopping (electron diffusion)

have been carried out. The parameter  $D_E$  is related to the rate of electron hopping, assuming nearest neighbour interactions, and is given by:  $D_E = k_{\text{HOP}}(\delta^2/6) = k_{\text{EX}}(\delta^2 C/6)$  where  $k_{\text{HOP}}$  and  $k_{\text{EX}}$  are the first order rate constants of electron transfer and self-exchange respectively.  $\delta$  is the equilibrium centre to centre core separation and  $C$  is the concentration of MPC cores in the nanoparticle film. The values determined are  $11 \times 10^{-8} \text{ cm}^2 \text{ s}^{-1}$ ,  $2.5 \times 10^6 \text{ s}^{-1}$  and  $2.1 \times 10^8 \text{ M s}^{-1}$  for  $D_E$ ,  $k_{\text{HOP}}$  and  $k_{\text{EX}}$  respectively.

## 20.5

### Probing Nanoparticles using Electrochemistry Coupled with Spectroscopy

A relatively recent technique that has been introduced to explore the local environment of a nanostructured material under potential control conditions is the use of solid state NMR coupled with electrochemistry [122–142]. This is a very challenging task for two basic reasons. The sensitivity of the measurement decreases due to the presence of a conducting electrode material in the NMR detection coil that reduces the so-called ‘quality factor’ of the probe [122]. A high field NMR instrument requires  $10^{18}$ – $10^{19}$  NMR active atoms (for example,  $^{13}\text{C}$  spins) to detect an observable signal for a reasonable period of time. The surface of a typical metal contains only about  $10^{15} \text{ atoms cm}^{-2}$ . Hence, a large surface area is required for the measurement. This disadvantage may be overcome when high surface area nanostructured materials are used. The use of solid state NMR to probe surface properties of metals, such as the Fermi level local density of states ( $E_F$ -LDOS) and the structure of adsorbates has been fairly well explored in the recent past [122, 124–128]. Electrochemical control along with solid state NMR allows access to molecular information on the static, dynamic and electronic structure of electrocatalytic materials on solid surfaces. Other advantages of electrochemical NMR (EC-NMR) include the ability to study surfaces at different temperatures, to follow the metal as well as the adsorbate relaxation times, to examine surface diffusion and surface reconstruction phenomena and particle size variation.

The two important probes that have been used in EC-NMR to study both the adsorbate and the substrate are  $^{13}\text{C}$  and  $^{195}\text{Pt}$ . All organic compounds contain carbon and hence can be selectively labeled with  $^{13}\text{C}$  while platinum is an important catalytic and electrocatalytic material. Additionally, the quadrupolar effects are absent since they have a nuclear spin,  $I = 1/2$ . Another major advantage of the EC-NMR is the possibility to study systems such as Pt-CN [129, 138] that are otherwise difficult to probe with the conventional gas/solid system. A schematic of EC-NMR instrumentation is shown in Figure 20.9. This configuration allows simultaneous potential control and NMR data acquisition of the sample. The use of a potentiostat may affect the NMR signal and the interfering noise can be removed by the use of appropriate filters [122, 124, 127]. The leakage of high power radio-frequency (RF) pulses is also prevented by the same mechanism. The NMR signals for the electrochemical interface remain steady and reproducible over several months, thus indicating that the interface is stable from the NMR point of view.

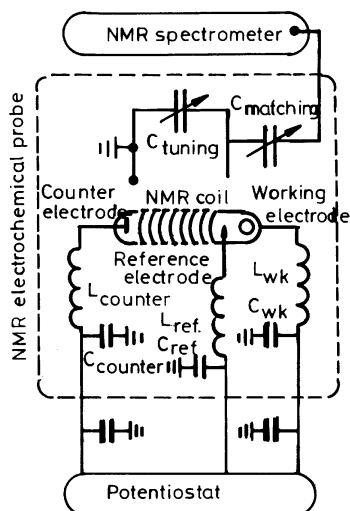
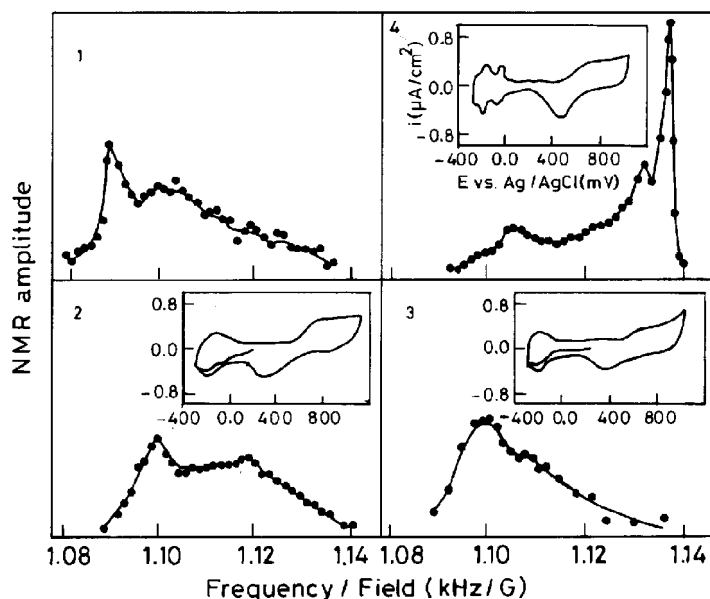


Fig. 20.9. Schematic of the EC-NMR probe circuitry showing the interface between NMR and electrochemistry. (Adapted from *Anal. Chem.*, 1998, 518A).

The Knight shift ( $K$ ) in a metal, corresponding to the chemical shift in a molecule, is known to be a fingerprint of the corresponding site or structure [143].  $K$  is the result of spin–spin interaction between nuclei and electrons. The electron spins at the Fermi energy can only be polarized and hence can produce non-zero spin density in an external magnetic field [143]. The Knight shift contains only static information. However, the dependence of spin–lattice relaxation time ( $T_1$ ) and spin–spin relaxation time ( $T_2$ ) on the temperature and the magnetic field can yield valuable information on the dynamics on the timescale of  $10^{-9}$  to  $10^2$  s.

The use of EC-NMR for the study of nanoparticles is exemplified by an investigation reported by Wieckowski and co-workers [122, 126, 128]. The working electrode is made of supported platinum catalyst particles of nanometer size, placed on a Pt boat. Figure 20.10 shows the point-by-point  $^{195}\text{Pt}$  NMR spectra under different conditions. The supported Pt crystallites show the characteristics of isolated, small Pt particles. Clear surface signals corresponding to the oxide of platinum on the as-received commercial sample are shown in Figure 20.10.1. The oxide reduction under potential control gives rise to the spectrum 20.10.2. The variations due to the particle size as well as the metallic versus oxide surface are clearly brought out in the spectra shown in Figure 20.10.

The adsorption properties of carbon monoxide and CN generated by the electrochemical decomposition of  $^{13}\text{C}$ -enriched methanol or  $^{13}\text{C}$ -enriched NaCN have been studied using EC-NMR [129, 130]. The  $^{13}\text{C}$  NMR of the adsorbed species on Pt nanoparticles reveals that the potential control affects the NMR output to varying extents [142]. A positive potential change leads to the shielding of  $^{13}\text{C}$  resonances and slopes of the order of  $-71 \text{ ppm V}^{-1}$  for  $^{13}\text{CO}$  (Figure 20.11) and  $-50$



**Fig. 20.10.** Point-by-point platinum NMR spectra of carbon-supported platinum electrodes. (1) As received, 2.5 nm average particle diameter; (2) cleaned, 2.5 nm; (3) cleaned, 2.0 nm; (4) cleaned, 8.8 nm. The

spectra were recorded at 80 K by manually sweeping the frequency and using a Hahn-echo pulse sequence. Insets are the corresponding electrochemical cyclic voltammograms. (Adapted from *Anal. Chem.*, **1998**, 518A).

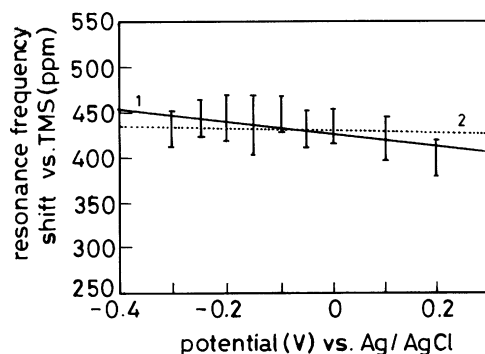


**Fig. 20.11.**  $^{13}\text{C}$  NMR line position of CO on Pt, as a function of electrode potential vs Ag/AgCl. Solid line: Least square fit with slope of  $-71 \pm 20 \text{ ppm V}^{-1}$ . Correlation coefficient 0.75; Dotted line: slope  $-15 \text{ ppm V}^{-1}$ . Correlation coefficient 0.46. (Adapted from *Phys. Rev. Lett.*, **1999**, **83**, 2457).

ppm  $V^{-1}$  for  $^{13}C$ N have been observed. The fact that the changes observed under potential control are entirely due to the Knight shift is confirmed by comparing the  $^{13}C$  chemical shift response of CO to an electric field in biomolecules, which is of the order of  $-15$  ppm  $V^{-1}$ . The changes in  $2\pi^*$  back donation are accounted for by the variations in the vibrational frequency,  $\nu_{CO}$ . The CO stretch frequency is lowered when the back donation is high. The above points suggest that the  $^{13}C$  NMR shift and the vibrational frequency of the adsorbed CO are electronic in nature. This originates from the changes in  $E_f$ -LDOS at the nanocrystalline metal surface and at the adsorbate, induced by electrochemical potential control [142]. A layer model analysis is used to describe the  $^{195}Pt$  NMR spectrum of nanoscopic materials [144]. It is also possible to correlate the electronegativity of the adsorbates with the Knight shift associated with the Pt nanoparticles [138]. The orientation of adsorbates on metallic substrates under potential control conditions has also been explored [122, 131]. Tong and co-workers have recently demonstrated the use of EC-NMR to investigate the electronic environment of the core of MPCs [145].

Other spectroscopic techniques that have been used with electrochemistry to probe nanoparticles include electronic and vibrational spectroscopies. The spectroelectrochemistry of nanosized silver particles based on their interaction with planar electrodes has been studied recently [146] using optically transparent thin layer electrodes (OTTLE). Colloidal silver shows a surface plasmon resonance absorption at 400 nm corresponding to 0.15 V vs. Ag/AgCl. This value blue shifts to 392 nm when an Au mesh electrode in the presence of Ag colloid is polarized to  $-0.6$  V (Figure 20.12). The absorption spectrum is reported to be quite reproducible and reversible. This indicates that the electron transfer occurs between the colloidal particles and a macroelectrode and vice versa. The kinetics of electron transfer is followed by monitoring the absorbance as a function of time. The use of an OTTLE cell ensures that the absorbance is due to all the particles in the cell between the cell walls and the electrode. The distance over which the silver particles will diffuse has been calculated to be 80  $\mu m$  in 150 s, using a diffusion coef-

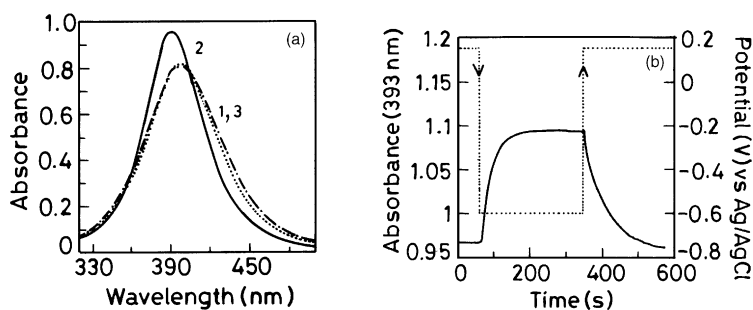


**Fig. 20.12** (a) Spectra of the silver sol obtained (1) at the open circuit potential of +0.15 V, (2) after a potential step to  $-0.6$  V and then (3) after stepping the potential back to +0.15 V vs Ag/AgCl. (b) Change in absorbance of a silver sol at 393 nm (continuous

line) as a function of time after application of a potential step to  $-0.6$  V from +0.15 V, and then reversal of the potential step back to +0.15 V (dashed line). (Adapted from Langmuir, 1997, 13, 1773).

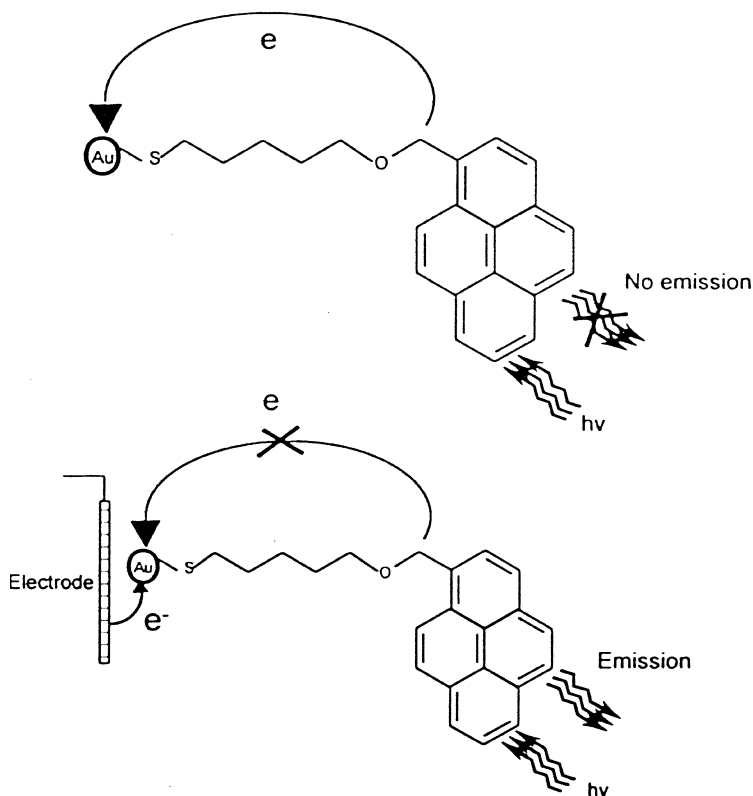
ficient value determined by the dynamic light scattering method. The OTTLE cell thickness is only 75  $\mu\text{m}$  and hence it is concluded that the electron transfer occurs close to the diffusion-limited rate of encounters of the metallic particles with the electrode surface. The potential window that is available for the study is limited by hydrogen evolution on the negative side ( $-0.8\text{ V}$ ) and the oxidation of silver particles on the positive side ( $0.4\text{ V}$ ). The spectroelectrochemical shift leads to a double layer capacitance value of  $(80 \pm 10)\text{ }\mu\text{F cm}^{-2}$  for the nanoparticles. Cottrell behaviour is satisfied for the equilibration of the particles with the planar electrode. Based on the spectral shift, a value of 1790 has been calculated for the number of electrons needed to shift the absorption peak from 404 nm to 392 nm in the case of particles of 11 nm size. This is equivalent to a shift of electrochemical potential from 0.4 V to  $-0.7\text{ V}$  that corresponds to a surface charge density increase of 6.2%. The particle charging current is associated with the electron tunneling across the particle and the electrode double layer and not by contact electrification.

Murray and co-workers reported similar observations on spectral shift by an electrochemical stimulus, for the gold MPCs [147]. The electronic charging of gold clusters stabilized by alkanethiolate monolayers effected by shifting the rest potential of  $-0.16\text{ V}$  to  $0.82\text{ V}$  is found to result in a change of about 9 nm in the absorbance maximum. The observed change is compared to the predictions from the theory based on a concentric sphere model [108] for cluster capacitance and the Mie theory of scattering [2, 146]. The sensitivity of plasmon positions to the charge associated with the metal particles opens up the possibility of tuning the absorption bands by electrochemical means. Nishihara and co-workers have demonstrated the electrochemical tuning of surface plasmon absorption for redox-active Au-MPCs. The shift in the absorbance maximum as a function of applied potential is reported to be predominantly due to the charging of the metal core. The contribution by the redox-active moiety, though small, should also be considered [62–64].

Kamat and co-workers demonstrated the electrochemical tuning of emission properties of a fluorophore using functionalized gold nanoparticles on a transparent ITO electrode [148]. The schematics of the assembly and the suppression of emission are given in Scheme 20.2. Spectroelectrochemical experiments using the pyrene-modified gold nanostructured film show that the communication between the fluorophore and the gold core is totally suppressed at  $-1.2\text{ V}$  versus SCE in acetonitrile medium. The emission is restored to about 90% by simply charging the electrode. The same authors have earlier shown that the nanocrystalline gold/ITO electrode allows the flow of electrons following Fermi level equilibration [149].

Weaver and co-workers [150] carried out potential-dependent infrared spectroscopy to characterize adsorption of CO on nanosized platinum particles. Large particles of diameter 4 nm and above show C–O stretching frequencies similar to those of platinum macroelectrodes. Small particles of diameter 2–4 nm, on the other hand, show a red shift in C–O frequency, approaching that of platinum carbonyl clusters. The authors ascribe this observation to the changes in the platinum surface coordination number, consistent with pseudo-spherical packing-density considerations. A time-resolved IR absorption technique has also been used to monitor electrocatalytic reactions using platinum nanoparticles [151].





**Scheme 20.2.** Deactivation of excited surface-bound pyrene (a) before and (b) after charging the gold nanocore. (Adapted from *Angew. Chem. Int. Ed. Engl.*, **2002**, 41, 2764).

Absorbance and electroreflectance studies involving viologen radicals that are placed in close proximity to electrochemically controlled gold nanoparticles reveal an anomalous electroreflectance spectrum around the formal potential of the viologen redox couple [152]. The spectra show characteristics of electrochemical charging and discharging of the gold particles at positive potentials. The authors suggest a strong interaction between viologen cation radical moieties and gold particles under plasmon excitation. The possibility of charge injection into gold nanoparticle ensembles and the consequent changes in the reflectance and transmittance of the nanostructured films has been explored by Schiffrin and co-workers [153]. The optical response to the electrochemical charge injection is explained in terms of electron density oscillations in individual particles [153]. The charge injection, according to the authors, occurs mostly on the outer layer and the rest of the film acts like a support for electron transfer. The behavior may be compared to that of individual quantum dots that can respond to electron injection. Potential-dependent surface enhanced Raman spectra (SERS) of pyridine using Ag

nanoparticles deposited electrochemically on colloidal gold assembled on a glass/SnO<sub>2</sub> electrode are found to be reasonably good substrates for SERS studies. Ag particles deposited on Pt electrodes by a chemical method show excellent potential-dependent SERS spectra for pyridine [24].

## 20.6

### Nanosensors

#### 20.6.1

##### Biosensors

Electrode surfaces can be modified with metal nanoparticles and such surfaces have found numerous applications in the field of bioelectrochemistry, particularly in biosensors [7, 155]. Gold nanoparticles are often utilized in such studies since they are known to retain the activity of the biomolecule with electrochemical activity intact as well [15]. It has also been observed that these nanoparticles can act as conduction centers facilitating the transfer of electrons. In addition, they provide large catalytic surface areas.

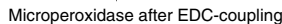
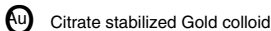
A vast amount of literature exists on enzyme-modified metal nanoparticles. Crumbliss and co-workers pioneered the use of metal nanoparticles for enzymatic sensors for various analytes such as H<sub>2</sub>O<sub>2</sub>, glucose, xanthine and hypoxanthine [156–158]. GCE or Pt electrodes are modified with enzyme-capped Au colloids, either by simple evaporation or electrodeposition. The nanoparticles act as mediators, transferring electrons between the redox-active site on the immobilized biomolecule and the electrode and thus eliminating the need for external mediators. These sensors are classified as “third generation biosensors”.

Carbon paste as an electrode has been well studied for biosensing applications. It has the advantage of ease of preparation, desired level of loading and good conductivity. Celej and Rivas developed a sensor for the determination of glucose using gold-dispersed carbon paste electrodes containing glucose oxidase (GOx) [159]. The gold particles catalyze the electrooxidation and reduction of the H<sub>2</sub>O<sub>2</sub> generated during the enzymatic catalysis. This sensor can also be used in flow injection systems.

Natan and co-workers have demonstrated the reversible electrochemistry of cytochrome-c at gold colloid-modified SnO<sub>2</sub> electrodes. The voltammetric behaviour depends strongly on the nanoscale morphology. Surfaces composed of isolated 12 nm Au particles give rise to reversible voltammetry while aggregates of particles of the same size result in irreversible behavior [160a]. Ju and co workers [160b] prepared similar nanoparticle-modified carbon paste electrodes and incorporated horse-heart cytochrome-c using a polishing procedure to detect micromolar (μM) concentrations of H<sub>2</sub>O<sub>2</sub>. More recently, tyrosinase–colloidal gold-modified carbon paste electrodes have been used for the detection of nanomolar (nM) concentrations of phenol [161]. The immobilized tyrosinase efficiently catalyzes the reaction

of phenol to form *o*-quinone that is electrochemically active. Gold nanoparticles allow a large degree of freedom in the orientation of the enzyme molecules. Additionally, the catalytic sites are easily accessible to substrate molecules. Casella and co-workers have electrochemically deposited gold nanoparticles on GCE surfaces and used these for sensing carbohydrates in flow injection and liquid chromatography modes [162]. Copper electrodeposited in a similar way leads to a sensor for glucose [163]. A very low detection limit of 0.8 pmol of glucose is obtained with a dynamic range extending over four orders of magnitude of the analyte.

Three-dimensional superstructures consisting of gold nanoparticles and a heme-containing undecapeptide, microperoxidase-11 (MP-11) have been assembled on ITO electrodes [164]. The base monolayer consists of an aminosilane that is cross-linked with MP-11 using 1-(3-dimethylaminopropyl)-3-methylcarbodiimide (EDC). When this assembly is treated with citrate-stabilized gold (13 nm diameter) colloid, the amino groups associated with the lysine and valine residues of the enzyme concentrate the metallic particles. This is further treated with cystamine to yield amino groups on the surface of the anchored gold particles. The procedure of enzyme modification is continued to obtain multilayers as shown in Scheme 20.3. Electrocatalytic reduction of  $\text{H}_2\text{O}_2$  is demonstrated using this assembly. Dong and co-workers [165] used the concept of immobilizing gold nanoparticles into a silicate network assembled on an electrode surface through specific Au–S interactions. This assembly is used to anchor horseradish peroxidase enzyme to analyze hydrogen peroxide. The biosensor has resulted in a fast amperometric response of 2.5 s for the detection of  $\text{H}_2\text{O}_2$  with a detection limit of 2  $\mu\text{M}$ . The sensor is also reported to exhibit high sensitivity, good reproducibility and long-term stability. The co-deposition of aminosilicate-stabilized gold particles and an enzyme, glucose oxidase on an ITO electrode surface is reported to result in a biosensor for glucose [166]. Since an all-aqueous medium is used in this process, the denaturation of the enzyme is largely hindered. Typical chronoamperometric traces (Figure 20.13) show the response of the sensor for various glucose additions. Chen and co-workers suggested yet another method for the amperometric determination of  $\text{H}_2\text{O}_2$  using HRP immobilized gold nanoparticles of different size via a long cysteamine/glutaraldehyde/cysteamine bridge [167]. This assembly, however, does not show an efficient direct electron transfer and hence catechol is used as an electron transfer mediator. Subsequently, the same authors directly immobilized HRP to uniformly small Au colloids via a short cystamine chain on a gold electrode [168]. This reduced the chain length, eliminating the need for an electron transfer mediator. D'Souza and Sampath have prepared bimetallic nanocomposites of Pt–Pd in a single step using organically modified silicates as a matrix as well as a stabilizer. XPS and CO adsorption studies on Pd–Pt bimetal suggest a Pd core and Pt shell type of structure. Thin films of Pd–Pt bimetal deposited on a GCE are found to be very good for the amperometric determination of ascorbic acid. The response of the sensor is fast, of the order of a few tens of seconds [169a]. The concept of immobilization of gold nanoparticles on a cystamine-modified gold mesh has been used to determine and separate dopamine (DA) from ascorbic acid



### Stepwise assembly of the MP-11/Au layered superstructure on an ITO Conductive support

**Scheme 20.3.** Stepwise assembly of the MP-11 Au layered superstructure on an ITO (or Au) conductive support. (Adapted from *Chem. Commun.*, **2000**, 1025).

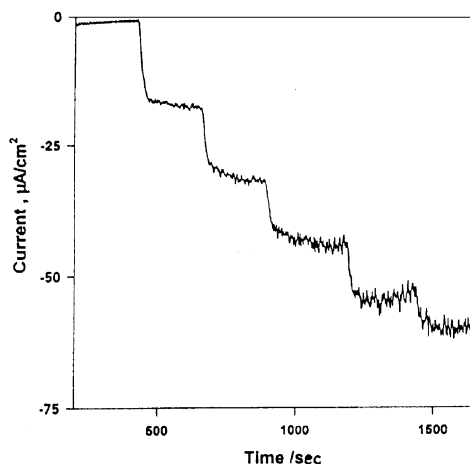


**Fig. 20.13.** Chronoamperometric responses of the glucose oxidase (Gox)-Au-Silicate thin film electrode at 0.6 V, for successive additions of 5 mM glucose in 0.1  $\text{KH}_2\text{PO}_4$  solution pH 5.6. (Adapted from *Langmuir*, **2001**, 17, 2602).

[169b]. It should be pointed out that DA and AA do not show separate peaks on a bare electrode surface. Thus good selectivity and sensitivity is achieved by this method.

The gold nanoparticle–enzyme modification procedure has also been used to probe the association of an enzyme and its cofactor [170]. Colloidal gold immobilized on a gold electrode using a dithiol linker is used to adsorb alcohol dehydrogenase (ADH). The interaction between ADH and the oxidized form of nicotinamide adenine dinucleotide [ $\text{NAD}^+$ ] is subsequently probed using electrochemical impedance studies [170]. The association is revealed by an increase in the charge transfer resistance for  $[\text{Fe}(\text{CN})_6]^{3-/4-}$  when the  $\text{NAD}^+$  concentration is increased in the bulk of the solution. Boal and Rotello synthesized diacyldiaminopyridine-derivatized gold nanoparticles [171] and further interacted them with flavin through non-covalent complexation. The molecular recognition based on host–guest interactions between flavin and the pyridine unit determines the redox activity of flavin. A cathodic shift in the potential is observed with increasing concentration of pyridine-functionalized gold particles.

The inactivation of certain enzymes such as cholesterol oxidase (CO) on interaction with Au nanoparticles is overcome by immobilizing CO and cholesterol esterase (CE) in a carrageenan hydrogel and coupling with Au particles loaded with HRP. This multienzyme device has been shown to be very useful in the determination of cholesterol in serum and whole blood [172]. The sensor operates at low potentials avoiding major interferences. The presence of the hydrogel enables the analysis of whole blood with no fouling of the electrode surface.

Electrochemical labels based on gold nanoparticles are of recent origin [173–177]. Kim and co-workers developed an immuno-chromatographic membrane strip

consisting of two interdigitated Ag electrodes [173] to determine human serum albumin (HSA). During the sensing action, a sandwich type complex consisting of the analyte, the immobilized antibody and the conjugate is formed at the electrode surface, generating a conductimetric signal. Electrochemical immunoassay of immunoglobulin G (IgG) has also been demonstrated using colloidal gold label [174]. This method involves an interaction of IgG with an immobilized antibody and a gold labeled antibody to form a sandwich type complex. The ASV of gold metal leads to a low detection limit of pM concentration. The electrochemical detection of DNA for the quantification of the human cytomegalovirus DNA sequence has been reported by Limoges and co-workers [178]. The assay is carried out in microwells where the single stranded (ss) target DNA is immobilized then undergoes hybridization with the corresponding oligonucleotide-modified Au particle. Gold is then electrochemically quantified using the ASV. Similar studies for the detection of DNA segments related to the breast cancer BRCA1 gene have also been reported [179]. Recently, Wang reported on a novel detection method for DNA based on a combination of magnetic separation and the already known concept of gold stripping analysis [180]. Very low detection limits of femtomoles (fM) have been achieved by this method.

Cai and co-workers used colloidal gold attached to a macroelectrode to increase the concentration of ss-DNA and consequently improving the sensitivity of DNA detection [181]. Hybridization of the DNA strand attached to the gold particles with a ferrocenecarboxaldehyde-labeled complementary strand from the bulk of the solution leads to a detection limit of the order of  $10^{-10}$  mol, as observed by DPV studies. The same authors demonstrated an electrochemical method for site-specific DNA analysis, based on the stripping of silver formed on gold nanoparticles [182]. This method involves the electrochemical stripping of catalytically formed Ag nanoparticles on Au to quantify the analyte. Even a single base pair mismatch is possible to detect by this method (Figure 20.14). Ye and co-workers [183] have recently reported the preparation of supported bilayer lipid membrane (BLM)-metal nanoparticle composites for designing biosensors. The deposition of Pt nanoparticles through non-conducting BLM is reported to be active for the electrocatalyzed reduction of oxygen. The nanoparticle array is a novel way of preparing electrodes similar to the NEEs reported by Martin and co-workers [5]. Direct electron transfer between hemoglobin and GCE has been demonstrated using synthetic lipid (didodecyldimethylammonium bromide, DDAB)-protected gold nanoparticles of size around 6 nm [184].

## 20.6.2

### Chemical Sensors

The use of nanoparticle arrays to generate surface-confined architectures has been extensively studied by Willner and co-workers [6]. The structural motif involves the sequential electrostatic assembly of nanoparticles and the desired molecules on planar electrodes. An ITO substrate is functionalized using an aminosilane molecule to yield a charged surface. Negatively charged citrate-stabilized gold

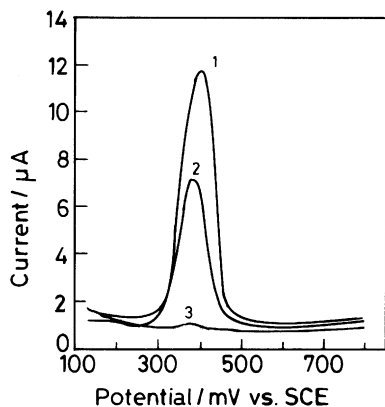
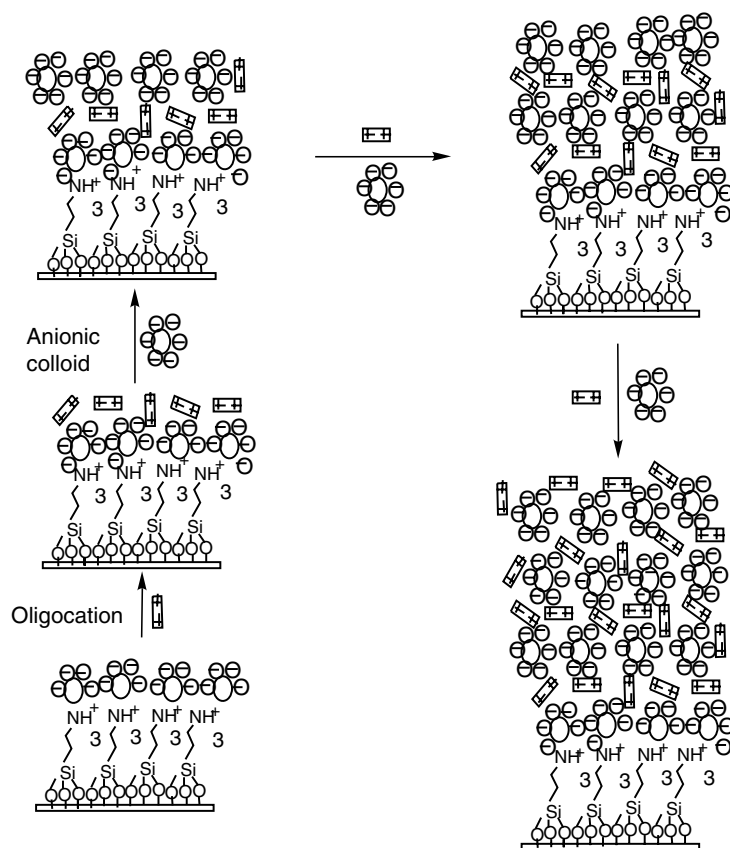


**Fig. 20.14.** DPV response for dsDNA detected by monitoring the silver in 0.1 M acetate buffer (pH 5.2) after 8 min. Silver enhancement of gold labels. Hybridization conditions: the ssDNA captured electrode was shaken in  $1.0 \times 10^{-7}$  M gold nanoparticle probe solution (0.3 M PBS buffer) for 60 min at 42 °C. Potential range, +0.10 to +0.80 V (vs. SCE); pulse amplitude, 50 mV; pulse width, 50 ms; pulse period, 0.2 s. (1) DPV response of the gold nanoparticle-labeled oligonucleotides

DNA probes hybridized with  $5.0 \times 10^{-9}$  M complementary oligonucleotides. (2) DPV response of the gold nanoparticle-labeled oligonucleotides. DNA probes hybridized with  $5.0 \times 10^{-9}$  M oligonucleotides containing single-base mismatch. (3) DPV response of the gold nanoparticle-labeled oligonucleotides DNA probes hybridized with  $5.0 \times 10^{-9}$  M non-complementary oligonucleotides. (Adapted from *Anal. Chim. Acta*, **2002**, 469, 165).

particles are electrostatically assembled on to this layer [22b, 24, 27]. The next step involves the assembly of polycationic molecules based on cyclophanes such as cyclobis (paraquat-*p*-phenylene) [185], cyclobis (paraquat-*p*-biphenylene) [186], pyridinium salts and an octacationic Pd(II) macrocycle [187] as given in Scheme 20.4. This procedure of metal particle and organic molecule attachment is repeated to yield multilayers of the assembly [28]. Similar preparation techniques have been reported where the crosslinking units are replaced by polymers, other nanoparticles or biomaterials [164, 188, 189]. The crosslinker molecule, cyclobis (paraquat-*p*-phenylene), is electro-active and hence the redox activity can be followed electrochemically. The redox activity increases with the number of layers anchored onto the surface, indicating that the assembly exhibits dimensional activity. Coulometric analysis yields coverages of  $1.5 \times 10^{-11}$  mol cm<sup>-2</sup> per layer, that leads to an estimate of 100 crosslinker molecules per gold particle. This is in excellent agreement with the number estimated to precipitate the gold colloid from the solution [190]. This further emphasizes that the interactions are electroactive in nature.

The  $\pi$  acceptor properties of the cyclobis (paraquat-*p*-phenylene) manifest in the complexation and sensing of  $\pi$  donors such as hydroquinones [190]. The sensing properties of the cyclobis (paraquat-*p*-phenylene)-modified surface towards hydroquinone are shown in Figure 20.15. It should be noted that the sensitivity for hydroquinone sensing could be tuned, based on the number of layers of the



**Scheme 20.4.** Method for the construction of oligocation-crosslinked Au-nanoparticle multilayers by electrostatic interactions. The first nanoparticle layer is formed by the

interaction of a nanoparticle solution with an amine-functionalized surface. (Adapted from *Chem. Commun.*, **2000**, 1025).

host molecule anchored onto the substrate. The cavity produced by the cyclobis (paraquat-*p*-phenylene) is also suitable for other hydroquinone-based molecules such as dihydroxyphenyl acetic acid, dopamine and adrenaline. The specificity of the assemblies can be manipulated by using different molecular linkers. For example, a higher generation cyclophane, cyclobis (paraquat-*p*-biphenylene) will result in a host assembly for bishydroxymethylferrocene [191].

Guo and co-workers have synthesized trioctyl phosphine oxide (TOPO) stabilized iron nanoparticles by the microemulsion method with an average diameter of 3 nm [192]. The amorphous particles are known to effectively catalyze reactions such as the decomposition of H<sub>2</sub>O<sub>2</sub>. A specific advantage of this method is that the presence of O<sub>2</sub> does not hamper the electrocatalytic currents obtained for H<sub>2</sub>O<sub>2</sub>. Gold colloids capped with a mixed monolayer of alkylthiol and amidoferrocenyl-



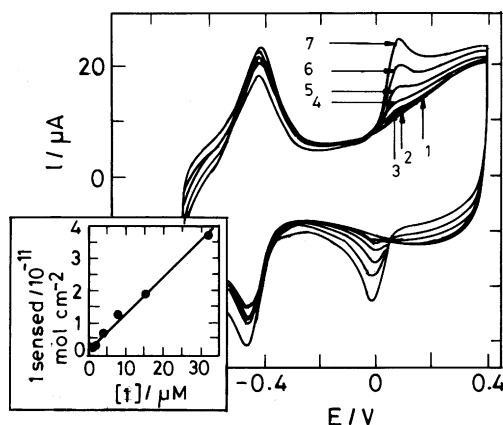


**Fig. 20.15.** Cyclic voltammograms of a layered bis-bipyridinium-Au-nanoparticle array (Five layers) in the absence of *p*-hydroquinone (curve 1) and in various concentrations of *p*-hydroquinone, (2)  $1 \times 10^{-6}$  M; (3)  $2 \times 10^{-6}$  M; (4)  $4 \times 10^{-6}$  M; (5)  $8 \times 10^{-6}$  M; (6)  $1.6 \times 10^{-5}$  M; (7)  $3.2 \times 10^{-5}$  M. Inset: Calibration curve corresponding to the electrochemical sensing of hydroquinone. All data were recorded under argon in 0.1 M phosphate buffer, pH 7.2, scan rate  $100 \text{ mV s}^{-1}$ . (Adapted from *J. Chem. Soc., Perkin Trans.*, **1999**, 1925).

alkylthiol are prepared using the Brust synthesis and the ligand place-exchange procedure [193]. In the solution phase, these mixed MPCs act as exo-receptors and can specifically sense oxo-anions such as  $\text{H}_2\text{PO}_4^-$  and  $\text{HSO}_4^-$  due to hydrogen bonding between the amide functionality and the anion. In the case of  $\text{H}_2\text{PO}_4^-$ , this manifests as a new wave in the cyclic voltammogram. The intensity of the wave increases at the expense of the initial  $\text{Fc}/\text{Fc}^+$  wave and completely replaces it once one equivalent of  $\text{H}_2\text{PO}_4^-$  is added, indicating the formation of a 1:1 complex between the amidoferrocenyl group and the oxo-anion. A progressive cathodic shift is observed with increasing concentration of  $\text{HSO}_4^-$ , rather than the appearance of a second wave. Here too, a 1:1 complex is formed though the association constant is smaller than for  $\text{H}_2\text{PO}_4^-$ . Other ions like  $\text{Cl}^-$ ,  $\text{Br}^-$ ,  $\text{NO}_3^-$  are not recognized by the MPC thus showing good selectivity. Israel and co workers [194a] reported on the affinity of metal ions towards gold nanoparticles modified with self-assembled monolayers containing acid end functionalities. The ion binding affinity is found to vary in the order  $\text{Fe}^{3+} > \text{Cu}^{2+} > \text{Zn}^{2+}$ . The ion gating or permselective properties of gold nanoparticles with self-assembled monolayers containing carboxylic acid functional groups have been reported for  $[\text{Ru}(\text{NH}_3)_6]^{3+/2+}$  and  $\text{Fe}(\text{CN})_6^{3-/4-}$  based on the solution pH and the analyte size [194b].

Nanoparticles have also been used successfully as amperometric gas sensors. Chiou and co-workers developed a dispersed catalyst gas-diffusion electrode for  $\text{SO}_2$  sensing [195]. Chloroauric acid is adsorbed on carbon black and subsequently reduced in a stream of hydrogen to obtain nanometer-sized particles. These are then shaped in the form of an electrode and used as a sensor. The electrochemical oxidation of  $\text{SO}_2$  gas is catalyzed by the nanoparticles with a fast response time. A

similar sensor based on the attachment of Au particles through a self-assembled monolayer has been developed by Li and co-workers [196]. Au nanoparticles are assembled on a Pt disk electrode using cysteine as a linker molecule. The presence of the nanoparticles increases the active surface area available for sensing and catalysis purposes.  $\text{SO}_2$  goes through a gas permeable membrane and comes into contact with the electrolyte. When NaOH is used as the electrolyte,  $\text{SO}_2$  dissolves in it, and, at a potential of 0.6 V, gives rise to an anodic reaction:  $\text{SO}_3^{2-} + 2\text{OH}^- - 2\text{e}^- \rightleftharpoons \text{SO}_4^{2-} + \text{H}_2\text{O}$ . This oxidation process is catalyzed by the Au nanoparticles. NaOH is found to give the best current response compared to other electrolytes with a minimum detectable concentration of 2.6 pM. Other gases such as CO, NO,  $\text{NH}_3$  and  $\text{CO}_2$  do not cause any interference. The same group also designed sensors for analytes such as  $\text{O}_2$  and CO based on a similar protocol [197, 198].

## 20.7

### Electrocatalysis

The use of nanoparticles for electrocatalysis has been well documented [40a, 199a–d]. Improving the performance of electrochemical energy devices has driven the research on the use of nanoparticles for catalyzing various redox reactions with the aim of using them in fuel cells. Since the literature on this topic is vast, we have attempted to summarize only the recent literature on the electrocatalysis of certain reactions. Excellent reviews on various aspects of electrocatalysis are already available [40a, 199a].

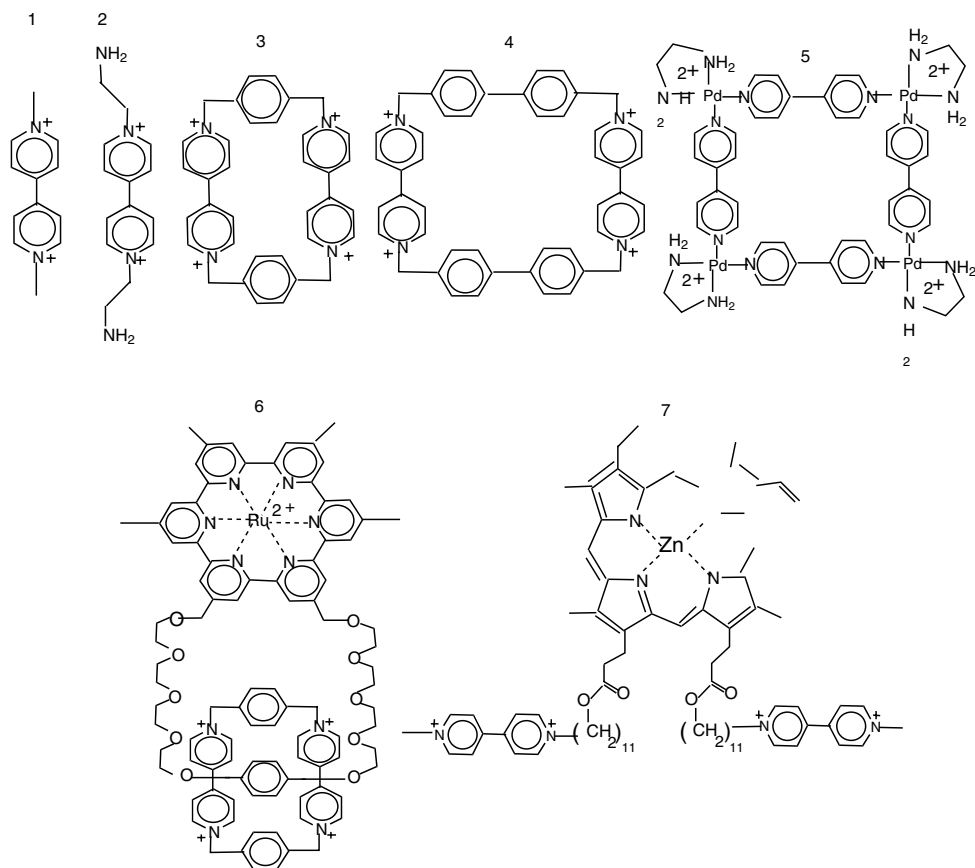
Nanometer-sized palladium islands on highly oriented pyrolytic graphite (HOPG) have been found to be very useful in catalyzing hydrogen electroadsorption and desorption and hydrazine oxidation [200]. The enhancement is related to the fractal nature of the metal island formed on HOPG. Polymer hosts such as Nafion have also been used for incorporating platinum nanoparticles to effect oxygen reduction electrocatalysis [201a]. Supriya and Sampath have prepared uniformly dispersed Au–Ag nanoalloy colloids in sol–gel-derived aminosilicate matrices and used them for oxygen reduction electrocatalysis [201b].

Platinised platinum electrodes have been used in electrocatalysis reactions for a long time [199b, 199c]. The effects of surface restructuring phenomena on the electrocatalysis are discussed in detail [202]. The catalytic surface is prepared by the electrodeposition of platinum nanoparticles on a planar platinum surface from 0.1 M chloroplatinic acid. An increase in the mean particle size of platinum is observed with aging by potential cycling, resulting in a decrease in the surface area and roughness. The consequences are observed in the oxygen coverage and activity of different electrodes. The strength of the Pt–O bond varies as the electrode is aged and hence the reactivity of adsorbed oxygen varies. The same authors also probed the desorption of hydrogen, oxygen and the oxidation of formic acid using Pt nanoparticles incorporated on gold electrodes [203]. The use of silver nanoparticles to enhance the redox activity of organosulfur compounds [204] and that of nanocrystalline platinum particles on the electrochemical oxidation of oxalic acid

[202, 203] has been recently reported. Gold nanoparticles electrodeposited on planar gold electrodes lead to a four-electron process for oxygen reduction in an acidic medium. The hydrodynamic voltammetric experiments do not show well-defined limiting waves; this may be due to a mixed control of diffusion and kinetic limitations [205].

Studies on the catalytic oxidation of CO and methanol are of great significance in several areas of research and technology [206]. The most commonly used catalysts for methanol oxidation belong to the Pt group. One disadvantage however, is that these catalysts tend to get poisoned by the CO-like species formed during the process. Zhong and co-workers have prepared faceted thiolate-capped Au–Pt alloy nanoparticles that possess the dual advantage of methanol oxidation at the Pt sites and CO oxidation at the Au sites [207]. The alloy particles are deposited on a GCE surface by the exchange-crosslinking-precipitation route and used for methanol oxidation [208]. The authors propose the involvement of gold oxide in the electrocatalytic process. In an earlier paper, the same group followed the electrocatalytic oxidation of CO using thiolate-capped gold particles [209]. Copper–palladium and silver–palladium alloy particles have also been explored as catalysts for methanol oxidation [210] in alkaline media. The alloying process causes deterioration in the performance of pure palladium clusters. Nanosized Pt–Pd particles have been synthesized and the electrocatalytic behaviour has been studied in order to understand the dissociative adsorption of methanol and formic acid [211]. Boron-doped diamond electrodes have recently come into prominence for a variety of applications including sensing, electrocatalysis and electrochemical decontamination [212, 213]. Platinum nanoparticles have been used to modify the boron-doped diamond electrodes [214] towards achieving electrocatalysis of methanol oxidation. The high dispersity inside the nano-honeycomb matrix and the high surface area of the nanoparticles leads to very good electrocatalytic activity. The electrocatalytic activities of nanosized platinum particles for methanol, formic acid and formaldehyde electrooxidation have been recently reported [215]. The sensitivity of the catalyst particles has been interpreted in terms of a ‘catalyst ensemble effect’ but the detailed microscopic behaviour is incomplete. Martin and co-workers [216] have demonstrated the incorporation of catalytic metal nanoparticles such as Pt, Ru and Pt/Ru into carbon nanotubes and further used them in the electrocatalysis of oxygen reduction, methanol electrooxidation and gas phase catalysis of hydrocarbons. A related work on the incorporation of platinum nanoparticles in carbon nanotubes has recently been reported to show promising electrocatalytic activity for oxygen reduction [217].

There have been many attempts to utilize nanosized materials for battery applications [218]. Nanosized alloys of Sn–Sb dispersed on carbon are found to be good anodes for lithium batteries [218b]. Though high reversible capacities have been reported for the alloy, there is considerable loss in subsequent cycles that is ascribed to the decomposition of surface oxide, formation of solid electrolyte interphase and aggregation of alloy particles during cycling. Dunn and co-workers [219] used nanosized ruthenium particles with carbon aerogels to develop supercapacitors having specific capacitances of the order of  $100 \text{ F g}^{-1}$ .



Scheme 20.5.



## 20.8

### Summary and Perspectives

The current efforts on electrochemistry with nanoparticles have been reviewed with a certain bias towards the contemporary areas of research namely, electrochemical charging, sensors and the use of spectroelectrochemical methods. There are many outstanding issues that require the attention of electrochemists in the years to come. Understanding the biological processes, bioassays and the stability of biomolecules under potential control is an area that is of immediate relevance. Mirkin and co-workers [10b] and Alivisatos and co-workers [9, 10a] have made significant contributions in the bioassembly of nanoparticles and their optical properties. The electrochemistry is still not well explored. Potential-dependent

SERS may lead to detection techniques and assays with good sensitivity and selectivity. The area of electrocatalysis is continuously expanding. It has great potential in the area of electrochemical energy systems, especially fuel cells and batteries. The fundamental questions on nucleation, electrocrystallization, faceting, energy dissipation in hot metals and redox potential of nanoparticles are some of the issues that will remain the focus of immediate research.

### Acknowledgement

The authors would like to acknowledge the immense help from Mr. Shaktivel in the preparation of the manuscript.

### References

- 1 M. FARADAY, *Philos. Trans. R. Soc.*, London, **1857**, 147, 145.
- 2 G. MIE, *Ann. Phys.*, **1908**, 25, 377.
- 3 *Handbook of Nanostructured Materials and Nanotechnology*, Vol. 1 Synthesis and Processing, ed. H. S. NALWA, Academic Press, New York 2000.
- 4 Nanoparticles and Nanostructured Films-Preparation, Characterisation and Applications, ed. J. H. FENDLER, Wiley-VCH, Weinheim 1998.
- 5 C. R. MARTIN, D. T. MITCHELL, *Electroanalytical Chemistry Series*, ed. A. J. BARD, I. RUBINSTEIN, Marcel Dekker, NY. **1999**. Vol. 21, p. 1.
- 6 (a) A. N. SHIPWAY, E. KATZ, I. WILLNER, *Chem. Phys. Chem.*, **2000**, 1, 18; (b) A. N. SHIPWAY, M. LAHAV, I. WILLNER, *Adv. Mater.*, **2000**, 12, 993; (c) A. N. SHIPWAY, I. WILLNER, *Chem. Commun.*, **2001**, 2035.
- 7 D. HERNANDEZ-SANTOS, M. B. GONZALEZ-GARCIA, A. COSTA-GARCIA, *Electroanalysis*, **2002**, 14, 1224.
- 8 D. E. CLIFFEL, J. F. HICKS, A. C. TEMPLETON et al., in *Metal Nanoparticles: Synthesis, Characterizations, and Applications*, eds. D. FELDHEIM, C. FOSS, Marcel Dekker, New York 2002, p. 297.
- 9 D. GERION, W. J. PARAK, S. C. WILLIAMS et al., *J. Am. Chem. Soc.*, **2002**, 124, 7070.
- 10 (a) A. P. ALIVISATOS, *Sci. Am.*, **2001**, 66, 285; (b) S. J. PARK, T. A. TATON, C. A. MIRKIN, *Science*, **2002**, 295, 1503.
- 11 P. MULVANEY, in *Nanoscale Materials in Chemistry*, ed. K. KLABUNDE, Wiley-VCH, Weinheim 2001, p. 121.
- 12 O. A. PETRII, G. A. TSIRLINA, *Russ. Chem. Rev.*, **2001**, 70, 285.
- 13 D. J. RILEY, *Curr. Opin. Colloid Surf. Sci.*, **2002**, 7, 186.
- 14 C. N. R. RAO, A. K. CHEETHAM, *J. Mater. Chem.*, **2001**, 11, 2887.
- 15 C. J. LOWETH, W. B. CALDWELL, X. PENG et al., *Angew. Chem. Int. Ed. Engl.*, **1999**, 38(12), 1808.
- 16 *Electrochemistry of Nanomaterials*, ed. G. HODES, Wiley-VCH, Weinheim 2000.
- 17 N. LI, C. R. MARTIN, B. SCROSATI, *J. Power Sources*, **2001**, 97–98, 240.
- 18 P. V. KAMAT, K. MURAKOSHI, Y. WADA et al., in *Handbook of Nanostructured Materials and Nanotechnology*, Vol. 3 Electrical Properties, ed. H. S. NALWA, Academic Press, New York 2000, p. 292.
- 19 O. I. MICIC, A. J. NOZIK, in *Handbook of Nanostructured Materials and Nanotechnology*, Vol. 3 Electrical Properties, ed. H. S. NALWA, Academic Press, New York 2000, p. 427.
- 20 M. GRAETZEL, in *Handbook of Nanostructured Materials and Nanotechnology*, Vol. 3 Electrical Properties, ed. H. S.

- NALWA, Academic Press, New York 2000, p. 527.
- 21 (a) S. J. GREEN, J. J. STOKES, M. J. HOSTETLER et al., *J. Phys. Chem. B*, **1997**, 101, 2663; (b) S. CHEN, R. W. MURRAY, *J. Phys. Chem. B*, **1999**, 103, 9996.
  - 22 (a) D. BETHELL, M. BRUST, D. J. SCHIFRIN et al., *J. Am. Chem. Soc.*, **1996**, 409, 137; (b) A. DORON, E. KATZ, I. WILLNER, *Langmuir*, **1995**, 11, 1313.
  - 23 (a) S. E. GILBERT, O. CAVALLERI, K. KERN, *J. Phys. Chem.*, **1996**, 100, 12123; (b) G. SANDMANN, H. DIETZ, W. PLIETH, *J. Electroanal. Chem.*, **2000**, 491, 78; (c) L. RODRIGUEZ-SANCHEZ, M. C. BLANCO, M. A. LOPEZ-QUINTELA, *J. Phys. Chem. B*, **2000**, 104, 9683; (d) Z. TANG, S. LIU, S. DONG et al., *J. Electroanal. Chem.*, **2000**, 502, 146.
  - 24 R. G. FREEMAN, K. C. GRABAR, K. J. ALLISON et al., *Science*, **1995**, 267, 1629.
  - 25 (a) D. S. MILLER, A. J. BARD, G. MCLENDON et al., *J. Am. Chem. Soc.*, **1981**, 103, 5536; (b) F.-R. F. FAN, A. J. BARD, *Science*, **1995**, 267, 871.
  - 26 M. LAHAV, V. HELEG-SHABATAI, J. WASSERMAN et al., *J. Am. Chem. Soc.*, **2000**, 122, 11480.
  - 27 G. CHUMANOV, K. SOKOLOV, B. W. GREGORY et al., *J. Phys. Chem.* **1995**, 99, 9466.
  - 28 R. BLONDER, I. SHEENEY, I. WILLNER, *Chem. Commun.*, **1998**, 1393.
  - 29 R. RIZZA, D. FITZMAURICE, S. HEARNE et al., *Chem. Mater.*, **1997**, 9, 2969.
  - 30 V. L. COLVIN, A. N. GOLDSTEIN, A. P. ALIVISATOS, *J. Am. Chem. Soc.*, **1992**, 114, 5221.
  - 31 (a) H. O. FINKLEA, in *Electroanalytical Chemistry*, Vol. 19, eds. A. J. BARD, I. RUBINSTEIN, Marcel Dekker, New York 1996, pp. 109–335; (b) D. V. LEFF, L. BRANDT, J. R. HEATH, *Langmuir*, **1996**, 12, 4723; (c) C. XU, L. SUN, L. J. KEPLEY et al., *Anal. Chem.*, **1993**, 65, 2102.
  - 32 (a) M. GIERSIG, P. MULVANEY, *J. Phys. Chem.*, **1993**, 97, 6334; (b) M. GIERSIG, P. MULVANEY, *Langmuir*, **1993**, 9, 3408; (c) T. TERANISHI, M. HOSOE, T. TANAKA et al., *J. Phys. Chem.*, **1999**, 103, 3818.
  - 33 S. BHARATHI, J. JOSEPH, O. LEV, *Electrochem. Solid-State Lett.*, **1999**, 2, 284.
  - 34 (a) M. D. MUSICK, D. J. PENA, S. L. BOTSKO et al., *Langmuir*, **1999**, 15, 844; (b) R. M. BRIGHT, M. D. MUSICK, M. J. NATAN, *Langmuir*, **1998**, 14, 5695.
  - 35 K. C. GRABAR, P. C. SMITH, M. D. MUSICK et al., *J. Am. Chem. Soc.*, **1996**, 118, 1148.
  - 36 V. PARDO-YISSAR, R. GABAI, T. BOURENKO et al., *Adv. Mater.*, **2001**, 13, 1320.
  - 37 C. DEMAILLE, M. BRUST, M. TSIONSKY et al., *Anal. Chem.*, **1997**, 69, 2323.
  - 38 Y. SHAO, M. V. MIRKIN, G. FISH et al., *Anal. Chem.*, **1997**, 69, 1627.
  - 39 (a) S. CHEN, *Langmuir*, **2001**, 17, 6664; (b) J. H. FENDLER, *Chem. Mater.*, **1996**, 8, 1616; (c) M. SASTRY, K. S. MAYYA, V. PATIL et al., *J. Phys. Chem. B*, **1997**, 101, 4954; (d) V. PATIL, M. SASTRY, *Langmuir*, **1998**, 14, 2707; (e) M. SASTRY, K. S. MAYYA, V. PATIL, *Langmuir*, **1998**, 14, 5921; (f) Y. TAIN, J. H. FENDLER, *Chem. Mater.*, **1996**, 8, 969; (g) S. PESCHEL, G. SCHMID, *Angew. Chem.*, **1995**, 107, 1568; (h) J. SCHMITT, G. DECHER, W. J. DRESSICK et al., *Adv. Mater.*, **1997**, 9, 61; (i) S. BHARATHI, N. FISHELSON, O. LEV, *Langmuir*, **1999**, 15, 1929; (j) T. A. TATON, C. A. MIRKIN, R. L. LETSINGER, *Science*, **2000**, 289, 1757; (k) P. ZHANG, P. S. KIM, T. K. SHAM, *Appl. Phys. Lett.*, **2003**, 82, 1470.
  - 40 (a) J. MCBREEN, S. MUKERJEE, in *Interfacial Electrochemistry*, ed. A. WIECKOWSKI, Marcel Dekker, New York 1999, p. 895; (b) G. GUNAWARDENA, G. HILLS, I. MONTENEGRO, *J. Electroanal. Chem.*, **1982**, 138, 241; (c) J. V. ZOVAL, P. R. BIERNACKI, R. M. PENNER, *Anal. Chem.*, **1996**, 68, 1585; (d) Z. CHEN, J. LI, E. WANG, *J. Electroanal. Chem.*, **1994**, 373, 83; (e) M. O. FINOT, G. D. BRAYBROOK, M. T. MCDERMOTT, *J. Electroanal. Chem.*, **1999**, 466, 234.
  - 41 (a) S. SAMPATH AND O. LEV, *J. Electroanal. Chem.*, **1997**, 426(1–2), 131; (b) M. J. HOSTETLER, C.-J. ZHONG, B. K. H. YEN et al., *J. Am. Chem. Soc.*, **1998**, 120, 9391; (c) S. W.

- HAN, Y. KIM, K. KIM, *J. Colloid Interface Sci.*, **1998**, 208, 272; (d) N. SANDHYARANI, T. PRADEEP, *Chem. Mater.*, **2000**, 12, 1755; (e) S. LINK, Z. L. WANG, M. A. EL-SAYED, *J. Phys. Chem. B*, **1999**, 103, 3529; (f) L. D'SOUZA, P. BERA, S. SAMPATH, *J. Colloid Interface Sci.*, **2002**, 246, 92; (g) N. TOSHIMA, M. HARADA, Y. YAMAZAKI et al., *J. Phys. Chem.*, **1992**, 96, 9927; (h) E. C. WALTER, M. P. ZACH, F. FAVIER et al., *Chemphyschem*, **2003**, 4, 131.
- 42 S. BHARATHI, M. NOGAMI, S. IKEDA, *Langmuir*, **2001**, 17, 1.
- 43 A. HENGLEIN, P. MULVANEY, A. HOLZWARTH et al., *Ber. Bunsen-Ges. Phys. Chem.*, **1992**, 96, 754.
- 44 P. MULVANEY, M. GIERSIG, A. HENGLEIN, *J. Phys. Chem.*, **1993**, 97, 7061.
- 45 A. HENGLEIN, *J. Phys. Chem.*, **1979**, 83, 2209.
- 46 A. HENGLEIN, P. MULVANEY, T. LINNERT et al., *J. Phys. Chem.*, **1992**, 96, 2411.
- 47 G. OLDFIELD, T. UNG, P. MULVANEY, *Adv. Mater.*, **2000**, 12, 1519.
- 48 S. M. PONDER, J. G. DARAB, J. BUCHER et al., *Chem. Mater.*, **2001**, 13, 479.
- 49 (a) M. PUMERA, J. WANG, E. GRUSHKA et al., *Anal. Chem.*, **2001**, 73, 5625; (b) G. A. ATTARD, A. AHMADI, D. J. JENKINS et al., *Chemphyschem*, **2003**, 4, 123.
- 50 M. BRUST, M. WALKER, D. BETHELL et al., *J. Chem. Soc., Chem. Commun.*, **1994**, 801.
- 51 (a) A. C. TEMPLETON, W. P. WUELFING, R. W. MURRAY, *Acc. Chem. Res.*, **2000**, 33, 27; (b) S. R. JOHNSON, S. D. EVANS, S. W. MAHON et al., *Langmuir*, **1997**, 13, 51; (c) A. C. TEMPLETON, M. J. HOSTETLER, C. T. KRAFT et al., *J. Am. Chem. Soc.*, **1998**, 120, 1906; (d) W. P. WUELFING, A. C. TEMPLETON, J. F. HICKS et al., *Anal. Chem.*, **1999**, 71, 4069; (e) M. J. HOSTETLER, A. C. TEMPLETON, R. W. MURRAY, *Langmuir*, **1999**, 15, 3782; (f) W. XU, W. LIU, D. ZHANG et al., *Colloids Surf. A*, **2002**, 204, 201; (g) H. FUJIHARA, H. NAKAI, *Langmuir*, **2001**, 17, 6393; (h) D. LI, J. LI, *Surf. Sci.*, **2003**, 522, 105.
- 52 M. J. HOSTETLER, S. J. GREEN, J. J. STOKES et al., *J. Am. Chem. Soc.*, **1996**, 118, 4212.
- 53 M. J. HOSTETLER, A. C. TEMPLETON, R. W. MURRAY, *Langmuir*, **1999**, 15, 3782.
- 54 M. J. HOSTETLER, J. J. STOKES, R. W. MURRAY, *Langmuir*, **1996**, 12, 3604.
- 55 R. S. INGRAM, M. J. HOSTETLER, R. W. MURRAY, *J. Am. Chem. Soc.*, **1997**, 119, 9175.
- 56 A. C. TEMPLETON, M. J. HOSTETLER, E. K. WARMOTH et al., *J. Am. Chem. Soc.*, **1998**, 120, 4845.
- 57 R. S. INGRAM, R. W. MURRAY, *Langmuir*, **1998**, 14, 4115.
- 58 S. CHEN, R. W. MURRAY, *Langmuir*, **1999**, 15, 682.
- 59 D. T. MILES, R. W. MURRAY, *Anal. Chem.*, **2001**, 73, 921.
- 60 J. J. PIETRON, R. W. MURRAY, *J. Phys. Chem. B*, **1999**, 103, 4440.
- 61 H. NAKAI, M. YOSHIHARA, H. FUJIHARA, *Langmuir*, **1999**, 15, 8574.
- 62 T. HORIKOSHI, M. ITOH, M. KURIHARA et al., *J. Electroanal. Chem.*, **1999**, 473, 113.
- 63 M. YAMADA, I. QUIROS, J. MIZUTANI et al., *Phys. Chem. Chem. Phys.*, **2001**, 3, 3337.
- 64 M. YAMADA, T. TADERA, K. KUBO et al., *Langmuir*, **2001**, 17, 2363.
- 65 S. CHEN, K. HUANG, *Langmuir*, **2000**, 16, 2014.
- 66 A. C. TEMPLETON, F. P. ZAMBORINI, W. P. WUELFING et al., *Langmuir*, **2000**, 16, 6682.
- 67 A. C. TEMPLETON, S. CHEN, S. M. GROSS et al., *Langmuir*, **1999**, 15, 66.
- 68 W. P. WUELFING, S. M. GROSS, D. T. MILES et al., *J. Am. Chem. Soc.*, **1998**, 120, 12696.
- 69 D. LEE, R. L. DONKERS, J. M. DESIMONE et al., *J. Am. Chem. Soc.*, **2003**, 125, 1182.
- 70 (a) R. H. TERRILL, T. A. POSTLETHWAITE, C.-H. CHEN et al., *J. Am. Chem. Soc.*, **1995**, 117, 12537; (b) W. P. WUELFING, R. W. MURRAY, *J. Phys. Chem. B*, **2002**, 106, 3139.
- 71 V. P. MENON, C. R. MARTIN, *Anal. Chem.*, **1995**, 67, 1920.
- 72 C. R. MARTIN, *Science*, **1994**, 266, 1961.

- 73 C. R. MARTIN, *Acc. Chem. Res.*, **1995**, 28, 61.
- 74 C. R. MARTIN, *Chem. Mater.*, **1996**, 8, 1739.
- 75 M. NISHIZAWA, V. P. MENON, C. R. MARTIN, *Science*, **1995**, 268, 700.
- 76 R. PARTHASARATHY, C. R. MARTIN, *Nature*, **1994**, 369, 298.
- 77 G. L. HORNYAK, C. J. PATRISSI, C. R. MARTIN, *J. Phys. Chem. B*, **1997**, 101, 1548.
- 78 G. CHE, B. B. LAKSHMI, C. R. MARTIN et al., *Chem. Mater.*, **1998**, 10, 260.
- 79 R. PARTHASARATHY, K. L. N. PHANI, C. R. MARTIN, *Adv. Mater.*, **1995**, 7, 896.
- 80 B. BRUNETTI, P. UGO, L. M. MORETTO et al., *J. Electroanal. Chem.*, **2000**, 491, 166.
- 81 C. SCHONENBERGER et al., *J. Phys. Chem. B*, **1997**, 101, 5497.
- 82 G. E. POSSIN, *Rev. Sci. Instrum.*, **1970**, 41, 772.
- 83 R. J. TONUCCI, B. L. JUSTUS, A. J. CAMPILLO et al., *Science*, **1992**, 258, 783.
- 84 J. M. SCHNUR, *Science*, **1993**, 262, 2669.
- 85 J. M. SCHNUR, R. SHASHIDHAR, *Adv. Mater.*, **1994**, 6, 971.
- 86 J. D. HARTGERINK, J. R. GRANJA, R. A. MILLIGAN et al., *J. Am. Chem. Soc.*, **1996**, 118, 43.
- 87 Z. QI, R. B. LENNOX, *Electrochem. Soc. Proc.*, **1997**, 97-5, 173.
- 88 J. S. BECK et al., *J. Am. Chem. Soc.*, **1992**, 114, 10834.
- 89 S. E. CREAGER, P. T. RADFORD, *J. Electroanal. Chem.*, **2001**, 500, 21.
- 90 R. M. PENNER, C. R. MARTIN, *Anal. Chem.*, **1987**, 59, 2625.
- 91 I. F. CHENG, L. D. WHITELEY, C. R. MARTIN, *Anal. Chem.*, **1989**, 61, 762.
- 92 J. C. HUTLEEN, V. P. MENON, C. R. MARTIN, *J. Chem. Soc., Faraday Trans.*, **1996**, 92, 4026.
- 93 K. B. JIRAGE, J. C. HUTLEEN, C. R. MARTIN, *Science*, **1997**, 278, 655.
- 94 J. C. HUTLEEN, K. B. JIRAGE, C. R. MARTIN, *J. Am. Chem. Soc.*, **1998**, 120, 6603.
- 95 S. B. LEE, C. R. MARTIN, *Anal. Chem.*, **2001**, 73, 768.
- 96 M.-S. KANG, C. R. MARTIN, *Langmuir*, **2001**, 17, 2753.
- 97 W. CHENG, S. DONG, E. WANG, *Anal. Chem.*, **2002**, 74, 3599.
- 98 W. CHENG, S. DONG, E. WANG, *Langmuir*, **2002**, 18, 9947.
- 99 (a) L. C. BROUSSEAU, III, S. M. MARINAKOS, J. P. NOVAK et al., *Cryst. Eng.*, **1998**, 1, 129; (b) R. P. ANDRES, T. BEIN, M. DOROGI et al., *Science*, **1996**, 272, 1323; (c) J. W. GERRITSEN, S. E. SHAFRANJUK, E. J. G. BOON et al., *Europhys. Lett.*, **1996**, 33, 279; (d) G. MARKOVICH, C. P. COLLIER, S. E. HENRICHS et al., *Acc. Chem. Res.*, **1999**, 32, 415; (e) R. L. WHETTEN, M. N. SHAFIGULLIN, J. T. KHOURY et al., *Acc. Chem. Res.*, **1999**, 32, 397; (f) A. C. TEMPLETON, W. P. WUELFING, R. W. MURRAY, *J. Am. Chem. Soc.*, **2000**, 33, 27.
- 100 X. WEAVER, X. GAO, *J. Phys. Chem.*, **1993**, 97, 332.
- 101 F. F.-R. FAN, A. J. BARD, *Science*, **1997**, 277, 1791.
- 102 R. S. INGRAM, M. J. HOSTETLER, R. W. MURRAY et al., *J. Am. Chem. Soc.*, **1997**, 119, 9279.
- 103 (a) A. E. HANNA, M. TINKHAM, *Phys. Rev. B.*, **1991**, 44, 5919; (b) M. AMMAN, R. WILKINS, E. BEN-JACOB et al., *Phys. Rev. B*, **1991**, 43, 1146.
- 104 P. MULVANEY, *Langmuir*, **1996**, 12, 788.
- 105 S. CHEN, R. S. INGRAM, M. J. HOSTETLER et al., *Science*, **1998**, 280, 2098.
- 106 S. J. GREEN, J. J. PIETRON, J. J. STOKES et al., *Langmuir*, **1998**, 14, 5612.
- 107 (a) J. F. HICKS, D. T. MILES, R. W. MURRAY, *J. Am. Chem. Soc.*, **2002**, 124, 13322; (b) V. L. JIMENEZ, M. C. LEOPOLD, C. MAZZITELLI et al., *Anal. Chem.*, **2003**, 75, 199.
- 108 J. F. HICKS, A. C. TEMPLETON, S. CHEN et al., *Anal. Chem.*, **1999**, 71, 3703.
- 109 S. CHEN, R. W. MURRAY, S. W. FELDBERG, *J. Phys. Chem. B*, **1998**, 102, 9898.
- 110 F. P. ZAMBORINI, J. F. HICKS, R. W. MURRAY, *J. Am. Chem. Soc.*, **2000**, 122, 4514.
- 111 J. F. HICKS, Y. SEOK-SHON, R. W. MURRAY, *Langmuir*, **2002**, 18, 2288.



- 112 S. CHEN, *J. Phys. Chem. B*, **2000**, *104*, 663.
- 113 S. CHEN, *J. Am. Chem. Soc.*, **2000**, *122*, 7420.
- 114 (a) S. CHEN, R. PEI, *J. Am. Chem. Soc.*, **2001**, *123*, 10607; (b) S. CHEN, F. DENG, *Langmuir*, **2002**, *18*, 8942.
- 115 S. D. JHAVERI, D. A. LOWY, E. E. FOOS et al., *Chem. Commun.*, **2002**, 1544.
- 116 F. P. ZAMBORINI, S. M. GROSS, R. W. MURRAY, *Langmuir*, **2001**, *17*, 481.
- 117 S. CHEN, K. HUANG, J. A. STEARENS, *Chem. Mater.*, **2000**, *12*, 540.
- 118 W. CHENG, S. DONG, E. WANG, *Electrochem. Commun.*, **2002**, *2*, 412.
- 119 S. CHEN, J. M. SOMMERS, *J. Phys. Chem. B*, **2001**, *105*, 8816.
- 120 J. J. PIETRON, J. F. HICKS, R. W. MURRAY, *J. Am. Chem. Soc.*, **1999**, *121*, 5565.
- 121 J. F. HICKS, F. P. ZAMBORINI, A. J. OSISEK et al., *J. Am. Chem. Soc.*, **2001**, *123*, 7048.
- 122 Y. Y. TONG, E. OLDFIELD, A. WIECKOWSKI, *Anal. Chem.*, **1998**, *518A*.
- 123 B. M. RUSH, J. A. RIEMER, E. J. CAIRNS, *J. Electrochem. Soc.*, **2001**, *148*, A137.
- 124 Y. Y. TONG, A. WIECKOWSKI, E. OLDFIELD, *J. Phys. Chem. B*, **2002**, *106*, 2434.
- 125 P. K. BABU, Y. Y. TONG, H. S. KIM et al., *J. Electroanal. Chem.*, **2002**, 524–525, 157.
- 126 Y. Y. TONG, E. OLDFIELD, A. WIECKOWSKI, *Electrochim. Acta*, **1998**, *43*, 2825.
- 127 Y. Y. TONG, C. RICE, N. GODBOUT et al., *J. Am. Chem. Soc.*, **1999**, *121*, 2996.
- 128 Y. Y. TONG, C. BELROSE, A. WIECKOWSKI et al., *J. Am. Chem. Soc.*, **1997**, *119*, 11709.
- 129 J. WU, J. B. DAY, K. FRANASZCZUK et al., *J. Chem. Soc., Faraday Trans.*, **1997**, *93*, 1017.
- 130 P. J. SLEZAK, A. WIECKOWSKI, *J. Magn. Res. A*, **1993**, *102*, 166.
- 131 M. S. YAHNKE, B. M. RUSH, J. A. REIMER et al., *J. Am. Chem. Soc.*, **1996**, *118*, 12250.
- 132 J. B. DAY, P.-A. VUISOZ, E. OLDFIELD et al., *J. Am. Chem. Soc.*, **1996**, *118*, 13046.
- 133 P.-A. VUISOZ, J.-P. ANSERMET, A. WIECKOWSKI, *Electrochim. Acta*, **1998**, *44*, 1397.
- 134 Y. Y. TONG, H. S. KIM, P. K. BABU et al., *J. Am. Chem. Soc.*, **2002**, *124*, 468.
- 135 P.-A. VUISOZ, J.-P. ANSERMET, A. WIECKOWSKI, *Electrochim. Acta*, **1998**, *44*, 1397.
- 136 P. SLEZAK, A. WIECKOWSKI, *J. Electroanal. Chem.*, **1992**, *339*, 401.
- 137 Y. Y. TONG, C. RICE, A. WIECKOWSKI et al., *J. Am. Chem. Soc.*, **2000**, *122*, 1123.
- 138 Y. Y. TONG, C. RICE, A. WIECKOWSKI et al., *J. Am. Chem. Soc.*, **2000**, *122*, 11921.
- 139 C. RICE, Y. Y. TONG, E. OLDFIELD et al., *J. Phys. Chem. B*, **2000**, *104*, 5803.
- 140 Y. Y. TONG, P. MERIAUDEAU, A. J. RENOUPREZ et al., *J. Phys. Chem. B*, **1997**, *101*, 10155.
- 141 Y. Y. TONG, E. OLDFIELD, A. WIECKOWSKI, *Faraday Discuss.*, **2002**, *121*, 323.
- 142 P.-A. VUISOZ, J.-P. ANSERMET, A. WIECKOWSKI, *Phys. Rev. Lett.*, **1999**, *83*, 2457.
- 143 C. P. SLICHTER, *Principles of Magnetic Resonance*, 3rd edition, Springer-Verlag, New York 1990, Vol. 135, p. 24.
- 144 (a) J. J. v. d. KLINK, J. BUTTET, *Phys. Rev. B*, **1984**, *29*, 6352; (b) J.-P. BUCHER, J. J. v. d. KLINK, *Phys. Rev. B*, **1988**, *38*, 11038; (c) J.-P. BUCHER, J. BUTTET, J. J. v. d. KLINK et al., *Surf. Sci.*, **1989**, *214*, 347.
- 145 B. S. ZELAKIEWICZ, G. C. LICA, Y. Y. TONG, 225th ACS Meeting, March 23–27, 2003.
- 146 T. UNG, M. GIERSIG, D. DUNSTAN et al., *Langmuir*, **1997**, *13*, 1773.
- 147 A. C. TEMPLETON, J. J. PIETRON, R. W. MURRAY, P. MULVANEY, *J. Phys. Chem. B*, **2000**, *104*, 564.
- 148 P. V. KAMAT, S. BARAZZOUK, S. HOTCHANDANI, *Angew. Chem. Int. Ed. Engl.*, **2002**, *41*, 2764.
- 149 V. SUBRAMANIAN, E. WOLF, P. V. KAMAT, *J. Phys. Chem. B*, **2001**, *105*, 11439.
- 150 (a) S. PARK, A. WASILESKI, M. J. WEAVER, *J. Phys. Chem. B*, **2001**, *105*,

- 9719; (b) S. PARK, M. J. WEAVER, *J. Phys. Chem. B*, **2002**, 106, 8667.
- 151 A. MIKI, S. YE, M. OSAWA, *Chem. Commun.*, **2002**, 1500.
  - 152 T. SAGARA, N. KATO, A. TOYOTO et al., *Langmuir*, **2002**, 18, 6995.
  - 153 T. BAUM, D. BETHELL, M. BRUST et al., *Langmuir*, **1999**, 15, 866.
  - 154 R. M. BRIGHT, D. G. WALTER, M. D. MUSICK et al., *Langmuir*, **1996**, 12, 810.
  - 155 A. L. CRUMBLISS et al., in *Proceedings of the Conference on Trends in Electrochemical Biosensors*, eds., G. COSTA, S. MIERTUS, World Scientific, Singapore, **1992**, pp. 43–58.
  - 156 J. ZHAO, R. W. HENKENS, J. STONEHUERNER et al., *J. Electroanal. Chem.*, **1992**, 327, 109.
  - 157 A. L. CRUMBLISS, S. C. PERINE, J. STONEHUERNER et al., *Biotech. Bioeng.*, **1992**, 40, 483.
  - 158 J. ZHAO, J. P. O'DALY, R. W. HENKENS et al., *Biosens. Bioelect.*, **1996**, 11, 493.
  - 159 M. S. CELEJ, G. RIVAS, *Electroanalysis*, **1998**, 10, 771.
  - 160 (a) K. R. BROWN, A. P. FOX, M. J. NATAN, *J. Am. Chem. Soc.*, **1996**, 118, 1154; (b) H. JU, S. LIU, B. GE et al., *Electroanalysis*, **2002**, 14, 141.
  - 161 S. LIU, J. YU, H. JU, *J. Electroanal. Chem.*, **2003**, 540, 61.
  - 162 I. G. CASELLA, A. DESTRADIS, E. DESIMONI, *Analyst*, **1996**, 121, 249.
  - 163 I. G. CASELLA, M. GATTA, M. R. GUASCITO et al., *Anal. Chem. Acta*, **1997**, 357, 63.
  - 164 F. PATOLSKY, T. GABRIEL, I. WILLNER, *J. Electroanal. Chem.*, **1999**, 479, 69.
  - 165 J. JIA, B. WANG, A. WU, G. CHENG et al., *Anal. Chem.*, **2002**, 74, 2217.
  - 166 S. BHARATHI, M. NOGAMI, O. LEV, *Langmuir*, **2001**, 17, 2602.
  - 167 Y. XIAO, H.-X. JU, H.-Y. CHEN, *Anal. Chim. Acta*, **1999**, 391, 73.
  - 168 Y. XIAO, H.-X. JU, H.-Y. CHEN, *Anal. Biochem.*, **2000**, 278, 22.
  - 169 (a) L. D'SOUZA, S. SAMPATH, *Langmuir*, **2000**, 16, 8510; (b) C. R. RAJ, T. OKAJIMA, T. OHSAKA, *J. Electroanal. Chem.*, **2003**, 543, 127.
  - 170 Y. LIU, F. YIN, L. YUMAI et al., *J. Colloid Interface Sci.*, **2003**, 258, 75.
  - 171 A. N. BOAL, V. M. ROTELLO, *J. Am. Chem. Soc.*, **1999**, 121, 4914.
  - 172 A. L. CRUMBLISS, J. STONEHUERNER, R. W. HENKENS et al., *Biosens. Bioelectron.*, **1993**, 8, 331.
  - 173 J.-H. KIM, J.-H. CHO, G. S. CHA et al., *Biosens. Bioelectron.*, **2000**, 14, 907.
  - 174 M. DEQUAIRE, C. DEGRAND, N. LIMOGES, *Anal. Chem.*, **2000**, 72, 5521.
  - 175 M. B. GONZALEZ GARCIA, A. COSTA-GARCIA, *Bioelectrochem. Bioenerg.*, **1995**, 38, 389.
  - 176 M. B. GONZALEZ GARCIA, C. FERNANDEZ-SANCHEZ, A. COSTA-GARCIA, *Biosens. Bioelectron.*, **2000**, 15, 315.
  - 177 H. LI, Q. WANG, J. XU et al., *Sens. Actuators B*, **2002**, 87, 18.
  - 178 L. AUTHIER, C. GROSSIORD, P. BROSSIER et al., *Anal. Chem.*, **2001**, 73, 4450.
  - 179 J. WANG, D. XU, A.-N. KAWDE et al., *Anal. Chem.*, **2001**, 73, 5576.
  - 180 J. WANG, Abstract of Papers, 225<sup>th</sup> ACS National Meeting, New Orleans, LA, USA. Mar. 23–27, **2003**.
  - 181 H. CAI, C. XU, P. HE et al., *J. Electroanal. Chem.*, **2001**, 510, 78.
  - 182 H. CAI, Y. WANG, P. HE et al., *Anal. Chim. Acta*, **2002**, 469, 165.
  - 183 J.-S. YE, A. OTTOVA, H. T. TIEN et al., *Bioelectrochemistry*, **2003**, 59(1–2), 65.
  - 184 X. HAN, W. CHENG, Z. ZHANG et al., *Biochim. Biophys. Acta-Bioenerg.*, **2002**, 273, 1556.
  - 185 A. N. SHIPWAY, M. LAHAV, R. BONDLER et al., *Chem. Mater.*, **1999**, 11, 13.
  - 186 M. LAHAV, A. N. SHIPWAY, I. WILLNER et al., *J. Electroanal. Chem.*, **2000**, 482, 217.
  - 187 M. LAHAV, R. GABAI, A. N. SHIPWAY et al., *Chem. Commun.*, **1999**, 1937.
  - 188 D. L. FELDHEIM, K. C. GRABAR, M. J. NATAN et al., *J. Am. Chem. Soc.*, **1996**, 118, 7640.
  - 189 A. KUMAR, A. B. MANDALE, M. SASTRY, *Langmuir*, **2000**, 16, 6921.
  - 190 M. LAHAV, A. N. SHIPWAY, I. WILLNER, *J. Chem. Soc., Perkin Trans. 2*, **1999**, 1925.
  - 191 A. N. SHIPWAY, M. LAHAV, I. WILLNER et al., *J. Electroanal. Chem.*, **2000**, 482, 217.
  - 192 L. GUO, Q. HUANG, X.-Y. LI et al., *Phys. Chem. Chem. Phys.*, **2001**, 3, 1661.

- 193 A. LABANDE, D. ASTRUC, *Chem. Commun.*, **2000**, 1007.
- 194 (a) L. B. ISRAEL, N. N. KARIUKI, L. HAN et al., *J. Electroanal. Chem.*, **2001**, 517, 69. (b) W. ZHENG, M. M. MAYE, F. L. LEIBOWITZ et al., *Anal. Chem.*, **2000**, 72, 2190.
- 195 C.-Y. CHIOU, T.-C. CHOU, *Electroanalysis*, **1996**, 8, 1179.
- 196 H. LI, Q. WANG, J. XU et al., *Sens. Actuators B*, **2002**, 87, 18.
- 197 H. LI, J. WEN, Q. CAI et al., *Analyst*, **2001**, 126, 1747.
- 198 G. SHI, M. LUO, J. XUE et al., *Fresenius' J. Anal. Chem.*, **2001**, 370, 878.
- 199 (a) J. O. M. BOCKRIS, S. U. M. KHAN, *Surface Electrochemistry*, Plenum Press, New York 1993; (b) A. M. FELTHAM, M. SPIRO, *Chem. Rev.*, **1971**, 71, 177; (c) K. KINOSHITA, in *Modern Aspects of Electrochemistry*, Vol. 14, eds. J. O. M. BOCKRIS, B. E. CONWAY, R. E. WHITE, Plenum Press, New York 1982, p. 557; (d) J. V. ZOVAL, J. LEE, S. GORER et al., *J. Phys. Chem. B*, **1998**, 102, 1166.
- 200 Y. GIMENO, A. H. CREUS, S. GONZALEZ et al., *Chem. Mater.*, **2001**, 13, 1857.
- 201 (a) O. ANTOINE, Y. BULTEL, R. DURAND, *J. Electroanal. Chem.*, **2001**, 499, 85; (b) D. SUPRIYA, S. SAMPATH, in preparation.
- 202 S. N. PRON'KIN, O. A. PETRII, G. A. TSIRLINA et al., *J. Electroanal. Chem.*, **2000**, 480, 112.
- 203 S. N. PRON'KIN, A. G. TSIRLINA, O. A. PETRII, S. Y. VASSILIEV, *Electrochim. Acta*, **2001**, 46, 2343.
- 204 J.-E. PARK, O. HATOZAKI, N. OYAMA, *Chem. Lett.*, **2003**, 32, 138.
- 205 M. S. EL-DEAB, T. OHSAKA, *Electrochim. Acta*, **2002**, 47, 4255.
- 206 (a) S. WASMUS, A. KUEVER, *J. Electroanal. Chem.*, **1999**, 461, 14; (b) T. D. JARVI, S. SRIRAMLU, E. M. STUVE, *J. Phys. Chem. B*, **1998**, 101, 3649.
- 207 Y. LOU, M. M. MAYE, L. HAN et al., *Chem. Commun.*, **2001**, 473.
- 208 F. L. LEIBOWITZ, W. X. ZHENG, M. M. MAYE et al., *Anal. Chem.*, **1999**, 71, 5076.
- 209 M. M. MAYE, Y. LOU, C.-J. ZHONG, *Langmuir*, **2000**, 16, 7520.
- 210 J. PRABHURAM, R. MANOHARAN, *J. Appl. Electrochem.*, **1998**, 28, 935.
- 211 J. S. GULLON, V. MONTLEL, A. ALDASZ et al., *Electrochem. Commun.*, **2002**, 4, 716.
- 212 T. N. RAO, A. FUJISHIMA, *Diamond Relat. Mater.*, **2000**, 9, 384.
- 213 G. M. SWAIN, *J. Electrochem. Soc.*, **1994**, 141, 3382.
- 214 K. HONDA, M. YOSHIMURA, T. N. RAO et al., *J. Electroanal. Chem.*, **2001**, 514, 35.
- 215 S. PARK, Y. XIE, M. J. WEAVER, *Langmuir*, **2002**, 18, 5792.
- 216 G. CHE, B. B. LAKSHMI, C. R. MARTIN et al., *Langmuir*, **1999**, 15, 750.
- 217 S. H. JOO, S. J. CHOL, I. OH et al., *Nature*, **2001**, 412, 169.
- 218 (a) K. GUO, Q. PAN, L. WANG et al., *J. Appl. Electrochem.*, **2002**, 32, 679; (b) H. LI, Q. WANG, L. SHI et al., *Chem. Mater.*, **2002**, 14, 103; (c) H. LI, L. SHI, W. LU et al., *J. Electrochem. Soc.*, **2001**, 148, 915; (d) H. LI, G. ZHU, X. HUANG et al., *J. Mater. Chem.*, **2000**, 10, 693.
- 219 (a) J. M. MILLER, B. DUNN, T. D. TRAN et al., *J. Electrochem. Soc.*, **1997**, 144, L309; (b) J. M. MILLER, B. DUNN, *Langmuir*, **1999**, 15, 799.

## 21

**Nanolithography and Nanomanipulation***A. K. Raychaudhuri***Abstract**

In this chapter we provide a brief review of different nanolithography and nanomanipulation techniques. We discuss mainly such techniques as templated growth, dip pen lithography, anodic oxidation and scanning probe microscope based nanomanipulation. The chapter contains an introduction to the basic techniques followed by examples of such nanostructure growth.

**21.1****Introduction**

The word lithography is generally used in the context of microelectronics where structures are defined in semiconductor wafers like Si or GaAs to make devices. Such a definition of lithography however refers to the top-down approach. In the context of fabrication of nanostructures one needs to broaden the definition of lithography to include bottom-up routes that are often employed to synthesize nanostructures or their arrays. In this route of lithography, the created pattern either directs the growth process or constrains the growth to within a nanometer or few tens of nanometers. Nanolithography also includes a mask for conventional dry or wet etching, as in conventional lithography albeit using novel routes. Nanomanipulation is intimately related to nanolithography. This is an enabling tool for assembly and manipulation of nanosized objects like nanoparticles, nanotubes and nanowires.

In the last five years the field of nanolithography has grown extensively and found innovative applications in the area of nanofabrication. The field of nanolithography starts where microlithography stops. It is important to have some acquaintance with the field of microlithography in order to appreciate the new field of nanolithography. I refer to a more recent reference to microlithography [1]. The scope of this chapter is limited and we will discuss only certain methods of nanolithography which use, directly or indirectly, chemical routes. We refer to some of the existing reviews for general aspects of nanofabrication [2, 3]. In this chapter we mainly include: (a) Templated growth and (b) Scanning probe microscopy (SPM)

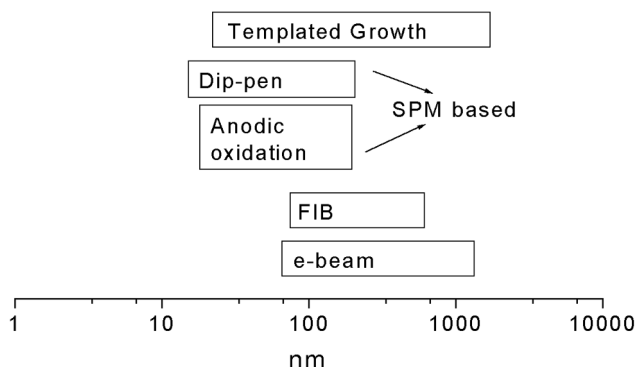


Fig. 21.1. Scope of nanolithography.

based lithography such as dip pen lithography and anodic oxidation. In Figure 21.1 we briefly sketch the scope of nanolithography. For comparison, we have included two techniques, electron beam lithography and focussed ion beam lithography (FIB), which are widely used lithography tools for features with sizes around 40–50 nm and greater. The type of nanolithography and nanomanipulation that has been discussed here has to effectively integrate with these two tools in order to enhance the capabilities of both classes of technique.

The chapter is arranged as follows. We first discuss the basics of each technique. This will be followed by some examples of nanostructures formed using these routes. We do not discuss physical measurements because this is outside the scope of the chapter. This is not an extensive review but it provides an overview of this rapidly expanding field.

To begin with it is best to place the field of nanolithography and its companion nanomanipulation in perspective. This is shown in Figure 21.2. Nanomanipulation, in principle, should also include “manipulation” using forces of self-assembly or other chemical forces and manipulations using optical tweezers. However, the word “nanomanipulation” is often used in a limited context where a SPM tip is used for manipulation of a nano-object. We stick to this definition, partly to reduce the scope of the review and partly because other manipulations are not in the area of expertise of the author.

A combination of optical and e-beam lithography provides a step down from the macroworld ( $\sim$ mm) to a length scale of tens to a hundred nanometers. Nanolithography fabricated objects in the sub 100 nm scale are then manipulated to make contact to electrodes created by an e-beam. Briefly, nanolithography and nanomanipulations not only make nanostructures but they enable us to make contact with existing lithographic tools so that one can make measurements or fabricate useful devices. This is illustrated in Figure 21.3, where we show the length scales that we encounter in different levels of lithography. A 100 nm gap has been created on a 500 nm wide line by e-beam lithography which acts as an electrode for nanoparticles and nanowires which can be placed in the gap using nanomanipulation. It can be seen that nanolithography and nanomanipulation are

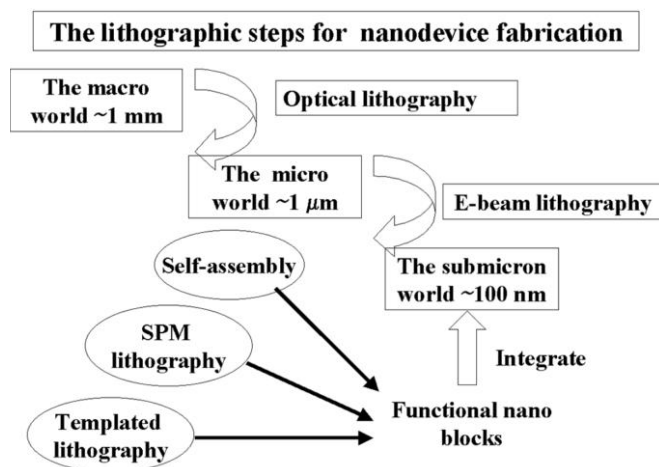


Fig. 21.2. A perspective of nanolithography and nanomanipulations.

the basic tools to provide the bridge to the world of optical and e-beam lithography which interfaces the world of macro-dimensions.

## 21.2

### Template Fabrication

One of the most popular and probably the cheapest method of nanolithography is to use nanometer size templates that can be used to fabricate nanowires. In some

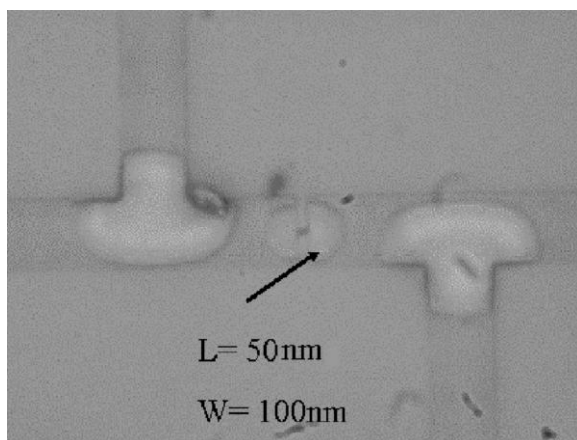


Fig. 21.3. Stepping down of length scales using optical and e-beam lithography to fabricate electrodes for accommodating nano-objects.

**Tab. 21.1.** Different types of membranes and templates that are used to grow nanowires.

Type of Membrane	Pore Diameter (nm)	Average Density ( $m^{-2}$ )
Etched ion track (polymer-mainly polycarbonates)	5–500	$10^{11}$ (random pores)
Etched mica	1–500	$10^{10}$ – $10^{11}$ (random pores)
Alumina	10–500	$10^{11}$ – $10^{13}$ (ordered pores)
Block copolymers	10–20	$10^{13}$ – $10^{14}$ (ordered pores)

cases this allows fabrication of arrays. This is a chemical route where the nanowires are actually grown by electrodeposition, the sol–gel technique or from the vapor phase. The advantage of this technique is that one can decouple the fabrication of nanowires and the templates and can have independent control of them. The templates used for synthesis are either anodized alumina membranes (AM) or etched track poly-carbonate or similar polymeric membranes (PM). There are other templates for such deposition, however AM and PM are the most popular. Ease of fabrication, handling and also commercial availability have made these membranes the mainstay of template growth. These templates can be procured from commercial suppliers and can also be tailor-made to a specific use. The templates contain cylindrical pores of diameter as small as 5–10 nm. In some cases the pores form an ordered hexagonal array and the packing density of the pores can be as large as  $10^{12}$ – $10^{13} m^{-2}$ . Table 21.1 lists different types of templates.

### 21.2.1

#### Polycarbonate Etched Track Templates

Etched track mica had been used for some time as a template for growth [4]. Etched tracks in PC (polycarbonate), PET (polyethylene terephthalate), PP (polypropylene), PVDF (polyvinylidene fluoride), PI (polyimide) are relatively new and are generally used for preparing high aspect ratio pores in free-standing membranes. These membranes, which are used as filters, are generally made from high purity polymer films which are exposed in a controlled way to high energy ( $>1$  MeV) charged particles in a nuclear reactor or in a high energy heavy ion accelerator. When high energy heavy ions of energy more than several hundreds of KeV move through an insulator the electronic energy loss (which predominates in this energy range over the nuclear loss) leads to latent track formation [5]. Such tracks can also be produced by using energetic  $\alpha$  particles in a nuclear reactor using the (n- $\alpha$ ) reaction. A schematic of track formation is shown in Figure 21.4.

During irradiation by swift ions, latent ion tracks are formed along the path of the ions. After irradiation, the material is subjected to chemical treatment leading to formation of the hollow channel from the latent ion track. The size and shape of the etched ion track is determined by the chemical processing. The etch process depends on the energy deposition density of the ion along its path, on the radiation

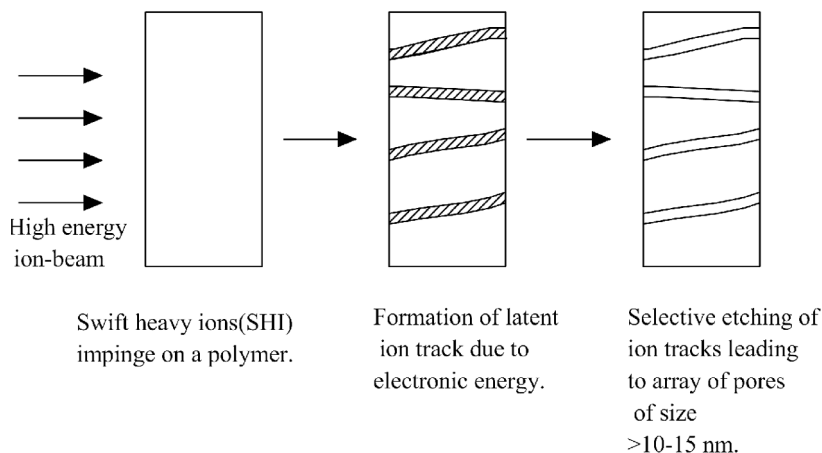


**Fig. 21.4.** Schematic of the process to produce etched ion tracks.

sensitivity of the material, on the storage conditions of the ion-irradiated material before etching, and on the etchant. The etching process is generally quantified by the *track etch ratio* which is the ratio between the track etch rate and the bulk etch rate. The optimum ion type seems to be Kr or Xe ions [6, 7] at specific energies up to about 20 MeV per nucleon.

If the material is stored in oxygen, oxidation of the radicals formed during the irradiation makes the latent ion track susceptible to selective track etching. Storing at temperatures close to the glass transition temperature of the polymer can enable it to rearrange on a molecular scale and may eventually anneal the ion track. Illumination, particularly UV radiation (300–400 nm) may lead to photooxidation which increases the track etch ratio by orders of magnitude. Soaking in weak solvents, such as dimethyl formamide or water-soluble gases [8] can sensitize ion tracks in certain polymers.

The requirement for use of these membranes as templates is to have high track etch ratios. For PC, track etch ratios above ten thousand have been observed. At the other extreme, addition of solvents, such as methanol, ethanol or propanol can dramatically decrease the track etch ratio, down to 2 to 4 in the case of PET. Although they accelerate the etching process, polymers like PMMA are generally etched with an acidic medium leading to very low etch track ratios  $\sim 1$ –10. In a recent study on the polymer polyallyl diglycol carbonate (PADG) [9] it was found that etch-rate values of the PADG increase nearly fourfold if the polymer is irradiated with 100 Mrad dose of electrons at 2 MeV prior to the heavy ion irradiation. The etch tracks were created by 140 MeV Si ions.

Generally the highest density of such pores in these polymers is  $\sim 10^9 \text{ cm}^{-2}$ . Commercially available membranes are etched polycarbonate or polyester of thickness typically in the range 10 to 30  $\mu\text{m}$  and with pore sizes down to 20 nm.



## 21.2.2

**Fabrication of Anodized Alumina Membrane**

A highly ordered structure of nanopores in alumina membranes is made generally by anodic oxidation of high purity (typically 5 N pure) aluminum foils. Typical pore sizes are in the range 15–100 nm and the pore density can be as high as  $10^{10}$ – $10^{11}$   $\text{cm}^{-2}$ . The highly reproducible nature of the alumina membrane makes it a very useful template for the formation of a number of different types of nanowire. The alumina membrane can be etched out after growth and this gives rise to free nanowires which can be used for a number of experiments and applications.

The growth of porous oxide on aluminum in various electrolytes under anodic bias has been studied for some time [10]. When aluminum is anodized in certain electrolytes, like phosphoric, sulfuric or oxalic acids, using a two-step process followed by etching, an array of close packed cells (pores) arranged in a near hexagonal pattern develops. Each cell contains a cylindrical pore and the axis of the cell is perpendicular to the surface.

The anodization process uses high purity Al foils. Before anodization the aluminum foil is de-greased with acetone or trichloroethylene for some time followed by a sodium carbonate wash at around 80 °C and vacuum annealed (typically  $10^{-3}$  Pa) at around 500 °C for a few hours. This is followed by an electrochemical polish in acidic solution (like perchloric acid and ethanol mixture or  $\text{H}_3\text{PO}_4$ ,  $\text{H}_2\text{SO}_4$  and  $\text{CrO}_3$  mixture). The anodization process is a two-step process as shown in Figure 21.5. In the first step the oxidation is carried out in 0.3 M–0.5 M acid medium at

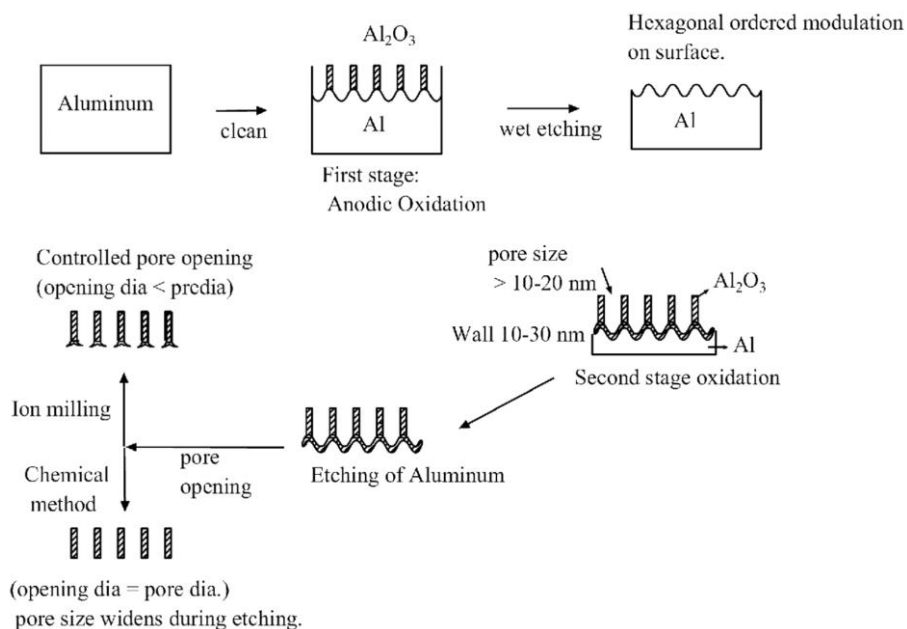


**Fig. 21.5.** Schematic of anodization for growth of alumina templates.

temperatures around 5–17 °C for 10 to 24 hours with applied voltage between 30 and 150 V. This leads to a layer of  $\text{Al}_2\text{O}_3$  on the Al foil. This alumina layer is then generally etched with a mixture of orthophosphoric acid and  $\text{H}_2\text{CrO}_4$  at around 50 to 60 °C for 10 to 12 hours (depending on the oxide thickness). The resulting aluminum has a hexagonal array surface structure. It is then oxidized again in a second step under the same conditions as before. The hexagonal structure that is left behind on the aluminum acts as the template for further growth of the oxide. This leads to typical circular tubes of alumina arranged in a hexagonal array and the bottom of the tube (where it terminates on the aluminum layer) closes on a barrier layer of  $\text{Al}_2\text{O}_3$  which has a U-shaped structure, as shown in Figure 21.5.

In the next step the Al layer at the bottom is generally removed with  $\text{HgCl}_2$ . This results in a honeycomb of porous alumina with one end closed by a U-tube type structure. The tube runs straight through the thickness of the membrane. The barrier layer at the bottom can be opened chemically or by using ion beams. Chemical methods of removing the bottom layer generally consist of an etch with  $\text{H}_3\text{PO}_4$ , the etching time generally depends on the thickness of the end  $\text{Al}_2\text{O}_3$ . It appears that if this etching is not performed properly it can lead to non-uniform end size. The chemical process of etching the barrier layer also leads to pore radius broadening. The removal of the bottom  $\text{Al}_2\text{O}_3$  and pore broadening is thus a crucial process.

Recently there has been a report of the use of  $\text{Ar}^+$  ion milling (500 eV) to open the bottom cap in the anodized alumina using a normal ion milling machine. The rate of milling can be controlled by the ion beam current density (generally  $\leq 1 \text{ mA cm}^{-2}$ ) and also the incident angle. The nominal milling rate is  $100 \text{ Å min}^{-1}$  at normal incidence for a current density of  $1 \text{ mA cm}^{-2}$  [12].

There are also reports of opening the barrier layer by anodic dissolution [13]. An applied voltage less than the anodic oxidation voltage ( $\sim 10\text{--}20 \text{ V}$ ) can lead to dissolution of the barrier oxide. For this to happen the dissolution rate has to be more than the anodic oxidation rate. This method is particularly suitable for cases where the alumina is being grown as a template on a substrate and the membrane is thin and supported by a substrate.

The applied bias can control the pore size as well as the pore separation. For growth voltages in the range 30–150 V the pore diameters are in the range 20–150 nm. Typical values are about  $1 \text{ nm V}^{-1}$  for the pore diameter and  $2.5\text{--}2.7 \text{ nm V}^{-1}$  for the cell spacing. The growth rate depends on the current density and also the temperature. Typical current density is in the range  $1\text{--}10 \text{ mA cm}^{-2}$ . The growth process is a result of two processes. The oxidation proceeds at the oxide metal interface and there is an electric field assisted chemical dissolution of oxide at the base of each pore. The growth rate is an equilibrium between these growth and dissolution processes.

A typical SEM picture of an AM is shown in Figure 21.6. In general one can get continuous pores over the complete thickness of the membrane. But occasionally one may get damaged pores.

Generally the AM films are composed of polycrystalline  $\gamma$ -alumina which is expected to have defects. The body of the membrane is more compact and crystalline

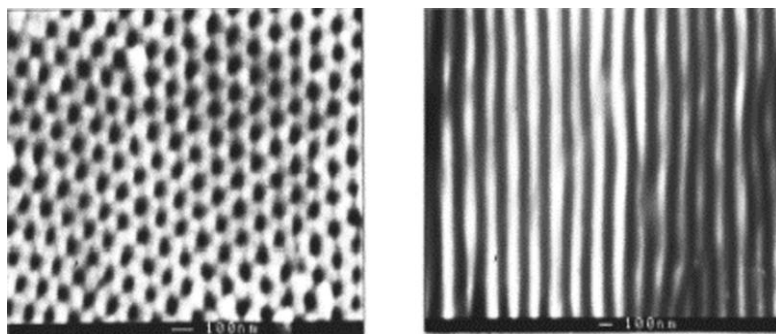


Fig. 21.6. Scanning electron microscopy image of an alumina template.

than the lining of the pore which is more amorphous. There are reports of photoluminescence (PL) from these grown templates in the frequency range 400–500 nm [14]. These seem to appear from the oxygen defects (charged) in the  $\text{Al}_2\text{O}_3$  and thus can be used as a probe to measure the defects in the grown layer. This becomes important when such templates are used for making PL or similar devices.

The two-stage anodization process for making the AM is necessary to produce a hexagonal pattern on the alumina for the oxidation in the second stage. In fact any patterning of the aluminum can act as a template for the oxidation and can produce the template. This has been shown by making a hexagonal array structure on aluminum film by nano-indentation [15]. It was shown that the anodization process leads to growth of hexagonal oxide tubes.

A recent application of the AM is to grow secondary templates of a polymer such as polyaniline. The nanopores have been filled with polyaniline nanowires [16] and even with carbon nanotubes (CNT) grown inside the pores [17]. The polyaniline was deposited by simply immersing the membrane in a solution of aniline and HCl. The aniline was then polymerized at room temperature following usual methods. The secondary templates, such as aligned CNTs, were generated in the alumina nanotubes by the catalytic pyrolysis of acetylene. These secondary templates, which have pores of much smaller diameter, are then used to grow new materials. The desired material, such as metal nanowires can be introduced into the aligned carbon nanotubes by methods such as electrodeposition. This leads to nanowires with a core structure, such as a Ni wire in a carbon nanotube.

### 21.2.3

#### Anodized Alumina Membrane as a Mask for Physical Vapor Deposition

A very important recent application is to use aluminized membranes as a mask for physical vapor deposition. In these cases the membrane is either attached to the substrate or a film of aluminum (typically a few microns thick) is grown on a substrate such as Si. This is followed by the anodic oxidation process to convert the aluminum film to an anodized template. The growth process is either physical

vapor deposition or CVD or the membrane is used for reactive ion etching to transfer the mask to the substrate. In this case the simple alumina mask acts as a simple nanometer level lithography mask.

Highly ordered arrays of quantum dots of GaAs and InGaAs with narrow dot-size distribution, have been grown on GaAs substrates using AM templates. This method can grow dots for latticed-matched systems as well as strained heterostructures [18]. The templates are prepared by the two-step anodic oxidation described previously. A lift-off process is used to separate thin templates from the aluminum substrates by etching away the unoxidized aluminum foil in a saturated  $\text{HgCl}_2$  solution. An etch with  $\text{H}_3\text{PO}_4$  was used to remove the oxide barrier at the end as well as to widen the pores to around 80 nm. The templates were bonded directly onto the GaAs substrate using van der Waals bonding. These ordered nanopores were then used directly as a mask for epitaxial growth of Q-dots by the standard MBE method. Q-dots with diameter as low as 20 nm were obtained.

60 nm size magnetic Fe nanodots were fabricated by e-beam evaporation over a  $1 \text{ cm}^2$  area of MgO substrate using an alumina membrane (thickness 300 nm, pore density  $10^{12} \text{ m}^{-2}$ ) as a shadow mask on a MgO substrate [19]. The membrane was subsequently removed in a 10% NaOH solution.

An alumina membrane mask has been used to generate a 100 nm period hexagonal pattern on Si by using  $\text{SF}_6$  reactive ion etching [20]. This also adjusted the hole diameter to around 60 nm. This mask was then used for ion etching. After the pattern formation the mask was etched out with  $\text{H}_2\text{SO}_4$  and  $\text{H}_2\text{O}_2$  (1:1) solution.

Bi nanowires have been grown from direct vapor into AM templates with diameters in the range 7 to 200 nm and their galvanomagnetic properties were studied [21]. The grown wires were single crystals. The method of growth is rather simple, the membrane is placed at the mouth of a crucible, which is kept in vacuum and contains molten Bi.

#### 21.2.4

##### Templates Made in Block Copolymers

Spontaneous pattern formation in diblock copolymers has been used to produce a high density ( $\sim 10^{13} \text{ m}^{-2}$ ) of uniform pores with diameter ( $\sim 10\text{--}30 \text{ nm}$ ) as wide area templates for deposition or synthesis of nanowires, nanoparticles or even a mask for ion milling or reactive ion etching (RIE) [22, 23]. In diblock copolymers different chains or blocks of polymers are covalently bonded. However, incompatibility between two blocks leads to spontaneous self-assembly when they are heated above the glass transition temperature of both. The self-assembled structures consist of separated monomers or segmented polymers. These patterns can exhibit highly ordered morphology and the pattern of the minority phase in the matrix of a majority phase can range from spherical to cylindrical or lamella. Template formation by the block copolymer route has certain advantages over the alumina templates. It is easier to achieve a large density, close to  $10^{13}\text{--}10^{14} \text{ m}^{-2}$  which in the case of the AM is around  $10^{12} \text{ m}^{-2}$  in most cases. Also AM is a two-step oxidation process whereas this is more or less a single-step process. A lower pore size ( $\sim 10 \text{ nm}$ ) is achievable. In the case of AM the process of opening up the oxide

barrier at the end of the oxidized membrane leads to increase in the pore size. However, in materials fabrication where the processing temperatures go beyond 150 °C to 170 °C these templates become unusable. In the case of AM a much higher processing temperature (~500 °C) is possible. This is a particular necessity where complex functional materials are synthesized in the templates.

Typical copolymer blends are PS (polystyrene)–PMMA (polymethylmethacrylate), PS–PB (polybutadiene) and PS–PI (polyisoprene). Generally the PS is the majority phase that makes the matrix and the other polymer is the minority phase which forms the ordered structure. The majority PS phase generally has a large molecular weight compared to the minority phase. The pattern formed depends on the relative chain lengths and the segmental interactions. As an example [22] the PS–PB block copolymers produce hexagonally ordered PB cylinders in a PS matrix, while in PS–PI one obtains spheres of PI. A schematic of the templates produced in block copolymers is shown in Figure 21.7.

For templates and etching masks that use a spherical particle one may restrict the film thickness to around the diameter of the particle (monolayer) to get ordered structures. In the PS–PMMA system one can obtain aligned cylinders of PMMA in PS if an electric field is applied during the curing process as shown in Figure 21.7. In this case one can get templates with sizes of the order of a micron.

Generally the block copolymer is spin-coated onto the substrate on which the pattern has to be grown or transferred. Some times the wetting of the substrate by the constituent homopolymer components can be controlled by a layer (~5 nm) of neutral brush layer of hydroxy-terminated random copolymer of the same constituents [24]. For instance PS homopolymer de-wets random copolymer surfaces of PS–PMMA with styrene fractions ( $f$ ) less than 0.65 while the PMMA de-wets for  $f > 0.5$ . Tuning the interfacial energy can thus control the orientation of the microphase-separated structures obtained from a diblock copolymer. The curing, lasting for a few hours to a day, is carried out at a temperature above the glass transition temperature  $T_g$  of both polymers. This leads to the formation of the separated phase. The etching of the pattern generally involves a chemical treatment that either stabilizes the matrix polymer or the separated phases against chemical or dry etching. As an example, with UV exposure and sonication in glacial acetic acid and deionized water the PMMS phase is degraded and can be removed [25]. Similarly ozonization attacks the carbon double bond in PB which thus can be degraded for preferential etching.

### 21.3

#### Fabrication of Nanostructures in the Templates

Making templates of ordered nanopores is the starting point for template based nanolithography. The next step involves “filling the pores” of the membrane with different materials of interest using one or more available methods. The methods include electrochemical deposition (ED), vapor phase deposition such as chemical vapor deposition (CVD), pressure injection of molten metals and sol–gel methods. In this section we describe some of the methods of deposition in the nanopores.

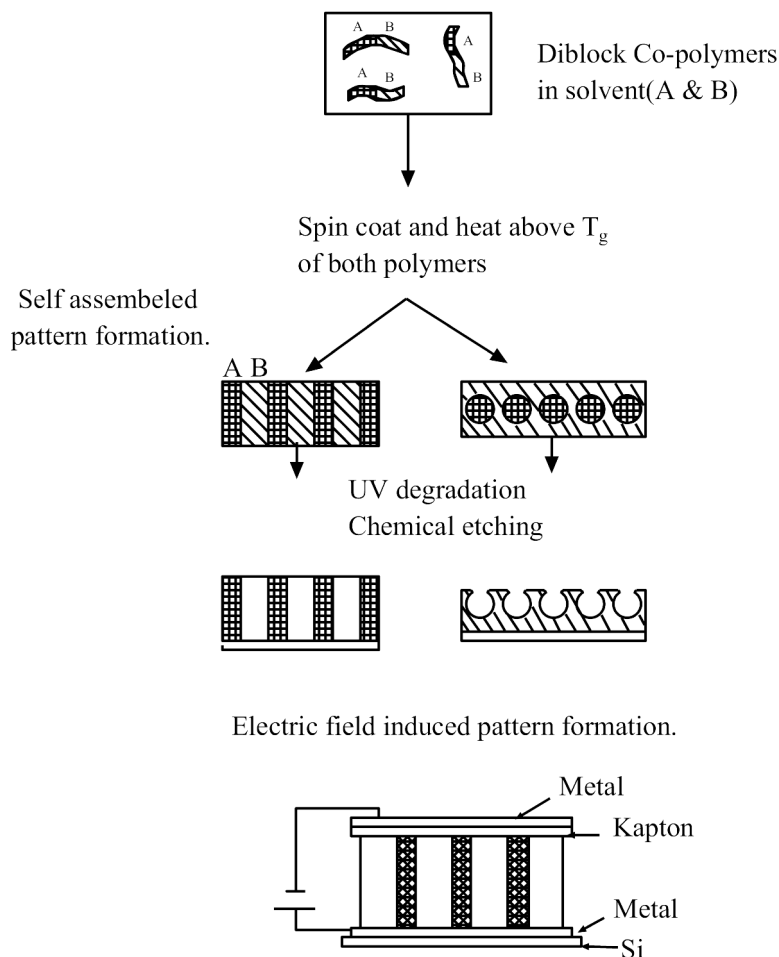


**Fig. 21.7.** Pattern formation in block-copolymers.

The chemical routes that are followed depend on the material to be deposited. In the case of metals or oxides that can be made easily by oxidizing the metal, the most popular route is electrochemical deposition. For more complex materials like functional oxides a sol-gel method is often used. For materials like GaN or carbon nanotubes the preferred method is CVD. In the subsequent subsections we give some details of the methods with examples.

### 21.3.1

#### Electrodeposition

Electrodeposition of metal inside the nanopores of a membrane is generally performed in baths containing metal salts. The baths are either acidic or basic and use

a three-terminal potentiostat. The art and science of electrodeposition of metals is well developed and well researched. The deposition of nanowires in the porous membranes can thus depend on the knowledge base available for the deposition process. However, the new feature that needs to be taken into consideration is the high aspect ratio holes through which the deposition has to take place. Such issues as the thermal diffusion of the ions from the opening of the pore to the interface of the deposition become important.

Generally for ED one needs a cathode where the metal is deposited. For this, generally, one end of the porous membrane is metallized with Au or Ag to a thickness of 500 nm or more by sputtering or evaporation. Often a thinner (20 nm) Ti layer is deposited prior to Au or Ag deposition. With the metallized membrane as the cathode (the working electrode), the counter electrode (anode) is graphite or Pt and Ag\AgCl or calomel forms the reference electrode. The deposition can be DC or pulsed deposition. The deposition conditions are varied to produce single crystalline or polycrystalline nanowires. One of the interesting aspect of ED is the deposition of metallic bilayers or multilayer structures from the same bath by changing the bias and adjusting the relative concentration of the two ions. For instance, multilayers of two metals are often deposited from the same bath by keeping the concentration of the more noble metal (that needs less bias for deposition) very low. At high bias, which is needed to grow the less noble metal, the deposition of the more noble metal becomes diffusion limited due to its low concentration. A schematic of the pore filling and electrodeposition of metals in the pores is shown in Figure 21.8.

One of the earliest studies of Au nanowire (diameter 8 nm) fabricated by electrodeposition in a 5  $\mu\text{m}$  thick etched track mica was reported in 1986 [26]. Effect of weak-localization and electron–electron interaction was studied down to 0.3 K. However, in the last decade especially in the last 5 years the field of electrodeposited nanowires in templates has been intensively investigated [27]. The application of such metallic nanowires in magnetism has been reviewed [28].

Co and Cu multilayer wire (40 nm diameter) has been grown in track etched polycarbonate membrane from a Co and Cu sulfate acidic bath using different voltage pulses [29]. The bath compositions were 1 mM of  $\text{CuSO}_4 \cdot 5\text{H}_2\text{O}$  and 0.5 M  $\text{CoSO}_4 \cdot 7\text{H}_2\text{O}$ . A voltage pulse of  $V_{\text{Cu}} \approx -0.2$  V was used for Cu and a pulse of  $V_{\text{Co}} \approx -0.9$  V was used to deposit Co. Evaporated Cu on one side of the membrane acted as the cathode for growth. These multilayer nanowires were investigated for their giant magnetoresistance (GMR) properties. Around 15% magnetoresistance (MR) was observed at room temperatures in a field of about 0.4 T. Multilayer nanowires of Cu and Co as well as alloy multilayer ((Ni–Fe)/Cu) nanowires have been grown in 6  $\mu\text{m}$  thick polycarbonate membranes using an acidic sulfate bath (using  $\sim 0.1$  M boric acid  $\text{H}_3\text{BO}_3$  as one of the components) [30]. In this pulsed deposition the Cu deposition was carried out with  $V_{\text{Cu}} \approx -0.3$ – $-0.5$  V while  $V_{\text{Co}} \approx -1$  V and  $V_{\text{NiFe}} \approx -1.3$  V. An evaporated layer of Au on the membrane was used as the cathode. Co/Cu multilayer nanowires have been deposited in a 60  $\mu\text{m}$ , 30 nm pore polymer membrane (with 0.3  $\mu\text{m}$  sputtered Cu as cathode) using an acidic single sulfate bath [31]. The multilayers (with 5 nm Co and 2 nm Cu) showed a

## Pore filling by electrodeposition.

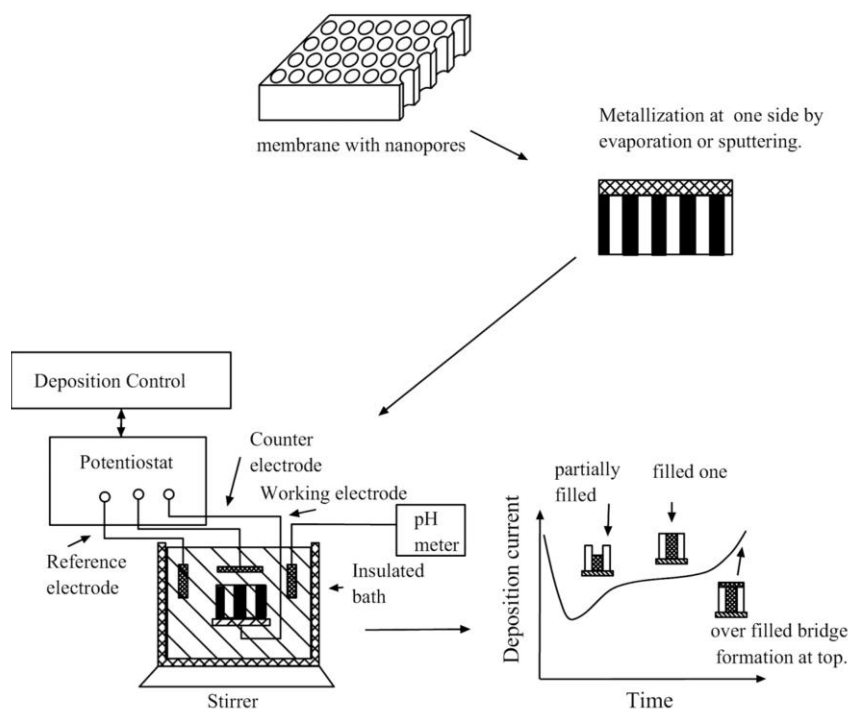


Fig. 21.8. Schematic of the electrodeposition process.

large perpendicular MR of 22% at 4.2 K and 11% at room temperature, in a field of 0.5 T. An interesting class of magnetic tunnel junction nanowires based on Ni/NiO/Co multilayers was made by a combination of electrodeposition and oxidation (to make NiO) [32]. There are very recent studies on magnetic shape anisotropy on nanowires of Co/Ag multilayer grown in 20  $\mu\text{m}$ , 120 nm pore polycarbonate membranes using a nearly neutral bath ( $\text{pH} \approx 7$ ). The bath had 0.15 M  $\text{CoSO}_4$ , 0.36 M  $\text{K}_4\text{P}_2\text{O}_7$  and 0.6 mM  $\text{AgCN}$ . 0.5  $\mu\text{m}$  sputtered Ag with a 20 nm Ti adhesion layer was used as the cathode [33].

There are a number of reports of the growth of good quality elemental nanowires in templates using ED techniques. They include Bi wires [21, 34] for positive GMR properties, an array of membrane-synthesized Ni [35] and Co [36] for magnetic recording applications and single crystalline Pb nanowires [37] for studying superconductivity in constrained systems. Bi wires are generally grown from an acidic bath ( $\text{pH} \approx 3$ ) consisting of 0.15 M  $\text{BiCl}_3$ , 0.3 M tartaric acid and glycerol. Bi wire shows giant positive MR which for the perpendicular geometry can be as high as 600–800% at 4.2 K (field perpendicular to wire) and 200% for the parallel geometry. 30 nm Pb wires are grown from 1 M Pb sulfamate using pulsed deposi-



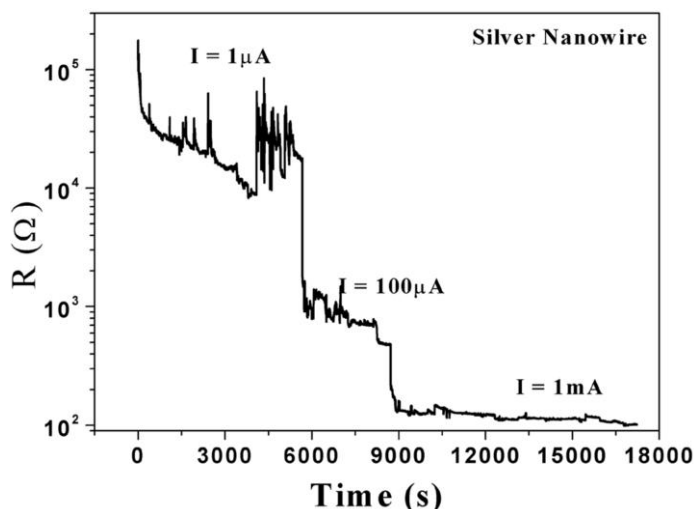


Fig. 21.9. Current induced changes in metallic silver nanowires made by template synthesis.

tion in a polycarbonate membrane. The pulsing condition determines whether the grown wire is single crystalline or polycrystalline. Single crystal nanowires have a superconducting  $T_c \approx 7.4$  K close to the bulk value while the polycrystalline nanowire with the same dimension has a  $T_c \approx 5.8$  K.

The nanowires grown in these templates are often not stable initially and it appears that there is significant current driven change in the resistance as current is passed through them [38]. The resistance changes also do not occur smoothly but by steps and jumps. This is shown in Figure 21.9. This is very similar to electromigration (em) phenomena that one sees in metal films when a high current is passed through them. The difference, however, is that in metal films em leads to mass transport, which leads to failure of the films, but in nanowires this actually reduces the resistance and is like a recovery process.

In recent years there have been reports of photoluminescence (PL) studies on metal oxide nanowires of  $\text{In}_2\text{O}_3$  [39] and  $\text{ZnO}$  [40].  $\text{In}_2\text{O}_3$  nanowires of 40–90 nm diameter were grown on alumina templates using a DC deposition ( $V_{\text{In}} = -1$  V) from a bath of  $\text{InCl}_3$  (38 mM) and  $\text{Na}_3\text{C}_6\text{H}_5\text{O}_7 \cdot 2\text{H}_2\text{O}$  (85 mM). The  $\text{In}_2\text{O}_3$  was made by oxidizing In wires at 100 K in oxygen and they showed a PL band at  $\sim 425$  nm.

An ordered array of  $\text{ZnO}$  nanowires on alumina membranes was prepared by oxidizing electrodeposited Zn nanowires in air at 300 °C. The electrodeposition was carried out from an acidic bath of  $\text{ZnSO}_4 \cdot 7\text{H}_2\text{O}$  (0.3 M Boric acid and 0.28 M  $\text{ZnSO}_4 \cdot 7\text{H}_2\text{O}$ ). The grown nanowires showed PL at  $\sim 55$  nm.

10 nm CdS Q-dots have been deposited in alumina membranes [41] by electrolyzing the membrane with  $\text{H}_2\text{SO}_4$  and then dipping it in boiling  $\text{CdSO}_4$ . The acid treatments leave S ions on the templates. The  $\text{Cd}^{2+}$  ions react with the S ions to form CdS in the nanopores. The array of Q-dots shows Raman lines that are red

shifted from the bulk. This is explained as arising due to confinement of the phonon modes.

### 21.3.2

#### Sol–Gel Method

The sol–gel method is a low temperature synthesis route for complex oxides [42]. It can be used to make complex functional oxide nanowires inside the pores of templates. In addition to the sol–gel method precursor-based solution deposition routes can also be used for nanostructure formation [43]. In both cases a post-deposition high temperature anneal ( $>500\text{--}600\text{ }^{\circ}\text{C}$ ) is needed to form the required stoichiometric phase. Due to the requirement of a high temperature anneal, alumina templates are used as the polycarbonate membranes decompose at a much lower temperature. For chemical solution deposition the membrane is dipped directly into the precursor solution. For sol–gel growth generally the required sol is prepared and the template is put into the sol for a required period (e.g. 0.5–1 h). After removing the membrane from the sol it is dried and then annealed at higher temperature before the required phase is formed. A schematic of the sol–gel route is shown in Figure 21.10.

An example of the formation of colossal magnetoresistive manganite nanowires is the formation of  $\text{La}_{0.7}\text{Ca}_{0.3}\text{MnO}_3$  (LCMO) in alumina templates [44]. These materials possess perovskite structure and the cell volumes are generally larger than those of metals and semiconductors. Hence it is comparatively difficult to structure them in the nanocrystalline form. Moreover, achieving the right stoichiometry of these multicomponent oxides at the nano-level is also a challenging task. The sol–gel technique is a powerful approach for preparing multicomponent inorganic materials as it is possible to precisely control the molecular microstructure, stoichiometry, high purity, and all at relatively low processing temperatures.

The sol used in the fabrication of LCMO nanowires was prepared by dissolving a stoichiometric ratio of lanthanum, calcium and manganese nitrates in an equal amount of water and adding ethylene glycol. The mixture was then heated on a hot plate till a sol of desired viscosity formed. Nanowires were fabricated by immersing the AM in the sol for 30–60 min and then heating to higher temperatures after wiping both surfaces clean. The membranes heated at different temperatures were subjected to XRD analysis to check the phase formation. Heating the membranes at  $700\text{ }^{\circ}\text{C}$  was sufficient to get the desired phase. Scanning electron microscopy was carried out on the nanowires embedded within the alumina membrane, both on the top surface and along the cross-section. The membranes were dissolved by immersing in 2 M NaOH for 30 min. The solution was then rinsed in triple distilled water several times before dispersing on the carbon grid to carry out transmission electron microscopy or on a metal substrate for SEM. An SEM of such a wire fabricated in AM is shown in Figure 21.11. In this case a metal was attached to the template before the sol–gel growth. The nanowires grow in an aligned fashion and retain their structure even after the template is etched away.

## Pore filling by Sol-Gel technique and oxide nanowire formation.

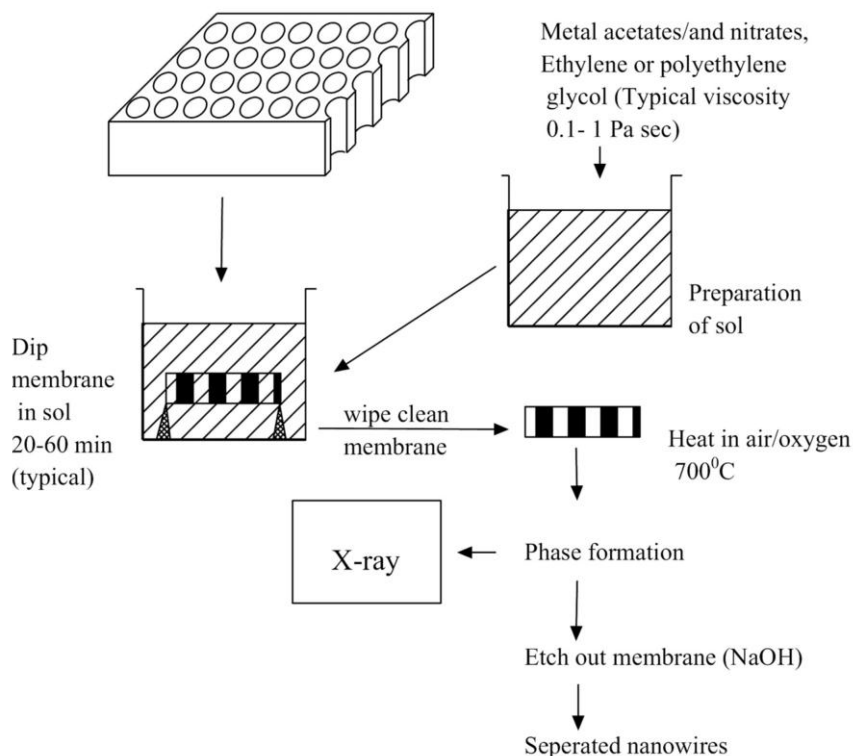


Fig. 21.10. The sol-gel route to the formation of oxide nanowires in templates.

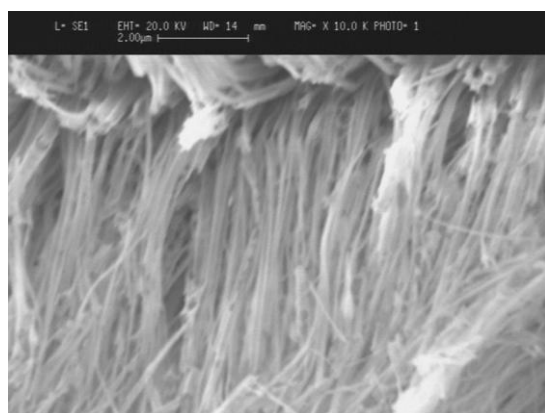


Fig. 21.11. SEM of nanowires of  $\text{La}_{0.7}\text{Ca}_{0.3}\text{MnO}_3$  (LCMO) grown by the sol-gel method in alumina templates.

Nanowires of  $\text{TiO}_2$  have been fabricated in nanoporous alumina membranes by sol-gel and other chemical methods.  $\text{TiO}_2$  nanotubes in AM have been prepared by the sol-gel method [45]. The sol-gel method has been used to fabricate highly ordered single crystalline anatase phase  $\text{TiO}_2$  nanowire arrays in anodic alumina membranes [46]. The wires have an average uniform diameter of around 60 nm and length 25  $\mu\text{m}$ . These wires have broad band visible PL at about 425, 465, and 525 nm that is attributed to self-trapped excitons, and oxygen defect centers. The  $\text{TiO}_2$  nanowires were fabricated using  $\text{TiO}_2$  sol made from alkoxide solution prepared by mixing tetrabutyl titanate, ethanol and  $\text{CH}_3\text{COOH}$ . The templates were immersed in the sol. The template was then allowed to dry at somewhat elevated temperature for the sol-gel transition to occur. The final phase formation occurs after heating to above 600  $^\circ\text{C}$ .

Nanowires of 60–200 nm anatase  $\text{TiO}_2$  were fabricated using liquid phase deposition in a track etched membrane [47]. The acidic precursor solution used was  $(\text{NH}_4)_2\text{TiF}_6$  (0.2 M) and  $\text{H}_3\text{BO}_3$  (0.1 M) and was adjusted to a pH of around 1.4 with 1:1 ammonia solution.

Arrays of concentric composite nanowires of  $\text{ZrO}_2$  with Co cores were made in an alumina template by the sol-gel method from  $\text{ZrO}_2$  sol [48]. The sol was made from  $\text{ZrOCl}_2 \cdot 8\text{H}_2\text{O}$ , ethanol,  $\text{HNO}_3$  and acetylacetone. The alumina membrane was dipped in the sol for 0.5–1 h and after drying was annealed at around 500  $^\circ\text{C}$ . The  $\text{ZrO}_2$  template was then filled with Co metal by electrodeposition. This composite nanostructure had an enhanced coercivity compared to that of bulk Co.

Transition metal oxide nanowires have been fabricated using the sol-gel method.  $\text{LiNiO}_2$  nanowires in alumina templates have been fabricated [49]. Highly ordered  $\text{LiNi}_{0.5}\text{Mn}_{0.5}\text{O}_2$  nanowires were fabricated from sol made from metal acetate cationic sources, citric acid and ethylene glycol [50]. The template was dipped into the sol, dried in vacuum and then annealed for 10 h at 600  $^\circ\text{C}$ . Preparation of nanowires of complex materials using alumina templates and a chemical route such as the sol-gel route is a profitable exercise. It gives the freedom of fabrication of a number of functional metallic oxides without changing the basic procedure significantly.

### 21.3.3

#### CVD Method

Templates have been used for the growth of semiconductor nanotubes, including ordered arrays of carbon nanotubes, by chemical and physical vapor deposition. This is a very promising route because it uses the existing knowledge base of physical and chemical vapor deposition in general and couples that to a rather ready made template that leads to an array formation. A schematic of nanowire formation using the vapor route is shown in Figure 21.12.

Early reports of the formation of carbon nanotube (CNT) arrays in templates are given in [51]. Aligned CNT with a diameter of about few nm with sufficient graphitic character were made by chemical vapor decomposition (CVD) using propylene gas. The CNTs were made with Fe and Co catalysts or without catalysts. The

## Pore filling & Nanowire formation using vapor route.

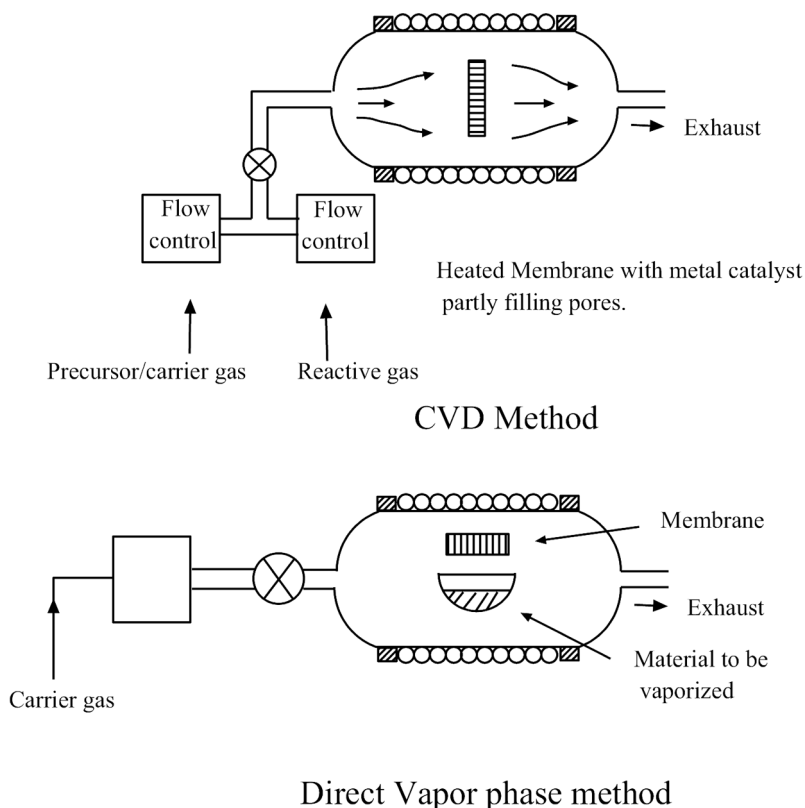


Fig. 21.12. Vapor route to nanowire formation in templates.

CVD process was carried out in a three-zone furnace with deposition temperatures varying from 500 to 1000 °C. The different temperatures of fabrication yielded different graphitic content with progressive increase in metallic appearance, decrease in resistance and enhanced tube wall structure at high temperatures. However, the graphitic content saturated at a deposition temperature of 800 °C. A recent paper reports the synthesis and magnetic behavior of Ni filled CNT [52]. A layer of Co was grown at the bottom of the template by electrodeposition and this acts as the catalyst. The template was then kept in a quartz reactor at 600 °C for 1 h in flowing gas of 98% Ar and 2% H<sub>2</sub>. Final deposition was carried out at 700 °C in a source gas of 2% C<sub>2</sub>H<sub>2</sub>, 2% H<sub>2</sub> and 96% Ar. Ni was electrodeposited within the pores of the CNT from an acidic bath of nickel sulfate. The wires with diameter of around 180 nm were found to have a strong uniaxial magnetic anisotropy with easy axis parallel to the wire axis. The parallel coercivity was as high as 185 Oe and much higher than the bulk Ni coercivity of 0.7 Oe.

Nanowires of GaN have been grown by vapor phase deposition in templates. Single crystalline GaN nanowires (hexagonal wurzite structure) of approximate diameter 14 nm and several micron in length were fabricated in an anodic alumina membrane of around 50  $\mu\text{m}$  thickness [53]. The four Raman lines of the nanowires in the range 531 to 745  $\text{cm}^{-1}$  agree with the phonon vibration frequencies of the crystalline wurtzite GaN. The growth was carried out in an alumina membrane prepared from 5 N aluminum. The deposition was performed at 1273 K from a vapor of  $\text{Ga}_2\text{O}$  with  $\text{NH}_3$  gas. The gaseous  $\text{Ga}_2\text{O}$  was prepared from heating in situ a mixture of Ga and  $\text{Ga}_2\text{O}_3$ . A highly ordered array of such GaN using a similar growth procedure to that above has been reported. The growth of the nanowires was catalyzed by electrodeposition of In in the pores from  $\text{InCl}_3$  electrolyte [54]. These wires with typical diameter 50 nm and 40–50  $\mu\text{m}$  length have visible PL in the region 360–540 nm at room temperature.

Aligned carbon nitride nanotubes have been fabricated in an alumina membrane using electron cyclotron resonance (ECR) plasma-assisted CVD of  $\text{C}_2\text{H}_2$  [55]. The membranes have a thickness of  $\sim 50$ –80  $\mu\text{m}$  and pore diameter of  $\sim 250$  nm. To promote the flow of ionic fluxes through the nanochannels of the alumina template a negative dc bias voltage was applied to the graphite substrate holder.

Si nanowires have been grown in templates using a direct vapour–liquid–solid route [56]. The wires were grown in a 60  $\mu\text{m}$  thick and 200 nm pore diameter alumina membrane. A thin layer ( $< 1$   $\mu\text{m}$ ) of Au is electrodeposited to form the catalyst. The growth was carried out using a 5% mixture of  $\text{SiH}_4$  in  $\text{H}_2$  in an isothermal low pressure reactor at 500  $^\circ\text{C}$ . The nanowire has a defect-free core of Si with a 2–3 nm oxide layer and is capped with Au at both ends. It has a growth direction of [100].

Application of CVD techniques, particularly plasma assisted CVD, to grow aligned nanotubes of complex semiconductor or oxides in alumina templates is a new tool. It is expected that in future this technique will find more applications.

## 21.4

### Scanning Probe Based Anodic Oxidation as a Tool for the Fabrication of Nanostructures

It is more than a decade since it was realized that the scanning probe microscope (SPM), like the scanning tunneling microscope (STM) and the atomic force microscope (AFM) could be used to create structures at the nanometer scale on a surface. It has also been demonstrated that even atoms can be manipulated using an STM [57]. There were reports of STM tip induced modification of resist as early as 1988 [58]. The field of SPM-based nanolithography is an established procedure to create patterns at nanometer level that can be transferred onto an underlying substrate, just like any other lithography mask in optical or e-beam lithography. This can lead to fabrication of nanoelectronic devices. The biggest advantage of the SPM-based lithography (despite its low writing speed) is that the same SPM can be used for writing the pattern and to image it after the writing process. Early reviews

on the use of SPM-based local oxidation for device fabrication sum up the development and basic issues in the field till 1996 [60].

Due to the finite force of contact, a contact-mode AFM (C-AFM) can mechanically modify a surface, particularly a soft surface. This leads to creation of a pattern on the substrate. However, in this review we do not discuss mechanical nanopatterning.

There are two ways to create reproducible patterns with nanometer size features on a surface using the “chemical route” and an SPM. They are dip-pen lithography and SPM-based anodic oxidation. In this section we discuss the anodic oxidation route. In both these methods the water meniscus that forms between the tip and the substrate plays the central role. In the case of dip-pen nanolithography there is transfer of matter (mostly organic molecules) from tip to substrate through the meniscus. In the case of anodic oxidation the meniscus acts like an electrochemical cell. A number of surfaces, both metallic and semiconducting, have been patterned using this route. Both STM and conducting probe AFM have been used for this purpose. The smallest resolution achieved is around 10 nm while in most cases a resolution of 30–40 nm can be achieved by controlling the humidity in which the microscope is being operated. The typical writing speed is  $1\text{--}10\ \mu\text{m s}^{-1}$ . This method combines the chemistry of anodic oxidation of a surface with the spatial resolution and scanning capability of an SPM.

The basic idea in SPM lithography based on anodic oxidation is described below. In Figure 21.13 we show a simple schematic. The tip is placed in close proximity to the substrate as in an STM or a non-contact mode AFM (NC-AFM) while it touches the surface with a contact force of around 1–10 nN in the case of C-AFM. Generally the writing operation is done in ambient air with a moisture content of more than 50% RH. The atmospheric moisture capillary condenses on the surface of the substrate forming a meniscus. It is the moisture meniscus that is the active electrolytic medium that is used in the anodic oxidation process. The moisture in this case is a “nano-reaction, vessel” for anodic oxidation. Formation of a meniscus around the SPM tip is one of the important core ideas that are used both in dip-pen lithography and in anodic oxidation. A bias is applied between the tip and the substrate and, for oxidation, the substrate is at a positive bias with respect to the tip. The oxidation process takes place under an applied field due to the bias and it has to be in excess of  $10^7\ \text{V cm}^{-1}$  for the oxidation process to begin. The applied field and its magnitude is thus the second important parameter for the oxidation process. The following pathway is envisaged for the anodic process. The  $\text{OH}^-$  ions are accelerated to the substrate under the applied field. The hydroxy ions oxidize the substrate. The mechanism for oxide growth follows the Mott mechanism [61] and the oxide growth rate depends on the electric field at the oxide/substrate interface. As the oxide grows to a certain thickness a significant portion of the applied field (due to the applied bias) drops across the oxide layer and the field at the oxide/substrate interface decreases. When this field falls below a critical value ( $\sim 10^7\ \text{V cm}^{-1}$ ) the oxidation process stops. This is thus a self-limiting process. The width and the height of the oxide grown will depend on the applied bias. As a rule of thumb, the higher the applied bias the greater the width and thickness of the

## SPM based nano-oxidation

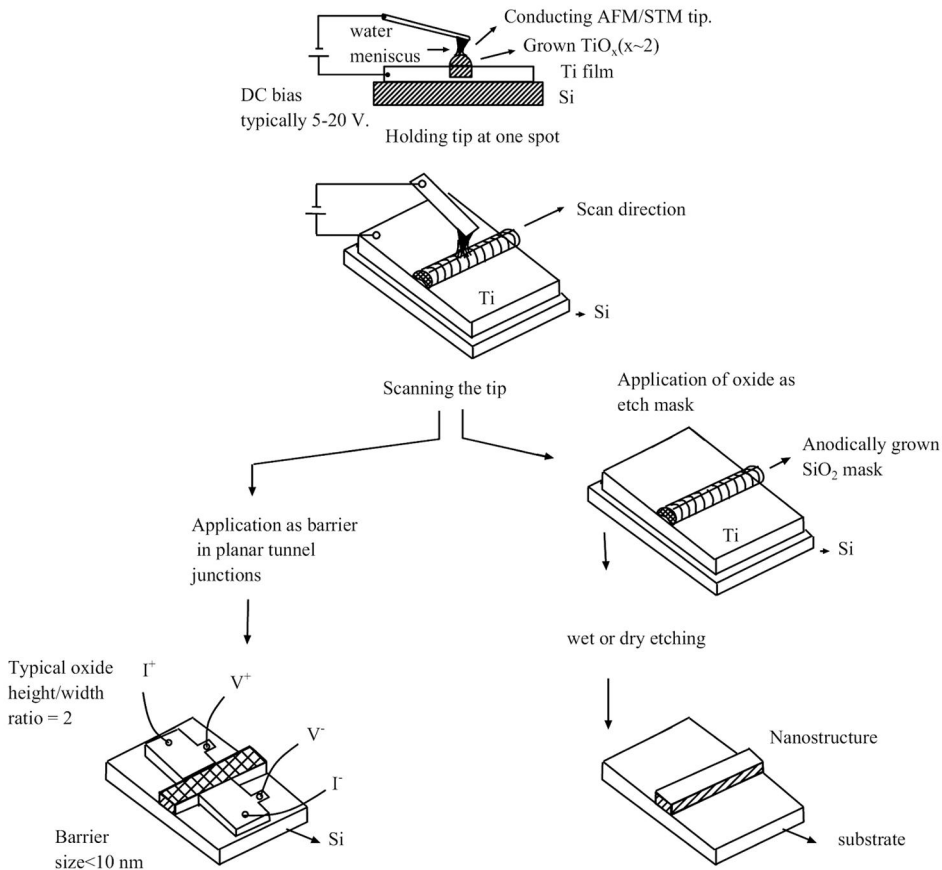


**Fig. 21.13.** Schematic of SPM-based nanooxidation.

grown line. In other words, a smaller bias and smaller time of interaction between the field and the substrate will lead to higher resolution. However, a bias lower than the critical bias will not lead to any oxidation.

Since the applied field is a key factor for the anodic oxidation process the radius of curvature of the tip is also important. Most AFM tips available commercially have a tip radius of curvature of  $\geq 10$  nm. This limits the minimum resolution that one can obtain in an AFM-based lithography. Since well defined and controlled micromachining lithography is used to make these tips on the AFM cantilevers, they are of reproducible size, shape and aspect ratio. This is a big advantage when it comes to doing reproducible lithography of a given resolution. A sharper tip can be obtained in STM but it is difficult to produce a tip of reproducible radius of curvature and aspect ratio.



The basic electrochemistry of the substrate is an important ingredient in the anodic oxidation process. The ease of doing the oxidation will definitely determine the material to be chosen for making the pattern. It appears that the two most popular substances which have been studied and used most extensively are Ti (for formation of  $\text{TiO}_x$ ) and H-passivated Si (for formation of  $\text{SiO}_2$ ).

In the last five years the field has matured and there are reports of actual devices being made using this route, as well as work on pattern transfer on a given wafer by wet or dry etching. There have been attempts to create parallel writing, thus enhancing the writing speed, which is inherently slow in SPM lithography [62]. In the following section we will describe some details of the lithographic work using SPM-based oxidation.

#### 21.4.1

##### Oxidation of Metallic Substrates

In the case of the oxidation of a metallic substrate the anodization depends strongly on the humidity of the adsorbed water molecules which is the working electrolyte. The anodization process is carried out in conventional configuration with the tip as the counter electrode and the metal substrate as the working electrode. The anodization takes place when the metallic substrate is biased positively with respect to the tip, which as mentioned before can be either the STM tip or the tip of a conducting AFM.

One of the first reports of the anodization was carried out in Ta using the STM tip [63]. Nanofabrication of a Ti surface by the STM tip induced anodization was carried out using a rather low bias in the range of 3 V and nanostructures with a resolution of 70 nm were produced [64]. An interesting example of the application of localized oxidation by proximity probe anodization is the fabrication of a lateral metal–oxide–metal junction on a film of Ti [65]. The Ti– $\text{TiO}_x$  lateral junction with a 15–25 nm wide and 30–50 nm long  $\text{TiO}_x$  pattern acted as a single electron transistor at room temperature. The pattern was produced on 3 nm Ti grown on Si with 100 nm of thermally grown oxide. The single electron transistor showed a Coulomb staircase of 150 mV period. Single atom point contact devices were fabricated with a conducting probe AFM on Al thin films [66]. The Al film (8 nm thick) was grown on a Si substrate with 100 nm  $\text{SiO}_2$ . The AFM tip was used to make an oxide pattern 500 nm long and about 40 nm wide in the middle of a 1  $\mu\text{m}$  wide Al wire. The anodization was done in 10%–20% ambient humidity with a bias between 8 and 12 V. The conductance  $G$  of the junction was monitored during the anodization process. The anodization was stopped when the conductance reached around  $2e^2/h$  which signified formation of a single atom point contact.

In this context of proximal probe induced oxidation it is worthwhile to point out an interesting observation where a high current passing through a metal film leads to its oxidation [67]. This process can be coupled to the SPM-based anodic oxidation to form patterns at the nanometer level. The planar oxidation was carried out with a current density of  $J \approx 10^7 \text{ A cm}^{-2}$ . The oxide growth rate was found to vary  $\propto J^n$  where  $n \approx 4$ .

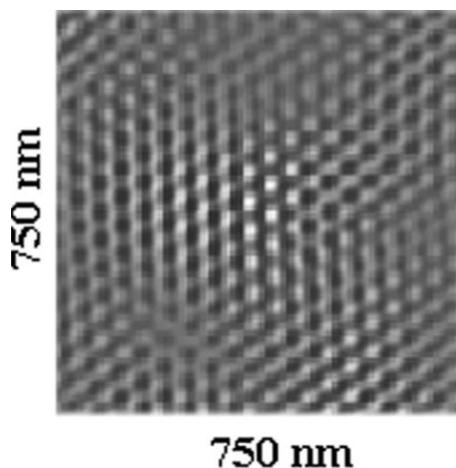


Fig. 21.14. Pattern created by anodic oxidation.

In recent years the anodic oxidation has been carried out by using pulsed mode bias on the conducting AFM tip [68]. A room temperature single electron memory was made by this method by growing  $\text{TiO}_x$  on 2.5 nm Ti film grown on atomically flat  $\alpha\text{-Al}_2\text{O}_3$ . In the pulsed mode one uses a much lower voltage. In pulsed mode while the positive bias of the substrate oxidizes the substrate the negative bias neutralizes the positive space charge from the front end of the growing  $\text{TiO}_x$ . The single electron memory cells formed by the AFM anodic oxidation are around 10 to 15 nm in size and can store around 25 electrons. The single electron memory cell showed hysteresis of a memory, even at room temperature.

The anodic oxide pattern of 100 nm dimension grown by SPM-based techniques can be used as a mask that can be transferred to a substrate below. An anodized alumina mask (produced by contact mode AFM on sputtered Al film) has been used to transfer pattern on Si by using a combination of wet and reactive ion etching. Anodic oxidation creates a protruding oxide pattern that can be etched. The pattern can form a positive or negative mask depending on what is etched, the aluminum or the oxides. In Figure 21.14 we show an example of a nanopattern (an array of points) created by anodic oxidation on a surface of aluminum.

It is expected that with more control of the anodic oxidation process, the local oxidation of metals will become a viable tool to create sub-100 nm patterns. However, there is a need to understand the process and the underlying factors that control the resolution somewhat quantitatively to enable more control of the process.

#### 21.4.2

#### Oxidation of Semiconducting Substrates

One of the first reports of single tip SPM-based oxidation of passivated Si (111) was made in 1990 [69]. This was followed by reports of oxidation of GaAs and other

semiconductor substrates. A conducting tip AFM ( $\text{Si}_3\text{N}_4$  tip metallized by 30 nm Ti) was used to make 1–2 nm high and 10–30 nm wide oxide structures on H-passivated n-type Si (100) substrates [70]. The writing was done by contact mode AFM using a contact force of around 100 nN with a cantilever with a force constant of around  $0.4 \text{ N m}^{-1}$ . The voltage bias used for the writing was in the range 1.5–2.5 eV. The threshold time for oxide formation was found to be around  $10^{-4}$  to  $10^{-5}$  s. The pattern was transferred to the Si substrate below using wet etching with KOH. The oxide grown by the SPM method is stoichiometric  $\text{SiO}_2$ , as has been shown by recent spectroscopic studies on such oxides [71].

UHV-STM has been used to form oxidation-based nanopatterns on an H-passivated Si (100) surface showing  $(2 \times 1)$  structure [72]. Line widths as small as 1.5 nm could be produced. Although UHV-STM offers a clean way of fabricating much smaller nanostructures of a few nm dimension as opposed to ten or few tens of nanometer sized features in SPM operating in the air most applications of SPM for nanofabrication were carried out in ambient air. This is presumably due to the ease of operation as well as the cost factor.

A nanometer scale pattern on n-type Si (100) was generated by field induced oxidation using Si cantilever tips which are made metallic by heavy p-type ( $10^{26} \text{ m}^{-3}$ ) doping [73]. It was found that the oxidation needs a threshold bias ( $\sim 10 \text{ V}$ ) before oxidation begins. The structures formed were oxides (1 nm high) which could be etched by leaving grooves on the substrate. (Growth of the oxide layer in Si consumes a layer of around  $0.5 h$  inside the Si where  $h$  is the height of the oxide layer grown. As a result it leaves a groove on removal of the protruding oxide formed by the tip-induced oxidation.)

In the models proposed for oxidation in the above experiments there is no role of the absorbed moisture layer that can act as the “electrolyte”. However, subsequent models show that the oxide formation can be explained using the moisture layer [74]. The process is similar to liquid electrolyte based anodization. The oxidation process is sensitive to the humidity. The diffusion limited electric field  $E$  at the surface determines the terminating thickness of the oxide grown. The model is similar to what has been proposed for the field-induced oxidation process proposed by Cabrera and Mott more than 50 years ago [61]. An electron tunnels from the conducting AFM tip (which is negatively biased with respect to the substrate) and creates negatively charged oxygen ions. The oxide growth stops when the electric field is no longer sufficient for the ionic diffusion.

Amorphous Si (a-Si) has been oxidized like crystalline Si in AFM-based lithography and has been used as a resist [75]. a-Si can be H passivated like its single crystalline counterpart. This makes SPM-based lithography possible in a-Si.

Application of non-contact mode AFM in anodic oxidation based lithography is an important step forward in this field [76]. Noncontact AFM has been used to create feature sizes  $< 30 \text{ nm}$  on a 65 nm resist (polymer resist) and was transferred through reactive ion etching (RIE) to the Si substrate (P-doped (100)) on which the resist is coated [77]. A scan speed of  $10 \mu\text{m s}^{-1}$  has been achieved using a heavily B-doped Si cantilever with a large spring constant ( $\sim 340 \text{ N m}^{-1}$ ) and mechanical resonance frequency ( $f_r \approx 1 \text{ MHz}$ ) and with a tip of radius of curvature

10 nm. The large spring constant prevents the cantilever being pulled down by the electrostatic force between the tip and the substrate which have opposite polarity. Due to noncontact operation the conducting AFM tip gives out an electron field emission. Typically, the current was in the range of a few tens of pA and it is the emission current that was kept constant by the feedback loop which moves the Z-piezo positioner. The line width written by this method depends on the voltage applied. For a fixed emission current a higher bias will ensure a larger line width due to the geometric effect.

Combination of a pulsed bias and noncontact AFM has been found to improve the control of the writing process [78]. This method reduces the tip-substrate interaction time and thus improves the reliability and lithographic resolution. The frequency of oscillation and the field pulsing frequencies need to be adjusted to create a definite phase relation between the two and it was found that the minimum line width is obtained when the applied field is on during the time the cantilever tip is furthest from the substrate. The process also needs adjustment of the duty cycle.

Recent applications of AFM for oxidation include lithography of amorphous chalcogenides such as  $\text{GeSb}_2\text{Te}_4$  films [79]. The particular choice of the material is due to its application potential as an electronic phase memory material. Selective oxide growth of Si using ultrathin  $\text{SiO}_2$  or  $\text{Si}_3\text{N}_4$  as a mask for AFM-based lithography has been done [80]. An ultrathin Pt-Si bilayer patterned by SPM oxidation has been used as a lithography mask [81]. An H-passivated Si surface was patterned by SPM-enabled oxidation. This local oxide prevents reaction of a deposited Pt film with the underlying Si, thus inhibiting silicide formation. The unreacted Pt on the oxide is removed by selective etching and the pattern is then annealed to transfer the pattern through silicide formation.

Judging by the present trend it is apparent that more innovative use of SPM-based oxidation of Si and other semiconductor materials will be applied in nano-electronic device fabrication.

## 21.5

### Use of Scanning Probe Microscopy in Dip Pen Nanolithography

One of the innovative applications of scanning probe microscopy for nanolithography is dip pen nanolithography (DPN). In this special technique the water meniscus formed between the tip and the substrate acts as a medium for molecular transport. The technique depends on the key phenomenon that the molecule to be deposited on the substrate (which is referred as the “ink”) can be transported in a controlled way from the tip (which is initially coated with the ink) to the substrate. The molecule (the ink) to be deposited on the substrate should interact with the substrate to form a chemical bond, leading to a stable structure [82].

The core concept that the water meniscus at the tip-substrate contact can indeed be controlled and can be used as the molecular transport medium came from basic investigations of water meniscus on lateral force microscopy (LFM) [83]. It was

observed that in conditions of low humidity ( $R_H \approx 10\%–20\%$ ) when the tip is in contact with the substrate (and resting on it) the water is transported from the tip to the substrate forming a meniscus. This changes the lateral force during scanning. When the humidity is high ( $R_H \approx 90\%$ ) for a hydrophilic substrate, there is transport of water from the substrate to the tip around the region of contact, leading to depletion of the water meniscus in the region around the contact. For a hydrophobic substrate, for the same high humidity there is transport of water from tip to substrate leading to growth of the water meniscus.

The scan speed of the AFM tip will determine the amount of water that is carried with the tip. At high scan rates the tip carries less water and the meniscus has less time to grow. The transport being essentially diffusion controlled the scale of growth is  $\propto t^{1/2}$ ,  $t$  being the time of contact. A schematic of the basic concepts involved in DPN is shown in Figure 21.15.

The observation that the relative humidity, the hydrophobic or hydrophilic nature of the substrate and the scan speed can be used to control the amount of water being transported from the tip to the substrate led to the technique of DPN. Currently the technique can achieve feature sizes down to 10–15 nm with the capability of using multiple “ink” [84] as well as both serial and parallel writing capability [85].

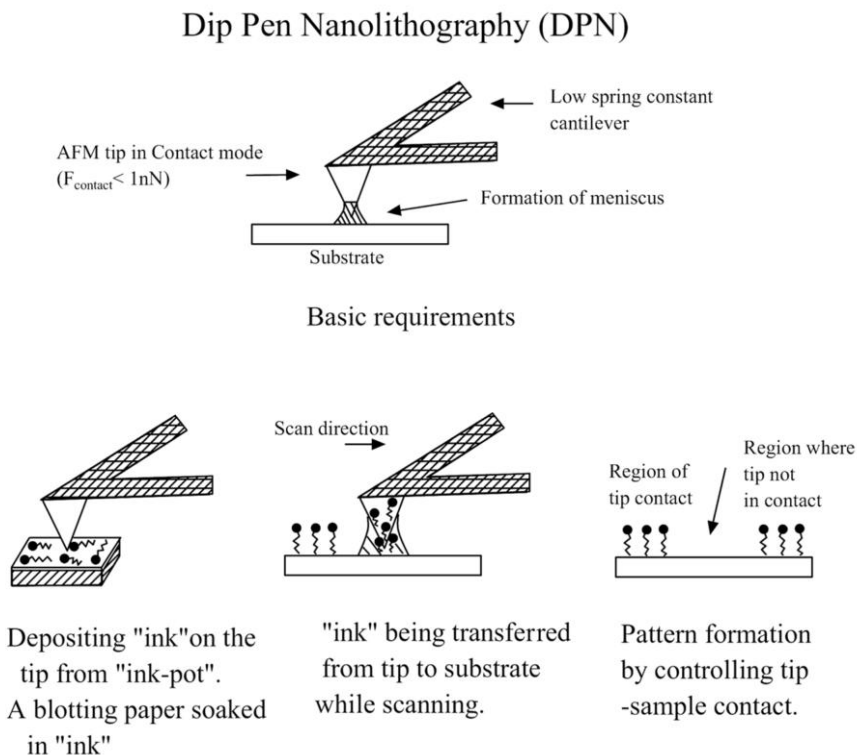


Fig. 21.15. Schematic of nanpattern formation by DPN.

The condition of deposition depends on the molecules to be deposited and their capability to form a self-assembled monolayer (SAM). The two widely used molecules are 16-mercaptohexadeconic acid (MHA) and 1-octadecane thiol (ODT) and the most used substrate is Au (111) film.

The writing is done with a rather soft AFM cantilever with a spring constant  $k \leq 0.05 \text{ N m}^{-1}$ . The tip of the cantilever has a typical radius of curvature of  $\sim 10 \text{ nm}$ . The “writing” or the deposition process is achieved by repeatedly making contact with the region where the molecule has to be transported. For example, to draw a line that region is repeatedly scanned. The contact force is kept rather low  $\sim 0.1\text{--}0.5 \text{ nN}$ . The LFM image is taken along with the AFM scan. Since the deposition of the molecule onto the substrate changes the lateral force (frictional force) during scanning, the LFM scan is used as a control or in situ diagnostic tool for the deposition, allowing the process to be stopped at any stage.

The patterning in DPN is done by forming a SAM of the molecule. As a result the hydrophobic/hydrophilic nature of the SAM becomes an important parameter. In the case of MHA the adsorbate is hydrophobic but the SAM is hydrophilic. In the case of ODT both are hydrophobic [86]. For a hydrophilic SAM the force of friction increases as more MHA (which is hydrophobic) is deposited and the wetting properties of the substrate increase with MHA deposition. In this case the meniscus can wet both the Au surface and the areas around it with deposited molecules. The effective DPN contact area grows as more molecules are deposited. For hydrophobic SAM and a molecule like ODT the wettability of the surface decreases as more and more molecules are deposited from the tip there by localizing monolayer growth. A summary of the transfer of molecules to and from the substrate during the dip-pen process is given in Table 21.2.

In the past two years this process has matured and has become a viable lithographic tool to create masks for etching [87]. In this method an oxidized Si (100) wafer on which pattern has to be created is coated with a layer (10 nm) of Au with a thin (5 nm) Ti adhesion layer. Using DPN a patterned SAM of ODT is created on the Au surface. ODT being a thiol, it binds to the Au surface. The exposed Au surface is then selectively etched using a ferri/ferrocyanide-based etching solution. The pattern of the exposed surface is then transferred to the Si below by anisotropic etching using KOH. The Ti–Au surface (which itself has been covered with SAM) covers the remaining Si surface thereby acting as a protective mask. This Ti–Au is removed with aqua regia thereby creating a clean patterned surface on Si.

**Tab. 21.2.** The dependence of molecular transport in the DPN process on the nature of the substrates.

<b>Surface</b>	<b>Humidity (%)</b>	<b>Direction of Ink Transport</b>
Hydrophilic (e.g., glass, mica)	Low ( $< 20$ )	Tip to substrate
Hydrophobic (e.g., PMMA, epoxy)	Low ( $< 20$ )	No transport
Hydrophilic	High ( $\geq 90$ )	Substrate to tip
Hydrophobic	High ( $\geq 90\%$ )	Tip to substrate

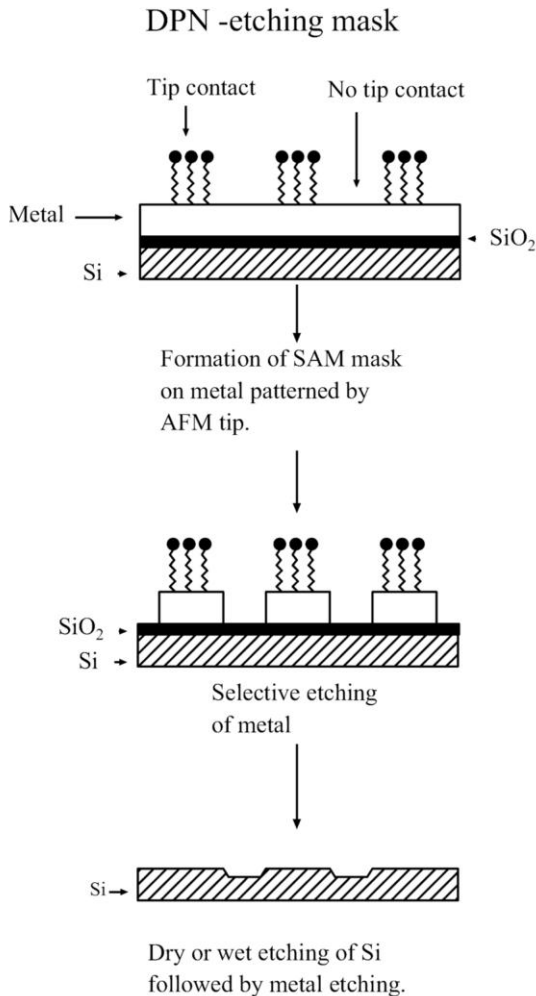


**Fig. 21.16.** Formation of nanoscale etch mask by DPN.

The lithographic definition of the mask has been done by DPN. An example of the process of mask formation by DPN is shown in Figure 21.16.

Most of the DPN applications have been done on Au substrates using thiol-based compounds as ink. However, the DPN has also been used to pattern directly on semiconductor surfaces like Si or GaAs [88]. In this work hexamethyl disilazane (HMDS) was used as the ink and monolayers of HMDS were patterned on the semiconductor surfaces.

An interesting extension of DPN is to use the meniscus formed between the tip and the substrate as an electrochemical cell, by applying a bias between the two. This is similar to the anodic oxidation using a conducting AFM tip as discussed before. An electrochemical DPN technique has been reported that can be used to

directly fabricate metal and semiconductor nanostructures [89]. It has been suggested that the application of the bias between the tip and substrate lead to better stability of the structure. The meniscus in this case contains metal salts that can be dissolved in water and it leads to deposition of the metal on the substrate from the meniscus electrolyte by cathodic reduction. As an example 30 nm wide, 0.4 nm high lines of Pt have been drawn on H-passivated P-type Si (100) wafers using 2 wt%  $\text{H}_2\text{PtCl}_6$  as the electrolyte.

It has been demonstrated that DPN can be used to create nanostructures on a surface which can then be used for directed assembly of nanoparticles [90]. In this application also the basic patterning by DPN was done with MHA as ink on an Au substrate. Subsequently, alkylamine-modified DNA was coupled to the MHA nanopatterns so created. By creating an ordered pattern of two distinct oligonucleotide sequences it was possible to create an ordered assembly of two different nanoparticles from a randomly dispersed system.

## 21.6

### Use of Scanning Probe Microscopy in Nanomanipulation

The field of nanolithography is intimately connected with nanomanipulation. In nanomanipulation generally a preformed nanoparticle, nanotube or a nanowire is manipulated to place it at a predetermined site. The most widely used tool for nanomanipulation is the cantilever of the AFM that provides a “robotic” arm to place the nano-objects in predetermined sites. A nanoparticle weakly adsorbed on a substrate can be moved by an AFM tip when it works in contact mode. This is not wanted but if the particle is “selected” and then moved by the AFM then it becomes a useful tool. The AFM-based manipulation turns the unwanted aspect to an advantage. For instance if one wants to place a nanowire between two electrodes an AFM cantilever can be used to image the wire and push it between the two electrodes. The advantage of the cantilever is that a predetermined force can be applied and also the same instrument can image it. The basic idea behind SPM-based nanomanipulation is shown in Figure 21.17.

The STM tip can also be used for nanomanipulation. In fact the first atomic level nanomanipulation was done by STM only [91]. However, in more recent context, by nanomanipulation we generally imply use of an AFM cantilever to manipulate nano-objects. This field, however, is in its early stages and there is a need to understand the physics of the manipulation in terms of the basic forces that are involved in this process. It is realized that it is different from what one sees in micromanipulation. There are three main road blocks that need to be solved effectively before this field can mature. First, there is the need to understand the basic physical and chemical processes that take place at the scale of a few nanometers, including the mechanics. Second, one need to develop effective hardware as well as control that has resolution and reproducibility of manipulation at this level. Third, there is a need for effective automation and software. Interestingly, these road-



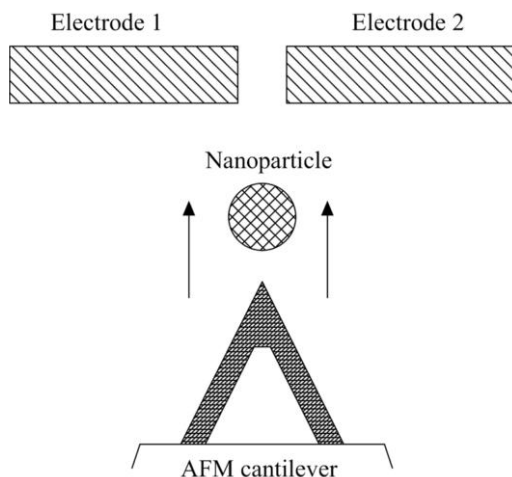


Fig. 21.17. Using an AFM tip to place a nanoparticle between two e-beam fabricated electrodes.

blocks notwithstanding there are good examples of effective nanomanipulation that have made this field progress.

Early reports on AFM-based nanomanipulation, which showed the feasibility of such a process, appeared as far back as 1995 [92, 93]. Subsequent publications also addressed the modeling and simulation of such a process and the issue of manipulation forces [94–97].

The process of nanomanipulation involves control of a number of forces. The main two forces are the force of adhesion ( $F_a^{tp}$ ) between the AFM tip and the adsorbate particle which will be manipulated and that between the particle and the substrate ( $F_a^{ps}$ ). These forces are mediated by the surface forces [98] and depend on the formation of a meniscus on the substrate. While  $F_a^{ps}$  stabilizes the particle on the substrate,  $F_a^{tp}$  makes the particle stick to the tip. The contact force between the tip and the particle  $F_c$  makes the particle move. The movement of the cantilever from its equilibrium position and the force constant of the cantilever determine the contact force in turn. In addition, since the experiments are carried out in ambient air, there are capillary forces between the tip and the particle as well as the van der Waal forces between the tip and the particle and between the particle and the substrate. It is the balance of these forces that determines the final dynamics of the particle movement.

As a simple model we consider  $F_a^{tp} \approx 4\pi R_{eff}\gamma_{sv}$  and  $F_a^{ps} \approx 4\pi R_p\gamma_{sv}$  where  $R_t$  = radius of curvature of the tip and  $R_p$  = radius of curvature of the particle and  $R_{eff} = (1/R_t + 1/R_p)^{-1}$ .  $\gamma_{sv}$  = surface energy at the solid/vapor interface. In order to move the particle from one place to another it is important to ensure (1) that the particle does not adhere to the tip and also (2) that the component of the contact force between the tip and the particle parallel to the surface ( $F_c^{\parallel}$ ) is larger than the force of friction so that the particle can be moved. As a rough estimate of the force

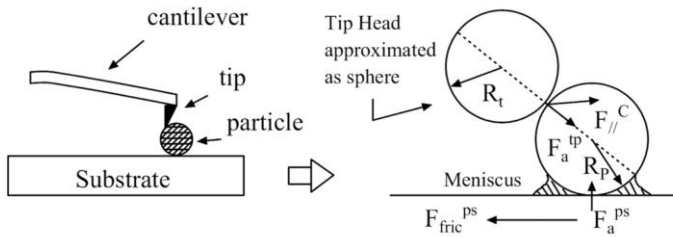
of friction we can have  $F_{\text{friction}}^{\text{ps}} \approx \mu^{\text{ps}}(F_a^{\text{ps}} + F_{\text{load}}^{\text{ps}})$  where  $F_{\text{load}}^{\text{ps}}$  = loading force and  $\mu^{\text{ps}}$  is the coefficient of friction between the particle and the substrate. The tip will “ride” smoothly along the surface of the particle when the tangential component of  $F_c$  on the surface of the particle is larger than the frictional force between the two, which is determined by  $F_a^{\text{tp}}$  and  $\mu^{\text{tp}}$ , the coefficient of friction between the particle and the tip. (The selection of the absorption chemicals is an important issue because it determines the force of adhesion. It depends on the type of the substrate and the particle. (For instance, in the manipulation of Au on mica poly-L-lysine is used.) To meet condition (1), i.e., to ensure that the particle does not stick to the tip, we should minimize  $F_a^{\text{tp}}$ , which for a given  $\gamma_{\text{sv}}$  happens for a minimum  $R_t$ . This can be achieved by a tip of long aspect ratio. When the tip and the particle have similar size,  $R_{\text{eff}} \approx R_p/2$  and  $F_a^{\text{tp}} \approx F_a^{\text{ps}}/2$  and the particle is not likely to adhere to the tip. Condition (2) would imply that there is a minimum contact force that is needed to move the particle. In order to have a substantial contact force that can make  $F_{\parallel}^c > F_{\text{friction}}^{\text{ps}}$ . This would imply that one would need a stiff cantilever (one with a large spring constant typically  $>10 \text{ N m}^{-1}$ ) for the manipulation. In Figure 21.18(a) we show a tentative force diagram for the nanomanipulation.

The scheme for nanomanipulation can be roughly described as below. Generally a noncontact mode image of the substrate is first taken to mark the particles to be manipulated and the trajectory of their movement. The noncontact mode ensures that  $F_{\parallel}^c \approx 0$ . The cantilever vibrating at an amplitude  $A$  is then lowered near the particle to be moved. At this stage, the feed back loop of the AFM is put to a hold mode so that the change in vibration amplitude does not make the feedback circuit adjust the tip–particle distance. Contact with the particle is detected by reduction in  $A$  and an increase in the static deflection. The cantilever carrying the tip is then moved along the desired trajectory. This movement would require a closed loop  $X$ – $Y$  scanner for the AFM. At the stop position the tip is again pulled out and the feedback is enabled to start the noncontact mode imaging process again. Sufficient  $F_a^{\text{ps}} > F_a^{\text{tp}}$  will ensure that the particle is parked at the desired spot as described before. This can be confirmed by the cantilever oscillating at its previous amplitude again. A schematic of the manipulation process described above is given in Figure 21.18(b). The description given above of the nanomanipulation process as well as the important forces is a simplification of the process that occurs, which in reality is rather involved. It is expected that in the years to come there will be an enhanced understanding of the basic processes.

## 21.7

### Nano-Electromechanical Systems

In the past 15 years the field of micro-electromechanical systems (MEMS) has progressed tremendously thanks to the innovative utilization of the techniques of microelectronic fabrication. In particular, techniques of lithography using optical and electron beams and the development of anisotropic etching (both dry and wet) led to the rapid progress in the field. In recent years there have been new efforts to



For particle not adhering to tip  $F_a^{tp} < F_a^{ps}$

For particle movement on substrate  $F_{//}^C > F_{frict}^{ps}$

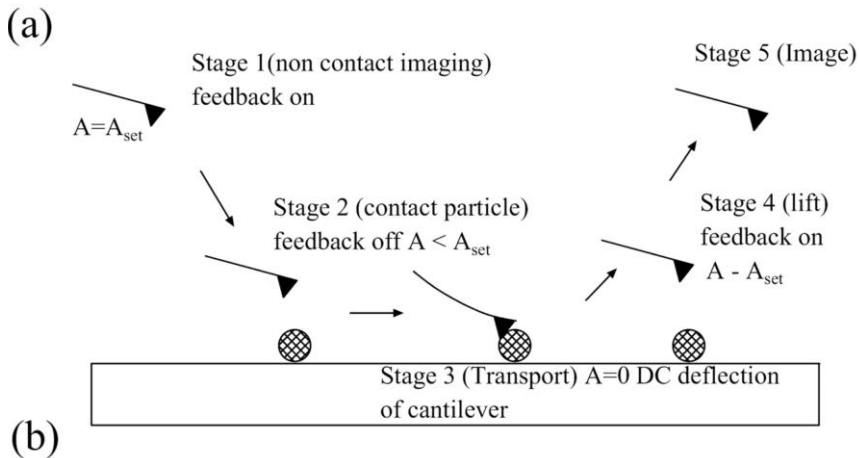


**Fig. 21.18.** (a) Schematic of the forces involved in nanomanipulation. (b) The scheme for nanomanipulation.

make mechanical structures of much smaller length scales deep in the submicron range. These efforts have initiated the field of nano-electromechanical systems (NEMS) [99].

The crucial aspect of NEMS fabricated structures is the realisation that one is dealing with mechanical vibrations of much higher frequencies. In the case of MEMS the resonance frequencies of the fabricated structures are in the range of tens to hundreds of kHz. For NEMS the frequencies are well into the RF range (1–100 MHz). Such a high frequency mechanical vibration needs investigation of physical properties (particularly mechanical properties) in a length scale that has not been done previously.

Interestingly, carbon nanotubes, due to their superior mechanical properties and their coupling of size and deformation to electronic structures are an exciting NEMS material. There are investigations of CNT from this viewpoint [100].

The field of NEMS has opened research challenges in the following well defined yet interdependent areas: (1) the design and fabrication of submicron mechanical

structures, (2) applications that transcend beyond simple extrapolation of MEMS to smaller length scales, (3) the actual electromechanical properties at nanometer scales and (4) actuation and sensing on a submicron scale.

Given the scope of the review and its focus on the techniques of nanolithography and nanomanipulation, we are not in a position to discuss these fields extensively. We mention some examples of recent progress in the fabrication of NEMS structures. Until now most of the NEMS structures have been made by innovative extensions of the techniques used for MEMS fabrications, like optical and e-beam lithography and anisotropic etching. The real 3D mechanical structures fabricated and investigated generally have a smallest length in the range of a few hundreds of nm ( $\geq 250$  nm). The new challenge is to use the techniques of nanolithography and nanomanipulation, described above, to fabricate NEMS structures. In principle, anodic oxidation and the DPN route can produce nanoscale masks for such processes. There are reports of the fabrication of NEMS structures on Si with length scales around 200–400 nm using aluminum masks fabricated using AFM-based local oxidation [101]. The fabrication of NEMS structures using nanolithography and nanomanipulation is in its infancy. It is expected that this field will grow, however, there are important road blocks which need to be attended to before any tangible progress can be made.

### Acknowledgements

The author wants to thank Mr. M. A. Paranjape, Ms. L. K. Brar and Ms. S. Kar for their help in the preparation of this manuscript.

### References

- 1 *Microlithography Science and Technology*, eds. J. R. SHEATS, B. W. SMITH, Marcel Dekker, New York 1998.
- 2 R. COONTZ, P. SZUROMI, *Science*, **2000**, 290, 1523–1539.
- 3 *Handbook of Nanostructured Materials and Nanotechnology*, ed. H. S. NALWA, Academic Press, New York. **2002**.
- 4 G. E. POSSIN, *Rev. Sci. Instrum.*, **1970**, 41, 772–77; W. D. WILLIAMS, N. GIORDANO, *Phys. Rev. B*, **1986**, 33, 8146–8154.
- 5 R. FLEISHER, P. B. PRICE, R. M. WALKER, *Nuclear Tracks in Solids*, University of California Press, Berkeley 1975; R. SPOHR, *Ion Tracks and Microtechnology: Basic Principles and Applications*, Vieweg, Wiesbaden 1990, 1–272.
- 6 P. YU. APEL, A. SCHULZ, R. SPOHR et al., *Nucl. Instrum. Methods Phys. Res. Sect. B*, **1997**, 130, 55–63.
- 7 P. YU. APEL, A. YU. DIDYK, A. G. SALINA, *Nucl. Instrum. Methods Phys. Res. Sect. B*, **1996**, 107, 276–280.
- 8 P. YU. APEL, I. V. BLONSKAYA, A. YU. DIDYK et al., *Nucl. Instrum. Methods Phys. Res. Sect. B*, **2001**, 179, 55–62.
- 9 R. MISHRA, S. P. TRIPATHY, A. KULSHRESTHA et al., *Pramana*, **2000**, 54, 777–784.
- 10 F. KELLER, M. S. HUNTER, D. L. ROBINSON, *J. Electrochem. Soc.*, **1953**, 100, 411–419.
- 11 Y. LI, G. W. MENG, L. D. ZHANG et al., *Appl. Phys. Lett.*, **2000**, 76, 2011–2013.
- 12 T. XU, G. ZANGARI, R. M. METZGER, *Nano Lett.*, **2002**, 2, 37–41.

- 13 K. NIELSCH, F. MULLER, AN-PONG LI et al., *Advanced Mater.*, **2000**, 12, 582–586.
- 14 Y. LEI, L. D. ZHANG, G. W. MENG et al., *Appl. Phys. Lett.*, **2001**, 78, 1125–1127; G. S. HUANG, X. L. WU, Y. F. MEI et al., *J. Appl. Phys.*, **2003**, 93, 582–585.
- 15 H. MASUDA, H. YAMADA, M. SATOH et al., *Appl. Phys. Lett.*, **1997**, 71, 2770–2772.
- 16 H. CAO, C. TIE, Z. XU et al., *Appl. Phys. Lett.*, **2001**, 78, 1592–1594.
- 17 J. BAO, Q. ZHOU, J. HONG et al., *Appl. Phys. Lett.*, **2002**, 81, 4592–4594.
- 18 X. MEI, D. KIM, H. E. RUDA et al., *Appl. Phys. Lett.*, **2002**, 81, 361–363.
- 19 KAI LIU, J. NOGUE'S, C. LEIGHTON et al., *Appl. Phys. Lett.*, **2002**, 81, 4434–4436.
- 20 Y. KANAMORI, K. HANE, H. SAI et al., *Appl. Phys. Lett.*, **2001**, 78, 142–143.
- 21 J. HAERMANS, C. M. THRUSH, Y. M. LIN et al., *Phys. Rev. B*, **2000**, 61, 2921–2930.
- 22 M. PARK, C. HARRISON, P. M. CHAIKIN et al., *Science* **1997**, 276, 1401–1404.
- 23 T. THURN-ALBRECHT, J. SCHOTTER, G. A. KASTLE et al., *Science*, **2000**, 290, 2126–2129.
- 24 P. MANSKY, Y. LIU, E. HUANG et al., *Science*, **1997**, 275, 1458–1460.
- 25 K. LIU, S. M. BAKER, M. TOUOMINEN et al., *Phys. Rev. B*, **2001**, 63, 060403(R).
- 26 W. D. WILLIAMS, N. GIORDANO, *Phys. Rev. B*, **1986**, 33, 8146–8154.
- 27 T. M. WHITENEY et al., *Science*, **1993**, 261, 1316.
- 28 W. SCHWARZACHER, K. ATTENBOROUGH, A. MICHEL et al., *J. Magn. Magn. Mater.*, **1997**, 165, 23–29; G. P. HEYDON, S. R. HOON, A. N. FARLEY et al., *J. Phys. D, Appl. Phys.*, **1997**, 30, 1083–1093.
- 29 L. PIRAUX, J. M. GEORGE, J. F. DESPRES et al., *Appl. Phys. Lett.*, **1994**, 65, 2484–2486.
- 30 A. BLONDEL, J. P. MEIER, B. DOUDIN et al., *Appl. Phys. Lett.* **1994**, 65, 3019–3021.
- 31 K. LIU, K. NAGODAWITHANA, P. C. SEARSON et al., *Phys. Rev. B*, **1995**, 51, 7381–7384.
- 32 B. DOUDIN, G. REDMOND, S. E. GILBERT et al., *Phys. Rev. Lett.*, **1997**, 79, 933–936.
- 33 S. VALIZADEH, J. M. GEORGE, P. LEISNER et al., *Thin Solid Films*, **2002**, 402, 262–271.
- 34 Z. ZHANG, X. SUN, M. S. DRESSELHAUS et al., *Appl. Phys. Lett.*, **1998**, 73, 1589–1591; Y. PENG, D. H. QUIN, R. J. ZHOU et al., *Mater. Sci. Eng. B*, **2000**, 77, 246–249; K. HONG, F. Y. YANG, K. LIU et al., *J. Appl. Phys.*, **1999**, 85, 6184–6186; K. LIU, C. L. CHEIN, P. C. SEARSON, *Phys. Rev. B*, **1998**, 58, R14681–14684.
- 35 K. NIELSCH, F. MULLER, A.-P. LI et al., *Adv. Mater.*, **2000**, 12, 582–586.
- 36 A. K. MUKENGA BANTU, J. RIVAS, G. ZARAGOZA et al., *J. Non Cryst. Solids*, **2001**, 287, 5–9.
- 37 G. YI, W. SCHWARZACHER, *Appl. Phys. Lett.*, **1999**, 74, 1746–1748.
- 38 A. BID, K. S. SHANKAR, A. K. RAYCHAUDHURI, submitted.
- 39 M. J. ZHENG, L. D. ZHANG, G. H. LI et al., *Appl. Phys. Lett.*, **2001**, 79, 839–841.
- 40 Y. LI, G. W. MENG, L. D. ZHANG et al., *Appl. Phys. Lett.*, **2000**, 76, 2011–2013.
- 41 A. BALANDIN, K. L. WANG, N. KOUKLIN et al., *Appl. Phys. Lett.*, **2000**, 76, 137–139.
- 42 C. J. BRINKER, G. W. SCHERER, *Sol-Gel Science*, Academic Press, New York 1990.
- 43 K. S. SHANKAR, S. KAR, A. K. RAYCHAUDHURI, *Solid State Communication*, accepted.
- 44 K. S. SHANKAR, S. KARR, A. K. RAYCHAUDHURI, submitted.
- 45 B. B. LAKSHMI, C. J. PATRISSI, C. R. MARTIN, *Chem. Mater.*, **1997**, 9, 2544–2550.
- 46 Y. LEI, L. D. ZHANG, G. W. MENG et al., *Appl. Phys. Lett.*, **2001**, 78, 1125–1127.
- 47 Y. L. SHI, X. G. ZHANG, H. L. LI, *Mater. Sci. Eng. A*, **2001**, 287, 1343–48.
- 48 J. BAO, C. TIE, Z. XU et al., *Adv. Mater.*, **2002**, 14, 44–47.
- 49 Y. ZHOU, *Mater. Sci. Eng. Sect. A*, **2001**, 287, 245–252.
- 50 Y. ZHOU, H. LI, *J. Mater. Chem.*, **2002**, 12, 681–686.

- 51 T. KYOTANI, L. TSAI, A. TOMITA, *Chem. Mater.*, **1996**, 8, 2109–2113; G. CHE, B. B. LAKSHMI, C. R. MARTIN et al., *Chem. Mater.*, **1998**, 10, 260–267.
- 52 J. BAO, Q. ZHOU, J. HONG et al., *Appl. Phys. Lett.* **2002**, 81, 4592–4594.
- 53 G. S. CHENG, L. D. ZHANG, Y. ZHU et al., *Appl. Phys. Lett.*, **1999**, 75, 2455–2457.
- 54 J. ZHANG, L. D. ZHANG, X. F. WANG et al., *J. Chem. Phys.*, **2001**, 115, 5714–5717; L. D. ZHANG, G. W. MENG, F. PHILLIP, *Mater. Sci. Eng. A*, **2000**, 286, 34–38.
- 55 S. L. SUNG, S. H. TSAI, C. H. TSENG et al., *Appl. Phys. Lett.*, **1999**, 74, 197–199.
- 56 K.-K. LEW, C. REUTHER, A. H. CARIM et al., *J. Vac. Sci. Technol. B*, **2002**, 20, 389–392.
- 57 D. M. EIGLER, E. K. SCHWEIZER, *Nature*, **1990**, 344, 524–527.
- 58 M. A. MCCORD, R. F. W. PEASE, *J. Vac. Sci. Technol. B*, **1988**, 6, 293–296.
- 59 J. A. DAHATA, *Science*, **1995**, 270, 1625–1626.
- 60 P. M. CAMPBELL, E. C. SNOW, *Semicond. Sci. Technol.*, **1996**, 11, 1558–1562.
- 61 N. CARBRERA, N. F. MOTT, *Rep. Prog. Phys.*, **1949**, 12, 163–181.
- 62 S. C. MINNE, J. D. ADAMS, G. YARALIOGLU et al., *Appl. Phys. Lett.*, **1998**, 73, 1742–1744.
- 63 T. THUNDAT, L. A. NAGAHARA, P. I. ODEN et al., *J. Vac. Sci. Technol. A*, **1990**, 8, 3537–3541.
- 64 H. SIGUMURA, T. UCHIDA, N. KITAMURA et al., *Jpn. J. Appl. Phys.*, **1993**, 32, L553–L555.
- 65 K. MATSUMOTO, S. TAKAHASHI, M. ISHII et al., *Jpn. J. Appl. Phys.*, **1995**, 34, 1387–1390; K. MATSUMOTO, M. ISHII, K. SEGUWA et al., *Appl. Phys. Lett.*, **1996**, 68, 34–36.
- 66 E. S. SNOW, D. PARK, P. M. CAMPBELL, *Appl. Phys. Lett.*, **1996**, 69, 269–271.
- 67 T. SCHMIDT, R. MARTEL, R. L. SANDSTROM et al., *Appl. Phys. Lett.*, **1998**, 73, 2173–2175.
- 68 K. MATSUMOTO, Y. GOTOH, T. MAEDA et al., *Appl. Phys. Lett.*, **2000**, 76, 239–241.
- 69 J. A. DAGATA, J. SCHNEIR, H. H. HARARY et al., *Appl. Phys. Lett.*, **1990**, 56, 2001–2003.
- 70 E. S. SNOW, P. M. CAMPBELL, *Appl. Phys. Lett.*, **1994**, 64, 1932–1934.
- 71 M. LAZZARINO, S. HEUN, B. RESSEL et al., *Appl. Phys. Lett.*, **2002**, 81, 2842–2844.
- 72 J. W. LYDING, T. C. SHEN, J. S. HUBACEK et al., *Appl. Phys. Lett.*, **1994**, 64, 2010–2012.
- 73 L. TSAU, D. WANG, K. L. WANG, *Appl. Phys. Lett.*, **1994**, 64, 2133–2135.
- 74 A. E. GORDON, R. T. FAYFIELD, D. D. LITFIN et al., *J. Vac. Sci. Technol. B*, **1995**, 13, 2805–2808.
- 75 S. C. MINNE, Ph. FLUECKIGER, H. T. SOL et al., *J. Vac. Sci. Technol. B*, **1995**, 13, 1380–1385.
- 76 P. A. FONTAINE, E. DUBOIS, D. STEVENARD, *J. Appl. Phys.*, **1998**, 84, 1776–1781.
- 77 K. WILDER, C. F. QUATE, D. ADDERTON et al., *Appl. Phys. Lett.*, **1998**, 73, 2527–2529.
- 78 B. LEGRAND, D. STEVENARD, *Appl. Phys. Lett.*, **1999**, 74, 4049–4051.
- 79 K. SUGAWARA, T. GOTOH, K. TANAKA, *Appl. Phys. Lett.*, **2001**, 79, 1549–1551.
- 80 T. YASUDA, S. YAMASAKI, S. GWO, *Appl. Phys. Lett.*, **2000**, 77, 3917–3919.
- 81 E. S. SNOW, P. M. CAMPBELL, H. TWIGG et al., *Appl. Phys. Lett.*, **2001**, 79, 1109–1111.
- 82 C. A. MIRKIN, S. HONG, L. DEMERES, *Chem. Phys. Chem.*, **2001**, 2, 237–39; R. D. PINER, J. ZHU, F. XU et al., *Science*, **1999**, 283, 661–663.
- 83 R. D. PINER, C. A. MIRKIN, *Langmuir*, **1997**, 13, 6864–6868.
- 84 S. HONG, J. ZHU, C. A. MIRKIN, *Science*, **1999**, 286, 523–525.
- 85 S. HONG, C. A. MIRKIN, *Science*, **2000**, 288, 1808–1811.
- 86 S. HONG, J. ZHU, C. A. MIRKIN, *Langmuir*, **1999**, 15, 7897–7900.
- 87 D. A. WEINBERGER, S. HONG, C. A. MIRKIN et al., *Adv. Mater.*, **2000**, 12, 1600–1603.
- 88 A. IVANISEVIC, C. A. MIRKIN, *J. Am. Chem. Soc.*, **2001**, 123, 7887–7889.
- 89 Y. LI, B. N. MAYNOR, J. LIU, *J. Am. Chem. Soc.*, **2001**, 123, 2105–2106.

- 90 L. M. DEMERS, S. J. PARK, T. A. TATON et al., *Angew. Chem. Int. Ed. Engl.*, **2001**, 40, 3071–3073.
- 91 J. A. STROSCIO, D. M. EIGLER, *Nature*, **1991**, 254, 1319–1326.
- 92 D. M. SCHAEFER, R. REIFENBERGER, A. PATIL et al., *Appl. Phys. Lett.*, **1995**, 66, 1012–1014.
- 93 T. JUNNO, K. DEPPERT, L. MONTELIUS et al., *Appl. Phys. Lett.*, **1995**, 66, 3627–3629.
- 94 C. BUAR, B. C. GAZEU, B. E. KOEL et al., *J. Vac. Sci. Technol. A*, **1997**, 15, 1577–1582; T. R. RAMACHANDRAN, C. BUAR, *Nanotechnology*, **1998**, 9, 237–245.
- 95 R. RESCH, A. BUGACOV, C. BAUR et al., *Appl. Phys. A*, **1998**, 67, 265–271.
- 96 M. SITTI, H. HASHIMOTO, International Conference on Advances in Intelligent Mechanotronics, September 1999, Athens, USA, *Proc. IEEE/ASME*, **1999**, 13–20.
- 97 G. SAGVOLDEN, I. GIAEVER, J. FEDER, *Rev. Sci. Instrum.*, **1999**, 70, 2769–2775.
- 98 J. ISRAELACHVILI, *Intermolecular and Surface Forces*, Academic Press, New York 1992.
- 99 M. L. ROUKES, *Phys. World*, **2001**, 14, 25–30.
- 100 W. T. THOMAS, C. W. ZHOU, L. ALESEYEV et al., *Nature*, **2000**, 405, 769–772.
- 101 G. ABDAL, A. BOISEN, Z. J. DAVIS et al., *Appl. Phys. Lett.*, **1999**, 74, 3206–3208.

## Index

### a

- ab initio calculation 365, 567
- ablation
  - laser 255, 309, 311, 313, 315, 318, 332, 336, 343, 365
  - soft ablation technique 540
- acetylene polymerization 563, 574–578
- adamantoid framework 440, 445
- ADH (alcohol dehydrogenase) 673
- adiabatic implosion 115
- adrenaline 676
- adsorption
  - energy 572
  - molecular 559
- AFM (atomic force microscopy) 122, 124, 706, 707
  - cantilever 716
- Ag
  - nanoparticle (*see* silver nanoparticle)
  - colloid 622
  - nanocrystal 61, 63
  - nanowire 273
- Ag<sub>3</sub>CuS<sub>2</sub> 173
- AgGaS<sub>2</sub> 173
- α-Ag<sub>9</sub>GaS<sub>6</sub> 173
- AgNO<sub>3</sub> 157
- AgS 20
- Ag<sub>2</sub>S, cluster 433–436
- AgSe 424
- Ag<sub>2</sub>Se, cluster 436–438
- Ag<sub>7</sub>Te<sub>4</sub> 172
- air separation, non-cryogenic 592
- akaganite 159
- ALH84001 (*see* Mars, life on)
- alloy, nanosized 679
- alluaudite 602
- Al-MCM-41 138, 139
- alumina, porous 267
- aluminium phosphate 595–598
  - AlPO-5 595–596
  - SAPO-n 595
  - ULM-n 597
- amorphous computing 86
- amorphous Fe/Co, nanophased 120
- amphiphilic structure 202
- anatase 141, 144, 248, 704
- annealing 21, 86, 124, 129, 140, 146, 220, 270, 319–326, 334, 342, 343, 350, 361, 362, 366, 398, 410, 491, 529
  - effect of 319
  - extended annealing 319
  - RTA (rapid thermal annealing) 333
  - post implantation 333
  - of SiNWs 343
- anodization 693, 709
- antiferromagnet 464
- anti-tumor agents 529
- aspect ratio 285, 287, 288, 290, 297, 299–305
- ATR-FTIR spectra silicon nanowire 342
- Au
  - nanoassembly 631
  - nanoparticle (*see* gold nanoparticle)
  - nanowire 270
  - polymer-stabilized 156
- Au<sub>n</sub><sup>–</sup> 556
- Au<sub>n</sub> nanocrystal 56, 61
  - two-dimensional arrays of size selection 63
- Au<sub>2</sub><sup>–</sup> 557, 559
- Au<sub>2</sub>(CO)O<sub>2</sub><sup>–</sup> 557, 559
- Au<sub>2</sub>O<sub>2</sub><sup>–</sup> 560
- Au<sub>3</sub>Sr/MgO(F5c) 574
- Au<sub>4</sub> 572, 573
- Au<sub>6</sub><sup>–</sup> 556
- Au<sub>8</sub> 568, 572
- Au<sub>10</sub><sup>–</sup> 556
- Au<sub>11</sub> 556
- (Au<sub>13</sub>)<sub>55</sub> 73



- Au<sub>15</sub> 556  
 Au<sub>19</sub> 556  
 Au<sub>55</sub> 56, 64  
 Au<sub>55</sub>(PPh<sub>3</sub>)<sub>12</sub>Cl<sub>6</sub> 56  
 Auger electron spectroscopy 552  
 autoclave 106, 170, 176  
 autooxidation 603  
 azodicarbonamide 137
- b**
- B<sub>4</sub>C (boron carbide), synthesis 189–192  
 BaCrO<sub>4</sub> 297  
 BaFe<sub>12</sub>O<sub>19</sub> 132  
 BaTiO<sub>3</sub> 109, 158, 162  
 Ba<sub>6</sub>Ti<sub>17</sub>O<sub>40</sub> 162  
 BaZrO<sub>3</sub> 162  
 bacterial strains, *Gram* positive/negative 536  
 band gap 175, 310, 355, 371, 372, 376, 383, 390, 392, 441, 443  
 – blue-shift 175, 274, 299–300, 372, 402, 441  
 – bulk 384  
 – closure 78, 79  
 – energy 621  
 – excitation 621  
 – red shifted 380, 386  
 – tuning 380  
 Beer-Lambert law (*see* Lambert Beer Law) 105  
 benzene (*see* C<sub>6</sub>H<sub>6</sub>)  
 Berzelius 551  
 betaine 103  
 BiTel 172  
 bias, pulsed mode 710  
 bilayer, metallic 699  
 binary metal oxides 158, 607, 608  
 binding energy 559, 563, 565, 571  
 bioassembly, nanoparticles 680  
 biocompatible nanoparticles 405  
 bioconjugation 410–413  
 biomineralization 462  
 biosensor 670–674  
 Blakemore's demonstration 96  
 block copolymer 476, 477, 697, 698  
 – morphology 484–486  
 – rod-coil diblock 502–507  
 block-selective solvent 477, 493  
 blue oxide (*see* molybdenum oxide)  
 BN  
 – nanotube 190, 244  
 – synthesis 189–192  
 Bohr exciton radius 371, 374, 385, 406, 441  
 bond angle constraints 481  
 bond-selected chemistry 583  
 borides, synthesis 189–192  
 borosilicate 594  
 bottleneck tubule 657  
 bottom-up routes 688  
 BP (boron phosphide), synthesis 189–192  
 brass, as microwave reflector 153  
 BRCA1 gene 674  
 breast cancer 674  
 breathing cycle 648, 649  
 Brillouin zone 386  
 BrNR<sub>4</sub>X 116  
 brookite 141, 144  
 Brunauer-Emmett-Teller (BET) analysis 521  
 Brust  
 – protocol 32  
 – synthesis 677  
 BSA (bovine serum albumin) 47  
 – simultaneous separation and detection 536  
 building block 422  
 – molybdenum 454
- c**
- C-13 NMR spectroscopy 145  
 C<sub>60</sub> 208, 220  
 CH<sub>3</sub>(CH<sub>2</sub>)<sub>12</sub>N(CH<sub>3</sub>) 116  
 CH<sub>3</sub>(CH<sub>2</sub>)<sub>17</sub>SiH<sub>3</sub> 145  
 C<sub>2</sub>H<sub>2</sub> 564  
 C<sub>6</sub>H<sub>6</sub> 43, 564, 565, 574, 575  
 CnH<sub>2n+1</sub>NH(CH<sub>2</sub>)<sub>2</sub>NH<sub>2</sub> 142  
 CCl<sub>4</sub> 128  
 CCVD (catalytic chemical vapor deposition) 214  
 CD (cyclodextrin) 40  
 CO, oxidation to CO<sub>2</sub> 561, 563, 565, 566, 569  
 α-CaCr<sub>2</sub>O<sub>4</sub> 159  
 calcification, porous silicon 527  
 cancer therapy, hyperthermic 109  
 capacitance 660–662  
 capacitor 154, 660  
 carbanions 479  
 carbide, synthesis 181–185  
 carbon XC-72 157  
 carbon matrix, sonochemical synthesis of encapsulated nanometals 127–129  
 carbothermal reaction 260–262  
 carrier gas 309, 327  
 – helium 327  
 – N<sub>2</sub> 327  
 – effect 327  
 Cassius, Andreas 95  
 catalysis (*see* nanocatalysis)  
 catalyst 620  
 – ensemble effect 679

- catalytic
  - cycles 561
  - reaction, turn-over frequency 578–581
  - selectivity, changing 574–578
- cathode, cold 350
- $\text{Cd}_x\text{Mn}_{1-x}\text{S}$  54
- $\text{Cd}_3\text{P}_2$  20, 22
- $\text{CdS}$  6, 7, 13, 14, 19, 20, 23, 24, 31, 42, 43, 52, 196, 201, 250, 373
  - $\text{CdS}$ -ferritin 25
  - cluster 438–444
  - Mn-doped 380
  - triangular 57
  - Zn-passivated 391, 392
- $\text{CdSe}$  6, 14, 20, 21, 24, 31, 52, 57, 65, 66, 149, 202, 250, 378
  - emission spectra 53
  - nanorod 57
  - neat preparation 22
  - spaced with PPV 73
- $\text{Cd}_2\text{S}_2$  core 193
- $\text{Cd}_{10}\text{S}_4(\text{SPh})_{16}$  55
- $\text{Cd}_{17}\text{S}_4(\text{SCH}_2\text{CH}_2\text{OH})_{26}$  56, 84
- $\text{Cd}_{32}\text{S}_{14}(\text{SC}_6\text{H}_5)_{36}(\text{DMF})_4$  55
- $\text{Cd}_{32}\text{S}_{14}(\text{SCH}_2\text{CH}(\text{CH}_3)\text{OH})_{36}$  56, 84
- $\text{CdInS}_2$  173
- $\text{CdS}_x\text{Se}_{1-x}$  54
- $\text{CdTe}$  nanocrystal 58
- $\text{CeO}_2$  105, 106, 110, 146, 160
- $\text{CeO}_{2-x}$  109
- ceramics 153
- chabazite (CHA) 597
- chalcogen, zerovalent 419
- chalcogenide
  - cluster 438–444
  - ligands 418, 419
  - – nickel 419–423
  - nanoparticle 95
  - – one-dimensional metal 193–198
  - – room temperature synthesis 170
  - nanophased 156
- chalcogenolate ligands, flexibility 418
- charge injection, sensitized 621
- charge transfer
  - interfacial 632
  - resistance 648
- charging effects, quantized 662
- chemical sensor 310, 674–678
- chemical valving effect 489
- chiral angle/vector 218
- chloroform 43
- cholesterol esterase (CE) 673
- cholesterol oxidase 673
- chromatography, size exclusion 217
- chromophore, redox 629
- cis-platin 529
- clinoptilolite (HEU) 592
- cloverite 599
- cluster
  - $\text{Ag}_2\text{S}$  433–436
  - $\text{Ag}_2\text{Se}$  436–438
  - Au, alkanethiolate stabilized 651
  - capacitance 661
  - $\text{CdS}$  438–444
  - chalcogenide 438–444
  - cold 566
  - compounds 56
  - copper tellurium 431
  - free cluster, synthetic way 555–562
  - $(\text{H}_2\text{O})_{20}$  cluster 472
  - $(\text{H}_2\text{O})_{60}$  cluster 472
  - $(\text{H}_2\text{O})_{100}$  cluster 470, 472
  - ‘magic number’ 56
  - molecules-to-cluster-to-solids pathway 420
  - monolayer-protected 651
  - nano-porous 452
  - size-distributed 580, 581
  - superclusters 73–75
  - supported 562–581
- CMC (critical micellar concentration) 267, 484
- CMR (colossal magnetoresistance) 95
- Co 116
  - nanocrystal 64
- $\text{Co}(\text{CO})_3\text{NO}$  138
- $\text{CoFe}_2\text{O}_4$  23, 160
- $\text{CoFe}_2\text{O}_4$  99, 101, 106
- $\text{Co}_3\text{O}_4$  143
- $\text{Co}_3\text{O}_4$  147
- $\text{Co}_2\text{P}/\text{CoP}$  189
- $\beta$ -cobalt hydroxide 144
- cobalt succinate 614
- coercivity 127
  - magnetic nanoparticles 80
- cognitive isomorphism 468
- cohesion energy 359
- colloidal
  - crystals 75, 77
  - MPC (monolayer protected colloidal particles) 32
  - sol 51
  - systems 469
- comb stabilizer 35
- computer circuits, self destructing 540
- conduction band (BCB) 371, 372, 378, 379, 400, 406, 621
- confined electrons 582
- confinement regime 385

- coordination polymer 590, 609–612
  - copper phosphate 603–605
  - copper tellurium cluster 431
  - core-shell CdSe/ZnSe particle, molecular limit 444
  - core-shell nanocrystal 59, 64, 68
  - Cottrell* behavior 668
  - Coulomb*
    - blockade 9
    - energy 567
    - stair-case model, semi-classical 659, 660, 662
  - cryptomelane 608
  - crystal field 381
    - strength 382
  - crystal growth 461
    - temperature effect, on crystal growth 151
  - crystallization process 18, 152, 170
  - CTAB (cetyltrimethylammonium bromide) 47, 142, 290–294, 297, 510
    - bilayer 304
    - pinholes 304
  - CTAT (cetyltrimethylammonium toluene sulfonate) 511
  - CuFeS<sub>2</sub> 173
  - CuGaS<sub>2</sub> 173
  - Cu(N<sub>2</sub>H<sub>3</sub>COO)<sub>2</sub>·2H<sub>2</sub>O 116
  - CuO 147, 162
  - Cu<sub>2</sub>O 103, 116, 126, 297
  - Cu<sub>3</sub>O<sub>4</sub> synthesis 146
  - Cu<sub>3</sub>P 189
  - CuSe 424
  - Cu<sub>2</sub>Se
    - $\alpha$ -Cu<sub>2</sub>Se 426
    - cubic 425
    - layered 424–426
    - spherical 426–430
  - Cu<sub>2x</sub>Se 23
  - Cu<sub>44</sub>Se<sub>22</sub>(PEt<sub>3</sub>Ph)<sub>18</sub> 428
  - Cu<sub>70</sub>Se<sub>35</sub>(PEt<sub>3</sub>)<sub>21</sub> 425
  - Cu<sub>70</sub>Se<sub>73</sub>(PR<sub>3</sub>)<sub>21</sub> 427
  - Cu<sub>147</sub>Se<sub>73</sub>(PEt<sub>3</sub>)<sub>22</sub> 55
  - cupferron 103, 106
  - current induced changes 701
  - curvature
    - negative 219, 460
    - positive 460
  - CVD (chemical vapor deposition) 23, 27, 181, 212, 225, 235, 247, 255, 262, 704–706
    - HFCVD (hot filament chemical vapor deposition or thermal evaporation) 335, 365
    - MOCVD (metal organic chemical vapor deposition) 12, 103, 271
    - plasma assisted 706
    - CCVD (catalytic chemical vapor deposition) 214
  - cyclobis (paraquat-*p*-phenylene) 675
  - cyclotrimerization 563, 577
    - acetylene 574
  - cysteine 678
  - cystine 460
- d**
- D4R (double 4-ring) cage, in zeolites 598
  - D-band 222
  - d-I* phase diagram, Pd nanocrystal 71
  - DBM (dibenzoylmethane) 147
  - DBS (dodecylbenzenesulfonate) 117
  - dead chains 478
  - Debye-Scherrer* equation 137, 373
  - decalin 115, 120, 121, 122, 138
  - decane 132
  - decomposition, heterolytic 552
  - dehydrocyclodimerization 605
  - dendron 506
  - dense device, highly 358
  - density of states 4
  - designed assembly 293, 298
  - DFT (density functional theory) calculations 315
  - diameter control, nanowire 326–328
  - diamond, synthesis 181–185
  - dibenzoylmethane 147
  - dielectric 96
    - heating, microwave 154
    - loss 155
    - material 153
    - molecule, low 662
    - polarization 154
  - diffraction data, X-ray 128
  - DIOS-MS (desorption/ionization on silicon mass spectrometry) 540–545
    - infrared (IR-DIOS-MS) 544
  - diphosphonate 611
  - dissolution, anodic 694
  - disulfide linkage 398
  - dithiothreitol 411
  - DLS (dynamic light scattering) 497, 500
  - DMAP (4-dimethylaminopyridine) 44, 46
  - DMF (dimethylformamide) 125, 127
  - DNA chip 9
  - DNA hybridization detection 413
  - DNT (dinitrotoluene) 536
  - DODAC (dimethyldioctadecylammoniumchloride) 511
  - dodecahedron 470

- dopamine 676
  - separation 671
- DOS (density of state) 387, 391, 394
  - local 79
  - partial 387
- double diamond superlattice 440
- double layer charging effect, quantized 631, 660
- DPhM (diphenylmethane) 129, 146
- DPN (dip pen nanolithography) 712–716
  - ink 742
  - molecular transport 714
  - multiple ink 713
  - patterning 714
  - writing 714
- DRIFT (diffuse reflectance infrared *Fourier* transform) 524
- drug carrier 507
- drug delivery, magnetic 109
- DS (dodecylsulfonate) 101
- DSC (differential scanning calorimetry) 134
- DSSC (dye-sensitized solar cells) 146
- DTAB (dodecyltrimethylammoniumbromide) 117
- DTAC (dodecyltrimethylammoniumchloride) 117
- dye assembly, semiconductor-organic 628
- e**
- EDAX (*see* EDX)
- eddy currents 155
- EDS (*see* EDX)
- EDX (energy dispersive X-ray) 138, 312, 330, 337, 521
- EELS (electron energy loss spectroscopy) 330, 337, 521, 553
- effective mass approximation 384, 385
- eigenvalue spectra 387
- electrocatalysis 649, 678–681
- electrochemical etching 519
- electrochemistry 646–681
  - electrocatalysis 678
  - metallic nanoparticles 649–657
  - nanosensors 670–678
  - preparation, nanostructures 647–649
  - single electron events 657–664
- electrochromic effects 627
- electrode
  - boron-doped 679
  - disk electrode, Pt rotating 660, 678
  - ensembles 653–657
  - indium tin oxide (ITO) 647, 668
  - Ir-Pt 658
  - optical transparent thin layer 667
  - sonoelectrode 149, 152
  - templated 653
- electrodeposition 695, 698–702
- electromagnetic radiation 152
- electromechanical actuators (nanotube) 228
- electromigration 701
- electron
  - diffusion 663
  - floodgun, low energy 400
  - hopping 663
  - transfer, kinetics 667
- electron-phonon relaxation 623
- electron-phonon coupling 382
- electronic structure calculation 383–393
- Eley-Rideal (ER)* mechanism 559
- EMA (effective mass approximation) 384–387
  - equation 390
  - IP-EMA (infinite potential effective mass approximation) 385, 392, 402
- endohedral functionalization 460
- EOLYS TM (*see also* CeO<sub>2</sub>) 110
- epitaxial casting 245
- EPR (electron paramagnetic resonance) 130, 131
- Eu<sub>2</sub>O<sub>3</sub>-TiO<sub>2</sub> nanocomposite 134
- europium-doped yttrium oxide 102
- evaporation
  - laser 182, 555, 562, 566
  - thermal 365
- exciton
  - definition 406
  - excitonic peak 374
- f**
- F/F<sup>+</sup> center 552, 553, 555, 562, 565
  - binding energy 564
- Fabry-Pérot* fringes 520, 532
- Faraday, Michael* 51, 94, 646
- “Farbe” 552
- fast flow reactor kinetics 555
- faujasite (FAU) 590, 591, 594
- Fe 115, 116
- Fe(CO)<sub>5</sub> 102, 118, 121, 125
- Fe<sub>4</sub>N 147
- Fe<sub>20</sub>Ni<sub>80</sub> 120
- Fe<sub>40</sub>Ni<sub>60</sub> 120
- Fe<sub>60</sub>Ni<sub>40</sub> 120
- β-FeOOH 159
- Fe<sub>2</sub>O<sub>3</sub> 115, 129, 130, 158
- Fe<sub>3</sub>O<sub>4</sub> 66, 130, 147, 159
- FeP 189
- Fe-Pt nanoparticles 109
- (Fe<sub>20</sub>Se<sub>38</sub>)<sup>18-</sup> 419

- $\alpha$ -Fe<sub>2</sub>O<sub>3</sub> 159
- $\gamma$ -Fe<sub>2</sub>O<sub>3</sub> 86, 96, 98, 99, 102, 103, 106, 109, 118, 159
- FEED (field-emitted electron energy distribution) 235
- Fermi*
  - energy 650
  - level 355, 392
  - – equilibration 634, 635, 668
  - – local density of state 664
- ferragels 650
- ferrite spinels 98
- ferrocene 153, 651, 655
- ferroelectrics 96
- ferromagnet, half-metallic 392
- ferrosilicate 594
- field emission 310, 350, 351
- films, semiconductor oxide 630
- filter, molecular 656
- flat panel display application 234, 235
- Flory-Huggins* interaction parameter 485, 502
- flow tube reactor kinetics 555
- flow-hydrothermal conditions 106
- fluorescence spectroscopy 377–383
- fluorescence-emission spectra 381
  - Eu-doped ZnS 382
- fluoroferrophosphate 602
- fluorophore 622, 625, 626
  - functionalized electrodes 631
- fluxionality, structural dynamical 572, 573
- foldamers 481
- form factors, symmetric/antisymmetric 386
- form-function relationship 457–465
- Fowler-Nordheim* (FN)
  - curve 350
  - plot 235, 351
  - theory 350
- Frank-Kasper* polyhedra 431
- FTIR (*Fourier* transform infra-red) 41, 122, 130, 142, 524
  - study, HF-dipped silicon nanowire 341
- fullerene 208, 454, 634
  - fullerene-like structure 135, 152
  - inorganic 135
  - thiol derivatives 626
- funnel effect 567
- furnace, three-zone 705
- FWHM (full-width at half maximum) 407
- g**
  - G-band 222
  - GaAs 22, 310
    - Mn-doped 392
  - GaCl<sub>3</sub> 134, 135
  - Ga<sub>1-x</sub>Mn<sub>x</sub>As 392
  - GaN 175, 310
    - nanowire 260
    - powder 177
    - wurtzite-type 176
  - GaO(OH) 115, 134
  - GaP 175, 310
  - GaI<sub>3</sub> 176
  - gallium phosphate 598, 599
  - gallophosphate 598
  - gallosilicate 594
  - gas sensing application 345
  - gas sensor, amperometric 677
  - Gaussian*
    - curves 397, 407
    - doublet 396
    - full width at half maximum 396
    - interparticle distances 294
    - spacing 295
  - Gd(NO<sub>3</sub>)<sub>3</sub> 539
  - Ge 310
  - gelatin 152
  - Gemini* surfactant 142
  - gene gun 9
  - Gibbs surface* excess 120
  - Gibbs-Thomson* effect 321
  - gismondine (GIS) 597
  - glass 153
    - glass former 129
    - transition temperature 480
  - glutathione 411
  - GMR (giant magnetoresistance) 699
  - gold colloid 52, 118, 120, 623
    - citrate-stabilized 671, 674
    - ruby red color 646
  - gold nanoparticle 140, 155, 669
    - C<sub>60</sub>-functionalized 652
    - crosslinked 676
    - hydrophobization 40
    - in water 43–48
    - isotropic 290
    - optical properties 35
    - synthesis 31, 32
      - – organic-solution-based 33, 34
      - – water-based 33
    - thionicotinamide capped 624
    - UV-vis spectra 46
  - graphite, highly oriented pyrolytic (HOPG) 353, 356, 543, 649, 678
  - growth process 18, 19, 55, 151, 196, 310
    - anisotropic 289, 291
    - control 273, 274
    - GaAs nanowire 337
    - isotropic 291

growth process (cont.)  
 – oxide-assisted 259, 328  
 – – discovery 311–314  
 – – mechanism 316, 317  
 – – morphology control 319–326  
 – – silicon-based nanowires 308–368  
 – – versus metal catalyst VLS growth 318  
 – solution based 265, 266  
 – twin-plane mechanism 331  
 – vapor-liquid-solid (VLS) 256–259  
 – vapor-solid 259, 260  
 guanadinium  
 – as guests 468  
 – as organic template 610

## h

(H<sub>2</sub>O)<sub>20</sub> cluster 472  
 (H<sub>2</sub>O)<sub>60</sub> cluster 472  
 (H<sub>2</sub>O)<sub>100</sub> cluster 470, 472  
 H<sub>2</sub>PtCl<sub>6</sub> 117, 128  
 halides 607  
 Hamaker constant 70  
 Hamiltonian 386, 387  
 – crystal orbital *Hamiltonian* overlap (COHP) 388  
 – matrix 389  
 hard colloidal rods 293  
 Hartree-Fock perturbation 365  
 Helium, as carrier gas 327  
 Helmholtz capacitance 631  
 hematite 159, 160  
 heptadecane 104  
 heptagon 219  
 HEU (clinoptilolite) 592  
 hexadecane 115, 118  
 hexafluoroacetylacetone 147  
 hexamethylenetetramine 146, 160  
 hexanedithiol 395  
 HFAA (hexafluoroacetylacetone) 147  
 HFCVD (hot filament chemical vapor deposition or thermal evaporation) 335, 365  
 Hg<sub>n</sub> nanoparticles 78  
 HgS 20  
 Hg<sub>32</sub>Se<sub>14</sub>(SeC<sub>6</sub>H<sub>5</sub>)<sub>36</sub> 56  
 high-silica material, direct synthesis 594  
 high-TC superconductivity 95  
 histidine 411  
 HMDS (hexamethyl disilazane) 715  
 hole scavenger 628  
 hole, photogenerated 633  
 hollandite 608  
 homopolymer contamination 480  
 honeycomb, porous alumina 694

HOPG (highly oriented pyrolytic graphite) 353, 356, 543, 649, 678  
 horseradish peroxidase 671  
 hot electron 624  
 hot spot mechanism 114  
 Huang-Rhys parameter 382  
 hureaulite 602  
 hybrid  
 – material 469  
 – metal oxides 612–614  
 – structure 308  
 hydrazine 116  
 hydrolysis 98–101  
 – forced 161  
 hydrophobization, nanoparticle 34, 40  
 hydrothermal method 22, 23, 172  
 hydrothermal route, microwave 159  
 hydroxyapatite, porous silicon 527, 528

## i

icosahedral sphere 470  
 icosidodecahedron 456  
 IgG (immunoglobulin G) 674  
 image charge, induced 567  
 immunoassay 413  
*in situ* catalyst 110  
 InAs 21  
 InCl<sub>3</sub> 134, 135, 173  
 In(OH)<sub>3</sub> 135  
 In<sub>2</sub>O<sub>3</sub> 268  
 indium phosphate 598, 599  
 ink, for DPN (*see also* DPN) 712  
 inorganic-organic hybrid probe, in fluorescence spectroscopy 625  
 InP 21, 175  
 – ZnS passivated 398  
 InSb 180  
 impurity-doping effect 573, 574  
 interferometry, laser 532  
 – sensor 533  
 intra-chain inter-segment interaction 481  
 intra-chain self-assembly 484  
 inverted micelle method 54  
 ion  
 – cyclotron resonance 555  
 – etching, reactive (RIE) 696, 711  
 – gating 677  
 – implantation 333  
 – tracks, etched 692  
 – transport, selective 656  
 ion-trap experiment 555  
 IP-EMA (infinite potential effective mass approximation) 385, 392, 402  
 Ir, polymer-stabilized 156

- iron (*see* Fe)
- iron oxide, amorphous 130
- iron phosphate 601, 602
- irradiation
  - $\gamma$ -ray 198, 203
  - laser pulse 624
  - time 134
  - ultrasonic 178
- isodurene 115
- isomorphism, cognitive 468
- isotropic material 197
  
- j**
- J-E* curves [*see also* Fowler-Nordheim (FN) plots] 351
  
- k**
- $K_2PdCl_4$  117
- $K_2(Pt(CN)_4)$  266
- Kagome lattice 608
- Keggin anions 463
- Keplerate 463, 465, 467
- KEVLAR™ 488
- kinetic energy distribution 566
- $KNbO_3$  158
- Knight shift 665
- Kubo gap 3, 5
  
- l**
- $La_{0.7}Ba_{0.3}MnO_3$  159
- $LaNiO_3$  143
- labeling, biological 405–416
  - fluorescent 408
- Lambert Beer Law 105
- Lanczos algorithm 389
- Langevin dynamics 566
- Langmuir-Blodgett film 54, 469
- Langmuir-Hinshelwood mechanism 559, 569
- LAPS (light-addressable potentiometric sensors) 539
- laser 80
  - ablation 255, 309, 311, 313, 315, 318, 332, 336, 343, 365
  - evaporation 182, 555, 562, 566
  - excimer 311
  - interferometry 532, 533
  - pulse irradiation 624
  - pyrolysis 99
  - QD-based 415
- lattice
  - contraction 361
  - expansion 364
  - phonon 406
- layer-rolled structure 197
- LCR circuits 96
- LCST (low critical solution temperature) 499
- LDA equation 386
- LDOS (local density of states) 355, 570
  - $E_f$ -LDOS 667
- LFM (lateral force microscopy) 712
- $Li_2O$  137
- ligand solvents 194
- light-emitting device 175
- $LiNbO_3$  171
- Lindemann theory 557
- liquid crystalline 201, 469
  - arrays 297
  - thermotropic phase 505
- liquid water, snap-shot 470
- lithiation-delithiation 137
- lithium ion cell 136
- lithographic template 491
- lithography (*see* nanolithography)
- $Li_xCoO_2$  137
- LMTO (linearized muffin tin orbital) 390
- LSM (lanthanum strontium manganate) 143
- LTMC (layered transition metal chalcogenide) 241, 242
- luminescence efficiency 409
- luminescent labels 405
- Luttinger-Kohn Hamiltonian 385
- lysis experiment 511
  
- m**
- M41S family 590
- M50 steel powder 121
- ‘magic number’, in cluster compounds 56
- magnetic data storage 286
- magnetic nanoparticles, coercivity 80
- magnetite 96, 97, 159
  - biogenic 97
  - biomineralization 97
- magnetoreception 96
- magnetoresistance (*see* GMR, CMR)
- magnetotactic spirillum 96
- magnetotaxis 96
- MALDI-MS (matrix assisted laser desorption ionization mass spectrometry) 463, 466, 540
- Marangoni effect 68
- Mars, life on 97
- mass spectrometry
  - matrix assisted laser desorption ionization mass spectrometry (MALDI-MS) 463, 466, 540
  - desorption/ionization on silicon mass spectrometry (DIOS-MS) 540–545
  - secondary ion mass (SIMS) 521

- mass spectrometry (cont.)
  - surface-assisted laser-desorption ionization mass spectrometry (SALDI-MS) 543
- matrix 24, 25
  - carbon matrix, sonochemical synthesis of encapsulated nanometals 127–129
  - electropolymerized 648
  - *Hamiltonian* 389
  - Ni matrix 126
  - nonablative 540
  - zeolite Y 24
- Maya blue paint 94
- MCM-41 (zeolite) 138–140, 267
- membrane
  - alumina 691, 693–695
  - MCM-41 138–140
  - MSP (mesoporous) materials 138
  - polycarbonate 654
  - polymeric 691
- MEMS (micro electromechanical systems) 9, 540
- mercapto compounds 411
- mercaptoethanol 201, 202
- mercaptoposilane 647, 650
- mesitylene 128
- mesophases
  - inverted 507
  - lyotropic 493–495
- MSP (mesoporous) materials 138, 590
  - M41S family 590
  - MCM-41 138–140, 267
  - *Mobil's* discovery 590
  - sonochemical synthesis 137–142
    - – silica 137
    - – SnO<sub>2</sub> 142
    - – titania 138, 141
  - zeolites 589–595
- metal
  - insulator, transition 393
  - – size-induced 78
  - nano-dispersed 13
  - nanoparticle 95
  - nitride, synthesis 186–189
  - pnictides 446, 447
- metal aluminiumphosphates 595
- metal silicoaluminiumphosphate 595
- metathesis reaction 103, 104
  - solid-state 175, 176
- methanol 116, 553
  - adsorbed on MgO 555
  - TDS spectra 554
- methylacrylate 125
- MEVVA (metal vapor vacuum arc) 333
- MFM (magnetic force microscope) 233
- MgCr<sub>2</sub>O<sub>4</sub> 159
- MgO
  - EELS 554
  - film 562, 565
  - MgO/Mo(100) thin film 566, 580
- MgO(F<sub>5c</sub>) 568
- MgO(F<sub>5c</sub>)/Au<sub>8</sub> catalyst 571, 573
- micelle 484
  - core-crosslinked 494
  - critical micelle concentration (CMC) 267, 484
  - cylindrical 269
  - formation 496
  - inter-micellar crosslinking 499
  - reverse 507
  - rod-like 501
  - shell-crosslinked 494
  - star 495
- micro enzyme reactor ( $\mu$ IMERS) 531, 532
- micro-twins 312
- microemulsion 106
- micrograph, polarizing optical 295
- microwave
  - absorber 153
  - reflector 153
  - transmitter 153
- microwave heating 113, 152–163
  - inorganic material 153
  - organic chemistry 153
  - solid-state reaction 153
- Mie theory, on scattering 35, 52, 140, 668
- MnFe<sub>2</sub>O<sub>4</sub> 23, 99, 101, 160
- Mn<sub>2</sub>O<sub>3</sub> 130
- MnS 376
- Mo<sub>17</sub> 453
- Mo<sub>36</sub> 453
- Mo<sub>132</sub> 452, 456, 458, 467
- Mo<sub>154</sub> 452, 454, 459
- Mo<sub>176</sub> 452, 458, 461, 462
- Mo<sub>248</sub> 462
- Mo<sub>368</sub> 452, 454, 459
- Mo(CO)<sub>6</sub> 130, 138
- Mo<sub>6</sub>O<sub>6</sub> 461
- Mo<sub>9</sub>O<sub>9</sub> 456
- MoS<sub>2</sub> 152, 172
  - nanotube 243, 254
- Mo<sub>57</sub>V<sub>6</sub> 453
- Mobil's* discovery 590
- MOCVD (metal organic chemical vapor deposition) 12, 103
- MOF-5 (metal organic framework) 610
- molecules-to-cluster-to-solids pathway 420
- Møller-Plesset perturbation level 365
- molybdenum blue, 452



- molybdenum chalcogenide 265  
 molybdenum oxide 130, 131  
 molybdenum oxide based structure 612  
 molybdenum phosphate 600, 601  
 monodisperse nanoparticles 95  
 Moore's law 1  
 morphology  
   – change 622  
   – control 308  
 Mössbauer  
   – spectroscopy 120, 129–131  
   – spectrum 120, 160  
   – studies 99  
 motor, molecular 9  
 Mott mechanism 707  
 Mott-Hubbard metal-insulator transition 83  
 MP-11 (microperoxidase-11) 671  
   – MP-11/Au layered superstructure 672  
 MPC (monolayer protected colloidal particles) 32  
 MRI (magnetic-resonance-imaging) 77  
   – functional 109  
 MS-1 (*Magnetotactic spirillum* unclassified) 96  
 MUA (mercaptoundecanoic acid) 47  
 mutinaite 594  
 Mysterium Cosmographicum, *Kepler* 465
- n**
- NaN<sub>3</sub> 176  
 Na<sub>2</sub>S 102, 422  
 NAD (nicotinamide adenine dinucleotide) 673  
 nanoaggregate, self-limiting 503  
 nanoantiferromagnets 462  
 nanoball 468  
 nanobelt 262  
 nanocable 202, 308, 332  
 nanocages 500–502  
 nanocapacitor 650  
 nanocapsule 497  
 nanocatalysis 551–586  
   – definition 551  
   – gold, strontium-doped 567–574  
 nanochain, silicon (SiNC) 325  
   – B-doped 350  
 nanochannel glass 653  
 nanocomputing 86  
 nanoconfinement 509  
 nanocrystal 4, 51–88, 95, 107, 361, 364  
   – core-shell semiconductor, for biological labeling 405–416  
   – formation 410  
   – GaAs 22  
   – InAs 21  
   – InP 21  
   – passivated 409  
   – programmed assemblies 61–76  
   – red-shifted emission 379  
   – semiconductor 54, 371–402  
   – size distribution 375  
   – synthesis strategies 53–61  
 nanodrop, water 471  
 nanoelectronics 8, 9, 401  
 nanofactory 32  
 nanofiber 203, 487  
 nanolithography 688–720  
   – dip pen (DPN) 712–716  
   – fabrication of nanostructures in the template 697–706  
   – optical and e-beam 689, 720  
   – scope 689  
   – template fabrication 690–697  
 nanomagnet 464  
 nanomanipulation 688–720  
   – scheme 718  
   – use of SPM 716–718  
 nanomaterials 1  
   – amorphous 158  
   – applications 8  
   – environmental cleansing 11  
   – investigation 2  
   – synthesis 2, 18, 26  
 nanometals, sonochemical fabrication 116–118  
 nanooxidation, SPM-based 708  
 nanophase materials 96  
 nanopillars 75  
 nanoporous material 589–615  
   – cluster 452  
   – hybrid 608–614  
 nanopowder 8  
   – synthesis 26  
 nanoreaction vessel 707  
 nanoreactor 459, 469  
 nanoribbons 308, 309, 318, 330–332, 506  
   – morphology 330  
   – silicon 309, 330–332  
   – SnO<sub>2</sub> 340  
   – ZnO 341  
   – ZnS 340, 341  
 nanorod 31, 57, 147, 285  
   – Au 52, 295  
   – CdIn<sub>2</sub>S<sub>4</sub> 193  
   – CdWO<sub>4</sub> 170  
   – DNA-linked 298  
   – inorganic, synthesis 287–293  
   – magnetite 101, 131  
   – metal, covered by carbon 269

- nanorod (cont.)
  - SiC 183
  - Si<sub>3</sub>N<sub>4</sub> 187
  - Sn<sub>4</sub>P<sub>3</sub> 188
- nanosensor 620, 670–678
- nanosheet 262
- nanosphere 456, 487
  - inorganic 286
  - porous 495, 496
  - surface 452
  - water dispersible 495, 498
- nanosponge 452, 468
- nanostucture, mushroom-shaped 503, 505
- nanostuctured landscape 459
- nano-super-supramolecular chemistry 452
- nanotechnology 1 ff.
  - sources of information 27
- nanotube 208–275, 489, 490
  - carbon 148, 210–239, 309, 348
  - – aligned bundles
    - – – crop circles 220
    - – – synthesis 212–214
    - – chemically modified 224–227
    - – electronic structure/properties/devices 227–239
    - – field emission 234–236
    - – formation, mechanism 222, 223
    - – hydrogen storage 238, 239
    - – limitation 309
    - – molecular sensor 237
    - – multi-walled (MWNT) 182, 209–269
    - – – synthesis 210, 211
    - – robotics 236
    - – sensors and probes 233, 234
    - – single-walled (SWNT) 128, 209, 214–271
    - – – synthesis 214–217
    - – structure/characterization 217–222
    - – synthesis 181–185
    - – Y-junction 231
  - inorganic 239–254
  - properties 253, 254
  - structures 246–253
  - synthesis 244–246
  - silicon 361
- nanowindow 470
- nanowire 31, 75, 171, 180, 255–275, 285, 693
  - CdS 193
  - core-shell 265
  - GaAs 337
  - GaN 339
  - GaP 339
  - Ge 256
  - magnetic tunnel junction 700
  - polyaniline 695
  - properties 274, 275
  - silicon, metalized (SiNW) 308
  - – chemical properties 340–347
  - – chemical sensing 345–347
  - – Co implanted 334
  - – diameter control 326–328
  - – large area aligned 328–330, 350
  - – modeling 359–365
  - – morphology evolution 324, 354
  - – nucleation scheme 316
  - – one-dimensional 322
  - – optical/electrical properties 347–358
  - – oriented, synthesis 334, 335
  - – thinnest stable short 361
  - silicon, oxide assisted growth 308–368
  - synthetic strategies 255–274
  - – inorganic 287–293
  - – solution-liquid-solid process 271–273
  - – template-based 266–271
- NEMS (nanoelectromechanical systems) 8, 9, 718–720
  - CNT (carbon nanotubes) 719
- Nernst equation 661, 663
- (NH<sub>4</sub>)<sub>2</sub>Ce(NO<sub>3</sub>)<sub>6</sub> 146, 160
- Ni 116
  - matrix 126
- Ni/NiO 162
- NiAl<sub>2</sub>O<sub>4</sub> 122, 143
- Nin carbonyl 562
- Ni(CO)<sub>4</sub> 128, 131
- Ni<sub>2</sub>(CO)<sub>x</sub> 562
- Ni<sub>3</sub>(CO)<sub>x</sub> 562
- Ni(COD)<sub>2</sub> 420
- Ni(cyclooctadiene)<sub>2</sub> 128
- α-Ni(OH)<sub>2</sub> 143
- NiFe<sub>2</sub>O<sub>4</sub> 23, 131, 132, 160
- Ni<sub>2</sub>P 189
- Ni<sub>15</sub>S<sub>15</sub>(PPh<sub>3</sub>)<sub>6</sub> 422
- Ni<sub>3n</sub>Se<sub>3n</sub>(PR<sub>3</sub>)<sub>6</sub> 422
- Ni<sub>20</sub>Se<sub>12</sub>(SeMe)<sub>10</sub>)<sup>2–</sup> 423
- Ni<sub>23</sub>Se<sub>12</sub>(PEt<sub>3</sub>)<sub>13</sub> 420, 421
- Ni<sub>34</sub>Se<sub>22</sub>(PPh<sub>3</sub>)<sub>10</sub> 422, 423
- Ni<sub>20</sub>Te<sub>18</sub>(PEt<sub>3</sub>)<sub>12</sub> 420, 421
- nickel phosphate 603–605
- nickel succinate 613
- nitride 147, 607
- NMR (nuclear magnetic resonance) 2, 25, 109
  - <sup>13</sup>C 665
  - electrochemical (EC-NMR) 664, 665
  - <sup>195</sup>Pt 665, 666
- nose, electronic 537
- NSA (normalized surface area) 139
  - MCM-supported catalyst 139

- NFSOM (near-field scanning optical microscopy) 274
- NTA (nitriolotriacetate) 152
- NT-FET (nanotube field effect transistor) 229, 331
- nucleation 18, 55, 99, 141, 151, 196, 310, 461, 466
- GaAs nanowire 337
  - oxide-assisted, mechanism 314–316, 324
  - silicon nanowire 328
- o**
- $O_{nc}$  sites 564
- OAG (oxide-assisted growth) 309
- octadecyltrihydrosilane 145
- ODA (octadecylamine) 37, 39
- ODT (octadecanethiol) 40, 42, 43
- OEMA (2-octanoylethylmethacrylate) 495
- oleic acid 118
- olympic rings, of  $BaFe_{12}O_{19}$  132
- onset potential 628
- open framework 589
- metal phosphates 595–605
  - stability 590, 591
- optical fiber communication 124
- optoelectronic nanodevice 620
- organic amines 594
- organic capping agent 380, 394
- organic solvent 42
- acetonitrile 19
  - benzene 43
  - chloroform 43
  - carbon tetrachloride 128
  - toluene 43
- organochalcogenolate ligands 419
- oxidation
- field-induced process 711
  - for preparation of isolated nanoparticles 101, 102
  - metallic substrates 709, 710
  - photocatalytic 633
  - semiconducting substrates 710–712
  - SPM based 708
- oxide nanoparticles 23, 94–110
- preparation 98–108
  - prospects 108–110
- oxide surface, size-selected clusters 566–578
- oxomolybdates 452–473
- p**
- PAA (polyacrylic acid) 495
- $P_3N_5$ , synthesis 186–189
- palladium nanoparticles 141
- paramelaconite 146
- particle-in-a-box problem 383
- PbS 14, 20, 23, 201
- PbSe 7, 201
- $PbSnS_3$  173
- $PbTiO_3$  103, 162, 246
- $PbWO_4$  171
- PCS (photon correlation spectroscopy) 161
- Pd 116, 117, 127, 128
- polymer-stabilized 156
- $Pd_{20}$  574
- $Pd_{20-25}$  577
- $Pd_{30}$  574, 577
- $Pd_{561}$  nanocrystal 56, 57, 63, 65, 73, 76
- $Pd_{1415}$  63, 65
- PdC 127
- $Pd(C_4H_4)$  565, 577
- surface complex 564
- $Pd(CO)_2(O_2)$  566
- $Pd(Co_3)(CO)$  566
- $Pd_{561}Ni_n$  64
- $Pd_{561}Ni_{3000}Pd_{1500}$  64
- PdO 146
- $Pd(O_2CCH_3)_2$  116
- PEG-MS (polyethylene glycol monostearate) 117, 146
- periodic solids 387
- permittivity 154
- perovskite 108
- structure 702
- phase-transfer process 31–48
- acid-facilitated 36, 41
  - proposed mechanism 48
- pH-gating 536
- PHI (phillipsite) 592
- phonon frequency 221
- phonon-phonon relaxation 623
- phosphides, synthesis 186–189
- phosphonate, zeolite-like 614
- photocatalyst 621
- reaction, efficiency 633
- photoconversion efficiency 630
- photocurrent 630
- photoemission studies 372, 394–401
- core level photoemission 395–399
- photofusion 624, 625
- photosynthesis 630
- pillared layered structures 612
- pinwheel-like structure 445
- PL (photoluminescence) 171, 172, 310, 347–350, 443, 695
- band edge 274, 406
  - irreversible quenching 536
  - redshift 536
  - room temperature 518

- PL (photoluminescence) (cont.)
    - spectra 407
  - plasma arc-jet 210
  - plasma effects, localized 155
  - plasmon absorption, surface 118
  - plasmon band 52, 285
    - longitudinal 299, 300
    - surface 623, 624
    - transverse 299
    - weak 303
  - plasmon resonance 37
    - surface 36
  - platinum
    - colloids 156
    - nanoparticle 32
  - plug and play approach, in sonochemistry 124
  - PMA (polymethylacrylate) 124
    - FePMA 126
    - CoPMA 126
  - PMMA (polymethylmethacrylate) 128
  - [PMo<sub>12</sub>O<sub>40</sub>]<sup>3-</sup> 463
  - point defects 552
  - polycarbonate membranes 267
  - polymer, nanostructured 476–514
    - coordination polymer 590, 609–612
    - macromolecular structural control 477–480
    - morphology, block copolymer 484–486
    - nanostructure 486–502
    - polymer conformational control 480–484
  - polymer chain, length 478
  - polymerization
    - acetylene 563, 574–578
    - anionic 479
    - atom-transfer radical 479
    - cationic 479
    - controlled radical 480
    - group-transfer 479
    - living 478–480
    - radical-mediated free-radical 479
    - reversible addition-fragmentation-chain transfer 479
  - polyol reaction 156
  - polyoxometalate chemistry 612
  - polysoaps 484
  - polystyrene 126, 127
  - potassium nitrilotriacetate 150
  - potential, screening 387
  - precipitative methods 19, 20
  - precursor 128, 175, 193
    - single-molecule 21, 198
    - volatile organic 121
  - proximal-probe patterning 255
  - PSD (post-source decay) 541
  - pseudo-first order rate constant 557
  - pseudo-first order reaction rate 557
  - pseudopotential
    - empirically determined 386
    - ionic 387
    - semi-empirical 386
  - PSMS (polystyrene microspheres) 123
  - Pt
    - nanoparticles 116, 117
    - nanocrystal 61
    - polymer-stabilized 156
  - Pt(111) 582
  - Pt<sub>n</sub><sup>-</sup> 560
  - [Pt<sub>38</sub>(CO)<sub>44</sub>H<sub>2</sub>]<sup>2-</sup> 56
  - Pt<sub>n</sub>O<sup>-</sup> 560
  - Pt<sub>n</sub>O<sub>2</sub><sup>-</sup> 560, 561
  - pulsed valve, molecular beam experiments 578–580
    - experimental scheme 579
  - purple of Cassius 95
  - PVA (polyvinyl alcohol) 197
  - PVP (polyvinylpyrrolidone) 54, 156, 157
  - pyridine 196
  - pyrolysis 170, 175, 182, 196, 335
    - laser 99
- q**
- Qdot™ 12
  - quantum confinement 52, 86, 383, 438
    - effects 442
  - quantum corral 1, 3
  - quantum dot 1, 9, 12–27, 41, 52, 75, 148, 385, 405
    - applications 17
    - – bar code 415
    - bioconjugation 410–413
    - – applications 413–416
    - core-shell 405
    - fluorescent properties 79
    - groups 170
    - PEG-based 653
    - synthesis 12
  - quantum yield 406, 409, 410
  - quantum-mechanical calculation 359
  - quartz 153
    - α-quartz 590
  - quench emission 632
  - quenching 129
- r**
- Raman microscopy 145
    - diamond 182
  - Raman scattering 310, 347–350

- SERS (surface-enhanced *Raman* scattering) 285, 286, 303
- – potential-depending 669
- RAMO (reactor autoclave micro onde) 160, 161
- rare-earth oxide, nanosized 133, 134
- rate constant 368
- reaction spectra, temperature programmed (TPR) 564, 569, 574, 575
- real space 383
- red-shifted emission 379, 443
- reduction, rate 118
- reduction-carburization 184
- reflector, microwave 153
- relaxation time
  - spin-lattice 665
  - spin-spin 665
- RESS (rapid expansion of supercritical fluid solutions) 118
- reverse micellar method 54, 73, 99
- Rh
  - nanoparticles 116
  - polymer-stabilized 156
- Rhodamine 6G 407
- rhombicosidodecahedron 470
- ring transfer process 48
- robotic arm 716
- Ru, polymer-stabilized 156
- rutile crystallization 162
- S**
  - $S_{10}$  non-bonded polyhedron 435
  - $S_{50}$  polyhedron 435
  - SAED (selected area electron diffraction) 135, 148, 290, 337
  - SALDI-MS (surface-assisted laser-desorption ionization mass spectrometry) 543
  - SAM (self-assembled monolayer) 32, 116, 626, 648, 677
  - saturation magnetization 127, 129, 147
  - SAXS (small angle X-ray scattering) 294
  - SBF (simulated body fluid) 527
  - SbSI 172
  - Schrödinger* equation 384, 386, 387
  - SDS (sodium dodecylsulfate) 117
  - $Se_{132}$  framework 438
  - Se–C bond scission 423
  - SECM (scanning electrochemical microscopy) 648, 650
  - selenide 606
  - selenium source 202
  - self-assembly 256, 453, 483
  - vs. designed chemical linkage 293–299, 305
  - self-association 483
  - self-cleaning glass 622
  - self-organization 128, 202
  - self-similarity 75
  - SEM (scanning electron microscopy) 2
    - AgSe 173
    - $\beta$ -SiC nanowire 261
    - diamond 182
    - GaAs nanowire 338
    - oriented silicon nanowire 329
    - porous silicon 520, 528, 530
  - semiconducting material (*see also* quantum dot) 310, 314
    - one-dimensional 309
  - sensitizer 625, 626
  - SERS (surface-enhanced *Raman* scattering) 285, 286, 303
    - potential-depending 669
  - SFLS (supercritical fluid-liquid-solid) 272
  - shape selective catalysts 593
  - Si nanostructure
    - chain-like 322
    - tadpole-like 322
  - Si/SiO<sub>x</sub> nanocomposite film 124
  - Si<sub>3</sub>N<sub>4</sub>
    - nanowire 260
    - synthesis 186–189
  - Si<sub>10</sub> 361
  - Si<sub>12</sub> 361
  - Si<sub>18</sub> 364
  - Si<sub>20</sub> 364
  - Si<sub>30</sub> 567
  - Si<sub>39</sub> 567
  - Si<sub>45</sub> 364
  - Si<sub>47</sub> 364
  - Si<sub>60</sub> 362
  - Si<sub>123</sub> 362
  - SiC 308, 310
    - $\beta$ SiC 335
  - Si<sub>100</sub>H<sub>20</sub> 367
  - Si<sub>100</sub>H<sub>40</sub> 367
  - Si<sub>100</sub>H<sub>60</sub> 366
  - Si<sub>100</sub>H<sub>86</sub> 366
  - SiO<sub>2</sub> 129
  - signature, spectroscopic 415
  - silent receptor 461
  - silica
    - microsphere 121, 133
    - polymorphs 594
  - silicalite (MFI) 594
  - siliceous ferrierite (FER) 594
  - silicoaluminiumphosphate 595
  - silicon 118
    - flat single-crystal 522

- silicon (cont.)
  - nanocrystallites 520
  - nanostructure, structural transition 360, 361
  - nanowire (*see* nanowire)
  - porous 118, 171, 518–547
  - as a test bed 524
  - bioactive 527–531
  - biodegradable 529, 530
  - calcification 527
  - culture, hepatocytes 531
  - explosive 539, 540
  - hydride passivated 525
  - hydroxyapatite 527, 528
  - photoluminescent 523
  - preparation/characterization 518–522
  - sensors 532–539
  - surface chemistry 522–527
  - wafer 310
- silver nanoparticle 40
  - acid-facilitated phase transfer 41
  - optical properties 44
- SIMS (secondary ion mass spectrometry) 521
- single domain size 96
- single electron device 80
- single electron transistor 9
- size distribution 375, 396
- size effects 3, 6, 10, 13, 79, 98, 309, 310, 330, 441, 551
  - catalytic property 562
  - electronic size effect 573
  - hydrogenated silicon cluster 365
  - quantum size effect 310
- size-confinement studies 407
- size-property relationship 439
- smart dust 534, 535
- SnO 136, 137, 162
- SnO<sub>2</sub> 136, 137, 161
  - nanostructure 340
- SOD (sodalite) 592
- SOFC (solid oxide fuel cells) 143
- soft template 289
- soft-landing 566, 567
- solar cells 80, 631
  - DSSC (dye-sensitized solar cell) 146
- sol-gel method 702–704
- solvothermal synthesis 22, 23, 105–108, 193
  - III–V nanomaterials 175–180
  - nanowire 273
  - non-oxide nanomaterials 170–204
- sonic
  - intensity 151
  - reaction 115
- sonochemistry 32, 113–148
  - coating polymers 123
  - decomposition 129
  - oxidation 130
  - plug and play approach 124
  - sonochemical deposition 121–124
  - sonochemical reduction 117
  - sonochemical synthesis
    - ferrites 131–133
    - hydroxides 143, 144
    - mesoporous material 137–142
    - metallic alloys 120, 121
    - mixed oxide 143
    - nano-metallic oxides 129–131
    - rare-earth oxide 133, 134
    - SnO<sub>2</sub>/SnO 136, 137
    - titania 144, 145
- sonoelectrochemistry 113, 148–152
  - effects of ultrasound 149
  - synthesis 149–152
- sonoelectrode 149, 152
- sonohydrolysis 134–136
- source-template-interface method, in-situ 199
- spectroscopy
  - Auger electron 552
  - C-13 NMR 145
  - EELS (electron energy loss spectroscopy) 330, 337, 521, 553
  - fluorescence 377–383, 625
  - Mössbauer 120, 129–131
  - pump-probe 622
  - STS (scanning tunneling spectroscopy) 310
  - SXA (soft X-ray absorption spectroscopy) 399
  - SXE (soft X-ray emission spectroscopy) 399
  - TDS (thermal desorption) 553
  - transient absorption 626
  - ultraviolet-visible absorption 372, 374–377
  - UV-Vis absorption spectroscopy 401
  - XPS (X-ray photoelectron spectroscopy) 109, 126, 130, 395, 396, 553
- sphalerite 201
- spherical nano-objects 462
- spheroidization mechanism 322, 325
- spin
  - coating 122
  - precession 109
  - spin-orbit coupling 390
- SPM (scanning probe microscopy) 688, 706–712
  - use in dip pen nanolithography 712–716
  - use in nanomanipulation 716–718
  - in oxidation 101–102

- squarate ion 610  
 SrAu<sub>n</sub> 568  
 SSA (specific surface area) 141  
 STA (scanning tip array) 122  
 stabilizing agent 54  
 STALION (lithium ion cell) 136  
 steric protection strategy 499  
 STM (scanning tunneling microscope) 1, 582, 706  
 – quantum corral 3  
 STM/STS measurement 351–355  
*Stober*  
 – method 121  
 – silica microspheres 130  
 STS (scanning tunneling spectroscopy) 310  
 sunscreen, transparent 110  
 supercapacitor 228  
 superclusters 73–75  
 superconductor 171  
 superoxo-like state 574  
 superparamagnetic 109, 121, 132  
 – blocking temperature 85  
 supramolecular chemistry 452–470,  
 – super-supramolecular chemistry 465, 470  
 surface chemistry 103  
 surfactant 54, 118, 201, 287, 477, 484, 507–513  
 – counter-ion polymerizable 510  
 – *Gemini* surfactant 142  
 SWNT (single-walled nanotube) 128, 209, 214–271  
 SXE (soft X-ray emission spectroscopy) 399  
 symmetry breaking 454  
 synchrotron radiation source 398, 399
- t**  
 TB (tight-binding) method 387–394  
 TBP (tri-n-butyl phosphine) 409  
 TDS (thermal desorption spectroscopy) 553  
 TEM (transmission electron microscopy) 2, 36, 39, 43, 45, 76, 100, 115, 118, 119, 130, 132, 161, 172, 300, 315  
 – Ag<sub>2</sub>Se 201  
 – Ag<sub>2</sub>Te 201  
 – AlN 178  
 – B<sub>4</sub>C 191  
 – Bi<sub>2</sub>Se<sub>3</sub> 199  
 – BN nanotube 190  
 – BP 192  
 – bright field 320, 323  
 – carbon nanotube  
 – – multiwall 183, 209  
 – – with catalyst 184  
 – CdIn<sub>2</sub>S<sub>4</sub> 195  
 – CdS 200  
 – – nanocrystal 195  
 – – nanowire 194  
 – CdSe 199  
 – Cu<sub>2–x</sub>Se nanotube 200  
 – DNA-linked gold nanorods 298  
 – GaN nanoparticle 176, 177  
 – Ga<sub>2</sub>O<sub>3</sub> nanowire 263  
 – gold nanorods 296  
 – HR-TEM 140, 161, 172, 183, 184, 202, 289, 290, 311, 319, 328, 337, 338, 339  
 – InP nanocrystals 174  
 – rippling-edge nanoribbon 331  
 – SiC nanowire 185, 258  
 – Si<sub>3</sub>N<sub>4</sub> 187  
 – silicon nanowire 312, 313, 329  
 – silver nitrate solution 344  
 – smooth-edge nanoribbon 331  
 – SnO<sub>2</sub> nanoribbon 340  
 – Sn<sub>4</sub>P<sub>3</sub> 189  
 – SnSe 199  
 – thiol derivatized Au nanoparticle 38  
 – TiB<sub>2</sub> 193  
 – VO<sub>x</sub> nanotube 252  
 – ZnS 376  
 – ZnSe 199  
 temperature effect, on crystal growth 151  
 template 310, 694, 695  
 template-based synthesis 266–271  
 templating effect 128  
 TEOS (tetraethyl orthosilicate) 118, 133  
 ternary  
 – compound semiconductors 198  
 – sulfide 173  
 tetrachalcogenomolybdate 444  
 tetrahedral Si nanocrystal 59  
 tetralin 22  
 ThC<sub>2</sub> 148  
 thermal evaporation (or HFCVD) 335, 365  
 thermogravimetric measurement 120, 130  
 thermolysis 102, 103, 106–108  
 THF 116  
 thiourea 102, 173, 202  
 Tin(II) phosphate 599, 600  
 TiO<sub>2</sub> 103, 158, 248, 631  
 TiO<sub>2</sub>/Au nanoparticles 633  
 Tl<sub>2</sub>O 135  
 Tl<sub>2</sub>O<sub>3</sub>–CaO–BaCu<sub>3</sub>O<sub>4</sub> 171  
 TlCl<sub>3</sub> 134, 135  
 titanate 162  
 titanium phosphate 605  
 titanosilicate 594  
 TMV (tobacco mosaic virus) 453  
 TNT (trinitrotoluene) 536

- todorokite 608  
 toluene 43  
 TOP (tri-n-octylphosphine) 20, 65, 409  
 TOPO (tri-n-octylphosphine oxide) 19–21, 104, 409, 411, 676  
 TOPS (tri-n-octylphosphine selenide) 20  
 total analysis system ( $\mu$ TAS) 531, 532  
 TPR (temperature programmed reaction spectra) 564, 569, 574, 575  
 –  $C_4H_6$  575  
 –  $C_4H_8$  575  
 –  $C_6H_6$  575  
 track etch ratio 692  
 track formation, latent 691  
 transformation, photoinduced 622–626  
 translational invariance 383  
 trapped emission 444  
 tribological properties 254  
 tris- $\mu$ -(dibenzylideneacetone)dipalladium 128  
 Triton X-100 106, 245, 267  
 tunneling 385  
 turn-on field 350  
 turn-over frequency, catalytic reaction 578–581  
 tweezers, optical 6, 689
- u**  
 Ullmann synthesis 585  
 ULM-n 597  
 ultrasound 117  
 – radiation 113, 114, 124  
 – application 113  
 urea 159, 462  
 UV-Vis  
 – absorption spectroscopy 401  
 – spectra 43, 45, 46, 300, 376  
 –  $Zn_{1-x}Mn_xS$  377
- v**  
 V centers 552  
 V(OH)(1,4-benzenedicarboxylate) 612  
 valence band (TVB) 371, 372, 378, 400, 406, 621  
 – photoemission 399, 400  
 van der Waals interaction 70  
 vanadium  
 – phosphate 600, 601  
 – silicate 594  
 vesicle 469  
 – bilayer 501  
 – ghost 510  
 – onion type, solid 501  
 – parachute-like 512  
 – templating 510
- vinylpyrrolidine 118  
 viologen 629, 669  
 virtual library, of building blocks 453  
 virus-ZnS nanocrystal hybrid material 61  
 VLS (vapor-liquid-solid) 308, 309, 319  
 – growth 311  
 – metal catalyzed 337  
 VLSE (vapor-liquid-solid epitaxy) 273  
 voltammogram, cyclic 652, 655  
 $VO_x$  nanotube 252, 253  
 VS (vapor-solid) process 322
- w**  
 W(CO) $_6$  146  
 wafer, Si 343  
 water 470–472  
 – autogenous pressure 170  
 – snapshot of liquid water 470  
 water pool 54  
 whiskers 259, 266  
 – nanowhiskers 272  
 – Si 321  
 – ZnO 308, 309, 336, 365  
 $WO_3$  nanoparticle 627  
 $WS_2$  nanotube 243  
 Wurtz-type reaction 181
- x**  
 XANES (X-ray absorption near-edge structure) 99, 126  
 Xenopus embryo, QD labeling 414  
 XPS (X-ray photoelectron spectroscopy) 109, 126, 130, 395, 396, 553
- y**  
 YSZ (Yttrium stabilized zirconia) 133, 138  
 yttrium oxide 102
- z**  
 Z-plots 662  
 zeolite 105, 217, 509  
 – A, synthetic sodium 592  
 – aluminosilicate 589, 591–595  
 – applications 593  
 – CHA (chabazite) 592  
 – FAU (faujasite) 592  
 – shape selective catalysts 593  
 – Si/Al ratio 593  
 – SOD (sodalite) 592  
 – UTD-1 592  
 – X 592  
 – Y 24  
 – ZSM-5 593, 594  
 “zipping” type mechanism 293



- zirconate 162
- zirconia 153, 161
- zirconium phosphate 605
- $\text{ZnFe}_2\text{O}_4$  23, 160
- $\text{ZnGa}_2\text{O}_4$  105
- $\text{ZnO}$  54, 101, 110, 146, 147, 244, 257, 260, 267, 273, 274, 308, 309, 336, 365, 381, 628, 630, 634
- $\text{Zn}_3\text{P}_2$  20
- $\text{ZnS}$  14, 19, 20, 24
  - Eu-doped 382
  - Mn-doped 380, 381
  - monodispersed 172
  - nanowire 201
- $\text{ZnSe}$  20, 22, 24, 196, 378
- $\text{ZrC}$ , nanocrystalline 185
- $\text{ZrO}_2$  106, 158, 161
- ZSM-5 593, 594